supporting partners

47th International Congress on Science Technology and Technology-based Innovation

"Sciences for SDGs: Challenges and Solutions"

STT47
Oct 5-7, 2021

~PROCEEDING BOOK~

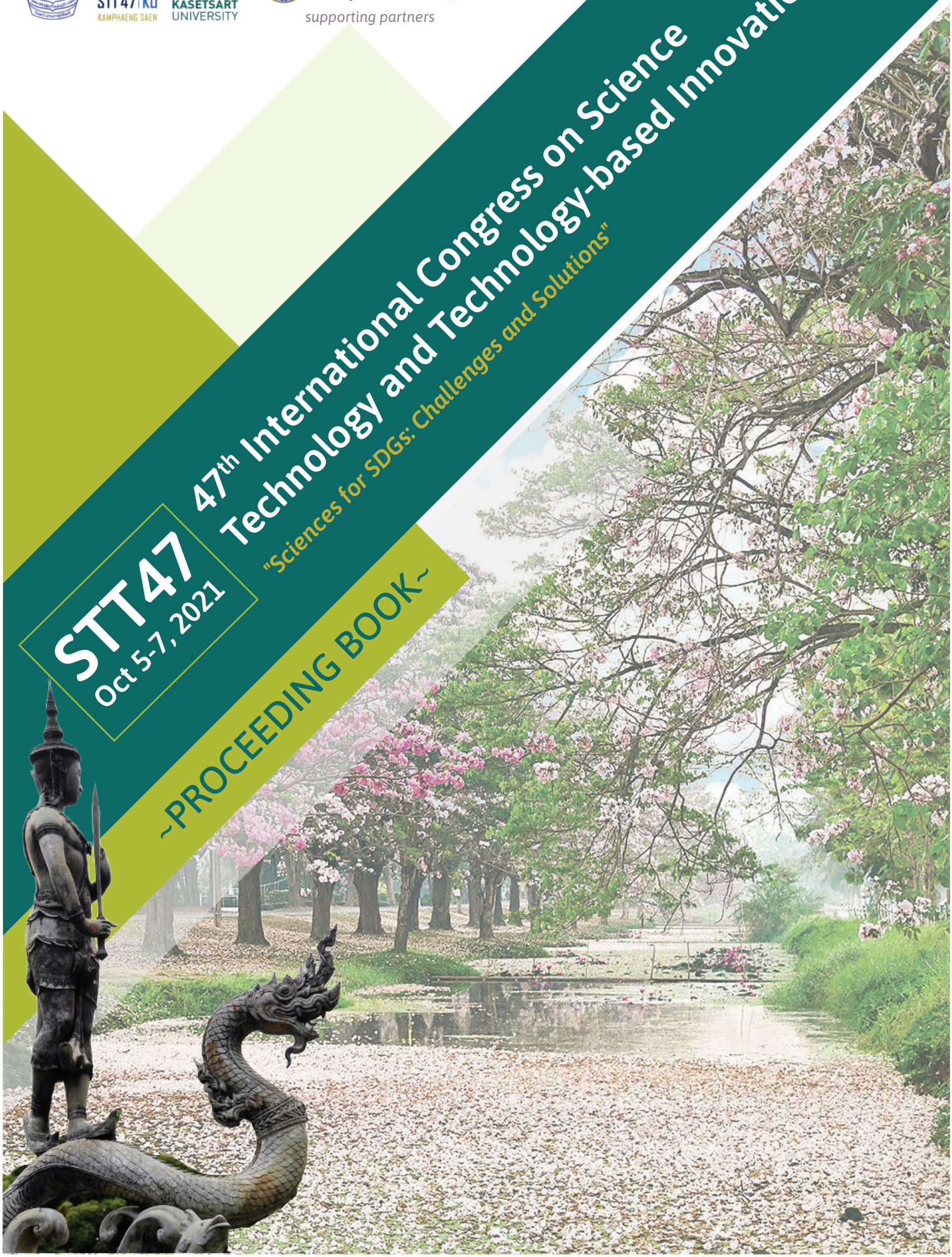

ทรงพระเจริญ

PROGRAM BOOK

The 47th International Congress on Science, Technology and Technology-based Innovation (STT47)

SCIENCES FOR SDGS:
CHALLENGES AND SOLUTIONS

October 5th-7th, 2021
Kasetsart University, Kamphaeng Saen Campus,
Nakhon Pathom, Thailand
Virtual Conference

Organized by:
The Science Society of Thailand under the Patronage of His Majesty the King
in Association with
Faculty of Liberal Arts and Science,
Kasetsart University, Kamphaeng Saen Campus

CONTENT

WELCOME MESSAGE FROM THE PRESIDENT OF THE SCIENCE SOCIETY OF THAILAND UNDER THE PATRONAGE OF HIS MAJESTY THE KING

On behalf of the Science Society of Thailand under the Patronage of His Majesty the King, I am delighted to invite you to the 47th International Congress on Science, Technology and Technology-based Innovation, or STT47, which will be held during October 5-7, 2021 in Nakon Pathom, Thailand. This event is our annual congress, jointly organized by Faculty of Art and Science, Kasetsart University, Kamphangsaen Campus.

United Nations has recognized the importance of basic sciences and proclaimed 2022 as the International Year of Basic Sciences for Sustainable Development (IYBSSD). The theme of STT47, "Sciences for SDGs: Challenges and Solutions" , is thus timely and vitally important for a better future of humankinds and nature. I believe this congress will provide all not only to network regionally and worldwide, but also will lead to a unique opportunity to join forces among scientists in Asia and the world for realizing the role of science in solving global challenges and finding solutions that are sustainable and beneficial to all life on earth.

In addition, the Young Rising Stars of Science award program of the society, firstly launched last year, will continue to attract young talents to attend the STT47 and meet with you all. These students will be our hope to work together and further on to create a better world for everyone. You can help shape them as well as the STT47 through submissions of your research abstracts and presentations at the congress.

I cordially invite you all to join us for the three intensive and interesting days of discussing contemporary scientific and science-related research.

Thank you.

Professor Dr. Supawan Tantayanon

President, the Science Society of Thailand Under the Patronage of His Majesty the King

WELCOME MESSAGE FROM THE CHAIRPERSON OF THE 47TH INTERNATIONAL CONGRESS ON SCIENCE, TECHNOLOGY AND TECHNOLOGY–BASED INNOVATION

The Science Society of Thailand under the Patronage of His Majesty the King is pleased to invite you to join the 47th International Congress on Science, Technology and Technology-based Innovation (STT47), which will be held at Kasetsart University, Kamphaeng Sean, Nakhon Pathom – Virtual Conference, Thailand, during October 5-7, 2021. The opening ceremony will be graciously presided over by Her Royal Highness Princess Maha Chakri Sirindhorn on 5th October, at 9 am.

International Congress on Science, Technology and Technology-based Innovation (STT) is one of the largest annual international scientific meeting with around one thousand local and oversea participants. The aim is to create scientific forum for national and international scientists and technologists as well as young Thai scientists from diversified fields of science and technology and to open an opportunity to share and exchange their experiences. In this year, there are 5 main sessions including

- Innovation Impacts Driven SDGS
- Mathematics, Statistical science and Computer science “Math Stat Comp For SDGS: Sustainable Solutions”
- Physics “Physics for Life in Space”
- Chemical Sciences “SDG Challenges: Chemical Solutions for Sustainable Society”
- Biological Sciences “Impact of Biological Science Towards SDGS: Active Learning for Biological Science Classes” and “Impact of Biological Science Towards SDGS: Biological Sciences Towards SDGS”

There are also approximately 20 symposiums such as Sustainable Hydrogen Production for Greener Environment and Chemical Products; Metal-Organic Composites in Material Science; Sustainable Use of Marine Biodiversity; Premium Agriculture: A Pathway Toward Sustainable and Inclusive BCG Economy Model; Acceleration of Sustainability towards Biobased Technological Platform Development; included in this event.

The Congress is highlighted by the Plenary Lecture from the world reputable scientist and the Honorable Lecture from the 2021 Outstanding Scientist(s) of Thailand. And during the Congress, lectures from several renowned invited speakers, and hundreds of contributed papers from various areas of Science and Technology will be presented orally (onsite or virtual) or in the form of posters. The Congress also includes high school competition of science projects to select the Best of the Best Projects of the year. Exhibition on advanced scientific and technological knowledge or instruments/appliances from various organizations and several suppliers will be displayed.

Looking forward to welcoming you in this STT47 Congress in October 5-7, 2021.

Professor Dr. Somkiat Ngamprasertsith

Chairperson STT47

WELCOME MESSAGE FROM THE HOST OF THE 47TH INTERNATIONAL CONGRESS ON SCIENCE, TECHNOLOGY AND TECHNOLOGY–BASED INNOVATION

It is our pleasure and honour to welcome you to Kasetsart University, Kamphaeng Saen Campus on behalf of the Faculty of Liberal Arts and Science to the 47th International Congress on Science, Technology and Technology–based Innovation (STT47).

The congress will give us opportunities to exchange the present and the future knowledge and experiences among national and international expertise scientists and technologists, as well as, the young scientists in various fields of Science, Technology and Technology–based Innovation.

The knowledge of science, technology and technology–based innovation have inspired many. They have become one of the crucial key factors for the world evolution. For all these years, a number of outstanding scientists, and numerous eminent scientists have contributed considerably to the world by presenting and sharing their latest research in this continual engraved congress.

We are grateful to our sponsors, advisory boards, invited speakers, reviewers, authors, and all participants, who have supported our initiative and have assisted in its organisation.

I take this opportunity to thank each and every one of you personally. I hope the congress would shed more light on our world of science, technology and technology–based innovation.

Assistant Professor Dr. Anamai Damnet

Dean of Faculty of Liberal Arts and Science,
Kasetsart University, Kamphaeng Saen Campus

HISTORY OF THE CONGRESS ON SCIENCE AND TECHNOLOGY OF THAILAND

International Congress on Science, Technology and Technology-based Innovation (STT), originally named "The Congress on Science and Technology of Thailand" with the same abbreviation of STT, is one of the most important scientific meetings in Thailand. It was firstly organized in 1974 by the Science Society of Thailand (SST) and Chulalongkorn University. Since then, the alternative Universities in Thailand have gone through the bidding for co-organizing the STT in the following years. It is the annual national congress for 45 years. To mark the 72nd Anniversary of the Science Society of Thailand in 2020, the congress has been changed to the international meeting.

The aim is to create scientific forum for national and international scientists and technologists as well as young Thai scientists from diversified fields of science and technology to meet and to provide them the opportunity to share and exchange their knowledge and experiences. It is our annual congress, which originally was the national meeting since 1971, but this year, it is its first time to be held as the international meeting.

Typically, the Congress Plenary Lecture is given by a Nobel Laureate in Science and Technology, followed by an honorable lecture of the Outstanding Scientist of Thailand in that particular year. During the Congress, lectures by several renowned invited speakers, panel discussions and hundreds of contributed papers from various areas of Science and Technology are presented orally or in the form of posters. In addition, the outstanding teacher awards, the young scientist awards, as well as the innovation awards and the national winners of high school student science projects are awarded in the Congress. An exhibition of advanced scientific and technological instruments and appliances from suppliers and enterprises are also the attractive event of the Congress.

ครั้งที่ ปี / วันที่ เดือน	ชื่อการประชุม	สถาบันเจ้าภาพร่วม	ประธาน (จำนวนผลงานวิจัย)	ประธานในพิธีเปิด
1. พ.ศ. 2514 26-27 พฤศจิกายน	การวิจัยทางวิทยาศาสตร์ กรุงเทพฯ 2514	คณะวิทยาศาสตร์ จุฬาลงกรณ์มหาวิทยาลัย	ศ.ดร.ประชุมสุข อาชวอำรุง (83 เรื่อง)	-
2. พ.ศ. 2516 30 พฤศจิกายน - 2 ธันวาคม	การวิจัยทางวิทยาศาสตร์ กรุงเทพฯ 2516	คณะวิทยาศาสตร์ จุฬาลงกรณ์มหาวิทยาลัย	ศ.ดร.ประชุมสุข อาชวอำรุง (219 เรื่อง)	-
3. พ.ศ. 2518 12-13 ธันวาคม	การวิจัยทางวิทยาศาสตร์ กรุงเทพฯ 2518	คณะวิทยาศาสตร์ คณะแพทยศาสตร์ มหาวิทยาลัยมหิดล	ศ.ดร.กำจร มนูญปิจุ (249 เรื่อง)	-
4. พ.ศ. 2520 16-17 ธันวาคม	การวิจัยทางวิทยาศาสตร์ กรุงเทพฯ 2520	คณะวิทยาศาสตร์ จุฬาลงกรณ์มหาวิทยาลัย	รศ.ดร.กำจัด มงคลกุล (344 เรื่อง)	-
5. พ.ศ. 2521 22-24 ธันวาคม	วิทยาศาสตร์และเทคโนโลยี เพื่อการพัฒนาภาคเหนือ	คณะวิทยาศาสตร์ มหาวิทยาลัยเชียงใหม่	ศ.ดร.พรชัย มาตังคสมบัติ (232 เรื่อง)	-
6. พ.ศ. 2522 21-23 ธันวาคม	วิทยาศาสตร์และเทคโนโลยี เพื่อการพัฒนาประเทศ	คณะวิทยาศาสตร์ มหาวิทยาลัยศรีนครินทรวิโรฒ บางแสน	ศ.ดร.พรชัย มาตังคสมบัติ (232 เรื่อง)	-
7. พ.ศ. 2523 4-6 ธันวาคม	วิทยาศาสตร์และเทคโนโลยี เพื่อการพัฒนาประเทศ	คณะวิทยาศาสตร์ คณะแพทยศาสตร์ มหาวิทยาลัยมหิดล	รศ.ดร.นัยพินิจ คชภักดี (233 เรื่อง)	สมเด็จพระเจ้าลูกเธอเจ้าฟ้าจุฬาภรณวลัยลักษณ์
8. พ.ศ. 2525 28-30 ตุลาคม	วิทยาศาสตร์และเทคโนโลยี เพื่อการพัฒนาประเทศ	คณะวิทยาศาสตร์ จุฬาลงกรณ์มหาวิทยาลัย	รศ.ดร.สัณห์ พณิชยกุล (245 เรื่อง)	-

ครั้งที่ ปี / วันที่ เดือน	ชื่อการประชุม	สถาบันเจ้าภาพร่วม	ประธาน (จำนวนผลงานวิจัย)	ประธานในพิธีเปิด
9. พ.ศ. 2526 27-29 ตุลาคม	วิทยาศาสตร์และเทคโนโลยีเพื่อการพัฒนาภาคตะวันออกเฉียงเหนือ	คณะวิทยาศาสตร์ มหาวิทยาลัยขอนแก่น	รศ.ดร.สัณห์ พณิชยกุล (174 เรื่อง)	รัฐมนตรีว่าการกระทรวงวิทยาศาสตร์เทคโนโลยีและการพลังงาน (ฯพณฯ ดำรง ลัทธพิพัฒน์)
10. พ.ศ. 2527 25-27 ตุลาคม	วิทยาศาสตร์และเทคโนโลยีแห่งประเทศไทย	คณะวิทยาศาสตร์ มหาวิทยาลัยเชียงใหม่	ศ.ดร.มนตรี จุฬาวัฒนทล (280 เรื่อง)	นายกรัฐมนตรี (พลเอก เปรม ติณสูลานนท์)
11. พ.ศ. 2528 24-26 ตุลาคม	วิทยาศาสตร์และเทคโนโลยีแห่งประเทศไทย	คณะวิทยาศาสตร์ มหาวิทยาลัยเกษตรศาสตร์	ศ.ดร.มนตรี จุฬาวัฒนทล (251 เรื่อง)	สมเด็จพระเจ้าลูกเธอเจ้าฟ้าจุฬาภรณวลัยลักษณ์
12. พ.ศ. 2529 20-22 ตุลาคม	วิทยาศาสตร์และเทคโนโลยีแห่งประเทศไทย	คณะวิทยาศาสตร์ มหาวิทยาลัยศรีนครินทรวิโรฒ ประสานมิตร	รศ.ดร.ภิญโญ พานิชพันธ์ (277 เรื่อง)	สมเด็จพระบรมโอรสาธิราชฯ สยามมกุฎราชกุมาร
13. พ.ศ. 2530 20-22 ตุลาคม	วิทยาศาสตร์และเทคโนโลยีแห่งประเทศไทย	คณะวิทยาศาสตร์ มหาวิทยาลัยสงขลานครินทร์ วิทยาเขตหาดใหญ่	รศ.ดร.ภิญโญ พานิชพันธ์ (420 เรื่อง)	สมเด็จพระเจ้าลูกเธอเจ้าฟ้าจุฬาภรณวลัยลักษณ์
14. พ.ศ. 2531 19-21 ตุลาคม	วิทยาศาสตร์และเทคโนโลยีแห่งประเทศไทย	คณะวิทยาศาสตร์ จุฬาลงกรณ์มหาวิทยาลัย	ศ.ดร.จริยา บรอดเคลแมน (259 เรื่อง)	นายกรัฐมนตรี (พลเอกชาติชาย ชุณหะวัณ)
15. พ.ศ. 2532 18-20 ตุลาคม	วิทยาศาสตร์และเทคโนโลยี เพื่อการพัฒนาทรัพยากรภาคเหนือ	คณะวิทยาศาสตร์ มหาวิทยาลัยเชียงใหม่	ศ.ดร.จริยา บรอดเคลแมน (394 เรื่อง)	ผู้แทนสมเด็จพระเจ้าลูกเธอเจ้าฟ้าจุฬาภรณวลัยลักษณ์
16. พ.ศ. 2533 25-27 ตุลาคม	วิทยาศาสตร์และเทคโนโลยีเพื่อการพัฒนาประเทศ	คณะวิทยาศาสตร์ สถาบันเทคโนโลยีพระจอมเกล้า เจ้าคุณทหารลาดกระบัง	ศ.ดร.วิชัย ริ้วตระกูล (369 เรื่อง)	-
17. พ.ศ. 2534 24-26 ตุลาคม	วิทยาศาสตร์และเทคโนโลยีเพื่อการพัฒนาทรัพยากรภาคเหนือ	คณะวิทยาศาสตร์ มหาวิทยาลัยขอนแก่น	ศ.ดร.วิชัย ริ้วตระกูล (349 เรื่อง)	-
18. พ.ศ. 2535 27-29 ตุลาคม	วิทยาศาสตร์และเทคโนโลยีเพื่อการพัฒนาประเทศ	คณะวิทยาศาสตร์ มหาวิทยาลัยเกษตรศาสตร์ ณ ศูนย์การประชุมแห่งชาติสิริกิติ์	ศ.ดร.สุชาติ อุปถัมภ์ (297 เรื่อง)	-
19. พ.ศ. 2536 27-29 ตุลาคม	วิทยาศาสตร์และเทคโนโลยีเพื่อการพัฒนาชายฝั่ง	คณะวิทยาศาสตร์ มหาวิทยาลัยสงขลานครินทร์ ณ โรงแรมดุสิต เจ.บี.หาดใหญ่	ศ.ดร.สุชาติ อุปถัมภ์ (438 เรื่อง)	-
20. พ.ศ. 2537 19-21 ตุลาคม	วิทยาศาสตร์และเทคโนโลยี เพื่อการพัฒนาเศรษฐกิจ สังคม และสิ่งแวดล้อม	คณะวิทยาศาสตร์และเทคโนโลยี มหาวิทยาลัยธรรมศาสตร์ ณ เซ็นทรัลพลาซ่า	ศ.ดร.สมศักดิ์ พันธุวัฒนา (252 เรื่อง)	นายกรัฐมนตรี (นายชวน หลีกภัย)
21. พ.ศ. 2538 25-27 ตุลาคม	วิทยาศาสตร์และเทคโนโลยีเพื่อการพัฒนาอุตสาหกรรม	คณะวิทยาศาสตร์ มหาวิทยาลัยบูรพา ณ โรงแรมแอมบาสซาเอร์ชิตี้ จอมเทียน ชลบุรี	ศ.ดร.สมศักดิ์ พันธุวัฒนา (354 เรื่อง)	นายกสภามหาวิทยาลัยบูรพา (นายเกษม จาติกวณิช)
22. พ.ศ. 2539 16-18 ตุลาคม	วิทยาศาสตร์และเทคโนโลยีเพื่อพัฒนาทรัพยากรมนุษย์	คณะวิทยาศาสตร์ มหาวิทยาลัยรามคำแหง ณ บางกอกคอนเวนชั่นเซ็นเตอร์ เซ็นทรัลพลาซา ลาดพร้าว	รศ.ดร.พิณทิพ รื่นวงษา (333 เรื่อง)	ผู้ว่าราชการกรุงเทพมหานคร (ดร.พิจิตต รัตตกุล)
23. พ.ศ. 2540 20-22 ตุลาคม	วิทยาศาสตร์และเทคโนโลยีเพื่อพัฒนาคุณภาพชีวิตในภูมิภาค	คณะวิทยาศาสตร์ มหาวิทยาลัยเชียงใหม่ ณ โรงแรมโลตัส ปางสวนแก้ว	รศ.ดร.พิณทิพ รื่นวงษา (495 เรื่อง)	รัฐมนตรีว่าการกระทรวงวิทยาศาสตร์เทคโนโลยีและสิ่งแวดล้อม (นายยิ่งพันธ์ มนะสิการ)
24. พ.ศ. 2541 19-21 ตุลาคม	วิทยาศาสตร์และเทคโนโลยีเพื่อการพัฒนาเศรษฐกิจที่มั่นคง	คณะวิทยาศาสตร์ มหาวิทยาลัยมหิดล ณ ศูนย์การประชุมแห่งชาติสิริกิติ์	ผศ.ดร.ทิพาพร ลิมปเสนีย์ (463 เรื่อง)	นายกรัฐมนตรี (นายชวน หลีกภัย)
25. พ.ศ. 2542 20-22 ตุลาคม	วิทยาศาสตร์และเทคโนโลยี เพื่อการพัฒนาทรัพยากรท้องถิ่น	คณะวิทยาศาสตร์ มหาวิทยาลัยนเรศวร ณ โรงแรมอมรินทร์ลากูน พิษณุโลก	ผศ.ดร.ทิพาพร ลิมปเสนีย์ (581 เรื่อง)	รัฐมนตรีว่าการกระทรวงวิทยาศาสตร์เทคโนโลยีและสิ่งแวดล้อม (ดร.อาทิตย์ อุไรรัตน์)
26. พ.ศ. 2543 18-20 ตุลาคม	วิทยาศาสตร์และเทคโนโลยีสู่สหัสวรรษใหม่	คณะวิทยาศาสตร์ จุฬาลงกรณ์มหาวิทยาลัย ณ ศูนย์การประชุมแห่งชาติสิริกิติ์	รศ.ดร.ศุภวรรณ ตันตยานนท์ (739 เรื่อง)	-
27. พ.ศ. 2544 16-18 ตุลาคม	วิทยาศาสตร์และเทคโนโลยีเพื่อการฟื้นฟูเศรษฐกิจไทย	มหาวิทยาลัยสงขลานครินทร์ โรงแรม ลี การ์เดนส์ พลาซ่า	รศ.ดร.ศุภวรรณ ตันตยานนท์ (921 เรื่อง)	ผู้ว่าราชการจังหวัดสงขลา
28. พ.ศ. 2545 24-26 ตุลาคม	วิทยาศาสตร์และเทคโนโลยีเพื่อการพัฒนาเศรษฐกิจที่ยั่งยืน	คณะวิทยาศาสตร์ประยุกต์ สถาบันเทคโนโลยีพระจอมเกล้าพระนครเหนือ ณ ศูนย์การประชุมแห่งชาติสิริกิติ์	รศ.ดร.สุรินทร์ เหล่าสุขสถิตย์ (834 เรื่อง)	สมเด็จพระเจ้าพี่นางเธอเจ้าฟ้ากัลยาณิวัฒนา กรมหลวงนราธิวาสราชนครินทร์

ครั้งที่ ปี / วันที่ เดือน	ชื่อการประชุม	สถาบันเจ้าภาพร่วม	ประธาน (จำนวนผลงานวิจัย)	ประธานในพิธีเปิด
29. พ.ศ. 2546 20-22 ตุลาคม	วิทยาศาสตร์และเทคโนโลยีเพื่อการพัฒนาท้องถิ่น	คณะวิทยาศาสตร์ มหาวิทยาลัยขอนแก่น ณ ศูนย์ประชุมอเนกประสงค์กาญจนาภิเษก	รศ.ดร.สุรินทร์ เหล่าสุขสถิตย์ (1039 เรื่อง)	รองนายกรัฐมนตรี (นายสุวิทย์ คุณกิตติ)
30. พ.ศ. 2547 19-21 ตุลาคม	วิทยาศาสตร์และเทคโนโลยีเพื่อสังคมและเศรษฐกิจฐานความรู้	คณะวิทยาศาสตร์ มหาวิทยาลัยศรีนครินทรวิโรฒ ณ ศูนย์แสดงสินค้าและการประชุมอิมแพ็ค เมืองทองธานี	รศ.ดร.สุรินทร์ เหล่าสุขสถิตย์ (854 เรื่อง)	สมเด็จพระเทพรัตนราชสุดา ฯ สยามบรมราชกุมารี
31. พ.ศ. 2548 18-20 ตุลาคม	วิทยาศาสตร์และเทคโนโลยีเพื่อการพัฒนาที่ยั่งยืน	เทคโนธานี มหาวิทยาลัยเทคโนโลยีสุรนารี	รศ.ดร.สุรินทร์ เหล่าสุขสถิตย์ (1021 เรื่อง)	สมเด็จพระเทพรัตนราชสุดา ฯ สยามบรมราชกุมารี
32. พ.ศ. 2549 10-12 ตุลาคม	วิทยาศาสตร์และเทคโนโลยีเพื่อการเศรษฐกิจพอเพียง เฉลิมฉลองการครองสิริราชสมบัติ ครบ 60 ปี ของพระบาทสมเด็จพระเจ้าอยู่หัว	คณะวิทยาศาสตร์ จุฬาลงกรณ์มหาวิทยาลัย ศูนย์การประชุมแห่งชาติสิริกิติ์	รศ.ดร.นภาวรรณ นพรัตนราภรณ์ (927 เรื่อง)	สมเด็จพระเทพรัตนราชสุดา ฯ สยามบรมราชกุมารี
33. พ.ศ. 2550 18-20 ตุลาคม	วิทยาศาสตร์และเทคโนโลยีเพื่อโลกยั่งยืน เฉลิมฉลองมหามงคลเฉลิมพระชนมพรรษาครบ 80 พรรษาของพระบาทสมเด็จพระเจ้าอยู่หัว	มหาวิทยาลัยวลัยลักษณ์ จังหวัดนครศรีธรรมราช	รศ.ดร.นภาวรรณ นพรัตนราภรณ์ (802 เรื่อง)	สมเด็จพระเทพรัตนราชสุดา ฯ สยามบรมราชกุมารี
34. พ.ศ. 2551 31 ตุลาคม - 2 พฤศจิกายน	วิทยาศาสตร์และเทคโนโลยีสำหรับโลกแห่งความท้าทาย	คณะวิทยาศาสตร์ สถาบันเทคโนโลยีพระจอมเกล้าเจ้าคุณทหารลาดกระบัง	รศ.ดร.นภาวรรณ นพรัตนราภรณ์ (777 เรื่อง)	สมเด็จพระเทพรัตนราชสุดา ฯ สยามบรมราชกุมารี
35. พ.ศ. 2552 15-17 ตุลาคม	วิทยาศาสตร์และเทคโนโลยีเพื่ออนาคตที่ดีขึ้น	คณะวิทยาศาสตร์ มหาวิทยาลัยบูรพา	รศ.ดร.นภาวรรณ นพรัตนราภรณ์ (854 เรื่อง)	ฯพณฯ องคมนตรี นายอำพล เสนาณรงค์
36. พ.ศ. 2553 26-28 ตุลาคม	วิทยาศาสตร์และเทคโนโลยีเพื่อสังคมที่ดีขึ้น	คณะวิทยาศาสตร์และเทคโนโลยี มหาวิทยาลัยธรรมศาสตร์	รศ.ดร.ธารารัตน์ ศุภศิริ (582 เรื่อง)	สมเด็จพระเทพรัตนราชสุดา ฯ สยามบรมราชกุมารี
37. พ.ศ. 2554 10-12 ตุลาคม	วิทยาศาสตร์สร้างสรรค์ เพื่อสรรค์สร้างอนาคต	คณะวิทยาศาสตร์ มหาวิทยาลัยมหิดล	รศ.ดร.ธารารัตน์ ศุภศิริ (699 เรื่อง)	สมเด็จพระเทพรัตนราชสุดา ฯ สยามบรมราชกุมารี
38. พ.ศ. 2555 17-19 ตุลาคม	วิทยาศาสตร์เพื่ออนาคตของมวลมนุษยชาติ	คณะวิทยาศาสตร์ มหาวิทยาลัยเชียงใหม่	รศ.ดร.ธารารัตน์ ศุภศิริ (690 เรื่อง)	สมเด็จพระเทพรัตนราชสุดา ฯ สยามบรมราชกุมารี
39. พ.ศ. 2556 21-23 ตุลาคม	นวัตกรรมวิทยาศาสตร์ เพื่อชีวิตที่ดีขึ้น	คณะวิทยาศาสตร์ มหาวิทยาลัยเทคโนโลยีพระจอมเกล้าธนบุรี	รศ.ดร.ธารารัตน์ ศุภศิริ (495 เรื่อง)	สมเด็จพระเทพรัตนราชสุดา ฯ สยามบรมราชกุมารี
40. พ.ศ. 2557 2-4 ธันวาคม	วิทยาศาสตร์และเทคโนโลยีสู่วิถีพัฒนาอาเซียน	คณะวิทยาศาสตร์ มหาวิทยาลัยขอนแก่น	ศ.ดร. เปี่ยมสุข พงษ์สวัสดิ์ (543 เรื่อง)	สมเด็จพระเทพรัตนราชสุดา ฯ สยามบรมราชกุมารี
41. พ.ศ. 2558 6-8 พฤศจิกายน	ประตูสู่อาเซียนด้วยวิทยาศาสตร์และเทคโนโลยี	มหาวิทยาลัยเทคโนโลยีสุรนารี	ศ.ดร. เปี่ยมสุข พงษ์สวัสดิ์ (384 เรื่อง)	สมเด็จพระเทพรัตนราชสุดา ฯ สยามบรมราชกุมารี
42. พ.ศ. 2559 30 พฤศจิกายน – 2 ธันวาคม	ศาสตร์แห่งแผ่นดิน สู่นวัตกรรมเพื่ออนาคตที่ยั่งยืน	คณะวิทยาศาสตร์ มหาวิทยาลัยเกษตรศาสตร์ ณ เซ็นทาราแกรนด์ แอท เซ็นทรัลพลาซา ลาดพร้าว	ศ.ดร. เปี่ยมสุข พงษ์สวัสดิ์ (290 เรื่อง)	สมเด็จพระเทพรัตนราชสุดา ฯ สยามบรมราชกุมารี
43. พ.ศ. 2560 17-19 ตุลาคม	เข้าใจวิทยาศาสตร์ เข้าถึงเทคโนโลยี สร้างนวัตกรรม นำสังคมยั่งยืน	คณะวิทยาศาสตร์ จุฬาลงกรณ์มหาวิทยาลัย ณ อาคารจามจุรี 10 จุฬาลงกรณ์มหาวิทยาลัย	ศ.ดร. เปี่ยมสุข พงษ์สวัสดิ์ (327 เรื่อง)	สมเด็จพระเทพรัตนราชสุดา ฯ สยามบรมราชกุมารี
44. พ.ศ. 2561 29-31 ตุลาคม	วิทยาศาสตร์ และเทคโนโลยีในยุคพลิกผัน	สมาคมวิทยาศาสตร์แห่งประเทศไทยในพระบรมราชูปถัมภ์ ณ ศูนย์นิทรรศการและการประชุมไบเทค	รศ.ดร.สายวรุพ ชัยวานิชศิริ (270 เรื่อง)	สมเด็จพระเทพรัตนราชสุดา ฯ สยามบรมราชกุมารี
45. พ.ศ. 2562 7-9 ตุลาคม	ต้นกล้านวัตกรรมสู่การพัฒนาที่ยั่งยืน	สำนักวิชาวิทยาศาสตร์ มหาวิทยาลัยแม่ฟ้าหลวง	รศ.ดร.สายวรุพ ชัยวานิชศิริ (338 เรื่อง)	สมเด็จพระกนิษฐาธิราชเจ้า กรมสมเด็จพระเทพรัตนราชสุดา ฯ สยามบรมราชกุมารี
46. พ.ศ. 2563 5-7 ตุลาคม	Power of Science to Achieve SDGs	คณะวิทยาศาสตร์ มหาวิทยาลัยรามคำแหง	ศ.ดร.สมเกียรติ งามประเสริฐสิทธิ์ (426 เรื่อง)	สมเด็จพระกนิษฐาธิราชเจ้า กรมสมเด็จพระเทพรัตนราชสุดา ฯ สยามบรมราชกุมารี

PROGRAM OVERVIEW

Code	Session/Symposium	October 5, 2021				October 6, 2021				October 7, 2021			
		AM		PM		AM		PM		AM		PM	
		Time: 8:00-11:00											
	Grand Opening Ceremony (Facebook Live / Youtube Live)		Time: 11:00-12:30						Time: 16:00-17:30				
	Poster Session			Time: 13:30-17:15		Time: 8:30-11:10							
A	SESSION A-INNOVATION IMPACTS DRIVEN SDGS												
B	SESSION B-MATH STAT COMP FOR SDGS: SUSTAINABLE SOLUTIONS			Time: 13:30-16:25		Time: 8:30-11:10		Time: 13:30-15:30					
C	SESSION C-PHYSICS FOR LIFE IN SPACE			Time: 13:30-15:00									
D	SESSION D-SDG CHALLENGES: CHEMICAL SOLUTIONS FOR SUSTAINABLE					Time: 9:00-11:50							
E1	SESSION E1-IMPACT OF BIOLOGICAL SCIENCE TOWARDS SDGS: ACTIVE			Time: 13:30-16:00		Time: 9:00-11:30							
E2	SESSION E2-IMPACT OF BIOLOGICAL SCIENCE TOWARDS SDGS:					Time: 8:30-11:10							
SYMP_A	SYMPOSIUM A: ACCELERATION OF SUSTAINABILITY TOWARDS BIOBASED			Time: 13:00-17:10									
SYMP_B	SYMPOSIUM B: CHALLENGES OF QUANTUM SCIENCE AND TECHNOLOGY					Time: 8:30-10:15							
SYMP_C	SYMPOSIUM C: CONSERVATION AND RESTORATION IN A CHANGING WORLD												
SYMP_D	SYMPOSIUM D: CRYSTALLOGRAPHY			Time: 13:00-15:45									
SYMP_E	SYMPOSIUM E: ENVIRONMENTAL (ECOLOGICAL) IMPACT OF									Time: 8:30-9:45			
SYMP_F	SYMPOSIUM F: FOREST BIODIVERSITY, CLIMATE CHANGE AND												
SYMP_G	SYMPOSIUM G: HOW CHEMISTRY CAN RESOLVE FOR COVID-19 PANDEMIC							Time: 13:00-14:20		Time: 8:30-11:25			
SYMP_H	SYMPOSIUM H: METAL-ORGANIC COMPOSITES IN MATERIAL SCIENCE												
SYMP_I	SYMPOSIUM I: PREMIUM AGRICULTURE: A PATHWAY TOWARD							Time: 13:30-15:15		Time: 8:30-10:30			
SYMP_J	SYMPOSIUM J: SUSTAINABLE HYDROGEN PRODUCTION FOR GREENER									Time: 8:30-11:50			
SYMP_K	SYMPOSIUM K: SUSTAINABLE USE OF MARINE BIODIVERSITY							Time: 13:00-15:30					
SYMP_L	SYMPOSIUM L: THE SUSTAINABLE TOURISM REVIEW IN A POST-PANDEMIC					Time: 8:30-12:00		Time: 12:30-16:30					
SYMP_M	SYMPOSIUM M: TUBERCULOSIS: OLD DISEASE, NEW APPROACHES									Time: 8:30-11:25			
SYMP_N	SYMPOSIUM N: SOLUTIONS FOR TOMORROW: DOW SUSTAINABILITY TO			Time: 13:30-16:30									
SYMP_O	SYMPOSIUM O: SYMPOSIUM ON SCIENCE EDUCATION FOR SUSTAINABILITY			Time: 13:30-16:00									
SYMP_P	SYMPOSIUM P: SUSTAINABLE FOOD SYSTEMS FOR GOOD HEALTH AND			Time: 13:30-15:30		Time: 9:30-12:00		Time: 13:00-16:00					
SYMP_Q	SYMPOSIUM Q: ADVANCE IN SCIENCE AND TECHNOLOGY TO ACCELERATE							Time: 14:00-16:00					
SYMP_R	SYMPOSIUM R: GREEN AND SUSTAINABLE CHEMISTRY: OPPORTUNITIES							Time: 14:00-15:30					
SYMP_S	SYMPOSIUM S: RECENT ADVANCES IN SYNTHETIC BIOLOGY AND GENOME					Time: 10:30-12:00							
	Annual Meeting of the SCISOC							Time: 14:00-16:00					
	Meeting of the STT48 Committee								Time: 16:00-18:00				
	Council of Science Deans of Thailand's Meeting			Time: 13:30-16:00									
	Head of Department Meeting (Physics)			Time: 13:30-16:00									
	Head of Department Meeting (Chemistry)			Time: 13:30-16:00									
	Head of Department Meeting (Biology)			Time: 13:30-16:00									
	Head of Department Meeting (CEPMART)			Time: 13:30-16:00									
	YRSS (Poster Session)					Time: 11:00-13:30							
	JYRSS (Poster Session)					Time: 11:00-13:30							
	YRSS (Oral Session)									Time: 8:30-12:00			
	YRSS / JYRSS (Awarding Session) [Facebook Live / Youtube Live]												Time: 15:30-16:30
	TYSA												Time: 13:00-15:00

KASETSART UNIVERSITY, KAMPHAENG SAEN CAMPUS

CONFERENCE ACCESS

Niwat Ruangpanit Building

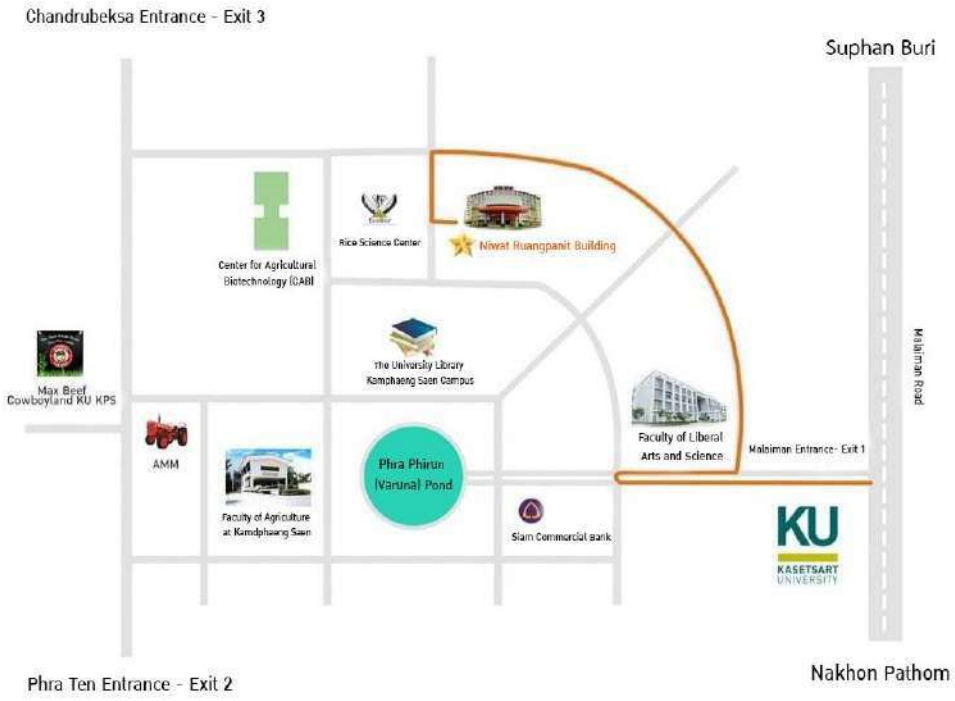

PROGRAM FOR GRAND OPENING CEREMONY OF STT47

OCTOBER 5th, 2021

Anamai Damnet Grand Ballroom, Niwat Ruangpanit Building
Kasetsart University, Kamphaeng Saen Campus, Nakorn Phatom, Thailand
[Zoom Meeting: https://us02web.zoom.us/j/85470660727]

Time	Events
8:00	All guests log in to virtual Opening Ceremony of STT47 Congress
8:45	VDO presentation on Kasetsart University
9:00	- Her Royal Highness Princess Maha Chakri Sirindhorn graciously presides over the opening ceremony of virtual STT47 Congress - Report on the society activities by Prof. Dr. Supawan Tantayanont, President of the Science Society of Thailand - Report on the STT47 Congress by Prof. Dr. Somkiat Ngamprasertsith, Chairman of STT47 Congress - Welcoming address by Dr. Chongrak Wachrinrat, President of Kasetsart University - Grand Opening Address by Her Royal Highness Princess Maha Chakri Sirindhorn
9:20	- Asst. Prof. Dr. Anamai Damnet, Dean of Faculty of Liberal Art and Science, Kasetsart University, Kamphaeng Saen Campus introduces Plenary lecturers: Plenary lecturer 1: Prof. Dr. Ben L. Feringa, 2016 Nobel Laureate in Chemistry Plenary lecturer 2: Prof. Dr. Vinich Promarak, 2021 Outstanding Scientist Short speech: Prof. Dr. Christopher Brett, President of International Union of Pure and Applied Chemistry (IUPAC)
9:25-9:55	Plenary Lecture 1: "The Art of Building Small " by Prof. Dr. Ben L. Feringa
10:00-10:20	Plenary lecture 2: “Efficient Solution-Processable Emissive Materials for Simple Structured Organic Light-Emitting Diodes (OLED)” by Prof. Dr. Vinich Promarak
10:25-10:35	Short speech: “IUPAC and Its Role as A Global Resource for Chemistry” by Prof. Dr. Christopher Brett
10:40	Her Royal Highness Princess Maha Chakri Sirindhorn graciously leaves STT47 Congress

PLENARY SPEAKER 1: Prof. Dr. Ben L. Feringa

THE ART OF BUILDING SMALL

Ben L. Feringa*

Stratingh Institute for Chemistry, University of Groningen,
Nijenborgh 4, 9747 AG Groningen, The Netherlands
*e-mail: b.l.feringa@rug.nl

Abstract:

Beyond the current frontiers of chemical sciences there is vast uncharted territory to control dynamic function based on molecular and supramolecular approaches. Far beyond Nature's design, the creative power of synthetic chemistry provides unlimited opportunities to realize our own molecular world as we experience every day with products ranging from pharmaceuticals to displays. Some challenges and opportunities for the future of society will be discussed. In the art of building small we explore the fascinating field of molecular nanoscience. Among the major challenges ahead in the design of complex artificial molecular systems is the control over dynamic functions and responsive far-from-equilibrium behaviour. A major goal is to gain control over translational and rotary motion. The focus is on my journey in the world of molecular switches and motors creating opportunities for smart medicines, molecular machines or responsive materials.

Information on http://www.benferinga.com

PLENARY SPEAKER 2: Prof. Dr. Vinich Promarak

EFFICIENT SOLUTION-PROCESSABLE EMISSIVE MATERIALS FOR SIMPLE STRUCTURED ORGANIC LIGHT-EMITTING DIODES (OLED)

Vinich Promarak*

Department of Materials Science and Engineering,
School of Molecular Science and Engineering,
Vidyasirimedhi Institute of Science and Technology (VISTEC),
Rayong, 21210 Thailand
*e-mail: vinich.p@vistec.ac.th; pvinich@gmail.com

Abstract:

OLED is a flat-lighting device composed of an organic layer that emits lights in response to an applied electrical current. OLEDs have many essential characteristics, such as self-luminescence, high flexibility, high resolution, and low power consumption, giving them vital advantages over existing display and lighting technology. Nowadays, OLEDs have become part of our daily life as they are already being integrated into various applications. Despite such tremendous progress, the development of some aspects of the OLEDs (materials and devices) is still necessary to bring this technology to the next level, such as flexible and foldable OLED devices. The currently used OLEDs are mainly manufactured with small-molecule emissive materials and sophisticated device architectures using vacuum evaporation processes, which are best suited for small dimension displays (smartphones and watches), and why the mid- to large-panel OLEDs are still expensive. However, the possibility to fabricate such devices on flexible substrates by simple, low-cost solution printing technologies (inkjet, slot-die, roll-to-roll, etc.) becomes more problematic. Therefore, the development of solution-processable and cost-effective emissive materials with high device performance is an important task to address.

In this presentation, the study and development of novel solution-processable emissive materials in which the essential elemental functions of an OLED, namely an intense solid-state light emission, electron/hole injection and transport capabilities, and solution-processability, would be incorporated by design into a single molecular architecture, will be illustrated. Several examples of solution-processable emissive materials will be discussed in terms of the structure-property relationships, with particular attention to the molecular design that affects the device performance. The optimized molecular design of these emissive materials has also allowed the construction of simple architectured solution-processed white light-emitting OLEDs (WOLEDs) with high electroluminescent performance and superior stability of white light emission.

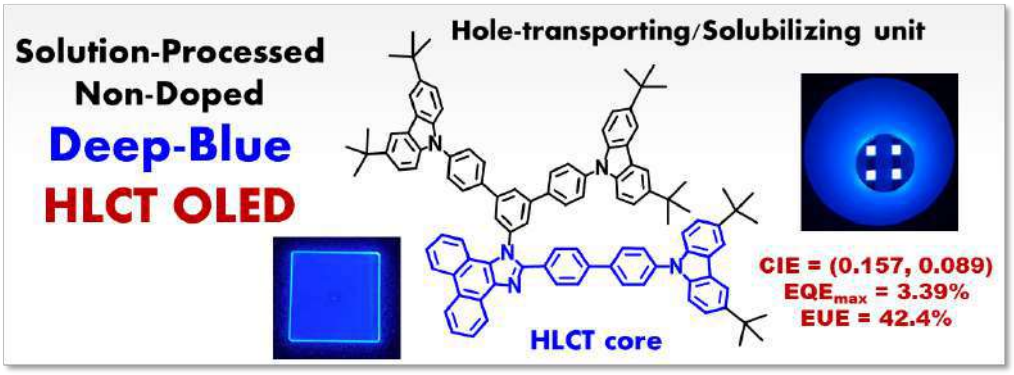

Figure. Solution-processed non-doped deep blue hybridized local and charge transfer (HLCT) excited state fluorescence molecule and device

SHORT SPEECH: Prof. Dr. Christopher Brett

IUPAC AND ITS ROLE AS A GLOBAL RESOURCE FOR CHEMISTRY

Christopher Brett[1,2]*

[1] Department of Chemistry, University of Coimbra, Coimbra, 3004-535, Portugal
[2] IUPAC, 79 T.W. Alexander Drive, Research Commons Building 4501, Suite 190, Research Triangle Park,
NC 27709, USA
*e-mail: cbrett@iupac.org

PROGRAM FOR SESSIONS, SYMPOSIUMS AND MEETINGS

OCTOBER 5th, 2021

Session:	POSTER PRESENTATION		
Link ZOOM:	https://zoom.us/j/92401135175		
Time	ID	Speaker	Title
11:00-12.30	-	-	Poster Presentation

Session:	SESSION A - INNOVATION IMPACTS DRIVEN SDGS		
Link ZOOM:	https://zoom.us/j/98815789296		
Chair person:	Dr. Mati Horprathum		
Time	ID	Speaker	Title
13:30-14:00	A_INV001	Teerakiat Kerdcharoen	INTERNET OF THINGS FROM FARM TO FORK
14:00-14:30	A_INV002	Takao Yasui	NANOWIRE MICROFLUIDICS FOR EARLY DISEASE DIAGNOSIS
14:30-15:00	A_INV003	Kazuki Nagashima	DIRECTING CHEMICAL REACTION PATHWAY ON NANOSTRUCTURED METAL OXIDE SURFACE FOR MOLECULAR SENSING APPLICATION
15:00-15:30	A_INV004	Jakrapong Kaewkhao	GLASS: FROM BASIC TO ADVANCED MATERIALS FOR INNOVATIVE LIFE
15:30-16:00	A_INV005	Supakij Suttiruengwong	INNOVATOR'S TOOLKIT
16:00-16:15	A_001	Ngamnete Phongpratheepchai	DETECTION OF CHIKUNGUNYA VIRUS USING REVERSE TRANSCRIPTION-PCR ASSAY COMBINED WITH LATERAL FLOW DIPSTICK
16:15-16:30	A_002	Nutthanun Moolsradoo	CORROSION RESISTANCE AND TRIBOLOGICAL STUDIES OF FLUORINATED-DLC FILM DEPOSITED BY PBII TECHNIQUE
16:30-16:45	A_003	Narakhan Khunsrimek	EFFECTS OF METEOROLOGICAL DATA SET SELECTION ON SIMULATION RESULTS OF ATMOSPHERIC DISPERSION CODE (NACAC)
16:45-17:00	A_004	Cheryanus Butkumchote	CONVERSION OF CASSAVA STARCH FACTORY SOLID WASTE TO COMPOST PRODUCTION BY BACTERIAL CONSORTIUM
17:00-17:15	A_005	Rajin Kakkoth Puthukkudi	IDENTIFYING FACTORS AFFECTING ELECTRICITY CONSUMPTION OF BANGKOK METROPOLITAN AREA IN THAILAND DURING COVID-19 SITUATION

Session:	SESSION C - PHYSICS FOR LIFE IN SPACE		
Link ZOOM:	https://zoom.us/j/97900743807		
Chair person:	Dr. Suparerk Aukkaravittayapun		
Time	ID	Speaker	Title
13:30-14:00	C_INV001	David Ruffolo	COSMIC RAYS: A RANDOM WALK THROUGH THE SOLAR WIND
14:00-14:30	C_INV002	Kitiyanee Asanok	RADIO ASTRONOMY FOR SUSTAINABLE DEVELOPMENT IN THAILAND AND FUTURE PROSPECTIVE
14:30-15:00	C_INV003	Phongsatorn Saisutjarit	SMALL SATELLITES – SPACE TECHNOLOGIES FOR LIFE
Break			
15:10-15:25	C_001	Chanin Maetmueang	DAM LEAKAGE DETECTION USING ELECTRICAL RESISTIVITY TOMOGRAPHY, GROUND-PENETRATING RADAR AND MULTICHANNEL ANALYSIS OF SURFACE WAVE: A CASE STUDY OF NONG PLA SAWAI RESERVOIR, LAMPHUN PROVINCE, NORTHERN THAILAND
15:25-15:40	C_002	Sorawat Siangpipop	SURFACE WAVE GROUP VELOCITY TOMOGRAPHY FROM AMBIENT SEISMIC NOISE CROSS-CORRELATION IN NORTHERN THAILAND
15:40-15:55	C_003	Paagjira Gajaseni	MONTE CARLO SIMULATION OF X-RAY GENERATION IN PLASMA FOCUS MACHINE
15:55-16:10	C_004	Karnjana Oncheurn	A STUDY OF ALIGNED ELECTROSPUN NANOFIBER USING MODIFIED RING-PARALELS COLLECTOR METHOD
16:10-16:25	C_005	Tanachporn Lukprang	GREEN SYNTHESIS AND CHARACTERIZATION OF CARBON DOTS FROM MANGOSTEEN

Session:	SESSION D - SDG CHALLENGES: CHEMICAL SOLUTIONS FOR SUSTAINABLE SOCIETY		
Link ZOOM:	https://zoom.us/j/99499675848		
Chair person:	Prof. Dr. Vudhichai Parasuk		
Time	ID	Speaker	Title
13:30-13:55	D_INV001	Rojana Pornprasertsuk	Zn AND Mn RECYCLING PROCESS FROM SPENT ALKALINE AND Zn-C BATTERIES TO BE RE-UTILIZED IN RECHARGEABLE Zn-ION BATTERY APPLICATION
14:00-14:25	D_INV002	Khamphee Phomphrai	HIGHLY ACTIVE METAL COMPLEXES SUPPORTED BY CONSTRAINED SCHIFF-BASE LIGANDS FOR CYCLOADDITION OF CO_2 TO EPOXIDES
14:30-14:42	D_001	Phatpasin Sumprasit	IMPACT OF ELECTROLYTE ADDITIVE ON IONIC SOLVATION AND TRANSPORT PROPERTIES FOR AQUEOUS ZINC-ION BATTERIES
14:45-14:57	D_002	Chaithawat Waikhani	EFFECT OF TEMPERATURE AND REDUCING AGENT CONCENTRATION ON THE Mn RECOVERY FROM SPENT ALKALINE AND Zn-C BATTERIES

Session:	SESSION E2 - IMPACT OF BIOLOGICAL SCIENCE TOWARDS SDGS: BIOLOGICAL SCIENCES TOWARDS SDGS		
Link ZOOM:	https://us02web.zoom.us/j/86926839567		
Chair person:	Prof. Dr. Chanpen Chanchao		
Time	ID	Speaker	Title
13:30-14:00	E2_INV001	Atsuo Kimura	NOVEL SINGLE- AND DOUBLE-ANCHOR-TYPE ISOMALTOMEGALOSACCHARIDES: PRODUCTION, FUNCTION, APPLICATION, AND CONTRIBUTION TO SDGS
14:00-14:15	E2_001	Prachakchit Chumkieo	DRAFT GENOME ANALYSIS OF A BEE SYMBIONT-DERIVED ANTIMICROBIL PRODUCER Streptomyces I-EHB-18
14:15-14:30	E2_002	Naeem Madsari	INNATE IMMUNITY ACTIVATION OF Litopenaeus vannamei BY Serine Protease AND HEAT-KILLED Vibrio parahaemolyticus
14:30-14:45	E2_003	Patcharee Phetthongyok	MICROBIAL DIVERSITY AND FUNCTION-BASED SCREENING FOR β-GALACTOSIDASES FROM WANG-PRA CAVE METAGENOME
14:45-15:00	E2_004	Pavinee Prapassornwattana	THE BINDING STUDY OF VIRAL CAPSID PROTEINS OF COXSACKIEVIRUS B3 WITH A BENZENE SULFONAMIDE DERIVATIVE AND RUPINTRIVIR BY USING COMPUTATIONAL METHODS
15:00-15:15	E2_005	Krittanai Trisakulwattana	TRANSCRIPTOME ANALYSIS OF DENGUE VIRUS INFECTION IN HUMAN HEPATOCYTE
15:15-15:30	E2_006	Ngoentra Samnaknit	β-GLUCOSIDASE ACTIVITY AND IN-SILICO STRUCTURAL ANALYSIS FROM THREE STRAINS OF ASPERGILLUS ACULEATUS
15:30-15:45	E2_007	Sirawit Jirawannaporn	DETECTION OF LEPTOSPIRES BY RPA-CRISPR-Cas12a TARGETING SecY GENE
15:45-16:00	E2_008	Thunyarat Surasiang	EFFECTS OF A6E MUTATION ON PROTEIN EXPRESSION AND STRUCTURE FORMATION OF Asn1p-GFP IN Saccharomyces cerevisiae

Symposium:	SYMPOSIUM B: CHALLENGES OF QUANTUM SCIENCE AND TECHNOLOGY TOWARDS SUSTAINABLE DEVELOPMENTS		
Link ZOOM:	https://zoom.us/j/97485819800		
Chair person:	Assoc. Prof. Dr. Anucha Watcharapasorn		
Co-chair:	Dr. Pimonpan Sompet		
Time	ID	Speaker	Title
13:00-13:30	SYMP_B_INV001	Rodney Van Meter	SDGS AND THE QUANTUM INTERNET
13:30-14:00	SYMP_B_INV002	Thiparat Chotibut	QUANTUM TECHNIQUES FOR EXPLAINABLE NATURAL LANGUAGE PROCESSING
14:00-14:30	SYMP_B_INV003	Ivan Rungger	QUANTUM COMPUTERS FOR MATERIALS SIMULATIONS USING EMBEDDING METHODS
14:30-14:50	SYMP_B_001	Naphan Benchasattabuse	DISTRIBUTING MULTIPARTITE ENTANGLED STATE OVER QUANTUM INTERNET
14:50-15:10	SYMP_B_002	Poramet Pathumsoot	OPTIMIZATION OF EXPECTED WAITING TIME IN NETWORK OF QUANTUM REPEATERS
Break			
Chair person:	Asst. Prof. Dr. Narupon Chattrapiban		
Co-chair:	Dr. Nuttachai Jutong		
Time	ID	Speaker	Title
15:20-15:50	SYMP_B_INV004	Tanapoom Poomaradee	TOWARD ULTRACOLD CAESIUM ISOMERS
15:50-16:20	SYMP_B_INV005	Pimonpan Sompet	EXPLORING FERMI-HUBBARD SYSTEM VIA QUANTUM GAS MICROSCOPE
16:20-16:50	SYMP_B_INV006	Nirpendra Singh	COMPUTATIONAL DESIGN FOR TWO-DIMENSIONAL MATERIALS FOR THERMOELECTRIC TRANSPORT
16:50-17:10	SYMP_B_003	Kritsana Saego	OPTICAL QUANTUM ERASER

Symposium:	SYMPOSIUM D: CRYSTALLOGRAPHY		
Link ZOOM:	https://zoom.us/j/94796182096		
Chair person:	Prof. Dr. Nongnuj Muangsin		
Time	ID	Speaker	Title
13:30-14:00	SYMP_D_INV001	Min Fey Chek	CRYSTAL STRUCTURE OF BIOPLASTIC-SYNTHESIZING PHA SYNTHASE (PhaC) REVEALING AN UNEXPECTED OPEN-CLOSED HETERODIMER
14:00-14:15	SYMP_D_001	Waralee Srinarawat	CRYSTALLIZATION AND CHARACTERIZATION OF MONOSODIUM URATE AND CALCIUM PYROPHOSPATE CRYSTALS AS CAUSE OF Gouty Arthritis
14:15-14:30	SYMP_D_002	Pasunee Laohawutthichai	CRYSTALLIZATION OF THE RECOMBINANT VIRAL RESPONSIVE PROTEIN 15 (PmVRP15) FROM THE BLACK TIGER SHRIMP Penaeus monodon
14:30-15:00	SYMP_D_INV002	Kanokwan Kongpatpanich	FUNCTIONALIZATION OF METAL-ORGANIC FRAMEWORKS FOR BIOMASS CONVERSION TO VALUE-ADDED CHEMICALS
15:00-15:15	SYMP_D_003	Chana Panyanon	STRUCTURES, PHOTOLUMINESCENCE AND CO_2 ADSORPTION PROPERTIES OF NOVEL POLYOXOMETALATES DERIVED FROM RICE HUSK BIOMASS
15:15-15:30	SYMP_D_004	Patcharin Jundee	PETROGRAPHY AND GEOCHEMISTRY OF MAFIC DIKES IN THAN SALAI ABANDONED QUARRY, THONG SAEN KHAN DISTRICT, UTTARADIT PROVINCE
15:30-15:45	SYMP_D_005	Kenika Khotchasanthong	FOUR NOVEL ZINC(II) COORDINATION POLYMERS BASED ON TRITOPIC AND HETEROCYCLIC N-DONOR MIXED LIGANDS

Symposium:	SYMPOSIUM N: SOLUTIONS FOR TOMORROW: DOW SUSTAINABILITY TO TACKLE WORLD CHANGE		
Link ZOOM:	https://zoom.us/j/92682911642		
Chair person:	Ms. Kanchana Un-Arom		
Time	ID	Speaker	Title
13:30-14:30	SYMP_N_INV001	Chompoonuch Junbua, Rangsun Chaosuwannakij, Thawatchai Tungkavet, Anurak Rassamee Amornwiwat	SUSTAINABLE INNOVATIONS FOR FUTURE PACKAGING BY DOW PACK GURU
Break			
14:45-15:30	SYMP_N_INV002	Loganathan Ravisanker	ADVANCING SAFETY AND CIRCULARITY OF RUBBERIZED SPORTS SURFACES THROUGH INNOVATION AND VALUE CHAIN PARTNERSHIPS
15:30-16:15	SYMP_N_INV003	Jens Schmidt	SUSTAINABLE CHEMICAL PRODUCTION – TECHNOLOGY & PATHWAYS TOWARDS A GREEN FUTURE FOR DOW
16:15-16:30	SYMP_N_001	Nattakarn Kruatong	USE OF BIOCHAR IMPREGNATED WITH IRON AND CHITOSAN FOR HEAVY METAL REMOVAL: SORPTION PERFORMANCES

Symposium:	SYMPOSIUM O: SYMPOSIUM ON SCIENCE EDUCATION FOR SUSTAINABILITY – LITERACY FOR ALL		
Link ZOOM:	https://zoom.us/j/91474796565		
Chair person:	Dr. Ganigar Chen		
Time	ID	Speaker	Title
13:30-14:00	SYMP_O_INV001	Yoshito Andou	FABRICATION OF BIODEGRADABLE CELLULOSE COMPOSITE THROUGH GREENER REACTION PROCESS
14:00-14:30	SYMP_O_INV002	Ruetai Chongsrid	INSPIRATION, MOTIVATION, AND CREATIVITY; HOW TO DESIGN STEM ACTIVITIES FOR SUSTAINABLE DEVELOPMENT
14:30-14:45	SYMP_O_001	Alvin Lim Teik Zheng	N-DOPED REDUCED GRAPHENE OXIDE/GRAPHENE NANOPLATELET (rGO/GNP) AEROGEL: PREPARATION AND CHARACTERIZATION
14:45-15:00	SYMP_O_002	Waraporn Rattanongphisat	EXPERIMENTAL INVESTIGATION ON SOLAR CHIMNEY STACK FOR NATURAL VENTILATION
15:00-15:15	SYMP_O_003	Mathivathani Kandiah	SILVER NANOPARTICLES: A SOLUTION FOR DEGRADING AZO DYES
15:15-15:30	SYMP_O_004	Abinaya Sathiskumar	BIOGENIC SYNTHESIS OF SILVER NANOPARTICLES USING THE EXTRACT OF ENVIRONMENTALLY BENIGN PLANT MATERIAL, BASIL (OCIMUM BASILICUM) AND DETERMINATION OF THEIR ANTIOXIDANT, ANTIBACTERIAL AND PHOTOCATALYTIC ACTIVITIES
15:30-15:45	SYMP_O_005	Ramlah Kamal	CONTRIBUTIONS OF A WEED: MICROWAVE ASSISTED GREEN SYNTHESIS OF SILVER NANOPARTICLES USING MORNING GLORY (Ipomoea spp.) FOR THE ASSESSMENT OF ITS ANTIOXIDANT, ANTIBACTERIAL AND PHOTOCATALYTIC ACTIVITY
15:45-16:00	SYMP_O_006	Napat Malathum	A REVIEW OF EDUCATIONAL PROGRAMMES AT THE RAMA 9 MUSEUM ASSOCIATED WITH THE UNITED NATIONS' SUSTAINABLE DEVELOPMENT GOALS

Symposium:	SYMPOSIUM P: SUSTAINABLE FOOD SYSTEMS FOR GOOD HEALTH AND WELL-BEING		
Link ZOOM:	https://zoom.us/j/95623018275		
Chair person:	Assoc. Prof. Dr. Chaleeda Borompichaichartkul		
Time	ID	Speaker	Title
13:30-14:00	-	Chair of the Symposium	SYMPOSIUM OPENING AND REGISTRATION
14:00-15:00	SYMP_P_INV001	Akkharawit Kanjana-opas	SUSTAINABLE FOOD SYSTEM FOR LOCAL INGREDIENTS, TREND AND SUPPORTING POLICY
15:00-15:30	-	Chair of the Symposium	Q&A

Session:	Council of Science Deans of Thailand's Meeting		
Link ZOOM:	https://us02web.zoom.us/j/86493611605		
Time	ID	Speaker	Title
13:30-16:00	-	-	Meeting

Session:	CEPMART Meeting		
Link ZOOM:	https://zoom.us/j/97036988638		
Time	ID	Speaker	Title
13:30-16:00	-	-	Meeting

Session:	The 36th Chemistry Department Heads of Thailand Meeting		
Link ZOOM:	https://us02web.zoom.us/j/81962233745		
Time	ID	Speaker	Title
13:30-16:00	-	-	Meeting

Session:	The 4th Physics Department Heads of Thailand Meeting		
Link ZOOM:	https://us02web.zoom.us/j/82758209021		
Time	ID	Speaker	Title
13:30-16:00	-	-	Meeting

Session:	The 3rd Biology Department Heads of Thailand Meeting		
Link ZOOM:	https://us02web.zoom.us/j/84038882921		
Time	ID	Speaker	Title
13:30-16:00	-	-	Meeting

OCTOBER 6th, 2021

Session:	SESSION B - MATH STAT COMP FOR SDGS: SUSTAINABLE SOLUTIONS		
Link ZOOM:	https://zoom.us/j/99929413009		
Chair person:	Assoc. Prof. Dr. Chartchai Leenawong		
Time	ID	Speaker	Title
8:30-9:00	B_INV001	Kannapha Amaruchkul	MULTI-OBJECTIVE LAND-WATER ALLOCATION MODEL FOR SUSTAINABLE AGRICULTURE WITH PREDICTIVE STOCHASTIC YIELD RESPONSE
9:00-9:30	B_INV002	Teerapong Suksumran	THE GEOMETRY OF N-DIMENSIONAL EINSTEIN GYROGROUP VIA KLEIN'S APPROACH
9:30-10:00	B_INV003	Thittaporn Ganokratanaa	UNSUPERVISED ANOMALY DETECTION FOR SURVEILLANCE VIDEOS
Break			
10:10-10:25	B_001	Thanomsak Laokul	ENDPOINT THEOREMS OF MULTI-VALUED MAPPING SATISFYING CONDITION (D) IN UNIFORMLY CONVEX HYPERBOLIC SPACES
10:25-10:40	B_002	Chadaporn Keatmanee	GUIDELINES of THAILAND PERSONAL DATA PRIVACY COMPLIANCE in UML: CASE of A PATIENT ASSISTANCE PROGRAM
10:40-10:55	B_003	Chanon Tantiwattanapaibul	THE PERTURBED RISK MODEL WITH INVESTMENT AND SURRENDER BASED ON POISSON NEGATIVE BINOMIAL COUNTING PROCESS
10:55-11:10	B_004	Sathit Prasomphan	TRACKING AND TAKE CARE AMNESIA PATIENT APPLICATION BY USING iBEACON

Session:	SESSION E1 - IMPACT OF BIOLOGICAL SCIENCE TOWARDS SDGS: ACTIVE LEARNING FOR BIOLOGICAL SCIENCE CLASSES		
Link ZOOM:	https://zoom.us/j/98949274106		
Chair person:	Asst. Prof. Dr. Noppadon Kitana		
Time	ID	Speaker	Title
9:00-9:30	E1_INV001	Nantana Gajaseni	NEW NORMAL, NEW MINDSET AND NEW SKILLSET: WHY AND HOW?
9:30-10:00	E1_INV002	Teck Keong Seow	CONVERSION OF A LARGE NON-MAJORS BIOLOGY COURSE TO ONLINE TEACHING – INSTRUCTIONAL RE-DESIGN AND ITS IMPACT ON STUDENT LEARNING
10:00-10:30	E1_INV003	Pongchai Dumrongrojwatthana	ACTIVE LEARNING VIA GAMING AND SIMULATIONS IN BIOLOGY AND SUSTAINABLE DEVELOPMENT COURSES
10:30-10:50	E1_001	Peeradon Sarnkaew	COMPUTER GAME OF CELL STRUCTURE AND FUNCTION IN BIOLOGY
10:50-11:10	E1_002	Alba Abad	CONNECTING THE CLIMATE CHALLENGE
11:10-11:30	E1_003	Sarnchai Viriyachat	PRACTICAL LEARNING WITH THE SIMULATED HUMAN DIGESTION - IN VITRO DIGESTION ANALYSIS ON GLUCOSE AVAILABILITY IN COMMON SOURCES OF CARBOHYDRATE CONSUMED IN THAILAND
11:30-11:50	E1_004	Raekkhwan Polthanya	THE USE OF MICROSCOPE LENS FOR SMARTPHONE AS AN ALTERNATIVE ACTIVE LEARNING TOOL FOR HIGH SCHOOL BIOLOGY CLASS

Session:	SESSION E2 - IMPACT OF BIOLOGICAL SCIENCE TOWARDS SDGS: BIOLOGICAL SCIENCES TOWARDS SDGS		
Link ZOOM:	https://us02web.zoom.us/j/86926839567		
Chair person:	Prof. Dr. Chanpen Chanchao		
Time	ID	Speaker	Title
9:00-9:30	E2_INV002	Preecha Phuwapraisirisan	SESAMOLIN: A VERSATILE PRECURSOR FROM SESAME SEED FOR DERIVATIZING BIOACTIVE LIGNANS
9:30-9:45	E2_009	Siriprapha Sudthonglang	ANTI-INFLAMMATORY ACTIVITY OF THE ETHANOLIC EXTRACT OF THE POWDER FORMULA OF A FUNGUS Cordyceps sinensis AND THREE HERBS (Panax ginseng, Kaempferia parviflora AND Houttuynia cordata) IN RAW264.7 CELLS
9:45-10:00	E2_010	Tattiya Kantasa	BIOLOGICAL ACTIVITY OF PROTEIN HYDROLYSATE FROM Lentinus squarrosulus Mont
10:00-10:15	E2_011	Khoa Anh Nguyen	FIRST IDENTIFICATION OF α-GLUCOSIDASE INHIBITORS FROM THE STEM OF Thunbergia laurifolia
10:15-10:30	E2_012	Thanakamol Khongsonthi	PREDICTION OF ANTI P. ACNES PEPTIDES FROM VARIOUS PROTEASES HYDROLYZED RICEBERRY RICE BRAN
10:30-10:45	E2_013	Thipwan Jiemanukunkij	DETERMINATION OF ORGANIC AND INORGANIC ELEMENTS IN THE BIOGAS DIGESTATE LIQUID
10:45-11:00	E2_014	Watcharapong Wimonchaijit	PROPICONAZOLE INHIBITS ROOT ELONGATION AND LATERAL ROOT DEPVELOPMENT IN RICE SEEDLINGS BY INTERFERING WITH AUXIN
11:00-11:15	E2_015	Luhur Septiadi	HEALTH STATUS OF THE RICE FROG Fejervarya limnocharis IN NAN PROVINCE, THAILAND, DURING PEAK HERBICIDE UTILIZATION PERIOD
11:15-11:30	E2_016	Sudarat Fueangmeekun	SUCCESSION OF CARRION INSECTS ON PIG CARCASSES RELOCATED FROM INDOOR TO OUTDOOR CONDITIONS

Symposium:	SYMPOSIUM A: ACCELERATION OF SUSTAINABILITY TOWARDS BIOBASED TECHNOLOGICAL PLATFORM DEVELOPMENT		
Link ZOOM:	https://zoom.us/j/99423993837		
Chair person:	Prof. Dr. Nuttha Thongchul		
Time	ID	Speaker	Title
9:00-9:30	SYMP_A_INV001	Hesham A. El Enshasy	MORPHOLOGY IN SUBMERGED CULTURE: THE MAIN CHALLENGE IN INDUSTRIAL BIOACTIVE COMPOUND PRODUCTION IN FUNGAL BIOFACTORIES
9:30-10:00	SYMP_A_INV002	Thana Sornchamni	THE POTENTIAL OF GREEN HYDROGEN
10:00-10:30	SYMP_A_INV003	Lalintip Hocharoen	BIOPROCESS DEVELOPMENT ON ANIMAL VACCINE PRODUCTION FOR A SUSTAINED TECHNOLOGY ENHANCEMENT
Break			
10:40-10:55	SYMP_A_001	Sitanan Thitiprasert	SUGAR TOLERANCE IN D-LACTIC ACID FERMENTATION BY Sporolactobacillus terrae SBT-1
10:55-11:10	SYMP_A_002	Panaya Kotchaplai	SCREENING AND ISOLATION OF LIGNIN-DEPOLYMERIZING BACTERIA FOR AN AROMATIC FEEDSTOCK PRODUCTION
11:10-11:25	SYMP_A_003	Suwattana Pruksasri	PREPARATION OF BIOACTIVE PECTIN FILMS FROM POMELO PEELS

Symposium:	SYMPOSIUM C: CONSERVATION AND RESTORATION IN A CHANGING WORLD		
Link ZOOM:	https://zoom.us/j/96712657482		
Chair person:	Prof. Dr. Suchana Chavanich		
Time	ID	Speaker	Title
8:30-9:00	SYMP_C_INV001	Kentaro Ando	RESEARCH OF IOC/WESTPAC
9:00-9:30	SYMP_C_INV002	Dominic Thomson	NET FREE SEAS - EXPLORING COMMUNITY-BASED SOLUTIONS TO MARINE POLLUTION
9:30-10:00	SYMP_C_INV003	Siriporn Sriaram	LESSONS LEARNED AND WAY FORWARD FOR MANGROVE RESTORATION IN THAILAND
10:00-10:15	SYMP_C_001	Sirikorn Pongtornkulpanich	AGE ESTIMATION OF MARINE FOSSILS FROM PHETCHABUN PROVINCE USING X-RAY ANALYSIS

Symposium:	SYMPOSIUM L: THE SUSTAINABLE TOURISM REVIEW IN A POST-PANDEMIC 2022: REBUILDING TOURISM TO SUSTAINABILITY		
Link ZOOM:	https://zoom.us/j/95250053060		
Chair person:	Dr. Chainarong Srirak		
Time	ID	Speaker	Title
8:30-9:00	-	-	REGISTRATION
9:00-9:30	-	Patthaphon Sukjai & Anamai Damnet	INTRODUCTION & WELCOME AND OPENING REMARKS
9:30-10:00	SYMP_L_INV001	Noel Scott	SUSTAINABLE TOURISM AS A STRATEGY FOR ADVENTURE TOURISM DEVELOPMENT
10:00-10:30	SYMP_L_INV002	Ann Suwaree Ashton	STRENGTHENING TOURISM SUSTAINABILITY WELLNESS TOURISM; THROUGH SOUTHEAST ASIA
10:30-11:00	SYMP_L_INV003	Robert C. Sinclair	COVID-19, SUSTAINABLE TOURISM, AND THE CHALLENGES FOR THE FUTURE
11:00-11:30	SYMP_L_INV004	Gina B. Alcoriza	THE SUSTAINABLE TOURISM REVIEW IN A POST-PANDEMIC 2022: REBUILDING TOURISM TO SUSTAINABILITY
11:30-12:00	-	-	ROUND TABLE DISCUSSION

Symposium:	SYMPOSIUM P: SUSTAINABLE FOOD SYSTEMS FOR GOOD HEALTH AND WELL-BEING		
Link ZOOM:	https://zoom.us/j/95623018275		
Chair person:	Assoc. Prof. Dr. Chaleeda Borompichaichartkul		
Time	ID	Speaker	Title
9:30-10:10	-	-	REGISTRATION
10:10-11:05	SYMP_P_INV002	Richard Archer	STATE-of-the-ART FOOD TECHNOLOGY FOR SUSTAINABLE FOOD SYSTEMS
11:05-12:00	SYMP_P_INV003	Lalana Thiranusornkij	LOCAL INGREDIENTS AND SUSTAINABILITY FOOD SYSTEM R&D FROM DEMAND SIDE

Symposium:	SYMPOSIUM S: RECENT ADVANCES IN SYNTHETIC BIOLOGY AND GENOME EDITING		
Link ZOOM:	https://zoom.us/j/92606820017 (WEBINAR)		
Chair person:	Dr. Verawat Champreeda		
Time	ID	Speaker	Title
10:30-11:00	SYMP_S_INV001	Chayasith Uttamapinant	GENETIC CODE REPROGRAMMING WITH ENGINEERED TRANSLATION MACHINERIES
11:00-11:30	SYMP_S_INV002	Wanatchaporn Arunmanee	BIOENGINEERING OF *Escherichia coli* OUTER MEMBRANE VESICLES AS DRUG AND VACCINE DELIVERY SYSTEM
11:30-12:00	SYMP_S_INV003	Weerawat Runguphan	ENGINEERING YEAST TO PRODUCE ADVANCED BIOFUELS AND HIGH-VALUE BIOCHEMICALS

Session:	YRSS & JYRSS SESSIONS		
Link ZOOM 1:	YRSS (Bio & Chem) > https://us02web.zoom.us/j/89550706931		
Link ZOOM 2:	YRSS (Others) > https://us02web.zoom.us/j/87973842561		
Link ZOOM 3:	JYRSS > https://us02web.zoom.us/j/82857200853		
Time	ID	Speaker	Title
11:00-13:30	-	-	Poster Presentation (YRSS & JYRSS)

Session:	Annual Meeting of the Science Society of Thailand Under the Patronage of His Majesty the King		
Link ZOOM:	https://zoom.us/j/98330395165		
Time	ID	Speaker	Title
14:00-16:00	-	-	Meeting

Session:	Meeting of the STT48 Committee		
Link ZOOM:	https://us02web.zoom.us/j/81811050099		
Time	ID	Speaker	Title
16:00-18:00	-	-	Meeting

Session:	SESSION D - SDG CHALLENGES: CHEMICAL SOLUTIONS FOR SUSTAINABLE SOCIETY		
Link ZOOM:	https://zoom.us/j/99499675848		
Chair person:	Prof. Dr. Vudhichai Parasuk		
Time	ID	Speaker	Title
13:30-13:55	D_INV003	Suwat Nanan	SUSTAINABLE DEGRADATION OF ORGANIC POLLUTANTS IN WASTEWATER BY PHOTOCATALYTIC PROCESS
14:00-14:25	D_INV004	Xuechuan Hong	SMALL-MOLECULE FLUOROPHORES FOR NIR-II BIOMEDICAL FLUORESCENCE IMAGING AND AND IMAGE-GUIDED THERAPY
14:30-14:42	D_003	Chaiwat Rujirasereesakul	SUBSTITUENT EFFECT ON THE KINETIC BEHAVIOR OF PHOSPHINE-CATALYZED CONJUGATE ADDITION REACTION OF ALLENIC ESTERS: A POTENTIAL SOLUTION FOR DEVELOPMENT OF A KINETICALLY FASTER CATALYTIC CONJUGATE ADDITION
14:45-14:57	D_004	Wannisa Vichit	THERMAL STABILITY OF ENCAPSULATED RED HOMMALI RICE EXTRACT WITH BETA-CYCLODEXTRINS
15:00-15:12	D_005	Boonyaras Sookkheo	OIL ADSORPTION IN WASTEWATER USING CHITIN EXTRACTED FROM CUTTLEFISH BONE
15:15-15:27	D_006	Jariya Jitdee	SYNTHESIS AND GENETIC CODE EXPANSION OF PLASTIC-DEGRADING ENZYMES FOR DETECTION OF MICROPLASTICS

Symposium:	SYMPOSIUM F: FOREST BIODIVERSITY, CLIMATE CHANGE, AND SUSTAINABLE USE FOR SAVING LIFE ON EARTH		
Link ZOOM:	https://zoom.us/j/99369031822		
Chair person:	Asst. Prof. Dr. Oraphan Sungkajanttranon		
Time	ID	Speaker	Title
13:00-13:20	SYMP_F_INV001	Alistair Monument	CONSERVE THE WORLD'S MOST IMPORTANT FORESTS TO SUSTAIN NATURE'S DIVERSITY, BENEFIT OUR CLIMATE, AND SUPPORT HUMAN WELL-BEING
13:20-13:40	SYMP_F_INV002	Jantrararuk Tovaranone	IMPACT OF CLIMATE CHANGE ON BIODIVERSITY FOR SUSTAINABLE USE
13:40-14:00	SYMP_F_INV003	Oh Cheow Sheng	SINGAPORE, BECOMING A CITY IN NATURE
14:00-14:20	SYMP_F_001	Ploypassorn Thirajitto	THE COMPARATIVE LEAF ANATOMY OF Erycibe ROXB. IN THAILAND

Symposium:	SYMPOSIUM H: METAL-ORGANIC COMPOSITES IN MATERIAL SCIENCE		
Link ZOOM:	https://zoom.us/j/98016113963		
Chair person:	Prof. Dr. Takiumi Konno		
Time	ID	Speaker	Title
13:30-14:00	SYMP_H_INV001	Yi-Chou Tsai	THE CAPRICIOUS Mo−Mo QUINTUPLE BOND
14:00-14:30	SYMP_H_INV002	Phimphaka Harding	STRATEGIES TOWARDS LIGHT-ACTIVATION IN IRON(III) SPIN CROSSOVER MATERIALS
14:30-15:00	SYMP_H_INV003	Yun Zong	METAL-ORGANIC FRAMEWORKS (MOFS) IN ENERGY STORAGE RESEARCH
15:00-15:15	SYMP_H_001	Saran Sukchit	SYNTHESIS AND CHARACTERIZATION OF HETEROBIMETALLIC COMPLEXES SUPPORTED BY POLYETHYLENE GLYCOL CHAINS-APPENDED 2,6-PYRIDINEDIMETHANAMINE

Symposium:	SYMPOSIUM K: SUSTAINABLE USE OF MARINE BIODIVERSITY		
Link ZOOM:	https://us02web.zoom.us/j/88114006148		
Chair person:	Assoc. Prof. Dr. Thamasak Yeemin		
Time	ID	Speaker	Title
13:00-13:30	SYMP_K_INV001	Janny D. Kusen	REPRODUCTION OF SOME CORAL REEF FISHES IN MANADO BAY AND BUNAKEN NATIONAL PARK INDONESIA TO SUPPORT THE SUSTAINABILITY RESOURCES
13:30-14:00	SYMP_K_INV002	Baria-Rodriguez MVB	THE FIRST SUCCESSFUL PRODUCTION OF AN F2 GENERATION FROM 12-YEAR-OLD SEXUALLY PROPAGATED MASSIVE CORAL COLONIES
14:00-14:30	SYMP_K_INV003	Sau Pinn Woo	BLUE ECONOMY: DRIVING GROWTH THROUGH SUSTAINABLE USE OF MARINE BIODIVERSITY
14:30-14:45	SYMP_K_001	Makamas Sutthacheep	COMMUNITY STRUCTURE OF CORALS ON A NEW DIVE SITE, PRATHONG UNDERWATER PINNACLE IN THE ANDAMAN SEA
14:45-15:00	SYMP_K_002	Charernmee Chamchoy	THE COLONY SIZE STRUCTURE OF CORAL POPULATIONS ON SHALLOW REEF FLAT AT KO RANG KACHIU, MU KO CHUMPHON NATIONAL PARK
15:00-15:15	SYMP_K_003	Nachaphon Sangmanee	THE RELATIONSHIP OF MEIOFAUNAL COMMUNITIES AND CORAL COVER AT MU KO SURIN NATIONAL PARK, THE ANDAMAN SEA
15:15-15:30	SYMP_K_004	Wichin Suebpala	DIVERSITY OF SMALL-SCALE FISHING GEARS IN RANONG, PHANG NGA AND PHUKET, THE NORTH ANDAMAN SEA

Symposium:	SYMPOSIUM L: THE SUSTAINABLE TOURISM REVIEW IN A POST-PANDEMIC 2022: REBUILDING TOURISM TO SUSTAINABILITY		
Link ZOOM:	https://zoom.us/j/95250053060		
Chair person:	Dr. Gina B. Alcoriza		
Time	ID	Speaker	Title
12:30-12:50	SYMP_L_001	Chainarong Srirak	A REVIEW OF NEW TOURISM IN THE POST-COVID ERA: OPPORTUNITIES AND CHALLENGES FOR SUSTAINABLE TOURISM DEVELOPMENT
12:50-13:10	SYMP_L_002	Piyapong Ketpiyarat	DEVELOPING AGRO-TOURISM STANDARDS TO SUPPORT NEW NORMAL TOURIST GROUPS: OPPORTUNITIES AND CHALLENGES FOR SUSTAINABLE TOURISM DEVELOPMENT IN THAILAND
13:10-13:30	SYMP_L_003	Patthaphon Sukjai	SOCIOLOGY OF TOURISM IN THE DIMENSION OF TRAVEL EXPERIENCE DESIGN WITH DEMOCRATIC CONCEPT
13:30-13:50	SYMP_L_004	Jong Saesong	GUIDELINES ON SELF-ADJUSTMENT OF TOURISM ENTREPRENEURS CAUSED BY EFFECTS OF COVID-19 IN PHRA NAKHON SI AYUTTHAYA
13:50-14:10	SYMP_L_005	Thanakorn Thangruang	POST NEW NORMAL TOURISM
Break			
14:20-14:40	SYMP_L_006	Theeranan Tanphanich	THE DEVELOPMENT OF A STAND UP PADDLE BOAT (SUP) ACTIVITY MODEL TO PROMOTE SUSTAINABLE SPORTS TOURISM
14:40-15:00	SYMP_L_007	Niramol Khwakhong	THE IMPORTANCE OF SERVICE QUALITY OF 5 STAR HOTELS IN RATCHAPRASONG AREA TO TRANSITION UNDERCORONAVIRUS-19 2019 SITUATION
15:00-15:20	SYMP_L_008	Apidet Changchai	THE PROCESS OF COORDINATING FORCES TO SHAKE SOCIETY THROUGH THE COVID-19 CRISIS: TOUR LEADER'S YOUTH CAPACITY DEVELOPMENT FOR SUSTAINABLE TOURISM DEVELOPMENT
15:20-15:40	SYMP_L_009	Apidet Changchai	THE WAY OF SURVIVAL OF THE THA - CHIN RIVERSIDE MARKET COMMUNITIES: APPROACH OF STEPPING THROUGH THE COVID - 19 CRISIS OF TOURISM COMMUNITY
15:40-16:00	SYMP_L_010	Varachoti Vitchalertphol	THE COMMUNICATION ACROSS CULTURE TO TOURISM IN THE NEW NORMAL WAY AFTER COVID-19
16:00-16:30	-	Gina B. Alcoriza	CLOSING REMARKS

Symposium:	SYMPOSIUM P: SUSTAINABLE FOOD SYSTEMS FOR GOOD HEALTH AND WELL-BEING		
Link ZOOM:	https://zoom.us/j/95623018275		
Chair person:	Assoc. Prof. Dr. Chaleeda Borompichaichartkul		
Time	ID	Speaker	Title
13:00-13:30	-	-	REGISTRATION
13:30-14:30	SYMP_P_INV004	Paola Pittia	FOOD INNOVATION FOR FOOD SYSTEM SUSTAINABILITY, GOOD HEALTH, AND WELL-BEING
14:30-15:00	SYMP_P_001	Naraporn Phomkaivon	PRE-GELATINIZED COLOR SWEET POTATOES: AN APPROACH IN POLYPHENOLS ENHANCEMENT AND ANTIOXIDANT POTENTIAL
15:00-15:30	SYMP_P_002	Lalita Lakkham	REPLACEMENT OF PHILANGKASA EXTRACTS TO NITRITE IN FERMENTED MEAT PRODUCT
15:30-16:00	-	Chair of the Symposium	SYMPOSIUM SUMMARY AND CLOSE

Symposium:	SYMPOSIUM Q: ADVANCE IN SCIENCE AND TECHNOLOGY TO ACCELERATE DECARBONIZATION FOR INDUSTRIES		
Link ZOOM:	https://zoom.us/j/99809595789		
Chair person:	Dr. Sumate Chareonchaidet		
Time	ID	Speaker	Title
14:00-14:30	SYMP_Q_INV001	Nannan Sun	-TBA-
14:30-15:00	SYMP_Q_INV002	Edman Tsang	-TBA-
15:00-16:00	SYMP_Q_INV003	Representative from CAS ICCB	-TBA-

Symposium:	SYMPOSIUM R: GREEN AND SUSTAINABLE CHEMISTRY: OPPORTUNITIES FOR ACADEMIA AND INDUSTRY		
Link ZOOM:	https://us02web.zoom.us/j/82159107076		
Chair person:	Prof. Joseph S.M. Samec		
Time	ID	Speaker	Title
14:00-14:30	SYMP_R_INV001	Adam Slabon	FROM INVENTION TO INNOVATION: CHEMICAL TECHNOLOGIES FOR ENVIRONMENTAL APPLICATIONS
14:30-14:45	SYMP_R_001	Chalinee Janta	MICROWAVE-ASSISTED EXTRACTION FROM FRUITS OF Lycium ruthenicum
14:45-15:00	SYMP_R_002	Patchayanan Suksamran	ANALYSIS OF CHEIMICAL COMPONENTS IN DEFFERENT TEA TAXA FROM CHIANG RAI USING UHPLC-MS/MS COMBINED WITH CHEMOMETRICS
15:00-15:15	SYMP_R_003	Achanai Buasri	RIVER SNAIL SHELL AS HIGHLY EFFECTIVE RENEWABLE HETEROGENEOUS BASE CATALYST FOR BIODIESEL PRODUCTION

Session:	POSTER PRESENTATION		
Link ZOOM:	https://zoom.us/j/92401135175		
Time	ID	Speaker	Title
16:00-17.30	-	-	Poster Presentation

OCTOBER 7th, 2021

Symposium:	SYMPOSIUM E: ENVIRONMENTAL (ECOLOGICAL) IMPACT OF MICROPLASTICS AND TECHNOLOGICAL POTENTIAL FOR MICROPLASTIC WASTE		
Link ZOOM:	https://us02web.zoom.us/j/84149957727		
Chair person:	Assoc. Prof. Dr. Taeng On Prommi		
Time	ID	Speaker	Title
8:30-8:45	SYMP_E_001	Suchanya Wongrod	ADSORPTION OF CADMIUM FROM AQUEOUS SOLUTIONS BY POLYETHYLENE MICROPLASTICS AND BAMBOO BIOCHAR
8:45-9:00	SYMP_E_002	Thanya Reunura	DETECTION OF MICROPLASTICS IN Litopenaeus vannamei (Penaeidae) AND Macrobrachium rosenbergii (Palaemonidae) IN CULTURED POND
9:00-9:15	SYMP_E_003	Witwisitpong Maneechan	OCCURRENCE OF MICROPLASTICS IN THE GASTROINTESTINAL TRACT OF Anax sp. (Odonata: Aeshnidae) FROM THE RICE FIELD
9:15-9:30	SYMP_E_004	Penkhae Thamsenanupap	ACCUMULATION OF MICROPLASTICS IN MACROINVERTEBRATES INHABITING IN HUAI KHAKHANG STREAM, MAHA SARAKHAM PROVINCE
9:30-9:45	SYMP_E_005	Pimchanok Patho	VARIATION OF THE PHYTOTOXICITY OF CRUMB RUBBERS WASTE ON WHEAT (Triticum aestivum L.) SEED GERMINATION WITH LEACHING CONDITIONS

Symposium:	SYMPOSIUM G: HOW CHEMISTRY CAN RESOLVE FOR COVID-19 PANDEMIC		
Link ZOOM:	https://zoom.us/j/98010238500		
Chair person:	Prof. Dr. Orawon Chailapakul		
Time	ID	Speaker	Title
8:30-9:00	SYMP_G_INV001	Charles S. Henry	LOW-COST MICROFLUIDIC SENSORS FOR BACTERIA AND VIRUS DETECTION
9:00-9:30	SYMP_G_INV002	Tanapat Palaga	HOW CHEMISTRY AIDS IN THE COVID-19 VACCINE DEVELOPMENT?
9:30-10:00	SYMP_G_INV003	Kittikhun Wangkanont	FLUORESCENT PROBE-BASED ASSAY FOR IDENTIFICATION OF SARS-COV-2 MAIN PROTEASE INHIBITORS
Break			
10:10-10:40	SYMP_G_INV004	Sudkate Chaiyo	RECENT DEVELOPMENT OF COLORIMETRIC AND ELECTROCHEMICAL BIOSENSORS FOR COVID-19 DIAGNOSIS
10:40-10:55	SYMP_G_001	Chirapha Prakobdi	COLORIMETRIC METHOD BASED ON THE SCHIFF'S TEST FOR DETECTION OF METHANOL ADULTERATION IN HAND SANITIZER
10:55-11:10	SYMP_G_002	Watcharapong Timklaypachara	PROGRAM FOR COMPARING HIGH PERFORMANCE CHEMICAL FINGERPRINTING OF SAMPLES WITH COMPREHENSIVE TWO-DIMENSIONAL GAS CHROMATOGRAPHY TO EVALUATE PERCENTAGE OF SIMILARITY OF COMPONENTS BETWEEN 2 SUBSTANCES
11:10-11:25	SYMP_G_003	Pakakan Ngernpradab	PDMS AS A MATERIAL FOR DIGITAL MAGNETOFLUIDICS FOR APPLICATIONS IN BIOMEDICAL ANALYSIS

Symposium:	SYMPOSIUM I: PREMIUM AGRICULTURE: A PATHWAY TOWARD SUSTAINABLE AND INCLUSIVE BCG ECONOMY MODEL		
Link ZOOM:	https://zoom.us/j/96019253904		
Chair person:	Dr. Worajit Setthapun		
Time	ID	Speaker	Title
8:30-9:00	SYMP_I_INV001	Chai Lay Ching	HEADING TOWARDS THE NEW ERA OF SMARTER FOOD SAFETY FOR A SUSTAINABLE FOOD SYSTEM
9:00-9:30	SYMP_I_INV002	Suvaluk Asavasanti	CIRCULAR FOOD PRODUCTION: VALORIZATION OF FOOD MANUFACTURING BY-PRODUCTS
9:30-10:00	SYMP_I_INV003	Alan Dronkers	HEMP AS A SUSTAINABLE CROP AND A RENEWABLE RESOURCE
10:00-10:30	SYMP_I_INV004	Korsak Towantakavanit	SYNBIO CONSORTIUM IS DRIVING THAILAND BCG ECONOMY TO THE NEW FRONTIER

Symposium:	SYMPOSIUM J: SUSTAINABLE HYDROGEN PRODUCTION FOR GREENER ENVIRONMENT AND CHEMICAL PRODUCTS		
Link ZOOM:	https://zoom.us/j/92367461035		
Chair person:	Prof. Dr. Suttichai Assabumrungrat		
Time	ID	Speaker	Title
8:30-9:00	SYMP_J_KEY001	Sibudjing Kawi	SUSTAINABLE BIOMASS TAR REFORMING FOR SYNGAS / HYDROGEN PRODUCTION VIA THERMAL & PLASMA CATALYSIS
9:00-9:30	SYMP_J_KEY002	Joongmyeon Bae	PORTABLE HYDROGEN ENERGY SYSTEM WITH AN ELECTROLYZER, METAL HYDRIDE, AND PEMFC FUEL CELL
9:30-10:00	SYMP_J_KEY003	Piyabut Charuphen	HANDLING GREEN HYDROGEN IN THE FORM OF AMMONIA FOR COMMERCIAL USE AIMING TO NET ZERO EMISSION AND SUSTAINABILITY
10:00-10:20	SYMP_J_INV001	Sakhon Ratchahat	HYDROGEN PRODUCTION FROM CATALYTIC METHANE DECOMPOSITION
Break			
10:30-10:50	SYMP_J_INV002	Jon Powell	MULTIFUNCTIONAL CATALYST PELLETS FOR HYDROGEN PRODUCTION
10:50-11:05	SYMP_J_001	Nopphon Weeranoppanant	MAKE IT FLOW: ITS APPLICATION IN PHOTOCATALYTIC WATER SPLITTING FOR HYDROGEN PRODUCTION
11:05-11:20	SYMP_J_002	Peat Khemnarong	HYDROGEN-RICH GAS PRODUCTION FROM STEAM REFORMING OF ETHANOL OVER Re-Ni/Al_2O_3 CATALYSTS
11:20-11:35	SYMP_J_003	Pasin Poung-Art	EFFECTS OF SUPPORT AND STEAM ADDITION ON CALCIUM CARBONATE REGENARATION IN THE COMBINED SORPTION-ENHANCED STEAM METHANE REFORMING WITH BI-REFORMING PROCESS
11:35-11:50	SYMP_J_004_P	Patid Poolthongkam	PRELIMINARY STUDY THE PALLADIUM CLUSTERS FOR HYDROGEN PRODUCTION FROM FORMALDEHYDE USING DFT CALCULATION

Symposium:	SYMPOSIUM M: TUBERCULOSIS: OLD DISEASE, NEW APPROACHES		
Link ZOOM:	https://zoom.us/j/98381009359		
Chair person:	Assoc. Prof. Dr. Roderick Bates		
Time	ID	Speaker	Title
8:30-9:00	SYMP_M_INV001	Gerhard Grüber	FROM MECHANISTIC- AND STRUCTURAL UNDERSTANDING OF Mycobacterium tuberculosis METABOLIC ENZYMES TO ANTI-TB COMPOUND DISCOVERY
9:00-9:15	SYMP_M_001	Pharit Kamsri	IDENTIFICATION OF NOVEL SERINE/THREONINE PROTEIN KINASES B INHIBITORS AS ANTI-TUBERCULOSIS AGENTS FROM KINASE LIBRARY: MULTISTAGE VIRTUAL SCREENINGS AND PHAMACOKINETIC PREDICTIONS
9:15-9:30	SYMP_M_002	Bandit Khamsri	INSIGHT INTO THE BINDING MODE AND BINDING INTERACTIONS OF BENZO[d]ISOTHIAZOLE DERIVATIVES AS POTENTIAL MTB DNA gyrase INHIBITORS USING MOLECULAR DYNAMICS SIMULATIONS
9:30-10:00	SYMP_M_INV002	Aasheesh Srivastava	HOT PURSUIT OF MYCOBACTERIA BY POLYASPARTAMIDE POLYELECTROLYTES
Break			
10:10-10:25	SYMP_M_003	Naruedon Phusi	PROPOSING NOVEL M. tuberculosis InhA INHIBITORS USING STRUCTURE-BASED DRUG DESIGN APPROACHES: MD SIMULATIONS AND FMO CALCULATIONS
10:25-10:40	SYMP_M_005	Pattarakiat Seankongsuk	SYNTHESIS OF Mycobacterium tuberculosis ATP SYNTHASE INHIBITORS
10:40-11:10	SYMP_M_INV003	Pornpan Pungpo	-TBA-
11:10-11:25	SYMP_M_004	Prabhu Yavvari	SELECTIVE TARGETING OF MYCOBACTERIAL BIOFILMS AND INTRACELLULAR MYCOBACTERIA BY SYNTHETIC ANTIMICROBIAL POLYAMIDES

Session:	YRSS		
Link ZOOM 1:	Bio > https://zoom.us/j/95834561717		
Link ZOOM 2:	Chem > https://zoom.us/j/94192185568		
Link ZOOM 3:	Com > https://zoom.us/j/98708723715		
Link ZOOM 4:	Env > https://zoom.us/j/98755366844		
Link ZOOM 5:	Food > https://zoom.us/j/96269948597		
Link ZOOM 6:	Mat > https://us02web.zoom.us/j/83119174158		
Link ZOOM 7:	Math > https://us02web.zoom.us/j/81278076901		
Link ZOOM 8:	Phy > https://us02web.zoom.us/j/89956723455		
Time	ID	Speaker	Title
8:30-12:00	-	-	Oral Presentation (YRSS)
Break			
Link ZOOM:	https://us02web.zoom.us/j/82966993052		
15:30-16:30		-	YRSS Awarding Session

Session:	TYSA		
Link ZOOM:	https://us02web.zoom.us/j/82702769403		
Time	ID	Speaker	Title
13:00-15:00	-	-	TYSA Workshop

SESSION A -
INNOVATION IMPACTS DRIVEN SDGS

INNOVATION IMPACTS DRIVEN SDGS

Chair: Dr. Mati Horprathum
Co-Chair: Asst. Prof. Dr. Narit Triamnak
Co-Chair: Asst. Prof. Dr. Kheamrutai Thamaphat

According to the COVID- 19 pandemic presents, global disruption has been being violently accelerated widespread. Meanwhile, technological innovations have been being highlighted as the potential solutions for distressed circumstances in such disruption era which can enable daily life activities such as works, businesses, industrials or educations to continue throughout the pandemic. The technological innovations can also significantly contribute to sustainable development and generate additional opportunities of the Sustainable Development Goals (SDGs) success. Hence, the technological innovations are crucial and need to be accelerated and scaled to strengthen the economic and social impact developments, especially, the SDGs. This session is to share new ideas, opportunities and the technological innovations among students, scientists, researchers, professionals, and innovators with an integrated approach including science, technology, and innovation (STI) that can aid to the achievement of SDGS. The presentation and discussion are comprehensive on the state-of- the- art expertise, emerging issues, crucial knowledge, and product development processes of innovations as well as the "innovation ecosystem" which will facilitate the STI knowledge based for healthcare, agriculture, environment, education, media and furthermore.

Invited Speakers

Assoc. Prof. Dr. Jakrapong Kaewkhao

Assoc. Prof. Dr. Kazuki Nagashima

Assoc. Prof. Dr. Takao Yasui

Asst. Prof. Dr. Supakij Suttiruengwong

Asst. Prof. Dr. Teerakiat Kerdcharoen

SESSION B –
MATH STAT COMP FOR SDGS: SUSTAINABLE SOLUTIONS

MATH STAT COMP FOR SDGS: SUSTAINABLE SOLUTIONS
Chair: Assoc. Prof. Dr. Chartchai Leenawong
Co-Chair: Dr. Witchaya Rattanametawee
Co-Chair: Dr. Punnarai Siricharoen

This session welcomes all researchers in Mathematics, Statistics, Computer Science, and related fields to present and exchange their academic views on the latest and novel research findings. The session's theme is, but not limited to, using the aforementioned fields to serve as sustainable solutions for achieving the 17 Sustainable Development Goals set by the United Nations.

Invited Speakers

Assoc. Prof Dr. Kannapha Amaruchkul

Assoc. Prof. Dr. Teerapong Suksumran

Dr. Thittaporn Ganokratanaa

SESSION C -
PHYSICS FOR LIFE IN SPACE

PHYSICS FOR LIFE IN SPACE
Chair: Dr. Suparerk Aukkaravittayapun

Nowadays, human life obviously depends much on technologies and innovations, life on earth has been forced to adapt new changes in order to catch up and utilize the new technologies and innovations. Ideas of life in space colonies has also become more and more realistic with even more advanced developing technologies and innovations. Human life, in this case, not only depends on but hangs by technologies and innovations in all aspects, such as food, air, energy, medicine, safety, transportation, communication, etc. To realize such ambitious space exploration, Physics plays as an essential role of new technologies and innovations to support life in space. However, there are still many crucial unsolved problems involved Physics inevitably which needs to be overcome to realize and make life in extreme conditions possible and comfortable. This session welcomes presentations from a wide spectrum of Physics to address (but not limit to) the possible solutions to current & future problems or to understand the unknown for better human life on earth and in space.

Invited Speakers

Prof. Dr. David Ruffolo

Dr. Kitiyanee Asanok

Dr. Phongsatorn Saisutjarit

SESSION D - SDG CHALLENGES: CHEMICAL SOLUTIONS FOR SUSTAINABLE SOCIETY

SDG CHALLENGES:
CHEMICAL SOLUTIONS FOR SUSTAINABLE SOCIETY
Chair: Prof. Dr. Vudhichai Parasuk
Co-Chair: Prof. Dr. Sumrit Wacharasindhu
Co-Chair: Prof. Dr. Patchanita Thamyongkit
Co-Chair: Assoc. Prof. Dr. Siwaporn Meejoo Smith
Co-Chair: Assoc. Prof. Dr. Pattaraporn Kim

Global warming and climate change are the grand challenges of the century. Although chemicals and chemical products make a better living for humankinds, it is undeniable that production processes and themselves cause harm to our environments and health, besides the global warming. To cope with these stagnant problems, the United Nations has launched "the 17 Sustainable Development Goals (SDGs)" campaign and persuade nations to join this program. In response to the program, Thai government has devised the BCG model (B=Bioeconomy, C=Circular Economy, G=Green Economy) to plan the nation economy development. Chemists have put considerable efforts towards this direction and established a new direction called "Green Chemistry". Today, there are numerous publications in the area of Green and Sustainable Chemistry and the number is expanding. This implies the increasing importance of this field in chemistry. In the 47th International Congress on Science, Technology and Technology-based Innovation, presentations and discussions in the session "SDG Challenges: Chemical Solutions for Sustainable Society" will be focused in four following areas:

- Green Materials for Environmental Protection and Remediation
- Green Materials for Clean Energy
- Green Materials for CO_2 Utilization
- Green Chemical Processes

Invited Speakers

Prof. Dr. Xuechuan Hong

Assoc. Prof. Dr. Khamphee Phomphrai

Assoc. Prof. Dr. Rojana Pornprasertsuk

Assoc. Prof. Dr. Suwat Nanan

SESSION E1 - IMPACT OF BIOLOGICAL SCIENCE TOWARDS SDGS: ACTIVE LEARNING FOR BIOLOGICAL SCIENCE CLASSES

IMPACT OF BIOLOGICAL SCIENCE TOWARDS SDGS: ACTIVE LEARNING FOR BIOLOGICAL SCIENCE CLASSES
Chair: Asst. Prof. Dr. Noppadon Kitana
Co-Chair: Asst. Prof. Dr. Ekaphan Kraichak

With this era of learning, 21st century skills are important for this generation. Biological sciences is one of the basic disciplines for SDGs. Previously, biological science classes were full of contents and memorization. Do we still need contents in classes? How can we develop 21st century skills in our students? We would like to invite all instructors to share your experiences in active learning or other learning methodology that can develop the required skills and knowledge in biological sciences in all areas, from molecular biology through ecology.

Invited Speakers

Assoc. Prof. Dr. Nantana Gajaseni

Assoc. Prof. Dr. Teck Keong Seow

Asst. Prof. Dr. Pongchai Dumrongrojwatthana

SESSION E2 - IMPACT OF BIOLOGICAL SCIENCE TOWARDS SDGS: BIOLOGICAL SCIENCES TOWARDS SDGS

IMPACT OF BIOLOGICAL SCIENCE TOWARDS SDGS: BIOLOGICAL SCIENCES TOWARDS SDGS
Chair: Prof. Dr. Chanpen Chanchao
Co-Chair: Prof. Dr. Supachitra Chadchawan

In order to reach SDGs, biological sciences research is one of the important pieces. The studies of life sciences in all disciplines and taxa are welcome to share your recent discovery in this conference. These include the researches in microbes, protozoans, plants, animals and human from molecular, cell, whole organism, and population through ecological system levels.

Invited Speakers

Prof. Dr. Atsuo Kimura

Prof. Dr. Preecha Phuwapraisirisan

SYMPOSIUM A

ACCELERATION OF SUSTAINABILITY TOWARDS BIOBASED TECHNOLOGICAL PLATFORM DEVELOPMENT
Chair: Prof. Dr. Nuttha Thongchul
Co-Chair: Assoc. Prof. Dr. Suwattana Pruksasri
Co-Chair: Dr. Siwaruk Siwamogsatham

As worldwide goals, the Sustainable Development Goals (SDGs) deliver a powerful determination for improving our planet. Fulfilling the SDG targets will take an unprecedented effort by all sectors in society. Recently, exploring the pathways to producing fuels and platform chemicals from sustainable feedstocks has attracted increased interest from researchers to entrepreneurs. With SDGs tools, future fuels and chemicals will be most likely produced from sustainable feedstocks. Renewable biomass including agricultural residues, municipal wastes, and industrial wastes is considered to be the sustainable resource with the potential to deliver renewable fuels and bio-based chemicals. In the past decade, research has been focusing on development of technologies to produce drop-in fuels/chemicals which could be used “as is” to substitute for conventional petroleum-derived fuels/chemicals. Bio-based functional replacement chemicals and novel products are promising new area of interest to academia and industry. This symposium aims to feature the current advancements in sustainable fuels/chemicals and identify the challenges in developing the novel conversion technologies via biological and/or chemical related pathways. All papers from both academia and industry relevant to novel sustainable product development and conversion technologies are invited. The topics include but are not limited to:

1. Biological or chemical production of drop-in bio-based fuels/chemicals from biomass;
2. Biological or chemical production of bio-based chemicals with functional replacement of the petroleum-derived products;
3. Biological or chemical production of novel products;
4. Drop-in or novel chemicals produced from other carbon feedstocks including municipal wastes, food wastes, waste fats/oils and other non-food/feed and renewable feedstocks

Invited Speakers

Prof. Dr. rer. Nat. Hesham A. El Enshasy

Dr. Thana Sornchamni

Dr. Lalintip Hocharoen

SYMPOSIUM B

CHALLENGES OF QUANTUM SCIENCE AND TECHNOLOGY TOWARDS SUSTAINABLE DEVELOPMENTS
Chair: Assoc. Prof. Dr. Anucha Watcharapasorn
Co-Chair: Asst. Prof. Dr. Narupon Chattrapiban
Co-Chair: Asst. Prof. Dr. Sujin Suwanna
Co-Chair: Dr. Pimonpan Sompet
Co-Chair: Dr. Nithiwadee Thaicharoen
Co-Chair: Dr. Nuttachai Jutong

As the world moves forward to achieve sustainable developments, how Quantum Science and Technology can help pave the way to attain these goals is certainly a great challenge. It has recently become apparent that with worldwide academic and research collaboration, the transition from basic quantum research to commercial applications will create the next generation of disruptive technologies that will impact local and global societies in various aspects. This symposium aims to introduce advances in quantum science and technologies that provide better solutions to grand challenges in such fields as energy, health, security and environment. Based on “superposition”, a property from which objects can be in different states at the same time, and “entanglement”, where they can be inherently correlated without any direct physical interaction, Quantum Mechanics can be implemented in a wide range of applications. For example, quantum computation can provide a breakthrough in the design of new chemical processes, new materials and medical drugs, new paradigms in machine learning and artificial intelligence. With the effects of quantum entanglement, data can be completely and securely protected within the network and in long-range communication. Quantum technologies will also give rise to clocks and sensors with unmatched sensitivity and accuracy, with potential impact in navigation, synchronization of future smart networks and medical diagnostics.
Potential Topics > All contributed presentations and papers from academia, research institutes, private sectors and industries are welcome. The symposium aims to cover the following (but not limited to) topics in theory, simulation and experiment: Quantum computation, including quantum simulation, quantum computing software and algorithms, quantum control, quantum machine learning, Quantum materials science, including quantum engineering, Quantum metrology, sensing and imaging, Quantum communication, including quantum network, cryptography, quantum key distribution, quantum internet, Quantum information, Foundation of quantum theory, including measurement theory, quantum trajectories, quantum stochastic process, Applications of quantum in fields such as economics, finance, and other sciences

Invited Speakers

Prof. Dr. Rodney Van Meter

Asst. Prof. Dr. Nirpendra Singh

Dr. Ivan Rungger

Dr. Pimonpan Sompet

Dr. Tanapoom Poomaradee

Dr. Thiparat Chotibut

SYMPOSIUM C

CONSERVATION AND RESTORATION IN A CHANGING WORLD
Chair: Prof. Dr. Suchana Chavanich
Co-Chair: Dr. Nontivich Tandavanitj

Our environment has been threated and impacted globally by anthropogenic activities, and the impacts are predicted to worsen in the next decade. How can we reimage conservation in our rapidly changing world? What are the key knowledge gaps that must be urgently addressed for a better conservation ? What are the challenges for conservation and restoration of the ecosystems ? This session welcomes presentations on both basic and advanced research topics related to conservation and restoration of the ecosystems including but not limited to novel tools and technological innovations, successful approaches and insightful lessons, engagement and participation of communities, and transdisciplinary collaborations.

Invited Speakers

Dr. Dominic Thomson

Dr. Kentaro Ando

Dr. Siriporn Sriaram

SYMPOSIUM D

CRYSTALLOGRAPHY
Chair: Prof. Dr. Nongnuj Muangsin
Co-Chair: Assoc. Prof. Dr. Kuakarun Krusong
Co-Chair: Asst. Prof. Dr. Kittipong Chainok

X-ray crystallography is the experimental science and is by far the most powerful method to determine the arrangement of atoms of a crystalline solid in three-dimensional space. This method has been used in structural chemistry and biological macromolecules for over a century. In the biological crystallography, three-dimensional structures of molecules such as proteins and nucleic acids are determined at atomic level. This helps us to understand the basic mechanisms of biomolecules, as well as aid in novel drug discovery. In chemical crystallography, the determination of crystal structures of organic, organometallic and coordination compounds (i.e. coordination polymers and metal-organic frameworks) is of great importance and highly valuable for understanding the structure-property relationship as well as supramolecular interactions (such as hydrogen bonds, halogen bonds, and π–π stacking) of the crystalline solids. Moreover, it also brings about crystal engineering for better structural design and achievement of desired functionalities.

Invited Speakers

Dr. Kanokwan Kongpatpanich

Dr. Min Fey Chek

SYMPOSIUM E

ENVIRONMENTAL (ECOLOGICAL) IMPACT OF MICROPLASTICS AND TECHNOLOGICAL POTENTIAL FOR MICROPLASTIC WASTE
Chair: Assoc. Prof. Dr. Taeng On Prommi
Co-Chair: Asst. Prof. Dr. Akekawat Viteepradit
Co-Chair: Asst. Prof. Dr. Orawan Chunhachart
Co-Chair: Asst. Prof. Dr. Kamontip Kuttiyawong

An increasingly serious and widespread problem of microplastics in ecosystem and impacts on food chains, the particular challenge and perspective of the smart technology can play a vital role in microplastic pollution crisis. The symposium aims to bring together leading academic scientists, researchers and research scholars to exchange and share their experiences and research results on all aspects of microplastic and its impacts and potential technology to eliminate microplastic waste and reduce microplastic pollution. The symposium focused on four themes:

- Monitoring and detection of microplastics in the environment
- Impacts of microplastic pollution on animal and human health
- Plastic waste management, recovery and conversion
- Smart technology for microplastic waste management
- Biotechnological approach for biodegradable of plastic

SYMPOSIUM F

FOREST BIODIVERSITY, CLIMATE CHANGE, AND SUSTAINABLE USE FOR SAVING LIFE ON EARTH
Chair: Asst. Prof. Dr. Oraphan Sungkajanttranon
Co-Chair: Asst. Prof. Dr. Sravut Klorvuttimontara
Co-Chair: Dr. Patchanee Vichitbandha

Human needs everything for living in daily life from nature. Biodiversity and ecosystem service are important and must be used carefully for sustaining life on earth. Human activities and climate change are the major causes effected to living things and livelihoods of people. These also play an important role in transmissible diseases between animals and humans. Forest Ecology and biodiversity are important and play a major role in the fight against climate change. People need forest products and services, but the forests should not be deforested or changing by desertification. We should talk together about vegetation, wildlife, insect, fungi, microorganisms, software and predict models, medicines, and products from the forest research. Let's lighten and forced the ideas for helping and saving life on earth together and to the next generation.

Invited Speakers

Dr. Jantrararuk Tovaranone

Mr. Alistair Monument

Mr. Oh Cheow Sheng

SYMPOSIUM G

HOW CHEMISTRY CAN RESOLVE FOR COVID-19 PANDEMIC
Chair: Prof. Dr. Orawon Chailapakul
Co-Chair: Dr. Sudkate Chaiyo

Recently, Coronavirus disease (COVID-19) is emerging as a global pandemic caused by severe acute respiratory syndrome coronavirus 2 (SARS-CoV-2). Globally, as of now, there have been about a billion confirmed cases, including 2 million deaths, reported to WHO. Due to the pandemic's current situation, knowledge and infection prevention have been continuously observed and developed. Chemistry also provides their essential contribution to the global fight against this outbreak. An understanding of viral structure to the isolation of vaccines as well as the development of materials and methods for diagnostic is played as a crucial role for chemistry area to tackle the covid-19 situation. This session aims to highlight cutting-edge chemical science research, including characterizing virus structure and mechanism of infection, novel compounds and their mechanism to inhibit virus structure for the treatment of COVID-19, advanced biosensing technologies for the rapid diagnosis of COVID-19, and other related. This will be achieved by taking the exploitation of a multidisciplinary approach. We hope this session will provide an opportunity for bringing together the chemists to help tackle the pandemic outbreak so as to open up new possibilities with practical use.

Invited Speakers

Prof. Dr. Charles S. Henry

Prof. Dr. Tanapat Palaga

Dr. Kittikhun Wangkanont

Dr. Sudkate Chaiyo

SYMPOSIUM H

METAL-ORGANIC COMPOSITES IN MATERIAL SCIENCE
Chair: Prof. Dr. Takiumi Konno
Co-Chair: Assoc. Prof. Dr. Preeyanuch Sangtrirutnugul
Co-Chair: Dr. Thanthapatra Bunchuay

The design and creation of metal-organic composite materials have been an important research subject in material science due to the synergistic functionalities arising from organic and inorganic components. Most of this class of materials involve the direct contacts between metallic elements and organic parts in a microscopic revel, which are well described as coordination bonds. Therefore, the profound understanding of the structures and functionalities of metal-organic composite materials based mainly on coordination chemistry is necessary for future development of material science. This session will focus on the design, structures, and functionalities of metal-organic composite materials that involve coordination compounds. We welcome papers discussing the molecular and solid structures containing metal centers, which lead to attractive solid-state functionalities, such as adsorption of molecules, dielectric properties, conducting and transporting phenomenon, catalytic activities, and photophysical properties.

Invited Speakers

Prof. Dr. Yi-Chou Tsai

Assoc. Prof. Dr. Phimphaka Harding

Dr. Yun Zong

SYMPOSIUM I

PREMIUM AGRICULTURE: A PATHWAY TOWARD SUSTAINABLE AND INCLUSIVE BCG ECONOMY MODEL

Chair: Dr. Worajit Setthapun
Co-Chair: Assoc. Prof. Dr. Poonpat Poonnoy
Co-Chair: Dr. Soracha Dechaumphai
Co-Chair: Asst. Prof. Dr. Pongsathorn Dechatiwongse

Bio-Circular-Green (BCG) Economy Model was conceptualized and promoted by the Thai government as a strategy to drive economic and social development. The model not only capitalizes strengths in robust agricultural activities in Thailand, but it also embraces different social and economic contexts in other countries that also aspire for an inclusive and sustainable growth. Bioeconomy, or bio-based economy, refers to the use and production of renewable biological resources especially in food, medical, and bioenergy sectors. Circular economy is based on the principles of reusing and recycling resources, extending product lifespan, and relocating waste efficiently. Green economy aims at an ultimate goal of sustainable development in a low carbon, resource efficient, and environmental-friendly society. Practically, the model conforms with the UN Sustainable Development Goals (SDGs) with an alignment in at least four goals: Goal 7 clean and affordable energy, Goal 11 sustainable cities and communities, Goal 12 responsible consumption and production, and Goal 13 climate action. Sustainability and inclusivity are essential factors of the BCG Economy Model to engage key stakeholders which will eventually create growth of local and global business opportunities, rate of employment, and countries' GDP. In particular, this session focuses on the way to develop the premium agriculture scheme as a part of the BCG Economy Model to upgrade the practices and product quality in the agricultural sector. Agricultural sector has been a basis for the economic and social development in Thailand so far, and it can serve as a good starting point of the discussion which can be further extended to other areas within BCG Economy, including food; medical and wellness; bioenergy, biomaterial and biochemical; and tourism and creative economy. Findings based on scientific research and technological development presented in this session will encourage an international collective effort of promoting the sustainable and inclusive growth through the concrete idea of the BCG Economy Model.

Invited Speakers

Asst. Prof. Dr. Suvaluk Asavasanti

Dr. Chai Lay Ching

Dr. Korsak Towantakavanit

Mr. Alan Dronkers

SYMPOSIUM J

SUSTAINABLE HYDROGEN PRODUCTION FOR GREENER ENVIRONMENT AND CHEMICAL PRODUCTS
Chair: Prof. Dr. Suttichai Assabumrungrat
Co-Chair: Assoc. Prof. Dr. Pattaraporn Kim- Lohsoontorn
Co-Chair: Assoc. Prof. Dr. Suwimol Wongsakulphasatch

The global hydrogen demand is found to continuously increase each year with the market value at hundreds of billions of dollars per year. Hydrogen can be used safely for a wide range of applications, i.e., in food, metal, glass and chemical industries. In addition, according to energy crisis and environmental concern, hydrogen is considered as a straightforward solution to issues related pollution and global warming. Hydrogen has been driven to become one of alternative energy carriers as well as used in carbon dioxide conversion to higher-valued products. To meet the requirement of global demand, technologies to produce hydrogen are therefore essential and is considered as significance. This conference session on "Sustainable Hydrogen Production for Greener Environment and Chemical Products" aims to gather outstanding researches and the comprehensive coverage of all aspects related to the hydrogen production technology for greener environment and chemical products. This session will bring together high-quality research on the different aspects of hydrogen production technology including current status and remaining challenges. Topics include, but not are limited to:

- Hydrogen production technologies, including chemical, electrochemical and biological processes
- Theoretical and experimental investigation for hydrogen production process design
- Integrated process development relating to the production of hydrogen and its utilization
- Hydrogen in CO_2 conversion to higher-valued products

Keynote and Invited Speakers

Prof. Dr. Joongmyeon Bae

Prof. Dr. Sibudjing Kawi

Mr. Piyabut Charuphen

Dr. Sakhon Ratchahad

Dr. Jon Powell

SYMPOSIUM K

SUSTAINABLE USE OF MARINE BIODIVERSITY
Chair: Assoc. Prof. Dr. Thamasak Yeemin
Co-Chair: Asst. Prof. Dr. Suchai Worachananant
Co-Chair: Asst. Prof. Dr. Makamas Sutthacheep

Marine biodiversity is comprised of several levels of organizations, from the genetic variability, to the species, populations, communities, and ecosystems. Over three billion people around the world depend on marine biodiversity for food and income, particularly fishing, mariculture and tourism. However, coastal and marine ecosystems have been greatly disturbed by over-exploitation of natural resources, habitat loss, pollution and climate change. In order to restore and conserve marine ecosystems, the sustainable use of marine biodiversity, from the shore to the deep sea, including coastal and offshore environments, is one of the key solutions for sustainable development. In this symposium, scientists and managers working in Thailand and other countries are invited to exchange their experiences in research, management, monitor and conservation aspects, focusing on sustainable use of marine resources. Some case studies from ecosystem services of sandy beach, mangrove, seagrass bed and coral reef ecosystems will be highlighted. The symposium will also cover the topics in ecotourism, capacity enhancement for monitoring and research, community-based management and marine protected areas.

Invited Speakers

Prof. Dr. Janny Dirk Kusen

Dr. Maria Vanessa Baria-Rodriguez

Dr. Abe Woo Sau Pinn

SYMPOSIUM L

THE SUSTAINABLE TOURISM REVIEW IN A POST-PANDEMIC 2022: REBUILDING TOURISM TO SUSTAINABILITY
Chair: Dr. Chainarong Srirak
Co-Chair: Dr. Gina B. Alcoriza
Co-Chair: Dr. Piyapong Ketpiyarat
Co-Chair: Ms. Patthaphon Sukjai

Covid-19 has disrupted tourism, hospitality, and leisure worldwide. It has also provided some space for academics, industry, and policy makers to think again about what tourism, hospitality and leisure are for, who they are for, and how they might be reconsidered as we transition into a post-pandemic future. The purpose of this symposium series is therefore to ask some big questions about what tourism, hospitality and leisure stand for in the post-pandemic world. Their purpose has long been understood as going far beyond simply offering satisfying experiences for their customers to generate incomes for the organizations involved. The sectors are widely understood to be integrally involved in contributing to sustainable development in the long term but what is their role in securing reliance in the short-term? How might all three sectors be involved in attempting to enrich communities and achieve local economic development? What is their role in providing health and wellbeing benefits, and how can this role be better harnessed? How are three sectors to work more closely together in a post-pandemic world? These and other major questions for the tourism, hospitality and leisure sectors in the post-pandemic age will be considered. Furthermore, the discussion panel also highlights the role of local communities and its leadership role for enhancement of sustainable tourism, thus how sustainable tourism could affect on wellbeing of local community under the shadow of SDG 1, 3 and 4. Similarly, the panel also discusses the role of sustainable logistics in tourism sector, which is beneficial for environmental sustainability.

Invited Speakers

Prof. Dr. Noel Scott

Assoc. Prof. Dr. Ann Suwaree Ashton

Dr. Robert C. Sinclair

Dr. Gina B. Alcoriza

SYMPOSIUM M

TUBERCULOSIS: OLD DISEASE, NEW APPROACHES
Chair: Assoc. Prof. Dr. Roderick Bates
Co-Chair: Assoc. Prof. Dr. Pornpan Pungpo

Tuberculosis (TB), caused by Mycobacterium tuberculosis, is a serious disease that claims more than one million lives each year. In addition, one third of the world's population is likely to be infected with the latent form of TB. The continuing challenge of TB is made greater for two reasons. The first is the appearance of drug-resistant strains. The second is that TB is likely to increase susceptibility to covid-19, and possibly vice-versa. Despite the seriousness of TB, most of the drugs currently used were developed decades ago and typically suffer from the disadvantage of requiring a very long treatment time to truly eliminate the bacterium. This symposium on "Tuberculosis: old disease, new approaches" will bring together aims three researchers who are using cutting edge tools such as structural biology and computational design to create new drugs that will be effective against this remarkably challenging bacterium. The session will also include presentations by students working on diverse projects in this critical area.

Invited Speakers

Prof. Dr. Aasheesh Srivastava

Prof. Dr. Gerhard Grüber

Assoc. Prof. Dr. Pornpan Pungpo

SYMPOSIUM N

SOLUTIONS FOR TOMORROW: DOW SUSTAINABILITY TO TACKLE WORLD CHANGE

Chair: Ms. Kanchana Un-Arom (Site Analytical & Quality Leader)

Co-Chair: Mr. Nattapong Jirawattanaworakul (Site Public Affairs Leader)

Co-Chair: Dr. Soparat Yudthavorasit (Senior Analytical Specialist)

Sponsored by Dow

Dow is the world's leading materials science company with an ambition to become the most innovative, customer centric, inclusive and sustainable. Dow's portfolio of plastics, industrial intermediates, coatings and silicones businesses delivers a broad range of differentiated science-based products and solutions for its customers in high-growth market segments, such as packaging, infrastructure, mobility and consumer care. Dow was founded in 1897 by Herbert Henry Dow and has started its business in Thailand since 1970, then expanded through a joint venture with SCG in 1987. Dow has started its sustainability journey in 1995 and growing our commitment overtime. Currently, Dow is embarking on the third stage of sustainability journey by rethinking business model and collaborating to grow impact. Dow sustainability targets in this stage are to 'Protect the climate, Stop the waste and Close the loop' focusing on carbon neutrality, circular economy/recycling, climate protection and safer material use. People and new science-and technology-based solutions become a key factor to tackle the sustainability challenges. In Thailand, Dow has various initiatives to tackle world challenges for sustainability, such as Public-Private Partnership for Plastics and Waste Management (PPP Plastics), Recycled Plastic Road, Dow for Sustainable Industry, International Coastal Clean-up and Dow Chemistry Classroom, ect. In this session, Dow aims to share and demonstrate actions to solve the sustainability world challenges. Innovation or research on topics related to Dow's focuses from academic and industrial sector are very welcome.

Invited Speakers

Dr. Jens Schmidt

Mr. Loganathan Ravisanker

Ms. Chompoonuch Junbua

Mr. Rangsun Chaosuwannakij

Dr. Thawatchai Tungkavet

Mr. Anurak Rassameeamornwiwat

SYMPOSIUM O

SYMPOSIUM ON SCIENCE EDUCATION FOR SUSTAINABILITY - LITERACY FOR ALL
Chair: Dr. Ganigar Chen
Co-Chair: Asst. Prof. Dr. Supakorn Boonyuen
Co-Chair: Asst. Prof. Dr. Watcharee Ketpichainarong
Co-Chair: Asst. Prof. Dr. Chanyah Dahsah

Education is a crucial element for preparing citizen to approach toward the Sustainable Development Goals. Particularly, scientific literacy is the cornerstone of SDG awareness and action. This symposium aims to be an effective platform for research communication among educators and researchers whose working on the interaction between science education and sustainable development by sharing best practice and carrying dialogue. The special attention will be paid to SDG3: Good Health and well-being, SDG6: Clean Water and Sanitation, SDG10 Sustainable cities and community, SDG12: Responsible Consumption and Production and SDG13: Climate Action but other topics linked science education to other SDGs also welcomed. The symposium is open for all levels (from kinder garden to vocational) and any styles (whether formal or informal or anything in between) of education.

Invited Speakers

Prof. Dr. Yoshito Ando

Ms. Ruetai Chongsrid

SYMPOSIUM P

SUSTAINABLE FOOD SYSTEMS FOR GOOD HEALTH AND WELL-BEING
Chair: Assoc. Prof. Dr. Chaleeda Borompichaichartkul
Co-Chair: Assoc. Prof. Dr. Cheunjit Prakitchaiwattana
Co-Chair: Assoc. Prof. Dr. Kitipong Assatarakul

The occurrence of coronavirus disease (COVID-19) pandemic leads to changes of lifestyle and working system, moreover it causes a high impact on a falling of world economy. Health and well-being problems are increased in attention markedly due to impact of COVID-19. Along with the occurrence of pandemic, according to WHO, about 690 million people were undernourished at the end of 2019 and absent rapid interventions, the COVID-19 pandemic could force an additional 130 million people into chronic hunger. Poor nutrition causes 45 per cent of deaths in children under five – 3.1 million children each year. Limitation of transportation during pandemic leads to food losses. Each year, an estimated one third of all food produced ends up rotting in the bins of consumers and retailers, or spoiling due to poor transportation and harvesting practices. Sustainable food systems support adequate nutrition, which helps people of all ages to achieve good health. Rebuilding our food systems to make them more sustainable, productive and resilient is essential--for solving long-term hunger challenges and managing acute shocks, like disease outbreaks and climate extremes. Sustainable food systems reduce waste and spoilage, and empower consumers to make smart choices in their food shopping and other innovations, sustainable food systems can deliver widespread benefits to people and plane. This session of "Sustainable Food Systems for Good Health and Well-being" opens for these following areas: Food cultivation and postharvest, Food processing and engineering, Food packaging and quality control, Product development of healthy and functional foods and ingredients, Zero waste in food systems and Food Logistic and supply chain.

Invited Speakers

Prof. Dr. Paola Pittia

Prof. Dr. Richard Archer

Asst. Prof. Dr. Akkharawit Kanchana-opas

Dr. Lalana Thiranusornkit

SYMPOSIUM Q

ADVANCE IN SCIENCE AND TECHNOLOGY TO ACCELERATE DECARBONIZATION FOR INDUSTRIES
Chair: Dr. Sumate Chareonchaidet
Co-Chair: Dr. Jirut Wattoom

Sponsored by SCG

New high records of temperature have been reported in news around the world recently. It is the real and direct impact of the global warming issue. World leaders have agreed to limit global warming to 2°C above pre-industrial temperature – the goal of the Paris Climate Agreement. Carbon emission is one of the key contributions to this problem and there are many actions that need to do in order to reach the goal. Adopting new technologies is also an option to accelerate the decarbonization pathway. SCG has already committed to becoming a net-zero carbon company by 2050. We are not only focused on implement available technologies but put tremendous effort into the science community to develop a more effective decarbonization innovation. We aim to foster the cooperation between academics and industries to develop new technology to bring Thailand to be net-zero carbon country in the near future. This symposium on "Advance in Science and Technology to Accelerate Decarbonization for Industries" aims to gather outstanding researches and implementation in the industries coverage of all aspects related to renewable energy, energy storage, carbon capture, storage, and utilization. This symposium will bring together high-quality research on the different aspects of decarbonization technology including current status and remaining challenges. Topics include, but not are limited to: Renewable energy, energy transition, energy storage and electrification, Carbon capture and utilization to new materials and chemicals and Integrated process development relating to the reducing carbon emission in heavy industries.

Invited Speakers

Prof. Dr. Nannan Sun

Prof. Dr. Edman Tsang

Representative from CAS ICCB

SYMPOSIUM R

GREEN AND SUSTAINABLE CHEMISTRY: OPPORTUNITIES FOR ACADEMIA AND INDUSTRY
Chair: Prof. Dr. Joseph S.M. Samec
Co-Chair: Asst. Prof. Dr. Duangamol Tungasmita

Even if climate change may not stop us from using fossil fuels, the supply will within 50 years according to BP:s latest report (https://www.bp.com/content/dam/bp/business-sites/en/global/corporate/pdfs/energy-economics/statistical-review/bp-stats-review-2019-full-report.pdf). Thus, we will need to find a new feedstock for our needs for producing chemicals for: food-, material-, transportation-, pharmaceutical production. The non-eatable part of biomass, lignocellulose is such a source that grows widely in both agriculture (stems, husks, etc) and in forestry. In addition to this, chemists will need to build up fundamental understanding and develop new methodologies and processes. This symposium will discuss how academia and industry can collaborate to smoothen this transition and welcomes papers regarding topics on Green and Sustainable Chemistry: -from fundamental studies to industrial implementations.

Invited Speakers

Prof. Dr. Adam Slabon

SYMPOSIUM S

RECENT ADVANCES IN SYNTHETIC BIOLOGY AND GENOME EDITING (WEBINAR)

Chair: Dr. Verawat Champreeda

Synthetic biology plays a crucial role in bio-industry where cell factories convert a range of raw materials to a variety of products, including biofuels, biochemicals, biopolymers, and specialty functional compounds. Capability of living organisms on biotechnological application can be enhanced by using synthetic biology to improve their ability to use a wider range of substrates from 1st Gen (sugar & starch), 2nd Gen (cellulosics) and CO_2, to synthesize new products, or make it tolerate to stressed operational conditions as well as to create new non-natural functionality. Genetic modification has been facilitated by the discovery of the CRISPR/Cas system, which leads to establishment of an efficient molecular tool for editing genomes of living organisms for desirable traits of interests. With the rapid development in omics technology and computational data analysis, synthetic biology is moving at a higher speed towards the design of cell factories with higher performances for target applications. These integrations of frontier technologies and knowledge advancement in recent years provide a platform for accelerating the scientist's capability on creating new organisms with desirable properties for the new era of biotechnology. In this session, the seminar will cover frontier researches in the field of synthetic biology in various model organisms by leading scientists. The topics cover the study on genetic code expansion for reprogramming translational machineries in mammalian cells, design and engineering of yeast cell factories for production of bio-based chemicals, and bioengineering of the bacterial membrane vesicles for biomedical applications. The webinar will give examples of inspired researches in synthetic biology for researchers working in this field.

Invited Speakers

Dr. Chayasith Uttamapinant

Dr. Wanatchaporn Arunmanee

Dr. Weerawat Runguphan

ABSTRACTS FOR INVITED SPEAKERS

INVITED SPEAKER: A_INV001

INTERNET OF THINGS FROM FARM TO FORK

Teerakiat Kerdcharoen*

Department of Physics, Faculty of Science, Mahidol University
*e-mail: teerakiat.ker@mahidol.ac.th

Abstract:
TBA

INVITED SPEAKER: A_INV002

NANOWIRE MICROFLUIDICS FOR EARLY DISEASE DIAGNOSIS

Takao Yasui[1-3,*]

[1] Department of Biomolecular Engineering, Graduate School of Engineering, Nagoya University
[2] Institute of Nano-Life-Systems, Institutes of Innovation for Future Society, Nagoya University
[3] Japan Science and Technology Agency (JST), PRESTO

*e-mail: yasui@chembio.nagoya-u.ac.jp

Abstract:

Analyzing microRNAs (miRNAs) within urine extracellular vesicles is important for realizing miRNA-based, simple and non-invasive early disease diagnoses and timely medical checkups. The urinary miRNA species differ in healthy and cancer groups of people, and they represent a warning sign for various cancer scenarios. However, the inherent difficulty in collecting dilute EVs from urine has hindered the development of such diagnoses and medical checkups. We propose a device composed of nanowire-integrated microfluidic device, which enables highly efficient EV collections and *in-situ* extraction of huge numbers of miRNAs to exceed the extraction numbers of the conventional ultracentrifugation method[1-3]. The mechanical stability of nanowires anchored into substrates during buffer flow and the electrostatic collection of EVs onto the nanowires are the two key mechanisms ensuring the success of the present device. We utilize our method to discover the numbers of potentially cancer-related miRNAs in urine. These urinary miRNAs would also act as miRNA groups for classifying cancer-related regulations. We also successfully identify miRNA groups in urine through a combination of nanowire-based miRNA extraction and machine learning-based analysis; the groups allow detection and localization of cancer. The machine learning-based analysis identified miRNA groups from almost all human miRNAs. The groups consisting of ~50 miRNA species could classify cancer and non-cancer subjects with high accuracy, sensitivity, and specificity. We expect these miRNA groups in urine will open a new era for work towards urine-based liquid biopsy. And the present device concept will be a foundation for work towards the long-term goal of urine-based early diagnoses and medical checkups of diseases.

1. T. Yasui, T. Yanagida, S. Ito, Y. Konakade, D. Takeshita, T. Naganawa, K. Nagashima, T. Shimada, N. Kaji, Y. Nakamura, I. A. Thiodorus, Y. He, S. Rahong, M. Kanai, H. Yukawa, T. Ochiya, T. Kawai and Y. Baba, *Sci. Adv.*, 2017, **3**, e1701133.
2. T. Suwatthanarak, I. A. Thiodorus, M. Tanaka, T. Shimada, D. Takeshita, T. Yasui, Y. Baba and M. Okochi, *Lab Chip*, 2021, **21**, 597-607.
3. T. Yasui, P. Paisrisarn, T. Yanagida, Y. Konakade, Y. Nakamura, K. Nagashima, M. Musa, I. A. Thiodorus, H. Takahashi, T. Naganawa, T. Shimada, N. Kaji, T. Ochiya, T. Kawai and Y. Baba, *Biosens. Bioelectron.*, 2021, in press.

INVITED SPEAKER: A_INV003

DIRECTING CHEMICAL REACTION PATHWAY ON NANOSTRUCTURED METAL OXIDE SURFACE FOR MOLECULAR SENSING APPLICATION

Kazuki Nagashima,[1,2*] Takuro Hosomi,[1,2] Jiangyang Liu,[1] Guozhu Zhang,[1] Masaki Kanai,[3] Tsunaki Takahashi,[1,2] Takeshi Yanagida[1,3]

[1] Department of Applied Chemistry, Graduate School of Engineering, The University of Tokyo, 7-3-1 Hongo, Bunkyo-ku, Tokyo, 113-8656, Japan
[2] Japan Science and Technology Agency (JST), PRESTO, 4-1-8 Honcho, Kawaguchi, Saitama, 332-0012, Japan
[3] Institute for Materials Chemistry and Engineering, Kyushu University, 6-1 Kasuga-Koen, Kasuga, Fukuoka, 816-8580, Japan
*e-mail: kazu-n@g.ecc.u-tokyo.ac.jp

Abstract:

Nanostructured metal oxides are prevailed materials for catalysts and molecular sensors due to their thermal/chemical robustness, which allow us to apply them for long-term used applications. An important challenge in these research fields is to direct the surface chemical reaction for realizing the desired chemical processes, however it has been restricted due to difficulty to understand the complex nature of metal oxide nanostructured surface. To overcome such limitation, we developed a platform based on metal oxide nanowire array for investigating the surface molecular behaviors on metal oxide. We fabricated the metal oxide nanowires with well-defined crystal facets and large surface area by designing their self-assembling process and used them to amplify the signals in spectrometric and spectroscopic analyses by concentrating the surface-adsorbed molecules. Such nanowire based analytical platform successfully demonstrated the impact of cation state on surface molecular behaviors and offered a rational strategy to direct the surface chemical reaction pathway. By employing organic and inorganic surface modifications, we successfully designed the surface cation state of metal oxide nanowires and suppressed the detrimental dimerization reaction of volatile carbonyl compounds. The directed chemical reaction pathway led to the fast recovery and the low temperature operation in molecular sensing device even without assistance of noble metal catalyst.

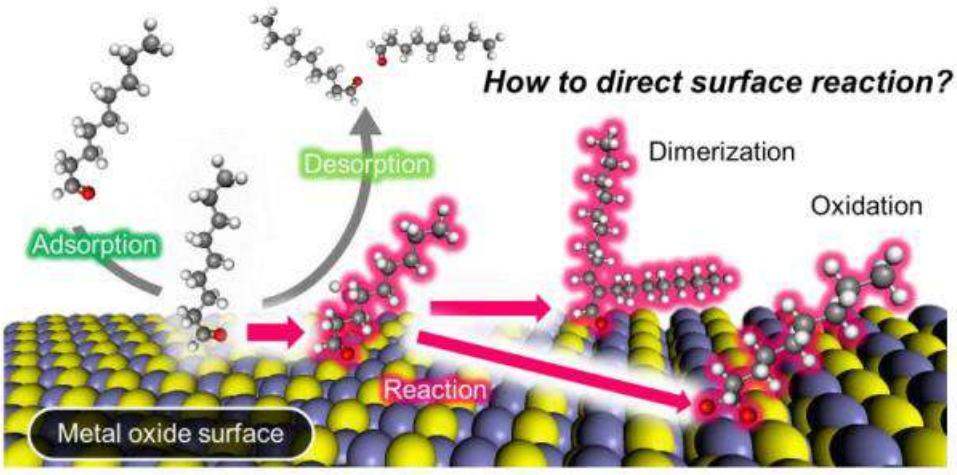

Figure.

INVITED SPEAKER: A_INV004

GLASS: FROM BASIC TO ADVANCED MATERIALS FOR INNOVATIVE LIFE

Jakrapong Kaewkhao[1,*]

[1]Center of Excellence in Glass Technology and Materials Science, Nakhon Pathom Rajabhat University, Nakhon Pathom, Thailand, 73000
*e-mail: jakrapong@webmail.npru.ac.th

Abstract:

Glass is an innovative material that has several of applications. Glass is an important component of many products in everyday life. Conventional and Innovative life is always be with glass material. In this talk, basic and advanced materials of glass will be explained. Several application for innovative life and impacted of human behavior be addressed. Moreover, advanced glass researches from Glass-Lab in Nakhon Pathom Rajabhat University are also demonstrated.

INVITED SPEAKER: A_INV005

INNOVATOR'S TOOLKIT

Supakij Suttiruengwong*

Department of Materials Science and Engineering, Faculty of Engineering and Industrial Technology, Silpakorn University
*e-mail: Suttiruengwong _S@su.ac.th

Abstract:
TBA

INVITED SPEAKER: B_INV001

Multi-Objective Land-Water Allocation Model for Sustainable Agriculture with Predictive Stochastic Yield Response

Kannapha Amaruchkul*

Graduate School of Applied Statistics, National Institute of Development Administration (NIDA),
118 Serithai Rd., Bangkapi, Bangkok 10240, Thailand
*e-mail: kamaruchkul@gmail.com

Abstract:

Consider an agricultural land-water resource allocation problem, in which yields are spatial dependent and stochastically correlated. To achieve sustainability, we formulate a multi-objective optimization problem, in which the decision maker determines the cultivation areas and the supplemental irrigation water levels at different locations, with social, economic and environmental goals in mind. For the social goal, we minimize the root mean squared difference of incomes among locations. For the economic goal, we minimize the production risk. We show that minimizing production risk is equivalent to maximizing the service level, when demand is normally distributed. For the environmental goal, we minimize the resource utilization. Assume that the yield vector at different locations follows a multivariate normal distribution. We formulate the multi-objective optimization problem using a weight global criterion method, and we provide a sufficient condition for convex quadratic programming. We demonstrate the applicability of our proposed framework in the case study of sugarcane production in Thailand. To capture yield response to water, we propose several models including linear and nonlinear regressions, and we obtain the closed-form expression for the linear and probit yield response models. The numerical experiment reveals that our solution significantly improves the social and economic goals, compared to the current policy. Finally, we illustrate how to apply our model to quantify the monetary value from reducing yield variability, which could be resulted from smart irrigation or precision agriculture.

INVITED SPEAKER: B_INV002

THE GEOMETRY OF N-DIMENSIONAL EINSTEIN GYROGROUP VIA KLEIN'S APPROACH

Teerapong Suksumran*

Department of Mathematics, Faculty of Science, Chiang Mai University, Chiang Mai, Thailand
*e-mail: teerapong.suksumran@cmu.ac.th

Abstract:

Einstein addition of relativistically admissible velocities in special relativity leads to the notion of a gyrogroup in mathematics. Roughly speaking, "gyrogroup" is a name for a peculiar mathematical structure consisting of one non-empty set and one non-associative binary operation. For example, the *n*-dimensional Einstein gyrogroup consists of the open unit ball $\mathbb{B} = \{\mathbf{v} \in \Upsilon^n : ||\mathbf{v}|| < 1\}$, together with Einstein addition $\oplus_E$ given by

$$\mathbf{u} \oplus_E \mathbf{v} = 1/(1+\langle \mathbf{u}, \mathbf{v} \rangle)(\mathbf{u} + 1/\gamma_{\mathbf{u}}\mathbf{v} + (\gamma_{\mathbf{u}}/1+\gamma_{\mathbf{u}})\langle \mathbf{u}, \mathbf{v} \rangle \mathbf{u}),$$

where Υ^n is the space of *n*-tuples with real components, $\langle \mathbf{u}, \mathbf{v} \rangle$ is the usual Euclidean inner product, and $\gamma_{\mathbf{u}} = 1/(1-||\mathbf{u}||^2)^{1/2}$. This gyrogroup arises as a model for studying hyperbolic geometry, which is non-Euclidean geometry, as shown in the work of Abraham A. Ungar. In this work, we study the geometry of *n*-dimensional Einstein gyrogroup, using Klein's approach. This approach indicates a strong connection between geometry and algebra. We then determine the isometry group of the *n*-dimensional Einstein gyrogroup in an explicit form.

INVITED SPEAKER: B_INV003

UNSUPERVISED ANOMALY DETECTION FOR SURVEILLANCE VIDEOS

Thittaporn Ganokratanaa*

King Mongkut's University of Technology Thonburi
*e-mail: thittaporn.gan@kmutt.ac.th

Abstract:

Anomaly detection is of great significance for intelligent surveillance videos. Current works typically struggle with object detection and localization problems due to crowded and complex scenes. Hence, we propose a Deep Spatiotemporal Translation Network (DSTN), novel unsupervised anomaly detection and localization method based on Generative Adversarial Network (GAN) and Edge Wrapping (EW). In training, we use only the frames of normal events in order to generate their corresponding dense optical flow as temporal features. During testing, since all the video sequences are input into the system, unknown events are considered as anomalous events due to the fact that the model knows only the normal patterns. To benefit from the information provided by both appearance and motion features, we introduce (i) a novel fusion of background removal and real optical flow frames with (ii) a concatenation of the original and background removal frames. We improve the performance of anomaly localization in the pixellevel evaluation by proposing (iii) the Edge Wrapping to reduce the noise and suppress non-related edges of abnormal objects. Our DSTN has been tested on publicly available anomaly datasets, including UCSD pedestrian, UMN, and CUHK Avenue. The results show that it outperforms other state-of-the-art algorithms with respect to the frame-level evaluation, the pixel-level evaluation, and the time complexity for abnormal object detection and localization tasks.

INVITED SPEAKER: C_INV001

COSMIC RAYS: A RANDOM WALK THROUGH THE SOLAR WIND

David Ruffolo[1,*]

[1]Department of Physics, Faculty of Science, Mahidol University
*e-mail: david.ruf@mahidol.ac.th

Abstract:

Cosmic rays are energetic particles or gamma rays from space, representing Earth's radiation environment, including sporadic bursts of solar energetic particles from solar storms that relate to "space weather" hazards for human activity and instruments in space, air passengers, and power outages at Earth. Space is filled with a tenuous, magnetized plasma (ionized gas) and the motion of charged cosmic rays in space is a random walk as the particles scatter from magnetic irregularities in the plasma. Thus time variations in the cosmic ray flux and directional distribution provide interesting information about plasma processes of the Sun and solar wind. We summarize recent research in Thailand regarding 1) the nature of magnetic fluctuations in the solar wind, using data from the Parker Solar Probe (PSP), mankind's first spacecraft to approach close to the Sun, 2) magnetic connectivity in space, also probed using PSP data, 3) particle acceleration by solar storms, as studied using ground-based neutron monitors (NMs) and soon to be studied using the Thai research satellite TSC-1, 4) particle drifts, as revealed by NM measurements of cosmic ray anisotropy, 5) particle diffusion, as revealed by NM measurements of cosmic ray anisotropy and flux variation with solar cycles, and 6) participation in the LHAASO collaboration to measure the highest-energy gamma rays and reveal "PeVatrons" that accelerate cosmic rays to PeV (10^{15} eV) energies in our Galaxy. Partially supported by the Program Management Unit for Human Resources & Institutional Development, Research and Innovation, NXPO [grant number B05F630115] and grant RTA6280002 from Thailand Science Research and Innovation.

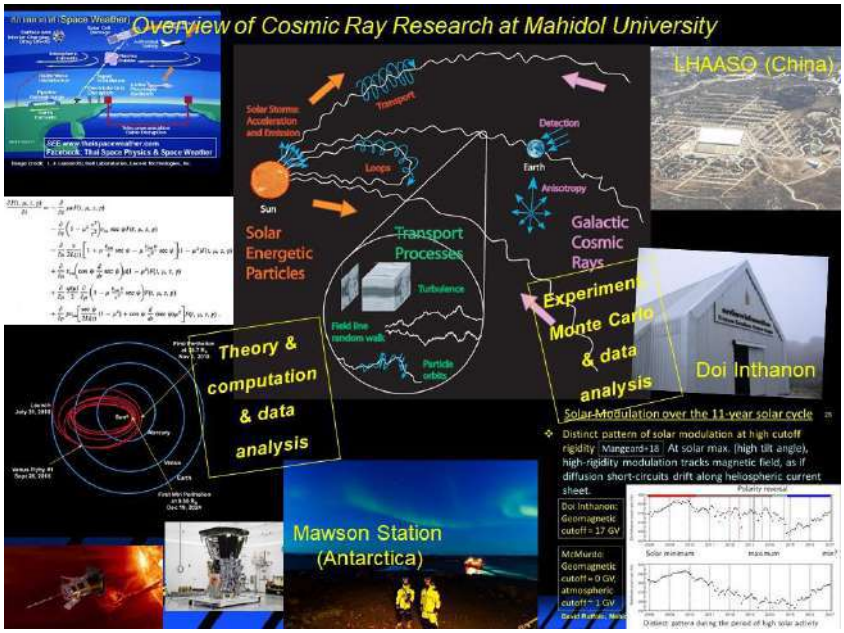

Figure 1. Overview of cosmic ray research at Mahidol University.

INVITED SPEAKER: C_INV002

RADIO ASTRONOMY FOR SUSTAINABLE DEVELOPMENT IN THAILAND AND FUTURE PROSPECTIVE

Kitiyanee Asanok*

(on behalf of RANGD project, NARIT, Thailand)
*e-mail: kitiyanee@narit.or.th

Abstract:

Radio astronomy (in 0.3 mm up to 30 m or 10 MHz up to 1 THz) is one of the essential study fields to understand the universe in the era of multi-wavelength and multi-messenger observations and to accelerate the understanding together with theoretical calculations. This astronomical study field with radio telescopes (i.e., generally parabolic structures) enables us to unveil a variety of the universe such as early, hot or cool, strange objects; because of its uniqueness and advantages: longer wavelengths than general astronomy at optical wavelengths and characterized emission. These emissions come from various types of objects in the universe, e.g., interstellar medium, cosmic microwave background, a region where new stars are born, pulsars, galaxies, active galactic nuclei (AGN), etc.

In spite of the importance of this radio astronomy, for a decade in Thailand elective courses have been given to undergrad and postgrad students just in a few universities. There are some researchers and students who are interested in this field but not as much flavor as other fields. To achieve sustainable development in Thailand, the National Astronomical Research Institute of Thailand (NARIT) (Public Organization) has initiated the project entitled Radio Astronomy Network and Geodesy for Development (RANGD) under the approval of the Ministry of Higher Education, Science, Research and Innovation (MHESI) since the year 2016. The main objectives of this project are to disseminate knowledge in radio astronomy and geodesy scientific research, development of microwave / digital technology, and human resources in many career paths, e.g., the researchers, scientists, engineers, lecturers, students, and other people who are interested in this field by learning integration with our Thai National Radio Telescope (TNRT). This telescope has a 40-m diameter size, which is the largest in South-East Asia, and is ongoing built at Huai Hong Khrai Royal Development Study Center, Doi Saket Chiang Mai, and will be completed within the year 2022. In this talk, therefore, I will introduce the importance of this project, why we need to do radio astronomy research in Thailand, which plans could achieve the development sustainability of Thailand? and research collaboration with other essential projects such as Thai Space Consortium (TSC) and other fields of astronomy.

INVITED SPEAKER: C_INV003

SMALL SATELLITES – SPACE TECHNOLOGIES FOR LIFE

Phongsatorn Saisutjarit*

International Institute of Space Technology for Economic Development (InSTED)
King Mongkut's University of Technology North Bangkok
1518 Pracharat 1 Rd. Wongsawang Bangsue Bangkok 10800 Thailand
*e-mail: phongsatorn.s@eng.kmutnb.ac.th

Abstract:

Space has been used as a tool for humankind for over 50 years. Many space technologies have an important contribution to the United Nations' Sustainable Development Goals (SDGs), such as utilizing of global navigation satellite system (GNSS), earth observation satellite (EOS), satellite communication, human space flight and microgravity research, space technology transfer, and inspiration via research/education. These space technologies can help countries pursue the SDGs such as access to clean water, food security, poverty alleviation, health care, environmental sustainability, and urban development. Small satellite missions can play a role as a part of a national strategies to respond to these needs in each area. The number of small satellite constellation missions is growing rapidly every year to provide more accurate observation data in near-real time or global communication and positioning. Besides, the potential societal benefits that space technologies would bring, exploring the new way to apply small satellites for optimizing and improving how we use resources, and capacity building through developing small satellite projects of the research group at Thai Space Consortium would be also introduced in this session.

INVITED SPEAKER: D_INV001

Zn AND Mn RECYCLING PROCESS FROM SPENT ALKALINE AND Zn-C BATTERIES TO BE RE-UTILIZED IN RECHARGEABLE Zn-ION BATTERY APPLICATION

Rojana Pornprasertsuk[1,2,3,4*], Theeranon Tankam[1,2], Jiaqian Qin[3,5], Nisit Tantavitchet[2,3,6], Jitti Kasemchainan[2,3,6], Prasit Pattananuwat[1,2,3], Soorathep Kheawhom[3,7], Patchanita Thamyongkit[8], Rongrong Cheacharoen[5], Anongnat Somwangthanaroj[7], Nattaporn Tonanon[7], Suthep Jongwannasiri[9], Kamonpan Manowilaikun[1,2], Kunchaya Thungsuai[1], Natnicha Kiatsiriwatthana[8], Kittima Lolupiman[5,7]

[1] Department of Materials Science, Faculty of Science, Chulalongkorn University, Thailand
[2] Center of Excellence in Petrochemical and Materials Technology, Chulalongkorn University, Thailand
[3] Research Unit of Advanced Materials for Energy Storage, Chulalongkorn University, Thailand
[4] Department of Materials Science and Technology, Nagaoka University of Technology, Japan
[5] Metallurgy and Materials Science Research Institute, Chulalongkorn University, Thailand
[6] Department of Chemical Technology, Faculty of Science, Chulalongkorn University, Thailand
[7] Department of Chemical Engineering, Faculty of Engineering, Chulalongkorn University, Thailand
[8] Department of Chemistry, Faculty of Science, Chulalongkorn University, Thailand
[9] Siamfrit Co., Ltd., Thailand
*e-mail: rojana.p@chula.ac.th

Abstract:

The Zn and Mn extraction processes from spent alkaline and Zn-C batteries by hydrometallurgical route and the synthesis of recycled Zn film and MnO_2 for Zn-ion battery application were developed in the project. The Zn and Mn extraction process involved the acid leaching of Zn and Mn ions from the spent alkaline and Zn-C battery electrodes in the lab-scale were initially investigated using various leaching conditions. The acid leaching using 0.5-2 M HCl and H_2SO_4 at ambient temperature providing Zn extraction efficiencies in a range of 72.3-95.3%. By introducing an inexpensive reducing agent namely sodium sulfide (Na_2S), sodium metabisulfite ($Na_2S_2O_5$) or hydrogen peroxide (H_2O_2) in 2M H_2SO_4, the Mn extraction efficiency for Mn was increased from 21.9% (no reducing agent) up to 48.4%, 82.8% and 98.9%, respectively. The upscale leaching study was subsequently performed in a 100-L pilot scale reactor demonstrated the Zn and Mn extraction efficiencies of 71% and 65%, respectively. Using the leaching/washing solutions from the upscale hydrometallurgical route, Zn-film deposition on the stainless steel/ Cu substrates and the MnO_2 synthesis via hydrothermal, reflux and electrodeposition techniques were performed. Both recycled Zn and MnO_2 were subsequently used as the anode and cathode main components in the CR2032 rechargeable Zn-ion battery, which in turn providing specific capacity more than 150 mAh/g and working performance more than 1,000 cycles.

INVITED SPEAKER: D_INV002

HIGHLY ACTIVE METAL COMPLEXES SUPPORTED BY CONSTRAINED SCHIFF-BASE LIGANDS FOR CYCLOADDITION OF CO_2 TO EPOXIDES

Jiraya Kiriratnikom, Nattiya Laiwattanapaisarn, Khamphee Phomphrai*

Department of Materials Science and Engineering, School of Molecular Science and Engineering, Vidyasirimedhi Institute of Science and Technology (VISTEC), Wang Chan, Rayong 21210, Thailand
*e-mail: khamphee.p@vistec.ac.th

Abstract:

Carbon dioxide (CO_2) is an attractive C1 feedstock for the chemical synthesis because of its availability, abundance, inexpensive, nontoxicity, and renewability. Nowadays, CO_2 has been converted to various valuable chemicals including methanol, urea, salicylic acids, and organic carbonates. Among these industrially important compounds, the cycloaddition reactions of CO_2 to epoxides affording cyclic carbonates are a commercially important reaction already exploited as polar aprotic solvents for catalytic reactions, electrolytes for lithium-ion batteries used in electric vehicles and mobile devices, and precursors for valuable polymers and chemicals. Motivated by these applications, we have set out to design a new highly active catalyst based on the famous bis(salicylidene)ethylenediamine (salen ligand) for the production of cyclic carbonates from CO_2 and epoxides. Although the development of salen ligands may seem matured, we found that the ligand can actually be further developed to add more constraint around the aromatic backbone giving a new constrained Schiff-base ligand (inden). In this work, the inden Cr and Al complexes were developed and found to be highly active for the CO_2/epoxide cycloaddition reaction giving 100% cyclic carbonates with very high turn-over frequency (TOF > 10,000 h^{-1}). Catalyst development and cycloaddition reactions will be discussed.

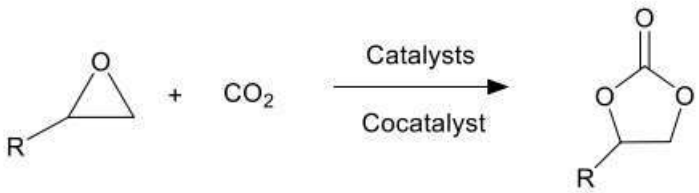

Figure. Cycloaddition of CO_2 to epoxides.

INVITED SPEAKER: D_INV003

SUSTAINABLE DEGRADATION OF ORGANIC POLLUTANTS IN WASTEWATER BY PHOTOCATALYTIC PROCESS

Teeradech senasu, Tammanoon chankhanittha, Suwat Nanan*

Materials Chemistry Research center, Department of chemistry, Faculty of Science, Khon Kaen University, Khon Kaen 40002 Thailand
*e-mail: suwatna@kku.ac.th

Abstract:

The incomplete degradation of the organic pollutants by various conventional treatments has been elucidated. In some cases, formation of the secondary pollutants was also found. Alternatively, photocatalytic treatment has been used as a clean and effective route for removal of the organic pollutants in wastewater. It is well accepted that one of the most important challenging topics in environmental protection is to develop novel photocatalysts with high sunlight harvesting capacity and high charge separation efficiency. In this talk, the heterojunctions based on two photocatalysts will be discussed. Interestingly, in the case of CdS/ BiOBr, the decoration of the hexagonal CdS on the surface of the tetragonal BiOBr for creation of the sunlight responsive photocatalyst will be demonstrated. The CdS/BiOBr-1:3 exhibited 100% removal of norfloxacin and ciprofloxacin antibiotics under visible light. In addition, complete degradation of the pollutants under natural solar light was also achieved. Construction of the heterojunction is a key strategy for improvement of the photocatalytic performance due to a decrease of the charge carrier recombination rate, an increase in visible light absorption range, and an enhancement of the surface area of the photocatalyst. The removal of the pollutants correlated well with the first- order reaction. Photogenerated hole played a crucial role in removal of the antibiotics. Confirmation of the stability of the prepared was also elucidated. The photoactivity of the photocatalyst remained the same after five times of use implying the excellent reusability. The present work demonstrates the promising potential of the heterojunction photocatalyst for detoxification of dyes and antibiotics in wastewater.

INVITED SPEAKER: D_INV004

SMALL-MOLECULE FLUOROPHORES FOR NIR-II BIOMEDICAL FLUORESCENCE IMAGING AND AND IMAGE-GUIDED THERAPY

Hui Zhou[1,2], Qianqian Li[1], Yishen Liu[1,2], Tian Tian[2], Xuechuan Hong*[,1,2], Yuling Xiao*[,1]

[1] State Key Laboratory of Virology, Hubei Province Engineering and Technology Research Center for Fluorinated Pharmaceuticals, Wuhan University School of Pharmaceutical Sciences, Wuhan 430071, China
[2] College of Science, Research Center for Ecology, Laboratory of Extreme Environmental Biological Resources and Adaptive Evolution, Tibet University, Lhasa, 850000, China
*e-mail: xiaoyl@whu.edu.cn, xhy78@whu.edu.cn

Abstract:

NIR-II fluorophores have shown great promise for biomedical applications with superior in vivo optical properties. Very recently, there has been an upsurge of interdisciplinary study focusing on developing versatile types of inorganic/organic fluorophores that can be used for non-invasive NIR-II imaging with low tissue auto-fluorescence and deeper tissue penetration. In this paper, we will provide an overview of the reports published to date on the design, properties, and molecular imaging of organic NIR-II fluorophores. Then, we will present the novel imaging modalities and versatile biomedical applicants brought by these superior fluorescent properties. Finally, we will report development of D-A type thiopyrylium-based NIR-II fluorophores with frequency upconversion luminescence (FUCL). H4-PEG-PT or H4-PEG-Glu can not only quickly and effectively image mitochondria in live or fixed osteosarcoma cells with subcellular resolution, but also efficiently achieving mitochondria-targeted cancer therapy.

Keywords:

Image-guided therapy, NIR-II imaging, small-molecule fluorophores, mitochondria-targeted

Refference

1. A. L. Antaris, H. Chen, K. Cheng, Y. Sun, G. Hong, C. Qu, S. Diao, Z. Deng, X. Hu, B. Zhang, X. Zhang, O. K. Yaghi, Z. R. Alamparambil, X. Hong, Z. Cheng, H. Dai. *Nat. Mater.* **2016**, *15*, 235–242**.**
2. H. Zhou, X. Zeng, A. Li, W. Zhou, L.Tang, W. Hu, Q. Fan, X. Meng, H. Deng, L. Duan, Y. Li, Z. Deng, X. Hong, Y. Xiao. *Nat. Commun.* **2020,** *11*，6183.
3. Y. Li, Y. Liu, Q. Li, X. Zeng, T. Tian, W. Zhou, Y. Cui, X. Wang, X. Cheng, Q. Ding, X. Wang, J. Wu, H. Deng, Y. Li, X. Meng, Z. Deng, X. Hong, Y. Xiao. *Chem. Sci.* **2020**, *11*, 2621–2626.
4. J. Lin, X. Zeng, Y. Xiao, L. Tang, J. Nong, Y. Liu, H. Zhou, B. Ding, F. Xu, H. Tong, Z. Deng, X. Hong. *Chem. Sci.* **2019**, *10*, 1219-1126.
5. B. Ding, Y. Xiao, H. Zhou, X. Zhang, C. Qu, F. Xu, Z. Deng, Z. Cheng, X. Hong. *J. Med. Chem.* **2019**, *62*, 2049−2059.
6. Y. Sun, X. Zeng, Y. Xiao, C. Liu, H. Zhu, H. Zhou, Z. Chen, F. Xu, J. Wang, M. Zhu, J. Wu, Z. Deng, Z. Cheng, X. Hong. *Chem. Sci.* **2018, *9*, 2092–2097**.

INVITED SPEAKER: E1_INV001

NEW NORMAL, NEW MINDSET AND NEW SKILLSET: WHY AND HOW?

Nantana Gajaseni*

Vice President, Mae Fah Luang University
Chiangrai 57100, Thailand
*e-mail: nantana.gaj@mfu.ac.th

Abstract:

Since COVID-19 pandemic the universities all around the world have been immediately switched the traditional teaching and learning (T&L) as face-to-face approach to online/distance learning instead. All stakeholders are struggle in copping fast enough in this disruption in particular on which T&L strategies would be applied and how we could teach our students to ensure and meet the same learning outcomes as before. Undeniably, this disruption enforced everyone to adopt "Digital Technology" that is seemingly a good choice to substitute face-to-face T&L approach. It is also acceptable that this quick digital transformation will enhance learning experiences with digital literacy development. However, it eventually brings up many questions on quality of T&L in terms of digital-ready skills, inequality of access, adaptability in online T&L; students' knowledge acquisition; practical skills in professional requirement; development of soft-skills, social-skills, and future-ready skills; etc. Therefore, it is essential for the university to consider a transformation in both appropriate facilities' support and rule & regulation of study programme to be more flexible and more partnership involvement to be ready to this higher education disruption. Even in a post-COVID-19 landscape we still live in the current COVID-19 preventive measures with social distancing, lower density classrooms and new learning environment and style, but the societal expectation on quality of graduate is still the same. By well preparing ourselves, we really need to rethink, redesign, reposition our mindset, our T&L strategies and our role as educators in science. There is no way of return to traditional T&L but the "Blended Learning (Face-to-Face and Online)" will be encouraging active learning as the trend of higher education in a new normal.

INVITED SPEAKER: E1_INV002

CONVERSION OF A LARGE NON-MAJORS BIOLOGY COURSE TO ONLINE TEACHING – INSTRUCTIONAL RE-DESIGN AND ITS IMPACT ON STUDENT LEARNING

Sylvia Sze Joo Law,[1] Teck Keong Seow[2]*

[1] Department of Biological Sciences, National University of Singapore, Singapore
[2] College of Alice & Peter Tan, Centre for Development of Teaching & Learning, and Department of Biological Sciences, National University of Singapore, Singapore
*e-mail: teckeong@nus.edu.sg

Abstract:

The sudden changes to human life that were brought about by the COVID-19 pandemic had also affected the global educational landscape. Just like many higher education institutions around the world, the universities in Singapore were not spared by the drastic changes either. While many had to switch to online teaching within a very short time, the General Biology course had the benefit of 2 to 3 months of vacation to re-design the instructional approach for the shift to online teaching. The instructional re-design was based on the Community of Inquiry framework, in which the three key elements of social, cognitive, and teaching presence converge to realise a collaborative constructivist educational experience (Figure 1).

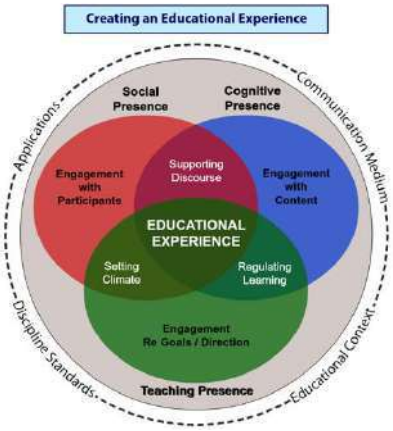

Figure 1. Community of Inquiry framework

The class of about 220 students was divided into 8 sections of not more than 30 students per section, with each section being assisted by two or three teaching assistants. Every e-class was conducted using the flipped classroom approach, with the students watching the instructional videos prior to the e-class and attempting formative diagnostic quizzes during the e-class. Each e-class of about 30 students was further sub-divided into 10 separate breakout rooms of not more than 3 students per room to discuss the quiz questions. The teaching assistants would move from one breakout room to another to guide the peer discussions with appropriate prompt questions. Preliminary analysis of the end-of-semester summative assessment data demonstrated that despite the conversion to online teaching, performance of the class was comparable to the performance of previous cohorts when the classes were conducted face-to-face. This finding showed that the use of the Community of Inquiry framework for the instructional re-designing towards online teaching of the large non-majors General Biology course had no unfavourable impact on student learning.

INVITED SPEAKER: E1_INV003

ACTIVE LEARNING VIA GAMING AND SIMULATIONS IN BIOLOGY AND SUSTAINABLE DEVELOPMENT COURSES

Pongchai Dumrongrojwatthana[1,*] Rattanapan Poomirat[2]

[1]Department of Biology, Faculty of Science, Chulalongkorn University, Bangkok, Thailand
[2]Former PhD student in Biological Science Program, Faculty of Science, Chulalongkorn University, Bangkok, Thailand
*e-mail: pongchai.d@chula.ac.th

Abstract:

Academic scholars, who are involved in primary, secondary, and higher educations, are responsible for advocating the concept of sustainable development, which integrates environmental, social, and economic aspects. Among various obligations, one of the most important is to teach, or coach, students on how to obtain the 21st century skills to meet job requirements, as well as serving as good citizens under recent 'volatile-uncertain-complex-ambiguous (VUCA)' world. These mandates can be accomplished via diverse activities, including teaching, research, student supports, and academic services. It is necessary to balance all activities while maintaining teaching standards and quality. Among several teaching techniques, gaming and simulation (G&S) has been proven as an effective tool to develop student's competency by applying their knowledge into action and practical learning. In this study, the applications of two G&S, namely 'ReHab' and 'Green Roof', serve as active learning tools in biology, sustainable development, and natural resource management courses. The ReHab game simulates a forest management situation. It can be applied in biology, ecology, and sustainable development courses, such as Principle of Natural Resource Management. The game involved of two groups of players with different goals of natural resource utilization, harvesters who generate incomes from plant biomass, and park rangers who protect the forest for rare migratory bird species. Two scenarios, 'no communication among players' and 'negotiation among players is allowed', are designed as game rules. Players have to apply their biological knowledge to sustain the system, which includes maintaining a steady source of income, conserve bird population, and reduce economic gap among players. The Green Roof game simulates an urban green space design. It is especially designed for shared learning regarding green roof ecosystem services in Ecology course. Two scenarios, 'construct green roof based on students' perception' and 'increase ecosystem services of the roof', are assigned for players. At the end of the game, a debriefing session is required to summarize the lessons learned. Implementing these two games in classes revealed that G&S can promote the concept of sustainable development goals and can assist students in obtaining diverse learning outcomes.

INVITED SPEAKER: E2_INV001

NOVEL SINGLE- AND DOUBLE-ANCHOR-TYPE ISOMALTOMEGALOSACCHARIDES: PRODUCTION, FUNCTION, APPLICATION, AND CONTRIBUTION TO SDGS

Weeranuch Lang, Takayoshi Tagami, Masayuki Okuyama, Atsuo Kimura*

Research Faculty of Agriculture, Hokkaido University, Sapporo 060-8589, Japan
*e-mail: kimura@abs.agr.hokudai.ac.jp

Abstract:

A scientific term of "megalosaccharide (MS)", proposed in 1959 by Thoma et al., was defined by sugar-size, of which the degree of polymerization (DP) ranged between oligosaccharide (DP = 2 to 9) and polysaccharide (DP > 100 or 200). However, this term became obsolete, since no efficient production method was available, while its valuable function was expected. We found that a mutant of dextran dextrinase (DDase) produced the α-1,6-glucosyl linked linear MS (isomaltomegalosaccharide; IMS), enabling us to analyze the function of MS for the first time. IMS exhibited the remarkable action to solubilize the compounds belonging to BCS-II (Biopharmaceutics Classification System Class II**)** like flavonoid, which will be mentioned in the last part of abstract**.**

DDase catalyzes a successive α-1,6-glucosyl transfer reaction to form dextran using maltooligosaccharide (MOS) as a substrate. Our initial research showed that wild-type DDase (or native DDase) synthesized less or no IMS from MOS, and only produced isomaltooligosaccharides and dextran. However, C-terminal deletion-mutant of DDase produced a large amount of IMS, indicating that structural element related to IMS-formation was present in C-terminal region. Our further study demonstrated that native DDase generated IMS under quite high substrate concentration, probably due to availability of enough MOS of accepter substrate.

Considering the transfer reaction of DDase, the reducing terminal of IMS is composed of MOS moiety, the portion of which is called as "anchor" (formed by rigid α-1,4-glucosyl chain). This IMS has only one anchor, since DDase originally produces the single-anchor-type IMS (Sa-IMS). We subjected Sa-IMS to the reaction of CGTase (cyclodextrin glucosyl transferase) with cyclodextrin, and succeeded in synthesis of double-anchor-type IMS (Da-IMS). Therefore, Da-IMS has two anchors of MOS moieties existing at its non-reducing and reducing ends.

Sa-IMS enhanced the rat intestinal uptake of quercetin-3-*O*-β-glucoside (Q3G; a flavonoid showing favorable physiological actions, e.g. anti-diabetic effect) by increasing solubility of Q3G. Sa-IMS also solubilized the water-insoluble ethyl red (azo-benzene dye, an environmental pollutant with less degradation in nature), and assisted azoreductase to degrade ethyl red, indicating potential ability to overcome pollution. Furthermore, the ibuprofen **(**IBP; anti-inflammatory medical agent**)** was also solubilized by Sa-IMS. It was found that Da-IMS had much stronger ability to solubilize Q3G and IBP than Sa-IMS did, due to double-anchor effect. Interestingly, those three compounds are members of BCS-II, which display the low water-solubility and high membrane-permeability. Since most of medicinal drugs and many functional food materials as well as azo-dyes belong to BCS-II, both of Sa-IMS and Da-IMS have the valuable function to solubilize the BCS-II compounds, contributing to dose-reduction of important BCS-II materials and thereby cutting down their production energy. Further contribution to SDGs is the enzymic degradation of pollutant (azo-dyes), providing clean environment.

INVITED SPEAKER: E2_INV002

SESAMOLIN: A VERSATILE PRECURSOR FROM SESAME SEED FOR DERIVATIZING BIOACTIVE LIGNANS

Wisuttaya Worawalai, Titiruetai Doungwichitrkul, Warin Rangubpit, Panyakorn Taweechat, Pornthep Sompornpisut, Preecha Phuwapraisirisan*

Department of Chemistry, Faculty of Science, Chulalongkorn University, Bangkok 10330, Thailand
*e-mail: preecha.p@chula.ac.th

Abstract:

Sesamolin is a major lignan found in sesame (*Sesamum indicum*) seeds. Unlike sesamin, one additional oxygen atom in sesamolin structure makes it more reactive as the presence of acetal. However, the controversial results between in *vitro* and in *vivo* bioactivities have raised the question of true bioactive metabolites possibly released after two major lignans are digested by animal models. We have prepared over 50 lignans using sesamolin as the starting material. Sesamolin was first converted to the more reactive hemiacetal derivative named samin, which was further derivatized into a wide variety of lignans by nucleophilic substitution. Upon bioactivity evaluation e. g. glucosidase inhibition of the synthesized lignans, the products containing more phenolic hydroxy showed more potent bioactivity. The synthesis of sesamolin derivatives and mechanism of inhibition investigated by kinetic study and molecular simulation will be presented.

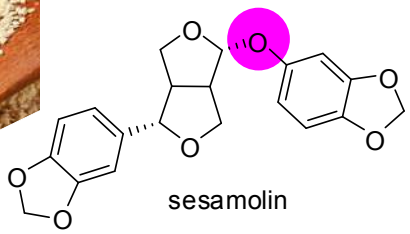

sesamolin

INVITED SPEAKER: SYMP_A_INV001

MORPHOLOGY IN SUBMERGED CULTURE: THE MAIN CHALLENGE IN INDUSTRIAL BIOACTIVE COMPOUND PRODUCTION IN FUNGAL BIOFACTORIES

Hesham Ali El Enshasy[1,2,*]

[1] Institute of Bioproduct Development (IBD), Universiti Teknologi Malaysia (UTM), Skudai, Johor Bahru, Malaysia
[2] City of Scientific Research and Technology Applications, New Burg Al Arab, Alexandria, Egypt.
*e-mail: henshasy@ibd.utm.my

Abstract:

Since centuries, fungal cells have been widely used for the production of many key bioactive molecules in chemical, food, feed, and pharmaceutical industries. This based on their high growth rate, the ability to utilize wide range of complex and economic substrates, and the capacity to produce metabolites in high concentration as extracellular product. In addition, they have been considered as one of the preferred biofactories for the production of different types of recombinant proteins based on their high excretion capacity which reduce the cost of downstream process. However, growth morphology of fungal cells in submerged culture is considered is one the main challenges for the cultivation of fungi in large scale. The same strain can show completely different morphological features (ranged from dispersed mycelium to complex pellet structure) with any minor change in cultivation conditions, cultivation conditions, or strain genetic manipulation. Therefore, for each cultivation process, a desired morphology needs to be controlled to produce the targeted product in high concentration. This presentation, will provide updated information about the recent development on factors affecting fungal morphology in submerged cultivation system using full scale approach from spore induction to large scale cultivation. Production of glucose oxidase and gluconic acid using a recombinant strain of *Aspergillus niger* (carrying multiple copy of *Gox* gene under regulation of *gpdA* promotor, with alpha amylase signal sequence) will be given as example to describe in details how growth morphology control and biopellet engineering design approaches can be used as tool in bioprocess development of bioproduct formation in industrial scale.

INVITED SPEAKER: SYMP_A_INV002

THE POTENTIAL OF GREEN HYDROGEN

Thana Sornchamni*

Innovation Institute, PTT Public Company Limited
*e-mail: thana.s@pttplc.com

Abstract:

Hydrogen is considered as one of the means to abate the climate change and most of countries, who aim to achieve net-zero carbon target, usually have hydrogen energy in their national energy agenda. The potential uses of hydrogen are growing in several applications, eg. mobility, heat and power, and chemicals. Currently, most of hydrogen is still produced either from coal or from natural gas and the production of this hydrogen still releases carbon dioxide to our atmosphere. Therefore, there is an effort to move to green hydroge, which is much more environment friendly.

Green hydrogen is defined as hydrogen produced from renewable energy, such as solar energy and wind energy, through the electrolysis technology. Green hydrogen has gained lots of attention due to two main factors. The first one is from the fact that the cost of renewable energy declined significantly during the last decade and the trend is still continue in the future. The second is that the cost of electrolysis technology is also declined within the last five year (2014-2019). In the presentation, comparison of different water electrolysis technologies, Alkaline Electrolysis (AEL), Proton Exchange Membrane (AEM) and Solid Oxide Electrolyzer (SOE) and the costs of producing green hydrogen from renewable energy will be discussed.

INVITED SPEAKER: SYMP_A_INV003

BIOPROCESS DEVELOPMENT ON ANIMAL VACCINE PRODUCTION FOR A SUSTAINED TECHNOLOGY ENHANCEMENT

Lalintip Hocharoen*

Bioprocess Research and Innovation Centre (BRIC), National Biopharmaceutical Facility (NBF), King Mongkut's University of Technology Thonburi (KMUTT)
*e-mail: lalintip.hoc@kmutt.ac.th

Abstract:

Thailand is confronting a number of challenges, such as inequality, an imbalanced economy, poverty in the country's regions, as well as a growing aging population. Overcoming these challenges aligns well with the UN Sustainable Development Goals (SDGs) and this work carried out by the South East Asia Research Collaboration (SEARC) team as a part of the Global Challenge Research Fund (GCRF) consortium contributes significantly towards achieving several SDGs, notably; SDG1: No poverty, SDG2: Zero hunger, SDG3: Global health and wellbeing, SDG9: Industry, innovation and infrastructure, and SDG17: Partnerships for the goals. This work has focused on the establishment of biopharmaceuticals and animal vaccine production capacity to reduce costs, increase accessibility, transform healthcare provision in Thailand and provide a sustained increase in the availability of high- tech drugs. Herein, we presented one of our collaborative technological platform developments for animal vaccines, particularly for swine vaccines, as Thailand's pig industry is relatively large while the pig vaccines are all imported, making the cost high and the farmer inaccessible. Porcine Circovirus type 2d (PCV2d) has become the predominant PCV genotype and considerably affected the swine industry, yet there is no commercially available PCV2d vaccine available. Currently, prevention is accomplished through the use of other genotype vaccines, which are relatively costly for veterinary applications. The novel PCV2d vaccine based on a subunit protein platform using *E. coli*, which is more reasonable, fast and provides a higher level of protein expression, was then designed. The production process was successfully scaled up from bench to large-scale (30L) production. This production platform technology has a high potential for successful industrial production on a local and global scale, enabling Thailand to become self-sufficient in terms of technology enhance.

INVITED SPEAKER: SYMP_B_INV001

SDGS AND THE QUANTUM INTERNET

Rodney Van Meter*

Keio University Shonan Fujisawa Campus, 5322 Endo, Fujisawa, Kanagawa 252-0882, Japan
*e-mail: rdv@sfc.keio.ac.jp

Abstract:

How will quantum computing help sustainable development goals? Quantum computers hold tremendous promise for revolutionizing computation. In this talk, I will present the seven key ideas for understanding quantum computing, focusing especially on how waves come together to solve interesting problems. In the latter part of the talk, I will present some of the problems that quantum computers are expected to help solve that will positively impact society's push to achieve the UN Sustainable Development Goals.

INVITED SPEAKER: SYMP_B_INV002

Quantum Techniques for Explainable Natural Language Processing

Chanatip Mangkang,[1] Jirawat Tangpanitanon,[2,3] Pradeep Bhadola,[4] Yuichiro Minato,[5] Dimitris Angelakis,[6] Thiparat Chotibut,[1,*]

[1] Chula Intelligent and Complex Systems, Department of Physics, Faculty of Science, Chulalongkorn University, Bangkok, Thailand
[2] Quantum Technology Foundation (Thailand)
[3] Thailand Center of Excellence in Physics, Chiang Mai, Thailand
[4] The Institute for Fundamental Study, Naresuan University, Thailand
[5] Blueqat Inc., Japan
[6] Centre for Quantum Technologies, National University of Singapore, Singapore
*e-mail: thiparatc@gmail.com, thiparat.c@chula.ac.th

Abstract:

Deep Learning (DL) has empowered computers with superior performance in modern Natural Language Processing (NLP) tasks, such as sentiment analysis and machine translation. Even for texts with long-range correlations such as sequences of characters in Wikipedia, DL can effectively express the power-law decay in the mutual information between two distant characters [H. W. Lin, M. Tegmark, Entropy, 19, 299 (2017)]. Despite empirical successes, its intrinsic non-linearity complicates the analysis of algorithmic behaviours. Which network architectures and how many parameters are essential to reproduce long-range correlations are important yet theoretically challenging questions to tackle. Here, we attempt to provide systematic answers through the mapping between DL and its matrix product state (MPS) counterpart [Y. Levine et al. Phys. Rev. Lett, 122, 065301 (2019)]. By recasting DL as MPS, we show that the number of parameters required to achieve high performance in sentiment analysis, and to reproduce power-law decay in the mutual information in Wikipedia texts, can be efficiently extracted from the entanglement entropy in the dual MPS. Our work utilises tools in many-body quantum physics to resolve explainability issues of NLP, and more generally of sequence modelling.

INVITED SPEAKER: SYMP_B_INV003

QUANTUM COMPUTERS FOR MATERIALS SIMULATIONS USING EMBEDDING METHODS

Ivan Rungger[1,*]

[1]National Physical Laboratory, TW11 0LW Teddington, United Kingdom
*e-mail: ivan.rungger@npl.co.uk

Abstract:

We present quantum algorithms to perform calculations for condensed matter systems on currently available quantum computers. We use the dynamical mean field theory (DMFT) embedding method, which is required to properly describe the large class of materials with strongly correlated electrons. We first apply a method based on the variational quantum eigensolver (VQE) to a 2-site system. This method made it possible to run DMFT calculations on quantum computing hardware for the first time (arXiv:1910.04735). We then present a recent method based on the maximally localised dynamical embedding (MLDE), which has the advantage that the number of qubits required for DMFT simulations is significantly reduced (Nature Computational Science **1**, 410 (2021)). We conclude by presenting our newly developed Krylov variational quantum algorithm with improved scaling properties, which allowed us to perform simulations for real material systems on quantum computing emulators (arXiv:2105.13298).

INVITED SPEAKER: SYMP_B_INV004

TOWARD ULTRACOLD CAESIUM ISOMERS

Tanapoom Poomaradee[1]*, Alexandros Giatzoglou[1], Ilkka Pohjalainen[2], Sami Rinta-Antila[2], Iain. D. Moore[2], Philip M. Walker[3], Luca Marmugi[1], and Ferruccio Renzoni[1]

[1] Department of Physics and Astronomy, University College London, Gower Street, London WC1E 6BT, United Kingdom
[2] Department of Physics, University of Jyväskylä, Survontie 9, 40014 Jyväskylä, Finland
[3] Department of Physics, University of Surrey, Guilford GU2 7XH, United Kingdom
*e-mail: ucaptpo@ucl.ac.uk

Abstract:

The text should be fully justified. Magneto Optical Trap (MOT) of 133Cs atoms was performed. The atomic source was provided by an ion beam generated from a surface ionisation source. The focused ion beam enters the cold atom setup through the small hole of vacuum impedance and is implanted and neutralised in a 25 mm thick foil. The foil is chosen to be yttrium due to a favourable imbalance between ionisation energy and work function. Then, neutralised atoms were extracted by resistive heating. After that, MOT loading from the neutraliser was performed. The implantation profile was numerically simulated, and a phenomenological model for the neutraliser was also developed. A model of 1D diffusion was used to extract the neutraliser activation energy.

In addition, preliminary implantation tests were also performed with radioactive beams, in this case to produce 135mCs. The 135mCs ion was generated by means of proton induced fission in a Uranium target. The ions were extracted and accelerated through a mass separator which directed the 135mCs ion beam to be implanted in a neutraliser. After implantation, gamma emission from the neutraliser was detected by a gamma detector. Then, by using the gamma spectrum, half-life of 135mCs was measured in order to verify implantation of the species. Moreover, preliminary tests for trapping of 135Cs were also conducted.

INVITED SPEAKER: SYMP_B_INV005

EXPLORING FERMI-HUBBARD SYSTEM VIA QUANTUM GAS MICROSCOPE

Pimonpan Sompet[1,2*]

[1]Max-Planck-Institut für Quantenoptik, Garching, Germany
[2]Research Center for Quantum Technology, Faculty of Science, Chiang Mai University, 239 Huay Kaew Road, Muang, Chiang Mai, 50200, Thailand
*e-mail: pimonpan.sompet@mpq.mpg.de

Abstract:

Many exotic phenomena in Fermi-Hubbard model are created by the interplay between charge and spin in the doped systems. Here, we study the influence of the charge motion in one- and two- dimensional antiferromagnet at the microscopic level by use a powerful quantum gas microscope of ultracold fermions (^{6}Li). In this system, the tunneling energy, the on-site interaction and chemical potential can be precisely controlled. With our high-resolution imaging, we can resolve both spin and charge density of individual lattice-site. This enables the measurements of spin-spin, density-density and spin-density correlations in the systems. In the talk, I will present our results on the time-resolved deconfinement between spin and charge in 1D system and the imaging of magnetic polarons in 2D system.

INVITED SPEAKER: SYMP_B_INV006

COMPUTATIONAL DESIGN FOR TWO-DIMENSIONAL MATERIALS FOR THERMOELECTRIC TRANSPORT

Nirpendra Singh*

Department of Physics and Center forCatalysis and Separation (CeCaS),
Khalifa University ofScience and Technology, Abu Dhabi, United Arab Emirates
*e-mail: nirpendra.singh@ku.ac.ae

Abstract:

The discovery of graphene, a one-atom-thick layer of carbon atoms, has opened up a window to the two-dimensional (2D) world of materials and triggered a surge of research activities on various 2D layered materials, including single layers of hexagonal-boron nitride (h-BN) and transition metal dichalcogenides (such as MoS2 and WSe2). Thermoelectric materials can convert heat into electricity directly and therefore have applications in waste heat recovery. Manipulating the carrier concentration and band structures of materials have effectively optimized the electrical transport properties, whereas nanostructure engineering and defect engineering can significantly reduce thermal conductivity. In the talk, I will discuss the thermoelectric properties of two-dimensional materials in the bulk and monolayer phase. I will also demonstrate various strategies to reduce the thermal conductivity and improve the Seebeck coefficient and discuss the design principles of two-dimensional materials for their applications in thermoelectric transport.

INVITED SPEAKER: SYMP_C_INV001

RESEARCH OF IOC/WESTPAC

Kentaro Ando[1, 2, *], Fangli Qiao[1, 3], Aileen Tan[1, 4], Wenxi Zhu [1]

[1] IOC/WESTPAC, UNESCO
[2] Japan Agency for Marine-Earth Science and Technology, Japan
[3] First Institute of Oceanography, Ministry of Natural Resources, China
[4] Centre For Marine & Coastal Studies, Universiti Sains Malaysia, Malaysia
*e-mail: andouk@jamstec.go.jp

Abstract:

Since the establishment as regional sub-commission of IOC in 1989, WESTPAC has been developed through the collaboration and contributions by 22 member states. In line with the Vision and High-Level Objectives (HLOs) of IOC, as well as the challenges faced by this particular region, WESTPAC has become recognized as a catalyst, advocate, coordinator and facilitator in promoting ocean knowledge, sustained observations and services for the improvement of governance towards a healthy ocean and coasts for shared prosperity in the last ten years. WESTPAC is committed to developing, coordinating and implementing marine scientific research, observations and services on four themes: Understanding Ocean Processes and Climate in the Indo-Pacific; Ensuring Marine Biodiversity and Seafood Safety; Safeguarding the Health of Ocean Ecosystems; and Enhancing knowledge of emerging ocean science issues. WESTPAC has formed 16 projects and working groups, implementing activities through them as shown in Figure 1. We will introduce some research projects, which may be related to the theme of the symposium. The first author will also introduce the research activities by JAMSTEC.

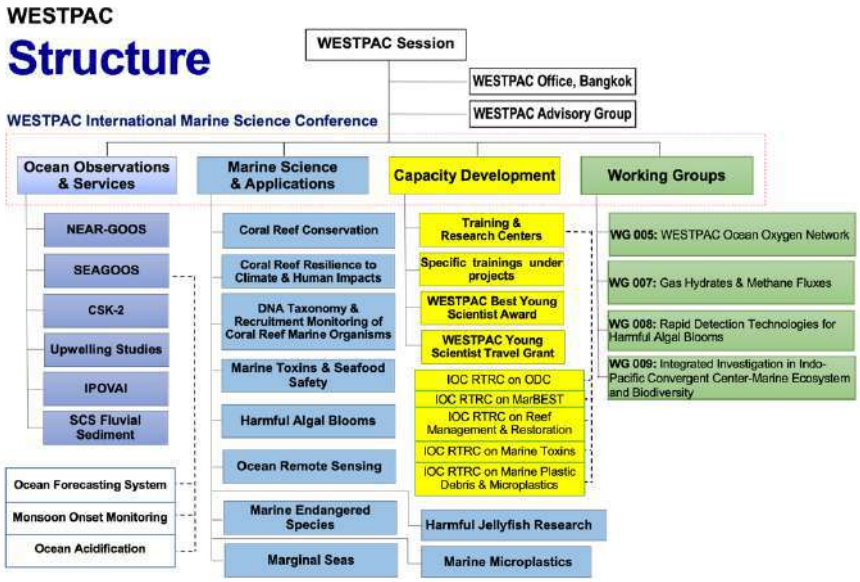

Figure 1. Structure of IOC/WESTPAC

INVITED SPEAKER: SYMP_C_INV002

NET FREE SEAS - EXPLORING COMMUNITY-BASED SOLUTIONS TO MARINE POLLUTION

Dominic Thomson[1,*]

[1] Environmental Justice Foundation (EJF), Global HQ: Unit 417, Exmouth House,
3/11 Pine Street, Farringdon, London, EC1R 0JH, UK
*e-mail: dominic.thomson@ejfoundation.org

Abstract:

Dominic Thomson is the Deputy Director and Project Manager for EJF based in Bangkok. In this presentation he will explore how communities can and should be at the core of any project designed to address environmental crises such as marine pollution. One of these projects is the Net Free Seas which collects discarded fishing nets to be recycled into new exciting products. It works with small-scale fishing communities across Thailand to collect and clean these nets ready to be taken to recycling factories.

These communities are often located in far-flung districts, far away from municipal waste management systems. Before Net Free Seas many communities relied on burning nets or sending them to landfill to dispose of them. This project aims to give them an alternative livelihood where they can actually get money for these old nets. Through engaging directly with communities such projects can maximise the environmental goals as well as the economic and societal gains from tackling marine pollution.

INVITED SPEAKER: SYMP_C_INV003

LESSONS LEARNED AND WAY FORWARD FOR MANGROVE RESTORATION IN THAILAND

Siriporn Sriaram*

International Union for Conservation of Nature (IUCN), Thailand Programme
*e-mail: Siriporn.Sriaram@iucn.org

Abstract:

Half of the world's mangroves or around 32 million hectares have been destroyed in the past decades. From 1990 – 2020, 10 million hectares of mangrove forests were lost (FAO, 2020). As a vital ecosystem which nourish juvenile fisheries and marine species as nursing grounds. Healthy mangrove ecosystem helps protect coastlines from extreme weather events and stabilise shorelines from erosion. Thailand has a total mangrove coverage of 277,923 hectares in 24 coastal provinces. From 1961 – 1995, due to charcoal concession, shrimp farming/aquaculture, mining and resettlement (Aksornkoae 2004; MFF 2011a), 55% of mangrove areas were lost.

In 2002, the Department of Marine and Coastal Resources (DMCR) was established and responsible for the mangroves monitoring and law enforcement, mangrove conservation and planting outside national parks and naval areas. On June 2021, the United Nations launched the UN Decade for Ecosystem Restoration (2021 – 2030) and encouraging global-wide afford on mangrove restoration as nature-based solution to tackle climate change issues. A large number of donors, NGOs and private companies have supported mangrove restoration in Thailand.

The presentation provides a summary of lessons learned from mangrove restoration projects in Thailand and identify opportunities for setting up the Public-Private-Partnership Mangrove restoration project that apply Forest Landscape Restoration (FLR) technique.

Keywords:

mangrove restoration, Forest Landscape Restoration, Nature-based solution, climate change

INVITED SPEAKER: SYMP_D_INV001

Crystal structure of bioplastic-synthesizing PHA synthase (PhaC) revealing an unexpected open-closed heterodimer

Min Fey Chek*, Sun-Yong Kim, Tomoyuki Mori, Toshio Hakoshima

Laboratory of Structural Biology and Protein Engineering,
Nara Institute of Science and Technology, Nara, Japan
*e-mail: chek.min_fey.ce9@bs.naist.jp

Abstract:

PHA synthase (PhaC) is the key enzyme in the biosynthesis of polyhydroxyalkanoate (PHA). PhaC forms an active dimer to polymerize acyl-moieties from the substrate acyl-coenzyme A (acyl-CoA) into PHA polymers. PHA is a type of biodegradable polyester produced by a wide-range of bacteria and archaea when there are plenty of carbon and limiting amount of other nutrients in surrounding environment. Additionally, the microbes also possess PHA depolymerase (PhaZ), which will biodegrade PHA in natural environments includes soil and ocean. These advantageous characteristics making PHA a promising alternative to the commodity petroleum-based plastics. Here, we report the crystal structure of the catalytic domain of PhaC from *Chromobacterium* sp. USM2, bound to CoA ($PhaC_{Cs}$-CAT). $PhaC_{Cs}$-CAT displayed an α/β hydrolase core subdomain, comprised of a catalytic triad (Cys291, Asp447, His477) and a CAP subdomain, which adopts a dynamic structure. In the open form, CAP subdomain restructured and retracted to allow substrate entry into the active site. In the current structure, $PhaC_{Cs}$-CAT form a dimer, where one protomer adopts an open conformation bound to a CoA, while the other protomer adopts a closed conformation in a CoA-free form. This open-closed heterodimer indicates the open conformation is stabilized by the asymmetric dimerization, enabling PhaC to accommodate CoA. The β-mercaptoethylamine moiety of the CoA is extended into the active site (Cys291) of PhaC, which is connected to a possible acyl-moiety binding cavity (Site A). The structure reveals the importance of dimerization in PhaC activity and the possible acyl-moiety binding site.

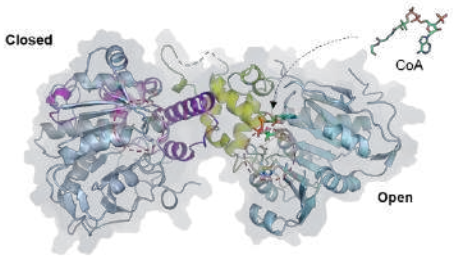

Figure. The open-closed heterodimer of $PhaC_{Cs}$-CAT. Catalytic triad (red circle) was covered by CAP subdomain in the closed form (Magenta). In the open form, the CAP subdomain (yellow) was restructure to allow substrate (e.g. acyl-CoA) enter into active site (red circle). The closed form CAP subdomain stabilized open form CAP subdomain in the heterodimer.

INVITED SPEAKER: SYMP_D_INV002

FUNCTIONALIZATION OF METAL-ORGANIC FRAMEWORKS FOR BIOMASS CONVERSION TO VALUE-ADDED CHEMICALS

Vitsarut Tangsermvit,[1] Taweesak Pila,[1] Vetiga Somjit,[1] Satoshi Horike,[1] Kanokwan Kongpatpanich,[1,*]

[1]Department of Materials Science and Engineering, School of Molecular Science and Engineering, Vidyasirimedhi Institute of Science and Technology, Rayong, 21210, Thailand
*e-mail: kanokwan.k@vistec.ac.th

Abstract:

5-Hydroxylmethylfurfural (HMF) is one of the key intermediate for the synthesis of several bio-based chemicals, polymers, and fuels. HMF is practically synthesized from fructose, while the one-pot synthesis of HMF from glucose is largely unexplored due to the necessary to have high density of both Lewis and Brønsted acid sites in the catalyst. In this work, the Lewis acid sites have been incorporated to the organic linker of the Brønsted MOF to achieve the efficient catalyst for glucose-to-HMF transformation. The local structure and acid density of the catalytic sites have been investigated to provide the understanding on the high catalytic performance of the presented acid-functionalized MOF. Moreover, the incorporation of the redox-active sites to MOF structure is also studied to demonstrate the use of MOF materials for the production 1,4-furandicarboxylic acid (FDCA), which is potentially used as monomer for bioplastic, from HMF at room temperature.

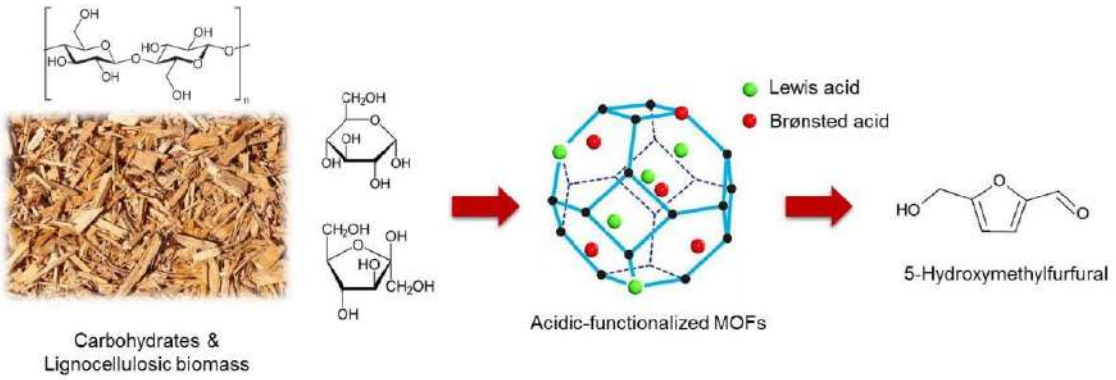

Figure. Functionalization of MOF materials for catalytic sugar conversion.

INVITED SPEAKER: SYMP_F_INV001

CONSERVE THE WORLD'S MOST IMPORTANT FORESTS TO SUSTAIN NATURE'S DIVERSITY, BENEFIT OUR CLIMATE, AND SUPPORT HUMAN WELL-BEING

Alistair Monument*

WWF International
*e-mail: amonument@wwfint.org

Abstract:

Forests are essential to our life on Earth, providing vital ecosystem services like clean air, water, food, timber, medicine and much, much more. After oceans, forests are the world's largest storehouses of carbon. Forests are home to more than three-quarters of the world's life on land. Approximately 750 million people, including 60 million Indigenous people, live in forests. Threats to the world's forests are growing. Expanding agriculture, due to an increased population and shifts in diet, is responsible for most of the world's deforestation. Illegal and unsustainable logging, usually resulting from the demand for cheap wood and paper, is responsible for most of the degradation of the world's forests—the largest threat to the world's forests. In degraded forests, small trees, bushes and plants often are severely damaged or dead; rivers are polluted; slopes are eroded; and more. Forests impact every part of our lives. The threats are so severe that we are losing huge swathes of forests at an alarming rate. The Amazon, the planet's largest rain forest, lost at least 17% of its forest cover in the last half century due to human activity—mainly clearing trees to create new or larger farms and ranches. the last 50 years our world has been transformed by an explosion in global trade, consumption and human population growth, as well as an enormous move towards urbanization. Until 1970, humanity's Ecological Footprint was smaller than the Earth's rate of regeneration. To feed and fuel our 21st century lifestyles, we are overusing the Earth's biocapacity by at least 56%. These underlying trends are driving the unrelenting destruction of nature, with only a handful of countries retaining most of the last remaining wilderness areas. Our natural world is transforming more rapidly than ever before, and climate change is further accelerating the change.

Finally, everyone has an important part to play in conserving forests for the future. Together, we can build a future that benefit both biodiversity and human well-being.

Figure.

INVITED SPEAKER: SYMP_F_INV002

IMPACT OF CLIMATE CHANGE ON BIODIVERSITY FOR SUSTAINABLE USE

Jantrararuk Tovaranonte[1,2]*

[1] School of Science, Mae Fah Luang University, Chiang Rai, Thailand
[2] Mae Fah Luang University Botanical Garden, Chiang Rai, Thailand
*e-mail: jantrararuk@mfu.ac.th

Abstract:

Climate change is one of the greatest challenges which its impact has adapted either through shifting habitat, losing species richness, changing life cycles, or the development of new physical traits biodiversity. The rate and magnitude of global climate change might be induced by the human activities to increased greenhouse gases emissions. As known, Human activities such as the production of goods and services for human well-being have resulted in the loss of biodiversity. Protecting the biodiversity is able to support the efforts to reduce the negative effects of climate change because it can help the storing carbon. Here, we try to use the meteorological approach of climate change model to predict the biological responses the climate change to augment the ability to mitigate future changes to global biodiversity and the services it provides to humans for their sustainable uses.

Figure.

INVITED SPEAKER: SYMP_F_INV003

SINGAPORE, BECOMING A CITY IN NATURE

Oh Cheow Sheng *

[1] Group Director (Streetscape), National Parks Board, Singapore
*e-mail: Oh_Cheow_Sheng@NParks.gov.sg

Abstract:

Singapore – A City in a Garden

At the start of Singapore's greening journey, the aim was to green up the island as quickly as possible to provide shade and access to green spaces for all. The greening strategy then evolved to provide colour through the planting of flowering trees and shrubs. Parks were linked up by the Park Connector Network and developments were encouraged to incorporate skyrise greenery to help improve the living environment. In the more recent years, the National Parks Board (NParks) has adopted biophilic design in restoring habitats and has been engaging the community in our efforts to sustain our greening efforts.

NParks has safeguarded more than 7,800 hectares of green spaces – nature reserves, gardens, and parks, linked by some 340km of park connectors as well as roadside greenery along streetscape – across Singapore, and has integrated greenery throughout the city. This is where we are today – a City in a Garden where greenery pervades our urban landscape.

Key Challenges

As Singapore continues to urbanise, the growing infrastructure will put increasing pressure on the established green cover. This, coupled with climate change and more extreme weather conditions, will result in higher urban temperatures and increased risks of localised flooding events. Therefore, the city needs to be developed in a way that continues to provide a high-quality living environment for Singaporeans, while ensuring that Singapore remains a distinctive global city that instils pride in our people, continue to be competitive, attract talent, investment and visitors.

Becoming a City in Nature

Singapore will be transformed into a City in Nature by the following strategies:

1. Extending Singapore's nature park network
2. Intensifying nature in parks and gardens
3. Restoring nature into the urban landscape
4. Strengthening connectivity between Singapore's green spaces

Enhancing stewardship of greenery and biodiversity

A City in Nature will enable the community to forge closer bonds through active stewardship of the environment. NParks will be expanding its outreach programmes to reach out to communities, schools, and individuals to encourage them to become stewards of greenery and biodiversity.

Under the enhanced stewardship programme, NParks has launched a new movement in Apr 2020 to plant a million trees across Singapore over the next 10 years.

INVITED SPEAKER: SYMP_G_INV001

LOW-COST MICROFLUIDIC SENSORS FOR BACTERIA AND VIRUS DETECTION

Charles S. Henry,[1,2,*] Jeremy Link,[1] Elijah Barstis,[1] Ilhoon Jang,[1] David Dandy,[2] Brian Geiss[3]

[1] Department of Chemistry, Colorado State University, Fort Collins, CO USA
[2] Department of Chemical & Biological Engineering, Colorado State University, Fort Collins, CO, USA
[3] Department of Microbiology, Immunology, and Pathology, Colorado State University, Fort Collins, CO, USA
*e-mail: chuck.henry@colostate.edu

Abstract:

Prior to the COVID-19 pandemic, infectious diseases accounted for millions of deaths worldwide. These bacterial and viral infections came from a wide range of sources including contaminated food, water, and contact with infected individuals. While these cases have been a significant burden, the world has feared the rise of a new pandemic like the Spanish Flu of 1918. We have now realized these fears with the rapid spread of SARS-CoV-2 infections around the globe. At present, more than 200M cases have been reported with more than 4M known fatalities worldwide. The economic and social losses have also been devastating. Diagnostics play a critical role in the fight against COVID-19 with their ability to identify infected individuals. The most common diagnostic assays are sensitive and specific but require expensive laboratories and highly trained individuals for operation increasing the time to get results and overall cost. Rapid diagnostic tests are an alternative that can be done outside of traditional laboratories but to date have largely under performed due to their limited complexity. Over the last decade, the Henry lab has been working to develop low-cost microfluidic devices for analysis of pathogenic bacteria and viruses. This talk will cover our recent research in this area leading to demonstration of how we are applying what we've learned to develop new systems to aid in the fight against the pandemic.

INVITED SPEAKER: SYMP_G_INV002

HOW CHEMISTRY AIDS IN THE COVID-19 VACCINE DEVELOPMENT?

Tanapat Palaga[1, 2]*

[1] Department of Microbiology, Faculty of Science, Chulalongkorn University, Bangkok, Thailand
[2] Chulalongkorn Vaccine Research Center, Faculty of Medicine, Chulalongkorn University, Bangkok, Thailand
*e-mail: Tanapat.p@chula.ac.th

Abstract:

Corona virus SARS-CoV2 is the cause of pandemic COVID-19. Effective and timely vaccine development and administration is the key for controlling the global impact of the diseases. Vaccine development relies on multidisciplinary effort mainly from immunologists, virologists and chemists. Various platforms of COVID-19 vaccines are available with speedy translating from lab bench to human arms. Adjuvants are one of the key components of successful vaccines. Adjuvants are not only used for delivery of vaccine or prolong vaccine half-life *in vivo*, but also plays a key role in determining immune response outcome. Different vaccine types require different adjuvants. Widely used mRNA vaccines are proved to be effective for preventing infections and/or disease severity of COVID-19. mRNA vaccines use antigen encoded genes in the form of mRNA with lipid nanoparticle for delivery. This presentation will review the different types of adjuvants currently in use with the focus on mRNA vaccine. Using *in vivo* imaging, the kinetics and biodistribution of mRNA delivered by lipid nanoparticles will be discussed with the implication in future use of mRNA vaccine for infectious diseases and cancer immunotherapy.

INVITED SPEAKER: SYMP_G_INV003

FLUORESCENT PROBE-BASED ASSAY FOR IDENTIFICATION OF SARS-COV-2 MAIN PROTEASE INHIBITORS

Peerapon Deetanya[1,2], Kowit Hengphasatporn[3], Patcharin Wilasluck[1,2], Yasuteru Shigeta[3], Thanyada Rungrotmongkol[4,5], Kittikhun Wangkanont[1,2,*]

[1] Center of Excellence for Molecular Biology and Genomics of Shrimp, Department of Biochemistry, Faculty of Science, Chulalongkorn University, Bangkok 10330 Thailand
[2] Molecular Crop Research Unit, Department of Biochemistry, Faculty of Science, Chulalongkorn University, Bangkok 10330 Thailand
[3] Center for Computational Sciences, University of Tsukuba, 1-1-1 Tennodai, Tsukuba, Ibaraki 305-8577, Japan
[4] Program in Bioinformatics and Computational Biology, Faculty of Science, Chulalongkorn University, Bangkok, 10330, Thailand
[5] Structural and Computational Biology Research Unit, Department of Biochemistry, Faculty of Science, Chulalongkorn University, Bangkok 10330 Thailand
*e-mail: kittikhun.w@chula.ac.th

Abstract:

The main protease of SARS-CoV-2 is responsible for viral polyprotein cleavage. This process is crucial for viral multiplication. Thus, the main protease is a promising target for antiviral drug development. Traditional enzyme activity assays for inhibitor identification rely on peptide-based substrates. However, the COVID-19 pandemic has limit or delay access to peptide synthesis services, especially for researchers in developing countries. We explored the application of 8-anilinonaphthalene-1-sulfonate (ANS) as a fluorescent probe for inhibitor identification. Fluorescence enhancement upon binding of ANS to the main protease was observed. This interaction was competitive with a peptide substrate, indicating that ANS bound within the active site. The utility of ANS-based competitive binding assay to identify main protease inhibitors was demonstrated with the flavonoid natural products baicalein and rutin. The molecular details of ANS and rutin interaction with the main protease was investigated with molecular modeling. Our results suggested that ANS could be utilized in a competitive binding assay to facilitate the identification of novel SARS-CoV-2 antiviral agents.

INVITED SPEAKER: SYMP_G_INV004

RECENT DEVELOPMENT OF COLORIMETRIC AND ELECTROCHEMICAL BIOSENSORS FOR COVID-19 DIAGNOSIS

Sudkate Chaiyo*,[1] Abdulhadee Yakoh,[1] Wanwisa Deenin,[1,2] Pawanrat Srithong,[3] Orawon Chailapakul[3]

[1] Institute of Biotechnology and Genetic Engineering, Chulalongkorn University, Bangkok, 10330, Thailand
[2] Program in Biotechnology, Faculty of Science, Chulalongkorn University, Bangkok, 10330, Thailand
[3] Electrochemistry and Optical Spectroscopy Center of Excellence (EOSCE), Department of Chemistry, Faculty of Science, Chulalongkorn University, Bangkok, 10330, Thailand
*e-mail: sudkate.c@chula.ac.th

Abstract:

Nowadays, the world has been facing the pandemic of severe acute respiratory syndrome coronavirus 2 (SARS-CoV-2) infection. As human-to-human transmission rapidly increased, this coronavirus disease 2019 (COVID-19) has spread globally and poses a threat to public health. Early and accurate diagnostics is undoubtedly needed for the containment of COVID-19 as it can facilitate the control of infection sources, thus limiting the spread of this viral contagious. Conventionally, the RT-PCR-based test for viral RNA detection is considered the gold-standard method for diagnosing COVID-19. However, the RT-PCR method might not be promptly available or affordable in many countries, as it is generally tested in a centralized laboratory/hospital by skilled personnel. To complement the detection of viral RNA, various immunosensing platforms have been developed for both antibody and antigen of SARS-CoV-2 detection. Two different techniques, colorimetric and electrochemical detection, were implemented with the sensing platforms and utilized for different sensing purposes. Both detectors can be simply miniaturized with the proposed sensors and enabled for on-field testing. In addition, the effectiveness of each sensor was demonstrated with the real-world samples (human sera for antibody testing and swab samples for antigen testing), in which the results were in good accordance with the traditional methods. These platforms can open the way to conceptually new biosensors for immunosensing applications, which are amenable to point-of-care applications and sensitive diagnostics.

INVITED SPEAKER: SYMP_H_INV001

THE CAPRICIOUS Mo–Mo QUINTUPLE BOND

Li-Teng Sun, Meng-Wei Lee, Yi-Chou Tsai*

Department of Chemistry and Frontier Research Center on Fundamental and Applied Sciences and Matters, National Tsing Hua University, Hsinchu 30013, Taiwan
*e-mail: yictsai@mx.nthu.edu.tw

Abstract:

Alkynes have two sets of mutually orthogonal π bonds, so alkynes can act as either a 2- or 4-electron donor ligand. We recently reported the metal-metal δ bonds and carbon-carbon π bond are in close resemblance in several ways. For instance, they are both two-center two-electron bonds formed by the highest occupied molecular orbital, and these two bonds are symmetry-adaptable for π interaction with the bonded atoms. As such, the quintuply bonded dimolybdenum amidinate contains two δ bonding pairs and are employed as a 2- and 4-electron donor to stabilize low-valent metal complexes. For example, the Mo-Mo quintuply bonded bis(amidinate) $Mo_2[\mu\text{-}\kappa^2\text{-}HC(N\text{-}2,6\text{-}{}^iPr_2C_6H_3)_2]_2$ readily displaced two CO ligands upon reacting with $W(CO)_6$ to give the 18-electron species $(OC)_4W\{\eta^2\text{-}Mo_2[\mu\text{-}\kappa^2\text{-}HC(N\text{-}2,6\text{-}{}^iPr_2C_6H_3)_2]_2\}$, where $Mo_2[\mu\text{-}\kappa^2\text{-}HC(N\text{-}2,6\text{-}{}^iPr_2C_6H_3)_2]_2$ is a four-electron donor ligand. More interestingly, two δ bonds in the Mo-Mo quintuple bond undergo double heterolysis upon reacting with $Fe(CO)_5$ and $CpCo(CO)_2$. In these two isolated products, one Mo atom is invariably ligated by a CO group, and the other Mo atom is bound to the 16-electron fragment "$(OC)_4Fe$" and "$Cp(CO)Co$." These two complexes are the transition metal analog of Fischer carbenes supported by experiments and theoretical investigations.

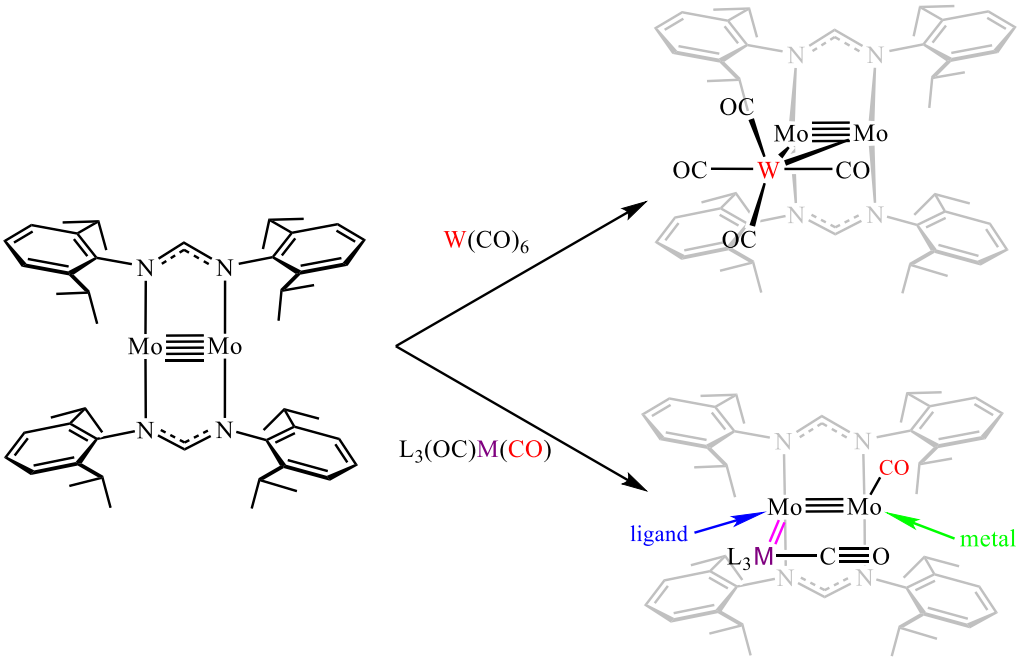

Figure.

INVITED SPEAKER: SYMP_H_INV002

STRATEGIES TOWARDS LIGHT-ACTIVATION IN IRON(III) SPIN CROSSOVER MATERIALS

Phimphaka Harding,[1*] David J. Harding,[1]Theerapoom Boonprab,[1] Warisa Thammasangwan,[1] Raul Diaz-Torres,[1] Shane G. Telfer,[2] Keith S. Murray,[3] Eric Collet,[4] Guillaume Chastanet,[5] Rodolphe Clérac[6]

[1] Functional Materials and Nanotechnology Center of Excellence, Walailak University, Thasala, Nakhon Si Thammarat, 80160, Thailand
[2] MacDiarmid Institute for Advanced Materials and Nanotechnology, Institute of Fundamental Sciences, Massey University, Wellington 6140, New Zealand
[3] School of Chemistry, Monash University, Clayton, Melbourne, Victoria, 3800, Australia
[4] Univ Rennes, CNRS, Institut de Physique de Rennes-UMR 6251, 35000 Rennes, France
[5] CNRS, Université de Bordeaux, ICMCB, 87 avenue du Dr A. Schweitzer, Pessac, F-33608, France
[6] Univ. Bordeaux, CNRS, Centre de Recherche Paul Pascal, UMR 5031, 33600 Pessac, France
*e-mail: kphimpha@mail.wu.ac.th

Abstract:

Spin crossover (SCO) is the reversible switching between two possible spin states, high spin and low spin.[1] The two spin states may be switched by a range of external stimuli including heat, light and pressure enabling their use in a rich array of applications. Octahedral iron(II) complexes form the bulk of SCO research but more recently work has been extended to iron(III) systems.[2] These complexes have the advantage of being air-stable, and allow a more diverse ligand set to enable SCO. Nevertheless, a weakness for iron(III) SCO systems is that they rarely undergo light activated SCO. In this talk, through a range of different examples, strategies towards enabling light activation in iron(III) SCO systems is discussed.

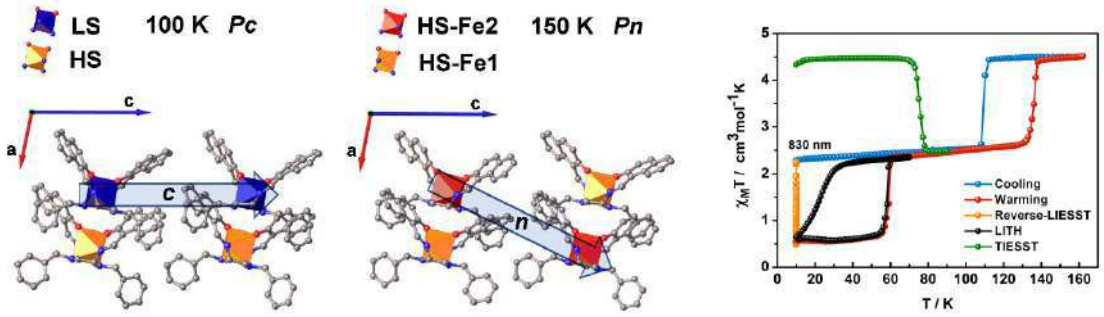

Figure. Structure of $[Fe(naphBzen)_2]I$ showing the reconstructive phase transition and the magnetic profile under thermal and light activation.

INVITED SPEAKER: SYMP_H_INV003

METAL-ORGANIC FRAMEWORKS (MOFS) IN ENERGY STORAGE RESEARCH

Yun Zong*

Agency for Science, Technology and Research (A*STAR), Singapore
*e-mail: zong_yun@hq.a-star.edu.sg

Abstract:

Metal-organic frameworks (MOFs) are ideal precursors to produce ultrahigh surface area heteroatoms-doped porous carbons which find excellent applications in energy storage as a whole. For zinc-air batteries reaping on high surface areas and critical transitional elements for high activity electrocatalysis, MOFs, particularly Co-based ones (e.g. ZIF-67) are good choices. To construct air-electrode of zinc-air batteries, binders are often needed which not only compromises electrochemically active surface area, but also the electrode conductivity. Moreover, due to the evolution of oxygen the catalyst particles may be flushed off, leading to degradation of electrocatalytic activities. Herein, MOFs in energy storage research, MOFs for zinc-air batteries, as well as immobilization of MOFs for performance enhancement of zinc-air batteries will be discussed. As example, we introduce in-situ selectively grown ZIF-67 onto electrospun polyacrylonitrile (PAN) fibers, forming PAN@ZIF-67 hybrid in "gems-on-string" structure. Thermal pyrolysis did not disturb the hierarchical structure, but furnish high ORR activity with excellent durability in alkaline electrolyte. In zinc-air battery (ZnAB) it delivers a stable discharge voltage of 1.24 V at a high current density of 20 mA cm^{-2}. A continuous operation over 38 days is demonstrated with the discharge voltage above 1.0 V at a current density of 10 mA cm^{-2}. A freestanding C-PAN@ZIF-67 mat as flexible cathode of thin and bendable ZnABs enables high discharge voltages in both flat and bent states, giving great promise to future flexible electronics.

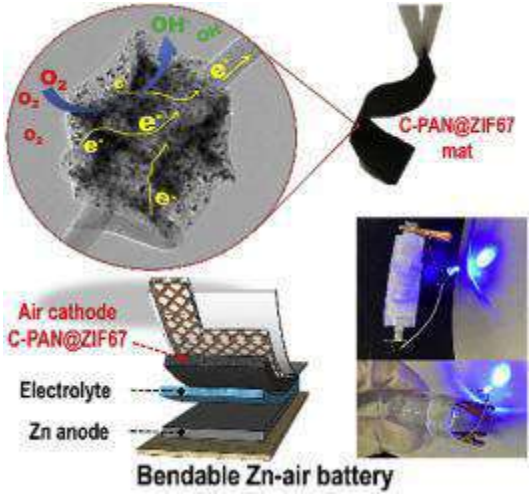

Figure. ZIF-67-derived Co and N co-doped particles strung on carbon fibers to form "gems-on-string" structure, represents a class of promising oxygen reduction reaction (ORR) catalyst with enhanced catalytic activity and stability for high-performance zinc-air batteries.

INVITED SPEAKER: SYMP_I_INV001

HEADING TOWARDS THE NEW ERA OF SMARTER FOOD SAFETY FOR A SUSTAINABLE FOOD SYSTEM

Filipe Magnum Silva Dos Santos[1], Alka[1], Low Kah Hin[2], Chai Lay Ching[1,*]

[1] Institute of Biological Sciences, Faculty of Science, University of Malaya, 50603 Kuala Lumpur, Malaysia.
[2] Department of Chemistry, Faculty of Science, University of Malaya, 50603 Kuala Lumpur, Malaysia.
*e-mail: lcchai@um.edu.my

Abstract:

As we are moving into the fourth wave of industrial revolution (4IR), we are about to experience a digital transformation of all industries, that includes agriculture, manufacturing, retail, banking and services, as well as the entire industrial value chain. 4IR is all about integrating information and communication technology such as the Internet of Things (IoT) with machines and processes for industry to form a smart and intelligent network of machines. It includes the emerging technologies of artificial intelligence (AI), cognitive computing, autonomous robots and more. These emerging smart technologies will drive a drastic industry transformation. The food industry network is complex as the food supply chain extend from farm (agriculture), food processing and manufacturing, packaging, logistics and transportation, retails, food service industry, last-mile delivery, and food waste management. Therefore, it is always challenging to manage and maintain the quality and safety of foods along these complex and dynamic food supply chain. In this presentation, various new smart technologies that enables better food traceability, foodborne disease management, food safety testing, and food packaging will be discussed.

INVITED SPEAKER: SYMP_I_INV002

CIRCULAR FOOD PRODUCTION: VALORIZATION OF FOOD MANUFACTURING BY-PRODUCTS

Suvaluk Asavasanti*

*e-mail: suvaluk.asa@kmutt.ac.th

Abstract:

TBA

INVITED SPEAKER: SYMP_I_INV003

HEMP AS A SUSTAINABLE CROP AND A RENEWABLE RESOURCE

Alan Dronkers[1]*
[1] Hemp Flax Group B.V.
*e-mail: panta67@hotmail.com

Abstract:

Sustainable agriculture is not only related to the non-use of herbicides and pesticides but is also related to improving and maintaining a healthy living top soil that has a good structure and is full of organic dust for a high absorption capacity. One of the main problems in agriculture around the world today is top soil erosion which reduces the capacity to hold water and fertilizer. The cultivation of hemp has a good effect on the soil structure because of its great and deep penetrating root system. At the same time at harvest the stalks are cut to a minimum of 15 centimeters above ground which leaves the soil protected for wind erosion and adds hemp fiber to the soil. Our company Hempflax grows its crops not with organic farmers but with normal farmers that normally have less attention for their top soil. So, most soils are heavily eroded when we start to grow our hemp. Both the crop itself and the application of organic fertilizers (mainly pig and cow manure) improve the top soil very much at just one cultivation cycle. The next following crop in the Netherlands is most time potatoes, the most lucrative crop for the farmers there. The hemp cultivation is not making a lot of money for the farmers but because of the better soil their potato crop after hemp can yield up to 10% more and because hemp reduced weeds (they can not compete with the fast growing hemp plants), less herbicide is needed in their following potato crop because the land after hemp was clean already. A true sustainable agriculture maintains a healthy and living top soil and has no further negative effects for the environment.

Many products we have in our society are produced and made from non renewable resources. So, if we use packaging materials made from plastics made from oil then we make those materials from a finite resource that one day will not be available anymore. But if we make packaging materials from bamboo then we make them from an endless renewable resource that can also be produced sustainable (organic with no negative effects for the soil or nature). Like bamboo, hemp can be cultivated sustainable and has even more uses for mankind.

We can also build a house with hemp when we build the walls from 'hempcrete'. Hempcrete is made from the wood core of the stalk (this has an open fiber). The wood is processed with hydraulic lime and because of that is instantly petrified (it becomes stone) and is not only very well insulating but also fire resistant. Where concrete can not 'breathe' especially humidity, hempcrete is a breathing wall product that regulates the humidity (no dangerous fungus in the house like with concrete). During this breathing process it also binds CO_2 and has self repairing properties when cracks might occur.

So, I can wake up in my hemp house, in my hemp bed (hemp MDF) with my hemp mattress (hemp fiber felt) and hemp pillows and hemp blankets (hemp textile). I stretch myself in my hemp underwear and put on my hemp slippers and open the hemp curtains. I go and take a shower with my hemp soap (made with seed oil) and hemp shampoo, brushing my teeth with CBD toothpaste (CBD is an anti inflammatory agent coming from the hemp flower). Then I put on my hemp shirt and hemp jeans and go to the kitchen to eat some hemp bread (made with the dehulled seeds) with hemp peanut butter and hemp cheese (made with hemp milk, made of the seed). I eat this while having some hemp tea and checking the 'hemp news'. Then I put on my hemp shoes and my hemp coat and go to my hemp electric car (with interior and exterior hemp fiber enforced plastics and other fiber interior components) with a hemp battery (hemp carbon/graphene) and drive to the hemp factory for another day at work. Life should be good in a world economy based on renewable resources and in balance with a healthy nature and environment for us to live.

INVITED SPEAKER: SYMP_I_INV004

SYNBIO CONSORTIUM IS DRIVING THAILAND BCG ECONOMY TO THE NEW FRONTIER

Korsak Towantakavanit*

Manager of Ecosytem and Incubation, Bangchak Initiative and Innovation Center (BiiC) Bangchak Corporation PLC.
Secretary of Food-Bio Industry Working Group under Innovation Institute for Industry (III), Federation of Thailand Industries
*e-mail: korsak@bangchak.co.th

Abstract:

Thailand Synthetic Biotechnology Consortium "SynBio Consortium" is about to be officially launched at the end of 2021 in order to gather key stakeholders to drive BCG economy. SynBio is a critical key success factor for the nation to shift into new paradigm of more sustainable economic and social development. The main driver of this mission is the agricultural sector. Let's imagine either we can produce milk without a cow or produce meat without animals but they are made of microbes. From the recently study funded by National Higher Education Science Research and Innovation Policy Council reported that SynBio combines various disciplines in genetics, molecular biology, systems biology, microbiology, biochemistry, and analytical chemistry. These skills need to be applied using quantitative engineering techniques of mathematics, computing, bioinformatics, biostatistics, and advanced computational modeling and simulation. Furthermore, additional skills are required in engineering, robotics, software engineering, artificial intelligence, and machine learning to support high throughput synthetic organism construction and testing. The preferred solution for integrating and developing these cross disciplinary skills is to fund focused flagship programs where scientists, engineers, and business skills can overlap and synergize.

Therefore, SynBio is determined as a secret source to tackle global challenges such as climate change, energy consumption, environmental protection, and health care. It could usher in a new normal of human being, after COVID-19 emerged, where agricultural biomass becomes the primary source of feedstocks for "Cell Factory" processing that currently manufactured from actual animals or plants. Already, SynBio is making its first steps as an enabling technology to produce various kinds of sustainable premium applications such as agriculture, renewable energy, food, supplement, ingredients, herbs, medical etc.

INVITED SPEAKER: SYMP_J_KEY001

SUSTAINABLE BIOMASS TAR REFORMING FOR SYNGAS / HYDROGEN PRODUCTION VIA THERMAL & PLASMA CATALYSIS

S. Kawi[1,*]

[1] Department of Chemical & Biomolecular Engineering, National University of Singapore, Singapore
*e-mail: chekawis@nus.edu.sg

Abstract:

Biomass has potential to provide about 25% of global total energy demand. The utilization of biomass by gasification is one of the promising routes for the production of not only hydrogen but also syngas, which is a prerequisite to produce higher valuable chemicals (methanol and ammonia) via the Fischer Tropsch process. Although biomass conversion is a promising route yet this process faces removal tar, mixture of heavy condensable hydrocarbons (1-5 ring aromatic compounds). The use of catalyst for tar cracking provides a promising way to make the process more economical and efficient as a catalyst can reduce the reaction temperature and increase the product yield. Plasma conversion process is also an emerging method to convert the reactant at lower (<300 °C) temperature [1-5].

In recent years, our research group has developed several strategies to solve this tar problem by designing and preparing stable catalysts for tar reforming by both thermal and plasma catalytic processes, using: Specific structure derived catalysts [6-13]; Addition of promoters [6,9]; Formation of bimetallic sites [6,14]; Bimetallic catalysts [6,10,11]; Organic-assistant catalyst synthesis [6,15]; Catalytic-plasma reaction [1-5]; Using waste derived materials as catalysts/support [6,16].

It is believed that effective conversion of tar produced during biomass gasification will continue to be a concern, and developing an excellent catalyst to convert tar is the crucial key to further improve the gasification technology to make it successful industrially.

References:

[1] J. Ashok, S. Kawi, *Energy Conv. & Manage.* (2021) in press.
[2] L.N. Liu, Z.K. Zhang, S. Das, S. Kawi, *Appl. Catal. B-Env.* 250 (2019) 250-272.
[3] L. Liu, S. Das, T. Chen, A. Borgna, S. Kawi, *Appl. Catal. B: Env.* 265 (2020) 118573.
[4] L. Liu, S. Das, S. Xi, S. Kawi, *Energy Conver. & Manage.* 206 (2020) 112475.
[5] S. Kawi, J. Ashok, N. Dewangan, S. Pati, *Waste & Biomass Valor.* 11 (2021) 1-30.
[6] J. Ashok, S. Das, K. Tomishige, S. Kawi, *Fuel Proc. Tech.* 199 (2020) 106252.
[7] S. Jayaprakash, A. Jangam, S. Kawi, *Fuel Proc. Tech.* 219 (2021) 106871.
[8] X. Gao, Z. Wang, J. Ashok, S. Kawi, *Chem. Eng. Sci.* X 7 (2020) 100065.
[9] J. Ashok, Y. Kathiraser, S. Kawi, *Appl. Catal. B-Env.* 172 (2015) 116-128.
[10] J. Ashok, S. Kawi, *Appl. Catal. A: Gen.* 613 (2021) 118013.
[12] Z.W. Li, Z.G. Wang, S. Kawi, *ChemCatChem* 11 (2019) 202-224.
[13] J. Ashok, S. Das, S. Kawi, *Energy Conv. & Manage.* X 1 (2019) 100003.
[14] U. Oemar, K. Hidajat, S. Kawi, *Appl. Catal. B-Env.* 148 (2014) 231-242.
[15] U. Oemar, K. Hidajat, S. Kawi, *ChemCatChem* 7 (2015) 3376-3385.
[16] J. Ashok, S. Das, S. Kawi, *Waste Manage.* 82 (2018) 249-257.

INVITED SPEAKER: SYMP_J_KEY002

PORTABLE HYDROGEN ENERGY SYSTEM WITH AN ELECTROLYZER, METAL HYDRIDE, AND PEMFC FUEL CELL

Joongmyeon Bae[1,*]

[1] Department of Mechanical Engineering, Korea Advanced Institute of Science and Technology, Republic of Korea
*e-mail: jmbae@kaist.ac.kr, +82-10-8772-1045

Abstract:

Production of green hydrogen to make sustainable environment attracts strong attentions nowadays. Likewise, hydrogen storage is also an important topic and there are various methods. Among those methods, metal hydride is studied to be applied to underwater equipment due to the high volumetric energy density.

Metal hydride has technical issues that it takes a long time to charge hydrogen and that thermal management is required.

In this study, a new system is suggested to overcome those problems. The system consists of a “charging unit” that stores hydrogen into metal hydride produced through water electrolysis and a “discharging unit” that utilizes the stored hydrogen in connection with the fuel cell.

In order to apply it to the target applications, AB2 type metal hydride is selected for the energy storage medium. However, the heat transfer coefficient of metal hydride is much lowered than usual metal powders. Consequently, the time it takes relatively long time for charging, which is an exothermic reaction. For discharging, which is an endothermic, the temperature of the hydrogen storage unit falls below zero. For internal thermal management, to solve this matter, design of heat transfer was eloquently built and the effective design was mechanically installed at the hydrogen storage system.

As a result, the time required for hydrogen charging was reduced to 1/4 compared to the system without thermal management and the temperature of the hydrogen storage unit could be maintained over zero during hydrogen discharge.

INVITED SPEAKER: SYMP_J_KEY003

HANDLING GREEN HYDROGEN IN THE FORM OF AMMONIA FOR COMMERCIAL USE AIMING TO NET ZERO EMISSION AND SUSTAINABILITY

Piyabut Charuphen[1,*]

[1] Bangkok Industrial Gas Co., Ltd., Bangkok, Thailand
*e-mail: CHARUPP@airproducts.com

Abstract:

As the world is pursuing the net zero emissions target driven by the climate change concerns, hydrogen produced from renewable sources, so-called green hydrogen, is ultimately an effective solution for bringing us there. Hydrogen is the most abundant substance on earth and can be found almost in every organic compound surrounding us, yet its light weight makes it challenging for getting stored and transported economically. Producing green hydrogen competitively is one thing while storing and transporting it to serve demands afar is another thing, putting hydrogen economy viability in question.

Air Products and Chemicals Inc. (AP), a global leading industrial gas company with the global largest hydrogen market, has leveraged its expertise in industrial gas technology to produce green ammonia by using green hydrogen as feedstock. Green ammonia is easier for being stored and transported, compared to hydrogen due to its property. Ammonia can then be dissociated to hydrogen at the point of hydrogen demand. The commercial-scale green ammonia production from green hydrogen has been recently invested by AP in Saudi Arabia, equivalent to total green hydrogen production of 650 ton per day. The green ammonia is aimed to serve green hydrogen demand in Europe and Japan for the mobility sector.

Hydrogen for mobility is driven by fuel cell electric vehicle (FCEV) using hydrogen as fuel presenting another alternative to battery electric vehicle (BEV) by resolving users' pain points from BEV's time-consuming battery charging. AP develops hydrogen refueling technology for FCEVs which provides not only safety, but also the same user experience as in refueling conventional gasoline for internal-combustion engine vehicles.

INVITED SPEAKER: SYMP_J_INV001

HYDROGEN PRODUCTION FROM CATALYTIC METHANE DECOMPOSITION

Sakhon Ratchahat[1,*], Suttichai Assabumrungrat[2], Ryo Watanabe[3], and Choji Fukuhara[3]

[1] Department of Chemical Engineering, Faculty of Engineering, Mahidol University, Nakhon Pathom, 73170, Thailand
[2] Center of Excellence in Catalysis and Catalytic Reaction Engineering, Department of Chemical Engineering, Faculty of Engineering, Chulalongkorn University, Bangkok 10330, Thailand
[3] Department of Applied Chemistry and Biochemical Engineering, Graduate School of Engineering, Shizuoka University, Shizuoka 432-8561, Japan
*e-mail: sakhon.rat@mahidol.edu

Abstract:

Hydrogen production from methane has been widely used and applied at commercial scale. Several process such as steam reforming, dry reforming, partial oxidation, and catalytic decomposition can convert methane into hydrogen. Recently the catalytic decomposition of methane (CDM) is great of interest due to its various advantages. Methane can be directly decomposed into pure hydrogen and remained deposit carbon on catalysts. By this way, hydrogen purity could be easily adjusted by controlling the process parameters. Meanwhile the formation of deposit carbon could be controlled to produce high value-added products such as carbon nanomaterials. Thus, catalysts play an important role in producing high-purity hydrogen and determining the property and quality of carbon nanomaterials. We have introduced CoMo/MgO catalyst for CDM process. As a results, it was found that the high-purity hydrogen of > 90% was obtained. In addition, the carbon nanomaterials were characterized to have crystalline structure higher than the commercial benchmark. However, the stability of catalyst is suggested to be further studied. In this research work, CDM process demonstrates a potential for production of high-purity hydrogen and carbon nanomaterials.

INVITED SPEAKER: SYMP_J_INV002

MULTIFUNCTIONAL CATALYST PELLETS FOR HYDROGEN PRODUCTION

Suwimol Wongsakulphasatch,[1] Suttichai Assabumrungrat,[2] Pasin Poung-Art,[1] Jon Powell[3,*]

[1] Department of Chemical Engineering, Faculty of Engineering,
King Mongkut's University of Technology North Bangkok, Bangkok, Thailand 10800
[2] Department of Chemical Engineering, Faculty of Engineering, Chulalongkorn University,
Bangkok, Thailand 10330
[3] International School of Engineering, Faculty of Engineering, Chulalongkorn University,
Bangkok, Thailand 10330
*e-mail: jdapowell@gmail.com:

Abstract:

Hydrogen has a wide range and increasing number of applications, including hydrogenation of organic compounds or fuel in transportation. Steam reformation of fossil fuels is the primary means of producing hydrogen, a by-product of which is CO_2. Current and recent work carried out be the authors involves the up-scaling of a process referred to as sorption enhanced steam reformation, with the development of catalyst pellets being an important part of that up-scaling process. Aims of this work include (i) the production of pellets that provide both catalysis of the steam reformation reaction and CO_2 sorption (ii) successful implementation of the pellets in a small pilot-scale plant. Results obtained using the $NiO/CaO-Al_2O_3$ multifunctional catalyst in both powder and pellet form show that hydrogen purities of 90 % and 85 % are achievable, respectively. The next phase of the research will involve the use of a small pilot-scale rig, and further development of the pellets. These developments will focus on addressing potential transport phenomena and mechanical strength issues caused by the up-scaling of the reactor and catalyst particle size. The authors discuss their approach in addressing these future challenges.

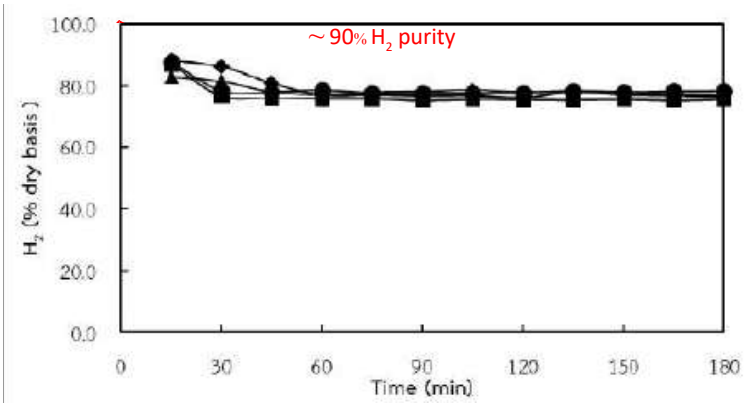

Figure.

INVITED SPEAKER: SYMP_K_INV001

REPRODUCTION OF SOME CORAL REEF FISHES IN MANADO BAY AND BUNAKEN NATIONAL PARK INDONESIA TO SUPPORT THE SUSTAINABILITY RESOURCES

Janny D. Kusen[1] Kakaskasen Andris Roeroe[1] Poppy Lintong[2,*]

[1] Faculty of Fisheries and Marine Sciences, Sam Ratulangi University Manado Indonesia
[2] Faculty of Medicine, Sam Ratulangi University Manado Indonesia
*e-mail: jannydkusen@unsrat.ac.id

Abstract:

Issue sustainability since the 1930s, especially in the USA has become an important scientific reference in the exploitation of marine fish with the presence of MSY (Maximum Sustainability Yield) against the exploitation that scientifically tends to over exploitation. The bottom line of this effort is to limitation the exploitation up to *ca*. 80 % from totally fish stock in knowing area to give time for remain fish community to recruitment naturally. Marine fishes as resources (biotic resources) that should be sustained in any reason, because it also impacts economic resources locally and globally. This is one of the reasons for the research on reproduction of several types of economically valuable coral fish in Bunaken National Park, North Sulawesi Indonesia. The main purpose of study is to analyze when these species spawning through approach with GSI (Gonado Somatix Index) and verified with gonad development histologically. By known their indices, it will be known well when these fishes will spawning down, therefore the concept to local government through the policy of exploration for when not be to exploited of certain types of fish and when it allowable. The result of six month data was figured up at some local economically species particularly to one family that famous coral reef fishes of the area. Some parts of these gonadal development could recognize the spawning time. The present rundown progress is to prepare academic base policy to government. In Indonesia's national scale since year 2016 set fish stocks at 12.5 million tons/year, whereas this stock fish number theoretically uncertainty parameters therefore to be called as fish stock assessment. No one might be secured for effort of 85 % from the national fish stock assessment, especially the number off exploitation unit. At least we have base officially number to monitor in the next survey it will going rise or down. Up to the present condition almost not reported yet the fish productivity country have field policy to limitation which economical species allowable or prohibited to exploitation. These decisions based on intensively scientific research is very important to maintain global fish stock sustained, while in the fact that some counties in the world have yearly high demand of fish stock from outside the country. Therefor the fish stock sustainability to secure the domestic high demand became the big economically business from this important biotic resources as one of their economically resources that also to be sustained. On the other hand, as biotic resources marine fishes cannot be converted like abiotic resources one, while it is unavoidable as daily needs of mostly world population. Through this small scale research could be remain again to all country to think seriously this issues and its technology. This era we have to decide how we are going to the real steps that we have to implemented the bioresources sustainability that important ecologically and economically. Because the future we just had been borrowed from our grand-grand children.

INVITED SPEAKER: SYMP_K_INV002

THE FIRST SUCCESSFUL PRODUCTION OF AN F_2 GENERATION FROM 12-YEAR-OLD SEXUALLY PROPAGATED MASSIVE CORAL COLONIES

Baria-Rodriguez MVB[1*], dela Cruz DW[2], Bonilla KG[1], Ligson CA[1], Toh TC, Edwards AJ[4], Harrison P[2], Guest JR[4]

[1] The Marine Science Institute, University of Philippines Diliman, 1101 Quezon City, Philippines
[2] Marine Ecology Research Centre, School of Environment, Science and Engineering, Southern Cross University, Lismore, New South Wales, Australia
[3] College of Alice and Peter Tan, National University of Singapore, 8 College Avenue East, Singapore, 138615
[4] School of Natural and Environmental Sciences, Newcastle University, Newcastle upon Tyne NE1 7RU, United Kingdom
* e-mail: vrodriguez@msi.upd.edu.ph

Abstract:

Coral sexual propagation for reef restoration offers several advantages compared to asexual propagation as it leads to high genetic diversity and provides access to millions of propagules. The majority of studies using the sexual mode of propagation focus on fast-growing *Acropora* species, which have been recently shown to successfully generate F_1 (first filial generation) in less than 4 years. However, there is still a lack of long-term studies on massive corals as material for reef restoration using the sexual mode of propagation, despite the fact that massive corals are generally more stress tolerant and slow to recruit naturally to degraded reefs. Here, we report on the survivorship, growth, and reproduction of two sexually propagated, massive coral species (*Favites abdita* and *F. colemani*), outplanted to the reef and monitored until 12 years post-fertilization (2009 - 2021). In 2009, gravid parent colonies were collected generating F1 parents which were outplanted in 2011. After 6 years, almost 90% of outplanted colonies were sexually mature and after 12 years, colony diameter ranged between 3.0 - 31.6 cm and 3.5 - 21.0 cm for *F. abdita* and *F. colemani*, respectively. In 2021, gravid F_1 colonies were spawned generating F_2 gametes. F_2 generation larvae were successfully collected with 100% fertilization (for *F. abdita*) and successfully settled on artificial substrates for both species. By far, this is the first study to demonstrate long-term sexual propagation of massive corals. It is highly recommended to use multiple species, with various life history strategies, via sexual propagation to restore and sustain coral population in degraded reef areas.

Keywords:

Favites abdita, *Favites colemani*, F_1 generation, F_2 generation, Spawning

INVITED SPEAKER: SYMP_K_INV003

BLUE ECONOMY: DRIVING GROWTH THROUGH SUSTAINABLE USE OF MARINE BIODIVERSITY

Sau Pinn Woo,[1,*] Annette Jaya-Ram,[1] Aileen Shau Hwai Tan[1,2]

[1] Centre for Marine and Coastal Studies (CEMACS), Universiti Sains Malaysia, 11800 USM, Penang, Malaysia
[2] School of Biological Sciences, Universiti Sains Malaysia, 11800 USM, Penang, Malaysia
*e-mail: abe_woo@hotmail.com

Abstract:

The Southeast Asia region is one of the fastest growing economy and population in the world. It sits at one of the world's marine mega biodiversity hotspot that accounts for about 76% species of corals and 37% of the fishes in the world. Rapid coastal development and rising populations have put tremendous pressure on the marine biodiversity resources especially on the demand of food. The enormous marine biodiversity resources in this region is thought to be under estimated and are under utilized that has the potential to leap the region's economic growth in the next decade. Blue food, marine pharmacognosy, and marine green tourism are some of the emerging industry in Blue Economy that are very much related to marine biodiversity that can be the game changer for Southeast Asia. A collaborative effort from academics, governments, as well as public and private sectors are essential in tapping the potentials of marine biodiversity resources and at the same time ensuring the conservation and sustainability of the marine environment and ecosystem in line with the visions of Sustainable Development Goals (SDG).

INVITED SPEAKER: SYMP_L_INV001

Sustainable Tourism as a Strategy for Adventure Tourism Development

Noel Scott*

Professor of Tourism Management, in the Sustainable
Research Centre, University of Sunshine Coast, Queensland, Australia.
*e-mail: nscott1@usc.edu.au

Abstract:

COVID 19 has put the international tourism market on hold and provided an opportunity for rethinking the experiences that adventure tour operators offer to their customers. This means innovation and new product development. This talk will discuss developing and involving sustainable tourism as a strategy for adventure tourism 'products'. Developing any new products requires a clear understanding of the target market. This presentation will discuss how to enhance tours by developing experiences meeting the needs of a particular segment.

INVITED SPEAKER: SYMP_L_INV002

STRENGTHENING TOURISM SUSTAINABILITY WELLNESS TOURISM; THROUGH SOUTHEAST ASIA

Ann Suwaree Ashton*

Graduate School of Tourism Management
National Institute of Development Administration, Thailand
*e-mail: suwaree.n@nida.ac.th, suwareeashton@hotmail.com

Abstract:

The main aim of this paper is to propose a strategy for developing wellness destinations in the next new normal tourism, especially in Southeast Asia case study: a theoretical and practical approach. In the past few years, even before the COVID-19 pandemic, the current phenomenon of a well-being lifestyle had already played an important role in peoples' everyday lives. Hence, due to a high demand in wellnesses activity and product, many events have occurred, for example: sports and leisure for heath in different places around the world (e.g. Japan, Thailand, Indonesia, and Cambodia). The healthy food market, slow food tourism development, including organic food products have been launched with highly competitive prices from many famous brands. In addition, in relation to an academic perspective it is clearly identified that a holistic wellness strategy destination development within the Southeast Asia region is still lacking, hence this chapter will fulfil those gaps (Hermon & Hazler, 1999; Lee, Denizci Guillet, & Law, 2018).

The wellness development theory and case studies in this chapter is to provide an understanding of the important concept will be proposed to match with a wellness current trend circumstance. The different case studies will be discussed in related to wellness activity and attributes. Particularly, four important wellness activities: including: sport and leisure for health; spa/ beauty; healthy food; and spiritual retreat concept (Bhumiwat & Ashton, 2020b). The significant insight of wellness attributes will be discussed, such as the well-being of: physical; mental; emotional; social and spiritual (Bhumiwat & Ashton, 2020a; Voigt, 2010; Voigt & Pforr, 2014).

Keywords:

Wellness strategy; Southeast Asia; Ageing healthy living; Wellness activity; Smart wellness destination.

References

Bhumiwat, A., & Ashton, A., S,. (2020a). Emotional Tourist Experience Model: Exploring the Health-wellbeing for the Active 50-plus Tourist Journal of Tourism, Hospitality & Culinary Arts, 12(3), 84-105.

Bhumiwat, A., & Ashton, A., S,. (2020b). Wellness Tourism Development: Spa for Health in the Hotel Industry and Tourist Perception Journal of Tourism Quarterly 2(3-4), 54-66.

Hermon, D. A., & Hazler, R. J. (1999). Adherence to Wellness Model and Perceptions of Psychological Well-being. Journal of Counseling & Development, 77(3), 339-343.

Lee, A. H., Denizci Guillet, B., & Law, R. (2018). Tourists' emotional wellness and hotel room colour. Current Issues in Tourism, 21(8), 856-862.

Voigt, C. (2010). Understanding Wellness Tourism: An Analysis of Benefits Sought, Health-Promoting Behaviours and Positive Psychological Well-being. University of South Australia Adelaide.

Voigt, C., & Pforr, C. (2014). Wellness Tourism A Destination Perspective NY, Milton Park: Routledge

INVITED SPEAKER: SYMP_L_INV003

COVID-19, SUSTAINABLE TOURISM, AND THE CHALLENGES FOR THE FUTURE

Robert C. Sinclair[1,*], R. Jeffrey Melton[2], Patthaphon Sukjai[3], Artan, Zell[4]

[1] President & CEO, Sinclair & Associates Consulting Incorporated, Advisory Director, Global Mining Sustainability
[2] Senior Partner, Ocean Editors
[3] Faculty of Liberal Arts and Science, Kasetsart University
[4] Zeta Labs
*e-mail: bob.sinclair76@gmail.com

Abstract:

The COVID-19 pandemic has had massive effects on economies worldwide. One industry that was particularly hard-hit on a global level was tourism. In this presentation, we discuss the impact of the pandemic in terms of psychological/cultural variables (e.g., collectivism versus individualism), which are the reasons that the East dramatically outperformed the West in terms of infection and death per million rates, and the impact of reopening economies in successful and unsuccessful manners. Furthermore, we discuss injustices in the distribution of vaccines and implications for the tourism industry. We describe the conditions that must be met in order to successfully reopen the tourism economy without threatening citizens' health. Finally, we advocate for vaccine passports that are formatted identically worldwide in the same manner as passports for international travel, the potential for use of dynamic face and voice recognition, and explicate our rationale.

Reference:

Sinclair, R. C., Melton, R. J., Sukjai, P., & Artan, Z. (2021, October 6-7). COVID-19, sustainable tourism, and the challenges for the future. Keynote address presented at *the 47th International Congress on Science, Technology and Technology-based Innovation: Sciences for SDGs; Challenges and Solutions*. Faculty of Arts and Sciences, Kasetsart University, Nakhon Pathom, Thailand.

INVITED SPEAKER: SYMP_L_INV004

THE SUSTAINABLE TOURISM REVIEW IN A POST-PANDEMIC 2022: REBUILDING TOURISM TO SUSTAINABILITY

Gina B. Alcoriza*

Associate Professor, Program Chairperson, Tourism Management
University of Santo Tomas-Legazpi, Legazpi City, Philippines
*e-mail: gb_alcoriza@yahoo.com.ph

Abstract:

Sustainable tourism development is now a buzzword worldwide because of the growing urbanization, climate change and social transformation. Nonetheless, the effects of COVID19 Pandemic to tourism is quite a serious problem and now a great concern on the recovery of the industry. The world now needs balance for the next generation's benefits that focuses on active participation of local residents in facilitating tourism in the countryside. The concern of rebuilding tourism now is more on a sustainable approach with greater emphasis on environmental preservation, economic stabilization and social security. The presentation describes sustainable tourism in a post- pandemic 2022. This emphasizes the activities in our rural communities as significant resources in developing sustainable tourism, and its importance and benefits. Sustainable tourism development strategies are considered in this presentation giving balance on planet, people and prosperity.

INVITED SPEAKER: SYMP_M_INV001

FROM MECHANISTIC- AND STRUCTURAL UNDERSTANDING OF *Mycobacterium tuberculosis* METABOLIC ENZYMES TO ANTI-TB COMPOUND DISCOVERY

Wuan-Geok Saw,[1] Priya Ragunathan,[1] Shin Joon, [1] Chui Fann Wong, [1] Amaravadhi Harikishore,[1] Roderick Wayland Bates[2], Gerhard Grüber,[1,*]

[1] School of Biological Science, Nanyang Technological University, Singapore
[2] Division of Chemistry and Biological Chemistry, School of Physical and Mathematical Sciences, Nanyang Technological University, Singapore 637371
[2] Experimental Drug Development Centre, The Agency for Science, Technology and Research, Singapore
[3]School of Biological Science, Nanyang Technological University, Singapore
*e-mail: ggrueber@ntu.edu.sg

Abstract:

Mycobacterium tuberculosis (*Mtb*) is one of the most successful human pathogens. Tuberculosis (TB), the deadly disease caused by this bacterium, kills more people than any other bacterial infectious disease.[1] There has been a recent resurgence of TB drug discovery activities, resulting in the identification of a number of novel enzyme inhibitors. Many of which targets the electron transport chain complexes and the F-ATP synthase as new target spaces for drug discovery, since the generation of ATP is essential for the bacterial pathogen's physiology, persistence, and pathogenicity. The mycobacterial F_1F_O-ATP synthase (F-ATP synthase**)** consists of nine subunits with a stoichiometry of α_3:β_3:γ:δ:ε:*a*:*b*:*b'*:c_9. The F_1 domain contains subunits α_3:β_3:γ:ε, the proton-translocating F_O domain subunits *a*:c_9, and subunits *b*:*b'*:*δ* are holding both domains together. Rotation of γε connects proton-conduction and ATP-formation within the α_3:β_3 hexamer. In the membrane-embedded F_O domain, each of the nine *c* subunits forms a helix-loop-helix structure, where the loop docks to the bottom of the N-terminal domain of subunit ε and the globular domain of γ, which both rotate and enable the coupling to the F_1 portion to transfer torque, derived by H^+-transport, to the catalytic $\alpha_3\beta_3$-headpiece. The talk describes how structural- and mechanistic insights into the molecular engine, F-ATP synthase, provided the platform for novel anti-TB targets and -compounds.

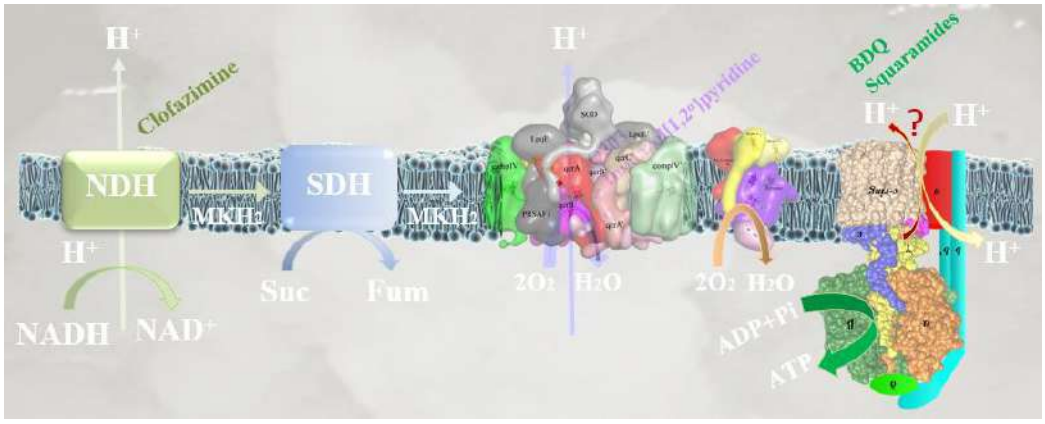

Figure. Respiratory chain of Mycobacteria

INVITED SPEAKER: SYMP_M_INV002

HOT PURSUIT OF MYCOBACTERIA BY POLYASPARTAMIDE POLYELECTROLYTES

Aasheesh Srivastava,*[1] Prabhu Srinivas Yavvari,[1] Anand Kumar Awasthi,[1] Siddhi Gupta,[2] Avinash Bajaj[2]

[1] Dept. of Chemistry, IISER Bhopal, Bhopal 462066 Madhya Pradesh India
[2] Regional Center for Biotechnology, NCR Biotech Cluster, Faridabad 122001 Haryana India
*e-mail: asrivastava@iiserb.ac.in

Abstract:

Infections caused by *Mycobacterium* are a cause of death and disfigurement for millions across the world. For example, tuberculosis (TB) accounts for approximately two million deaths every year, largely in the developing countries. The 'next generation' of this challenge is already staring at us in the form of Multi-drug resistant forms of TB (MDR-TB) and extensively drug-resistant TB (XDR-TB). In this talk, I will discuss about our efforts in designing and developing polyaspartamide polyelectrolytes as novel antimicrobial polymers that can selectively kill *Mycobacterium* with high potency. These biodegradable and biocompatible polymers are easy to prepare and modify chemically. They achieve the killing of *Mycobacterium* through a non-membrane lytic process, which is somewhat uncommon in antimicrobial polymers.

Mycobacteria also uses our own macrophage cells as a safe hideout to escape the common antimycobacterial drugs. These macrophage-residing *Mycobacteria* are therefore especially challenging to target by current drugs and become a source for recurrent infections. In the later part of my talk, I will present how we further improved our polyamide polyelectrolytes to achieve the killing of *Mycobacteria* that reside within macrophages. Not only this, but our polymers could also degrade the biofilms formed by *Mycobacteria*, further confirming their potent antimycobacterial potential. The talk will cover such polymer-based approaches that we are taking to create antimicrobial and antifouling surfaces.

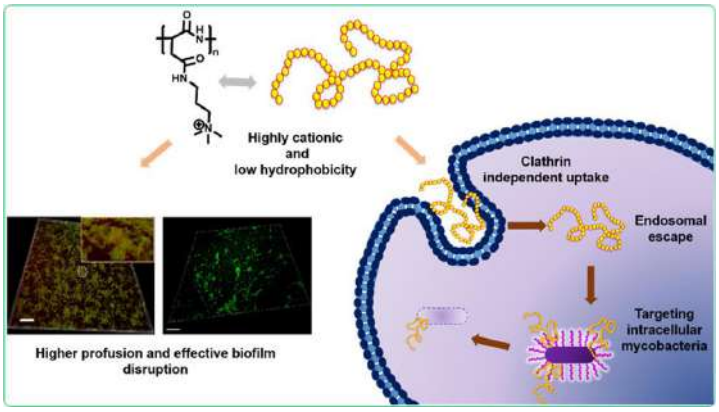

Figure. Schematic of cationic polyelectrolytes targeting Mycobacterium residing within macrophages.

INVITED SPEAKER: SYMP_M_INV003

-TBA-

Pornpan Pungpo*

*e-mail: pornpan.p@ubu.ac.th

Abstract:

TBA

INVITED SPEAKER: SYMP_N_INV001

SUSTAINABLE INNOVATIONS FOR FUTURE PACKAGING BY DOW PACK GURU

Chompoonuch Junbua*, Rangsun Chaosuwannakij, Thawatchai Tungkavet, Anurak Rassamee Amornwiwat

Dow Thailand Group, Thailand
*e-mail: JChompoonuch@dow.com

Abstract:

Nowadays, sustainability plays a major key for global innovation development, especially for future packaging trends. Material development in packaging industry is by far having a huge growth in terms of application from the broad and increase demand of people to fulfil the daily well-being. Dow Thailand Group, the leading materials science company with packaging experts " Dow Pack Guru team" succeed on the introduction of innovative science and technology to turn idea for solutions to become an action in real life. In this panel discussion, the fundamentals of polyethylene, the applications of using innovative material, mega-market trends in packaging industry, how plastic packaging can reduce Green House Gas emissions, the research and development in terms of science aiming to close the loop for a circular economy are presented. Zero-waste for long-term sustainability starting from product designing, production usage and disposal of waste as a value feedstock for other industry are also included with the real-world case sharing on sustainable packaging innovations in Thailand and the Asia Pacific.

INVITED SPEAKER: SYMP_N_INV002

ADVANCING SAFETY AND CIRCULARITY OF RUBBERIZED SPORTS SURFACES THROUGH INNOVATION AND VALUE CHAIN PARTNERSHIPS

Loganathan Ravisanker[1]*, Paul Fong[1], Dr. Zhang Liang[2], Wei Li[2]

[1] Dow Inc., Singapore
[2] Dow Inc., Shanghai, P.R. China
*e-mail: Lravisanker@dow.com

Abstract:

Field applied rubberized sports surfaces such as running tracks and playgrounds consist of an adhesive system that binds the elastic components such as EPDM and SBR rubber granules. Once cured, the surface provides desired strength and cushioning properties to reduce fall-related injuries for the users. However, the presence of harmful substances such as aromatic solvents, heavy metals, TDI, MOCA in the rubberized surfaces has been a cause of concern for the users' health and safety. In 2015, news of a 'poisonous running track' in China further highlighted the concerns and the need for sustainable and safe alternative materials.

ECOGROUND™ binder technology from Dow is a safe alternative for installing rubberized surfaces. Based on water-based acrylic copolymers, this novel binder technology has very low VOC, low odor, and is free of hazardous substances. In addition, a unique accelerator system in this binder technology enables better chemical bonding and mechanical interlocking with the granules and provides desired mechanical and cushioning properties.

As a water-based system, ECOGROUND™ is easy and safe to store and handle on sites and provides superior UV resistance, and thus helps retain aesthetics for a longer time. This innovative binder won the 2017 R&D 100 awards for Green Technology and has enabled safe and sustainable sports surfaces in many schools and universities in the region.

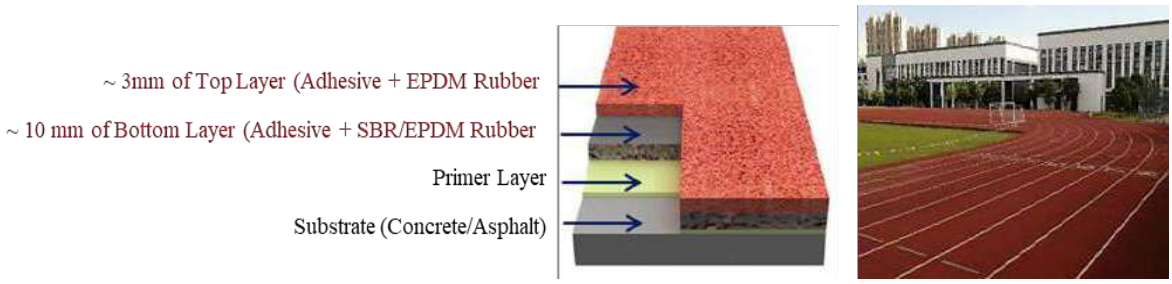

Recycled SBR granules from tires are widely used at the bottom layer of the rubberized play surfaces, while EPDM granules are used in the top layer for better aesthetics. However, SBR granules raise safety concerns with the presence of hazardous substances. As a result, the trend in some regions is to use all EPDM granules that only further increases the carbon footprint of such rubberized systems.

In Singapore, in partnership with various industry stakeholders, including educational institutions, Dow has successfully demonstrated the use of granules from used sports and school shoes as a potential replacement for the SBR granules.

The used shoes usually are thrown away into waste bins and eventually end up in incinerators and landfills. Thus, recycling used shoes into sports surfaces reduces carbon footprint and potentially improves the safety profile of the rubberized play surfaces.

INVITED SPEAKER: SYMP_N_INV003

SUSTAINABLE CHEMICAL PRODUCTION – TECHNOLOGY & PATHWAYS TOWARDS A GREEN FUTURE FOR DOW

Jens Schmidt[1]*

[1] DOW Inc. Germany
*e-mail: JSSchmidt3@dow.com

Abstract:

Society and regulatory bodies are getting more and more concerned about climate change and drive required changes in our society to keep global warming below a critical level. With industrial emissions from required energy and direct process emissions accounting for ~30% of the total global greenhouse gas emissions (source: Climate Watch / World Resources Institute) there is a clear need for industry players to define and implement transitions to a more sustainable production.

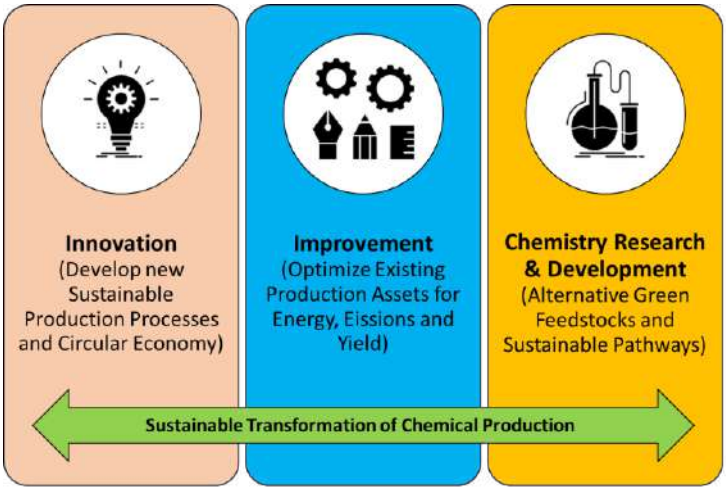

Fig.1: Key elements of a sustainable transformation of chemical production

DOW Inc as a major chemical producer has also defined Sustainability goals, such as a GHG reduction target to support society in this transformation, not only through the benefit its products bring in the value chains via energy savings downstream but also directly in Dow' s production processes around the world.

A successful transition will have to tackle all 3 scopes (1, 2, 3) of GHG emissions by developing innovative new processes which require less energy and don' t depend on fossil sources, allow for circular economies via recycling as well as optimizing existing assets regarding their energy footprint and emissions profile. In addition, a company needs to look beyond their own emissions and understand the footprint of key raw materials as these can drive over 50% of the final products carbon footprint. Here, besides improved production processes, research and development activities are needed to identify alternative green raw materials and different chemical production routes which allow for sustainable value chains.

Last not least the transformation to sustainable chemical production has to be accompanied by economic feasibility and business models which are highly dependent on incentives for green products in the market, government subsidies to overcome market barriers for entry and societal and investor preferences towards sustainable producers.

The presentation will outline the high level framework and illustrate the concept above with a few selected examples.

INVITED SPEAKER: SYMP_O_INV001

FABRICATION OF BIODEGRADABLE CELLULOSE COMPOSITE THROUGH GREENER REACTION PROCESS

Yoshito Andou[1,2 *], Safarul Mustapha[3], Tessei Kawano[3]

[1] Organization for Promotion of Research and Open Innovation,
Kyushu Institute of Technology, Fukuoka 808-0196, Japan
[2] Collaborative Research Centre for Green Materials on Environmental Technology,
Kyushu Institute of Technology
[3] Department of Life Science and Systems Engineering,
Graduate School of Life Science and Systems Engineering, Kyushu Institute of Technology
*e-mail: yando@life.kyutech.ac.jp

Abstract:

Reduction of carbon dioxide is a big concern for relaxation of global warming. The carbon dioxide increases due to the consuming of petroleum-derived products and human activities, which must reduce and replace resources based on petroleum to other. We also need to change our lifestyle. Since the use of non-biodegradable products is not sustainable, sustainable environmental science and green chemistry is certainly important nowadays.

Lignocellulose can be one candidate for low carbon resources to replace from petroleum. With increasing environmental concern our research has focused on green materials such as sustainable, renewable, and biodegradable. In this time, the author focused on celluloses as a bio-based filler and its modification as eco-friendly methods. Especially, the study of polymer composite with cellulose filler will introduce, which has been growing exponentially its study as a low-carbon material because of high strength, and stiffness, lighter in weight and biodegradability. In one of our studies, poly(lactic acid)[PLA] composite with nanocellulose was prepared through twin-screw extruder as a molding method (Figure 1). Although it is difficult to disperse cellulose in polymer matrix, this PLA composite showed high dispersibility of nanocellulose in the matrix resin.

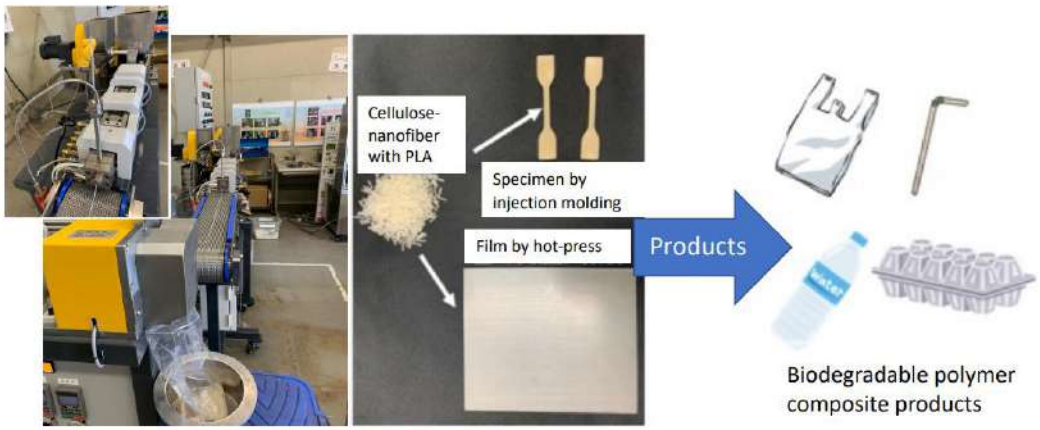

Figure 1. Preparation of PLA composites with cellulose nanofiber through twin-screw extruder and its molding products.

INVITED SPEAKER: SYMP_O_INV002

INSPIRATION, MOTIVATION, AND CREATIVITY:
HOW TO DESIGN STEM ACTIVITIES FOR SUSTAINABLE DEVELOPMENT

Ruetai Chongsrid*

National Science and Technology Development Agency, Pathum Thani, 12120, Thailand
*e-mail: reutai@nstda.or.th

Abstract:

In Thailand, Sirindhorn Science Home is one of the national learning centres for STEM activities for teachers and children under the STEM academy program, National Science and Technology Development Agency (NSTDA), Ministry of Higher Education Science Research and Innovation.

STEM activities at the Sirindhorn Science Home academy program aims to equip children and youth young people with three major skills for a worthwhile future: inspiration, motivation, and creativity.

The key pillars of the work that Sirindhorn Science Home is doing are STEM teachers' training, a STEM camp for students, and the development of curricula and science educational content and material such as books and, multimedia. Building on this, the STEM program can encourage and help develop essential skills, such as critical thinking, communication, collaboration, and creativity which are essential. Above all, it is one of the main organizations that contribute to STEM education for sustainable development.

The STEM academy program offers develops activities for children which are related with the 17 goals of sustainable development. For example, Biomimicry program, Climate action program, STEM plus culture program, Energy and transportation program, Food and feed program, Agriculture program, Robotics and automation program, Smart material for sustainable city program, Good health program, and Biodiversity program.

The STEM program academy has incorporates 7 pedagogies: 1) Making it a meaningful learning experience 2) Cultivating creativity through powerful ideas 3) Allowing students them to construct their own understanding and knowledge of the world 4) Creating challenging activities in specific contexts 5) Nurturing curiosity continuously with the Learning Spiral model 6) Teaching children how to think rather than what to think. Thus, there is metacognition process in students through recording, refection, and discussion and 7) Setting an inspiring learning environment and offering fun hands-on activities with related their daily life to motivate students to bring out their inspirations for their best learning efficiency.

Keywords:

inspiration, motivation, creativity, STEM Activity, Education for Sustainable Development, ESD

INVITED SPEAKER: SYMP_P_INV001

SUSTAINABLE FOOD SYSTEM FOR LOCAL INGREDIENTS, TREND AND SUPPORTING POLICY

Akkharawit Kanjana-opas*

Vice President of National Science and Technology Development Agency
*e-mail: akkharawit.kan@nstda.or.th

Abstract:
TBA

INVITED SPEAKER: SYMP_P_INV002

STATE-of-the-ART FOOD TECHNOLOGY FOR SUSTAINABLE FOOD SYSTEMS

Richard Archer,[1,*]

[1] School of Food & Advanced Technology, Massey University, New Zealand
[1]Riddet Institute, Palmerston North, New Zealand

*e-mail: r.h.archer@massey.ac.nz

Abstract:

For the last six years a major research programme called FIET (Food Industry Enabling Technologies) has been running across three New Zealand universities plus three research institutes. FIET covered "new" food process technologies targeted at making the New Zealand food system more sustainable. Some are new inventions, some new to New Zealand, and two are modern incarnations of ancient food preservation processes. The talk will cover ten of the more interesting projects and their technologies:

Ice Bank – the best-performed format now on offer for storing and retrieving "cold"
Rapid Liquid Freezer – robust, compact freezer for sheep or goat milk
Meat Tenderisation – new technologies for accelerating industrial scale sous vide
Precision Smoking – new device for generating culinary smoke without the undesirables
Creamed Pomace – new process to convert pomace to smooth, high fibre ingredient
Atmospheric Freeze Drying – drying from frozen more cheaply than vacuum freeze drying
Drying Sticky Products – dry juice or honey to a non-sticky powder with minimal agent
Pulsed Electric Field – reduced oil and energy use on potato chips
Microwave Sterilisation – fast thermal treatment of packaged RTE meals at retort pressures
UV of Rolling Berries – extended shelf life by even UV treatment on all sides of berries

These FIET-developed technologies are now ready for, or are undergoing, commercialisation.

INVITED SPEAKER: SYMP_P_INV003

LOCAL INGREDIENTS AND SUSTAINABILITY FOOD SYSTEM R&D FROM DEMAND SIDE

Lalana Teeranusornkit*

Senior Deputy Managing Director In terms of food innovation and new product development, CPF
*e-mail: lalana.thi@cpf.co.th

Abstract:
TBA

INVITED SPEAKER: SYMP_P_INV004

FOOD INNOVATION FOR FOOD SYSTEM SUSTAINABILITY, GOOD HEALTH, AND WELL-BEING

Paola Pittia*

Faculty of Bioscience and Technology for Food, Agriculture and Environment, University of Teramo
*e-mail: ppittia@unite.it

Abstract:

TBA

INVITED SPEAKER: SYMP_Q_INV001

-TBA-

Nannan Sun*

*e-mail: TBA

Abstract:

TBA

INVITED SPEAKER: SYMP_Q_INV002

-TBA-

Edman Tsang*

*e-mail: TBA

Abstract:

TBA

INVITED SPEAKER: SYMP_Q_INV003

-TBA-

Representative from CAS ICCB*

*e-mail: TBA

Abstract:

TBA

INVITED SPEAKER: SYMP_R_INV001

FROM INVENTION TO INNOVATION: CHEMICAL TECHNOLOGIES FOR ENVIRONMENTAL APPLICATIONS

Adam Slabon*
Department of Materials and Environmental Chemistry, Stockholm University Svante Arrhenius väg 16c 10691 Stockholm, Sweden
*e-mail: adam.slabon@mmk.su.se

Abstract:

The success of Green Chemistry is reflected both in academic research and sustainable commercial applications. In this talk, I will discuss the challenges and opportunities of scientific research with respect to its path from successful validation in the laboratory toward potential implementation and commercialization. Two examples from our on-going work will be used to elucidate the critical aspects for the transition from invention to innovation:

a) Efficient treatment of domestic and industrial wastewater is one of the major challenges of the 21st century. Among the inorganic pollutants, nitrogen species are significant contaminants, and the management of the nitrogen cycle is one the most crucial parts of wastewater purification. The company AquaBioSolve Stockholm AB has patented a solution that substitutes the required chemicals for denitrification by using electricity.

b) The growing demand for Li-ion batteries (LIBs) has made their postconsumer recycling an imperative need toward the recovery of valuable metals, such as cobalt and nickel. Nevertheless, their recovery and separation from active cathode materials in LIBs, via an efficient and environmentally friendly process, have remained a challenge. A bio-inspired metal-organic framework (MOF) achieves efficient cobalt separation at room temperature.

Figure. Toward sustainable recycling of Li-ion batteries *via* Green Chemistry.

INVITED SPEAKER: SYMP_S_INV001

GENETIC CODE REPROGRAMMING WITH ENGINEERED TRANSLATION MACHINERIES

Chayasith Uttamapinant[1,*]

[1] School of Biomolecular Science and Engineering, Vidyasirimedhi Institute of Science and Technology (VISTEC), Rayong 21210, Thailand
*e-mail: chayasith.u@vistec.ac.th

Abstract:

I will outline research efforts in my laboratory in developing labeling strategies for proteinogenic species not amenable to commonly used labeling techniques such as GFP. These species include microproteins, proteins produced from alternative open reading frames, and proteolytically processed peptides. Central to our efforts is the genetic code expansion technology, in which several components of the cellular protein translation machineries are engineered to allow production of proteins bearing new building blocks with useful reporting properties. We developed variants of genetic code expansion-based labeling strategies, including a molecular beacon reporter for processed peptides and subcellular proteome tagging tools, and demonstrated their utilities in imaging microproteins and peptides, including *de novo* generated amyloid-beta peptides, and proteomes in living mammalian cells.

INVITED SPEAKER: SYMP_S_INV002

BIOENGINEERING OF *Escherichia coli* OUTER MEMBRANE VESICLES AS DRUG AND VACCINE DELIVERY SYSTEM

Sedthawut Laotee,[1] Thitirat Rattanawongwiboon,[2] Najet Mahmoudi,[3]
Wanatchaporn Arunmanee[1,*]

[1] Department of Biochemistry and Microbiology, Faculty of Pharmaceutical Sciences, Chulalongkorn University, Bangkok, 10330, Thailand
[2] Thailand Institute of Nuclear Technology (Public Organization), Ongkharak, Nakorn Nayok, 26120, Thailand
[3] STFC ISIS Facility, Rutherford Appleton Laboratory, Chilton, Didcot, OX11 0QX, United Kingdom
*e-mail: wanatchaporn.a@chula.ac.th

Abstract:

To tackle antimicrobial resistance, antibiotic use is currently being reduced in farming. However, food production yields can be reduced due to increased disease outbreaks. One solution is vaccination, which is very cost effective and does not promote antibiotic resistance. The most effective vaccines are live-attenuated vaccines that closely mimic the biology of the pathogen. However, despite showing the best efficacy, they can revert to a virulent form and increase the risk of disease transmission in both the agricultural environment and humans. Thus, new safer and effective vaccine platforms should be developed. Outer membrane vesicles (OMVs) are released by Gram-negative bacteria and contain lipopolysaccharide (LPS), outer membrane proteins (OMP), toxins, DNA, etc. Genetically engineered OMVs can be created to attach any antigens to OMVs. Benefits of using OMVs as vaccines: 1) easy and cheap production from genetically well-defined *E. coli* 2) LPS serves as an internal adjuvant even when modified to reduce toxicity 3) safe; OMV-based vaccines have been approved for humans.

OMV's are an increasingly mature technology but a remaining hurdle to their use, noted in recent reviews, is OMV heterogeneity which makes quality control difficult. Even though a meningitis serogroup B OMV vaccine, Bexsero, has been approved for human use by EMA in 2013, it is currently the only OMV-based vaccine on the market. The main challenges in OMV development are the high reactogenicity of LPS and unwanted OMV-associated immunogens, and batch to batch consistency of OMV production. We are interested in finding the minimal redesign to make reproducible and stable OMVs. In the *E. coli* outer membrane, OMPs vary in number, size, and characteristics and may hold the key to OMV consistency. Some OMPs consisted of specific LPS binding sites which create ordered regions within the outer membrane. Certain OMPs may thus help stabilise OMVs and control the amount of LPS present. Our project uses a new approach that combine genetic engineering with accurate physical analysis to understand the qualities of reproducible, simple and stable OMVs. Furthermore, OMVs were also modified to display antigens for further applications. Therefore, the OMVs with these qualities would be a promising platform to produce safe and effective vaccines for clinical use.

INVITED SPEAKER: SYMP_S_INV003

ENGINEERING YEAST TO PRODUCE ADVANCED BIOFUELS AND HIGH-VALUE BIOCHEMICALS

Weerawat Runguphan,[1,*] Akaraphol Watcharawipas[1], Kittapong Sae-tang[1], Kitisak Sansatchanon[1], Wiparat Siripong[1], Philipp Wolf[2], Theodora Puspowangi Kusumoputri[3], Clara Angela[4], Joe James Downes[4], Pipat Sudying[1], Kriengsak Boonchoo[1], Kanokarn Kocharin[1], Sutipa Tanapongpipat[1]

[1] National Center for Genetic Engineering and Biotechnology, Thailand
[2] Leipzig University, Germany
[3] Atma Jaya University, Indonesia
[4] Indonesia International Institute for Life-Sciences
[5] University of Kent, United Kingdom
*e-mail: weerawat.run@biotec.or.th

Abstract:

As the effects of climate change become increasingly severe, metabolic engineers and synthetic biologists are looking towards greener sources for transportation fuels, platform chemicals and high-value chemicals. The design and optimization of microorganisms to produce these compounds from renewable feedstocks can significantly reduce dependence on fossil fuels and thereby produce fewer emissions. In this presentation, we provide an overview of our recent work including: 1) Engineering the yeast *Pichia pastoris* and *Saccharomyces cerevisiae* to produce the advanced biofuels isobutanol, isoamyl alcohol and the fragrant compounds acetate esters and 2) Engineering the yeast *S. cerevisiae* to produce D-lactic acid. For the first work, our strategy exploited the yeast's amino acid biosynthetic pathway and diverted the amino acid intermediates to the 2-keto acid degradation pathway for higher alcohol production. Rewiring of the cells' primary metabolism using CRISPR/Cas9 further improved product yields. Efforts are underway to create a consolidated bioprocessing platform based on a single microorganism that directly converts sugarcane bagasse into advanced biofuels. For the second work, we identified highly efficient D-lactate dehydrogenase variants after screening 600 lactic acid bacteria isolates. Systematic deletions and down-regulation of genes in the ethanol and glycerol pathways resulted in a strain that can produce D-lactic acid at near theoretical yield. Altogether, our work represents progress towards efficient microbial production of fuels, platform chemicals and high-value chemicals.

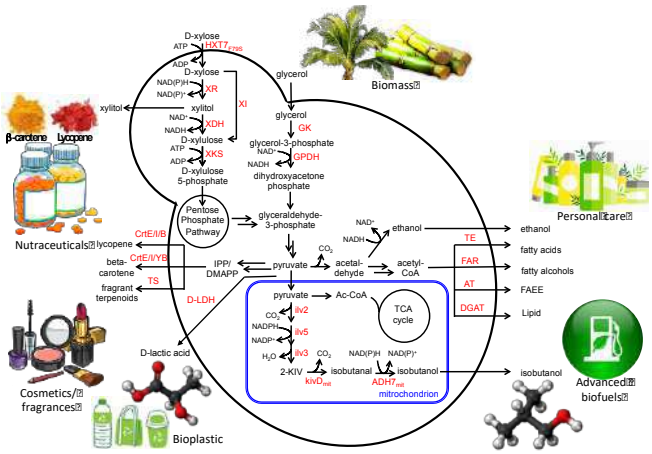

ORAL PRESENTATION SESSIONS

INFORMATION FOR ORAL PRESENTATION

Oral presentations will include a pre-recorded video presentation and a live discussion with other speakers and attendees of the session.

Oral presentations need to be pre-recorded before the conference, and uploaded to the virtual conference platform as an mp4. **The deadline to upload oral presentations to the conference e-mail (stt47congress@gmail.com) is September 24, 2021. In addition, please use the STT47 virtual background during the recording if possible.**

Presentations should be a maximum of 12 to 15 minutes based on your time slot. Select invited speakers have been asked to provide 25 minute presentations. If your video presentation exceeds the maximum time restriction, we will contact you and ask you to re-record and upload the presentation.

Video presentations will be available to attendees on the assigned date-time of each session. Each session will also have a live, Q&A-style discussion. The time and date of the discussion for your session can be found in this program book.

These live discussions will bring together the speakers, depending on the number of speakers in the session. They will provide an opportunity to answer questions from attendees, discuss your work with like-minded peers, and build connections. Live discussions will occur over ZOOM platform. You will be able to access the live discussion session through the conference platform. Access to the Zoom Meeting room will be provided 15 minutes prior to the start of the discussion time. As a presenter you should rename yourself as "ID – NAME," during the live discussion. We highly encourage all presenters to be available to take part in their live discussion session.

POSTER PRESENTATION SESSIONS

INFORMATION FOR POSTER PRESENTATION

Poster presentations will include a high-quality PDF poster, an optional pre-recorder video flash talk (as an mp4 format), and a live discussion with conference attendees on assigned conference schedule.

Posters will be accessible to conference attendees in the main conference platform for the duration of the event. You have the option of pre-recording a three-minute flash talk to accompany your poster. The flash talk will also be available in the main conference platform throughout the event. The flash talks can include excerpts of your high-quality poster in the form of a PowerPoint presentation or a high-level walkthrough. If your optional flash talk exceeds the maximum time restriction, we will contact you and ask you to re-record and upload the new video.

The deadline to upload posters to the conference support e-mail (stt47congress@gmail.com) is September 24, 2021. In addition, please use the STT47 virtual background during the recording if possible.

Presenters will also take part in a 180-minute live poster session hosted through ZOOM platform on 5th and 6th October. During this time, speakers should be present in ZOOM platform to discuss their presentations with conference attendees. We highly encourage all presenters to be available to take part in their live discussion session. As a presenter you should rename yourself as “ID – NAME SURNAME,” during the live discussion.

SESSION A -
INNOVATION IMPACTS DRIVEN SDGS

ID	Presenter	Title
A_001_P	Penpark Sirimark	THE STUDY OF EFFICIENCY OF LPG HOT AIR DRYER COMPARED WITH ELECTRICAL HOT AIR DRYER; CASE STUDY OF DRIED SLICED PORK

SESSION D - SDG CHALLENGES:
CHEMICAL SOLUTIONS FOR SUSTAINABLE SOCIETY

ID	Presenter	Title
D_001_P	Sokkeang Be	ENCHANING MANGROVE BIOCHAR RESIDUE FOR PHOSPHATE ADSORPTION BY MODIFIED WITH Fe3+, K+ AND Na+
D_002_P	Narumon phonrung	FABRICATION CHARACTERIZATION AND LEACHING PROPERTIES OF POLYACRYLONITRILE ELECTROSPUN NANOFIBROUS MEMBRANES CONTAINING BIOCHAR AND ZINC NANOPARTICLES
D_003_P	Sirintip Sangsawang	IDENTIFICATION OF NON-COVALENT INHIBITORS OF SARS-CoV-2 MAIN PROTEASE THOUGHT VIRTUAL SCREENING AND PHARMACOKINETIC PREDICTION
D_004_P	Kanlapangha Rattanasaikaew	PREPARATION AND CHARACTERIZATION OF POLYMETHACRYLATE EUGENOL-BASED PARTICLES
D_005_P	Latdamanee Phuththatham	SYNTHESIS AND CHARACTERIZATION OF NEARLY UNIFORM BIOBASED POLYMER PARTICLES FOR USE AS ANTIMICROBIAL FILM

SESSION E2 - IMPACT OF BIOLOGICAL SCIENCE TOWARDS SDGS: BIOLOGICAL SCIENCES TOWARDS SDGS

ID	Presenter	Title
E2_001_P	Panus Yingjamsiri	REGULATION OF HUMAN ID1 GENE PROMOTER BY MICRORNA-221/222
E2_002_P	Orapan Sripichai	ANTIBACTERIAL ACTIVITY OF ETHANOLIC EXTRACTS FROM THAI MEDICINAL PLANTS AGAINST Porphyromonas gingivalis
E2_003_P	Orapan Sripichai	ANTIMICROBIAL SUSCEPTIBILITY PROFILE OF Cutibacterium acnes ISOLATES FROM ACNE PATIENTS IN THAILAND
E2_004_P	Kanokorn Wechakorn	ANTIOXIDANT AND ANTIDIABETIC INHIBITORY ACTIVITY OF CRUDE EXTRACTS FROM EDIBLE INSECTS
E2_005_P	Pimchanok Puthong	COMPARATIVE STUDY ON BIOACTIVE INGREDIENTS AND ANTIOXIDANT POTENTIAL OF SOME CABBAGES (BRASSICA OLERACEA VAR. CAPITATA)
E2_006_P	Passanan Bawornkrailerd	IDENTIFICATION OF TOXIC PLANTS FROM MORPHOLOGICALLY SIMILAR EDIBLE PLANTS IN THAILAND USING DNA BARCODE
E2_007_P	Ekachai Chukeatirote	ISOLATION AND CHARACTERIZATION OF BACTERIOPHAGE INFECTING Bacillus cereus
E2_008_P	Sompradtana Worabandit	MEDIA AFFECTING GERMINATION RATE OF ORCHID SEEDS IN Seidenfadenia mitrata (Rchb. f.) Garay
E2_009_P	Phanthipha Runsaeng	METHOD FOR PROTEIN EXTRACTION AND PAPER DEVICE FOR PROTEIN SEMI-QUANTITATIVE SCREENING IN NATURAL RUBBER LATEX
E2_010_P	Supawee Kinnonkok	PREVALENCE AND CHARACTERISATION OF ANTIMICROBIAL RESISTANCE GENOTYPES AND PHENOTYPES OF CAMPYLOBACTER ISOLATES FROM PATIENTS IN THAILAND
E2_011_P	Jenjira Chalerm	RAPID AND ACCURATE IDENTIFICATION OF HUMAN-ASSOCIATED STAPHYLOCOCCI BY USE OF MULTIPLEX REAL-TIME PCR
E2_012_P	Chanoknant Thongsuk	STUDY ON PHYTOCHEMICAL COMPOSITION AND BIOLOGICAL ACTIVITIES OF Aspidistra sutepensis K. Larsen
E2_013_P	Burassakorn Tongmee	CHARACTERIZATION OF CRUDE PROTEASE EXTRACTE FROM VISCERA OF SEA BASS (Lates calcarifer)

SYMPOSIUM A

ID	Presenter	Title
SYMP_A_001_P	Jirabhorn Piluk	EFFICACY OF UVC LIGHT IN DECONTAMINATION OF INDICATOR PATHOGENS AND ITS SURFACE CLEANING APPLICATION

SYMPOSIUM C

ID	Presenter	Title
SYMP_C_001_P	Damisa Kaminsin	GENETIC DIVERSITY OF PAINTED STORK Mycteria leucocephala IN DUSIT ZOO, THAILAND, BASED ON MITOCHONDRIAL CYTOCHROME B SEQUENCES

SYMPOSIUM D

ID	Presenter	Title
SYMP_D_001_P	Yupa Wattanakanjana	CRYSTAL STRUCTURE OF SILVER (I) BROMIDE COMPLEX CONTAINING 4-PHENYLTHIOSEMICARBAZIDE AND TRIPHENYLPHOSPHINE LIGANDS
SYMP_D_002_P	Nanthawat Wannarit	CRYSTAL STRUCTURES AND HIRSHFELD SURFACE ANALYSIS OF NEW MONO- AND DINUCLEAR COPPER(II) COMPLEXES CONTAINING MIXED DIIMINE AND HYDROXYBENZOATE DERIVATIVE LIGANDS
SYMP_D_003_P	Nareekarn Meebua	SYNTHESIS, CHARACTERIZATION, X-RAY STRUCTURES OF NEW COPPER(II) COORDINATION POLYMERS INCORPORATING IMIDAZOLE-BASE DERIVATIVES AND SULFATO ANIONIC BRIDGING LIGAND
SYMP_D_004_P	Vipada Petson	SYNTHESIS, CHARACTERIZATION AND CRYTAL STRUCTURE OF A NEW DINUCLEAR COPPER(II) COMPLEX CONTAINING 1,10-PHENANTHROLINE AND 3-NITROBENZOATE LIGANDS
SYMP_D_005_P	Chayanin Nisaimun	EFFECT OF GYPSUM WASTE ADDITIONS ON THE LOW-DENSITY CALCIUM SILICATE INSULATING BOARD USING RICE HUSK ASH AS SiO_2 SOURCE
SYMP_D_006_P	Kulwadee Ponanunrirk	CRYSTAL STRUCTURE OF ONE-DIMENSIONAL LADDER CHAIN-LIKE STRUCTURE CADMIUM(II) COORDINATION POLYMER

SYMPOSIUM F

ID	Presenter	Title
SYMP_F_001_P	Kajonsak Vongshewarat	SPECIES DIVERSITY OF LICHEN AT THE UTHOKKAWIPATPRASIT WATER GATE IN PAKPHANANG DISTRICT, NAKHON SI THAMMARAT PROVINCE

SYMPOSIUM G

ID	Presenter	Title
SYMP_G_001_P	Thanathip Kosawatphat	STRAIGHTFORWARD SIGNAL AMPLIFICATION FOR A SENSITIVE DETECTION OF HORMONAL CORTISOL USING THE CONSTRICTED LATERAL FLOW TEST STRIP
SYMP_G_002_P	Umaporn Pimpitak	DEVELOPMENT OF LATERAL FLOW IMMUNOASSAY FOR RAPID AND SENSITIVE DETECTION OF anti-SARS-CoV-2 IgG

SYMPOSIUM H

ID	Presenter	Title
SYMP_H_001_P	Kann Jiwattayakul	RATIONALIZATION OF REACTIVITY OF NICKEL AND PALLADIUM PINCER COMPLEXES AS CATALYSTS FOR IODOBENZENE AND 1,2-DIMETHYLDISULFANE: THEORETICAL STUDY
SYMP_H_002_P	Napat Misrisuk	STRUCTURAL CHARACTERIZATION OF ONE POT SYNTHESIZED NANO-SIZED B-TRICALCIUM PHOSPHATE
SYMP_H_003_P	Kanyaporn Thubthong	A PERYLENE DIIMIDE/TITANIUM DIOXIDE HYBRID AS ELECTRON TRANSPORTING LAYER IN PEROVSKITE SOLAR CELLS
SYMP_H_004_P	Juntasak Wangrangsimakul	EFFECTS OF TYPES OF ARYLAMINES BASED BENZOXAZINE BINDERS IN BRAKE PADS ON THERMAL DEGRADATION KINETICS

SYMPOSIUM I

ID	Presenter	Title
SYMP_I_001_P	Rachata Lueachan	VALUE ADDED MANGO PEELS POWDER AS DIETARY FIBER IN CRISPY MIXED-VEGETABLE SHEET

SYMPOSIUM K

ID	Presenter	Title
SYMP_K_001_P	Arirush Wongnutpranont	MACROBENTHIC FAUNA AND TOURISM ACTIVITIES WITHIN UNDERWATER PINNACLE DIVE SITES IN THE NORTH ANDAMAN SEA, THAILAND
SYMP_K_002_P	Laongdow Jungrak	SPECIES DIVERSITY AND ABUNDANCE OF MACROBENTHIC INVERTEBRATES IN SEAGRASS AT KO PHRA THONG, PHANG NGA PROVINCE
SYMP_K_003_P	Ploypailin Rangseethampanya	THE INITIAL STUDY OF FISH ASSEMBLAGE IN THE CORAL NURSERIES OF HIGH STRESS-TOLERANT CORAL FRAGMENTS IN THE WESTERN GULF OF THAILAND

SYMPOSIUM N

ID	Presenter	Title
SYMP_N_001_P	Chayanit Sripradit	EFFECT OF PHOSPHATE COMPOUND AS LIQUID PHASE SINTERING ADDITIVE ON PROPERTIES OF ALUMINA CERAMICS
SYMP_N_002_P	Pimrampa Kititarakul	PREPARATION OF PERVIOUS PAVING BRICK FROM CERAMIC PITCHER USING CERAMIC GLAZE AS BONDING MATERIAL

SYMPOSIUM O

ID	Presenter	Title
SYMP_O_001_P	Supakorn Boonyuen	THE INTEGRATION OF GREEN CHEMISTRY AND SMALL SCALE FOR BASIC REDOX REACTIONS
SYMP_O_002_P	Rasitvich Panichvatana	PHYTOFABRICATION OF SILVER NANOPARTICLES (AgNPs) WITH PHARMACEUTICAL CAPABILITIES BY USING Oroxylum Indicum (L.) Kurz BARK EXTRACT
SYMP_O_003_P	Tanyalak Nuntakulkaisak	A SIMPLE PIEZOELECTRIC CALIBRATION METHOD OF THE LOW-COST OPTICAL INTERFEROMETRY KIT FOR UNDERGRADUATE TEACHING LABORATORY

SYMPOSIUM Q

ID	Presenter	Title
SYMP_Q_001_P	Soravich Mulinta	EFFECTS OF POTTERY STONE ON PHYSICAL – MECHANICAL PROPERTIES MICROSTRUCTURE AND PORCELAIN OF TABLEWARE FOR SINGLE-FAST FIRING

SYMPOSIUM R

ID	Presenter	Title
SYMP_R_001_P	Chidchanok Tabtimhin	ELEMENTAL CONTENT IN ARABICA GREEN COFFEE BEAN FROM NORTHERN THAILAND USING INDUCTIVELY COUPLED PLASMA MASS SPECTROMETRY COMBINED WITH CHEMOMETRICS
SYMP_R_002_P	Satipat Suttayasorranakhom	OLECULAR DOCKING INVESTIGATION TOWARDS GELDANAMYCIN ANALOGUES FOR HSP90 TARGETED ANTI-CANCER DRUG THERAPY
SYMP_R_003_P	Pheeraphong Bunroek	DEVELOPMENT OF SEA BASS SCALES GELATIN/NANO-TiO2 BLENDED FILMS FOR INHIBITION OF Staphylococcus aureus BY THE PHOTOCATALYTIC
SYMP_R_004_P	Keeradara Hiruntrakool	DENSITY FUNCTIONAL THEORY STUDY OF THE GLYPHOSATE ADSORPTION ON LEWIS ACIDIC BEA ZEOLITES: EFFECT OF LEWIS ACID
SYMP_R_005_P	Ornanong Opasmongkolchai	DIRECT CARBOXYLATION OF METHANE WITH CARBON DIOXIDE OVER 3d-TRANSITION METALS SUPPORTED ON METAL–ORGANIC FRAMEWORK NU-1000: A DENSITY FUNCTIONAL THEORY STUDY
SYMP_R_006_P	Athittaya Rasrichai	EFFECTS OF THE ZEOLITE FRAMEWORK ON THE ADSORPTION OF GLYPHOSATE ON HAFNIUM-CONTAINING ZEOLITES: A DFT STUDY

Junior Young Rising Stars of Science Award 2021

ID	Presenter	Title
JYRSS-01	Prapawarin Wanabodeenimit Voratha Assavasirijinda Sasikanchana Khongraksa	ANTI-BACTERIAL AND BIODEGRADABLE FILM FOR FOOD PRESERVING PACKAGING
JYRSS-02	Romteera Boongor Palika Sangtongsittichok	THE IDENTIFICATION OF VIBRIO SPP. CONTAMINATION IN FRESH AND PRESERVED SEAFOOD USING NUCLEOTIDE SEQUENCE OF 16S rRNA GENE
JYRSS-03	Palin Chokjindachai	SYNTHESIS OF FUNCTIONALIZED IONIC LIQUIDS FOR EVALUATION OF ANTIBACTERIAL ACTIVITY
JYRSS-04	Phattharaset Anantaviriya Pirada Saelee Chanyapas Thongyam	ISOLATION AND SCREENING OF BACTERIA PRODUCING BACTERIOCIN TO INHIBIT THE GROWTH OF GASTROINTESTINAL TRACT PATHOGENIC BACTERIA
JYRSS-05	Aleeta Ardcharoen Jirath Kanaraksanti Pitchayut Sangchery	ENZYMATIC PRODUCTION OF XYLOOLIGOSACCHARIDES FROM BANANA PEELS
JYRSS-06	Paravee Santikulluk Chalisa Pornsukjantra Chirayu Intaratanoo	SMART FARMING: LEAF SPOT DETECTING APPLICATION FOR HYDROPONIC GREEN OAK
JYRSS-07	Chawin Butdisuwan Premsiri Nitkamhan	MICROSTRUCTURE, BIOACTIVE COMPOUNDS, AND PHYSICAL PROPERTIES OF GLUTEN-FREE MACARONI FROM RED RICE
JYRSS-08	Kanchaporn Srisamai Kanyanat Churaya	ALPHA-AMYLASE INHIBITORY ACTIVITY OF PROTEIN AND PROTEIN HYDROLYSATES FROM HANG JASMINE RICE 105
JYRSS-09	Khwanchira Wannahom Chidapha Suepsin Laksikarn Lakornthip	A STUDY OF FATIGUE ON GRADE 9 AND 11 STUDENTS OF THE MAHASARAKHAM UNIVERSITY DEMONSTRATION SCHOOL (SECONDARY), ACADEMIC YEAR 2020
JYRSS-10	Kan Senklang Penpitcha Phongtui Nutthakit Pichai	PACKAGING CONTAINS ACTIVATED CARBON FROM LONGAN SEEDS, EMITTING ESSENTIAL OIL AND INHIBITING RIPENING OF MANGO DURING THE TRANSPORTATION
JYRSS-11	Kamonchanok Sukpaona	INHIBITION OF DENTAL CARIES BACTERIA USING ASSAM TEA EXTRACTS CULTIVATED ON THE NORTH OF THAILAND
JYRSS-12	Kritchanat Rattanasaiyai Phonkrit Angsupokai Koon Senklang	INSTRUMENT DESIGN FOR MEASURING PM 2.5 FILTRATION EFFICIENCY OF SURGICAL MASK
JYRSS-13	Kongpob Pakaranodom Mawin Srichart	SENTIMENT ANALYSIS OF COMMENTS ABOUT SMARTWATCH ON SOCIAL MEDIA BY DATA ANALYTIC METHOD
JYRSS-14	Mawaddah Billateah Nada Surerat	WOOD PLASTIC COMPOSITE FROM PLASTIC AND PARA WOOD WASTE

ID	Presenter	Title
JYRSS-15	Mumin Waealee Sakirin Sakayae	OCCURRENCE AND DISTRIBUTION OF MICROPLASTICS IN PATTANI BAY WITH SPECIAL REFERENCE TO MANGROVE HABITATS
JYRSS-16	Basla Siripatana Kittipong Nopchanasuphap	INTELLIGENT TRAFFIC LIGHT SYSTEM
JYRSS-17	Pitchayapa Muangjaila Pannaporn Pleeroy	THE EFFECT OF ZINC OXIDE AND TITANIUM DIOXIDE ON GROWTH OF MELON AND THAI PEPPER
JYRSS-18	Napat Rattanaburee Ratima Sirikat	BACTERIAL CELLULOSE COATED BY VIRGIN COCONUT OIL FOR WOUND DRESSING APPLICATION
JYRSS-19	Kittipong Tapyou Pannawich Chaisil	SMART SCHOOL ATTENDANCE SYSTEM USING FACE RECOGNITION WITH NEAR OPTIMAL IMAGING
JYRSS-20	Sopida Rakprathum Tanadol Phoyoo Waranon Kaewket	DEVELOPMENT OF ALTERNATIVE METHOD FOR DETERMINATION OF POTASSIUM IN AGRICULTURAL SAMPLES
JYRSS-21	Thidarat Promjabok Kwanchanok Thitawannonate	DIVERSITY OF BACTERIA ISOLATED FROM KLONGTUP MANGROVE FOREST AT SATTAHIP DISTRICT, CHONBURI PROVINCE AND SURVEY OF PROTEASE PRODUCING BACTERIA
JYRSS-22	Chanyanut Promkhan Napat Chonkuljana Supawit Srinithiwat	A STUDY OF EMISSIVITY OF HUMAN SKIN USING THERMAL INFRARED SENSOR
JYRSS-23	Supat Saengmanee Natcha Suttirat	NANOFLUIDS SYNTHESIS FROM MANGOSTEEN PEEL EXTRACT
JYRSS-24	Natwadee Boonrit Pattarasuda Jeenjam	THERMAL PROPERTIES OF SOLID FUEL BRIQUETTES PRODUCED FROM RICE HUSK MIXED WITH PLASTICS BY EXTRUSION TECHNIQUE
JYRSS-25	Visaruta Butburee Sasitorn Rakthong	THE DEVELOPMENT OF CHILD SLEEPING PAD OF RUBBER FOAM WITH ADDITION SILVER NANOCOMPOSITE
JYRSS-26	Chayanit Panjak Mingkwan Anna Wasanruk	DEVELOPMENT OF TOOL FOR ESTIMATING ALZHEIMER'S DISEASE RISK BY USING MIRNA AS BIOMARKER
JYRSS-27	Nitikorn Poondechalarp Poopha Suwananek	DEVELOPMENT OF OIL-BASED FORMULATION OF TRICHODERMA SP. AS A BIOCONTROL AGENT AGAINST PHYTOPATHOGENIC MICROBES
JYRSS-28	Thanakorn Hengsoontorn Pimwalan Kesornbubpha	PROTEIN HYDROLYSATE FROM SOY-MILK RESIDUE AS AN ALTERNATIVE NITROGEN SOURCE FOR AURANTIOCHYTRIUM SP. CULTIVATION
JYRSS-29	Phiriyaporn Jen-aksorn Krongsiri Pongfai	UNDERSTANDING OF REGIOSELECTIVITY IN THE ALPHA-GALACTOSIDASE WITH QM/MM
JYRSS-30	Phawat Pien-ngam	THE STUDY ON CATALYTIC ACTIVITY OF PALLADIUM ON ALUMINA FOR SYNTHESIS OF 3,4- DIHYDROPYRIMIDIN-2(1H)-ONES AND ITS DERIVATIVES UNDER GREEN CHEMISTRY APPROACH

ID	Presenter	Title
JYRSS-31	Tanatcha Chaichana Chattarin Jomkham	ITERATIVE METHODS FOR SOLVING SPLIT FEASIBILITY PROBLEM AND APPLICATION
JYRSS-32	Kittapat Manasil Thaksaporn Nantapornsiripong	EXPRESSION OF MONOPOLAR SPINDLE 1 KINASE (MPS1/TTK) IN HEPATOCELLULAR CARCINOMA

Young Rising Stars of Science Award 2021

ID	Presenter	Title
Bio-01	Sirawit Ngammaungpak	BIOCHEMICAL EFFECTS FROM VARIOUS PARTS OF *Moriga oleifera* ON GROWTH INHIBITION OF *Mimosa pigra*
Bio-02	Nuchanart Suntornnont	EFFECTS OF COENZYME Q10 ON OXIDATIVE STRESS OF HUMAN KERATINOCYTES
Bio-04	Pichsinee Sapparojpattana	EVOLUTION OF ANDROGENESIS IN BASKET CLAM GENUS *Corbicula* IN THAILAND
Bio-05	Chamawee Lertwattanaporn	PRODUCTION OF BACTERIAL BIODEGRADABLE POLYHYDROXYALKANOATES (PHAS)
Bio-06	Matchapon Anchaleepornsan	A STUDY OF THE MATING SYSTEM IN A RARE MORNING GLORY SPECIES IN THAILAND, *Blinkworthia lycioides* CHOISY (CONVOLVULACEAE)
Bio-07	Nalapat Leangnim	BIOCHEMICAL CHARACTERIZATION OF A CELL-ASSOCIATED TANNASE FROM TANNIN-TOLERANT YEAST, *Cyberlindnera rhodanensis* A22.3 FOR FEED ADDITIVE APPLICATION
Bio-08	Chanakan Thepyoo	IDENTIFICATION OF LIVESTOCK ANIMAL *ACE2* NUCLEOTIDE SEQUENCE IN REGIONS ENCODED FOR AMINO ACIDS BINDING FOR SPIKE 1 PROTEIN OF THE SARs-COV-2
Bio-09	Nutcha Sa-ingthong Anukoon Ketnak	EVALUATING PHYSIOLOGICAL RESPONSES OF NEWLY IMPROVED RD6 (RD6 BC4F4) RICE TO SALT STRESS AT SEEDLING STAGE
Bio-11	Dhup Bhukdee	IMPROVED COLORECTAL CANCER SUBTYPING WITH MACHINE LEARNING AND BIOINFORMATICS ANALYSIS
Bio-12	Wathusiri Khongsiri	ISOLATION AND CHARACTERIZATION OF LYTIC BACTERIOPHAGES AGAINST *Aeromonas hydrophila*
Bio-13	Papitchaya Taluptong	DETECTION OF *Phytophthora palmivora* from durian BY LOOP-MEDIATED ISOTHERMAL AMPLIFICATION (LAMP) ASSAY
Bio-14	Krissana Komolwanich	A STUDY ON ANTIBACTERIAL ACTIVITIES OF FRUIT PEEL WASTES FROM RAMBUTAN, LONGAN AND BANANA
Bio-15	Paphanaphak Prakopphon	MICROPLASTIC POLLUTION IN COMMERCIALLY DRIED ANCHOVY FISH IN CHUMPHON PROVINCE
Bio-16	Kanyanat Kaewutai	DISTRIBUTION OF WEDGE CLAMS *Donax* spp. ON SANDY BEACHES OF SOUTHERN THAILAND
Bio-18	Kanthida Pamornpol	THE EFFECT OF PROPOLIS EXTRACT FROM *Geniotrigona thoracica* TO INHIBIT *Propionibacterium acnes* AND *Staphylococcus aureus*
Bio-19	Intouch Khunanopparat	VARIATION IN SKULL MORPHOLOGY OF THE PANHA'S CROCODILE NEWT *Tylototriton panhai* IN LOEI-PHETCHABUN RANGES

ID	Presenter	Title
Bio-20	Jirakit Jaroonrunganan	LOW-COST PRODUCTION OF SUPER EFFECTIVE BIOBOOM IN FLUIDIZED-BED BIOREACTOR FOR CRUDE OIL REMOVAL
Bio-21	Sudarat Sukphanao	IDENTIFICATION OF *Streptomyces* sp. STRAIN SBTS01 AND W18L9 AS NOVEL SPECIES AND GENOME DATA MINING REVEALED THE BIOSYNTHESIS POTENTIAL AS PLANT GROWTH PROMOTER
Bio-22	Fah Lertkulvanich	MORPHOLOGY AND GENETIC DIVERSITY OF GOLDEN SILK ORB-WEAVER (*Nephila*) IN THAILAND
Bio-23	Anotai Suklom	THE TAXONOMIC STUDIES OF GENUS *Floresorchestia* IN KASETSART UNIVERSITY
Bio-24	Hathaichanok Vanviratikul	GENERATION OF *Chlamydomonas reinhardtii*'S MUTANT LIBRARY
Bio-26	Kanyanee Srikaewfathong	SCREENING OF PROBIOTIC BACTERIA AND PREBIOTIC CONCENTRATION TO PROMOTE PROBIOTIC GROWTH FOR INCREASING EFFICIENCY AND INHIBITING POTENTIAL PATHOGENS IN CHICKEN
Chem-01	Aphiwan Saenonphut	PORTABLE NON-ENZYMATIC ELECTROCHEMICAL SENSORS FOR PROTEIN DETECTION IN RUBBER
Chem-02	Anawat Khanonkun Pittayaporn Ardnarong	FLOW IMPROVEMENT ON MICROFLUIDIC PAPER-BASED ANALYTICAL DEVICES
Chem-03	Atchareeya Boonthana-Arkrapat Penpicha Janprasert	GREEN PROCESS FOR *Camellia Oleifera* SEED OIL PRODUCTION
Chem-04	Kajjana Boonpalit	MECHANISMS OF HYDROGEN ACTIVATION AND STYRENE HYDROGENATION BY LEWIS ACID-TRANSITION METAL CATALVSTS
Chem-05	Phanawat Charoensuk	SYNTHESIS AND CHARACTERIZATION OF CARBOXYMETHYLCELLULOSE HYDROGELS FROM RICE STRAW FOR POTENTIAL USE IN AGRICULTURAL AND BIOMEDICAL APPLICATIONS
Chem-06	Kanokwan Sakunrungrit	RAPID AND SENSITIVE METHOD FOR DETERMINATION OF MERCURY IN PHARMACEUTICAL PRODUCTS BASED ON GREEN SYNTHESIS OF CARBON NANODOTS
Chem-07	Nureesa Jehmong Sitirokiyoh Chehheng	SYNTHESIS OF HYDROXYAPATITE FROM BUDU WASTE USING ORGANIC ACID EXTRACTION
Chem-08	Siripreeya Phankingthongkum	VIRTUAL ALTERNATIVES TO MOLECULAR MODEL SET FOR CHEMISTRY EDUCATION
Chem-09	Chanon Chanloi	Cu-CATALYZED HYDROFLUORINATION OF α,β-ACETYLENIC ESTERS WITH PhC(O)F AS A F-SOURCE : A DFT STUDY
Chem-10	Asmah Narongraksakhet	FORMULATION AND STABILITY TESTING OF PERFUME CONTAINING WAN SAO LONG (*Amomum bioforum* Jack) AS MAIN INGREDIENTS
Chem-13	Nutthawan Sangnawakit	STRUCTURE AND TRANSPORT PROPERTIES OF ELECTROLYTES IN AQUEOUS ZINC-LON BATTERIES

ID	Presenter	Title
	Siriporn Teeraburanapong	
Chem-14	Chaninat Sriaudcha Potjana Ponil Sayamon Sonbuddee	NOVEL STARCH-BASED SUPERABSORBENT POLYMERS: SYNTHESIS, CHARACTERIZATION AND SWELLING PERFORMANCE
Chem-15	Chantalaksana Chantarangkul	STRUCTURAL STUDIES AND DFT CALCULATIONS OF MANGANESE(III) SCHIFF BASE COMPLEXES
Chem-16	Sudarat Laihang	THE FABRICATION OF N AND P-DOPED VEGETABLE ROOT-DERIVED HIERARCHICAL POROUS CARBON FOR SUPERCAPACITORS WITH ULTRAHIGH CAPACITANCE
Chem-18	Kulpon Makjaroen Meta Wongsa	DESIGNING A PROTEIN-BASED BIOSENSOR FOR METAL DETECTION USING PROTEIN ENGINEERING APPROACH
Com-01	Chanaporn Chaisumritchoke Tup Kongthaworn Borvorntat Nirandmongkol	A DEEP LEARNING-BASED MOSQUITO SPECIES AND GENDER CLASSIFICATION SYSTEM
Com-02	Kannika Wiratchawa	DEVELOPMENT OF A NATURAL LANGUAGE PROCESSING DATASET AND A MACHINE LEANING MODEL FOR IDENTIFYING TYPE OF LAW OF POST IN LEGAL WEBBOARDS
Com-03	Luigi Alfonso Macaraig Jeerapan Sudsawad Eric Bergum	NLP EMOTION CLASSIFICATION
Com-05	Werayut Pornanek Yutthaphum Kaewkbil	MEDICAL PROFESSIONALS AND FUNDAMENTALS HELP CARE CHAT BOT
Com-06	Put Phapon	FREE-WEARABLE FALL DETECTION FOR ELDERLY WITH DEEP LEARNING
Com-07	Sirawit Phoyoo	FLOOD DISASTER FORECASTING SYSTEM WITH LOT TECHNOLOGY
Com-09	Damrong Tongsiri	AIR QUALITY FORECASTING MODEL USING TIME-SERIES DATA
Com-10	Korrakot Triwichian Malada Leewalan	SHARE TRAVEL EXPENSES MICRO-SERVICES PLATFORM
Com-12	Aung Khant Oo Siyu Han Prasong Chonsathian	NEARBY FESTIVAL
Env-01	Ratchanon Ampornpitak	A LANDSCAPE TREE (*Tabebuia argentea)* EXHIBITS HIGHER SENSITIVITY TO SOIL MOISTURE THAN A LANDSCAPE PALM (*Ptychosperma macarthurii)* GROWING IN THE SAME ROOF GARDEN: AN IMPLICATION FOR SUSTAINABLE URBAN WATER USE
Env-02	Nutchapon Chaiwanich	EFFECTS OF ARSENIC ON GROWTH AND BIOETHANOL PRODUCTION OF CASSAVA
Env-03	Arrat Chuaichat	EFFECTS OF SEDIMENT ON JUVENILE CORAL ABUNDANCE AT KO MAPHRAO, THE WESTERN GULF OF THAILAND

ID	Presenter	Title
Env-04	Prakaidao Nontasri Tanunnut Thammasorn	DESIGNING ENVIRONMENTALLY FRIENDLY BUILDINGS: A CASE STUDY OF THE BANG PU WETLANDS NATURE STUDY CENTER, SAMUT PRAKAN PROVINCE
Env-05	Kanapon Kiranon Pornnapa Watada Hataichanok Kaewkunjorn	MODELLING FINE ATMOSPHERIC PARTICULATE MATTER USING MACHINE LEARNING
Food-01	Isaya Kijpatanasilp	KINETIC MODELING OF MICROBIAL DEGRADATION AND QUALITY OF LONGAN JUICE BY UV RADIATION
Food-03	Sukal Wasutaputtipong Chinananth Limtanapunyaporn	WILD BITTER GOURD KIMCHI
Food-04	Kamonchanok Kumlao	DEVELOPMENT OF PLANT-BASED CHEDDAR CHEESE USING RESPONSE SURFACE METHODOLOGY (RSM)
Food-05	Kanchanaphon Chumthong Nattana Kongchoosi	PRODUCTION AND CHARACTERIZATION OF pH-SHIFT-PRODUCED PROTEIN ISOLATES FROM SAGO PALM WEEVIL (*Rhynchophorus ferrugineus*) LARVAE
Food-06	Kanyakorn Thauparong Phatcharida Buaklee	DEVELOPMENT OF ROASTED RICE TEA PRODUCT FROM *Cordyceps millitaris*
Food-07	Sasitorn Khuntong	EVALUATION OF 5'-Ribonucleotides AS THE UMAMI FLAVOR IN FRESH TOMATO
Mat-01	Yolada Issaraseree Nattapan Phongpala	SUPERHYDROPHOBIC RUBBER-COATED FABRIC FOR OIL-WATER SEPARATION
Mat-02	Teepich Houtae	RECYCLING PEROVSKITE SOLAR CELLS BY NOVEL SPRAY PROCESSES
Mat-04	Chanatphapa Cunrawahthanarrong	EFFECT OF STACKING SEQUENCE ON THE STRENGTH OF CARBON FIBER SANDWICH PANEL FOR A COMPOSITE MONOCOQUE CHASSIS OF AN ELECTRIC FORMULA STUDENT RACING CAR
Mat-07	Patcharee Kulrit	BIOCOMPOSITE HYDROGEL LOADED WITH INDIGO EXTRACT FOR COSMETIC APPLICATIONS
Mat-09	Sarawut Changart	QUANTITY OF MICROPLASTIC FIBERS FROM WASHING SYNTHETIC FABRICS BY HAND WASHING
Mat-10	Supaporn Kamlue	DEVELOPMENT OF GAS SENSOR BASED ON 2D TITANIUM CARBIDE (Ti3C2Tx MXene)
Mat-11	Sasiprapa Loosungnoen Titinan Pintakorn Saranyu Khiaokhoen	A STUDY OF THE NANO STAMPING PROCESS TO FABRICATE A METALLIC NANOSTRUCTURE FOR LSPR PLASMONIC BIOSENSING APPLICATION
Math-01	Nichakan Loesatapornpipit	ASYMPTOTIC PROOERTIES OF DISCRETE MINIMAL S,LOGT-ENERGY CONSTANTS AND CONFIGURARTION
Math-02	Sukrid Petpradittha	ENTIRE SOLUTIONS OF SOME FUNCTIONAL EQUATIONS
Math-03	Arlisa Janjing	SOME NUMBER-THEORETIC PRODUCTS
Math-04	Suphawich Sengpanich	GRAPHS ASSOCIATED WITH THE MAP x-->x+x-1 ON Zn

ID	Presenter	Title
Math-05	Krongkhwan Paksonisit Nadthapong Sritecha Suktorn Bundok	FORECASTING MODEL FOR THE CHANCE OF THUNDERSTORMS IN UPPER NORTHEASTERN, THAILAND
Math-06	Pornnapat Yamphram	OPTIONS PORTFOLIO SELECTION AND INDIFFERENCE PRICING UNDER MEAN-VARIANCE UTILITY WITH FINITE LIGUIDIFY
Phy-01	Noppachanin Kongsathitporn	EXOPLANET TRANSIT TIMING VARIATION AND TRANSIT DURATION VARIATION
Phy-02	Panupol Untarabut	MOLECULAR DYNAMICS SIMULATIONS OF LITHIATION AND DELITHIATION PROCESS IN POROUS SILICON ELECTRODE MATERIAL FOR HIGH-PERFORMANCE LI-LON BATTERIES
Phy-03	Rattachanok Chongprasit	SYNTHESIS OF VANADIUM DIOXIDE (VO2) NANOPARTICLES FOR THERMOCHROMIC APPLICATIONS
Phy-04	Siriporn Silapat Siriwan Laophilai	ANALYSIS OF SPATIAL TEMPORAL VARIATIONS OF CHLOROPHYLL-A USING DATA FROM AQUA MODIS SATELLITE
Phy-05	Suriya Nongkae Khacharin Tangphanit	DEVELOPMENT OF ELECTRODE MATERIALS FROM $Ni(OH)_2$ FOR SUPERCAPACITOR APPLICATION
Phy-06	Grit Saowanit	TRACKING ORIGINS OF GAMMA RAYS IN THE MILKY WAY GALAXY BY FERMI-LAT ALL SKY MAPS
Phy-07	Worathat Paenthong	MULTI-CHANNEL RESONANCE SPECTROSCOPY FOR VOCS OPTICAL SENSOR ARRAY

ABSTRACTS AND PROCEEDINGS

CONVERSION OF CASSAVA STARCH FACTORY SOLID WASTE TO COMPOST PRODUCTION BY BACTERIAL CONSORTIUM

Cheryanus Butkumchote [1,3], and Warawut Chulalaksananukul [2,3*]

[1] Program in Biotechnology, Faculty of Science, Chulalongkorn University, Bangkok 10330, Thailand
[2] Department of Botany, Faculty of Science, Chulalongkorn University, Bangkok 10330, Thailand
[3] Biofuels by Biocatalysts Research Unit, Faculty of Science, Chulalongkorn University, Bangkok 10330, Thailand
*e-mail: warawut.c@chula.ac.th

Abstract:

In Thailand, cassava starch processing plant generates various solid waste such as cassava pulp (thippi) and wastewater treatment sludge that creating serious environmental pollution. The study of thippi and wastewater treatment sludge converted to compost by a bacterial consortium. Bacterial consortium formulated with five groups of bacteria containing *Bacillus subtilis* isolate CV1031 and S51041 (amylolytic bacteria), *B. subtilis* isolate CV103C and *Paenibacillus polymyza* isolate MALS1B (cellulolytic bacteria), *B. ginsengihumi* isolate NP1 (nitrogen fixation bacteria), *B. shackletonii* isolate PCS1041A (phosphate solubilizing bacteria), and *B. batavensis* isolate KCS1043-1 (potassium solubilizing bacteria). The effect of consortium inoculation on thippi and wastewater treatment sludge compost demonstrated nitrogen (N), phosphorus (P), potassium (K), calcium (Ca), magnesium (Mg), zinc (Zn), manganese (Mn), iron (Fe), copper (Cu) were 1.36%, 0.74%, 1.64%, 41.16%, 2.65, 0.29, 125.69, 695.77, 0.47 and 20.8 mg/kg, respectively, which is 4, 5, 5, 5, 3, 112, 14 and 16 times than thippi. Whereas, cyanide and C:N ratio of waste compost were reduced. Furthermore, the combination of thippi, wastewater treatment sludge, rice husk, cow dung, phosphate rock and feldspar has potential to improve the nutrients in waste compost.

CORROSION RESISTANCE AND TRIBOLOGICAL STUDIES OF FLUORINATED-DLC FILM DEPOSITED BY PBII TECHNIQUE

Nutthanun Moolsradoo,[1,*] Shuichi Watanabe,[2]
[1]Faculty of Industrial Education and Technology, King Mongkut's University of Technology Thonburi, Bangkok 10140, Thailand
[2]Faculty of Fundamental Engineering, Nippon Institute of Technology, Saitama 345–8501, Japan
*e-mail: nutthanun.moo@kmutt.ac.th

Abstract:
Fluorinated Diamond-Like Carbon Film fabricated from C_2H_2:CF_4 mixtures were used to compare and study the effects of fluorine content on the deposition, corrosion and tribological properties of the films prepared by plasma-based ion implantation. The structure of the films was analyzed using Raman spectroscopy. The composition at the top surface of the films was measured using Energy Dispersive X-ray Spectroscopy. The surface hardness of the films was measured using a nanoindentation hardness tester. The corrosion performance of the films was determined using potentiodynamic polarization. The tribological property of all films was measured using a ball on disk friction tester. The results indicate that with increasing fluorine content from 6.7 at.% to 20.6 at.%, the friction coefficient and corrosion current density increases, while the film hardness and corrosion potential decrease. The film hardness and corrosion potential of F-DLC film can increase the value up to 21.5 GPa and 0.009 V with fluorine content of 6.7 at.%, respectively. This is due to the formation of sp^3 sites in the film. The friction coefficient of the F-DLC film with a fluorine content of 6.7 at.% is relatively stable and demonstrates a considerable improvement in the tribological property, with the lowest friction coefficient of 0.2. This is due to high hardness and an increase in the sp^3 bonds.

Introduction:
Coating thin film technology has been studied for many applications such as in the magnetic storage, automobile, tooling, biomedical and other industries. In particular, Diamond-Like Carbon film (DLC) shows excellent properties including high hardness and elastic modulus, good biocompatibility properties, low friction coefficients and high wear resistance [1-3]. Electrochemical corrosion behavior and tribological properties of DLC film are known to be dependent on the film composition and structure, which depend on the deposition technique and precursor gas [4]. Many investigations have been dedicated to the introduction of additional foreign elements in the structure to improve the properties of DLC films [5-6]. Previous studies have shown that DLC films doped with hydrogen, fluorine and sulfur elements are improved their performance, while silicon is improved corrosion properties due to the formation of a passive film on their surfaces [7–12]. PBII (Plasma-based ion implantation) has been developed to improve DLC film properties. In this technique, low working temperature avoids film quality degradation, such as loose and rough surface structure, and avoids DLC graphitization caused by normal CVD technique which is performed at a higher working temperatures [13-14]. Currently, there is no report on the deposition of fluorine-added DLC films, on the silicon wafers by PBII aimed at comparing the corrosion and tribological performances. In this paper, the PBII technique was utilized to prepare fluorine-added DLC films (henceforth denoted as F-DLC film). The aim study was to

compare and study the effects of fluorine content on the deposition, corrosion and tribological properties of the films.

Methodology:

A system of the Plasma-based ion implantation (PBII) apparatus used in this study is shown in **Figure 1.** [15]. The inner dimensions of the vacuum chamber were 600x630x200 mm^3, with a residual pressure of approximately $1x10^{-4}$ Pa. The plasma was generated by a radio frequency (RF 13.6 MHz) glow discharge and a negative high voltage pulse power supply connected to the sample holder.

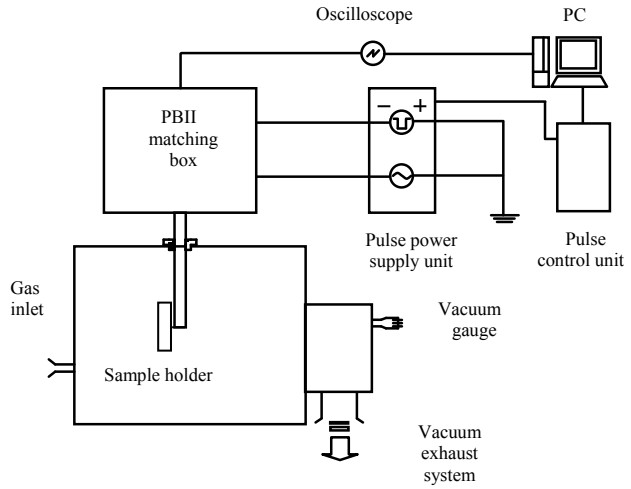

Figure 1.
System of the PBII apparatus used in this experiment [15]

Silicon (100) wafers with a thickness of 0.7 mm were used as substrates. The silicon substrates were prepared by sputter-cleaning, and then interlayer deposition using the PBII technique. The silicon substrate was sputter-cleaned with Ar^+ for 20 min to remove surface contaminants. Then, the interlayer was first deposited with CH_4 for 60 mm, to improve the adhesion between the film and the substrate. The negative pulse bias voltage of the sputter-cleaning and interlayer deposition was set to -10 kV and -20 kV, respectively. The RF power and pressure of the sputter-cleaning and interlayer deposition were set to 300 W and 1 Pa, respectively. The pulse frequency of the sputter-cleaning and interlayer deposition was set to 1 kHz at a pulse width of 5 μs and a pulse delay of 25 μs and 60 μs.

The pure DLC and F-DLC films were deposited using the PBII technique. The pure DLC film was deposited using a C_2H_2 precursor gas. The F-DLC film was deposited from gaseous mixtures of C_2H_2:CF_4 at three different flow rate ratios of 1:2, 1:4 and 1:6. The bias voltage of the deposited film was set to -5 kV at an RF power of 300 W. The pulse frequency of the deposition was set to 1 kHz at a pulse width of 5 μs and a pulse delay of 25 μs. The deposition pressure was set to 2 Pa. The total deposited thickness of the films was approximately 500 nm.

The structure of all films was analyzed using Raman spectroscopy with a beam diameter of 4 μm and a wavelength of 532 nm. The Raman spectra in the wavelength of 1,000-1,800 cm^{-1} of all films were deconvoluted into Gaussian G peaks. The composition at the top surface of all films was measured using Energy Dispersive X-ray Spectroscopy (EDS) with the acceleration voltage of 15 kV. The surface hardness of all films was measured using

a nanoindentation hardness tester. A diamond ball indenter (Berkovich-type) was used with an indentation load of 1,000 μN. The corrosion performance of all films was determined using potentiodynamic polarization experiments in an aqueous 0.05 M NaCl solution. A Pt sheet and Ag/AgCl were used as the counter and the reference electrodes, respectively. The potential voltage was varied from -3V to +3 V at a scanning rate of 10 mV/s. The tribological property of all films was measured using a ball on disk friction tester. A dry sliding test was carried out using a ball indenter, A5052 Aluminium alloy with a diameter of 6 mm. The normal applied load was set to 1 N with a linear speed of 31.4 mm/s, and 3,000 frictional rotations. The test was performed under ambient air at room temperature.

Results and Discussion:

The Raman spectra of all films are shown in **Figure 2**. The results show the Raman spectra of the pure DLC and F-DLC films deposited on the silicon substrate. All films in this experiment show a broad spectrum composed of a D band (1,350 cm^{-1}) and a G band (1,580 cm^{-1}), which are similar to the peaks observed in the conventional DLC films. From **Figure 2**, the results show that the G peak of the F-DLC films shifted from 1,505 cm^{-1} (1:2 flow rate ratio) to 1580 cm^{-1} (1:6 flow rate ratio) with fluorine addition, while the pure DLC film shows the G peak at 1,528 cm^{-1}. The G peak of the F-DLC film shift is believed to be partly due to the changes in the microstructure. This is because the addition of foreign elements in the film can revert the sp^3 network to a sp^2 network [16]. The G peak shift indicates an increase in the number or size of graphitic domains [17], which is an increase in sp^2 bonds (sp^3 decreases) and the formation of sp^2 clusters with an increase in the fluorine content. This lead to a decrease in the film hardness and elastic modulus.

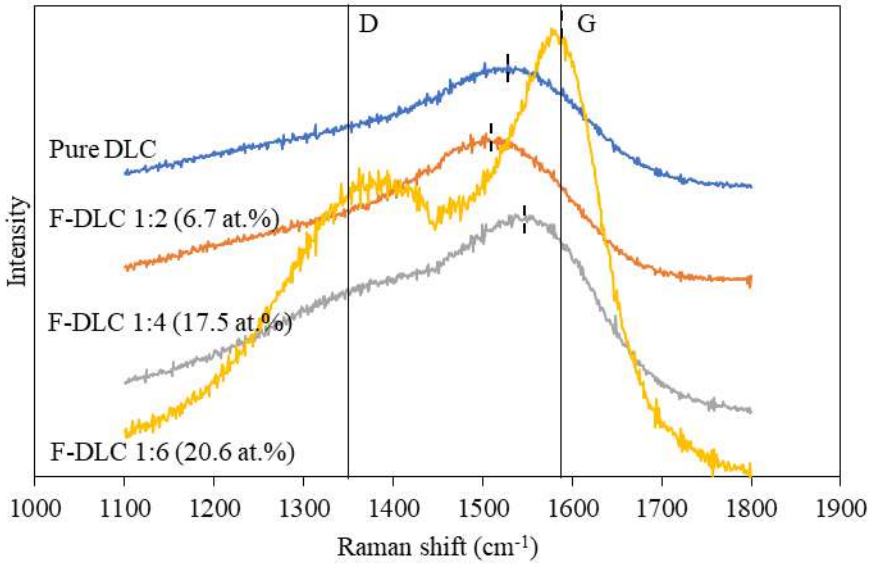

Figure 2.
Raman spectra of the pure DLC and F-DLC films

The relative atomic contents measured on the top surface of the film deposited on the silicon substrate are shown in **Table 1**. The carbon, fluorine, and oxygen were measured using EDS. The concentrations were normalized to a total of 100 at.%, neglecting the hydrogen contribution. From **Table 1**, the results of the F-DLC film show that the fluorine and oxygen contents increase from 6.7 at.% to 20.6 at.% and 0.3 at.% to 4.2 at.% when the gas flow rate ratio changed from 1:2 to 1:6, respectively.

Table 1.
G peak, Relative atomic content and film hardness of pure DLC and F-DLC films

Film type	Gas flow rate ratio	Relative atomic contents (at.%)				Film hardness (GPa)	Corrosion potential (E_{corr} (V))	Corrosion current density (i_{corr} (A/cm^2))
		C	F	O	Other			
Pure DLC	-	91.1	-	0.3	8.6	25.5	-0.010	0.949×10^{-6}
F-DLC	1:2	82.3	6.7	0.3	10.7	21.5	0.009	9.34×10^{-7}
	1:4	70.6	17.5	1.5	10.4	20.9	-0.100	9.30×10^{-6}
	1:6	64.3	20.6	4.2	10.9	10.2	-0.150	3.67×10^{-6}

The surface hardness values measured on the top surface of the film deposited on the silicon substrate are shown in **Table 1**. The hardness of the films decreased from those of pure DLC film (25.5 GPa) as the fluorine content increased. It is clear that the hardness of the F-DLC films decreased from 21.5 GPa to 10.2 GPa with fluorine and oxygen additions. That is the fluorine and oxygen gradually increased from 6.7 at.% to 20.6 at.% and 0.3 at.% to 4.2 at.% when the gas flow rate ratio changed from 1:2 to 1:6, respectively. The decreases in the film hardness are believed to be partly due to the changes in the microstructure, as concluded from Raman spectra.

The potentiodynamic polarization curves of all films are shown in **Figure 3**. The results obtained from the polarization curves are given in **Table 1**. In general, the sample in the corrosion behavior with the lower current density and greater potential indicates a better corrosion resistance [18]. An improvement in the corrosion resistance of a film is demonstrated by a shift in the polarization curve towards the region of lower current density and greater potential [18]. Moreover, the difference in the corrosion behavior of the film was attributed to the difference in the microstructure of the films [19]. An increase in the sp^3 bonds in the DLC films reduce the electrochemical corrosion and increase the electrochemical protection efficiency [18, 20].

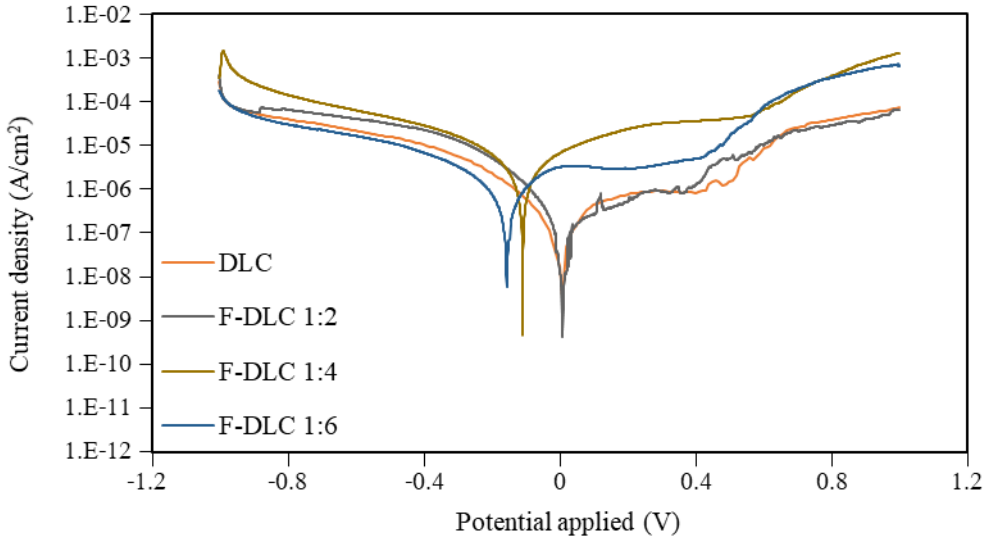

Figure 3.
Potentiodynamic polarization curve of pure DLC and F-DLC films

From **Table 3**, the results show that the corrosion potential (E_{corr}) of the pure DLC film shifted to a more positive value, while the current density (i_{corr}) decreased with fluorine content at 6.7 at.%. The greater corrosion potential and lower current density of F-DLC at fluorine content of 6.7 at.% compared with the pure DLC reveal that the introduction of fluorine into the DLC film increases the corrosion resistance because of the increased sp^3 sites in the film [21], as concluded from Raman spectra. Therefore, the greatest corrosion potential value of 0.009 V was observed in the F-DLC film with fluorine content of 6.7 at.%. Moreover, the F-DLC film shows the corrosion potential (E_{corr}) decreased from 0.009 V to -0.150 V, and the current density (i_{corr}) increased from $9.34x10^{-7}$ A/cm^2 to $3.67x10^{-6}$ A/cm^2 with fluorine content increased from 6.7 at.% to 20.6 at.%.

The friction coefficient of all films measured under ambient air is shown in **Figure 4**. The friction coefficient of the F-DLC film with fluorine content of 6.7 at.% (1:2 flow rate) is relatively stable and demonstrates a considerable improvement in the tribological property, with the lowest friction coefficient of 0.2. This is due to high hardness of 21.5 GPa and an increase in the sp^3 bonds, as concluded from Raman spectra. Moreover, the F-DLC film with fluorine content of 20.6 at.% (1:6 flow rate) had an unstable and failed easily during tests at 2,250 cycles. It is due to the lowest hardness of 10.2 GPa. The decreased film hardness results in difficultly supporting the load, which can increase the contact area at the ball-film interface, the friction coefficient can increase and tends to fail easily during the test.

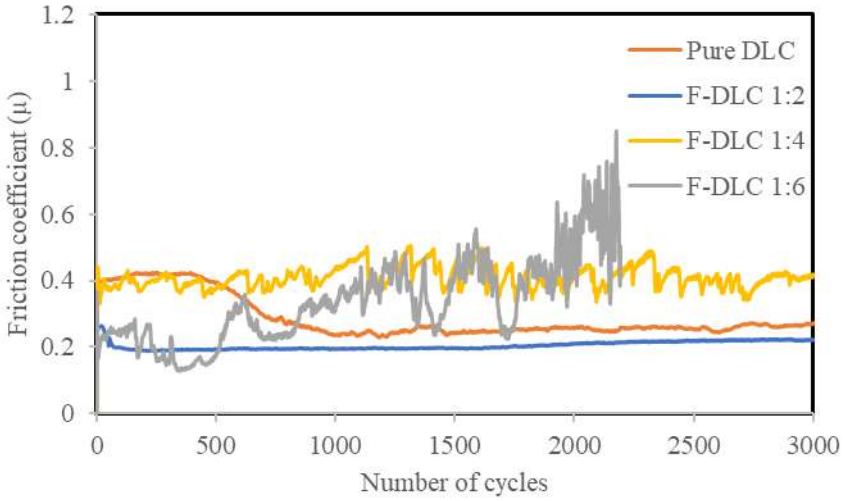

Figure 4.
Changes in friction coefficients of pure DLC and F-DLC films

Conclusion:

Fluorine added diamond-like carbon film (F-DLC) were prepared on Si (100) wafer by the PBII technique. The films were investigated in terms of their structure, atomic content, surface hardness, corrosion resistance and tribological property by using Raman spectroscopy, Energy Dispersive X-ray Spectroscopy, nanoindentation hardness testing, potentiodynamic polarization and ball on disk friction testing. It was observed that by increasing fluorine content from 6.7 at.% to 20.6 at.%, friction coefficient and corrosion current density increases, while the film hardness and corrosion potential decreases. Moreover, the film hardness and corrosion potential of F-DLC film can increase the value up to 21.5 GPa and 0.009 V with a fluorine content of 6.7 at.%, respectively. This is due to the formation of sp^3 sites in the film. The friction coefficient of the F-DLC film with fluorine content of 6.7 at.% is relatively stable and demonstrates a considerable improvement in the

tribological property, with the lowest friction coefficient of 0.2. This is due to high hardness and an increase in the sp^3 bonds.

Acknowledgements:
This research project is supported by Thailand Science Research and Innovation (TSRI) Basic Research Fund: Fiscal year 2021 under project number 64A306000031

References:
1. Kwak SCH, Wang J, Chu PK. Diamond and Related Materials. 2005;14:78-85.
2. Cruz R, Rao J, Rose T, Lawson K, Nicholls JR. Diamond and Related Materials. 2006;15:2055-2060.
3. Shirakura A, Nakaya M, Koga Y, Kodoma H, Hasebe T, Suzuki T. Thin Solid Films. 2006;494:84-91.
4. Wang Z, Wang C, Wang Q, Zhang J. Applied Surface Science. 2008;254:3021-3025.
5. Huang N, Yang P, Leng YX, Wang J, Sun H, Chen JY, Wan GJ. Surface and Coatings Technology. 2004;186:218-226.
6. Yu GQ, Tay BK, Sun Z. Surface and Coatings Technology. 2005;191:236-241.
7. Azzi M, Amirault P, Paquette M, Klemberg-Sapieha JE, Martinu L. Surface and Coatings Technology. 2010;204:3986-3994.
8. Papakonstantinou P, Zhao JF, Lemoine P, McAdams ET, McLaughlin JA. Diamond and Related Materials. 2002;11:1074-1080.
9. Moolsradoo N, Watanabe S. Advanced in Materials Science and Engineering. 2010;2010:1-8.
10. Choi J, Nakao S, Kim J, Ikeyama M, Kato T. Diamond and Related Materials. 2007;16:1361-1364.
11. Choi J, Kim J, Nakao S, Ikeyama M, Kato T.: Nuclear Instruments and Methods in Physics Research Section B: Beam Interactions with Materials and Atoms. 2007;257:718-721.
12. Choi J, Nakao S, Ikeyama M, Kato T. Surface and Interface Analysis. 2008;40:806-809.
13. Xia L, Sun M, Liao J. Diamond and Related Materials. 2005;14:42-47.
14. Wang Y, Ma X, Tang G, Sun M. Vacuum. 2013;89:74-78.
15. Moolsradoo N, Watanabe S. Advanced in Materials Science and Engineering. 2017;2017:1-8.
16. Ray SC, Pong WF, Papakonstantinou P. Thin Solid Films. 2016;610:42-47.
17. Freire Jr FL, Mariotto G, Brusa RS, Zecca A, Achete CA. Diamond and Related Materials. 1995;4:499-502.
18. Sui JH, Zhang ZG, Cai W. Nuclear Instruments and Methods in Physics Research Section B: Beam Interactions with Materials and Atoms. 2009;267:2475.
19. Liu E, Kwek HW. Thin Solid Films. 2008;516:5201-5205.
20. Ferrari AC, Robertson J. Physical Review B. 2000;61:14095-14107.
21. Khun NW, Liu E, Zeng XT. Corrosion Science. 2009;51:2158-2164.

DETECTION OF CHIKUNGUNYA VIRUS USING REVERSE TRANSCRIPTION-PCR ASSAY COMBINED WITH LATERAL FLOW DIPSTICK

[1] Ngamnete Phongpratheepchai, [2] Areekit Supatra, [3] Chansiri Kosum

[1] Faculty of Medicine, Srinakharinwirot University, Thailand
[2] Faculty of Medicine, Srinakharinwirot University, Thailand, Innovative Learning Center, Srinakharinwirot University, Thailand and Center of Excellence in Biosensors, Srinakharinwirot University, Thailand
[3] Faculty of Medicine, Srinakharinwirot University, Thailand and Center of Excellence in Biosensors, Srinakharinwirot University, Thailand
*e-mail: [1] ngamnete.net@g.swu.ac.th, [2] supatraa@g.swu.ac.th, [3] kchansiri@yahoo.com

Abstract:

Chikungunya fever is a disease caused by chikungunya virus (CHIKV), spread to people by the bite of an infected mosquito. At present, CHIKV is one of the major public health problems in tropical and subtropical countries around the world. In this study, the reverse transcriptase-polymerase chain reaction (RT-PCR) combined with a lateral flow dipstick (LFD) method was developed as a paper-based platform for CHIKV detection. The method was sensitive and specific which could be accomplished within 80 minutes. Hence, it is suitable for the use as screening test for at the outbreak areas as well as beneficial for prevention and control planning of the virus.

Introduction:

Chikungunya fever is a disease caused by Chikungunya virus (CHIKV) [(1)]. The virus was transmitted to people by the bite of infected Aedes mosquitoes [(2)] causing joint inflammation and swelling which is the main organ that suffers from the infected and often debilitating [(3)]. In the few years, the CHIKV has become one of the major problems in Southeast Asia such as Singapore, Malaysia, and Thailand [(4)].

The two species of *Aedes mosquitoes* causing Chikungunya fever are *Aedes aegypti* and *Aedes albopictus*[(5)]. In human, when infected with CHIKV, acute symptoms usually appearing 3-12 days after a bite from a mosquito. The common symptoms include fever, muscle pain and joint pain[(6)]. However, occasionally the joint pain may be last for months or even years. The mortality rate following CHIKV infection is relatively low, but severe joint pain can affect long-term quality of life[(7)] [(8)].

The diagnosis of CHIKV can be achieved in several ways, such as antigen or serological test [(9)], viral culture, viral isolation[(10)] and molecular techniques such as reverse transcriptase polymerase chain reaction (RT-PCR) [(11)] [(12)] has been developed for diagnostic use. However, these methods are costly, complicated procedures and time-consuming. Hence, we have developed the screening test for CHIKV diagnosis based on RT-PCR combined with a lateral flow dipstick (LFD) [(13)]. The results can be easily read from the color bar appearance based on chromatography principle. Therefore, it is suitable for use preliminary disease screening in outbreak areas.

Methodology:

1. Sample collection

In this study was approved by Ethic Committees, Srinakharinwirot University (Ethic Approval number : SWUEC/X-450/2563) and Ramathibodi Hospital, Mahidol University (Ethic Approval number : MURA2021/105). All CHIKV RNA specimens were obtained from Department of Pathology, Faculty of Medicine Ramathibodi Hospital, Mahidol University.

2. Extraction of viral RNA

The plasma samples were extracted by using the Nucleic acid extractions MagDEA® Dx reagents (Precision System Science, Chiba, Japan) according to manufacturer's protocol. The genomic RNA extracted were kept at - 4 °C until use. The concentrations of RNA were measured by using NanoDrop™ 2000 Spectrophotometer (Thermo Scientific; Wilmington, DE, USA).

3. Reverse transcriptase polymerase chain reaction (RT-PCR)

The primers for RT-PCR amplification were designed based on the CHIKV envelope glycoprotein 1 (E1) gene from the NCBI database (GenBank accession number; AB857841.1). The forward primer (CHIKV E1-F3) and reverse primer (CHIKV E1-B3) were designed by using software Primer explorer V5 programed (http://primerexplorer.jp/lampv5e /index.html).

Reverse transcription of CHIKV RNA was performed by the addition of random hexamers, 10X RT buffer, 0.1 M DTT, 25 mM $MgCl_2$, dNTP mix, RNase OUT, superscript II reverse transcriptase and RNase H.

The PCR amplification for detection of envelope glycoprotein 1 gene was performed in 25 µl reaction containing 1X PCR buffer, 2 mM $MgCl_2$, 0.4 mM dNTPs mix, 0.05 U/µl Taq polymerase (Invitrogen, USA), 0.4 µM of each primer, and 9 ng/µl of genomic DNA. The amplification step contained pre-denaturation step at 95 °C for 5 minutes, followed by 30 cycles of denaturation at 95 °C for 30 second, annealing 56 °C for 30 second, extension 72 °C for 1 minute, and finally post-extension 72 °C for 5 minutes. Then, 3 µl of PCR amplicon was examined by using 2 % agarose gel electrophoresis in 0.5X TAE buffer at 100 volts and observed under UV light using gel-doc (UVITEC Cambridge).

4. Optimization of DNA probe hybridization

The specific oligonucleotide probe was designed between CHIKVE1-F3 and CHIKVE1-B3 regions based on the envelope glycoprotein 1 gene (GenBank accession number; AB857841.1). The Specific FITC-labeled oligonucleotide probe was hybridized with PCR amplified products. After PCR amplification, the DNA hybridization was performed by the addition of 9 µl of PCR product into a microcentrifuge tube and 1 µL of FITC-DNA probe was added. The reaction incubated at 56 °C for 10 minutes prior to the addition of 100 µl of the running buffer. The FITC-DNA probe concentrations for hybridization were carried out at 10, 1, 0.1 µM, respectively.

5. Lateral Flow Dipstick assay (LFD)

After DNA hybridization, the LFD strips (Milenia, HybriDtect, Germany) was dipping into the hybridization mixture and left for another 5-10 minutes until the liquid reaches to the top of the membrane and stop reacting by dipping the LFD strip into distilled water for 10 minutes.

6. Limit of Detection (LOD) and specificity test

The limit of detection (LOD) and specificity tests were performed at optimal conditions of the RT-PCR-LFD. The limit of detection test was performed with 10-fold serial

DNA dilution of CHIKV concentration to reach the range of 90.0 ng/µl – 0.9 pg/µl. The specificity test was investigated against Dengue virus type 1, Dengue virus type 2, Dengue virus type 3, Dengue virus type 4, Zika virus, Influenza virus, Hepatitis C virus and *Staphylococcus aureus*.

Results and Discussion:

1. RT-PCR

The optimization of RT-PCR amplification was accomplished at optimal temperature of 56 °C. The size of PCR the amplicon is 200 bp (Figure 1).

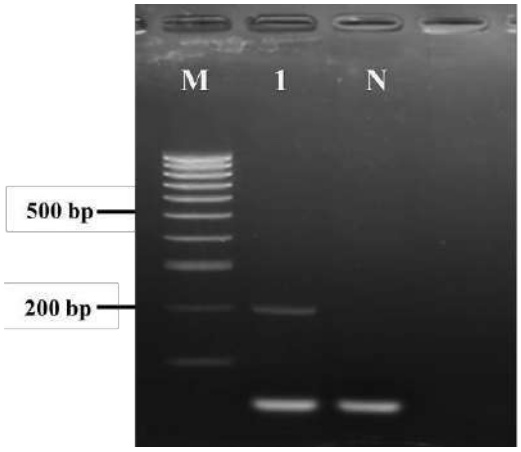

Figure 1.

DNA pattern for CHIKV PCR amplification analyzed by 2% gel electrophoresis at 56 °C. Lane M represents 100 bp+ DNA marker. Lane 1 represents PCR the amplicon of CHIKV. Lane N represents negative control.

2. Optimization of DNA probe concentration

The optimization of DNA probe concentration, the 1.0 µM was suitable for the RT-PCR-LFD assay (Figure 2).

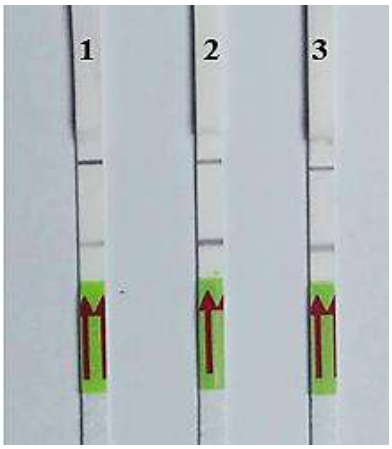

Figure 2.

The comparison of DNA probe concentration for RT-PCR-LFD assay. Strips 1 , 2 and 3 represent DNA probe concentration at 10 µM, 1.0 µM, 0.1 µM.

3. Limit of Detection (LOD) and specificity test

The Limit of detection of RT-PCR-AGE and RT-PCR-LFD assays for CHIKV detection CHIKV performed with 10-fold serial DNA dilutions, the optimized condition was 0.9 ng/µl. (Figures 3A and 3B). The RT-PCR-AGE assays showed cross reaction to Dengue virus type 1 and *S. aureus*. The RT-PCR-LFD assays showed no cross reaction to other viral and bacterial in human such as (Figure 4A and 4B).

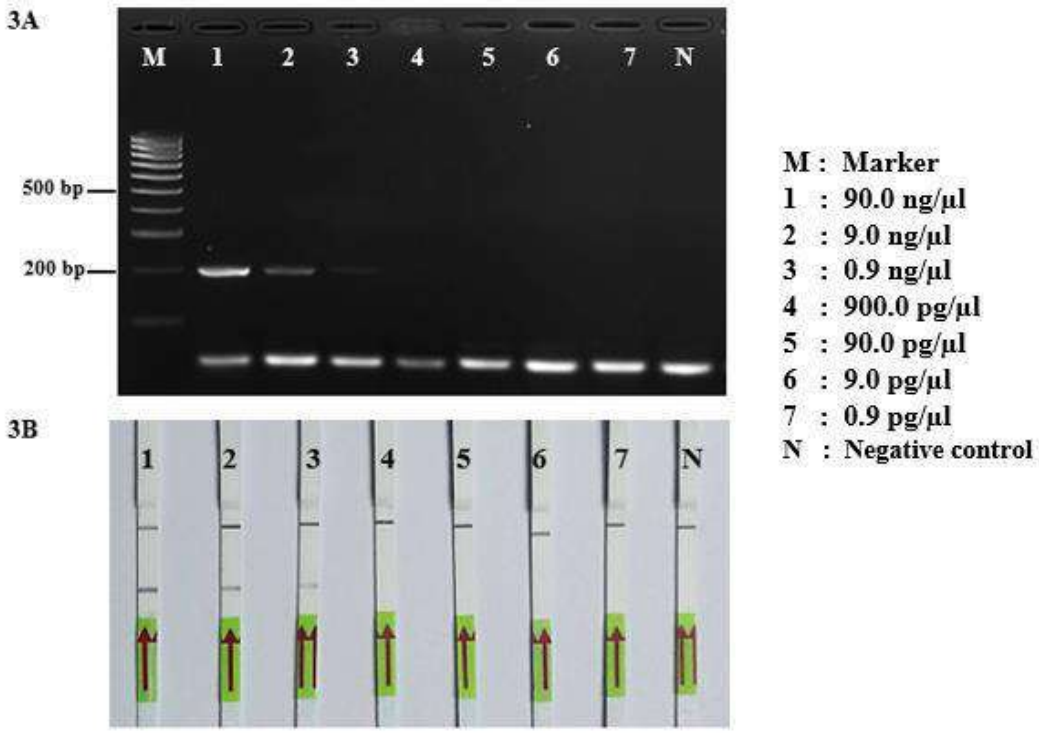

Figure 3.

Limit of detection of (A) RT-PCR-AGE assay (B) RT-PCR-LFD assay. Lane M represents DNA marker. Lanes 1-7 represent PCR the amplicon of serial DNA dilutions at 90 ng/µl, 9 ng/µl, 0.9 ng/µl, 900 pg/µl, 90 pg/µl, 9 pg/µl, 0.9 pg/µl, respectively. Lane N represents negative control.

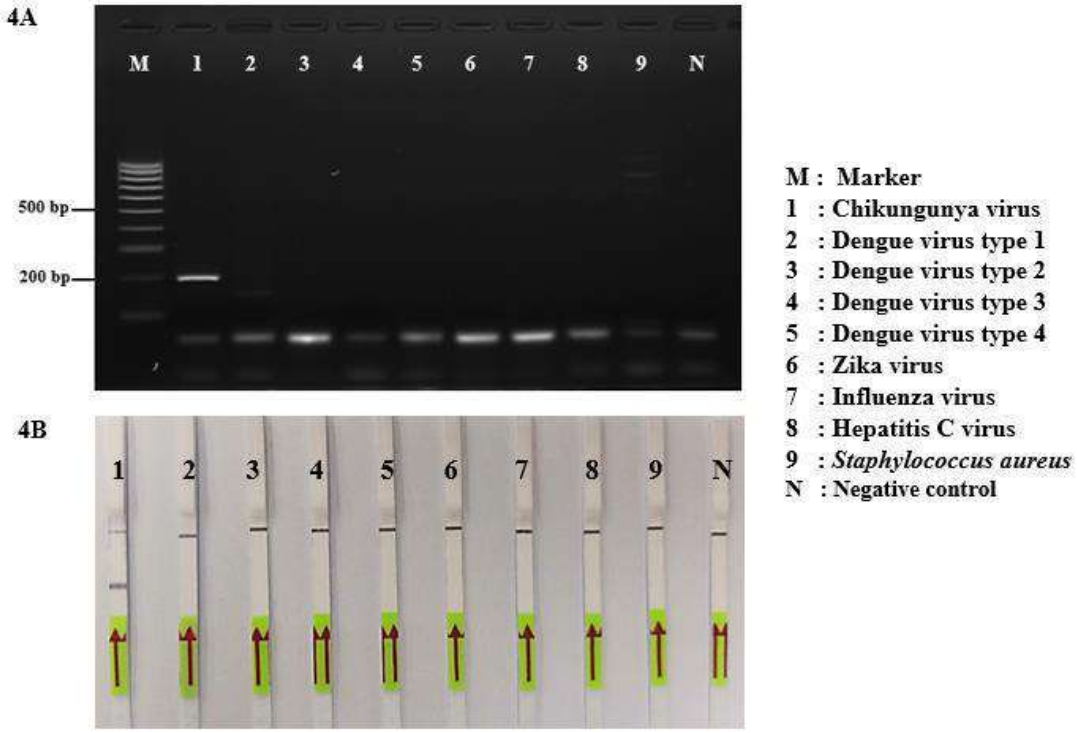

Figure 4.

Specificity test of (A) RT-PCR-AGE assay (B) RT-PCR-LFD assay using DNA templates from other viral and bacterial. Lane M represents a DNA marker. Lanes 1-7 and Strips 1-7 represent PCR the amplicon of viral and bacterial include CHIKV, Dengue virus type 1-4, Zika virus, Influenza virus, Hepatitis C virus and *S. aureus*, respectively. Lane N represents negative control.

The gold standard for diagnosis of CHIKV is RT-PCR [(14) (15)], Currently, despite of highly sensitivity and specificity, RT-PCR required complicated procedures and time-consuming. The RT-PCR LFD assay[(16)] developed in this study aimed to be used as point-of-care detection. The sensitivity of RT-PCR-LFD and RT-PCR-AGE assay were similar. According to specificity test, the RT-PCR-LFD assay showed no cross reaction against other treated virus and bacteria while RT-PCR-LFD was positive to Dengue virus type 1 and S. *aureus.* In addition, the process time of RT-PCR-LFD was 80 minutes whereas RT-PCR-AGE was up to 2-3 hours.

Conclusion:

The application of LFD instead of AGE could reduce detection time, which is suitable for point-of-care detection. In addition, LFD the results can be easily observed from color bar, convenient which is suitable for low-cost testing.

Acknowledgements:

This study was financially supported by Faculty of Medicine, Srinakarinwirot University. We would like to thank the Laboratory of Biochemistry, Faculty of Medicine, Sirnakarinwirot University and Center of Excellence in Biosensors, Sirnakarinwirot University for supporting molecular equipment facilities. Also, thank to Department of Pathology, Faculty of Medicine Ramathibodi Hospital, Mahidol University for supporting the CHIKV specimens.

References:

1. Intayot P, Phumee A, Boonserm R, Sor-Suwan S, Buathong R, Wacharapluesadee S, et al. Pathogens. 2019;8(3):121.
2. Matusali G, Colavita F, Bordi L, et al. Viruses. 2019;11(2):175.
3. Pathak H, Mohan MC, Ravindran V. Clin Med (Lond). 2019;19(5): 381-385.
4. Diop D, Meseznikov G, Sanicas M.: MOJ Public Health. 2015;2(6):181–187.
5. Powell JR.. Am J Trop Med Hyg. 2018;98(6):1563-1565.
6. Horwood PF, Buchy P. Rev Sci Tech. 2015;34(2):479-89.
7. Haese NN, Broeckel RM, Hawman DW, Heise MT, Morrison TE, Streblow DN. J Infect Dis. 2016;214(suppl 5):S482-S7.
8. Burt, FJ, Rolph, MS, Rulli, NE, Mahalingam S, Heise, MT. The Lancet. 2012;379(9816):662–671.
9. Natrajan MS, Rojas A, Waggoner JJ. J Clin Microbiol. 2019;57(6):e00350-19
10. Rahman, M. Pulse. 2018;10(1):18-24.
11. Faggioli F, Luigi M, Boubourakas IN. Viroids and Satellites. 2017;pp.381-91.
12. Artika IM, Wiyatno A, Ma'roef CN. Genet Evol. 2020;81:104215.
13. Koczula KM, Gallotta A. Essays Biochem. 2016;60(1):111-20.
14. Johnson BW, Russell BJ, Goodman CH. J Infect Dis. 2016;214(suppl 5):S471-S474.
15. Pfeffer M, Linssen B, Parker MD, Kinney RM. J Vet Med B. 2002;49(1):49–54.
16. Xiong Y, Luo Y, Li H, Wu W, Ruan, X, Mu X. International Journal of Infectious Diseases. 2020;95:406-412.

EFFECTS OF METEOROLOGICAL DATA SET SELECTION ON SIMULATION RESULTS OF ATMOSPHERIC DISPERSION CODE (NACAC)

Narakhan Khunsrimek,[1,*] Piyawan Krisanungkura,[2] Wasin Vechgama,[3] Somboon Rassame,[1] Kampanart Silva[4]

[1] Department of Nuclear Engineering, Faculty of Engineering, Chulalongkorn University, 254 Phayathai Rd., Patumwan, Bangkok 10330, Thailand

[2] Office of Atoms for Peace, 16 Vibhavadi Rangsit Rd., Lat Yao, Chatuchak, Bangkok 10900, Thailand

[3] Thailand Institute of Nuclear Technology (Public Organization), 9/9 Moo 7, Sai Mun, Ongkharak, Nakhon Nayok 26120, Thailand

[4]Renewable Energy and Energy Efficiency Research Team, National Energy Technology Center, National Science and Technology Development Agency 114 Thailand Science Park, Phahonyothin Road, Khlong Nueng, Khlong Luang, Pathum Thani 12120, Thailand

*e-mail: 6171454721@student.chula.ac.th

Abstract:

Fukushima nuclear accident demonstrated that the released radionuclides disperse through and accross atmospheric layers with no regards to the national boundaries. Therefore, even for countries without nuclear power plants, transboundary radiation impact assessment is essential for emergency planning. Simulation with an atmospheric dispersion is widely used in this kind of assessment. Inappropriate selection of meteorological input data leads to unrepresentative simulation results. In this study, the effects of meteorological data set selection on the simulation results is investigated. Two hypothetical severe accidents consisting of loss of offsite power and large-break loss of coolant scenarios are used as initial conditions. The meteorological data in 2020 from NCEP is formatted into three cases: extreme climate data, representative data from climate data ranking, and hourly climate data. Nuclear Accident consequence Analysis code (NACAC) is used for the comparative assessment. The extreme case provides conservative results, either high concentration or dispersion covering large area. In contrast, the representative data case provides similar results to the hourly data case with much less calculation time. This indicates that representative data case can provide results that are suitable for emergency planning without spending extensive calculation resources.

Identifying Factors Affecting Electricity Consumption of Bangkok Metropolitan Area in Thailand during COVID-19 Situation

Rajin Rajan Kakkoth Puthukkudi,[1] Naraphorn Paoprasert,[2] Kampanart Silva [3]

[1]Department of Industrial Engineering, Faculty of Engineering, Kasetsart University, Chatuchak, Bangkok 10900, Thailand.
[2]Department of Industrial Engineering, Faculty of Engineering, Kasetsart University, Chatuchak, Bangkok 10900, Thailand.
[3]Renewable Energy and Energy Efficiency Research Team, National Energy Technology Center (ENTEC), Pathum Thani 12120, Thailand.
*e-mail: rajin07@gmail.com

Abstract: This study explored factors that could affect electrical consumption during COVID-19 in Thailand. Several sectors were investigated separately consisted of residential area, small general service, medium general service, large general service, governmental institution and non-profit organization, temporary tariff, EV charging station, and public lighting. The number of COVID-19 cases was one primary factor of interest whether this would potentially affect consumptions in these sectors. The results showed that stock index seemed to be the most obvious significant factor, especially for the overall consumption on Electrical consumption, Small General Service and Specific Business Service with 95% confidence level. On the contrary, residential was the only sector that was not impacted by stock index. Rather, oil price was significant in this sector. The number of cases was not a significant factor of even at least 90% confidence level and even with a one-month time lag. The only case that showed number of cases as the significant factor was the overall consumption with only 80% confidence level.

Introduction: Thailand is the third-largest power producer and consumer in Asia, behind Indonesia and Vietnam. Although the contribution of the sector to the overall economy is small, electricity is one of the most important infrastructures for industry and business sectors. In 2019, the power sector accounted for 2.7% of the nominal GDP and about 0.3% of the total employment. Thailand is heavily dependent on the natural gas-fired power plants accounting for a 58% share of total power supply. About 12% of total power supply is imported from Laos and Cambodia, while renewal and alternative energy account for a 13.1% share. The overall transmission line length is more than 36,400 km and is entirely owned and operated by the state-owned Electricity Generating Authority of Thailand (EGAT).

During the COVID-19 situation, presumably, there could be a change in electricity consumption as seen in [1]. As per world health organization report about Thailand, from January 2020 to March 2021, there were 28,346 confirmed cases of COVID-19 with 92 deaths, reported to WHO. As of 19 March 2021, a total of 69,927 vaccine doses administered inside Thailand.

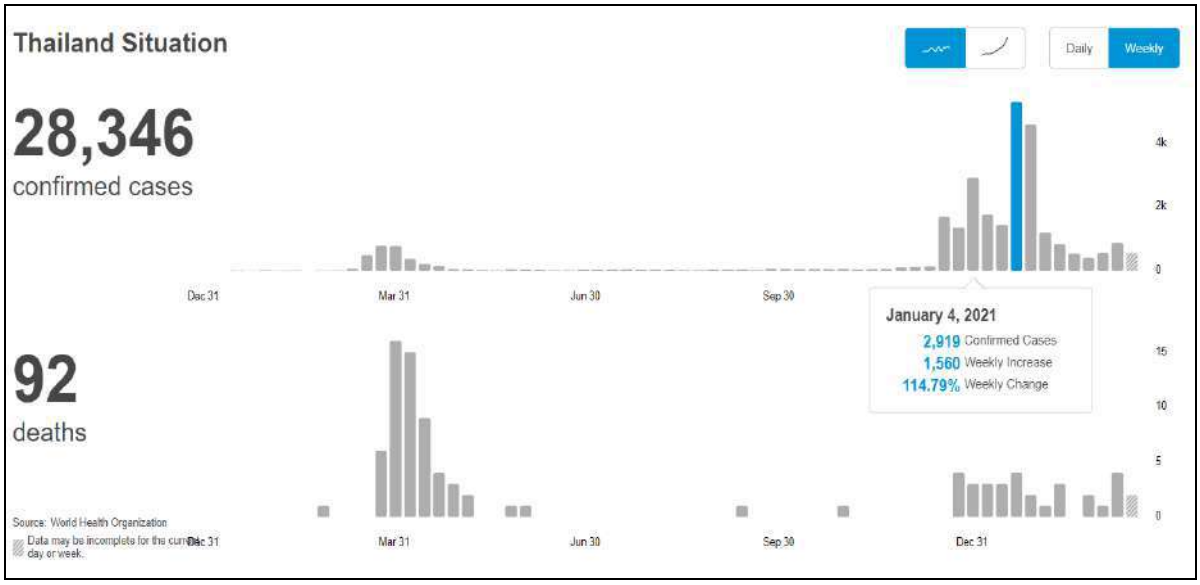

Figure 1. COVID dashboard in Thailand - 2020- 2021

The first serious spike was around April 2020 resulting in the first lockdowns in Bangkok Metropolitan Area. People were asked to keep social distancing and work from home. As mentioned, a few studies have been studying the impact of COVID-19 to electrical consumption. For example, Aruga et al. [1] explored electrical consumption in India during the country lock down under COVID-19 pandemic crisis. In this study, NIFTY 50 (Indian stock market) was found to be a factor that impacted electrical consumption.

Other studies that explored several other factors that were assumed to impact electrical consumptions are as follows. Damrongsak et al. [2] analyzed electrical consumption in Thailand, especially in department stores, to analyze the factors including shopping area for rent, center area, hall area, ambient temperature and relative humidity Since stock market was used as one factor that could potentially impact electrical consumption, a study by Alamgir and Amin [3] investigated the relationship between oil price and stock market using a Nonlinear Autoregressive Distributed Lag (NARDL) model. In this study they found a positive relation between world oil price and stock market index.

Other studies explored the aspect of reducing electrical consumption in Thailand. For example, Jareemit and Limmeechokchai [4] claimed that the electrical consumption in the commercial and residential building in Thailand was increasing at a rate of five percent per year. They searched for solutions to decrease energy consumption in residential sectors. Pachanawan et al. [5] providing a guideline to save electrical energy for each tooling process in rice mills in Thailand. Assawamartbunlue et al. [6] collected data in different cement factories in Thailand and performed a regression analysis to identify factors that could reduce consumption. Assawamartbunlue and Luknongbu [7] discussed about the Thailand native starch energy efficiency plan and suggested a strategy that the government can reduce 30% consumption by 2036. Poolsawat et al. [8] surveyed residents regarding to the electric appliance's usage. They attempted to extract characteristics of appliances usage to better suggest more efficient appliances to users.

Moreover, there have also been a few studies that explored the impact of COVID-19 to several factors. For example, Sutrisno et al. [9] examined the impact of COVID-19 on six stock market indices of countries listed on ASEAN Exchanges and three stock market indices

of countries listed on ASEAN Exchanges which had sectoral index of consumer products and property. Rajatanavin et al. [10] investigated COVID-19 pandemic first wave in Thailand and its related safety measures executed by the Thai government. The proactive response from the health ministry and related departments was claimed to help reducing the spread. Chen et al. [11] also explored COVID-19 pandemic study in Thailand economy and attempted to suggest a quick win solution to boost the Thailand economy.

In this paper, we explored factors that could affect electrical consumption during COVID-19 in Thailand. Several sectors were investigated separately consisted of residential area, small general service, medium general service, large general service, governmental institution and non-profit organization, temporary tariff, EV charging station, and public lighting. The number of COVID-19 cases was one primary factor of interest whether this would potentially affect consumptions in these sectors.

Methodology: In order to explore the impact of COVID-19 on the consumption of electricity, consumption data were analyzed for various sectors consisted of Residential, Small General Service, Medium General Service, Large General Service, Specific Business Service, Government Institutions and Non Profit Organizations, Temporary Tariff, EV Charging Station, and Public Lighting.

As mentioned in the introduction, two parameters were selected as factors that could potentially impact electrical consumption in addition to the number of COVID-19 cases—oil price and stock index. Since the first wave in Thailand happened in April 2019, data were gathered during the period of 2019-2020. Data of electrical consumptions for all sectors in 2019-2020 are shown in Tables 1 and 2. Although in 2019, there had not yet been any confirmed case in Thailand, it was still beneficial to also include more data in 2019 in the first analysis to explore the impact from other factors apart from the number of cases and the compare the results with those when using only the year 2020. Hence, in this study, three analyses were conducted on the following datasets to carefully investigate the number of cases factor as follow:

1. Electrical consumption during 2019- 2020 versus various factors
2. Electrical consumption only during 2020 versus various factors
3. Electrical consumption during 2019- 2020 versus the number of cases with 1-month time lag

For this last case, the one month time lag was assumed since typically, when there was a spike, the government would not suddenly shut down all businesses and required a work-from-home policy until about a couple weeks later.

Table 1. Bangkok Metropolitan Electrical Consumption

Month	Electrical consumption	Residential	Small General Service	Medium General Service	Large General Service	Specific Business Service	Public Lightings
Jan.	4075	1035	634	707	1484	173	42
Feb.	4144	1122	661	706	1438	178	38
Mar.	4611	1223	707	805	1633	201	42
Apr.	4663	1425	745	737	1508	208	41
May	4925	1440	772	816	1647	208	42
Jun.	4589	1270	725	784	1575	194	41
Jul.	4475	1208	696	759	1579	190	42
Aug.	4475	1185	698	776	1582	192	42
Sep.	4261	1119	670	733	1522	176	41
Oct.	4440	1181	688	762	1572	194	43
Nov.	4234	1115	668	736	1495	179	41
Dec.	3839	973	603	654	1399	168	43
Total	52731	14296	8267	8975	18432	2261	499

Table 2. Bangkok Metropolitan Electrical Consumption 2020

Month	Electrical consumption	Residential	Small General Service	Medium General Service	Large General Service	Specific Business Service	Public Lightings
Jan.	4284	1142	674	726	1509	190	43
Feb.	4157	1143	668	707	1435	163	40
Mar.	4465	1310	699	741	1510	162	43
Apr.	4073	1455	677	611	1178	111	42
May	4311	1757	531	563	1296	120	43
Jun.	4215	1527	548	660	1325	114	42
Jul.	4270	1402	593	691	1409	132	43
Aug.	4282	1344	599	717	1443	136	43
Sep.	4273	1322	598	713	1457	141	42
Oct.	3959	1102	547	687	1454	126	43
Nov.	3920	1118	543	671	1415	132	42
Dec.	3791	1072	527	652	1368	129	43
Total	50001	15694	7203	8141	16799	1655	509

Regression analysis was used to identify significant factors. In this study, regression analysis was conducted in using the fit regression model in Minitab. In the fit regression model, it could describe the relationships between a set of predictors and a continuous response using the ordinary least squares method. Interaction and polynomial terms were also explored.

Results and Discussion: Tables 3 and 4 illustrated the results from running regression models on the first two datasets as described in the methodology section. The cells without numbers showed that they were not significant factors (at 90% confidence level). Factors with numbers showed the p-values of those factors toward consumptions in each sector (asterisks showed that they are significant at 95% confidence level).

Table 3. Electrical consumptions during 2019- 2020 versus number of cases, oil price, and stock index

No.	Sector	Cases	Oil Price	Stock Index
1	Electrical Consumption	-	-	0.035*
2	Residential	-	0.047*	-
3	Small General Service	-	-	0.003*
4	Medium General Service	-	-	0.062
5	Large General Service	-	-	0.084
6	Specific Business Service	-	-	0.033*
7	Public Lightings	-	-	0.069

Table 4. Electrical consumptions during 2020 versus number of cases, oil price, and stock index

No.	Sector	Cases	Oil Price	Stock Index
1	Electrical consumption	-	0.022*	-
2	Residential	-	-	-
3	Small General Service	-	-	-
4	Medium General Service	-	-	-
5	Large General Service	-	-	-
6	Specific Business Service	-	-	0.119
7	Public Lightings	-	-	-

From Table 3, stock index seems to be the most obvious significant factor, especially for the overall consumption on Electrical consumption, Small General Service and Specific Business Service with 95% confidence level. On the contrary, residential was the only sector that was not impacted by stock index. Rather, oil price was significant in this sector. Surprisingly, if considering only the year 2020, stock index was no longer the significant factor for most sectors. However, these two tables show that the number of COVID-19 cases has no impact at all on electrical consumption in any sector in Thailand. Hence, to investigate in a deeper level, it was interesting to find out whether this factor alone would impact electrical consumption with a one-month time lag as shown in Table 5. In Table 5, the number of cases was still not a significant factor of even at least 90% confidence level. The only case that showed number of cases as the significant factor was the overall consumption with only 80% confidence level.

Table 5. Electrical consumptions versus number of cases

No.	Sector	Cases
1	Electrical consumption	0.189
2	Residential	0.458
3	Small General	0.961
4	Medium General Service	0.686
5	Large General Service	0.524
6	Specific Business Service	0.685
7	Public Lightings	0.407

Conclusion: The purpose of this research was to explore whether the number of COVID-19 cases, oil price, and stock index would impact electrical consumption in Bangkok Metropolitan Area in Thailand for various sectors. However, the results clearly showed that the number of cases still did not significantly impact consumption even with a one-month time lag. This may due to the fact that perhaps, the majority of the workforces who typically worked in any general office around Bangkok may still need to work in the actual office anyway to maintain workflow. Only a few workforces were allowed to work-from-home with no impact to the companies' operations.

Rather, stock index seemed to be identified as the statistically significant factor when considering two-year period (2019-2020). Hence, during normal situations, stock index was found to be the major factor that affected consumptions in most sectors. Unfortunately, although the second wave happened in 2021 with a huge spike in April, data of electrical usage by sectors have not been officially released yet. So, it would also be interesting to include data in the year 2021 and update the findings which may reveal different results since the second wave was much more serious by a large order of magnitude than the first wave.

References:

1. Aruga k, Islam Md. M, Jannat A. Effects of COVID-19 on Indian Energy Consumption Sustainability. 2021;12(14):1-15.
2. Damrongsak D, Wongspai W, Thinate N. Investigation on the Energy Consumption of Department Store in Thailand Energy Procedia. 2019;156 (2019):217-221.
3. Alamgir F, Amin S.B. The nexus between oil price and stock market Evidence from South Asia Energy reports. 2021;7(2021):693-703.
4. Jareemit D, Limmeechokchai B. Influence of Changing Behavior and High Efficient Appliances on Household Energy Consumption in Thailand Energy Procedia. 2017;138 (2017):241-246.
5. Pachanawan A, Chuan-Udom S, Saengprachatanarug K, Wongpichet S. Electrical Energy Consumption and Energy Conservation of Rice Mills in the Northeastern of Thailand Engineering Journal. 2017;21(4):ISSN 0125-8281.
6. Assawamartbunlue K, Surawattanawan P, Luknongbu W. Specific energy consumption of cement in Thailand Energy Procedia. 2019;156(2019):212-216.
7. Assawamartbunlue K, Luknongbu W. Specific energy consumption of native starch industry in Thailand Energy Procedia. 2020;6(2020):299-303.
8. Poolsawat K, Tachajapong W, Prasit S, Wongsawat W. Electricity consumption characteristics in Thailand residential sector and its saving potential Energy Reports. 2020;6(2):337-343.
9. Sutrisno, Panuntun B, Adristi F.I. PANDEMIC IMPACT OF COVID-19 ON THE STOCK MARKET INDEX AND RETURN OF STOCK MARKET INDEX MODUS. 2020;33(1):47-66.
10. Rajatanavin N, Tuangratananon T, Suphanchaimat R, Tangcharoensathein V. Responding to the COVID-19 second wave in Thailand by diversifying and adapting lessons from the first wave BMJ Global Health. 2021;6(7):1-9.
11. Chen R, Chaiboonsri C, Wannapan S. The Perspective of Thailand Economy After the Effect of Coronavirus-19 Pandemics Explication by Dynamic I-O Models and Agent-Based Simulations SAGE. 2021;1-17:2021.

THE STUDY OF EFFICIENCY OF LPG HOT AIR DRYER COMPARED WITH ELECTRICAL HOT AIR DRYER; CASE STUDY OF DRIED SLICED PORK

Penpark Sirimark[1], Sanchai Yotmanee[2], Wasinee Pradubsri [1], Praphanpong Somsila [3,*]
[1] Department of Science and Mathematics, Rajamangala University of Technology Isan Surin Campus, Surin 32000 Thailand
[2] Faculty of Science and Technology, Phuket Rajabhat University, Phuket, Thailand
[3] Department of Mechanical Engineering, Rajamangala University of Technology Isan Surin Campus, Surin 32000 Thailand
*e-mail: praphanpong.so@rmuti.ac.th

Abstract:
LPG hot air dryer has been used as an alternative dryer, which could reduce the producing costs. It has been used for many food drying process, such as beef drying, coconut flesh drying and garlic sheet drying. However, the study of dried sliced pork is rarely found. Therefore, this research aimed to study the drying process of sliced pork comparing the efficient of LPG hot air dryer and electrical hot air dryer. Sliced pork was dried in either an electrical hot air dryer or a LPG hot air dryer with the 3 different temperatures of 50, 55 and 60°C, and 3 different air velocities of 1.0, 1.5 and 2.0 m/s. During drying process, the moisture content was measured every 10 mins. The results showed that the moisture content of dried sliced pork was decreased when increasing the drying temperature, regardless of air velocities. Moreover, the quality of dried sliced pork using LPG hot air dryer was not significantly different from those using electrical hot air dryer.

ENDPOINT THEOREMS OF MULTI-VALUED MAPPING SATISFYING CONDITION (D) IN UNIFORMLY CONVEX HYPERBOLIC SPACES

Thanomsak Laokul
Department of Mathematics and Computing Science, Mahidol Wittayanusorn School, Nakorn Pathom 73170, Thailand
e-mail: thanom.kul@mwit.ac.th

Abstract: This paper introduces the notion of mapping satisfying condition (D) generalized nonexpansive mappings for the multi-valued case in metric spaces. Such mapping is not included within the notion of Suzuki mappings, and it is stronger than the notion of semi-nonexpansive mappings. A sufficient condition for the existence of endpoints for the mapping satisfying condition (D) in uniformly convex hyperbolic space is established. We also prove a common endpoint theorem for a pair of multi-valued mappings satisfying condition (D). Furthermore, strong and Δ convergence theorems of the S-iteration for this class of mappings are also discussed.

1. Introduction:

Let E be a nonempty subset of a metric space (X,d). A mapping $T : E \to 2^X$ is called a multi-valued mapping where 2^X is the family of nonempty subsets of X. In particular, if Tx is a singleton for every x in E then T is called a single-valued mapping. An element $x \in E$ is called a *fixed point* of T if $x \in Tx$. Moreover, x is called an *endpoint* (or a *stationary point*) of T if $x \in Tx$ and $\{x\} = Tx$. We denote by $\mathrm{Fix}(T)$ the set of all fixed points of T and $\mathrm{End}(T)$ the set of all endpoints of T. We can see that $\mathrm{End}(T) \subseteq \mathrm{Fix}(T)$. This implies that the concept of endpoints seems to be more complicated than the concept of fixed points. Nevertheless, both concepts are coincident when T is a single-valued mapping. Theorems regarding fixed points' existence and properties are known as *fixed point theorems*. Since an answer to a mathematical problem can be viewed as a fixed point of a proper mapping. Thus, the fixed point theory is vital in many areas of mathematics and other sciences. In the same way, the endpoint theory has many applications as well. For instance, Corley[6] proved that a maximization with respect to a cone is equivalent to the problem of finding an endpoint of a particular multi-valued mapping. Tarafdar and Yuan[26] established an endpoint theorem and applied it to obtain the existence of Pareto optima for multi-valued mappings in ordered Banach spaces. For other applications, the reader is referred to Haddad[9], Khanh and Long[11], and Turinici[27].

A single-valued mapping $T : E \to X$ is said to be nonexpansive if

$$d(Tx,Ty) \leq d(x,y) \quad \text{for all } x,y \in E.$$

The first result concerning the existence of endpoints for nonexpansive mappings was obtained by Panyanak[18] in 2015. After that, it was extended from uniformly convex Banach spaces to the general setting of Banach spaces with the Dominguez-Lorenzo condition by Espinola et al.[8]. Furthermore, Kudtha and Panyanak[14] generalized to Suzuki mappings in uniformly convex hyperbolic spaces. Recently, in 2020, Bejenaru and Postolache[4] introduced a new generalized nonexpansiveness but stronger than quasi-nonexpansiveness for single-valued mappings so-

called condition (D). It states that a single-valued mapping T from a nonempty subset E of a Banach space $(X,\|\cdot\|)$ into itself is said to be endowed with property (D) if

$$\| Tx - Ty \| \leq \| x - y \|$$

for all $x \in E$, $y \in E(T,x)$, where $E(T,x) = \{ Tp \mid p \in E, \| Tp - p \| \leq \| Tx - x \| \}$.

In this paper, we introduce the notion of multi-valued mappings satisfying condition (D) and some of its properties. We give sufficient conditions for the existence of endpoints for the multi-valued mappings satisfying condition (D) in uniformly convex hyperbolic spaces with monotone moduli of uniform convexity. Moreover, we also prove a common endpoint theorem for a pair of multi-valued mappings satisfying condition (D) in such spaces. The strong and Δ convergence theorems for the S-iteration for the class of multi-valued mappings satisfying condition (D) under some given conditions, are discussed.

2. Preliminaries:

Throughout this paper, $\mathbb{N}$ stands for the set of natural numbers, and $\mathbb{R}$ stands for the set of real numbers. Let E be a nonempty subset of a metric space (X,d) and $x \in X$. The *distance* from x to E is defined by

$$\operatorname{dist}(x,E) := \inf \{ d(x,y) : y \in E \}.$$

The *radius* of E relative to x is defined by

$$R(x,E) := \sup \{ d(x,y) : y \in E \}.$$

For a multi-valued mapping T, we note that $x \in \operatorname{Fix}(T)$ if and only if $\operatorname{dist}(x,Tx) = 0$. Moreover, $x \in \operatorname{End}(T)$ if and only if $R(x,Tx) = 0$. A sequence $\{x_n\}$ in E is called an *approximate endpoint sequence* for T if

$$\lim_{n\to\infty} R(x_n, Tx_n) = 0,$$

and the mapping T is said to have the *approximate endpoint property*[1] if it has an approximate endpoint sequence in E.

We denote by $\mathcal{CB}(E)$ the family of nonempty closed bounded subsets of E and by $\mathcal{K}(E)$ the family of nonempty compact subsets of E. The *Pompeiu-Hausdorff distance* on $CB(E)$ is defined by

$$H(A,B) := \max\left\{ \sup_{a\in A} \operatorname{dist}(a,B), \sup_{b\in B} \operatorname{dist}(b,A) \right\} \text{ for all } A,B \in \mathcal{CB}(E).$$

It follows from Theorem 2.1.7 of Takahashi[24] that the Pompeiu-Hausdorff distance on $\mathcal{CB}(E)$ is a metric.

A multi-valued mapping $T : E \to \mathcal{CB}(E)$ is said to be *nonexpansive*[12] if

$$H(Tx,Ty) \leq d(x,y) \tag{2.1}$$

for all $x,y \in E$. If (2.1) is valid for all $x,y \in E$ with $\frac{1}{2}\operatorname{dist}(x,Tx) \leq d(x,y)$, then T is called a *Suzuki mapping* or a *C-type generalized nonexpansive mapping*[23]. T is called *quasi-nonexpansive* if $\operatorname{Fix}(T) \neq \emptyset$ and $H(Tx,Tp) \leq d(x,p)$ for all $p \in \operatorname{Fix}(T)$ and $x \in E$. Moreover, if $\operatorname{End}(T) \neq \emptyset$ and $H(Tx,Tq) \leq d(x,q)$ for all $q \in \operatorname{End}(T)$ and $x \in E$, then T is said to be *semi-nonexpansive*. It is known from Panyanak[20] that if T is nonexpansive and $\operatorname{Fix}(T) \neq \emptyset$, then T is quasi-nonexpansive. Moreover, if T is quasi-nonexpansive and $\operatorname{End}(T) \neq \emptyset$, then T is semi-nonexpansive.

Now, we define condition (D) for multi-valued mappings.

Definition 2.1. Let E be a nonempty subset of a metric space (X,d). A multi-valued mapping $T:E\to \mathcal{CB}(E)$ is said to be endowed with property (D) if

$$H(Tx,Ty)\le d(x,y)$$

for all $x\in E$, $y\in E(T,x)$, where $E(T,x)=\left\{v\in Tp \middle| p\in E, d(p,v)=\text{dist}(p,Tp)\le \text{dist}(x,Tx)\right\}$.

The following result is an immediate consequence of the definition.

Proposition 2.1. The following statements hold.

(i) If T is a nonexpansive, then T satisfies condition (D).

(ii) If T satisfies condition (D) with $\text{Fix}(T)\neq\varnothing$, then T is a quasi nonexpansive.

(iii) If T satisfies condition (D) with $\text{End}(T)\neq\varnothing$, then T is a semi-nonexpansive.

The following example shows that the mapping class that meets the (D) condition is not included in the Suzuki mapping class.

Example 2.1. Let $E=[0,3]$ and $T:E\to\mathcal{K}(E)$ be defined by

$$Tx=\begin{cases}\{3\} & ,\text{if } x=0\\ \left\{\frac{3}{2}\right\} & ,\text{if } x\in\left(0,\frac{3}{2}\right)\\ \left[\frac{3}{2},x\right] & ,\text{if } x\in\left[\frac{3}{2},3\right].\end{cases}$$

It is easy to see that $E(T,x)=\left[\frac{3}{2},3\right]$ for all x in E. We will show that T satisfies condition (D), but is not a Suzuki mapping.

Case I. If $x=0$ and $y\in E(T,x)$, then

$$H\left(Tx,Ty\right)=H\left(\{3\},\left[\frac{3}{2},y\right]\right)=|3-y|=3-y$$

and

$$d(x,y)=|0-y|=y.$$

Since $y\ge 3/2$, we have $3-y\le y$, so $H\left(Tx,Ty\right)\le d(x,y)$.

Case II. If $x\in\left(0,\frac{3}{2}\right)$ and $y\in E(T,x)$, then

$$H\left(Tx,Ty\right)=H\left(\left\{\frac{3}{2}\right\},\left[\frac{3}{2},y\right]\right)=0\le d(x,y).$$

So $H\left(Tx,Ty\right)\le d(x,y)$.

Case III. If $x\in\left[\frac{3}{2},3\right]$ and $y\in E(T,x)$, then

$$H\left(Tx,Ty\right)=H\left(\left[\frac{3}{2},x\right],\left[\frac{3}{2},y\right]\right)=0\le d(x,y).$$

So $H\left(Tx,Ty\right)\le d(x,y)$. Thus, T satisfies condition (D). Next, we show that T is not a Suzuki mapping. Put $x=1$ and $y=0$. Then,

$$\frac{1}{2}\text{dist}(x,Tx)=\frac{1}{2}\text{dist}\left(1,\left\{\frac{3}{2}\right\}\right)=\frac{1}{2}\left|1-\frac{3}{2}\right|=\frac{1}{4}<1=d(x,y).$$

Since $H(Tx,Ty)=H\left(\left\{\frac{3}{2}\right\},\{3\}\right)=3/2>1=d(x,y)$, T is not a Suzuki mapping.

The following list provides basic properties of mappings satisfying condition (D).

Lemma 2.1. Let E be a nonempty closed subset of a metric space (X,d) and let $T:E\to\mathcal{K}(E)$ be a multi-valued mapping satisfying condition (D). For any $x,y\in E$, let $u_x\in Tx$ and $v_y\in Ty$ such that $d(x,u_x)=\text{dist}(x,Tx)$ and $d(y,v_y)=\text{dist}(y,Ty)$, respectively. Then the following conclusions hold.

(i) $H(Tx,Tu_x)\le d(x,u_x)$.

(ii) If $\text{dist}(x,Tx)\le\text{dist}(y,Ty)$, then $H(Ty,Tu_x)\le d(y,u_x)$.

(iii) $\text{dist}(x,Ty)\le 3\text{dist}(x,Tx)+d(x,y)$ whenever $\text{dist}(x,Tx)\le\text{dist}(y,Ty)$.

(iv) $H(Tx,Ty)\le 2\min\{\text{dist}(x,Tx),\text{dist}(y,Ty)\}+d(x,y)$.

Proof. Since $d(x,u_x)=\text{dist}(x,Tx)\le\text{dist}(x,Tx)$, then $u_x\in E(T,x)$. Thus

$$H(Tx,Tu_x)\le d(x,u_x)=\text{dist}(x,Tx),$$

and hence (i) is proved.

To prove (ii), suppose $\text{dist}(x,Tx)\le\text{dist}(y,Ty)$. We have $u_x\in E(T,y)$, this implies that

$$H(Ty,Tu_x)\le d(y,u_x).$$

To prove (iii), suppose $\text{dist}(x,Tx)\le\text{dist}(y,Ty)$. Then we have $u_x\in E(T,y)$, this implies that $H(Ty,Tu_x)\le d(y,u_x)$. It follows from (i) that

$$\begin{aligned}\text{dist}(x,Ty)&\le d(x,u_x)+\text{dist}(u_x,Tu_x)+H(Tu_x,Ty)\\&\le d(x,u_x)+H(Tx,Tu_x)+d(y,u_x)\\&\le d(x,u_x)+d(x,u_x)+\left(d(y,x)+d(x,u_x)\right)\\&=3d\left(x,u_x\right)+d\left(x,y\right)\\&=3\text{dist}\left(x,\ Tx\right)+d\left(x,y\right).\end{aligned}$$

To prove (iv), it is enough to consider only the case when $\text{dist}(x,Tx)\le\text{dist}(y,Ty)$. Then we have $u_x\in E(T,y)$, $H\left(Tu_x,Ty\right)\le d(u_x,y)$. It follows from (i) that

$$\begin{aligned}H(Tx,Ty)&\le H(Tx,Tu_x)+H(Tu_x,Ty)\\&\le\text{dist}(x,Tx)+d(u_x,y)\\&\le\text{dist}(x,Tx)+d(u_x,x)+d(x,y)\\&=2\text{dist}\left(x,Tx\right)+d\left(x,y\right)\\&=2\min\{\text{dist}(x,Tx),\text{dist}(y,Ty)\}+d(x,y).\end{aligned}$$

The notion of uniformly convex hyperbolic spaces was introduced by Leustean[16].

Definition 2.2. A *hyperbolic space* is a metric space (X,d) together with a function $W:X\times X\times[0,1]\to X$ such that for all $x,y,z,w\in X$ and $\alpha,\beta\in[0,1]$, we have

(W1) $d(z,W(x,y,\beta))\le(1-\beta)d(z,x)+\beta d(z,y)$;

(W2) $d\left(W(x,y,\beta),W(x,y,\alpha)\right)=|\beta-\alpha|\,d(x,y)$;

(W3) $W(x,y,\beta)=W(y,x,1-\beta)$;

(W4) $d(W(x,z,\beta),W(y,w,\beta))\le(1-\beta)d(x,y)+\beta d(z,w)$.

For convenience, from now on, we will use the notation $(1-\beta)x\oplus\beta y$ instead of $W(x,y,\beta)$. A nonempty subset E of X is said to be *convex* if $\{(1-\beta)x\oplus\beta y:\beta\in[0,1]\}\subseteq E$

for all $x, y \in E$. The hyperbolic space (X, d, W) is called *uniformly convex* if for any $r \in (0, \infty)$ and $\varepsilon \in (0, 2]$ there exists $\delta \in (0, 1]$ such that for all $x, y, z \in X$ with $d(x, z) \le r$, $d(y, z) \le r$ and $d(x, y) \ge r\varepsilon$, we have

$$d\left(\frac{1}{2}x \oplus \frac{1}{2}y, z\right) \le (1 - \delta)r.$$

In this case, we call δ a modulus of uniform convexity. In particular, if δ is a nonincreasing function of r for every fixed ε, then we call it a monotone modulus of uniform convexity. It is well known that every Uniformly convex Banach space is a uniformly convex hyperbolic space. Moreover, every CAT(0) space is a uniformly convex hyperbolic space, see, e.g., Leustean[16].

The concept of p-uniform convexity was used extensively by Xu[29]. Khan and Khamsi[10] studied its nonlinear version for $p = 2$.

Definition 2.3. Let (X, d, W) be a uniformly convex hyperbolic space. For each $r \in (0, \infty)$ and $\varepsilon \in (0, 2]$, we define

$$\Psi(r, \varepsilon) := \inf\left\{\frac{1}{2}d^2(x, z) + \frac{1}{2}d^2(y, z) - d^2\left(\frac{1}{2}x \oplus \frac{1}{2}y, z\right)\right\},$$

where the infimum is taken over all $x, y, z \in X$ such that $d(x, z) \le r$, $d(y, z) \le r$, and $d(x, y) \ge r\varepsilon$. We say that (X, d) is 2-*uniformly convex* if

$$c_M := \inf\left\{\frac{\Psi(r, \varepsilon)}{r^2\varepsilon^2} : r \in (0, \infty), \varepsilon \in (0, 2]\right\} > 0.$$

Laokul and Panyanak[15] prove the following property in any 2-uniformly convex hyperbolic space (X, d, W),

$$d^2\left((1 - \beta)x \oplus \beta y, z\right) \le (1 - \beta)d^2(x, z) + \beta d^2(y, z) - 4c_M\beta(1 - \beta)d^2(x, y) \qquad (2.2)$$

for all $x, y, z \in X$ and $\beta \in [0, 1]$.

From now on, X stands for a complete uniformly convex hyperbolic space with a monotone modulus of uniform convexity. Let E be a nonempty subset of X and $\{x_n\}$ be a bounded sequence in X. The *asymptotic radius* of $\{x_n\}$ relative to E is defined by

$$r(E, \{x_n\}) = \inf\left\{\limsup_{n \to \infty} d(x_n, x) : x \in E\right\}.$$

The *asymptotic center* of $\{x_n\}$ relative to E is defined by

$$A(E, \{x_n\}) = \left\{x \in E : \limsup_{n \to \infty} d(x_n, x) = r(E, \{x_n\})\right\}.$$

It is known that in uniformly convex Banach spaces and CAT(0) spaces, there is a common property that each bounded sequence has a unique asymptotic center with respect to a closed convex subset. This property also holds in a complete uniformly convex hyperbolic space. The following fact can be founded in Leustean[16].

Lemma 2.2. Every bounded sequence $\{x_n\}$ in X has a unique asymptotic center with respect to any nonempty closed convex subset E of X.

Now, we give the concept of Δ-convergence for bounded sequences and the concept of semiclosedness for mappings.

Definition 2.4. Let E be a nonempty closed convex subset of X and $x \in E$. A bounded sequence $\{x_n\}$ in X is said to be Δ-*converges* to x if $A(E, \{u_n\}) = \{x\}$ for every subsequence $\{u_n\}$ of $\{x_n\}$. In this case we write $x_n \xrightarrow{\Delta} x$ and call x the Δ-*limit* of $\{x_n\}$.

It is known from Kirk[13] that every bounded sequence in X has a Δ-convergent subsequence.

Definition 2.5. Let E be a nonempty closed convex subset of X and $T : E \to \mathcal{K}(E)$. Let I be the identity mapping on E. We say that $I - T$ is semiclosed if for any sequence $\{x_n\}$ in E such that $x_n \xrightarrow{\Delta} x \in E$ and $R(x_n, Tx_n) \to 0$, one has $Tx = \{x\}$.

3. Endpoint theorems:

We begin this section by proving the semiclosed principle for multi-valued mappings satisfying condition (D) in uniformly convex hyperbolic spaces.

Lemma 3.1. Let E be a nonempty closed convex subset of X, let I be the identity mapping on E, and let $T : E \to \mathcal{K}(E)$ be a multi-valued mapping satisfying condition (D). Then $I - T$ is semiclosed.

Proof. Let $\{x_n\}$ be a sequence in E such that $x_n \xrightarrow{\Delta} x \in E$ and $R(x_n, Tx_n) \to 0$. For each $n \in \mathbb{N}$, we can choose $y_n \in Tx_n$ and $z_n \in Tx$ such that

$$d(x_n, y_n) = R(x_n, Tx_n) \text{ and } d(y_n, z_n) = \text{dist}(y_n, Tx).$$

Since Tx is compact, there exists a subsequence $\{z_{n_k}\}$ of $\{z_n\}$ such that $\lim_{k\to\infty} z_{n_k} = v$ for some $v \in Tx$. By Lemma 2.1 (iv), we have

$$\begin{aligned} d(x_{n_k}, v) &\le d(x_{n_k}, y_{n_k}) + d(y_{n_k}, z_{n_k}) + d(z_{n_k}, v) \\ &\le R(x_{n_k}, Tx_{n_k}) + H(Tx_{n_k}, Tx) + d(z_{n_k}, v) \\ &\le R(x_{n_k}, Tx_{n_k}) + 2\min\left\{\text{dist}(x_{n_k}, Tx_{n_k}), \text{dist}(x, Tx)\right\} + d(x_{n_k}, x) + d(z_{n_k}, v) \\ &\le R(x_{n_k}, Tx_{n_k}) + 2\text{dist}(x_{n_k}, Tx_{n_k}) + d(x_{n_k}, x) + d(z_{n_k}, v) \\ &\le 3R(x_{n_k}, Tx_{n_k}) + d(x_{n_k}, x) + d(z_{n_k}, v). \end{aligned}$$

This implies that $\limsup_{k\to\infty} d(x_{n_k}, v) \le \limsup_{k\to\infty} d(x_{n_k}, x)$. Therefore, $v \in A(E, \{x_{n_k}\}) = \{x\}$ and hence $x = v \in Tx$. We next show that $x \in \text{End}(T)$. Let $w \in Tx$. For each k, there exists u_{n_k} in Tx_{n_k} such that $d(w, u_{n_k}) = \text{dist}(w, Tx_{n_k})$. By Proposition 2.1 (ii), we have

$$\begin{aligned} d(x_{n_k}, w) &\le d(x_{n_k}, u_{n_k}) + d(u_{n_k}, w) \\ &\le R(x_{n_k}, Tx_{n_k}) + \text{dist}(w, Tx_{n_k}) \\ &\le R(x_{n_k}, Tx_{n_k}) + H(Tx_{n_k}, Tx) \\ &\le R(x_{n_k}, Tx_{n_k}) + d(x_{n_k}, x). \end{aligned}$$

This implies that $\limsup_{k\to\infty} d(x_{n_k}, w) \le \limsup_{k\to\infty} d(x_{n_k}, x)$, and hence $w \in A(E, \{x_{n_k}\}) = \{x\}$. Therefore, $w = x \in Tx$. Thus, $Tx = \{x\}$.

As a consequence of Lemma 3.1, we can obtain the following results.

Theorem 3.1. Let E be a nonempty bounded closed convex subset of X and $T : E \to \mathcal{K}(E)$ be a multi-valued mapping satisfying condition (D). Then T has an endpoint if and only if T has the approximate endpoint property.

Proof. The necessity is clear. For the sufficiency, we suppose that $\{x_n\}$ is an approximate endpoint sequence for T. Since $\{x_n\}$ is bounded, there exists a subsequence $\{x_{n_k}\}$ of $\{x_n\}$ such that $x_{n_k} \xrightarrow{\Delta} x \in E$. By Lemma 3.1, x is an endpoint of T.

We also obtain a common endpoint theorem as the following result.

Theorem 3.2. Let E be a nonempty bounded closed convex subset of X and let $S,T : E \to \mathcal{K}(E)$ be two multi-valued mappings satisfying condition (D). If S has an approximate endpoint sequence in $\mathrm{End}(T)$, then S and T have a common endpoint.

Proof. Let $\{x_n\}$ be an approximate endpoint sequence for S in $\mathrm{End}(T)$. Since $\{x_n\}$ is bounded, there exist a subsequence $\{x_{n_k}\}$ of $\{x_n\}$ such that $x_{n_k} \xrightarrow{\Delta} x \in E$. By Lemma 3.1, $x \in \mathrm{End}(S)$. Let $w \in Tx$. Then

$$\begin{aligned} d(w, x_{n_k}) &= \mathrm{dist}(w, Tx_{n_k}) \\ &\le H(Tx, Tx_{n_k}) \\ &\le 2\min\left\{\mathrm{dist}(x, Tx), \mathrm{dist}(x_{n_k}, Tx_{n_k})\right\} + d(x_{n_k}, x) \\ &\le 2\mathrm{dist}(x_{n_k}, Tx_{n_k}) + d(x_{n_k}, x). \end{aligned}$$

This implies that $\limsup_{k\to\infty} d(x_{n_k}, w) \le \limsup_{k\to\infty} d(x_{n_k}, x)$, and hence $w \in A(E, \{x_{n_k}\}) = \{x\}$.

Therefore, $w = x$ for all $w \in Tx$. Thus, $x \in \mathrm{End}(T)$.

4. Convergence theorems:

In 2018, Panyanak[19] modified the Ishikawa iteration process, which is a generalization of the Mann iteration process, for approximating endpoints of multi-valued nonexpansive mappings in a uniformly convex Banach space. Recently, Laokul and Panyanak[15] extended Panyanak's result[19] to a multi-valued Suzuki mapping in the general setting of 2-uniformly convex hyperbolic spaces.

The *S-iteration process* was introduced by Agarwal et al.[2], which is independent from Mann and Ishikawa iteration process. It is defined by for E a convex subset of a Banach space X and T a mapping of E into itself, the iterative sequence $\{x_n\}$ is generated from $x_1 \in E$,

$$\begin{cases} x_{n+1} = (1-\alpha_n)Tx_n + \alpha_n Ty_n, \\ y_n = (1-\beta_n)x_n + \beta_n Tx_n, \quad \text{for all} \quad n \in \mathbb{N}, \end{cases} \tag{4.1}$$

where $\{\alpha_n\}$ and $\{\beta_n\}$ are real sequences in $(0,1)$. We know from Bauschke and Combettes[3] (Proposition 3.1) that the convergence rate of S-iteration process is similar to the Picard iteration process and faster than both Mann and Ishikawa iteration process.

In this section, we prove Δ and strong convergence theorems of the S-iteration process for the mapping satisfying condition (D). Let E be a nonempty convex subset of X, and $\{\alpha_n\}$, $\{\beta_n\}$ be sequences in [0,1], and $T : E \to \mathcal{K}(E)$ be a multi-valued mapping. The sequence of S-iteration process is defined by $x_1 \in E$,

$$y_n = (1-\beta_n)x_n \oplus \beta_n z_n, \quad n \in \mathbb{N},$$

where $z_n \in Tx_n$ such that $d(x_n, z_n) = R(x_n, Tx_n)$, and

$$x_{n+1} = (1-\alpha_n)z_n \oplus \alpha_n w_n, \quad n \in \mathbb{N}, \tag{4.2}$$

where $w_n \in Ty_n$ such that $d(y_n, w_n) = R(y_n, Ty_n)$.

A sequence $\{x_n\}$ in X is said to be Fejer monotone with respect to E if

$$d(x_{n+1}, p) \le d(x_n, p) \text{ for all } p \in E \text{ and } n \in \mathbb{N}.$$

The following lemma shows that the sequence of S-iteration defined by (4.2) is Fejer monotone with respect to the endpoint set of the mapping satisfying condition (D).

Lemma 4.1. Let E be a nonempty convex subset of X and let $T: E \to \mathcal{K}(E)$ be a multi-valued mapping satisfying condition (D) with $\mathrm{End}(T) \neq \varnothing$. Let $\{x_n\}$ be the sequence of S-iteration defined by (4.2). Then $\{x_n\}$ is Fejer monotone with respect to $\mathrm{End}(T)$.

Proof. Let $p \in \mathrm{End}(T)$. For each $n \in \mathbb{N}$ and by Proposition 2.1 (iii), we have

$$\begin{aligned} d(y_n, p) &\leq (1-\beta_n)d(x_n, p) + \beta_n d(z_n, p) \\ &\leq (1-\beta_n)d(x_n, p) + \beta_n H(Tx_n, Tp) \\ &\leq (1-\beta_n)d(x_n, p) + \beta_n d(x_n, p) \\ &= d(x_n, p). \end{aligned}$$

This implies that

$$\begin{aligned} d(x_{n+1}, p) &\leq (1-\alpha_n)d(z_n, p) + \alpha_n d(w_n, p) \\ &\leq (1-\alpha_n)H(Tx_n, Tp) + \alpha_n H(Ty_n, Tp) \\ &\leq (1-\beta_n)d(x_n, p) + \beta_n d(y_n, p) \\ &\leq (1-\beta_n)d(x_n, p) + \beta_n d(x_n, p) \\ &= d(x_n, p). \end{aligned}$$

Thus, $\{x_n\}$ is Fejer monotone with respect to $\mathrm{End}(T)$.

The following fact can be founded in Chuadchawna, Farajzadeh, and Kaewcharoen[5].

Lemma 4.2 Let E be a nonempty closed convex subset of X and $\{x_n\}$ a Fejer monotone sequence with respect to E. Then $\{x_n\}$ converges strongly to an element of E if and only if $\lim_{n\to\infty} \mathrm{dist}(x_n, E) = 0$.

The following fact can be founded in Dhompongsa and Panyanak[7].

Lemma 4.3. Let E be a nonempty closed convex subset of X and $\{x_n\}$ be a bounded sequence in X. If $A(E, \{x_n\}) = \{x\}$ and $\{u_n\}$ is a subsequence of $\{x_n\}$ with $A(E, \{u_n\}) = \{u\}$ and the sequence $\{d(x_n, u)\}$ converges, then $x = u$.

Now, we prove Δ-convergence theorem.

Theorem 4.1. Let E be a nonempty closed convex subset of a 2-uniformly convex hyperbolic space X and let $T: E \to \mathcal{K}(E)$ be a multi-valued mapping satisfying condition (D) such that $\mathrm{End}(T) \neq \varnothing$. Let $\alpha_n, \beta_n \in [a, b] \subset (0,1)$ and $\{x_n\}$ be the sequence of S-iteration defined by (4.2). Then $\{x_n\}$ Δ-converges to an endpoint of T.

Proof. We divide the proof into two steps as follows.

Step I. We show that $R(x_n, Tx_n) \to 0$. Let $p \in \mathrm{End}(T)$. It follows from (2.2) that

$$\begin{aligned} d^2(y_n, p) &\leq (1-\beta)d^2(x_n, p) + \beta_n d^2(z_n, p) - 4c_M \beta_n (1-\beta_n) d^2(x_n, z_n) \\ &\leq (1-\beta)d^2(x_n, p) + \beta_n H^2(Tx_n, Tp) - 4c_M \beta_n (1-\beta_n) d^2(x_n, z_n) \\ &\leq (1-\beta)d^2(x_n, p) + \beta_n d^2(x_n, p) - 4c_M \beta_n (1-\beta_n) d^2(x_n, z_n) \\ &\leq d^2(x_n, p) - 4c_M \beta_n (1-\beta_n) d^2(x_n, z_n) \end{aligned}$$

which yields

$$\begin{aligned} d^2(x_{n+1},p) &\le (1-\alpha_n)d^2(z_n,p)+\alpha_n d^2(w_n,p)-4c_M\alpha_n(1-\alpha_n)d^2(z_n,w_n) \\ &\le (1-\alpha_n)d^2(z_n,p)+\alpha_n d^2(w_n,p) \\ &\le (1-\alpha_n)H^2(Tx_n,Tp)+\alpha_n H^2(Ty_n,Tp) \\ &\le (1-\alpha_n)d^2(x_n,p)+\alpha_n d^2(y_n,p) \\ &\le (1-\alpha_n)d^2(x_n,p)+\alpha_n\left(d^2(x_n,p)-4c_M\beta_n(1-\beta_n)d^2(x_n,z_n)\right) \\ &\le d^2(x_n,p)-4c_M\alpha_n\beta_n(1-\beta_n)d^2(x_n,z_n). \end{aligned}$$

Then,

$$a^2(1-b)d^2(x_n,z_n)\le \alpha_n\beta_n(1-\beta_n)d^2(x_n,z_n)\le \frac{d^2(x_n,p)-d^2(x_{n+1},p)}{4c_M}.$$

Thus,

$$\sum_{n=1}^{\infty}a^2(1-b)d^2(x_n,z_n)\le \sum_{n=1}^{\infty}\alpha_n\beta_n(1-\beta_n)d^2(x_n,z_n)<\infty. \tag{4.3}$$

This implies that $\lim_{n\to\infty} d^2(x_n,z_n)=0$, and hence

$$\lim_{n\to\infty} R(x_n,Tx_n)=\lim_{n\to\infty} d(x_n,z_n)=0. \tag{4.4}$$

Step II. We show that $\{x_n\}$ Δ-converges to an endpoint of T. We denoted by

$$\omega_w(x_n):=\bigcup A(E,\{u_n\})$$

where the union is taken over all subsequences $\{u_n\}$ of $\{x_n\}$. Let $u\in\omega_w(x_n)$, then there exists a subsequence $\{u_n\}$ of $\{x_n\}$ such that $A(E,\{u_n\})=\{u\}$. Since $\{u_n\}$ is bounded, there exists a subsequence $\{v_n\}$ of $\{u_n\}$ such that $v_n \xrightarrow{\Delta} v\in E$. It follows from Lemma 3.1 that $I-T$ is semiclosed and Lemma 4.3 that $u=v\in \mathrm{End}(T)$, which implies that $\omega_w(x_n)\subseteq \mathrm{End}(T)$. Next, we show that $\omega_w(x_n)$ consists of exactly one point. Let $\{u_n\}$ be a subsequence of $\{x_n\}$ with $A(E,\{u_n\})=\{u\}$ and let $A(E,\{x_n\})=\{x\}$. Since $u\in\omega_w(x_n)\subseteq \mathrm{End}(T)$, $\{d(x_n,u)\}$ converges. Again by Lemma 4.3, $x=u$. This shows that $\{x_n\}$ Δ-converges to an endpoint of T.

Next, we prove strong convergence theorem. Recall that a mapping $T:E\to\mathcal{K}(E)$ is said to satisfy condition (J) if $\mathrm{End}(T)\neq\varnothing$ and there exists a nondecreasing function $g:[0,\infty)\to[0,\infty]$ with $g(0)=0$, $g(r)>0$ for $r\in(0,\infty)$ such that

$$R(x,Tx)\ge g\left(\mathrm{dist}(x,\mathrm{End}(T))\right) \text{ for all } x\in E.$$

The mapping T is said to be semicompact if for any sequence $\{x_n\}$ in E such that

$$\lim_{n\to\infty} R(x_n,Tx_n)=0,$$

there exists a subsequence $\{x_{n_k}\}$ of $\{x_n\}$ such that $\lim_{k\to\infty} x_{n_k}=q\in E$.

The following fact founded in Panyanak[17] also needed.

Lemma 4.4. Let $\{\alpha_n\},\{\beta_n\}$ be two real sequences in $[0,1)$ such that $\beta_n\to 0$ and $\sum\alpha_n\beta_n=\infty$. Let $\{\gamma_n\}$ be a nonnegative real sequence such that $\sum\alpha_n\beta_n(1-\beta_n)\gamma_n<\infty$. Then $\{\gamma_n\}$ has a subsequence which converges to zero.

Theorem 4.2. Let E be a nonempty closed convex subset of a 2-uniformly convex hyperbolic space X and let $T:E\to\mathcal{K}(E)$ be a mapping satisfying condition (D) such that $\mathrm{End}(T)\neq\varnothing$.

Let $\alpha_n, \beta_n \in [a,b] \subset (0,1)$ and $\{x_n\}$ be the sequence of S-iteration defined by (4.2). If T satisfies condition (J), then $\{x_n\}$ converges strongly to an endpoint of T.

Proof. First, we show that $\operatorname{dist}(x_n, \operatorname{End}(T)) \to 0$. Assume that $\lim_{n\to\infty} \operatorname{dist}(x_n, \operatorname{End}(T)) = r > 0$, that is, for any $\varepsilon > 0$, there exists a positive number N such that

$$|\operatorname{dist}(x_n, \operatorname{End}(T)) - r| < \varepsilon \text{ for all } n > N.$$

Put $\varepsilon = \frac{r}{2}$, $|\operatorname{dist}(x_n, \operatorname{End}(T)) - r| < \frac{r}{2}$, this implies that

$$\operatorname{dist}(x_n, \operatorname{End}(T)) < \frac{3r}{2}. \tag{4.5}$$

Let g be a nondecreasing function of the mapping T which satisfies condition (J). It follows from (4.4) and (4.5) that

$$0 < g\left(\frac{3r}{2}\right) < g\left(\operatorname{dist}(x_n, \operatorname{End}(T))\right) \le R(x_n, Tx_n) \to 0$$

a contradiction, and hence $\lim_{n\to\infty} \operatorname{dist}(x_n, \operatorname{End}(T)) = 0$. By Lemma 4.1, $\{x_n\}$ is Fejer monotone with respect to $\operatorname{End}(T)$. The conclusion follows from Lemma 4.2.

Theorem 4.3. Let E be a nonempty closed convex subset of a complete 2-uniformly convex hyperbolic space X and let $T : E \to \mathcal{K}(E)$ be a mapping satisfying condition (D) such that $\operatorname{End}(T) \neq \varnothing$. Let $\alpha_n, \beta_n \in [0,1)$ be such that $\beta_n \to 0$ and $\sum \alpha_n \beta_n = \infty$ and let $\{x_n\}$ be the sequence of S-iteration defined by (4.2). If T is semicompact, then $\{x_n\}$ converges strongly to an endpoint of T.

Proof. From (4.3) we get that

$$\sum_{n=1}^{\infty} \alpha_n \beta_n (1 - \beta_n) d^2(x_n, z_n) < \infty.$$

By Lemma 4.4, there exist a subsequence $\{d^2(x_{n_k}, z_{n_k})\}$ of $\{d^2(x_n, z_n)\}$ such that $\lim_{k\to\infty} d^2(x_{n_k}, z_{n_k}) = 0$, and hence

$$\lim_{k\to\infty} R(x_{n_k}, Tx_{n_k}) = \lim_{k\to\infty} d(x_{n_k}, z_{n_k}) = 0. \tag{4.6}$$

Since T is semicompact, by passing to a subsequence, we may assume that $x_{n_k} \to q \in E$. It follows from Lemma 2.1 (iv) that

$$\begin{aligned} \operatorname{dist}(q, Tq) &\le d(q, x_{n_k}) + \operatorname{dist}(x_{n_k}, Tx_{n_k}) + H(Tx_{n_k}, Tq) \\ &\le d(q, x_{n_k}) + \operatorname{dist}(x_{n_k}, Tx_{n_k}) + 2\min\left\{\operatorname{dist}(x_{n_k}, Tx_{n_k}), \operatorname{dist}(q, Tq)\right\} + d(x_{n_k}, q) \\ &\le 2d(q, x_{n_k}) + 3\operatorname{dist}(x_{n_k}, Tx_{n_k}). \end{aligned}$$

Thus, $q \in Tq$. Let $w \in Tq$. For each k, there exists w_{n_k} in Tx_{n_k} such that $d(w, w_{n_k}) = \operatorname{dist}(w, Tx_{n_k})$. By Proposition 2.1 (ii) and (4.6), we have

$$\begin{aligned} d(x_{n_k}, w) &\le d(x_{n_k}, w_{n_k}) + d(w_{n_k}, w) \\ &\le R(x_{n_k}, Tx_{n_k}) + H(Tx_{n_k}, Tq) \\ &\le R(x_{n_k}, Tx_{n_k}) + d(x_{n_k}, q) \to 0 \text{ as } k \to \infty. \end{aligned}$$

Thus, $w = q$, and hence $q \in \operatorname{End}(T)$. By Lemma 4.1, $\lim_{n\to\infty} d(x_n, q)$ exists and hence q is the strong limits of $\{x_n\}$.

Acknowledgements:

The authors would like to thank the anonymous reviewers for their careful reading and valuable suggestions which led to the present form of the paper. This research was supported by Mahidol Wittayanusorn School.

References:

1. Amini-Harandi A. Endpoints of set-valued contractions in metric spaces. Nonlinear Anal. 2010;72:132–134.
2. Agarwal RP, O' Regan D, Sahu DR. Iterative construction of fixed points of nearly asymptotically nonexpansive mappings. J. Nonlinear Convex Anal. 2007;8:61–79.
3. Bauschke HH, Combettes PL. Convex analysis and monotone operator theory in Hilbert spaces. CMS Books in Mathematics/Ouvrages de Mathematiques de la SMC. 2011.
4. Bejenaru A, Postolache M. A unifying approach for some nonexpansiveness conditions on modular vector spaces. Nonlinear Anal. Model. Control. 2020;25:827–845.
5. Chuadchawna P, Farajzadeh A, Kaewcharoen A. Convergence theorems and approximating endpoints for multi-valued Suzuki mappings in hyperbolic spaces. J. Comp. Anal. Appl. 2020;28:903–916.
6. Corley HW. Some hybrid fixed point theorems related to optimization. J. Math. Anal. Appl. 1986;120:528–532.
7. Dhompongsa S, Panyanak B. On Δ-convergence theorems in $CAT(0)$ spaces. Comput. Math. Appl. 2008;56:2572–2579.
8. Espinola R, Hosseini M, Nourouzi K. On stationary points of nonexpansive set-valued mappings. Fixed Point Theory Appl. 2015;236.
9. Haddad G. Monotone viable trajectories for functional-differential inclusions. J. Differential Equations. 1981;42:1–24.
10. Khamsi MA, Khan AR. Inequalities in metric spaces with applications. Nonlinear Anal. 2011;74:4036–4045.
11. Khanh PQ, Long VST. Invariant-point theorems and existence of solutions to optimization related problems. J. Global Optim. 2014;58:545–564.
12. Kirk WA. A fixed point theorem for mappings which do not increase distance. Amer. Math. Month.1965;72:1004–1006.
13. Kirk WA, Panyanak B. A concept of convergence in geodesic spaces. Nonlinear Anal. 2008;68:3689–3696.
14. Kudtha A, Panyanak B. Common endpoints for Suzuki mappings in uniformly convex hyperbolic spaces. Thai J. Math. 2018;Special issue:159–168.
15. Laokul T, Panyanak B. Common endpoint for non-commutative Suzuki mappings. Thai J. Math. 2019;17:821–828.
16. Leustean L. A quadratic rate of asymptotic regularity for CAT(0)-spaces. J. Math. Anal. Appl. 2007;325:386–399.
17. Panyanak B. Mann and Ishikawa iteration processes for multi-valued mappings in Banach spaces. Comput. Math. Appl. 2007;54:872–877.
18. Panyanak B. Endpoints of multi-valued nonexpansive mappings in geodesic spaces. Fixed Point Theory Appl. 2015;147.
19. Panyanak B. Approximating endpoints of multi-valued nonexpansive mappings in Banach spaces. J. Fixed Point Theory Appl. 2018;77:1–8.
20. Panyanak B. Endpoint iterations for some generalized multi-valued nonexpansive mappings. J. Nonlinear Convex Anal. 2020;21:1287–1295.
21. Reich S. Fixed point of contractive functions. Bull. Un. Mat. Ital. 1972;5:26–42.
22. Shahzad N, Markin J. Invariant approximations for commuting mappings in CAT(0) and hyperconvex spaces. J. Math. Anal. Appl. 2008;337:1457–1464.

23. Suzuki T. Fixed point theorems and convergence theorems for some generalized nonexpansive mapping. J. Math. Anal. Appl. 2008;340:1088–1095.
24. Takahashi W. Nonlinear functional analysis. Fixed point theory and its applications. Yokohama Publishers. 2000.
25. Tarafdar E, Watson P, Yuan XZ. Poincare's recurrence theorems for set-valued dynamical systems. Appl. Math. Lett. 1997;10:37–44.
26. Tarafdar E, Yuan XZ. The set-valued dynamic system and its applications to Pareto optima, Acta. Appl. Math. 1997;46:93–106.
27. Turinici M. Differential Lipschitzianness tests on abstract quasimetric spaces. Acta Math. Hunger. 1983;41:93–100.
28. Kohlenbach U. Some logical metatheorems with applications in functional analysis. Trans. Amer. Math. Soc. 2005;357:89–128.
29. Xu HK. Inequalities in Banach spaces with applications. Nonlinear Anal. 1991;16:1127–1138.

GUIDELINES of THAILAND PERSONAL DATA PRIVACY COMPLIANCE in UML: CASE of A PATIENT ASSISTANCE PROGRAM

Chadaporn Keatmanee[1,*], Songphon Klabwong[2], Umaporn Kithgrapan[2]
[1]Department of Computer Science, Faculty of Science, Ramkhamkaeng University, Thailand
[2]Nextmed Co.,Ltd., Bangkok, Thailand
*email: chadaporn.ru.ac.th

Abstract:
Firms in healthcare strive to improve the quality of the programs they provide. To achieve this, they require access to health data. Personal health information is categorized in sensitive information. Governments have legislation to ensure that privacy is respected, and healthcare firms must comply with it. Thailand Privacy Data Protection Act (PDPA) sets new standards by increasing and improving online personal data protection. To take and safeguard a firm compliance, privacy concerns should be addressed both by design (risk-approach), as well as, by default. Therefore, the guidelines that were created by combining regulation, information privacy, and best practices for web development, were needed. These guidelines based on Behavioral Diagrams were emphasized on designing the sequence diagram for a patient assistance program. The online program must comply right of the data subjects which is a patient. Ultimately the proposed guidelines aimed to equip web developers with a PDPA-standards compatible software incorporation.

Introduction:
One of the most important industry sectors that requires digital transformation is life sciences and healthcare. Currently, healthcare companies worldwide collect and process personal health information digitally. Health information is considered personal sensitive information. Therefore, the increased in quantity of health data has raised concerns throughout society regarding personal privacy violation. In recent years, Thai people have gained awareness of privacy concerns because the enactment of person data protection act (PDPA)[1] will become effective in upcoming years. This act contains provisions in relation to the restriction of rights and freedom of a person that aims to protect personal data and put in place effectively remedial measures of data subjects whose rights to the protection of personal data are violated. The act was prepared by the Ministry of Digital Economy and Society and reflected global trends in personal data protection (e.g., EU GDPR[2]). The government published PDPA in the Government Gazette on 27 May 2019. In addition, there is a grace period of 2 years before the act completely effective. Nevertheless, according to the pandemic, Covid-19, the law enforcement was postponed being effective on June 1st, 2022.

PDPA protects data subjects who is alive and ignores deceased person. The personal data are information about identifiable individuals which can be as little as name, address, email, Internet Protocol (IP), and website cookies. One of the most concerned data categorized in sensitive information (Section 26), is healthcare data for example, medical histories, demographic information, laboratory results, and any form of data obtained from healthcare professional for personal appropriate care that can identify an individual[3]. In addition, the modern healthcare industry has invented various technologies to digitize patient's health information not only for enhancing the diagnosis but also collecting the individual information for profiling[4]. Examples of

the digital health information are various kinds of medical images, blood pressures, heart rate, etc. Numerous profiling of patients combined with Artificial Intelligence algorithms could be beneficial for further individual diagnosis and better living. Consequently, volume of collected healthcare data has continued to exponentially increase. Therefore, the privacy of personal health information is a crucial concern.

There were many previous papers worldwide that paid attention to the study of privacy of personal health information in several contexts[5-7]. In Thailand, this area of interest is increasingly investigated aiming to understand the privacy concerns and its compliance. One of the papers was the exploration of behavioral intention of Thais' personal health information by applied the internet users' information privacy concerns model[8]. In addition, the study of the differentiation of IT implementation for data privacy between the United States and Thailand to understand the variation in order to make appropriate decision[9].

Patient Assistance Program (PAP) is one of the healthcare sectors that is designed for supporting patients and pharmaceutical companies. The program's goals are administrative tasks to ensure that patients get well treatment for examples; confirming vaccine appointment; reporting adverse events; tracking dorses of used jabs; providing financial support solutions. Thus, a third-party company who operates this program must effectively handle the patient's health information which considered confidential data. Currently, various companies use the digital platform to tackle those tasks instead of paper based. Applying functional web application could reduce human errors for tracking and making reports. For instant, one of the data subject rights for PDPA is that consumers can request their personal data in digital form.

Ensuring that a web application is PDPA compliance is an important task. PDPA compliance touches all aspects of the application. PDPA poses specific requirements on the storage of data, as well as how it is processed. In addition, it requires that applications provide users with specific functionality, such as a mean to retrieve all that users' data. In web applications design focus on modularity and separation of concerns (e.g., model-view-controller architecture), ad-hoc PDPA compliance may result in sprinkling the logic for such compliance throughout these modules. Therefore, host applications interact with the backend system via traditional SQL statements called sharded design would be more appropriate[10].

Consequently, the guidelines for required PDPA functions in web applications is mandatory. This research aims to introduce the basic process in web application design to comply PDPA. The UML behavioral diagrams were especially utilized for Section 34: the data subject rights. The proposed interaction diagrams emphasize the time orderly of messages for each data subject right in the patient assistant program guiding the company to increase consumer trust, as well as avoid penalty both administrative and criminal fines, and reputation damage.

Methodology:

The patient assistant program is considered as a data controller. Therefore, the basic tasks should be performed are following; consider using only necessary information to operate its tasks (data minimization); notify usage of their personal data; acquire consent from the patients (data subjects) in its' program for profiling; restrict the period of data detention; apply data security techniques (encryption, data anonymization, and pseudorandom); response to data subject rights; and finally, notify data breach. These required tasks are summarized in **Figure 1.** In this case, the company could consider appointing an officer called data privacy officer (DPO) who responses for data handling, executive coordination, data privacy and security policy management.

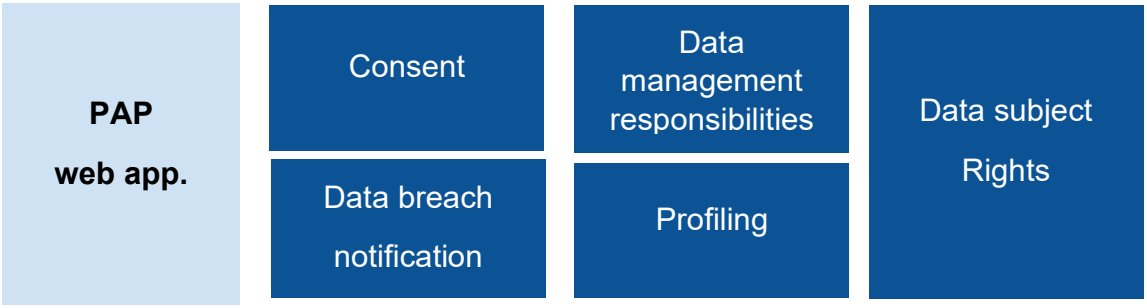

Figure 1. Basic components in data privacy were emphasized in PAP digital platform.

Complete design of web application to conform PDPA are tedious tasks, consequently, this research focused on applying data subject rights. Patients or customers who are called data subject can interact with PAP web application to acquire their rights as shown in Figure 2.

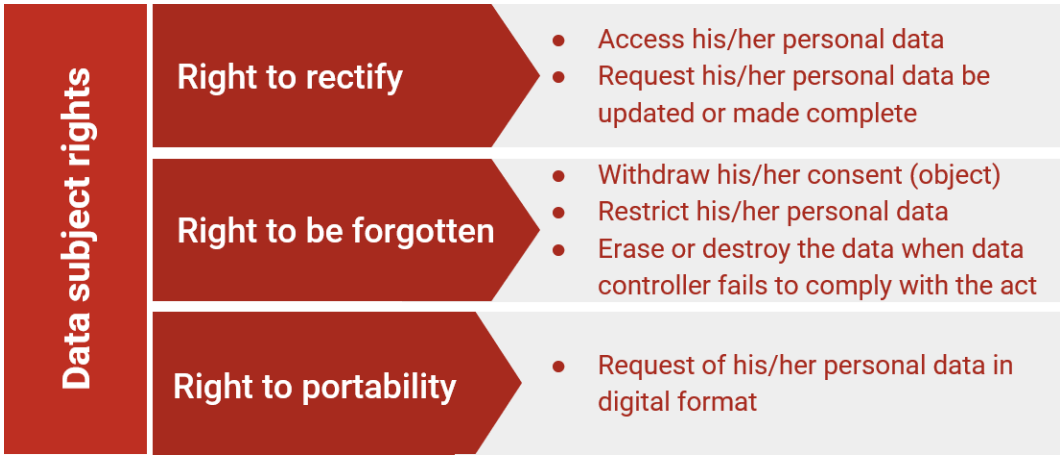

Figure 2. Conformation design regards rights of data subject in PAP web application.

First and foremost, the data security architecture shown in **Figure 3.** should be emphasized for user verification which are user identification and authentication. Identification is the process of verifying that consumer is who he/she says he/she is whereas authentication is the process by verifying that consumer is real, genuine, or authentic. Basically, encryption is used for both identification and authentication in the digital world. Thus, encryption algorithms should be applied to enhance data security. Data access of each participant in the PAP web application can be controlled by the Policy maker. Finally, activities related to personal data called logs should be stored and examined by internal and external audits.

The additional diagram in **Figure 4.** shows design of data storages. The storages composted of two kinds of data. The first one stored general information and the latter kept the sensitive data including personally identifiable information (PII) and protected health information (PHI). The last one strongly required encryption for data security.

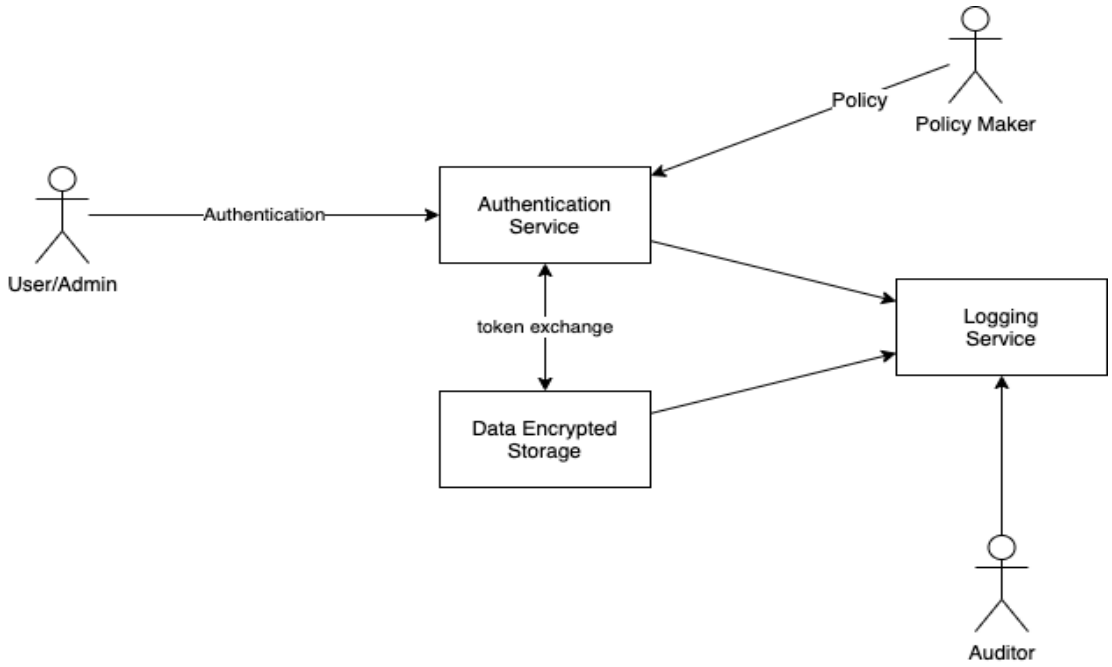

Figure 3. Data security architecture was applied to PAP digital platform.

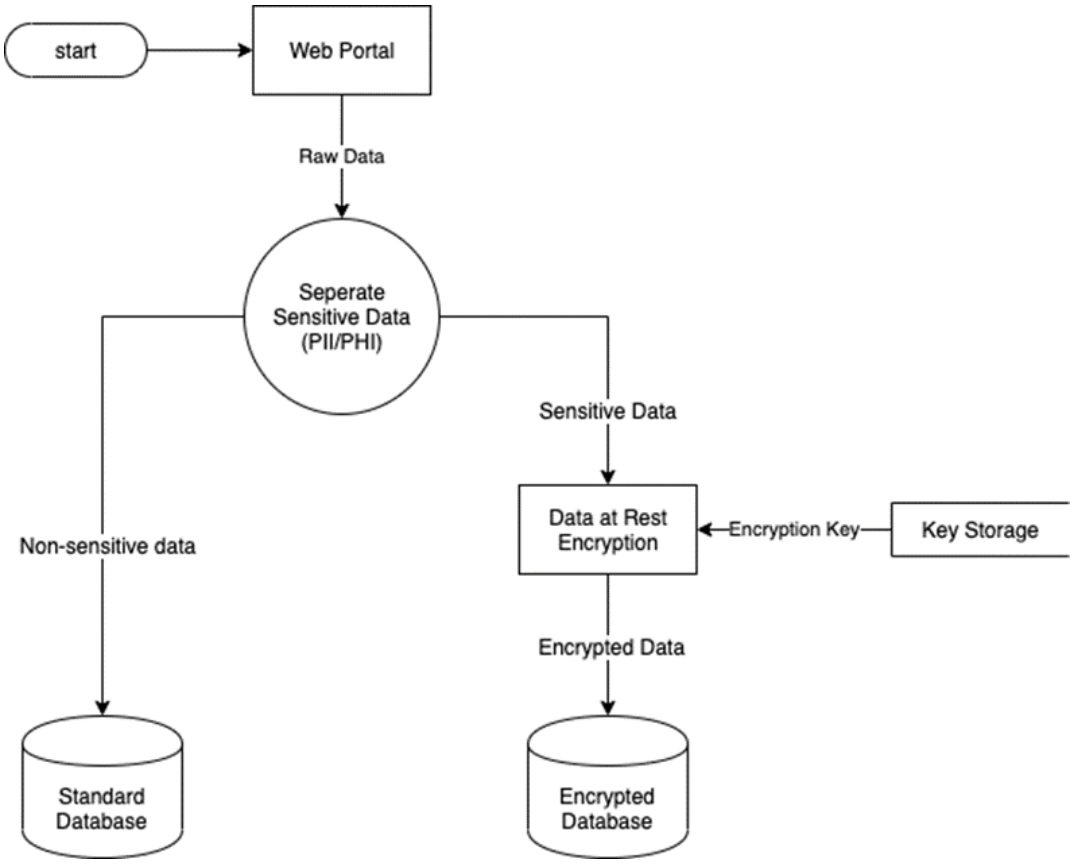

Figure 4. Secure data storage is designed for PAP digital platform.

Considering to the rights of data subject shown in **Figure 2.**, PAP web application shall allow the data subject to access and update his/her information. The data subject is entitled to request access to the personal data related to him or her which is shown in sequence diagram in **Figure 5.** After authentication, the data subject independently viewed his/her personal data. However, to protect mistakenly edited the user's information. The process required verification of the system administrator.

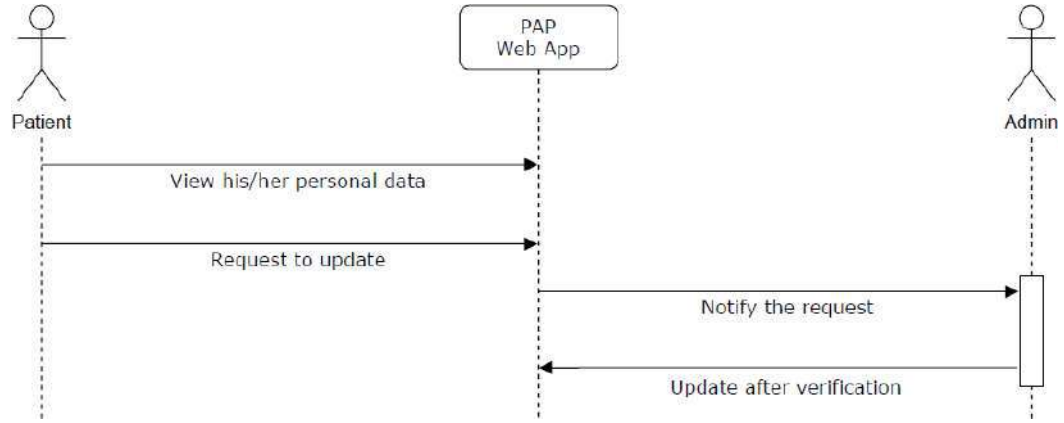

Figure 5. Right of data subject to access and update his/her personal data is shown in the UML.

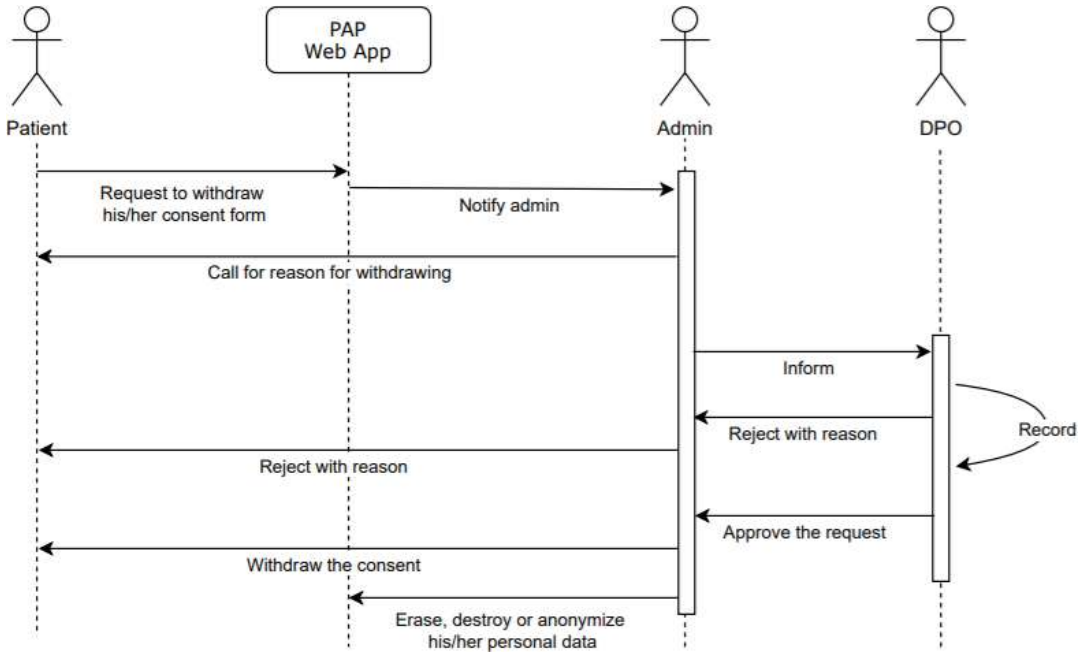

Figure 6. Right of data subjects to object the collection, use, or disclose of his/her personal data is shown in the UML.

The data subject shall have the right to object (withdraw) the collection, use, or disclosure of the personal data concerning him/her at any time. The data subject also can request the data controller to erase or destroy the personal data or anonymize the personal data to become the anonymous data which cannot identify the data subject. In addition, the data subject can restrict the personal data. All requests were categorized in right to be forgotten shown in **Figure 6. to Figure 8.** The system administrator should consult to the customer and DPO before the requests were eighter approved or rejected. In addition, the DPO has responsibility to record of each request.

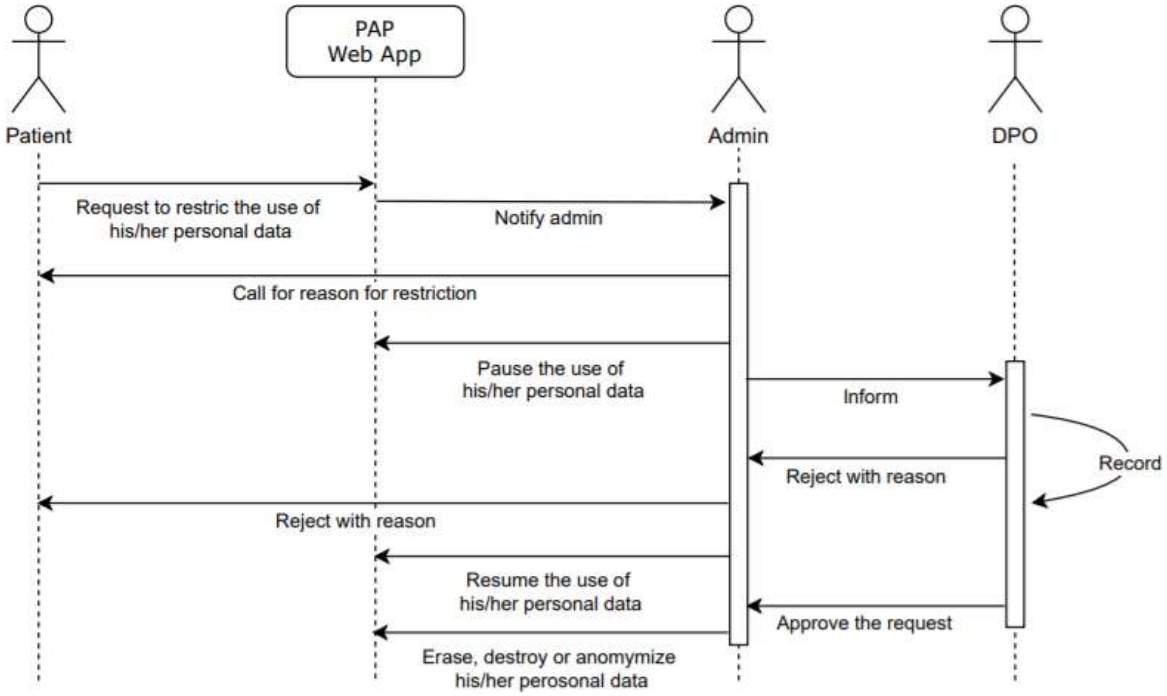

Figure 7. Right of data subjects to restrict the collection, use, or disclose of his/her personal data is shown in the UML.

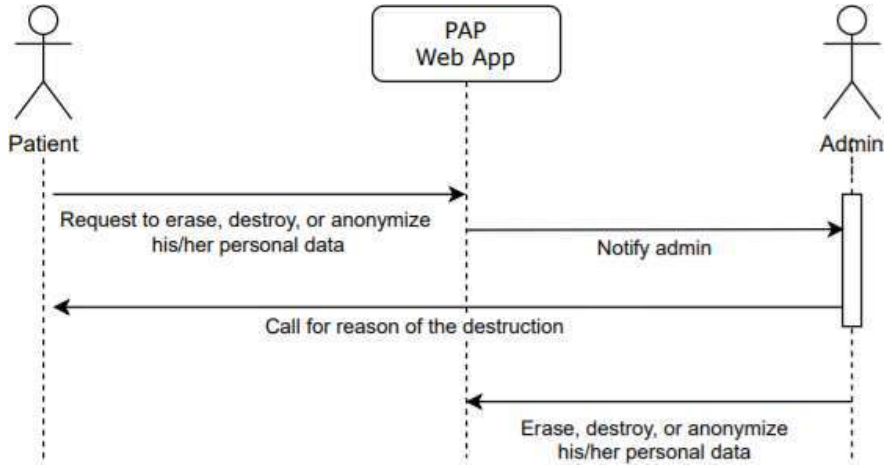

Figure 8. Right of data subjects to erase, destroy, or anonymize his/her personal data is shown in the UML.

Finally, the right to portability can be digitally performed by the system when the data subject requested. The data controller shall arrange such personal data to be in the format which is readable or commonly used by ways of automatic tools or equipment and can be used or disclosed by automated means as shown **in Figure 9.**

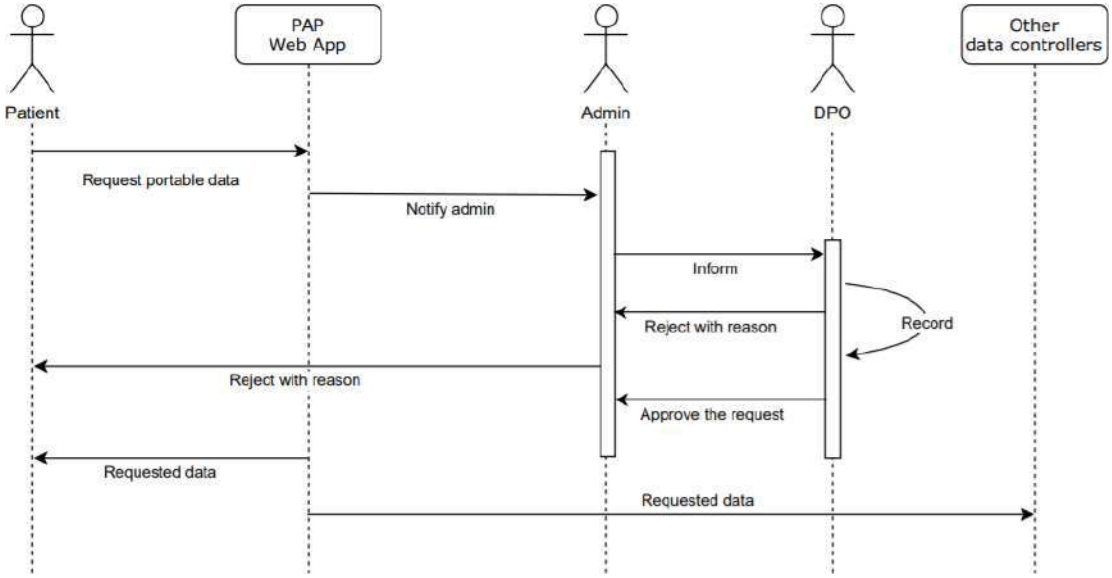

Figure 9. Right of data subjects for receive his/her information is shown in the UML.

Evaluation and discussion:

The proposed UML sequence diagram from Figure 4. to Figure 9. Conform PDPA in Chapter III, Rights of the data subjects. Their personal data were considered throughout these sections in a row; section 30: access; section 31: portability; section 32: withdrawal; section 33: destruction; section 34: restriction; and section 35: completeness. In addition, this research also guided the overview of basic process for data privacy and security. However, to complete all of concerns in the act, the additional designs for data anonymization, policy management, and secure protocol will investigated in the future.

Conclusion:

Coming to effect on 1.6.2022, PDPA sets the foundations on safeguarding personal data of services and on-line application users. Its universal application affects all entities collecting, storing and in general processing Thai citizens' personal data as part of service. Privacy and data protection is widely ignored by traditional engineering. These UML behavioral diagram partly contributed from expected limitations of IT sector in terms of compliance awareness and legislative understanding.

References:

1. Thai Government, 2019. Personal Data Protection Act. [online] Available at: https://drive.google.com/open?id=1MzGNi3kdDPA0E52n8bDybeuDNklM8xJe.

2. European Union, 2019. Complete Guide to GDPR Compliance. [online] Available at: https://gdpr.eu/

3. Pratt W, Kenton U, Andrea C, Meredith M S. Communications of the ACM. 2006;49(1):51-55.

4. Agapito G, Barbara C, Ilaria C, Daniela F, Pietro Hiram G, Nicola I, Theodora L, Marianna M, Mariadelina S,Mario C. In 2014 International Conference on High Performance Computing & Simulation (HPCS).2014:616-620.

5. Zerka F, Barakat S, Walsh S, Bogowicz M, Leijenaar R T, Jochems A, Lambin P. JCO clinical cancer informatics.2021;4:184-200.

6. Keshta I, Odeh A. Egyptian Informatics Journal.2021; 22(2):177-183.

7. Deepa N, Pandiaraja P. Journal of Ambient Intelligence and Humanized Computing.2021;12(5): 4877-4887.

8. Srisawatsakul C, Boontarig W. Current Applied Science and Technology.2021;21:774-787.

9. Theera Ampornpunt N. Ramathibodi's Fourth Decade: Best Innovation to Daily Practice.2009:10-13.

10. Supreeth S, Vinay B, Melissa W, Arun K, Vijay C. Proc. VLDB Endow. 2020;13(7):1064–1077.

THE PERTURBED RISK MODEL WITH INVESTMENT AND SURRENDER BASED ON POISSON NEGATIVE BINOMIAL COUNTING PROCESS

Chanon Tantiwattanapaibul,[1] Jiraphan Suntornchost[1*]
[1]Department of Mathematics and Computer Science, Faculty of Science, Chulalongkorn University, Bangkok, Thailand
*e-mail: Jirapahan.S@chula.ac.th

Abstract:

In this paper, we introduce a dependent risk model with investment and surrender perturbed by Brownian motion where the numbers of policies and investments are Poisson-Negative binomial counting processes. In addition, the occurrences of claims and surrenders are defined by thinning operators of the number of policies. Moreover, we obtain the probabilistic properties of surplus process, the adjustment coefficient function, and an upper bound of the ruin probability by the martingale approach. Finally, we discuss graphical trends of the upper bound of the ruin probability accumulated with risk model influenced by different variables in the model.

Introduction:

The insurance risk model is one of the most powerful tools for insurance companies to measure their risks of business. The classical risk model, known as Cramer-Lundberg risk model for the surplus process $R(t)$ is defined as

$$R(t) = u + ct - \sum_{i=1}^{N(t)} Y_i, \tag{1}$$

where $u \geq 0$ is the initial capital, $c > 0$ is the premium rate per unit of time and $N(t)$ is the Poisson process with intensity λ. The sequence $\{Y_i\}_{i=1}$ is a sequence of claim sizes which are assumed to be independent and identically distributed with mean μ_Y and variance σ_Y^2, respectively. The premium income in the classical model is assigned to constantly accumulated with time and is independent from claim sizes. However, the assumption of constant premium rate might not be applicable to some situations as mentioned in Boikov[2] where the premium incomes are not linear in time. Additionally, extensions of the classical model by modelling a relationship between the number of premiums and the number of claims by a thinning process is also brought attentions from researchers such as in Si et al.[5]and Yu and Huang[8].

Beside claims and premiums, other components are also added to risk models in several extensions of the classical risk models such as uncertainty of premiums and investments in terms of perturbation by a Brownian motion. Pioneered works in perturbed risk models can be found in Dufresne and Gerber[3] and Furrer and Schmidli[4]. Moreover, the developments of the perturbed risk model are more favorable in some real situations. For example, Cai and Yang[6] added the investment factor in the risk model to reflect the behavior of companies allocate money to invest and make profit.

In this study, we propose a risk model by incorporating different important components into the risk model such as investment, surrender, dependence between the numbers of claims and premiums, and uncertainty from unexpected events. The underlying counting process considered in our study is a compound Poisson called as the Poisson-Negative binomial counting process.

The organization of this paper is as follows. In the section of methodology, we introduce the risk model, derive its probabilistic properties, and obtain an upper bound of ruin probability. In the section of results and discussion, we present graphical results of trends of the upper bound of the ruin probability influenced by some important variables in the risk model. Finally, the last section concludes our study.

Methodology:

The surplus process considered in this study includes of six components which are initial capitals, investment capitals, premiums, claims, surrenders, and fluctuations from uncertain benefits and payments. Particularly, the surplus at time t which is denoted by $R(t)$, can be written as

$$R(t) = u + S(t), \tag{2}$$

where $u > 0$ is the initial capital and $S(t)$ is the profit process defined as

$$S(t) = AN_1(t) + \sum_{k=1}^{N_2(t)} X_k - \sum_{k=1}^{N_2(t,p)} Y_k - \sum_{k=1}^{N_2(t,q)} Z_k + \sigma B(t). \tag{3}$$

The components in the profit process (3) are as follows. The variable $A < u$ is the investment capital, $N_1(t)$ is the number of investment capitals following a compound Poisson Negative Binomial process with parameters λ_1, k_1, p_1; namely $N_1(t) \sim PNB(\lambda_1, k_1, p_1)$. $\{X_k, k \geq 1\}$ is a sequence of nonnegative i.i.d. random variables representing the amounts of premiums with mean μ_X and variance σ_X^2. The counting process $N_2(t,p)$ is the p-thinning process of $N_2(t)$ denoting the number of claims up to time t, represented by $N_2(t,p) \sim PNB(\lambda_2 p, k_2, p_2)$. The sequence of claim sizes $\{Y_k, k \geq 1\}$ are i.i.d. random variables with mean μ_Y and variance σ_Y^2. The counting process $N_2(t,q)$ is the q-thinning process of $N_2(t)$ denoting the number of surrenders up to time t, represented by $N_2(t,q) \sim PNB(\lambda_2 q, k_2, p_2)$. The sequence of $\{Z_k, k \geq 1\}$ are i.i.d. random variables with mean μ_z and variance σ_Z^2. $\{B(t), t \geq 0\}$ is a standard Brownian motion denoting the uncertainty benefits and payments of insurance companies $\sigma > 0$ is a constant that represents the diffusion volatility parameter. We suppose that $\{X_k, k \geq 1\}$, $\{Y_k, k \geq 1\}$, $\{Z_k, k \geq 1\}, \{N_1(t), t \geq 0\}, \{N_2(t), t \geq 0\}, \{N_2(t,p), t \geq 0\}, \{N_2(t,q), t \geq 0\}, \{B(t), t \geq 0\}$ are mutually independent.

To study properties of the risk model, we first introduce the counting processes used in our study. The underlying distribution for counts considered in this paper follows a compound Poisson distribution called as the Poisson-Negative binomial distribution constructed from the compound Poisson random variable $N = \sum_{h=1}^{M} D_h$ where M is a Poisson random variable with intensity λ and $D_h (h \geq 1)$ follows a negative binomial distribution with parameters k and p. Therefore, the moment generating function of the random variable N can be obtained as

$$
\begin{aligned}
m_N(r) &= E(e^{rN}) \\
&= E\left(e^{r\sum_{h=1}^{M} D_h}\right) \\
&= E\left(E\left(e^{r\sum_{h=1}^{M} D_h}\right)|M\right) \\
&= E((m_D(r))^M) \\
&= G_M(m_D(r)) \\
&= \exp\{\lambda(m_D(r)-1)\}.
\end{aligned}
$$

Consequently, we define the counting process based on the Poisson-Negative binomial distribution as follows.

Definition 1. The counting process $N(t)$ is said to be a Poisson-Negative binomial counting process with parameters λ, k, p, denoted as $N(t) \sim PNB(\lambda, k, p)$, if it satisfies

1. $N(0) = 0$,
2. $\{N(t), t \geq 0\}$ has stationary and independent increments,
3. for all $t > 0$, $N(t)$ is Poisson-Negative binomial counting process with the moment generating function
$$m_{N(t)} = \exp\{\lambda t(m_D(r)-1)\},$$
where D follows the Negative binomial distribution with parameters k and p,
4. the mean and variance are $E[N(t)] = \lambda t\frac{k}{p}$ and $Var[N(t)] = \lambda t\frac{k}{p^2}(k+1-p)$.

Another type of counting process considered in this study is the p-thinning counting process for the number of claims and the number of surrenders. The definition of p-thinning counting process of the counting process $N(t)$ is defined as

$$p \circ N(t) = \sum_{i=1}^{N(t)} \delta_i\,(p),$$

where $\{\delta_i,\ i = 1,2,\ldots\}$ are i.i.d. Bernoulli random variables with parameter p.

Having introduced counting processes used in our surplus process, we will derive some important properties of the profit process $S(t)$ as the following.

Lemma 1. The profit process $S(t)$ has the following properties.

1. $S(0) = 0$,
2. $\{S(t), t \geq 0\}$ has stationary and independent increments,
3. The expectation and variance of $S(t)$ are defined as
$$E[S(t)] = \alpha t \text{ and } Var[S(t)] = \beta t,$$

where

$$\alpha = \frac{A\lambda_1 k_1}{p_1} + \frac{\lambda_2 k_2}{p_2}\mu_X - \frac{\lambda_2 p k_2}{p_2}\mu_Y - \frac{\lambda_2 q k_2}{p_2}\mu_Z,$$

$$\begin{aligned}
\beta = {} & A^2\lambda_1\frac{k_1}{p_1^2}(k_1+1-p_1) + \lambda_2\frac{k_2}{p_2^2}(k_2+1-p_2)\mu_X^2 + \lambda_2\frac{k_2}{p_2}\sigma_X^2 + \lambda_2 p\frac{k_2}{p_2^2}(k_2+1-p_2)\mu_Y^2 \\
& + \lambda_2 p\frac{k_2}{p_2}\sigma_Y^2 + \lambda_2 q\frac{k_2}{p_2^2}(k_2+1-p_2)\mu_Z^2 + \lambda_2 q\frac{k_2}{p_2}\sigma_Z^2 + \sigma^2.
\end{aligned}$$

4. There is a function $g(r)$ such that

$$E[\exp\{-rS(t)\}] = \exp\big(tg(r)\big).$$

Proof. 1. From (3), we obtain

$$S(0) = AN_1(0) + \sum_{k=1}^{N_2(0)} X_k - \sum_{k=1}^{N_2(0,p)} Y_k - \sum_{k=1}^{N_2(0,q)} Z_k + \sigma B(0) = 0.$$

2. Since $N_2(t)$ has stationary and independent increments and $\{X_k, k \geq 1\}$ are i.i.d., the process $\sum_{k=1}^{N_2(t)} X_k$ has stationary and independent increments. Similarly, since $N(t,p)$, and $N(t,q)$ have stationary and independent increments and the sequences $\{Y_k, k \geq 1\}$ and $\{Z_k, k \geq 1\}$ are sequences of i.i.d. random variables, the processes $\sum_{k=1}^{N_2(t,p)} Y_k$ and $\sum_{k=1}^{N_2(t,q)} Z_k$ have stationary and independent increments. Therefore, the profit process $S(t)$ has stationary and independent increments.
3. The mean of $S(t)$ can be directly obtained as

$$\begin{aligned} E(S(t)) &= E(AN_1(t)) + E\left(\sum_{k=1}^{N_2(t)} X_k\right) - E\left(\sum_{k=1}^{N_2(t,p)} Y_k\right) - E\left(\sum_{k=1}^{N_2(t,q)} Z_k\right) \\ &\quad + E(\sigma B(t)) \\ &= \frac{A\lambda_1 k_1}{p_1} t + \frac{\lambda_2 k_2}{p_2}\mu_X t - \frac{\lambda_2 p k_2}{p_2}\mu_Y t - \frac{\lambda_2 q k_2}{p_2}\mu_Z t \\ &= \alpha t. \end{aligned}$$

Using the independence properties of different components in the surplus process and the variance formula of compound random variables, the variance of $S(t)$ can be obtained as

$$\begin{aligned} Var\big(S(t)\big) &= Var\big(AN_1(t)\big) + Var\left(\sum_{k=1}^{N_2(t)} X_k\right) + Var\left(\sum_{k=1}^{N_2(t,p)} Y_k\right) \\ &\quad + Var\left(\sum_{k=1}^{N_2(t,q)} Z_k\right) + Var(\sigma B(t)) \\ &= A^2 Var(N_1(t)) + Var\big(N_2(t)\big)E^2(X_k) + Var(N_2(t,p))E^2(Y_k) \\ &\quad + Var\big(N_2(t,q)\big)E^2(Z_k) + E(N_2(t))\,Var(X_k) + E(N_2(t,p))\,Var(Y_k) \\ &\quad + E\big(N_2(t,q)\big)Var(Z_k) + \sigma^2\,Var(B(t)) \\ &= A^2\lambda_1\frac{k_1}{p_1^2}(k_1 + 1 - p_1)t + \lambda_2\frac{k_2}{p_2^2}(k_2 + 1 - p_2)\mu_X^2 t + \lambda_2\frac{k_2}{p_2}\sigma_X^2 t \end{aligned}$$

$$+\lambda_2 p\frac{k_2}{p_2^2}(k_2+1-p_2)\mu_Y^2 t+\lambda_2 p\frac{k_2}{p_2}\sigma_Y^2 t\ +\lambda_2 q\frac{k_2}{p_2^2}(k_2+1-p_2)\mu_Z^2 t$$
$$+\lambda_2 q\frac{k_2}{p_2}\sigma_Z^2 t+\sigma^2 t$$
$$=\beta t.$$

4. Using the definition of moment generating functions and the independence properties of each component in the surplus process, we can show that

$$E[\exp\{-rS(t)] = E[\exp\{-rAN_1(t)\}]\cdot E\left[\exp\left\{-r\sum_{k=1}^{N_2(t)}X_k\right\}\right]$$
$$\cdot E\left[\exp\left\{r\sum_{k=1}^{N_2(t,p)}Y_k\right\}\right]\cdot E\left[\exp\left\{r\sum_{k=1}^{N_2(t,q)}Z_k\right\}\right]$$
$$\cdot E[\exp\{-r\sigma B(t)\}]$$
$$=\exp\left\{t\left(\lambda_1\left(m_{D_1}(-rA)-1\right)+\lambda_2\left(G_{D_2}(m_X(-r))-1\right)\right)\right\}$$
$$\cdot\exp\left\{t\left(\lambda_2 p\left(G_{D_2}(m_Y(r))-1\right)+\lambda_2 q\left(G_{D_2}(m_Z(r))-1\right)\right)\right\}$$
$$\cdot\exp\left\{\frac{1}{2}t\sigma^2 r^2\right\}$$
$$=\exp\left(tg(r)\right),$$

where

$$g(r)=\lambda_1\left(m_{D_1}(-rA)-1\right)+\lambda_2\left(G_{D_2}(m_X(-r))-1\right)+\lambda_2 p\left(G_{D_2}(m_Y(r))-1\right)$$
$$+\lambda_2 q\left(G_{D_2}(m_Z(r))-1\right)+\frac{1}{2}\sigma^2 r^2. \qquad (4)$$

In the next theorem, we will show that the function $g(r)$ obtained in (4) has a unique positive real root. To prove the property, we need the common assumption of the stability property of the company's business. That is the assumption that $E\left(S(t)\right)>0$ which implies that,

$$\frac{A\lambda_1 k_1}{p_1}+\frac{\lambda_2 k_2}{p_2}\mu_X>\frac{\lambda_2 p k_2}{p_2}\mu_Y+\frac{\lambda_2 q k_2}{p_2}\mu_Z\,. \qquad (5)$$

Theorem 2. The adjustment coefficient equation $g(r)=0$ has a unique positive solution which is called as the adjustment coefficient and is denoted as R.

Proof. To prove the theorem, we need to show that; (a) $g(0)=0$, (b) $g'(0)<0$, (c) $g''(r)>0$, for all $r\in(0,+\infty)$, and (d) $\lim_{r\to+\infty}g(r)=+\infty$.

For (a), substitute $r=0$ into $g(r)$, we can see that $g(0)=0$.

To prove (b), we first compute the derivative of $g(r)$ as

$$g'(r)\ =\ -A\lambda_1\left(m'_{D_1}(-rA)\right)-\lambda_2\left(G'_{D_2}\left(m_X(-r)\right)m'_X(-r)\right)+\lambda_2 p\left(G'_{D_2}\left(m_Y(r)\right)m'_Y(r)\right)$$
$$+\lambda_2 q\left(G'_{D_2}\left(m_Z(r)\right)m'_Z(r)\right)+\sigma^2 r.$$

From (5) and the properties that $m_X(0)=m_Y(0)=m_Z(0)=1$, $G'_{D_i}(1)=m'_{D_i}(0)=\frac{k_i}{p_i}$

for $i = 1, 2$ and $m_X'(0) = \mu_X$, $m_Y'(0) = \mu_Y, m_Z'(0) = \mu_Z$, we can show that

$$g'(0) = -\frac{A\lambda_1 k_1}{p_1} - \frac{\lambda_2 k_2}{p_2}\mu_X + \frac{\lambda_2 p k_2}{p_2}\mu_Y + \frac{\lambda_2 q k_2}{p_2}\mu_Z < 0.$$

To prove (c), note that the second derivative of $g(r)$ is

$$\begin{aligned} g''(r) = A^2\lambda_1\left(m_{D_1}''(-rA)\right) + \lambda_2\left(m_X''(-r)G_{D_2}'\left(m_X(-r)\right) + \left(m_X'(-r)\right)^2 G_{D_2}''\left(m_X(-r)\right)\right) \\ +\lambda_2 p\left(m_Y''(r)G_{D_2}'\left(m_Y(r)\right) + \left(m_Y'(r)\right)^2 G_{D_2}''\left(m_Y(r)\right)\right) \\ +\lambda_2 q\left(m_Z''(r)G_{D_2}'\left(m_Z(r)\right) + \left(m_Z'(r)\right)^2 G_{D_2}''\left(m_Z(r)\right)\right) + \sigma^2. \end{aligned}$$

By letting $c_1 \coloneqq m_{D_1}(-rA) - 1$, $c_2 \coloneqq G_{D_2}(m_X(-r)) - 1$, $c_3 \coloneqq G_{D_2}(m_Y(r)) - 1$, and $c_4 \coloneqq G_{D_2}(m_Z(r)) - 1$. Then $c_i'(r) < 0$ and $c_i''(r) > 0$ for $i = 1, \ldots, 4$ while other terms are greater than zero. Therefore, $g''(r) > 0$ for all $r \in \mathbb{R}^+$.

For (d), we can see from the definition of $g(r)$ that $\lim_{r\to+\infty} g(r) = +\infty$.

From (a) - (d), we can conclude that the equation $g(r) = 0$ has a unique positive solution.

Next, we will obtain an upper bound of the ruin probability by first introducing the definitions of time of ruin and the ruin probability. The ruin probability given the initial capital u is defined as

$$\psi(u) = P(T < \infty | R(0) = u),$$

where T is the time of ruin defined as

$$T = \inf_{t\geq 0}\{R(t) \leq 0\}.$$

To obtain the upper bound of the ruin probability, we follow the same approach as in the classical risk model by constructing a martingale and applying the martingale stopping time theorem. To define a martingale, we first introduce the filtration $\mathcal{F}_t$ generated by the profit process $S(s)$ for $s \leq t$ as $\mathcal{F}_t = \sigma(S(s), s \leq t)$. The construction of the martingale is a direct application of Lemma 1(4) as the following.

Theorem 3. Define $\mathcal{M}_u(t) = \exp\{-r(u + S(t)) - tg(r)\}$. Then $\mathcal{M}_u(t)$ is a $\mathcal{F}_t - martingale$.

Proof. By the conditional expectation, let $s < t$

$$\begin{aligned} E[\mathcal{M}_u(t)|\mathcal{F}_s] &= E[\exp\{-r(u + S(t)) - tg(r)\}|\mathcal{F}_s] \\ &= E\big[\exp\{-r\big(S(t) - S(s)\big) - r(u + S(s)) - sg(r) - \\ &\qquad (t - s)g(r)\}|\mathcal{F}_s\big] \\ &= \exp\{-r(u + S(s)) - sg(r)\} \\ &\qquad \cdot E\big[\exp\{-r\big(S(t) - S(s)\big) - (t - s)g(r)\}|\mathcal{F}_s\big] \\ &= \exp\{-r(u + S(s)) - sg(r)\} \\ &= \mathcal{M}_u(s), \end{aligned}$$

where we use Lemma 1(4) to obtain the last two equations. Therefore, $\mathcal{M}_u(t)$ is martingale.

Having obtain a martingale, we follow Yu and Huang[8] by applying the martingale stopping theorem to obtain the upper bound of the ruin probability. The theorem 4 and Corollary are originally presented in Yu and Huang[8]. However, for the smoothness of this presentation, we restate their theorems and proofs below.

Theorem 4. (Yu and Huang[8]) The ultimate ruin probability satisfies

$$\psi(u) \leq \exp\{-ru\}E\left[\sup_{t\geq 0}\{\exp[tg(r)]\}\right]. \tag{6}$$

Proof. Note that, for a fixed time t_0, $t_0 \wedge T$ is a stopping. Then, by the stopping time theorem, we obtain

$$\begin{aligned} exp\{-ru\} &= E[\mathcal{M}_u(0)] = E[\mathcal{M}_u(t_0 \wedge T)] \\ &= E[\mathcal{M}_u(T)|T \leq t_0]P(T \leq t_0) + E[\mathcal{M}_u(t)|T > t_0]P(T > t_0) \\ &\geq E[\mathcal{M}_u(T)|T \leq t_0]P(T \leq t_0) \end{aligned} \tag{7}$$

Then

$$\begin{aligned} P(T \leq t_0) &\leq \frac{\exp\{-ru\}}{E[\mathcal{M}_u(T)\,|T \leq t_0\,]} \\ &= \frac{\exp\{-ru\}}{E[\exp\{-rR(T) - Tg(r)\}|T \leq t_0]} \end{aligned} \tag{8}$$

Since $R(T) < 0$ and (8), we know that $\exp\{-rR(T)\} \geq 1$ for all $r > 0$.
Hence

$$P(T \leq t_0) \leq \frac{\exp\{-ru\}}{E[\exp\{-Tg(r)\}|T \leq t_0]}$$

Consider the denominator $E[\exp\{-Tg(r)\}|T \leq t_0]$, we know that

$$E[\exp\{-Tg(r)\}|T \leq t_0] \geq \inf_{0\leq t\leq t_0}[\exp\{-Tg(r)\}|T \leq t_0].$$

Therefore,

$$\begin{aligned} P(T \leq t_0) &\leq \frac{\exp\{-ru\}}{\inf_{0\leq t\leq t_0}[\exp\{-Tg(r)\}|T \leq t_0]} \\ &= \exp\{-ru\}\sup_{0\leq t\leq t_0}\{\exp\{tg(r)\}\}, \end{aligned} \tag{9}$$

Taking expectation on both sides of (9) and limit $t_0 \to +\infty$, then the theorem is proved.
Corollary 1. (Yu and Huang[8]) The upper bound of ultimate ruin probability denoted by

$$\psi(u) \leq \exp\{-Ru\}, \tag{10}$$

when $R = \sup\{r : g(r) \leq 0\}$.
Proof. Taking supremum over r in both sides in (9), we obtain that

$$\begin{aligned} \psi(u) &\leq \sup_{r>0}\left(\exp\{-ru\}E\left[\sup_{t\geq 0}\{\exp[tg(r)]\}\right]\right) \\ &\leq \exp\{-Ru\}. \end{aligned}$$

Results and Discussions:

In this section, we perform numerical simulations to study trends of the upper bound of ruin probability, e^{-Ru}, which is influenced by different parameters in the risk model. The parameters considered are the initial capital (u), the size of investment capital (A), the parameter (λ_1) of the rate of investments and the proportion of the occurring of surrender (q), and the diffusion volatility parameter. The values of parameters used in our numerical study are as follows. $u = 5,\ \lambda_1 = 20,\ \lambda_2 = 30,\ A = 5,\ k_1 = 2,\ k_2 = 3,\ p_1 = 0.5,\ p_2 = 0.4, p = 0.05,\ q = 0.001,$ $\sigma = 5$. The random variables X_k, Y_k, Z_k, representing the premium sizes, claim sizes, and surrender sizes are exponentially distributed with means $\mu_X = 0.3,\ \mu_Y = 0.4,$ and $\mu_Z = 0.2$, respectively. Figure 1-5 show trends of the upper bound influenced by the initial capital u, the size of investment capital (A), the parameter (λ_1) of the rate of investments and the proportion of the occurring of surrender (q), and the volatility parameter (σ) respectively.

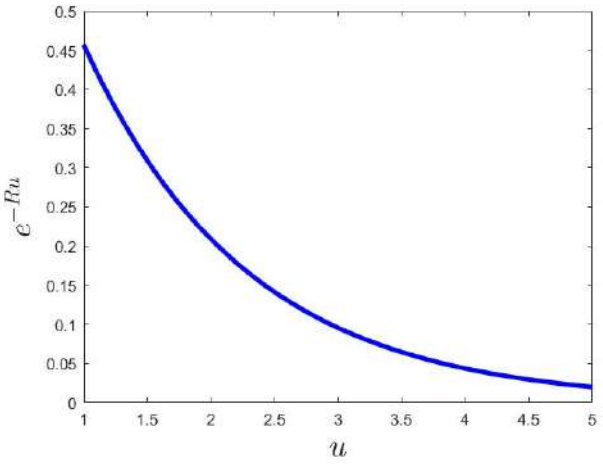

Figure 1:

Plot of the upper bound of the ruin probability e^{-Ru} against the initial capital u.

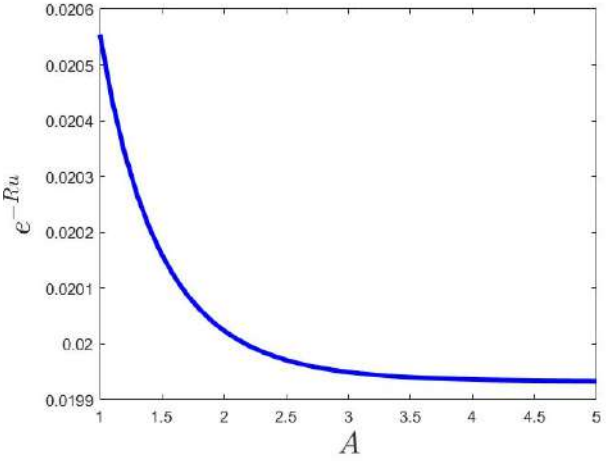

Figure 2:

Plot of the upper bound of the ruin probability e^{-Ru} against the investment capital A.

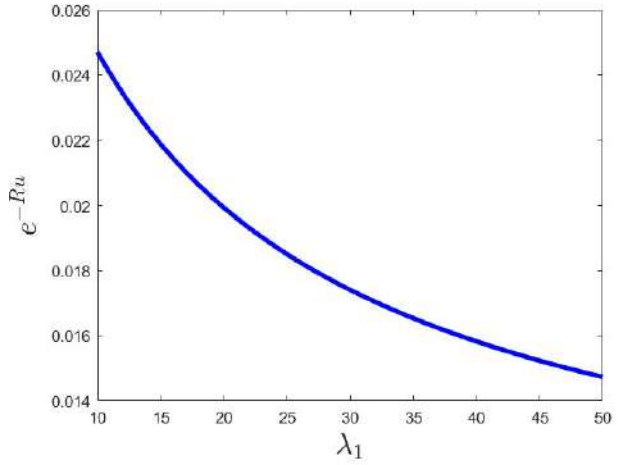

Figure 3:

Plot of the upper bound of the ruin probability e^{-Ru} against the rate of investments λ_1.

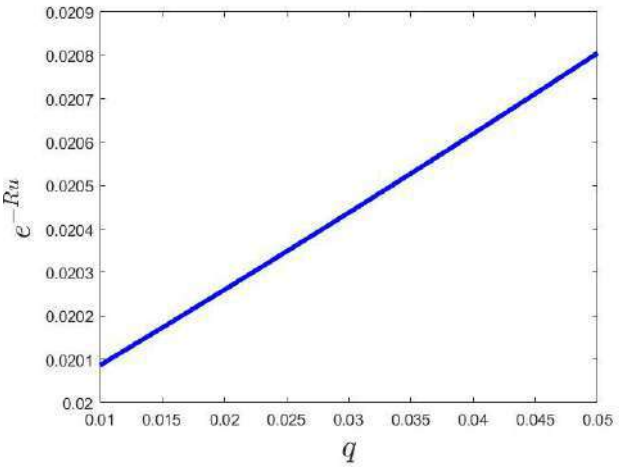

Figure 4:

Plot of the upper bound of the ruin probability e^{-Ru} against the proportion of the occurring of surrender q.

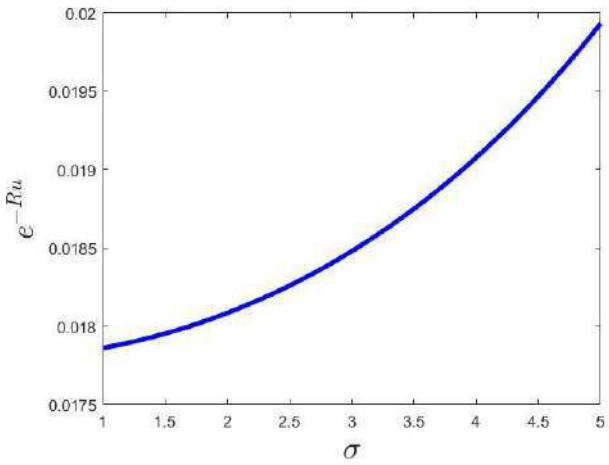

Figure 5:

Plot of the upper bound of the ruin probability e^{-Ru} against the volatility parameter σ.

From Figures 1-5, we can see that the upper bound of ruin probability decreases as one of the initial capital, investment amount, and rate of investments increases. In opposite direction, the upper bound of the ruin probability increases as either the proportion of surrender or the volatility variable increases. The results agree with theoretical and realistic insurance risk models. For example, the volatility variable presenting the behavior of chaos occurrence such as the insurance companies allocate money to stock markets as a result that the trend of the upper bound of ruin probability in Figure 5 dramatically increases when σ increases.

Conclusion:

In this paper, we introduced the perturbed risk model with investment and surrender based on the Poisson-Negative binomial counting process. The model incorporates many different components used in insurance business such as investment and surrenders. Moreover, by using the Poisson-Negative binomial underlying distribution of counts instead of the Poisson distribution commonly used current risk models, we can accommodate data with overdispersion commonly occurred in insurance data. In our study, we also derived the probabilistic properties of the model and obtained the formula to obtain the adjustment coefficient and the upper bound of ruin probability. Furthermore, we showed numerical simulations to study trends of the upper bound of the ruin probability as functions of different parameters in the risk models including investment (A), frequency of investment (λ_1), the portion of surrender (q), and the volatility variable (σ). These relations will help policymakers in predicting the trend of ruin probability based on the trends of the specified parameters in the model. The model and its probabilistic properties derived in our study should be applicable to a wider situations of insurance business than other risk models available in literature. However, some further developments of our model can be considered such as an extension to a multidimension to accommodate insurance company with multiple policies.

References:

1. Gerber HU. S.S. Heubner Found. Monogr. Ser. Heubner Foundation. 1979.
2. Boikov AV. Theory Probab. Appl. 2002;47:489-493.
3. Dufresne F., Gerber HU. Insur Math Econ. 1991;10:51-59.
4. Furrer HJ., Schmidli H. Insur Math Econ. 1994;15:135-169.
5. Si JD., Wang ZY., Wang GJ. Appl. Math. J. Chinese Univ. Ser. B. 2002;17(4):435-441.
6. Cai J., Yang HL. Adv Appl Probab. 2005;37:819-835.
7. Huang YJ., Yu WG. Discrete Dyn Nat Soc. 2013;2013:1-8.
8. Yu WG., Huang YJ. Math Probl Eng. 2015;2015:1-8.

TRACKING AND TAKE CARE AMNESIA PATIENT APPLICATION BY USING iBEACON

Sathit Prasomphan1,* Yasintorn Sirijaruwong, Sopon Hiruntiwakul

Department of Computer and Information Science,
King Mongkut's University of Technology North Bangkok, Bangkok, 10800 THAILAND
*e-mail: sathit.p@sci.kmutnb.ac.th

Abstract:
Tracking system and take care amnesia patient is a mobile application where the user can monitor patients' location in crowded environments. In addition to patients, there is also the elderly people, so user can use this application to track their location. It can be used for any safety purpose tracking which will work in android platform and use GPS to track the location. Our application can use to track the location of older people at a distance within 50 meters along with beacon and it can use with the older patient in hospital who lives in Bangkok. We hope that our application can be used efficiently and respond the need of user as well. Moreover, most importantly, our application has functions related to patient care, whether calling emergency numbers, recording activities and finding nearby hospitals as an option for users to consider safety and can reduce the mortality rate of patients. We also developed simulation results of the location error mode by comparing several location methods utilizing Received Signal Strength indicator (RSSI) data to find the most accurate localization for this system.

Introduction:
Public Health Service Center 65 Ruksasuk Bang Bon was established to be responsible for public health work with communities in the area. To promote health for the people according to the policy of the Bureau of Health, which has been divided into areas of responsibility as well as other public health service centers throughout Bangkok. The operations are organized into four dimensions, both proactive and reactive. To enhance the efficiency of physical and mental health along with the development of public health of the community by allowing the community to participate in the promotion and protection of their own health and people in the community.

Nowadays, the technology is widely used and the aging society is coming. Most population in the country are older. Thus, one problem that occurs is the forgetfulness of these older people. This problem make an effect to the older people that they cannot perform daily routine normally. From this problem, our goal is to make an application that can help reminds some activities of the elderly people. However, with the patient tracking system the user can track and monitor their patient location in just a simple app when the user is anywhere.

In the mobile application. We have proposed a system for tracking the location of the beacon network. This is a low power device capable of transmitting broadcast signals via Bluetooth Low Energy (BLE), so it is mainly used for detecting the close presence of patients.

The device consists of a module that communicates independently and has the ability to work simultaneously with the local GSM network (DTMF, SMS, GPRS and GSM) [1]. It

provides effective real time location. Using this system, we can get accurate location of the beacon that is to be tracked.

Databases and software determine the coordinates of each track point recorded in the database. This can be displayed on the screen using Google Maps later using the api rental method. However, to view the patient's location. User must be connected to the Internet. The patient's coordinates can be viewed every 30 seconds.

For our system, we use XAMPP software which provides access to a database of patient activity records, emergency calls, patient history, admin profiles, admin assign, function of finding nearby hospitals and the location of beacons on Google map from anywhere in the world. The system also facilitates reducing patient mortality and providing a reminder to patients.

Related Theory:

A. GPS signal transmission

A GPS tracking unit is a device that uses the Global Positioning System to determine the precise location of beacons. Users on Earth operate GPS receivers. It measures the time it takes for a radio signal to travel from four or more satellites to its location. Then the distance from each satellite is calculated. In addition, from this calculation, the device determines the longitude, latitude, and altitude of the location. The tracking system easily and accurately locates the vehicle by following the triangular method or trilateration. It is a method of determining the relative position of an object using the geometry of a triangle. To "quantify the triangle", a GPS receiver measures the time it takes for a satellite to travel to Earth in a very short period of time (less than one tenth of a second) and thereby measure the distance from the satellite as the travel time of the radio signal. To determine the distance between the satellite and the satellite, the measured time is multiplied by the radio frequency speed of 300,000 km (186,000 miles) per second [1]. The latitude and longitude coordinates can be sent to the user every 30 seconds to track the patient's coordinates in order to see if every 30 seconds, where did the patient go or it may be transmitted and stored in a database using a mobile modem which allows the user to display real-time location of both beacons and smartphones on our application.

B. Definition of beacon device [2]

A beacon, in the context of location-based services, is a small hardware device that enables data transmission to mobile devices within a specific range of the device. For most applications, recipients must have Bluetooth turned on, have the associated mobile app installed with location services enabled and must have opted in to accept the sender's transmissions.

Beacons are usually small standalone devices that are attached to walls or objects in the environment. The simplest beacons simply send out a signal to devices in range but they may also be Wi-Fi- and cloud-connected and can contain memory, processing resources and sensors for temperature and motion detection (among other possibilities). A typical configuration might include an ARM processor, a Nordic Semiconductor or Texas Instruments chipset, a Bluetooth Low Energy (BLE) module and a battery. The devices are low power and inexpensive, with a battery life of several years.

Beacons are often said to work like lighthouses, sending out an intermittent signal that can be detected by an entity within range. Instead of the light signals that guide ships, however, the beacon emits a radio signal that can be picked up by nearby mobile devices equipped with the associated app. As Google developers commented at the release for the company's Eddystone beacon profile, "Just like lighthouses have helped sailors navigate the

world for thousands of years, electronic beacons can be used to provide precise location and contextual cues within apps to help you navigate the world."

Google's Eddystone and Apple's iBeacon are the two most commonly implemented beacon protocols. Here's a brief explanation of how iBeacon works. Any hardware device that supports Bluetooth 4.0 can, in theory, become a beacon in an iBeacon network, which means that smartphones, PCs and tablets can function as beacons. The beacon continuously scans for iOS-based mobile devices that have Bluetooth open and are running the associated mobile app. When the beacon detects such a device, it sends a connection request to wake up the app. Information within the request includes the information required to push the desired communication to the device in real time.

Beacons are increasingly implemented in retail environments, where they are used to streamline mobile payment systems and enable proximity marketing: the wireless delivery of promotional material to mobile users within range. The location may be so precise that the communications target a shopper standing in front of a particular product with coupon offers, flash sales and suggestions for related products -- among many other possibilities.

Beacon technology has many other applications. The same precision of targeting that finds consumers can enable communications directed to someone in a particular seat at a stadium or standing in front of a museum installation or an artwork in a gallery. The technology can provide users with directions or maps to airport locations such as gates, ticket counters, shops and restaurants, as well as identifying the closest elevators, restrooms and courtesy phones. Similar apps can help guide people in other large facilities, such as hospitals and help them find their cars when they leave those locations.

Figure 1.
Beacon image

C. Dart language

Dart is a programming language designed for client development [4] [5] such as for the web and mobile apps. It is developed by Google and can be used to build server and desktop applications. Dart is an object-oriented, class-based, garbage-collected language with C-style syntax [6] Dart can compile to either native code or JavaScript. It supports interfaces, mixins, abstract classes, reified generics, and type inference.[7]. Dart was unveiled at the GOTO conference in Aarhus, Denmark, October 10–12, 2011.[8] The project was founded by Lars Bak and Kasper Lund.[9] Dart 1.0 was released on November 14, 2013.[10]

Dart initially had a mixed reception and the Dart initiative has been criticized by some for fragmenting the web, due to the original plans to include a Dart VM in Chrome. Those plans were dropped in 2015 with the 1.9 release of Dart to focus instead on compiling Dart to JavaScript [11]. In August 2018, Dart 2.0 was released, with language changes including a sound type system [12]. Dart 2.6 introduced a new extension, dart2native. The feature extends native compilation to the Linux, macOS, and Windows desktop platforms. Earlier developers were able to create new tools only using Android or iOS devices. Moreover, with this extension it becomes possible to compose a Dart program into self-contained executables. Thus, according to the company representatives, it is not obligatory now to have Dart SDK installed, the self-contained executables can now start running in a few seconds. The new extension is also integrated with Flutter toolkit, thus making it possible to use the compiler on small services (backend supporting for example) [13][14] .

D. RSSI [15]

RSSI stands for Received Signal Strength Indicator. It is the strength of the beacon's signal as seen on the receiving device, e.g. a smartphone. The signal strength depends on distance and Broadcasting Power value. At maximum Broadcasting Power (+4 dBm) the RSSI ranges from -26 (a few inches) to -100 (40-50 m distance). RSSI is used to approximate distance between the device and the beacon using another value defined by the iBeacon standard: Measured Power (see below). Due to external factors influencing radio waves—such as absorption, interference, or diffraction—RSSI tends to fluctuate. The further away the device is from the beacon, the more unstable the RSSI becomes.

E. Measured Power [16]

Measured Power is a factory-calibrated, read-only constant, which indicates what is the expected RSSI at a distance of 1 meter to the beacon. Combined with RSSI, it allows estimating the distance between the device and the beacon. However, you can change it in the raw chips using Arduino etc. if you have access to the AT-commands of the BLE chip.

F. Related work.

Bellini et.al [12] employed data collected by an iBeacon-based system that consists of two components: a network of antennas strewn across the facility and a Bluetooth bracelet worn by the patients. They applied the concepts of Relational and Popularity Indexes to describe, display, and explain the social behavior of AD patients. They redefine the Relational Index to capture roaming and casual interactions, which are widespread among AD patients. They used data analytics to create prediction tools and applications to improve social activity scheduling, sociability monitoring, and promotion, with the ultimate goal of improving patient quality of life. Roosan et.al [13], the goal of this research is to use heatmap visualization to present progress notes data. The researchers used unstructured text from deidentified patient data progress notes in their investigation. The study team used the clinical complexity model to conduct qualitative content coding and created a heatmap based on the processed frequency data. The researchers created a color-coded heatmap based on the severity and acuity of a patient's condition acquired across several previous visits. Future study into developing an automated procedure for constructing a heatmap from an unstructured dataset could pave the way for big data in healthcare to be operationalized. Rafferty et.al [14], this study provides a novel technique for detecting and alerting caregivers of at-risk residents leaving a care facility. Wearable Bluetooth beacons and beam-formed listening devices are used to power this system. This approach demonstrated to be accurate in a test including 275 egress occurrences, with no false positives. This approach, in particular, has been in use at a real residential care home for over a year. Future work that has been proposed focuses on how to improve this solution. In [15], this study looks at the scholarly literature on mHealth apps that help caregivers of Alzheimer's patients. Between January 2014 and January 2021, they searched published literature in five electronic databases, using the PRISMA guidelines for scoping reviews. The final review comprised twelve papers. Based on the functionality provided by the examined caregiver applications, six themes emerged. They are caregiver tracking, task management, monitoring, mental support, education, and a communication platform for caregivers. The analysis found that mHealth apps for caregivers of Alzheimer's patients are lacking. Industry, government, and academics have an opportunity to meet the unmet needs of these caregivers.

Methodology:

In this section, we describe procedures and methods of developing application as follows

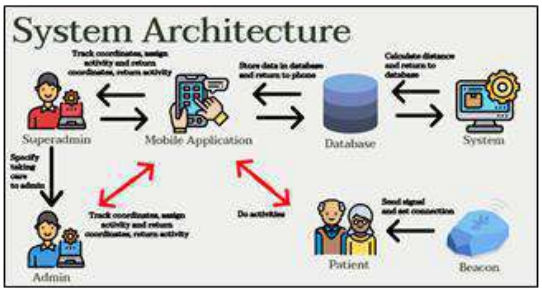

Figure 2.
System Architecture overview

Superadmin and admin will follow-up patient process via a mobile application. Superadmin is responsible for managing which admin are taking care of which patient and can increase the number of admin. Admin is responsible to track patient by viewing information via mobile applications and increasing activity, add medicines to patients by filling out information through a mobile application to save data through a database. Process of Adding, Deleting, and editing patient information will be stored in the database by superadmin and admin. Those data will sent server and information is sent in the system. Patient is followed by superadmin and admin. Devices used to track patients have phone and beacon. Beacon will transmit signals distance of 50 meters and telephones will transmit signals over a distance of 50 meters.

Beacons do not broadcast constantly. They 'blink' instead. Advertising Interval describes the time between each blink. The value ranges between 100 ms and 2000 ms. The shorter the interval, the more stable the signal. Keep in mind that adjusting Advertising Interval will affect battery life in a big way. The formula used to calculate the distance is

$$\text{Distance} = 10 \wedge ((\text{Measured Power} - \text{RSSI})/(10 * N))$$

Where N is Constant depends on the Environmental factor. Obviously, the Distance calculated is the approximated distance and not the exact distance as for calculating exact distance we have to make the loss factor (from environmental factors).

Results and Discussion:

From the experiments conducted at Public Health Service Center 65 Ruksasuk Bang Bon, it can be concluded that users or admin and superadmin can monitor patients using both beacons and smartphones to track the signal with a GPS system as shown in this figure.

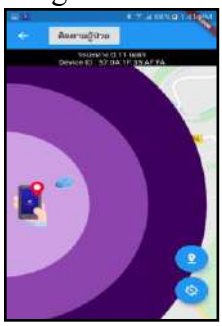

Figure 3.
Patient tracking page with beacon

From this figure, it can be seen that there are all 3 borders. The first level purple dot is outside the building, the 2nd level purple dot is inside the building, and the 3rd level purple dot is closest to the admin and superadmin.

This application admin can take care of patients by adding details of activities as shown in this picture.

Figure 4.
Patient activity page

From this figure, when admin and superadmin add details of patient activities. A notification sound using Siri as a reminder can be sent to the patient's phone.

However, if the patient is in a serious accident, the user can use the "EMERGENCY CALL" function to immediately call an ambulance.

Finally, superadmin determines which admin to take care of patients using. "Assign patient" button to manage for the convenience of care.

Figure 5.
Assign admin page

We also have simulation results of the location error mode by comparing several location methods utilizing Received Signal Strength indicator (RSSI) data to find the most accurate localization for this system. To verify our hypothesis, we installed the Beacons in their designated places and calculated the path-loss model and RSSI values at ten different sites. The IEEE model route loss equation was utilized to determine the path loss model. In order to measure RSSI in a room, raw data must be collected. This information is based on the presence of many beacons in the room. The RSSI per one meters is -65 db.

We were able to collect RSSI measurements at different power levels using Estimate's Beacons to find the most effective and efficient way to put the Beacons in a room to ensure comprehensive coverage. This required a variety of arrangements in which Beacons were mounted around the walls while RSSI readings were taken from multiple spots throughout the room and compared to a computed path loss. The ideal setup would have the highest overall RSSI values in every position in the room, with the fewest weak points. We

calculated that three iBeacons would be enough to cover the entire room based on the measurements of the multiple iBeacons. The RSSI using three iBeacons at 10 locations are shown as follows.

Table 1.
The RSSI of iBeacon at 10 locations.

Point	Distance from iBeacon	RSSI
1	331.16	-80
2	369.48	-86
3	305.89	-75
4	165.98	-81
5	208.53	-84
6	265.22	-80
7	387.77	-84
8	497.19	-85
9	231.96	-83
10	558.77	-87

Conclusion:

This research was presented to Public Health Service Center 65 Ruksasuk Bang Bon on patient follow-up and care for amnesia patients to help determine the patient's location for safety and to provide patient care by use a smartphone activity recorder method and use an emergency number to call an ambulance immediately. Most of the system architecture is built on two basic features, the Global Positioning System (GPS) and Siri, voice that are used to track location and to sound alerts to the patient's phone. The tracked location is determined by tracked parameters such as latitude and longitude. Using this parameter allows the user to verify the location by entering the values obtained on Google of latitude and longitude. The advantages of the proposed system are users are provided with a iBeacon accessory that can be used to track patients at close distances.

References:

1. Mistary P., Chile R. Real time Vehicle tracking system based on ARM7 GPS and GSM technology. 2015:1-6.
2. Mrunalv A. K., Pranoti S. T., Atul D. R. Comparative Study on vehicle Tracking System. IJFEAT. 2015: 3(4):1-5.
3. Upadhaya A., Bothra S., Sing R., Gupta S. Tracking System Using GSM, GPS & ARM7. 2020.
4. Valerie M., Outcomes Research and the Quality of Health Care:: The Beacon of an Ethics of Evidence. Evaluation & the Health Professions. 1999: 22(1): 3-32
5. Bracha G., Ungar D., "Mirrors: design principles for meta-level facilities of object-oriented programming languages", ACM SIGPLAN Notices. 2004:39(10):331–344.
6. Walrath K., Ladd S., What is Dart? (1st ed.). O'Reilly Media. 2012:20.
7. Walrath, K., Ladd S., Dart: Up and Running (1st ed.). O'Reilly Media. 2012.
8. Buckett C. Dart in Action (1st ed.). Manning Publications. 2012:475.
9. Lui G., Gallagher T., Li B., "Differences in RSSI readings made by different Wi-Fi chipsets: A limitation of WLAN localization". 2011 International Conference on Localization and GNSS (ICL-GNSS). 2011:53–57.
10. Parameswaran A. T., Husain M. I., Upadhyaya S., "Is RSSI a Reliable Parameter in Sensor Localization Algorithms – An Experimental Study" (PDF). 28th International Symposium On Reliable Distributed Systems, New York. September 2009.

11. Alhasanat A.,Sharif B., Tsemendis C., "Efficient RSS-based collaborative localisation in wireless sensor networks".International Journal of Sensor Networks, 2016: 22(1):27-36.
12. Bellini G., Cipriano M., Comai S., De Angeli N., Gargano J.P., Gianella. M., Goi G., Ingrao G., Masciadri A., Rossi G., Understanding Social Behaviour in a Health-Care Facility from Localization Data: A Case Study. Sensors. 2021:21:2147.
13. Roosan, D., Karim, M., Chok, J. & Roosan, M. Operationalizing healthcare big data in the electronic health records using a heatmap visualization technique. 2020.
14. Rafferty, J.; Synnott, J.; Nugent, C.; Cleland, I.; Ennis, A.; Catherwood, P.; Orr, C.; Selby, A.; McDonald, G.; Morrison, G. Safe Beacon: A Bluetooth Based Solution to Monitor Egress of Dementia Sufferers within a Residential Setting. Proceedings. 2018:2:1218.
15. Kim, E., Baskys, A., Law, A.V. et al. Scoping review: the empowerment of Alzheimer's Disease caregivers with mHealth applications. npj Digit. Med. 2021:4.

A STUDY OF ALIGNED ELECTROSPUN NANOFIBER USING MODIFIED RING-PARALELS COLLECTOR METHOD

Karnjana Oncheurn and Yingtot Infahsaeng*

Division of Physics, Faculty of Science and Technology, Thammasat University, Pathum Thani 12120 Thailand

***E-mail:** yingyot.infahsaeng@gmail.com

Abstract:

Currently, the nanofiber has been widely interested in numerous applications. To functionalize the nanofiber application, the optimization of diameter size, orderly alignment, and characteristics of nanofiber is required. The simple technique for nanofiber fabrication is electrospinning method. Moreover, an interesting feature is the orderly alignment of nanofibers developed by a modified electrospinning technique. In this work, the electrospun effect obtained from the ring-parallels collector revealed the increased electrostatic forces from the ring to parallel collector. As a result, the average diameter of nanofiber about 168.5 nm for the small ring diameter size. However, high percentage alignment of about 24% was achieved for the large ring diameter of 24 cm. Thus, the electrostatic force of the ring and parallel plates collector exhibit a significant effect on the diameter and percentages alignment as well as optical transmittance. This works suggest that they are able to achieve the nanofiber with highly ordering alignment and high transmittance by modified electrospinning. The results of this experiment are useful and can be applied to the applications that require these features in the future.

Introduction:

Nanofiber is fiber generated from polymers with the nanometer diameter range and the high ratio of length per mass. Nanofiber have been extensively studied due to its numerous application[1] such as tissue engineering[2], drug delivery[3], energy storage[4], and optoelectronic device[5]. Such a wide range of nanofiber applications is due to the versatile characteristics, such as flexibility, being light weight, large surface area to volume ratio, and having small diameter. Thus, a nanofiber functionality could be enhanced due to its properties. To control the diameter size of nanofiber, proper method is required. An interesting and widely used method is electrospinning technique, which has been continuously developed since 1990s until the present[6]. Because of their easy steps, a continuous nanofiber can be reproduced in a short time and in large industrial scale.

Electrospinning is a popular nanofiber manufacturing process with three main components, which are syringe, needle, high voltage power supply and conducting collector. In the electrospinning process, the polymer solution is prepared in the syringe. Then, high positive voltage is applied to the needle at syringe electrode and the negative voltage is applied to the collector electrode. During the solution injection, the solution at the tip become a cone, called a Taylor cone[7] due to the presence of electrostatic force. When the electrical force greater than the surface tension of the solution, the jet solution straight to the collector. As the substance descends, it moves in a spiral and the solvent is completely evaporated before the fibers deposit on the collector. The characteristics difference of fiber may be obtained from the electrospinning, that depend on the used conditions[8], for example the distance between tip to collector, the solution concentration[9], syringe flow rate, and applied voltage[10].

Usually, the resulting nanofibers are randomly arranged in a disorderly. Thus, an orderly arrangement pattern is interestingly developed by the parameter's optimization or the setup modification technique. Upon the general electrospun setup, modification have been made by adding components that increase the strength of the fibers, for example change the shape of a collector from planar to be drum or plate collector[11], using a magnetic force[12] or extra electrical forces[13–15]. By adding a parallel collector, the electric field geometry can enhance the orientation of the nanofibers[14]. However, the addition of various components is limited, result to the difference of nanofiber characteristics. From the previous research, it was found that the electric force modification, such as additional ring electrode, is the most simply technique for low cost and more aligned nanofibers fabrication.

Therefore, in this research, the focus is to study the effect of nanofiber obtained from the electrospinning technique by replacing the common collector by part of the parallel plates and adding ring copper electrode between the tip and collector terminals to increase the electrical load as part of the control over the fiber fall area. Then, the diameter and alignment of nanofiber were investigated as well as the optical property.

Material and Method:

Nanofiber fabrication: The polyvinyl alcohol (PVA) at concentration of 7.5% w/v was prepared in deionized water at 80°C for 1 hour and stirred until the solution is completely dissolved. Then, the electrospinning experiment was set using an aluminum foil as reference collector and a parallel plates collector. The ring copper electrode between the tip and collector was added as shown in Figure 1. The PVA solution was prepared in to a 20 ml syringe, the flow rate was set at 0.1 ml/hour and the spinning time of 1 hour. The random reference nanofiber was deposited on the aluminum foil substrate as a collector, while the aligned nanofiber was produced using parallel plates collector and ring copper electrode. The two-copper parallel plate collector with size of 20x5x0.65 cm are located with a gap between plate of 2 cm. The distance between needle tip and the collector was set at 15 cm. The ring copper electrodes with diameter of 12, 18 and 24 cm were used. The distance between the needle tip to ring was set at 5 cm. Finally, the applied voltage between the tip and collector was fixed at 15 kV and between the ring copper and collector was set at 5 kV. The nanofibers on the collector were collected by the cleaned glass substrate.

Characterization: The diameter and alignment of nanofiber were characterized by field emission scanning electron microscopes (FE-SEM, JSM 7800F, JEOL) at 2 kV. Before the investigation, the nanofibers on glass substrate were sputter-coated with Au to enhance the electrical conductivity. The alignment of nanofiber image was analyzed by imageJ software, using Fast Fourier transform analysis to average the nanofiber and calculate the percentage degree of alignment. The transmission of nanofiber was characterized by UV-Vis spectrophotometer (Cary 7000 UMS, Agilent) in the wavelengths range 300 to 800 nm.

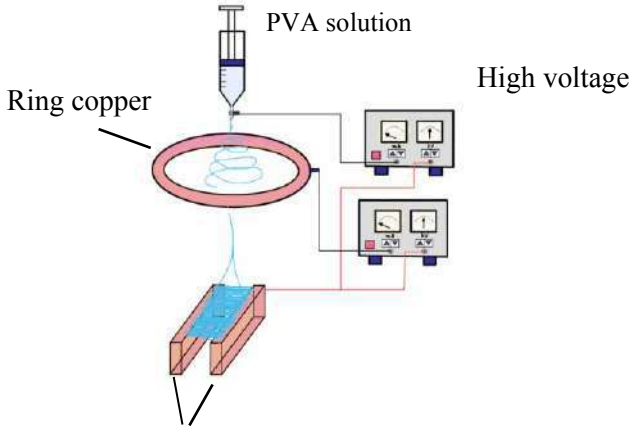

Figure 1. schematic of the component electrospinning process

Results and Discussion:

Morphology properties: From Figure 2 (a-d), the average diameter of nanofiber on aluminum foil collector is 229.8±9.7 nm and the average diameters of nanofiber by ring-parallel collector are 168.6±5.3, 168.1±5.9 and 186.6±7.2 nm at the ring diameters of 12, 18 and 24 cm, respectively. The results show that all average nanofiber diameters of ring-parallels collector are smaller than that of aluminum foil collector. In addition, the uniformly nanofiber can be observed when the ring-parallels collector is applied. This indicate that the electrode and collector modification is significantly affected on the nanofiber diameter. Interestingly, the nanofiber diameters at the ring diameters of 12 and 18 cm are not significantly difference. Thus, the diameter of nanofiber may be limited at the ring electrode diameter lower than 18 cm. The decrease in diameter was due to the electrostatic force from the ring copper between the tip and collector. The constantly gradient in electric force affects the charges inside the solution beam, contributing to the increasing force between the internal charges. This allows the jet solution stream to move out of the tip faster and in a smaller diameter size. At this point, the decreasing of ring diameter cause the extra high electric force between charge on jet solutions, compared to other ring diameter size, and, therefore, reduce the diameter of electrospun nanofiber. In addition, the fiber dispersion density seems to be decrease when the ring diameter increase as seen from SEM image.

The percentage alignment of nanofiber was calculated from the alignment distribution at the angles from 0^o to 180^o as shown in Figure 2(e-h). It was found that the distribution of nanofiber on aluminum foil was randomly distributed, resulting in a high peak intensity graph distribution over all angles as shown in Figure 2(e) and the percentage of alignment of 11.22% was obtained as shown in Figure 3. In Figures 2(f-h), the peak intensity graph has the highest values at the angle of 150°, 61° and 64° for the ring diameters of 12, 18 and 24, respectively. It was found that the most pronounced peak distribution at specific angle was presented for all conditions of ring-parallel collector, while other angles present a low peak distribution, indicating that the nanofiber from ring-parallels exhibit an orderly alignment. The percentages of alignment from ring-parallels collector were 17.31% 15.78% and 23.81% for the ring diameters of 12, 18 and 24 cm, respectively as shown in Figure 3.

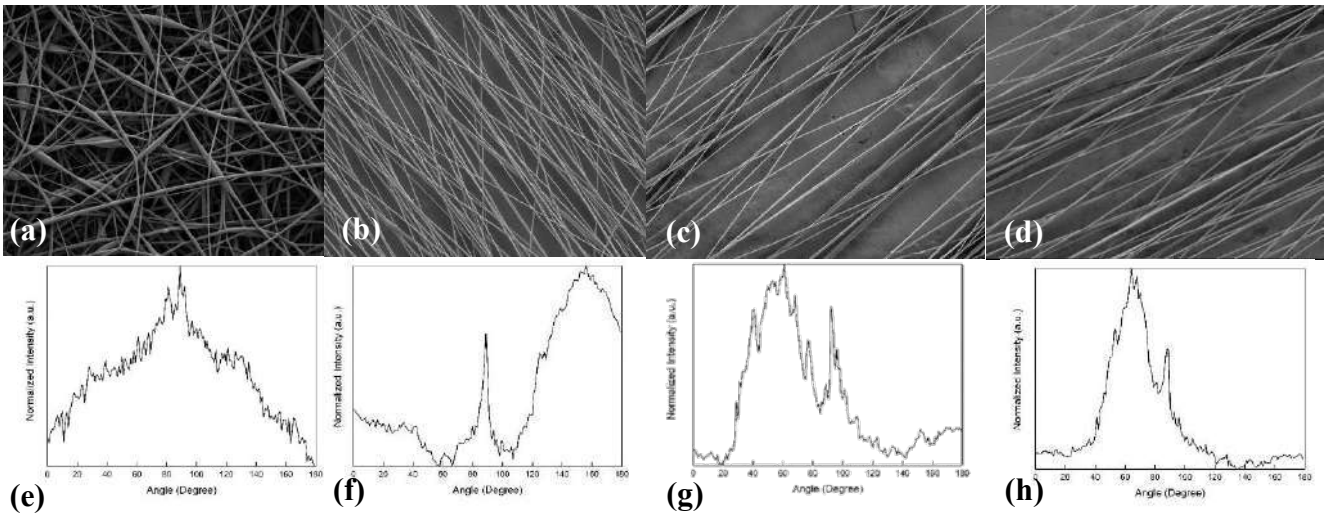

Figure 2. Scanning electron microscope (SEM) image of PVA layers on aluminum foil collector (a) and ring-parallels plate collector (b-d) for ring diameter of 12, 18 and 24 cm, respectively. Distribution of fiber alignment of PVA nanofiber layers on aluminum foil collector (e) and ring-parallels plate collector (f-h) for ring diameter of 12, 18 and 24 cm, respectively.

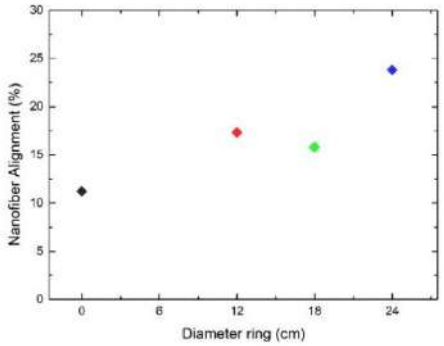

Figure 3. The comparative percentage alignment of nanofiber on aluminum foil and ring parallels collector at 12, 18 and 24 cm, respectively.

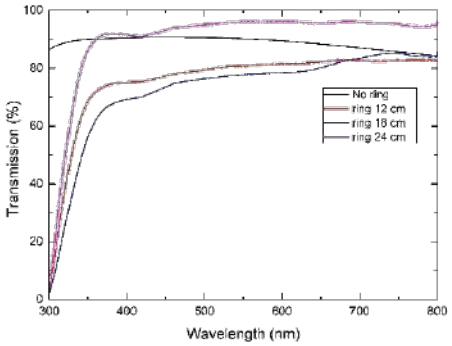

Figure 4. Transmission of electrospun fiber from aluminum foil and ring parallels collector.

Optical transmittance: Figure 4 shows the transmission percentage of electrospun nanofiber from the aluminum foil and ring-parallels collector in the wavelength ranges of 300-800 nm. Without ring-parallels collector, the transmittance was higher than 80% for all wavelength ranges. By using the ring-parallels collector, high transmission percentage of greater than 60% was observed at the wavelength > 400 nm. It should be noted that the curves for the aluminum foil collector are consistently consistent. In contrast, the transmittance of the ring-parallels collector at all ring diameters are sharply dropped at the wavelength < 350 nm. The result indicate that the alignment of nanofiber causes the low transmittance in ultraviolet region. In addition, the percentage of transmission is increased, when the ring diameter increase. However, the transmittances for the

small ring diameter sizes of 12 and 18 cm are slightly on the same level. This result is consistent with the nanofiber alignment as shown in Figure 3.

Conclusion:

In summary, we successfully fabricated the nanofiber by the ring-parallels collector modified electrospinning technique. It found that the average diameter of nanofiber was reduced to 168.1±5.91 nm at the ring diameter of 18 cm. In addition, the percentage alignment is significantly increased as the ring diameter increase. Compared with the common setup, the higher percentage alignment of 23.81% was achieved. In addition, the nanofiber alignment corresponds to the high percentages of transmission of nanofiber. This works suggest that they are able to achieve the nanofiber with highly ordering alignment and high transmittance by modified electrospinning. However, more parameters of the setup are required to optimize the nanofiber characteristics and functionality.

Acknowledgements

This study was supported by Thammasat University Research Fund, Contract No. TUFT 46/2564.

Reference

1. Lou, L.,Osemwegie, O.,Ramkumar, S. S. Industrial & Engineering Chemistry Research 2020;59 (13);5439–5455.
2. Mehrasa, M.,Asadollahi, M. A.,Ghaedi, K.,Salehi, H.,Arpanaei, A. International Journal of Biological Macromolecules 2015;79;687–695.
3. Yu, D.-G.,Zhu, L.-M.,White, K.,Branford-White, C. Health 2009;01 (02);67–75.
4. Tamura, T.,Kawakami, H. Nano Letters 2010;10 (4);1324–1328.
5. Buyuktanir, E. A.,Frey, M. W.,West, J. L. Polymer 2010;51 (21);4823–4830.
6. Reneker, D. H.,Yarin, A. L.,Zussman, E.,Xu, H. 2007; pp 43–346.
7. Geoffrey Ingram Taylor. Proceedings of the Royal Society of London. Series A. Mathematical and Physical Sciences 1964;280 (1382);383–397.
8. Nayak, R.,Padhye, R.,Arnold, L. In *Electrospun Nanofibers*; Elsevier, 2017; pp 11–40.
9. Yarin, A. L.,Koombhongse, S.,Reneker, D. H. Journal of Applied Physics 2001;90 (9);4836–4846.
10. Reneker, D. H.,Yarin, A. L.,Fong, H.,Koombhongse, S. Journal of Applied Physics 2000;87 (9);4531–4547.
11. Dabirian, F.,Sarkeshik, S.,Kianiha, A. Current Nanoscience 2009;5 (3);318–323.
12. Beachley, V.,Wen, X. Materials Science and Engineering: C 2009;29 (3);663–668.
13. Huang, Z.-M.,Zhang, Y.-Z.,Kotaki, M.,Ramakrishna, S. Composites Science and Technology 2003;63 (15);2223–2253.
14. Zhao, J.,Liu, H.,Xu, L. Materials & Design 2016;90;1–6.
15. Li, D.,Wang, Y.,Xia, Y. Nano Letters 2003;3 (8);1167–1171.

Dam Leakage Detection Using Electrical Resistivity Tomography, Ground-Penetrating Radar and Multichannel Analysis of Surface Wave: A Case Study of Nong Pla Sawai Reservoir, Lamphun Province, Northern Thailand

Chanin Maetmueang,[1,*] Suwimon Udphuay,[2] Siriporn Chaisri,[3]
Mingkhwan Kruachanta,[4] Adul Yawichai[5]
[1,2,4,5]Department of Geological Sciences, Faculty of Science, Chiang Mai University
[3]Department of Physics and Materials Science, Faculty of Science, Chiang Mai University
*e-mail: chanin_ma@cmu.ac.th

Abstract:

Geophysical techniques including electrical resistivity tomography, ground-penetrating radar, and multichannel analysis of surface wave have been applied for dam leakage detection of Nong Pla Sawai reservoir, Lamphun province, northern Thailand. It is suspected that the reservoir may have had leakage problems since it cannot retain adequate volume of water even in the rainy season. The geophysical surveys are employed in finding leakage locations within and beneath the dam core. All geophysical data were acquired along the flat surface of the dam ridge. The electrical resistivity data from the electrical resistivity tomography survey and the shear velocity data from the multichannel analysis of surface wave survey show inhomogeneity in the dam core and the basement indicating several suspicious leakage locations of the dam. However, the ground-penetrating radar data present information only at very shallow depth of the dam core and the leakage is not detected at this depth. In this study, the geophysical results provide information about the leakage locations of the dam, which is very useful for the reservoir remediation.

Introduction:

Nong Pla Sawai reservoir is located in Ban Hong district, Lamphun province, northern Thailand (Figure 1). The reservoir is one of 22 reservoirs of the Royal-Initiated Ping River Watershed Comprehensive Development Project, under the responsibility of Huai Hong Khrai Royal Development Study Center. It was built in 1995 with the dam dimension of 298 m in length, 6 m in width, and 14.5 m in height. The dam core of the reservoir is the earth-filled type. This reservoir has been used as water resource for agricultural purposes as well as for conservation of the local watershed. However, Nong Pla Sawai reservoir has not served its purposes since it cannot store water in the rainy season and the water in the reservoir decreases rapidly. It has been suspected that the reservoir may be of leakages. Moreover, it also has been observed that some amount of surface water in the watershed channel disappears before storing in the reservoir (C. Suddan, personal communication, January 9, 2020).

To solve the leakage problem, information about true locations and directions of the leakages is needed before the reservoirs can be repaired. The best way to find locations of the leakage is field observations such as drilling, sampling, in-situ testing, analyzing, and modeling. However, the drilling may destroy the internal structure of the dam ridge and it is time and cost consuming. An alternative method for reservoir leakage detection without destroying the dam internal structure is geophysical surveys. Not only the method is nondestructive, but it is also time and cost effective, and technically acceptable[1].

Geophysical methods are based on physical principles to investigate physical properties of the subsurface such as density, electrical resistivity, velocity, etc. The

geophysical techniques can be used to image subsurface structure or subsurface cross section for several purposes such as in petroleum industry, geotechnical engineering problems, etc. There are many types of geophysical surveys including seismic, magnetic, gravity, electrical resistivity, electromagnetic induction, and ground-penetrating radar surveys.

Electrical resistivity tomography (ERT), ground-penetrating radar (GPR), and multichannel analysis of surface wave (MASW) have been effectively and widely applied for leakage detections[2,3,4]. Therefore, this study proposes combined nondestructive geophysical surveys including ERT, GPR, and MASW to detect leakage locations within and beneath the dam core of Nong Pla Sawai reservoir.

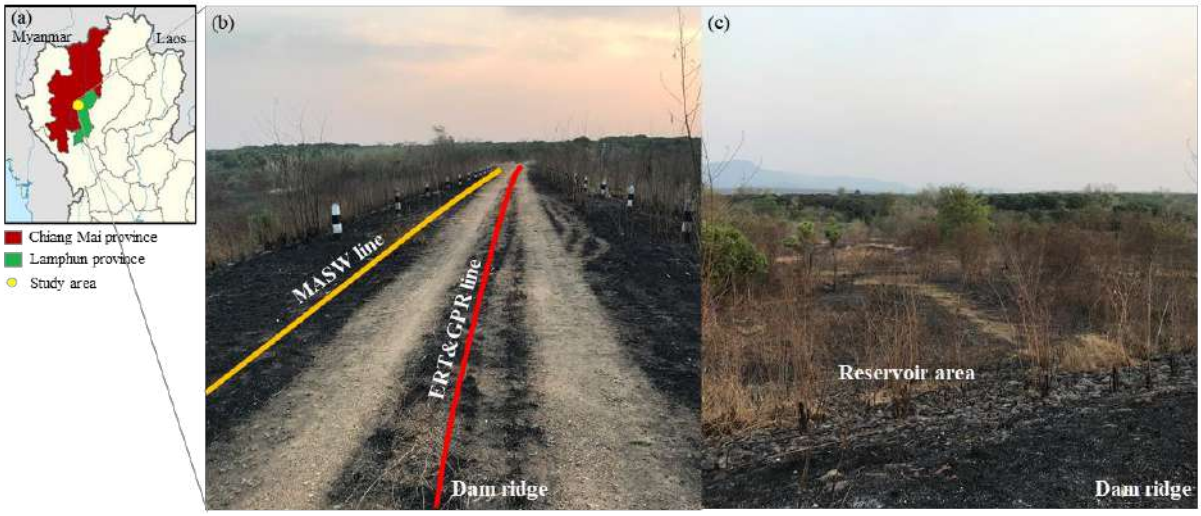

Figure 1.
(a) Location of Nong Pla Sawai reservoir in Lamphun province, northern Thailand, (b) a photo showing the dam ridge, and (c) a photo showing the reservoir area

Methodology:

The geophysical surveys; ERT, GPR, and MASW were acquired on the flat surface of the dam ridge at Nong Pla Sawai reservoir (Figure 1). The ERT and GPR survey lines are at the same location, which is at the center of the dam core (Figure 1b). The MASW survey line is parallel to the ERT and GPR lines and is 2 m distance away from the upstream side of the dam (Figure 1b). All the survey lines are 280 m long that is shorter than the dam core length, which is 298 m. The reservoir was dry during the survey time. Figure 2 shows photos taken during the geophysical data acquisition at the dam ridge.

ERT Method

ERT method is an electrical geophysical method for imaging ground structure from changes of electrical properties in subsurface. The main principle of ERT is transmitting a direct current (DC) into subsurface and measuring a voltage in a set of electrodes. An apparent resistivity (ρ_a) of the subsurface is calculated from Ohm's law (R=V/I, where R is resistance, V is the measured potential, and I is current) that applying a geometric factor (K) (ρ_a=K × R)[5]. The geometric factor is based on the electrode configuration of the survey such as dipole-dipole, Wenner, and Schlumberger configurations[6]. An apparent resistivity will be inverted into a true resistivity to display an estimated subsurface resistivity distribution[7]. The ERT method is an effective method to detect area of subsurface containing high water content because water has very low resistivity. Any water leakage zone often has more humidity than the surrounding area. Therefore, leakage locations of a reservoir may be detected using the resistivity method.

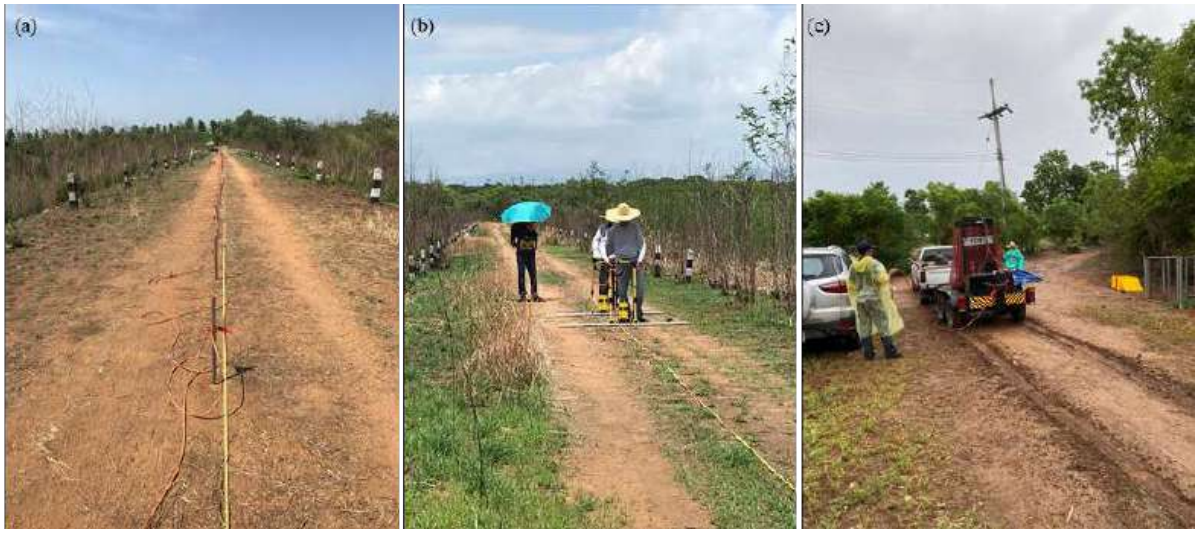

Figure 2.
Photos showing geophysical surveys at Nong Pla Sawai reservoir; (a) ERT, (b) GPR, and (c) MASW

ERT data in this study were collected using ABEM TERRAMETER SAS 4000 with ABEM Electrode Selector ES10-64C, which was powered by a direct current power source. A minimum of 2 m electrode spacing with dipole-dipole configuration was used. The ERT raw data were inverted to inverted resistivity section by AGI EarthImager^{TM} 2D software.

GPR Method

GPR is an electromagnetic (EM) geophysical method, which uses high frequency EM wave to scan and image shallow subsurface structure. The main principle of the GPR is transmitting high frequency band of 10 MHz to 2 GHz EM waves from a transmitting antenna to subsurface then reflected with an object and return to a receiving antenna. The reflection will generate when subsurface has different dielectric property[8]. The dielectric property of subsurface material is a material physical property dependent on water content, type of material, etc. GPR is most effective in the area where subsurface has low conductivity because an attenuation of GPR wave depends on the material conductivity. High conductivity material has high attenuation[9]. The subsurface structure can be imaged by the measuring of two-way travel times of the EM waves traveling in the subsurface. Because any leakage location has dielectric property different from surrounding area, hence GPR may be used for leakage detection.

GPR data, in this study, were acquired using three center frequencies of antenna, 50 MHz, 100 MHz, and 250 MHz at the same survey line with the ERT data. This survey used pulseEKKO Pro GPR system of Sensors&Software Inc. The GPR survey data were processed using Ekko_project software. The processing steps were DC removal, dewow, background subtraction, time median filtering, bandpass filtering, and auto gain control (AGC)[10,11] respectively. The processing flowchart is shown in Figure 3a. Leakage location was interpreted using the processed GPR data.

MASW Method

MASW is a seismic method executed on the ground surface, which utilizes the Rayleigh-type surface wave to characterize the near-surface shear wave velocity (V_s) distribution. V_s is an elastic constant, closely related to Young's, shear modulus and a direct indicator of the ground strength known as the stiffness[12]. MASW works by 3 main steps (Figure 3b). First, measure seismic surface wave, which is generated from seismic source

such as sledgehammer, weight drop, and buffalo gun. Then, a dispersion curve of surface wave (Rayleigh or Love waves) is plotted to analyze its propagation velocities. Finally, shear wave velocity cross section is generated. This step is most responsible for the analyzed propagation velocity pattern of the surface waves. MASW method can be used to locate a potential leakage area with low V_s that is interpreted as loose soil or a weathering zone. This zone may associate with a fracture or a void that is a cause of water leakage.

In this case study, MASW data were acquired using the Geometrics Geode seismograph with 24-bit resolution with 4.5 Hz vertical geophones. The geophone spacing is 2 m, the sampling rate is 0.5 ms, and total acquisition time is 2 s. The source generating the seismic wave is the elastic wave generator (EWG) or weight drop. Note that due to the use of the EWG as the source that had to be towed by a truck at the center of the dam ridge, the MASW survey line was moved to the upstream side of the dam ridge, 2 m away from the ERT and GPR lines. The MASW data from the survey were processed using ParkSEIS software for extracting dispersion curve and inversion.

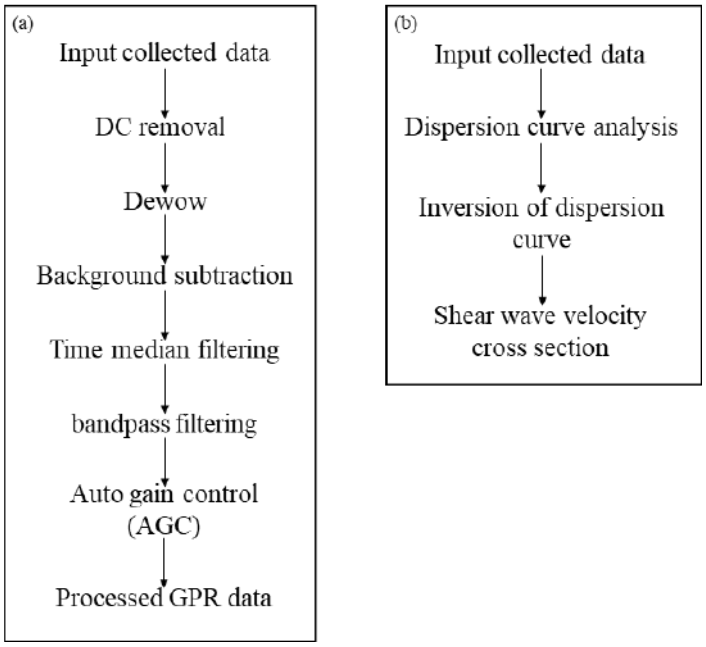

Figure 3.
Data processing flowcharts; (a) GPR and (b) MASW

Results:

ERT method

Inverted ERT section shown in Figure 4a represents the subsurface resistivity distribution of the dam core and the basement. The resistivity values range from less than 15 ohm-m as shown in blue color scale to higher than 80 ohm-m as shown in red color scale, while the medium resistivity values of 15-80 ohm-m are shown in green color scale.

The interpretation of inverted ERT section is shown in Figure 4b in which the estimate dam-core/basement contact and the reservoir floor level are marked according to the available original dam construction plan information. The first part is the dam core layer. The thickness of this layer is about 2-16 m. The geologic material of the dam core is compressed clay that acts as a water barrier because of its low permeability. The electrical resistivity of clay is relatively low, thus, this zone should show uniform low resistivity. In this case, however, the ERT section shows that the dam core is inhomogeneous as there are high resistivity anomalies presented in lower resistivity layer. These high anomalous zones in the

dam core may be due to a present of other materials such as gravel, loose clay or cavity. All high resistivity anomalies are shown as table 1 and red circle in Figure 4b. These zones are interpreted as possible leakage locations within the dam core. Note that the other red spots at the very near surface are not considered to be leakage anomalies because they are found at very shallow depth or below the estimate dam core contact.

The basement of the dam below the dam core, according to the available borehole data, is composed of silty sand, silty gravel with sand, silty clay cobbles and boulders. Therefore, the resistivity section of this zone should be higher than the dam core zone. In the inverted ERT section, however, the resistivity distribution of the basement is inhomogeneous, with zones of lower resistivity than the surrounding area (Figure 4b). This may indicate that the basement is not in a dense state. As a result, this may be another cause of leakage problems of the reservoir.

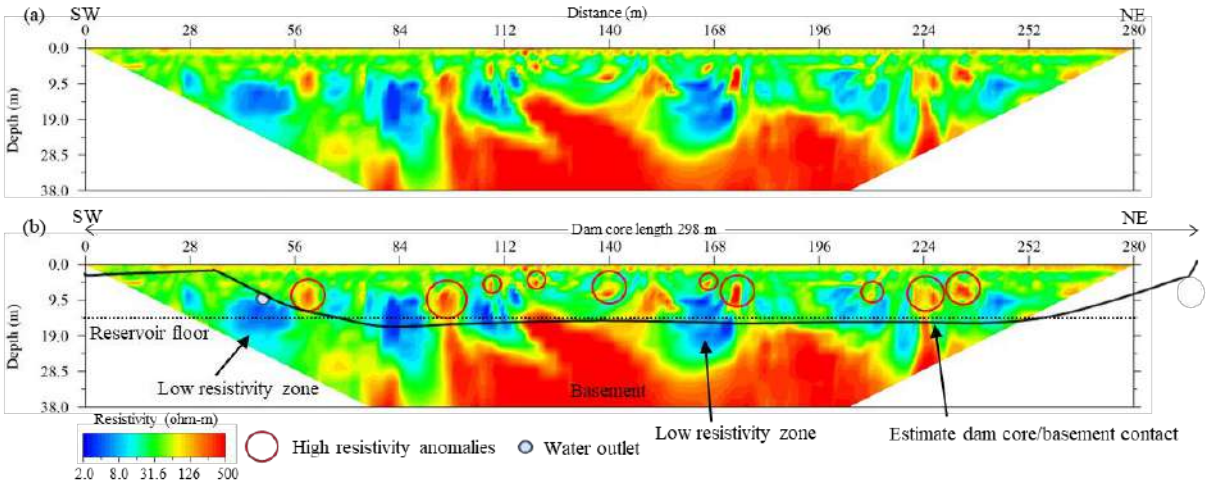

Figure 4.
Inverted ERT sections; (a) without interpretation, and (b) with interpretation. Red circles are suspected leakage anomalies. Black line is dam core bottom (dam core/basement contact). Dot line is reservoir floor level.

Table 1.
Location of high resistivity anomalies

Anomaly	Surface distance (m)	Depth (m)
1	58	7
2	98	7
3	110	4.5
4	120	4
5	140	5
6	166	4.5
7	174	4.5
8	210	6
9	224	5.5
10	234	4.5

GPR method

GPR method is used to investigate subsurface information at very shallow depth that the ERT and MASWA methods cannot detect. The processed GPR data are displayed in sections as shown in Figure 5. It can be noticed that depth of investigation (DOI) of the GPR

using the low frequency of 50 MHz is approximately 5 m, while that of the 100 and 250 MHz is only about 4 and 1 m, respectively. As a result, The GPR sections show almost flat reflectors that indicate thin near-surface layers. Leakage anomaly does not show in the GPR sections. This may be due to there is not a leakage zone or the leakage zone cannot be detected by the GPR.

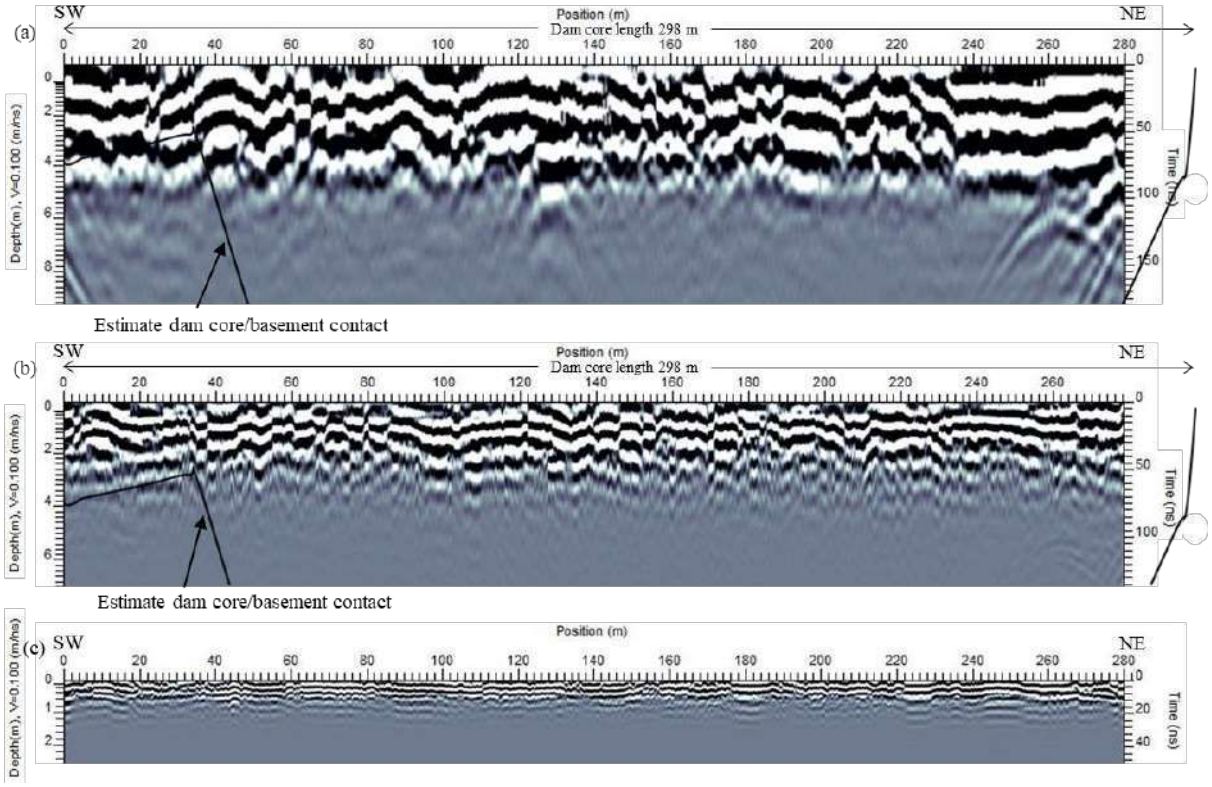

Figure 5.
GPR sections; (a) 50 MHz, (b) 100 MHz and (c) 250 MHz. Black line is dam core bottom (dam core/basement contact).

MASW method

The processed MASW data are presented as a V_s section in Figure 6. Blue color indicates low V_s (less than 270 m/s), green color indicates medium V_s (270-340 m/s), and yellow to red color indicates high V_s (greater than 340 m/s). DOI of the section is 30 m. The section can be divided into 3 zones: top, middle, and bottom. The thickness of the top zone is about 5-7 m and that of the middle zone is about 10-15 m. The V_s of the top, middle and bottom zones is about 300, 230, and greater than 400 m/s respectively. This V_s represents material of stiff clay/soil, soft clay/soil, and soft rock[13] respectively that relate to data from the dam construction document. There are 3 anomalous zones in the MASW section. The first anomaly is shown in the red rectangle located at surface distance of 45-60 m and at depth of about 10 m. It shows discontinuity of V_s that indicates discontinuity of the subsurface material. The second anomalies are shown in the yellow rectangles that locate at depth of 10-15 m and surface distance of 120, 170, and 190 m. These show lower V_s than the surrounding area that may indicate an inhomogeneity of the dam core. The third anomaly is located below the dam-core/basement contact representing low V_s zone of the basement. This may be because the basement is not a permanent rock showing an inhomogeneous feature that found along MASW profile. Moreover, the third anomaly increases in thickness at the beginning and the end of the profile. These may affect to leakage problem.

The MASW anomalies are consistent with the ERT anomalies. Both anomalies are the same locations and have similar physical characteristics. The anomaly in red rectangle is

related to the basement at 56 m surface distance of the inverted ERT section. The basement problems are founded in both methods. Therefore, this can verify an accuracy of the leakage interpretation.

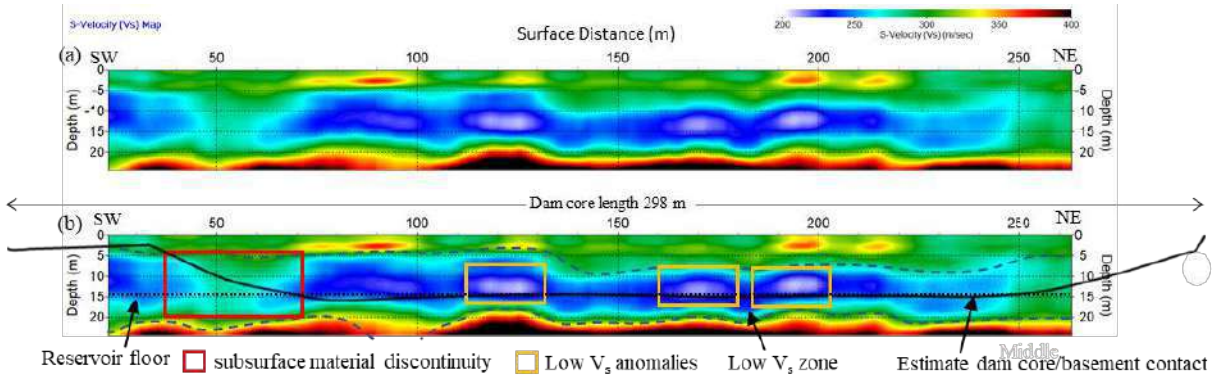

Figure 6.

MASW V_s section; (a) Without interpretation, and (b) with interpretation. The red rectangle is a subsurface material anomaly. The yellow rectangle are Low V_s anomaly. Black line is dam core bottom (dam core/basement contact).

Discussion and Conclusion:

Geophysical surveys, especially ERT and MASW can be used to detect possible leakage locations of the dam core at Nong Pla Sawai reservoir. From this case study, there are 2 reasons that cause the leakage problem. First, the resistivity section has high resistivity anomalies above dam-core/basement contact zone that represent inhomogeneous character in the dam core. Second, the basement may be inhomogeneous or impermanent that shows in both ERT and MASW surveys. In this study, however, the GPR survey does not show the reservoir leakage anomaly at very shallow depth of the dam core.

To improve the data interpretation accuracy, geological data by geological field mapping of the study area are required to verify the geophysical interpretation. Overall, the geophysical results provide information about the leakage locations, which is very useful in the remediation of the reservoir. The result from this study has already been reported to Huai Hong Khrai Royal Development Study Center, which is an organization under the Royal Irrigation Department of Thailand.

Acknowledgements:

The author would like to thank Department of Geological Sciences, Faculty of Science, Chiang Mai University for supplying all research facilities. Research funding is sponsored by Development and Promotion of Science and Technology Talents Project (DPST) and National Astronomical Research Institute of Thailand (NARIT).

References:

1. Poomvises N, Pakdeerod P, Kongsuk A, Sintuboon N, Sawasdipong B, Husain M, Harith Z. The geophysical risk matrix: an innovative risk analysis tools for earth-rock dam failures inspection: the 1st International Conference on Dam Safety Management and Engineering, Singapore. 2020:175-183.
2. Al-Fares W. Application of electrical resistivity tomography technique for characterizing leakage problem in Abu Baara earth dam, Syria: International Journal of Geophysics. 2014:1-9.
3. Li H., Ma H. Application of ground penetrating radar in dam body detection: Procedia engineering. 2011;26:1820-1826.

4. Nolan J., Sloan S., Broadfoot S., McKenna J., Metheny O. Near-surface void identification using MASW and refraction tomography techniques: SEG San Antonio 2011 Annual Meeting, SEG, Expanded Abstracts. 2011:1401-1405.
5. Neyamadpour A. Detection of subsurface cracking depth using electrical resistivity tomography: A case study in Masjed-Soleiman, Iran: Construction and Building Materials. 2018;191:1103-1108.
6. Ebraheem A.M., Al Mulla M.M., Sherif M.M. Mapping groundwater conditions in different geological environments in the northern area of UAE using 2D earth resistivity imaging survey: Environmental Earth Sciences. 2014;72:1599-1614.
7. Loke M. H., Barker R.D. Rapid least-squares inversion of apparent resistivity pseudosections using a quasi-Newton method: Geophysical Prospecting. 1996;44:131-152.
8. Knight R. Ground Penetrating Radar for Environmental Applications: Earth Planet. Sci. 2001;29:229-255.
9. Davis J.L., Annan A.P. Ground Penetrating Radar for high-resolution mapping of soil and rock stratigraphy: Geophysical Prospecting. 1989;37:531-551.
10. Annan A.P. Practical Processing of GPR Data: Proceedings of the Second Government Workshop on Ground Penetrating Radar. 1999.
11. Jol H. M., Bristow C. S. GPR in sediments: advice on data collection, basic processing and interpretation, a good practice guide: The Geological Society of London. 2003;211:9-27.
12. Park C. B., Miller R. D., Xia J. Multichannel analysis of surface waves: Geophysics. 1999;64:800-808.
13. Kandpal G.C., John B., Joshi K.C. Geotechnical Studies in Relation to Seismic Microzonation of Union Territory of Chandigarh: Geotechnical Studies in Relation to Seismic Microzonation of Union Territory of Chandigarh. 2009;13:75-83.

GREEN SYNTHESIS AND CHARACTERIZATION OF CARBON DOTS FROM MANGOSTEEN

Tanachporn Lukprang,[1] Monthon Lertworapreecha,[2] Pakorn Preechaburana,[3]
Supaluck Amloy[1*]
[1]Optical Sensing Laboratory, Department of Physics, Faculty of Science, Thaksin University, Phatthalung 93210, Thailand
[2]Microbial Technology for Agriculture, Food and Environment Research Center, Department of microbiology, Faculty of Science, Thaksin University, Phatthalung 93210, Thailand
[3]Applied Optics Laboratory, Department of Physics, Faculty of Science and Technology, Thammasat University, Pathumthani, 12120, Thailand

*e-mail: supaluckam@gmail.com

Abstract:

Carbon dots (CDs) have received significant attention because they can be synthesized from both natural raw materials containing carbon (C) as the main constituent and green synthesis method. In this work, CDs were synthesized from a part of mangosteen such as peels, pulps and leaves with hydrothermal method. The CDs exhibit a significant size variation in the range of 8.03 ± 1.88 nm, 11.25 ± 1.72 nm and 416.69 ± 53.05 nm as estimated from TEM images of mangosteen peels, pulps and leaves, respectively. This behavior leads to the broadened absorption spectra, which demonstrates two peaks located at 230-285 nm and 320-356 nm. The absorption results indicate that the CDs were affected by transitions of organic substance, including aromatics and carbonyl compounds. Moreover, the existences of functional groups such as C-O, C-N, C=C, C=O, C-H, N-H and O-H, on the surface of CDs are indicated from FTIR spectra. Furthermore, the CDs solutions would appear brown color under daylight and exhibited bright green fluorescence under UV irritation. This result is interesting as our CDs can be utilized as dye cells for bioluminescence imaging application in the future.

Introduction:

Carbon dots (CDs) have been attracted great attention in recent years because of unique photoluminescence and physicochemical properties, such as multi-color fluorescence, good solubility in aqueous or organic solvents, low toxicity and biocompatibility.[1,2,3] CDs are a kind of carbonaceous materials with a size of less than 10 nm[1,2], which have found broad applications, e.g., bioimaging, biosensing, targeted drug delivery and photocatalysis. These fluorescent nanoparticles were initially separated from the synthetic process of single-walled carbon nanotubes by Xu et al. in 2004 and named as CDs by Sun et al. in 2006.[1]

Currently, CDs have been synthesized using several approaches such as including arc-discharge,[4] laser ablation,[5] electrochemical oxidation,[6] microwave,[7] pyrolysis[1,2,8] and hydrothermal methods.[3,9-16] Although significant methods have been developed to produce CDs, these conventional synthetic methods usually require toxic chemical reagents or organic

solvents as precursor. Thus, hydrothermal synthesis has received significant attention because of this technique require only deionized water as precursor.

Nowadays, the various green raw materials have utilized as carbon source for CDs synthesis such as jackfruit,[9] saffron,[10] broccoli,[11] willow bark,[12] cherry blossom flowers,[3] red lentils,[13] apple juice,[14] unripe peach[15] and prunus cerasifera fruits.[16] Thus, CDs made from different raw material contribute various surface groups and special performance.

Even though, among the reported works, mangosteens have been used as a raw material for CDs, but they were synthesized by pyrolysis method.[2,8] In this work, we aimed to synthesize CDs from both natural product and green method by hydrothermal. Therefore, we have synthesized CDs from mangosteen peels, pulps and leaves as carbon source, using a simple approach for preparation without the assistance of any chemical reagent by hydrothermal method. Our CDs exhibit green fluorescence under UV light exposure, which is interesting to be utilized as dye cells for bioluminescence imaging application in the future.

Methodology:

CDs were prepared from a part of mangosteen such as peel pulp and leave using hydrothermal method (see Figure 1). The mangosteen peels (50 g) were cut into small pieces, dissolved in deionized water (350 mL) and ground using a blender until obtained homogeneous solution. The suspension was passed through a filter paper and then the solution (40 ml) was transferred into a Teflon-lined stainless steel autoclave and heated at 200 °C for 3 h in a furnace. The upper yellowish-brown solution was further purified through two membrane filter sizes, 0.45 μm and 0.22 μm, respectively. The processes were repeated by above steps but replaced the raw materials form mangosteen pulps and mangosteen leaves. The CDs were stored at below 4 °C for transmission electron microscopy (TEM) and UV-visible (UV-Vis) spectroscopy. Finally, the solutions were freeze-dried to obtain a brown solid powder for further characterization by Fourier transform infrared spectroscopy (FTIR).

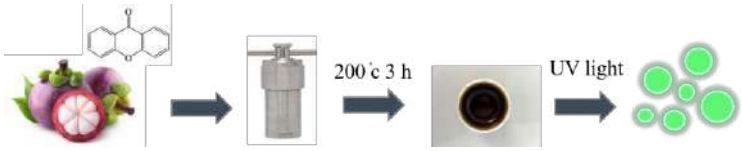

Figure 1.
Schematic representation of synthesis process of CDs from mangosteen

Results and Discussion:

The CDs were determined using TEM, UV-Vis and FTIR techniques. TEM images show spherical shape of CDs with average diameters of 8.03 ± 1.88 nm, 11.25 ± 1.72 nm, and 416.69 ± 53.05 nm for mangosteen peels, pulps and leaves, respectively (see Figure 2).

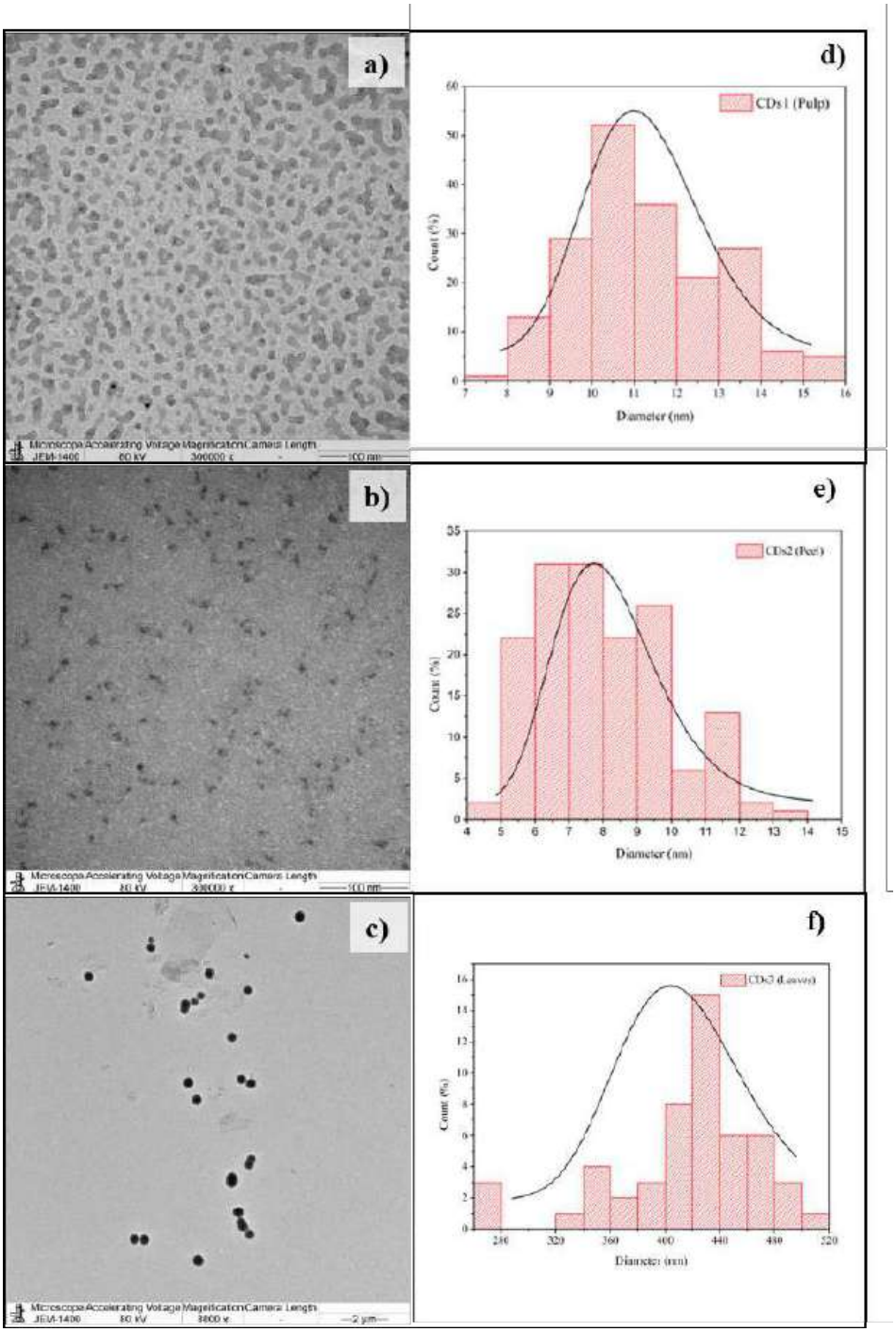

Figure 2.
TEM images of CDs prepared from mangosteen (a) pulps, (b) peels and (c) leaves and their size distribution histogram shown in (d)-(f), respectively.

The existence of functional groups on the CDs surface was characterized using FTIR spectroscopy (see Figure 3). The peaks in the region of 1000-1300 cm^{-1} and 1200-1410 cm^{-1} correspond to stretching vibrations of C-O (alcohol, phenol and ether) and C-N, respectively. The amide group is caused from the nitrogen chains formation during the transformation process from mangosteen structure to CDs. Additionally, the strong peak at 1450-1600 cm^{-1} is attributed to C=C stretching of organic compounds of the carbon atoms in benzene of the aromatic hydrocarbon structure (Phenyl group). The peaks at 1650-1850 cm^{-1} are generated

from the stretching vibrations of C=O, whereas the C-H stretching occurs at around 2850-2962 cm^{-1}. The broad band in the range of 3100-3500 cm^{-1} is identified of O-H stretching (hydroxyl and carboxylate group) and N–H stretching (amine group).[1,2,15] The FTIR spectra of CDs demonstrate the surface organic functional group such as hydrocarbon, oxygen and nitrogen compositions. Thus, CDs can be justified as a good compatibility with aqueous or organic solvents.

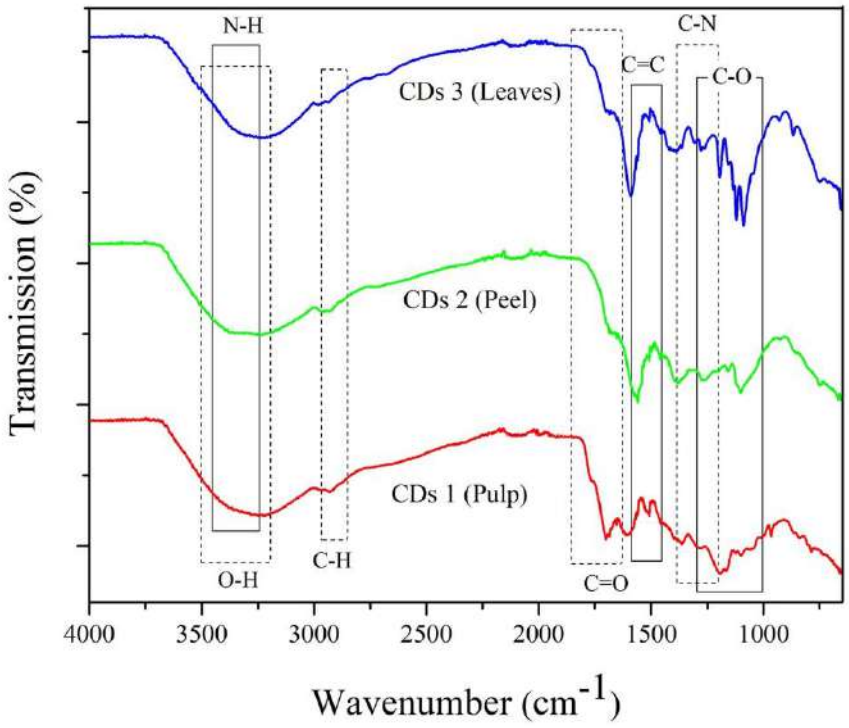

Figure 3.
FTIR spectra of CDs1 (pulp), CDs2 (peel) and CDs3 (leaves)

The optical properties of CDs were characterized using UV-Vis. As shown in the Figure 4, CDs aqueous solutions appear brown color under daylight and emitted bright green fluorescence under UV irritation (wavelength 253.7 nm). In the UV-vis spectra (see Figure 5), absorbance peaks of CDs show significant wavelength in ultraviolet region, which are 285 nm, 275 nm and 270 nm for mangosteen pulps, peels and leaves, respectively. The absorption band at 230-285 nm could be ascribed to the π-π^* transition of aromatic SP^2 domains and the peak at 320-356 nm is associated with n-π^* transition of the unsaturated groups with nitrogen atoms. As a result, the excited state energies are trapped by surface states leading to a strong emission.[8,17]

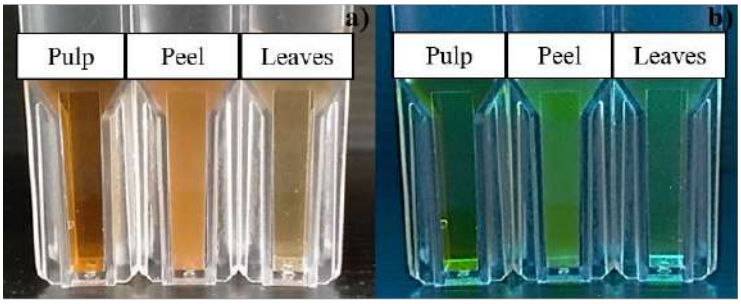

Figure 4.
Photographs of CDs were synthesized from pulps, peels and leaves of mangosteens dispersed in water, (a) under daylight and (b) 253.7 nm irradiation.

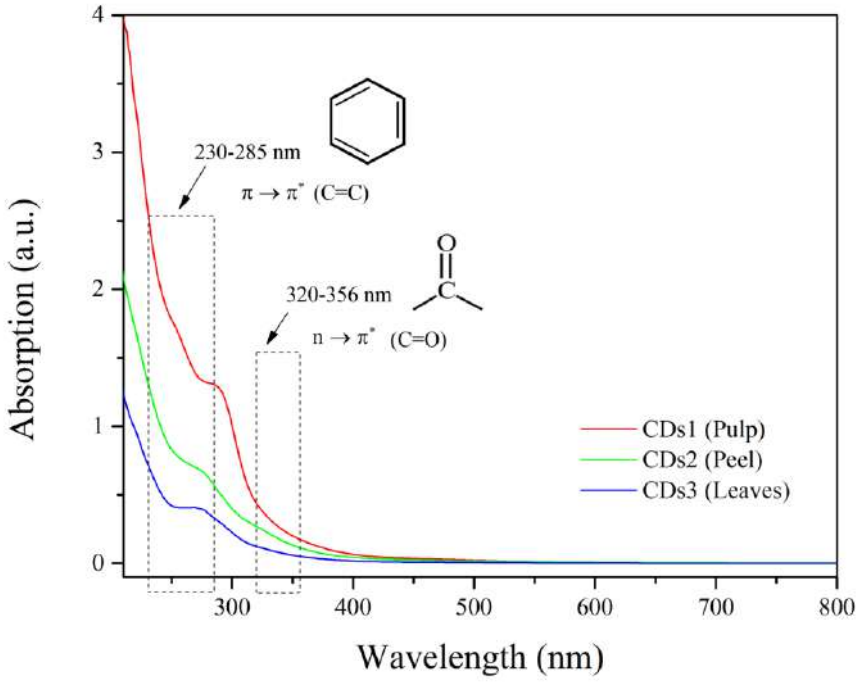

Figure 5.
Absorption spectra of CDs1 (pulps), CDs2 (peels) and CDs3 (leaves)

Conclusion:

In summary, the green synthesized CDs were successfully using hydrothermal method and mangosteen as natural raw materials. Due to the interesting CDs properties such as nanoparticle sizes, low toxicity, compatibility with aqueous or organic solutions and fluorescence under UV irradiation, thus they exhibit potential for bioimaging application.

Acknowledgements:

This work has been supported by Department of Physics, Faculty of Science, Thaksin University. The authors also gratefully acknowledge to Department of Chemistry for the instrumental support (UV-Vis, FTIR) and other necessary facilities.

References:

1. Jiao, X.Y., Li, L.s., Qin, S., Zhan, Y., Huang, K. and Xu, L. Colloids and Surfaces A. 2019;577:306-314.
2. Aji, M.P., Susanto, Wiguna, P.A. and Sulhadi. J Theor Appl Phys. 2017;11:119-126.
3. Huang, K., He, Q., Sun, R., Fang, L., Song, H., Li, L., Li, Z., Tian, Y., Cui, H. and Zhang, J. Chemical Physics Letters. 2019;731:136586.
4. Dey, S., Govindaraj, A., Biswas, K. and Rao, C.N.R. Chemical Physics Letters. 2014;595-596:203-208.
5. Hu, S.L. Niu, K.Y., Sun, J., Yang, J., Zhao, N.Q. and Du, X.W. Journal of Materials Chemistry. 2012;19:484-488.
6. Li, H., He, X., Kang, Z., Huang, H., Liu, Y., Liu, J., Lian, S., Tsang, C.H.A., Yang, X. and Lee, S.T. Angewandte Chemie International. 2012;49:4430-4434.
7. Hu, Q., Paau, M.C., Zhang, Y., Gong, X., Zhang, L., Lu, D., Liu, Y., Liu, Q., Yao, J. and Choi, M. F.M. The Royal Society of Chemistry. 2014;4:18065-18073.
8. Yang, R., Guo, X., Jia, L., Zhang, Y., Zhao, Z. and Lonshakov, F. Applied Surface Science. 2017; http://dx.doi.org/10.1016/j.apsusc.2017.05.252.
9. Thongsai, N., Jaiyong, P., Kladsomboon, S., In I., and Paoprasert, P. Applied Surface Science. 2019;487:1233-1244.
10. Ensafi, A.A., Sefat, S.H., Kazemifard, N., Rezaei, B. and Moradi, F. Sensors and Actuators B. 2017;http://dx.doi.org/10.1016/j.snb.2017.06.163.
11. Arumugam, N. and Kim, J. Materials Letters. 2018;https://doi.org/10.1016/j.matlet. 2018.02.043.
12. Qin, X., Lu, W., Asiri, A.M., Al-Youbi, A.O. and Sun, X. The Royal Society of Chemistry. 2013;3:1027-1035.
13. Khan, Z.M.S.H., Rahman, R.S., Shumaila, Islam, S. and Zulfequar, M. Optical Materials. 2019;91:386-395.
14. Mehta, V.N., Jha, S., Basu, H., Singhal, R.K. and Kailasa, S.K. Sensors and Actuators B: Chemical. 2015;http://dx.doi.org/10.1016/j.snb. 2015.02.104.
15. Atchudan, R., Immanuel Edison, T.N.J. and Lee, Y.R. Journal of Colloid and Interface Science. 2016;482:8-18.
16. Ma, H., Sun, C., Xu, G., Wu, G., Zhang, X., Hana, X., Qi, X., Lv, X., Sun, H. and Zhang, J. Spectrochimica Acta Part A: Molecular and Biomolecular Spectroscopy. 2019;213:281-287.
17. Bandia, R., Dadigala, R., Gangapuram, B.R. and Guttena, V. Journal of Photochemistry & Photobiology, B: Biology. 2018;178:330-338.

Monte Carlo simulation of X-ray Generation in Plasma Focus Machine

Paagjira_Gajaseni[1,*], Phongphaeth Pengvanich[1] Arlee Tamman[2]
[1]Department of Nuclear Engineering, Faculty of Engineering, Chulalongkorn University
[2]Thailand Institute of Nuclear Technology
*e-mail: paagjira.gajaseni@gmail.com

Abstract:
An x-ray emission from a 1.5 kJ Mather type plasma focus was simulated using the Geant4 simulation toolkit which was based on the Monte Carlo method. The simulation traced the interaction between the electron beam formed during the focus and the anode in order to analyze the profile and characteristics of the x-ray that was generated from the interaction. Various anode materials and shapes were tested. The simulation showed that the highest x-ray dose was found between 60-70 degree angles when using a solid cylindrical tungsten anode.

Introduction:
X-ray is a type of electromagnetic radiation that was first discovered in 1896[1] and has been used in various non-destructive diagnostic applications such as medical imaging[2] and industrial radiography. These applications are essential to modern society as they help detect anomaly that may be too small to be seen visually such as small material defects[3], or locate deep inside an object such as a tumor. Characteristics such as profile and energy of an x-ray determine the type and design of application it is suitable for. Different design of x-ray generators in turn generate x-ray with different characteristics. In this article, the x-ray characteristics from a 1.5 kJ Mather type plasma source, namely TPF-II, designed and constructed by Thailand Institute of Nuclear Technology (TINT) has been analyzed

Plasma focus device (PFD) was discovered in the early 1960s[4].It remains one of the devices for studying nuclear phenomena as it can generate several of products such as high density plasma, electron beam, ion beam and x-ray in a wide energy range.[5] TPF-II
Although the fundamental of x-ray generation in a plasma focus device is similar to that of an x-ray tube, the device is more complicated in term of charge particle generation and structure. The change in the structure of the plasma focus (such as the anode) will cause change in the x-ray.

The effect of structural change has been conducted numerically for the Mather type plasma focus "TPF-II" as shown in **Figure 1.** The study utilizes the Geant4 computer simulation toolkit to trace the passage of electron particles and x-ray during the focus. Geant4 algorithm is based on the Monte Carlo method[6] to simulate the motion of particles. The program relies on the calculation of non-deterministic parameters such as directions and distances of particle motion through matter or a particle detectors. Geant4 has variety of data library with different physics models such as the bremsstrahlung processes available, making it suitable for x-ray generation study[7].

Figure 1.
Mather type plasma focus TPF-II

Methodology:

The simulations were performed when the electron beam was formed after the compression of the plasma approached and collided with the anode and emitted x-ray. A previous study on x-ray emission of plasma focus[8] found that the x-ray was produced after electrons collided with the anode, and were distributed at 70-80 degree angle to the electrode axial.

To setup the simulation, the position of the anode was placed at the center of the system. An electrons beam was created with a number of sample particles at 100000 and energy of 200 keV, and shot into anode at 0 degree angle as shown in **Figure 2.** Simulated detectors with a 1 mm beryllium window (high x-ray transmission, preventing electrons from reaching the detectors) were placed at the distance of 22 cm from the top of anode at various angles for the total of 15 positions from -70 to +70 degrees as shown in **Figure 3.**

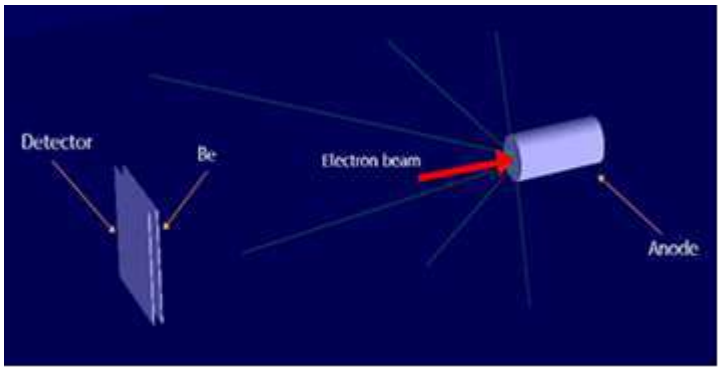

Figure 2.
The virtual experiment setup

Additional input parameters for Geant4 included the anode geometry which had the same dimension as the actual anode used in the TPF-II plasma focus and the gas used in the system. The radius and length of the anode were 1.25 cm and 6.5 cm respectively. Argon was used as a working gas of the system. In the simulation, the effect of the wall chamber was neglected.

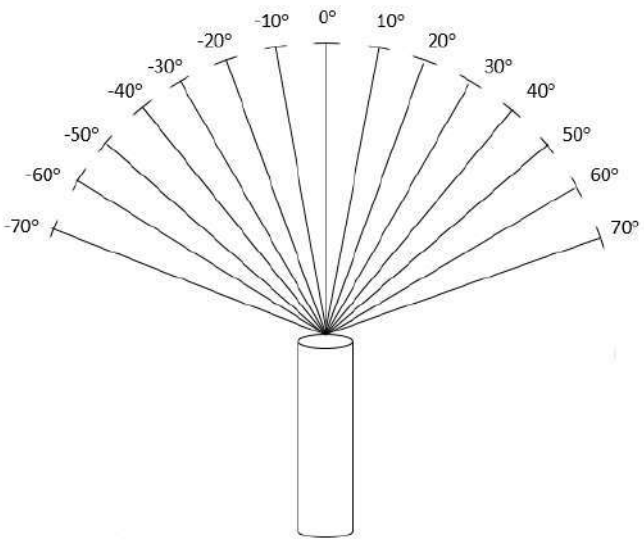

Figure 3.
15 different positions of detector

To study the factor of anode that effect to X-ray dosage. The experiment will be using the 3 type of anode (**Figure 4.**): 1) Solid copper cylindrical anode. (The original design of TPF – II) 2) A hollow copper cylindrical anode. 3) A Solid tungsten cylindrical anode.

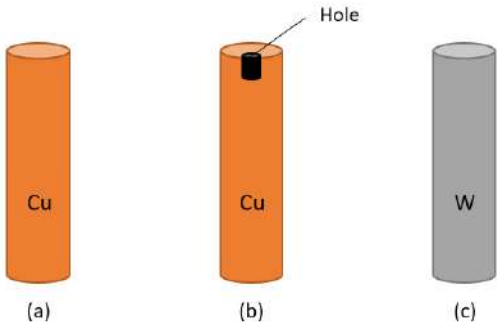

Figure 4.
The 3 type of anode. From left: a) Solid cylindrical copper anode, b) Hollow cylindrical copper anode and c) Solid cylindrical tungsten anode

Results and Discussion:
The dosages output x-ray were recorded by the detectors at different angular positions between -70 and 70 degrees. **Figures 5-7** show the dosages at various positions averaged from 10 runs for the three anodes.

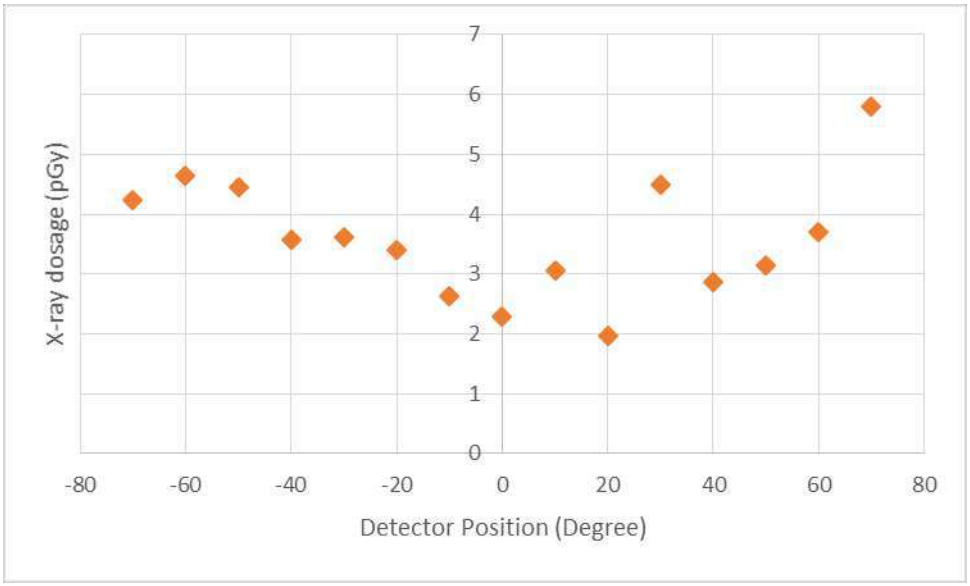

Figure 5.
The output X-ray for different position of detector by using a solid copper anode

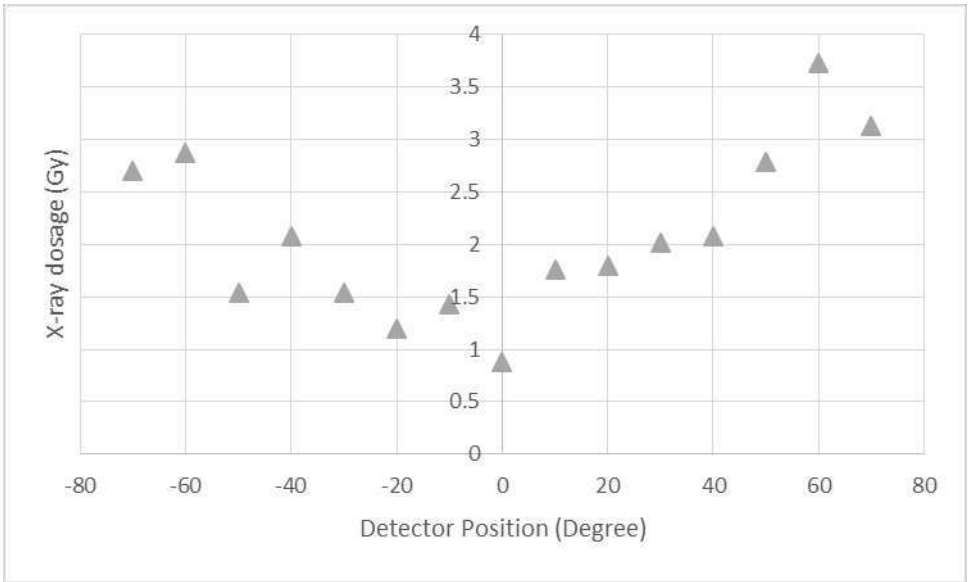

Figure 6.
The output X-ray for different position of detector by using a hollow copper anode

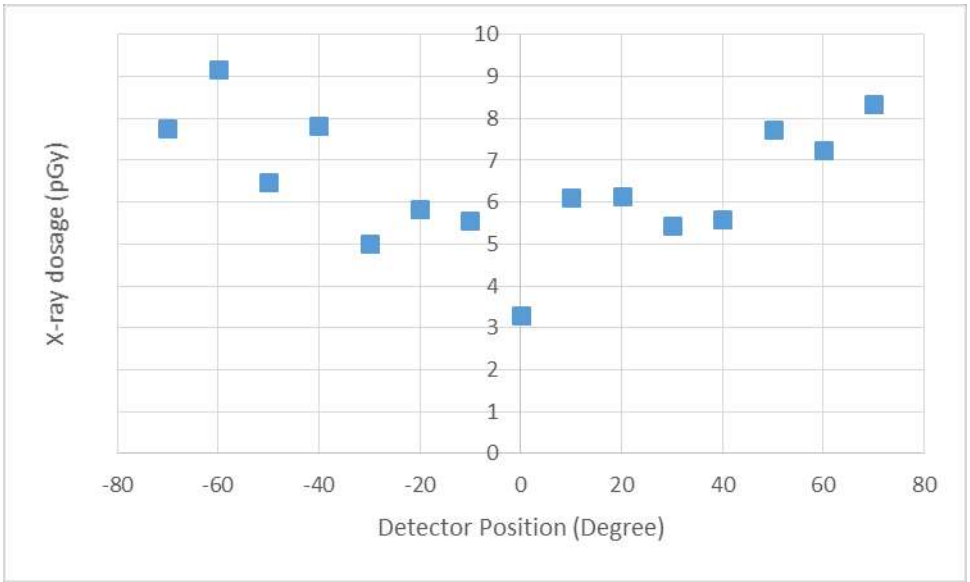

Figure 7.
The output X-ray for different position of detector by using a solid tungsten anode

In all three cases, the x-ray dosage showed increasing trend toward higher positive or negative degree angles, corresponding to the finding of the previous study[8]. The fluctuations in the data were due to the limit number of simulation particles, and has been slightly mitigated by using the average values from multiple runs.

Figure 8.shows comparison of the results among the three anode types. The highest dosage of x-ray output was produced by using the solid tungsten anode. Tungsten, which has higher atomic number than copper, can produce higher intensity of Bremsstrahlung x-ray which is generated in addition to the characteristic x-ray when an electron beam hitting a target material. A large part of x-ray dose is contributed by this Bremsstrahlung x-ray. Depending on the position of the detector, the solid tungsten anode can produce approximately twice x-ray dose of the solid copper anode.

The lowest x-ray output found among the three anode type was the output from the hollow copper anode. This anode design was initially proposed to test the possibility of generating more secondary x-ray by increasing probability of interaction via the hollow shape. Depending on the position of the detector, the x-ray dosage of the hollow anode case was approximately half of the solid anode. The design is subject for further investigation.

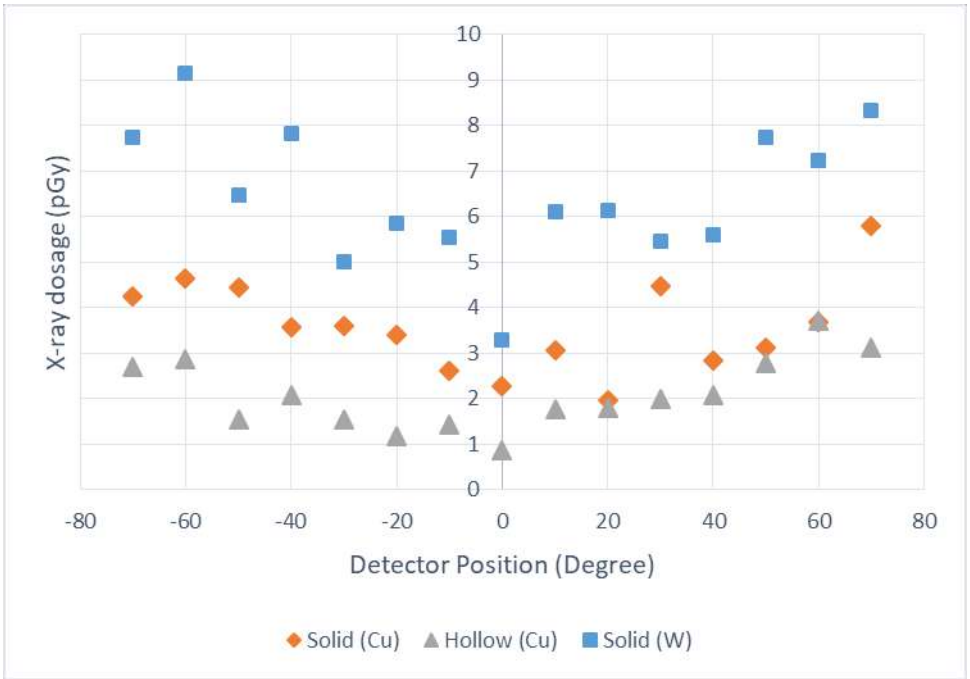

Figure 8.
The comparison of the output of 3 type of anode

Conclusion:

X-ray emission from a 1.5 kJ Mather type plasma focus was investigated using the Geant4 simulation toolkit based on the Monte Carlo method. The simulation traced the interaction between the electron beam formed during the focus and the anode in order to analyze the profile and characteristics of the x-ray that was generated from the interaction. Output x-ray dosages when using solid copper, hollow copper, and solid tungsten anodes were compared at different detector position. The highest x-ray dose was found between 60-70 degree angles when using a solid cylindrical tungsten anode. The increase due to changing from copper to tungsten anode was approximately twice. On the contrary, decrease in x-ray output was observed when changing from solid copper to hollow copper.

Acknowledgement:

The authors would like to Associate Professor Doctor Mudtorlep Nisoa and Thailand Institute of Nuclear Technology for allowing the usage of data of the TFP-II plasma focus.

References:

1. Spiegel, P. K American Journal of Roentgenology.1995. 164 (1): 241–243
2. Huda, W., & Abrahams, R. B. American Journal of Roentgenology, 2015. 204(4), W393–W397.
3. K. Gawdzińska, J. Grabian, W. Przetakiewicz. Metalurgija. 2008. 47 (3). 199-201
4. Decker, G., and R. Wienecke Physica B+C, vol. 82, no. 1, 1976, pp. 155–164
5. Habibi, M., Amrollahi, R., & Farrahi, M. Brazilian Journal of Physics, 2008. 38(2), 264–267.
6. HŘivnáčová, I. Journal of Physics: Conference Series. 2012.396(2), 022024.
7. Nasseri, Mohammad M. Nuclear Engineering and Technology, 2016. vol. 48, no. 3, pp. 795–798
8. Knoblauch, P., et al. Radiation Physics and Chemistry, vol. 145, 2018, pp. 39–426.

SURFACE WAVE GROUP VELOCITY TOMOGRAPHY FROM AMBIENT SEISMIC NOISE CROSS-CORRELATION IN NORTHERN THAILAND

Sorawat Siangpipop[1,*], Siriporn Chaisri[2], Niti Mankhemthong[1]
[1]Department of Geological Sciences, Faculty of Science, Chiang Mai University, Thailand
[2]Department of Physics and Materials Science, Faculty of Science, Chiangmai University, Thailand
*e-mail: sorawat_s@cmu.ac.th

Abstract:
The ambient seismic noise in northern Thailand was used as the diffuse wavefields to reconstruct the empirical Green's function (EGF) by cross-correlation between pair stations C1. In the case of inadequately synchronized station pair, the cross-correlation of cross-correlation function (C2) is applied to enhance the quality of EGF by stacking C1 and C2. From EGF, the surface waves waveform can be seen, and dispersion curves were extracted by frequency-time analysis (FTAN) method. The quality control of dispersion curves measuring is based on signal to noise ratio criteria. The final dispersion curves from each pair stations were employed for estimating the group velocity tomography.

Introduction:

There are two primary seismological networks in Thailand, TM network operate by the Thai Meteorological Department (TMD) and TH network operate by the Department of Mineral Resources (DMR), generally aiming at detecting seismological events. By monitoring ground movement continuously, the continuous raw data were also recorded at each seismology station. These ambient seismic noises (ASNs) contain some information similar to the signal from an earthquake event. The analysis of ambient seismic noises has significant advantages over the analysis of source dependent methods because they are independent of the source's error. The enormously recorded data can be utilized to analyze given more resolution's solutions. However, the daily data collections from seismological networks in Thailand are still under development, then some problems might occur during the data collecting procedure, for example, gapping and asynchronization between stations.

To analyze ASN data, the ambient continuous noise u_A and u_B functions observed at pair stations A and B are cross correlated to estimate the empirical Green's function (EGF) of the diffuse wavefields,[1-4] called C1 express as

$$CCF_{AB} = \int u_A(t)\, u_B(t+\tau)dt \qquad (1)$$

Under the assumption of full-aperture seismic sources, CCF_{AB} represents the seismic signal that either station A or B acted like the virtual source, Figure 1 (Left), which equivalent to seismic waveforms as the data obtained from source event. The surface waves can be easily recognized from C1 and extracted for further analysis.[5] However, sometimes data from the pair stations might be partially missing or shifting in time from other stations (poorly synchronized station) causing inferior quality of EGF. To overcome the synchronization problems, the cross-correlation of cross-correlation function (C2), Figure 1 (Right), using the same reference station could be applied to resolve this problem.[6] The C2 function is comparable with the C1 function, and more information can be obtained for data analysis. Moreover, the CCF from all possible station pairs can also be improved by stacking C1 and C2. The successfully EGFs reconstructed from stacking C1+C2 are analyzed for surface wave velocity tomography maps which related to geological structures.[7-10]

Figure 1.
(Left) C1 is the cross-correlation function between signal of station A and B. (Right) C2 is the cross-correlation of cross-correlation function C1 from pair stations A-S and B-S when S is the reference station.

This study is focusing on northern Thailand region, the most active province in the country. To focus on the Rayleigh waves, this research will utilize the vertical component (Z) signal for analyzing. The one-year continuous seismic noises data from October 2019 to October 2020 are obtained from the 22 seismic stations (Figure 2) that mainly located in northern Thailand and some in central Thailand including short-band, broad-band, and high broad-band stations from network operated by DMR, TMD, and the Incorporated Research Institutions for Seismology (IRIS).

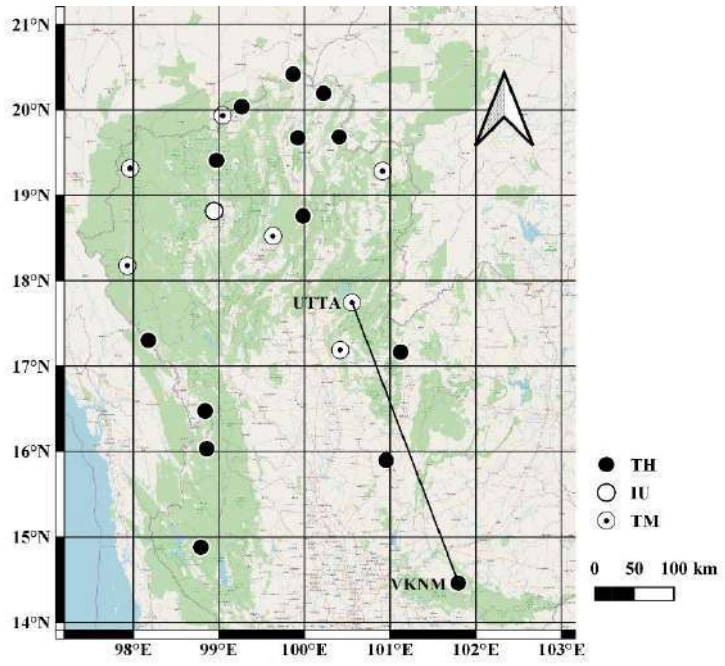

Figure 2.
The location of 22 seismic stations, black circles are TH network from DMR, dotted circles are TM network from TMD, and white circle is IU network from IRIS.

Methodology:

All continuous raw data from seismic stations were filtered with a low-cut filter 0.2s (high-cut filter 5 Hz) to prevent aliasing from resampling sample interval to 0.1s, which is covering our interested period (5-23s). This will reduce the calculation time during CCF calculations.

Figure 3 presents the procedure methodology. First step, the routines pre-processing for data preparation are 1) removing the instrument response, 2) band-pass filtering (3-60s), 3) normalizing the signal by the running-absolute-mean, and 4) whitening the amplitude spectrum in the band-pass period.

There have been demonstrated that the highest correlation rate from one-year correlation can be obtained in the correlation window around the 2000s to 5000s.[11-13] Then, the cross-correlation function C1 were generated for all possible pair stations using correlation window 5000s and then stacked daily. Next, the dispersion curves of surface waves were extracted from daily C1 by frequency-time analysis (FTAN).[11,12,14] This method applying along with FTAN called phase-matched filters helps solving multiple arrival issue.[15,16] The extracted surface wave dispersion curves will be verified, based on the signal to noise ratio (SNR) defined as the ratio of the maximum absolute value of the signal in the considered signal window to the standard deviation of values in the noise window. The waveform's quality can be improved with stacking of C2. In details, the C2 calculation procedure consists of five steps: 1) defining the positive and time-reversed negative lags of C1 from pair station and reference stations, 2) filtering the defined signal with 5 to 25 seconds and whitening within the same considered period, 3) cross-correlation calculation of all possible C1, 4) summing up all CCFs to obtain C2, and 5) stacking C1 with C2s.

All quality-controlled dispersion curves are then inverted. This method is called surface wave tomography. The surface wave's paths are assumed to follow great circle between pairs of stations, respecting slowness for a specific period. The slowness model was approximated along a regular $0.2^o \times 0.2^o$ grid.[17] Then, the inversion procedure turned slowness model into group velocity model. The modern inversion methods provide tools to know how close the image is to the actual structure named the resolution matrix.[20] To estimate spatial resolution, cones were fit to each resolution matrix. The cones whose best fitting is smaller than 5 per cent of the maxima considered as noise and discarded. Noted, the resolution cannot be less than twice the inter-node spacing, which around 44 km in our case (twice of grid spacing).

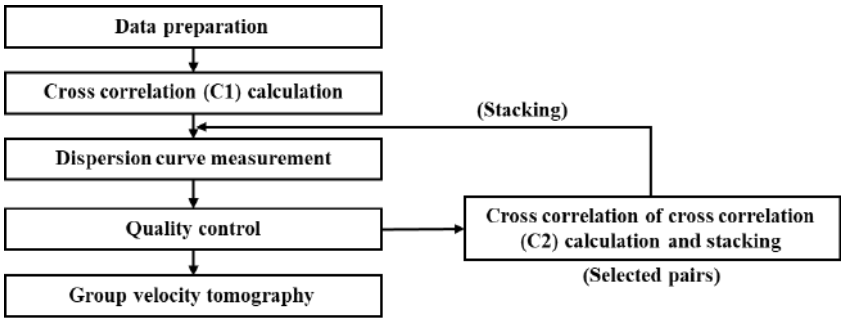

Figure 3.
Schematic of methodology.

Results and Discussion:

Figure 4 displays all normalized CCF from C1 according to interstation distance with two lines represent surface wave signal between propagation speed 2.0-4.0 km/s. Then, daily C1 were summed between causal (positive) and acausal (negative) lag turning into one-side signal by averaging, under the symmetric waveform assumption. The raw FTAN solutions were enhanced by phase-matched filters achieving clean FTAN. From daily stacked EGF, three-months stacking with one-month stepping functions were used for dispersion curves extraction and displayed with quality control in Figure 5 (Right), showing a selected pair stations UTTA-VKNM with 387km interstation distance.

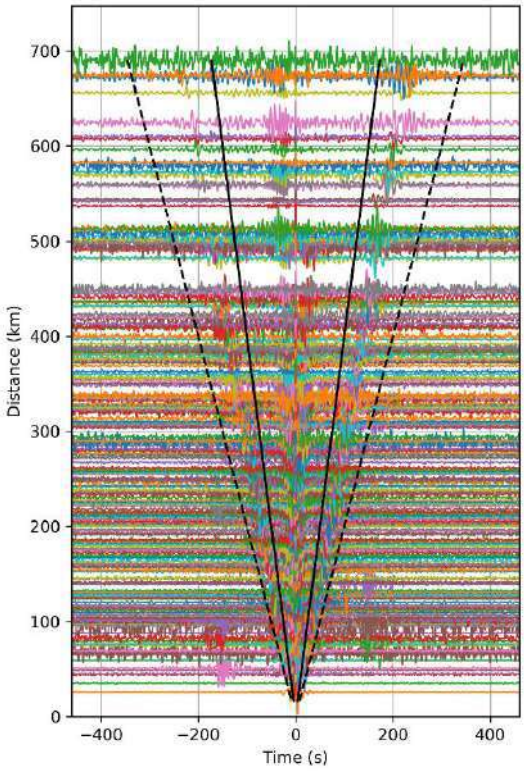

Figure 4.
Normalized CCF from C1 (one year data) according to interstation distance, the total of 249 pairs. Dashed lines indicate speed 2.0km/s and black lines indicate speed 4.0 km/s.

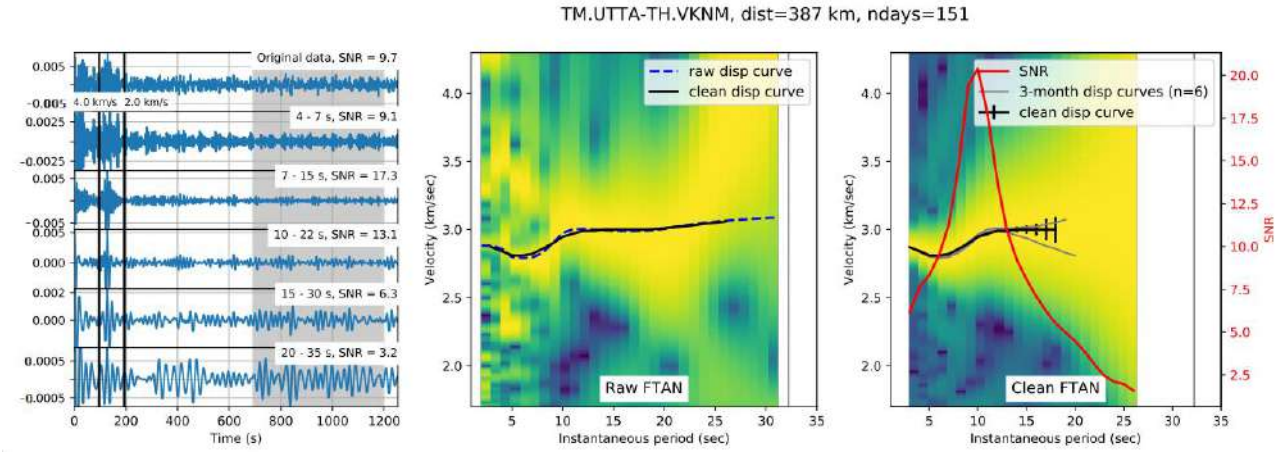

Figure 5.
(Left) Original CCF and band pass filtered cross-correlation with SNRs and velocity spectrum (Center) raw FTAN, and (Right) clean FTAN with dispersion curve and SNR.

In quality control, the signal to noise ratio (SNR) is calculated from the ratio of the maximum absolute value of the signal in between black vertical lines in Figure 5 (Left), to the standard deviation of the value in the noise window (grey areas 500s width and 500s after the signal window). The quality control selection criteria are as following:

1) Interstation distances (D in kilometers) must be at least three times of wavelengths.[11,12,18,19] If consider phase velocity of 4km/s, the cut-off period equals to D/12.
2) If group velocity standard deviation (σ_{vg}) $\leq$ 0.2 km/s, the SNR $\geq$ 5.[20]
3) If σ_{vg} > 0.2 km/s, the SNR $\geq$ 7.[18]

Figure 6 compares the waveform from C1 and C2 and Figure 7 displays the similarity of C1 and stacking C1+C2. We focus the discussion on the improvement of EGF by stacking C1+C2. The results are displayed in Figure 8 to Figure 10. By comparison, a small SNRs improvement (Figure 8) and a longer dispersion curve (Figure 9) can be observed. The higher SNR allows the more stable dispersion curve to be passed in quality control. Figure 10 shows the enlarger and more finely spatial resolution of tomography map indicated by black circles. Then, the inversion procedure turned slowness model into group velocity model shown in Figure 11.

However, there are some factors that probably affected the quality of C2: 1) the poor quality of C1 in the first place, 2) reference stations are in the non-stationary phase zone, 22.5 degree around azimuth and back azimuth of the considered pair, and 3) virtual sources are not well aligned with the considered pairs.[6]

Figure 11 shows the variation of surface wave velocity with periods that related to shear wave velocity structure underneath the study area. This means the shear wave velocity of lower north of Thailand is approximately higher than that of upper north region. How surface wave velocities connect to the geological structures could be examined for further studies.

Nevertheless, these results are from one-year ASN data and still undergoing research. We could apply more data if that become available. The data set would benefit from longer time series and more seismic stations, which would allow more uncertainties to be measured and more measurements to pass the selection criteria. The more stable EGF and more reference stations would yield a more stable C2 function.

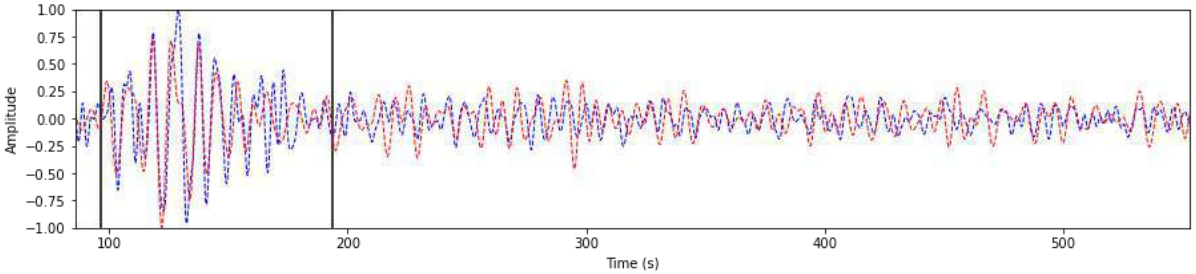

Figure 6.

Normalized CCF between UTTA and VKNM, blue-dash wave is C1 result, and red-dash wave is C2 result. The black vertical lines indicate velocity windows between 2-4 km/s cover the surface wave signal.

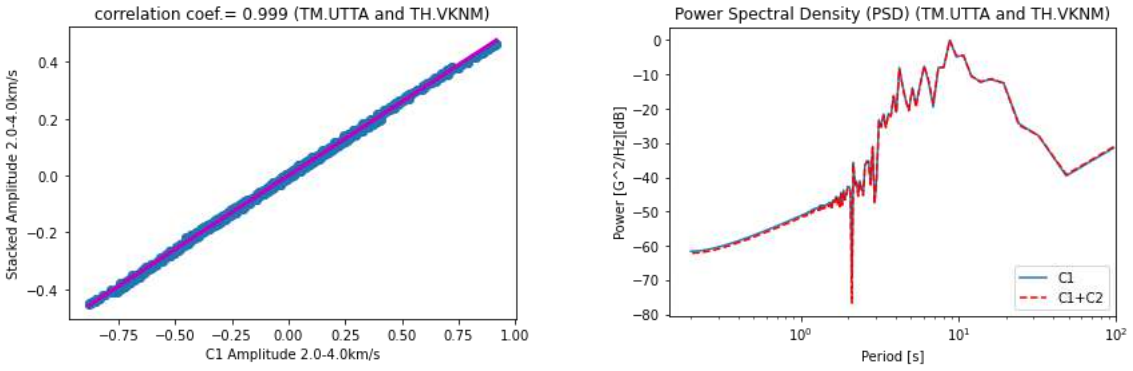

Figure 7.

(Left) Correlation coefficient between stacked C1+C2 amplitude and C1 at defined signal windows, and (Right) their power spectrum density.

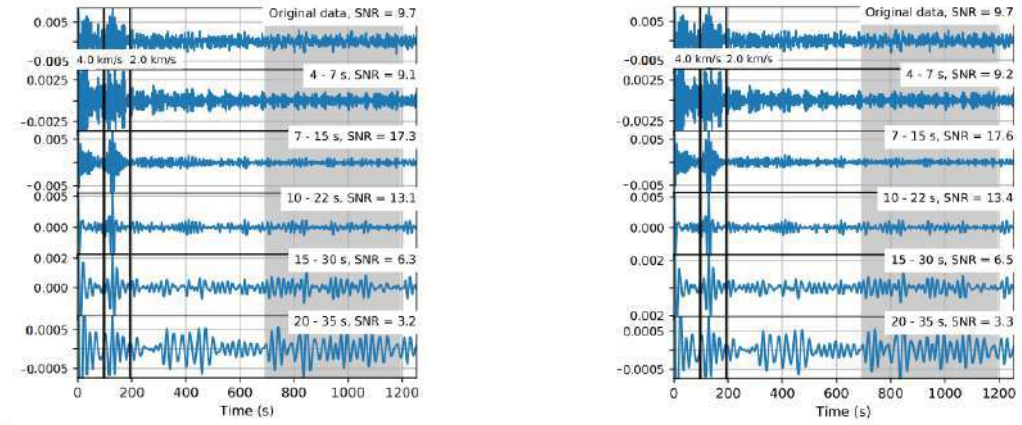

Figure 8.
Comparison SNRs in each period band of (Left) C1 and (Right) stacked C1 with C2 from UTTA and VKNM pair stations.

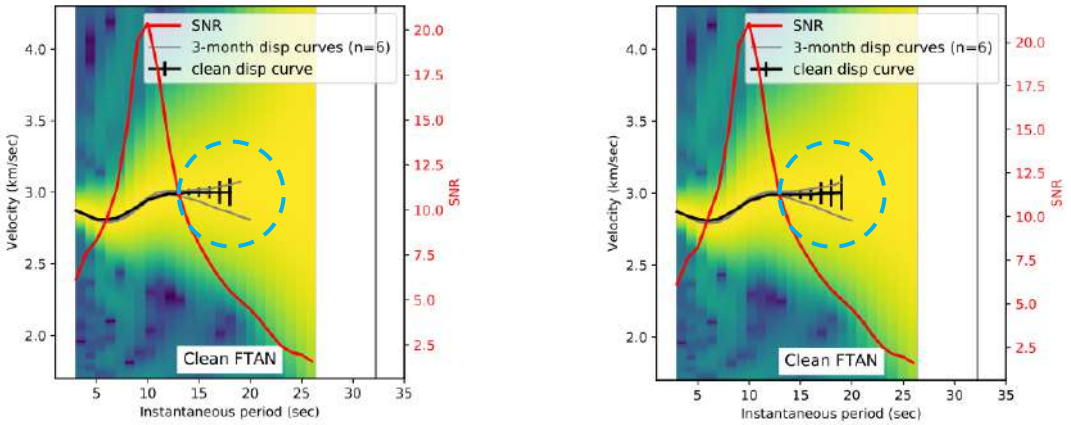

Figure 9.
Comparison dispersion curve extracted from (Left) C1 and (Right) stacked C1 with C2 from UTTA and VKNM pair stations.

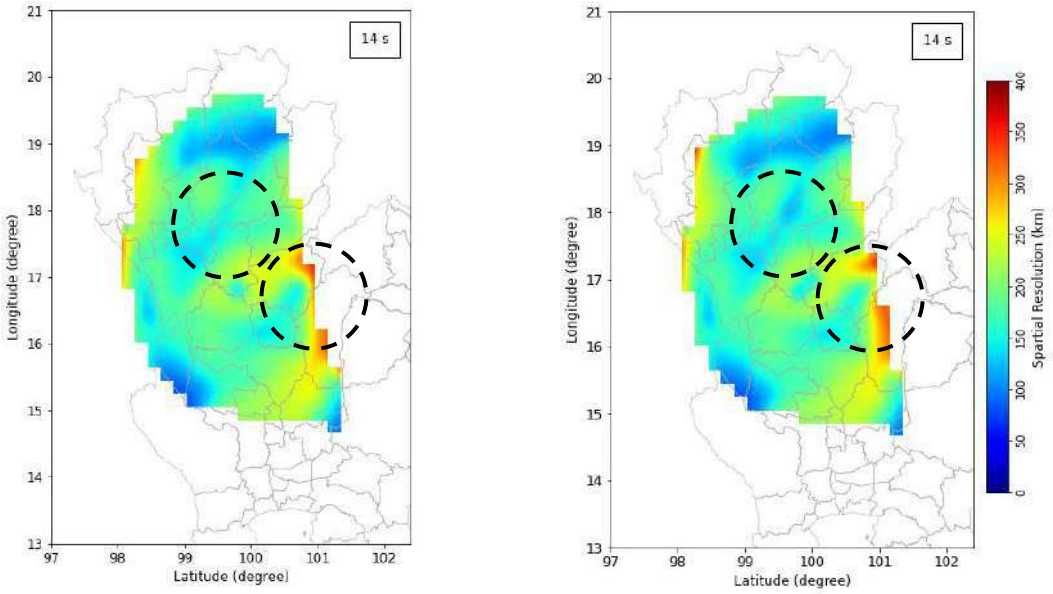

Figure 10.
Spatial resolution comparison, solutions from (Left) C1 and (Right) stacked C1 with C2.

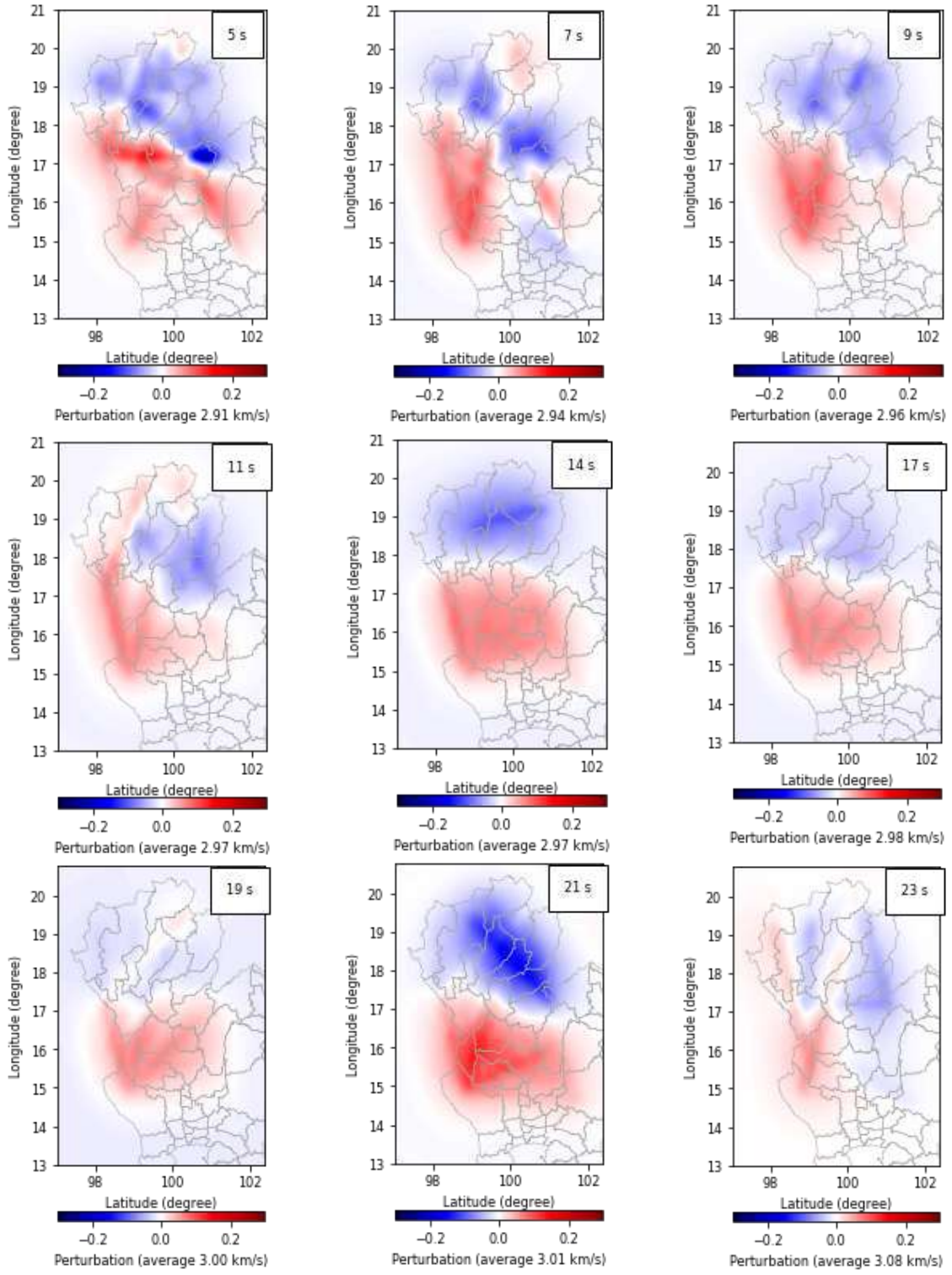

Figure 11.
The final group velocity tomography in northern Thailand region.

Conclusion:

We have determined EGFs from cross-correlation of ambient noise within the period from 3 to 60s in daily segments, with a maximum duration of one year. Then, by a phase-matched filtering FTAN, Rayleigh wave group velocities are measured from EGFs. Uncertainties are estimated based on seasonal variations using three-month time series. A data selection procedure is applied to all dispersion measurements using SNR related criteria. To improve

EGF solutions from poorly synchronized paths, the cross-correlation of cross-correlation C2 were applied within period band 5-25s and then stacked with C1. The SNR of the empirical Green's function EGF were increased, and the longer dispersion curves could be measured. Finally, the improvement in the spatial resolution and the group velocity tomographic images in period range 5-23s were obtained.

Acknowledgements:
I would like to express my special thanks of gratitude to the National Science and Technology Development Agency (NSTDA), Thailand, who supported all financial funding. The ambient seismic noise data were acquired from the Department of Mineral Resources (DMR), the Thai Meteorological Department (TMD), and the Incorporated Research Institutions for Seismology (IRIS). The ObsPy Python framework massively utilizes to manage and process the seismic data.[21] I would also like to extend my gratitude to Goutorbe et al. (2015) for the Python-based programs Seismic noise tomography.[12]

References:

1. Larose E, Derode A, Campillo M, Journal of Applied Physics. 2004;67:8393-8399.
2. Roux P, Sabra K G, Kuperman W A, Roux A, The Journal of the Acoustic Society of America. 2005;117:79-84.
3. Garnier J, Papanicolaou G, SIAM Journal on Imaging Sciences. 2009;2:396-437.
4. Wapenaar K, Draganov D, Sneider R, Campman X, Verdel A, Geophysics. 2010;75:75A195-175A209.
5. Campillo M, Paul A, Science. 2003;299:547-549.
6. Chen Y, Saygin E, Journal of Geophysical Research: Solid Earth. 2019;125.
7. Shapiro N M, Campillo M, Stehly L, Ritzwoller M H, Science. 2005;307:1615-1618.
8. Sabra K G, Gerstoft P, Roux P, Kuperman W A, Fehler M C, Geophysical Research Letters. 2005;32:L14311.
9. Gerstoft P, Sabra K G, Roux P, Kuperman W A, Fehler M C, Geophysics. 2006,71:SI23-SI31.
10. Cho K H, Herrmann R B, Ammon C J, Lee K, Bulletin of the Seismological Society of America. 2007,97:198-207.
11. Bensen G, Ritzwoller M, Barmin M, Levshin L, Lin F, Moschetti M, Shapiro N, Yang Y, Geophysical Journal International. 2007;169:1239-1260.
12. Goutorbe B, de Oliveira Coelho D L, Drouet S, Geophysical Journal International. 2015;203:869-882.
13. Seats K J, Lawrence J F, Prieto G A, Geophysical Journal International. 2012,188:513-523.
14. Levshin A, Ratnikova L, Berger J, Bulletin of the seismological Society of America. 1992;82:2464-2493.
15. Herrin E, Goforth T, Bulletin of the Seismological Society of America. 1977;67:1259-1275.
16. Goforth T, Herrin E, Bulletin of the Seismological Society of America. 1979;69:27-44.
17. Lin F C, Tsai V C, Schmandt B, Geophysical Journal Internationl. 2014;198:656-670.
18. Yang Y, Ritzwoller M H, Levshin L, Shapiri N M, Geophysical Journal International. 2007;198:259-274.
19. Bao X, Song X, Li J, Earth and Planetary Science Letters. 2015;417:132-141.
20. Lu Y, Stehly L, Paul A, Group A W, Geophysical Journal Internationl. 2018;214:1136-1150.
21. Beyreuther M, Barsch R, Krischer L, Megies T, Behr Y, Wassermann J, Seismological Research Letters. 2010;81:530-533.

EFFECT OF TEMPERATURE AND REDUCING AGENT CONCENTRATION ON THE Mn RECOVERY FROM SPENT ALKALINE AND Zn-C BATTERIES

Chaithawat Waikhani[1,2], Kamonpan Manowilaikun[1,2,] Theeranon Tankam[1,2], Rojana Pornprasertsuk[1,2,3,4,*]
[1]Center of Excellence on Petrochemical and Materials Technology, Chulalongkorn University, Bangkok, Thailand
[2]Department of Materials Science, Faculty of Science, Chulalongkorn University, Bangkok, Thailand
[3]Research Unit of Advanced Materials for Energy Storage, Chulalongkorn University, Bangkok, Thailand
[4]Department of Materials Science and Technology, Nagaoka University of Technology, Niigata, Japan
*e-mail: rojana.p@chula.ac.th

Abstract:
This research focused on the Mn recovery from the electrode powder of spent alkaline and zinc carbon batteries by leaching process and MnO_2 synthesis. The mixed electrode powder of spent batteries was leached by sulfuric acid (H_2SO_4) without a reducing agent at room temperature and 80°C, and with the addition of H_2O_2 as a reducing agent at various concentrations at room temperature. Depending on the leaching conditions, the Mn leaching efficiency of 8-87% were obtained. The leaching solutions at various conditions were subsequently used as precursors for MnO_2 synthesis by mixing with $(NH_4)_2S_2O_8$ and heating at 90°C. The mixed phases of ε- and γ-MnO_2 were obtained when the leaching solution at room temperature was used, while γ- and α-MnO_2 were obtained when the leaching solution at 80°C was utilized. The single phase of γ-MnO_2 with the higher Mn recovery efficiency of 64% was achieved when 0.6 M H_2O_2 was added in the leaching process.

Introduction:
Primary batteries such as alkaline and Zn-C batteries, are single-use and usually disposed in landfill. The unused alkaline batteries mainly consisted of a Zn-powder anode, a separator, MnO_2 and graphite cathode and KOH electrolyte, while the Zn-C batteries consisted of a Zn-foil anode, a separator, MnO_2 and amorphous carbon cathode, $ZnCl_2$ or NH_4Cl_2 electrolyte and a graphite rod.[1, 2] The general reaction pathways of the alkaline and Zn-C batteries are shown in Eq. 1-3 and Eq. 4-8, respectively.[3] After used, MnO_2 in the cathodes of both types of battery were converted to Mn_2O_3 Mn_3O_4 or $ZnMn_2O_4$ depending on the electrochemical reaction pathways (Eq. 2,5,7,11-15).[4]

Electrochemical reactions of alkaline battery:

Anode: $Zn + 2OH^- \rightarrow ZnO + H_2O + 2e^-$ (1)

Cathode: $2MnO_2 + H_2O + 2e^- \rightarrow Mn_2O_3 + 2OH^-$ (2)

Total: $Zn + 2MnO_2 \rightarrow ZnO + Mn_2O_3$ (3)

Electrochemical reactions of Zn-C battery

Anode: $Zn + 2Cl^- \rightarrow ZnCl_2 + 2e^-$ (4)

For ammonium chloride electrolyte

Cathode : $2MnO_2 + 2NH_4Cl + H_2O + 2e^- \rightarrow Mn_2O_3 + 2NH_4OH + 2Cl^-$ (5)

Total: $Zn + 2MnO_2 + 2NH_4Cl + H_2O \rightarrow ZnCl_2 + Mn_2O_3 + 2NH_4OH$ (6)

For zinc chloride electrolyte

Cathode : $2MnO_2 + ZnCl_2 + H_2O + 2e^- \rightarrow Mn_2O_3 + Zn(OH)_2 + 2Cl^-$ (7)

Total: $Zn + 2MnO_2 + H_2O \rightarrow Mn_2O_3 + Zn(OH)_2$ (8)

Other electrochemical reaction pathways

Anode: $Zn + 2OH^- \rightarrow ZnO + H_2O + 2e^-$ (9)

$Zn + 4OH^- \rightarrow Zn(OH)^{2-}_4 + 2e^-$ (10)

Cathode: $3MnO_2 + 2H_2O + 4e^- \rightarrow Mn_3O_4 + 4OH^-$ (11)

$2MnO_2 + 2H^+ + 2e^- \rightarrow 2MnOOH$ (12)

$Zn(OH)^{2-}_4 + 2MnOOH \rightarrow ZnMn_2O_4 + 2H_2O + 2OH^-$ (13)

Total: $2Zn + 3MnO_2 \rightarrow Mn_3O_4 + 2ZnO$ (14)

$Zn + 2MnO_2 \rightarrow ZnMn_2O_4$ (15)

The previous reported works on the recovery of Mn from spent primary batteries by acid leaching process showed the leaching reactions using sulfuric acid as in Eq. 16-20.[5] Depending on the final products of the spent electrode powder, the leaching process usually yields $MnSO_4$ and $ZnSO_4$ with MnO_2 and H_2O as by-products. The leaching of MnO_2 to $MnSO_4$ in Eq. 20 is usually unflavored, which in turn lower the Mn-ion leaching efficiency in the form of $MnSO_4$;[5] therefore, the addition of reducing agent to lower oxidation state of Mn^{4+} in MnO_2 was implemented to enhance the Mn-ion leaching efficiency.

$Mn_2O_3 + H_2SO_4 \rightarrow MnSO_4 + MnO_2 + H_2O$ (16)

$Mn_3O_4 + 2H_2SO_4 \rightarrow 2MnSO_4 + MnO_2 + 2H_2O$ (17)

$ZnMn_2O_4 + 2H_2SO_4 \rightarrow ZnSO_4 + MnSO_4 + MnO_2 + 2H_2O$ (18)

$ZnO + 2H_2SO_4 \rightarrow ZnSO_4 + 2H_2O$ (19)

$MnO_2 + H_2SO_4 \rightarrow MnSO_4 + H_2O + 1/2O_2$ (20)

Several types of reducing agent such as $C_6H_8O_6$, $C_6H_8O_7$ and $H_2C_2O_4$ were reported to promote the Mn leaching efficiency in Zn-MnO_2 batteries. By leaching in 0.5 M H_2SO_4 at 25°C for 3 h, the Mn leaching efficiency was increased from 50 % without the reducing agent to 98.79%, 91.59% and 87.45% with the above reducing agents, respectively.[1] By using $FeSO_4$ as a reducing agent in 1.5 M H_2SO_4, the Mn leaching efficiency of more than 90% was achieved.[6] Furthermore, using 2 M H_2SO_4 with 0.6 M H_2O_2, the Mn leaching efficiency was increased from 43.5% (no reducing agent) up to 97.54%.[5] Thus, in this study, H_2O_2 was employed as a reducing agent (Eq. 21) due to its high reducing activity and cost effectiveness.

$MnO_2 + H_2SO_4 + H_2O_2 \rightarrow MnSO_4 + 2H_2O + O_2$ (21)

This study also focused on the Mn recovery in a form of MnO_2, which can later be used in several energy storage applications including both primary and secondary batteries.[7] The leaching solutions from the previous acid leaching step were used as a precursor for MnO_2 synthesis. In previous reported works, $MnSO_4 \cdot H_2O$ (1.352 g, 0.008 mol) and $(NH_4)_2S_2O_8$ (1.826 g, 0.008 mol) were dissolved in 35 mL of water. The solution was heated in an oil bath at 80°C for 4 h to obtain the γ-MnO_2.[8] γ-MnO_2 synthesis was also achieved by mixing $MnSO_4$ 0.4 g and $(NH_4)_2S_2O_8$ 1.0 g, then hydrothermally treated in an autoclave 90°C for 36 h.[9] Furthermore, pure γ-MnO_2 was synthesized from the 20-mL leaching solution from alkaline battery (using 0.5 M H_2SO_4 with 0.6 M H_2O_2 at room temperature) with $(NH_4)_2S_2O_8$ (1.826 g, 0.008 mol) dissolved in 15-mL DI water.[10] Therefore, in this study, the Mn recovery by γ-MnO_2 synthesis from the leaching solution at various leaching conditions using the similar process as that of Ref.10 was investigated.

Methodology:

Preparation and characterization of mixed electrode powders

Spent alkaline and Zn-C batteries (Panasonic, size AA) were separately dismantled to obtain the spent electrode powders. After grinding and mixing in a blender, the mixed electrode powder of each type of spent battery was washed three times by deionize water and ethanol in

ultrasonic bath for 20 min. The powder was then dried at 105°C for 48 h.[11] The phase and chemical composition of the spent electrode powder was subsequently analyzed by X-ray diffraction (XRD) and X-ray fluorescence spectroscopy (XRF) techniques, respectively.

Leaching process

The leaching process of the spent electrode powder was carried out in a plastic beaker with a magnetic stirrer. Sulfuric acid (H_2SO_4) was initially used without a reducing agent at room temperature and 80°C with the leaching conditions as summarized in **Table 1**. After that, the effect of reducing agent concentration on the Mn leaching efficiency was investigated by adding hydrogen peroxide (H_2O_2) at the concentration of 0.1-0.6 M to 0.5 M H_2SO_4 as summarized in **Table 2**. The Mn-ion concentration in the leaching solutions was subsequently determined by atomic absorption spectroscopy (AAS) technique to obtain the Mn leaching efficiency which was calculated from Eq. 22 (averaged over 3 samples per condition).

$$\text{Mn leaching efficiency} = \frac{C_{Mn}\left(^{g}/_{100mL}\right)}{\%Mn \times W_{electrode}\left(^{g}/_{100mL}\right)} \times 100\% \quad (22)$$

C_{Mn} = Mn-ion concentration in the leaching solution from AAS (g/100mL)

%Mn = Percentage of Mn in raw electrode powder from XRF (%)

$W_{electrode}$ = Weight of the spent electrode powder used in the leaching process (g/100mL)

Table 1.

Summary of leaching conditions without a reducing agent at room temperature (RT) and 80°C.

H_2SO_4 Concentration (M)	Solid:Liquid (S:L) ratio	Temperature (°C)
0.5	1:20	RT
0.5	1:20	80
1	1:10	80
2	1:5	80
5	1:5	80

Table 2.

Summary of leaching conditions with the addition of H_2O_2 as a reducing agent at RT.

H_2SO_4 Concentration (M)	S:L ratio	H_2O_2 Concentration (M)
0.5	1:20	0
		0.1
		0.3
		0.6

Synthesis of recycled MnO_2 from leaching solutions

The precursor solution was prepared by mixing the leaching solutions obtained from previous step (20 mL) with a solution of ammonium persulfate (1.826 g, 0.008 mol) dissolved in DI water (15 mL). The precursor solution was subsequently put in an autoclave and heat in an oil bath at 90°C for 24 h. After that, the samples were washed with DI water and ethanol, filtered, and dried at 60°C.[10] Phases of the obtained MnO_2 were analyzed by XRD technique, and the Mn recovery efficiency was subsequently calculated from Eq. 23 (averaged over 3 samples per condition).

$$\text{Mn recovery efficiency} = \frac{W_{Mn}(^{g}/_{100mL})}{\%Mn \times W_{electrode}(^{g}/_{100mL})} \times 100\% \quad (23)$$

W_{Mn} = Weight of Mn in the recycled MnO_2 if using 100 mL leaching solution (g/100mL)
%Mn = Percentage of Mn in raw electrode powder from XRF analysis (%)
$W_{electrode}$ = Weight of electrode powder used in the leaching process (g/100mL)

Results and Discussion:

Phase and chemical composition of spent electrode powders

The chemical composition analysis by XRF technique of the spent electrode powders from spent alkaline and Zn-C batteries is summarized in **Table 3**. The Zn-C battery consisted of 39.60 wt% Mn, while and alkaline batteries contained 54.90 wt% Mn. Other than Mn and Zn, the XRF results reveal other minor metal contents, such as K, S, Al, Si, Ti, Fe, and Ca in the mixed electrode powders.

Table 3.
Chemical composition of the spent electrode powders of alkaline and Zn-C batteries analyzed by XRF technique.

Type of battery	Element composition (wt%)									
	Mn	**Zn**	**K**	**S**	**Al**	**Si**	**Ti**	**Fe**	**Ca**	**Others**
Zn-C	39.60	29.50	526 ppm	0.23	0.88	0.22	-	0.28	0.12	697 ppm
Alkaline	54.90	14.90	6.59	0.40	0.12	0.25	0.22	0.17	447 ppm	1741 ppm

The phase of spent electrode powders of alkaline and Zn-C batteries analyzed by XRD technique are shown in **Figure 1**. The mixed phases of $Zn_xMn_{2-x}O_4$ (located between Mn_3O_4 and $ZnMn_2O_4$) and graphite were found in the electrode powder of spent alkaline batteries (**Figure 1a.**), while for spent Zn-C batteries (**Figure 1b.**), the mixed phases of $Zn_xMn_{2-x}O_4$ ZnClOH and ZnO were mainly observed, which is similar to previous work by Biswas, et al.[12] No carbon peak was shown in the spent Zn-C electrode XRD result due to the utilization of amorphous carbon.[13] ZnO was not clearly shown in the electrode powder of alkaline battery, which was due to the smaller weight fraction of anode powder compared to that of cathode powder. According to the XRD result, the main phase of electrode powders in both types of primary battery was $Zn_xMn_{2-x}O_4$; therefore, the leaching result reported this this study will be first focused on the Mn leaching efficiency of spent alkaline electrode powder.

Mn leaching efficiency in various leaching conditions

The Mn leaching efficiency without a reducing agent of spent alkaline electrode powder is summarized in **Figure 2a**. The Mn leaching efficiency of 8-14% was observed when the leaching temperature increased to 80°C and the H_2SO_4 concentration increased from 0.5 M to 10 M. The result reveals that the increase in the leaching temperature and H_2SO_4 concentration did not significantly promote the Mn leaching ability. By using H_2O_2 as a reducing agent at room temperature, the Mn leaching efficiency was increased from 11% to 87% (**Figure 2b.**). The increasing H_2O_2 concentration led to the higher Mn leaching efficiency as expected due to the reduction reaction of by-product MnO_2 to the leachable Mn^{2+}as described in Eq. 21.

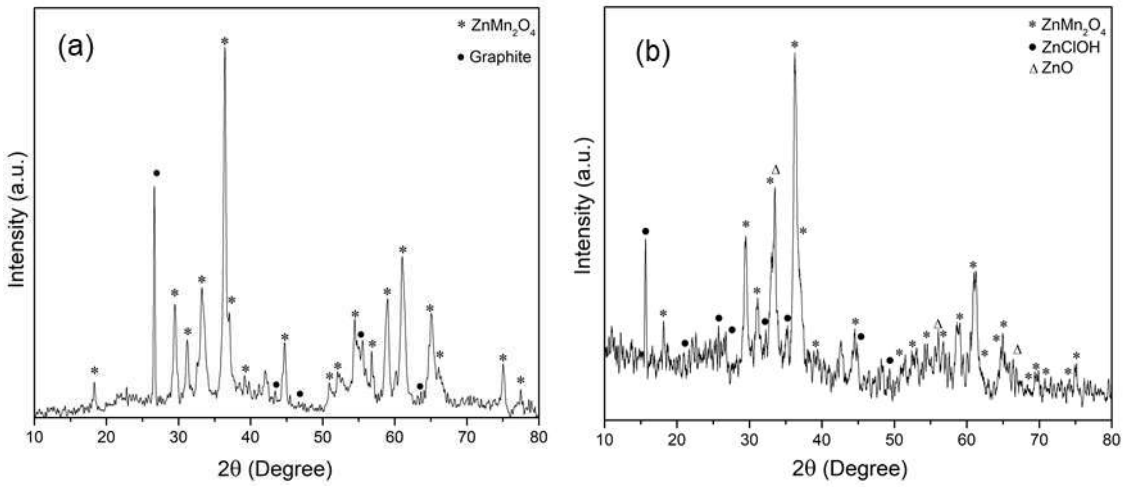

Figure 1.
XRD patterns of the spent electrode powders of (a) alkaline and (b) Zn-C batteries ($ZnMn_2O_4$: JCPDS 01-071-2499 , graphite:JCPDS 01-075-2078, ZnClOH: JCPDS 01-072-0525, ZnO: JCPDS 03-065-2880).

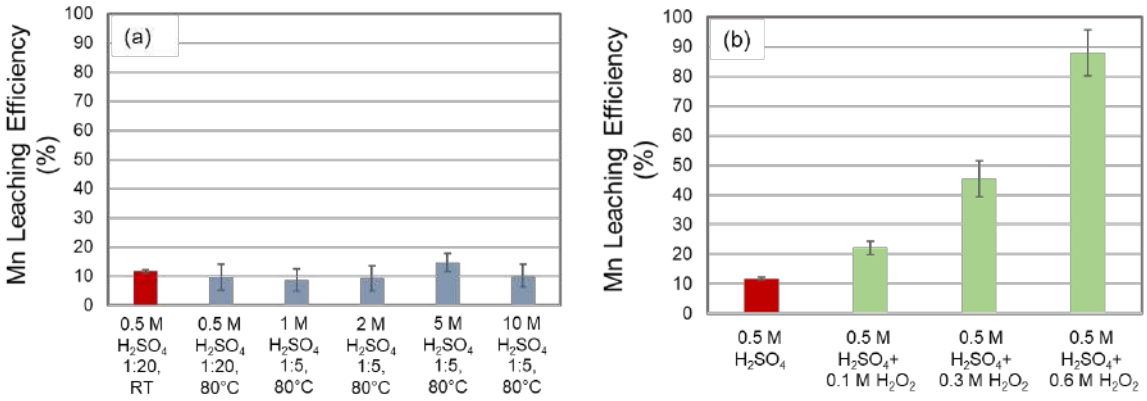

Figure 2.
The Mn leaching efficiency of spent alkaline electrode powder in sulfuric acid (a) without a reducing agent and (b) with 0.1-0.6 M H_2O_2 as a reducing agent.

Phase and recovery efficiency of the recycled MnO_2 synthesized from the leaching solutions

The phases of the recycled MnO_2 synthesized from the leaching solutions at various conditions were analyzed by XRD technique (**Figure 3.)**. The results reveal that the phases of the recycled MnO_2 were dependent on the leaching conditions. Once the leaching solution without a reducing agent was utilized as a precursor, the mixed phases ε- and γ- MnO_2 were obtained (leaching at room temperature), while the γ- and α- MnO_2 phases were obtained when leaching at 80°C at all H_2SO_4 concentrations. On the contrary, if using the leaching solution with H_2O_2 addition as a precursor, the single phase of γ-MnO_2 was obtained. The different phases of MnO_2 observed when using the precursors from different leaching conditions were possibly caused by the difference in the Mn concentrations and pH of the precursor solutions as previously reported in Ref. 14. Additionally, no impurity phase was observed, thus suggesting that other phases were not formed under this hydrothermal condition or may be formed in water-soluble phases which were subsequently removed by the washing process.

The Mn recovery efficiency in a form of MnO_2 were summarized in **Figure 4**. Overall, the Mn recovery efficiency had a similar trend as that of Mn leaching efficiency, thus

suggesting that the Mn recovery was highly dependent on the leaching step. Without the reducing agent, the highest Mn recovery efficiency of 17% was observed when leaching with 5 M H_2SO_4 at solid:liquid ratio of 1:5 at 80°C (**Figure 4a.**). When H_2O_2 was utilized as a reducing agent, the highest Mn recovery efficiency of 64% was achieved at 0.6 M H_2O_2 (**Figure 4b.**).

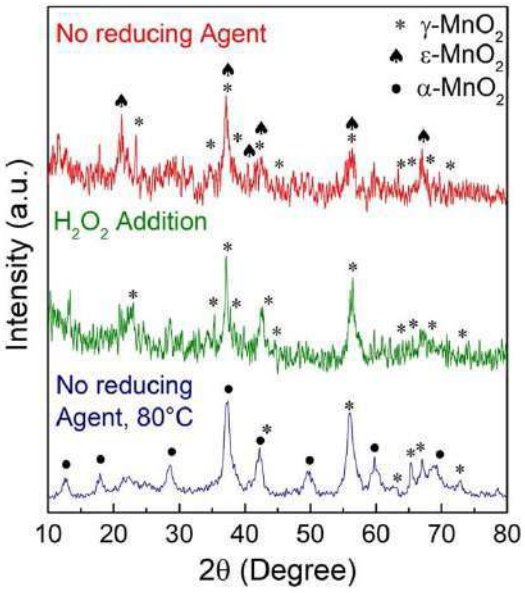

Figure 3.

The XRD patterns of the recycled MnO_2 synthesized from the leaching solutions with various leaching conditions.

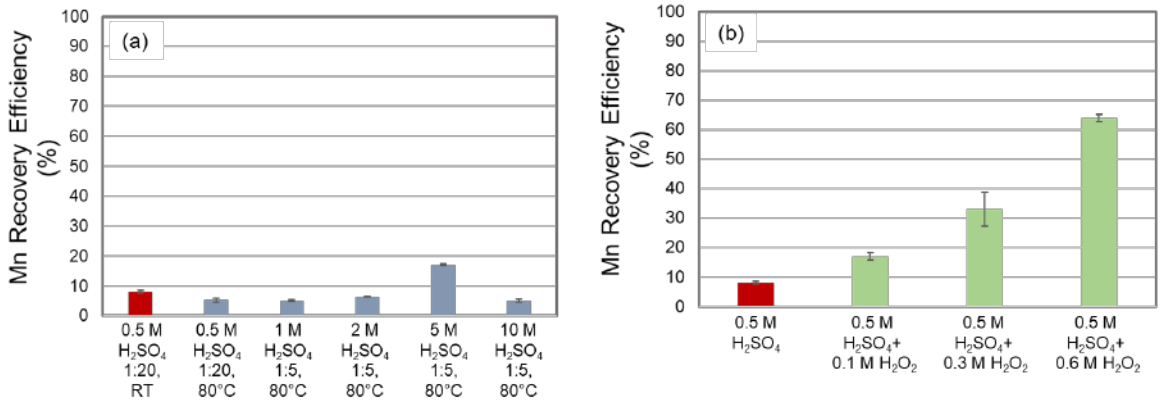

Figure 4.

The Mn recovery efficiency of the recycled MnO_2 from the leaching solutions (a) without a reducing agent and (b) with an addition of H_2O_2 as a reducing agent.

Conclusion:

The Mn leaching efficiency was increased from 11% (0.5 M H_2SO_4) to 87% when 0.5 M H_2SO_4 with addition of 0.6 M H_2O_2 was used in the leaching process. The increasing Mn leaching efficiency was also observed with increasing reducing-agent concentration. The phases of recycled MnO_2 synthesized from the leaching solutions were highly dependent on the leaching condition. Without a reducing agent in the leaching process, the mixed phases of MnO_2 at the lower Mn recovery efficiencies in a range of 8-17 were obtained, while the single phase of γ-

MnO_2 at the higher Mn recovery efficiency of 64% was achieved when 0.6 M H_2O_2 was added in the leaching process.

Acknowledgement:
We would like to thank Center of Excellence on Petrochemicals and Materials Technology (Petromat) for Mr. Chaithawat Waikhani's scholarship, the research fund from Office of National Higher Education, Science Research and Innovation Policy Council by Program Management Unit for National Competitiveness Enhancement, GAICCE Research Grant from ASEAN University Network/Southeast Asia Engineering Education Development Network (AUN/SEED-net), and Mr. Suthep Jongwanasiri at Siamfrit Co., Ltd. for his consultation on the upscaled leaching and synthesis process.

References:
1. Chen W-S, Liao C-T, Lin K-Y. Energy Procedia. 2017;107:167-174.
2. Farzana R, Rajarao R, Hassan K, Behera PR, Sahajwalla V. J Clean Prod. 2018;196:478-488.
3. Collins J, Gourdin G, Qu D. Green Chem.2018;1:771-860.
4. Ingale ND, Gallaway JW, Nyce M, Couzis A, Banerjee S. J Power Sources. 2015;276:7-18.
5. Buzatu M, Săceanu S, Petrescu MI, Ghica GV, Buzatu T. J Power Sources. 2014;247:612-617.
6. Sinha MK, Purcell W. Hydrometallurgy. 2019;187:168-186.
7. Julien C M, Mauger A. Nanomaterials (Basel). 2017;7(11):396-438.
8. Liu Y, Wei J, Tian Y, Yan S. J Mater Chem. A. 2015;3(37):19000-19010.
9. Zheng H, Modibedi M, Mathe M, Ozoemena K. Mater Today. 2017;4(11):11624-9.
10. Manowilaikun M. Master's Thesis. Department of Material Science, Chulalongkorn University. 2020
11. Andak B, Özduğan E, Türdü S, Bulutcu AN. Journal of Environmental Chemical Engineering. 2019;7(5).103372-103381.
12. Biswas R-K, Karmakar A-K, Kumar S-L, Hossain M-N. Waste Manag. 2015;46:529-535.
13. Sundén B. Hydrogen, Batteries and Fuel Cells. 2019;1:57-79.
14. Gangwar D, Rath C. Appl. Surf. Sci. 2021;557:149693-149704.

ENHANCING MANGROVE BIOCHAR RESIDUE FOR PHOSPHATE ADSORPTION BY MODIFIED WITH Fe^{3+}, K^+, AND Na^+

Sokkeang Be*, Anawat Pinisakul
Chemistry for Green Society and Healthy Living Research Unit (ChGSH), Department of Chemistry, Faculty of Science, King Mongkut's University of Technology Thonburi 10140, Bangkok, Thailand
*e-mail: be.sokkeang@mail.kmutt.ac.th

Abstract:

Biochar has been used as an environmentally friendly adsorbent to adsorb the nutrients. Four types of biochar were used to adsorb phosphate (one unmodified biochar and three modified biochars. This study's objectives were (i) to compare phosphate adsorption removal with different biochar modifications and (ii) to study the adsorption kinetic. 0.1 mol L^{-1} of Fe^{3+}, K^+, and Na^+ solutions with a volume of 500 mL were used to modified 20 g of biochar. The batch experiment was conducted to investigate phosphate adsorption removal. The result showed that unmodified biochar could not adsorb phosphate. However, biochar modified with Fe^{3+} can remove phosphate than those of K^+ and Na^+. The equilibrium time of 300 min of BC-Fe^{3+}, the phosphate removal efficiency was 48.50% ± 0.22. In addition, the experiment was fitted with pseudo-first-order with an R^2 value of 0.95 and giving adsorption capacity (0.15 mg g^{-1}) closed to the experiment value (0.12 mg g^{-1}). The phosphate adsorption followed reversible adsorption reactions. Furthermore, the K_d value increased from 11.61-24.24 L kg^{-1}, while increasing contact time from 5-360 min. This study suggested that biochar modified with Fe^{3+} can use to remove phosphate from contaminated water or reduce phosphate leaching from agriculture.

Introduction:

Phosphate (P) is an essential macronutrient required for plants growth and supports living organisms in aquatic environments.[1] However, the excessive application of phosphate in agriculture led to leaching and runoff P, resulting in negative environmental impact and effect on water bodies (eutrophication).[2,3] In addition, increase phosphate concentrations on water bodies causes human health due to the production of cyanotoxins.[4] Therefore, to remove phosphate, many techniques, such as biological processes, chemical precipitation, ion exchange, and adsorption have been used.[5] However, the adsorption process is recognized as the most attractive technique compared to other processes due to multiple advantages, including operational simplicity, high effectiveness, high removal rate, low cost, no generation of secondary pollutions, and most importantly, the availability of a wide range of adsorbents.[6,7]

In current years, biochar was used as an environmentally friendly adsorbent to remove phosphate from water and used for soil improvement, as shown in several studies.[2, 8, 9] However, the use of raw biochar has low phosphate adsorption capacity due to limited effective functional groups, specific surface area values, active sites, and anion exchange capacities.[10] To improve the phosphate adsorption capacity, modifications have been used to active biochar surface properties and pore structure.[11] Many studies have been worked on biochar modified using different metals (**Table 1**), such as Zheng, Q. et al.[12] used $MgCl_2$, $AlCl_3$, and $MgCl_2$ mixed $AlCl_3$ modified wheat straw biochar. Zhong, Z. et al.[8], Wu, L. et al.[13], and Li, T. et al.[14] were used $FeCl_3$, MgO, and $La(OH)_5$ to modified on coconut shells,

peanut shells, and pineapple peels, respectively. In addition, this study was used Fe^{3+}, K^{+}, and Na^{+} to modified mangrove biochar. These elements have a positive charge for electrostatic force to attach PO_4^{3-} with Fe^{3+}, K^{+}, and Na^{+}. Furthermore, the plant can be used Fe^{3+}, K^{+}, and Na^{+} as their nutrient and salt for growing.

This study's objectives were (i) to compare phosphate adsorption removal with different biochar modifications and (ii) to study the kinetic adsorption using pseudo-first-order and pseudo-second-order models. The batch experiments were conducted to determine phosphate adsorption. This study hypothesized that biochar modified with Fe^{3+}, K^{+}, and Na^{+} could have more ability to adsorb phosphate than unmodified biochar.

Table 1. P adsorption capacity of biochar using different modification agents

Biochar feedstock	Modification	Phosphate adsorption capacity (mg g^{-1})	References
Wheat Straw	$MgCl_2$	9.64	12
	$AlCl_3$	82.78	
	$MgCl_2 + AlCl_3$	153.40	
Coconut Shell	$FeCl_3$	4.2	8
Hardwood	$MgCl_2 \cdot 6H_2O$	463.5	3
Sugarcane Leaves	Mg/Al-LDHs	81.83	15
Poplar Chips	$AlCl_3 \cdot 6H_2O$	47.84	16
Peanut Shells	MgO	18.94	13
Pineapple Peels	$La(OH)_3$	101.16	14
Waste Activated Sludge	$FeCl_3 \cdot 6H_2O$	111	17
	$FeSO_4 \cdot 7H_2O$ and $FeCl_3 \cdot 6H_2O$	34.2	

Methodology:

Modified biochar preparation

Biochar (BC) was made from mangrove trees collected from Bann Khao Yi San, Samut Songkhram Province, Amphawa District, Thailand. The biochar sample was sieved to pass a <2 mm sieve before being used as an adsorbent. BC-Fe^{3+}, BC-K^{+}, and BC-Na^{+} were prepared by mixing 20 g of biochar in an Erlenmeyer flask with 500 mL 0.1 M $FeCl_3.6H_2O$, KCl, and NaCl, respectively. The flask was shaken at 180 rpm for 48 h at a room temperature of 30 °C. The mixtures were filtered through Glass Microfiber filter paper (GF/C^{TM}), and the residue was washed with deionized water until the pH of the solution was between 6.5-7.5 and dried at 105 °C.

Batch adsorption experiment

KH_2PO_4 analyzed grade was used to make a stock solution of 1000 mg L^{-1}. The desired concentration of phosphate solution was prepared from the stock solution. The effect of contact time on phosphate adsorption removal was determined using 2 g L^{-1} of BC, BC-Fe^{3+}, BC-K^{+}, and BC-Na^{+} mix with 50 mL of 10 mg L^{-1} phosphate concentration in Erlenmeyer flask. The mixtures were shaken for 5, 10, 20, 30, 60, 120, 180, 240, 300, and 360 min at 180 rpm using a shaker. The solutions were filtered through (GF/C^{TM}) for analyses of phosphate concentration at each contact time. The ascorbic acid method was used to determine phosphate concentration at the wavelength of 882 nm. The removal efficiencies (%), the amount adsorbed per unit weight of adsorbent (q_e in mg g^{-1}), and sorption coefficient (K_d in L Kg^{-1}) were calculated using Equation (1), (2), and (3) below:

$$\% \text{ Removal} = \frac{C_i - C_e}{C_i} \times 100 \quad (1)$$

$$q_e = \frac{(C_i - C_e) \times 100}{m} \quad (2)$$

$$K_d = \frac{(C_i + C_{adsorbent} - C_e) \times V}{(\frac{m}{1000}) \times (C_e - C_{adsorbent})} \quad (3)$$

where C_i and C_e are the initial concentration and equilibrium concentration (mg L^{-1}), $C_{adsorbent}$ is the concentration release from biochar (mg L^{-1}), q_e is the adsorbed amount per adsorbent (mg g^{-1}), m is mass of biochar (g), V is the volume of solution (L), and K_d is the sorption coefficient (L Kg^{-1}).

Statistical analysis

The phosphate concentrations were determined in triplicate, and the results were indicated as mean ± standard deviation (mean ± SD). Statistical analysis was performed using Minitab v16 (Minitab, LLC, Pennsylvania, USA, Version 16). A one-way analysis of variance (ANOVA) was used to test for significant differences at 95% ($p < 0.05$). The Tukey comparison was performed to confirm which treatments were significantly different from all other treatments.

Results and discussion:

Effect of contact time on phosphate adsorption removal

The phosphate adsorption with different modifications such as BC, BC-Fe^{3+}, BC-K^+, and BC-Na^+ are shown in **Table 2**. **Figure 1** shows the percentage of phosphate removal and remains concentration on biochar modified with Fe^{3+} (BC-Fe^{3+}). The results showed that unmodified biochar could not adsorb PO_4^{3-}. In addition, BC-K^+ and BC-Na^+ have less adsorption removal by 2.1% and 1.3%, respectively. The most experiment of BC-K^+ and BC-Na^+ were P desorption. However, **Figure 1** showed that phosphate removal by biochar modified with Fe^{3+} increased from 30.7% to 48.5%, with an increase in contact time from 5 to 360 min. The adsorption process reaches equilibrium within 300 min. The biochar modified with Fe^{3+} can remove phosphate than those of K^+ and Na^+ due to Fe^{3+} having three positive charges, while K^+ and Na^+ have only one positive charge. In addition, when comparison of charge density (charge per volume), it was found that the charge density of Fe^{3+} greater than Na^+ and Na^+ greater than K^+ ($Fe^{3+} > Na^+ > K^+$) by following the charge density values of 349, 24, and 11 C mm^{-3}, respectively. The adsorption by modification of Fe^{3+} gave a higher affinity to P. On the other hand, it was reported that the Fe hydroxide (Fe-OH) formed on the surfaces of materials could easily be protonated in acid solutions (Fe-OH + H^+ = Fe-OH_2^+), leading to the formation positively charged surface that enhances phosphate adsorption. Furthermore, the phosphate uptake by the BC-Fe^{3+} was influenced by the pH values of the solution.[8] By comparing the final pH to initial pH values after the adsorption process, the final pH was decreased from 5.83 to 3.89 along with contact time, while the initial pH was 6.36. This finding might be due to releasing some H^+ and Fe^{3+} during shaking of different contact times. However, the oxygen-contamination functional group also enhances the Fe^{3+} attracted to the surface of biochar during the modification process. Moreover, the NH_2 functional group could adsorb P via the reaction between $NH_2 + H^+ = NH_3^+$ (at acidic pH) and $NH_3^+ + PO_4^{3-} = NH_3^+$-$PO_4^{3-}$. In addition, the acidic pH in water can become from Fe^{3+} dissolve in water because Fe^{3+} is acidic species.

Table 2. The effect of contact time on phosphate adsorption removal.

Time (min)	BC-Fe^{3+}	BC-K^+	BC-Na^+	BC
	P adsorption removal (%)			
5	31.01 ± 0.09^{f}	-3.21 ± 0.06^{c}	-2.18 ± 0.07^{c}	-372 ± 0.91^{b}
10	30.70 ± 0.09^{f}	-7.61 ± 0.03^{g}	-4.61 ± 0.09^{e}	-368 ± 0.43^{a}
20	33.27 ± 0.25^{e}	-6.83 ± 0.13^{f}	-3.40 ± 0.06^{d}	-376 ± 0.00^{c}
30	33.03 ± 0.12^{e}	2.10 ± 0.16^{a}	-6.03 ± 0.22^{g}	-376 ± 0.57^{c}
60	33.00 ± 0.09^{e}	-2.37 ± 0.09^{b}	-5.33 ± 0.46^{f}	-391 ± 0.47^{e}
120	40.51 ± 0.34^{d}	-2.63 ± 0.09^{b}	-4.26 ± 0.12^{e}	-396 ± 0.11^{g}
180	43.31 ± 0.23^{c}	-4.36 ± 0.16^{e}	-5.95 ± 0.20^{g}	-388 ± 0.28^{d}
240	44.20 ± 0.06^{b}	-3.27 ± 0.28^{c,d}	1.30 ± 0.16^{a}	-392 ± 0.00^{f}
300	48.50 ± 0.22^{a}	-7.75 ± 0.37^{g}	-4.24 ± 0.22^{e}	-399 ± 0.65^{h}
360	48.07 ± 0.30^{a}	-3.79 ± 0.13^{d}	0.56 ± 0.11^{b}	-399 ± 0.11^{h}

BC-Fe^{3+} is biochar modified with Fe^{3+}, BC-K^+ is biochar modified with K^+, BC-Na^+ is biochar modified with Na^+, and BC is unmodified biochar. Significant differences are indicated by different letters ($p < 0.05$). The negative number of P adsorption removal meant that the experiment was P desorption.

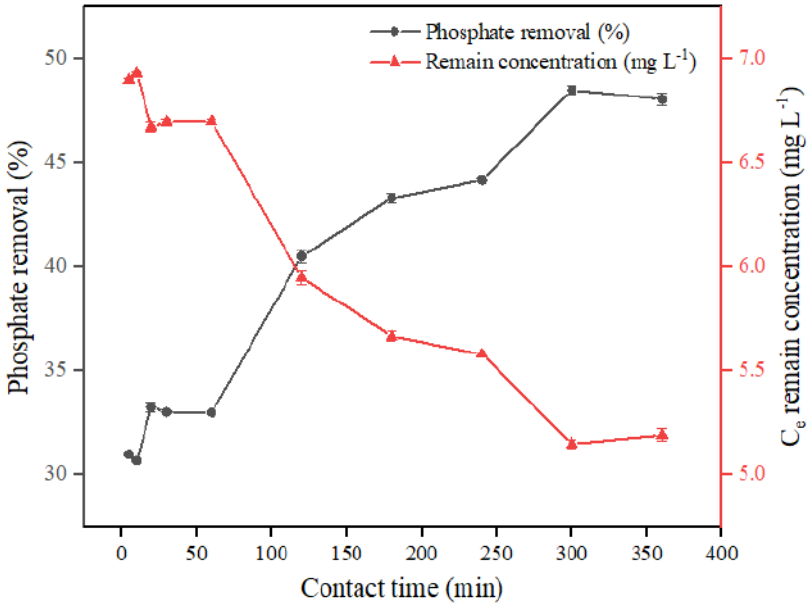

Figure 1. Effect of contact time on phosphate adsorption removal and remain phosphate concentration of BC-Fe^{3+}.

Table 3 showed the effect of contact time on phosphate desorption concentration (Control experiment). The results showed that unmodified biochar was release or desorption of phosphate concentration more than BC-Fe^{3+}, BC-K^+, and BC-Na^+ samples. In addition, the pH of BC, BC-K^+, and BC-Na^+ was in basic pH which is give the result of lower adsorption and more phosphate desorption. The BC-Fe^{3+} sample was in acidic pH which is more phosphate adsorption and less desorption.

Table 3. The effect of contact time on phosphate desorption concentration (Control experiment)

Time (min)	BC-Fe^{3+}	BC-K^{+}	BC-Na^{+}	BC
	Phosphate concentration (Control experiment) mg L^{-1}			
5	0.07	0.24	0.17	2.66
10	0.06	0.25	0.18	2.85
20	0.07	0.42	0.23	2.98
30	0.11	0.43	0.23	3.32
60	0.11	0.62	0.38	3.80
120	0.14	0.70	0.34	4.13
180	0.15	0.64	0.76	4.53
240	0.04	0.68	0.40	4.63
300	0.06	0.78	0.38	4.79
360	0.07	0.77	0.50	5.11

BC-Fe^{3+} is biochar modified with Fe^{3+}, BC-K^{+} is biochar modified with K^{+}, BC-Na^{+} is biochar modified with Na^{+}, and BC is unmodified biochar.

Sorption coefficient (K_d) of biochar modified with Fe^{3+}

Figure 2 shown the sorption coefficient (K_d) of biochar modified with Fe^{3+}. The results show that the K_d value increased with the P adsorption removal increase. The K_d value by biochar modified with Fe^{3+} increased from 11-24.14 L Kg^{-1} with an increase in the percentage of P removal from 30.7-48.5% and contact time from 5-360 min. This finding indicated that when the percentage removal increased, the K_d also increase.

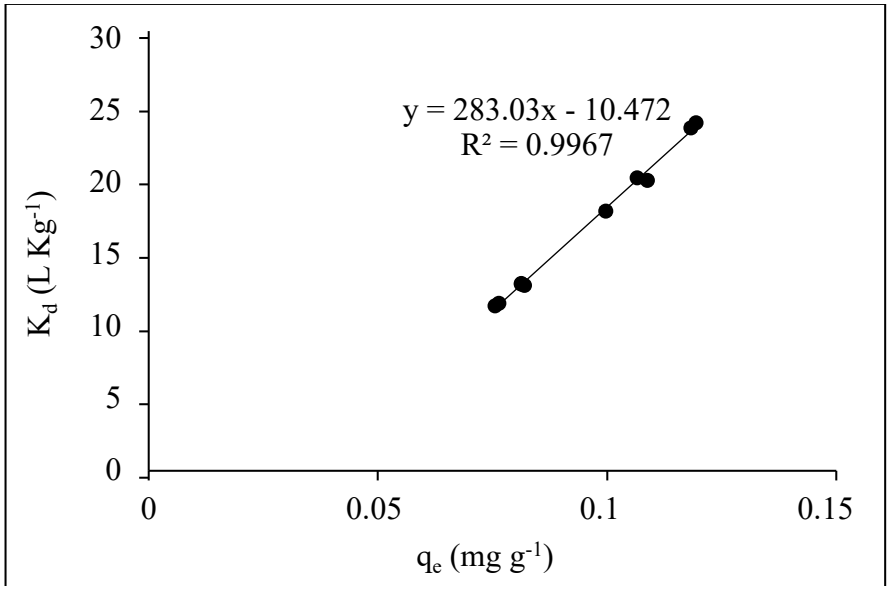

Figure 2. The sorption coefficient (K_d) of phosphate adsorption on biochar modified with Fe^{3+}.

The functional group (FTIR)

The FTIR spectra of the BC and BC-Fe^{3+} before and after phosphate adsorption are shown in **Figure 3**. After P adsorption, the FTIR spectrum of the BC- Fe^{3+}-P exhibited differences compared to the BC-Fe^{3+} and BC. At wavenumber 1041 cm^{-1}, the P-O bond occurred in BC-Fe^{3+} after P adsorption, which is revealed that phosphate was firmly adsorbed

at this bond. The peak located at 3418-3547 cm^{-1} can be attributed to the O-H stretching vibration of hydrogen-bonded groups and water molecules. The band 2924- 2852 cm^{-1} were attributed to the CH_2 group. The NH_2 stretching (amide) vibration is found at 1619 cm^{-1}. The peak at 1400 cm^{-1} and 1317 cm^{-1} were for the stretching vibrations of the C=C and C-O, respectively.[8]

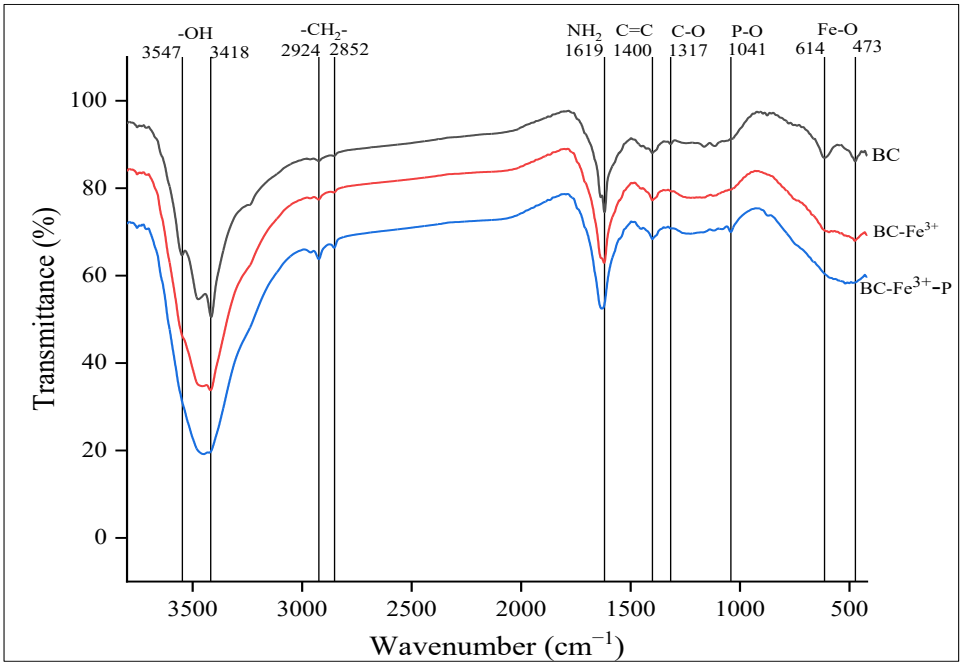

Figure 3. FTIR spectrum of the unmodified biochar (BC), biochar modified with Fe^{3+} (BC-Fe^{3+}), and biochar modified with Fe^{3+}after P adsorption (BC-Fe^{3+}-P).

Biochar phosphate adsorption kinetic

Adsorption kinetic models can be used to describe the main phosphate adsorption mechanisms by biochar. Pseudo-first-order models are commonly used to describe reversible adsorption reactions that involve weak interactions between phosphate and biochar, while pseudo-second-order models are generally responded to chemical reactions. The parameters and correlation coefficients (R^2) of adsorption kinetic with two models are listed in **Table 4**. After comparing the R^2 values, it was found the R^2 of pseudo-first-order and pseudo-second-order models were closed values (0.95-0.96). When adsorption capacity was compared between two models, it was found that the adsorption capacity from the experiment ($q_{e,exp}$) was closed to adsorption capacity from the pseudo-first-order model ($q_{e,cal}$). Thus, the P adsorption by biochar modified with Fe^{3+} was better fitted with the pseudo-first-order model. This result is suggesting that phosphate adsorption onto BC-Fe^{3+} occurs via a reversible adsorption reaction.[12] In addition, Zhong, Z. et al.[8] and Yang, Q. et al.[17] found that the adsorption capacity were 4.2 mg g^{-1} and 111 mg g^{-1}, respectively. However, the adsorption capacity was depended on the initial concentration of metals used to modified biochar and feedstock used.

Table 4. Kinetic parameters for P adsorption by BC-Fe^{3+}

Sample	$q_{e,exp}$ (mg g^{-1})	Pseudo-first-order			Pseudo-second-order		
		$q_{e,cal}$ (mg g^{-1})	k_1 (min^{-1})	R^2	$q_{e,cal}$ (mg g^{-1})	k_2 (L mg^{-1} min^{-1})	R^2
BC-Fe^{3+}	0.12	0.15	0.0009	0.95	6.89	5 x 10^{-5}	0.96

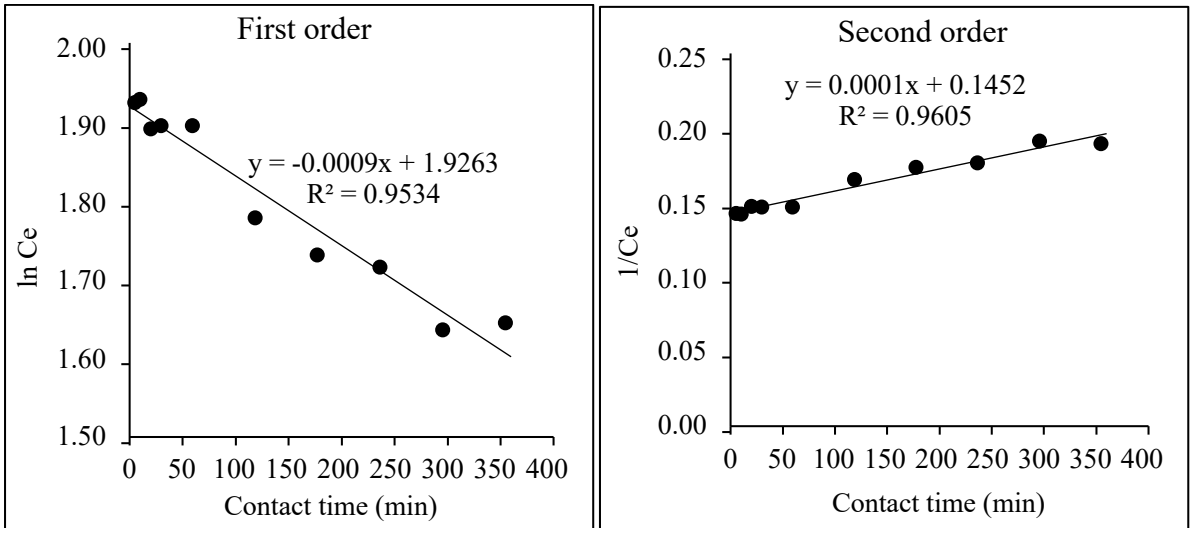

(a) **(b)**

Figure 4. P adsorption kinetic (a) pseudo-first-order and (b) pseudo-first-order by BC-Fe^{3+}

Conclusion:

This study revealed that BC-Fe^{3+} deriving from mangrove trees has the ability for phosphate adsorption. The BC-Fe^{3+} showed high adsorption removal up to 48%, while BC-K^{+} and BC-Na^{+} up to 2% and 1%, respectively, and no P adsorption by unmodified biochar. Adsorption kinetics were well fitted by a pseudo-first-order model. Phosphate adsorption by the BC-Fe^{3+} followed the reversible adsorption reaction. Thus, the BC-Fe^{3+} could be useful for removing phosphate from contaminated water and reducing phosphate leaching from agriculture.

Acknowledgment:

The authors would like to thank the Department of Chemistry, Faculty of Science, and Environmental Technology Program, School of Energy, Environment and Materials, King Mongkut's University of Technology Thonburi, Thailand, for laboratory analysis.

References:

1. Jung, K.-W., Lee, S., and Lee, Y.J. Synthesis of Novel Magnesium Ferrite ($MgFe_2O_4$)/Biochar Magnetic Composites and Its Adsorption Behavior for Phosphate in Aqueous Solutions. 2017;245:751-759.
2. Huang, Y., Lee, X., Grattieri, M., Yuan, M., Cai, R., Macazo, F.C., and Minteer, S.D. Modified Biochar for Phosphate Adsorption in Environmentally Relevant Conditions. 2020;380:122375.
3. Arbelaez Breton, L., Mahdi, Z., Pratt, C., and El Hanandeh, A. Modification of Hardwood Derived Biochar to Improve Phosphorus Adsorption. 2021;8:41.
4. Jung, K.-W., Jeong, T.-U., Choi, J.-W., Ahn, K.-H., and Lee, S.-H. Adsorption of Phosphate from Aqueous Solution Using Electrochemically Modified Biochar Calcium Alginate Beads: Batch and Fixed-Bed Column Performance. 2017;244:23-32.
5. Liu, H., Guo, W., Liu, Z., Li, X., and Wang, R. Effective Adsorption of Phosphate from Aqueous Solution by La-Based Metal-Organic Frameworks. 2016;6:105282-105287.

6. Chen, J., Yan, L.-g., Yu, H.-q., Li, S., Qin, L.-l., Liu, G.-q., Li, Y.-f., and Du, B. Efficient Removal of Phosphate by Facile Prepared Magnetic Diatomite and Illite Clay from Aqueous Solution. 2016;287:162-172.
7. Goscianska, J., Ptaszkowska-Koniarz, M., Frankowski, M., Franus, M., Panek, R., and Franus, W. Removal of Phosphate from Water by Lanthanum-Modified Zeolites Obtained from Fly Ash. 2018;513:72-81.
8. Zhong, Z., Yu, G., Mo, W., Zhang, C., Huang, H., Li, S., Gao, M., Lu, X., Zhang, B., and Zhu, H. Enhanced Phosphate Sequestration by Fe (III) Modified Biochar Derived from Coconut Shell. 2019;9:10425-10436.
9. Be, S., Vinitnantharat, S., and Pinisakul, A. Effect of Mangrove Biochar Residue Amended Shrimp Pond Sediment on Nitrogen Adsorption and Leaching. 2021;13:7230.
10. Wan, S., Wang, S., Li, Y., and Gao, B. Functionalizing Biochar with Mg-Al and Mg-Fe Layered Double Hydroxides for Removal of Phosphate from Aqueous Solution. 2017;47:246-253.
11. Novais, S.V., Zenero, M.D.O., Barreto, M.S.C., Montes, C.R., and Cerri, C.E.P. Phosphorus Removal from Eutrophic Water Using Modified Biochar. 2018;633:825-835.
12. Zheng, Q., Yang, L., Song, D., Zhang, S., Wu, H., Li, S., and Wang, X. High Adsorption Capacity of Mg-Al-modified Biochar for Phosphate and Its Potential for Phosphate Interception in Soil. 2020;259:127469.
13. Wu, L., Wei, C., Zhang, S., Wang, Y., Kuzyakov, Y., and Ding, X. MgO-Modified Biochar Increases Phosphate Retention and Rice Yields in Saline-Akaline Soil. 2019;235:901-909.
14. Li, T., Su, X., Yu, X., Song, H., Zhu, Y., and Zhang, Y. $La(OH)_3$-Modified Magnetic Pineapple Biochar as Novel Adsorbent for Efficient Phosphate Removal. 2018;263:207-213.
15. Li, R., Wang, J.J., Zhou, B., Awasthi, M.K., Ali, A., Zhang, Z., Gaston, L.A., Lahori, A.H., and Mahar, A. Enhancing Phosphate Adsorption by Mg/Al Layered Double Hydroxide Functionalized Biochar with Different Mg/Al Ratios. 2016;559:121-129.
16. Yin, Q., Ren, H., Wang, R., and Zhao, Z. Evaluation of Nitrate and Phosphate Adsorption on Al-Modified Biochar: Influence of Al Content. 2018;631:895-903.
17. Yang, Q., Wang, X., Luo, W., Sun, J., Xu, Q., Chen, F., Zhao, J., Wang, S., Yao, F., and Wang, D. Effectiveness and Mechanisms of Phosphate Adsorption on Iron-Modified Biochars Derived from Waste Activated sludge. 2018;247:537-544.

Fabrication characterization and leaching properties of Polyacrylonitrile electrospun nanofibrous membranes containing biochar and zinc nanoparticles.

Narumon Phonrung,[1,2] Orawan Suwantong,[1,2] Khamphe Phongthong,[3] Thitipone Suwunwong,[1,2*]
[1]School of Science, Mae Fah Luang University, Tasud, Muang, Chiang Rai, 57100, Thailand
[2]Center of Chemical Innovation for Sustainability (CIS), Mae Fah Luang University, Tasud, Muang, Chiang Rai, 57100, Thailand
[3]Environmental Assessment and Technology for Hazardous Waste Management Research Center, Faculty of Environmental Management, Prince of Songkla University, Songkhla 90112, Thailand
*e-mail: thitipone.suw@mfu.ac.th

Abstract:

Electrospun nanofibrous membranes were fabricated based on Polyacrylonitrile (PAN) doped with biochar 5% w/w (base on the weight of PAN) and Zinc nanoparticles 5% w/w (base on the weight of PAN) via the electrospinning method. Throughout the experiment, the best results from all combinations tested were achieved for biochar and zinc behenate doped nanofibers. These had homogenous nanoparticle coverage (some particles <100 nm in diameter) with uniform fiber morphology scanning electron microscope (SEM). Efficient biochar and Zinc nanoparticles-based nanofiber filter technique electrospinning and adding biochar to make nanofibers the electrospinning polymer is stronger, the resulting polymer plate is thicker, retains its shape, and has a smaller fiber size, allowing the air filter to capture fine particles. Moreover, biochar and Zinc nanoparticles doped nanofibers displayed the lowest biochar and Zinc leaching of all samples prepared in this study. These nanofibers, therefore, represent a promising alternative to current biochar and Zinc nanoparticles doped nanofibers prepared in situ.

IDENTIFICATION OF NON-COVALENT INHIBITORS OF SARS-CoV-2 MAIN PROTEASE THOUGHT VIRTUAL SCREENING AND PHARMACOKINETIC PREDICTION

Sirinthip Sangsawang,[1] Siripen Modmuang,[1] Bandit Khamsri,[1] Pharit Kamsri,[2] Auradee Punkvang,[2] Patchreenart Saparpakorn,[3] Supa Hannongbua,[3] Prasat Kittakoop, [4,5,6] Khomson Suttisintong,[7] Noriyuki Kurita,[8] James Spencer,[9] Adrian J. Mulholland,[10] Pornpan Pungpo[1,*]

[1] Department of Chemistry, Faculty of Science, Ubon Ratchathani University, Ubon Ratchathani, 34190, Thailand

[2] Division of Chemistry, Faculty of Science, Nakhon Phanom University, Nakhon Phanom, 48000, Thailand

[3] Department of Chemistry, Faculty of Science, Kasetsart University, Bangkok, 10900 Thailand

[4] Chulabhorn Research Institute, Kamphaeng Phet 6 Road, Laksi, Bangkok 10210, Thailand

[5] Chulabhorn Graduate Institute, Chemical Biology Program, Chulabhorn Royal Academy, Kamphaeng Phet 6 Road, Laksi, Bangkok 10210, Thailand

[6] Center of Excellence on Environmental Health and Toxicology (EHT), Thailand

[7] National Nanotechnology Center (NANOTEC), 111 Thailand Science Park, Klong Luang, Pathum Thani, 12120, Thailand

[8] Department of Computer Science and Engineering, Toyohashi University of Technology, Toyohashi 441-8580, Japan

[9] School of Cellular and Molecular Medicine, Biomedical Sciences Building, University of Bristol, Bristol, BS8 1TD, United Kingdom

[10] Centre for Computational Chemistry, School of Chemistry, University of Bristol, Bristol, BS8 1TS, United Kingdom

*e-mail: pornpan_ubu@yahoo.com

Abstract:

SARS-CoV-2 main protease has been identified as a promising target for COVID-19 drug development. Herein, we attempt to identify novel non-covalent based SARS-CoV-2 main protease inhibitors from Specs database, commercially available database, based on virtual screening combined with pharmacokinetic predictions. The top 5 compounds with good binding affinity, physicochemical properties and pharmacokinetic properties were **AF-886/30573012**, **AE-473/30364057**, **AH-034/04564025**, **AG-690/10484053** and **AG-205/05876008**. Crucial interactions for binding of these 5 compounds are hydrogen bond interaction, pi-pi interaction and hydrophobic interactions with amino acid residues in the SARS-CoV-2 main protease binding site. The BBB, Caco2 permeability, HIA and MDCK cell level predicted values suggested that the selected compounds were medium to high absorption and permeability properties. Therefore, these finding compounds aided to identify novel SARS-CoV-2 main protease inhibitors as potentially against the COVID-19.

IMPACT OF ELECTROLYTE ADDITIVE ON IONIC SOLVATION AND TRANSPORT PROPERTIES FOR AQUEOUS ZINC-ION BATTERIES

Phatpasin Sumprasit,[1,2] Jitti Kasemchainan,[1,2] and Manaswee Suttipong[1,2,*]
[1]Department of Chemical Technology, Faculty of Science, Chulalongkorn University, Bangkok 10330, Thailand
[2]Center of Excellence on Petrochemical and Material, Chulalongkorn University, Bangkok 10330, Thailand
*e-mail: manaswee.s@chula.ac.th

Abstract:

Aqueous zinc-ion batteries (ZIBs) are recognized as a possible alternative to lithium-ion batteries for large scale energy storages. It is known that the adding of electrolyte additives can improve the ionic mobility, and thus the performance of ZIBs. However, uncertainties still remain on the fundamental interactions in electrolyte solutions, as well as the dynamical properties of ions. In the present work, molecular dynamics (MD) simulations were employed to study the role of electrolyte additive on zinc ion (Zn^{2+}) solvation structure and transport properties. Systems of aqueous zinc sulfate ($ZnSO_4$) electrolyte at 0.1, 0.5, 1, and 2 M concentrations with and without addition of 0.1 M manganese sulfate ($MnSO_4$) were considered at ambient conditions. The Zn^{2+} ion solvation structure changed with the concentration and the addition of $MnSO_4$ electrolyte additive. Adding of $MnSO_4$ resulted not only in stronger coordination between Zn^{2+} ions and water, but also in weaker coordination between Zn^{2+} ions and anions. With an increase in concentration, the ionic conductivity, like diffusion coefficient of Zn^{2+} ions, decreased for both $ZnSO_4$ solutions with and without $MnSO_4$. The trends observed in ionic conductivity from simulation were in agreement with experimental results. Apart from the fundamental insights and experimental findings provided, the results perhaps suggest ways to design novel electrolytes for aqueous ZIBs.

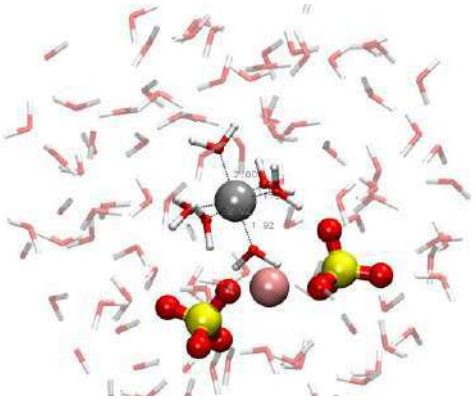

Figure 1.
Zn^{2+} ion is solvated by 6 water molecules in the solution of 1 M $ZnSO_4$ + 0.1 M $MnSO_4$

OIL ADSORPTION IN WASTEWATER USING CHITIN EXTRACTED FROM CUTTLEFISH BONE

Ratchakrich Patthamasopasakul and Boonyaras Sookkheo*
Department of Chemistry, Faculty of Science, Rangsit University, Patumthani, Thailand
*e-mail: boonyaras.s@rsu.ac.th

Abstract:
In this work, the extraction of chitin from cuttlefish bone was investigated to apply for oil adsorption in wastewater. The deproteinization and demineralization of cuttlefish bone were performed by refluxing with 8% w/v NaOH solution at 80 °C for 3 h and soaking in 8% w/v HCl solution at ambient temperature (28 °C) for 24 h, respectively. The physical appearance of extracted chitin was light orange. The amount of extracted chitin (5.73% w/w of total weight of the bone) was obtained. The extracted chitin was further applied as an adsorbent for oil adsorption using the synthetic wastewater containing 2% w/v oil via mild conditions: adsorption temperature of 28 °C, pH of 9.0 and shaking speed of 125 rpm for 15 min. It was observed that the sorbent amounts of 1.00, 2.00, 3.00, 4.00 and 5.00 g gave the oil adsorption efficiencies of 65.25, 76.10, 78.33, 79.13 and 80.25%, respectively. Moreover, oil adsorption efficiency was also tested in local restaurants (5 points) at Rangsit University, Thailand, and the result found that high ability for oil adsorption with an average of 86.55% was obtained.

Introduction:

Nowadays, wastewater originating from oil spills in food/chemical industries is a common environmental pollutant in everyday life[1]. Thus, cleaning up oil has become an exigent issue. To date, several methods have been tried to solve this problem such as combustion, adsorption, air flotation, gravitational sedimentation and chemical condensation[2]. Among these methods, the adsorption exhibits excellent efficiency for treatment of oily wastewater due to its easy operation and low cost. It is also presented some good advantages such as easy operation and low cost which can really applied in practical process[3-4]. In general, commercial adsorbents such as zeolite, silica, clay, rubber gels, aerogel and polyurethane foam are utilized for oil adsorption process[5-7]. Unfortunately, they are expensive and difficult to be entirely degraded in the environment. In recent years, chitin is one of the abundant polysaccharide polymers which can be used as a low-cost and eco-friendly material for oil adsorption[8]. It can be generally found in crustacean exoskeletons and insect shells such as shrimp, cuttlefish, crab, cockroach, grub and others[9]. Chitin has rigid crystalline structure via strong molecular H bonds between the polymer chains which is not soluble in water[10]. It is substantially composed of 2-acetamido-2-deoxy-D-glucopyranose (N-acetyl-D-glucosamine, GlcNAc) units linked by β (1, 4) linkage (Figure 1)[11].

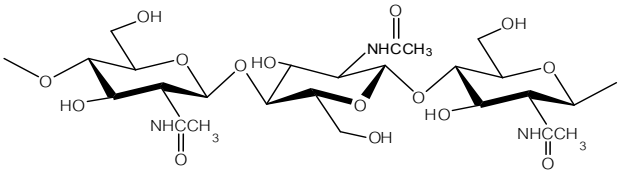

Figure 1.
Chemical structure of chitin

In this work, chitin, as a low-cost sorbent, was produced from cuttlefish bone via extraction process including deproteinization and demineralization. It should be noted that the objectives of this work were not only increase the value of waste (cuttlefish bone) from the seafood industry by converting into chitin, but it also could reduce the environmental problems. The physicochemical properties of chitin were investigated in details. To obtain optimum conditions for oil adsorption from synthetic wastewater, various factors such as contact time, pH value and chitin sorbent amount were systematically investigated. Moreover, oil adsorption efficiency in local restaurants (5 points) at Rangsit University, Thailand was also tested in order to know the possibility for further application in environmental wastewater.

Methodology:

Preparation of cuttlefish bone

Cuttlefish bone corrected from Yaring seaside, Pattani province, Thailand was used as a feedstock for chitin extraction (Figure 2). It was cleaned by washing process, dried at 70 °C for 3 h and finally crushed by using grinding machine.

Figure 2. Cuttlefish bone.

Deproteinization of cuttlefish bone

In brief, 100 g of prepared cuttlefish bone was added into round bottom flask containing 8% w/v NaOH solution, and then refluxed at 80 -90 °C for 3 h. The deproteinized product was separated by filtration process using filter paper grade 42 circles, washed with washed with distilled water until natural pH and dried at 70 °C for 3 h.

Demineralization of cuttlefish bone

In brief, a certain amount of cuttlefish bone obtained after deproteinization was soaked in HCl solutions with different concentrations at ambient temperature for 24 h. The demineralized product was separated by filtration process using filter paper grade 42 circles, washed with washed with distilled water until natural pH and dried at 70 °C for 3 h. Finally, the chitin sorbent was obtained. Here, the physical properties of as-prepared chitin were investigated in each condition. The existence of each functional group on the surface of chitin sorbent was also determined by Fourier transform infrared spectrometry (FT-IR) using a PerkinElmer Spectrum 100 FT-IR spectrometer.

Gravimetric analysis of oil using hexane extraction

In brief, pH value of sample (50 mL) containing of oil was defined (pH = 2) using HCl solution. The prepared sample was transferred into separatory funnel containing of 30 mL hexane, and then vigorously slewed for 2 min. After finishing process, it was separated into two layers. For bottom layer (water phase) was corrected for repetitive extraction. The mixture solution of oil and hexane in upper layer was corrected in evaporating dish. Then, the hexane in mixture solution was eliminated by using water bath. The obtained sample was

kept in oven at 70 °C for 3 h. Finally, the sample was kept in desiccator for further gravimetric analysis.

Optimization for oil adsorption
Effect of contact time
1.00 g of chitin was added into 50 mL of synthetic wastewater containing 2% w/v oil and stirred with a speed of 125 rpm at ambient temperature (28 °C) for 5, 10, 15, 20, 25 and 30 min. After finishing the process, the chitin sorbent was separated via filtration and the obtained sample solution was then analyzed to find the remaining amount of oil and to evaluate the adsorption efficiency.

Effect of pH value
1.00 g of chitin was added into 50 mL of synthetic wastewater containing 2% w/v oil and stirred with a speed of 125 rpm at ambient temperature (28 °C) for 15 min. Here, the pH value of mixture solution was adjusted from 5.0 to 11.0 through adding HCl and NaOH solution as required. After finishing the process, the chitin sorbent was separated via filtration and the obtained sample solution was then analyzed to find the remaining amount of oil and to evaluate the adsorption efficiency.

Effect of chitin sorbent amount
Various chitin amounts of 0.00, 1.00, 2.00, 3.00, 4.00 and 5.00 g of chitin were added into 50 mL of synthetic wastewater containing 2% w/v oil and stirred with a speed of 125 rpm at ambient temperature (28 °C) for 15 min. Here, mixture solution (pH value = 9.0) was defined since it is an optimum condition for oil adsorption. After finishing the process, the chitin sorbent was separated via filtration and the obtained sample solution was then analyzed to find the remaining amount of oil and to evaluate the adsorption efficiency.

Investigation on oil adsorption efficiency in wastewater
200 mL of wastewater containing oil was collected from various local restaurants such as (I) Islamic restaurant, (II) beef noodle restaurant, (III) cooked to order dish restaurant, (IV) chicken rice restaurant and (V) curry and rice restaurant at Rangsit University, Thailand. Here, oil amount containing in wastewater was gravimetrically analyzed using hexane extraction. In a typical adsorption process, 2.00 g of chitin were added into 50 mL of wastewater obtained from each restaurant and stirred with a speed of 125 rpm at ambient temperature (28 °C) for 15 min. Here, mixture solution (pH value = 9) was defined since it is an optimum condition for oil adsorption. After finishing the process, the chitin sorbent was separated via filtration and the obtained sample solution was then analyzed to find the remaining amount of oil and to evaluate the adsorption efficiency.

Results and Discussion:
Optimization for deproteinization and demineralization
From our previous study, the refluxing with 8% w/v NaOH solution at 80 °C for 3 h was found to be an optimum condition for deproteinization process. Thus, the effect of HCl concentration was investigated on demineralization of cuttlefish bone for 24 h, and the results found that the use of HCl concentration amount of 8-16% w/v resulted in physical appearance of very light orange chitin flake as required (Table 1). However, the yield or weight of extracted chitin was also decreased to some extent with the increasing of HCl concentration amount. Thus, HCl concentration amount of 8 w/v was selected as an optimum condition for demineralization process.

Table 1
Yield and physical properties of chitin extracted from cuttlefish bone via demineralization process using different concentrations of HCl

HCl (% w/v)	Weight of chitin (g)	Yield (%)	Physical appearance (Color)
2	8.3258	8.33	Orange
4	7.0163	7.02	Orange
6	5.8093	5.81	Light orange
8	.57310	.573	Very light orange
10	3.4961	3.50	Very light orange
12	1.7776	1.78	Very light orange
14	1.7645	1.76	Very light orange
16	1.7334	1.73	Very light orange

Characterization of sorbent using FT-IR analysis

Figure 3 shows the FT-IR spectrum of chitin extracted from cuttlefish bone. One can see that the broad peaks at range of 3500-3250 cm^{-1} were attributed to the bands of -OH and -NH stretching vibration[12]. The peaks at around of 3000-2800 and 1380 cm^{-1} could be assigned to the $-CH_3$ stretching and deformation, respectively. The C=O secondary amide could be observed at 1650 cm^{-1} while the bands at 1200-890 cm^{-1} was vibrations for C-O and C-O-C stretching. As observed, a similar FT-IR spectrum of chitin extracted in this study was found when compared with previous studies[13-14].

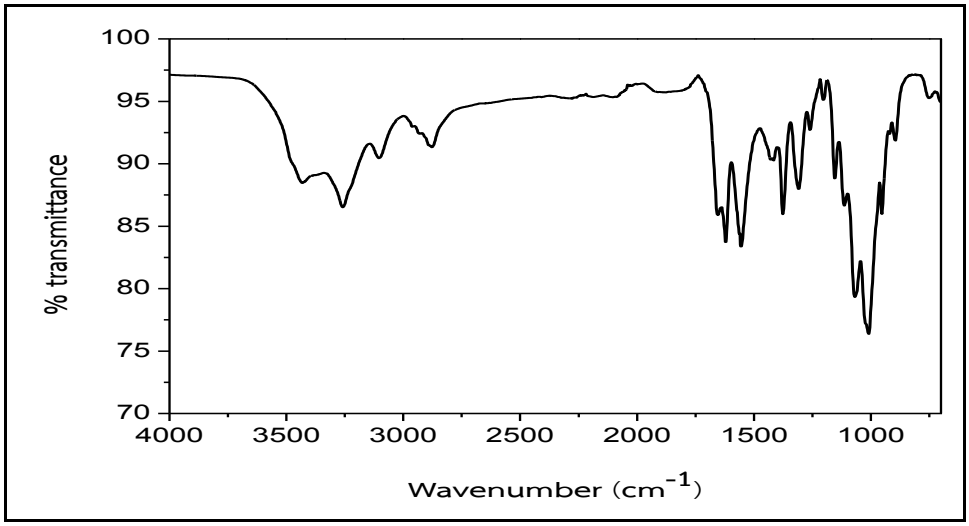

Figure 3.
FT-IR spectrum of chitin extracted from cuttlefish bone.

Effect of contact time for oil adsorption

Figure 4 shows the effect of contact time for oil adsorption from synthetic wastewater using chitin sorbent extracted from cuttlefish bone. As expected, the oil adsorption efficiencies were continuously increased from 52.30 to 61.24% with the increasing of contact times from 5 to 30 min. It should be noted that and oil adsorption ability became close to equilibrium for 15 min. Therefore, the contact time for 15 min was selected as an optimum condition for oil adsorption process.

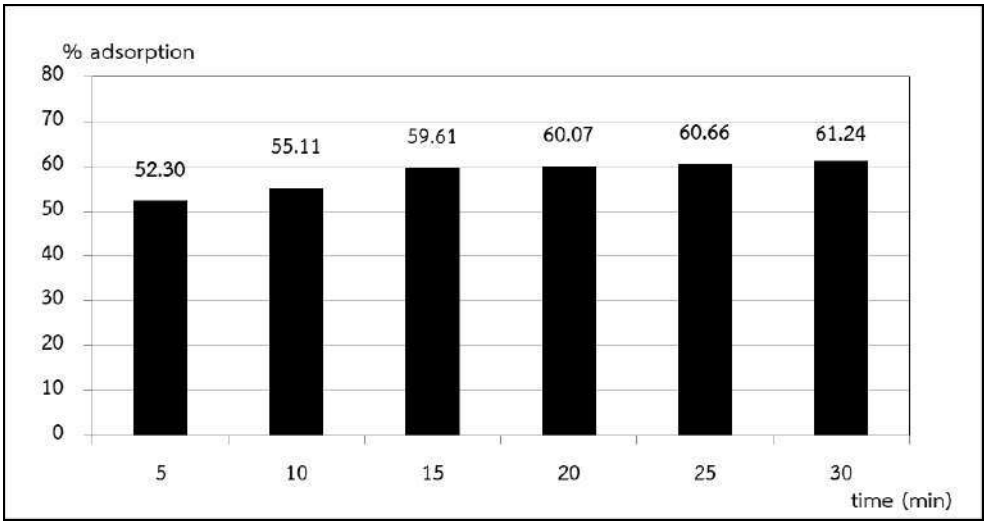

Figure 4.
Oil adsorption efficiency in synthetic wastewater at different contact times using chitin sorbent extracted from cuttlefish bone.

Effect of pH value for oil adsorption

Figure 5 shows the effect of pH value for oil adsorption from synthetic wastewater using chitin sorbent extracted from cuttlefish bone. It is found that the increasing of pH values from 5.0 to 9.0 caused a strong enhancement in the oil adsorption efficiencies with a maximum percentage of 65.05%, and then decreased to some extent. This indicates that when the pH was slightly basic, the adsorption process was more efficient. In the other words, the increasing in pH value facilitated the interaction between the negatively charged chitin with oil molecules. Therefore, the pH value of 9.0 was selected as an optimum condition for oil adsorption process.

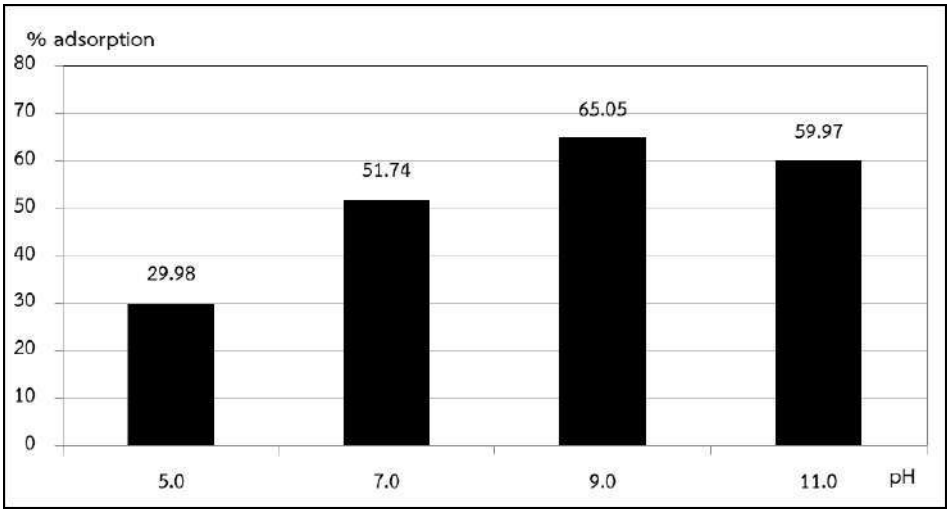

Figure 5.
Oil adsorption efficiency in synthetic wastewater at different pH values using chitin sorbent extracted from cuttlefish bone.

Effect of chitin sorbent amount for oil adsorption

Figure 6 shows the effect of chitin sorbent amount for oil adsorption from synthetic wastewater. As expected, the oil adsorption efficiency onto chitin steeply increased along

with increasing amount of chitin sorbent. This phenomenon should be attributed to the increase of the surface area of chitin sorbent for oil adsorption. After chitin sorbent amount of 2.00 g, the oil adsorption efficiency was slightly changed from 76.10 to 80.25% since the adsorption equilibrium was reached even though the number of binding sites available for adsorption enhanced with increasing the sorbent amount. Based on this result, the chitin sorbent amount of 2.00 g was selected as an optimum condition for oil adsorption process.

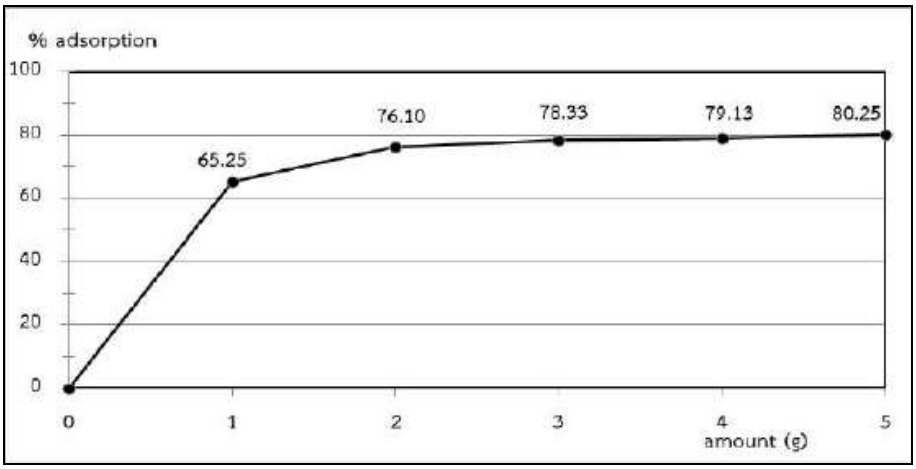

Figure 6.
Oil adsorption efficiency in synthetic wastewater at different amounts of chitin sorbent.

Oil adsorption efficiency in wastewater
Figures 7 and 8 show the oil adsorption efficiency in wastewater derived from various local restaurants such as (I) Islamic restaurant, (II) beef noodle restaurant, (III) cooked to order dish restaurant, (IV) chicken rice restaurant and (V) curry and rice restaurant at Rangsit University, Thailand. It is found that oil adsorption efficiencies from these local restaurants were averaged about 86.55%. This indicates that chitin sorbent extracted from cuttlefish bone had good performance for oil adsorption in environmental wastewater.

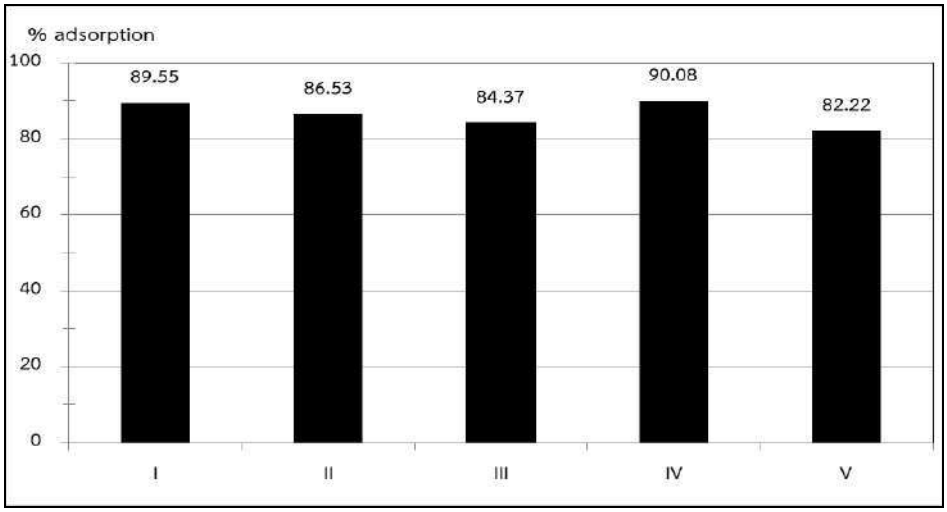

Figure 7.
Oil adsorption efficiency in wastewater derived from various local restaurants using chitin sorbent extracted from cuttlefish bone.

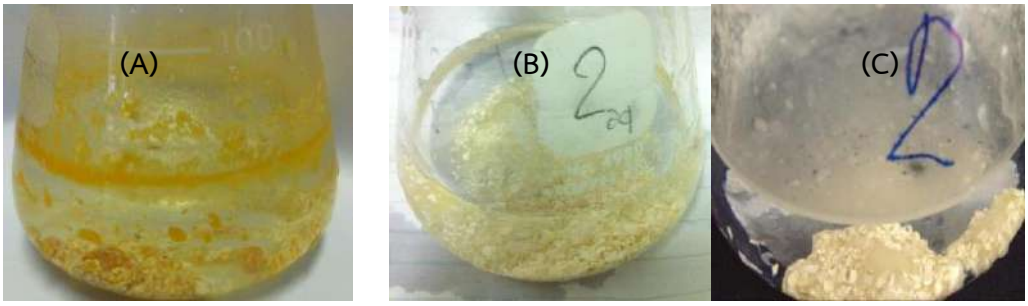

Figure 8.
Oil adsorption in wastewater derived from (A) cooked to order dish restaurant, (B) beef noodle restaurant and (C) chicken rice restaurant.

Conclusion:
In summary, chitin sorbent was easily extracted from cuttlefish bone via deproteinization (8% w/v NaOH solution at 80 °C for 3 h) and demineralization (8% w/v HCl solution at ambient temperature (28 °C) for 24 h), providing a chitin yield of 5.73 %w/w. Several effects such as contact time, pH value and chitin sorbent amount exhibited significantly results for increasing the oil adsorption efficiency in synthetic wastewater. Here, the optimum conditions for the oil adsorption in synthetic wastewater using chitin sorbent extracted from cuttlefish bone were as follows (I) contact time of 15 min, (II) pH value of 9.0 and (III) chitin sorbent amount of 2.00 g, providing an oil adsorption efficiency (76.10%) in synthetic wastewater. Moreover, the oil adsorption efficiencies in wastewater from local restaurants (5 points) at Rangsit University, Thailand were successfully achieved with a total average of 86.55%. This research is expected that as-extracted chitin from cuttlefish bone will further be developed on chemical and physical modification in order to improve the oil adsorption efficiency.

References:
1. Zhou X, Fu Q, Liu H, Gu H, Guo Z. J. Colloid Interface Sci. 2021; 581: 299-306.
2. Li R, Li Z, Yang R. Yin X. Lu J, Zhu L, Yang R. Mater. Chem. Phys. 2020; 241: 122338.
3. Chen J, Wang X, Huang Y, Lu S, Cao X, Yun J, Cao D. Eng. Sci. 2018; 5: 4-16.
4. Dashairya L, Rout M, Saha P, Adv. Compos. Hybrid Mater. 2017; 1: 135-148.
5. Carmody O, Frost R, Xi Y, Kokot S, J. Colloid Interface Sci. 2007; 305: 17-24.
6. Zhang A, Yin X, Shen X, Liu Y, ES Energy Environ. 2018; 1: 89-98.
7. Chin SF, Binti Romainor AN, Pang SC. Mater. Lett. 2014; 115: 241-243.
8. Cao YL, Pan ZH, Shi QX, Yu JY. Int. J. Biol. Macromol. 2018; 114: 392-399.
9. Shaqsi N, Hoqani HA, Hossain MA, Biochem. Biophys. Rep. 2020; 23: 100779.
10. Sugimoto M, Morimoto M, Sashiwa H, Shigemasa Y.Carbohydr. Polym.1998; 36: 49–59.
11. Kittur FS, Prashanth K, Sankar K, Tharanathan R. *Carbohydr. Polym.* 2002; 49: 185–193.
12. Rinaudo M. *Prog. Polym.* Sci. 2006; 31: 603–632.
13. Dotto G, Santos JM, Rodrigues L, Lima C. J. Colloid Interface Sci. 2015; 446; 133–140.
14. Gopi S, Pius A, Thomas S. J. Water Process Eng. 2016; 14: 1–8.

Preparation and characterization of polymethacrylate eugenol-based particles

Kanlapangha Rattanasaikaew, [1] Korawinwich Boonpisuttinant,[2] Supanida Winitchai,[3] Patchara Punyamoonwongsa,[4] Preeyaporn Chaiyasat [1,*]

[1] Department of Chemistry, Faculty of Science and Technology, Rajamangala University of Technology Thanyaburi, Klong 6, Thanyaburi, Pathumthani 12110, Thailand
[2] Thai Traditional Medicine College, Rajamangala University of Technology Thanyaburi, Prachathipat, Thanyaburi, Pathumthani 12110, Thailand
[3] Kasetsart Agricultural and Agro-Industrial Product Improvement Institute (KAPI), Kasetsart University, Ladyao, Chatujuk, Bangkok 10900, Thailand
[4] School of Science, Mae Fah Luang University, Chiang Rai 57100, Thailand

*e-mail: p_chaiyasat@mail.rmutt.ac.th

Abstract: This research aims to prepare poly(methacrylate eugenol) (ME)-based polymer particles by suspension polymerization. The ME as a biomonomer was prepared by the esterification of eugenol with methacrylic anhydride. The ^{1}H-NMR and FT-IR spectra confirmed the addition of methacrylate group on the structure. The ME was subsequently used to prepare polyME-based polymer particles at various ratios of ME: methyl methacrylate (MMA): divinylbenzene (DVB) (wt%). The milky suspensions with high colloidal stability were observed in all cases. The micrometer size, spherical particles were formed. The stability of the obtained polymer particles in an organic solvent as tetrahydrofuran was determined. The results showed that approximately 1-2 %wt of the polymer was dissolved according to the amount of MMA and DVB. The prepared polyME-based polymer particles were surface modified with a specific functional group for enzyme immobilization and then used to encapsulate magnetic nanoparticles for enzyme recovery application.

SUBSTITUENT EFFECT ON THE KINETIC BEHAVIOR OF PHOSPHINE-CATALYZED CONJUGATE ADDITION REACTION OF ALLENIC ESTERS: A POTENTIAL SOLUTION FOR DEVELOPMENT OF A KINETICALLY FASTER CATALYTIC CONJUGATE ADDITION.

Chaiwat Rujirasereesakul,[1] Piyatep Ngernklay,[1] Torsak Luanphisarnnont[1,2]*
[1]Department of Chemistry, Faculty of Science, Mahidol University, Bangkok 10400, Thailand
[2]Center of Excellence for Innovation in Chemistry (PERCH-CIC), Faculty of Science, Mahidol University, Bangkok 10400, Thailand
*e-mail: torsak.lua@mahidol.ac.th

Abstract:

Green and sustainable chemistry is currently one of the most important challenges in chemistry as minimization or elimination of the environmental impact of chemical processes is necessary for sustainable development of the world. One approach to achieve a greener chemical process is to improve the kinetic behavior of a chemical reaction, which leads to a more efficient chemical process. Phosphine-catalyzed conjugate addition reaction of allenic esters is an important mechanism in chemical synthesis that can be found as part of the first mechanistic step in many organic reactions. A better understanding of this key step may lead to an improvement of the efficiency of many organic syntheses. This work focuses on the effect of substituent on the kinetic behavior of the reaction. Alkyl and aryl allenic esters were used for the comparison in the kinetic investigation using a pseudo-first order approximation. The rate of the conjugate addition of triphenyl phosphine into aryl allenic esters was found to be approximately two-fold faster than that of alkyl allenic esters.

Introduction:

Development of green and sustainable chemical processes for chemical synthesis is one of the most important challenges in current chemical research.[1-3] Catalysis has played an important role in development of new chemical reactions with lower damage to the environment as catalysis can reduce the amount of reagent and thereby produces less waste and by-product.[4-6] In the past few decades, many catalysts for fundamental organic reactions have been developed. Among these reactions, catalytic conjugate addition reactions have been widely investigated as the reactions provide a convenient method for construction of a carbon-carbon bond or carbon-heteroatom bond. Conjugate addition reactions are important for syntheses of natural products,[7,8] chiral compounds,[9,10] sensors,[11] and drug delivery.[12]

Conjugate addition reactions have also been used in development of new synthetic methodology in which a conjugate addition reaction is a key mechanistic step in the reaction, providing a more structurally complexed product.[13-15] Tertiary phosphines have been reported to be an effective catalyst for conjugate addition reactions of allenic esters, resulting in a phosphine-incorporated intermediate which is vital in development of many organic reactions such as [3 + 2] annulations,[16] [4 + 2] annulations,[17] and asymmetric γ-additions.[18] Development of these green catalytic synthetic methods often focuses on variation on the type of phosphine catalysts and the reaction condition optimization to provide the product in high yield. However, a kinetic approach to improve the efficiency of the reaction has not been well investigated although the outcome might provide a solution to improve the rate and the efficiency of the reaction. Herein, this research studied the effect of substituent on the kinetic

behavior of the conjugate addition of phosphines into allenic esters using a pseudo-first order approach to determine the rate of the reaction (**Scheme 1**).

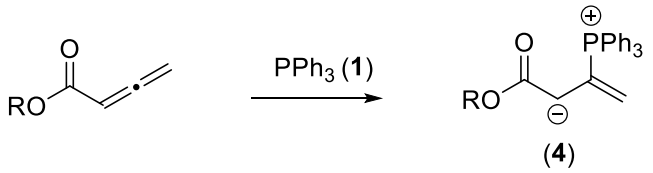

R = ethyl (**2**) R = ethyl (**4a**)
2-naphthyl (**3**) 2-naphthyl (**4b**)

Scheme 1 Conjugate addition between triphenylphosphine (**1**) and allenic esters (**2** or **3**)

Methodology:

General Procedure: ^{1}H-NMR and ^{31}P-NMR spectra were obtained from Bruker Avance 400 MHz NMR spectrometer. Chemical shifts are reported in ppm from tetramethylsilane (TMS) with the residual solvent resonance as an internal standard ($CDCl_3$ at δH 7.26 ppm) and the resonance of PPh_3 as an external standard (δP –4.70 ppm). Data are reported as follows: s = singlet, d = doublet, t = triplet, m = multiplet; coupling constant(s) in Hz, integration. Thin layer chromatography was performed on aluminum sheet with a Merck silica gel 60 F254 plate and compounds were visualized under UV light. Merck silica gel 60(0.063 – 0.200 nm) was used as a stationary phase on column chromatography. Mass spectra were obtained from high resolution mass spectra (HRMS) on a Bruker microTOF spectrometer in the ESI mode.

Material: Commercial reagents and organic solvents were purchased from TCI and Merck and were used without further purification unless otherwise noted.

Synthesis of 2-naphthyl 2,3-butadienoate:

To a round bottom flask were added a solution of CrO_3 (5.50 g, 55 mmol) in water (150 mL). The reaction was cooled down to 0 ^{o}C, and concentrated H_2SO_4 (40 mL) was added dropwise. A solution of 3-butyn-1-ol (2.00 g, 28 mmol) in acetone (30 mL) was added dropwise into the reaction at 0 ^{o}C, and the reaction was stirred at 0 ^{o}C for 3.5 hours. The reaction was extracted with EtOAc (6x 100 mL), and the combined organic layer was extracted with water (4x 100 mL) and saturated brine (2x 100 mL), dried over $NaSO_4$, and concentrated in vacuo. The desired 3-butynoic acid was obtained as an off-white solid (1.99 g, 85 %). The ^{1}H NMR spectrum was found to be identical to the published data.[19] ^{1}H NMR (400 MHz, $CDCl_3$), δ (ppm) 3.36 (d, *J*=2.67 Hz, 2H), 2.23 (t, *J*=2.67 Hz, 1H).

To a round bottom flask were added 2-chloro-1-methylpyridinium iodide (Mukaiyama reagent, 393 mg, 1.54 mmol), K_2CO_3 (430 mg, 3.08 mmol), 3-butynoic acid (129.5 mg, 1.54 mmol), 2-naphthol (200 mg, 1.4 mmol) and CH_2Cl_2 (14 mL). The reaction was stirred at room temperature for 4 hours. The reaction was filtered through a plug of silica. The solvent was removed in vacuo. The residue was purified by flash column chromatography (30% EtOAc/Hexane) to afford the title compound as a solid (96.5 mg, 54 %). The ^{1}H NMR spectrum was found to be identical to the published data.[20] ^{1}H NMR (400 MHz, $CDCl_3$), δ (ppm) 7.89–7.80 (m, 3H), 7.63–7.60 (m, 1H), 7.51–7.45 (m, 2H), 7.29–7.24 (m, 1H), 5.88 (t, *J* = 6.48 Hz, 1H), 5.37 (d, *J* = 6.48 Hz, 2H).

General procedure for UV-Visible kinetic experiments: The stock solutions of ethyl 2,3-butadienoate (0.01 M), 2-naphthyl 2,3-butadienoate (0.001 M), and triphenyl phosphine (0.1 and 0.01 M) in acetonitrile were prepared. To investigate the reaction, allenic ester (500 µl) was added to a cuvette with a 1 cm pathlength. Triphenyl phosphine (500 µl) was added to the cuvette for the 10x experiment. The scanning UV spectra of the reaction was performed using UV-2600 Shimadzu spectrophotometer. The absorbance at 440 mM was used for the kinetic

study. Other experiments (20x, 30x, and 40x) were performed in a similar manner with appropriate volumes of the substrates.

Results and Discussion:

To investigate the substituent effect of a conjugate addition of phosphine into allenic esters, aryl and alkyl allenoates were selected for the study. Aryl and alkyl substituents from the alcohol component of allenic esters possess different electronic and steric environment. This difference may lead to a different kinetic behavior in the conjugate addition reaction, which thereby may lead to higher efficiency and better environmental impact of phosphine-catalyzed conjugate addition reactions. Model compounds (**Figure 1**) were chosen to represent the substrates in the kinetic study. Triphenylphosphine (PPh_3, **1**) was selected as a representative for phosphine. Ethyl 2,3-butadienoate (**2**) and 2-naphthyl 2,3-butadienoate (**3**) were chosen as representatives for alkyl allenoate and aryl allenoate, respectively. Although triphenylphosphine and ethyl 2,3-butadineoate are commercially available, 2-naphthyl 2,3-butadienoate was synthesized from 3-butyn-1-ol using a two-step procedure (**Scheme 2**): oxidation of the alcohol and esterification with concomitant isomerization of the double bond. Conversion of 3-butyn-1-ol to 3-butynoic acid was accomplished by using Jones oxidation,[21] and the acid was obtained in 85%. The esterification between the acid and 2-naphthol was performed using Mukaiyama reagent, and the desired product **3** was obtained in 54%.

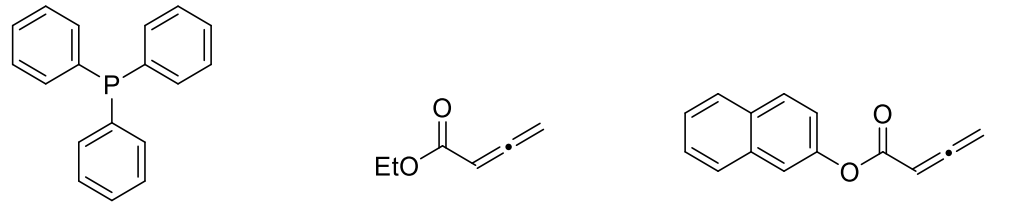

Triphenylphosphine (PPh_3, **1**) | Ethyl 2,3-butadienoate (**2**) | 2-Naphthyl 2,3-butadienoate (**3**)

Figure 1 Representative compounds for kinetic investigation

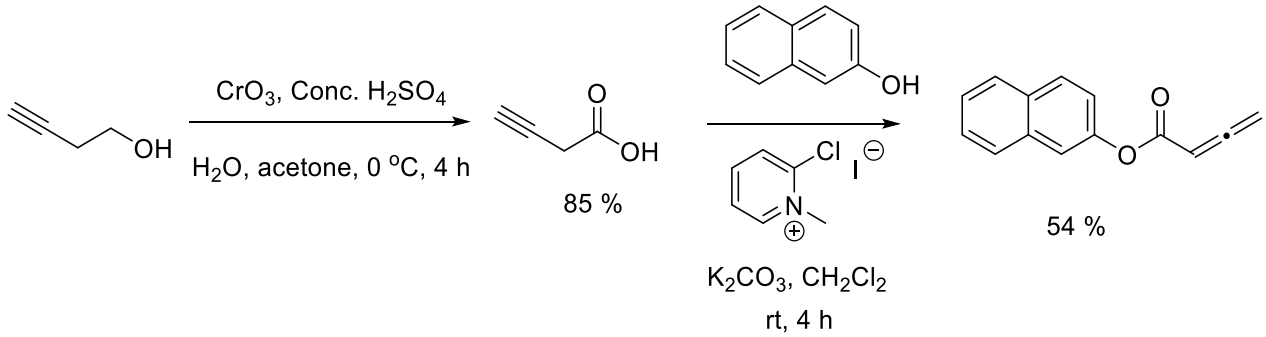

Scheme 2 Synthesis of 2-naphthyl 2,3-butadienoate (**3**)

To investigate the kinetic behavior of the conjugate addition reaction of phosphine, UV-visible spectroscopy was used to monitor the concentration of the conjugate product (**4**, **Scheme 1**). Although the conjugate product (**4**) have been proposed as an intermediate in previously reported literature, reported characterization of this compound has only been performed with mass spectrometry[22] possibly because of the high instability of the compound. We confirmed the presence of the conjugate product by high resolution mass spectrometry

(HRMS), ^{31}P nuclear magnetic resonance (NMR) spectroscopy, and UV-visible spectroscopy. Upon addition of the phosphine solution into ethyl 2,3-butadinoate, a new species with the same characteristic peak in HRMS as the conjugated product **4a** was observed. The peak (m/z value) was found to be 375.1506, which belonged to an exact mass of $[M+H]^+$ (the calculated value is 375.1508). A ^{31}P-NMR spectrum of the reaction also showed the presence of a new phosphorous peak at 29.91 ppm, which was speculated to belong to the conjugate product **4a** (**Figure 2**). The downfield shift in ^{31}P-NMR from the phosphine **1** was consistent with the proposed structure of the conjugate product **4a.**[22] Upon addition of the phosphine into ethyl 2,3-butadienoate, a new peak in UV-visible spectra emerged at 440 nm and its absorbance increased as the time passed (**Figure 3** and **4**). With the HRMS and ^{31}P-NMR data, we speculated that the new peak belonged to compound **4a**. Similarly, addition of triphenylphosphine (**1**) into 2-naphthyl 2,3-butadienoate (**3**) also gave a new peak in UV-visible spectra at 440 nm (**Figure 5**), which we speculated to be a conjugate product **4b**.

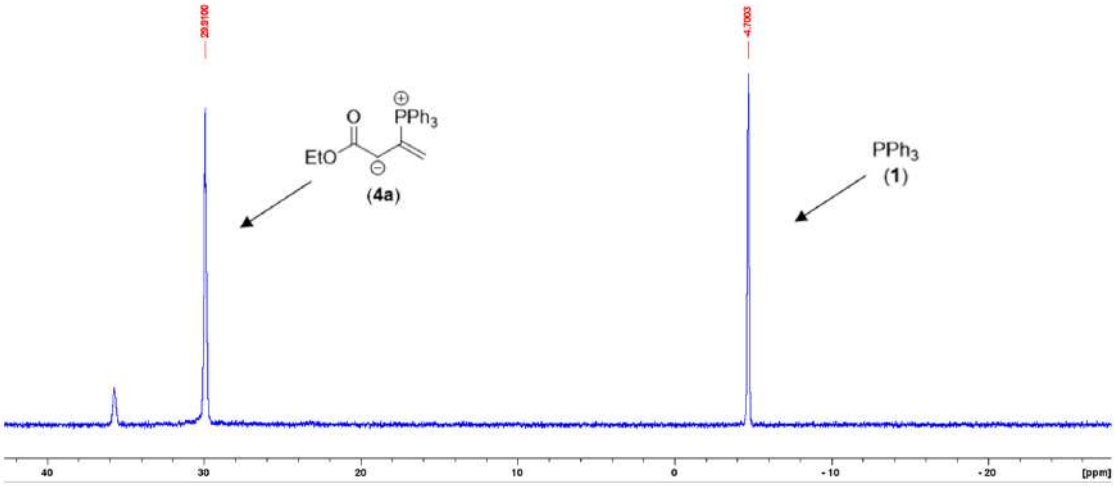

Figure 2 ^{31}P NMR spectrum of the conjugate addition between triphenylphosphine (**1**) and ethyl 2,3-butadienoate (**2**)

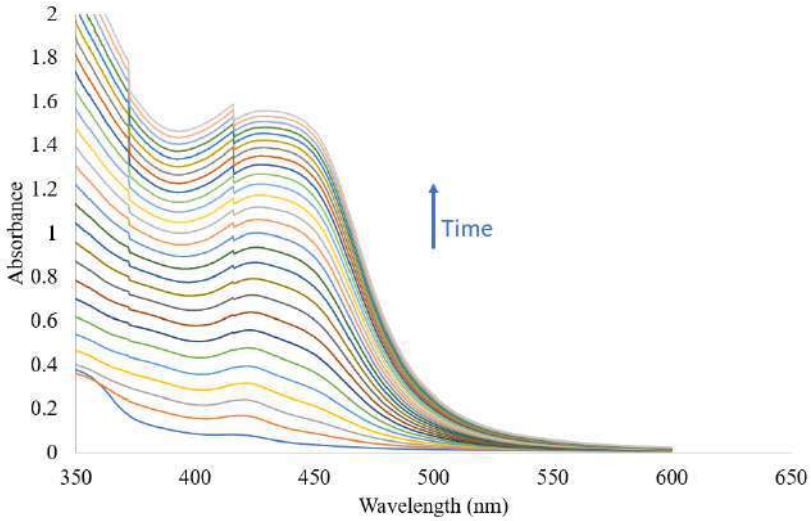

Figure 3 Absorbance versus wavelength at different times of the conjugate addition between triphenylphosphine (**1**) and ethyl 2,3-butadienoate (**2**)

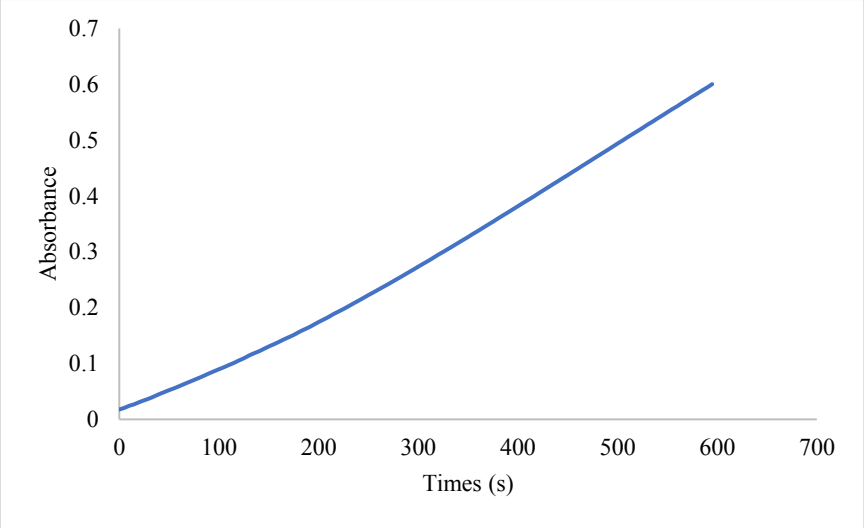

Figure 4 Absorbance at 440 nm versus reaction time of the conjugate addition between triphenylphosphine (**1**) and ethyl 2,3-butadienoate (**2**)

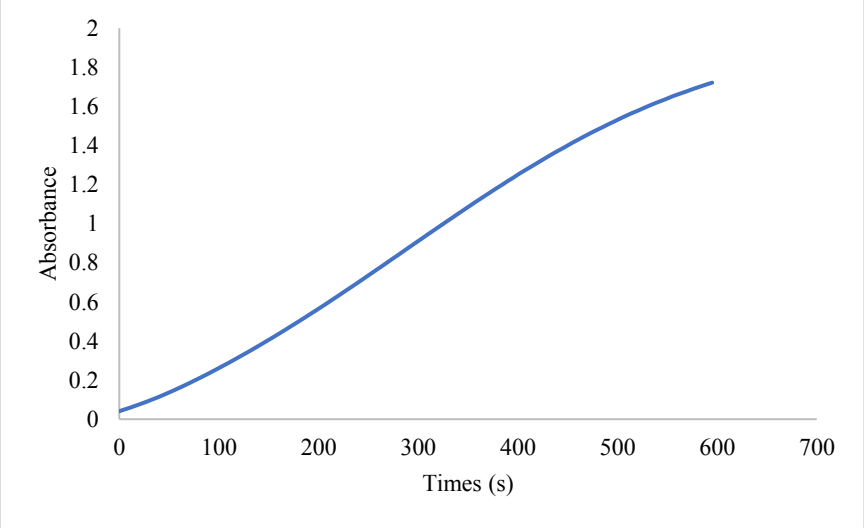

Figure 5 Absorbance at 440 nm versus reaction time of the conjugate addition between triphenylphosphine (**1**) and 2-naphthyl 2,3-butadienoate (**3**)

Quantitative determination of the rate constant of the conjugate addition of phosphines to allenic esters was performed using a pseudo-first order approximation. The conjugate addition reaction was expected to obey a second order rate law, similar to the reported kinetic study of the conjugate addition of amines into allenic esters.[21] The approximation could be used to simplify a second order rate law into a first order rate law reaction, by performing the reaction using one substrate at a much higher concentration (>10x) than the other substrate. The concentration of the substrate with much higher concentration was assumed to be constant during the reaction. The rate of the reaction thus depended on the concentration of only one substrate, making the rate determination simpler.

According to the second order rate law

$$\text{Rate} = k[A][B] \quad (1)$$

If $[A] >> [B]$, $[A] \approx$ constant,

$$\text{Rate} = k'[B] \quad (2)$$

Where $k' = k[A]$ (3)

From (2), the rate is first order

$$\ln[B] = -k't + \ln[B]_0 \quad (4)$$

In this investigation, triphenylphosphine (**1**) was used at a large excess. The graphs in **Figure 6** were plotted between the ln[ethyl 2,3-butadienoate] values or ln[2-naphthyl 2,3-butadienoate] values versus time at the excess concentration (10x) of triphenylphosphine. The slope from these plots gave the pseudo first order rates (k') for compounds **2** and **3**. The k' values were found to be 3.85×10^{-4} s^{-1} for **2** and 3.11×10^{-3} s^{-1} for **3** at 10x excess concentration of triphenylphosphine. Conjugate addition reactions at different concentrations of triphenylphosphine (20x, 30x, and 40x) were performed, and their plots were constructed to determine k' values at different concentrations of triphenylphosphine.

a

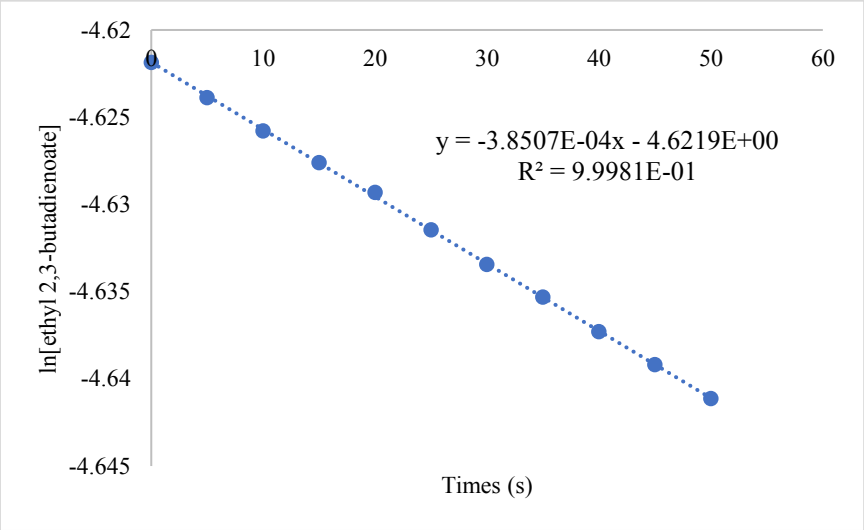

b

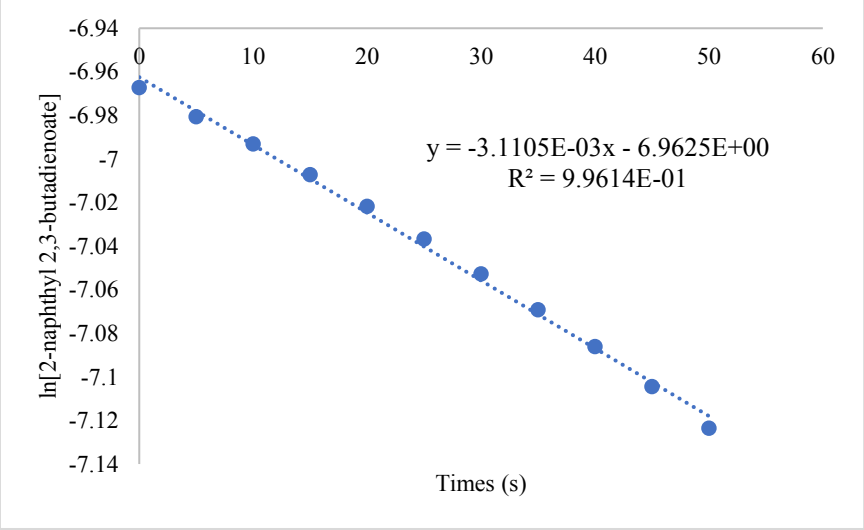

Figure 6 Examples of pseudo-first order plots between **a**) ln[ethyl 2,3-butadienoate] or **b**) [2-naphthyl 2,3-butadienoate] versus time (at 10x concentration of triphenylphosphine)

To determine the second order rate constant of the conjugate reaction, pseudo-first order rates (k' values) were plotted against the concentrations of triphenylphosphine. The slope of this new plot was the second order rate constant. The rate constant (k) of the conjugate addition reaction between ethyl 2,3-butadienoate (**2**) and triphenylphosphine was determined to be

$7.85x10^{-3}$ $M^{-1}s^{-1}$ (**Figure 7a**). The rate constant of the conjugate addition reaction between 2-naphthyl 2,3-butadienoate (**3**) and triphenylphosphine was determined to be $8.20x10^{-1}$ $M^{-1}s^{-1}$ (**Figure 7b**).

a

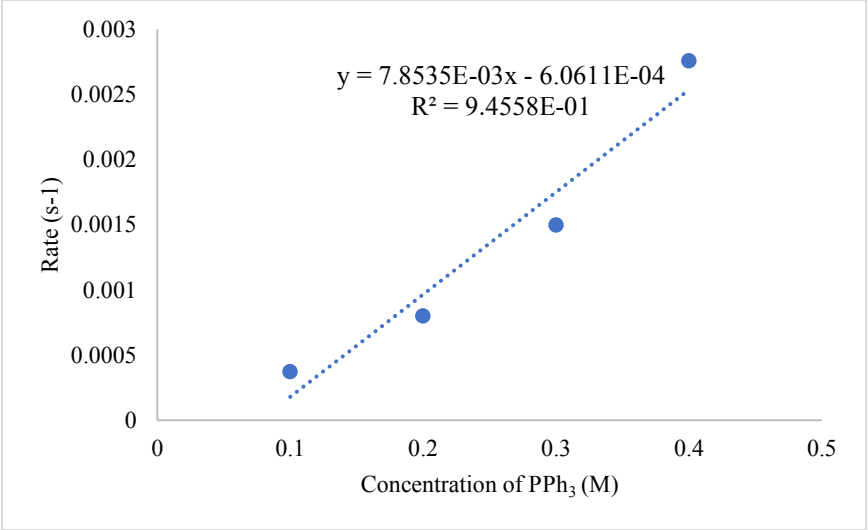

b

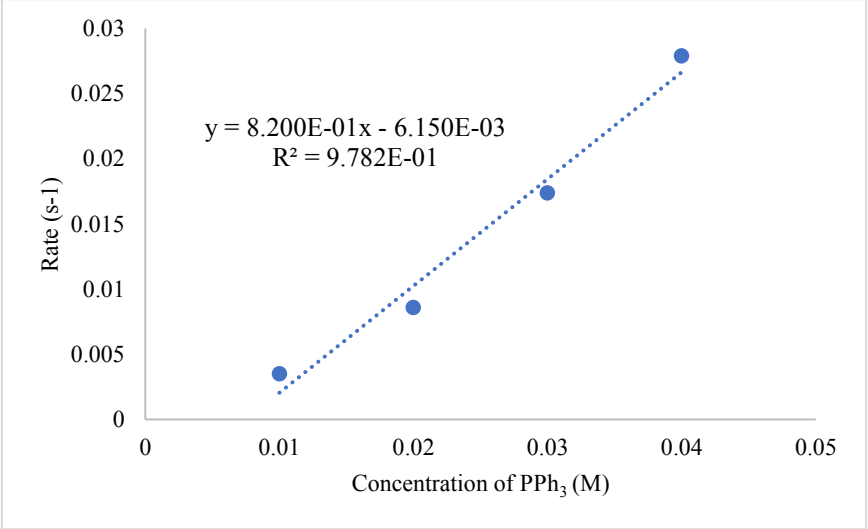

Figure 7 Plots between pseudo-first order rates (k' values) versus concentrations of triphenylphosphine (10x, 20x, 30x, and 40x) for the conjugate addition of **a**) ethyl 2,3-butadienoate (**2**) and **b**) 2-naphthyl 2,3-butadienoate (**3**)

The rate of the conjugate addition of ethyl 2,3-butadienoate (**2**) was approximately 2 order of magnitude slower than that of 2-naphthyl 2,3-butadienoate (**3**). The presence of an aromatic group at the alcohol component of the allenic ester may play an important role in increasing the electrophilicity of the ester, making the conjugate addition faster. This result may potentially be used to develop a synthetic method based on conjugate addition of phosphine into allenic esters with a better kinetic behavior by changing the substrate from alkyl allenic esters to aryl allenic esters.

Conclusion:

The second order rate constants of conjugate addition reaction of alkyl and aryl allenic esters were studied using a pseudo-first order approximation. The kinetic behavior of aryl allenic esters is approximately 100–time faster. This result may provide a solution to improve the kinetic behavior of many synthetic methods involving a conjugate addition of phosphine into allenic esters, and thereby making these methods more efficient. Application of the finding to develop new synthetic methods with better kinetic profile is currently undergoing and will be reported in due course.

Acknowledgements:

This research was supported by the Development and Promotion of Science and Technology Talents Project (DPST); the Institute for the Promotion of Teaching Science and Technology (IPST); Center of Excellence for Innovation in Chemistry (PERCH-CIC), Ministry of Higher Education, Science, Research and Innovation; and the Department of Chemistry, Faculty of Science, Mahidol University. We also thank the Central Instrumental Facility (CIF) at the Faculty of Science, Mahidol University for research facilities.

References:

1. Huang Y, Ji X, Ma Z, ŁężYk M, Xue Y, Zhao H. RSC Adv. 2021;11:23922-23942.
2. Raveendran P, Fu J, Wallen SL. J Am Chem Soc. 2003;125:13940-13941.
3. Varma RS. ACS Sustainable Chem Eng. 2016;4:5866-5878.
4. Phukan S, Mahanta A, Kakati D, Rashid MH. Appl Organometal Chem. 2019;33:4758-4767.
5. Yamaguchi S, Fujita S, Nakajima K, Yamazoe S, Yamasaki J, Mizugaki T, Mitsudome T. ACS Sustainable Chem Eng. 2021;9:6347-6354.
6. Kozell V, McLaughlin M, Strappaveccia G, Santoro S, Bivona LA, Aprile C, Gruttadauria M, Vaccaro L. Sustainable Chem Eng. 2016;4:7209-7216.
7. Stamm P, Etl F, Maia ACD, Dötterl S, Schulz S. J Org Chem. 2021;86:5245-5254.
8. He X, Xie M, Li R, Choy PY, Tang Q, Shang Y, Kwong FY. Org Lett. 2020;22: 4306-4310.
9. Bella M, Jørgensen KA. J Am Chem Soc. 2004;126:5672-5673.
10. Hajra A, Yoshikai N, Nakamura E. Org Lett. 2006;8:4153-4155.
11. Zhu D, Yan X, Ren A, Xie W, Duan Z. Anal Chim Acta. 2019;1058:136-145.
12. Xu CR, Qiu L, Pan CY, Hong CY, Hao ZY. Bioconjugate Chem. 2018;29:3203-3212.
13. Yamada K, Mogi Y, Mohamed MA, Takasu K, Tomioka K. Org Lett. 2012;14:5868-5871.
14. Germain N, Guénée L, Mauduit M, Alexakis A. Org Lett. 2014;16:118-121.
15. Alexakis A, March S. J Org Chem. 2002;67:8753-8757.
16. Ni H, Yu Z, Yao W, Lan Y, Ullah N, Lu Y. Chem Sci. 2017;8:5699-5704.
17. Wurz RP, Fu GC. J Am Chem Soc. 2005;127:12234-12235.
18. Chen Z, Zhu G, Jiang Q, Xiao D, Cao P, Zhang X. J Org Chem. 1998;63:5631-5635.
19. Tiambeng TN, Roberts DS, Brown KA, Zhu Y, Chen B, Wu Z, Mitchell SD, Guardado-Alvarez TM, Jin S, Ge Y. Nat Commun. 2020;11:3903-3920.
20. Conner ML, Brown MK. J Org Chem. 2016;81:8050-8060.
21. Kiattisewee C, Kaidad A, Jiarpinitnun C, Luanphaisarnnont T. Monatsh Chem. 2018;149: 1059-1068.
22. Zhang K, Cai L, Jiang X, Garcia-Garibay MA, Kwon O. J Am Chem Soc. 2015;137:11258-11261.

Synthesis and characterization of nearly uniform biobased polymer particles for use as antimicrobial film

Latdamanee Phutthatha[1], Utt Eiamprasert[1], Chariya Kaewsaneha[2], Preeyaporn Chaiyasat[1,3], Amorn Chaiyasat[1, 3*]

[1] Department of Chemistry, Faculty of Science and Technology, Rajamangala University of Technology Thanyaburi, Klong 6, Thanyaburi, Pathumthani 12110, Thailand
[2] School of Bio-Chemical Engineering and Technology, Sirindhorn International Institute of Technology (SIIT), Thammasat University, Pathum Thani 12121, Thailand
[3]Advanced Materials Design Development (AMDD) Research Unit, Faculty of Science and Technology, Rajamangala University of Technology Thanyaburi, Pathum Thani 12110, Thailand

*e-mail: a_chaiyasat@mail.rmutt.ac.th

Abstract:

This research aims to synthesize and characterize biobased polymer particles for use as antimicrobial film. Because of the environmental problem based on the residual of fossil polymer, using biopolymer is an excellent solution. Eugenol is hydroxyphenyl propene extracted from essential oils is mainly used in both foods and cosmetic. It is showed significant antimicrobial activity. Therefore, eugenol was copolymerized with tetrahydrogeraniol in emulsion polymerization to produce biobased polymer particles in this work.Eugenol and tetrahydrogeraniol were first introduced double bond via esterification with methacrylic anhydride to obtain methacrylate eugenol (ME) and methacrylate tetrahydrogeraniol (THGMA), respectively. Before emulsion polymerization, a macro chain transfer again (macro CTA) of poly(2-(dimethylamino)ethyl methacrylate)-iodide (PDMAEMA-I) was synthesized. After that, PDMAEMA-I was used as a macro CTA in the emulsion polymerization of ME and THGMA copolymer (P(ME-THGHA)). The obtained polymer particles were highly stable with a zeta potential of over +30 mV. Moreover, they were spherical with a nearly uniform size (pdi < 0.09) of about 200 nm. P(ME-THGHA) particle represented high-performance antimicrobial property. In addition, the biobased polymer emulsion can easily coat on various substrates with adhesive properties due to low glass transition temperature.

SYNTHESIS AND GENETIC CODE EXPANSION OF PLASTIC-DEGRADING ENZYMES FOR DETECTION OF MICROPLASTICS

Jariya Jitdee,[1] Piyachat Meesawat,[2] Bhumrapee Eiamthong,[2] Chayasith Uttamapinant,[2] Worawan Bhanthumnavin[1,*]

[1]Department of Chemistry, Faculty of Science, Chulalongkorn University, Bangkok 10330, Thailand

[2]School of Biomolecular Science and Engineering, Vidyasirimedhi Institute of Science and Technology (VISTEC), Rayong 21210, Thailand

*e-mail: worawan.b@chula.ac.th

Abstract:

Petrochemical plastics can degrade into the size level of microplastics. One source of microplastics is polyethylene terephthalate (PET or PETE). Enzymes used to degrade PET have been reported. In our work, we wish to repurpose the activity of PET-degrading enzymes, into PET-detecting enzymes, and use the engineered enzyme for microplastic detection, *via* enzyme engineering to create enzyme variants which can form covalent adducts with microplastic particles. The enzyme-microplastic adduct is generated *via* the use of 2,3-diaminopropionic acid (DAP) derivative, which we will incorporate in place of the catalytic serine residue at the active site of *I. sakeinesis*—PETase *via* the genetic code expansion technique. Working toward this goal, we have successfully synthesized 2,3-diaminopropionic acid (DAP) derivative. The synthetic methods were carried out with improvements to the protocols previously reported in literature, in seven steps and an overall yield of 7 %. The compound was structurally characterized by nuclear magnetic resonance (NMR) spectroscopy. Moreover, we cloned an expression vector for PETase, in which its catalytic serine codon is replaced with an amber stop codon—marking it as a site for unnatural amino acid incorporation and demonstrated the expression of the PETase protein bearing an unnatural amino at the active site serine in *Escherichia coli* using amber-suppressor pyrrolysyl tRNA and its corresponding pyrrolysyl-tRNA synthetase enzyme.

Introduction:

Petrochemical plastics are non-biodegradable and can persist in the environment for a long time and can also be degraded into the size level of microplastics (≤5 mm) which is harmful to the environment. One type of plastics majorly contributing as a source of microplastics is polyethylene terephthalate (PET), which are primarily used in clothes, packaging, and drink bottles. PET is a thermoplastic that can be produced by the reaction of ethylene glycol and terephthalic acid. Unlike most plastics, PET can be biochemically degraded with many hydrolytic enzymes such as *Ideonella sakeiensis*—PETase.

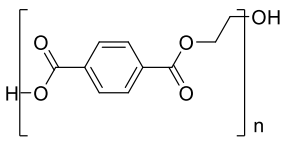

Figure 1. Polyethylene terephthalate (PET) structure

In 2016, Yoshida *et al.*[1] began a search for microbial PET degraders from natural sources. The microbials were cultivated in test tubes containing a defined culture medium supplemented with a PET film. One sediment sample containing a distinct microbial consortium had been observed to form on the PET film and showed clear signs of degradation (induced morphological change in the PET film). *Ideonella sakaiensis* 201-F6, the bacterium capable of degrading PET, was isolated. Compared to previously known PET-degrading enzymes, this newly identified enzyme, PETase, had a higher performance for PET degradation.

In 2018, Austin *et al.*[2] had also studied the adaptations that contribute to the substrate specificity of PETase. The active site of PETase, the catalytic triad, comprises Ser160, Asp206, and His237. The improvement and development of the microplastics detection method by synthesizing an unnatural amino acid to use in a genetic code expansion technique with plastic degrading enzyme were reported.

Genetic code expansion is a technique used for modification of genetic code. Specific codons have been re-allocated to encode an unnatural amino acid. The key to expanding the genetic code are aminoacyl-tRNA synthetase/tRNA (aaRS/tRNA) pairs which specifically with unnatural amino acid. This system must be orthogonal with the native translation system, including endogenous tRNA, natural amino acids, as well as endogenous aaRS. As for this work, a 2,3-diaminopropionic acid (DAP) derivative will be used as an unnatural amino acid due to the similarity of the structure of this DAP derivative with serine which is an active site of PETase that plays an important role to bind to the carbonyl carbon by a hydroxyl group and break the ester bond of PET.

The general mechanism of PET-PETase degradation of polymer chains is shown in **Figure 2a**. On the other hand, DAP-modified enzymes **(Figure 2b)** could act as a nucleophile to form a stable covalent substrate-enzyme adduct *via* an amide linkage with the substrates of enzymes without degrading it.

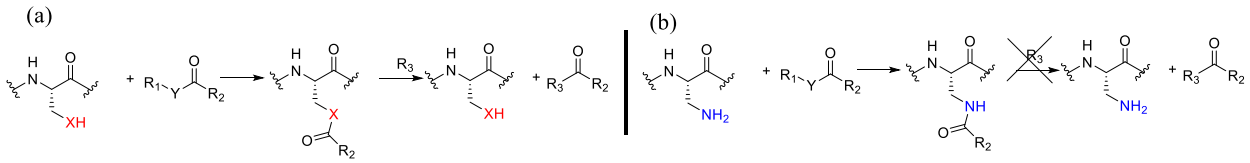

Figure 2. (a) Active-site Ser or Cys residues react with C=O that collapse to acyl-enzyme intermediates. (b) replacing Cys or Ser with DAP derivative may result in a first intermediate resistant to cleavage.[3]

Structural similarity of DAP derivative to cysteine and serine makes it challenging to discover an aminoacyl-tRNA synthetase that is selective for DAP derivative *in vivo*. Huguenin-Dezot *et al.*[3] had found a DAP derivative that is able to evolve *Methanosarcina barkeri (Mb) pyrrolysyl*-tRNA synthetase (PylRS)/tRNA (Pyl/CUA) pair variant for the site-specific incorporation.

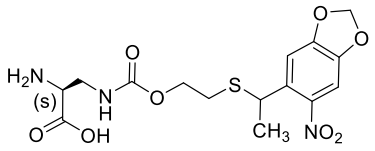

1

Figure 3. Structure of protected version of DAP derivative ((2S)-2-amino-3-{[(2-{[1-(6-nitrobenzo[d][1,3]dioxol-5-yl)ethyl]thio}ethoxy)carbonyl]amino}propanoic acid TFA salt (1))

Therefore, we wish to convert a PET-degrading enzyme into a sensitive PET detector by using a genetic encode expansion technique to insert DAP derivative.

Methodology:

Materials and instruments: All chemicals and reagents were purchased from commercial sources and used without further purification. NMR spectra were obtained from Jeol NMR spectrometer and were recorded at 500 MHz for ^{1}H NMR experiments and 126 MHz for ^{13}C NMR experiments, using deuterated dimethylsulfoxide (DMSO-d_6), deuterated chloroform ($CDCl_3$), and deuterated methanol-d_4 as NMR solvents. The chemical shifts (δ) are reported in parts per million (ppm) relative to tetramethylsilane signal (δ_H = 0.00 ppm) employing residual protonated signal of deuterated solvent as a reference. In the genetic code expansion technique. Cloning: T100TM Thermal Cycler (Bio-rad), Mupid-exU (Submarine electrophoresis system, Run agarose gel). Protein expression: Mini-PROTEAN Tetra system (SDS-PAGE and Western blot, Bio-rad), Shaker (Innova44, eppendorf), Nanodro.

Synthesis of 2,3-diaminopropionic acid derivative: The synthesis was carried out using a method of Nicolas Huguenin-Dezot's[3] with a major modification in some steps and slight modification in others. The desired compound was successfully synthesized in seven steps.

*Step 1: Synthesis of 4',5'-methylenedioxy-2'-nitroacetophenone (**3**):*

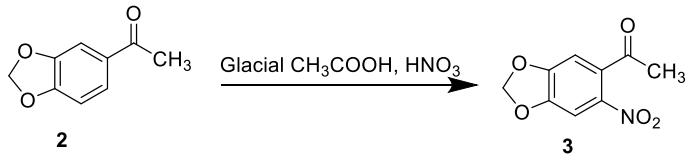

2 **3**

3',4'-(methylenedioxy) acetophenone (**2**) (4 g, 0.02 mol, 1 eq) was dissolved in glacial acetic acid (24 mL) and stirred for 30 min to dissolve. The solution was added dropwise to a 250 mL 3 necked-round bottom flask containing HNO_3 (44 mL) at 0 °C (4 Pasteur pipettes / 5 min), over a 30 minute addition. The reaction mixture was maintained at 0 °C during addition and for an additional 30 minutes while stirring under a N_2 atmosphere. Then the mixture was warmed to 40 °C and stirred under N_2 atmosphere for an additional 30 minuntes. The mixture was cooled to room temperature and poured slowly into ice in a beaker (500 mL). A yellow precipitate appeared. The mixture was then stirred for 15 min and filtered using suction pump. The dark yellow gum was neutralized with Na_2CO_3, washed with water and dried in an oven. The crude yellow solid was then purified by column chromatography on SiO_2 (eluent: 1:1 CH_2Cl_2: Hexane to 100% CH_2Cl_2). The desired compound, 4',5'-Methylenedioxy-2'-nitroacetophenone (**3**) was obtained as the major product (1.8048 g, 35%): R_f= 0.66. ^{1}H NMR (500 MHz, $CDCl_3$) δ (ppm): δ 7.54 (s, 1H), 6.74 (s, 1H), 6.16 (s, 2H), 2.48 (s, 3H). ^{13}C NMR (126 MHz, $CDCl_3$) δ (ppm): 199.35, 152.82, 148.95, 140.24, 135.29, 106.32, 104.96, 103.72, 30.36.

*Step 2: Synthesis of (R,S)-1-[4',5'-(Methylenedioxy)-2'-nitrophenyl]ethanol (**4**):*

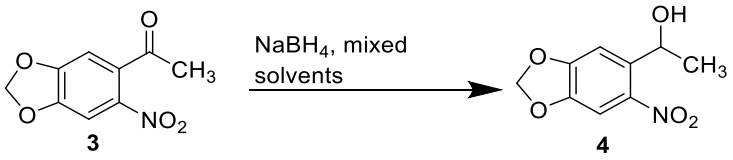

3 **4**

4',5'-Methylenedioxy-2'-nitroacetophenone (**3**) (1.2528 g, 5.99 mmol, 1eq) was suspended in a solvent mixture of CH_2Cl_2 (12 mL), CH_3OH (19 mL), and absolute ethanol (13 mL) in 100 mL single-necked round bottom flask. $NaBH_4$ granules (0.3408 g, 9 mmol,

1.5 eq.) were added in 4 portions to the yellow suspension every 5 min (total time = 20 min addition) at 15 °C. After the addition was complete, the reaction mixture was stirred at room temperature for 30 min (or until the starting material was completely consumed as determined by TLC analysis: SiO_2, TLC eluent: 100% CH_2Cl_2). The reaction was quenched by the addition of acetone (3 mL), left stirring at room temperature for 10 min. The mixture was then evaporated to dryness under reduced pressure to obtain a yellow solid. The solid was re-dissolved in CH_2Cl_2 (10 mL×2) and washed with saturated aq. NH_4Cl solution (30 mL×2) and finally with saturated aq. NaCl solution (30 mL×2). The organic layer was separated, dried over anhydrous Na_2SO_4, filtered, and evaporated to dryness in an oven to obtain (*R*,*S*)-1-[4',5'-(Methylenedioxy)-2'-nitrophenyl]ethanol (**4**) as a yellow solid (1.2569 g, 99%): R_f= 0.33. ^{1}H NMR (500 MHz, $CDCl_3$) δ (ppm): 7.45 (s, 1H), 7.26 (s, 1H), 6.12 – 6.08 (m, 2H), 5.45 (qd, *J* = 6.2, 3 Hz, 1H), 2.26 (d, *J* = 3.5 Hz, 1H), 1.53 (d, *J* = 6.3 Hz, 3H). ^{13}C NMR (126 MHz, $CDCl_3$) δ (ppm): 152.51, 147.02, 141.61, 139.05, 106.44, 105.23, 103.01, 65.78, 24.28.

*Step 3: Synthesis of (R,S)-1- bromo-1-[4',5'-(methylenedioxy)-2'-nitrophenyl]ethane (**5**)*

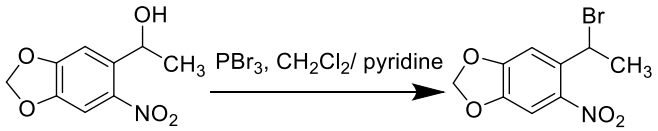

4 **5**

A 250 mL, 3 necked round-bottom flask was dried in an oven for 15 minute then further with a heat gun and purged with N_2 gas. After that, the flask was charged with (*R*,*S*)-1-[4',5'-(Methylenedioxy)-2'-nitrophenyl]ethanol (**4**) (1.9741 g, 9.34 mmol, 1 eq) dissolved in CH_2Cl_2 (30 mL) was adde. The flask was then wrapped with aluminium foil to shield from the light and stirred at 0 °C under N_2 atmosphere. After 20 min, PBr_3 (0.4 mL, 4.25 mmol, 0.45 eq) was added drop wise into the reaction mixture for 10 min using syringe pump at 0 °C. Subsequently, pyridine (0.07 mL) was added and the solution was stirred at 0˚C for 15 min. Afterwards, the reaction was warmed to room temperature and stirred continuously for 30 min. The reaction was judged to be complete by TLC analysis (SiO_2, TLC eluent: 100% CH_2Cl_2). It was then cooled to 0 °C and stirred for 5 min then quenched by addition of MeOH (2 mL), brought to room temperature and stirred for 10 min under N_2 atmosphere. After the quenching was complete, the reaction mixture was evaporated to dryness under reduced pressure. The yellow gum was dissolved in CH_2Cl_2 (15 mL), and saturated aq. $NaHCO_3$ solution (2×20mL). The contents were loaded into a separatory funnel, the organic phase was washed sequentially with a saturated aq. $NaHCO_3$ solution (2×30 mL) and saturated aq. NaCl solution (3×40 mL). The organic layer was separated, dried over anhydrous Na_2SO_4, filtered, and evaporated to dryness to obtain a yellow gum. The crude product was purified by column chromatography on SiO_2 (eluent: CH_2Cl_2:Hexane (2:8 to 1:1)) to obtain (*R*,*S*)-1- bromo-1-[4',5'-(methylenedioxy)-2'-nitrophenyl]ethane (**5**) in 77% yield (1.9832 g). ^{1}H NMR (500 MHz, $CDCl_3$) δ (ppm): 7.33 (s, 1H), 7.25 (s, 1H), 6.11 (d, *J* = 1.0 Hz, 1H), 5.88 (q, *J* = 6.8 Hz, 1H), 2.02 (d, *J* = 6.8 Hz, 3H). ^{13}C NMR (126 MHz, $CDCl_3$) δ (ppm): 152.06, 147.67, 141.60, 134.79, 108.75, 105.05, 103.27, 42.77, 27.59.

*Step 4: Synthesis of 2-{[1-(6-Nitrobenzo[d][1,3]dioxol-5-yl)ethyl]thio}ethan-1-ol (**6**):*

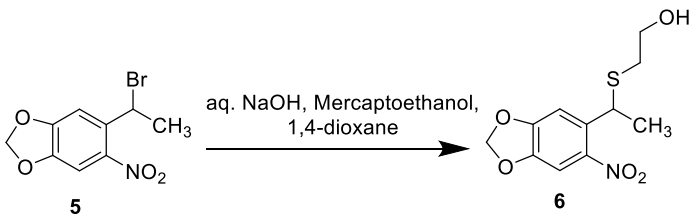

5 6

A freshly prepared solution of NaOH (0.5 M, 2 mL, 1 mmol, 1.2 eq) was loaded in a 3 necked round bottom flask and degassed. After 10 min, mercaptoethanol (0.08 mL, 1.13 mmol, 1.36 eq) was added to the flask and degassing was continued for a further 10 min. Separately, the starting (*R*,*S*)-1- bromo-1-[4',5'-(methylenedioxy)-2'-nitrophenyl]ethane (**5**) (0.2288 g, 0.83 mmol, 1 eq) was dissolved in 1,4-dioxane (2 mL) and degassed for 10 min. Both round bottom flasks were wrapped with aluminium foil to shield from the light. Compound **5** was transferred into the flask containing NaOH and mercaptoethanol using cannula over 10 min in the dark under positive pressure of N_2 gas. A yellow precipitate formed, which was then dissolved with 1,4-dioxane (2 mL). The solution was subjected to a sonication for 20 min in the dark until the reaction mixture became a clear yellow solution. The contents were left stirring for 6 h at room temperature in the dark under N_2 atmosphere. The reaction was judged to be complete by TLC (3:7 EtOAC:Hexane) and the solvent was evaporated. The yellow gum was then extracted with EtOAC (10mL×2), aq. NH_4Cl (10 mL×2), and saturated NaCl (10mL×3). The organic layer was separated and dried over anhydrous Na_2SO_4, filtered, and the solvent was evaporated. The crude product was purified by column chromatography on SiO_2 (eluent: 15% EtOAc:Hexane to 50%EtOAc/Hexane) in the dark to obtain 2-{[1-(6-Nitrobenzo[d][1,3]dioxol-5-yl)ethyl]thio}ethan-1-ol (**6**) as a sticky yellow paste (0.2121 g, 94%). ^{1}H NMR (500 MHz, $CDCl_3$) δ (ppm): δ 7.27 (s, 1H), 7.26 (s, 1H), 6.09 (d, *J* = 3.6 Hz, 2H), 4.78 (q, *J* = 7.0 Hz, 1H), 3.68 – 3.57 (m, 2H), 2.62 – 2.48 (m, 2H), 1.55 (d, *J* = 7.0 Hz, 3H). ^{13}C NMR (126 MHz, $CDCl_3$) δ (ppm): 152.26, 146.88, 143.95, 136.02, 107.97, 104.76, 103.01, 60.85, 38.31, 34.88, 23.15.

Step 5: Synthesis of 2-((1-(6-nitrobenzo[d][1,3]dioxol-5-yl)ethyl)thio)ethyl (4-nitrophenyl) carbonate (7):

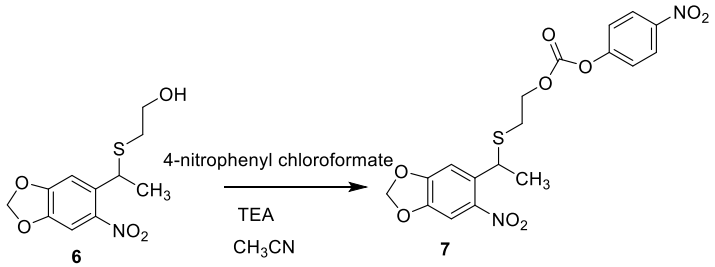

6 7

A 3 necked round-bottomed flask was dried in an oven. The dry flask was charged with a solution of 2-{[1-(6-Nitrobenzo[d][1,3]dioxol-5-yl)ethyl]thio}ethan-1-ol (**6**) (0.2897 g, 1.06 mmol, 1 eq) in dry CH_3CN. 4-Nitrophenyl chloroformate (0.3598 g, 1.78 mmol, 1.68 eq) was added in one portion, followed by addition of triethylamine (0.6 mL, 4.30 mmol, 4.05 eq). The reaction turned turbid and white precipitates were formed. The solution was then left stirring at rt for 6 hours. The reaction was judged to be complete by TLC (3:7 EtOAC:Hexane) and was evaporated to dryness under reduced pressure. The product was purified by column chromatography on SiO_2 (eluent: 5% to 30% EtOAc:Hexane) in the dark to obtain 2-((1-(6-nitrobenzo[d][1,3]dioxol-5-yl)ethyl)thio)ethyl (4-nitrophenyl) carbonate (**7**) as a yellow gum (0.2853 g, 65%) with an R_f = 0.48 (SiO_2 plate, EtOAc/n-hexane = 3:7). ^{1}H NMR (500 MHz, $CDCl_3$) δ (ppm): 8.27 (d, *J* = 9.2 Hz, 2H), 7.38 (d, *J* = 9.1 Hz, 2H), 7.30 (s,

1H), 7.27 (s, 1H), 6.09 (s, 2H), 4.87 (q, *J* = 7.0 Hz, 1H), 4.32 (qt, *J* = 11.1, 6.6 Hz, 2H), 2.77 – 2.63 (m, 2H), 1.56 (s, 3H). ^{13}C NMR (126 MHz, $CDCl_3$) δ (ppm): 155.56, 152.32, 152.08, 146.75, 145.51, 143.37, 135.72, 125.39, 121.86, 107.97, 104.88, 103.05, 68.01, 38.98, 31.02, 23.14.

*Step 6: Synthesis of (2S)-2-[(tert-Butoxycarbonyl)amino]-3-{[(2-{[1-(6-nitrobenzo [d][1,3]dioxol-5-yl)ethyl] thio}ethoxy)carbonyl]amino}propanoic acid (**8**):*

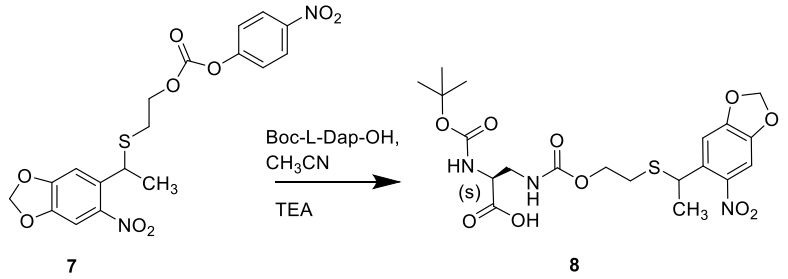

7 8

Compound **7** (0.2853 g, 0.65 mmol, 1 eq) was dissolved with dry CH_3CN (8 mL) and transferred into a three-necked round bottom flask. Boc-Dap-OH (0.1460 g, 0.71 mmol, 1.09 eq) was added in one portion to the flask, followed by addition of triethylamine (0.55mL, 3.94 mmol, 6.06 eq). The reaction flask was wrapped with aluminium foil and stirred at rt for 6 h under N_2 atmosphere. After this time, the reaction was judged to be complete by TLC (98:2 EtOAc:CH_3COOH), then dried under reduced pressure. This was purified by column chromatography (eluent: 50:50 EtOAc:Hexane to 100% EtOAc then 5%>40% MeOH:EtOAc) in the dark to obtain(2*S*)-2-[(*tert*-butoxycarbonyl)amino]-3-{[(2-{[1-(6-nitrobenzo[d][1,3]dioxol-5-yl)ethyl]thio}ethoxy)carbonyl]amino}propanoic acid (**8**) as a yellow gum (0.3098 g, 94 %). ^{1}H NMR (500 MHz, $CDCl_3$) δ (ppm): 7.28 (s, 1H), 7.25 (s, 1H), 6.09 (d, *J* = 15.1 Hz, 2H), 5.99 (s, 1H), 5.86 (s, 1H), 4.78 (q, *J* = 7.0 Hz, 1H), 4.17 (s, 1H), 4.07 – 4.01 (m, 2H), 3.51 (s, 2H), 2.51 (tq, *J* = 13.3, 6.7 Hz, 2H), 1.51 (d, *J* = 6.9 Hz, 3H), 1.38 (s, 9H). ^{13}C NMR (126 MHz, $CDCl_3$) δ (ppm): 173.74, 157.92, 156.49,152.06, 146.86, 143.25, 136.20, 108.11, 104.76, 103.07, 81.77, 64.63, 54.44, 43.24, 38.94, 32.02, 28.43.

*Step 7: Synthesis of (2S)-2-amino-3-{[(2-{[1-(6- nitrobenzo[d][1,3]dioxol-5 yl)ethyl]thio}ethoxy) carbonyl]amino}propanoic acid TFA (**1**):*

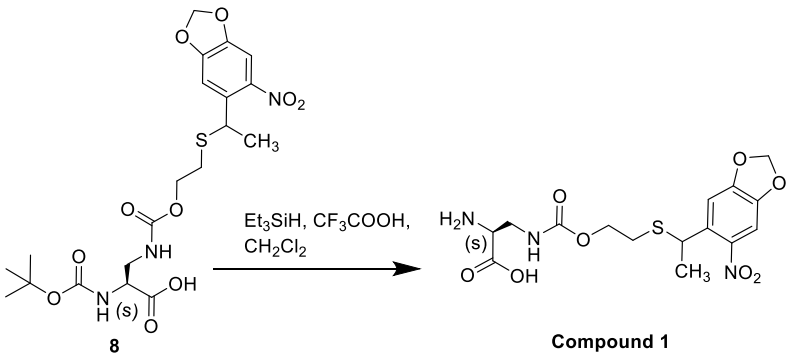

8 Compound 1

Compound **8** (0.5044 g, 1.00 mmol, 1 eq) was dissolved with CH_2Cl_2 (12 mL) and loaded to a dry single necked round bottom flask, the flask was wrapped with aluminium foil to shield from the light, stirred at rt for 5 min. After that Et_3SiH (1.6 mL, 10.01 mmol, 10.01 eq) was added to the solution and stirred for 5 min. Subsequently, CF_3COOH (1.6 mL, 20.89 mmol, 20.89 eq) was added drop-wise *via* syringe over 5 min at room temperature. The reaction mixture tuned from light yellow to dark yellow color and was left stirring at room

temperature for 2 h. The reaction was judged to complete by TLC (98:2 EtOAc:CH_3COOH), then the solution was concentrated to dryness under reduced pressure to obtain a yellow-brown gum. This was dissolved with CH_3OH (10 mL) and evaporated to dryness under reduced pressure; repeated five time to remove any CF_3COOH, Et_3SiH, H_2O. The yellow gum was dissolved with CH_3OH (10 mL) and transferred to dry three-necked round bottomed flask. The solution was stirred at 0 °C under N_2 atmosphere for 10 min. Et_2O was then transferred into the flask *via* cannula under positive pressure of N_2 gas while the contents were vigorously stirred. A white yellow precipitate formed, and the contents stirred vigorously at 0 °C for 30 min, then r.t. for an additional 2 h. The precipitate was then filtered and washed with dry Et_2O (3×10 mL), followed by dry *n*-hexane (10 mL×2). The product was left dried at room temperature overnight in the dark to obtain (2*S*)-2-amino-3-{[(2-{[1-(6-nitrobenzo[d][1,3]dioxol-5-yl)ethyl]thio}ethoxy)carbonyl]amino}propanoic acid TFA salt (**1**) as a pale-yellow powder (0.1942 g, 48%). ^{1}H NMR (500 MHz, $CDCl_3$) δ (ppm): 7.31 (s, 1H), 7.27 (s, 1H), 6.11 (d, *J* = 4.5 Hz, 2H), 4.96 (dt, *J* = 11.8, 6.4 Hz, 56H), 4.73 (q, *J* = 6.9 Hz, 1H), 4.15 – 3.98 (m, 3H), 3.69 (ddd, *J* = 14.9, 5.1, 3.9 Hz, 1H), 3.54 (dd, *J* = 15.1, 6.2 Hz, 2H), 2.66 – 2.47 (m, 2H), 1.52 (d, *J* = 6.9 Hz, 3H). ^{13}C NMR (126 MHz, Methanol-d4) δ (ppm): 168.48, 161.37, 160.02, 152.08, 147.12, 141.04, 135.37, 115.84, 107.4, 104.03, 103.33, 64.34,53.61,40.47,38.44, 29.86, 21.69.

Genetic code expansion:

Cloning of an expression construct for His6-SUMO-PETase(S160TAG):

The coding sequence for *Ideonella sakeiensis* PETase gene with its signal peptide removed was PCR-amplified using Q5® High-Fidelity DNA Polymerase from pET21b-Is-PETase plasmid (Addgene # 112202) with primers PETase_S160*_F (23-mer, GATGGGCTGGtagATGGGGGGCG) and PETase_S160*_R (20-mer, ACACCCATGCGGGCAGTATC). During the amplification, the catalytic residue S160 in the PETase gene was replaced by an amber stop codon (TAG). The PETase gene was circularized by a KLD reaction in a thermal cycler. The PETase gene was circularized by a KLD reaction in a thermal cycler.

The putatively mutated PETase gene was amplified by primers nonsigPETase_OVL_SUMO_F (cagagaacagattggtggatcccagaccaatccgtatgcgcg) and PETase_TGA_OVL_XhoI_R(AGCAGCCTAGGTTAATTAAGCCTCGAGTCAggaacagttcg cggtgcg) to generate overhangs for Gibson assembly. The solubility tag SUMO gene was amplified from pC013 - Twinstrep-SUMO-huLwCas13a using primers His-SuMO pHND-OVL F (TTTGTTTAACTTTAAGAAGGAGATGTACATATGcatcatcatcatcatcacagcagc) and His-SUMO R (ggatccaccaatctgttctctgtgag). An acceptor plasmid p-His-Lipoyl_TEV-Strep plasmid (a kind gift from Jason Chin, MRC LMB, United Kingdom) was digested with NdeI and XhoI, and assembled with the PETase and SUMO inserts *via* Gibson assembly before transformation into *E.coli*. Plasmids were isolated from single colonies and sequence-analyzed for confirmation.

Expression of His6-SUMO-PETase(S160BocK) in E.coli BL21:

Two expression plasmids for His6-SUMO-PETase(S160TAG) **(**Figure 4) and *Methanosarcina Mazei* pyrrolysyl tRNA synthetase and its cognate amber-suppresor tRNAPyl were transformed into *E. coli* BL21. Upon reaching the OD_{600} of 0.5-0.6, the culture was supplemented with 1mM tert-butyloxycarbonyl lysine (BocK) and 1mM isopropyl-β-D thiogalactopyranoside (IPTG), and protein expression was carried out at 37 °C for 4 h. Whole cell lysates were electrophoretically separated in SDS-PAGE, and analyzed *via* Coomassie blue staining and anti-His6 western blotting.

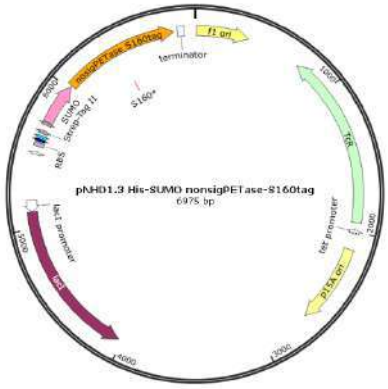

Figure 4. An expression construct for His6-SUMO-PETase(S160TAG)

Results and Discussion:

Synthesis of 2,3-diaminopropionic acid derivative: The model compound 2,3-diaminopropionic acid derivative (**1**) was successfully synthesized in seven steps. Starting from step 1, a nitration reaction by an addition of HNO_3 to an aromatic ring of 3',4' (methylenedioxy)acetophenone (**2**) at the meta position. First, the starting compound dissolved in glacial acetic acid was added dropwise to a nitric acid flask, then warm-up to 40 °C. In the first modification, we decrease the time of warm-up from 2.5 h to 30 min. The product compound was obtained as a major product among three other by-products. The second modification is to dilute an acidic precipitate with Na_2CO_3 in a filtration step before purification by column chromatography without recrystallization. The method has been optimized to give a compound **3** in a higher percent yield from 7% to 35% in a shorter period of time.

Step 2 involved a reduction reaction of ketone **3** using granules $NaBH_4$. The procedure has been optimized by decreasing the time from 4 h to 30 min. The yields were as high as those reported yields of **4**.

In step 3, in order to replace the hydroxyl group in **4** by bromine, PBr_3 was used as a reagent. The reaction conditions were optimized in a small scale and could be reproduced at a larger scale. In addition, optimization by decreasing the reaction time showed no effect on the reaction and resulted in even a higher percent yield of **5** than those reported in the reference.[3] The product of this step is relatively sensitive to light and everything needs to be done with minimum light.

A substitution reaction in step 4 was carried out by an addition of mercaptoethanol to replace the bromine atom in compound **5**. First, a freshly prepared NaOH solution was mixed with mercaptoethanol. After that, the degassed solution of starting compound **5** in 1,4-dioxane was transferred into the flask containing a mixture of aq. NaOH and mercaptoethanol solution by using a cannula under positive pressure N_2 gas. It was found that with a fresh 1,4-dioxane, the reaction proceeded really cleanly without any by-products. In addition, the stirring time was decreased from overnight to 6 hours without any effect to the reaction yield of **6**. However, the reaction was required to be performed in the dark.

In step 5, compound **6** was dissolved in CH_3CN followed by addition of *N*,*N*′-disuccinimidyl carbonate (DSC) and triethylamine. Firstly, the reaction was carried out with DSC as a reagent. However, the reaction failed everytime. No reaction was observed. Changing the solvent system from CH_3CN to THF or 1,4-dioxane could not get the reation going. Attempts have been made to change the base from DIPEA to TEA. Again, the starting material did not react. Due to the unsuccessful result of the use of DSC, 4-nitrophenyl chloroformate had been used as a substitute. The reaction of **6** proceeded nicely and the

product compound **7** was obtained in good yield. An additional optimization was to decrease the reaction time from overnight to 6 h. A stable crude product was obtained using 4-nitrophenyl chloroformate as a reagent. Subsequent purification with column chromatography resulted in pure compound **7**.

In step 6, attempts to treat a solution of **7** with Boc-Dap-OH failed to give the product. Boc-Dap-OH is an amino acid molecule that is a zwitterion. Therefore, the addition of a base is required to prepare a nucleophilic amino acid. DIPEA and TEA have been used for comparison. It was observed that this procedure was successfully when TEA was used. With DIPEA, the reaction was incomplete, and by-products were also obtained. On the other hand, as TEA is a slightly stronger base, reaction had gone to completion. Apart from that, the time of the procedure was decreased from overnight to 6 h to give compound **8**.

In the last step, Et_3SiH and CF_3COOH were used as a reagent to dispose of the Boc-group. It was found that in order to get good yield of the desired DAP derivative (compound **1**), the precipitate should not be allowed to dry at rt more than 1 night to reduce the decomposition.

Genetic code expansion:

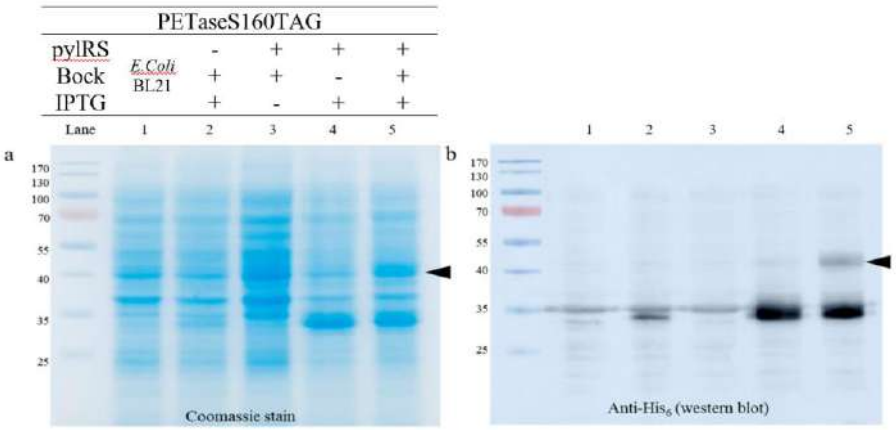

Figure 5. SDS-PAGE analysis. (a) Different components of PETaseS160TAG were expressed in *E. coli* BL21 (Coomassie stain). (b) anti-His6 western blotting.

The expression analysis is as shown in **Figure 5a**. Lane 1: Empty *E.coli* BL 21. Lane 2: A Combination of PETase plasmid, unnatural amino acid (BocK), and IPTG without pylRS plasmid results in incomplete expression. Lane 3: A combination of pylRS plasmid and unnatural amino acid (BocK), without inducing by IPTG results in the protein is unexpressed. Lane 4: A combination of 2 plasmids and IPTG, without unnatural amino acid (BocK), results in incomplete expression protein was observed (30.1 kDa). Land 5: A combination of all components result in a preferred protein was observed (44 kDa). The reaction was confirmed by anti-His_6 western blotting to identify the complex (**Figure 5b**).

Conclusion:

The photocaged derivative of 2,3-diaminopropionic acid (Compound **1**) was successfully synthesized in seven steps and 7 % overall yield. The synthesis was carried out with a major modification in several steps over a previously published protocol. The reaction conditions were optimized at a small scale and could be reproduced at a larger scale. A system for genetic code expansion of *Ideonella sakeinesis* PETase, allowing incorporation of unnatural amino acids—including the DAP derivative into PETase was prepared. Our near future goals are to produce DAP-modified PETase capable of forming a stable covalent

adduct with PET plastics, and develop a sensitive and specific PET microplastic detection assay based on this engineered enzyme.

Acknowledgements:

This research is supported by Department of Chemistry, Faculty of Science, Chulalongkorn University, Bangkok and School of Biomolecular Science and Engineering, Vidyasirimedhi Institute of Science and Technology (VISTEC), Rayong.

References:

1. Yoshida S, Hiraga K, Takehana T, Taniguchi I, Yamaji H, Maeda Y, Toyohara K, Miyamoto K, Kimura Y, Oda, K. Science. 2016;351:1196-1199.
2. Austin H.P, Allen M.D, Donohoe B.S, Rorrer N. A, Kearns F.L, Silveira R.L, Pollard B.C, Dominick G, Duman R, Omari K.E, Mykhaylyk V, Wagner A, Michener W.E, Amore A, Skaf M.S, Crowley M.F, Thorne A.W, Johnson C.W, Woodcock H. L, McGeehan J.E, Beckham G.T. PNAS. 2018;115:E4350-E4357.
3. Huguenin-Dezot N, Alonzo D.A, Heberlig G.W, Mahesh M, Nguyen D.P, Dornan M.H, Boddy C.N, Schmeing T.M, Chin, J.W. Nature. 2019;565:112–117.

THERMAL STABILITY OF ENCAPSULATED RED HOMMALI RICE EXTRACT WITH BETA-CYCLODEXTRINS

Wannisa Vichit[1], Nisakorn Saewan[1,2]*, Nattakan Panyachariwat[1,2], Ampa Jimtaisong[1,2]
[1]School of Cosmetic Science, Mae Fah Luang University, Chiang Rai, 57100, Thailand
[2]Cosmetic and Beauty Innovations for Sustainable Development (CBIS) Research Group, Mae Fah Luang University, Chiang Rai, 57100, Thailand
*e-mail: nisakorn@mfu.ac.th

Abstract:
Red hommali rice (RHR), a well-known red rice in Thailand, provides high antioxidant and anti-inflammation activities due to high phenolic and procyanidin contents. However, these compounds are comparatively thermal sensitive and unstable. The aim of the present study was to encapsulate the extract by molecular inclusion with beta-cyclodextrin by using freeze drying method. The inclusion complexes were evaluated for the percentage of encapsulation efficacy. The encapsulated RHR extract powder was characterized by fourier transform infrared spectroscopic (FTIR), differential scanning calorimetry (DSC), and scanning electron microscope (SEM). The stability of the encapsulated powders was evaluated in solution form in comparison to free extract. Freeze drying methods provided a high encapsulation efficacy of RHR extract (88.40 and 86.33 % for total phenolic and procyanidin content, respectively). The encapsulated RHR extract in beta-cyclodextrin enhanced the remaining of phenolic and procyanidin compounds about 2.5 times under high temperature (50 °C). The results showed that beta-cyclodextrin can be used as wall material for encapsulation of RHR and protected the active molecules against thermal degradation which increase the potential of using this extract in cosmetic formulation.

Introduction:
Red rice (*Oryza sativa* L.) is a pigmented rice that has antioxidant, anti-inflammatory, and anticarcinogenic potential (Laokuldilok, Shoemaker, Jongkaewwattana, & Tulyathan, 2010; Oki et al., 2002; Ratanavalachai et al., 2012). RHR is well known as commercial red rice cultivar of Thailand that possesses antioxidant activities with phenolic and procyanidin compounds and has potential use in cosmetics, functional food and pharmaceuticals (Vichit & Saewan, 2015). However, red rice extract is not stable and easily susceptible to degradation through many factors such as light, pH, and temperature. Thus, in order to use RHR extract as a cosmetic ingredient, the stability of extract is required. To enhance stability of natural extract, various techniques such as metal complexation, co-crystallization, and encapsulation were used to protect active compounds against oxidation, evaporation, reaction or migration (Munin & Edwards-Lévy, 2011; Madene, Jacquot, Scher, & Desobry, 2006). One of the most popular encapsulation techniques is to form an inclusion complex with cyclodextrins which are chemically and physically stable molecules with cyclic oligosaccharides consisting of six, seven, or eight units, linked by 1,4-α-glucosidic bonds and called α-, β-, and γ-cyclodextrins, respectively (Del Valle, 2004). Beta-cyclodextrin has ability to form inclusion complexes with a wide variety of organic compounds which enter partly into the cavity of beta-cyclodextrins (Mourtzinosa, Papadakisb, Igoumenidisc, & Karathanosca, 2011).

In this study, the encapsulation of RHR extract was prepared by inclusion complex with beta-cyclodextrin by using freeze drying method. The encapsulated powder was

evaluated for its percentage of encapsulation efficacy and characterized by FTIR, DSC, and SEM. Moreover, thermal stability was studied in solution by storage at 50 °C for 6 weeks and evaluated the remaining of phenolics and procyanidins.

Methodology:

Materials

RHR was collected in Chiang Rai, Thailand. The rice (5 kg) was extracted with 8 L of ethanol for 24 hours then filter though Whatman No. 1 filter paper and removed the solvent by rotary evaporator. The extract was washed with hexane and stored at 4 °C until used. Beta-cyclodextrin, folin-ciocalteu reagent, gallic acid, potassium bromide, sodium bicarbonate, and vanillin were purchased from Sigma-Aldrich Co., USA. Ethanol and sulfuric acid were purchased from Merck, Germany.

Preparation of encapsulation

Beta-cyclodextrin (BC) was selected to use as wall material. The ratio between RHR extract (RHR) and the wall material was 1:2. The extract solution was slowly added dropwise into the beaker containing BC solution with magnetic stirring. This complex mixture was kept under constant stirring for 24 h. After completing the reaction, the complex solution was frozen by cooling ethanol bath and then lyophilized in a freeze dryer (Freezone 6 plus, Labconco, USA).

The percentage of encapsulation efficiency

The encapsulation efficiency was determined by centrifugation method (Yallapu, Gupta, Jaggi, & Chauhan, 2010). The encapsulated powder was dissolved in ethanol (25 mg/ml) and centrifuged at 4 °C at 14,000 rpm for 1 h. Supernatant layer consisted of unencapsulated extract, while the encapsulated was precipitated. Then, both fractions were determined amount of total phenolic content (Folin-Ciocalteu method) and total procyanidin content (vanillin method) (Vichit & Saewan, 2015). For total phenolic content, the 20 µl of samples were mixed with 20 µl of Folin-ciocalteu reagent, 125 µl of 7% sodium hydrogen carbonate and 50 µl of water. The mixture was incubated at room temperature for 60 min. Then the sample measured the absorbance at 750 nm and calculated as mg gallic acid equivalents. For total procyanidin content, the 20 µl of samples were added with 100 µl of 1% vanillin in sulfuric acid. The mixture was incubated at room temperature for 15 min. Then, the sample determined the absorbance at 500 nm and expressed as epicatechin equivalent. Encapsulation efficiency (% EE) was calculated using the following equation:

Encapsulation efficiency (%) = (Encapsulated RHR content/Total RHR content) x 100

Fourier transform infrared spectroscopic (FTIR)

The sample was prepared by using diffuse reflectance method with potassium bromide powder (KBr). FTIR spectra of sample powders were obtained in range 400 to 4000 cm^{-1}, using a FTIR spectrophotometer (Spectrum GX, PerkinElmer, USA). The resolution was 1.0 cm^{-1} and the spectra were the result of average 4 scans.

Differential scanning calorimetry (DSC)

The differential scanning calorimetry was performed by using a 822e, Mettler Toledo, Switzerland. Approximately 2 mg of sample powders were placed in aluminum pans with lid. The samples were heated from room temperature to 360°C at a heating rate of 10 °C/min. The measurements were carried out under dry nitrogen at the flow rate of 50 ml/min.

Scanning electron microscope (SEM)

The external morphology of sample powders was analyzed by scanning electron microscope (SEM). The sample powders were prepared by gold coating with sputter coater. Samples were observed under the scanning electron microscopy 1450 VP, LEO, Germany.

Thermal stability study

Thermal stability of free extract and encapsulated extract were studied at 5 % in solution by storage at 50 °C for 6 weeks. The remaining phenolics and procyanidins was evaluated.

Results and Discussion:

Encapsulated RHR extract powder

An inclusion complex of RHR extract with beta-cyclodextrin (BC) was prepared upon mixing in aqueous solution and subsequent freeze dying. The encapsulation of RHR was successfully prepared with the percentages of yield were 96.82 % based on powder weight. Freeze dry method produced light pink softly sponge powder as shown in Fig.1.

Figure 1.
Encapsulated RHR extract powder

The percentage of encapsulation efficiency

Encapsulation efficiency of encapsulated RHR was quantified by total phenolic and results showed that encapsulated RHR with freeze drying methods provided a high encapsulation efficacy at 88.40 % for total phenolic content. This suggests that RHR is suitable for inclusion into BC.

Fourier transform infrared spectroscopic (FTIR)

The encapsulation of RHR in BC was confirmed using FTIR for comparing chemical bonds and molecular structure. The FTIR spectra of BC, free RHR, and encapsulated RHR were shown in Fig. 2. The spectral region of O-H stretching (3,550 – 3,200 cm^{-1}), alkyl C-H stretching (2,950 – 2,850 cm^{-1}) and aromatic C=C bending (1,700-1,550 cm^{-1}) spectral region was obviously shifted after encapsulation. The spectral region of O-H stretching of BC and free RHR were found at 3,369 and 3,383 cm^{-1}, respectively. The peak of encapsulated RHR was shifted to 3,371 cm^{-1}. Free RHR appeared C-H stretching aliphatic band at 2,854 cm^{-1}, but it disappeared after encapsulation. Moreover, the major peak of free RHR was 1,741, 1,711, and 1,633 cm^{-1} can be correlated to the stretching of aromatic C=O in extract. This spectral region was obviously shifted to 1,731 and 1,637 cm^{-1} after encapsulated in BC. These shifts indicated the occurring of complex formation between RHR and wall materials.

Differential scanning calorimetry (DSC)

The thermogram of BC showed two endothermic peaks at 167 and 315 °C (Fig. 3a), while free RHR showed two endothermic peaks at 158 and 314 °C (Fig. 3b). The DSC analysis showed difference endothermic (167 and 301 °C) and exothermic (315 °C) peaks for encapsulated RHR (Fig. 3c). These results indicated that there is major interaction between RHR extract and beta-cyclodextrin. The change of peak related the total enthalpy change and generally considered as a proof of complex formation.

Scanning electron microscope (SEM)

SEM microphotographs of BC and encapsulated RHR were shown in Fig. 4. Microphotograph of BC appeared as polygon shape and encapsulated RHR showed as sponge sheet. The drastic change in the surface morphology of encapsulated powder indicated the presence of a new solid phase which was due to molecular encapsulation with freeze drying method of the rice extract in BC complex.

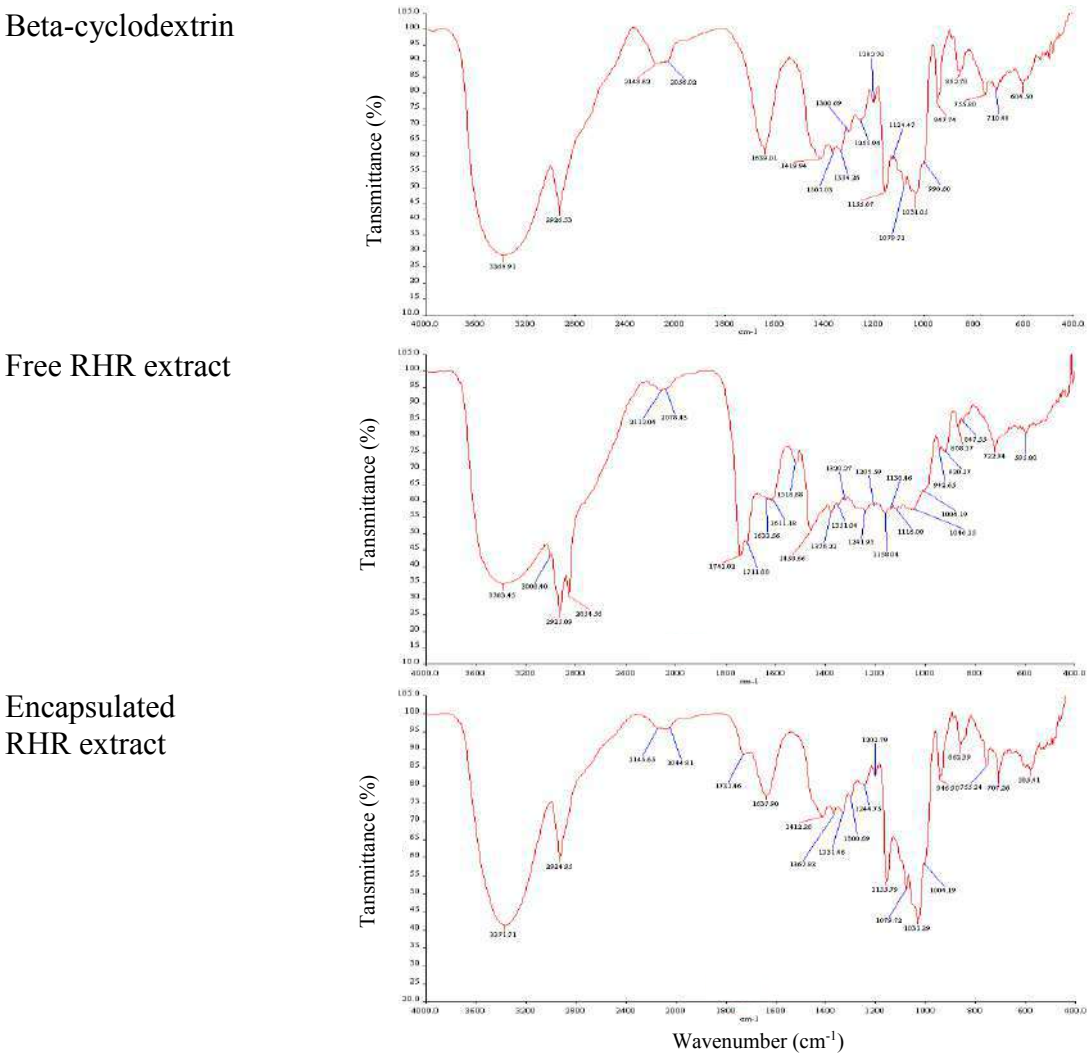

Figure 2.
IR spectra of beta-cyclodextrin, free and encapsulated RHR extracts

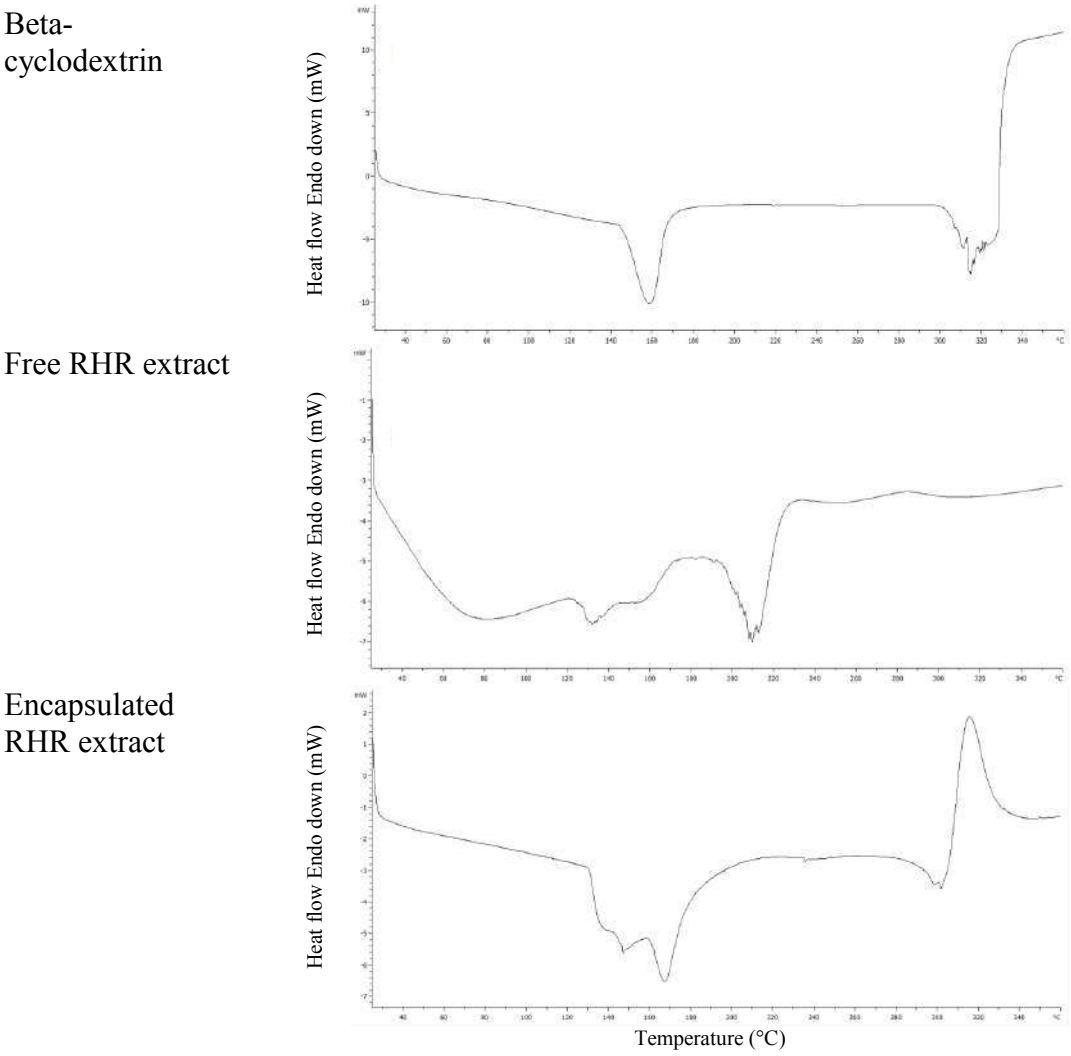

Figure 3.
DSC thermograms of beta-cyclodextrin, free and encapsulated RHR extracts

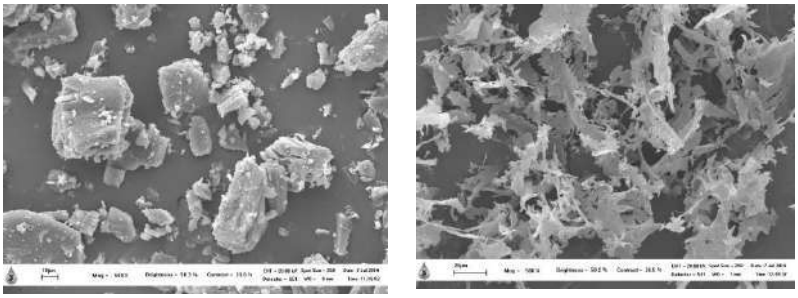

Figure 4.
Scanning electron microphotographs of beta-cyclodextrin (left) and encapsulated RHR extracts (right)

Thermal stability study

According to stability of phenolic compound of RHR extract affected by temperature, in this study, thermal degradation of phenolic and procyanidin of encapsulated RHR was investigated at 50°C with storage period of 6 weeks. Physical appearance of free and

encapsulated RHR solution were shown in Fig. 5. The free RHR was high color changing from yellow to dark red at 6 weeks. While the color of encapsulated RHR showed slower release of extract and more stable.

As expected, the degradation of free extract was attributed to large decrease in phenolic (38.03 %) and procynidin (24.75 %), as shown in Fig. 6. The results showed that the encapsulated RHR was slowly degraded comparison to free extract which indicated the protection of the phenolic and procyanidin molecules (77.70 and 59.61 %, respectively). Moreover, the encapsulated was higher half-life than free extract which showed more than 2.5 times in both phenolic and procyanidin contents. The result concluded that the interaction strength between the extract and BC preserved the complex against thermal degradation providing higher stability of phenolic and procyanidin molecule.

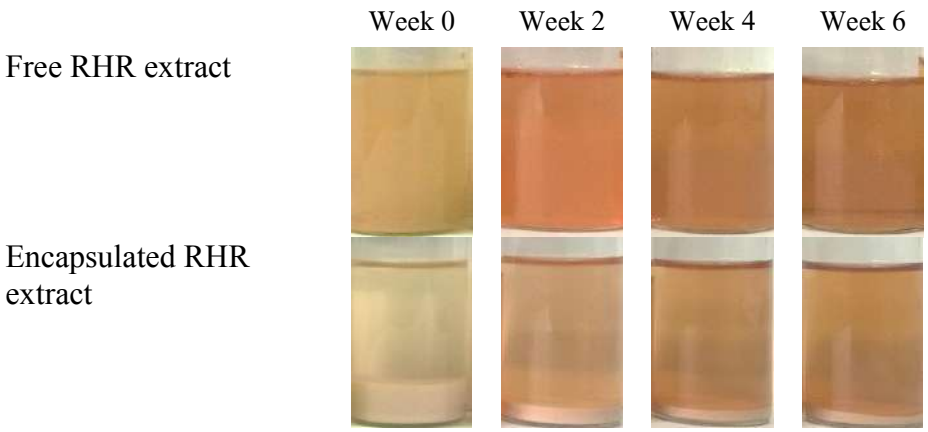

Figure 5.
The appearance of free and encapsulated RHR extract in solution at 50 °C

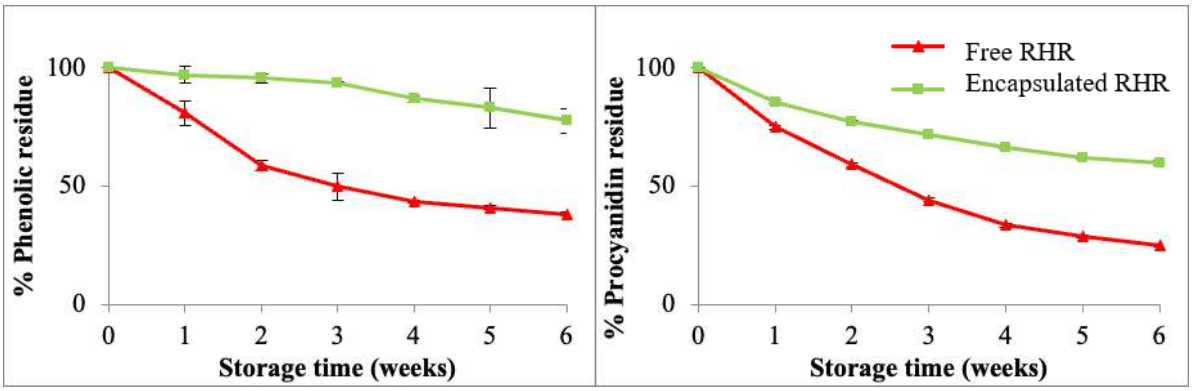

Figure 6.
Thermal stability of free and encapsulated RHR extract
by evaluated the phenolic (left) and procyanidin degradation (right)

Conclusion:

The encapsulated RHR extract powder produced from freeze drying methods providing a high encapsulation efficacy and enhancing stability of phenolic and procynidin content in RHR extract. Therefore, the increasing of shelf life of these bioactive compounds can be done by encapsulating with BC and encapsulated RHR extract was considered as high potential for using as a natural active ingredient in cosmetic products.

Acknowledgements:
The authors also would like to thanks Mae Fah Luang University for providing scientific equipment and facilities for this work.

References:
1. Del Valle EMM. Proc Biochem. 2004;39(9):1033-1046.
2. Laokuldilok T, Shoemaker CF, Jongkaewwattana S, Tulyathan V. J Agri Food Chem. 2010;59(1):193-199.
3. Madene A, Jacquot M, Scher J, Desobry S. Inter J Food Sci Tech. 2006;41(1):1-21.
4. Mourtzinosa I, Papadakisb S. E, Igoumenidisc P, Karathanosca VT. Procedia Food Sci. 2011;1:1679-1685.
5. Munin A, Edwards-Lévy F. Pharmaceu. 2011;3(4):793-829.
6. Oki T, Masuda M, Kobayashi M, Nishiba Y, Furuta S, Suda I, Sato T. J Agri Food Chem. 2002:50(26):7524-7529.
7. Ratanavalachai T, Thitiorul S, Tanuchit S, Jansom C, Uttama S, Itharat A. J Med Ass Thai. 2012;95(1):S109-S114.
8. Vichit W, Saewan N. Inter J Pharm Pharmaceu Sci. 2015;7(7):329 -334.
9. Yallapu MM, Gupta BK, Jaggi M, Chauhan SC. J Colloid Inter Sci. 2010;351(1):19-29.

ANTI-INFLAMMATORY ACTIVITY OF THE ETHANOLIC EXTRACT OF THE POWDER FORMULA OF A FUNGUS *Cordyceps sinensis* AND THREE HERBS (*Panax ginseng*, *Kaempferia parviflora* AND *Houttuynia cordata*) IN RAW264.7 CELLS

Siriprapha Sudthonglang, Suppawit Utaiwat, Thanaset Senawong*
Department of Biochemistry, Faculty of Science, Khon Kaen University, Thailand
*e-mail: sthanaset@kku.ac.th

Abstract:
The powder formula of a fungus *Cordyceps sinensis* and three herbs (*Panax ginseng*, *Kaempferia parviflora* and *Houttuynia cordata*) (PFCPKH) was developed as a dietary supplement to enhance health. In this research, the anti-inflammatory activity of ethanolic extract of PFCPKH was studied in RAW264.7 cells. The cell viability remained above 90% until a concentration of 60 µg/mL. The concentrations of ethanolic extract of PFCPKH used for studying the anti-inflammatory activity were 10-60 µg/mL. All these concentrations exhibited anti-inflammatory activity as the nitric oxide (NO) and prostaglandin E2 (PGE_2) productions in RAW264.7 cells were significantly decreased ($p < 0.05$) when compared with lipopolysaccharide (LPS) alone treatment. The identified phenolic compounds of PFCPKH ethanolic extract including *p*-Hydroxybenzoic acid, Vanillic acid, Syringic acid, *p*-Coumaric acid, Ferulic acid and Sinapinic acid. The results demonstrated for the first time the anti-inflammatory activity of the industrialized PFCPKH *in vitro*, thus validating its promising anti-inflammation potential.

Introduction:

Inflammation is an immune response against harmful stimuli such as tissue injury by physical and chemical exposure, viral or bacterial infection. Normal part of defense response is acute inflammation subsequently is chronic inflammation[1]. During the inflammation process many type of immune cells are activated[1]. The macrophage is a very important role in the inflammatory process that secrete pro-inflammatory mediators and cytokines such as tumor necrosis factor alpha (TNF-α), interleukin-1 (IL-1) and interleukin-6 (IL-6) as well as increase nitric oxide (NO), prostaglandin E2 (PGE_2)[2] to stimuli inflammatory cells produce the secondary mediators in the inflammatory process. Lipopolysaccharide (LPS) is a component of the gram-negative bacterial cell wall, can stimulate macrophage cells to release inflammatory cytokines[3] and activate immune cells to up-regulate inflammatory state. However, the overproduction of mediators leads to chronic inflammation and can cause many diseases such as ischemic heart disease, stroke, cancer, diabetes mellitus, chronic kidney disease, non-alcoholic fatty liver disease (NAFLD), auto-immune and neurodegenerative conditions[4]. The mechanisms of action for anti-inflammatory drugs are focus on therapies that inhibit pro-inflammatory cytokine release as well as decrease leucocyte recruitment[5]. At present, the generally used inflammatory drugs are non-steroidal anti-inflammatory drugs (NSAIDs) but many NSAIDs have adverse reactions to the digestive system such as gastrointestinal bleeding including cardiovascular side effects, and NSAID induced nephrotoxicity[6]. Therefore, the herbs that have a property in anti-inflammatory effects but

fewer side effects, maybe alternative for inflammation treatment and beneficial in the development of anti-inflammatory drugs for safe drugs in clinical use.

Herbal medicines are widely used in Asian countries[7]. Thai people still use many herbs for health maintenance and therapy in addition many herbals were processed as dietary supplements. Recently, the powder formula of a fungus *Cordyceps sinensis* and three herbs consist of *Panax ginseng*, *Kaempferia parviflora* and *Houttuynia cordata* (PFCPKH) was developed as a dietary supplement and commercially available. *Cordyceps sinensis* is a valuable macro fungus and has various pharmacological activities from chemical constituents. Most of them have a key role to regulate our immune system and several compounds have potential in anti-viral and anti-tumor activity[8]. The three herbs that were mixed in the formula were improving from their biological activity and use for enhancing health. First, *P. ginseng* is a well-known that the ethanolic extract of ginseng has anti-inflammatory properties in LPS activated-macrophage cells[9] and patients with nonalcoholic fatty liver disease[10]. Second, *K. parviflora* is one of the plants in the Zingiberaceae family, locally known in Thai as kra-chai-dam has been reported about the active constituents for anti-allergic activity[11]. In addition, the flavonoid extract also has anti-inflammatory activity in RAW264.7 cells and animals, these results supported the traditional use of *K. parviflora* for the treatment of inflammation[11]. Third, *H. cordata* Thunb. or "Khao-tong," or "Plu-khao" in Thai, is a plant in Saururaceae family. This plant has been widely used for a long in the eastern and southern regions of Asia[12], which is used as an anti-pyretic, detoxicant and anti-inflammatory agent[13,14]. In summary, these three plants possessed many pharmacological activities such as anti-aging, anti-cancer[13,15,16], immune stimulation and anti-oxidant activity[18], and anti-allergic activity[19]. However, the anti-inflammatory activity of PFCPKH has not been studied yet. Thus, the objective of this study is to investigate the anti-inflammatory activity of PFCPKH ethanolic extract through the inhibition of nitric oxide (NO) and prostaglandin E2 (PGE_2) production in LPS-stimulated RAW macrophage 264.7 cells and demonstrate the phenolic acid profile of the PFCPKH product.

Methodology:

Materials

The powder formula of a fungus *Cordyceps sinensis* (62.19%) and three herbs [*Panax ginseng* (21.14%), *Kaempferia parviflora* (12.94%) and *Houttuynia cordata* (3.73%)] was obtained from the Prolac (Thailand) Co., Ltd. in Lamphun Province, Thailand. The plant ingredients of this PFCPKH were calculated from the information labels on the containers. RAW264.7 cells were obtained from Dr. Pramote Mahakunakorn, Faculty of Pharmaceutical Science, Khon Kaen University. LPS (*E. coli* 0111: B4) and diclofenac sodium were purchased from Sigma-Aldrich (St. Louis, MO, USA). Griess reagent for nitrite determination was purchased from Promega (Madison, WI). PGE_2 ELISA kit was purchased from Abcam (ab133021) (Cambridge, MA, USA). RPMI 1640 medium, fetal bovine serum (FBS), trypsin-EDTA and penicillin/streptomycin were obtained from Gibco/Invitrogen Crop. (Grand Island, NY, USA).

Cell culture

The murine macrophage cell line RAW264.7 were cultured in RPMI 1640 medium supplemented with 10% fetal bovine serum (FBS), penicillin (100 U/mL), and streptomycin (100 µg/mL). The cells were incubated at 37°C with a humidified atmosphere of 5% CO_2.

Preparation of ethanolic extract

15 g of the powder formula of the *C. sinensis* and three herbs (*P. ginseng*, *K. parviflora* and *H. cordata*) obtained from Prolac (Thailand) Co., Ltd., Lamphun province, Thailand, was

dissolved in 150 mL of absolute ethanol by stirring for 48 h at room temperature, and then subjected to centrifugation at 4,807 x g for 10 min. After the supernatant was filtered, evaporation and dryness were ultimately achieved under a gentle stream of nitrogen to obtain a final product with a yield of 12.47%w/w before kept at -20 °C until use.

Cell viability assay

The viability of RAW264.7 cells was determined by the MTT (3-(4,5-dimethylthiazolyl)-2-2,5-diphenyltetrazolium bromide) assay. RAW264.7 cells were seeded in 96-well plate at a density of 8×10^3 cells/well. After 24 h, the cells were treated with various concentrations (10-200 µg/mL) of PFCPKH ethanolic extract and the control group was treated with 0.5% DMSO for 24 h at 37 ºC. After indicated times, the MTT solution was added to each well and incubated for 2.5 hours at 37 ºC. After removing the solution, formazan crystal in each well was dissolved by DMSO and measured at the absorbance at 550 nm with a microplate reader (Biochrom, UK). The absorbance at 655 nm was used as a reference wavelength.

Nitrite determination

The nitrite concentration in the cultured medium of RAW264.7 cells was measured as an indicator of NO production according to Griess reaction with some modification[20]. RAW264.7 cells were seeded in 96-well plate (2×10^4 cells/well) in volume of 200 µL for 22 h before the cell culture medium was replaced with serum-free (1% FBS) medium. Thereafter, the cells were pre-treated with various concentrations of the PFCPKH ethanolic extract, and the positive control group was treated with 25 µg/mL diclofenac (DCF) for 2 h. After 2 h incubation, the cells were incubated with LPS (1 µg/mL) for 24 h. After that, the cultured medium from each well was collected and mixed with Griess reagents (Promega, USA), incubated in darkness at room temperature for 10 min. The absorbance was then measured at 540 nm by a microplate reader.

Prostaglandin E_2 (PGE_2) determination.

The RAW264.7 cells were seeded in 96-well plate (200 µL/well, 1×10^5 cells/mL) and incubated for 22 h before replacing the cell culture medium with serum-free (1% FBS) medium. The cells were then pre-treated with various concentrations of the PFCPKH ethanolic extract except the treatment of positive control group that was treated with 25 µg/mL Diclofenac (DCF) for 2 h and LPS (1 µg/mL) before an incubation for 24 h. Thereafter, PGE_2 was determined by using PGE_2 ELISA kit (Abcam, USA) according to manufacturer's protocol.

HPLC analysis

Inertsil®-ODS-4 C18 column (4.6 mm i.d. x 250 mm, 5 µm particle size) was used for reverse phase HPLC to analyze the phenolic acid compositions in PFCPKH ethanolic extract following the condition as previously described with some modifications[21]. The gradient of mobile phase for determination of the phenolic acid was composed of solvents A (100% acetonitrile) and B (1% acetic acid in deionized water) as follows: 0 min, 3% A: 97% B; 2 min, 8% A: 92% B; 10 min, 8% A: 92% B; 20 min, 10% A: 90% B; 50 min, 20% A: 80% B, 60 min, 20% A: 80% B, 100 min, 3% A: 97% B. The accuracy of phenolic acid identification was ensured by 1 µg of *m*-hydroxybenzaldehyde as the internal standard.

Statistical analysis

Data are expressed as mean ± SD from two or three independent experiments. The data analysis was performed by one-way ANOVA coupled with Duncan's post hoc test. Differences were significant at * $p < 0.05$, ** $p < 0.01$, and # $p < 0.001$)

Results and Discussion:

Effect of PFCPKH ethanolic extract on cell viability in RAW264.7 cells

To investigate the anti-inflammatory activity of PFCPKH ethanolic extract *in vitro* (LPS-induced RAW264.7 model), the concentrations that are safe for RAW264.7 cells were determined. The PFCPKH ethanolic extract was tested for its toxicity to the cells by MTT assay with concentrations of 10-200 µg/mL (Fig. 1). The concentrations that cause a percentage of cell viability more than 90% were considered as safe to the cells. The concentrations of PFCPKH ethanolic extract 10-60 µg/mL were considered safe for the cells with cell viability more than 90% compared with control (C). Therefore, the concentrations of 10-60 µg/mL were used in the subsequent experiments.

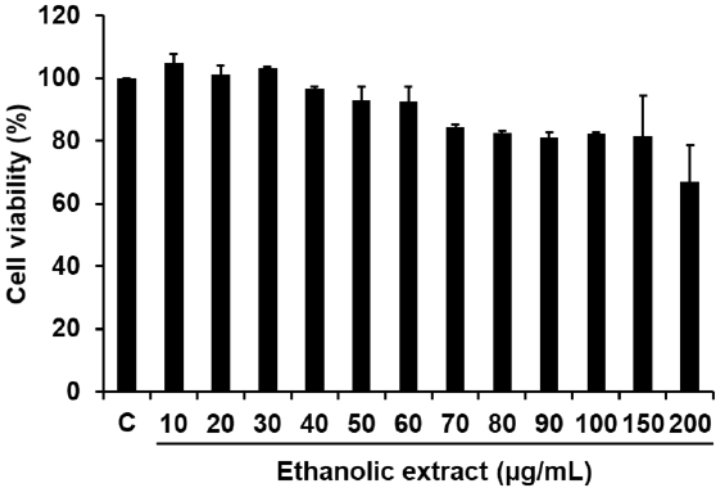

Figure 1. Effect of PFCPKH ethanolic extract on cell viability of RAW264.7 cells. RAW264.7 cells were incubated with various concentrations (10-200 µg/mL) of PFCPKH ethanolic extract in RPMI 1640 medium for 24 h. Cell viability was assessed by MTT assay. The result was reported as a percentage compared with untreated control and expressed as means ± SD of three dependent experiments.

Effect of PFCPKH ethanolic extract on nitric oxide (NO) production of LPS-stimulated RAW264.7cells

PFCPKH ethanolic extract at concentrations of 10-60 µg/mL inhibited the NO production (Fig. 2) under 1 µg/mL LPS-stimulated condition. The control groups of cells without and with LPS-treatments were also demonstrated. LPS treatment stimulated RAW264.7 cells to increase NO production. The ethanolic extract inhibited NO production significantly (* $p < 0.05$ and # $p < 0.001$) in a dose-dependent manner as shown by less nitrite concentration than that of control (LPS-treatment alone) 20-83% and DCF inhibited NO production 35% of control. The positive control diclofenac (DCF; NSAID drug) at a concentration of 25 µg/mL was also studied comparatively and lipopolysaccharide (LPS) from gram-negative bacteria at a concentration of 1 µg/mL was used in the present study for activation of inflammatory response of RAW264.7 cells, and this concentration was not toxic to RAW264.7 cells, consistent with the result from a previous study[22].

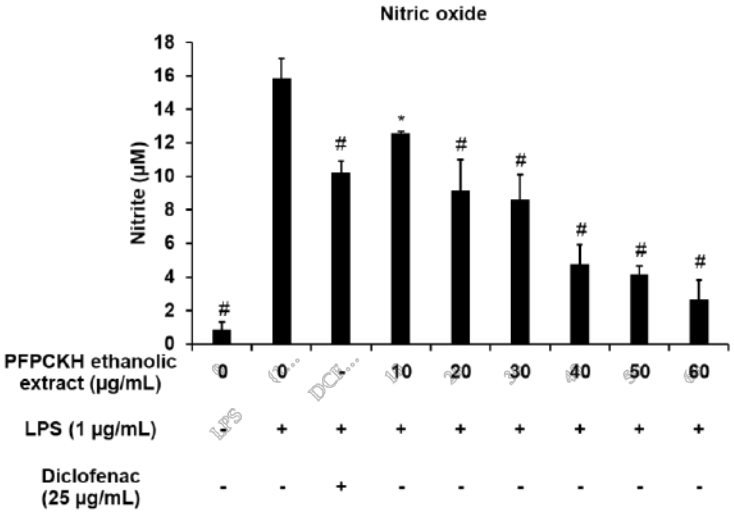

Figure 2. Effect of PFCPKH ethanolic extract on NO production in RAW264.7 cells. RAW264.7 cells were seeded in RPMI 1640 medium for 22 h and then replaced with serum-free medium and pre-treated with PFCPKH ethanolic extract at various concentrations (10-60 µg/mL) for 2 h before was stimulated with LPS (1 µg/mL) and incubated at 37 °C for 24 h. Nitrite concentration was estimated by Griess reagent compare with nitrite standard. The result was reported as a concentration of nitrite by and expressed as means ± SD of three dependent experiments. Statistic significant inhibition of NO production (* $p < 0.05$ and ** $p < 0.01$) were compared with LPS group.

Effect of PFCPKH ethanolic extract on PGE_2 production of LPS-stimulated RAW264.7 cells

In PGE_2 determination, the ethanolic extract at concentrations of 2.5-60 µg/mL inhibited PGE_2 production 69-93% and DCF inhibited PGE_2 production 99% compared with the control (LPS-treatment alone). These results demonstrated that the ethanolic extract has potential anti-inflammatory activity as the decreased PGE_2 productions in LPS-stimulated RAW264.7 cells were observed and comparative to the anti-inflammatory drug (DCF).

This manifested those concentrations of all tested extracts could inhibit PGE_2 production significantly ($p<0.001$). Although, PFCPKH at concentrations of 2.5-20 µg/mL could inhibit PGE_2 production in dose-dependent manners, at higher concentrations of PFCPKH ethanolic extract could inhibit PGE_2 production less than that low concentration. This may cause by the higher concentrations contained more substituents that affect to COX-2 enzyme expression that activated PGE_2 production. Further studies are needed to elucidate the effect of PFCPKH on COX-2 expression by LPS-stimulated RAW264.7 cells.

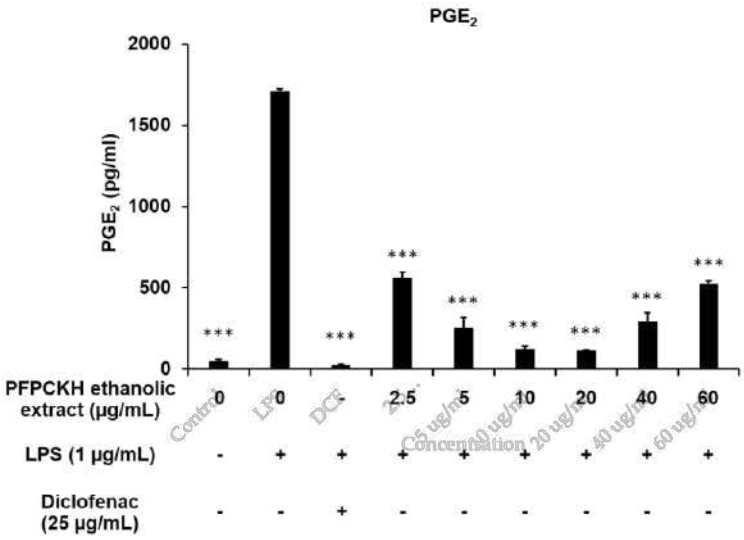

Figure 3. Effect of PFCPKH ethanolic extract on PGE_2 production in RAW264.7 cells. RAW264.7 cells were seeded in RPMI 1640 medium for 22 h and then replaced medium to be serum-free medium and pre-treated with PFCPKH ethanolic extract various concentration (2.5-60 µg/mL) for 2 h. Thereafter, the cells were stimulated with LPS (1 µg/mL) and incubated at 37 °C for 24 h. PGE_2 concentration was estimated by PGE_2 ELISA Kit compared with PGE_2 standard. The result was reported as a concentration of PGE_2 and expressed as means ± SD of three dependent experiments. Statistical significance inhibition of PGE_2 production (*** $p < 0.001$) was compared with LPS group.

In the process of inflammation, many inflammatory mediators, such as nitric oxide (NO) and Prostaglandins (PGs) were synthesized by iNOS and COX-2 enzyme. Our results demonstrated that PFCPKH ethanolic extract has potential anti-inflammatory activity as it could decrease NO and PGE_2 productions in LPS-stimulated RAW264.7 cells (Figs. 2, 3) in the same way as the anti-inflammatory drug (DCF). Therefore, PFCPKH ethanolic extract may be considered as an anti-inflammatory agent.

However, the effect of PFCPKH ethanolic extract on other inflammatory mediators, pro-inflammatory cytokines and proteins implicated in the inflammation pathway will be studied in the future.

Quantification of phenolic composition in PFCPKH by HPLC

The phenolic acid compositions of PFCPKH ethanolic extract were analyzed by reverse-phase HPLC. The HPLC result showed that 6 phenolic acids such as *p*-hydroxybenzoic, vanillic, syringic, *p*-coumaric, ferulic and sinapinic acids were identified when compared with the available phenolic acid standards (Fig. 4A). The HPLC analysis revealed that the levels of phenolic acids in this ethanolic extract were 9.60 ± 0.15, 15.79 ± 1.01, 17.13 ± 1.76, 23.07 ± 8.86, 64.45 ± 1.45 and 13.49. ± 1.54 µg/g of sample in powder form, respectively (Fig 4B), calculated by comparison with phenolic standards (Fig 4A). Among the identified phenolic acids of PFCPKH, the most abundant phenolic acid in ethanolic extract was ferulic acid (Table 1). In previous study, ferulic acid was demonstrated to inhibit NO and PGE_2 production[23–25].

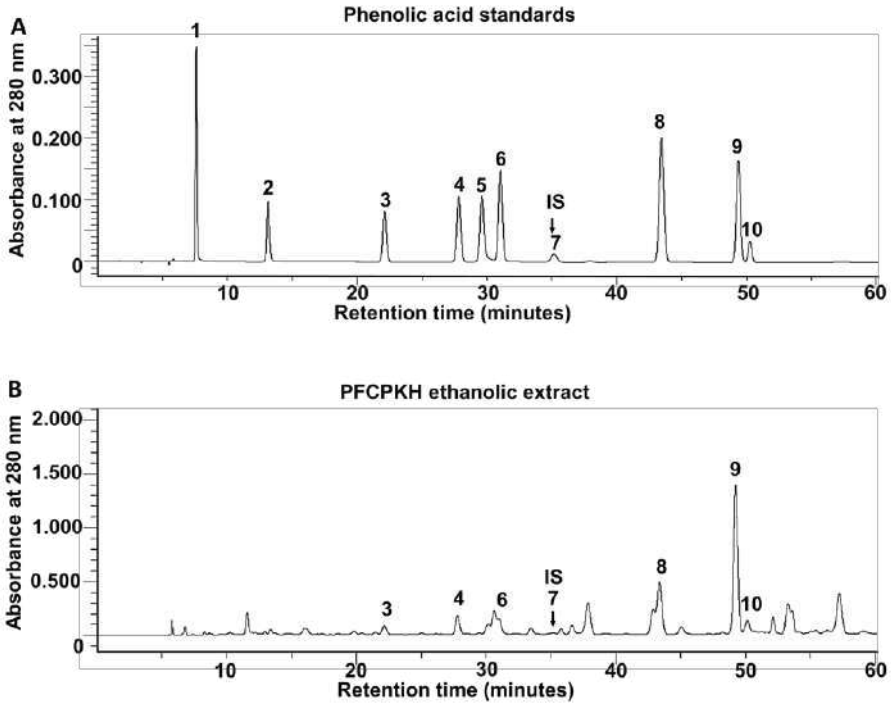

Figure 4. HPLC chromatograms of phenolic acid standards (A) and base hydrolyzed-PFCPKH ethanolic extract (B), where 1= gallic acid, 2 = protocatechuic acid, 3 = *p*-hydroxybenzoic acid, 4 = vanillic acid, 5 = caffeic acid, 6 = syringic acid, 7 = m-hydroxybenzaldehyde, 8 = *p*-coumaric acid, 9 = ferulic acid and 10 = sinapinic acid. The *m*-hydroxybenzaldehyde was used as an internal standard (I.S.).

Tabel 1 Phenolic acid compositions of PFPKH ethanolic extract

Phenolic acids[a] (µg/g of sample in powder form of PFPKH)					
***p*-Hydroxy-benzoic acid**	**Vanillic acid**	**Syringic acid**	***p*-Coumaric acid**	**Ferulic acid**	**Sinapinic acid**
9.60 ± 0.15	15.79 ± 1.01	17.13 ± 1.76	23.07 ± 8.86	64.45 ± 1.45	13.49 ± 1.54

a Results are expressed as means ± SD of three determinations.

Conclusion:

Our results suggested that the PFPCKH ethanolic extract possesses anti-inflammatory activity as demonstrated by inhibition of NO and PGE_2 productions in LPS-stimulated RAW264.7 cells. For further study, the effect of PFPCKH ethanolic extract on many pro-inflammatory cytokines and proteins implicated in the inflammation pathway should be studied in order to confirm its anti-inflammatory activity.

Acknowledgements:

This study was supported by Thailand Research Fund (TRF) in the project Research and Researcher for Industry (RRi). We acknowledge the Prolac (Thailand) Co., Ltd., Lamphun, Thailand, for providing the samples and partial financial support.

References:

1. Woranam K, Senawong G, Utaiwat S, Yunchalard S, Sattayasai J, Senawong T. Plos One. 2020;15:1-18.
2. Kim EA, Kim SY, Ye BR, et al. Int Immunopharmacol. 2018;59:339-346.
3. Rao YK, Fang SH, Tzeng YM. J Ethnopharmacol. 2007;114:78-85.

4. Furman D, Campisi J, Verdin E, et al. Nat Med. 2019;25:1822-1832.
5. Szollosi DE, Manzoor MK, Aquilato A, Jackson P, Ghoneim OM, Edafiogho IO. J Pharm Pharmacol. 2018;70:18-26.
6. Wongrakpanich S, Wongrakpanich A, Melhado K, Rangaswami J. Aging Dis. 2018;9:143-150.
7. Kanjanahattakij N, Kwankhao P, Vathesatogkit P, et al. BMC Complement Altern Med. 2019;19:1-9.
8. Joshi DR, Adhikari N. Adv J Chem. 2020;2:226-238.
9. Han SY, Kim J, Kim E, et al. J Ginseng Res. 2018;42:496-503.
10. Hong M, Lee YH, Kim S, et al. J Ginseng Res. 2016;40:203-210.
11. Sae-wong C, Tansakul P, Tewtrakul S. J Ethnopharmacol. 2009;124:576-580.
12. Meng Z, Wen T, Kang J, Lei B, Hyde KD. Chiang Mai J Sci. 2015;42:317-330.
13. Kim SK, Ryu SY, No J, Choi SU, Kim YS. Arch Pharm Res. 2001;24:518-521.
14. Shin S, Joo SS, Jeon JH, et al. J Vet Sci. 2010;11:273-275.
15. Leardkamolkarn V, Tiamyuyen S, Sripanidkulchai B. Asian Pacific J Cancer Prev. 2009;10:695-698.
16. Ru W, Wang D, Xu Y, et al. Drug Discov Ther. 2011;9:23-32.
17. Cheng D, Sun L, Zou S, et al. Molecules. 2019;24:1835.
18. Jang MH, Piao XL, Kim JM, Kwon SW, Park JH. Phyther Res. 2008;22:544–549.
19. Tewtrakul S, Subhadhirasakul S, Kummee S. J Ethnopharmacol. 2008;116:191-193.
20. Wu Y, Liu Z, Wu W, et al. Biosci Rep. 2018;38:1-10.
21. Chuenchom P, Swatsitang P, Senawong T, Jogloy S. Chiang Mai J Sci. 2016;43:123-137.
22. Shin JY, Kang JS, Byun HW, Ahn EK. Mol Med Rep. 2017;16:5137-5142.
23. Kim EO, Min KJ, Kwon TK, Um BH, Moreau RA, Choi SW. Food Chem Toxicol. 2012;50:1309-1316.
24. Lampiasi N, Montana G. Immunobiology. 2016;221:486-493.
25. Yoo S-R, Seo C-S, Lee N-R, Shin H-K, Jeong S-J. Pharmacogn Mag. 2015;11:585-591.

ANTIBACTERIAL ACTIVITY OF ETHANOLIC EXTRACTS FROM THAI MEDICINAL PLANTS AGAINST *Porphyromonas gingivalis*

Thanitchai Kamthalang,[1] Chutima Jittaprasatsin,[1] Piyada Wangroongsarb,[1] Patamaporn Pruksakorn,[2,*]

[1]National Institute of Health, Department of Medical Sciences, Ministry of Public Health, Nonthaburi, Thailand

[2]Medical Life Sciences Institute, Department of Medical Sciences, Ministry of Public Health, Nonthaburi, Thailand

*e-mail: patamaporn.p@dmsc.mail.go.th

Abstract:

Periodontitis is a chronic inflammation of the gums and the supporting tissues of the tooth that is triggered by bacteria in dental plaque. *Porphyromonas gingivalis* is a Gram-negative oral anaerobic bacteria that is considered a keystone pathogen in periodontitis. The objective of this study was to evaluate the antibacterial activity of ethanolic extracts from Thai medicinal plants against *P. gingivalis*. Three hundred and thirty extracts from 200 plants were tested antibacterial activity using a broth microdilution assay. For this assay, chlorhexidine (2.0 μg/mL) was used as positive control and DMSO (dimethyl sulfoxide) was used as negative control. Of these, the rhizomes of mango ginger (*Curcuma amada* Roxb.), the leaves of dracaena (*Dracaena fragrans* (L.) Ker-Gawl), the aerial parts of the rough chaffed flower (*Achyranthes aspera* L.), and the leaves and fruits of bushwillow (*Combretum attenuatue* Wall.) exhibited the most potent antibacterial activity against *P. gingivalis* with minimum inhibitory concentration (MIC) values of 25 μg/mL. In addition, the rhizomes of mango ginger showed the minimum bactericidal concentration (MBC) value of 25 μg/mL whereas the leaves of dracaena, the aerial parts of the rough chaffed flower, and the leaves and fruits of bushwillow showed the MBC values of 50 μg/mL. The findings suggest that these plant extracts could be promising sources for the isolation of antimicrobial substances against *P. gingivalis*, consequently the formulation of oral health products for protection and treatment of periodontitis.

ANTIMICROBIAL SUSCEPTIBILITY PROFILE OF *Cutibacterium acnes* ISOLATES FROM ACNE PATIENTS IN THAILAND

Nattapong Cheunban,[1] Peera Udomjarumane,[2] Apiyut Nettakul,[2] Orapan Sripichai[1,*]
[1]National Institute of Health, Department of Medical Sciences, Ministry of Public Health, Nonthaburi, Thailand
[2]Pornkasem Clinic, Bangkok, Thailand
*e-mail: orapan.s@dmsc.mail.go.th

Abstract:
Cutibacterium acnes plays an important role in the development of acne. Antimicrobials have been widely used for several decades to improve inflammatory lesions, which may result in development of resistant strains. Alarmingly, antimicrobial-resistant *C. acnes* has become a worldwide problem, but there are limited data on antimicrobial resistant pattern in Thailand. This study aims to determine the antimicrobial susceptibility of *C. acnes*, isolated from patients with acne, to different prescribed antimicrobial agents. Cutaneous samples were collected from facial acne lesions of 70 patients with acne vulgaris attending the dermatology clinic in Thailand, from January to June 2021. All samples were cultured in anaerobic conditions to identify the presence of *C. acnes*, and final identification of isolates was performed by real-time polymerase chain reaction. Isolates of *C. acnes* were then subjected to the susceptibility test for ten antimicrobial agents using a minimum inhibitory concentration (MIC) test strip. Fifty-four isolates (77.1%) were resistant to macrolide group (erythromycin and clarithromycin) and lincosamide group (clindamycin), with very high MIC value (>256 µg/mL). This finding suggests that any information for past exposure to antimicrobials within the macrolide-lincosamide-streptogramin (MLS) group; chemically distinct but have similar mechanisms of action to inhibit protein synthesis and cross-resistance due to target modification, should suggest avoidance of prescription of these agents. The MIC of tetracycline, doxycycline, minocycline, gentamicin, amoxicillin, ciprofloxacin, and trimethoprim/sulfamethoxazole were all below the breakpoint of antimicrobial resistance, but an increasing trend of MIC was observed. The present results provide useful information to guide antimicrobial prescribing strategies in Thai patients with acne. However, determination of antimicrobial susceptibility patterns of *C. acnes* should be taken before treating patients with antimicrobial agents and long-term therapy should be avoided to reduce the spread of antimicrobial-resistant strains.

ANTIOXIDANT AND ANTIDIABETIC INHIBITORY ACTIVITY OF CRUDE EXTRACTS FROM EDIBLE INSECTS

Jintana Masoongnoen, Sompong Sansenya, Kanokorn Wechakorn*
[1]Department of Chemistry, Faculty of Science and Technology, Rajamangala University of Technology Thanyaburi, Pathumthani 12110, Thailand
*e-mail: kanokorn_w@rmutt.ac.th

Abstract:
The consumption of edible insects has been significantly increased in Thailand due to their high protein contents and nutritional values. In this work, several edible insect extracts, including silkworm pupae, house cricket, short-tailed cricket, field cricket, bamboo caterpillar, and Bombay locust, were investigated the biological activities such as free radical scavenging activity (DPPH) as well as α-glucosidase and α-amylase inhibitory activities. The edible insect powder was extracted by using hexane, dichloromethane, ethyl acetate, and methanol, respectively. The methanolic extracts of Bombay locust showed the highest free radical scavenging activity among other insects but lower than the ascorbic acid as the standard inhibitor. For the antidiabetic inhibition, almost crude extracts of field cricket and short-tailed cricket exhibited the potent α-glucosidase inhibitory activity as same as the acarbose. In comparison, the α-amylase inhibitory activity of ethyl acetate extract from silkworm pupae was as same as that of acarbose. From these results, the crude extract of diverse edible insects revealed a variety of potent biological activities.

BIOLOGICAL ACTIVITY OF PROTEIN HYDROLYSATE FROM MUSHROOM *Lentinus squarrosulus* Mont

Tattiya Kantasa,[1] and Jongrak Attarat[1, *]
[1] Department of Biochemistry, Faculty of Medical Science, Naresuan University, Phitsanulok, 65000
*e-mail: jongrukau@nu.ac.th

Abstract:
The skin is constantly submitted to oxidative stress. reactive oxygen species (ROS) not only cause cell damage, but they contribute to dermis collagen depletion by matrix metalloproteinases (MMPs) which leads to premature skin ageing. Furthermore, ROS increase melanin synthesis resulting in hyperpigmentation. Thereby, the composition of skincare often includes chemicals that reduce the skin problems. However, the compounds cause side effects at high concentrations. Therefore, safer alternatives are needed, and proteins hydrolysates are promising candidates. In this study, proteins hydrolysates from the *Lentinus squarrosulus* Mont, was completely digested by pepsin, lyophilized and ultrafiltered using a MWCO 3 kDa. The protein hydrolysate inhibited the highest tyrosinase activity (IC_{50} 11 mg/ml), while the inhibition of 1 µg/µL kojic acid inhibited at 47%. For the MMPs inhibition assay, 20 mg/mL of protein hydrolysate decreased the MMPs activity by 31% while 1 M of 1,10-phenanthroline reduced it by 86%. The antioxidant activity, ABTS and DPPH assays gave different results. The protein hydrolysate at 20 mg/mL showed 12% inhibition by ABTS assay but the inhibition of DPPH was 67%. The protein hydrolysate exhibited interesting tyrosinase and MMPs inhibitory effects, and strong antioxidant activity by DPPH assay. The further purification of the hydrolysate could lead to the identification of peptides sequences that may have even more pronounced activities, and could be used in anti-ageing or skin whitening cosmetics.

Introduction:

Skin problems cause from intrinsic and extrinsic factors; hormone, heredity, and ultraviolets.[1] Melanin synthesis will occur at the epidermis area for skin protection. The melanin is synthesized by both monophenolase and diphenolase reaction of tyrosinase.[2] The melanin is pigment for iris, hair and skin color. If there are over production of melanin synthesis, it leads to hyperpigmentation and cause dark spot, freckles, melasma.[3, 4] The ultraviolet radiation affect photo aging because of reactive oxygen species (ROS). The ROS also has a role to activate a sign of mitogen-activated protein kinase (MAPK) that will turn off the defense of of antioxidant enzymes expression in cells and activate matrix metalloproteinase (MMPs) reaction. The expression of extracellular proteinases decomposes collagen and elastic fibers and the make wrinkle and skin-aging.[5] Cosmetic products; cream, lotion, toner skin care have substance such as kojic acid, hydroquinone, vitamin C, and arbutin to reduce those skin problems.[6] However using of those substance at high concentration or for long term cause side effects such as sensitive skin, irritated, dermatitis. Nowadays, bioactive peptides or protein hydrolysate are popular used in the cosmetic products to inhibit tyrosinase activity. The advantage of peptide using is small size that is potential to absorb into skin. Many peptides are antioxidant, stability and less side effect. Some peptide also activates a collagen formation, anti-wrinkle, and increase cell growth.[7]

Here, researchers focused to study protein hydrolysate activities of *Lentinus squarrosulus* Mont or Khonkaw. which is commonly found in North-East region of Thailand. This mushroom is rich of nutrient, high protein and low fat. There is report about antioxidant activity and able to decrease level of blood pressure and cholesterol.[8] The aim of this study is protein hydrolysate preparation from *L. squarrosulus* Mont. using pepsin and study its biological activities.

Methodology:

1. Extraction of Lentinus squarrosulus* Mont *protein

L. squarrosulus Mont powder 200 mg with 2 L distilled water, pH value to 10 with 1mol/L NaOH, then blender with an overhead stirrer at 1000 rpm for 2 hrs. The supernatant was then pooled, and the pH was adjusted to the pH 4.2 using 1 mol/L HCl and it was then centrifuged at 4000rpm, 4°C for 20 min. The precipitate was collected and solubilized with distilled water, and then the pH was adjusted to 3.7 using 1 mol/L HCl and freeze-dried. The resultant *L. squarrosulus* Mont protein concentrate was stored at -20 °C until required for further analysis.

2. Preparation of Lentinus squarrosulus Mont. protein hydrolysate

The *L. squarrosulus* Mont protein extract powder was hydrolyzed with a pepsin. The hydrolysis was performed at 37° C for 24 h at pH 3.7 by pepsin (1% enzyme/substrate), the protein reaction was heated at 95 °C for 20 min. to stop the reaction. And final step for protein hydrolysate preparation, the mixture was centrifuged at 4000rpm, 4°C for 20 min and collected the supernatant and filtered using ultrafiltration membranes with molecular cut off of 3 kDa. Finally, the suspension was freeze-dried. The resultant *L. squarrosulus* Mont protein concentrate was stored at -20 °C until using for further analysis.

3. Measurement of tyrosinase inhibitor potency

Tyrosinase inhibition assay was followed method by Song, W et al., 2020[9] 5 mM L-dopa 1 2 0 µL was mixed in a 5 mM Potassium phosphate buffer solution (pH 6.8) 70 µL. Commercial tyrosinase 15 µL was added in the reaction and then the *L. squarrosulus* Mont protein hydrolysate or positive control; kojic acid was appended. The absorbance of the resulting solution was measured at 475 nm after reaction L-dopaquinone expression. The resulting value will be calculated % inhibition.

$$\% \text{ Tyrosinase inhibition} = \frac{\text{Activity}_{(\text{Enzyme})} - \text{Activity}_{(\text{Inhibition})}}{\text{Activity}_{(\text{Enzyme})}} \times 100$$

4. DPPH radical scavenging activity

DPPH reagent was prepared by dissolving 0.1 mM DPPH in ethanol. Protein hydrolysate was added in100 µL of DPPH reagent. The reaction was incubated for 30 min in the dark at room temperature. The absorbance of the resulting solution was measured at 517 nm. The result was expressed as 0.5 mg/mL Trolox as a standard substance. The resulting value will be calculated % inhibition.

$$\% \text{ Inhibition of DPPH} = \frac{\text{OD517nm}_{(\text{Control})} - \text{OD517}_{(\text{Sample})}}{OD517_{(\text{Control})}} \times 100$$

5. ABTS radical scavenging activity

ABTS reagent was prepared by dissolving 7mM ABTS reagent. Protein hydrolysate was added in 2.45 mM potassium persulphate and 7 mM ABTS. The mixture nurtured for 30 min in the dark at room temperature. The absorbance of the resulting solution was measured at 734 nm. The result was expressed as 0.5 mg/mL Trolox as a standard substance. The resulting value will be calculated % inhibition.

$$\% \text{ Inhibition of ABTS} = \frac{\text{OD734nm}_{(\text{Control})} - \text{OD734}_{(\text{Sample})}}{OD734_{(\text{Control})}} \times 100$$

6. Measurement of MMPs inhibitor potency

Anti-collagenase Activity of *L. squarrosulus* Mont protein hydrolysate was performed according to the method described in Collagenase Activity Colorimetric Assay Kit (Catalog Number MAK293). Reaction mix was composed of collagenase Substrate (FALGPA) 40 µL, Collagenase (0.35 U/mL) 10 µL, *L. squarrosulus* Mont protein hydrolysate, Inhibitor (1 M, 1,10-Phenanthroline), collagenase assay buffer 50 µL. The mixture was stranded for 5-15 min in the dark, at 37°C. The absorbance of the resulting solution was measured at 345 nm.

7. Statistical analysis

Data are presented as the mean ± standard error (SE) of determinations made for each sample. Data were tested by one-way analysis of variance (ANOVA) using SPSS version 26.0. Least significant differences (LSD, $P \leq 0.05$) were calculated to compare differences between means following determination of a significant effect by ANOVA.

Results:

Tyrosinase inhibition of the Lentinus squarrosulus Mont protein hydrolysate

Tyrosinase inhibition of the protein hydrolysate from *L. squarrosulus* Mont was hydrolyzed by pepsin shown in Fig 1, The protein hydrolysate inhibited the highest tyrosinase activity (IC_{50} 11 mg/ml). All each concentration exhibited a concentration-dependent response within tested concentrations. Within the concentration range from 0.1-20.0 mg/mL, the capacity of tyrosinase inhibition increased with the sample's concentration. By here 1 µg/µL Kojic acid as a positive control inhibited activity of tyrosinase for 47%.

Antioxidant activity evaluation of DPPH radical-scavenging activity assay and ABTS radical-scavenging activity assay

The antioxidant activities of *L. squarrosulus* Mont protein hydrolysate determined using two in vitro assays are presented in Fig 2. DPPH is a stable free radical that shows maximum absorbance at 517 nm in ethanol. When DPPH encounters a proton-donating substance such as an antioxidant, the radical is scavenged and the absorbance is reduced. In this study, Antioxidant activity of *L. squarrosulus* Mont protein hydrolysate was performed with Trolox used as a standard substance. As observed in Fig 2a. At protein concentration 20 mg/mL exhibited a stronger radical scavenging capacity by 78% inhibition of DPPH. All each concentration exhibited a concentration-dependent response within tested concentrations, the capacity of scavenging DPPH radicals increased correspond to the sample's concentration. While testing with ABTS radical-scavenging activity assay show different result. Fig 2b. The protein hydrolysate at all concentrate exhibited a concentration-independent response within tested concentrations by DPPH assay.

MMPs inhibition

MMPs inhibition of the *L. squarrosulus* Mont protein hydrolysate is presented in Fig 3, protein hydrolysate at protein concentration 20 mg/mL represented strong collagenase inhibition activity by 31%. All each concentration exhibited a concentration-dependent response. Within the concentration range from 0.1-20.0 mg/mL, the capacity of collagenase inhibition increased with the sample's concentration. While 1 M 1,10- Phenanthroline as a positive control has anti-collagenase at 86%. This show that a protein decomposed from dry

fruiting body of *L. squarrosulus* Mont with pepsin can increase an inhibition process of MMPs.

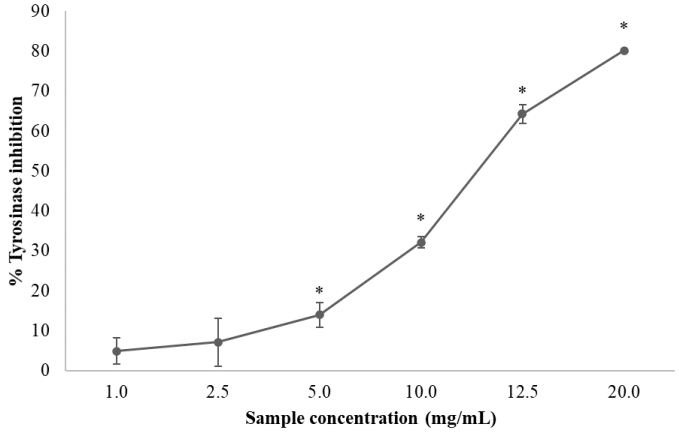

Figure 1 Tyrosinase inhibition of protein hydrolysate from *L. squarrosulus* Mont. Data were tested by one-way analysis of variance (ANOVA) using SPSS version 26.0. *. The mean difference is significant at the 0.05 level. (*; Sample concentration exhibited a concentration-dependent response within tested concentrations)

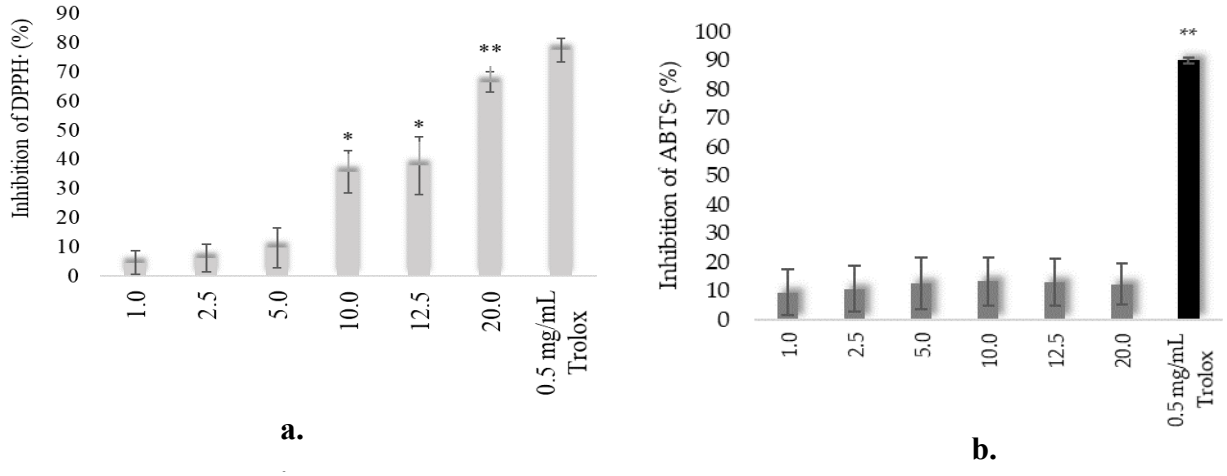

Figure 2 Antioxidant activity of *L. squarrosulus* Mont protein hydrolysates. **(a.)** DPPH radical scavenging activity of protein hydrolysate from *L. squarrosulus* Mont. **(b.)** ABTS radical scavenging activity of protein hydrolysate from *L. squarrosulus* Mont. Data were tested by one-way analysis of variance (ANOVA) using SPSS version 26.0. ***, **;** The mean difference is significant at the 0.05 level. (*; Sample concentration exhibited a concentration-independent response within tested concentrations, **; Sample concentration exhibited a concentration-dependent response within tested concentrations.)

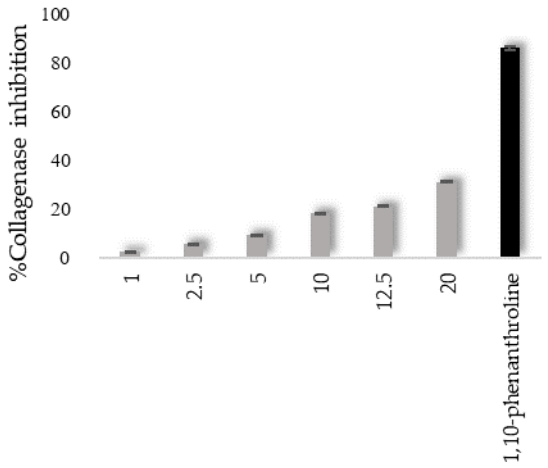

Figure 3 %MMPs inhibition of protein hydrolysate from *L. squarrosulus* Mont. Data are presented as the mean ± standard error (SE) of determinations made for each sample.

Discussion:

According to the experimental result, protein hydrolysate of *L. squarrosulus* Mont showed stronger of antioxidant by DPPH assay than ABTS assay. This study corresponded to Chang-Feng Chi' study, protein hydrolysate from head of bluefin leather jacket, were decomposed by papain and produced three peptides; BHH-P1, BHH-P2 and BHH-P3.[10] Refer to the antioxidant action used antioxidant testing showed that BHH-P1 and BHH - P2 peptide have strong antioxidant action that tested with DPPH assay higher than ABTS assay. Therefore, the DPPH assay and ABTS assay did not coincide and the resulting value will not be reported by IC50. The DPPH was a stable radical interact in Methanol solvent, while ABTS interact with a water solvent.[11] They concluded that the major content of two peptide (BHHs) is hydrophobic or aromatic amino acids. From previous report, the antioxidative peptide depends on size of molecular and composition of hydrophobic amino acids, The hydrophobic amino acids such as Trp, Pro, Tyr, Lys, Leu, Val and His. This is first study to extract protein hydrolysate from dried fruiting body of *L. squarrosulus* Mont and then hydrolyzed using pepsin. From the experimental result show that protein hydrolysate at concentration of 20 mg/mL, inhibit the process of tyrosinase about 80% while1 mg/mL Kojic acid is able to inhibit the tyrosinase activity about 47%.

From our previous study (data not shown), the preparation of protein hydrolysate from dried fruiting body of *L. squarrosulus* Mont extract using pepsin give also showed tyrosinase inhibitory as similar to this study. However, the tyrosinase inhibition from the extract should be also from phenolic compound content in the dried fruiting body; catechin[12] and tannins which have been reported for tyrosinase inhibition.[13,14] In this study, we developed method to first extraction protein from dried fruiting body and then used pepsin to hydrolyze protein before study the tyrosinase activity of protein hydrolysate. At protein concentration 0.2 µg/µL of protein hydrolysate from dried fruiting body of *L. squarrosulus* Mont extract using pepsin (Do not protein extraction) exhibited a stronger reduced tyrosinase activity by 33%. Then extraction of protein hydrolysate from dried fruiting body of *L. squarrosulus* Mont by pepsin can decrease tyrosinase activity more than extraction of protein hydrolysate method in previous study when compared. The report to show production of tyrosinase inhibitory peptides from a food protein source. The protein hydrolysate from dried fruiting body of *L. squarrosulus* Mont as similar rice bran protein (RBP Hydrolysates;RBP). RBP a significant inhibition of both tyrosinase reactions was observed in fractions containing low-molecular-weight peptides of <3000Da.[2]

According to result of MMPs inhibition in this study, the protein hydrolysate from mushroom is able to inhibit activity of MMP-1 as similar to protein hydrolysate from cod skin gelatin[15] and walnut (*Juglans regia* L.). In vitro study, protein hydrolysates are able to inhibit process of MMP-1 via MMP-1 signaling pathway.[16]

Conclusion:

This study showed that protein hydrolysate from *Lentinus squarrosulus* Mont which decomposed by pepsin have an inhibitory effect of tyrosinase and MMPs. The protein hydrolysate exhibited interesting strong antioxidant activity. Even though the antioxidant action that tested by ABTS assay is less than DPPH assay. However, the more purification process will be performed to identify peptide sequence and test its cytotoxicity before using in anti-aging cosmetic or brightening product.

References:

1. Megaw, L., Clemens, T., & Stock, S. (2017). Pregnancy outcome and ultraviolet radiation; A systematic review. Environ Res, 155, 335-343.
2. Ochiai, A., Tanaka, S., Tanaka, T., & Taniguchi, M. (2016). Rice Bran Protein as a Potent Source of Antimelanogenic Peptides with Tyrosinase Inhibitory Activity. J Nat Prod, 79(10), 2545-2551.
3. Sato, K., & Toriyama, M. (2009). Depigmenting effect of catechins. Molecules, 14(11), 4425-4432.
4. Banna, H., Hasan, N., &Yoo, J.-W. (2018). In vitro and in vivo evaluation of MHY908-loaded nanostructured lipid carriers for the topical treatment of hyperpigmentation. Journal of Drug Delivery Science and Technology, 48, 457-465.
5. Jesumani, V., Du, H., & Huang, N. (2019). Potential Use of Seaweed Bioactive Compounds in Skincare-A Review. Mar Drugs, 17(12).
6. Vijayakumar, R., Abd Gani, S. S., & Mohd Mokhtar, N. F. (2017). Anti-Elastase, Anti-Collagenase and Antimicrobial Activities of the Underutilized Red Pitaya Peel: An in Vitro Study for Anti-Aging Applications. Asian Journal of Pharmaceutical and Clinical Research, 10(8), 251.
7. Piyanan, C., & Romanee, S. (2014). Protein hydrolysate from tilapia frame: antioxidant and angiotensin I converting enzyme inhibitor properties. International Journal of Food Science and Technology, 50, 1436-1444.
8. De Leon AM, G. L., De Ramos PDV, Kalaw SP. (2017). Enriched cultivation of Lentinus squarrosulus (Mont.) Singer: A newly domesticated wild edible mushroom in the Philippines. Mycosphere, 8 (3), 615–629
9. Song, W., Liu, L. L., & Yang, H. B. (2020). Inhibitory effects and molecular mechanism on mushroom tyrosinase by condensed tannins isolation from the fruit of Ziziphus jujuba Mill. var. spinosa (Bunge) Hu ex H. F. Chow. *Int J Biol Macromol, 165*(Pt B), 1813-1821.
10. Chi, C.-F., Wang, B., & Deng, S.-G. (2015). Isolation and characterization of three antioxidant peptides from protein hydrolysate of bluefin leatherjacket (*Navodon septentrionalis*) heads. *Journal of Functional Foods, 12*, 1-10.
11. Memarpoor-Yazdi, M., Mahaki, H., & Zare-Zardini, H. (2013). Antioxidant activity of protein hydrolysates and purified peptides from Zizyphus jujuba fruits. *Journal of Functional Foods, 5*(1), 62-70.
12. Jongrak ATTARAT, a. T. P. (2015). Bioactive Compounds in Three Edible Lentinus Mushrooms. Agriculture Technology and Biological Sciences, 12(6), 491-504.

13. Chen, T., Hou, H., & Li, B. (2016). Protective effect of gelatin peptides from pacific cod skin against photoaging by inhibiting the expression of MMPs via MAPK signaling pathway. *J Photochem Photobiol B, 165*, 34-41.

14. KUBO, Q.-X. C. A. I. (2002). Kinetics of Mushroom Tyrosinase Inhibition by Quercetin. J. Agric. Food Chem., 50, 4108−4112.

15. Abuine, R., Rathnayake, A. U., & Byun, H.-G. (2019). Biological activity of peptides purified from fish skin hydrolysates. *Fisheries and Aquatic Sciences, 22*(1).

16. Xu, D., Wang, W., & Zhao, M. (2020). Walnut protein hydrolysates, rich with peptide fragments of WSREEQEREE and ADIYTEEAGR ameliorate UV-induced photoaging through inhibition of the NF-kappaB/MMP-1 signaling pathway in female rats. *Food Funct, 11*(12), 10601-10616.

CHARACTERIZATION OF CRUDE PROTEASE EXTRACTE FROM VISCERA OF SEA BASS (*Lates calcarifer*)

Burassakorn Tongmee,[1]Theeraphol Senphan [2,*]
[1] Prince Royal's College, Chiangmai, Thailand, 50000
[2] Program in Food Science and Technology, Faculty of Engineering and Agro-industry, Maejo University, Sansai, Chiangmai, Thailand, 50290
*e-mail: theeraphol_s@mju.ac.th, Tel: 053-875030 ext.207

Abstract:

Sea bass (*Lates calcarifer*), a brackish aquatic animal, is an economically important in Thailand. Sea bass is commonly processed into frozen fillet products and other products. After fish processing, fish viscera were found as a major byproduct with low-values added but fish viscera were rich in protease enzyme. Therefore, the objective of this study was to study the preparation and characterization of crude protease extract (CPE) from sea bass viscera. The result showed that CPE had enzyme activity of 0.0038 unit/ml, protein content of 7.81 mg/ml and specific activity value of 0.0005 unit / mg. When studying the protein patterns of CPE by SDS-PAGE (sodium dodecyl sulphate–polyacrylamide gel electrophoresis) and activity staining (zymography) techniques. It was found that CPE was found two major band proteins by SDS-PAGE with molecular weights (MWs) of 68 and 45 kDa, respectively. For activity staining, a protein bands of CPE with the MWs of 68 and 45 kDa were estimated from the activity bands on the casein substrate gel electrophoresis. The presence of the two major clear zones (68 and 45 kDa) suggested that it is the protease that can hydrolyze casein in the gel. Therefore, CPE from the sea bass viscera can be recovered and further used, in which the cost of commercially available proteases can be reduced.

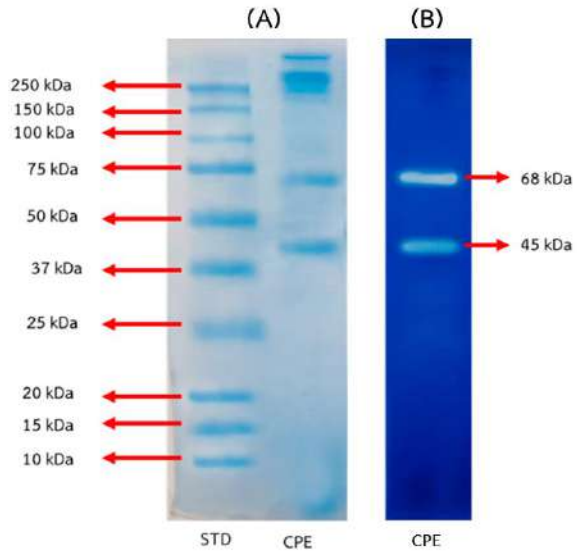

Figure 1 Protein pattern (A) and activity staining (zymography) (B) of crude protease extract (CPE) from sea bass viscera.

COMPARATIVE STUDY ON BIOACTIVE INGREDIENTS AND ANTIOXIDANT POTENTIAL OF SOME CABBAGES *(Brassica oleracea* var. *capitata***)**

Pimchanok Puthong,[1] Sirinya Taya,[2] Napaporn Khuanphram,[3] Mongkhon Panyarat,[1] Rawiwan Wongpoomchai[3,*]

[1] Yupparaj Wittayalai School, Chiang Mai 50200, Thailand

[2] Functional Food Research Unit, Science and Technology Research Institute, Chiang Mai University, Chiang Mai 50200, Thailand

[3]Department of Biochemistry, Faculty of Medicine, Chiang Mai University, Chiang Mai 50200, Thailand

*e-mail: rawiwan.wong@cmu.ac.th

Abstract:

Cabbage (*Brassica oleracea*), a famous vegetable, is composed of various varieties including green cabbage (var. *capitata* f. *alba*) and red cabbage (var. *capitata* f. *rubra*). Vegetable color influences on various biological activities. The aim of this study was to compare the content of bioactive compounds and antioxidant capacities between green and red cabbage varieties. Fresh organic cabbages were extracted by distilled water as a pattern of daily life consumption. One gram of red cabbage extract (RCE) contained 17.29±0.07, 3.66±0.03 and 3.80±0.64 milligrams of total phenolic compounds, total flavonoids and total anthocyanins, respectively, while green cabbage extract (GCE) consisted of 3.52±0.08, 0.48±0.03 and 0.45±0.01 milligrams of these phenolic compounds. The amount of hydrophilic phytochemicals in RCE were higher than those in GCE. The antioxidant activities of RCE using DPPH, FRAP and ABTS assays were 36.16±2.47, 31.70±1.29 and 47.15±3.00 mg TE/g extract, respectively, while the antioxidant activities of GCE were 6.98±1.28, 4.47±0.13 and 4.75±0.53 mg TE/g extract, respectively. It might be suggested that red cabbage exhibited higher antioxidant activities than green cabbage due to its polyphenol content especially anthocyanins. The potential of B. *oleracea* f. *rubra* might be not only as healthy food but also as functional ingredients in some health products.

COMPUTER GAME OF CELL STRUCTURE AND FUNCTION IN BIOLOGY

Peeradon Sarnkaew, Naphat Samitthikorn, Kittapas Boonyom, Supanan Sucharit *
Department of Biology, Mahidol Wittayanusorn School, Phutthamonthon, Nakorn Pathom, Thailand
*e-mail: supanan.suc@mwit.ac.th

Abstract:

COVID-19 pandemic outbreak has had a huge impact on education, especially learning and teaching methods. The topic of biology on cell structure and function is the basis for building on the content of other chapters at a higher level, which is the topic learned in Grade 7. Creating a game about cell structure and function is media creation to promote learning for the online platform. The purpose of this project is to develop media for learning content, to enhance understanding of the content, to make learners enjoy, and to create a positive attitude for further learning in biology on the topic of structure and function of cells. The game was created by using the Unity engine and tested with a sample group of 30 of grade 7 students at Krabi Provincial Administrative Organization School. In a gaming session, pretest, posttest, and satisfaction assessment forms were completed by students. For the game system, the game is an adventure, action, and problem-solving in 2D. The average game time is 40 minutes, and the analysis is done by using descriptive statistics to measure the effectiveness of the game. The results showed that, the sample group indicated improvement in their learning in such content after playing the game significantly, using T-test at 0.01 statistical significance. All of them statistically had scores more than 60% at 0.01 statistical significance, which is the minimum passing scores in the post-test. These results suggested that they have a good understanding of the subject content. In addition, the sample had a positive attitude for further learning with a satisfaction level of 83.4% on average. In conclusion, the game media could enhance understanding in the topic of biology. This teaching method might be suitable to use for students, especially during the pandemics.

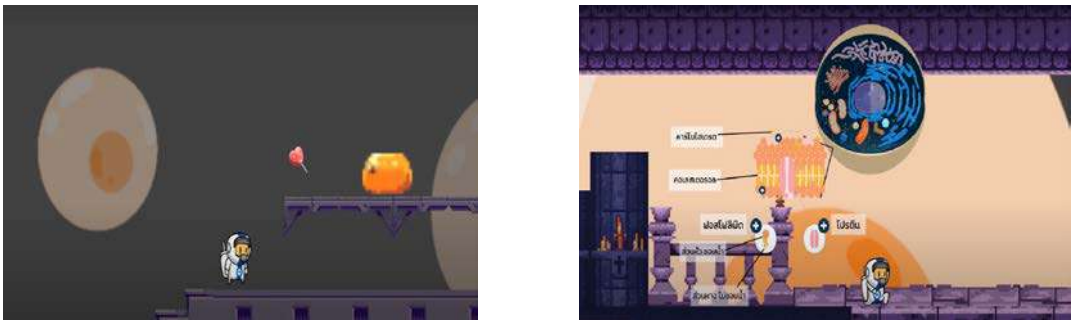

Figure 1.
Examples of gameplay in “Intro the Cell” game.

CONNECTING THE CLIMATE CHALLENGE

Alba Abad[1*], Prajwal Rhajbandhari[2]
[1]Wellcome Centre for Cell Biology, University of Edinburgh, Edinburgh, UK
[2]Research Institute for Bioscience and Biotechnology, Kathmandu, Nepal
*e-mail: mabadfe@staffmail.ed.ac.uk

Abstract:
Engage Nepal with Science is an organization that works with Nepalese communities to spread the culture of engaging with science to empower and build confidence in STEM. We are a group of researchers and educators from different parts of the world that believe that empowerment in STEM is crucial to promote critical thinking, problem-solving skills, boost curiosity and help us understand the world around us, which are key to make informed decisions, create a fairer, more inclusive society and to foster positive change. One of the projects we are currently running is named Connecting the Climate Challenge and is one of the 17 COP26 Creative Commissions funded by the British Council. The aim of this project is to digitally connect communities in Nepal and Scotland to work together to find innovative solutions to tackle the climate crisis and inspire climate action, while highlighting the importance of creating global connecting to tackle global issues like climate change.

Figure 1.

Detection of *leptospires* by RPA-CRISPR-Cas12a targeting *SecY* gene

Sirawit Jirawannaporn[1,2], Umaporn Limothai[1], Sasipha Tachaboon[1], Patcharakorn Kiatamornrak[1], Watchadaporn Chaisuriyong[1], Oraphan Mayuramart[9], Sunchai Payungporn[9], Nattachai Srisawat[1,3,4,5,6,7*]

[1] Excellence Center for Critical Care Nephrology, King Chulalongkorn Memorial Hospital, Bangkok, Thailand

[2] Ph.D. candidate in Doctor of Philosophy Program in Medical Sciences, Faculty of Medicine, Chulalongkorn University, Bangkok, Thailand

[3] Critical Care Nephrology Research Unit, Faculty of Medicine, Chulalongkorn University, Bangkok, Thailand

[4] Division of Nephrology, Department of Medicine, Faculty of Medicine, Chulalongkorn University, and King Chulalongkorn, Memorial Hospital, Bangkok, Thailand

[5] Academy of Science, Royal Society of Thailand, Bangkok, Thailand

[6] Tropical Medicine Cluster, Chulalongkorn University, Bangkok, Thailand

[7] Excellence Center for Critical Care Medicine, King Chulalongkorn Memorial Hospital, Bangkok, Thailand

[8] Department of Critical Care Medicine, Center for Critical Care Nephrology, The CRISMA Center, University of Pittsburgh School of Medicine, PA, USA

[9] Research Unit of Systems Microbiology, Department of Biochemistry, Faculty of Medicine, Chulalongkorn University, Bangkok, Thailand

[*]Corresponding author, E-mail: drnattachai@yahoo.com

Abstract:

The clinical signs and symptoms of leptospirosis shared similarities with various infectious diseases such as dengue, sepsis, and malaria. Moreover, the clinical signs and symptoms of leptospirosis shared similarities with various infectious diseases such as dengue, sepsis, and malaria. Therefore, it is difficult to be diagnosed. One of the key barriers to reducing the impact of leptospirosis is the insensitive diagnostic tools currently available such as rapid tests, microscopic agglutination tests (MAT), and real-time PCR. Therefore, we need a better diagnostic tool. RPA-CRISPR-Cas12a-based detection platform was designed to detect the *SecY* gene of pathogenic *leptospira spp.* with approximately 10^2 copies/reaction limit of detection in pure culture without false positive or false negative. In conclusion, the new RPA-CRISPR-Cas12 targeting *SecY* gene was capable of *leptospires* detection without the need for expensive laboratory equipment.

Keyword: Detection, *leptospira spp.* , Leptospirosis, CRISPR-Cas

Introduction:

Leptospirosis is a zoonotic disease that affects global health, with over a million cases per year and 58,900 deaths (1). The disease is caused by pathogenic gram-negative spirochete Leptospira, which can adapt to the broad spectrum of mammalian hosts and environments (2, 3). The clinical signs and symptoms of leptospirosis shared similarities with various infectious diseases such as dengue, sepsis, and malaria. Therefore, it is difficult to be diagnosed.

One of the key barriers to reducing the impact of leptospirosis is the insensitive diagnostic tools currently available. There are three major standard methods recommended by WHO which are 1) Microscopic agglutination test (MAT), a serological-based diagnosis method. MAT is accurate but required a skilled technician, a well-equipped laboratory, and time-consuming. 2) Dark-field microscope diagnosis from sample culture collected from blood at the early stage of infection can also present *leptospira spp.* infection evidence. However, *leptospira spp.* is a slow-growing bacterium, so it might take weeks to get the results. 3) Real-time PCR, a nucleic acid detection method that is faster, accurate, and has been widely using as the primary diagnostic method. The Real-Time PCR equipment is expensive and not available for every hospital, especially the hospital in the rural area. (4, 5). Besides, most leptospirosis cases are often admitted to hospitals in rural areas without proper laboratory equipment. Therefore, we need a better diagnostic tool.

Rapid diagnostic tests (RDTs) could be the best tools for limited-resource settings. However, according to the previous study, the rapid test for leptospirosis IgM available in Thailand still lacks sensitivity, especially for early diagnosis (6). Recently, Recombinase Polymerase Amplification (RPA) is an isothermal nucleic acid amplification developed as a new diagnostic technique based on three enzymes: recombinase, A single-stranded DNA binding (SSB), and polymerase. RPA is simple, not requiring expensive laboratory equipment to perform, so it is ideal for low-resource diagnostics (7). Moreover, RPA can work with CRISPR-Cas12a that has been shown promising results of nucleic acid detection. (8-10). Our objective is to develop a Leptospirosis diagnostic tool using the RPA combined with CRISPR-Cas12a for early leptospirosis detection. We expect that RPA-CRISPR-Cas12a can detect *Leptospires* DNA using *SecY* genes which have been a good target for pathogenic *Leptospira spp.* detection in a human's blood allow us to develop a point-of-care diagnosis (POCD) for Leptospirosis (11-13).

Methodology:

Culture of *Leptospira*

The *leptospira spp.* isolated from the blood of *leptospira spp* infected patients were cultured in semi-solid Ellinghausen, McCullough, Johnson and Harris (EMJH) medium (14, 15) in 30^{o}C incubator for three weeks, then the culture was examined using dark field microscopy to confirm the existence of *leptospira spp*.

Primers, Probes, and CRISPR-Cas12 guide RNA

The forward and reverse primers selected from a conserved region part of the gene SecY from *leptospira interrogans* serovar Lai str. (16) The Both primers were then confirmed with in-silico analysis with Basic Local Alignment Search Tool (BLAST) (Table 1).

Oligonucleotides for single guide RNA (sgRNA) (1µM) and T7 promoter (1 µM) were used to generate the sgRNA with HiScribe™ T7 High Yield RNA Synthesis Kit (New England Biolabs (UK) Ltd) then purified by Monarch® RNA Cleanup Kit. (New England Biolabs (UK) Ltd) The concentration purified of crRNA product will be measured with Qubit 4 Fluorometer (Thermo Scientific) Then store at -80^{o}C.

Table 1: gRNA, RPA primers and DNA probe design

Materials	Design
T7 Promoter	5'-TAATACGACTCACTATAGGG-3'
SecYIV crRNA oligo	5'-ATGAACCCACCGTATTTTTTATCTACA CTTAGTAGAAATTACCCTATAGTGAGTCGTATTA-3'
*SecY*ctRNA	5'-AUGAACCCACCGUAU UUUUUAUCUACACUUAGUAGAAAUUA- 3'
SecYIV Forward Primer	5'-GCGATTCAGTTTAATCCTGC-3' (16)
SecYIV Reverse Primer	5'-GAGTTAGAGCTCAAATCTAAG-3'(16)
DNA probe	5'/56-FAM/AAAGCCAGGACAAGCGCCG/3IABkFQ/3' (9)

DNA extraction

The *leptospira* spp. From culture was counted using Petroff-Hauser counting chamber under darkfield microscopy as previously described. (17) A total of 10^8 copies of *leptospira sp.* will then processed for DNA extraction using High Pure PCR Template Preparation Kit (Roche, USA). After the DNA extraction, the concentration and quality of the extracted DNA will be determined by using Nanodrop (Thermo Scientific nd 1000, USA) at OD 260/280. The good purity of DNA OD should be between 1.6 to 1.8. Then store at -20^o C.

Recombinase Polymerase Amplification (RPA)

Leptospires *SecY* genes was amplified with RPA Basic kit (TwistDX, Cambridge, UK) with 0.48µM of forward primer and 0.48µM of reverse primer, 1µl template, and 14mM of MgOAC. Then incubated at 39ºC for 40 minutes followed by 75ºC for 5 minutes for heat inactivation.

CRISPR-Cas12a-based detection system for *Leptospires* infection.

The reaction of CRISPR-Cas12a composed of 30nM sgRNA, 330nM of EnGen® *Lba* Cas12a (cpf1) (New England Biolabs, USA), 600nM DNA probe, 1X NEBuffer 2.0 (New England Biolabs, USA), and 1µl of RPA amplicons. Total reaction volume was 15µl. The

CRISPR-Cas12a reaction was incubated with 39ºC for 20 minutes then the fluorescent signal was observed with naked eye using B-BOX™ Blue Light LED Epi-illuminator (SMOBIO Technology, Inc.) (Figure 1).

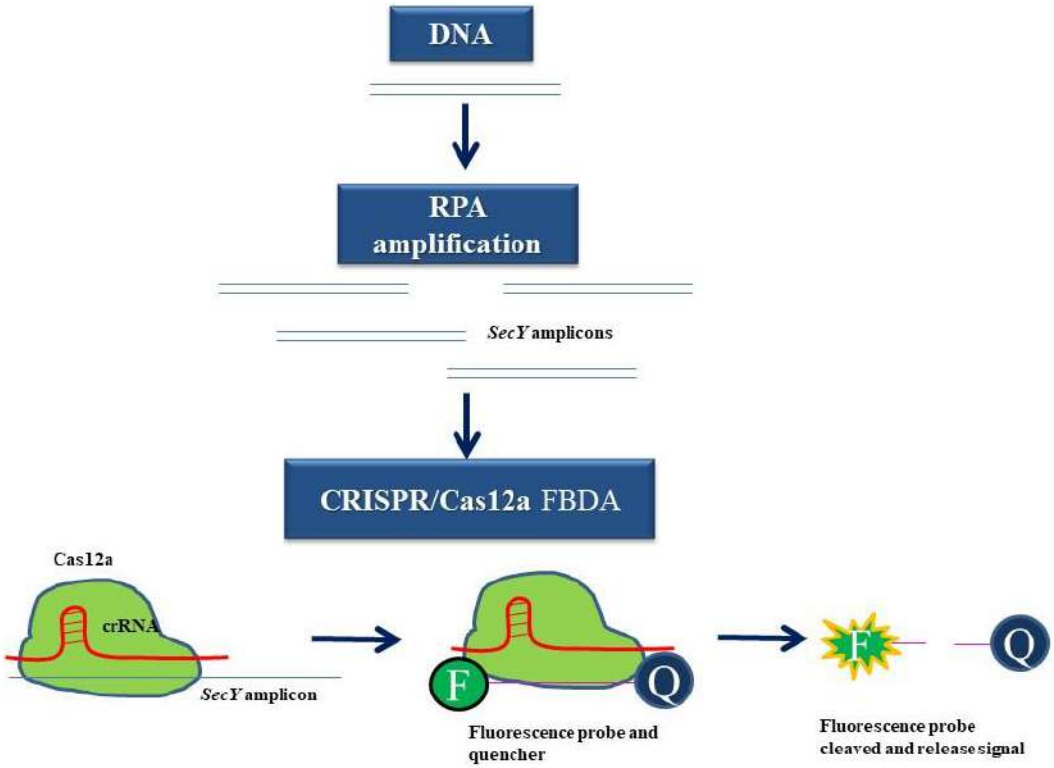

Figure 1. Detection of *leptospires* by RPA-CRISPR-Cas12a targeting *SecY* gene
Adapted from (18)

Limit of detection testing

The extracted DNA of 10^8 copies *leptospira spp.* was 10-fold serial diluted ranging from 10^6 to 10 copies/reaction. The limit of detection (LOD) was observed from the lowest concentration tube with a visible fluorescent signal. The two duplicated experiments were operated.

Results and Discussion:

In order to test the ability to detect *Leptospires* using RPA-CRISPR-Cas12a, the *leptospira spp.* standard ranging from 10^6 to 10 copies/reaction were amplified using RPA, followed by CRISPR-Cas12a-based detection. Two duplicated experiments showed that the limit of this new method's detection was approximately 10^2 copies/reaction without false positive or false negative (Figure 3).

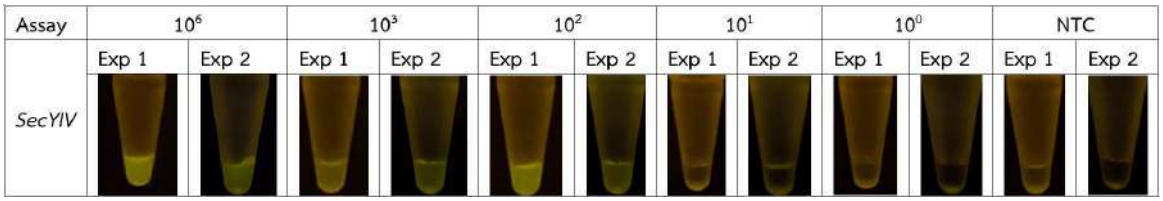

Figure 2. (b) Limit of detection for RPA-CRISPR-Cas12a targeting *SecY* gene. NTC is non-template control.

The RPA-CRISPR-Cas12a-based detection system is a new detection platform for nucleic acid detection of infectious diseases and has been used for many infectious disease detection.(18, 19) This study is the first report for *leptospires* detection using RPA-CRISPR-Cas12a-based detection targeting *SecY* gene with the 10^2 copies/reaction limit of detection. Although in earlier research, the *SecY* qPCR results showed the LOD at 10^0 (11), it is enough to detect the leptospirosis patient and give the treatment before the symptom is getting more severe, according to a previous study that 10^4 copies/ml of leptospires in the blood associated with severe leptospirosis.(20, 21)

Our study's strength is RPA-CRISPR-Cas12a-based detection targeting *SecY* is ideal for rural area hospital setup with less requirement of expensive laboratory equipment such as Real-Time PCR machine. We only need a heat-box for the isothermal reaction. However, confirmation tests with gold standard methods such as Real-Time PCR and Microscopic Agglutination Test (MAT) are still required. Moreover, clinical sample validation is still needed to investigate the sensitivity, specificity, and accuracy of our new assay and cross-reactivity testing with other infectious diseases or non-pathogenic *leptospira spp*.

Conclusion

Our study showed promising results with The RPA-CRISPR-Cas12a-based detection system targeting *SecYIV* gene with acceptable LOD, and it was capable of leptospires detection, which will help rural area hospitals. It is practical, simple, portable, rapid, and cost-effective.

Acknowledgments

We thank the Critical Care Nephrology Research Unit, Faculty of Medicine, Chulalongkorn University; the Excellence Center for Critical Care Nephrology (EC-CCN), King Chulalongkorn Memorial Hospital, Tropical Medicine Cluster, Chulalongkorn University; and Sisaket Provincial Public Health Office for their collaborative effort during data collection and participation in the study. We thank Suppalak Brameld (Section of Immunology Leptospirosis, Melioildosis, and Brucellosis, National Institute of Health, Department of Medical Sciences, Ministry of Public Health) for the MAT testing. The 100th Anniversary Chulalongkorn University Fund for Doctoral Scholarship and The 90thAnniversary of Chulalongkorn University Fund (Ratchadaphiseksomphot Endowment Fund for financial support).

References

1. Costa F, Hagan JE, Calcagno J, Kane M, Torgerson P, Martinez-Silveira MS, et al. Global Morbidity and Mortality of Leptospirosis: A Systematic Review. PLoS neglected tropical diseases. 2015;9(9):e0003898.
2. Levett PN. Leptospirosis. Clinical microbiology reviews. 2001;14(2):296-326.
3. Soo ZMP, Khan NA, Siddiqui R. Leptospirosis: Increasing importance in developing countries. Acta tropica. 2019;201:105183.
4. Ahmad SN, Shah S, Ahmad FM. Laboratory diagnosis of leptospirosis. Journal of postgraduate medicine. 2005;51(3):195-200.
5. Budihal SV, Perwez K. Leptospirosis Diagnosis: Competancy of Various Laboratory Tests. Journal of Clinical and Diagnostic Research : JCDR. 2014;8(1):199-202.

6. Dinhuzen J, Limothai U, Tachaboon S, Krairojananan P, Laosatiankit B, Boonprasong S, et al. A prospective study to evaluate the accuracy of rapid diagnostic tests for diagnosis of human leptospirosis: Result from THAI-LEPTO AKI study. PLoS neglected tropical diseases. 2021;15(2):e0009159.
7. Daher RK, Stewart G, Boissinot M, Bergeron MG. Recombinase Polymerase Amplification for Diagnostic Applications. Clinical chemistry. 2016;62(7):947-58.
8. Gootenberg JS, Abudayyeh OO, Lee JW, Essletzbichler P, Dy AJ, Joung J, et al. Nucleic acid detection with CRISPR-Cas13a/C2c2. Science (New York, NY). 2017;356(6336):438-42.
9. Gootenberg JS, Abudayyeh OO, Kellner MJ, Joung J, Collins JJ, Zhang F. Multiplexed and portable nucleic acid detection platform with Cas13, Cas12a, and Csm6. Science (New York, NY). 2018.
10. Chen JS, Ma E, Harrington LB, Da Costa M, Tian X, Palefsky JM, et al. CRISPR-Cas12a target binding unleashes indiscriminate single-stranded DNase activity. Science (New York, NY). 2018.
11. Bourhy P, Bremont S, Zinini F, Giry C, Picardeau M. Comparison of Real-Time PCR Assays for Detection of Pathogenic Leptospira spp. in Blood and Identification of Variations in Target Sequences. Journal of Clinical Microbiology. 2011;49(6):2154-60.
12. Waggoner JJ, Pinsky BA. Molecular diagnostics for human leptospirosis. Current opinion in infectious diseases. 2016;29(5):440-5.
13. Yap M-L, Sekawi Z, Chee H-Y, Alan Ong H, Neela V. Comparative analysis of current diagnostic PCR assays in detecting pathogenic Leptospira isolates from environmental samples. Asian Pacific Journal of Tropical Medicine. 2019;12(10):472-8.
14. Johnson RC, Harris VG. Differentiation of pathogenic and saprophytic letospires. I. Growth at low temperatures. J Bacteriol. 1967;94(1):27-31.
15. Chideroli RT, Gonçalves DD, Suphoronski SA, Alfieri AF, Alfieri AA, de Oliveira AG, et al. Culture Strategies for Isolation of Fastidious Leptospira Serovar Hardjo and Molecular Differentiation of Genotypes Hardjobovis and Hardjoprajitno. Frontiers in microbiology. 2017;8:2155-.
16. Ahmed A, Engelberts MF, Boer KR, Ahmed N, Hartskeerl RA. Development and validation of a real-time PCR for detection of pathogenic leptospira species in clinical materials. PLoS One. 2009;4(9):e7093.
17. Larson AD, Treick RW, Edwards CL, Cox CD. Growth studies and plate counting of leptospires. J Bacteriol. 1959;77(3):361-6.
18. Caliendo AM, Hodinka RL. A CRISPR Way to Diagnose Infectious Diseases. New England Journal of Medicine. 2017;377(17):1685-7.
19. Li Y, Li S, Wang J, Liu G. CRISPR/Cas Systems towards Next-Generation Biosensing. Trends in biotechnology. 2019;37(7):730-43.
20. Truccolo J, Serais O, Merien F, Perolat P. Following the course of human leptospirosis: evidence of a critical threshold for the vital prognosis using a quantitative PCR assay. FEMS microbiology letters. 2001;204(2):317-21.
21. Segura ER, Ganoza CA, Campos K, Ricaldi JN, Torres S, Silva H, et al. Clinical spectrum of pulmonary involvement in leptospirosis in a region of endemicity, with quantification of leptospiral burden. Clinical infectious diseases : an official publication of the Infectious Diseases Society of America. 2005;40(3):343-51.

DETERMINATION OF ORGANIC AND INORGANIC ELEMENTS IN THE BIOGAS DIGESTATE LIQUID

Thipwan Jiemanukunkij[1], Thunyaphat Amawatchana[2], Pimchai Chaiyen[2], Thanyaporn Wongnate[2], Somchart Maenpuen[1,*]
[1]Department of Biochemistry, Faculty of Science, Burapha University, Chonburi 20131, Thailand
[2]School of Biomolecular Science and Engineering, Vidyasirimedhi Institute of Science and Technology (VISTEC), Rayong 21210, Thailand
*e-mail: somchart@go.buu.ac.th

Abstract:

In this report, the organic and inorganic elements serving as macronutrients and micronutrients as well as toxicants in biogas digestate liquid (BDL) were investigated. Samples from 5 batches of anaerobic co-digestion of animal manure inoculum and food waste harvested during January-May, 2020 were quantitatively measured using atomic absorption spectrometry and carbon-nitrogen-sulfur analyses. The results showed that for the macronutrients measured among 5 batches, the nitrogen, potassium, phosphorus and sulfur contents were fluctuated due to food waste intake, while the calcium contents were in a broad range of 20-43 ppm. For measurement of the micronutrients such as iron, zinc and copper, their contents were consistent in all batches. For the analysis of toxic elements in BDL, we could not detect any arsenic and cadmium while chromium (12-23 ppb) and lead (7-77 ppb) contents were detected in trace amount and lower than the regulation level required by Department of Agriculture (DOA) of Thailand. The study presented herein demonstrates that BDL contains all essential without toxic elements, supporting that BDL is suitable for serving as an environmentally friendly plant-promoting biostimulant.

Introduction:

The rising world population demands increase of energy, water and food which can result in the generation of more organic wastes that could affect the environment. There are three main groups of organic wastes including crop wastes from agricultural industry, food wastes from daily consumption and animal wastes from livestock such as pig, cow, and chicken farming.[1,2] These wastes can cause air pollution, environmental problems, and global warming. For example, animal manure wastes can cause unpleasant odor. One of the methods employed to solve this problem is using an anaerobic digestion (AD) process in which no oxygen is required for digestion. The major product obtained from AD process is biogas such as methane (CH_4) which can be used as a household energy.[3] The main byproduct from biogas production is digestated liquid or "biogas digestate liquid (BDL)" which can be used as an organic fertilizer because BDL usually contains nitrogen (N), phosphorus (P), potassium (K), zinc (Zn), iron (Fe), and sulfur (S), *etc*. that are essential for plant growth.[4]

Most of organic fertilizers contain plant nutrients that can be divided into 2 groups including macronutrients and micronutrients. N, P, K, Ca, S, and Mg serve as macronutrients while trace elements such as Fe, Zn, manganese (Mn), copper (Cu), boron (B), molybdenum (Mo) and chlorine (Cl) are classified as micronutrients.[5] Plants need these nutrients to promote growth. The macronutrients play crucial roles in plant developments such as promoting chlorophyll synthesis or green color development in plant, initiating the root protrusion, seeding, fruiting and flowering, controlling the turn-on and turn-off switches of the leaf stomata that are involved in cell division. In addition, the macronutrients play an important role in syntheses of chlorophyll components, amino acids and vitamins and the enhancements of the growth of roots and seeds. While the micronutrients

are involved in the synthesis of auxin, chlorophyll and starch, and also promote growth of the plant reproductive system.[6,7]

Because of their important roles in plant growth and development, in this study, plant nutrients –organic and inorganic elements– and toxic elements in BDL obtained from anaerobic co-digestion of animal manure inoculum and food waste have been quantitatively measured by atomic absorption spectrometry (AAS) and carbon-nitrogen-sulfur (CNS) analyses. The study will provide the data set that can be used as a quality control and beneficial for evaluation of BDL as an environmentally friendly organic fertilizer.

Methodology:

Instruments, chemical reagents and sample collection

The instruments used in this study were AAS (PinAAcle 900T PerkinElmer) for analysis of elements, CNS 628 series elemental analyzer (LECO corporation) for analysis of carbon, nitrogen and sulfur. All chemical reagents used were of high purity and analytical grades. All metal standards for AAS analysis were commercially available as a solution with 1000 ppm stock in 2% (v/v) HNO_3 (Perkin Elmer Pure). For CNS analysis, EDTA and coal (LECO Certified Reference Materials) was used a reference for determining N and S content, respectively.

The biogas digestate liquid (BDL) obtained from anaerobic co-digestion of animal manure inoculum and food waste was kindly provided by the Biosynthai Biotechnology Co., Ltd., and was harvested in 5 batches during the period of 5 months in 2020 (January, February, March, April and May).

Sample preparation for AAS analysis

Different batches of BDL were pre-treated prior to performing AAS analysis. For AAS analysis of general elements, the treatment process was carried out by the standard protocol described in the American Society for Testing and Materials (ASTM; designation number D1971-16). In principle, the sample was digested with mineral acids and heated at atmospheric pressure. 100 ml of each BDL sample was added into 0.5 ml of the concentrated HNO_3 (63% (w/w)) and 5 ml of the concentrated HCl (37% (w/w)). Then, the sample was heated at 80 ^oC on a hot plate with care of avoiding sample boiling until the sample volume was reduced to 20 ml. After that, the acidified sample was centrifuged at 15,000 rpm for 30 min and the supernatant was added with 2% (v/v) HNO_3 to obtain the final volume of 100 ml and then stored at 4 ^oC until use. Before applying the digested sample into the AAS instruments, the digested sample was filtered by a 0.22 μm syringe filter to remove small particulates. For arsenic (As) analysis, the digested sample received additional treatment. In a total volume of 10 ml, 1 ml of the digested sample was added into 6 ml of a Milli-Q® Type I ultrapure water, 2 ml of a mixture solution (5% (w/v) potassium iodide (KI) and 5% (w/v) ascorbic acid) and 1 ml of the concentrated HCl. The reaction was placed in a fume hood for 1 h to allow the reduction of As^{5+} into As^{3+}, as the As^{3+} gives good signals in AAS analysis.

Atomic absorption spectroscopy

The conditions used in AAS analysis were as follows: the light sources that generate the particular wavelengths for detection of each type of element were a hollow cathode lamp (HCL) for analysis of P, K, Fe, Zn, Cd, Cr, Cu and Pb, and an electrodeless discharge lamp (EDL) for analysis of As. The source of energy for free-atom production from heating an air/acetylene flame was used for analyzing K, Fe, Zn, Cd, Cr, Cu and Pb, while nitrous oxide/acetylene flame was used for analyzing P. The sample flow rate was 8.8 mL/min. Different types of burners were used for different types of flames. For air/acetylene flame, the stainless-steel burner should be used while nitrous oxide/acetylene flame was compatible with the titanium burner.

CNS analysis

For analysis of carbon, nitrogen and sulfur in BDL samples, no pretreatment process was required. A sample was directly placed in a nickel boat liner within the oven. The sample was then heated sequentially at 950 ºC in a primary furnace, then 850 ºC in secondary furnace for analysis of nitrogen and carbon, respectively. For sulfur analysis, heating at 1,350 ºC was applied. During the combustion process, the 99.99% oxygen gas (O_2) was applied to oxidize C, S and N to detectable gas forms–carbon dioxide (CO_2), sulfur dioxide (SO_2) and nitric oxide (NOx), respectively. The gases were detected by the infra-red (IR) and thermal conductivity (TC) cells. The non-dispersive IR (NDIR) cell was used for detection of CO_2 and SO_2 for determination of C and S, while TC cell was used to detect NOx for quantitation of N. EDTA and coal were used as reference materials (RMs) to determine the content of N and S, respectively.

Results and Discussion:

Quantitation of macronutrients

The macronutrients that were analyzed including N, P, K, Ca, and S. The CNS analyzer was used to determine N and S contents by using EDTA and coal as RMs, respectively. The results in Figure 1A showed that the N contents in BDL harvested in January and March 2020 were closely similar with 0.03-0.04% (w/w). While in February and April 2020, The N contents were lower than those in January and March for about 2 folds. In contrast, the N content in BDL harvested in May 2020 was incredibly high. This could be due to a variety of feeding food wastes.[8] While the S contents were likely increased from January to May 2020 (Figure 1B). This may depend on the different sources of feeding.[9]

For P, K and Ca content analyses, AAS was used to determine the concentration of each element using an individual calibration curve plot. To determine the concentration of P, the absorbance at 213.55 nm was measured. Based on the P standard curve in a range of 25-800 ppm, the P contents in BDL were determined and found to be increased from January to May 2020 (Figure 1C). For K analysis, the absorbance at 766.49 nm was measured and a calibration curve plot was constructed in a range of 0.1-5 ppm. The results in Figure 1D indicated that the K contents measured in BDL of 4 batches (January, February, March and April) were similar in a range of 1,126-1,517 ppm, while it was lower in May (858 ppm). The previous report demonstrated that the K concentration at 6 mM could enhance the N source assimilation and photosynthesis.[10] Based on the formula weight of K of 39.098 g/mol, the concentration of K determined for each batch (from January to May) could be estimated as about 39, 32, 29, 36 and 22 mM, respectively. These concentrations were rather high and could inhibit the growth and root development. However, in the real use, BDL is generally diluted 10-fold to obtain the potassium salt in a range of about 3 mM, which is at the concentration beneficial for plant growth.[10]

For analyses of the Ca contents, it should be noted that the measurement was not done by absorption but by emission instead. Based on a Ca calibration curve plot in a range of 10-200 ppm, the results showed that the Ca contents in February and March were higher than those in January, April and May about 2 folds (Figure 1E). The high Ca contents detected in BDL were beneficial for controlling the water content in plant cells as the previous report indicated that Ca is involved in regulating the stomatal opening and closure.[11]

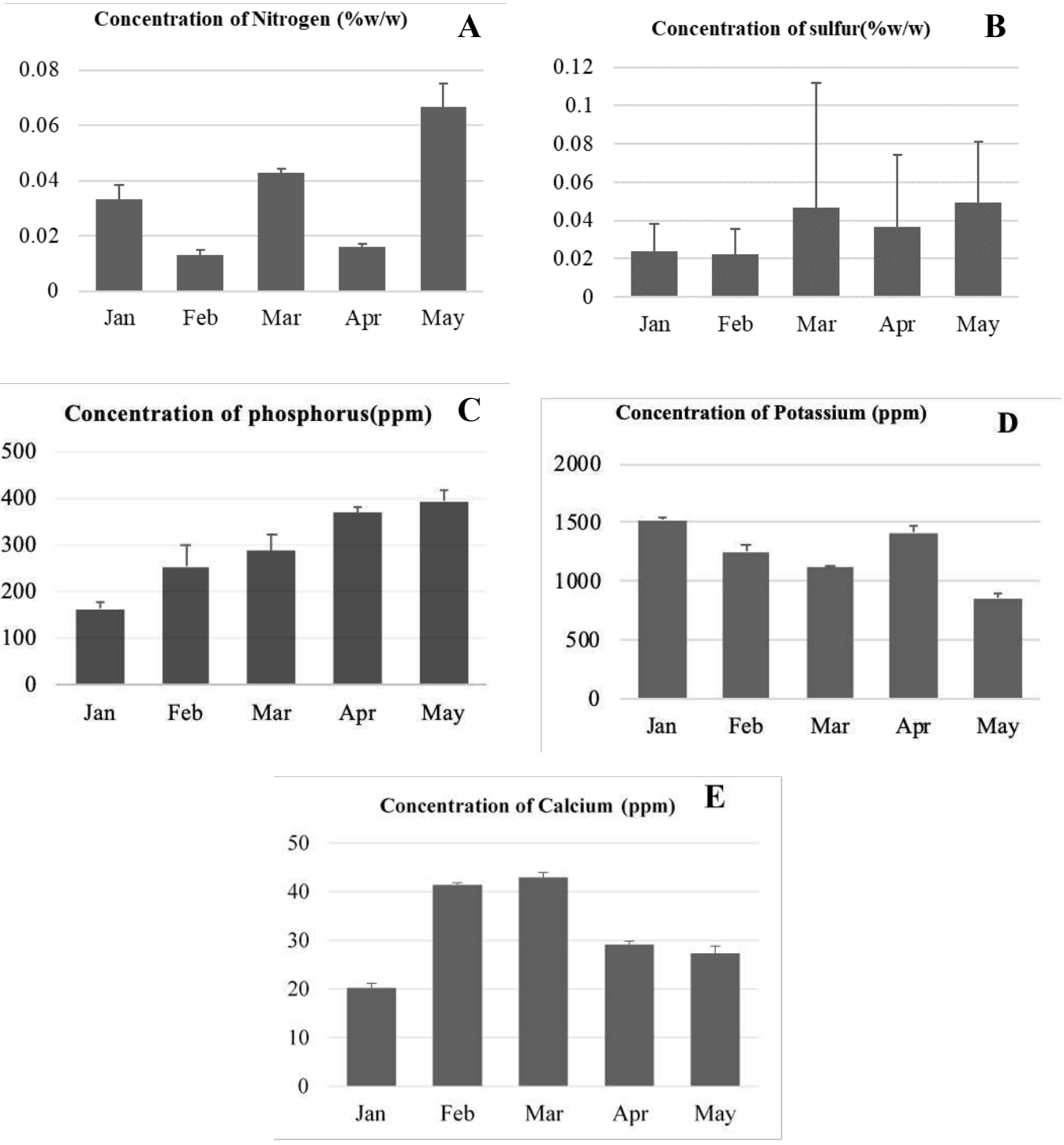

Figure 1. Quantitation of macronutrients in BDL harvested in 5 batches (from January to May 2020) by CNS analyzer and AAS. Analyses of the nitrogen (A) and sulfur (B) contents by CNS analyzer. Analyses of the phosphorus (C), potassium (D) and calcium (E) contents by AAS. Error bars represent standard deviations (S.D.) from three replications of the data. All concentrations determined were summarized in Table 1.

Quantitation of micronutrients

The micronutrients including Cu, Fe and Zn were quantitatively analyzed by AAS techniques. These elements are involved in synthesis of crucial substances such as auxin, chlorophyll and starch during plant growth. The Cu content analysis at absorbance 324.75 nm using a calibration

curve plot with a range of 5-500 ppm showed that the Cu contents in January and May were higher than those in February, March and April 2020 for about 2 folds (Figure 2A). For the measurement of the Fe contents at absorbance 248.33 nm, the results indicated that using a standard curve with a range of 0.25-5 ppm, the Fe contents in 5 batches were similar with 1.5-2 ppm (Figure 2B). While the Zn contents measured absorbance at 213.86 nm and using a standard curve with a range of 0.1-2 ppm were found the highest in January and May with 1.3 ppm (Figure 2C). The presence of these micronutrients in BDL could be because of the food that were good source of Fe, Zn and Mg.[12]

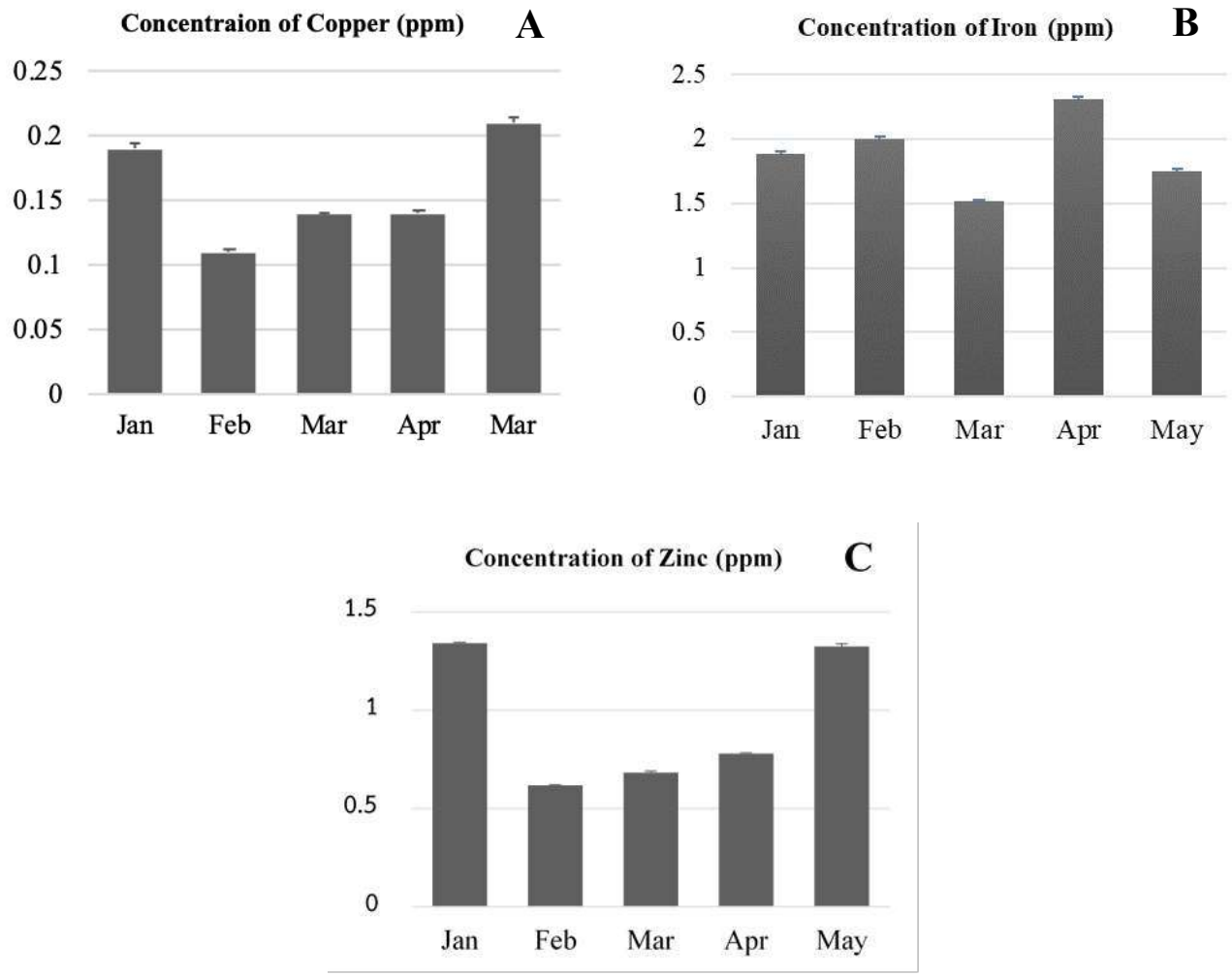

Figure 2. Quantitation of micronutrients in BDL harvested in 5 batches from January to May 2020 by AAS. Analyses of the copper (A), iron (B) and zinc (C) contents by AAS. Error bars represent standard deviations (S.D.) from three replications of the data. All concentrations determined were summarized in Table 1.

Quantitation of toxic elements

According to the declaration by Department of Agriculture (DOA) of Thailand, the toxic elements affecting plant growth include As, Cd, Cr and Pb. The quantity of these elements must be controlled to not exceed the values regulated by DOA. All toxic elements were determined based on a standard curve plot of each element in the ppb concentration range. The results showed that only two toxic elements –Pb (Figure 3A) and Cr (Figure 3B)– could be detected by AAS analysis, while the other two elements, As and Cd, could not be detected. The Pb contents in BDL harvested in January and February was 75-77 ppb, 30-40 ppb in March and April, and only 7 ppb in May (Figure 3A). For the Cr contents in BDL harvested during this period, they were detected at very low

concentration around 12-23 ppb (Figure 3B). The detection of toxic elements in BDL could be due to organic nutrient sources (animal feed or human food) that contained trace amount of these elements.[13] However, the amount of Pb and Cr detected in BDL are rather low when compared to the level required by the DOA regulation (Pb ≤5,000 ppb and Cr ≤3,000 ppb), suggested that BDL is safe for users and serving as an environmentally friendly plant-promoting biostimulant.

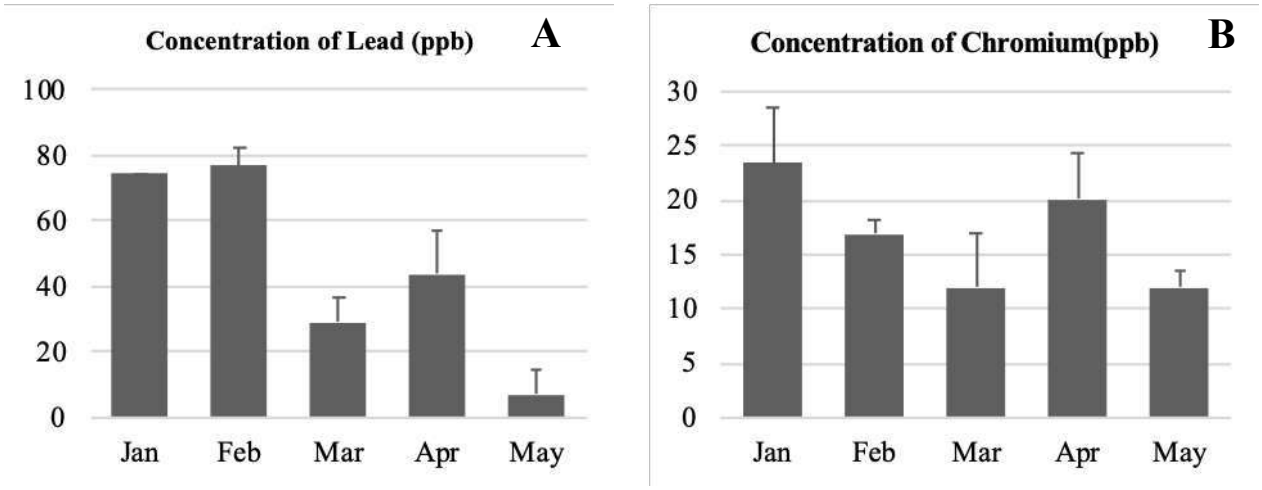

Figure 3. Quantitation of toxic elements in BDL harvested in 5 batches from January to May 2020 by AAS. Analyses of the lead (A) and chromium (B) contents by AAS. Error bars represent standard deviations (S.D.) from three replications of the data. All concentrations determined were summarized in Table 1.

Determination of C/N ratio

The carbon-to-nitrogen (C/N) ratio is the ratio of total element of carbon (C_{total}) and total nitrogen (N_{total}) that is used as a representative for analyzing the source of sedimentary organic matters.[14] In this report, the C/N ratio in BDL harvested during 5 batch periods were analyzed. The results shown in Figure 4 demonstrated that the C/N ratios were in a range of about 1.5-3.8 which were within the specified range recommended by DOA (≤20). The C/N ratios are crucial indicators for energy and nutrient sources in the AD process. It should be noted that when the carbon substances are present more than nitrogen sources, it can cause changes in the microorganism's community in the system and affect the AD process.[15] The higher C/N ratios, the slower composting reactions.[16]

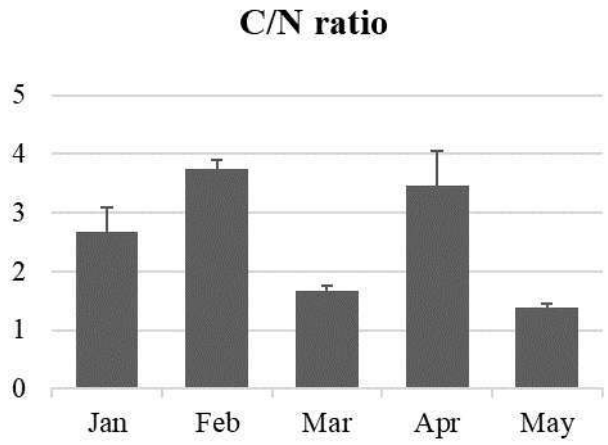

Figure 4. The C/N ratios in BDL harvested in 5 batches from January to May 2020. Error bars represent standard deviations (S.D.) from three replications of the data. All concentrations determined were summarized in Table 1.

Table 1. Summary of the quantitation of organic and inorganic elements in BDL harvested in 5 batches from January to May 2020.

Parameters	Month				
	January	**February**	**March**	**April**	**May**
Macronutrients (ppm)					
Total nitrogen[a]	0.030 ± 0.005	0.010 ± 0.002	0.040 ± 0.002	0.010 ± 0.001	0.070 ± 0.008
Total phosphorus	163 ± 16	255 ± 44	287 ± 37	370 ± 11	394 ± 25
Total potassium	1,517 ± 19	1,255 ± 54	1,126 ± 11	1,410 ± 62	858 ± 35
Sulfur (S)[a]	0.02 ± 0.01	0.02 ± 0.01	0.03 ± 0.05[*]	0.04 ± 0.04[*]	0.05 ± 0.03
Calcium (Ca)	20 ± 1	41 ± 1	43 ± 1	29 ± 1	27 ± 2
Micronutrients (ppm)					
Iron (Fe)	1.90 ± 0.02	2.00 ± 0.02	1.500 ± 0.004	2.30 ± 0.02	1.80 ± 0.01
Zinc (Zn)	1.300 ± 0.004	0.600 ± 0.001	0.700 ± 0.008	0.800 ± 0.003	1.300 ± 0.013
Copper (Cu)	0.200 ± 0.005	0.100 ± 0.003	0.100 ± 0.001	0.100 ± 0.003	0.200 ± 0.005
Toxic element (ppb)					
Arsenic (As)	ND	ND	ND	ND	ND
Cadmium (Cd)	ND	ND	ND	ND	ND
Chromium (Cr)	23 ± 5	17 ± 1	12 ± 5	20 ± 4	12 ± 1
Lead (Pb)	75 ± 0	77 ± 6	29 ± 8	44 ± 13	7 ± 8[*]
Nutrient balance in AD process					
C/N ratio	2.2	3.6	1.6	3.8	1.5

[a]Analysis by CNS analyzer and the unit presents as %w/w.
[*]The data obtained are fluctuated among three replications.
ND, not detected.

Conclusion

In this study, plant macronutrients and micronutrients consisting of organic and inorganic elements in BDL harvested in 5 batches during January to May, 2020 were quantitatively measured using CNS and AAS analyses. The data indicate that BDL from different batches contained plant nutrients that are essential for plant growth. In addition, toxic elements were not detected or detected

in trace amount, suggesting that BDL is suitable for serving as an environmentally friendly plant-promoting biostimulant.

Acknowledgements

This work was supported by The National Research Council of Thailand (NRCT) Grants NRCT5-RSA63012-01 (to S. M.) and NRCT5-RSA63025-02 (to T. W.) and funding supports from Vidyasirimedhi Institute of Science and Technology (VISTEC) and Global Partnership Program from Program Management Unit-B and Royal Academy of Engineering (UK) (to P. C., T. W. and T. A.). We thank Science Innovation Facility (SIF) at Faculty of Science, Burapha University for AAS support, and School of Biomolecular Science and Engineering at Vidyasirimedhi Institute of Science and Technology (VISTEC) for kind support of CNS analyzer. We also thank the Biosynthai Biotechnology Co., Ltd. for providing BDL for this study.

References

1. Wainaina S, Awasthi MK, Sarsaiya S, Chen H, Singh E, Kumar A, Ravindran B, Awasthi SK, Liu T, Duan Y, Kumar S, Zhang Z, Taherzadeh MJ. Bioresour Technol. 2020;301:122778–122791.
2. Westerman PW, Bicudo JR. Bioresour Technol. 2005;96:215–221.
3. Cheong JC, Lee JTE, Lim JW, Song S, Tan JKN, Chiam ZY, Yap KY, Lim EY, Zhang J, Tan HTW, Tong YW. Sci Total Environ. 2020;715:136789–1367800.
4. Iocoli GA, Zabaloy MC, Pasdevicelli G, Gómez MA. Sci Total Environ. 2019;647:11–19.
5. Maathuis FJ, Diatloff E. Methods Mol Biol. 2013;953:1-21.
6. Osman KT. In: Soils, Principles, Properties and Management. Springer, Dordrecht. 2013:129–159.
7. Uchida R. In: Plant Nutrient Management in Hawaii's Soils, Approaches for Tropical and Subtropical Agriculture. 2000:31–55.
8. Jamaludin SN, Kadir AA, Azhari NW. MATEC Web Conf. 2017;103:05015–05022.
9. Wickham R, Galway B, Bustamante H, Nghiem LD. Int biodeter biodegr. 2016;113:3–8.
10. Xu X, Du X, Wang F, Sha J, Chen Q, Tian G, Zhu Z, Ge S, Jiang Y. Front Plant Sci. 2020;11:904–916.
11. Yoshioka K, Moeder W. Nature. 2020;585:507–508.
12. Amarakoon D, Thavarajah D, McPhee K, Thavarajah P. J Food Compos Anal. 2012;27:8–13.
13. Bloem E, Albihn A, Elving J, Hermann L, Lehmann L, Sarvi M, Ylivainio K. Sci Total Environ. 2017;607-608:225–242.
14. Nasir A, Lukman M, Tuwo A, Hatta M, Tambaru R. Front Mar Sci. 2016;3:266–273.
15. Liang X, Yuan J, Yang E, Meng J. Eur J Soil Biol. 2017;82:50–55.
16. Martin AM. In: Maximising the Value of Marine By-Products. Elsevier. 2007:486–515.

DRAFT GENOME ANALYSIS OF A BEE SYMBIONT-DERIVED ANTIMICROBIAL PRODUCER *Streptomyces* I-EHB-18

Prachakchit Chumkieo,[1] Pinidphon Prombutara[2] Tanapat Palaga,[1] Chompoonik Kanchanabanca[1],*
[1] Department of Microbiology, Faculty of Science, Chulalongkorn University, Thailand
[2] Omics Sciences and Bioinformatics Centre, Chulalongkorn University, Thailand
*e-mail: chompoonik.k@chula.ac.th

Abstract:

Bee symbiont *Streptomyces* I-EHB-18 with broad spectrum of antimicrobial activity was subjected for genome analysis to predict the potential to be novel natural product producer. A draft genome sequence had a size of 8.8 Mbp with the G+C content of 73%. The genome assembly resulted in 168 contigs containing 7,539 coding sequences. The complete 16S rRNA analysis revealed *Streptomyces andamanensis* KC-112^T (99.86%) as the most closely related strain. The phylogeny analysis with other reported bee symbiont-derived *Streptomyces* species showed the diversity among difference sources of bees. The secondary metabolites biosynthetic gene clusters (BGCs) analysis predicted that *Streptomyces* I-EHB-18 genome contained multiple gene clusters with the potential for the production of various types of compounds such as terpene, polyketide, non-ribosomal peptide, peptide, butyrolactone, phosphoglycolipid and amglyccycl. Thus, this study spotlights the bioactive potential of *Streptomyces* I-EHB-18 using genomics-based approach.

Introduction:

Actinomycetes are free-living bacteria which are ubiquitously found in natural ecosystems. This group plays an important role in terrestrial, fresh water, and marine environments as decomposers. Moreover, many actinomycetes have co-existed with other species such as plants, animals, fungi, and insects by symbiosis[1].

Streptomyces, the largest genus of actinomycetes, is best known as a producer of various secondary metabolite such as geosmin (earth odor), siderophore (nutrient pirating molecules), and especially bioactive compounds, e.g., antibiotics, antifungals, antivirus, antiparasitic, and immunosuppressive agents. Most of the bioactive compounds produced are antibiotics[2]. However, the number of new metabolites as novel bioactive compounds has decreased because most common compounds were discovered[3]. Isolation of strains of microorganisms from unexplored extreme habitats, e.g. deep sea, dessert, volcanoes and etc., should enhance chances of deriving novel compounds[4]. In addition, investigating symbiosis species, such as endophytes[5] and insects[6], also leads to discover a wide variety of new strains and compounds. Cyphomycin, is an example for a new antifungal compound from a Brazilian *Streptomyces* (ISID311) isolated from the microbiome of the fungus-growing ant *Cyphomyrmex* sp.[6].

From our previous study of Tangwichai (2016)[7], several *Streptomyces* strains with antimicrobial activities were isolated from eastern honeybee (*Apis cerana*). The results showed that the isolated *Streptomyces* I-EHB-18 presented broad spectrum of antimicrobial activity against *Bacillus subtilis*, *Escherichia coli*, *Staphylococcus aureus*, and *Candida albicans*. Previous strain identification by 16S rRNA gene sequencing revealed that

Streptomyces. I-EHB-18 was closely related to *Streptomyces andamanensis* (98% identity)[8]. However, there has been no information on *S. andamanensis* whole genome sequence.

As types of metabolites produced by *Streptomyces* could be determined based on sequences of biosynthetic gene clusters situated on their chromosome. Examination of genomic sequence using bioinformatics tools could help indicating the number of biosynthesis gene clusters (BCGs) and also predicting expected metabolite types[9]. Therefore, the purpose of this work was to analyze draft genome of *Streptomyces* I-EHB-18 to evaluate its secondary metabolites biosynthetic gene clusters. This will contribute to new databases and genetic information of *Streptomyces* I-EHB-18 for further study as a highly potential antimicrobial producer.

Methodology:

1. Strain and cultivation

Streptomyces I-EHB-18 was recovered from Microbial Culture Collection, Department of Microbiology, Faculty of Science, Chulalongkorn University and cultured in International Streptomyces Project-2 (ISP-2) medium (0.4% yeast extract, 1% malt extract, 0.4% dextrose)[10] at 30˚C.

2. Electron microscopy

The morphology of *Streptomyces* I-EHB-18 for scanning electron microscopy (SEM) was prepared by culturing the strain on ISP-2 agar for 14 days. Observation under SEM was conducted at Scientific and Technological Research Equipment Centre, Chulalongkorn University.

3. Whole genome sequencing

Genomic DNA of *Streptomyces* I-EHB-18 was extracted using TIANamp Bacterial DNA Kit (Tiangen Biotech, Beijing, China). The extracted genomic DNA was sequenced and generated a draft genomic DNA sequence by Omics Sciences and Bioinformatics Centre, Chulalongkorn University using Illumina MiSeq system.

4. Draft genome analysis

The draft genomic DNA sequence was analysed for general features using Galaxy[11]. CGView Server was used to construct a circular draft genome map[12]. Gene annotation was analysed via CGView by Prokka[13]. JSpeciesWS was used for comparing the genome sequence with a group of closely related species[14]. MEGA11 was used for sequence alignment and creation of a neighbor-joining phylogenetics tree based on 16S rRNA gene sequence of *Streptomyces* I-EHB-18 among others *Streptomyces* isolated from bees[15]. antiSMASH was used for the analysis of secondary metabolite biosynthesis gene clusters[9].

Results and Discussion:

1. General features of Streptomyces I-EHB-18

Streptomyces I-EHB-18 from eastern honeybee (*Apis cerana*) was isolated and preserved by Tangwichai (2016)[7]. General properties are aerobic, Gram-positive, filamentous actinomyces. When cultured on solid medium ISP-2 agar, *Streptomyces* I-EHB-18 colonies appeared greenish white (color code 153) to light olive gray color (color code 112) (Figure 1) according to ISCC-NBS color system. From SEM result (Figure 1), the individual spore shape is oval with smooth surface forming spiral spore chains as same as described for *S. andamanensis* KC-122^T on Sripreechasak (2016)[8].

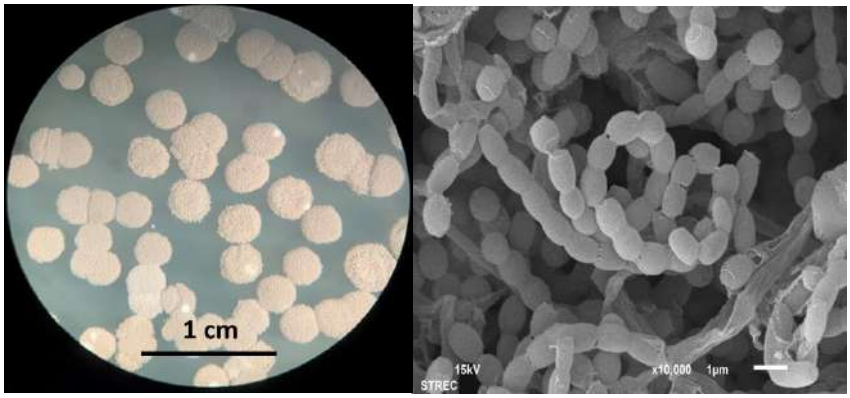

Figure 1 *Streptomyces* I-EHB-18 colony morphology on ISP-2 agar plate under stereo microscope (left), and under SEM, Bar 1 μm (right).

2. General genomic information and phylogeny of Streptomyces I-EHB-18

Streptomyces I-EHB-18 draft genome sequence had a size of 8,831,774 bp with a contig length of N50 at 156,168 bp. The average G+C content was predicted as 73%. The genome assembly resulted in 168 contigs containing 2 rRNAs and 93 tRNAs (Table 1 and Figure 2). In regard to genome size and %G+C, *Streptomyces* genomes with the high %G+C content produced many homopolymer G and C stretches resulting in displaying errors during base-calling and genome assembly and causing difficulty during short read. Accordingly, roughly 90% of the available genomes were only available in draft status[16]. Thus, in order to achieve a complete whole genome of *Streptomyces* I-EHB-18, combination of long and short read sequencing would enable generating genome to be more complete[17]. Actinobacteria have two different topologies which are linear and circular genome forms. Most Actinobacteria have circular form but some genera such as *Streptomyces*, *Actinomyces*, *Amylolatopsis*, *Actinoplanes*, *Streptoverticillium*, and *Micromonospora* present linear genome[18]. Referring to the *Streptomyces* genus, *Streptomyces* I-EHB-18 could possibly have linear form. However, CGView Server has limitation on inability of constructing more conventional linear maps[12]. The number of predicted proteins by Prokka showed the total of 7,539 coding sequences (CDSs) consisting of 713 putative proteins (9.45%), 3,085 hypothetical proteins (40.9%), and 3,741 unknown proteins (49.65%). Identification of these hypothetical and unknown function genes in *Streptomyces* I-EHB-18 could be further conducted to verify their roles.

Table 1. Characteristics of *Streptomyces* I-EHB-18 genome

Attribute	Value
Number of contigs	168
Genome size (bp)	8,831,774
GC content (%)	73
N50	156,168
L50	18
rRNA	2
tRNA	93
Protein-coding sequence (CDs)	7,539

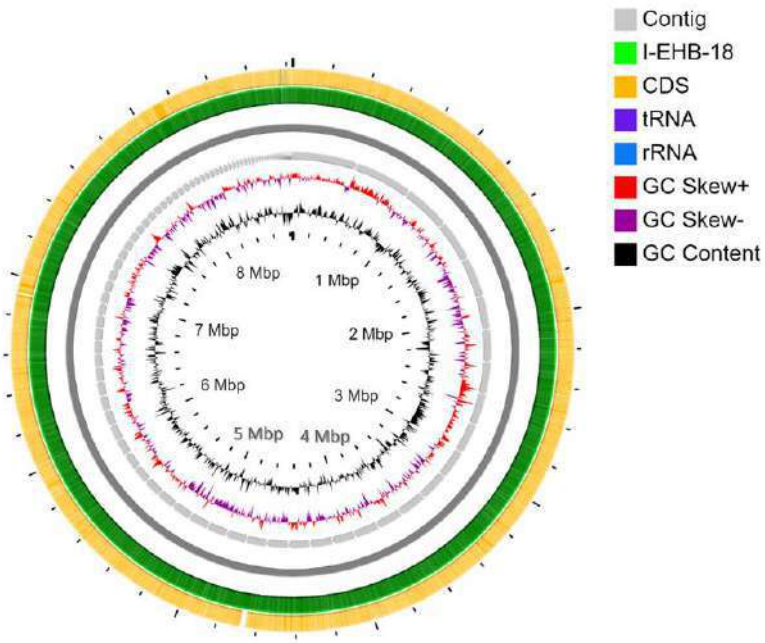

Figure 2. Circular representation of *Streptomyces* I-EHB-18 genome created by CGView Server

3. Streptomyces I-EHB-18 identification

To reidentify *Streptomyces* I-EHB-18 using the new genomic sequence information, 8,831,774 base pair of the draft genome sequence was aligned with close species assigned by Jspecies. The result showed that the closest species according to genomic sequence was *Streptomyces* sp. SAT1 which had average nucleotide identity (ANI) 97.54%. *Streptomyces* sp. SAT1 closely related species is *Streptomyces anandii* NRRL B-3590^T based on its 16s rRNA sequence[19]. *Streptomyces* sp. SAT1 presented antifungal activity highly active against pathogenic filamentous fungi *Dothiorella gregaria*, and moderate activity against *Botryospaeria dothidea* and *Sclerotinia sclerotiorum*[19]. Thus, it is possible that *Streptomyces* I-EHB-18 can be beneficial as biocontrol agents for plant pathogens inhibition. However, when analysed with EzBioCloud using the complete 16S rRNA gene sequence of *Streptomyces* I-EHB-18 from the draft genome sequence (1,525 base pair) the closest candidate was *S. andamanensis* KC-112^T (99.86%). Nevertheless, the soil isolated *S. andamanensis* KC-112^T which was identified as new species by Sripreechasak[8] still has not been undertaken whole genome sequencing yet. According to the morphology observation of *Streptomyces* I-EHB-18 and SEM results, the aerial mycelium color and spore chain form were very similar to *S. andamanensis* KC-112^T. Therefore, our *Streptomyces* I-EHB-18 draft genome sequence could probably represent genome sequence of *S. andamanensis*.

As a source of *Streptomyces* I-EHB-18 was bee, the phylogeny of *Streptomyces* I-EHB-18 and others *Streptomyces* previously isolated from bees reported could describe relationship and variety of bee associated *Streptomyces* as endosymbiont. Gene sequences of 16s rRNA of *Streptomyces* isolated from variety sources of bees including South-East Asian stingless bee (*Tetragonilla collina*)[20], stingless bee *(Tetragonisca angustula*)[21], Hymenoptera[22] and beehives[23], were used to generate a neighbor-joining phylogenetics tree (figure 3). *Micromonospora siamensis* was used as an out group. The tree illustrated that *Streptomyces* I-EHB-18 has never been previously isolated from other bees, and *Streptomyces* strains isolated from difference source of bees are very diverse. Thus, bee-symbiont is a potential sources of novel bioactive compound producers, especially, *Streptomyces* species.

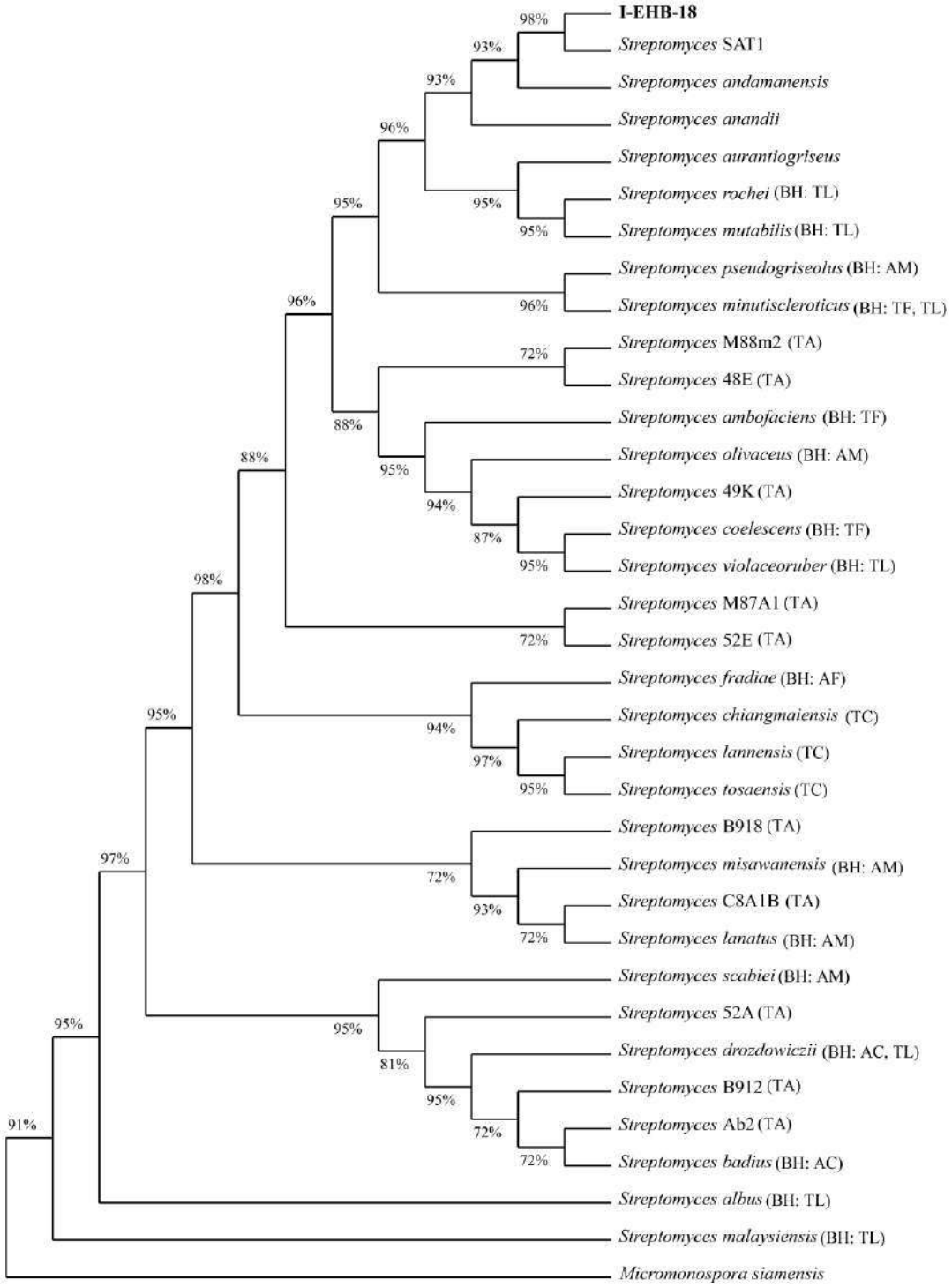

Figure 3. Neighbour-joining tree analysis of 16S rRNA of *Streptomyces* I-EHB-18 and bee-associated *Streptomyces*. Bootstrap values based on 1,000 replications were shown at branch nodes. The evolutionary distances were computed using Maximum Composite Likelihood method. *Micromonospora siamensis* was used as an out group. Abbreviation after species and strains shown source of isolation: AC; *Apis cerana*, AF; *Apis florea*, AM; *Apis mellifera*, BH; beehive, TA; *Tetragonisca angustula*, TC; *Tetragonilla collina*, TF; *Trigona fuscobalteata* and TL; *Trigona laeviceps*

4. Prediction of secondary metabolite biosynthesis gene clusters

According to the ability of *Streptomyces* I-EHB-18 to inhibit tested Gram-positive, Gram-negative and fungi strains, the genome of this strain might contain several BGCs. To evaluate the presence of secondary metabolite gene clusters in *Streptomyces* I-EHB-18, antiSMASH was used as a tool for rapid genome-wide identification, annotation and analysis of secondary metabolite biosynthesis gene clusters in bacterial genomes[9]. Secondary metabolite BGCs in genome of *Streptomyces*. I-EHB-18 were predicted as 41 regions. BGCs that related with antimicrobial activity was showed in Table 2. The result revealed variety types of potential antimicrobial clusters, such as terpene, polyketide synthase type I (PKS-I), non-ribosomal peptide synthetase (NRPS), peptide, butyrolactone, phosphoglycolipid, amglyccycl, and hybrids clusters. Most possible known BGCs (100% similarity) were albaflavenone and coelibactin. Albaflavenone is an antibiotic produced from *Streptomyces albidoflavus* which has activity against *B. subtilis* ATCC6633[24]. Coelibactin is a putative non-ribosomal peptide produced from *S. coelicolor* A3(2) with chelate zinc molecule activity[25]. This mechanism is identical to siderophore which help bacteria uptake nutrient and survive in the environments, including a mechanism to kill other microorganisms[26].

The promising BGCs (50-80% similarity) were sceliphrolactam, informatipeptin, bafilomycin B1, and teichomycin. Sceliphrolactam derived from wasp-associated *Streptomyces* sp. exhibited antifungal activity which inhibited the growth of amphotericin B-resistant *Candida albicans*[27]. Informatipeptin BGCs was found in many *Streptomyces* strains including *Streptomyces viridochromogenes*[28] via genome mining-guided discovery[29]. Informatipeptin is a class III lanthipeptide. This peptide is one of the ribosomally-synthesized and post-translationally-modified peptides (RiPPs)[30]. It has characteristic of thioether cross-links imperative for bioactivity and stability[31]. Lantipeptides has potential applications which include human and veterinary medicine as well as in the biochemical, pharmaceutical, agricultural, and food industries[32]. Bafilomycins, macrolide antibiotics, isolated from the fermentation broth of three *Streptomyces griseus* strains (TU 1922, TU 2437, TU 2599) exhibited antimicrobial activity against gram-positive bacteria and fungi[33]. Moreover, Bafilomycin B1 was used for studies of autophagy and cell death[34]. Teichomycin A_1 and A_2 were obtained from *A. teichomyceticus* nov. sp. (ATCC 31121). Both are highly active against gram-positive bacteria and teichomycin A_1 shows some activity against gram-negative bacteria[35]. The less possible BGCs (about 50% similarity) were streptobactin and hygromycin A. Streptobactin, catechol-type siderophore, isolated from the marine-derived actinomycete *Streptomyces* sp. YM5-799 and showed iron-chelating activity[36]. Hygromycin (A and B) antibiotics produced by *Streptomyces hygroscopicus* were inhibitors of bacterial ribosomal peptidyl transferase[37-38]. However, the lower similarity score might indicate the possibility of these BGCs to be novel BGCs.

Further chemical analytical experiments should be conducted to confirm that *Streptomyces* I-EHB-18 is a highly potential producer for both known and novel compounds. Detection of metabolites by genome mining approach could confirm substances produced by this organism. Moreover, a combination of metabolomic, transcriptomics and genomic information could reveal the complete metabolites production and also pathway regulation of these BGCs. Therefore, in the future we might have a potential lead compound that enter the drug discovery pipeline from *Streptomyces* I-EHB-18.

Table 2. Predicted antimicrobial secondary metabolite biosynthesis cluster of *Streptomyces* I-EHB-18 by antiSMASH.

Group of biosynthetic gene cluster	Cluster region	Size (bp)	Most similar known biosynthetic cluster (% similarity)	Possible functional activity
Terpenes:				
	1.1	21,023	Oxalomycin B (9%)	Antiviral Antibacterial Immunosuppressant
	26.1	21,047	Albaflavenone (100%)	Antibacterial
PKS:				
Type 1 PKS	19.1	29,438	Bafilomycin B1 (16%)	Antimicrobial Immunosuppressant
	39.1	86,578	Sceliphrolactam (60%)	Antifungal
NRPS:				
	10.2	31,523	Streptobactin (47%)	Siderophore
	29.2	54,128	Coelibactin (100%)	Zincophore
	34.2	26,777	Atratumycin (7%)	Antibacterial
	73.1	17,984	α,β-expoxyketone (15%)	Enzyme inhibitor
Peptide:				
Lantipeptide	10.1	22,628	Informatipeptin (71%)	Antimicrobial
Butyrolactone:				
	6.1	10,957	Streptoseomycin (4%)	Antibacterial
	69.1	11,122	Lactonamycin (7%)	Antimicrobial
Hybrids:				
NRPS-hgIE-KS	8.1	49,307	Auroramycin (14%)	Antimicrobial
T1PKS-bacteriocin	23.1	22,528	Bafilomycin B1 (83%)	Antimicrobial Immunosuppressant
NRPS-bacteriocin	27.1	47,923	(2S,6R)-diamino-(5R,7) dihydroxyheptanoic acid (21%)	Immunosuppressant Antimicrobial
Others:				
Phosphoglycolipid	28.1	28,935	Teichomycin (83%)	Antibacterial
Amglyccycl	29.1	23,289	Hygromycin A (54%)	Antibacterial

Conclusion:

Insight exploration of bee-symbiont *Streptomyces* I-EHB-18 genetic materials via draft genome analysis and secondary metabolite biosynthetic gene clusters prediction in this study showed genetic basis of *Streptomyces* I-EHB-18 that could define the identity of the strain. The variety of predicted antimicrobial BGCs enhanced potential of this strain to be a candidate of novel secondary metabolites producer. *Streptomyces* I-EHB-18 will be used as a strain to production bioactive compounds for many aspects, such as medical remediation against severe human pathogens, as well as crops pathogens biocontrol.

Acknowledgements:

This project was supported by The Scholarship from the Graduate School, Chulalongkorn University to commemorate the 72nd anniversary of His Majesty King Bhumibol Aduladej, Chulalongkorn University Graduate School Thesis Grant and Ratchadaphiseksomphot Endowment Fund, Chulalongkorn University.

References:

1. van der Meij A, Worsley SF, Hutchings MI, van Wezel GP. FEMS Microbiol Rev. 2017; 41: 392-416.
2. Watve MG, Tickoo R, Jog MM, Bhole BD. Arch Microbiol. 2001; 176 (5): 386-90.
3. González-Zorn B, Escudero JA. Int Microbiol. 2012; 15: 101-109.
4. Baltz RH. J Ind Microbiol Biotechnol. 2006; 33(7): 507-513.
5. Christina A, Christapher V. Bhore SJ. Pharmacogn Rev. 2013; 7 (13): 11–16.
6. Chevrette MG, Carlson CM, Ortega HE, Thomas C, Ananiev GE, Barns KJ, Book AJ, Cagnazzo J, Carlos C, Lanigan W, Grubbs KJ, Horn HA, Hoffmann FM, Klassen JL, Knack JJ, Lewin GR, McDonald BR, Muller L, Melo WGP, Pinto-Tomás AA, Schmitz A, Wendt-Pienkowski E, Wildman S, Zhao M, Zhang F, Bugni TS, Andes DR, Pupo MT, Currie CR. Nat Commun. 2019; 10: 516.
7. Tangwichai O, Kanchanabanca C, Palaga T. Prodeeding of the 26th TSB; Chiang Mai, Thailand. 2016; 1139-1156.
8. Sripreechasak P, Tamura T, Shibata C, Suwanborirux K, Tanasupawat S. Int J Syst Evol Microbiol. 2016; 66: 2030-2034.
9. Medema MH, Blin K, Cimermancic P, de Jager V, Zakrzewski P, Fischbach MA, Weber T, Takano E, Breitling R. Nucleic Acids Res. 2011; 39: 339–346.
10. Shirling EB, Gottlieb D. Int J Syst Bacteriol. 1966; 16: 313-340.
11. Afgan E, Baker D, Batut B, van den Beek M, Bouvier D, Cech M, Chilton J, Clements D, Coraor N, Gruning BA, Guerler A, Hillman-Jackson J, Hiltemann S, Jalili V, Rasche H, Soranzo N, Goecks J, Taylor J, Nekrutenko A, Blankenberg D. Nucleic Acids Res. 2018; 2 (46): 537-544.
12. Grant JR, Stothard P. Nucleic Acids Res. 2008; 36: 181-184.
13. Seemann T. Bioinformatics. 2014; 30: 2068- 2069.
14. Richter M, Rossello-Mora R, Glockner FO, Peplies J. Bioinformatics. 2016; 32 (6): 929-931.
15. Tamura, K, Stecher G. Kumar S. Mol Biol Evol. 2021; 38: 3022-3027.
16. Heinsch SC, Hsu SY, Otto-Hanson L, Kinkel L, Smanski MJ. BMC Genomics. 2019; 20: 994.
17. Lee N, Kim W, Hwang S, Lee Y, Cho S, Palsson B, Cho BK. Sci Data. 2020; 7: 55.
18. Redenbatch M, Scheel J. Sscmidt U. Antonie van Leeuwenhoek. 2000; 78 (3-4): 227-235.
19. Liu X, Dou G, Ma Y. J Gen Plant Pathol. 2016; 82: 165-173.
20. Promnuan Y, Kudo T, Ohkuma M, Chantawannakul P. Int J Syst Evol Microbiol. 2013; 63: 1896-1901.
21. Cambronero-Heinrichs JC, Matarrita-Carranza B, Murillo-Cruz C, Araya-Valverde E, Chavarría M, Pinto-Tomás AA. Microbiology. 2019; 165: 292-301.
22. Matarrita-Carranza B, Moreira-Soto RD, Murillo-Cruz C, Mora M, Currie CR, Pinto-Tomás AA. Front Microbiol. 2017; 8: 2016.
23. Promnuan Y, Kudo T, Chantawannakul P. World J Microbiol Biotechnol. 2009; 25: 1685-1689.
24. Gurtler H, Pedersen R. J Antibiot. 1994; 47 (4): 343-349.

25. Zhao B, Moody SC, Hider RC, Lei L, Kelly SL, Waterman MR, Lamb DC. Int J Mol Sci. 2012; 13 (7): 8500-8513.
26. Morey JR, Kehl-Fie TE. mSytems. 2020; 5 (4): 554-574.
27. Oh DC, Poulsen, M, Currie CR, Clardy J. Org Lett. 2011; 13: 752-755.
28. Liu W, Sun F, Hu Y. ChemistryOpen 2018; 7: 558-561.
29. Zhong Z, He B, Li J, Li YX. Synth Syst Biotechnol. 2020; 5: 155-172.
30. Mohimani H, Kersten RD, Liu WT, Wang M, Purvine SO, Wu S, Brewer HM, Pasa-Tolic L, Bandeira N, Moore BS, Pevzner PA, Dorrestein PC. ACS Chem Biol. 2014; 9: 1545-1551.
31. Knerr PJ, van der Donk WA. Annu Rev Biochem. 2012; 81: 479-505.
32. Barbosa J, Caetano T, Mendo S. J Nat Prod. 2015; 78: 2850-2866.
33. Werner G, Hagenmaier H, Drautz H, Baumgartner A, Zahner H. J Antibiot. 1984; 37: 110-117.
34. Shacka JJ, Klocke BJ, Roth, KA. Autophagy. 2006; 2: 228-230.
35. Parenti F, Beretta G, Berti M, Arioli V. J Antibiot. 1978; 31: 276-283.
36. Matsuo Y, Kanoh K, Jang JH, Adachi K, Matsuda S, Miki O, Kato T, Shizuri Y. J Nat Prod. 2011; 74: 2371-2376.
37. Habib ESE, Scarsdale JN, Reynolds KA. Antimicrob Agents Chemother. 2003; 47: 2065-2071.
38. Borovinskaya MA, Shoji S, Fredrick K, Cate JH. RNA. 2008; 14: 1590-1599.

EFFECTS OF A6E MUTATION ON PROTEIN EXPRESSION AND STRUCTURE FORMATION OF Asn1p-GFP IN *Saccharomyces cerevisiae*

Thunyarat Surasiang and Chalongrat Noree*
Institute of Molecular Biosciences, Mahidol University, Salaya, Nakhon Pathom 73170, Thailand
*e-mail: chalongrat.nor@mahidol.edu

Abstract:
Asparagine synthetase is a metabolic enzyme responsible for ATP-dependent conversion of L-aspartate to L-asparagine. A metabolic disease called "asparagine synthetase deficiency" (ASD) is caused by certain mutations in the *ASNS* gene coding for human asparagine synthetase (ASNS). The phenotypes of ASD include microcephaly (small head/brain size) and some other neurological defects. Among 30 identified mutations, A6E mutation has been demonstrated to have the most negative impact on the abundance of human ASNS. In budding yeast, asparagine synthetases (Asn1/2p) have been revealed the extraordinary feature of reversible assembly into micron-sized cytosolic structures (foci/filaments) in response to the presence/absence of their nutrients and/or regulators. However, A6E mutation originally identified in humans, has not yet been tested in the yeast system. So, this study aims to investigate the effects of A6E mutation on (1) protein abundance, (2) overall growth of yeast, and (3) supramolecular structure formation of yeast asparagine synthetase (Asn1p) being fused with a green fluorescent protein (GFP), thus allowing both the protein detection with anti-GFP and the direct visualization under the microscope. The genome of yeast BY4741 was engineered by first knocking out *ASN2* (known as a minor contributor to yeast asparagine biosynthesis) to prevent the complication in the characterization of A6E mutation effect on its paralog, *ASN1* (known as a major contributor to the asparagine biosynthesis), and then introducing A6E mutation codon to the chromosomal *ASN1*, together with *GFP*, in order to produce the mutant enzyme Asn1p(A6E)-GFP. The results of Western blot analysis of yeast expressing Asn1p(A6E)-GFP vs. yeast expressing Asn1p(WT)-GFP revealed that A6E mutation adversely impaired the expression of the enzyme in all yeast growth stages. Moreover, the growth curve analysis showed that yeast expressing Asn1p(A6E)-GFP grew significantly slower than yeast expressing Asn1p(WT)-GFP. For the assays of the enzyme assembly/disassembly kinetics and dynamics, A6E mutation obviously affected the structure formation frequency of the enzyme, especially when cells were grown to the stationary phase. Interestingly, in contrast to Asn1p(WT)-GFP, assembly and disassembly states of Asn1p(A6E)-GFP were insensitive to rapid changes in the intracellular energy levels upon treatment with sodium azide (assembly trigger) during log-phase or fresh glucose addition (disassembly trigger) at stationary phase. Altogether, these results have confirmed that the effect of A6E mutation on protein expression levels of asparagine synthetase is common across eukaryotic species. So, this has implied that the yeast construct in our study could be used as an alternative model of ASD, and probably be used as an initial platform to screen for any potent drug that can rescue the expression of asparagine synthetase for further development of the ASD treatments in humans.

FIRST IDENTIFICATION OF α-GLUCOSIDASE INHIBITORS FROM THE STEM OF *Thunbergia laurifolia*

Khoa Nguyen Anh, Preecha Phuwapraisirisan*
Center of Excellence in Natural Products, Department of Chemistry, Faculty of Science, Chulalongkorn University, Bangkok 10330, Thailand
*e-mail: preecha.p@chula.ac.th

Abstract:

Bioactive-guided phytochemical investigation of *Thunbergia laurifolia* L. led to the isolation of eleven compounds. Their chemical structures were determined by analysis of one-dimensional, two-dimensional nuclear magnetic resonance (NMR) and high-resolution mass spectrometry, as well as by comparison with literature data. All isolated compounds were evaluated for α-glucosidase inhibition. Syringaresinol (**1**) and rosmarinic acid (**7**) showed the most significant inhibitory activity against α-glucosidase with the IC_{50} values of 60.53 and 78.28 μM respectively. Further study on mechanism underlying rat intestinal α-glucosidase inhibition indicated that syringaresinol (**1**) could retard the maltase and sucrase function by non-competitive while rosmarinic acid (**7**) was identificated as a non-competitive inhibitor against maltase and a mixed manner inhibitor against sucrase.

Introduction:

The group of diseases due to defects in insulin secretion, insulin action, or both is collectively referred to diabetes, which is mainly classified into two types: type-I and type-II. It has been considered as one of the most remarkable public health problems in the 21st century.[1,2] To date, acarbose, miglitol, and other related α-glucosidase inhibitors are a few drugs approved for type-II diabetes treatment. However, these agents cause gastrointestinal harm such as flatulence, abdominal bloating, and diarrhea. Many researchers have searched for effective α-glucosidase inhibitors from natural sources to pave the way for alternative antidiabetic drugs that may substitute acarbose and its family.[3]

In the search for α-glucosidase inhibitors from medicinal plants that have been evidenced for antidiabetic activity in animal models, the stem extract of *Thunbergia laurifolia* has been noted for significant inhibition against α-glucosidase in our screening. However, the active components responsible for this inhibition remained unexplored.

In Thailand, *T. laurifolia* is used in traditional medicine as an antipyretic, as well as an antidote to detoxify poisons. *T. laurifolia*, commonly known in Thai as 'Rang-Jeud', belongs to the family Acanthaceae. Its leaves are opposite, heart-shaped with serrated leaf margin and taper to a pointed tip. The hermaphrodite flower is trumpet-shaped with a short broad tube, white outside and yellowish inside (Figure 1). The leaves of *T. laurifolia* are believed to have detoxifying effects. They are used as an antidote for poisons and drugs, including the treatment of drug addiction. To date, the crushed dried leaves are commercially packed and sold as tea back to drink as a detoxifying drink.[4,5] Although there have been a few reports of antidiabetic activity of *T. laurifolia*,[6-7] a comprehensive investigation on the active components responsible for such activity remained unexplored. In the present study, we applied α-glucosidase inhibition-gauided isolation to discover the active components presented in the stem extract.

Figure 1. *Thunbergia laurifolia L.*

Methodology:

General experimental procedure

^{1}H-NMR and ^{13}C-NMR spectra were recorded with JEOL JNM-ECZ500R/S1 NMR spectrometers operating at 500 MHz for ^{1}H or 125 MHz for ^{13}C nuclei. High-resolution mass spectra (HRMS) were recorded using electronspray ionization (ESI) with a MicroTOF Bruker mass spectrometer. Analytical thin layer chromatography (TLC) was performed with precoated Merck silica gel 60 F_{254} plates (0.25 mm for thick layer) and visualized at 254 nm using an ultraviolet lamp. Column chromatography was performed with Merck silica gel 60 (70-230 mesh).

Plant material and extraction

The stems of *T. laurifolia* were collected from Nakhonratchasima, Thailand in 2018. The dried stems of *T. laurifolia* (5 kg) were ground and extracted by methanol (3 × 20 L) to give a methanol extract. The methanol extract was partitioned with hexane, ethyl acetate to give hexane extract (HE) (10 g), ethyl acetate extract (EE) (30 g) and the remaining water layer (WL). The solvent was evaporated in vacuo using a rotary evaporator to obtain the crude extracts.

Isolation and purification

The ethyl acetate extract (30 g) was separated by column chromatography (silica gel, ethyl acetate-hexane, a gradient of 0:100 to 100:0) to give 8 fractions (A-H). Fraction G (800 mg) was chromatographed on Sephadex LH-20 column eluted with CH_2Cl_2-MeOH (1:1, v/v) to yield 5 subfraction (G1-G5). Subfraction G3 (120 mg) was separated by repeated Sephadex LH-20 column chromatography (CC) using CH_2Cl_2-MeOH (1:1, v/v) to obtain 3 subfraction (G3.1-G3.3). Subfraction G3.3 (40 mg) was separated by reverse-phase flash column chromatography (FCC) - C18 using mobile phase of MeOH-water (2:1, v/v) to afford compound **1** (5.5 mg). Fraction H (5 g) was fractioned by Sephadex LH-20 column eluted with MeOH to yield 4 subfractions (H1-H4). Subfraction H1 (500 mg) was purified by repeated Sephadex LH-20 column using MeOH to give 3 subfrations (H1.1-H1.3). Compound **2** (50 mg) was obtained by purification of subfraction H1.1 (120 mg) with reverse-phase FCC (C18) using mobile phase MeOH-water (3:2, v/v). Compound **3** (20 mg) was isolated from subfraction H1.3 (100 mg) by reverse-phase FCC (C18) using mobile phase MeOH-water (1:1, v/v). Subfraction H2 (600 mg) was chromatographed on Sephadex LH-20 column with MeOH to obtain 3 subfractions (H2.1-H2.3). Compound **4** (15 mg) was purified from subfration H2.2 (100 mg) by reverse-phase FCC (C18) using mobile phase MeOH-water (3:2, v/v). Subfraction H3 (650 mg) was separated by reverse-phase FCC (C18) using mobile phase MeOH-water (7:3, v/v) to isolate compound **5** (20 mg). Subfraction H4 (900 mg) was fractioned by Sephadex LH-20 column eluted with MeOH to give 4 subfractions (H4.1-H4.4). Compound **6** (30 mg) was purified by reverse-phase FCC (C18) using mobile phase MeOH-water (3:2, v/v) from subfraction H4.2 (120 mg). Subfraction

H4.4 (250 mg) was separated by repeated Sephadex LH-20 column using MeOH to obtain 3 subfraction (H4.4.1-H4.4.3). Compound **7** (15 mg) was isolated from subfraction H4.4.2 (100 mg) by reverse-phase FCC (C18) using mobile phase MeOH-water (8:3, v/v). Fraction D (4g) vas fractioned by Sephadex LH-20 column eluted with MeOH-CH_2Cl_2 (1:1, v/v) to obtain 8 subfractions (D1-D8). Fraction D7 (300 mg) was separated by reverse-phase FCC (C18) using MeOH-water (5:1, v/v) to give 2 subfractions (D7.1-D7.2). Compound **8** (8 mg) was purified from subfraction D7.2 (110 mg) by column chromatography (silica gel, CH_2Cl_2). Compounds **9** (9 mg) and **10** (8.1 mg) were obtained from subfraction D7.1 (160 mg) by reverse-phase FCC (C18) using mobile phase MeOH-water (5.5:1, v/v). Compound **11** (5 mg) was isolated from subfraction D4 (200 mg) by repeated Sephadex LH-20 column using MeOH-CH_2Cl_2 (1:1, v/v) as mobile phase.

α-Glucosidase inhibition assay

α-glucosidase inhibition against rat intestinal maltase and sucrase was evaluated using the method previously described.[8] The enzyme solution prepared from rat intestinal acetone powder (Sigma, St. Louis) was used as a source of maltase and sucrase. The isolated compounds were added with 30 µL the phosphate buffer solution (pH 6.9), 20 µL of the substrate solution (maltose: 10 mM, sucrose: 100 mM) in the phosphate buffer solution, 80 µL of glucose assay kit (SU-GLLQ2, Human), and 20 µL of the enzyme solution. Then, the mixture was incubated at 37^oC for 10 minutes (maltose) and 40 minutes (sucrose). The quantity of glucose is thus proportional to quinoneimine and can be determined by absorption at 500 nm using Bio-Rad 3550 microplate reader. The percentage of inhibition was calculated by $[(A_0-A_1)/A_0]*100$, with A_1 and A_0 are respectively the absorbance with and without the samples.

Kinetic study of α-glucosidase inhibition

Kinetic study was investigated by constructing Lineweaver Burk plot parameters which are determined by varying the concentration of the substrates (maltose and sucrose) and rat intestinal α- glucosidase in the absence and presence of tested compounds. The α-glucosidase and active compounds were incubated with increasing concentration of maltose (2-10 mM) and sucrose (20-100 mM). Data from kinetic study provide the insights about the mechanism of inhibition.[8]

Results and Discussion:

The glucosidase inhibition assay indicated that ethyl acetate extract shows the highest activity over hexane extract and remaining water layer (WL) (Figure 2). Chromatographic purification of ethyl acetate extract led to the isolation of eleven known compounds (Figure 3). The structures of these isolated compounds were characterized by analysis of their ^{1}H-NMR, ^{13}C-NMR, MS data, and the comparison with the previous reports.

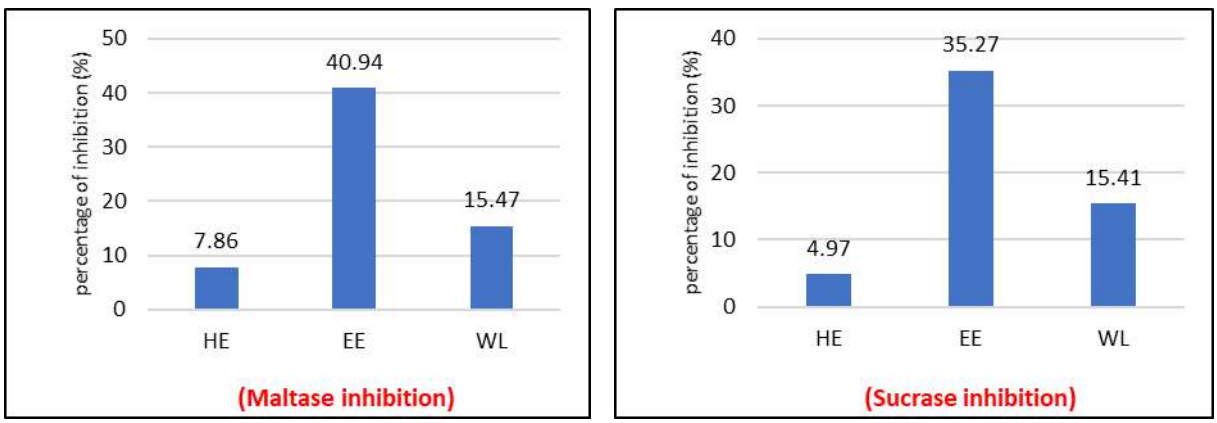

Figure 2. The percentage of inhibition of crude extracts against maltase and sucrase

at 1 mg/mL

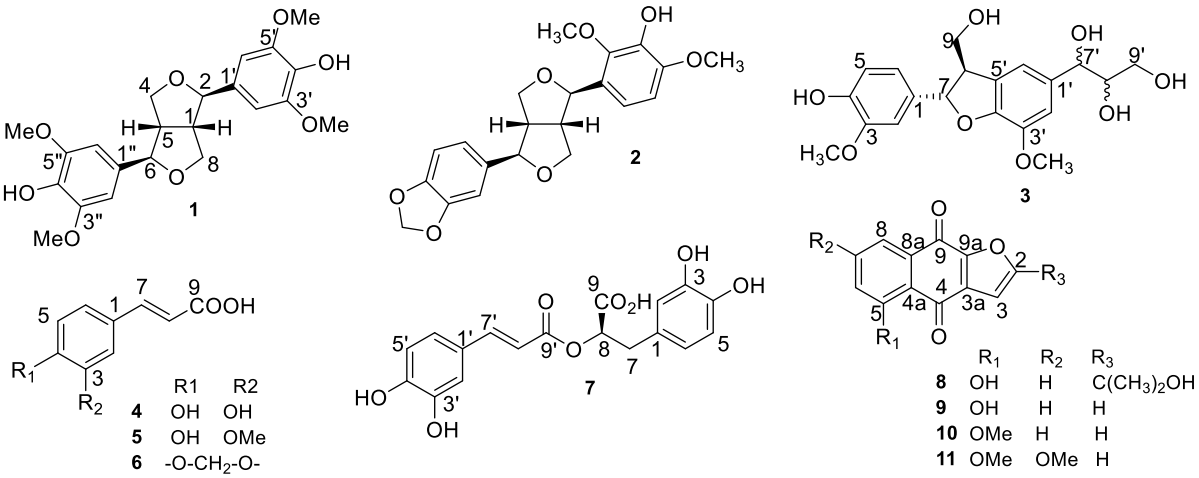

Figure 3. The structures of isolated compounds

Syringaresinol (**1**): white powder; ^{1}H-NMR (500 MHz, chloroform-*d*) δ (ppm) 6.58 (4H, s, H2′, H6′, H2′′, H6′′), 4.73 (2H, d, *J* = 4.1 Hz, H2, H6), 4.28 (4H, dd, *J* = 9.0, 6.8 Hz, H4, H8), 3.09 (2H, s, H1, H5), 3.90 (12H, s, MeO-3′, MeO-5′, MeO-3′′ MeO-5′′); ^{13}C-NMR (125 MHz, chloroform-*d*) 54.5 (C-1), 86.2 (C-2), 71.9 (C-4), 54.5 (C-5), 86.2 (C-6), 71.9 (C-8), 132.2 (C-1′), 102.8 (C-2′), 146.3 (C-3′), 134.4 (C-4′), 146.3 (C-5′), 102.8 (C-6′), 132.2 (C-1′), 102.8 (C-2′′), 146.3 (C-3′′), 134.4 (C-4′′), 146.3 (C-5′′), 102.8 (C-6′′), 56.5 (MeO-3′′), 56.5 (MeO-5′′), 56.5 (MeO-3′′), 56.5 (MeO-5′′).[9]

Lignan α-7a (**2**): white powder; ^{1}H-NMR (500 MHz, chloroform-*d*) δ (ppm) 6.86 (1H, d, *J*= 1.4 Hz, H2′′), 6.77 (1H, d, *J* = 8.0 Hz, H5′′), 6.81 (1H, dd, *J* = 8.0, 1.5 Hz, H6′′). 6.62 (1H, d, *J* = 8.5 Hz, H5′), 6.84 (1H, d, *J* = 8.5 Hz, H6′), 5.94 (2H, s, O-CH_2-O), 3.05 (1H, m, H1), 5.05 (1H, d, *J* = 4.8 Hz, H2), 4.31 (1H, dd, *J* = 9.1, 7.4 Hz, H4a), 4.21 (1H, dd, *J* = 9.1, 6.6 Hz, H4), 4.68 (1H, d, *J* = 5.8 Hz, H6), 2.97 (1H,m, H5), 4.01 (1H, dd, *J* = 9.2, 4.7 Hz, H8a), 3.90 (1H, dd, *J* = 9.2, 4.7 Hz, H8), 3.92 (3H, s, MeO-2′), 3.88 (3H, s, MeO-4′); ^{13}C-MR (125MHz, chloroform-*d*) 54.1 (C1), 82.3 (C2), 73.1 (C4), 54,7 (C5), 85.5 (C6), 73.1 (C8), 128.1 (C′), 144.5 (C2′), 138.6 (C3′), 147.2 (C4′), 105.9 (C5′), 115.8 (C6′), 135.3 (C1′′), 106.7 (C2′′), 148.0 (C3′′), 147.3 (C4′′), 108.3 (C5′′), 119.6 (C6′′), 60.5 (MeO-2′), 56.3 (MeO-4′), 101.1 (O-CH2-O).[10,11,12]

Meliasendanin B (**3**): yellow gum; ^{1}H-NMR (500 MHz, methanol-d_4) δ (ppm) 6.92 (1H, br, H2), 6.73 (1H, d, *J*= 8.1 Hz, H5), 6.79 (1H, dd, *J*= 8.1, 1.8 Hz, H6), 6.91 (1H, br, H2′), 6.87 (1H, br, H6′), 5.51 (1H, d, *J*= 6.2 Hz, H7), 3.46 (1H, br, H8), 3.80 (1H, m, H9a), 3.75 (1H, m, H9b), 4.55 (1H, m, H7′), 3.65 (1H, m, H8′), 3.36 (1H, dd, *J*= 11.2, 6.3 Hz, H9′a), 3.5 (1H, dd, *J*= 11.2, 4.0 Hz, H9′b), 3.78 (3H, s, MeO-3), 3.84 (3H, s, MeO-3′); ^{13}C-NMR (125 MHz, Methanol-d_4) 134.6 (C1), 110.5 (C2), 149.1 (C3), 147.5 (C4), 116.1 (C5), 119.7 (C6), 89.1 (C7), 55.4 (C8), 64.8 (C9), 127.8 (C1′), 112.5 (C2′), 145.3 (C3′), 148.9 (C4′), 129.8 (C5′), 116.6 (C6′), 75.5 (C7′), 77.5 (C8′), 64.2 (C9′), 56.3 (MeO-3), 56.7 (MeO-3′).[13]

Caffeic acid (**4**): white powder; ^{1}H-NMR (500 MHz, methanol-d_4) δ (ppm) 6.97 (1H, br, H2), 6.71 (1H, d, *J* = 8.2 Hz, H5), 6.86 (1H, d, *J* = 8.2 Hz, H6), 7.46 (1H, d, *J*= 15.9 Hz, H7), 6.16 (1H, d, *J* = 15.9 Hz, H8); ^{13}C-NMR (125 MHz, methanol-d_4) 126.5 (C1), 113.8 (C2), 148.1 (C3), 145.5 (C4), 115.2 (C5), 121.5 (C6), 145.5 (C7), 114.5 (C8), 169.9 (C9).[3]

Ferullic acid (**5**): white powder; ^{1}H-NMR (500 MHz, Methanol-d_4) δ (ppm) 7.13 (1H, brs, H2), 6.8 (1H, d, *J*= 8.2 Hz, H5), 7.02 (1H, *J*= 8.2 Hz, H6), 7.6 (1H, d, *J*= 15.9 Hz, H7),

6.27 (1H, d, *J*= 15.9 Hz, H8), 3.85 (3H, s, MeO-3); ^{13}C-NMR (125 MHz, Methanol-*d*$_4$) 126.5 (C1), 110.3 (C2), 149.2 (C3), 148.0 (C4), 115.1 (C5), 122.7 (C6), 145.6 (C7), 114.6 (C8), 169.0 (C9), 55.1 (MeO-3).[14]

3′,4′-Methylenedioxycinnamic acid (**6**): white powder; ^{1}H-NMR (500 MHz, Methanol-*d*$_4$) δ (ppm) 7.13 (1H, brs, H2), 6.72 (1H, d, *J*= 8.0 Hz, H5), 6.93 (1H, d, *J*= 8.0 Hz. H6), 7.27 (1H, d, *J*= 15.9 Hz, H7), 6.16 (1H, d, *J*= 15.9 Hz, H8), 5.84 (2H, s, O-CH2-O); ^{13}C-NMR (125 MHz, Methanol-*d*$_4$) 129.2 (C1), 107.2 (C2), 148.6 (C3), 149.7 (C4), 109.6 (C5), 125.2 (C6), 144.4 (C7), 117.6 (C8), 168.4 (C9), 102.1 (O-CH_2-O).[15]

Rosmarinic acid (**7**): yellow powder; ^{1}H-NMR (500 MHz, Methanol-*d*$_4$) δ (ppm) 6.74 (1H, brs, H2), 6.65 (1H, d, *J*=8.0 Hz, H5), 6.60 (1H, d, *J*=8.0 Hz, H6), 7.0 (1H, d, *J*= 2.0 Hz, H2′), 6.75 (1H, d, *J*= 8.2 Hz, H5′), 6.89 (1H, d, *J*= 8.2 Hz, H6′), 7.49 (1H, d, *J*= 15.9 Hz, H7′), 6.24 (1H, d, *J*= 15.9 Hz, H8′), 5.06 (1H, d, *J*= 9.3 Hz, H8), 3.06 (1H, m, H7a), 2.91 (1H, m, H7b); ^{13}C-NMR (125 MHz, Methanol-*d*$_4$) 130.8 (C1), 117.5 (C2), 146.7 (C3), 144.9 (C4), 116.2 (C5), 121.7 (C6), 38.6 (C7), 77.3 (C8), 127.9 (C1′), 115.1 (C2′), 146.9 (C3′). 149.4 (C4′), 116.4 (C5′), 123.0 (C6′), 146.7 (C7′), 115.4 (C8′), 169.0 (C9′).[16]

5-Hydroxyisopropylnaptho[2,3-b]furan-4,9quinone (**8**): yellow powder; ^{1}H-NMR (500 MHz, chloroform-*d*) δ (ppm) 6.79 (1H, s, H3), 7.23 (1H, d, *J*=8.1 Hz, H6), 7.62 (1H, dd, *J*=8.1, 7.8 Hz, H7), 7.74 (1H, d, *J* = 7.8 Hz, H8), 1.76 (6H, s, H11, H12); ^{13}C-NMR (125 MHz, Chloroform-*d*) 168.4 (C2), 102.4 (C3), 131.2 (C3a), 186.8 (C4), 115.4 (C4a), 163.5 (C5), 125.4 (C6), 136.4 (C7), 120.1 (C8), 132.9 (C8a), 172.8 (C9), 152.1 (C9a), 69.6 (C10), 28.9 (C11, C12).[17]

5-Hydroxynaptho[2,3-b]furan-4,9quinone (**9**): yellow powder; ^{1}H-NMR (500 MHz, chloroform-*d*) δ (ppm) 7.78 (1H, d, *J*= 2.0 Hz, H2), 6.99 (1H, d, *J*= 2.0 Hz, H3), 7.29 (1H, d, *J*= 8.5 Hz, H6), 7.62 (1H, dd, *J*= 8.5, 7.3 Hz, H7), 7.77 (1H, d, *J*= 7.3 Hz, H8); ^{13}C-NMR (125 MHz, Chloroform-*d*) 149.0 (C2), 108.5 (C3), 130.4 (C3a), 186.6 (C4), 115.5 (C4a), 162.6 (C5), 125.5 (C6), 136.5 (C7), 120.2 (C8), 132.8 (C8a), 173.0 (C9a), 153.0 (C9).[17]

5-Methoxynaptho[2,3-b]furan-4,9quinone (**10**): yellow powder; ^{1}H-NMR (500 MHz, chloroform-*d*) δ (ppm) 7.73 (1H, d, *J*= 1.4 Hz, H2), 6.97 (1H, d, *J*=1.4 Hz, H3), 7.33 (1H, d, *J*= 8.4 Hz, H6), 7.69 (1H, dd, *J*= 8.4, 7.6 Hz, H7), 7.91 (1H, d, *J*= 7.6 Hz, H8), 4.02 (3H, s, MeO-5); ^{13}C-NMR (125 MHz, Chloroform-*d*) 148.9 (C2), 109.2 (C3), 132.2 (C3a), 186.6 (C4), 120.7 (C4a), 160.7 (C5), 118.8 (C6), 135.2 (C7), 120.1 (C8), 134.2 (C8a), 173.4 (C9), 151.2 (C9a), 56.7 (MeO-5).[17]

5,7-Dimethoxynaptho[2,3-b]furan-4,9quinone (**11**): yellow powder; ^{1}H-NMR (500 MHz, chloroform-*d*) δ (ppm) 7.71 (1H, d, *J*= 1.8 Hz, H2), 6.97 (1H, d, *J*= 1.8 Hz, H3), 6.74 (1H, d, *J*= 2.4 Hz, H6), 7.41 (1H, d, *J*=2.4 Hz, H8), 3.99 (3H, s, MeO-5), 3.97 (3H, s, MeO-7); ^{13}C-NMR (125 MHz, Chloroform-*d*) 148.9 (C2), 109.4 (C3), 132.6 (C3a), 179.3 (C4), 115.1 (C4a), 162.9 (C5), 104.4 (C6), 164.9 (C7), 104.7 (C8), 137.2 (C8a), 173.0 (C9), 151.0 (C9a), 56.7 (MeO-5), 56.17 (MeO-7).[17]

α-Glucosidase inhibitory activity of isolated compounds

All the isolated compounds were evaluated for their α-glucosidase inhibitory activity and the results are shown in Table 1. Syringaresinol (**1**) and romarinic acid (**7**) showed highly active inhibition among isolated compounds with IC_{50} values of 60.53 and 72.21 μM, respectively; while the furano napthoquinones (**8**-**10**) showed no-inhibition activity. The result indicated that the compounds containing phenolic moiety show higher activity than others. It is likely that α- glucosidase inhibitory potency increases according to the number of free phenolic and methoxy groups on the aromatic ring.

Table 1. α-Glucosidase inhibitory effect of isolated compounds

Compound	**IC_{50}**

	Maltase (μM)	Sucrsse (μM)
1	61.58	60.53
2	>300	>300
3	>300	>300
4	119.44	125.69
5	202.07	103.41
6	NI[a]	>300
7	78.28	72.21
8	NI	NI
9	NI	NI
10	NI	NI
11	NI	NI
Acarbose	2.76	5.13

[a]NI: no-inhibition

Kinetic study of syringaresinol (1) and rosmarinic acid (7)

Syringaresinol (**1**), caffeic acid (**4**), ferulic acid (**5**), and rosmarinic acid (**7**) were published as the potential α-glucosidase inhibitors in the previous report.[18,19] Caffeic acid (**4**) and ferullic acid (**5**) were identified as the mixed manner inhibitors against maltase. In addition, ferullic acid (**5**) inhibited intestinal sucrase in a mixed manner whereas caffeic acid (**4**) was a non-competitive inhibitor.[19] However, there is no report about the kinetic study of syringaresinol (**1**) and rosmarinic acid (**7**) against maltase and sucrase. Therefore, to address how can 1 and 7 retard the function of glucosidases, we herein carried out kinetic study.

The Lineweaver-Burk plots of syringaresinol (**1**) displayed a set of traight lines, all of which intersected in X-axis. Kinetic analysis revealed that V_{max} decreased with unchanged K_m in the presence of increasing concentration of syringaresinol (**1**). This observation allowed the identification of a non-competitive manner against maltase and sucrase with K_i values of 37.01 and 57.05 μM, respectively.

Kinetic study of rosmarinic acid (**7**) suggested that maltase was inhibited through non-competitive manner (Figure 4-A) with K_i value of 53.71 μM. However, rosmarinic acid (7) inhibited sucrase by mix-type manner (Figure 4-B) with the K_i and K_i' values of 137.22 and 129.51 μM, respectively. The kinetic study parameters of syringaresinol (**1**) and rosmarinic acid (**7**) against maltase and sucrase are summarized in Table 2.

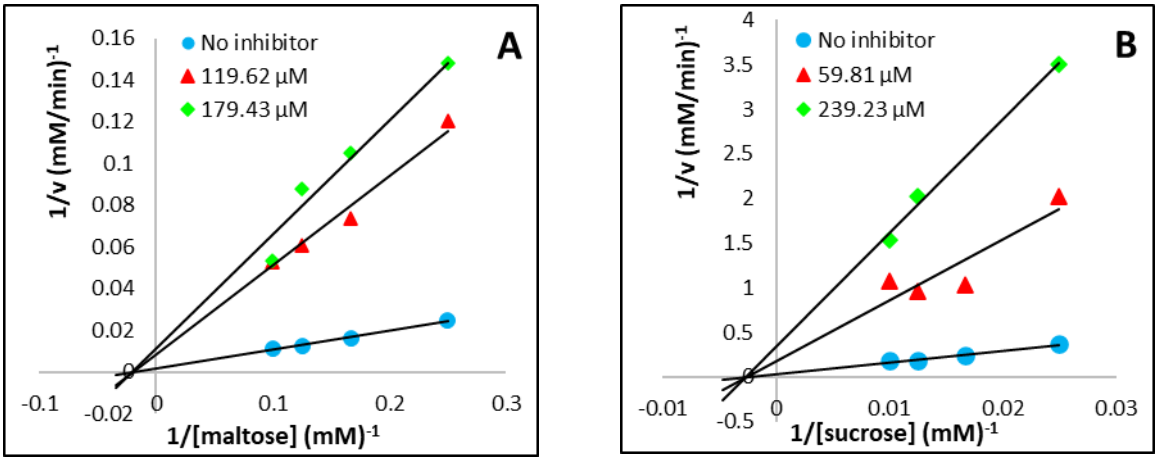

Figure 3. Lineweaver-Burk plots for inhibitory activity of syringaresinol (**1**) against A (maltase) and B (sucrase)

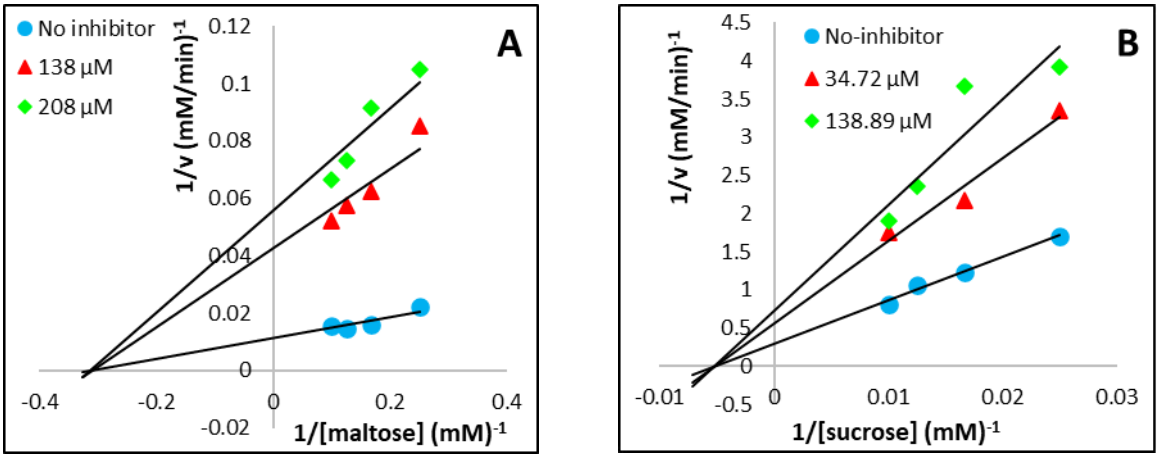

Figure 4. Lineweaver-Burk plots for inhibitory activity of rosmarinic acid (**7**) against A (maltase) and B (sucrase)

Table 2. Inhibition types and kinetic parameters of syringaresinol (**1**) and rosmarinic acid (**7**) on α-glucosidase

		Syringaresinol (**1**)	Rosmarinic acid (**7**)
Maltase	Inhibition type	Non-competitive	Non-competitive
	K_i (µM)	37.01	53.71
	K_i' (µM)	-	-
Sucrase	Inhibition type	Non-competitive	Mixed
	K_i (µM)	57.05	137.22
	K_i' (µM)	-	129.51

Conclusion:

α-Glucosidase inhibitory guided isolation of the stems of T. laurifolia yielded eleven compounds. To the best of our knowledge, compounds **1-6** and **8-11** were isolated from this plant for the first time. Of isolated compounds, syringaresinol (**1**) and rosmarinic acid (**7**) were the most active inhibitors against rat intestinal maltase and sucrase with non-competitive and mix-type manners. In this study, we demonstrated that T. laurifolia is a prolific source of bioactive phenolic compounds such as lignans and could be used as biomarkers for future investigation.

Acknowledgements:

KAN is grateful thank to the Graduate school, Chulalongkorn University for the H.M. the King Bhumibhol Adulyadej's 72nd Birthday Anniversary Scholarship. Center of Excellence in Natural Products is supported by Ratchadapiseksompot Endownment Fund, Chulalongkorn University.

References:

1. American diabetes association. Diabetes Care. 2008; 31: 55-60.
2. Laar FAVD. Vasc Health Risk Manag. 2007; 3: 673-689.
3. Yin Z, Zhang W, Feng F, Zhang Y, Kang W. Food Sci Hum Well. 2014; 3: 136-174.
4. Chan EWC, Eng SY, Tan YP, Wong ZC. Pharmacogn. Mag. 2011;24:1-6.
5. Boonyarikpunchai W, Sukrong S, Towiwat P. Pharmacol. Biochem. Behav. 2014;124: 67-73.

6. Aritajat S, Wutteerapol S, Saenphet K. Southeast Asian J. Trop. Med. Public Health. 2004;35:53-58.
7. Hongsing P, Palanuvej C, Ruangrungsi N. Walailak J. Sci. & Tech. 2020;17:776-787.
8. Rattanangkool E, Kittikhunnatham P, Damsud T, Wacharasindhu S, Phuwapraisirisan P. Eur. J. Med. Chem. 2013;66:296-304.
9. Monthong W, Pitchuanchom S, Nuntasaen N, Pompimon W. Am. J. Appl. Sci. 2011;8:1268-1271.
10. Worawalai W, Doungwichitrkul T, Rangubpit W, Taweechat P, Sompornpisut P, Phuwapraisirisan P. Bioorg. Chem. 2009;87:783-793.
11. Jing Y, Zhang YF, Shang MY, Liu GX, Li YL, Wang X, Cai SQ. Molecules. 2017;22: 125-144.
12. Tran HQ, Nguyen TTN, Chau VM, Phan VK, Bui HT, Nguyen PT, Seok BS, Young HK. Bioorg. Med. Chem. Lett. 2012;22:2527-2533.
13. Lun W, Fu L, Yang CY, Khan AA, Liu X, Wang MK. Fitoterapia. 2014;99:92-98.
14. Abaston J, Richard T, Cluzet S, Palos Pinto A, Dufour MC, Corio-Costet M-F, Mérillon JM. J. Agric. Food Chem. 2017;65:8884-8891.
15. Zhou K, Chen D, Li B, Zhang B, Miao F, Zhou L. PloS one. 2017;12:1-13.
16. Akoury, E. Am. Res. J. Chem. 2017;1:15-23.
17. Abeygunawardena C, Kumar V, Marshall DS, Thomson RH, Wickramaratne DBM. Phytochemistry. 1991;30:942-945.
18. Duong TTT, Do TNV, Nguyen HX, Le TH, Dang PH, Nguyen NT, Nguyen TNT, Nguyen TD, Nguyen MTT. Tetrahedron Lett. 2017;58:2280-2283.
19. Adisakwattana S, Chantarasinlapin P, Thammarat H, Yibchok-Anun S. J Enzym Inhib Med Ch. 2009; 24:1194-1200.

HEALTH STATUS OF THE RICE FROG *Fejervarya limnocharis* IN NAN PROVINCE, THAILAND, DURING PEAK HERBICIDE UTILIZATION PERIOD

Luhur Septiadi,[1] Panupong Thammachoti,[1, 2] Julien Claude,[3] Noppadon Kitana[1, 2]*
[1]Department of Biology, Faculty of Science, Chulalongkorn University, Bangkok 10330, Thailand
[2]BioSentinel Research Group (STAR), Faculty of Science, Chulalongkorn University, Bangkok 10330, Thailand
[3]Institut des Sciences de l'Évolution de Montpellier, Université de Montpellier, CNRS, IRD, EPHE, Montpellier, France
*e-mail: noppadon.k@chula.ac.th

Abstract:
Herbicides have been continuously and intensively used in Thailand's agriculture, leading to a potential hazard to human and non-target organisms. Prior studies using sentinel species showed that frogs living in herbicide-contaminated paddy fields had higher residues and changes in morphological and physiological status. In this study, we monitor the potential influence of herbicides on health of the rice frog *Fejervarya limnocharis* populations based on organismal parameters (condition factor, gonadosomatic index, hepatosomatic index) and population parameters (growth pattern, size-frequency distribution). Samplings of frogs were conducted from two paddy fields with different degrees of herbicide utilization at Nan province, northern Thailand, during the peak herbicide utilization period (wet season, July 2020). Frogs from these sites were compared and analyzed statistically. The weight-length relationship shows differences in growth patterns between sites. At organismal level, condition factor on adult male frogs showed significant site-related differences. Gonadosomatic index on adult female frogs showed significant site-related differences, indicating potential effect of xenoestrogens. Hepatosomatic index on both sexes shows significant site-related differences, indicating a higher exposure to xenobiotics. At population level, size-frequency distribution showed significant site-related differences and disproportionate distribution. It can be concluded that herbicides could influence non-target organisms at organismal and population levels and may lead to subtle and perpetual changes in agroecosystem health.

Introduction:
Environmental contamination has become one of the serious threats to the global environment. Southeast Asia as the densely populated region utilizing agricultural activity as the backbone of its economy[1], are prone to the health hazards of agrochemicals[2]. Not only affecting many communities[3], but agrochemicals utilization also poses a risk to the non-target organism living in the vicinity due to their persistence which may result in adverse effects[4].

The adverse effects caused by agrochemicals can be monitored on any vertebrates tested in physical conditions and vertebrates living in affected areas. Due to the shared similarities of metabolic process and susceptibility to humans, a variety of vertebrates as sentinel species has been studied before, e.g., mammals[5], turtles[6], fish[7], and amphibians[8]. The observed adverse effect on sentinel species may provide forewarning to the danger of continuous and intensive utilization of agrochemicals.

Amphibians have been considered as one of the most applicable sentinel species due to their susceptibility and sensitivity to environmental change and stressors, especially

chemical contaminants during their complex life cycles[9]. For instance, amphibians have been used for study on environmental exposure[10], an animal model for endocrine-disruptor study[11], a model organism for environmental genotoxicity[12], and other physiological studies[13]. Also, a concern was raised on the global decline of amphibians where one of the underlying factors was agrochemicals contaminations, which indirectly affecting amphibian growth and survival in a population[14].

In Thailand, agricultural activities are considered as the foundation of its economy which resulting in the inevitably high demand for imported pesticides[15]. Herbicides make up the largest portion of imported pesticides with the most common type including 2,4 D, ametryn, paraquat, glyphosate, atrazine[15]. Furthermore, it was decided that the use of paraquat is prohibited (along with tightening restrictions on several pesticides) due to its potential effect on health hazards[15]. Nan Province (northern part of Thailand) has become one of the areas with a major agricultural activity which includes crops of paddy, tamarind, and maize. Several efforts to monitor the degree of herbicide impact to a non-target organism in paddy field has been conducted, including in rice field crab[16], freshwater mussel[17], and rice frog[18]. It is important to monitor the adverse effect of herbicide on amphibians living in the affected areas. In this study, we investigate the adverse effect by using rice frog *Fejervarya limnocharis* as sentinel species of agrochemical contamination. We confirmed the impact by using organismal and population parameters, by comparing the frog living in paddy fields with different degrees of herbicide utilization.

Methodology:

Study Sites and Field Sampling

Frogs were collected from contaminated site (a paddy field with intensive herbicide utilization; Loc: 47Q 0686734 UTM 02047312) and reference site (a paddy field with no history of herbicide utilization; Loc: 47Q 0687013 UTM 02054799) in Wiangsa district, Nan Province, Thailand, during 18–19 July 2020. These two sites have similar geographic and climatic conditions but approximately 7 km far away from each other and separated by a big river (Figure 1). It was reported that water from contaminated site has been contaminated by atrazine herbicide[16], and tissue of rice frogs have been exposed to a higher concentration of atrazine, glyphosate, and paraquat herbicides[19]. The highest herbicide utilization was reported in the wet or rainy season (April–July)[18, 20] which corresponds to cultivation period and mean rainfall in Thailand.

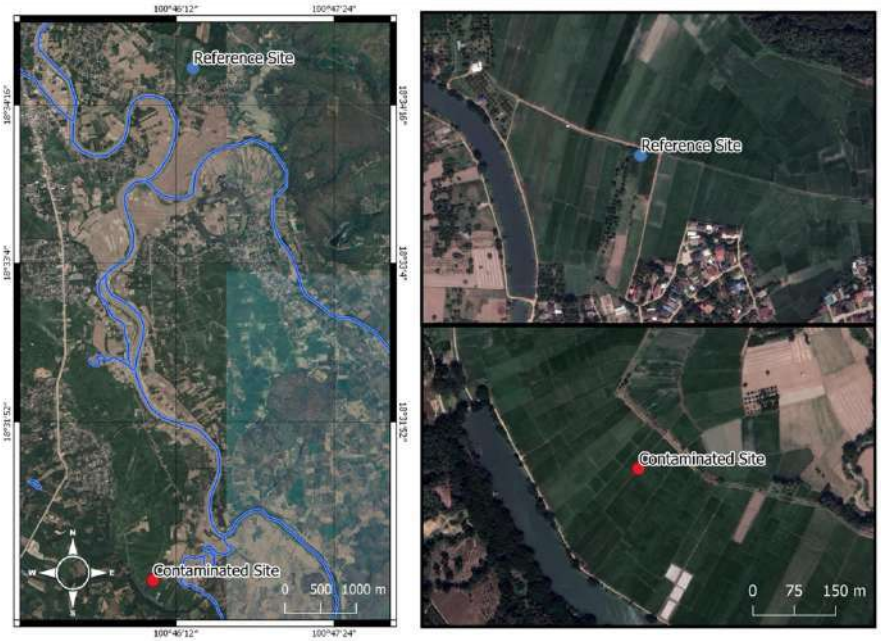

Figure 1. Location map showing the contaminated and reference site in Nan Province, Thailand.

Field samplings were conducted using visual encounter survey where several stages of frogs (i.e., froglet, juvenile, sub-adult, adult) were caught by hand at night. To obtain the best comparable data, the survey was restricted to 45 minutes and limited to 4–6 surveyors. The total sample of rice frogs collected from contaminated and reference sites is shown in Table 1.

Table 1. Sample size of rice frog *F. limnocharis* population from contaminated and reference sites in Nan Province, Thailand, during the peak herbicide utilization period

Month Year/ Period	Contaminated Site	Reference Site
July 2020/ Rainy season	Froglet: 26 Juvenile: – Subadult: – Adult: 54	Froglet: 21 Juvenile: – Subadult: 16 Adult: 86
Total	80	123

Estimation of Growth Pattern, Condition Factor, Gonadosomatic index, and Hepatosomatic index

Frogs were immediately transported to the laboratory at Chulalongkorn University Forest and Research Station, Nan Province, and euthanized by immersion in 0.5% tricaine methane sulfonate solution (Sigma-Aldrich, St. Louis, MO, USA). Frogs were measured for body weight (BW) and snout-vent length (SVL) using Ohaus Pioneer Analytical Balances (accuracy 0.0001 g) and Mitutoyo Absolute Digimatic Caliper (accuracy 0.01 mm), respectively. The frogs were dissected and measured for the weight of liver and gonad (testis and ovary) with the aid of Olympus stereomicroscope and Ohaus Pioneer Analytical Balances.

Regression analysis was calculated based on log-transformed data of body weight and snout-vent length represented in Equation (1),

$$\log BW = b \log SVL + \log a \quad (1)$$

where constant *b* is a scaling coefficient—indicating the growth pattern of population[21], while constant *a* and *b* were used for Condition Factor (CF)—the indicator of overall health of frog populations[22], represented in Equation (2).

$$CF = (BW \times 100) / (a \times SVL^{b}) \quad (2)$$

Gravimetric indices were used to investigate the somatic change on organs, including gonadosomatic index (GSI; relative weight of gonad to body weight) and hepatosomatic index (HSI; relative weight of liver to body weight)[18]. These were estimated based on following Equation (3).

$$HSI/GSI = \text{organ weight} \times 100 / \text{body weight} \quad (3)$$

The data based on parameters of organismal level (i.e., CF, GSI, HSI) were represented in boxplot using ggplot2 R-packages[23] analyzed in R v.3.4.1.

Estimation of Size-frequency distribution

The dissected frogs were determined for stage and sex then categorized into froglet, male, and female. The data from each site were represented in relative frequency in percentage using base in R v.3.4.1.

Statistical analysis

Differences in growth patterns were compared between sites by analysis of covariance (ANCOVA) using logSVL as a covariable followed by Bonferroni tests. Data on organism parameters (i.e., CF, GSI, HSI) were priorly tested for normal distribution and homogeneity of variance, and were analyzed separately between sexes. Mean comparisons were analyzed by Student's *t*-test to investigate the difference between contaminated and reference sites. In case normality and variance from the organismal data were not fulfilled, the data were subjected to Mann-Whitney rank-sum test. The power of test for growth pattern and organismal parameters were also estimated. A two-sample Kolmogorov-Smirnov test was used to test the difference in Size-frequency distribution between contaminated and reference sites.

Results and Discussion:

Weight-length relationship and Growth Pattern

The weight-length relationship (Figure 2) shows that there are differences in growth patterns between sites. The scaling coefficient of frogs from contaminated site (2.8222) was higher than those from reference site (2.5596), indicating different growth pattern between two populations. As the logSVL increases, corresponding logBW also increased (contaminated site: $r = 0.9955$, reference site: $r = 0.9738$). After controlling for the influence of logSVL, ANCOVA showed a significant difference of logBW between sites ($p < 0.05$, power of test [$\alpha = 0.05$] = 0.80). The estimated marginal mean of logBW in frogs from contaminated site (0.495) was significantly higher than those from reference site (0.467), indicating the differences in growth pattern between sites. Differences in growth patterns have been observed from other frog species[24, 25, 26] and within the same frog species[18, 27] exposed to various agrochemical contaminants. It can be concluded that the difference in the growth pattern of the frog population is likely influenced by herbicide contamination.

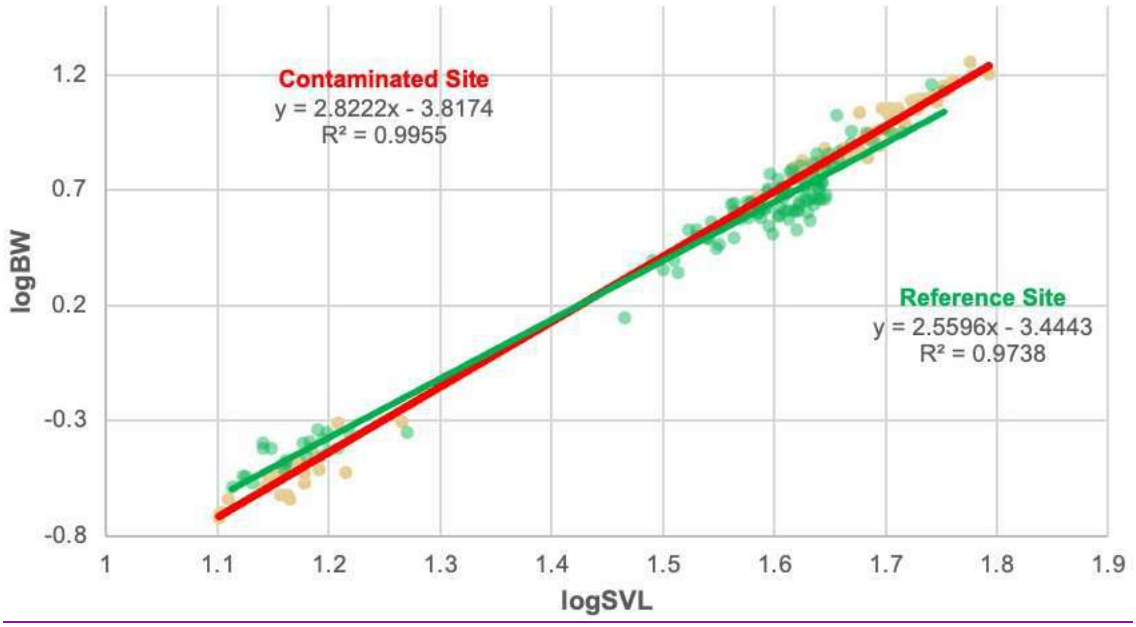

Figure 2. Regression analyses of log-transformed bodyweight (BW) and snout-vent length (SVL) of rice frog *F. limnocharis* population from contaminated and reference site in Nan Province, Thailand, during the peak herbicide utilization period.

Condition Factor, Gonadosomatic Index, and Hepatosomatic Index

Condition factor on adult male frogs from contaminated site (104.69 ± 2.126) was significantly higher than those from reference site (94.78 ± 2.163) (Mann Whitney rank sum test, $p < 0.05$, power of test [$\alpha = 0.05$] = 0.67). There was no significant difference in CF on adult female frogs between contaminated site (105.18 ± 1.973) and reference site (105.56 ± 2.266) (Student's *t*-test, $p > 0.05$, power of test [$\alpha = 0.05$] = 0.05). Based on CF results, the differences between contaminated and reference sites were observed only in adult male frogs. Studies from another frog species[22, 28, 29] and within the same frog species[18, 27] generally show that contaminated site has significantly lower CF than those from reference site, indicating frogs from contaminated site have lesser health fitness. The lesser health fitness could imply that the disruption of growth hormone secretion caused by herbicide[24, 30] may lead to smaller frogs, thereby could be easily caught by a predator. In contrast, our study shows high CF observed in adult male frogs living in contaminated sites which does not indicate the herbicide influence on the overall health.

There was no significant different in GSI on adult male frogs between contaminated site (0.30 ± 0.013) and reference site (0.30 ± 0.015) (Student's *t*-test, $p > 0.05$, power of test [$\alpha = 0.05$] = 0.05), partly due to high individual variation and small sample size. However, GSI on adult female frogs from contaminated site (8.77 ± 0.439) was significantly higher than those from reference site (6.98 ± 1.013) (Mann Whitney rank sum test, $p < 0.05$, power of test ([$\alpha = 0.05$] = 0.43). Previous studies using the combined dataset of several common frogs shows no site-related difference of GSI in male frogs, except for female frogs from contaminated site which showing significantly higher GSI[31]. It was also similar within the same frog species showing significantly higher GSI of adult female frogs from contaminated site[18]. The larger ovary of frogs from contaminated site is likely influenced by herbicides, as it was previously reported, the higher GSI in adult female frogs of *Fejervarya limnocharis* from Thailand was primarily observed in the wet/rainy season[18, 20] where herbicides (i.e., glyphosate, paraquat, atrazine) were utilized intensively. Atrazine is known as endocrine-disrupting chemicals (EDCs)[32] capable to interrupts the hormonal sex regulations[24]. Nonetheless, the presumption of atrazine as EDCs is still under scrutiny, whether it may or

may not be the cause of potent effect on reproductive health[33, 34, 35]. Still, other herbicides present in the study sites (i.e., glyphosate, paraquat) may cause a potential effect on reproductive health, as previously observed on other frog species[36]. There are limited studies that focused on the estrogenic effect on female frogs[18] and in addition to our study, there is an observable herbicide impact on reproductive health of adult females' frogs living in contaminated sites.

Hepatosomatic index on adult male frogs from contaminated site (2.39 ± 0.091) was significantly higher than those from reference site (1.90 ± 0.041) (Student's *t*-test, $p < 0.05$, power of test [$\alpha = 0.05$] = 0.99). Similarly, HSI on adult female frogs from contaminated site (2.81 ± 0.070) was significantly higher than those from reference site (2.15 ± 0.133) (Mann Whitney rank sum test, $p < 0.05$, power of test [$\alpha = 0.05$] = 0.99). Based on the combined dataset of common frogs, it reveals similar trends showing significantly higher HSI on both sexes from contaminated site[31]. Studies on another frog species[28] and within the same frog species[18] also reveals similar results showing significantly higher HSI on both sexes from contaminated site. The heavier liver was regarded as the coping mechanism of the body to the unfavorable conditions[28] which also suggests xenobiotic contaminant accumulation[18]. It was reported that paraquat can reduce glutathione levels in the liver of fish[37]. Therefore, since liver serves as the main organ to detoxicate and accumulate contaminants, it must work harder to eliminate such compounds. In line with our study, there is an observable herbicide impact to the frog living in contaminated site by the changes of liver somatic indicating potential exposure of xenobiotics. The results summary of health parameters at organismal level (i.e., CF, GSI, HSI) is shown in Table 2 and Figure 3.

Table 2. Health parameters at organismal level including CF, GSI, and HSI (Mean ± SEM) of adult male and adult female rice frog *F. limnocharis* population from contaminated and reference site in Nan Province, Thailand, during the peak herbicide utilization period

Parameter	Sex	Contaminated site	Reference site	Power of test ($\alpha = 0.05$)[a]
Condition Factor	Adult male	104.69 ± 2.126 (N=23)	94.78 ± 2.163[*] (N=61)	0.67
	Adult female	105.18 ± 1.973 (N=30)	105.56 ± 2.266[ns] (N=40)	0.05
Gonadosomatic index	Adult male	0.30 ± 0.013 (N=20)	0.30 ± 0.015[ns] (N=35)	0.05
	Adult female	8.77 ± 0.439 (N=28)	6.98 ± 1.013[*] (N=14)	0.43
Hepatosomatic index	Adult male	2.39 ± 0.091 (N=20)	1.90 ± 0.041[*] (N=35)	0.99
	Adult female	2.81 ± 0.070 (N=28)	2.15 ± 0.133[*] (N=14)	0.99

[a]indicates the power of samples from both contaminated and reference sites (two-sample *t*-test, $\alpha = 0.05$)

[*]indicates significant difference between the contaminated and reference site (Mann-Whitney rank sum test/ Student's *t*-test, $p < 0.05$)

[ns]indicates no significant difference between the contaminated and reference site (Student's *t*-test, $p > 0.05$)

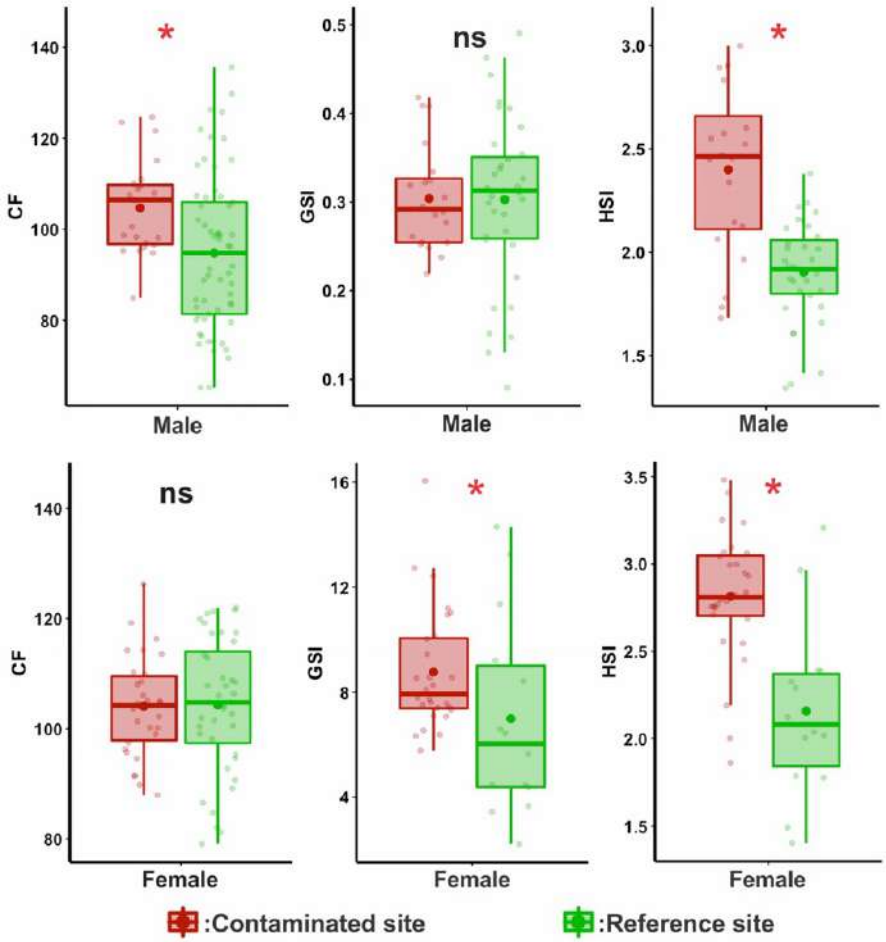

Figure 3. Boxplot of health parameters (CF, GSI, and HSI) of adult male and adult female rice frog *F. limnocharis* population from contaminated and reference site in Nan Province, Thailand, during the peak herbicide utilization period.

Size-frequency distribution

Both sexes show a higher means of SVL from contaminated site (38.30 ± 1.186) than those from reference site (36.74 ± 0.654). The size-frequency distribution shows significant site-related difference (two-sample Kolmogorov-Smirnov test, D = 0.4312, $p < 0.05$). Disproportionate distribution was observed prominently in contaminated sites, indicating the impact of herbicide contamination on the population structures. There are limited studies that directly focused on the population structure (i.e., size-frequency distribution). However, these irregular distributions might be due to reproductive failure, as one of the sexes could be dominant in the population which is likely caused by EDCs[38]. The global decline of amphibian population has also been linked to the immunotoxicity effect partly caused by agrochemicals, leading to the higher parasite load[39] in which certain life-stages (e.g., newly metamorphosing frogs) are found to be more sensitive[40]. To gains more insight into herbicide impacts on amphibian populations, additional studies (e.g., age structure, hatchling ratio, mortality rate) apart from size-frequency distribution should be widely encouraged. There is an observable herbicide impact on the size-frequency distribution of frogs living in contaminated sites showing disproportionate distribution, yet further investigations are needed to confirm this trend. The mean SVL and size-frequency distribution as a parameter on a population level is shown in Figure 4.

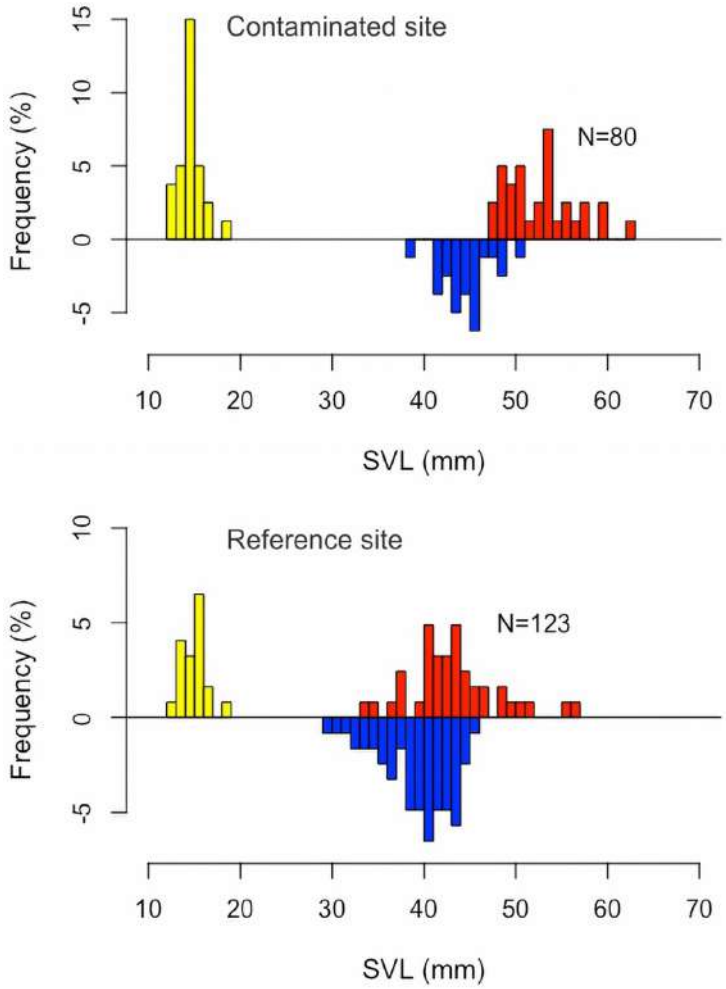

Figure 4. Size-frequency distribution (in percentage) of rice frog *F. limnocharis* population from contaminated and reference site in Nan Province, Thailand, during the peak herbicide utilization period. Yellow bar, red bar and blue bar correspond to froglets, female frogs and male frogs, respectively.

Conclusion:

Rice frogs plays important role in agroecosystem health by providing regulating services (controlling pest species), supporting ecosystem structure (soil burrowing, aquatic bioturbation), and nutrient cycling (food web)[41]. Due to their susceptibility and sensitivity to environmental stressors[9], amphibians are experiencing global decline[14], and by inference, humans may be losing the associated ecosystem services[41]. Our monitoring shows that herbicides could influence non-target organisms (i.e., rice frog) at organismal (CF, GSI, HSI) and population levels (growth pattern, size-frequency distribution) and may lead to subtle and perpetual changes in agroecosystem health. Further studies on contamination analysis and herbicide impacts on amphibian populations should be widely encouraged.

Acknowledgements:

We thank Dr.Jirarach Kitana and Dr.Wichase Khonsue (Chulalongkorn University, Thailand) for their supports. We are grateful to Mr.Ekkachai Punya-in for his expertise and assistance in the field. We thank Mr.M. Fathoni (Brawijaya University, Indonesia) for his valuable idea on data interpretation. We are grateful to the BioSentinel Lab members of Chulalongkorn University for their constructive comments to improve this study. This study was funded by

The Sci-Super VI fund from Faculty of Science of Chulalongkorn University, and the 90th Anniversary of Chulalongkorn University Fund.

References:

1. Xiao X, Boles S, Frolking S, Li C, Babu JY, Salas W, Moore III B. Remote Sens Environ. 2006;100(1):95–113.
2. Lam S, Pham G, Nguyen-Viet H. Int J Occup Med Environ Health. 2017;23(3):250–260.
3. Nicolopoulou-Stamati P, Maipas S, Kotampasi C, Stamatis P, Hens L. Front Public Health. 2016;4:148.
4. Mancini F, Woodcock BA, Isaac NJ. Curr Opin Environ Sustain. 2019;11:53–58.
5. Bossart GD. Vet Pathol. 2011;48(3):676–690.
6. Kitana N, Callard IP. J Environ Sci Health A. 2008;43(3):262–271.
7. Ali D, Nagpure NS, Kumar S, Kumar R, Kushwaha B, Lakra WS. Food Chem Toxicol. 2009;47(3):650–656.
8. Sparling DW, Bickham J, Cowman D, Fellers GM, Lacher T, Matson CW, McConnell L. Ecotoxicol. 2015;24(2):262–278.
9. Venturino A, Rosenbaum E, Caballero De Castro A, Anguiano OL, Gauna L, Fonovich De Schroeder T, Pechen De D'Angelo AM. Biomarkers. 2003;8(3–4):167–186.
10. Roy D. J Biosci. 2002;27(3):187.
11. Kloas W, Lutz I. J Chromatogr A. 2006;1130(1):16–27.
12. Burlibaşa L, Gavrilă L. Appl Ecol Environ Res. 2011;9(1):1–15.
13. Burggren WW, Warburton S. ILAR J. 2007;48(3):260–269.
14. Gahl MK, Pauli BD, Houlahan JE. Ecol Appl. 2011;21(7):2521–2529.
15. Laohaudomchok W, Nankongnab N, Siriruttanapruk S, Klaimala P, Lianchamroon W, Ousap P, Jatiket M, Kajitvichyanukul P, Kitana N, Siriwong W, Hemachudhah T, Satayavivad J, Robson M, Jaacks L, Barr DB, Kongtip P, Woskie S. Hum Ecol Risk Assess. 2020;27(5):1147–1169.
16. Maneein R, Khonsue W, Varanusupakul P, Noppadon K. Res J Chem Environ. 2011;15(2):1018–1023.
17. Thitiphuree T, Kitana J, Varanusupakul P, Kitana N. EnvironmentAsia. 2013;6(1):13–18.
18. Thammachoti P, Khonsue W, Kitana J, Varanusupakul P, Kitana N. J Environ Prot. 2012a;3(10):1403–1408.
19. Jantawongsri K, Thammachoti P, Kitana J, Khonsue W, Varanusupakul P, Kitana N. EnvironmentAsia. 2015;8(1):68–74.
20. Othman MS, Khonsue W, Kitana J, Thirakhupt K, Robson MG, Kitana N. Asian Herpetol Res. 2011;2(1):41–45.
21. Othman MS, Khonsue W, Kitana J, Thirakhupt K, Robson MG, Kitana N. Malaysian Journal of Health Sciences. 2016;14(2):57–64.
22. Brodeur JC, Suarez RP, Natale GS, Ronco AE, Zaccagnini ME. Ecotoxicol Environ. 2011;74(5):1370–1380.
23. Wickham H. Elegant graphics for data analysis. Media. 2009;35(211):1000–1007.
24. Hayes TB, Stuart AA, Mendoza M, Collins A, Noriega N, Vonk A, Johnston G, Liu R, Kpodzo D. Environ Health Perspect. 2006;114(Suppl 1):134–141.
25. Storrs SI, Semlitsch RD. Gen Comp Endocrinol. 2008;156(3):524–530.
26. Lenkowski JR, Sanchez-Bravo G, McLaughlin KA. J Environ Sci. 2010;22(9):1305–1308.
27. Hegde G, Krishnamurthy SV. EEC. 2014;9(1):69–76.
28. Zhelev ZM, Popgeorgiev GS, Mehterov NH. Bulg J Agric Sci. 2015;21(3):534–539.
29. Zhelev ZM, Tsonev SV, Arnaudova DN. Acta Zool. Bulg. 2017;8:169–176.

30. Schulte-Hostedde AI, Zinner B, Millar JS, Hickling GJ. Ecol. 2005;86(1):155–163.
31. Hegde G, Krishnamurthy SV, Berger G. Chem Ecol. 2019;35(5):397–407.
32. McKinlay R, Plant JA, Bell JN, Voulvoulis N. Environ Int. 2008;34(2):168–183.
33. Carr JA, Gentles A, Smith EE, Goleman WL, Urquidi LJ, Thuett K, Kendall RJ, Giesy JP, Gross TS, Solomon KR, Van Der Kraak G. Environ Toxicol Chem. 2003;22(2):396–405.
34. Murphy MB, Hecker M, Coady KK, Tompsett AR, Jones PD, Du Preez LH, Everson GJ, Solomon KR, Carr JA, Smith EE, Kendall RJ. Aquat Toxicol. 2006;76(3–4):230–245.
35. Hansen SP, Messer TL, Mittelstet AR. J Environ Manage. 2019;250:109424.
36. Quassinti L, Maccari E, Murri O, Bramucci M. Pestic Biochem Physiol. 2009;93(2):91–95.
37. Parvez S, Raisuddin S. Arch Environ Contam Toxicol. 2006;50(3):392–397.
38. Lambert MR, Giller GS, Barber LB, Fitzgerald KC, Skelly DK. PNAS. 2015;112(38):11881–11886.
39. Köhler HR, Triebskorn R. Science. 2013;341(6147):759–765.
40. Rollins-Smith LA, Ramsey JP, Pask JD, Reinert LK, Woodhams DC. Integr Comp Biol. 2011;51(4):552–562.
41. Hocking DJ, Babbitt KJ. Herpetol. Conserv. Biol. 2014;9(1):1–17.

IDENTIFICATION OF TOXIC PLANTS FROM MORPHOLOGICALLY SIMILAR EDIBLE PLANTS IN THAILAND USING DNA BARCODE

Passanan Bawornkrailerd,[1] Nattana Chokboonjarern,[1] Fahsai Totanarungroj,[1] Supajit Sraphet,[2] Nattaya Srisawad,[2] Supanan Sucharit[1,*], Kanokporn Triwittayakorn[2]
[1]Mahidol Wittayanusorn School, THAILAND
[2]The Institute of Molecular Biosciences Mahidol University, THAILAND
*e-mail: supanan.suc@mwit.ac.th

Abstract:

As there are reported cases about patients with poisoning from consumption of; *Alocasia macrorrhizos Schott* (giant taro), *Phytolacca americana* (pokeweed), and *Datura metel L.* (thorn apple), due to the similar morphological features to those of its edible counterparts which are *Colocasia gigantea Hook.f.* (giant elephant ear), *Talinum paniculatum* (fameflower), and *Brugmansia suaveolens* (angel's trumpet). This study sets out to use DNA Barcode to help distinguish these three pairs of toxic plants from edible plants having similar morphology features, to determine the most suitable DNA markers, and to contribute as a reference for further research of these plants. Therefore, the DNA of sample plants was extracted by C-TAB protocol and replicated for specific regions: *rbc*L, *mat*K472, and ITS2, by PCR. The qualification control of DNA was examined by gel electrophoresis technique and NanoDrop Spectrophotometer, then PCR products were sequenced by a company to determine the nucleic acid sequence. Finally, the obtained DNA sequencing data was analyzed and constructed into phylogenetic trees by using Chromas and MEGA-X program. These phylogenetic trees show the evolutionary relationship between toxic plants and morphologically similar edible plants and verify that these toxic plants and edible plants can be distinguished using DNA Barcode from region *rbc*L, *mat*K472, and ITS2 as each outgroup clearly separates from the edible plants. Overall, the sequence information from *mat*K472 shows the most distinction. Therefore, *mat*K472 is the most suitable DNA marker for the identification of these plants.

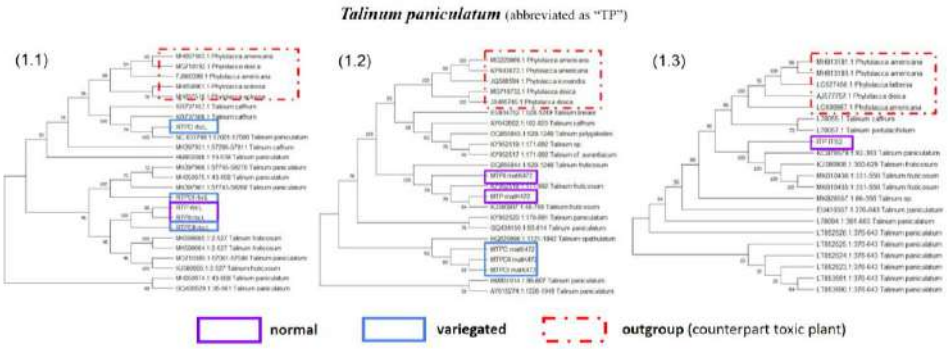

Figure 1. Phylogenetic tree of *Talinum paniculatum* (fameflower) using (1.1) *rbc*L, (1.2) *mat*K472, and (1.3) ITS2 as the DNA marker.

Innate Immunity Activation of *Litopenaeus vannamei* by Serine Protease and Heat-Killed *Vibrio parahaemolyticus*

Naeem Madsari, Phanthipha Runsaeng*
Division of Applied and Health Sciences, Faculty of Science, Prince of Songkla University, Songkhla 90112, Thailand
*e-mail: phanthipha.r@psu.ac.th

Abstract:

The transmittable disease problem affects the penaeid shrimp farming industry. Acute hepatopancreatic necrosis disease (AHPND) is a bacterial disease causing a high mortality rate and making economic losses. Since a serine protease is a critical virulence factor from *Vibrio parahaemolyticus*, it is to be remarkable to use as an immune stimulant or a shrimp vaccine. In the present study, a mutated serine protease gene was used for creating a DNA vaccine. To study the efficacy of shrimp responsive stimulation, the DNA vaccine mixed with heat-killed *Vibrio parahaemolyticus* (HkVP) was inoculated in white shrimp (*Litopenaeus vannamei*) compared with HkVP and NaCl injection. After immune priming for one week, the shrimp were injected again with *V. parahaemolyticus* and collected the hemocytes. The cellular immune response such as phagocytosis, encapsulation, and nodule formation were investigated. The results demonstrated that mixed vaccine could stimulate cellular immune responses including phagocytic rate, nodulation and encapsulation. The results indicated that a serine protease DNA vaccine mixed with the HkVP might enhance the shrimp responsive system and reduce the harshness of *V. parahaemolyticus.* In the future, the vaccine may be developed to be an effective adjuvant or vaccine that controls AHPND in shrimp aquaculture.

Introduction:

Pacific white shrimp or *Litopenaeus vannamei* is the predominant commercial shrimp species worldwide. Nevertheless, the menace of infectious diseases is one of the major causative factors for shrimp aquaculture development. Acute hepatopancreatic necrosis disease syndrome or called early mortality syndrome (AHPND or EMS) is the most common disease in *L. vannamei* farming and creates serious problems for farmers. A gram-negative bacteria named *Vibrio parahaemolyticus* is a cause of this disease, the pathogen obtains a unique plasmid that translates toxin homologous to Photorhabdus insect-related (Pir) toxins ($Pir^{vp}A$ and $Pir^{vp}B$). These Pir-like toxins cause hepatopancreas necrosis and disfunction which led to the death of shrimp [1]. A variety of approaches were attempted to reduce the severity of the disease. On the part of the shrimp immune system, it relies on innate immunity consisting of cellular and humoral responses. The cellular immunities rely upon the functions of hemocytes as well as nodules formation, phagocytosis, and encapsulation. Phagocytosis involves the internalization of small pathogens by adherence, ingestion, pathogen destruction and exocytosis [2,3]. Encapsulation is a process to destroy larger microorganisms that are unable to phagocytose by a single hemocyte, microbes will be eliminated or restricted the movement by aggregated hemocytes [3]. Nodule formation is performed by hemocyte aggregation around the microbe leading to a multilayered capsule forming and melanization activation. Finally, the microbes are eliminated [4]. Moreover, the humoral immunity

depends on the interaction of several proteins for example antimicrobial peptides, protease cascade and prophenoloxidase (proPO) [5, 6]. Therefore, the point of AHPND control in shrimp by using vaccines is perceived as useless because the invertebrate immunity is lacking any kind of immunological memory comparable to the vertebrates. However, many current studies can stimulate shrimp immunity and reduce the severity of disease with vaccines. In the previous study, the vaccines may accordingly provide some assistance to control this disease by increasing of basal immune. Furthermore, inactivated bacteria used as vaccines had been indicated to be efficacious in laboratory experiments. Inactivated vaccines such as heat-killed and formalin-killed vaccines of *Vibrio harveyi* and *Vibrio alginolyticus* demonstrated not only the increase of survival percentage but also activate phagocytosis, bacterial clearance, and phenoloxidase activity [7,8,9]. Presently, DNA vaccine becomes an exciting procedure to increase the duration of immune stimulation. Although, a lot of virulence factors from *V. parahaemolyticus* have been considered as a DNA vaccine for AHPND disease. Serine proteases are proteolytic enzymes which play important roles in various processes of the body. In *V. parahaemolyticus*, this protease has been reported as a virulence factor which making injury by host tissue degradation [10]. Since a serine protease DNA vaccine from *V. parahaemolyticus* revealed the ability to prevent the mortality of zebrafish, it was selected to a candidate of DNA vaccine [10]. However, the role of a serine protease from *V. parahaemolyticus* in shrimp has not been certainly investigated. In this study, the mixed vaccine between DNA vaccine encoding a mutated serine protease of *V. parahaemolyticus* and heat-killed *V. parahaemolyticus* (HkVP) was used for exploring its efficiency in shrimp immune system comparing with HkVP and NaCl group. The cellular immune parameters in shrimp including *in vitro* encapsulation, nodule formation, and phagocytic activity were examined.

Methodology:

Vaccine preparation

From all virulence factors of *V. parahaemolyticus*, a serine protease (NC_004605.1) was selected to design a DNA vaccine. To create the DNA vaccine that could stimulate shrimp immunity but could not harm the shrimp cell, the conserved residues of serine protease were mutated from His82, Asp131, and Ser231 to Gly, Asp, and Pro, respectively. Then, the mutated serine protease (mutVpSP) was cloned into pcDNA3.1 plasmid (GeneScript, USA). Afterward, to prepare the HkVP, a pathogenic strain of *V. parahaemolyticus* obtained from Department of aquatic science, Faculty of natural resources, PSU was grown in tryptic soy broth (TSB) added with 2% NaCl (Difco, Sparks, MD, USA) at 37 ◦C for 15 h. Then, the cultured broth was centrifuged at 1000xg at 4 ◦C for 25 min. After washing with 0.85% normal saline solution (NSS), the bacterial pellet was resuspended in NSS. Accordingly, the bacterium was autoclaved at 120 ◦C for 20 min. Then, HkVP ($5x10^5$ CFU/ml) was used for experimental group. In addition, the mixed vaccine (DNA vaccine combining with HkVP was prepared by mixing DNA vaccine (5 µg/g shrimp) with HkVP ($5x10^5$ CFU/ml). Finally, mixed vaccine and HkVP were separately injected into shrimp for investigating the immune response in *L. vannamei* compared with control group.

Shrimp inoculation

The healthy *L. vannamei* with bodyweight 2±1.0 g was procured from local shrimp pond in Songkla, Thailand and maintained for one week. The shrimp was fed three times per day with formulated diet (40% protein) produced by Krungthai Food company (Bangkok, Thailand). Shrimp were divided into three groups with 20 shrimp for each group. The first group, shrimp were individually injected with mixed vaccine. The second group, shrimp were

stimulated by only HkVP whereas the shrimp in the last group were only received NSS. After 7 days post-vaccinated, the shrimp was challenged with lived *V. parahaemolyticus* ($5x10^5$ CFU/ml). Then, hemolymph was collected after 24 h of injection.

Phagocytosis assay

The phagocytosis was investigated succeeding the earlier procedure [11]. For hemocytes harvesting, the mixture of fresh hemolymph and anticoagulant (50 mM Tris-HCl, 2% glucose, 2% NaCl, 20 mM EDTA, pH 7.4) were centrifuged at 800×g, 4°C for 20 min and then it was resuspended in TBS buffer containing 50 mM $CaCl_2$. After inactivating *V. parahaemolyticus* (A600 = 0.4) in TBS buffer at 72 °C for 20 min, the inactivated bacterium was added (1-2 µl) into hemocyte suspension. The reaction was incubated at 18 °C for 1 hour. The solutions were mounted onto a microscope slide and placed in a watery chamber at 18 °C for 1 h. Afterwards, the slide was dried at room temperature. The dried sample slide was dipped in absolute methanol for 3-5 min and soaked in 1:20 Giemza staining. The phagocytized hemocytes were observed by a light microscope. Each of the treatments were investigated on three microscope slides for statistical analysis. The activity of shrimp phagocytosis represented by phagocytic rate (PR) and phagocytic index (PI). PR = (phagocytic hemocytes)/(total hemocytes) × 100%. A moderate number of bacteria in hemocytes were identified as PI. The experiment was performed in triplicate for statistical analysis.

In vitro encapsulation test

The *in vitro* encapsulation was performed succeeding the previous research [11, 12]. Ni-NTA agarose beads were equilibrated in TBS containing 50 mM $CaCl_2$ (equilibrated buffer). Then, the beads were incubated and shaken with C-type lectin (rFmLdlr) at 4 °C overnight. After rinsing with equilibrated buffer four times, the beads were resuspended with equilibrated buffer. Thereby, the hemocytes in K-199 medium were added into the wells of a 24 well culture plate layered with 1% agarose and left for 10 min. Finally, the protein-coated beads 1-2 µl was dropped and incubated at 18 °C. The encapsulated bead was observed at 0, 6, and 24 h after being incubated with a light microscope. The experiment was carried out in triplicate for statistical test.

Nodule formation assay

The formation of the nodule was evaluated following the preceding study [13]. In brief, K-199 medium was utilized for hemolymph dilution in ratio 1:10. After mixing instantly, the combination was incubated at room temperature for 0, 5, 10, 15, 30, and 60 min with shaking 45 rpm. Then, the fixative buffer (0.5 ml of 2.5% glutaraldehyde in 0.1 M sodium cacodylate, pH 7.4, containing 12% glucose) was added a half of the sample volume and mixed immediately. Therefore, the nodules of each time point were monitored by the light microscope. The experiment was performed in triplicate for statistical analysis.

Results & Discussion:

Phagocytosis activity

The hemocyte from vaccinated shrimp gets to be phagocytized which was observed under the light microscope (Table.1). The phagocytic rate of HkVP and a mixed vaccine was 62.0% and 66.67%, respectively, whilst a control shrimp was 41%. Moreover, the phagocytic index of shrimp receiving a mixed vaccine or only HkVP also higher than control shrimp which it was 1.325, 2.100, and 2.260, respectively. The results indicated that both a mixed vaccine and only HkVP might provoke the phagocytosis like as reported for shrimp receiving an inactivated *V. alginolyticus* that showed heightened in phagocytic activity [14].

Table 1.

The data of phagocytic rate and phagocytic index.

	Phagocytic rate (%)	Phagocytic index
NaCl	41.00±6.25	1.325±0.07
HkVP	62.00±4.58	2.100±0.24
HkVP+DNA	66.67±3.21	2.260±0.05

In vitro encapsulation activity

The results from the encapsulation test showed encapsulated beads were found at 6 h after incubation. Fig.1 exhibited the larger size of hemocytes agglutination covered beads in the vaccinated group both 6 and 24 h. The encapsulation percentage at 6 h of each vaccinated group was 60% while the control group had only 30%. However, the encapsulation was triggered as time increases, the percentage of encapsulation at 24 h was increased to 80 and 90% in HkVP and mixed vaccine, respectively. However, the encapsulation activity at 24 h in control group displayed only 75%. In previous study, FmLdlr could enhance encapsulation by hemocytes [15]. Therefore, the results revealed that the hemocytes of vaccinated shrimp that was promoted by rFmLdlr showed higher encapsulation more than control group which was promoted by rFmLdlr as well (Table.2), suggesting that HkVP and mixed vaccine might induce hemocytes in encapsulating foreign molecules.

Figure 1.

In vitro encapsulation activity. The Ni-NTA agarose beads were encapsulated by the hemocytes from NaCl, HkVP, and mixed vaccine (HkVP+DNA vaccine) injected shrimp. The encapsulated beads were observed at 0, 6, and 24 h after incubation.

Table 2.

The data of encapsulation percentage.

	Encapsulation bead (%)		
	0 h	6 h	24 h
NaCl	0±0.00	30±5.00	75±5.00
HkVP	0±0.00	60±8.66	80±8.66
HkVP+DNA	0±0.00	60±8.66	90±5.00

Nodule formation

Figure 2 revealed that most of hemocytes are single cells at 0 min. At 5 min later, many tiny nodules were found in control and both vaccinated shrimp. After incubation for 10 min, the nodules were exhibited in control and vaccinated shrimp. However, the size of nodules between the three groups is not much different. The distinguish size of nodulation was observed after incubation for 15 min. The nodules of the vaccinated shrimp exhibited a larger size nodule more than a control shrimp. The average number of hemocytes was 13.2 in the control group whereas 18.3 and 19.27 hemocytes were found in HkVP and mixed vaccine group. After continuous incubation for 30 and 60 min, the scale of the nodules was enlarged as the number of nodules was dropped because individually of the nodules was merged to a larger nodule. Therefore, the average number of hemocytes in the nodule of HkVP and mixed vaccine groups was boosted to 24.38 and 28.86 after incubation for 30 min as well as boosted to 50 and 52.5 for 60 min, respectively. The average number in a control group was only 15.38 and 23.13 after incubation for 30 and 60 min, respectively. The larger and more numerous nodules are exhibited in vaccinated shrimp (Table.3). The among of hemocytes was increased leading to the induction of *in vitro* bacterial clearance [16]. In addition, inactivated *V. alginolyticus* was reported to be an inducer for increasing the immune response by augmentation of total hemocyte counts in vaccinated shrimp [14]. Therefore, increased number of hemocytes corresponded to the enhanced immunity, it could be that higher aggregated hemocytes or high levels of nodules mean an improved immune response that could eliminate pathogens rapidly. The results demonstrated that mixed vaccine and HkVP showed better capability to stimulate innate immune consisting of phagocytosis, encapsulation, and nodulation assay compared with control group. These results suggested that serine protease DNA vaccine and HkVP activate cellular immunity by enhancing the nodule formation.

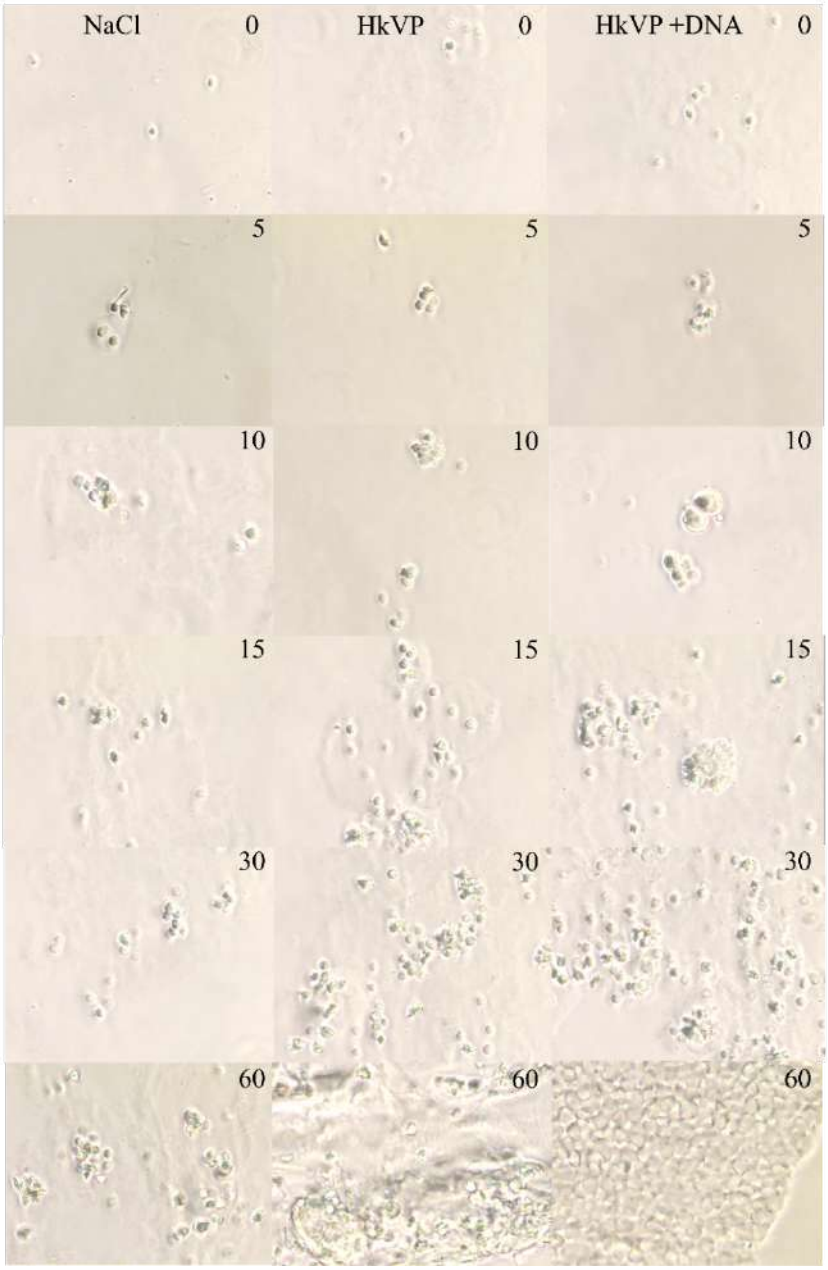

Figure 2.

Nodule formation assay. The formation of nodules from the hemolymph of NaCl, HkVP, and mixed vaccine (HkVP+DNA vaccine) injected shrimp were observed at various time points.

Table 3.

The average number of hemocytes in nodules.

	The average number of hemocytes in nodules					
	0 min	5 min	10 min	15 min	30 min	60 min
NaCl	5.60±0.20	9.30±0.33	11.57±0.16	13.20±0.16	15.38±0.35	23.13±0.57
HkVP	5.50±0.50	9.40±0.38	11.75±0.36	18.30±0.43	24.38±0.36	50.00±0.28
HkVP+DNA	5.50±0.30	9.45±0.32	12.38±0.37	19.27±0.34	28.86±0.36	52.50±0.67

Conclusion:

Recently, the heat-killed vaccine (HkVP) and the DNA vaccine from *V. parahaemolyticus* were successfully prepared. The shrimp were inoculated with each vaccine possessed the higher responses in cellular immunity. The phagocytic rate of both vaccinated was higher than control shrimp. The encapsulation percentage of each vaccinated group was higher than control shrimp and the bigger size of agglutinated hemocytes covering the beads was found in experiment group. Besides, an enlarge of nodule in the vaccinated group discriminated after incubation for 15 to 60 min. Although, the shrimp possess only innate immune response and do not result in immune memory like the adaptive immune system, both vaccines show the ability of immunostimulants in the cellular immune response of shrimp. From the data presented here, it could be presumed that HkVP and mixed vaccine can be used as an adjuvant or immune enhancer that promoted the shrimp immune induction. These results will be applied to an effective candidate vaccine to provoke the immune capability against AHPND in *L. vannamei* or other penaeid shrimp farming.

Acknowledgements:

This work was supported by the government budget of Prince of Songkla University (Grant No. SCI6202088S) and the PSU-Ph.D. Scholarship (PSU_PHD2561-002) from the Graduate School, Prince of Songkla University.

References:

1. Lee CT, Chen IT, Yang YT, Ko TP, Huang YT, Huang JY, Huang MF, Lin SJ, Chen CY, Lin SS, Lightner DV, Wang HC, Wang AHJ, Wang HC, Hor L., Lo CF. Proc Natl Acad Sci USA. 2015;112:10798–10803.
2. Kondo M, Itami T, Takahashi Y, Fujii R, Tomonaga, S. Fish Pathol. 1998;33:421-427.
3. Vargas-Albores F, Yepiz-Plascencia G. Trends Comp. Biochem. Physiol. 1998;5:195-210.
4. Satyavathi VV, Minz A, Nagaraju J. Cell. Signal. 2014;26:1753-1763.
5. Jiravanichpaisal P, Lee BL, Söderhäll K. Immunobiology. 2006;211:213–236.
6. Vazquez L, Alpuche J, Maldonado G, Agundis C, Pereyra-Morales A, Zenteno E. Innate Immun. 2009;15:179–188.
7. Hettiarachchi M, Pathirage SG, Hettiarachchi, DC. J Natn Sci Found SRI. 2005;33:257-263.
8. Lin YC, Chen JC, Morni WZ, Putra DF, Huang CL, Li CC, Hsieh JF. PLoS One. 2013;8:e69722.
9. Hsu CH, Chen JC, Lin Y.C, Chen YY, Liu PC, Lin BW, Hsieh JF. Fish Shellfish Immunol. 2021;112:151-158.
10. Liu R, Chen J, Li K, Zhang X. Fish Shellfish Immunol. 2011;30:1241-1248.11. Yang J, Wang L, Zhang H, Qiu L, Wang H, Song L. PLoS One. 2011;6:e17089.
12. Wang L, Wang L, Zhang D, Li F, Wang M, Huang M, Zhang H, Song L. Fish Shellfish Immunol. 2013;34:832–842.
13. Martin GG, Kay J, Poole D, Poole C. Inver bio. 1998;117:155-168.
14. Lin YC, Chen JC, Morni WW, Putra DF, Huang CL, Li CC, Hsieh JF. PLoS One. 2013;8;e69722.
15. Kwankaew P, Praparatana R, Runsaeng P, Utarabhand P. Fish Shellfish Immunol. 2018;74:295-308.
16. Martin GG, Poole D, Poole C, Hose JE, Arias M, Reynolds L, McKrell N, Whang A. J Invertebr Path. 1993;62:517-522.

ISOLATION AND CHARACTERIZATION OF BACTERIOPHAGE INFECTING *Bacillus cereus*

Wallapat Phongtang, Ekachai Chukeatirote*
School of Science, Mae Fah Luang University, Chiang Rai 57100, Thailand
*e-mail: ekachai@mfu.ac.th

Abstract:
Bacillus cereus is a causative agent especially for the foodborne disease causing diarrhea and vomiting. In this study, the presence of *B. cereus* bacteriophages was studied using Thua Nao, a Thai fermented soybean product as the isolating source. Two bacteriophages (BaceFT01 and BaceCM02) were isolated based on their ability to form plaques on *B. cereus* host. The purified phages were then characterized in terms of morphology, host range, and stability. Both phages appeared to be the member of the *Myoviridae* family based on their structure in electron micrographs. The two phages could infect only *B. cereus*, and were able to survive in a pH range between 5 and 12. Both phages were inactive when incubating at 50°C for 2h. The characterization of these two phages would be useful in generating fundamental data of the phages that might be further explored for possible biocontrol use in food industry.

MEDIA AFFECTING GERMINATION RATE OF ORCHID SEEDS IN *Seidenfadenia mitrata* (Rchb. f.) Garay

Sompradtana Worabandit,[1] Naphaphan Jaidee,[2] Jantrararuk Tovaranonte[1,2,*]
[1]School of Science, Mae Fah Luang University, Muang, Chiang Rai, 57100, Thailand
[2]Mae Fah Luang University Botanical Garden, Mae Fah Luang University, Muang, Chiang Rai, 57100, Thailand
*e-mail: Jantrararuk@mfu.ac.th

Abstract:

Seidenfadenia mitrata (Rchb. f.) Garay, a monotypic genus, grows slowly and has decreased its population in wild habitat due to low fruiting rate and low germination, habitat loss, deforestation and illegal collection. In general, the production of plantlets on a large scale has been successful using the tissue culture technique. The purpose of this study was to evaluate the most efficient culture medium for *in vitro* on seed germination of *S. mitrata* (Rchb. f.) Garay. Seeds were cultured in three culture media as half-strength MS in semi-solid medium (½ MS-SS), half-strength MS in solid medium (½ MS-S) and half-strength MS in solid medium with activated charcoal (half-strength MS-S-ACh) with 5 replications. The seed germination was recorded in terms of Growth index (GI), germination speed index (GSI), and germination percentage (%germination) every week for 8 weeks after culture The results showed that the highest of GI, GSI and % germination were 4.36, 21.4 and 100% in ½ MS-SS medium, respectively at 95% confidence level.

METHOD FOR PROTEIN EXTRACTION AND PAPER DEVICE FOR PROTEIN SEMI-QUANTITATIVE SCREENING IN NATURAL RUBBER LATEX

Panwadee Wattanasin,[1] Apichat Phengdaam,[1] Phanthipha Runsaeng[2,*]
[1]Division of Physical Science, Faculty of Science, Prince of Songkla University, Hat Yai, Songkhla, 90110, Thailand
[2]Division of Health and Applied Sciences, Faculty of Science, Prince of Songkla University, Hat Yai, Songkhla, 90110, Thailand
*e-mail: phanthipha.r@psu.ac.th

Abstract:
The allergy to natural rubber latex (NRL) proteins is a significant occupational health hazard. The entrepreneurs often use several methods to clear protein in NRL. It leads to increasing of costs. An effective method for protein extraction and simple method for quantitative screening are required. In this study, the highest protein extraction yields were obtained using microwave for 30 min with buffer containing 0.4 M Urea, 0.04 M SDS, 0.43 M acetone (4.18 mg/g for RRIM600 and 5.20 mg/g for RRIT251). However, the lower levels of protein were detected in condition prepared by sonication (3.69 mg/g for RRIM600 and 4.44 mg/g for RRIT251). In addition, we developed a microfluidic paper-based analytical device for protein concentration screening. The device is a filter paper containing hydrophobic barrier and hydrophilic zone. In the zone contained modified bromocresol green reacted with extracted proteins. The device has a linear range of 0.05-5.00 mg/ml, with coefficient of determination (r^2) > 0.9968. Using the device for screening the quantity of proteins in each step of protein elimination will help the entrepreneurs to save time and cost for protein elimination processes. Moreover, the method is simple, low-cost, easy-to-use, and instrument-free for on-site analysis.

MICROBIAL DIVERSITY AND FUNCTION-BASED SCREENING FOR β-GALACTOSIDASES FROM WANG-PRA CAVE METAGENOME

Patcharee Phetthongyok,[1] Apirak Wiseschart[1,2], Duriya Chantasingh[2], Kusol Pootanakit[1]*
[1]Institute of Molecular Biosciences, Mahidol University, Salaya, Phutthamonthon, Nakhon Pathom 73170, Thailand.
[2]National Center for Genetic Engineering and Biotechnology (BIOTEC), 133 Thailand Science Park, Paholyothin Rd, Klong 1, Klongluang, Pathumthani 12120, Thailand.
*e-mail: kusol.poo@mahidol.ac.th

Abstract:
Microorganisms play essential roles in every aspect of our lives (e.g. human health, nutrient cycles, and ecological balance). However, only limited numbers of microorganisms found in nature can be cultured under the laboratory conditions. Therefore, metagenomics approach was developed to investigate both the identities of the microorganisms and the potential microbial products that can be found within a given niche. Novel microorganisms are usually found in extreme environments. Cave ecosystem is considered an extreme environment due to their oligotrophic conditions. Here, the taxonomic community structure of Wang-Pra cave-dwelling microorganisms was investigated using 16S rRNA amplicon sequencing via Ion Personal Genome Machine System (PGM). Most of the microorganisms identified were distributed into the phyla *Proteobacteria* (21.5%), *Actinobacteria* (9.5%), and *Firmicutes* (3.1%). However, the majority of microbes cannot be classified (64.2%) into any known phyla. Furthermore, to test for the functionality of the cave metagenome, its ability to hydrolyze X-gal was also investigated. The extracted eDNA were used to construct a fosmid library, yielding 3.5 x 10^4 recombinant clones. Of these, 22 clones showed β-galactosidase activity. Our results suggested a great potential for Wang-Pra cave as a habitat for novel microorganisms that might be a promising source of novel microbial products of biotechnological and industrial interests.

Introduction:

Cave ecosystem is considered as extreme environment because they are in general of limited nutrient and biomass. It has been reported that caves are colonized by highly specialize microorganisms who have well-adapted metabolic activities to thrive under the cave-specific conditions[1]. Normally, soil environments are the major reservoir of microorganisms with many industrial enzymes and pharmacologically valuable compounds[2-3]. However, due to the limitation of microbes that can be grown under the laboratory conditions (less than 1%)[4], the indirect molecular approach was developed based on the isolation and analysis of nucleic acids from soil samples without cultivation, so called "metagenomics". Based on targeted 16S rRNA metagenomic amplicon sequencing, previous studies revealed unexpected diversity of microorganisms from various cave samples[4-7]. In general, *Actinobacteria*, *Acidobacteria,* and *Proteobacteria* are the most frequently found phyla in the cave environments[1, 8].

β-galactosidase (E.C. 3.2.1.23) also known as lactase, is one of the important enzymes in the dairy industry. It hydrolyzes disaccharide lactose to release monosaccharides, glucose and galactose[9]. Consequently, when this enzyme is added to milk or milk products, it solves the problem of lactose intolerance in human. β-galactosidase can be found in bacteria, fungi, plants, and yeast. Also, this enzyme is used to convert whey into ethanol or syrup to solve the water waste pollution of whey disposal problem[10]. Due to the demands for enzymes

especially in their thermostability and pH, the need for novel β-galactosidases with those properties for industrial used are still needed. For instance, a thermostable β-galactosidase was isolated from soil sample in China[11], and also from the sediments of a hot spring in Spain[12].

In Thailand, caves are a general landscape which in general, is mostly undisturbed from visitors or tourists. Previously, 16S rRNA metagenomic sequencing was used to explore Manao-Pee cave microbiome[13]. The results showed contrasting taxonomic community structure between the cave soil community and its outside samples. However, the study of cave metagenomic and functional analysis of microbial products in Thailand are barely investigated. Here, the taxonomic structure of Wang-Pra cave microorganisms was investigated using 16S rRNA amplicon sequencing using an Ion Personal Genome Machine (Thermo Fisher Scientific, USA). The functionality of the cave metagenome was also explored by constructing cave eDNA library and screening for β-galactosidase activity.

Methodology:

Site description and sampling

Wang-Pra cave is part of the extensive Khao Wang Khamen karst ecosystem, located on the mountainside at an altitude of about 90 meters above sea level in Sai Yok district, Kanchanaburi province. This cave is occupied by many animals especially Kitti's hog-nosed bat (*Craseonycteris thonglongyai*). As this bat species is a near-threatened species, this cave is officially closed to visitors[14]. Cave soil pH exhibited slightly alkaline condition. Soil samples were collected from five different locations in the dark zone at the dept of 5 cm. The samples were stored at -20°C before DNA extraction.

Environmental DNA (eDNA) extraction and purification

Soil samples (WPI) were extracted by the modified SDS-based DNA extraction method with slight modification[13]. Specifically, 3 g of soil samples were mixed with 16 ml of DNA extraction buffer (100 mM Tris-HCl, pH 8.0, 100 mM sodium ethylenediaminetetraacetic acid (EDTA), pH 8.0, 100 mM sodium phosphate, pH 8.0, 1.5 M NaCl, 4% (w/v) cetyltrimethylammonium bromide (CTAB) and 100 µl of proteinase K (20 mg/ml). The mixture was vigorously shaken at 250 rpm, 37 °C for 30 min. Then, 2 ml of 20% (w/v) sodium dodecyl sulfate (SDS) was added to the mixture and incubated at 65 °C for 2 h. During this time, the mixture was gently mixed every 15-20 min. Next, the mixture was centrifuged at 8,000 ×g for 10 min at room temperature. The supernatant was transferred to a new 50 ml centrifuge tube, and the soil pellet was re-extracted again by adding 6 ml of DNA extraction buffer and 1.5 ml of 20% (w/v) SDS. After mixing thoroughly, the mixture was incubated at 65 °C. After 15 min, the supernatant was collected as described above. All supernatants were combined and mixed with equal volume of chloroform: isoamyl alcohol (24:1 (v/v)). The upper phase was transferred to a new tube after centrifugation at 8,000 ×g for 10 min at 4 °C. eDNA was precipitated with 0.6 vol of isopropanol and incubated for 1 h at room temperature. The precipitated eDNA was pelleted by centrifugation at 16,000×g for 20 min at 4 °C. Then, 300 µl of ice-cold 70% ethanol (v/v) was carefully added to the pellet and centrifuged again at 16,000×g for 10 min at 4 °C. Extracted eDNA pellet was air-dried at room temperature and then dissolved in 100 µl of sterilized Tris-EDTA (TE) Buffer. The extracted eDNA were combined and purified using electroelution technique as previously described[13]. Finally, the concentration and purity of extracted eDNA was determined using a NanoDrop 2000 spectrometer (Thermo Fisher Scientific).

Targeted 16S rRNA metagenomic amplification and sequencing

Purified eDNA from inside of Wang-Pra cave (WPI) was used as DNA template to amplify the V5-V6 regions of 16S rRNA gene using universal primers Ee785F (5'-GGATTAGATACCCTGG TAGTCC-3') and E1081R (5'- CTCACGRCACGAGCTGACG-

3'). In a 25 μL PCR reaction mixture contained 1x Phusion HF buffer (Thermo Scientific), 0.4 mM of each primer, 0.4 mM of each dNTP, 1 U Phusion High-Fidelity DNA polymerase (Thermo Scientific), and 25 ng of purified eDNA template. The PCR cycles were: an initial denaturation at 98 °C for 30 sec, followed by 35 cycles of 98 °C for 10 sec, 68 °C for 30 sec, and 72 °C for 30 sec, and a final extension at 72 °C for 5 min. PCR products from three independent reactions were combined and purified using QIAquick Gel Extraction Kit (Qiagen, Germany) according to the manufacturer's protocol. The concentration and purity of purified PCR products were determined using a NanoDrop 2000 spectrometer (Thermo Fisher Scientific). Finally, the purified PCR products were sequenced at the Genome Institute, National Center for Genetic Engineering and Biotechnology (BIOTEC), Thailand, using an Ion Personal Genome Machine (Thermo Fisher Scientific, USA).

Bioinformatic analysis and community structure comparison based on targeted 16S rRNA metagenomic sequencing

From sequencing datasets, primers and low-quality reads (Phred ≤ Q20) were removed. Also, chimeric sequences were identified and filtered out by UCHIME[16] using the referenced dataset from the Ribosomal Database Project (RDP)[17]. To determine taxonomic community structure, qualified reads were processed through a pipeline in QIIME (Quantitative Insights Into Microbial Ecology) version 1.9.1 for clustering sequences into Operational Taxonomic Units (OTUs), and taxonomic classification[18]. The OTUs were clustered with an open-reference method using UCLUST at 97% similarity cut off[19].

Wang-Pra cave fosmid library construction

The library was constructed using CopyControl Fosmid library Production Kit with pCC2FOS vector according to the manufacturer's protocol (Lucigen, USA). The extracted eDNA was blunt-ended, 5'-phosphorylated and ligated to pCC2FOS vector. After incubation overnight, recombinant fosmid was packaged into lambda phage particles using *in vitro* packaging extract. The *E. coli* EPI300-T1^{R} strain was used for lambda phage infection. The transformants were subsequently plated on LB agar plate supplement with 12.5 μg/ml chloramphenicol and incubated at 37º C overnight to select for recombinant fosmid clones. The fosmid libraries were kept at -80ºC in 30% glycerol stock for further use.

Determination of average insert size of the fosmid library

10 fosmid clones were randomly picked from the library for fosmid extraction. The average eDNA insert size was measured using restriction fragment length polymorphism (RFLP). After digestion of the extracted fosmids with *Not*I, pulsed-field gel electrophoresis (PFGE) was subsequently run on the CHEF DRIII system (Bio-Rad, USA) at 14ºC for 14 h. The switch time was logarithmically ramped from 0.22 – 0.92 sec with a ramped factor of 0.357. The forward and reverse voltage gradient were 9 V/cm and 6V/cm, respectively.

Functional screening of the fosmid library for β-galactosidase activity

Pooled recombinant fosmid clones were diluted in LB broth to obtain approximately 1,500 colonies per plate. Then, they were directly screened using LB agar plate supplement with12.5 μg/ml of chloramphenicol, X-gal (20 μg/ml), and 100mM IPTG. After overnight incubation at 37 °C and left for 1-2 weeks. The positive clones were identified by blue colony phenotype.

Results and Discussion:

Wang-Pra cave eDNA extraction and purification

In this study, crude eDNA was extracted from a total of 144 g of soil samples. The results showed that the size of the crude eDNA was greater than 23 kb (Fig. 1A). In total, four crude eDNA extractions were performed. The obtained extracted eDNAs were then pooled and purified. The purified eDNAs from the four extractions are shown in figure 1B. The eDNA quality and quantity is shown in table 1.

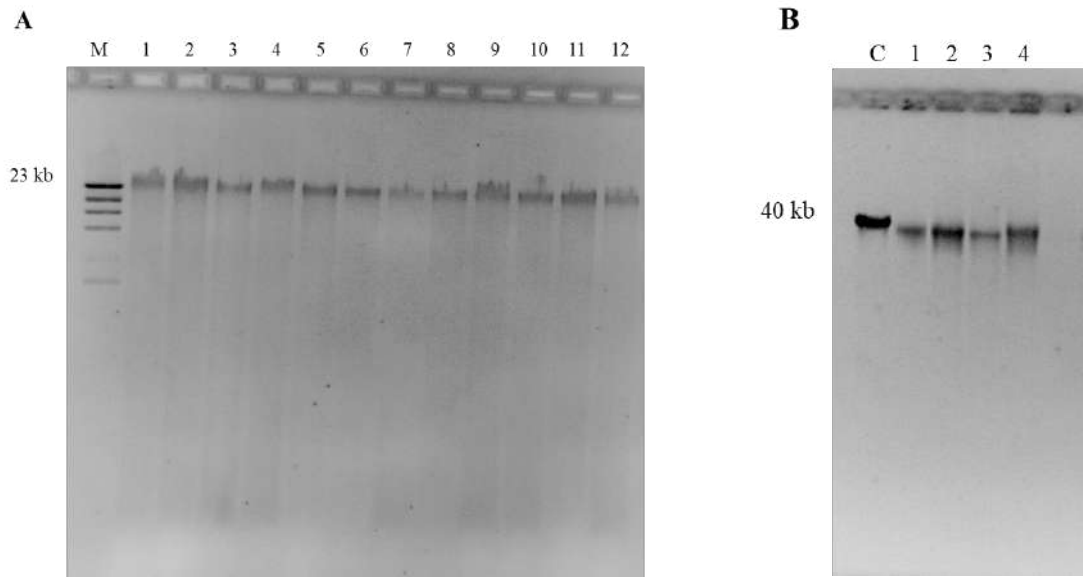

Figure 1. **Agarose gel electrophoresis of Wang-Pra cave eDNA samples. A. Crude eDNA samples, M is ƛ DNA *Hind*III marker and lanes 1-12 represent crude eDNA samples. B. Purified eDNA using electroelution technique. Lane C is fosmid control DNA (40 kb) (Lucigen, USA). Lanes 1- 4 represent purified eDNA samples.**

Table 1. The quality and quantity of purified eDNA from soil sample inside Wang-Pra cave.

Samples	DNA (ng/µl)	260/280	260/230	Total (µg)
1	29.2	1.65	1.41	1.752
2	62.7	1.69	1.31	1.254
3	16.3	1.74	0.97	0.652
4	40.2	1.73	1.45	1.608

Taxonomic community structure based on targeted 16S rRNA metagenomic sequencing

The purified eDNA was used as DNA template to amplify 16S rRNA gene with universal primers targeted the hypervariable V5 and V6 regions. After sequencing, the results showed a total high-quality read of 33,643. Taxonomic distribution analysis at phylum level showed that the most dominant phyla in Wang-Pra cave soil community were *Proteobacteria* (21.5%), *Actinobacteria* (9.5%), and *Firmicutes* (3.1%). This confirmed other reports whereby *Actinobacteria* and *Proteobacteria* are the commonly found bacterial phyla in cave ecosystems[1, 8, 13, 20]. Interestingly, 64.2% of sequence identified could not be assigned into any known phyla (Fig. 2). Again, confirming that caves are well-known as extreme habitat which are a good source of novel microorganisms and very likely novel microbial products[21].

Construction of fosmid library from Wang-Pra cave metagenome

The fosmid library was constructed using CoppyControl HTP production kit with pCC2FOS as cloning vector and *E. coli* as the heterologous host due to its high transformation efficiency[22]. From 5.2 µg of purified eDNA, approximately 3.5 x 10^4 clones were obtained. The size of the insert fragments was approximately 27 kb as estimated using RFLP technique coupled with pulsed-field gel electrophoresis (PFGE). Therefore, in total, the size of this Wang-Pra cave fosmid library was of approximately 953 Mb.

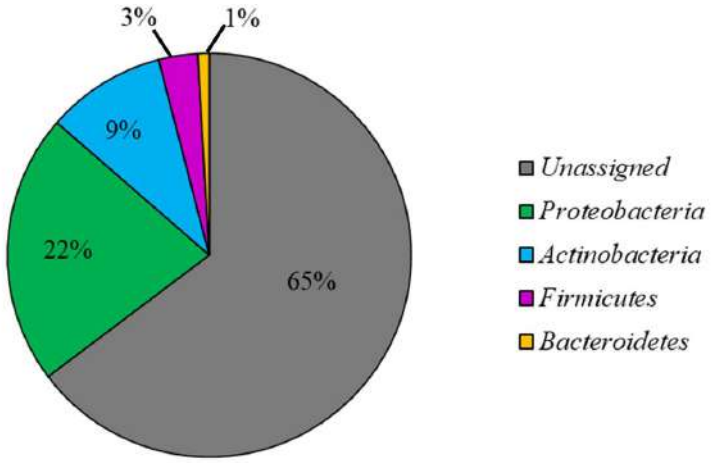

Figure 2. The taxonomic community structure of soil inside Wang-Pra cave.

Activity screening for transformants showing β-galactosidase activity

X-gal agar plate assay is commonly employed to discover β-galactosidase activity. When X-gal is hydrolyzed, it gives galactose and 5-bromo-4-chloro-3-hydroxyindole. The later subsequently dimerizes and oxidized to 5,5'-dibromo-4,4'-dichloro-indigo, forming blue precipitates[11, 23]. Therefore, clones with β-galactosidase activity will be shown as blue color colonies. From the screening of $3.5x10^4$ clones, 22 clones showed β-galactosidase activity (Fig. 3), yielding a hit ratio of 1:1590. This result is higher than other studies which also used X-gal in functional screening[11, 24]. However, the limitation to functional screening is that the genes must be able to be expressed in the heterologous host. The efficiency of gene expression will therefore depend on the vector-host selection and also codon usage[25-26].

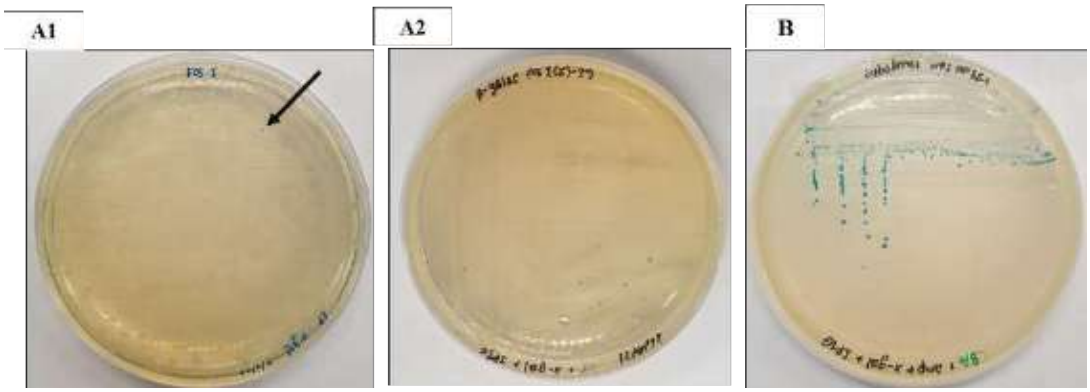

Figure 3. Examples of β-galactosidase-positive clones from Wang-Pra cave metagenomic library. The β-galactosidase activity was screened using X-gal as a substrate. A1 and A2 are examples of clones that can hydrolyze X-gal. B, β-galactosidase positive control.

Conclusion:

Metagenomics approach was employed to determine the microbial taxonomic community from Wang-Pra cave. A fosmid library was constructed and functionally screened for X-gal hydrolysis. Twenty-two clones showed this ability, and they may encode for novel β-galactosidase enzyme. Our results suggested that this cave hosts potential novel microorganisms that might be a promising source for unique microbial products of biotechnological and industrial interests.

Acknowledgement:

This work was supported by the Plant Genetic Conservation Project under the Royal Initiation of Her Royal Highness Princes Maha Chakri Sirindhorn (RSPG) and the 60th Year Supreme Reign of His Majesty King Bhumibol Adulyadej Scholarship, Mahidol University.

References:

1. Tomczyk-Żak K, Zielenkiewicz U, *Geomicrobiology Journal* 2016;33(1):20-38.
2. Rosselló-Mora R, Amann R, *FEMS Microbiology Reviews* 2001;25(1):39-67.
3. Daniel R, *Nature reviews. Microbiology* 2005;3470-8.
4. Torsvik V, Goksøyr J, Daae F L, *Applied and environmental microbiology* 1990;56(3):782-787.
5. Ortiz M, Neilson J W, Nelson W M, Legatzki A, Byrne A, Yu Y, Wing R A, Soderlund C A, Pryor B M, Pierson L S, Maier R M, *Microbial Ecology* 2013;65(2):371-383.
6. Riesenfeld C S, Goodman R M, Handelsman J, *Environmental microbiology* 2004;6(9):981-989.
7. De Mandal S, Chatterjee R, Kumar N S, *BMC Microbiology* 2017;17(1):90.
8. Oliveira C, Gunderman L, Coles C A, Lochmann J, Parks M, Ballard E, Glazko G, Rahmatallah Y, Tackett A J, Thomas D J, *Diversity (Basel)* 2017;9(3).
9. Neri D F M, Balcão V M, Carneiro-da-Cunha M G, Carvalho Jr L B, Teixeira J A, *Catalysis Communications* 2008;9(14):2334-2339.
10. Saqib S, Akram A, Halim S A, Tassaduq R, *3 Biotech* 2017;7(1):79.
11. Zhang X, Li H, Li C-J, Ma T, Li G, Liu Y-H, *BMC Microbiology* 2013;13(1):237.
12. Knapik K, Becerra M, González-Siso M-I, *Scientific Reports* 2019;9(1):11195.
13. Wiseschart A, Mhuanthong W, Tangphatsornruang S, Chantasigh D, *BMC Microbiology* 2019;19(1):144.
14. Bates P, Bumrungsri, S. & Francis, C., *The IUCN Red List of Threatened Species 2019* 2019; e.T5481A22072935.
15. Wang Y, Qian P-Y, *PLOS ONE* 2009;4(10):e7401.
16. Zhu W, Lomsadze A, Borodovsky M, *Nucleic Acids Res* 2010;38(12):e132-e132.
17. Zhao Y, Tang H, Ye Y, *Bioinformatics* 2012;28(1):125-126.
18. Caporaso J G, Kuczynski J, Stombaugh J, Bittinger K, Bushman F D, Costello E K, Fierer N, Peña A G, Goodrich J K, Gordon J I, Huttley G A, Kelley S T, Knights D, Koenig J E, Ley R E, Lozupone C A, McDonald D, Muegge B D, Pirrung M, Reeder J, Sevinsky J R, Turnbaugh P J, Walters W A, Widmann J, Yatsunenko T, Zaneveld J, Knight R, *Nature Methods* 2010;7(5):335-336.
19. Edgar R, *Bioinformatics* 2010;262460-1.
20. Wiseschart A, Mhuanthong W, Thongkam P, Tangphatsornruang S, Chantasigh D, *Geomicrobiology Journal* 2018;35518-527.
22. Boni I V, *Molecular Biology* 2006;40(4):587-596.
23. Erich S, Kuschel B, Schwarz T, Ewert J, Böhmer N, Niehaus F, Eck J, Lutz-Wahl S, Stressler T, Fischer L, *Journal of Biotechnology* 2015;21027-37.
24. Wang K, Li G, Yu S Q, Zhang C T, Liu Y H, *Applied Microbiology and Biotechnology* 2010;88(1):155-165.
25. Martínez A, Osburne M S, *Methods Enzymol* 2013;531123-42.
26. Frumkin I, Lajoie M J, Gregg C J, Hornung G, Church G M, Pilpel Y, *Proceedings of the National Academy of Sciences* 2018;115(21):E4940.

PRACTICAL LEARNING WITH THE SIMULATED HUMAN DIGESTION - IN VITRO DIGESTION ANALYSIS ON GLUCOSE AVAILABILITY IN COMMON SOURCES OF CARBOHYDRATE CONSUMED IN THAILAND

Sarnchai Viriyachat[1], Sukanya Jaroenporn[1, 2, *]
[1]Department of Biology, Faculty of Science, Chulalongkorn University, Thailand
[2]The University to Tambon Project (U2T: Phasing District, Nan Province), Faculty of Science, Chulalongkorn University, Thailand
*e-mail: Sukanya.ja@chula.ac.th

Abstract:
Malnutrition is a serious challenge facing our global community and ending malnutrition is one of the sustainable development goals. The modern concept of malnutrition of the WHO includes the notion of the double burden of malnutrition which expresses the challenge of malnutrition as two sides problem including 1) the traditional undernourishment which causes growth stunt, micronutrient deficiency, and other related issues, and 2) the problem of obesity which causes the non-communicable diseases that are the major challenge facing the healthcare system worldwide. The Thai healthcare system is experiencing increases in diabetes and obesity-related diseases, even in rural area. These diseases are correlated with high blood sugar levels while lowering blood sugar levels can alleviate these diseases. The food glycemic index is a conventional index that helps us understand and predict the effect that each food item has on the blood sugar level. However, this index has many limitations. To find a possible alternative method that is effective and can be conducted easily, therefore, this experiment is aimed to compare post digestion glucose levels from different groups of carbohydrates and find the correlation between glucose levels obtained from the study vs. glycemic index values as reported in the International Glycemic Index Table. Two groups of carbohydrate including unmodified carbohydrates (riceberry, brown rice, mixed rice, sticky rice, jasmine rice) and modified carbohydrates (spaghetti, egg noodle, mung bean noodle, instant noodle, rice noodle, fine rice noodle, and white bread) were digested in test tubes mimicking the carbohydrate digestion process in the human body. The method of *in vitro* digestion consists of three-step enzymatic hydrolysis that simulates the mouth (digest 15 min with alpha-amylase), gastric (digest 2 hr with pepsin), and small intestinal (digest 2 hr with pancreatin and amyloglucosidase) phases. Samples were collected and the glucose levels were determined at 0, 30, 60, 90, and 120 min after the carbohydrate digestion process reach its *in vitro* equivalent of the small intestinal phase. The results showed that modified carbohydrates contributed to both ends of the extreme producing both highest and lowest post digestion glucose level while unmodified carbohydrates from the rice produce moderate levels of glucose, and cluster together tightly within the group. The correlation between glucose level and the glycemic index value was not statistically significant (Spearman's rho = 0.102). This might be due to the difference in sources of carbohydrates between this study and those reported in the International Table. Nevertheless, this experiment demonstrates the unique trend of sugar content in Thai food. For example, mung bean noodles showed the lowest glucose concentration, while instant noodles and rice noodles showed the highest glucose concentration after the *in vitro* digestive processes. Overall, this assay provides important tools for local educators to further use in teaching Biology class as well as examining the glycemic index of the local food.

PREDICTION OF ANTI *P. acnes* PEPTIDES FROM VARIOUS PROTEASES HYDROLYZED RICEBERRY RICE BRAN.

Thanakamol Khongsonthi,[*] Noprada Masuwan,[**] Pornpinit Prasartkul[***]
364 Salaya, Phutthamonthon District, Nakorn Pathom, Thailand, 73170
*e-mail: sweetphak.12@gmail.com
**e-mail: noprada23@gmail.com
***e-mail: pornpinit2547@gmail.com

Abstract:

Nowadays, chemicals and antibiotics are the major treatment drugs for acne vulgaris caused by *P. acnes* infection. There are some reported cases of drug allergies and drug-resistant pathogenic microbes. Instead of acne drugs, the alternative treatment as natural compound and biomimetic molecules provide the better solutions. In the light of natural compound and biomimetic molecules, the *in silico* peptidomes from riceberry rice bran protein hydrolysates against anti *P. acnes* properties were studied. By predictive digestion peptidomes of the four major proteins in rice bran; albumin, glutelin, globulin, prolamin with three protease enzymes (chymotrypsin, pepsin, and trypsin) and collected as the input data sets. Then, the prediction of the antibacterial properties was performed by online bioinformatics tools i.e. iAMP and DBAASP programs while the cytotoxicity was analyzed by ToxinPred. To screen for multifunctional peptides, Venny 2.1.0 online tool was used. Several modes of action against the bacteria were predicted, such as anti-quorum sensing with the QSPpred, anti-biofilm with dPABBs, and the cell penetration with CellPPD program. Moreover, the amino acid composition-based, physicochemical, and structural analyses were performed with COPid and PEP-FOLD3.5 programs. The best-predicted score of all properties were identified. It was found that the best predicted score of antibacterial peptide and anti-biofilm was from the peptide sequence GRRKLIVTKILHTISVPGQIQF, the best predicted score of antibacterial and anti-quorum sensing peptide was MKIIF and a peptide that has multifunctional properties was HQKIHRF. There were no dual functional antibacterial peptides with cell penetrating ability. The majority of the appropriated peptides have the length of 5-22 amino acids, positive net charge, and the structure of random coiled, or alpha helix. This study would be an alternative treatment molecule against *P. acnes*, and further be one of the datasets for antibacterial treatment screening.

PREVALENCE AND CHARACTERISATION OF ANTIMICROBIAL RESISTANCE GENOTYPES AND PHENOTYPES OF *Campylobacter* spp. ISOLATES FROM PATIENTS IN THAILAND

Supawee Kinnonkok, Nattapong Cheunban, Thanitchai Kamthalang, Chutima Jittaprasatsin, Piyada Wangroongsarb, Orapan Sripichai*
National Institute of Health, Department of Medical Sciences, Ministry of Public Health, Nonthaburi, Thailand
*e-mail: orapan.s@dmsc.mail.go.th

Abstract:
Campylobacter, a common foodborne zoonotic pathogen, is the main cause of bacterial gastroenteritis worldwide. Additionally, *Campylobacter* is an opportunistic pathogen which causes bacteremia and other invasive infections in immunocompromised patients. Antimicrobial resistance (AMR) in *Campylobacter* spp. is a concern due to its importance in public health, particularly when it involves with the drugs of choice for treatment of patients. The present study aimed to determine species spectrum and AMR pattern of *Campylobacter* spp. in Thailand, using 180 isolates from various human clinical samples. Identification of *Campylobacter* species was performed by real-time polymerase chain reaction (PCR) assay. *C. jejuni* was the predominant species recovered from diarrheal patients following by *C. coli*, whereas *C. fetus* was main species isolated from septicemia patients. The resistance phenotypes of the isolates were determined by minimum inhibitory concentrations against seven commonly-used antimicrobial drugs, and AMR-associated genes were detected by real-time PCR. High rates of resistance were observed against quinolones (ciprofloxacin and/or nalidixic acid; 72% in *C. jejuni*, 77% in *C. coli* and 42% in *C. fetus*) and cyclines (doxycycline and/or tetracycline; 40% in *C. jejuni*, 82% in *C. coli* and 21% in *C. fetus*). Alternatively, lower resistance rates to macrolides (azithromycin and/or erythromycin) and gentamicin were presented. Strong correlations between phenotypic resistance and putative gene mutations were revealed, with a high prevalence of the *gyrA* T86I substitution among quinolone resistant isolates, present of *tet(O)* among cycline resistant isolates, and *23S rRNA* A2075G transition mutation among macrolide resistant isolates. Interestingly, some of the isolates that displayed multidrug resistant phenotype lacked the corresponding genetic determinants. Better understanding of the AMR mechanisms in *Campylobacter* is necessary to provide the most appropriate therapies to patients and develop new strategies for improving AMR control programs.

PROPICONAZOLE INHIBITS ROOT ELONGATION AND LATERAL ROOT DEPVELOPMENT IN RICE SEEDLINGS BY INTERFERING WITH AUXIN

Watcharapong Wimonchaijit, Juthamas Chaiwanon*
Center of Excellence in Environment and Plant Physiology, Department of Botany, Faculty of Science, Chulalongkorn University, Bangkok, 10330, Thailand
*e-mail: juthamas.c@chula.ac.th

Abstract:

Propiconazole is a systemic fungicide which is widely used to control fungal diseases in many crop plants including rice. The constant use of propiconazole can worsen the environmental pollution because propiconazole is highly persistent and difficult to be degraded after its application. Therefore, there is the need to evaluate how propiconazole affects plant growth and development. Our results found that propiconazole inhibited plant growth. Propiconazole-treated plants showed shorter plant height, reduced plant weight, and lower emerged lateral root density than untreated plants. We also investigated the auxin response in propiconazole-treated plants and found that auxin treatments were able to rescue lateral root density in propiconazole-treated plants to the untreated level. This suggested that propiconazole may cause the defect in auxin response in roots and lead to the reduced lateral root density.

Introduction:

Root system is the underground part of plants, which plays pivotal roles in water uptake and nutrient acquisition from soil. Plant roots not only provide storage function and mechanical support for the aboveground parts, but also serve as the major interface that perceives and responds to external stimuli, triggered by both biotic and abiotic factors.[1] Previous studies demonstrated that modifying root traits has been shown to be a promising way to improve crop performance, resulting in increasing yield.[2]

Propiconazole (PPZ) is a triazole compound widely used as a systemic fungicide in many crop plants to reduce the loss of plant productivity caused by fungal diseases such as rice false smut disease.[3] However, the constant use can potentially cause environmental pollution. PPZ is highly persistent in soil, and its accumulation has been detected in the topsoil of paddy rice field.[4] In addition, PPZ also inhibits plant growth, as it is a specific inhibitor of CYP450 enzymes in the brassinosteroid biosynthesis pathway.[5] To elucidate hormone actions in various plant species, researchers have used triazole chemicals such as PPZ or brassinazole and paclobutrazole to block brassinosteroid and gibberellin synthesis, respectively.

Rice root systems consist of primary root, crown roots, and lateral roots, which emerge from the primary and crown root axes. The branching and growth of lateral roots account for a large proportion of the total root length and surface area and are controlled by plant hormones.[6] Brassinosteroid (BR) is a class of plant steroid hormones that control various growth and developmental processes. Rice mutants with defects in BR biosynthesis or signalling show dwarf shoot and short root phenotypes,[7] suggesting that BR is critical for promoting root development. Auxin is another plant hormone, which plays an indispensable role in the initiation and subsequent development of lateral roots. Auxin signalling or transport mutants show reduced number of lateral roots, due to the inhibition of lateral root primordia initiation.[8,9]

In this study, the effects of PPZ treatment on rice shoot and root growth were evaluated. PPZ treatments not only inhibited root growth but also reduced lateral root density. In addition, when exogenous auxin was applied together with PPZ, lateral root density could be rescued.

Methodology:

1. Plant materials and growth condition

Seeds of Thai local rice, Puang Tawng, were obtained from Pathum Thani rice research center. Dehusked seeds were surface sterilized by soaking with 70 % ethanol for 2 minutes, 40 % Haiter commercial bleach for 15 minutes, and then rinsed with sterilized dH2O for 4-5 times. The sterilized seeds were germinated on sterile plates containing Yoshida's solution with 1 % sucrose, 0.55 g/L MES, and 0.25 % gellan gum under dark condition at room temperature for two days. Uniform seedlings were selected and transferred to a glass tube (one plant per tube) containing the same media with control or PPZ treatments at the concentration of 5, 10, and 20 μM, or 1-Naphthaleneacetic acid (NAA) at the concentration of 20, 50, and 100 nM. All plants were grown in a phytotron room (30 ^{O}C and 12-hour-light-dark cycle). Each treatment contained at least 12 to 15 replicates.

2. Measurement of shoot and root growth parameters

Growth parameters were collected including shoot fresh weight, shoot dry weight, root fresh weight, root dry weight, plant height, primary root length, and lateral root density. All roots were scanned by Epson Perfection V700 Photo scanner and fixed in FAA solution (Formaldehyde Alcohol Acetic Acid, 10%:50%:5% + 35% water). Primary root length was measured from the scanned photo by using ImageJ software. The number of lateral roots was counted under a stereo microscope and used to calculate the lateral root density, which is calculated as the number of emerged lateral roots divided by primary root length.

3. Statistical Analysis

All experiments used completely randomized design (CRD), and the results were analyzed by ANOVA. All statistical analysis will be performed by using SPSS software version 22.

Results and Discussion:

1. PPZ inhibits shoot and root growth in rice seedlings

To evaluate the effects of PPZ on plant growth, we treated rice seedlings with the varying concentrations of PPZ. Five μM PPZ obviously inhibited shoot growth in terms of plant height, shoot fresh weight, and shoot dry weight, and higher concentrations of PPZ at the concentration of 10 and 20 μM also showed stronger inhibitory effects, which shoot traits were about 50% lower than the untreated plants as shown in Figure 1. In terms of root growth, root fresh weight and primary root length were significantly reduced only in the rice seedling treated with 20 μM of PPZ. These results suggested that PPZ negatively affects plant growth. This finding is consistent with previous reports of phenotypes of rice BR biosynthesis mutants and PPZ-treated rice and maize,[5,10,11] supporting that BR is important for cell elongation and leaf expansion.

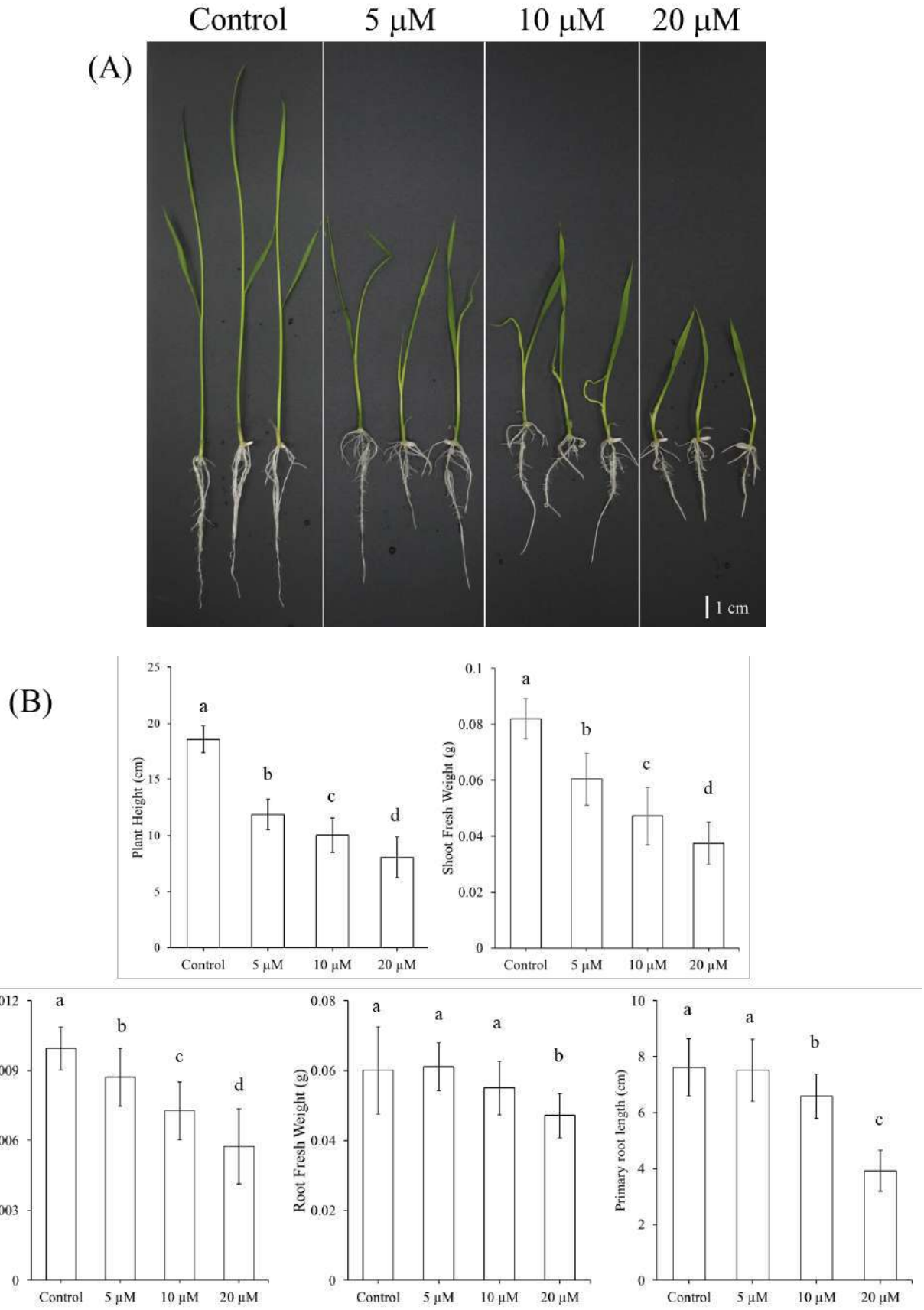

Figure 1. Plant growth response of rice seedlings treated with PPZ. (A) Rice seedlings treated with the varying concentrations of PPZ for 5 days. (B) Plant growth traits of the rice seedlings treated with PPZ for 5 days. Error bar at each point represents ± SD. Significant

differences of the mean were analyzed by Tukey's range test ($P < 0.05$) and indicated by different letters above the bar graph.

2. PPZ inhibits lateral root development by interfering with auxin-mediated mechanisms

Our results also showed that PPZ inhibited lateral root development as shown in Figure 2. Emerged lateral root density in PPZ-treated plants was reduced to about 70% compared to the untreated plants. These results suggest that PPZ-inhibited BR biosynthesis is important for lateral root development.

Auxin is known to regulate lateral root development. To investigate whether PPZ inhibits lateral root development by interfering with auxin, roots were grown in the presence of PPZ as well as NAA auxin. From the results in Figure 3, NAA treatments were able to rescue emerged lateral root density in PPZ-treated plants, of which emerged lateral root density was higher than the plants treated with only 5 μM PPZ. Interestingly, emerged lateral root density of PPZ-treated plants with 50 nM and 100 nM NAA was significantly higher than the untreated plants. These results suggested the reduced lateral root density in PPZ-treated plants is possibly due to the defects in auxin-mediated mechanisms, such as interfering with auxin transport and/or downregulation of auxin biosynthesis or positive regulators of auxin signalling pathway at the lateral root primordia. This is consistent with previous studies that BR promotes lateral root formation by promoting polar auxin transport in Arabidopsis roots.[12]

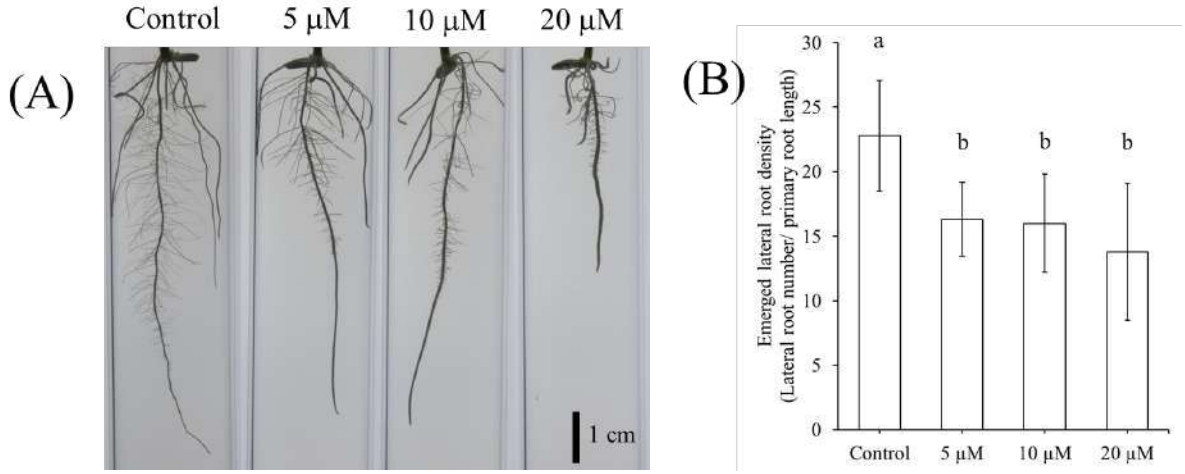

Figure 2. Effects of PPZ on lateral root development. (A) Roots of the rice seedlings treated with the varying concentrations of PPZ for 5 days. (B) Quantification of emerged lateral root density of the rice seedlings treated with PPZ for 5 days. Error bar at each point represents ± SD. Significant differences of the mean were analyzed by Tukey's range test ($P < 0.05$) and indicated by different letters above the bar graph.

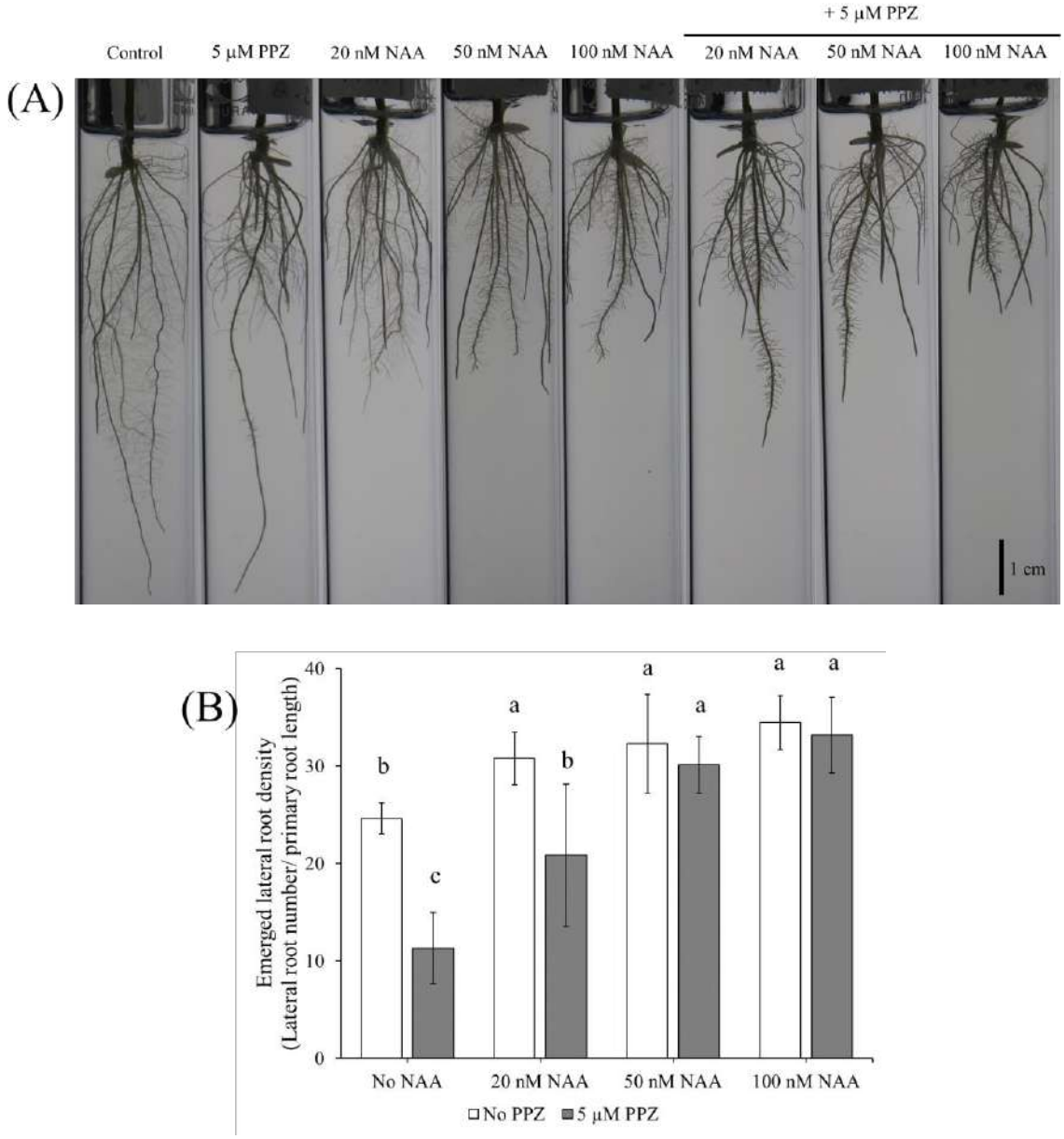

Figure 3. Response of roots treated with auxin (NAA) with/without 5 μM PPZ. (A) Roots of the rice seedlings treated with the varying concentrations of NAA with/without 5 μM PPZ for 8 days. (B) Quantification of emerged lateral root density of the rice seedlings treated with NAA with/without 5 μM PPZ for 8 days. Error bar at each point represents ± SD. Significant differences of the mean were analyzed by Tukey's range test ($P < 0.05$) and indicated by different letters above the bar graph.

Conclusion:

Here, we demonstrated that PPZ treatment negatively affects shoot growth, root elongation and lateral root density in rice seedlings. The findings from this study provide a better understanding of the impact of PPZ contamination in agricultural fields on development of rice root system, which could potentially affect crop productivity. It also suggests roles of BR biosynthesis in regulating root development. Identification of genes and molecular mechanisms of root growth and lateral root formation will be important for engineering crop root systems to improve crop performance under non-favorable soil conditions.

Acknowledgements:

This research was supported by the graduate scholarship from the Faculty of Science, Chulalongkorn University to W.W., and Research Grant for New Scholar Ratchadaphisek somphot Endowment Fund Chulalongkorn University (RGN_2559_032_11_23) to J.C..

References:

1. Lynch JP. New Phytol. 2019;223:548–564.
2. Zhan A, Schneider H, Lynch JP. Plant Physiol. 2015:168: 1603–1615.
3. Fan J, Yang J, Wang YQ, Li GB, Li Y, Huang F, Wang WM. Mol. Plant Pathol. 2016:17:1321-1330.
4. Kim IS, Beaudette LA, Shim JH, Trevors JT, Suh YT. Plant Soil. 2002:239:321-331.
5. Hartwig T, Corvalan C, Best NB, Budka JS, Zhu JY, Choe S, Schulz B. PLoS One. 2012:7:e36625.
6. Gowda VRP, Henry A, Yamauchi A, Shashidhar HE, Serraj R. Field Crops Res. 2011:122:1-13.
7. Tong H, Xiao Y, Liu D, Gao S, Liu L, Yin Y, Jin, Y, Qian Q, Chu C. Plant Cell. 2014:26:4376-4393.
8. Kitomi Y, Inahashi H, Takehisa H, Sato Y, Inukai Y. Plant Sci. 2012:190:116-122.
9. Wang M, Qiao JY, Yu CL, Chen H, Sun CD, Huang LZ, Li CY, Geisler M, Qian Q, Jiang DA, Qi YH. Plant Cell Environ. 2019:42:1125-1138.
10. Best NB, Johal G, Dilkes BP. Plant Direct. 2017:1-18.
11. Hong Z, Ueguchi-Tanaka M, Shimizu-Sato S, Inukai Y, Fujioka S, Shimada Y, Takatsuto S, Agetsuma M, Yoshida S, Watanabe Y, Uozu S, Kitano H, Ashikari M, Matsuoka M. Plant J. 2002:32:495-508.
12. Bao F, Shen J, Brady SR, Muday GK, Asami T, Yang Z. Plant Physiol. 2004:134:1624–1631.

RAPID AND ACCURATE IDENTIFICATION OF HUMAN-ASSOCIATED STAPHYLOCOCCI BY USE OF MULTIPLEX REAL-TIME PCR

Jenjira Chalerm,[1] Supawee Kinnonkok,[1] Jintana Sotkaew,[1] Thanatchaya Puangchaba,[1] Parichat Andon,[1] Nattapong Cheunban,[1] Orapan Sripichai[1,*]
[1]National Institute of Health, Department of Medical Sciences, Ministry of Public Health, Nonthaburi, Thailand
*e-mail: orapan.s@dmsc.mail.go.th

Abstract:
The genus *Staphylococcus* is normal inhabitants of skin and mucous membranes, and can causes opportunistic infections in humans and animals. Staphylococci are the most common cause of nosocomial bloodstream infections. Fast and accurate identification of staphylococci is critical for immediate treatment with effective antimicrobial drugs. Staphylococci contain 55 known and many unnamed species which are identified by phenotypic analysis in many clinical laboratories, however these results are often incorrect because of phenotypic variation. Thus, genetic analysis is necessary for definitive species identification. The purpose of the present study was to develop a multiplex real-time polymerase chain reaction (M-PCR) for species identification of the most clinically significant *Staphylococcus* spp., which contained the following: *S. aureus*, *S. epidermidis*, *S. haemolyticus*, and *S. hominis*. The assay was included 16S rRNA specific for staphylococci as internal control. The specificity of the newly developed method was tested on 50 different bacterial reference strains and 200 different field strains that were isolated from the human skin. In consequence, the single-tube M-PCR assay demonstrated a sensitivity of 100% and a specificity of 100% that performed better than conventional identification methods. The entire specimen preparation and assay can be finished within 2 hours. This method thus provides a rapid and accurate approach to the identification of staphylococcal species in the clinical laboratory and research.

MICRORNA-221/222-RESPONSIVE ELEMENTS OF HUMAN ID1 GENE PROMOTER

Panus Yingjamsiri,[1] Saowakon Paca-uccaralertkun[2,*]
[1] Toxicology International Program, Faculty of Science, Mahidol University, Bangkok, Thailand
[2] Department of Microbiology, Faculty of Science, Mahidol University, Bangkok, Thailand
*e-mail: saowakon.pac@mahidol.ac.th

Abstract:

Inhibitor of DNA binding1 (Id1) is a protein that plays the versatile roles in cell cycle, cell proliferation and cell differentiation. The aberrant expression of Id1 has been reported in many kinds of cancer including cervical cancer. High level of Id1 is found to be correlated with the HPV-positive cancer cell. However, the mechanism in regulating Id1 expression is still unclear. microRNA-221/222 expression is reported to be altered in many kinds of cancer including HPV-positive cervical cancer cell. This study aimed to investigate the promoter regulation of Id1 involved with microRNA-221/222 in HPV-positive cervical cancer cell, HeLa cell. The results showed that the region between -1477 to -656 upstream Id1 promoter was essential for Id1 expression. Moreover, miRNA-221/222 performed a negative regulation role on the expression of Id1 promoter involved with the region between -1477 to -656 upstream. These results demonstrated that miR-221/222 regulated Id1 promoter activity and suggested that the -1477/656 region may play a role in miR-221/222-mediated Id1 promoter regulation.

Introduction:

Inhibitor of DNA binding (Id) family members are key regulatory proteins which play the essential roles in the cell cycle and cellular processes and function by inhibiting target proteins that include the basic helix-loop-helix domain. Since the basic helix-loop-helix proteins are associated with the cell differentiation, the altered Id protein expression can lead to the change in cell differentiation, cell proliferation and cell cycle depending on cell types. ID proteins compose of 4 major types: ID1, ID2, ID3 and ID4. Each ID protein has specific difference in binding to the basic-loop-helix protein targets and has different expression pattern. ID1, among the ID family, is the most studied. The ID1 gene is located on chromosome 20 at 20q11.21 and contains 1,239 bp encoding for 2 exons. The function of ID1 involve with many processes in the body. ID1 contribute to the cell-cycle regulation, stem cell, developmental process, neural process, bone formation and angiogenesis. Basically, in cell cycle regulation, ID1 antagonizes the transcription activation of differentiation-associated genes, promote cell-cycle progression, and inhibits cell senescence.

ID1 is positively regulated in undifferentiated, highly proliferative, embryonic or cancer cells. Id1 is controlled by the 2.2 kilobases pairs upstream promoter[1]. However, the molecular pathway that regulate Id1 promoter is still unclear. An aberrant expression of ID1 is associated with the progression of tumors and poor prognosis[2]. Many studies have found the association between Id1 up-regulation and HPV-infected carcinogenesis in various type of cancers including colorectal carcinoma[3], breast carcinoma[4] and cervical carcinoma[5]. High level of Id1 has been found to be correlated with the HPV-positive cancer cell[6].

MicroRNAs are the single-strand oligonucleotide of about 22 nucleotide which regulate gene expression and cause the downregulation and up-regulation of molecular

signaling pathway. MiRNA-221/222 deregulation has been implicated in many different types of human cancers including cervical cancer[7]. This study aimed to investigate the effect of miR-221/222 on Id1 expression in the HPV-positive cancer cell.

Methodology:

Cell culture and transfection: HeLa cell was cultured in Dulbecco's Modified Eagle Media (DMEM) supplemented with 10% fetal bovine serum. The cells were grown at 37 °C in the presence of 5% CO_2.

Plasmid construction: Id1 promoter region of normal human chromosome was amplified and cloned into *BglII* and *HindIII* sites of pGL3 basic vector using the specific primers named as
1477Id1Forward (5' TTT AGA TCT CTC TTC ATA CAG TGC CCG CT 3'),
985Id1Forward (5' TTT AGA TCT TTC AGA CGC TGA CAC AGA CC 3'),
656Id1Forward (5' TTT AGA TCT GGG TCT CAG GAA CAC GAA CA 3'),
367Id1Forward (5' TTT AGA TCT TTA GCT TCC TTG CCT CCT TCC 3'),
181Id1Forward (5' TTT AGA TCT GCC CAT TGG CTG CTT TTG AA 3'),
Id1Reverse (5' TTT AAG CTT TCT TGG CGA CTG GCT GAA ACA 3')

The recombinant constructs were screened by restriction endonuclease digestion followed by gel electrophoresis. Then, they were verified by DNA sequencing analysis. The plasmids were named according to the length of Id1 promoter regions: pGL3-1477Id1, pGL3-985Id1, pGL3-656Id1, pGL3-367Id1, and pGL3-183Id1.

pcDNA3+miRNA-221/222, a miRNA-221/222 expression vector, was kindly provide by Professor Silvia Anna Ciafre (Departments of Experimental Medicine and Biochemical Sciences and Internal Medicine and Endocrinology, University of Rome, Italy).

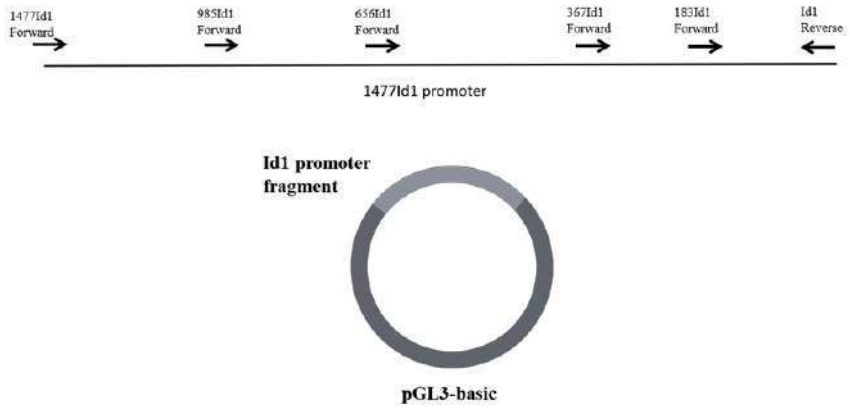

Figure 1.
Id1 promoter constructs were amplified using the specific primers and cloned into pGL3 basic vector

Transfection: Transient transfection was done when the cells reached confluency of 90%. Transfections were performed with Lipofectamine 3000 reagent (Invitrogen, USA) according to the manufacturer's instructions. 500 ng mixture of pGL3-Id1, pSV-β-galactosidase with or without pcDNA3+miRNA-221/222 plasmid was used in each well in a 24- well plate. pSV-β-galactosidase plasmid was used as an internal control. The transfection reagent and DNA were diluted in Opti-MEM® I Reduced Serum (Gibco Life Technologies). Diluted DNA and diluted transfection reagent were mixed and introduced onto the cells in the plate. The cells were harvested for luciferase assay and galactosidase assay after 48 hours incubation.

Luciferase Assay and β-Galactosidase Assay: Equal volume of protein was used for luciferase and β-galactosidase assay. The β-galactosidase assay was carried out using β-galactosidase enzyme assay system with reporter lysis buffer (Promega). Protein was mixed with the buffer and incubated at 37^{O}C until the solution turned yellow after which 1M sodium carbonate was added to stop the reaction. The absorbance was read at 405 nm in a Biochrom EZ Read 400 Microplate Reader. For luciferase assay, the protein was mixed with luciferase assay reagent (Promega) and luciferase assay was performed using TECAN Spark microplate reader M10. The luciferase activities were normalized using β- galactosidase as an internal control[8]. The relative luciferase activities were calculated.

Results and Discussion:

Characterization of Id1 promoter expression in HeLa cell

To study the regulatory elements on Id1 promoter, Id1 promoters with luciferase reporter were constructed using the pGL3 base vector, named pGL3-Id1. The luciferase with 1477 bp length of Id1 promoter was -1477 Id1. The other constructs with Id1 promoter at 985, 656, 367 and 183 bp were named -985 Id1, -656 Id1, -367 Id1 and -183 Id1 respectively. The luciferase-Id1 constructs were transfected into HeLa cell and the relative luciferase activities were measured and calculated. The results showed that the deletion of a region between -1477 and -985 caused the great reduction of Id1 promoter activities. The further deletion of region between -985 to -656 significantly reduced Id1 promoter to only 25.81%. The deletion of region between -656 to -183 showed no significant difference in activities. The regulatory element of Id1 promoter has been studied in a few types of cells and context. Constitutive expression of Id1 was regulated by the proximal promoter region, while the distal promoter region seems to be responsible for stimulated expression by specific molecular signalling[9]. However, the regulation and expression of Id1 were cell-specific and context dependent[10]. For example, in myoblast, Id1 was regulated by several responsive elements between -985 and -956 bp region[11]. The region -1105 to -1080 played a role in regulating Id1 in HepG2[12]. The results in this study suggested that the important regulatory element of Id1 promoter in HeLa was most likely presented within the region between -1477 to -656 upstream Id1 promoter.

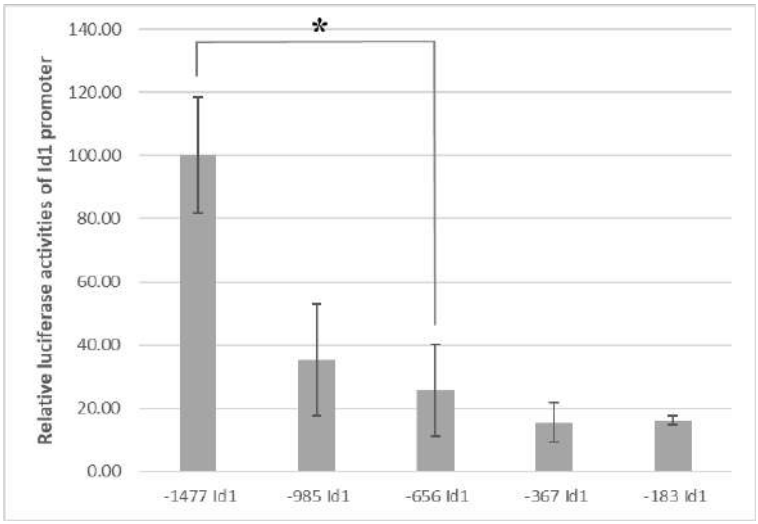

Figure 2.

Id1 promoter activities in HeLa cells. The relative luciferase activities of Id1 promoter were represented as mean±SD. *, $p<0.05$

miR-221/222 regulate Id1 promoter expression via specific element

miR-221/222 are reported to be associated with many types of cancers including HPV-positive cervical cancer. To investigate the effect of miR-221/222 on the expression of Id1 promoter, plasmid expressing miR-221/222 were co-transfected along with different pGL3-Id1. The results showed highly decreasing activity when miR-221/222 was co-transfected with -1477 Id1. However, effect of miR-221/222 on the construct -656 Id1 and -183 Id1 was not significant. Normally miRNA regulate the gene expression by targeting 3' UTR of the target mRNA, however, in some case they can regulate the promoter activities[13]. A study in squamous cell carcinoma of the head and neck cell lines demonstrated that miR-221 was downregulated in HPV-positive squamous cell carcinoma[14]. Another study in breast cancer showed that Id1 can be altered by the expression of miR-221/222[15]. These results demonstrated that miR-221/222 could regulate Id1 promoter in HeLa cells and suggested that the -1477/656 region may play a role in miR-221/222-mediated Id1 promoter regulation.

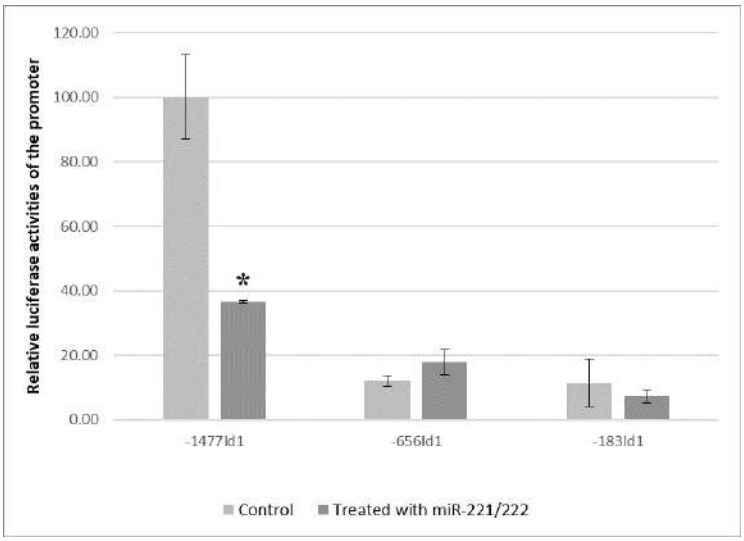

Figure 3.

miR-221/222 affect Id1 promoter activities in HeLa cells. miR-221/222 expression vectors were transfected to HeLa and the relative luciferase activities were measured. The relative luciferase activities of Id1 promoter were represented as mean±SD. *, $p<0.05$

Conclusion:

The expression of Id1 promoter in HeLa cells might be mainly regulated by the region between -1477 and -656 bp upstream. miR-221/222 exerted their effect via the region between -1477 and -656 bp upstream by reducing Id1 promoter activities to about 36%. This study demonstrated the regulation of Id1 by miRNA-221/222. The deeper understanding about how Id1 would be regulated by miRNA-221/222 is remained for further investigated.

Acknowledgements:

This research has been supported by Science Achievement Scholarship of Thailand. The authors also gratefully acknowledge to Faculty of Science, Mahidol University, Thailand for analytical instrument facility.

References:

1. Jan O. Nehlin EH, Wen-Lin Kuo, Colin Collins, and Judith Campisi. Biochemical and biophysical research communications. 1997;231:628–634.
2. Roschger C, Cabrele C. Cell Communication and Signaling. 2017;15.

3. Ricciardi R, Ghabreau L, Yasmeen A, Darnel AD, Akil N, Al Moustafa AE. Cell Cycle. 2009;8(12):1964-1965.
4. Yasmeen A, Bismar TA, Kandouz M, Foulkes WD, Desprez PY, Al Moustafa AE. Cell Cycle. 2007;6(16):2038-2042.
5. Li JK, Xie LX, Gan XL, Liu B, Zhang Y, Song B, et al. International Journal of Gynecological Cancer. 2011;21(7):1276-1281.
6. Zhao Z, Bo Z, Gong W, Guo Y. International journal of medical sciences. 2020;17(8):995-1005.
7. Pan ZX, Zhang XY, Chen SR, Li CZ. Eur Rev Med Pharmacol Sci. 2019;23(9):3645-53.
8. Solberg N, Krauss S. Methods in molecular biology (Clifton, NJ). 2013;977:65-78.
9. Gautschi O, Tepper CG, Purnell PR, Izumiya Y, Evans CP, Green TP, et al. Cancer research. 2008;68(7):2250-2258.
10. Simonson MS, Rooney A, Herman WH. Nucleic Acids Res. 1993;21(24):5767-5774.
11. Katagiri T, Imada M, Yanai T, Suda T, Takahashi N, Kamijo R. Genes to Cells. 2002;7(9):949-960.
12. Korchynskyi O, ten Dijke P. J Biol Chem. 2002;277(7):4883-4891.
13. O'Brien J, Hayder H, Zayed Y, Peng C. Frontiers in Endocrinology. 2018;9:402.
14. Wald AI, Hoskins EE, Wells SI, Ferris RL, Khan SA. Head & neck. 2011;33(4):504-512.
15. Rao X, Di Leva G, Li M, Fang F, Devlin C, Hartman-Frey C, et al. Oncogene. 2011;30(9):1082-1097.

STUDY ON PHYTOCHEMICAL COMPOSITION AND BIOLOGICAL ACTIVITIES OF *Aspidistra sutepensis* K. Larsen

Chanoknant Thongsuk[1], Arpamas Chariyakornkul[2], Orapin Kantawet[1], Rawiwan Wongpoomchai[2,*]

[1]Chiang Mai University Demonstration School, Chiang Mai University, Chiang Mai 50200, Thailand

[2]Department of Biochemistry, Faculty of Medicine, Chiang Mai University, Chiang Mai 50200, Thailand

*e-mail: rawiwan.wong@cmu.ac.th

Abstract:

Aspidistra sutepensis K. Larsen is a local plant in northern Thailand. Its flower and root are used as an ingredient in food and traditional medicine, respectively. However, there are no reports about phytochemical profile and biological activities of *A. sutepensis*. This study aimed to investigate phytochemical composition and biological activities of *A. sutepensis* root. The dry root of *A. sutepensis* was extracted by ethanol and water to obtain ethanolic extract (AE) and water extract (AW). Both AE and AW were determined total phenolic and flavonoid contents using colorimetric and high-performance liquid chromatography (HPLC) methods. Their antioxidant properties were analyzed using ABTS, DPPH and FRAP assay. Total phenolic and flavonoid contents in AE were higher than AW. These contents in AE were 6.20 ± 0.28 and 1.62 ± 0.27 mg/g extract, respectively. AE presented greater antioxidant activities than AW. The radical scavenging activity of ABTS and DPPH of AE showed 43.98 ± 7.04 and 68.24 ± 10.40 %, respectively. For FRAP assay, AE was 7.35 ± 0.55 mg Trolox/g extract. The antioxidant activities of *A. sutepensis* extracts were correlated with its phytochemical contents. From these data, *A. sutepensis* root might be an attractive source for functional ingredients for health promotion.

SUCCESSION OF CARRION INSECTS ON PIG CARCASSES RELOCATED FROM INDOOR TO OUTDOOR CONDITIONS

Sudarat Fueangmeekun, Buntika Areekul Butcher*

Integrative Ecology Laboratory, Department of Biology, Faculty of Science, Chulalongkorn University, Bangkok, Thailand
*e-mail: buntika.a@chula.ac.th

Abstract:
Corpse relocation is one of several methods used to prevent the discovery of the cadaver. Many scientific evidences such as CCTV and testimony from the witnesses are used to solve the cadaver relocation cases. Entomological evidence could also be used to estimate primary crime scene using the knowledge of the restriction of carrion insect habitat. However, the study of insect succession on relocated carcass have never been conducted in Thailand. Therefore, this research aims to study insect succession on pig carcasses relocated from indoor to outdoor conditions at Nong Hin District, Loei Province during November 2020 – February 2021. There were 3 experiments in this study: A) non-relocated or control group, only laid in the outdoor condition B) relocated from indoor to outdoor conditions C) refrigerated before relocated to outdoor condition. *Chrysomya rufifacies*, *C. megacephala*, *C. nigripes*, *Necrobia ruficollis*, *N. rufipes*, and *Dermestes maculatus* are the dominant carrion insect species in all three experiments. In the experiment 2, adults and larvae of *Megaselia scalaris* were found both before and after relocated to the outdoor condition. This species was also reported in the indoor case and other indoor study from Malaysia. Therefore, it could be used to determine the relocation case. In the experiment 3, no insect was found on the carcass before relocation, therefore, entomological evidence does not work for this condition.

Introduction:

After the crime was committed, the discovery of the corpse would bring the evidence lead to murderer arrested, therefore, the murderer tend to conceal the corpse. There are many approaches the murderer used to prevent the discovery of the corpse for example, concealment, wrapping, displacement and cadaver relocation. Postmortem relocation of the corpse can be either short or long distance. Most cases of cadaver relocation, the place where the cadaver was found are different from where the crime scene was committed (1). When the corpse was found, the police would not know whether the body was committed at the place where the body discovery or the body was relocated from the primary crime scene after death. Several evidences are used to investigate the cadaver relocation cases such as testimony from the witness, CCTV, and forensic botanical evidence.

Forensic entomology can be used to estimate not only postmortem interval but also primary crime scene because the insects discovered on the body varies on the environment factors (2,3). If the insects found on the corpse were not the species that restrict to the habitat the corpse was discovered, then this corpse might be relocated from another location (4). The cadaver relocation case investigation using forensic entomological evidence had been reported in Italy. Two-woman corpses were found next to each other at a mountainous wooded area in Morterone, Lecco, northern Italy. Stage of decomposition of both corpses were different. *Chrysomya albiceps* was reported from one corpse, however there was no *C.*

albiceps found in two baited traps that were laid in this area but the fly was found in two baited traps placed at the lower altitude in vicinity of Olginate, 9 km from the place where the corpses were discovered. This suggested that one corpse was infested by *C. albiceps* before relocated to the location where the corpse was discovered (5).

Previous forensic entomological studies in Thailand focused on morphology of the forensic flies, development of carrion insects, insect succession and stage of decomposition in different habitats and conditions in various regions of Thailand (6–10). However, there is no report of forensic entomological study in the upper northern Thailand. Moreover, the study of cadaver relocation has never been reported in Thailand. Therefore, this research aims to study insect succession on pig carcasses relocated from indoor to outdoor conditions and study insect succession on refrigerated pig carcasses relocated to outdoor conditions. This work will be the first forensic entomological study on cadaver relocation in Thailand.

Methodology:

The study was conducted during November 2020 – February 2021. There are 3 experiments: A) non-relocated, only laid in the outdoor condition B) relocated from indoor to outdoor conditions and C) refrigerated before relocated to outdoor condition. Each experiment will be referred as experiment 1, experiment 2, and experiment 3, respectively.

Study site

The study sites located at Nong Hin district, Loei Province. The tamarind plantation (17°06'01" N 101°52'38" E) was used as the outdoor condition. The farm shed (17°05'50" N 101°49'55" E) was used as indoor condition and the refrigerator for the experiment 3 was also placed here. The distance between indoor and outdoor study sites was 5 km.

Animal carcass

Domestic pig *Sus sacrofa domestica* carcasses weighing approximately 30 kg were used in these experiments because some of the pig's anatomy such as lack of heavy fur, size of chest cavity and fat distribution are similar to human anatomy (4) therefore they were used as animal models in this study The pig carcasses were dressed before starting the experiment to be similar to the human death.

Field protocol

In the experiment 1, the dressed pig carcass was laid on the ground in the tamarind plantation. In experiment 2, the dressed pig carcass was laid in the farm shred for 3 days then relocated to the tamarind plantation. In experiment 3, the dressed pig carcass was refrigerated at approximately 4 °C for 3 days then relocated to the tamarind plantation. The carcass in experiment 1 was covered with the wire mesh cages (1x1x0.8 m) to prevent disturbance of other animals, especially vertebrates. For relocated carcasses, they were covered with the wire mesh cages after relocation. Each carcass was approximately 50 – 70 m. away from each other. Physical data such as ambient temperature, relative humidity, carcasses temperature, maggot masses temperature were recorded. Climate data of Loei Province were recorded from Thai Meteorological Department website: https://www.tmd.go.th. The field work was performed during 8.00 am – 3.00 pm.

Collecting techniques

Collecting techniques are different for each stage of development. Eggs were collected using fine paintbrush and preserved in 75% ethanol. Larvae (maggots) were collected using forceps then boiled in 90 °C of hot water for 30 seconds to fix size and length of the maggots then preserved in 75% ethanol. Pupae were collected by digging the soil

around the carcasses to discover the pupae and preserved in 75% ethanol. Adults were collected using aerial net and hand collecting then preserved in 75% ethanol (11).

Collecting time

Insect specimens were collected during 8.00 am – 3.00 pm on the field-work day. For the first 14 days (weeks 1 and 2), the insect specimens were collected every day, except the experiments 2 and 3 the carcasses were not disturbed, no insect collecting for the first 3 days (day0 – day2) then relocation at experimental day 3, observed for any insect specimen before relocating the carcasses, and one hour after relocating to the outdoor condition. At week 3, the carcasses were visit and the specimens were collected every other day. At week 4, the carcasses were visit and the specimens were collected once every 3 days. At week 5 – 9, 11, 13, the carcasses were visit and the specimens were collected once a week.

Determination of decomposition stage

Every field- work day, the carcasses was noted and photographed to determine the stage of decomposition. There are 5 stages: fresh stage, bloated stage, decay stage, post-decay stage, remain stage determining by carcass change after death. Fresh stage begins right after the body dead and end when the body become bloated. Bloated stage, the corpse's abdomen bloats like a balloon because of the gas from the process of anaerobic bacteria in the gut. This stage begins when the abdomen slightly inflates. Decay stage begins when the abdomen of the corpse deflates. Post-decay stage start when the corpse was decay to dry flesh, skin, cartilage and bone. Remain stage when the corpse remains only bone and hair (19).

Laboratory works

All insect specimens from the study site were identified at least to the genus level. Blow fly specimens were identified using the key for identification of Thai species (12). Other fly specimens were identified using key for identification from Flies: the natural history and diversity of Diptera (13). Beetle specimens were identified using American beetles volume 1 (14) and American beetles volume 2 (15)

Results and Discussion:

The dominant carrion insect species in all experiments were not different. *Chrysomya rufifacies* were the most blow fly species found in all experiments followed by *C. nigripes* and *C. megacephala*. The dominant carrion beetle species in all experiment were similar. *Necrobia rufipes*, *N. ruficollis*, and *Dermestes maculatus* were the most common beetle species that can be randomly collected in all experiments.

In the experiment 2, the carcass was in the bloated stage at the relocation day. The insect specimens were collected before relocating to the outdoor condition, unidentified flesh fly larvae, adults and larvae of *Megaselia scalaris* were collected from the carcass, therefore, this species could be used as forensic entomological evidence for relocation cases from indoor habitat. *Megaselia scalaris* was found on the rabbit carcass left in the indoor environment in Malaysia, *M. scalaris* was the dominant species and the first species arrived the carcass but there was no flesh fly species access the carcass (16). Moreover, *M. scalaris* can be used to estimate postmortem interval more accurate than other species because it was the first fly species access to the indoor carcass (17). Furthermore, several studies of insect succession in indoor condition found *M. scalaris* on the carcasses (16, 17, 20) Therefore, if the carcass was discovered in the outdoor condition but *M. scalaris* was found on the carcass then *M. scalaris* could be the evidence to indicate that the carcass might be relocated from the indoor condition. In contrast, flesh fly species was recorded in the experiment 1 which conducted only in outdoor condition. This result similar to the study of insect succession on Samae-sarn Island, flesh flies were the first insect species colonized the carcass (18). These

results showed that flesh fly can colonize both indoor and outdoor cases, therefore, flesh fly cannot be the entomological evidence to indicate where the primary crime scene is. However, *M. scalaris* was found on the carcass only one day after relocation because in outdoor condition, there were the predator of the maggot such as ants came to prey the maggots. In the real situation, *M. scalaris* could be used to determine the relocation case from indoor condition if that corpse were found not more than one day after relocation.

There are few forensic entomological studies on relocated carcasses. The methods of the previous studies before were not actually relocated the carcasses but laid them in 2 study sites then compared the carrion insects from these 2 study areas. From the two previous studies some carrion beetle species were the indicator species for corpse relocation (21,22). In this study, the carcasses were relocated 3 days after starting the experiment, the colonization of carrion beetle did not present in this period, therefore, the carrion insect species potentially used for indicating the cadaver relocation were fly species. If these 2 previous studies had relocated the carcasses, the indicator species for relocated carcass might not found. The different methods also affect the results. The report of relocation case in Italy, *C. albiceps* was used to determine the relocation case (5). However, this species is not recorded in Thailand therefore it cannot be used as an indicator for carcass relocation.

In the experiment 3, no insect specimen found on the carcass before carcass relocation to the outdoor condition which implies that forensic entomological evidence might not work for the refrigerated before relocated to other places. The concealment of the refrigerator prevents the colonization of the insect and low temperature in the refrigerator can keep the carcass fresh longer than the normal temperature. After the relocation, the insect specimens collected from the carcass were similar to those of the experiment 1. Refrigerating the carcass did not affect to insect succession pattern but affected the time in fresh stage of decomposition.

The stage of decomposition in each experiment can be divided into 5 stages: fresh stage, bloated stage, decay stage, post-decay stage, and remain stage, respectively (figure 1). The colonization of carrion insects on the carcasses were different in each stage. Insect succession pattern of each experiment were similar (figure 2–4). In the initial phase, many fly species infested the carcasses then the carrion beetle species came to colonize the carcass. Fresh stage took 3 days in the experiment 1 and 6 days in the experiment 3 but no data for the experiment 2 because the carcass was not visited in this stage, experiment 3 took the longest time at this stage due to carcass refrigerated. Carrion insect specimens can be collected from the experiments 1 and 3 were fly eggs and adults of *Chrysomya rufifacies* and *C. megacephala.* Bloated stage took 3 days in all experiment. Larvae and adults of *C. rufifacies* and *C. megacephala* and adults of *C. nigripes* and *Hydrotaea spinigera* were collected from every experiment in this stage. In decay stage, every experiment took 3 days. Third instar larvae of *C. rufifacies*, *C. megacephala,* and *C. nigripes* and adults of *Protopiophila latipes* were collected from every experiment. The carrion beetles such as *Saprinus* spp. which were the predator of maggot colonized the carcasses followed by *Necrobia rufipes* and *N. ruficollis*, the carrion feeder, came to feed the carcasses. In post-decay stage, every experiment took approximately 70 days in this stage. Pupae of *C. rufifacies*, *C. megacephala,* and *C. nigripes* were collected in this stage. The carrion feeder beetles were still at the carcasses. Another carrion feeder beetle, *Dermestes maculatus*, came to colonize the carcasses in this stage. The last stage of decomposition, remain stage, *N. rufipes*, *N. ruficollis*, and *D. maculatus* were collected from every experiment.

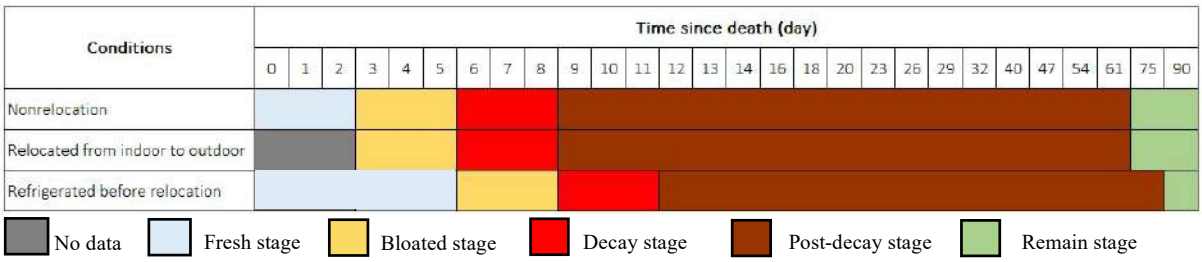

Figure 1 Stage of decomposition in the three experiments

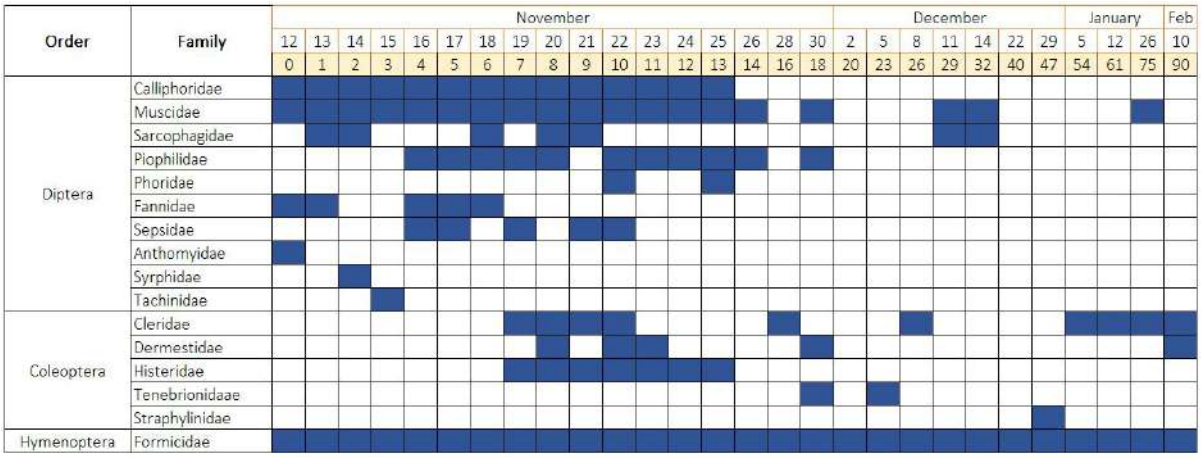

Figure 2 Insect succession pattern of non-relocated pig carcass (experiment 1)

Figure 3 Insect succession pattern of relocated pig carcass from indoor to outdoor conditions (experiment 2)

Order	Family	November																December							January			Feb
		12	13	14	15	16	17	18	19	20	21	22	23	24	25	26	28	30	2	5	8	11	14	22	29	5	12	26	10
		0	1	2	3	4	5	6	7	8	9	10	11	12	13	14	16	18	20	23	26	29	32	40	47	54	61	75	90
Diptera	Calliphoridae																												
	Muscidae																												
	Sarcophagidae																												
	Piophilidae																												
	Fannidae																												
	Sepsidae																												
	Syrphidae																												
	Tachinidae																												
	Anthomyidae																												
	Stratiomyidae																												
	Neriidae																												
Coleoptera	Cleridae																												
	Dermestidae																												
	Histeridae																												
	Scarabaeidae																												
	Staphylinidae																												
Hymenoptera	Formicidae																												

Figure 4 Insect succession pattern of refrigerated pig carcass before relocation (experiment 3)

When compared stage of decomposition in the experiment 1 and previous study on hanging pig carcasses conducted at Nan province during the winter (November 2010 – February 2011), both fresh and bloated stages of this study took 3 days which was longer than the Nan study (10). However, it could be affected by the environmental factors, especially temperature and humidity (figures 5, 6). And also condition of the carcasses, one laid on the ground and the other hung about 1.20 m above ground. In this research, temperature at the study site were less than 25 °C that is not the optimum temperature for the bacterial activities (23), therefore the decomposition was slow and longer than the previous study. At the decay stage, this study took 3 days while it was 4 days in the Nan study. The hanging condition might affect the decomposition stage period especially during the decay stage, the maggots that play an important role to decompose the carcass at this stage fell from the hanging carcass on the ground therefore, only the remained maggots on the carcass can continue the carcass decomposition led to delayed of this decomposition stage. In post-decay stage, this study took longer time than the previous study to reach the remain stage because of the lower temperature and the higher relative humidity of this study (24). However, the information of these two studies cannot be compared because each study was conducted in different areas, time and other environmental factors.

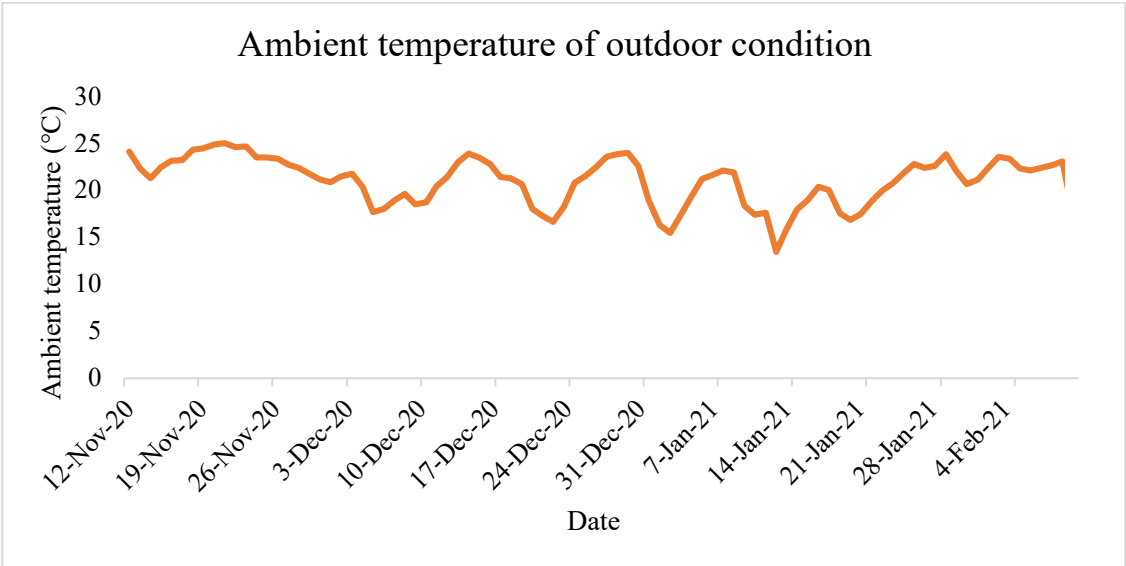

Figure 5 The ambient temperature of the outdoor condition since the first day until the last day of the experiment

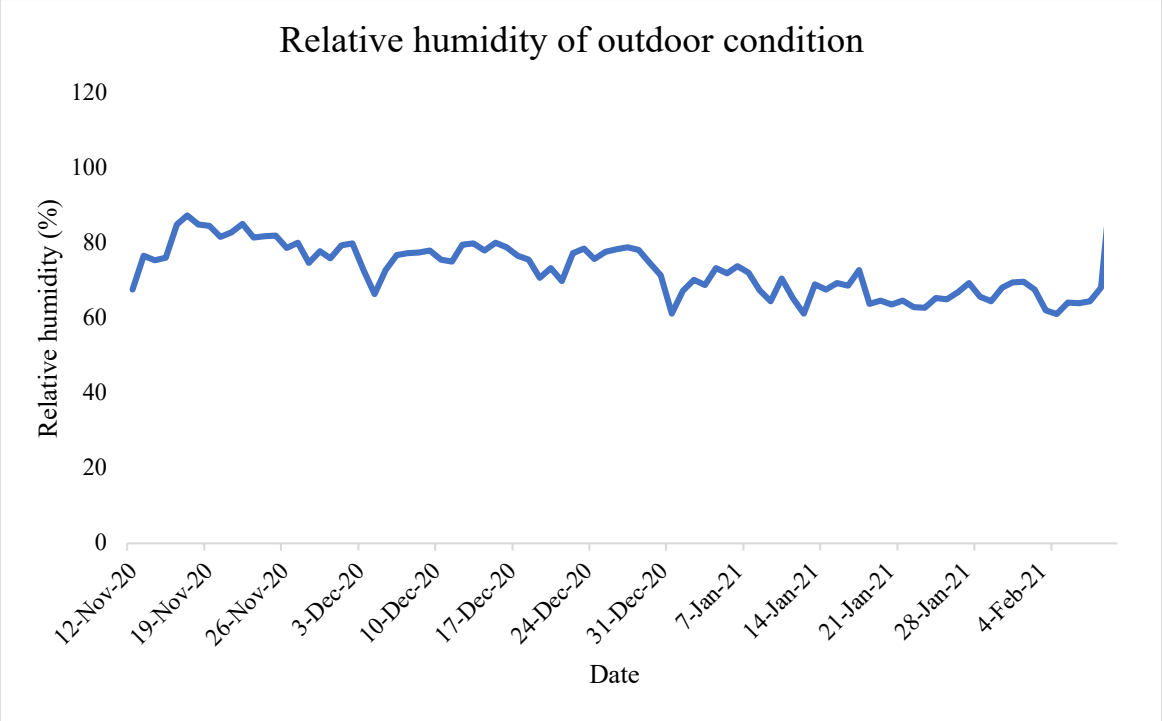

Figure 6 The Relative humidity of the outdoor condition since the first day until the last day of the experiment

Conclusion:

Forensic entomological evidence could be used to solve the cadaver relocation cases. From this preliminary study, *M. scalaris* were found both before and after relocated the pig carcasses from indoor to outdoor conditions. This species might be the indicator species for indoor condition in relocation case but it cannot be used in case of refrigerated the carcass before relocating. In Thailand, more studies should be done on cadaver relocation in other conditions and many more replications.

Acknowledgements:

This study was supported by CU Graduate School Thesis Grant. We thank Ms. Wilai Pakdee for allowing us to use her land as the study site.

References:

1. Charabidze D, Gosselin M, Hedouin V. PeerJ. 2017:5;e3506.
2. Byrd JH, Castner JL. Forensic Entomology: The Utility of Arthropods in Legal Investigation. 2009. Second edition. Boca Raton: CRC Press.
3. Amendt J, Richards CS, Campobasso CP, Zehner R, Hall MJR. Forensic Sci Med Pathol. 2011:7;379–392.
4. Catts EP, Goff, ML. Annu. Rev. Entomol. 1992:37;253–272.
5. Lambiase S, Camerini G. J. Forensic Sci. 2012:57;799–801.
6. Sukontason K, Piangjai S, Siriwattanarungsee s, Sukontason KL, Parasitol Res. 2008:102;1207–1216.
7. Sukontason K, Bunchu N, Chaiwong T, Moopayak K, Sukontason K. Parasitol Res. 2010:106;1055–1064.
8. Bunchu N, Thaipakdee C, Vitta A, Sanit S, Sukontason K, Sukontason KL, J. Parasitol. Res. 2012; 1–10

9. Vitta A, Pumidonming W, Tangchaisuriya U, Poodendean C, Nateeworanart1 S. Trop. Biomed. 2007:24;1–5
10. Sukchit M, Deowanish S, Butcher BA. Trop. Nat. Hist. 2015:15;137–153
11. Amendt J, Campobasso CP, Gaudry E, Reiter C, LeBlanc HN, Hall MJR. Int. J. Leg. Med. 2007:121;90–104.
12. Sukontason K, Sukontason KL. Blow Flies of Importance in Thailand. 2010.
13. Marshall SA. Flies: The Natural History and Diversity of Diptera. 2012. New York: Firefly Books.
14. Amett RH, Thomas MC. American Beetles Volume 1. 2000. Boca Raton: CRC Press.
15. Amett RH, Thomas MC, Skelley PE, Frank JH. American Beetles Volume 2. 2002. Boca Raton: CRC Press.
16. Zuha RM, Ankasha SJ, Disney RHL, Omar B, Egypt. J. Forensic Sci.2016:216–222.
17. Reibe S, Madea, B. Parasitol Res. 2010:106;637–640
18. Fueangmeekun, F. Insects and Other Arthropods Succession on Pig Carcasses at Beach Forest of Samae-San Island, Sattahip District, Chonburi Province. Senior Project. 2018 Department of Biology, Faculty of Science, Chulalongkorn University.
19. Goff ML. Exp. Appl. Acarol. 2009:49;21–36
20. Zeariya MGM, Hammad KM, Fouda MA, Al-Dali AG, Kabadaia MM. J. Entomol. Zool. 2015:3;473–482
21. Matuszewski S, Szafałowicz M, Jarmusz M. Forensic Sci. Int. 2013:231;234–239
22. Madra A, Konwerski S, Matuszewski S. Forensic Sci. Int. 2014:242;32–37
23. Campobasso CP, Vella GD, Introna F. Forensic Sci. Int. 2001:120;18–27
24. Cockle DL, Bell LS. Forensic. Sci. Int. 2015:253;136.e1–136.e9

THE BINDING STUDY OF VIRAL CAPSID PROTEINS OF COXSACKIEVIRUS B3 WITH A BENZENE SULFONAMIDE DERIVATIVE AND RUPINTRIVIR BY USING COMPUTATIONAL METHODS

Pavinee Prapassornwattana, Aunlika Chimprasit, Supa Hannongbua, and Patchreenart Saparpakorn*
Department of Chemistry, Faculty of Science, Kasetsart University, Bangkok, Thailand
*e-mail: fscipnsk@ku.ac.th

Abstract: Coxsackievirus B3 (CVB3) was one of the highest clinical samples of viral pathogens in Thailand. CVB3 used the viral capsid proteins (VPs) for binding with host-cell receptors. These VPs consist of four proteins (chains A-D). The novel druggable pocket of CVB3 was revealed in chain A and C. Previously, the rupintrivir was one of the available drugs for target of CVB3 protease. However, the rupintrivir and other drugs have side effects on patients. In 2019, a benzene sulfonamide derivative has been reported as a new inhibitor for VPs of CVB3. The benzene sulfonamide derivative has half maximal effective concentration (EC_{50}) better than the rupintrivir. To get insight for development of the new inhibitors and investigate whether the rupintrivir can be an inhibitor against VPs of CVB3, the aim of this work is to study the binding of VPs of CVB3 with the benzene sulfonamide derivative and rupintrivir. In this research, molecular dynamics (MD) simulations and molecular mechanics Poisson−Boltzmann surface area (MM-PBSA) calculations were applied to study the complexes of VPs CVB3 with the benzene sulfonamide derivative and rupintrivir. The results showed that the benzene sulfonamide derivative and rupintrivir can form key interactions with residues in chain A (i.e. Cys73, Val74, Tyr75, Phe76, Gln96 and Ala97) and in chain C (i.e. Gln233, Gln234, Asn235 and Phe236) of CVB3. From the study, rupintrivir might be able to inhibit VPs of CVB3.

Introduction: In 2016, the armed forces research institute of medical sciences (AFRIMS) in Thailand revealed that coxsackievirus B3 (CVB3) was one of the majorities of the identified clinical samples of viral pathogens in Thailand.[1] In worldwide, CVB3 was an outbreak through each country in 1983-2016.[2] CVB3 caused diseases in humans including hand, foot and mouth disease (HFMD), meningitis, myocarditis, pancreatitis, pericarditis, and encephalitis.[2] After people contact with the CVB3, the viral capsid proteins of CVB3 bind with host-cell receptors including DAF (decay-accelerating factor) and CAR (coxsackievirus and adenovirus receptor).[3]

The available drugs were used for inhibition of CVB3 including pleconaril, enviroxime and rupintrivir. However, those available drugs possessed some undesirable side effects.[4] Lastly, a benzene sulfonamide derivative was found as a new inhibitor for target at viral capsid proteins of CVB3.[5] The viral capsid proteins of CVB3 consisted of chain A-D.[6] A novel binding pocket was revealed at chain A and C of CVB3.[5] The positions of novel binding pocket at chain C accorded with the positions of CVB3 binding with DAF receptor including 232, 233, 234, 235 and 236 in chain C of CVB3.[3,5] The benzene sulfonamide derivative showed the inhibition with CVB3 (The half maximal effective concentration (EC_{50})=0.7 ± 0.1 μM). It was compared the inhibition with the rupintrivir (EC_{50}=2.8 ± 0.5 μM).[5] Rupintrivir was reported a target for 3C protease of viral species of picornavirus[7], norovirus[8], and coronaviruses[9]. The 3C protease of norovirus revealed the interactions with rupintrivir by studied in molecular docking.[8] The structures of the benzene sulfonamide

derivative and rupintrivir are shown in Figure 1a and 1b. In order to confirm the experiment for the binding of the benzene sulfonamide derivative and rupintrivir to VPs of CVB3, computational methods using molecular dynamics simulations and molecular mechanics Poisson−Boltzmann surface area (MM-PBSA) calculations were applied to investigate the stable conformations and interactions of the compounds with CVB3.

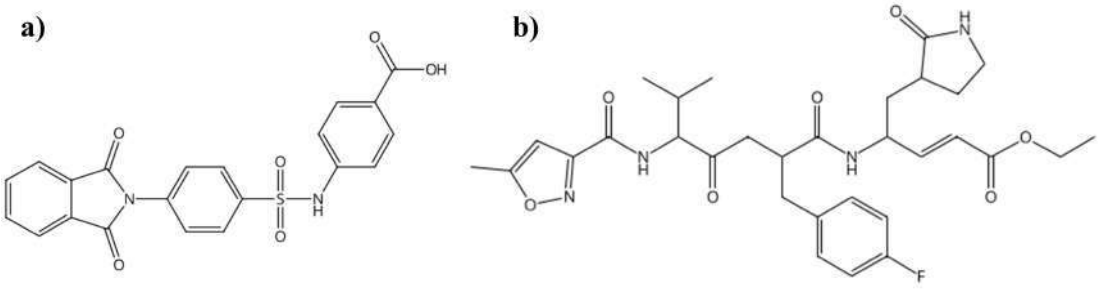

Figure 1. Structures of (a) the benzene sulfonamide derivative and (b) rupintrivir

Methodology: *Preparation of complexes:* The complex of viral capsid proteins of CVB3 with the benzene sulfonamide derivative was obtained from RSCB protein data bank (PDB code:6GZV).[5] The rupintrivir structure was also selected from RSCB protein data bank (PDB code:3SJI).[10] Afterwards, the rupintrivir was docked to CVB3 by using GOLD V5.7.1 program.[11] The scoring function was goldscore scoring function. The 12 Å from the rupintrivir were defined as the active site of CVB3. The cluster analysis was chosen in 1.5 Å of conformational results. Lastly, a highest score of conformations was selected for molecular dynamics simulations.

Molecular dynamics (MD) simulations: Both of CVB3 with the benzene sulfonamide derivative and rupintrivir systems were carried out by GROMACs V5.1.4 program with the AMBER99SB protein force field. In the energy minimization step, both systems were performed in 100 ps. In two steps of equilibration, (1) NVT ensemble, the both systems were heated 300 K in 100 ps. (2) NPT ensemble, the both systems were performed 300 K and 1 bar in 100 ps. In the production molecular dynamics step, both systems were carried out 100 ns. Root-mean-square deviation (RMSD), number of hydrogen bond interactions, middle cluster analysis and molecular mechanics Poisson−Boltzmann surface area (MM-PBSA) calculations were analyzed.

Molecular mechanics Poisson−Boltzmann surface area (MM-PBSA) calculations: The conformations of 12 Å CVB3 (12 Å of CVB3 from the benzene sulfonamide derivative and rupintrivir) with the benzene sulfonamide derivative and rupintrivir in 50-100 ns from MD simulations were calculated the binding free energy by using MM-PBSA calculations[12,13] in GROMACs program. The binding free energies were calculated as follows.

$$\Delta G_{binding} = \Delta E_{vdw} + \Delta E_{ele} + \Delta G_{pol} + \Delta G_{nonpol(SASA)} \quad (1)$$

Where $\Delta G_{binding}$ is the binding free energy, ΔE_{vdw} is the energies of van der Waal interactions, ΔE_{ele} is the energies of electrostatic interactions, ΔG_{pol} is the polar solvation free energy, and $\Delta G_{nonpol(SASA)}$ is the non-polar solvation free energy

Results and Discussion: The stability of structure was investigated from the root-mean-square deviation (RMSD). RMSD of backbone atoms of CVB3 in the complexes of CVB3 with the benzene sulfonamide derivative and rupintrivir are shown in Figure 2. The fluctuations of RMSD stabilized in the range of 3.0-4.5 Å. The 50-100 ns of MD trajectories were applied to study the number of hydrogen bond interactions, the middle cluster analysis and molecular mechanics Poisson−Boltzmann surface area (MM-PBSA) calculations.

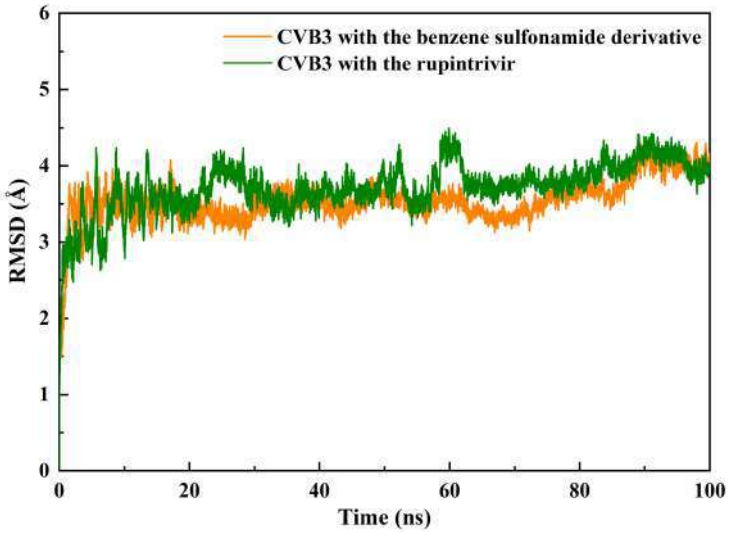

Figure 2. Root-mean-square deviation of CVB3 with the benzene sulfonamide derivative and rupintrivir

The number of hydrogen bond interactions of CVB3 with the benzene sulfonamide derivative and rupintrivir in 50-100 ns of MD trajectories are shown in Figure 3. The hydrogen bond interactions of CVB3 with the benzene sulfonamide derivative and rupintrivir revealed 88.5% and 27.9%, respectively. There were one to four hydrogen bond interactions. The percentage of hydrogen bond interactions in the complex of CVB3 with the benzene sulfonamide derivative were higher than those in the complex of CVB3 with the rupintrivir. The results agreed with the experimental results with the better inhibition of the benzene sulfonamide derivative than rupintrivir[5].

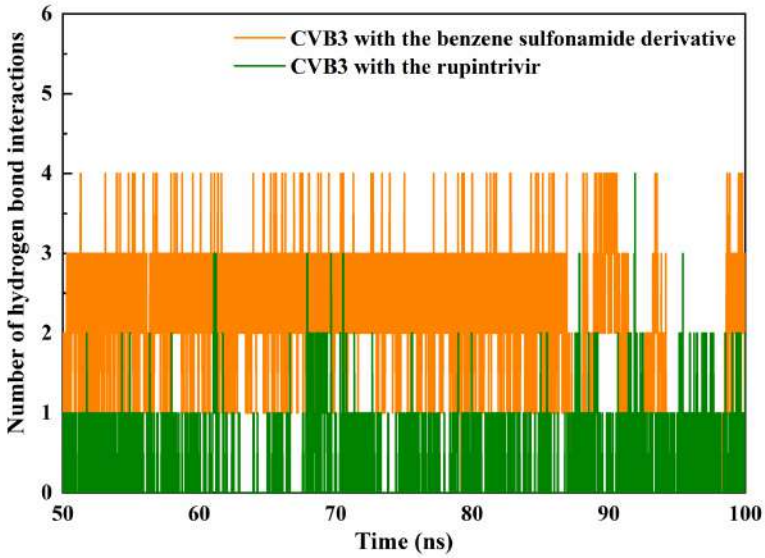

Figure 3. Number of hydrogen bond interactions of CVB3 with the benzene sulfonamide derivative and rupintrivir

The selected structure from cluster analysis using RMSD cutoff of 1.5 Å from 50 to 100 ns MD trajectories of CVB3 with the benzene sulfonamide derivative is shown in Figure 4a. The structure indicated that the benzene sulfonamide derivative located in the binding pocket (chain A and C) of CVB3. The benzene sulfonamide derivative could bind with

residues in chain A and C of CVB3 (Figure 4b and 6). The benzene sulfonamide derivative formed pi-alkyl interactions at Cys73 in chain A of CVB3 with -1.40 kJ/mol and it formed hydrogen bond interactions at Val74, Phe76 in chain A and Gln233 in chain C of CVB3 with -0.07, -6.34 and 0.80 kJ/mol, respectively. The benzene sulfonamide derivative also bound with Tyr75, Gln96 in chain A and Asn235, Phe236 in chain C of CVB3 via hydrogen bond interactions with -3.81, -0.95, -3.65 and -12.30 kJ/mol, respectively. Moreover, the benzene sulfonamide derivative formed van der Waal interactions with Ala97 in chain A of CVB3 with the values of -4.18 kJ/mol and formed pi-pi interactions at Phe236 in chain C of CVB3.

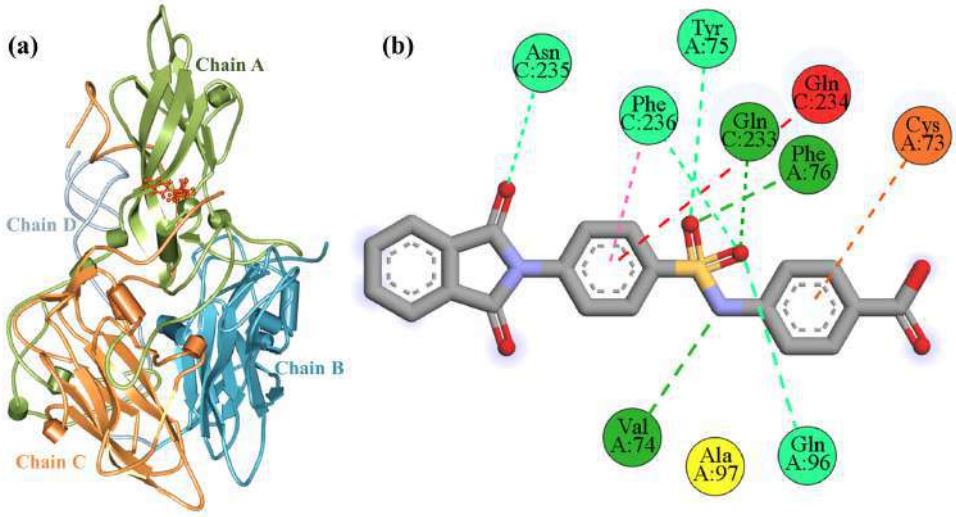

Figure 4. (a) Structure of CVB3 with the benzene sulfonamide derivative, (b) interactions of residues in CVB3 with the benzene sulfonamide derivative (pi-pi interaction (dark pink), pi-alkyl interaction (orange), pi-amide interaction (red), hydrogen bond interaction (dark green), carbon hydrogen bond interaction (light green) and van der Waal interaction (yellow)) from middle cluster analysis

The structure of CVB3 with the rupintrivir from the middle cluster analysis (Figure 5a) indicated that the rupintrivir could be located in the binding pocket of viral capsid proteins of CVB3. Moreover, the rupintrivir could interact with residues in chain A and C of CVB3 as demonstrated in Figure 5b and 6. The rupintrivir bound with chain A of CVB3 at residues Cys73 (-2.22 kJ/mol) and Ala97 (-2.24 kJ/mol) by alkyl interactions. The rupintrivir also formed hydrogen bond interactions at Val74, Phe76 in chain A and Gly9, Gln233, Gln234, Asn235 in chain C of CVB3 with -0.88, -5.21, -0.71, 1.36, -0.43 and -2.67 kJ/mol, respectively. The rupintrivir bound at Tyr75 and Gln96 in chain A of CVB3 via van der Waal interactions with -1.49 and -0.19 kJ/mol, respectively. The rupintrivir also formed pi-alkyl interactions at Cys73 in chain A and Cys11, Phe236 in chain C of CVB3 with -2.22, -2.00 and -7.02 kJ/mol, respectively.

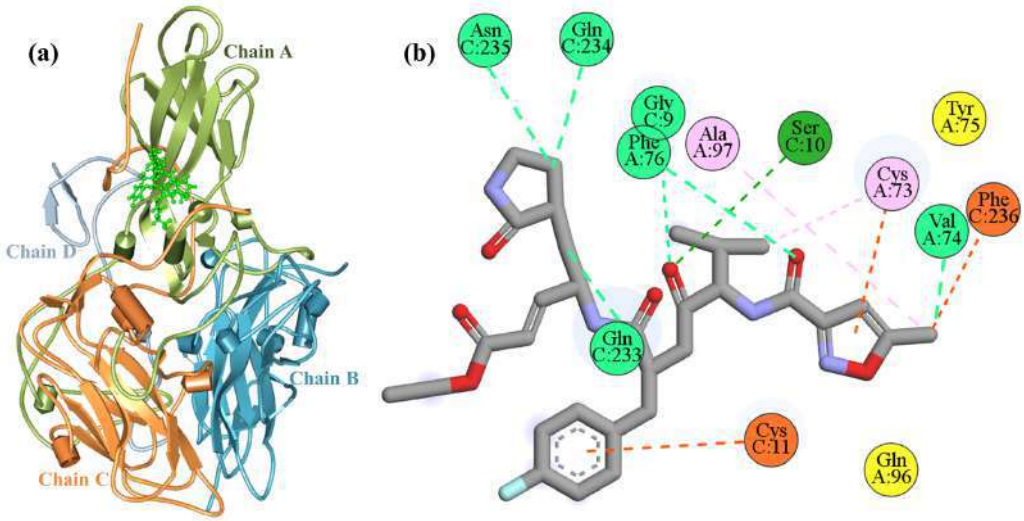

Figure 5. (a) Structure of CVB3 with the rupintrivir, (b) interactions of residues in CVB3 with the rupintrivir (pi-alkyl interaction (orange), hydrogen bond interaction (dark green), carbon hydrogen bond interaction (light green), alkyl interaction (light pink) and van der Waal interaction (yellow)) from middle cluster analysis

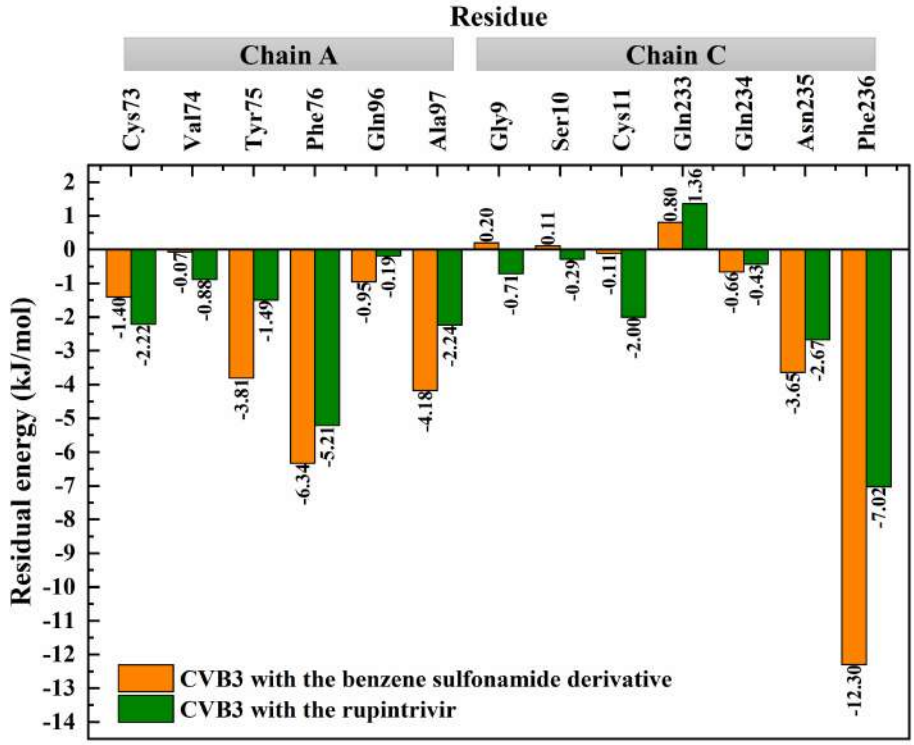

Figure 6. Residual energy of CVB3 with the benzene sulfonamide derivative and rupintrivir from MM-PBSA calculations

Both complexes of CVB3 with the benzene sulfonamide derivative and rupintrivir showed the interactions at Gln233, Gln234, Asn235 and Phe236 in chain C (the positions of CVB3 binding with DAF receptor). The residual energy of Gln233 in chain C of CVB3 with both the benzene sulfonamide derivative and rupintrivir were positive energy due to the residual energies from MM-PBSA calculations had some overestimated values. However, the residual energies between Gln233, Gln234, Asn235 and Phe236 in chain C of CVB3 and the benzene sulfonamide derivative were lower than the rupintrivir. From the results, the binding

between these residues in chain C of CVB3 with the benzene sulfonamide derivative was stronger than with the rupintrivir. The residual energies of CVB3 in chain A (Cys73, Val74, Tyr75, Phe76, Gln96 and Ala97) with the benzene sulfonamide derivative also showed the stronger interactions than with the rupintrivir. Additionally, the residues at Cys73, Phe76 in chain A, and Gln233, Phe236 in chain C, which formed the interactions with the benzene sulfonamide derivative and rupintrivir, were the same residues that formed interactions in experiment[5,14]. The binding energies of both complexes are shown in Table 1 which the higher negative values of the binding energies ($\Delta G_{binding}$) are the better binding affinity of CVB3 with the benzene sulfonamide derivative and rupintrivir. It indicated that CVB3 bound with the benzene sulfonamide derivative (-207.10 kJ/mol) better than with the rupintrivir (-120.33 kJ/mol). These binding energies also agreed well with the experimental results[5].

Table 1. The energies of CVB3 with the benzene sulfonamide derivative and rupintrivir from MM-PBSA calculations

Energy terms	Binding energy (kJ/mol)	
	CVB3 with the benzene sulfonamide derivative	CVB3 with the rupintrivir
ΔE_{vdw}	-149.93±0.20	-170.95±0.23
ΔE_{ele}	-340.03±0.77	-13.76±0.14
ΔG_{pol}	296.74±0.91	82.89±0.20
$\Delta G_{nonpol(SASA)}$	-13.90±0.01	-18.51±0.02
$\Delta G_{binding}$	-207.10±0.37	-120.33±0.20

Conclusion: The complexes of CVB3 with the benzene sulfonamide derivative and rupintrivir were applied in order to study insight of these complexes. From the results of these complexes, the number of hydrogen bond interactions, residual energies and binding energies of the benzene sulfonamide derivative showed the binding with CVB3 better than the rupintrivir. It accorded with the experimental results[5]. Cys73, Val74, Tyr75, Phe76, Gln96, Ala97 in chain A and Gln233, Gln234, Asn235 and Phe236 in chain C of CVB3 were formed interactions with both the benzene sulfonamide derivative and rupintrivir. Then, these residues are the important residues of CVB3 for creation of new inhibitors in order to inhibit CVB3. In addition, the results of the interactions, residual energies and binding energies supported that the rupintrivir can form interactions with VPs of CVB3. Then, the rupintrivir might be able to bind with VPs of CVB3.

Acknowledgements: P.P. is grateful to Development and Promotion of Science and Technology Talents Project (DPST) for a scholarship. This work was supported by Kasetsart University Research and Development Institute. We also acknowledge the Laboratory for Computational and Applied Chemistry (LCAC) at Kasetsart University (KU).

References:

1. Zhou Y, Fernandez S, Yoon IK, Simasathien S, Watanaveeradej V, Yang Y, Marte-Salcedo OA, Shuck-Lee DJ, Thomas SJ, Hang J, Jarman RJ. Am. J. Trop. Med. Hyg. 2016;95:663 – 669.
2. Fu X, Mao L, Wan Z, Xu R, Ma Y, Shen L, Jin X, Zhang C. IJID. 2019;87:1-7
3. Joshua DY, Cifuente JO, Pan J, Bergelson JM, Hafenstein S. J. Virol. 2012;86:12571–12581.
4. Kang H, Kim C, Kim DE, Song JH, Choi M, Choi K, Kang M, Lee K, Kim HS, Shin JS, Kim J, Han SB, Lee MY, Lee SU, Lee CK, Kim M, Ko HJ, van Kuppeveld FJM, Cho S. Antivir. Res. 2015;124:1-10.

5. Abdelnabi R, Geraets JA, Ma Y, Mirabelli C, Flatt JW, Domanska A, Delang L, Jochmans D, Kumar TA, Jayaprakash V, Sinha BN, Leyssen P, Butcher SJ, Neyts J. PLoS Biol. 2019;17:1-17.
6. Muckelbauer JK, Kremer M, Minor I, Diana G, Dutko FJ, Groarke J, Pevear DC, Rossmann MG. Structure. 1995;3:653-667.
7. Patick AK, Binford SL, Brothers MA, Jackson RL, Ford CE, Diem MD, Maldonado F, Dragovich PS, Zhou R, Prins TJ, Fuhrman SA, Meador JW, Zalman LS, Matthews DA, Worland ST. Antimicrob Agents Chemother. 1999;43:2444-2450.
8. Rocha-Pereira J, Nascimento MS, Ma Q, Hilgenfeld R, Neyts J, Jochmans D. Antimicrob Agents Chemother. 2014;58:4675-4681.
9. Liu C, Zhou Q, Li Y, Garner LV, Watkins SP, Carter LJ, Smoot J, Gregg AC, Daniels AD, Jervey S, Albaiu D. ACS Cent Sci. 2020;6:315-331.
10. Guangwen L, Jianxun Q, Zhujun C, Xiang X, Feng G, Daizong L, Wangke Q, Hong L, Hualiang J, Jinghua Y, George FG. J. Virol. 2011;85:10319-10331.
11. Gareth J, Peter W, Robert CG, Andrew RL, Robin T. J. Mol. Biol. 1997;267:727-748.
12. Genheden S, Ryde U. Expert Opin Drug Discov. 2015;10:449–461.
13. Huang K, Luo S, Cong Y, Zhong S, Zhang JZH, Duan L. Nanoscale. 2020;2:10737-10750.
14. Flatt JW, Domanska A, Seppälä AL, Butcher SJ. Commun. Biol. 2021;4:1-8.

THE USE OF MICROSCOPE LENS FOR SMARTPHONE AS AN ALTERNATIVE ACTIVE LEARNING TOOL FOR HIGH SCHOOL BIOLOGY CLASS

Raekkhwan Polthanya,[1,*] Andaman Kaosung,[1] Intouch Khunanopparat,[1] Pitchaporn Soykratok,[1] Surapa Chinplikanon,[1] Thanaporn Bubparam,[1] Vichaya Auvichayapat,[1] Warot Thuvadarakul,[1] Pongchai Harnyuttanakorn,[1, 2] Noppadon Kitana,[1, 2, 3]

[1]Department of Biology, Faculty of Science, Chulalongkorn University, Bangkok, Thailand
[2]The University to Tambon Project (U2T: Phasing District, Nan Province), Faculty of Science, Chulalongkorn University, Thailand
[3]Center of Learning Network for the Region, Chulalongkorn University, Bangkok, Thailand
*e-mail: khwanbbgun41@gmail.com

Abstract:
A microscope is a ubiquitous tool for science education generally used in high school as well as introductory classes at university. With the mandatory hand-on skills, the microscope can improve biology learning experience of students in the active learning environment. However, the cost of microscope has become as a major burden for schools to provide equal opportunity for every student to use the equipment. As a result, the use of this equipment as the active learning tool is limited and not widely effective. Recently, a microscope lens that once attached onto a smart phone or a computer tablet can produce high resolution magnified image in the range of 20 - 50 times has been developed and known as CU SmartLens. Although the magnification is relatively lower and require a specific tip to acquire a decent image for biology class, the price of each lens (590 to 890 Thai Baht) is affordable and much lower than that of a light microscope used in high school. Using this equipment in rural school could bring about an equitable quality education and promote lifelong learning opportunities (SDG4). In this project, we aim to organize a learning unit for high school teachers in rural areas at Nan Province to use CU SmartLens as an alternative tool for the active learning in biology class. In the learning unit, once the teachers learn about the working principle of CU SmartLens compared to the light microscope and important tips for taking digital photograph with the CU SmartLens, a biology laboratory module for plant morphology and anatomy will be demonstrated. Each school will be provided with a number of CU SmartLens and assigned to independently develop a semester long, active learning module for students with the use of local plant as a subject for macroscopic and microscopic study of external and internal structure of root, stem, leaf, flower, fruit and seed. Pre-test and post-test will be used as tools for learning outcome evaluation within school. At each school, the students will be given a group activity to take scientific photography and draft a scientific description of the photos before being reviewed and revised by their classmates. After that, a social media (Facebook page) will be used as a forum for online communications between our team and students from the participating schools. A scientific photography exhibition will be used as a tool to encourage student engagement. The satisfaction of students and teachers will also be evaluated. Overall outcome and further implementation of this project will be presented and discussed.

TRANSCRIPTOME ANALYSIS OF DENGUE VIRUS INFECTION IN HUMAN HEPATOCYTE

Krittanai Trisakulwattana[1], Sarin Chimnaronk[1,*]
[1]Institute of Molecular Biosciences, Mahidol University, Nakhon Pathom 73170, Thailand.
*E-mail: sarin.chi@mahidol.ac.th

Abstract

Dengue virus (DENV) infection contributes to a wide range of clinical complications. One of the most lethal manifestation is dengue-induced acute liver failure (ALF), which may raise the mortality rate to nearly 70%. To date, dengue pathogenesis is still poorly understood and molecular pathways involved in ALF have not been characterized. This study aimed at investigation of impact of DENV infection in human hepatocytes through the transcriptome analysis. A human hepatoblastoma cell line, HuH-7, was used for infection with two different virus serotypes of DENV-2 and -4, which has been reported as the most prevalent in Thailand. We revealed here that DENV-2 caused 855 significantly up-regulated and 949 down-regulated genes in HuH-7, whereas 195 and 128 genes were significantly up-regulated and down-regulated, in case of DENV-4, respectively. While both serotypes commonly showed activation of ER stress and unfolded protein response (UPR), DENV-2 repressed DNA replication initiation at G1-to-S phase transition, and markedly, DENV-4 induced NF-κB signaling-mediated interferon (IFN) activation important for pro-inflammatory responses. To our knowledge, this is the first report of distinct transcriptional landscapes between DENV-2 and DENV-4. Our findings provide a better understanding of dengue pathophysiology in human hepatocytes as well as important clues to DENV-induced ALF which could contribute to a wide range of applications such as diagnosis, prognosis, and treatment of ALF in the future.

Introduction

Beyond 390 million people around the world especially in tropical and sub-tropical regions were infected with dengue virus (DENV) annually[1]. DENV is a positive-sense single-strand RNA virus classified in flavivirus genus within family *Flaviviridae*, transmitted to humans through the bite of the female mosquito (*Aedes aegypti*). Clinical manifestations can range from non-specific patterns such as mild fever, aches, nausea, vomit, thrombocytopenia and leukopenia to severe disease forms including mucosal bleeding, plasma leakage, and hepatic injury. The severe stage of dengue infection is called dengue hemorrhagic fever (DHF) that is characterized by internal bleeding, and dengue shock syndrome (DSS) with impaired permeability of endothelial layer[2]. It has been reported that DENV is capable of infection and replication in multiple human cell targets including hepatocyte, monocyte or macrophage, and epithelium[3]. This may contribute to a wide range of clinical characteristics of the diseases.

Dengue-induced acute liver failure (ALF) is one of the most lethal clinical signs that was found in late stage of severe dengue (SVD). ALF is characterized by increasing hepatic enzymes (AST, ALT > 1000 U/L), hyperbilirubinemia, hepatic encephalopathy, and coagulopathy. Despite a low occurrence of about 0.3-1.1% of ALF in dengue patients, its mortality rate could be as high as 68.3%[4] because liver is tightly involved in multiple physiological processes, e.g., nutritional metabolism, detoxification, and coagulation. To

date, dengue pathogenesis is still poorly understood and molecular pathways involved in ALF have not been yet characterized. It has been assumed that direct attack by the virus, immune-mediate injury, and ischemic hepatic perfusion could be responsible for the diseases[5]; however, sufficient supporting evidence is lacking. Although some recent studies reported the gene expression profiles of DENV-infected liver cells[6,7], the genes or pathways related to DENV-induced ALF have been not yet identified.

Understanding of the consequences of infection in host cell targets could be directly investigated through global changes in gene expression, which can be performed by RT-quantitative (q)PCR, microarray, and RNA sequencing (RNA-seq) technology. RT-qPCR is the most traditional approach to detect transcript levels but in a low-to-medium throughput manner. Both RT-qPCR and microarray require well-defined and valid target sequences[8]. To overcome these limitations, RNA-seq, whose principle is to sequence total transcribed RNA in cells at a specific time and condition using the next-generation sequencing technology, can provide more high-throughput transcriptomic profile at the whole genome scale[9].

To provide deep insight into ALF mechanism, this study employed the bulk RNA-seq and bioinformatics to investigate significant changes upon DENV infection in human hepatic cells. Furthermore, we also compared the differences between dengue serotypes in host responses for the first time. Our results provided important clues as to how DENV alters host cell fates and a possible link to the onset of ALF in severe dengue patients.

Methodology

1. Virus infection

Human hepatoblastoma (HuH-7) cells were infected with DENV serotypes 2 and 4 (DENV-2 strain 16681 and DENV-4 strain H241) for 2 hours at 37°C under 5% CO_2. Each serotype was varied in multiplicity-of-infection (MOI) of 0 (mock control), 0.5, 1, and 5. Cells were harvested at two different post-infection time points at 18 hours or "early stage of infection" and 48 hours or "late stage of infection", according to a previously reported DENV replication model[10]. Cells were divided into two aliquots for construction of the RNA library for subsequent RNA-seq and for the high-content imaging to calculate the infection efficiency. Two biological replicates were performed for each condition.

2. Assessment of DENV infection

Cells were fixed using 4% paraformaldehyde prior to immunostaining with an anti-double-stranded (ds)RNA antibody as a primary antibody, followed by the secondary antibody tagged with Alexa Fluor 488, to visualize intracellular viral genomes that are assumed to be in perinuclear areas in cytoplasm[1]. Then, cells were treated with the DAPI dye to stain chromosomal DNA at AT-rich regions for counting number of cells.

The high-content imaging analysis (HCA) system was utilized to quantify fluorescence signal in a single-cell manner. All image files were processed on the Columbus server, and infection efficiency was calculated as follows:

$$\text{Infection efficacy} = \%\left(\frac{Number\ of\ cell\ with\ signal\ of\ anti-dsRNA\ (Alexa\ Fluor\ 488)}{Total\ number\ of\ cells\ (DAPI)}\right)$$

3. Transcriptome analysis

3.1. *Differentially expressed gene analysis (DEA)*

Downstream analyses of RNA-seq were performed using the R scripts. Useful read counts that were successfully mapped onto the human genome (hg38) from mock (uninfected) and infected cells at 48 hours post-infection (HPI) with an MOI of 5 were used as input for differentially expressed gene analysis using DESeq2[11] to compute log2 fold change of differential gene expression between uninfected and infected cells, and the *p*-value (or *p*-adjusted value, statistical significance).

3.2. *Pathway analysis and gene set enrichment analysis (GSEA)*
Outputs from DEA were subjected to both pathway analysis and gene set enrichment analysis. Pathway analysis was performed via the clusterProfiler[12] package, and GSEA via the ReactomePA[13] package. Pathway analysis is technically GO-based gene annotation in biological process modules, while GSEA is focusing on a specific gene set in each pathway, scanned by the descending-ranked list of genes based on log2 fold change, and provides enrichment score as an output.

Results and Discussion
1. DENV-2 and DENV-4 efficiently infected HuH-7 cells

In the DENV replication cycle, the virus attaches to cell surface receptors to invade cell targets through receptor-mediated endocytosis. The viral particle-containing endosome deforms virus envelope under acidification to release positive-single stranded RNA genome into cytoplasm. The viral positive genome serves for 2 major purposes: (1) translation into viral proteins that facilitate virion assembly and viral genome replication, and (2) a template for negative strand synthesis, the process by which double-stranded RNAs (ds-RNAs) are produced[10,14]. Viral ds-RNAs further associate with viral non-structural proteins to initiate synthesis of plus-strand RNA prior to packaging into new virus particles. As aforementioned, here we employed ds-RNA as an indicator of infection represented by green fluorescence of Alexa Fluor 488.

The infection efficiency of DENV-2 and DENV-4 in HuH-7 cells were precisely measured by high-content analysis (HCA) (**Fig. 1** upper panel). As expected, the more HPI and multiplicity of infection (MOI), the more infected cells were. DENV-2 showed slightly higher infectivity than DENV-4 at the same timepoints. The result suggested that infection at MOI 5 at 48 HPI was the most appropriate condition for cDNA library construction and RNA-seq since HuH-7 cells showed approximately 80-90% infection similarly in both serotypes (**Fig. 1** lower panel). Mock infection (MOI 0) cells at 48 hours were used in DEA as basal gene expression. It is noted that our HCA is superior to current assays such as flow cytometry in the low background and only living cells were counted upon cell phenotypic observation.

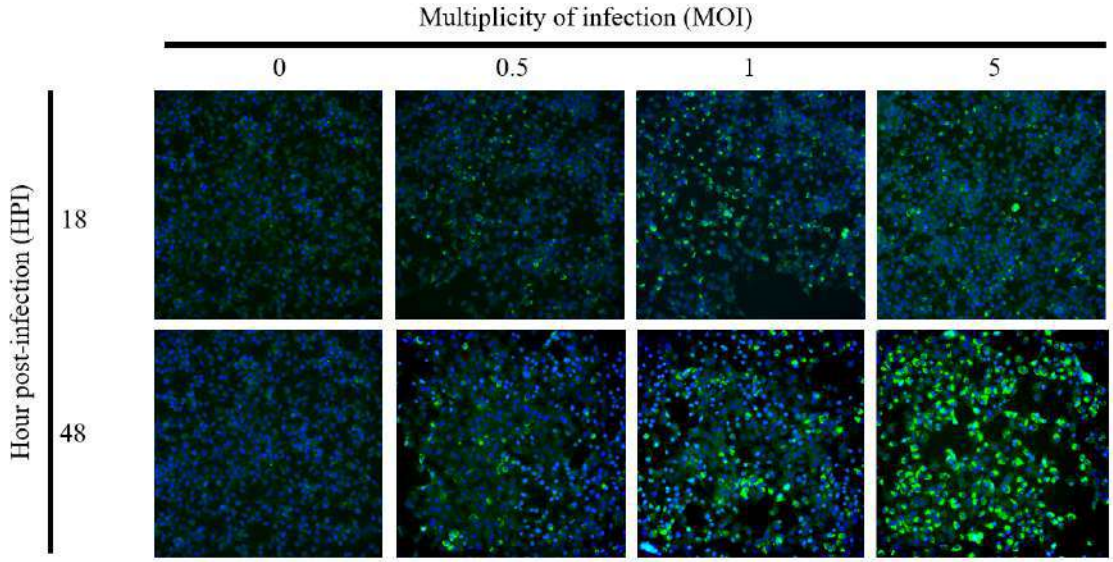

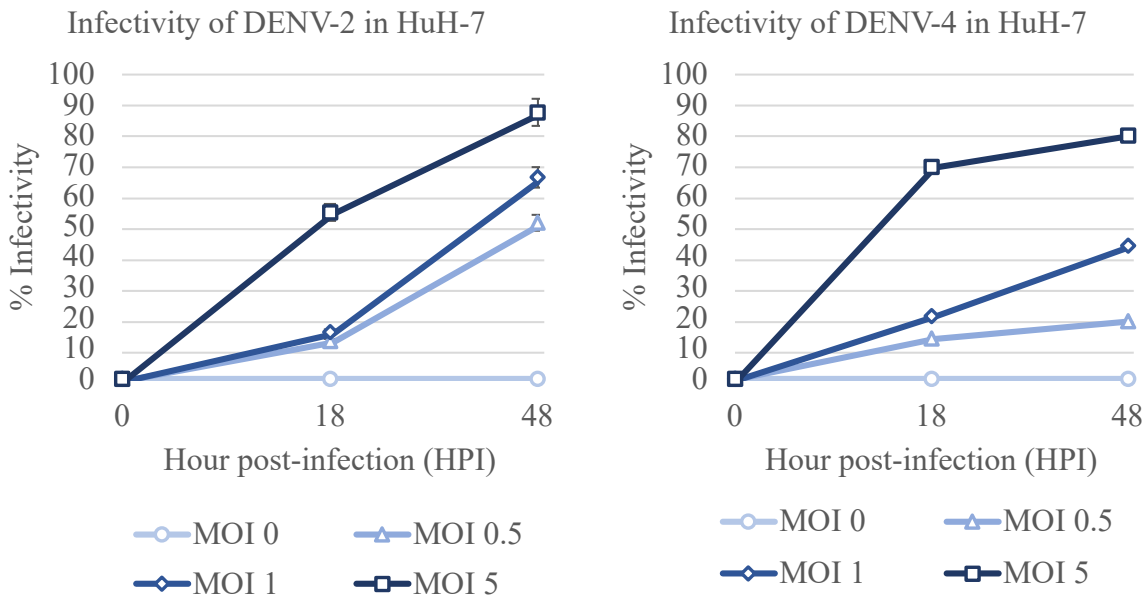

Figure 1. Measurement of infectivity using HCA. Immunofluorescence images of HuH-7 cells infected with DENV-2 with different MOIs of 0, 0.5, 1, and 5 at different HPIs (upper panel). The quantitative results of infectivity of DENV-2 (left) and DENV-4 (right) are shown in the lower panel.

2. DENV-2 and DENV-4 infections showed differences in differential gene expression

Initially, we observed and compared the pattern of 2,679 differentially expressed genes among samples with and without infection using the heatmap (**Fig. 2**). The gene expression patterns among uninfected vs infected HuH-7 cells, as well as those of cells infected with DENV-2 vs DENV-4 were obviously distinct. The results also suggested that HuH-7 cells exhibited different host responses between DENV-2 and DENV-4. It is noted that gene expression patterns in uninfected HuH-7 cells or mocks for DENV-2 and DENV-4 experiments were grouped together but showed some subtle differences. This was likely due to batch effect inevitably occurring during sample preparation and the next-generation sequencing procedure.

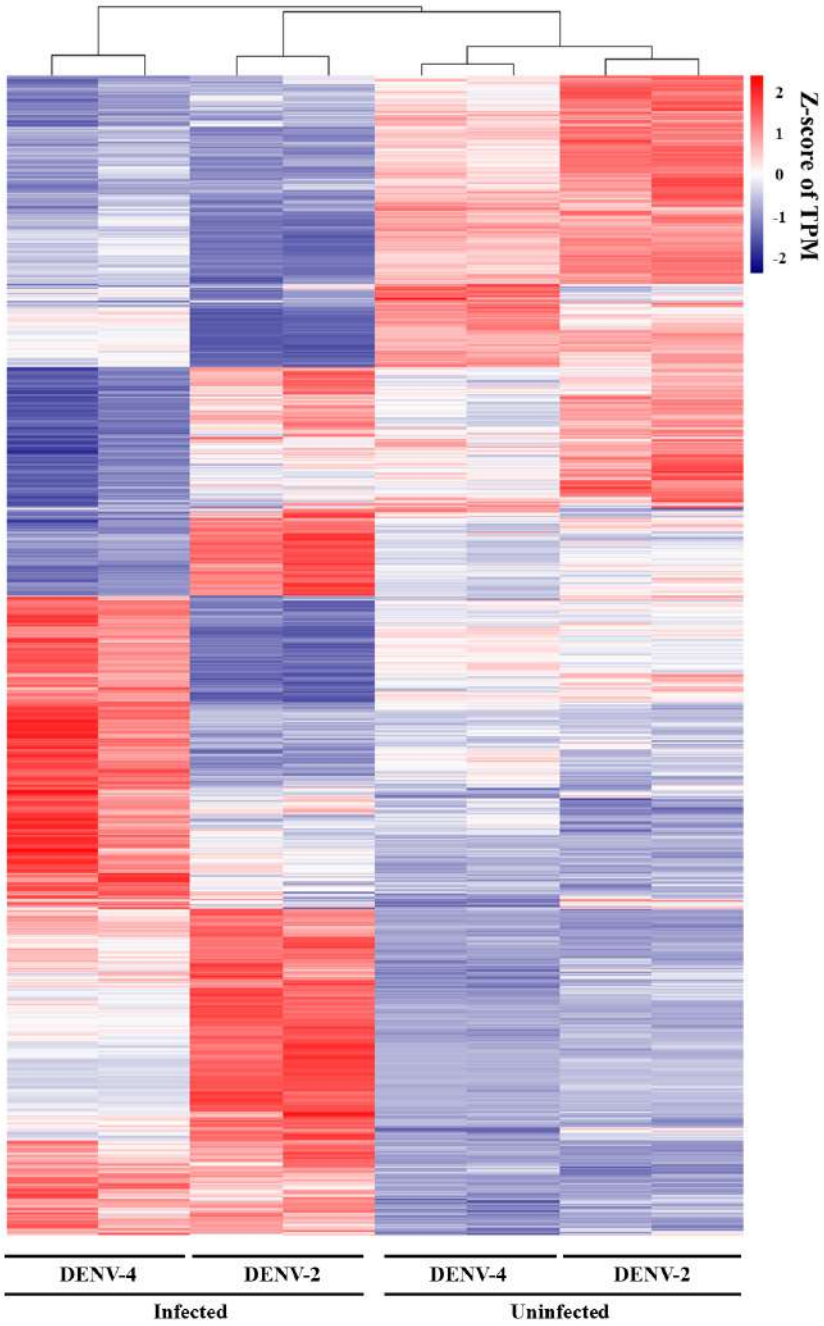

Figure 2. Heatmap illustrates global patterns of gene expression in both infected (MOI 5) and mock (MOI 0) samples at 48 HPI. Each condition was performed in two biological replicates. The color scale represents the Z-score of transcripts per million (TPM). 2,679 expressed genes are listed along the y-axis.

Given that DENV-2 and DENV-4 have been the most prevalent in Thailand[15], we decided to investigate global differences of host response between these two strains. We noted that this study paid attention on only reads that were associated with coding sequences, i.e., mRNA transcripts. We set up the criteria for significance being adjusted *p*-value less than 0.05 and log2 fold change more than absolute of 1 (dotted lines in **Fig. 3**).

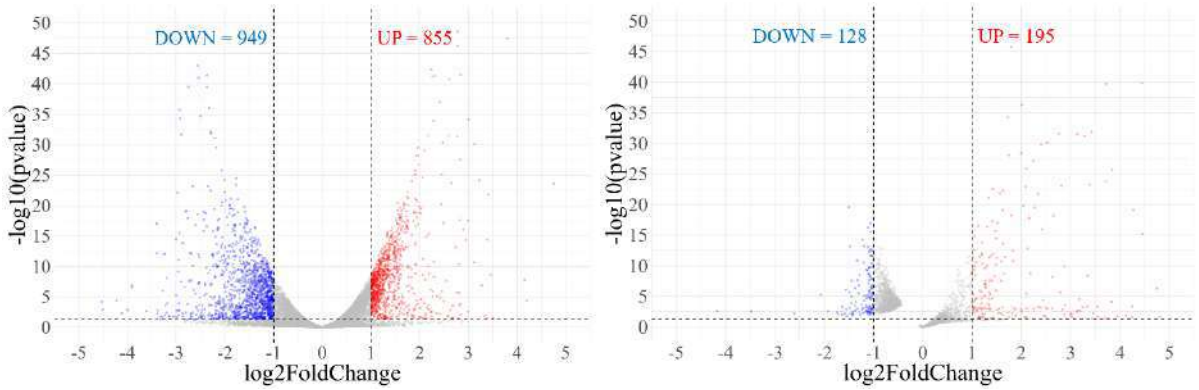

Figure 3. Volcano plot represents overview of differentially expressed genes in HuH-7 cells infected with DENV-2 (left panel) and DENV-4 (right panel) when compared with uninfected cells (MOI 0). X-axis indicates magnitude of differential expression by "log2 fold change" and Y-axis indicates statistical significance in term of "-log *p*-value". Up-regulated and down-regulated genes are shown as red and blue dot, respectively.

Our transcriptome results revealed that DENV-2 caused 855 significantly up-regulated genes and 949 down-regulated genes, whereas 195 and 128 genes were up-regulated and down-regulated, in case of DENV-4, respectively (**Fig. 3**). Given that the genome sequences of two strains used here are 67.6% identical and the percent of infected cells were similar (**Fig. 1**), it should not be straightforward to explain why DENV-2 created more impact on gene expression in HuH-7. To our knowledge, this is the first report of distinct transcriptional landscapes between DENV-2 and DENV-4.

3. DENV-2 down-regulated DNA replication; DENV-4 up-regulated inflammatory response

Next, we used significantly differentially expressed genes from DEA to perform pathway analysis to understand how differentiated genes are involved in cellular processes during infection. It should be noted that the term "pathway analysis" in this work was GO-based gene annotation in biological process modules.

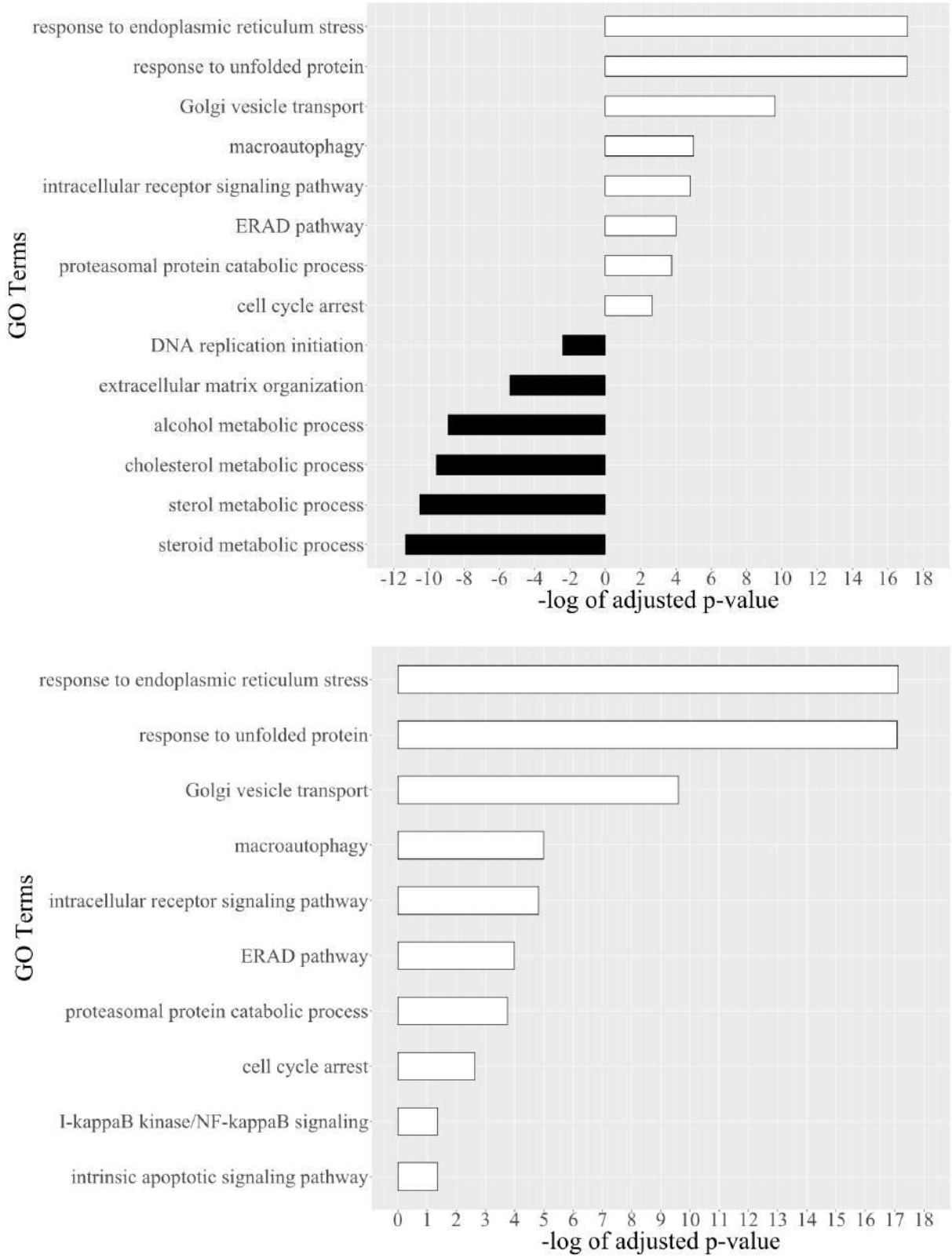

Figure 4. Pathways significantly affected by DENV-2 (upper panel) and DENV-4 (lower panel) in HuH-7 cells. The plots show biological processes defined by GO database (Y-axis) and their statistical significance in term of "-log of adjusted *p*-value" (X-axis). White bars represent up-regulation and black bars are down-regulation.

It is interesting that while DENV-2 made changes in both directions of up- and down-regulations, DENV-4 showed only significant up-regulated pathways (**Fig. 4**). The pathways

commonly disrupted by both DENV-2 and DENV-4 were, from the most to the least significance, ER stress and unfolded protein response (UPR), Golgi vesicle transport or membrane trafficking, macroautophagy, intracellular receptor signaling pathway, ERAD pathway, protein catabolic process, and cell cycle arrest. Notably, up-regulation of pro-inflammatory signaling as NF-κB was unique in DENV-4 infected cells. In DENV-2 infection, the most down-regulated process was the lipid and alcohol metabolisms, followed by extracellular matrix (ECM) organization and DNA replication.

In addition, we also performed gene set enrichment analysis (GSEA) in which the ranked log2 fold changes of gene expression are taken into consideration to calculate the pathway "enrichment score".

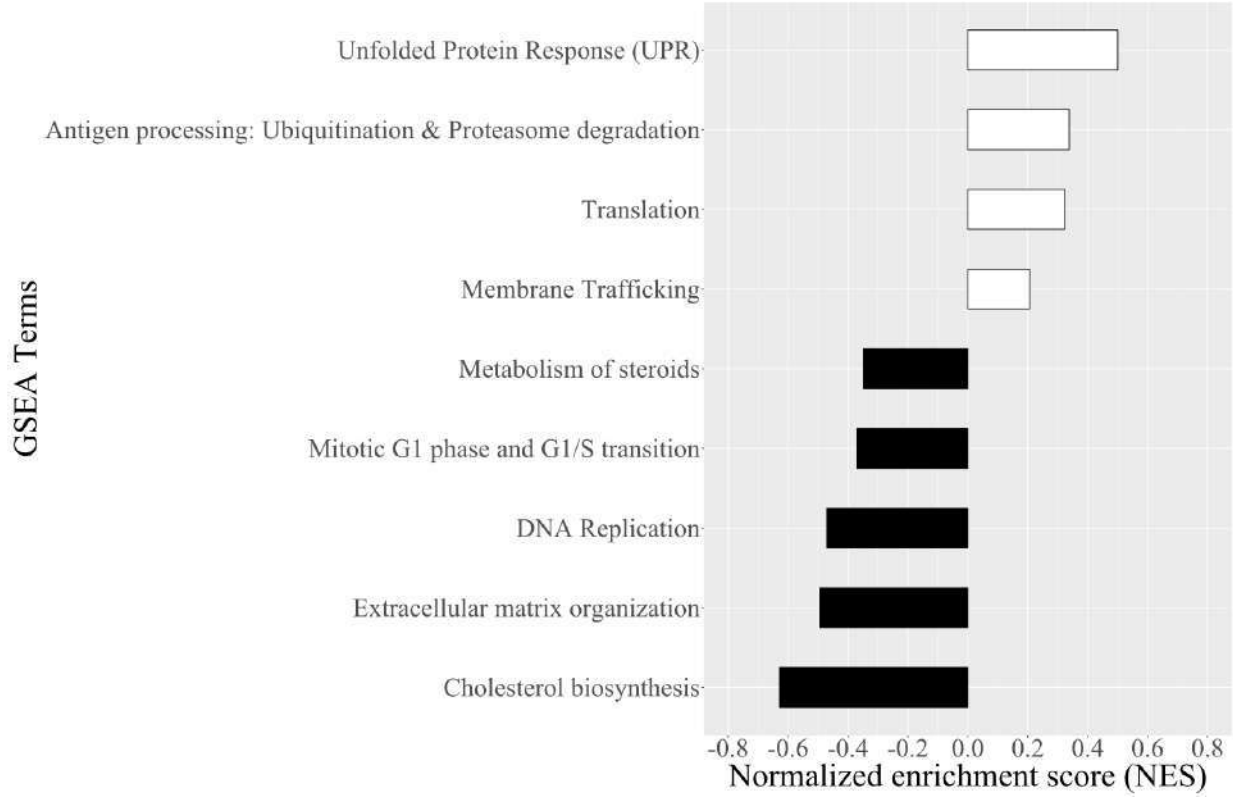

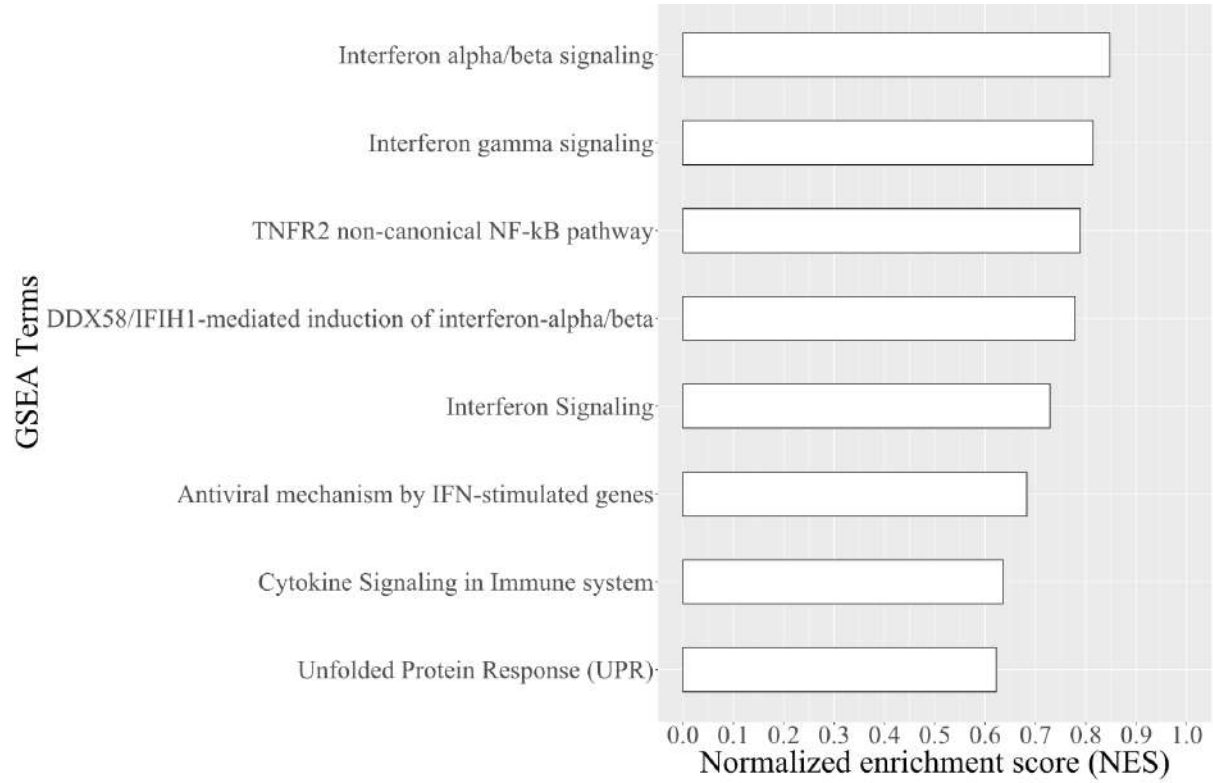

Figure 5. Plots of results from GSEA of DENV-2 (upper panel) and DENV-4 (lower panel) infection in HuH-7 cells. The Y-axis represents biological processes defined by GO database and the X-axis is their normalized enrichment score (NES). White and black bars represent the pathways showing up-regulation and down-regulation, respectively.

GSEA showed relevant results that both DENV-2 and DENV-4 stimulated UPR upon infection. Our findings were collaborated by previous studies in which UPR played major roles in dengue infection[16]. The process responded to ER stress stemmed from the ER membrane usage by DENV. UPR activates the crosstalk of IRE1, PERK and ATF6 pathways to induce expression of chaperones and protein folding-related factors. Our transcriptome also provided new pathways, which have not been mentioned, associated with DENV-2 infection including DNA replication initiation (**Fig. 4** upper panel), corresponding to G1-to-S phase transition[17] in GSEA (**Fig. 5** upper panel). Markedly, DENV-4 but not DENV-2 induced NF-κB signaling-mediated interferon (IFN) activation important for pro-inflammatory responses (lower panels in **Figs. 4** and **5**), which was the most up-regulated pathway in cells infected with DENV-4. This could be an important clue to the relationship to DENV-induced ALF.

Altogether, we provided solid evidence to describe, for the first time, distinct host responses upon infection by DENV-2 and DENV-4, suggesting the molecular pathways involving in DENV-induced ALF. The findings in this work would be a crucial knowledge for further study to understand dengue pathogenesis and development of treatment in the future.

Conclusion

Our transcriptome analysis revealed that 855 genes were significantly up-regulated, and 949 genes were down-regulated in HuH-7 cells upon DENV-2 infection, whereas DENV-4 induced up-regulation of 195 genes and down-regulation of 128 genes. The UPR pathway is the most commonly up-regulated in both DENV-2 and DENV-4. We also found a unique feature of DENV-4 in which NF-κB and interferon signaling pathways were significantly activated.

Acknowledgment

This work was supported by the Young Researcher Development Program and a Grants-in-Aid for Scientific Research from National Research Council of Thailand (NRCT) to KT and SC, respectively.

References

1. Bhatt S, Gething PW, Brady OJ, Messina JP, Farlow AW, Moyes CL, et al. Nature. 2013;496(7446):504–7
2. Nedjadi T, El-Kafrawy S, Sohrab SS, Desprès P, Damanhouri G, Azhar E. Virol J. 2015;12(1):1–11.
3. Cruz-Oliveira C, Freire JM, Conceição TM, Higa LM, Castanho MARB, Da Poian AT. FEMS Microbiol Rev. 2015;39(2):155–70.
4. Teerasarntipan T, Chaiteerakij R, Komolmit P, Tangkijvanich P, Treeprasertsuk S. WORLD J GASTROENTERO. 2020;9327:4983–4994.
5. Fernando S, Wijewickrama A, Gomes L, Punchihewa CT, Madusanka SDP, Dissanayake H, et al. BMC Infect Dis. 2016;16(1):1–9.
6. Sessions OM, Tan Y, Goh KC, Liu Y, Tan P, Rozen S, et al. PLoS Negl Trop Dis. 2013;7(3).
7. Zanini F, Pu S-Y, Bekerman E, Einav S, Quake SR. Elife. 2018;7.
8. Lowe R, Shirley N, Bleackley M, Dolan S, Shafee T. PLoS Comput Biol. 2017;13(5):1–23.
9. Costa-Silva J, Domingues D, Lopes FM. PLoS One. 2017;12(12)
10. Zitzmann C, Schmid B, Ruggieri A, Perelson AS, Binder M, Bartenschlager R, et al. Front Microbiol. 2020;11(April).
11. Love MI, Huber W, Anders S. Genome Biol. 2014; 15, 550.
12. Yu G, Wang L, Han Y, He Q. OMICS. 2012; 16(5), 284–287.
13. G Yu, QY He. Mol. Biosyst. 2016; 12(2):477–479.
14. Clyde K, Kyle JL, Harris E. J Virol. 2006;80(23):11418–11431.
15. Limkittikul K, Brett J, L'Azou M. PLoS Negl Trop Dis. 2014;8(11).
16. Perera N, Miller JL, Zitzmann N. Cell Microbiol. 2017;19(5):1–9.
17. Fragkos M, Ganier O, Coulombe P, Méchali M. Nat Rev Mol Cell Biol. 2015;16(6):360–74.

β-GLUCOSIDASE ACTIVITY AND IN-SILICO STRUCTURAL ANALYSIS FROM THREE STRAINS OF *ASPERGILLUS ACULEATUS*

Ngoentra Samnaknit[1], Duriya Chantasingh[2], Kusol Pootanakit[1]*
[1]Institute of Molecular Biosciences, Mahidol University, Salaya, Phutthamonthon, Nakhon Pathom 73170, Thailand.
[2]National Center for Genetic Engineering and Biotechnology (BIOTEC), 133 Thailand Science Park, Paholyothin Rd, Klong 1, Klongluang, Pathumthani 12120, Thailand.
*e-mail: kusol.poo@mahidol.ac.th

Abstract:

β-glucosidases (BGLs) are members of glycoside hydrolase family 3 (GH3) and can be found in various microorganisms, especially fungi. *Aspergillus aculeatus* is a promising fungus for cellulolytic enzymes production. Recently, using transcriptomic analysis, differential gene expressions were studied in three strains of *A. aculeatus* (HUT2365, BCC199, and BCC56535). The β-glucosidase gene was found to be highly upregulated in the HUT2365 strain. Here, its activity was determined. The results showed approximately 3- and 9-folds over the other two strains on day 6. Protein analysis by multiple sequence alignment revealed a conserved active site of GH3 family enzyme in all three strains. Moreover, homology modeling was used to predict the 3D-structure and explore the different functional domains of these β-glucosidases. Three homologous structures were obtained by using crystal structure of *Km*BglI (PDB: 3ABZ) as a template for homology modeling. The results showed that the β-glucosidase structures contain TIM barrel-like domain with a catalytic GH3 family active site (aspartate), an α/β sandwich domain and a FnIII domain. However, the FnIII domain was found only in HUT2365 and BCC199. This suggested that the FnIII domain may be involved in the β-glucosidase activity. Thus, to improve the β-glucosidase efficiency the focus should be first on this domain.

Introduction:

Biofuel is a promising alternative energy to reduce the consumption of fossil fuels. The production of bioethanol from cellulosic biomass consists of pretreatment for deconstruction of lignin and hemicellulose, hydrolysis of holocellulose into fermentable sugars by various enzymes, and finally the fermentation of obtained sugars into bioethanol. However, high cost of hydrolysis process is a major problem in bioethanol production. Therefore, to reduce the manufacturing cost, improvement in enzyme activity is needed.

Cellulosic biomass is a complex substrate of cellulose, hemicellulose, and lignin[1]. Cellulose is the major component, composed of glucan chains with repeating β-1,4-D-glucose units. Cellulases act as cellulose-degrading enzymes. There are three major cellulases, comprised of cellobiohydrolases (E.C. 3.2.1.91), endoglucanases (E.C. 3.2.1.74), and β-glucosidases (BGLs; E.C. 3.2.1.21)[2]. These cellulase enzymes are produced by various organisms including filamentous fungi, such as *Trichoderma reesei*. Although *T. reesei* contains highly effective cellulases, its BGL activity is low, resulting in limited hydrolysis of cellulosic molecule[3]. Meanwhile, another fungus, *Aspergillus aculeatus* has the ability to produce multi-polysaccharide degrading enzymes as well as BGL[4]. Therefore, *A. aculeatus* may be a promising cellulase producer for improved efficiency in bioethanol production.

BGLs are members of the GH3 (glycoside hydrolase) families[5]. The crystal structure of *A. aculeatus* BGL (AaBGL1) shows three domains: a catalytic TIM (triosephosphate

isomerase) barrel-like domain, an α/β sandwich domain, and a FnIII (fibronectin type III) domain. In addition, the active site of AaBGL1 contains highly hydrophobic and aromatic residues. However, the positions and the identities of the acid/base catalytic residues of GH3 family members are highly diverse and not identical[6]. Therefore, BGLs from other fungal strains may have different structure, domain, and active site.

Recently, transcriptomic analysis of three *A. aculeatus* strains (HUT2365, BCC199, and BCC56535), possessing different cellulase activities (HUT2365 showed highest cellulase activity, followed by BCC199 and BCC56535) were performed in our laboratory[7]. The results, as expected, showed diverse transcriptional patterns. Specifically, a gene encoding for β-glucosidase (acu03887_1) was highly expressed in HUT2365 when compared to the other two strains. This gene may therefore be the candidate for improving the cellulase activities in other strains. In this study, β-glucosidase activity of the three *Aspergillus aculeatus* strains were initially determined. The results showed that the high cellulase strain (HUT2365) had the highest activity in all days tested when compared to the other two strains. Then, to determine if this difference in activity is due to their 3D structure, *in-silico* technique was used to perform homology modeling and to explore the functional domains of these three β-glucosidases.

Methodology:

Enzyme preparation

Three *A. aculeatus* strains (HUT2365, BCC199 and BCC56535) were grown on potato dextrose agar (PDA) plates and then incubated at 30°C for 4 days. To generate fungal spores, mycelium were grown in liquid spore induction medium (2% peptone, 2% yeast extract, 1% glucose and 1% KH_2PO_4) supplemented with rice grains at the ratio of 1 g rice grain: 1 ml medium[6]. The growing spores were separated from rice grains by using 0.05% Triton X-100. Then the spores were washed with sterile water, 3 times, before further used as starter culture. The starter culture (1 x 10^7 spores/ml) were inoculated into 50 ml of wheat bran (4% w/v) and soybean meal (3% w/v) medium (WS) as a submerged (liquid) culture for enzyme production. Fungal strains were cultured for 6 days under aerobic cultivation condition at 30°C, 150 rpm. Crude enzymes were collected after cultivation for 1-, 3-, and 6-day. The supernatant containing crude β-glucosidase enzyme were separated from residual substrates by centrifugation at 8,000 rpm for 20 min.

Enzyme assay

β-glucosidase activity was determined by using p-nitrophenyl-β-D-glucopyranoside (pNPG; Sigma) as a substrate[6]. The reaction mixture contained 100 mM sodium acetate buffer (pH 5.0), 0.1% (w/v) pNPG and diluted in a total volume of 500 µl. After 30 min incubation at 50°C, the reaction was terminated by adding 350 µl of 1M Na_2CO_3. The quantity of p-nitrophenol was measured spectrophotometrically at 405 nm. One unit of the enzyme refers to the amount of enzyme that produces 1 µmol p-nitrophenol per minute. The reactions were performed in triplicate. The total protein concentrations of the crude enzyme extracts were determined by Bradford's method with the Bio-Rad protein assay reagent (Bio-Rad, USA).

Homology modeling

β-glucosidase DNA sequences from three *A. aculeatus* strains were derived from RNA-seq analysis. The online website (https://web.expasy.org/translate/) was used to translate the DNA sequences to amino acid sequences. Then, these amino acid sequences were blast searched at NCBI by choosing Protein Data Bank (PDB). The website ESPript 3.0 (https://espript.ibcp.fr/ESPript/cgi-bin/ESPript.cgi) and CLUSTAL O (https://www.ebi.ac.uk/Tools/msa/clustalo/) were used to carry out multiple sequence alignment. InterPro (https://www.ebi.ac.uk/interpro/) was used for protein classification. The SWISS-MODEL sever (https://swissmodel.expasy.org/) was utilized for homology modeling.

Results and Discussion:

β-glucosidase activity assay

Previously, the HUT2365 strain was found to express the highest level of β-glucosidase transcript among the three strains[7]. However, we do not know if this is true at the protein level. Therefore, the β-glucosidase activity of the three strains were determined in this study. The results showed significant difference among the three strains in all days investigated (Table 1). This is still true on day 3, even though the range of β-glucosidase activity for HUT2356 strain is large. As this is the beginning of our investigation, it may be due to the limited number of experimental replicates (n = 3). The HUT2365 strain showed the highest β-glucosidase activity at all days tested, followed by BCC199 and BCC56535 (Fig. 1). Our results suggested that *A. aculeatus* HUT2365 strain produced the most highly efficient β-glucosidase among the three strains investigated. Therefore, it has the potential to be of used in the biomass conversion industry.

Multiple sequence alignment

The β-glucosidase protein blast search of three *A. aculeatus* strains showed the highest identity to a β-glucosidase I (PDB: 3ABZ) from *Kluyveromyces maxianus* (*Km*BglI). Specifically, it has 34.92%, 36.18% and 31.85% protein identity against HUT2365, BCC199, and BCC56535, respectively. Multiple sequence alignment showed the highly conserved glycosyl hydrolase family 3 (GH3) active site with an Asp^{242} identified as the active site residue (Fig. 2). This active site is also found in other fungal β-glucosidases such as thermophilic fungi *Chaetomium thermophilum*[8] and *Thermotoga neapolitana*[9].

Homology modeling

The BGL amino acid sequences were submitted to the SWISS-MODEL sever and the template search were performed using PDB database. The β-glucosidase I template (PDB: 3ABZ) from *K. maxianus* and the three BGLs shared the highest identity (32-36%). Even though the protein identity is not that high, it is however in the range of feasible homology cutoff of >30%[10]. Homology modeling indicated that the BGL structure of all three *A. aculeatus* strains contained the TIM barrel-like domain with the nucleophile aspartate at the active site, and an α/β sandwich domain (Fig. 3). Interestingly, the FnIII domain was found only in the BCC199 and HUT2365 strains (Fig. 3B and 3C). This domain is thought to be involved in the positioning of the enzyme on very large polymeric substrates and also in its thermostability[5, 9]. The results from *in-silico* analysis suggested that the FnIII domain may affect the β-glucosidase activity of *A. aculeatus*. Therefore, improving the β-glucosidase activity in *A. aculeatus* should focus on this domain.

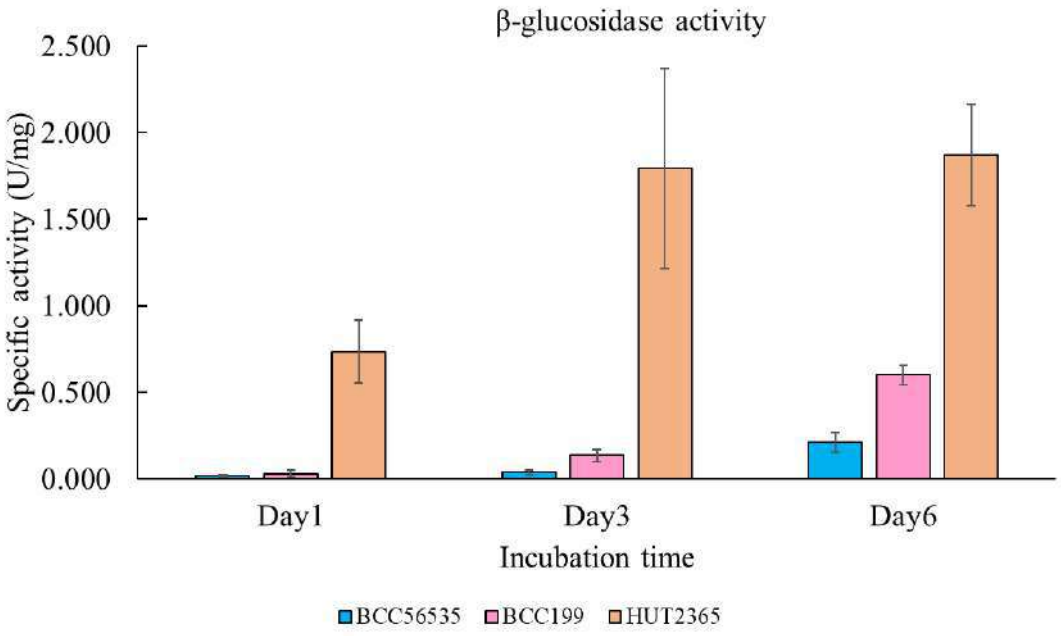

Figure 1. Specific activity of β-glucosidases from *A. aculeatus* BCC56535 (blue), BCC199 (pink), and HUT2365 (orange).

Table 1. Specific activity of β-glucosidases

A. aculeatus	**Specific activity (U/mg)**		
	Day 1	**Day 3**	**Day 6**
BCC56535	0.017±0.01[a]	0.037±0.01[a]	0.211±0.06[a]
BCC199	0.031±0.02[b]	0.136±0.04[b]	0.601±0.06[b]
HUT2365	0.734±0.18[c]	1.792±0.58[c]	1.872±0.29[c]

[a,b,c] Different letters in the same column are significantly different ($p < 0.05$)
BCC : Biotec Culture Collection
HUT : Hiroshima university culture collection

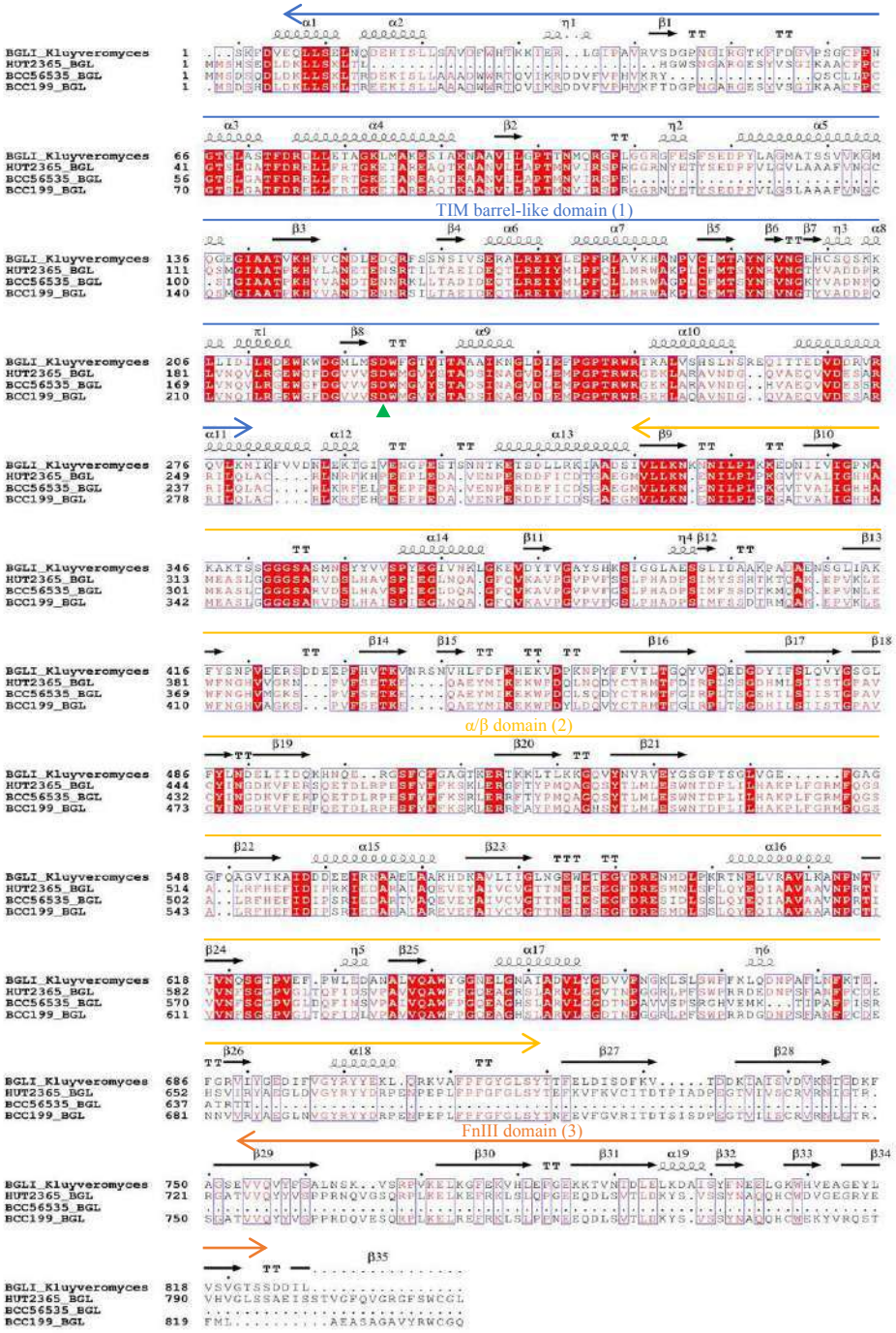

Figure 2. Multiple sequence alignment of β-glucosidases from *A. aculeatus* BCC56535, BCC199, HUT2365 and *K. maxianus*. Secondary structure elements are shown on the top of the alignment. The green triangle below the alignment indicates the catalytic conserved residue (aspartate). The three domains are also indicated. Red box indicates strict identity. Red character indicates similarity in a group. Blue frame indicates similarity across groups. α-Helices, β-strands, strict β-turns, and strict α-turns are displayed as coils, black arrows, TT, and TTT letters, respectively. The figure was constructed using ESPript[11].

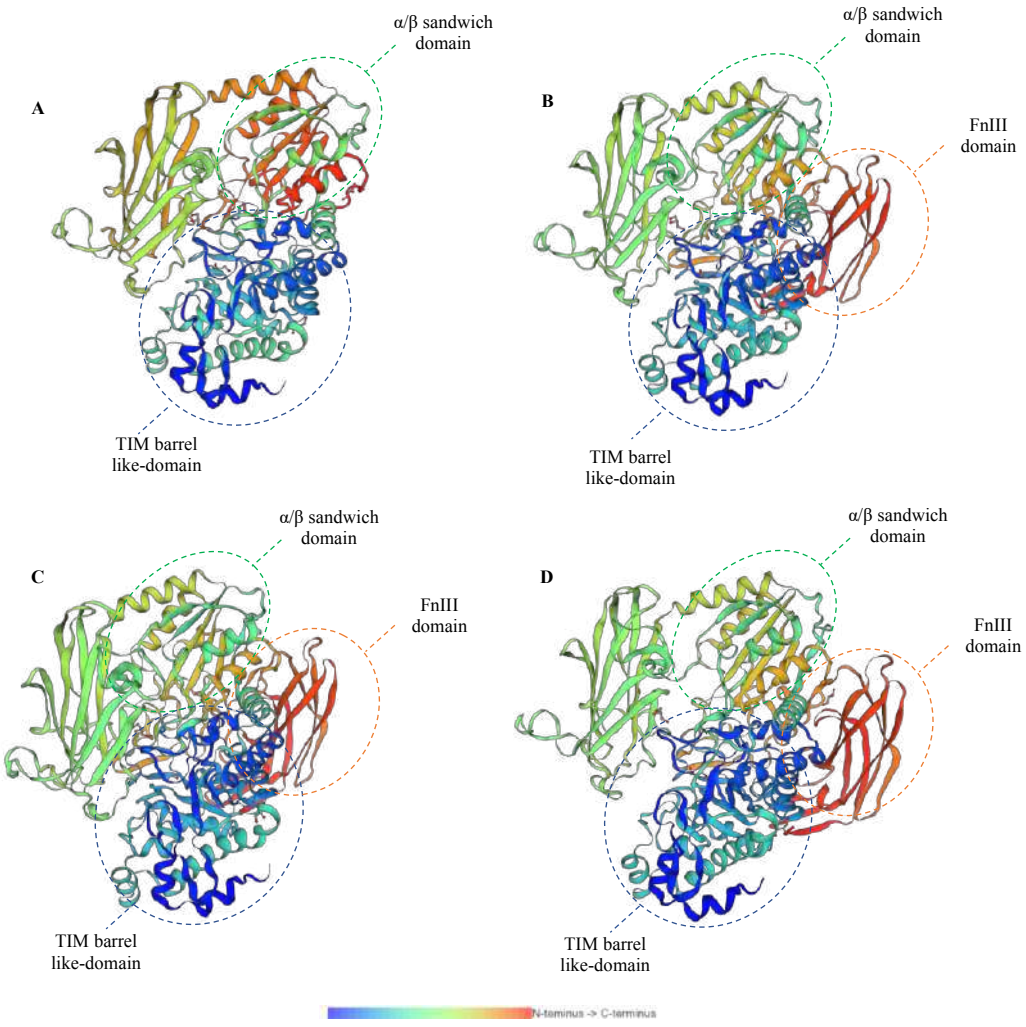

Figure 3. 3D homology modeling of β-glucosidases from *A. aculeatus* BCC56535 (A), BCC199 (B), HUT2365 (C), and *K. maxianus* (chain A) (D). The TIM barrel like-domain, α/β sandwich domain, and FnIII domain are shown in blue, green, and orange, respectively.

Conclusion:

In this study, *A. aculeatuse* HUT2365 showed the highest β-glucosidase activity, followed by BCC199 and BCC56535. Homology modeling showed that they are closely related to BGL1 from *K. maxianus*. Overall, the 3D structure of these three enzymes are very similar except at the TIM barrel-like (C-terminal) domain and also at the α/β sandwich (N-terminal) domain. It is possible that the low β-glucosidase activity of BCC56535 may be the lack of FnIII domain. Therefore, to improve the activity of this enzyme the initial target may be at the FnIII domain.

Acknowledgements:

We would like to thank the Thailand Graduate Institute of Science and Technology (TGIST), National Science and Technology Development Agency (NSTDA) and Mahidol University for all supports provided.

References:

1. Anwar Z, Gulfraz M, Irshad M, Journal of Radiation Research and Applied Sciences 2014;7(2):163-173.
2. Behera S, Arora R, Nandhagopal N, Kumar S, Renewable and sustainable energy reviews 2014;3691-106.
3. Saloheimo M, Kuja-Panula J, Ylösmäki E, Ward M, Penttilä M, Applied and environmental microbiology 2002;68(9):4546-4553.
4. Suwannarangsee S, Arnthong J, Eurwilaichitr L, Champreda V, J Microbiol Biotechnol 2014;24(10):1427-37.
5. Suzuki K, Sumitani J-I, Nam Y-W, Nishimaki T, Tani S, Wakagi T, Kawaguchi T, Fushinobu S, Biochemical Journal 2013;452(2):211-221.
6. Poonsrisawat A, Paemanee A, Wanlapatit S, Piyachomkwan K, Eurwilaichitr L, Champreda V, 3 Biotech 2017;7(5):290-290.
7. Mhuantong W, Charoensri S, Poonsrisawat A, Pootakham W, Tangphatsornruang S, Siamphan C, Suwannarangsee S, Eurwilaichitr L, Champreda V, Charoensawan V, Chantasingh D, Frontiers in Bioengineering and Biotechnology 2021;8(1594).
8. Mohsin I, Poudel N, Li D-C, Papageorgiou A C, International Journal of Molecular Sciences 2019;20(23):5962.
9. Pozzo T, Pasten J L, Karlsson E N, Logan D T, Journal of molecular biology 2010;397(3):724-739.
10. Xiang Z, Curr Protein Pept Sci 2006;7(3):217-27.
11. Robert X, Gouet P, Nucleic Acids Res 2014;42(Web Server issue):W320-4.

EFFICACY OF UVC LIGHT IN DECONTAMINATION OF INDICATOR PATHOGENS AND ITS SURFACE CLEANING APPLICATION

Jirabhorn Piluk,[1] Sitanan Thitiprasert,[1] Phetcharat Jaiaue,[2] Jesnipit Thammakes,[2] Nuttha Thongchul[1,*]

[1]Research Unit in Bioconversion and Bioseparation for Value-Added Chemical Production, Institute of Biotechnology and Genetic Engineering, Chulalongkorn University, Phayathai, Pathumwan, Bangkok 10330 Thailand

[2]Program in Biotechnology, Faculty of Science, Chulalongkorn University, Phayathai, Pathumwan, Bangkok, 10330, Thailand

*e-mail: Nuttha.T@chula.ac.th

Abstract:

Due to the pandemic outbreak of COVID-19, people are aware of living in hygienic conditions. General practices of decontamination require heat or chemical to disinfect the objects or surfaces. However, in some applications, heat or chemicals cannot be applicable. UV light is typically used for decontamination in drinking water and fruit juice industries as it has been approved by FDA. Therefore, it is believed that the application of UV light can be extended for surface cleaning. In this work, we investigated the efficacy of UVC light for decontamination of indicator pathogens contaminated on different surfaces. Chick-Watson Model was applied for dose prediction to disinfect 5 bacteria including *Escherichia coli*, *Klebsiella pneumoniae*, *Streptococcus faecalis*, *Staphylococcus aureus* and *Bacillus subtilis* spores on 4 different surfaces. UVC intensity and type of bacteria and their initial concentrations as well as the materials affected the decontamination efficacy. Using the predicted UVC exposure time to inactivate the tested bacteria contaminated on aluminum sheet seemed effective while the inactivation on wood seemed to be very poor. In addition, inactivation of the tested bacteria to 4-log reduction on plastic sheet and paper seemed not very effective as the bacteria still existed the swabbed surfaces after UVC exposure. The finding here could perhaps be explained by the different surface roughness of each material. Among the tested materials, aluminum sheet has the smoothest surface while wood surface is rough. The surface roughness could be contributed to UVC absorption and transmission to the targeted bacteria. The findings in this study suggested that with proper dose prediction and well defined conditions including surface characteristics, majority of contaminant and its population, UVC light can be successfully used for as an environmentally friendly process for disinfection purpose.

Keywords: UVC light, Pathogenic bacteria, Surface cleaning, Decontamination

PREPARATION OF BIOACTIVE PECTIN FILMS FROM POMELO PEELS

Nattariya Trasri, Suwattana Pruksasri*
Department of Biotechnology, Faculty of Engineering and Industrial Technology, Silpakorn University, Nakhon Pathom 73000 Thailand
*e-mail: pruksasri_s@su.ac.th

Abstract:
Pomelo is a citrus fruit that is largely cultivated in Southeast Asia including Thailand. Its peel, which contributes up to 30% of the total fruit weight, is generally discarded as agricultural waste. However, it consists of many valuable compounds such as flavonoids, essential oil, cellulose, hemicellulose, and pectin. Then, pomelo peel might be efficiently used as a raw material for pectin production. Therefore, the focus of this work was on the utilization of pomelo peel pectin extract as a biopolymer material to form edible films with antioxidant properties. Pectin was extracted from the albedo part (spongy white peel) of pomelo using 1.0 M citric acid solution at 90 °C for 30 min. The methoxyl content and the degree esterification of the obtained pectin were 13.6 and 71.4%, respectively. The pomelo peel extract solution was mixed with glycerol at different ratios to form bioactive films. The total phenolic contents of all films were in the range of 1.26-1.68 mg gallic acid equivalents (GAE)/g dry film. The results of the present study demonstrated that pomelo peel extract could be used in producing edible films with improved quality characteristics. Further study on the applications of bioactive pectin films for food applications should be explored.

Keywords: Pomelo peel, Pectin, Edible film, Antioxidant

SCREENING AND ISOLATION OF LIGNIN-DEPOLYMERIZING BACTERIA FOR AN AROMATIC FEEDSTOCK PRODUCTION

Panaya Kotchaplai*
Research Unit in Bioconversion and Bioseparation for Value-Added Chemical Production, Institute of Biotechnology and Genetic Engineering, Chulalongkorn University, Thailand, 10330
*e-mail: panaya.k@chula.ac.th

Abstract:
Lignin, due to its structure, is a promising source for the renewable feedstock for many industries. However, the heterogeneity of the lignin-derived product is one of the major challenges for the valorization of lignin. In this study, the lignin-depolymerizing microbial strains were screened from soil samples and decayed barks by using the nitrated lignin-based colorimetric assay. Three isolates which showed positive result were further identified as *Bacillus* strains based on 16S rRNA gene sequencing. The isolated strains were then investigated for the growth-dependent production of aromatic compound in M9-based medium containing 0.25 g/L lignin. Glucose was added as co-carbon source since all tested strains could not use lignin as their sole carbon source. *Bacillus* sp. strain P1 and W1 grew well only in the presence of yeast extract whereas *Bacillus* sp. strain CU2-1 could grow well in either organic or inorganic carbon source. The obtained metabolites at the 144th hour were identified by using Gas Chromatography-Mass Spectrometry (GC-MS). Interestingly, the substantial accumulation of coumaryl alcohol derivatives was observed in all three isolates. While 4-hydroxyphenyllactic acid was the sole major metabolite for *Bacillus* sp. strain P1, phenyllactic acid and 4-hydroxyphenylpyruvic acid were detected in *Bacillus* sp. strain W1. In addition to phenyllactic acid and 4-hydroxyphenyllactic acid, vanillic acid was also accumulated in *Bacillus* sp. strain CU2-1.

SUGAR TOLERANCE IN D-LACTIC ACID FERMENTATION BY *Sporolactobacillus terrae* SBT-1

Sitanan Thitiprasert[1*], Jirabhorn Piluk[1], Vasana Tolieng[1], Somboon Tanasupawat[2], Nuttha Thongchul[1]

[1]Research Unit in Bioconversion/Bioseparation for Value-Added Chemical Production, Institute of Biotechnology and Genetic Engineering, Chulalongkorn University, Phayathai Road, Wangmai, Pathumwan, Bangkok 10330, Thailand

[2]Research Unit in Bioconversion/Bioseparation for Value-Added Chemical Production, Department of Biochemistry and Microbiology, Faculty of Pharmaceutical Sciences, Chulalongkorn University, Phayathai Road, Wangmai, Pathumwan, Bangkok 10330, Thailand

[*]Corresponding author: E-mail: Sitanan.T@chula.ac.th

Abstract:

Lactic acid is over a decade known as a useful organic acid with a wide application in food, pharmaceutical, cosmetic, and chemical industries. The natural lactic acid exists in two optical isomers, including D(-) and L(+) lactic acid. Additionally, pure enantiomers are more preferrable which provides various advantages compared with a racemic mixture of lactic acid (DL-lactic acid). The recent process of optically pure lactic acid production can be achieved by microbial fermentation. Focusing on optically pure D-lactic acid production, the most lactic acid producers are from the genus *Lactobacillus* and *Sporolactobacillus*; however, fewer bioprocess development studies of D-lactic acid are investigated, compared with L-lactic acid production. In particular, large-scale production of D-lactic acid has not yet been commercialized along with the increasing demand in specific applications, leading to raising the challenge to develop fermentation technology for improving D-lactic acid production. In this study, *Sporolactobacillus terrae* SBT-1 was found as an efficient D-lactic acid-producing strain that could grow and produce D-lactic acid at a very high glucose and sucrose concentration. In batch cultivation using 360 g/L glucose, SBT-1 produced 290.30 g/L D-lactic acid with a sufficiently high glucose conversion yield of 86%, the production rate of 3.02 g/Lh, and optically pure D-lactic acid of 96.80% enantiomer excess. The use of high sucrose concentration (440 g/L), SBT-1 could also effectively produce 276.50 g/L lactic acid with a conversion yield of 90%, a production rate of 2.88 g/L, and an optical purity of 98%. In addition to the experimental results, SBT-1 exhibited superior activity to ferment relatively high glucose or sucrose concentrations without the catabolite repression and byproduct formation.

DISTRIBUTING MULTIPARTITE ENTANGLED STATE OVER QUANTUM INTERNET

Naphan Benchasattabuse,[1,*] Clement Meignant,[2] Ryosuke Satoh,[1] Michal Hajdušek,[1] Damian Markham[2,3], Frédéric Grosshans[2], Rodney Van Meter[1]
[1]Keio University Shonan Fujisawa Campus, 5322 Endo, Fujisawa, Kanagawa 252-0882, Japan
[2]Laboratoire d'Informatique de Paris 6, CNRS, Sorbonne Université, 4 place Jussieu, 75005 Paris, France
[3]Japanese-French Laboratory for Informatics, CNRS, National Institute of Informatics, University of Tokyo, Tokyo, Japan
*e-mail: whit3z@sfc.wide.ad.jp

Abstract:
Interconnected quantum networks, the so-called Quantum Internet, have been attracting increasing interest from academia as well as the industry due to the tremendous advancements in quantum technologies over the last decade. Quantum Internet promises a multitude of enhanced as well as novel functionalities ranging from ultra-secure communication and sensing to better clock synchronization and distributed quantum computation. An important resource for many of these services is multipartite entangled states shared between the nodes of the quantum network. We propose an algorithm to distribute such states using a RuleSet-based protocol, a software contract that defines a sequence of instructions to execute after certain conditions are met on each node, allowing the nodes' autonomy and requiring minimal classical communication. The algorithm does not require full knowledge of the network topology nor is it dependent on the routing algorithm. Our approach is based on enlarging multipartite states from smaller sets of direct neighbours to all final participants. We also discuss the tradeoff between lockstep synchronized operations and the number of total classical messages. Further investigation is required to analyze how to balance said tradeoff.

OPTICAL QUANTUM ERASER

Kritsana Saego*, Poompong Chaiwongkhot, Sujin Suwanna

Optical and Quantum Physics Laboratory, Department of Physics, Faculty of Science,
Mahidol University, Bangkok 10140, Thailand
*e-mail: kritsana.sae@student.mahidol.edu

Abstract:
A photon that is split into two paths, either by double slit or beam splitter, will interfere with itself and show interference fringes. The state of photon can be represented by a superposition of paths information. By observing which-path information, the superposition state is collapsed. Subsequently, the interference fringe will be disappeared. However, one can restore the fringe by erasing which-path information, this process is known as the "Quantum eraser experiment". One scheme of this experiment can be set up based on Mach–Zehnder interferometer. At the output port of the interferometer, we can see the interference fringes. Path information can be marked by placing one polarizer at each path of the interferometer, one with angle 0^o and another one with angle 90^o with respect to the horizontal polarization. In this case, the interference fringe will be lost. By adding the third polarizer with angle 45^o with respect to the horizontal polarization at the outpot port of the interferometer to erasing which -path information. Then, the interference fringe is back. This work is focus on the interference fringe from setup when the third polarizer is rotated at different angles. We observe how the interference pattern changes and characterize it by measuring visibility of interference fringe. We found that the fringe visibility from the third polarizer at angle 0^o, 22.5^o and 45^o giving 0.017, 0.271 and 0.585 respectively.

OPTIMIZATION OF EXPECTED WAITING TIME IN NETWORK OF QUANTUM REPEATERS

Poramet Pathumsoot,[1] Ryosuke Satoh,[2] Naphan Benchasattabuse,[2] Michal Hajdušek,[2] Rodney Van Meter,[2] Sujin Suwanna,[1,*]
[1]Optical and Quantum Physics Laboratory, Department of Physics, Faculty of Science, Mahidol University, Bangkok 10400, Thailand
[2]Keio University Shonan Fujisawa Campus, 5322 Endo, Fujisawa, Kanagawa 252-0882, Japan
*e-mail: sujin.suw@mahidol.ac.th

Abstract:
Many quantum algorithms offer advantages over classical counterparts when they are executed on quantum computers. In the era of noisy intermediate-scale quantum (NISQ) devices, a quantum computer consists of a small number of qubits, which cannot operate for sufficiently long, while a novel quantum algorithm requires many qubits and a long operation time. Such limitation puts dampers on the advantages that theory offers. However, just as a traditional network of computers enhances the computation performance of classical computers, we envision a quantum internet to bring together smaller quantum computers and enhance the power of quantum computation. In order to achieve a high-quality connection between quantum computers, many techniques to suppress noises in quantum channels have been proposed. One is a well-known network of quantum repeaters capable of executing error-correcting protocols. In this work, we have created a simulator using discrete-event simulation package, SimPy 4.0.1 in Python, to analyze the performance of a network of quantum repeaters under various circumstances for a real-world, which should save time and budget for trials and errors and help designing experiments. We then investigate the expected waiting time to connect two end nodes under two topological configurations, which can be characterized as series-then-parallel and parallel-then-series. This expected waiting is measured by the expected number of trials and depend on the rate of photon connection are modelled as Bernoulli trials with success probability p. The analytical results and simulation results agree very well.

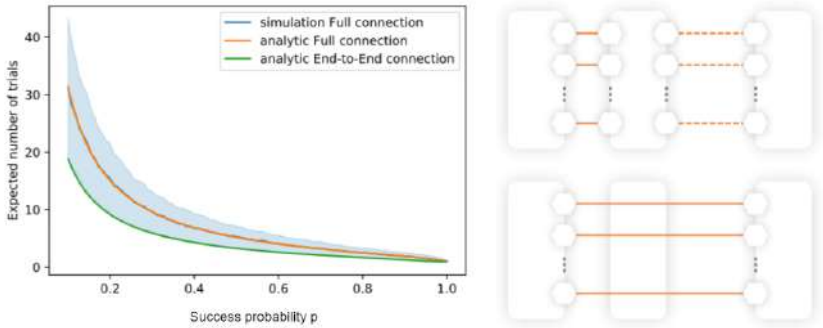

Figure 1.
Expected waiting time to connect two end nodes (left) and two topological configurations of a network (right): parallel-then-series (top-right) and series-then-parallel (bottom-right)

AGE ESTIMATION OF MARINE FOSSILS FROM PHETCHABUN PROVINCE USING X-RAY ANALYSIS

Sirikorn Pongtornkulpanich,[1] Kanokwan Boonsook,[1] Patcharin Naemchanthara,[2] Sumalee Ninlapruk[3], Kittisakchai Naemchanthara[1,*]

[1]Department of Physics, Faculty of Science, King Mongkut's University of Technology Thonburi, Bangkok, Thailand
[2]Department of Material and Process Engineering Technology, Faculty of Engineering and Technology, King Mongkut's University of Technology North Bangkok, Rayong Campus, Rayong, Thailand
[3]High Dose Radiation Dosimetry Calibration Laboratory, Office of Atom for Peace, Bangkok, Thailand

*e-mail: puri_kit@hotmail.com

Abstract:
The aim of this research is to apply the material characterization such as the crystal structure and chemical composition for fossil age estimation. The marine fossil consisted of three samples were collected from Nong Phai district, Phetchabun province. All marine fossils were prepared and characterized crystal structure by X-ray diffractometer. The chemical composition of all marine fossils was analyzed by X-ray fluorescence spectrometer. The chemical composition result was used to calculate the strontium and calcium ratio for age estimation of marine fossil. The results showed the marine fossil-1 and marine fossil-2 had like shell embedded in the rock while the marine fossil-3 had like the coral fossil. The main crystal structure of marine fossil-1 and marine fossil-2 were calcite phase but the marine fossil-3 was quartz phase. The main crystal phase of all marine fossils were confirmed with the chemical composition. The Sr and Ca ratio of marine fossil-1, marine fossil-2 and marine fossil-3 were 1.330, 1.711 and 0.386, respectively relating with the geological time of Permian period. From this experiment indicated that the crystal structure and chemical composition can be used to estimate the age of fossil.

Key words: Age Estimation, Geological Time, Marine Fossil, Sr/Ca Ratio, X-ray Analysis

Introduction:

Phetchabun province was the center part of Thailand, which cover area about 12,688 square kilometer.[1] This province was confirmed by the many archeological and geological studies about the collision between Shan Thai and Indochina Earth's crust[2]. This collision was the result in the transformation of ocean to land that corresponded with the presence of marine fossils in Phetchabun province. The marine fossils were discovered in various areas of Phetchabun province such as Nam Nao, Ban Nong Pla and Lom Sak district.[3,4] In recent year, there are report about the discovery of marine fossil in Nong Phai district. The Nong Phai district is the fertile rainforest in the past and then, this is decadent leading to the community currently. Moreover, the characteristic of marine fossil in this area have different from the others.[5] The geologist and archeologist is interested to investigate the characteristic and estimate the age of fossil from this area. However, there are only reports in geological field but no seen the scientific report. The scientific methods to evaluate the fossil

such as radiocarbon, K-Ar and ESR dating are complicate and high cost.[6] The appearance and characteristic of marine fossil can be indicated the oldness of fossil but cannot estimate the real age of fossil. The material characteristic such as crystal structure and chemical composition is the alternative technique that is simple and low cost. The crystal structure and chemical composition can be primary estimated the marine fossil age. Therefore, the marine fossil collected from Nong Phai district was estimated age by material characterization technique. The marine fossil were characterized the crystal structure by X-ray diffraction and the chemical composition by X-ray fluorescence techniques. All results were used to primary estimate age of marine fossil from Nong Phai district.

Methodology:

The marine fossils were collected from Nong Phai district in Phetchabun province, Thailand that located at latitude and longitude of 15.92 and 100.94, respectively as shown in Figure 1.

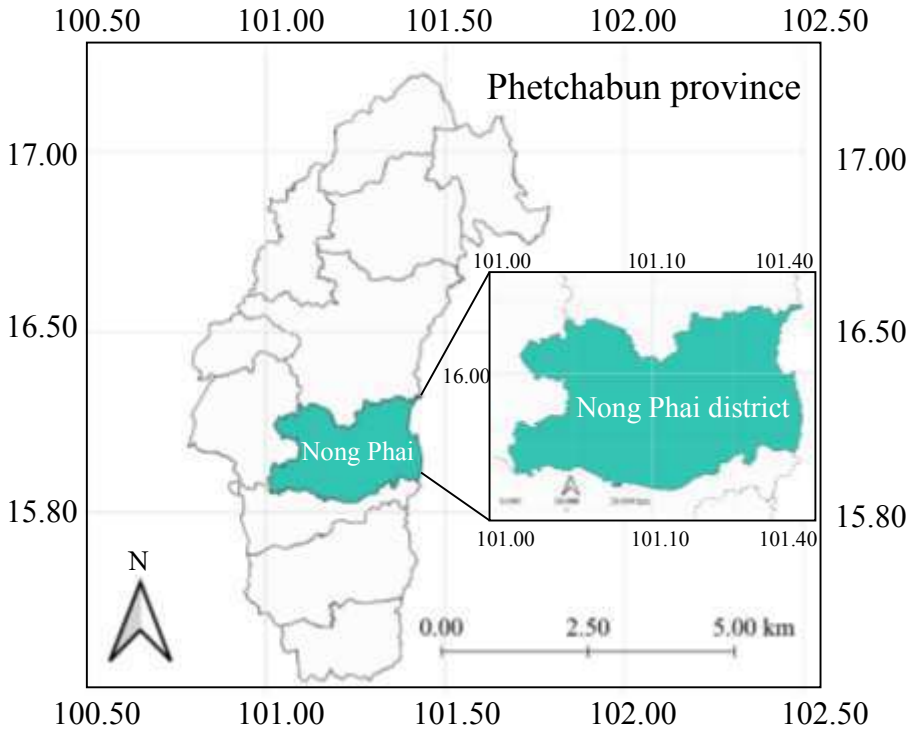

Figure 1. The location sites of collected marine fossil at Nong Phai district.

The collected marine fossil consist of three pieces of shell and coral fossils. The marine fossils were washed by distilled water in the ultrasonic bath to remove the soil impurity covering on the surface. The marine fossil were removed the organic matter by soaking in hydrogen peroxide solution and dried at room temperature for 24 h. Each marine fossil were ground and sieved into powders until particle size less than 150 µm. All powders of each marine fossil were kept in the amber plastic bags for preventing the sunlight exposure. The crystal structure of marine fossil were investigated by X-ray diffractometer (XRD, D2 phaser, Bruker) with scanning range from 10 to 70 degree in 2Theta at step rate 0.2 degree per second. The chemical composition were examined by X-ray fluorescence spectrometer (XRF, S8 Tiger, Bruker). The XRF results were used to calculate the ratio of strontium and calcium for age estimation of marine fossil.

Results and Discussion:

The marine fossil were observed anatomical feature by photography as shown in Figure 2.

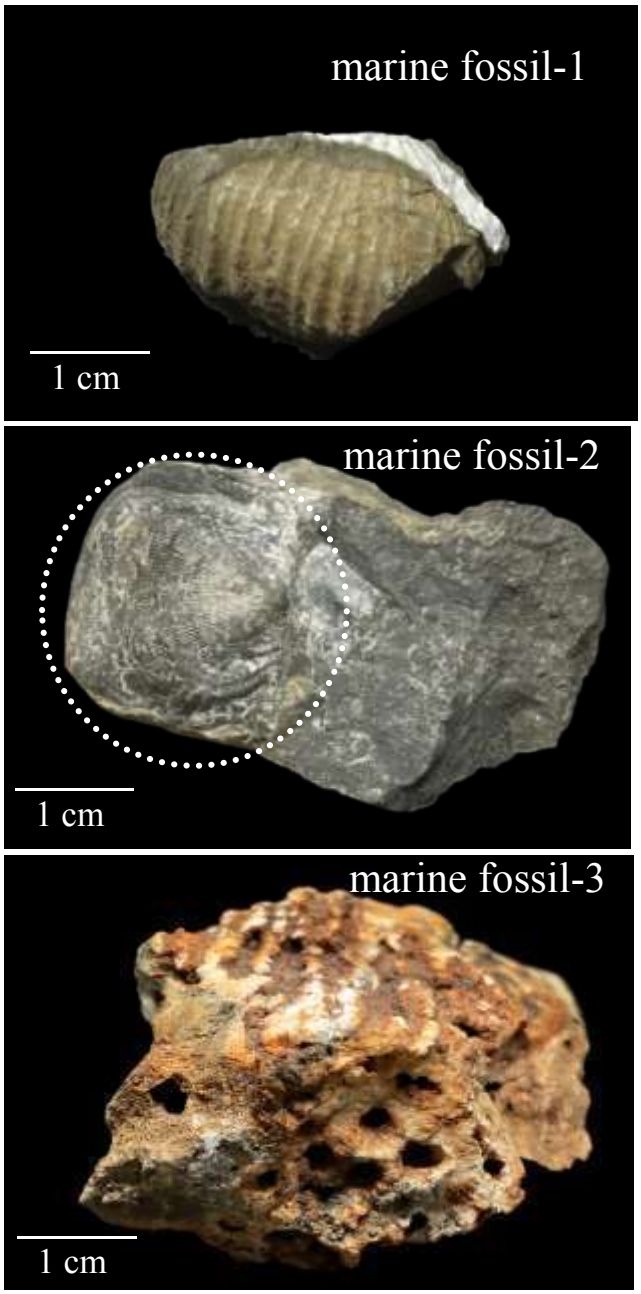

Figure 2. The photography of extracted marine fossils.

The marine fossil-1 showed the shapes like shell embedded in the bulk as like rock. The shell of marine fossil had gray colour, shell vary convex. The shape shell marine fossil-1 have circular and width about 3 cm. The characteristics of marine fossil-2 had similarly with marine fossil-1 but it was smaller size. From the characteristics of both marine fossils indicated that brachiopods shell corresponding with the archaeological reports.[7] The marine fossil-3 had the shape like coral and brown colour. The surface of marine fossil-3 had the large pores leading to the high roughness. The characteristics of marine fossil-3 indicated that the coral limestone with according to

the archaeological report also.[8] To more information, the XRD technique was selected to investigate the crystal structure and phase compound of marine fossils as shown in Figure 3. To more information, the XRD technique was selected to investigate the crystal structure and phase compound of marine fossils as shown in Figure 3.

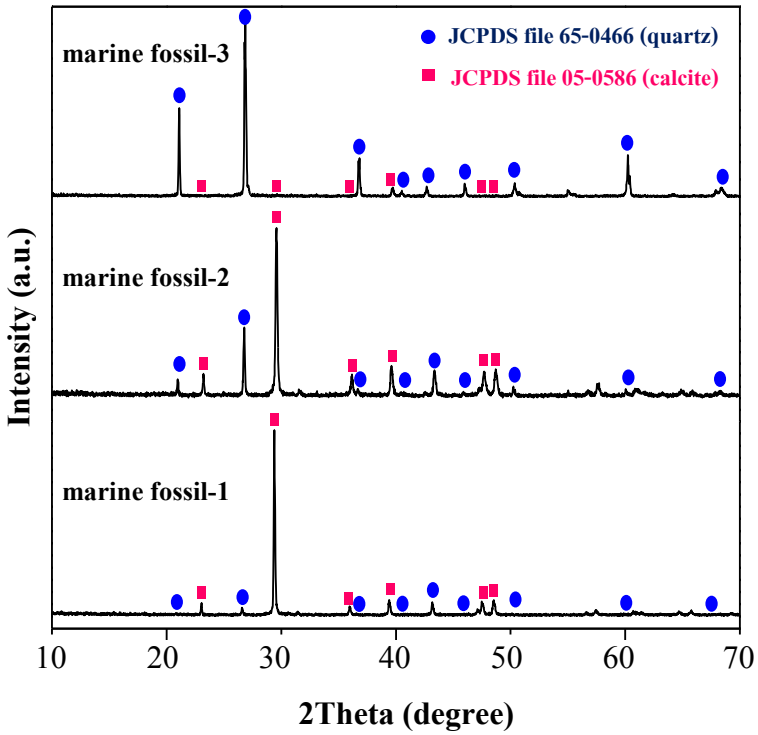

Figure 3. The XRD pattern of the marine fossils.

Figure 3 showed the XRD patterns of all marine fossils were considered in the range of 2theta from 10 to 70 degree. The XRD pattern of marine fossil-1 showed the highest main peak at 2Theta of 26.636 and other peaks at 20.856, 36.540, 42.446, 45.788, 50.132, 59.95 and 68.302 degree, corresponding to the joint committee on powder diffraction standard (JCPDS) file number 65-0466, which was the crystal structure of quartz phase (SiO_2).[9] In addition, the XRD pattern of marine fossil-1 occur at 23.022, 29.405, 35.965, 39.401, 47.489 and 48.512 degree, according to JCPDS file number 05-0586 of calcite phase ($CaCO_3$).[10] The marine fossil-2 and marine fossil-3 showed the XRD pattern similar with marine fossil-1. Considering the intensity of XRD pattern of calcite phase, the marine fossil-1 was higher more than other while the intensity of quartz phase of marine fossil-3 was the highest. The quantity of phase composition was calculated from XRD pattern by Rietveld refinement analysis as shown in Table 1.

Table 1. The phase composition of marine fossils.

Sample	Phase composition (%)	
	Calcite	Quartz
marine fossil-1	96.752	3.248
marine fossil-2	80.524	19.476
marine fossil-3	6.155	93.844

From Table 1, the calcite phase of marine fossil-1, marine fossil-2 and marine fossil-3 were 96.752, 80.524 and 6.155 %, respectively while the quartz phase of marine fossil-1, marine fossil-2 and marine fossil-3 were 3.248, 19.476 and 93.844 %, respectively.

In general, the shell from marine fossil-1 and marine fossil-2 consist of the main calcium carbonate more than 95 % .[11] The decreasing of calcium carbonate in marine sample-2 and marine fossil-3 indicated silicification effect. This means that the shell deposal induced the calcium carbonate decomposition leading to the pore appearance on surface shell.[12] Then, the silica from sediment, surrounding the shell diffused in these pores until quartz formation. From the increasing quartz and decreasing calcite phase of marine fossil implied the decomposition of shell for a long time.[13]

To clear age estimation, the marine fossil must investigated on the chemical composition by XRF as shown in Table 2.

Table 2. The chemical composition of samples from XRF.

Sample	Concentration (%)									
	CaO	**SiO_2**	**Al_2O_3**	**K_2O**	**Fe_2O_3**	**MnO**	**MgO**	**BaO**	**SrO**	**Other**
marine fossil-1	86.38	2.82	0.58	0.03	7.39	0.17	0.56	0.63	0.11	1.36
marine fossil-2	69.98	19.41	2.96	0.22	4.56	0.14	1.07	-	0.18	0.73
marine fossil-3	0.84	89.60	6.60	0.33	1.84	0.06	0.44	-	27 ppm	0.61

Table 2 showed the main chemical composition of marine fossil-1 and marine fossil-2 was calcium oxide (CaO) that indicated the calcium content from calcite ($CaCO_3$) phase.[14] The presence of silicon dioxide (SiO_2) of all marine fossil was the results of the quartz phase from the silicification effect.[15] For the amount of calcium and silicon from XRF results was corresponded with the XRD results. The barium oxide (BaO), magnesium oxide (MgO), and strontium oxide (SrO) were found in marine fossil.[16] A few concentration of these chemical composition indicated that the all of fossil is a marine animals in the past. While, the aluminium oxide (Al_2O_3), potassium oxide (K_2O), iron oxide (Fe_2O_3) and manganese oxide (MnO) were found in all marine fossils that these chemical composition are the soil composite.[17] The amount of Al_2O3 and K_2O increased with decreasing of CaO indicating the both diffusion in marine fossil. The increasing of SiO_2 results in the decreasing of Fe_2O_3 and MnO. Because the completely formation of quartz phase depleted the Fe_2O_3 and MnO as an impurity from soil surrounding.[18] Thus, the difference of chemical composition between marine fossil and modern shell is important data that used to evaluate the age of them. Especially, the using chemical composition ratio of strontium (Sr) and calcium (Ca) is well known for preliminary age estimation.

The chemical composition from XRF result was used to calculate the ratio of Sr and Ca from Eq1 and showed in Table 3. The value of Sr and Ca ratio related to the geological time of marine fossil.[19]

$$\text{The ratio of Sr and Ca} = \frac{\text{Sr concentration}}{\text{Ca concentration}} \text{ x } 1000 \qquad (1)$$

Table 3. The composition of calcium and strontium of marine fossils.

Sample	Concentration (%)		Sr and Ca ratio	Geological time
	Ca	Sr		
marine fossil-1	61.330	0.093	1.330	Permian period
marine fossil-2	49.686	0.085	1.711	
marine fossil-3	0.596	23 ppm	0.386	

From the Table 3 showed the Sr and Ca ratio value of marine fossil-1 and marine fossil-2 are 1.330 and 1.711, respectively, while the marine fossil-3 is 0.386. From the result indicated that the value of Sr and Ca ratio of marine fossil-3 is the lowest corresponding with the lapse of time. This phenomenon can describe the transformation of marine fossil as follow: the initial phase of marine fossil is the aragonite phase and then transformed to calcite phase along with loss of strontium in the short period about ten million years. After that, the loss of strontium has continue.[20] Moreover, the surface of coral fossil was roughness more than other shell fossil resulting in high level of silicification effect.[21] However, all value of Sr and Ca ratio are the similar range with the geological time of Permian period. From the results indicated that all marine fossil from Nong Phai district have the geological time corresponding with the archeology reports.[22]

Acknowledgements:

The authors would like to thank Mr. Vikij Phenphak, the officer in Phetchabun province, Ministry of Interior, Thailand for the marine fossils. For the analysis equipment, we are grateful to Thailand Institute of Nuclear Technology (TINT) and Office of Atom for Peace, Thailand (OAP). This research has been supported the financial fund by Science Achievement Scholarship of Thailand (SAST). Finally, thanks to the department of Physics, King Mongkut's University of Technology Thonburi (KMUTT), Thailand for facility supporting in this work.

References:

1. Karns DR, Murphy JC, Voris HK. Trop Nat Hist. 2010;10(1):1-25.
2. Boonsoong A, Panjasawatwong Y, Metparsopsan K. Island Arc. 2011;20(1):107-124.
3. Paungya N, Singtuen V, Won-in K. Geoj. Tour. Geosites. 2020;31:1057-1067.
4. Roberts TR, Jumnongtha J, Nat. Hist. Bull. Siam Soc. 1999;47:153-189.
5. Chitnarin A, Crasquin S, Charoentitirat T, Tepnarong P, Thanee N. Geodiversitas. 2012; 34(4): 801–835.
6. Grün R. Am. J. Phys. Anthropol. 2006.131:2-48.
7. Baliński A. Acta Palaeontologica Polonica. 2012;57(4):897-924.
8. Roche RC, Abel RL, Johnson KG, Perry CT. Coral Reefs. 2011;30(1):195-201.
9. Yu C, Wang M, Dong X, Shi Z, Zhang X, Lin Q. RSC Adv. 2017;7:55748–55749.
10. Koroglu L, Ayas E. Adv Powder Technol. 2018;29: 2835-2844.
11. Zhang J, Chen H, Mu T, Pan Y. Earth Environ. Sci. 2018;170:1-4.
12. Butts SH. The Paleontological Society Papers. 2014;20:15–34.
13. Butts SH. Briggs DEG. Topics in Geobiology. 2010;32:411-430.
14. Wongsaenmai S. SNRU Journal of Science and Technology. 2018;10(1):32-36.
15. Conley DJ, Frings PJ, Fontorbe G, Clymans W, Stadmark J, Hendry KR, Marron AO. Rocha CLDL. Front. Mar. Sci. 2017;4:1-19.
16. Thomas JM, Schop F, Manheim FT. J Paleontol. 1967;41(5):1197-122
17. Yu H, He Z, Shi Z, Kong B. Acta Geochim. 2018;37(4):571-577.

18. Duchac KC, Hanor JS. Precambrian Res. 1987;37(2):125-146.
19. Purton LMA, Shields GA, Brasier MD, Grime GW. Geology. 1999;27(12): 1083-1086.
20. Kazuo S. Mem Fac Sci, Kyoto Univ. Ser. Geol. Mineral. 1970;37:181-187.
21. Majeski AL, Garvin PL. J Int AIDS Soc. 2006;113(3-4):87-99.
22. Fontaine H, Salyapongse S, Suteethorn V. Nat. Hist. Bull. Siam Soc. 2003; 51(1): 37-67.

GENETIC DIVERSITY OF PAINTED STORK *Mycteria leucocephala* IN DUSIT ZOO, THAILAND, BASED ON MITOCHONDRIAL CYTOCHROME *B* SEQUENCES

Damisa Kaminsin,[1] Krittee Piamsanga,[1] Rangsinee Sankhom,[2] Saowaphang Sanannu,[3] Natapot Warrit,[1] Amporn Wiwegweaw[1,*]

[1] Department of Biology, Faculty of Science, Chulalongkorn University, Bangkok, Thailand

[2] Durrell Institute of Conservation and Ecology, School of Anthropology and Conservation, University of Kent, Canterbury, Kent CT2 7NR, UK

[3] Bureau of Conservation and Research, The Zoological Park Organization of Thailand, Bangkok, Thailand

*e-mail: amporn.w@chula.ac.th

Abstract:

The painted stork *Mycteria leucocephala* is a large waterbird in the tropical wetland ecosystem, which is currently experiencing a steady decline in population primarily due to habitat degradation. Thus, captive breeding at the zoo plays an important role in restoring the decreasing numbers and helping the survival of this species. This study aimed to evaluate the level of genetic diversity of painted storks at Dusit Zoo (n = 50) using mitochondrial cytochrome *b* sequence data. The results demonstrated that the genetic diversity of captive painted storks was relatively low with a haplotype diversity of 0.543 and nucleotide diversity of 0.00061. Three distinct haplotypes were identified based on two variable sites of 1,029 nucleotides, with Hap-1 being the most common haplotype (66%). Tajima's D and Fu's F_s revealed no significant deviation from neutrality. Our results suggest that the current population of painted storks at Dusit Zoo may have experienced founder effect (a limited number of female founders) and/or inbreeding depression, resulting in low genetic variation. Our findings provide preliminary genetic information for future painted stork breeding programs in Thailand. However, further studies using co-dominant microsatellite markers are required to quantify the level of inbreeding and to ensure the amount of genetic diversity in this captive population.

Introduction:

The painted stork, *Mycteria leucocephala*, is a non-migratory and a large fish-eating wading bird in the Ciconiidae family. Its distribution is mostly found throughout South and Southeast Asia in coastal mangroves, freshwater marshes, swamp forest, flooded fields, and riverbanks.[1,2,3] The species can therefore be an excellent bioindicator for the abundance of food sources, assessing wetland habitat changes and detecting environmental toxicity and pollution of water.[4,5] In the last few decades, painted stork populations have been declining as a result of urbanization, the conversion of wetlands to agricultural regions, pollution, and hunting for eggs and chicks.[2,6,7] Although the painted stork was classified as a near threatened species on the IUCN Red List, its population continues to decline globally, raising conservation concerns and putting it at risk of local extinction in some areas where habitat degradation is heavily affected.[8,9]

Historically, painted storks were commonly found in the southwestern and peninsular parts of Thailand.[10] Owing to habitat degradation, most of them can now be found in a few locations in the central of Thailand, where wetlands still remain and are suitable for their viability, such as Pak Thale (Phetchaburi Province), Bang Pu (Samut Prakan Province), and

Laem Phak Bia (Phetchaburi Province).[11,12] Accordingly, wetland preservation is one of the important conservation measures for preserving this bird species. In addition, *ex situ* conservation techniques, such as captive breeding programs, can also prevent the imminent population decline of the species.[13,14] At present, five breeding facilities (zoos) for painted storks have been established under the Zoological Park Organization of Thailand under the Royal Patronage of H.M. The King. These zoos are: Dusit Zoo, Bangkok; Nakhon Ratchasima Zoo, Nakhon Ratchasima Province; Khon Kaen Zoo, Khon Kaen Province; Songkhla Zoo, Songkhla Province and Chiang Mai Zoo, Chiang Mai Province. The painted stork's breeding program has been initially established in Dusit Zoo since 1997 by using 70 stork individuals as initials without records of their provenance (i.e., sources, ages, or sexes). A captive breeding program from 1997 to 2018 could enlarge the population number of painted storks to 173 individuals. All of them were raised together in a large aviary under semi-natural conditions (Figure 1). However, a successful breeding program in terms of increasing the number of individuals could not individually guarantee the population's adaptive ability to novel conditions related to environmental changes, genetic diversity is also significant as well. A high level of genetic diversity would allow captive individuals to re-establish self-sustaining populations in the wild if they were reintroduced to their historically distributed.[15,16,17] Thus, sufficient genetic variation of captive populations is crucial for long-term effective breeding programs and conservation management strategies. Therefore, understanding the genetic diversity of currently existing captive populations is necessary prior to conducting further breeding or reintroduction programs. This study aimed to examine the genetic variation of captive painted storks in Dusit Zoo based on the mitochondrial cytochrome *b* sequences. Our results will provide fundamental data for effective breeding program management and conservation planning of the painted stork population in the future.

Figure 1.
The painted storks (right) and their captivity at Dusit Zoo (left), Bangkok, Thailand.

Methodology:

Sample collection and DNA extraction

173 captive *M. leucocephala* in Dusit Zoo were caught by zookeepers and staff using drop net traps for collecting blood samples for an annual health check. All birds were recorded their body weight and rung for individual identification using a mark recapture ring. Approximately 300 µl of blood was collected from the subclavian vein by the zoological park veterinarian team using a 1 ml syringe. Blood samples were immediately stored in a 1.5 ml tube coated with EDTA for blood coagulating prevention. In this study, only 50 adult birds (24 males and 26 females) were selected for genetic analyses. Total DNA was subsequently

extracted from blood samples using the FavorPrep™ tissue genomic DNA extraction mini kit (Favorgen Biotech corp., Taiwan) following the manufacturer's protocol. The experimental protocol was approved by the Animal Care and Use Committee of Faculty of Science, Chulalongkorn University (Protocol Review No. 1823015).

DNA amplification and sequencing

The mitochondrial cytochrome *b* gene was amplified by polymerase chain reaction (PCR), using primer L14990 (5'-CCATCCAACATCTCAGCATGATGAAA-3') and H16065 (5'-GGAGTCTTCAGTCTCTGGTTTACAAGAC-3').[18] The PCR reaction was set up for a 45 µl reaction containing 2 µl of DNA template (approximately 30–50 ng), 0.5 µM of each primer and 1x premix of EmeraldAmp® MAX PCR master mix (Takara, Japan). PCR amplification was proceeded on Bio-Rad T100 (Biorad) under thermal cycling conditions: initial denaturation at 93°C for 3 min, followed by 35 cycles of denaturation at 93°C for 30 sec, annealing at 52°C for 1 min, extension at 72°C for 1.15 min, and a final extension at 72°C for 10 min. The sizes of amplicons were checked by electrophoresis using 0.8% (w/v) agarose gel, staining with SYBR®Safe DNA gel stain (Invitrogen™), and visualized under blue light transilluminator. The desired PCR products were purified via gel extraction and sequenced by Bionics Inc. in South Korea.

Genetic data analyses

All sequences were manually checked and aligned using Clustal W algorithm embedded in MEGA v.7.01.[19] The number of polymorphic sites (p), average number of pairwise nucleotide differences (*k*), the number of haplotypes (H), haplotype diversity (*h*) and nucleotide diversity (π) were calculated by DnaSP v.6.12.03.[20] Mean transition/transversion ratio and pairwise genetic distance (p-distance) were determined using Kimura 2-parameter distance via MEGA. Phylogenetic trees were constructed using Maximum likelihood and Bayesian Inference methods. The Maximum likelihood tree was conducted in PhyML v.3.0[21] using GTR+G+I model based on the Bayesian Information Criteria (BIC) and 1,000 bootstrap replicates. The Bayesian tree was performed in MrBayes v.3.2.1[22] running 10 million generations with sampling every 100 steps and a burn-in of 25,000 generations, and the resulted tree was visualized via Figtree v.1.4.4[23]. Nucleotide sequences of cytochrome *b* genes of *M. cinerea* (Genbank Accession No. U72778.1), *M. ibis* (U72784.1) and *M. americana* (AF082066) were used as outgroups for both analyses.

Results and Discussion:

A total of 1,029 bp of cytochrome *b* sequence data was successfully obtained from all 50 painted stork samples. No indels were observed in the alignments and they could be translated into amino acid sequences without internal stop codons. The average A, T, C, and G compositions were 25.3, 23.1, 37.8, and 13.8%, respectively, and the C+G (51.6%) content was slightly higher than A+T (48.4%). This result is similar to those found in cytochrome *b* sequences of other bird species.[18,24] Kimura-2-parameter genetic distance between stork individuals ranged from 0 to 0.002. Two variable sites (0.19%) were detected from all aligned sequences, defining three haplotypes for *M. leucocephala* mtDNA, with Hap-1 is the most common haplotype shared by 33 individuals (Table 1); resulted phylogenetic trees also support this. According to the Bayesian and maximum likelihood trees, all painted stork haplotypes were nested within the same clade and formed a monophyletic group, and were clearly separated from the outgroups with high support values (Figure 2). We additionally found that the nucleotide sequence of Hap-2 is 100% identical to the cytochrome *b* sequence of painted stork from San Diego Wild Animal Park, USA (U72777.1), implying that the Hap-2 haplotype is not unique to Thai painted stork. Moreover, of 26 females analyzed, our results

indicated that only three possible maternal lineages would be able to contribute to future generations if these female storks were used as breeding stock. As a result, further genetic examination of the remaining stork individuals at Dusit zoo is required to find more female birds with distinct mtDNA haplotypes in order to enhance genetic variation of the subsequent generation.

Table 1.
Variable sites of haplotypes in the cytochrome *b* sequences of 50 painted storks. The number of individuals and frequency of each haplotype are shown in the two columns on the right.

Haplotype	Nucleotide position		Number of individuals	% Frequency
	801	1017		
Hap-1	T	A	33 (PS16, 20, 41, 43, 49, 50, 51, 76, 79, 80, 81, 91, 92, 97, 99, 104, 105, 106, 107, 108, 110, 114, 115, 116, 117, 121, 127, 129, 132, 137, 147, 157 & 171)	66
Hap-2	C	A	12 (PS15, 18, 46, 72, 84, 94, 95, 112, 113, 130, 136, & 165)	24
Hap-3	C	G	5 (PS7, 14, 37, 48 & 58)	10

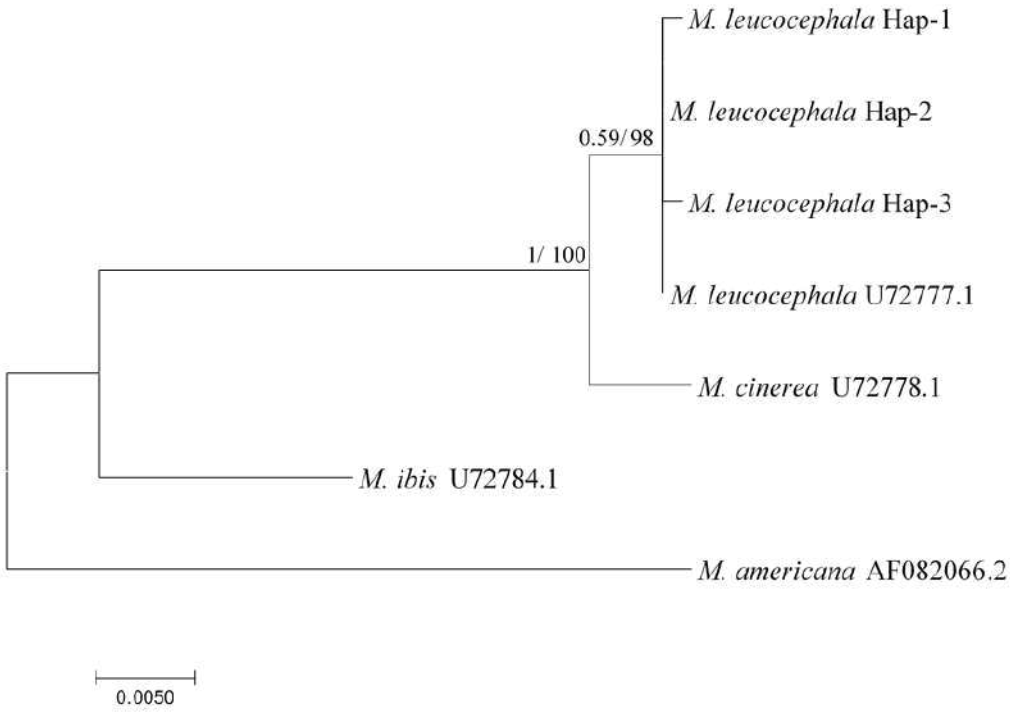

Figure 2.
Phylogenetic tree constructed by Bayesian Inference and Maximum likelihood methods based on mitochondrial cytochrome *b* sequences of *M. leucocephala* from Dusit zoo and its related species. Numbers at each node indicated Bayesian posterior probabilities (left) and maximum likelihood bootstrap values (right).

Table 2.
Genetic diversity in the mitochondrial cytochrome *b* sequences of captive painted storks at Dusit Zoo

Population	n	p	*k*	H	*h* ± S.D.	π ± S.D.	Tajima's D (*p*-value)	Fu's F_s (*p*-value)
DZ	50	2	0.642	3	0.507 ± 0.064	0.00062 ± 0.00009	0.780 (p>0.1)	0.927 (0.278)

n; number of individuals, p; number of polymorphic sites, *k*; average number of pairwise nucleotide differences, H; number of haplotypes, *h*; haplotype diversity, π; nucleotide diversity

Tajima's D and Fu's F_s revealed positive values with no significant difference, suggesting that the mtDNA region under examination did not depart from the neutral mutation model. Haplotype (*h*) and nucleotide (π) diversity indices were 0.507 ± 0.064 and 0.00062 ± 0.00009, respectively, indicating low genetic diversity in the captive painted stork population (Table 2). These results are similar to those previously reported in other captive birds such as black-winged myna *Acridotheres melanopterus* (h = 0.606, π = 0.00242, n = 24)[25], blue-crowned laughingthrush *Garrulax courtoisi* (h = 0.380, π = 0.11, n = 23)[26] and eclectus parrot *Eclectus roratus* (h = 0.500, π = 0.00443, n = 13)[27]. According to records, approximately 70 stork individuals were used as breeding stock at the beginning, hence the low genetic diversity of painted stork in Dusit Zoo in terms of haplotype diversity, may result from a small number of female founders (founder effect), since Witzenberger and Hochkirch (2011) proposed that a minimum number of 15 founders may be sufficient to minimize the loss of genetic diversity in captivity. Unfortunately, there is no information on the founders' origins and backgrounds to draw any conclusions. Furthermore, the presence of low genetic diversity may also be linked to other factors such as the reproductive capability of female founders, inbreeding, human interference in captive facilities, and the use of genetic markers.[28] In the latter case, since the cytochrome *b* gene for the whole avian mitochondrial genome is a conserved region with approximately a substitution rate of 2%/Myr and often evolves at a substantially slower rate than non-protein-coding regions (e.g., control region).[18,29] The genetic diversity observed in the present study was therefore considerably lower than those studies with the control region.[30,31] We were originally interested in using control region as a genetic marker to evaluate genetic diversity, but we failed to amplify a desired fragment of this region. We recommended that a comprehensive assessment of genetic diversity should not depend on a single marker, especially mitochondrial DNA which displays only one maternal inheritance, other nuclear markers should be included (e.g., microsatellite markers) in order to ensure a certain amount of intrinsic genetic diversity as well as inbreeding in this captive stork population.[17] Finally, for the effective management of the breeding program for painted stork conservation in Thailand, the genetic diversity analysis of this stork species in other zoos (e.g., Nakhon Ratchasima Zoo, Khon Kaen Zoo, Songkhla Zoo and Chiang Mai Zoo) and wild populations are required. Zoo-to-zoo genetic exchange, periodic additions of wild-caught specimens to captivity as well as precise procedures for preventing inbreeding (i.e., avoiding mating between closely related individuals), would be critical to reducing genetic diversity loss.[15,17] Although the painted stork has not yet been listed as an endangered species, its population trend is declining as habitat destruction intensifies. Therefore, for the long-term survival of the painted stork in Thailand, the preservation of its wetland habitats and ecosystem should be done in

combination with population recovery in captivity, not only in population numbers but also in the maintaining of genetic variation.

Conclusion:

Our findings revealed low genetic variation of mitochondrial cytochrome *b* sequences, with three common haplotypes found among 50 painted stork individuals in Dusit Zoo. The results provide preliminary information for future painted stork breeding programs and conservation planning as well as awareness of the low level of genetic diversity, in terms of haplotype diversity, of this captive population. We additionally recommended that the genetic diversity of other populations of painted stork both in captivity and in the wild should be evaluated.

Acknowledgements:

This research was financially supported by the Graduate School of Chulalongkorn University Fund, the Development and Promotion of Science and Technology Talents Project (DPST) and the Department of Biology, Faculty of Science, Chulalongkorn University. We would like to express our sincere gratitude to the chief and staff of Dusit Zoo for their support and assistance in sample collecting. We are grateful to the Zoological Park Organization of Thailand under the Royal Patronage of H.M. The King for giving permission for this study. We would also like to thank Miss Kotchaporn Phansawat and Miss Jiratchaya Rattanasila for their assistance in the field and sample collection.

References:

1. Sundar KSG, Waterbird. 2006;29:365–374.
2. Sundar KSG, Chauhan AS, Kittur S, Babu S. Wetlands. 2014;35:115–125.
3. Kushwaha S, Kumar A. Int. j. trend res. dev. 2018;3:958–965.
4. Lopes IF, Miño CI, Del Lama SN. Braz. J. Biol. 2007;67:849–857.
5. Urfi AJ. Waterbirds. 2011;34:448–456.
6. Urfi AJ. Forktail. 2007;23:150–153.
7. Prabhakar CS, Dudhmal D. Sci. Res. Repot. 2016;6:50–57.
8. Luthin CS. Col. Waterbirds. 1987;10:181–202.
9. IUCN. The IUCN Red List. 2016. Downloaded from http://www.iucnredlist.org/
10. Morioka H, Yang CM. Jap. J. Ornithol. 1990;38:149–150.
11. Nabhitabhata J, Lekhakul K, Sanguansombat W. Bird of Thailand. 2007;1:234–235.
12. Thai National Parks. 2021. Downloaded from http://www.thainationalparks.com/
13. Fraser DJ. Evol Appl. 2008;1:535–586.
14. Schulte-Hostedde AI, Mastromonaco GF. Evol Appl. 2015;8:413–422.
15. Ballou JD. Zoo Biol. 1984;3:311–323.
16. Robert A. Biol. Conserv. 2009;142:2915–2922.
17. Witzenberger KA, Hochkirch A. Biodivers Conserv. 2011;20:1843–1861.
18. Kocher TD, Thomas WK, Meyer A, Edwards SV, Paabo S, Villablanca FX, Wilson AC. Proc. Natl. Acad. Sci. 1989;86:6196–6200.
19. Kumar S, Stecher G, Tamura K. Mol Biol Evol. 2016;33:1870–1874.
20. Rozas J, Ferrer-Mata A, Sanchez-DelBarrio JC, Guirao-Rico S, Librado P, Ramos-Onsins SE, Sanchez-Gracia A. Mol Biol Evol. 2017;34:3299–3302.
21. Guindon S, Dufayard JF, Lefort V, Anisimova M, Hordijk W, Gascuel O. Syst. Biol. 2010;59:307–321.
22. Ronquist F, Teslenko M, van der Mark P, Ayres DL, Darling A, Hohna S, Larget B, Liu L, Suchard MA, Huelsenbeck JP. Syst. Biol. 2012;61:539–542.

23. Rambaut A. Institute of Evolutionary Biology, University of Edinburgh, Edinburgh. 2010. Downloaded from http://tree.bio.ed.ac.uk/software/figtree/
24. Uddin A, Chakraborty S. Mitochondrial DNA A. 2017;28:187–196.
25. Astuti D, Rachmatika R. AIP Conf. Proc. 2019;2120:1–7.
26. Chen G, Chenqing Z, Wan N, Liu D, Fu VWK, Yang X, Yu YT, Liu Y. PeerJ. 2019;7:e6643.
27. Astuti D. IOP Conf. Ser.: Earth Environ. Sci. 2020;591:1–6.
28. Ping-ping J, Qiu-lei L, Sheng-guo F, Ping D, Li-ming C. J Zhejiang Univ SCI. 2004;6:413–417.
29. Lovette IJ. The Auk. 2004;121:1–6.
30. Lopes IF, Tomasulo-Seccomandi AM, Bryan Jr AL, Brisbin Jr IL, Glenn TC, Del Lama SN. Genet. Mol. Res. 2011;10:1910–1922.
31. Yamamoto Y. Reintroduction. 2011;1:77–80.

CRYSTAL STRUCTURE OF ONE-DIMENSIONAL LADDER CHAIN-LIKE STRUCTURE CADMIUM(II) COORDINATION POLYMER

Kulwadee Ponanunrirk,[1,2] Kittipong Chainok,[2] Nanthawat Wannarit[1,2]*
[1]Department of Chemistry, Faculty of Science and Technology, Thammasat University, Klong Luang, Pathum Thani 12121, Thailand,
[2]Materials and Textile Technology, Faculty of Science and Technology, Thammasat University, Klong Luang, Pathum Thani 12121, Thailand.
*Correspondence e-mail: nwan0110@tu.ac.th

Abstract:

A new 1D coordination polymer, $[Cd(benz)(4,4'\text{-bipy})(NO_3)]_n$ (**1**) (benzH = benzoic acid and 4,4′-bipy = 4,4′-bipyridine) has been synthesized and characterized. The crystal structure of **1** was determined by using single-crystal X-ray diffraction. Compound **1** crystallizes in the monoclinic crystal system with $P2_1/c$ space group. For the structure of this compound, each Cd(II) center has coordination environment with $[CdN_2O_4]$ chromophore from two benzoate, two 4,4′-bipy molecules, and a coordinated nitrate ion, resulting a distorted-octahedral geometry. Two closed Cd(II) ions are connected by carboxylate group of two bridging benzoate with *syn-anti* coordination mode and these dimeric units are further linked by 4,4′-bipy ligands to form a 1D ladder chain-like structure in crystallographic *a* axis. The packing structure is stabilized by supramolecular interactions such as hydrogen bonding, π···π and C-H···π interactions. In addition, the solid-state photoluminescent properties of compound **1** exhibits wavelength-dependent emission in the range of 330-370 nm.

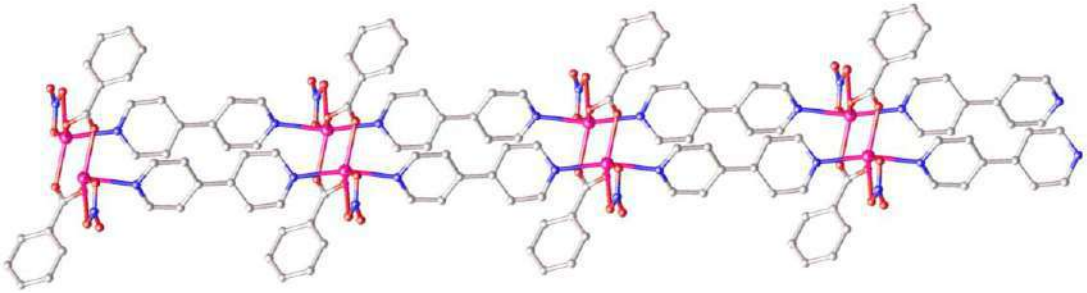

Figure 1. View of 1D ladder chain-like structure of compound **1**

CRYSTAL STRUCTURE OF SILVER (I) BROMIDE COMPLEX CONTAINING 4-PHENYLTHIOSEMICARBAZIDE AND TRIPHENYLPHOSPHINE LIGANDS

Kantima Muangjeen[1], Yupa Wattanakanjana[1]*
[1]Division of Physical Science, Faculty of Science, Prince of Songkla University, Hatyai, Songkhla 90112, Thailand
*e-mail: yupa.t@psu.ac.th

Abstract:
The reaction of silver(I) bromide with triphenylphosphine (PPh_3) and 4-phenylthiosemicarbazide (4-PTSC) gave mononuclear complex of formula [AgBr(4-PTSC)(PPh_3)$_2$]·H_2O. The structure of the complex was characterized by infrared (IR) spectra, single crystal X-ray diffraction. The Ag(I) ion exhibits distorted tetrahedral coordination with two P atoms from two PPh_3 ligands, one terminal S atom from the 4-PTSC ligand and bromide ion. Intramolecular N—H···Br and N—H···N hydrogen bonds are observed (graph set motif S(6) and S(5), respectively). In the crystal, the complex molecules are linked to form dimers via bifurcated N—H···Br hydrogen bonds involving the amine and bromide groups.

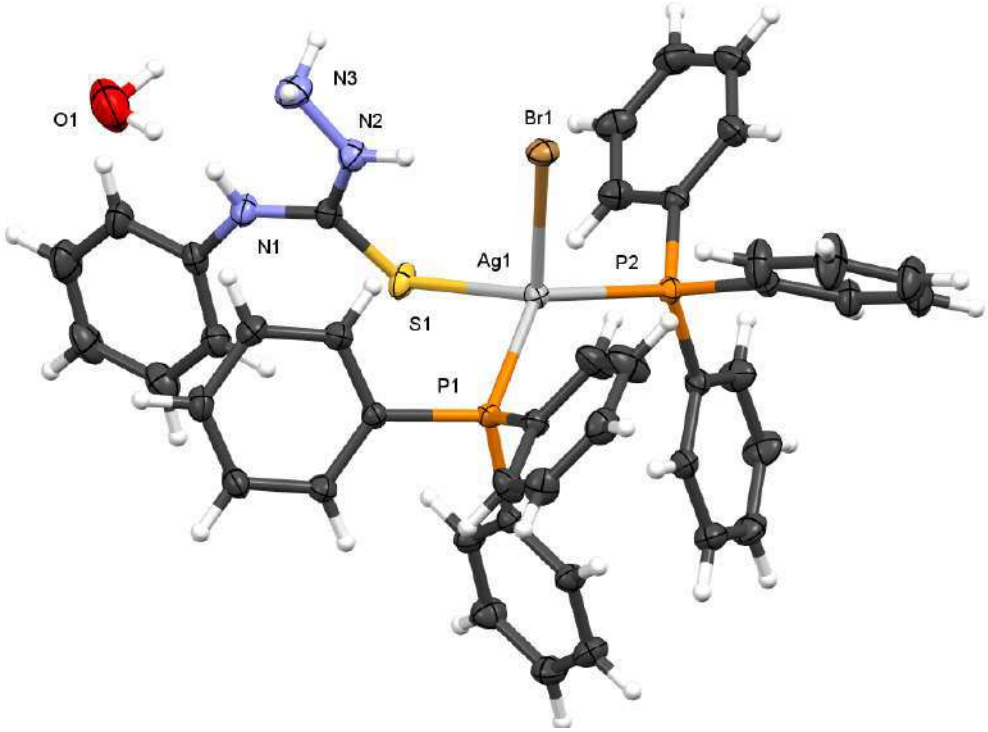

Figure 1. The molecular structure of [AgBr(4-PTSC)(PPh_3)$_2$] ·H_2O, with displacement ellipsoids drawn at the 50% probability level.

CRYSTAL STRUCTURES AND HIRSHFELD SURFACE ANALYSIS OF NEW MONO- AND DINUCLEAR COPPER(II) COMPLEXES CONTAINING MIXED DIIMINE AND HYDROXYBENZOATE DERIVATIVE LIGANDS

Wanussanun Chaisuriya[1,2], Kittipong Chainok[2], and Nanthawat Wannarit[1,2*]

[1]Department of Chemistry, Faculty of Science and Technology, Thammasat University, Pathum Thani, Thailand, 12121
[2]Thammasat University Research Unit in Multifunctional Crystalline Materials and Applications (TU-MCMA), Faculty of Science and Technology, Thammasat University, Klong Luang, Pathum Thani 12121, Thailand
*e-mail: nwan0110@tu.ac.th

Abstract:

Three new copper(II) complexes namely $[Cu(2,2'\text{-bpy})_2(3\text{-OHbenz})_2]NO_3$ (**1**), $[Cu(dpyam)(4\text{-OHbenz})_2]\cdot H_2O$ (**2**) and $[Cu_2(phen)_2(2\text{-Obenz})_2](2\text{-OHbenzH})$ (**3**) when diimine ligands: 2,2′-bpy = 2,2′-bipyridine, dpyam = 2,2′-dipyridylamine and phen = 1,10-phenanthroline; hydroxybenzoate derivatives: 2-OHbenzH = 2-hydroxybenzoic acid, 3-OHbenz = 3-hydroxybenzoate and 4-OHbenz = 4-hydroxybenzoate have been successfully synthesized and characterized. The crystal structures of these complexes have been determined by single-crystal X-ray diffraction. Mononuclear complexes **1** and **2**, the Cu(II) ion adopts a distorted trigonal-bipyramidal geometry for complex **1**, while that of complex **2** exhibits a distorted square planar geometry. For dinuclear complex **3**, the environment of Cu(II) ion is distorted trigonal bipyramidal geometry. Two Cu(II) ions in complex **3** are bridged by two monoatomic hydroxo bridges from deprotonated hydroxy group of 2-OHbenz ligands. The crystal structures of these complexes have been stabilized by intermolecular interactions including hydrogen bonding, π···π and C–H···π. To study the intermolecular interactions of all synthesized complexes, the Hirshfeld surfaces analysis and fingerprint plots have been investigated.

CRYSTALLIZATION AND CHARACTERIZATION OF MONOSODIUM URATE AND CALCIUM PYROPHOSPATE CRYSTALS AS CAUSE OF GOUTY ARTHRITIS

Waralee Srinarawat, and Jirarut Wongkongkatep*

Department of Biotechnology, Faculty of Science, Mahidol University, Bangkok 10400, Thailand
*E-mail: jirarut.chu@mahidol.ac.th

Abstract:

Almost all elderly confronts multiple health problems that prevent their full participation in society. Gouty arthritis is one of aging diseases that frequently found. This disease is caused by the prolonged hyperuricemia leading to the formation of monosodium urate crystal (MSU). The crystals induce innate immune response and cause inflammation in and around the joint. Another disease that related with crystal-induced inflammation is pseudogout. The excessive concentration of inorganic pyrophosphate induces the crystallization of calcium pyrophosphate dihydrate (CPPD) and leads to inflammation. This study aimed to prepare and characterize the crystals of MSU and 2 polymorphs of CPPD, which are monoclinic calcium pyrophosphate dihydrate (m-CPPD) and triclinic calcium pyrophosphate dihydrate (t-CPPD). The as-synthesized MSU, m-CPPD and t-CPPD crystals were characterized by complementary techniques including powder X-ray diffraction (XRD), Fourier-transform infrared spectroscopy (FT-IR), Raman spectroscopy, scanning electron microscopy (SEM) and thermogravimetry analysis (TGA). The crystallization method gave high yield of needle-shaped MSU, rod-shaped m-CPPD and rhomboid-shaped t-CPPD crystals which are 72.5%, 97.6% and 93.8%, respectively. The characterization techniques confirm the composition and polymorph of the crystals. The characterized crystals were further stained with some suitable fluorescent dyes as a newly proposed methodology for crystal identification which will definitely assist the diagnosis of gouty arthritis.

Keywords: calcium pyrophosphate dihydrate; fluorescence; gout; monosodium urate; pseudogout

Introduction:

Arthritis is aging-associated diseases that generate the infliction of pain and severe joint inflammation. Gout is one of arthritis, and produces serious illness as a result of crystal-induced inflammation process. The long term of hyperuricemia or high level of urate in blood induces the crystallization of monosodium urate monohydrate (MSU) crystals.[1] The accumulation of MSU crystals activates NOD-like receptor related protein 3 (NLRP3) inflammasome signaling pathway and generates interleukin-1β (IL-1β).[2] Aside from MSU crystal, calcium pyrophosphate dihydrate (CPPD) crystal is considered as a root cause of another type of arthritis which is previously known as pseudogout or calcium pyrophosphate dihydrate deposition disease. The crystallization of CPPD crystal occurs when the activity of ecto-nucleotide pyrophosphatase/phosphodiesterase 1 (ENPP1) is abnormal which causes the over-production of inorganic pyrophosphate (PPi). The excessive PPi binds with calcium ion and leads to the formation of CPPD crystals.[3] There are two polymorphs of CPPD crystals found in pseudogout patient's synovial fluids which are monoclinic calcium pyrophosphate

dihydrate (m-CPPD) and triclinic calcium pyrophosphate dihydrate (t-CPPD). Both m-CPPD and t-CPPD were reported to cause acute and chronic inflammation.[4] The symptoms of gout and pseudogout are quite similar which are pain, stiffness, erythema and swelling around the affected joint. Acute pain reaches its highest point within 24 to 48 hours and relieves in 7 to 10 days without treatment. However, the pain will be occurred again after 6 months to 2 years.[5]

The medical diagnosis for gout and pseudogout starts with the physical examination, patient's history and uric acid level investigation. In equivocal cases, synovial fluids are collected to identify the type of crystal by a compensated polarized light microscopy. MSU crystal is needle-like shape which show negative birefringence under compensated polarized light microscopy. While CPPD crystal appears weakly positive birefringence of rhomboid-shaped crystal. In some cases, X-rays will be used to observe the accumulation of CPPD crystals or chondrocalcinosis[6] and show asymmetric swelling within a joint or subcortical cyst without erosions for gout.[7] However, the downside of compensated polarizing light microscopy method is its moderate sensitivity, depending on operator's skill which may result as high as 30% false-negative rate.[8] While X-rays is also lack of sensitivity in diagnosis because only 45% of gout patients show radiographic bone change and only after 6-8 years of the first attack.[9]

Herein, we studied the formation and characterization of MSU, m-CPPD and t-CPPD crystals using powder X-ray diffraction (XRD), Fourier-transform infrared spectroscopy (FT-IR), Raman spectroscopy, scanning electron microscopy (SEM) and thermogravimetric analysis (TGA). Then the screening of fluorescent dyes for crystal identification was conducted further as a novel and useful tool for differentiation of gout and pseudogout cases.

Methodology:

Materials. All commercially available chemicals are of reagent grade and were used as received without further purification. Thioflavin T, 7-hydroxycoumarin ($C_9H_6O_3$), sodium pyrophosphate decahydrate ($Na_4O_7P_2{\bullet}10H_2O$), uric acid ($C_5H_4N_4O_3$) and Nile red ($C_{20}H_{18}N_2O_2$) were purchased from Wako Pure Chemical Industries, Ltd., Japan. Calcium chloride ($CaCl_2$) and sodium hydroxide (NaOH) were obtained from Ajax Finechem Pty Ltd, Taen Point, Australia. Acetic acid glacial 100%, Alizarin red S monosodium salt ($C_{14}H_7NaO_7S$) and 25% ammonia solution were bought from Merck KGaA, Darmstadt, Germany. Acridine orange hydrochloride hydrate ($C_{17}H_{19}N_3{\cdot}HCl{\cdot}xH_2O$), Berberine chloride form ($C_{20}H_{18}ClNO_4$) were purchased from Sigma-aldrich, Co., Saint Louis, USA. Nonyl acridine orange ($C_{26}H_{38}BrN_3$) was obtained Invitrogen (Thermo Fisher), Oregon, USA.

Crystallization of MSU crystals. MSU crystals were prepared as described by Denko and Whitehouse (1976).[10] Typically, 2.00 g of uric acid was weighed and added to 400 ml of deionized water under ambient air. The solution was continuously stirred and heated to 60 ºC for 30 minutes, then an appropriate volume of 2 M NaOH was added to adjust pH of the solution to 8.9 to obtain the clear solution. Then the solution was cooled down to room temperature and allowed to crystallize for 18 hours at room temperature. The obtained white powder was filtered through Whatman grade 1 filter paper and dried in hot-air oven at 180 ºC for 2 hours. The obtained MSU crystal was 1.84 g (yield 72.5%) and kept in a sealed vial stored inside a desiccator at room temperature.

Crystallization of CPPD crystals. The methods for m- and t-CPPD synthesis were slightly modified from Gras's method.[4] Ammonium acetate buffer was prepared by mixing 6 ml of glacial acetic acid with 200 ml of deionized water before the pH was adjusted to 5.8

and 3.6 with 25% ammonia solution for synthesis of m- and t-CPPD, respectively. The buffer was continuously stirred and heated until the temperature reached 90ºC. Next, $CaCl_2$ aqueous solution (100 ml) (76.25 mM for m-CPPD and 302.97 mM for t-CPPD) and sodium pyrophosphate decahydrate (NaPPi) (100 ml) (50.35 mM for m-CPPD and 151.02 mM for t-CPPD) were fed simultaneously into the buffer solution at feeding rate of 4.5 ml/min using Masterflex L/S® 77202-50. After 22 minutes of vigorous stirring, the feedings were stopped and the solution was continuously heated for 1 hour. The solution was filtered and the residue was dried in a hot air oven at 180°C for 2 hours. The dried weights of the obtained m- and t-CPPD crystals were 1.46 g (yield 97.6%) and 4.11 g (yield 93.8%), respectively. The crystals were kept in a sealed vial and stored inside a desiccator at room temperature.

Characterization of the crystals. XRD measurements were performed with a Bruker AXS model D8 discover equipped with Cu radiation set at 40 mA current and 40 kV voltage. The crystals were scanned from 2-70º in the 2θ range with a scanning rate of 0.0116º per minute at 25ºC. FT-IR spectrums of the crystals were characterized by a PerkinElmer frontier FTIR with 4 cm^{-1} resolutions and 16 scans per spectrum over the wavenumber range of 4000 - 400 cm^{-1}. Raman spectroscopy was performed to characterize the crystal using a Horiba XploRA PLUS confocal Raman microscope over the wavenumber range of 50-3400 cm^{-1} with laser source at 532 nm. SEM was employed to clearly observe the micro-scaled structure of the crystal. The crystals were observed on a Hitachi SU 8010 ultra-high resolution field emission scanning electron microscope operated under vacuum with an accelerating voltage of 10 kV. The sample were coated with platinum/palladium for 1.5 minutes before observation. TGA was performed with PerkinElmer TGA 4000 in the temperature range of 30-500°C at a heating rate of 5°C per minute.

Screening of fluorescent dyes. Approximately 0.04 mg of each MSU, m- or t-CPPD crystal was gently placed on a glass coverslip. Then, 1 µl of the selected fluorescent dye solution (1 mM), or 0.006% w/v in the case of Alizarin red S, was dropped on the crystal and pipetted up and down for a complete mixing. The coverslip was then heated on a hotplate at 75°C for 5 minutes to dry the stained sample. Then the coverslip was placed on a cavity slide using a hanging drop technique. The morphology, birefringence and fluorescence of the stained crystals was observed under Olympus BX51 fluorescence microscope equipped with U-GAN gout analyzer.

Results and Discussion:

Crystal formation. A complete dissolution of uric acid under alkaline pH is considered as a key process to successfully obtain the MSU crystals in the test tube. The needle-shaped crystals with negative birefringence of MSU were imaged under a microscope equipped with U-GAN gout analyzer which provided a polarized light suitable for the birefringence analysis. The as-prepared MSU crystals displayed a strong negative birefringence as shown in Figure 1a, with the yield of 72.5% and average size of 32.56±10.46 µm. The synthesis of m- and t-CPPD required different pH to obtain different polymorphism because pH 5.8 was suitable for m-CPPD but pH 3.6 was essential for t-CPPD synthesis. The molar ratio of calcium and PPi ions needed to be maintain at 2:1 throughout the crystallization process to obtain the pure phase of m- and t-CPPD. As displayed in Figure 1b, the rod-shaped of m-CPPD crystals were observed with the average size of 16.72±1.50 µm. While t-CPPD crystal appeared as rhomboid shape with 6.45±1.99 µm wide and 30.66±9.80 µm long (Figure 1c). Both m-CPPD and t-CPPD showed a weakly positive birefringence as

shows in Figure 1. Adaptation from Gras' method[4] gave the synthesis yield of 97.6% and 93.8% for m-CPPD and t-CPPD, respectively.

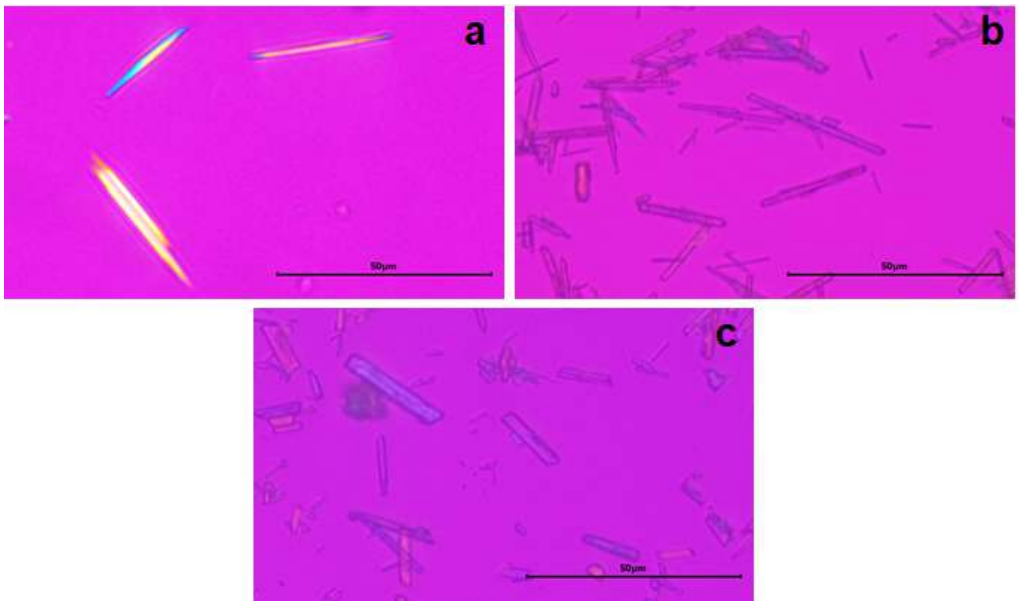

Figure 1. The microscopic images of MSU (a), m-CPPD (b) and t-CPPD (c) crystals observed under polarized light microscope.

Crystal characterization. XRD is generally used for phase identification of a crystalline material and can provide information on unit cell dimensions. The obtained XRD pattern of as-synthesized MSU crystals is shown in Figure 2, and matched well with the previous data reported by Molloy et al. (2019).[11] The pattern suggests the triclinic unit cell of MSU crystals which are a = 10.888 Å, b = 9.534 Å, c = 3.567 Å, α = 95.060º, β = 99.470º and γ = 97.170º, denoted as space group $P\bar{1}$. The crystal structure of MSU was clarified by Mandel and Mandel (1976).[12] The urate anions are bound via hydrogen bonds which aligned along the edges of purine rings, and created 2D parallel sheets of purine rings. Sodium ions are located between the sheet space and bound to 1) urate via cation-π interactions, and 2) one molecule of water through cation-oxygen interaction.[12] One water molecule also binds with the negatively charged nitrogen atom by a hydrogen bonding interaction. Therefore, the MSU crystals contains 1 water molecule per 1 MSU molecule, and should be denoted as monosodium urate monohydrate.

The XRD patterns of m-CPPD and t-CPPD crystals are congruous with the patterns reported by Gras et al. (2013).[4] As showed in Figure 2, the XRD pattern of t-CPPD shows 2 patterns of phased characterization in which the majority is triclinic space group $P\bar{1}$ (a = 7.365 Å, b = 8.287 Å, c = 6.691 Å, α = 102.960º, β = 72.730º and γ = 95.010º) and the minority is monoclinic space group $C2/c$ (a = 15.106 Å, b = 5.672 Å, c = 6.668 Å, α = 90º, β = 102.360º and γ = 90º). The XRD results implied that t-CPPD was not pure phase but contaminated with a small amount of m-CPPD. The XRD pattern obtained for the m-CPPD phase was comparable with the data published by Brown et al. (1963),[13] Liu et al. (2009)[14] and Gras et al. (2013)[4] but did not correspond to the lattice constant determined by Mandel et al. (1988).[15] The structure of m-CPPD has not been resolved by X-ray crystallography but Rietveld refinements suggested a monoclinic space group (a = 12.618 Å, b = 9.250 Å, c = 6.760 Å, α = 90º, β = 104.970º and γ = 90º).[4]

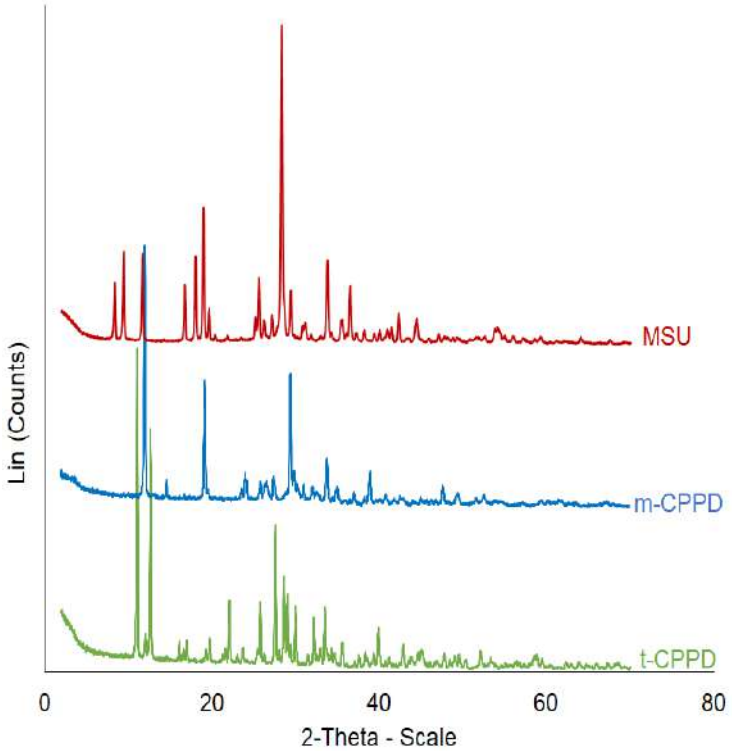

Figure 2. XRD patterns of MSU (red), m-CPPD (blue) and t-CPPD (green)

FT-IR and Raman spectroscopy provide the valuable information on characterization of a pure compound. The obtained MSU crystals were subjected to FT-IR and Raman spectroscopic analyses and the results are shown in Figures 3 and 4, red line. As can be seen in Figure 3, two vibration regions corresponding to O-Na peaks appeared at 531 and 556 cm^{-1} were recorded. The vibration peak of N-H stretching is indicated at 800 cm^{-1} and the peaks of O-H vibration is observed at 1660 and 2700-3500 cm^{-1}. Raman spectrum of MSU crystals also confirmed the N-H peak at 785 cm^{-1}, purine ring vibration at 627 cm^{-1} and C-N-C vibrations at 381 and 587 cm^{-1}. The results are in good agreement with the previous reported by Li et al. (2020).[16]

Both m-CPPD and t-CPPD crystals were analyzed by FT-IR and Raman spectroscopy as showed in Figures 3 and 4, respectively, and the vibrational regions of FT-IR and Raman spectra are summarized in Table 1. The O-H vibrations in FT-IR spectra of both forms of CPPD were observed around 3700-2900 cm^{-1}. While the peaks of the spectra between 1200 and 700 cm^{-1} can be assigned to P-O and P-O-P vibration. The FT-IR and Raman spectra obtained in this study were comparable with the data reported by Gras et al. (2013).[4]

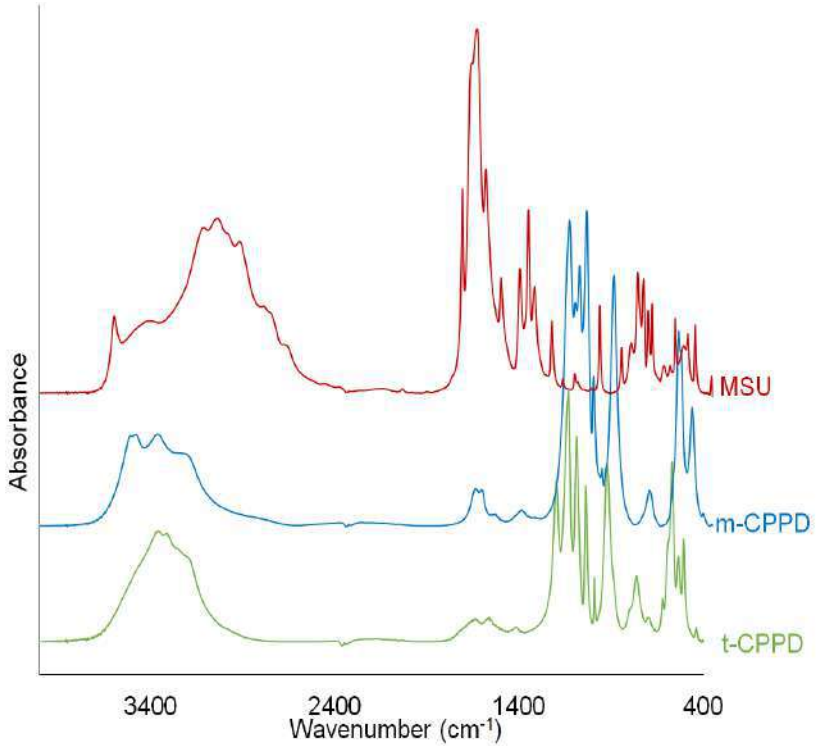

Figure 3. FT-IR spectra of MSU (red), m-CPPD (blue) and t-CPPD (green)

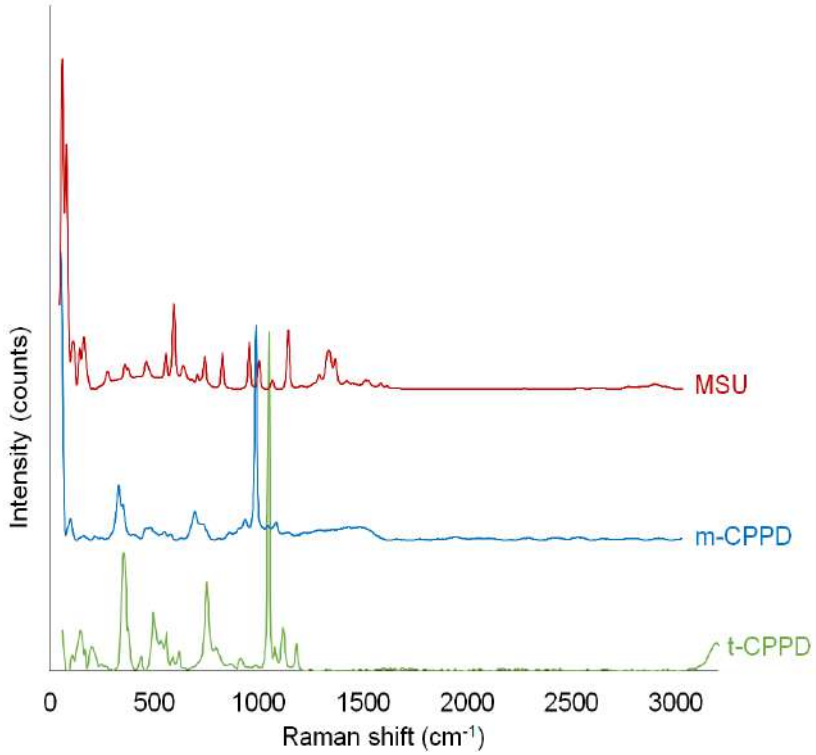

Figure 4. Raman spectrums of MSU (red), m-CPPD (blue) and t-CPPD (green)

Thermogravimetric analysis (TGA) is generally utilized for characterization of the thermal properties of materials. The technique provides information about the composition and purity, decomposition and transition temperatures, and absorbed moisture content of the materials of interest. TGA curve between temperature of 30 and 500ºC showed two steps of weight loss in the crystalline phases for MSU crystal and one step of weight loss in the case

of the m-CPPD and t-CPPD as showed in Figure 5. The first step of 8.7% weight loss of MSU crystal was observed in the temperature range of 108-252 ºC, which is almost identical to the theoretically value of weight loss calculated for one water molecule. For the m-CPPD and t-CPPD crystals, the theoretical value of weight loss of two molecule of water in $Ca_2P_2O_7 \cdot 2H_2O$ was calculated to be 12.4%. The analysis result indicates that the weight loss of the m-CPPD and t-CPPD were found to be 12.4 and 13.1%, respectively, which confirmed that there are two water molecules per one formula unit of calcium pyrophosphate in the crystal lattice of CPPD.

Table 1. Vibrational region of FTIR and Raman spectrum of m-CPPD and t-CPPD crystals

m-CPPD		t-CPPD		Assignment
FT-IR	Raman	FT-IR	Raman	
3519 3485 3369	3355	3359 3311	3233 3197	O-H vibrations
1037	1044	1039	1051	Symmetric PO_3 vibrations
1166 1135 1112 1074 993	1145 1104 990	990	988	Asymmetric PO_3 vibrations
928	912	920	913	Asymmetric POP vibrations
737	770 734	796 762	797 752	Symmetric POP vibrations

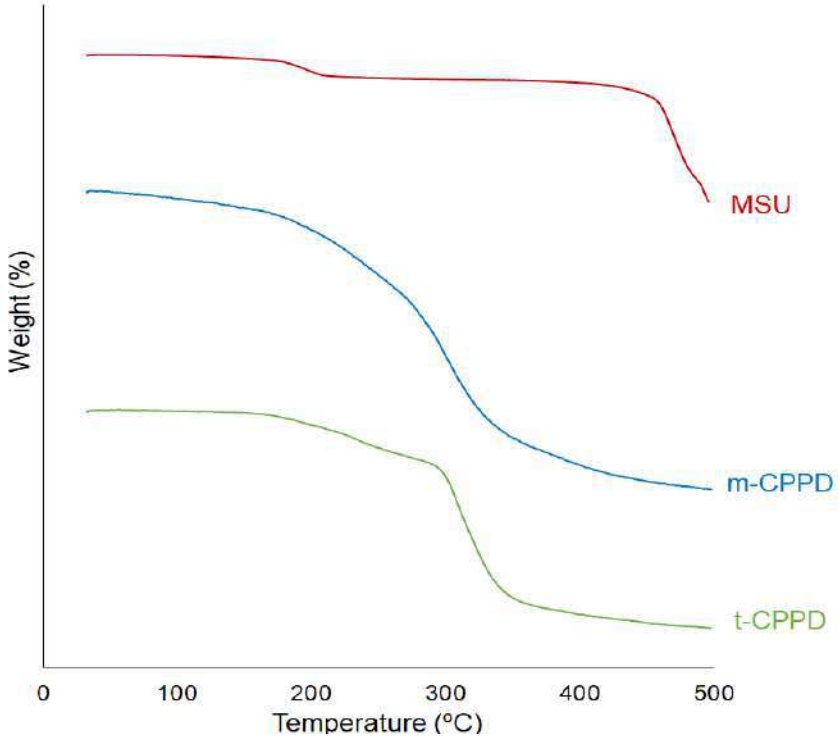

Figure 5. TGA curves of MSU (red), m-CPPD (blue) and t-CPPD (green)

Scanning electron microscope (SEM) technique provides information about the surface topography of the sample. As shown in Figure 6, the surface topographies of MSU, m- and t-CPPD crystals were smooth with some layers appeared especially in the case of m- and t-CPPD. The microscopic images of MSU and m-CPPD crystals revealed the long rod-shaped crystal, however, the habit of MSU is more likely needle shaped crystals. Notably, the observation via a light microscope during the crystallization yielded clearly the needle shape of MSU as displayed in Figure 1a. It is possible that the fragile edge of the needle MSU would be broken during the filtration process before SEM analysis, therefore, only the thin rod shape of MSU crystal was remained in the SEM samples. The t-CPPD is clearly a rhomboid shape with smooth surface and some layers as displayed in Figure 6c.

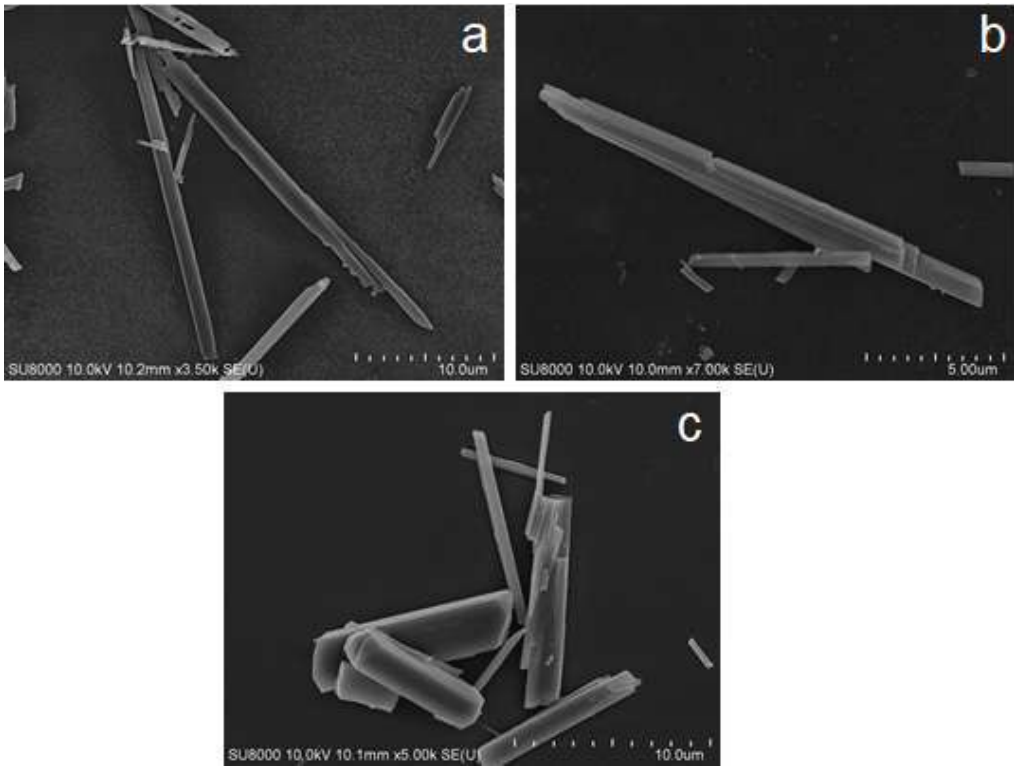

Figure 6. SEM images of MSU (a), m-CPPD (b) and t-CPPD (c) crystals

Screening of fluorescent dyes for crystal staining. Because gouty arthritis can be divided into gout and pseudogout, which the inflammation is caused by the crystals of MSU and CPPD, respectively. Therefore, the discrimination of MSU and CPPD crystal using fluorescent technique would be a rapid and simple method for crystal identification which will definitely assist the proper management of gouty arthritis. Totally 8 fluorescent dyes were selected based on their environmental responses, and the staining was performed. Staining with 7-hydroxycoumarin and berberine showed the brightest blue and green fluorescence in the case of m-CPPD over MSU and t-CPPD, although some spots of the dried 7-hydroxycoumarin could be imaged in blue (Table 2). All of the three crystals displayed a very bright red fluorescence after staining with acridine orange and nonyl acridine orange, therefore it might be not possible to distinguish the MSU and CPPD crystals using the acridine orange dye series.

Table 2. Fluorescence staining of MSU, m-CPPD and t-CPPD crystals. Exposure time and gain used to acquire each image was noted.

Fluorescent dyes	MSU	m-CPPD	t-CPPD
7-Hydroxycoumarin exposure time: 100 ms gain: 100%		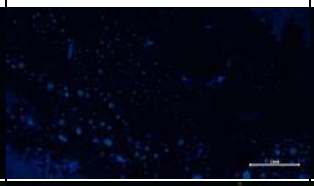	
Berberine exposure time: 100 ms gain: 100%	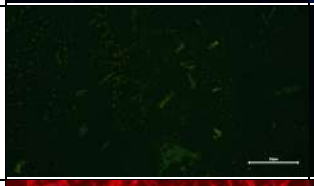	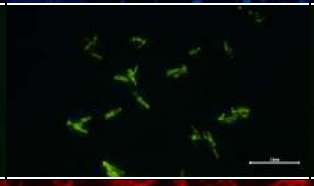	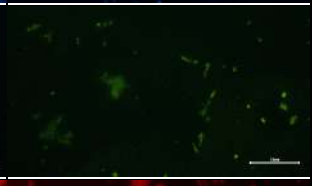
Acridine orange exposure time: 350 ms gain: 100%	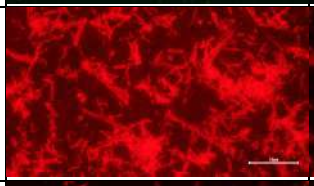	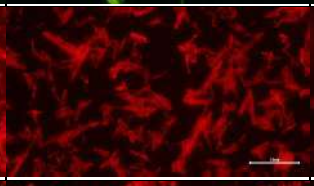	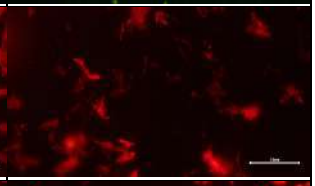
Nonyl acridine orange exposure time: 100 ms gain: 100%	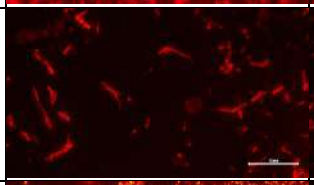	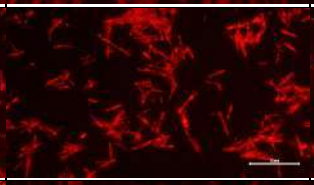	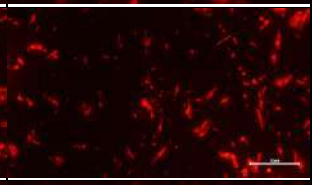
Neutral red exposure time: 350 ms gain: 500%	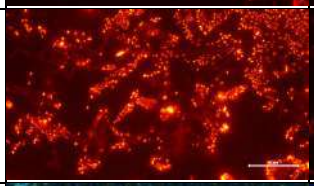	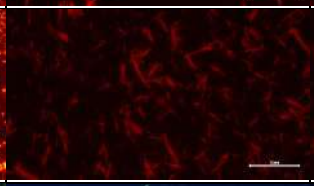	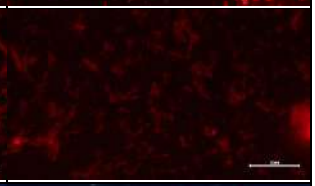
Thioflavin T exposure time: 350 ms gain: 100%	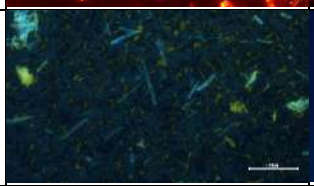		
2,6-TNS exposure time: 100 ms gain: 100%	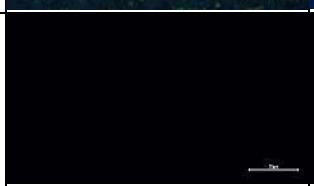	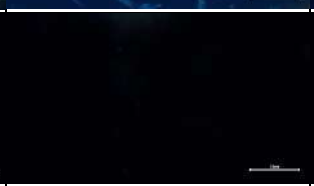	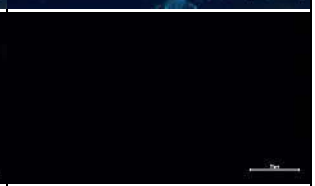
Alizarin Red S exposure time: 350 ms gain: 500%	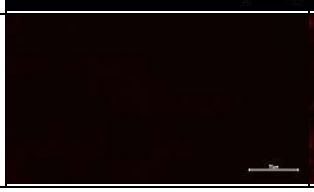	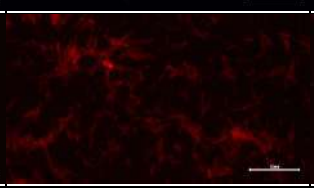	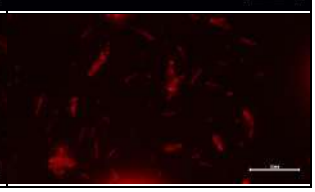

Neutral red could stain the two polymorphs of CPPD crystals as the periphery of the crystals appeared in weak red, but the extremely bright orange spots were found only when MSU crystals were presented. Because the dried spots of neutral red did not emit any fluorescence under similar condition, therefore, it is highly possible to distinguish between CPPD and MSU using neutral red. Even the greenish fluorescence was observed only in the case of MSU staining with Thioflavin T, but the same greenish fluorescence was also appeared when the solution of Thioflavin T was dried without MSU on the glass cover slide

under similar condition. Therefore, Thioflavin T may be inappropriate for the crystals staining. On the other hand, CPPD could be selectively stained in red with Alizarin red S when increasing the exposure time and gain to 350 ms and 500%, respectively. Therefore, further investigation is required for the Neutral red and Alizarin red S in the crystals staining.

Conclusion:

In this study, the root causes of gouty arthritis, i.e. needle-like MSU crystal, rod-shaped m-CPPD crystal and the rhomboid crystal of t-CPPD crystal, were synthesized with high yields and almost pure phase. The as-synthesized crystals were well-characterized using XRD, FT-IR, Raman spectroscopy and TGA, Meanwhile the surface topology and birefringence were observed by SEM and polarized light microscope. Neutral red and Alizarin red S may be useful as a selective dye for the MSU and CPPD crystals identification purpose.

References:

1. Martillo M A, Nazzal L, Crittenden, D B. Curr Rheumatol Rep. 2014; The crystallization of monosodium urate. Current rheumatology reports. 16: 400-400.
2. Mahon O, Dunne A. Front Immunol. 2018;9:1145.
3. Stefan C, Jansen S, Bollen M. TIBS 2005;30:542-550.
4. Gras P, Rey C, Marsan O, Sarda S, Combes C. Eur J Inorg Chem. 2013;2013:5886-5895.
5. Grassi W, Angelis R D. Reumatismo. 2011;63:238-245.
6. Rosenthal A K, Ryan L M. NEJM. 2016;374:2575-2584.
7. Hainer B L, Matheson E, Wilkes R T. AFP. 2014;90:831–836.
8. Li B, Singer N G, Yeni Y N, Haggins D G, Barnboym E, Oravec D, Lewis S, Akkus O. A&R. 2016; 68:1751-1757.
9. Schlesinger N. Am J Manag Care. 2005;11:S443-S450.
10. Denko C W, Whitehouse M W. J Rheumatol. 1976;3:54-62.
11. Molloy R G E, Sun W, Chen J, Zhou W. Chem Commun (Camb). 2019;55:2178-2181.
12. Mandel N S, Mandel G S, J Am Chem Soc. 1976;98:2319–2323.
13. Brown E H, Lehr J R, Smith J P, Frazier A W. J. Agric. Food Chem. 1963;11:214–222.
14. Liu Y Z, Jackson A P, Cosgrove S D. Osteoarth. Cartil. 2009;17:1333–1340.
15. Mandel G S, Renne K M, Kolbach A M, Kaplan W D, Miller J D, Mandel N S. J. Cryst. Growth 1988;87:453–462.
16. Li M, Li S, Tang W, Gong J. Cryst Growth Des. 2020;20:804-812.

CRYSTALLIZATION OF THE RECOMBINANT VIRAL RESPONSIVE PROTEIN 15 (*Pm*VRP15) FROM THE BLACK TIGER SHRIMP *Penaeus monodon*

Pasunee Laohawutthichai,[1,2] Min Fey Chek,[3] Tomoyuki Mori,[3] Sun Yong Kim,[3] Toshio Hakoshima,[3] Anchalee Tassanakajon,[2] Kuakarun Krusong[1,*]

[1]Structural and Computational Biology Research Unit, Department of Biochemistry, Faculty of Science, Chulalongkorn University, Bangkok 10330, Thailand

[2]Center of Excellence for Molecular Biology and Genomics of Shrimp, Department of Biochemistry, Faculty of Science, Chulalongkorn University, Bangkok 10330, Thailand

[3]Structural Biology Laboratory, Nara Institute of Science and Technology, Nara, 630-0192, Japan

*e-mail: Kuakarun.K@chula.ac.th

Abstract:

White spot syndrome virus (WSSV) causes a gigantic loss in black tiger shrimp (*Penaeus monodon*) farming. Viral responsive protein 15 (*Pm*VRP15) is a novel protein that significantly responses to WSSV infection in black tiger shrimp. Previous results showed that *Pm*VRP15 is a membrane-associated protein, which probably contains a single transmembrane α-helix. *Pm*VRP15 plays a role in viral exit from the nucleus. In this study, we aim to crystallize *Pm*VRP15. A series of truncated *Pm*VRP15 genes were constructed and expressed in *E. coli*. Crystallization trials were performed in 96-well crystallization plate using vapour diffusion method. Data collection was performed at RIKEN SPring-8 Center, Japan. Structure of *Pm*VRP15 will help elucidate the protein function.

EFFECT OF GYPSUM WASTE ADDITIONS ON THE LOW-DENSITY CALCIUM SILICATE INSULATING BOARD USING RICE HUSK ASH AS SiO_2 SOURCE

Chayanin Nisaimun,[1,*] Natthanon Phonchai,[1,2] Charusporn Mongkolkachit,[3] and Thanakorn Wasanapiarnpong[1,2]

[1] Department of Materials Science, Faculty of Science, Chulalongkorn University, Bangkok

[2] Center of Excellence on Petrochemical and Materials Technology, Chulalongkorn University, Bangkok

[3] National Metal and Materials Technology Center (MTEC), Klong Luang, Pathumthani

[*] e-mail: chayanin.nis@hotmail.com

Abstract:

This study focuses on using industrial wastes as a substitute for the main raw materials in calcium silicate insulating board for instance rice husk ash (RHA) as an alternative silica source that is an amorphous silica and gypsum from the waste plaster mold. Traditionally, calcium silicate product is prepared through reaction between silica source and calcium source such as silica sand and lime in high pressure hydrothermal conditions. The influence of gypsum waste on the phase formation of calcium silicate product using rice husk ash during autoclave was investigated. The samples were prepared by mixing the raw materials with a molar ratio of CaO/SiO_2 as 1:1. Ceramic fiber 2.5 wt% and eucalyptus paper pulp 2.5 wt% were added as the fiber reienforcement with water added to form slurry. Then the samples were casted and cured in plastic molds at room temperature for 2 days. Samples were demolded and placed in an autoclave for hydrothermal reaction at 200 ^oC for 2 hours. Finally, they were dried at 60 ^oC for 2 days until they reached their constant weight. Low bulk density samples of 0.23 g/cm^3 with a bending strength of 456.63 kPa were successfully prepared by 1 wt% of gypsum waste addition. The samples were characterized by XRD and SEM and observed physical properties. The addition of gypsum waste had a positive effect on the tobermorite phase formation.

Introduction:

The calcium silicate is often used as a heat-insulating material for walls or ceilings of buildings and construction to prevent heat from entering the building. It is also used in high-temperature environment such as refractory kiln due to its good insulating properties, low density, fire resistance, durability, machinability, and inertness. In addition to this, it can use at very wide range temperatures up to 600-1100 ^oC, depending on the quality and use, easy to install and inexpensive.[1-2]

Various crystalline hydrated calcium silicates can be prepared by reacting calcareous with siliceous in different rations under hydrothermal conditions. Among them, tobermorite and xonotlite phases are mainly employed as an insulation building material due to their fibrous and strengthen of the structures. The tobermorite phase can be synthesized through adjusting the mole ration of CaO/SiO_2 varying from 0.8-1.5. At the initial stage, the calcium silicate hydrate (CSH) gel can occur in atmospheric conditions. The structure of CSH(I) is very similar to that of tobermorite phase, however, it possesses poor crystallinity. It was also found that such material can be changed to the tobermorite phase when temperature increased to above 120 ^oC.[3-5] The overall chemical reactions can be illustrated in the following equation:

$$xCaO_{(s)} + ySiO_{2(s)} + zH_2O_{(l)} \rightarrow CSH(I)_{(gel)} \rightarrow Tobermorite_{(crystal)} \quad (1)$$

Compared with that of crystalline silica, amorphous silica can be more easily dissolved due to the nature of the disordered structure as well as higher surface area, which are more reactive with a calcium source. Notably, the dissolution rate of silica is related to the silanol group on the surface. It has been reported that large number of silanol groups are known as an increasing solubility.[6]

On the other hand, the gypsum is often used as an activator because the sulfate (SO_4^{2-}) group in its structure can accelerate the transformation of CSH gel to tobermorite by substituting the tobermorite structure. This also resulted in an imperfection of tobermorite structure.[7-8]

Methodology:

Rice husk ash (RHA) was received from A.T. Biopower Co.,Ltd. Thailand. Gypsum waste was received from Crystal Ceramics Co.,Ltd., Thailand. Calcium hydroxide (73.41%CaO) was used as calcium source. Reinforcement materials were paper pulp and ceramic fiber (Isowool 1430 bulk, Isolite insulating products company), and the chemical composition of such raw materials is provided in **Table 1.**

Table 1.
Chemical composition (wt%) of raw materials

Raw materials	SiO_2	Na_2O	K_2O	MgO	CaO	Al_2O_3	Fe_2O_3	ZnO	MnO	P_2O_3	SO_3	ZrO_2
RHA	95.79	0.16	2.58	0.35	0.58	0.08	0.05	0.02	0.03	0.36	-	-
Calcium hydroxide	2.06	0.12	0.03	0.51	73.41	0.27	0.03	-	-	-	-	-
Gypsum waste	2.18	0.74	0.11	-	31.15	0.13	0.09	-	-	-	45.42	-
Ceramic fiber	49.0	-	-	-	-	35.4	-	-	-	-	-	15.2

The samples were prepared by blend the raw materials in the molar ratio of 1:1 between CaO and SiO_2 in water to form a slurry by adding gypsum 0, 1, 3, 10 wt%, **Table 2**, and then mixed in a mechanical ball mill for 30 min at room temperature by using the water/solid mass ratio of 5. Subsequently, the calcium silicate slurry was mixed with 2.5 wt% paper pulp and 2.5 wt% ceramic fiber. The resulting slurry mixture was maintained at 80 ^oC for blending. After 1 h, the samples were cast and cured in plastic molds at room temperature for 2 days to obtain the rigid body. Then, hydrothermal reactions were carried out by using an autoclave bomb at 200 ^oC with autogenous pressure around 210 psi for 2 h. Finally, the resulting solid samples were dried at 60 ^oC until they were a constant weight. The sample size was 5 x 5 x 2 cm^3 as depicted in **Figure 1.**

The phase analysis of the prepared samples was determined by power X-ray diffraction (XRD: Bruker, D8 Advance, Germany). The morphology of the prepared samples was observed by Scanning electron microscopy (SEM: JOEL, JSM-6480LV, Japan).

Table 2.
Formulation of samples (wt%)

Raw materials	RHA0	RHA1	RHA3	RHA10
Rice husk ash	45.09	44.64	43.74	40.58
Calcium hydroxide	54.91	54.36	53.26	49.42
Gypsum waste	0	1	3	10
Ceramic fiber	2.5	2.5	2.5	2.5
Paper pulp	2.5	2.5	2.5	2.5
Sum	105	105	105	105

Results and Discussion:

The XRD patterns of samples prepared by RHA and $Ca(OH)_2$ with 0, 1, 3, and 10 wt% of gypsum cured under hydrothermal conditions are shown in **Figure 2**. Apparently, the sample contained 0 wt% of gypsum displayed a small broad peak of tobermorite. It was clearly seen that the CSH gel began to form the tobermorite crystals at 2θ ~7^o. At 1, 3, 10 wt% gypsum samples, the diffraction patterns showed the high and sharp characteristic peaks of tobermorite phase. It should be noted that the peaks intensity of the tobermorite phase was found to be almost the same as the patterns of adding gypsum. However, in cases of the samples with 3 and 10 wt% gypsum, the basanite phase was observed with the excess of sulfate ions in calcium silicate product. Meanwhile, the formation of the basanite phase was clearly seen in the sample with 10 wt% gypsum.

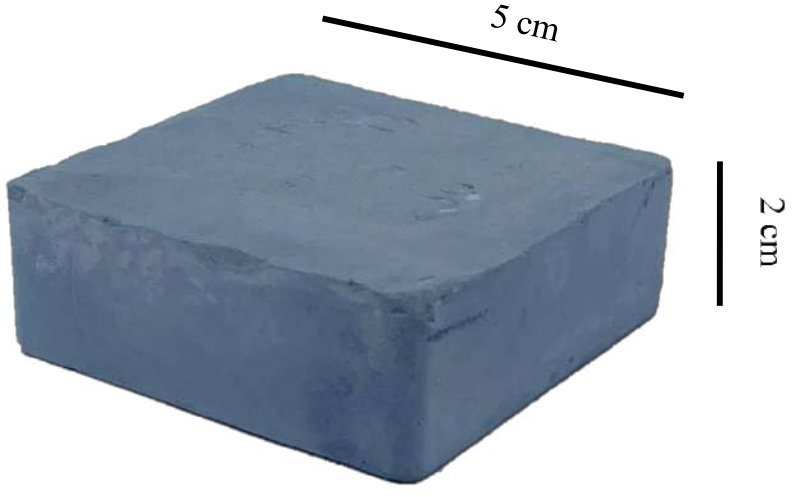

Figure 1.
View of the prepared sample

The SEM micrograph of the samples with adding 0, 1, 3, and 10 wt% gypsum cured after hydrothermal reactions are shown in **Figure 3.** The different morphologies of the tobermorite crystals could be observed. In the absence of gypsum (**Figure 3 a)**), the

tobermorite product appears in the form of lath-like crystals. By adding gypsum, the crystal habit of the product was changed to the plate-like shape as shown in **Figure 3 b), c), d)**. It should be noted that the size of plate-like crystals become larger in the case of 10 wt% gypsum **(Figure 3 d).** From this result, it exhibited in the same way as Mostafa N et al.[7] and Helanova E et al.[9] that sulfate accelerated the formation of tobermorite and effected on imperfection of crystal structure.

In addition, the bulk density of the samples was investigated. It appeared that the addition of the gypsum can affect the lower bulk density and more apparent porosity as shown **Figures 4** and **5**. Meanwhile, the bending strength of the samples with different gypsum content presented in **Figure 6**. Indeed, the RHA1 sample exhibited the highest bending strength of 456.63 kPa. When the amount of gypsum was increased, the bending strength was reduced to 390.50 kPa and 371.62 kPa for RHA3 and RHA10, respectively. The bending strength for the sample without adding the gypsum (RHA0) was found to be 341.11 kPa. The strength of all specimens was lower than that of the results of Chen M et al.[4] at 9 MPa, which were autoclaved at 185 ^{o}C for 2h due to the higher bulk density than this study.

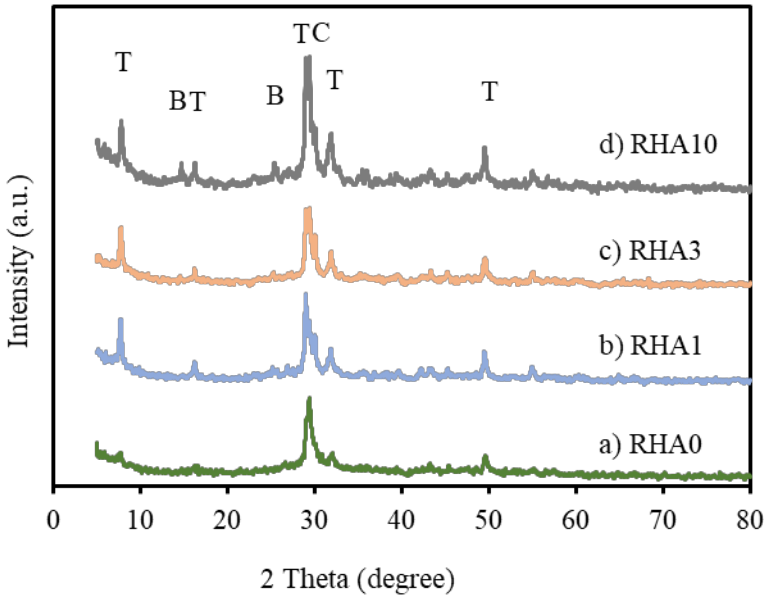

Figure 2.
XRD patterns of samples with adding a) 0 wt% b) 1 wt% c) 3 wt% d) 10 wt% gypsum (T=Tobermorite, C=Calcite, B=Basanite)

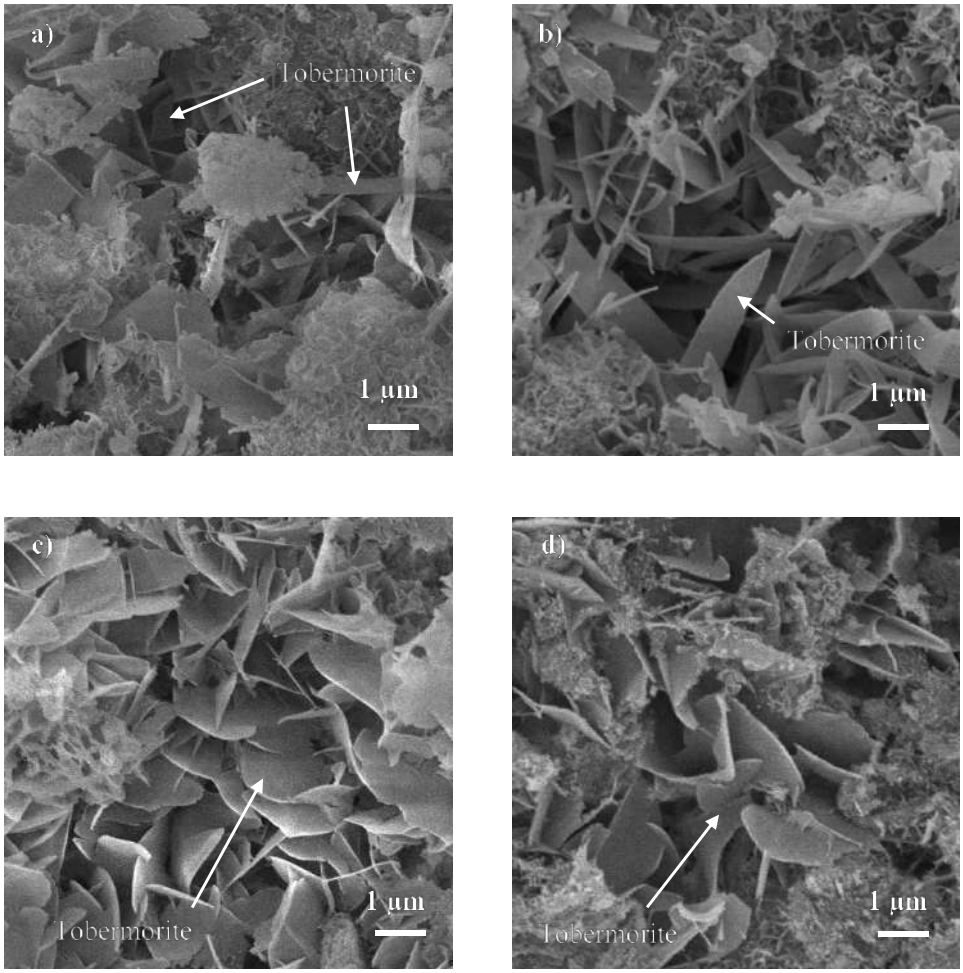

Figure 3.
SEM micrograph of samples with adding a) 0 wt% b) 1 wt% c) 3 wt% d) 10 wt% gypsum

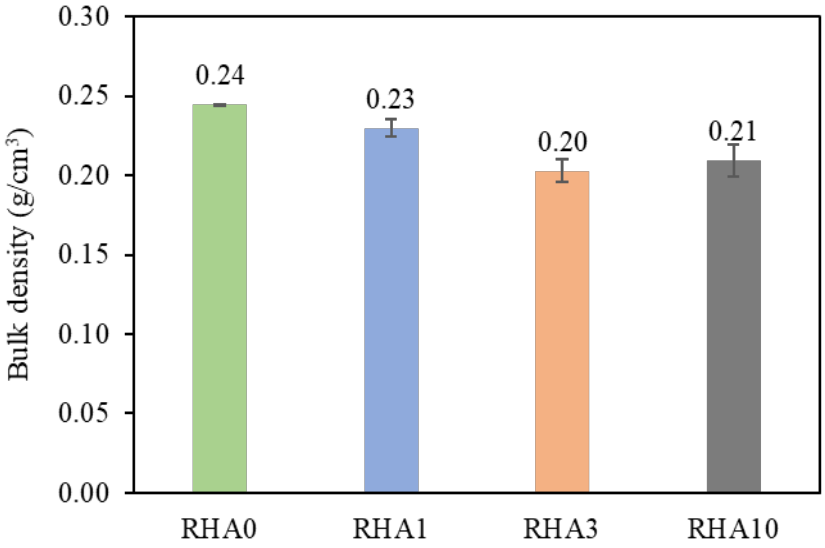

Figure 4.
Bulk density of samples

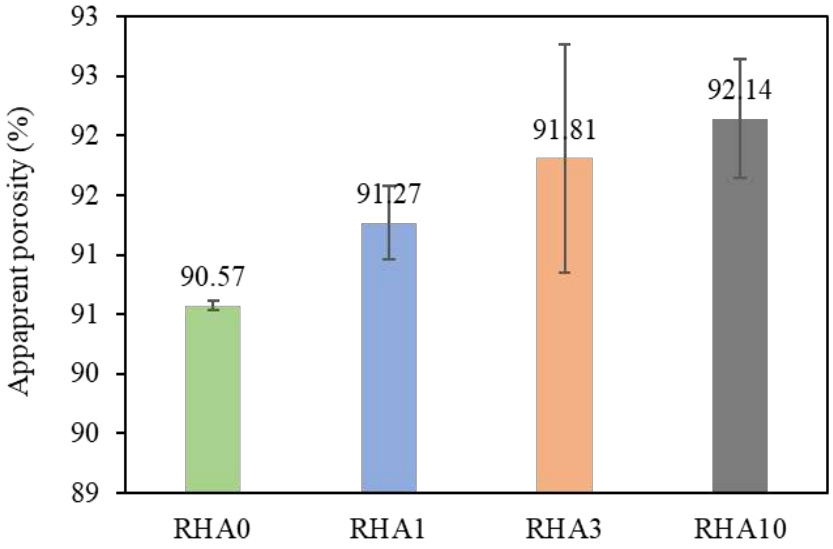

Figure 5.
Apparent porosity of samples

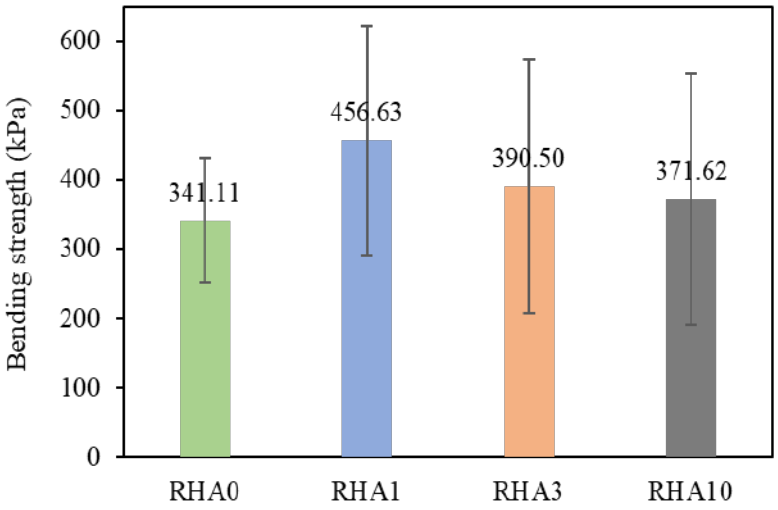

Figure 6.
bending strength of samples

Conclusion:

In this study, adding gypsum effect on calcium silicate prepared by using rice husk ash as SiO_2 source was observed at autoclave 200 ^oC for 2 h. Low bulk density samples of 0.23 g/cm^3 with a bending strength of 456.63 kPa were successfully prepared by 1 wt% of gypsum waste addition. Adding gypsum also influenced the morphology of tobermorite crystal grew larger and flatter. It related to the bending strength. The results from this study verified the gypsum as an accelerated material to encourage tobermorite phase formation.

Acknowledgements:

This research is funded by Thailand Graduate Institute of Science and Technology, TGIST and the authors would like to gratefully acknowledge Department of Materials Science, Faculty of Science, Chulalongkorn University. The financial support has been

provided by GAICCE Research Grant from ASEAN University Network/Southeast Asia Engineering Education Development Network (AUN/SEED-net).

References:

1. Kristanto L, Sugiharto H, Agus SD, Pratama SA. Procedia Eng. 2017;171:679-688.
2. Harper S. Compos. 1982;13(2):123-128.
3. Oh JE, Clark SM, Monteiro PJ. Cem Concr Res. 2011;41(1):102-106.
4. Chen M, Lu L, Wang S, Zhao P, Zhang W, Zhang S. Constr Build Mater. 2017;143:280-288.
5. Meller N, Hall C, Phipps JS. Mater Res Bull. 2005;40(5):715-723.
6. Haastrup S, Bødker MS, Hansen SR, Yu D, Yue Y. J Non Cryst Solids. 2018;481:556-561.
7. Mostafa N, Shaltout A, Omar H, Abo-El-Enein S. J Alloy Compd. 2009;467(1-2):332-337.
8. Cerný V, Melichar J, Fleischhacker J, Drochytka R. Mater Sci Forum. 2018;916:179-183.
9. Helanova E, Drochytka R, Černý V. Key Eng Mater. 2016;714:116-121

FOUR NOVEL ZINC(II) COORDINATION POLYMERS BASED ON TRITOPIC AND HETEROCYCLIC *N*-DONOR MIXED LIGANDS

Kenika Khotchasanthong,[1] Winya Dungkaew,[2] Filip Kielar,[3] Mongkol Sukwattanasinitt,[4] Kittipong Chainok[1,*]

[1]Thammasat University Research Unit in Multifunctional Crystalline Materials and Applications, Faculty of Science and Technology, Thammasat University, Thailand
[2]Department of Chemistry, Faculty of Science, Mahasarakham University, Thailand
[3]Department of Chemistry, Faculty of Science, Naresuan University, Thailand
[4]Department of Chemistry, Faculty of Science, Chulalongkorn University, Thailand
*e-mail: kc@tu.ac.th

Abstract:

Four new Zn(II) coordination polymers with tritopic and heterocyclic *N*-donor mixed ligands, $[Zn_2(btb)_2(im)_2][DMA]_2 \cdot sol$ **(1)**, $[Zn(btb)(ppy)][DMA] \cdot sol$ **(2)**, $[Zn_2(btb)_2(apm)][DMA]_2 \cdot sol$ **(3)**, and $[Zn_3(\mu_4\text{-}O)(btb)_2(pyz)][DMA] \cdot sol$ **(4)** (apm = aminopyrimidine, btb = benzene-1,3,5-tribenzoate, DMA = dimethylammonium, im = imidazole, pyz = pyrazine, ppy = 4-phenylpyridine, sol = solvents) were synthesized and characterized. The sizes and shapes of *N*-donor co-ligands play a crucial role in the assembly of titled coordination polymers. Compounds **1-3** exhibit a two-dimensional network with **hcb** topology. Whereas, **4** exhibits two-fold interpenetrated 3D network with **sit** topology. It is fascinating that all these compounds not only show unique selectivity for detection of Pb^{2+}, Cu^{2+}, Hg^{2+}, Fe^{2+}, Fe^{3+}, and Cr^{3+} ions through fluorescence quenching mechanism but also exhibit adsorption of CO_2 at room temperature.

PETROGRAPHY AND GEOCHEMISTRY OF MAFIC DIKES IN THAN SALAI ABANDONED QUARRY, THONG SAEN KHAN DISTRICT, UTTARADIT PROVINCE

Patcharin Kosuwan Jundee[1,*], Thanapat Wongboonruang,[2] Boontarika Srithai[1]
[1]Department of Geological Sciences, Faculty of Science, Chiang Mai University, Chiang Mai, 50200 Thailand
[2]Ground Data Probe Company Limited, Ladprao, Bangkok, Thailand
*e-mail: patcharinkosuwan.j@cmu.ac.th

Abstract:
Spectacular sets of mafic dike that cut across Permian limestone were observed at Than Salai abandoned quarry, Bo Thong Sub-District, Thong Saen Khan District, Uttaradit Province. Ten dike samples were, therefore, collected for petrography and geochemical analyses. These rocks were classified into 2 groups; including altered porphyritic micrograbbro and least-altered seriate microgabbro/microdiorite. The altered porphyritic micrograbbro composed mainly of plagioclase phenocrysts in a groundmass that made up of plagioclase and clinopyroxene with minor amount of unidentified mafic minerals and opaque minerals. The least-altered seriated microgabbro/microdiorite showed ophitic/sub-ophitic phenocrysts and consisted mainly of plagioclase and clinopyroxene, with minor amount of orthopyroxene and opaque minerals. Geochemically, least-mobile elements suggested that these intrusive igneous rocks were gabbroic diorite/diorite with calc-alkaline affinity, which were later interpreted as tectonically arc-related magma.

STRUCTURES, PHOTOLUMINESCENCE AND CO_2 ADSORPTION PROPERTIES OF NOVEL POLYOXOMETALATES DERIVED FROM RICE HUSK BIOMASS

Chana Panyanon,[1] Winya Dungkaew,[2] Kittipong Chainok[1,*]
[1] Thammasat University Research Unit in Multifunctional Crystalline Materials and Applications (TU-McMa), Faculty of Science and Technology, Thammasat University, Thailand
[2] Department of Chemistry, Faculty of Science, Mahasarakham University, Thailand
*e-mail: kc@tu.ac.th

Abstract:
Rice husk ash (RHA) generated by the direct-fried combustion process of the biomass electricity generating plants is one of the most abundant and available waste materials in Thailand. In the present work, silica (SiO_2) powder was extracted from RHA (provided by Kamalasia Bio Power 2010 Co., Ltd), and were used as Si resources for the production of value chemicals. Herein, the synthesis and structural characterization of three new silica-based polyoxometalates, $[SiW_{12}O_{40}]\cdot 2ImH\cdot 2H_3O$ (**1**), $[Eu_2(H_2O)_2(Im)_2(ox)(SiW_{11}O_{39})_2]$ (**2**), and $[(Eu(H_2O)_5)_2(ox)(Eu(H_2O)_3SiW_{11}O_{39})_2]$ (**3**) (Im = imidazole, ImH = imidazolium, ox = oxalate), are described. The single crystal X-ray diffraction analyses revealed that the crystal structures of these hybrid materials consist of polyanion $[SiW_{12}O_{40}]$ clusters. All these materials exhibit good thermal stabilities up to *ca*. 500 °C. The maximum CO_2 uptake capacity under high pressure (50 bar) of the activated **1** reached 52.5 and 48.6 $cm^3\ g^{-1}$ at 45 and 55 °C, respectively. Notably, **2** and **3** display red luminescence emission in the solid state at room temperature with the decay lifetime of 0.76 and 0.22 ms, respectively. This work demonstrates that silica powder that extracted from biomass waste can be utilized to develop functional polyoxometalate materials for various potential applications in gas adsorption, luminescence, *etc*.

SYNTHESIS, CHARACTERIZATION AND CRYTAL STRUCTURE OF A NEW DINUCLEAR COPPER(II) COMPLEX CONTAINING 1,10-PHENANTHROLINE AND 3-NITROBENZOATE LIGANDS

Vipada Petson,[1,2] Preawmai Khongdechsakda,[1,2] Wanassanan Chaisuriya,[1,2] Kittipong Chainok,[2] and Nanthawat Wannarit[1,2]*

[1]Department of Chemistry, Faculty of Science and Technology, Thammasat University, Klong Luang, Pathum Thani 12121, Thailand

[2]Thammasat University Research Unit in Multifunctional Crystalline Materials and Applications (TU-MCMA), Faculty of Science and Technology, Thammasat University, Klong Luang, Pathum Thani 12121, Thailand

*e-mail: nwan0110@tu.ac.th

Abstract:

A new dinuclear copper(II) complex containing 1,10-phenanthroline (phen) and 3-nitro-benzoate (3-NO_2benz) ligands with the chemical formula of [Cu_2(phen)$_2$(3-NO_2benz)$_2$(μ-3-NO_2benz)$_2$]·3-NO_2benzH was synthesized by direct preparation method. The structure of complex has been determined by using single-crystal X-ray diffraction. This complex crystallizes in triclinic crystal system with *P*-1 space group. The coordination environment of Cu(II) ion presents a square pyramidal geometry with [CuN_2O_3] chromophore. Two Cu(II) ions are doubly-bridged by two 3-NO_2benz bridging ligands with *syn-anti* coordination mode. The packing structure of this complex has been stabilized by supramolecular interactions such as hydrogen bonding, π···π, C–H···π and N–O···π interactions.

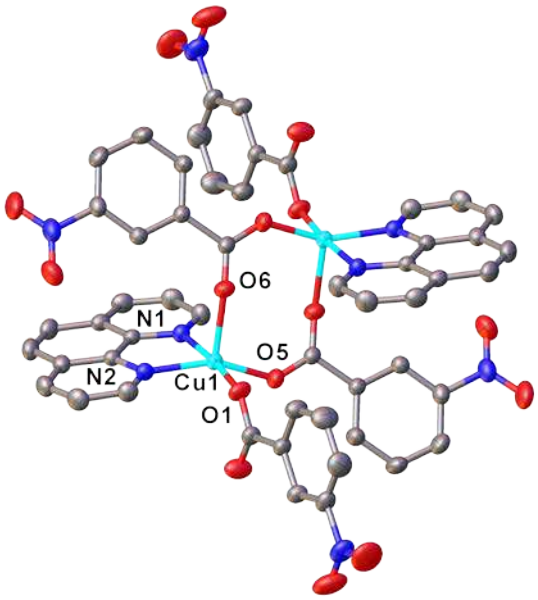

Figure 1. Molecular structure of [Cu_2(phen)$_2$(3-NO_2benz)$_2$(μ-3-NO_2benz)$_2$] dinuclear unit. Hydrogen atoms are omitted for clarity.

SYNTHESIS, CHARACTERIZATION, X-RAY STRUCTURES OF NEW COPPER(II) COORDINATION POLYMERS INCORPORATING IMIDAZOLE-BASE DERIVATIVES AND SULFATO ANIONIC BRIDGING LIGAND

Nareekarn Meebua,[1,2] Wanatchaporn Pentes,[1,2] Kittipong Chainok,[2] and Nanthawat Wannarit,[1,2]*

[1]Department of Chemistry, Faculty of Science and Technology, Thammasat University, Klong Luang, Pathum Thani 12121, Thailand
[2]Thammasat University Research Unit in Multifunctional Crystalline Materials and Applications (TU-MCMA), Faculty of Science and Technology, Thammasat University, Klong Luang, Pathum Thani 12121, Thailand
*e-mail: nwan0110@tu.ac.th

Abstract:

Two new copper(II) coordination polymers namely $[Cu(Im)_4(\mu\text{-}O_2SO_2)]_n$ (**1**) and $\{[Cu(bzi)_3(\mu\text{-}O_2SO_2)]\cdot H_2O\cdot DMF\}_n$ (**2**) containing imidazole-base derivatives, Imidazole (Im) and 1-benzylimidazole (bzi) have been successfully synthesized and characterized. The crystal structures of these compounds have been determined by using single-crystal X-ray diffraction (SCXRD). Compound **1** crystallizes in monoclinic crystal system with *C*2 space group. The structure of compound **1** consists of Cu(II) ions which show with a distorted octahedral geometry with $[CuN_4O_2]$ chromophore linked by $\mu\text{-}O_2SO_2$ ligand, providing a one-dimensional zigzag chain-like structure along crystallographic *c* axis. While, compound **2** crystallizes in monoclinic crystal system with $P2_1/c$ space group. There are two crystallographically independent Cu(II) ions in the structure showing different geometries, distorted square planar geometry with $[CuN_4O_2]$ chromophore and distorted octahedral geometry with $[CuN_4O_2]$ chromophore for Cu(1) and Cu(2), respectively. These Cu(II) ions are connected alternatively together by $\mu\text{-}O_2SO_2$ ligand providing a one-dimensional alternating zigzag chain-like structure along crystallographic *c* axis. Interestingly, the difference in structural topology of compounds of **1** and **2** were affected by the steric hindrance of imidazole derivative ligand.

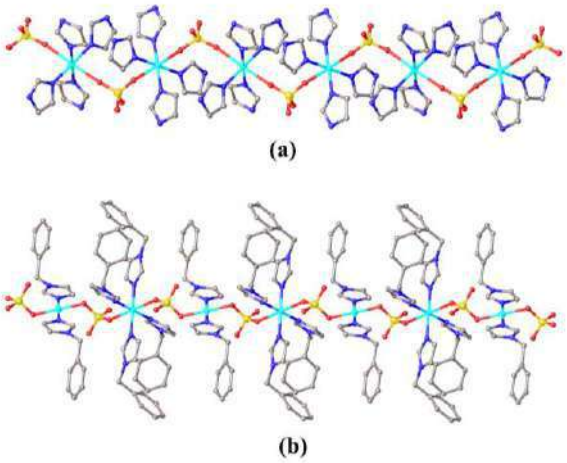

Figure 1. one-dimensional zigzag chain-like structures of compounds **1** (a) and **2** (b)

ACCUMULATION OF MICROPLASTIC IN MACROINVERTEBRATES INHABITING IN HUAI KAKANG STREAM, MAHA SARAKHAM PROVINCE

Penkhae Thamsenanupap[a], Jatuporn Teanma[a], Tawatchai Tanee[a,b]

[a] Faculty of Environment and Resource Studies, Mahasarakham University, Maha Sarakham 44150, Thailand
[b] Genetics and Environmental Toxicology Research Group, Khon Kaen University, Khon Kaen 40002, Thailand

Abstract:

Huai Kakang stream is an important water resource for local people for many activities, including agriculture, aquaculture, recreation and for receiving wastewater. This stream was reported a poor water quality with the exceeding limits of Lead and cadmium. However, there was no report on microplastics. Hence, the occurrence of microplastic and macroinvertebrates inhabiting in Huai Kakang stream was aimed for this study. Macrointervertebrates were randomly collected base on functional feeding group for studying the accumulation of microplastic. Sediment and water samples were also collected from four sites along Huai Kakang stream. All sample were prepared and examined under the microscope and microscope-FTIR. Color, shape, type and size of microplastics were studied. The result showed that predators (i.e. Coenagrionidae, Libellulidae, Notonectidae, Belostomatidae) were found the highest amount of microplastics with the average of 2.4 items per individual. The grazer (i.e. Lymnaea sp., Melanoides tuberculate, Viviparoidea and Baetidae) were found the second most abundant of microplastic with 2.25 items per individual. Blue fibered polypropylene was the most abundant microplastic found in macroinvertabrates with the predominant size of 10-1000 µm. Sediment and water sampler were found the highest abundant of transparent fibered polypropylene with the predominant size of 10-1000 µm. All four sampling sites were polluted by microplastics. The occurrence of microplastic in the Huai Kakang stream indicated that this stream needs local people and relevant authorities' attention on improving water quality.

Keywords; microplastic, macroinvertebrates, freshwater, Chi river tributary

ADSORPTION OF CADMIUM FROM AQUEOUS SOLUTIONS BY POLYETHYLENE MICROPLASTICS AND BAMBOO BIOCHAR

Suchanya Wongrod*, Siriluk Chirakorn, Soydoa Vinitnantharat
Environmental Technology Program, School of Energy, Environment and Materials, King Mongkut's University of Technology Thonburi, Bangkok, 10140, Thailand
Environmental and Energy Management for Community and Circular Economy (EEC&C) Research Group, King Mongkut's University of Technology Thonburi, Bangkok, 10140, Thailand
*e-mail: suchanya.won@kmutt.ac.th

Abstract:

This study investigates the capability of cadmium (Cd) sorption on polyethylene (PE) microplastics and on bamboo biochar (BB) through adsorption isotherm studies. Cadmium was prepared at different concentrations (50-4000 µg/L). For batch sorption experiments, the PE or BB was separately added in the Cd solutions under controlled conditions at laboratory scale. The model-fittings of adsorption isotherms (i.e., Langmuir and Freundlich) were performed in non-linear regression. Biochar properties including Fourier transform infrared spectroscopy, X-ray powder diffraction, X-ray fluorescence and Brunauer–Emmett–Teller surface area were analyzed. Results show that the Cd sorption by BB was in good agreement with Freundlich model, implying that Cd could be sorbed on the BB via multilayer adsorption. The sorption of Cd on PE was well-described by Langmuir model. The maximum adsorption capacity of PE was 108.6 µg/g within 24 hr, which affirms the Cd sorption at homogenous sites of PE. This study highlights that PE can act an important vector to carry microplastic-metal co-contaminant properties, which pose serious threats to aquatic lives, while BB serves as a potential adsorbent for Cd removal from water. Further studies on the PE-Cd removal by biochars could be achieved to provide suitable treatments towards microplastic-metal co-contaminants from aquatic environments.

Keywords: Biochar, Cadmium, Microplastic, Polyethylene

Introduction:

Nowadays, plastic production has been continuously increased and reached 348 million tons in 2017 in which Asia countries are the largest producer globally. Regarding the long lifetime, spatial mobility and possible interaction of plastic in the environment, the plastic accumulation in the ecosystem is nowadays an emerging environmental issue. In addition, since plastic can be broken down into small particles known as microplastics (MPs), unforeseen environmental problems that threatens aquatic environments.

Microplastics (MPs) can be classified into two main types: primary and secondary MPs. The primary MPs are small plastics that have been directly produced for consumer products, while the secondary MPs are small plastic particles that were gradually degraded from large plastic debris due to erosion and/or exposure to several environmental conditions such as water, wind and sunlight (Sharma & Chatterjee, 2017). Erni-Cassola et al. (2019) reported that in the aquatic environment, about 10^3-10^4 particles/m^3 were found in sediments, while 0.1-1 particles/m^3 were enriched in surface water. Erni-Cassola et al. (2019) reported

that polyethylene (PE) was the most abundant plastic type in aquatic environments, followed by polyester, polyamide and acrylic (PP&A), polypropylene (PP), and polyesters (PS).

Apart from MPs, metal contamination in the water bodies has also appeared as a major environmental issue due to rapid development of agricultures, and industrial activities and urbanization to support the economic growth over the past decades (Worakhunpiset, 2018). Distribution of metal concentrations in aquatic environments can be as results of natural activities such as volcanic eruption and soil erosion, and anthropogenic sources such as the inappropriate waste disposal, discharges of untreated wastewater, and excessive uses of fertilizers in agricultures. Once metal elements are entered into water bodies, they can be deposited in soils and water bodies, accumulated in sediments and living organisms through food chain, which can be finally affected human health (Thongra-ar et al., 2008).

Cadmium (Cd) is one of common toxic metals that often contaminates in water bodies and affects aquatic organisms. Mclaren et al. (2004) reported that the Cd concentrations in the water and sediments of the Chao Phraya River and associated waterways were 0.62 µg/L and 953 µg/kg, respectively (at dry season, worst case scenario). Although the Cd concentration in water are relatively low, the Cd concentrations in crabs in the Gulf of Thailand were exceeded the maximum ranges according to standards (Chaiyara et al., 2013). This highlights that the removal of Cd from water bodies are still necessary to prevent a potential health risk to human.

Regarding the contamination of MPs and metals that can be co-occurred in aquatic environments, the information on the sorption of Cd onto MPs can be useful to understand their transport behaviors and toxicity. Metal sorption capacity by MPs may be varied, depending on various factors, for instances, plastic types, complexation and stabilization of metal ions (e.g., Cd(II) and Pb(II)) by water anions, competition for active pore sites of cationic metals and divalent water cations, and compression of the electrical double layer by water ions (Yu et al., 2019).

Adsorption is well-known as a cost effective approach that has been widely applied for pollution treatments such as metals (e.g., Pb(II) and Cd(II)) and MPs (e.g., high-density polyethylene (HDPE) and polystyrene (PS)) (Tong et al., 2020). There are several mechanisms involved in the sorption for organic and inorganic pollutants by adsorbents including ion exchange, electrostatic attraction, surface complexation, physical adsorption, precipitation, pore-filling and surface partition. Moreover, surface precipitation can be taken place if the adsorbent contains anionic compounds such as PO_4^{3-} and CO_3^{2-} on its surface. In addition, high porosities of the adsorbents can accelerate the physical adsorption of pollutants onto available pore sites (Agrafioti et al., 2014). Typically, the sorption interactions between pollutants and adsorbents depend mainly on the nature of the feedstocks.

There are various types of adsorbents used to remove MPs such as activated carbon, biochar, etc. Biochar, a black solid char derived from bio-waste material, is considered as an alternative to recycle by-product residues and produce valuable-added product, and thus promoting the zero waste and environmental sustainability to the community. Biochars can be produced from several feedstock types such as agricultural residues, wood and solid digestate from anaerobic digestion process via thermal conversion processes (Li et al., 2014; Wongrod et al., 2018).

To date, there are restricted data on the toxicity and behaviors of Cd and MPs, which can be co-occurred in water and subsequently threaten aquatic lives in water. This study examined the Cd sorption on polyethylene (PE) and on bamboo biochar (BB) to investigate the sorption capability and toxicity of Cd towards PE and BB through the adsorption isotherm studies.

Methodology:

Biochar Preparation and Characterization: Biochar derived from bamboo was produced at 1000°C for 20 days in a kiln under slow pyrolysis technology. The physical, chemical and structural characteristics of bamboo biochar including specific surface area, Fourier transform infrared spectroscopy (FTIR), X-ray powder diffraction (XRD) and X-ray fluorescence (XRF) were analyzed. Fourier transform infrared spectroscopy (FTIR) was analyzed to identify the functional groups present on the bamboo biochar. The X-ray diffraction (XRD) was employed to identify the crystalline structures presented in the bamboo biochar. The sample was grounded to less than 100 µm particle size and was characterized using a powder diffractometer. X-ray fluorescence (XRF) was analyzed to determine the elemental composition of the biochar. Brunauer-Emmett-Teller (BET) specific surface area of bamboo biochar was determined using the N_2 adsorption method at 77 K (3Flex, Micromeritics, USA). After that, the bamboo biochar was kept in a close container prior to its uses as an adsorbent.

Preparation of synthetic wastewater and microplastics: Cadmium nitrate ($Cd(NO_3.4H_2O)$ at analytical grade was used to prepare synthetic wastewater. The synthetic Cd(II) solutions were prepared in ranges of 50-4000 µg/L. Polyethylene (PE) at particle size of 125 µm (average) was selected for microplastic studies.

Batch sorption experiments: Adsorption isotherms of Cd(II) onto PE and BB were separately conducted at initial concentrations ranging from 50 to 4000 µg/L at 30°C at 180 rpm for 24 h by using an incubator shaker (Innova 42, New Brunswick Scientific™, USA). Initial pH of solutions was adjusted to 5 using 0.1 M HNO_3 and 0.1 M NaOH. For sorption experiments, PE or BB (400 mg) were separately added to 100 mL of Cd(II) solution. Experiments were performed in duplicates with controls (without PE and BB). After sorption, samples were filtered using syringe filters (0.45 µm) and Cd concentrations were analyzed using AAS at λ 228.8 nm. Langmuir and Freundlich adsorption isotherm models were used to describe the experimental data.

Results and Discussion:

Characterization of biochar and microplastics:

FTIR analysis of bamboo biochar: Figure 1 shows the FTIR of bamboo biochar (BB). FTIR spectroscopy is used to identify structural property, i.e., functional groups contained in the biochar. The peak band of 3448 cm^{-1} referred to the asymmetric stretching vibration of O–H functional groups (H-bonded) present in the biochar (Cantrell et al., 2012). The peak band of 1633 cm^{-1} was assigned to the stretching vibrations of C=C, while the band at 1399 cm^{-1} was attributed to $–CH_2$ scissoring. The presence of band at 523 cm^{-1} indicated bending vibration of the Cu–O bond (Raul et al., 2014). It is clear that the FTIR spectra provide the qualitative information of functional groups present on the surfaces of the biochar, which can be linked to possible sorption interactions of Cd(II) onto the biochar surface.

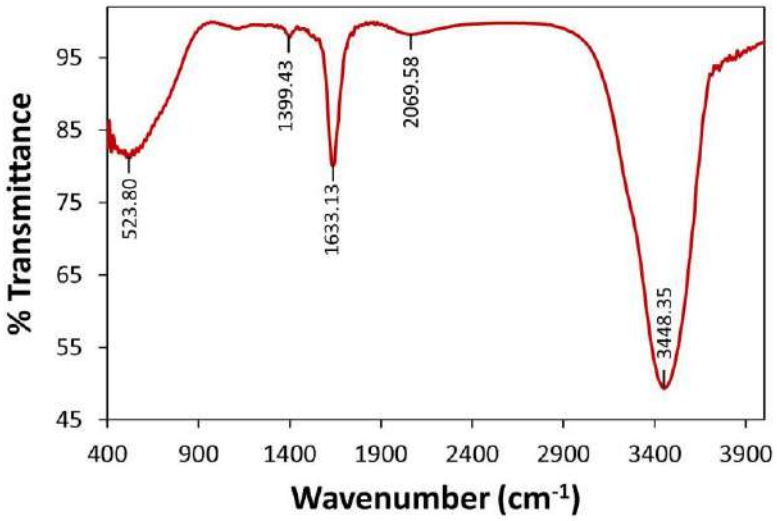

Figure 1. FTIR analysis of bamboo biochar.

XRD analysis of biochar: The XRD spectral analysis of the BB are presented in Figure 2. The inorganic components in amorphous and/or crystalline forms presented in the biochar were identified by search-match software with reference from the American Mineralogist Crystal Structure Database. From Figure 2, there were three broad peaks appear at 2θ around 10.4-12.2°, 23.7-24.5° and 40.2-48.5° (without any sharp and strong peak), which probably attributed to the combination of turbostratic structure of disordered carbon (Rybarczyk et al., 2016). The quartz (SiO_2) in the bamboo biochar was also affirmed by the presence of diffraction peak at 24.2° (Liou & Wu, 2009). In addition, another peak at around 43.8° implied the existence of graphite in the bamboo biochar, which supported by Li et al. (2020).

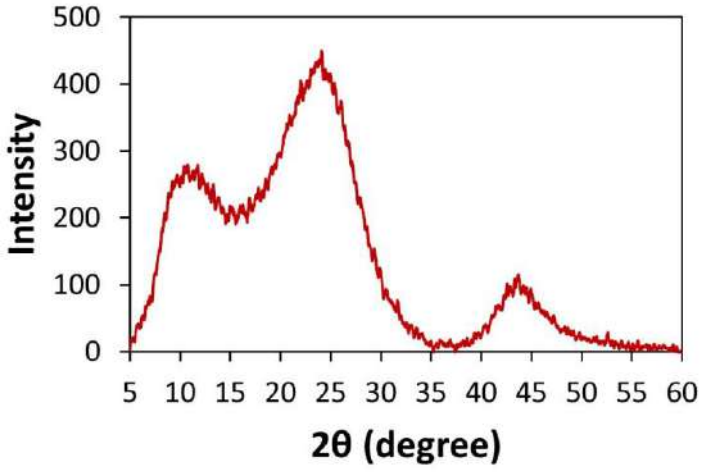

Figure 2. XRD analysis of bamboo biochar.

XRF analysis of biochar: Table 1 shows the elemental composition of the BB. The results showed that the BB contained significant fractions of Si-, Al-, P- and K-oxides. The biochar had highest contents of K_2O (39%) followed by SiO_2 (22%), CaO (10%), and P_2O_5

(10 %). These results clearly suggested that these main elemental compositions contained in the biochar can be possibly involved during the sorption towards water pollutants.

Table 1. XRF analysis of bamboo biochar.

Formula	Chemical composition
K_2O	39.30
SiO_2	22.20
CaO	10.70
P_2O_5	10.10
SO_3	4.67
Cl	4.09
Fe_2O_3	3.37
MgO	3.25
MnO	1.59
Al_2O_3	0.29
ZnO	0.25
CuO	0.20

Sorption isotherm experiment:

Figure 3(a) and 3(b) show the adsorption isotherms for Cd(II) by polyethylene (PE) and by bamboo biochar (BB), respectively. Parameter constants from the Cd(II) adsorption isotherms by PE and BB with Langmuir and Freundlich models are present in Table 2. Results demonstrate that the Cd(II) adsorption isotherms on PE fitted with Langmuir model, while the adsorption of Cd(II) on BB was well-described by Freundlich model (Figure 3(a, b) and Table 2). Based on the empirical isotherm equations (Song et al., 2013), the Langmuir model assumed that the adsorption of Cd(II) was at homogenous sites on PE, while the Freundlich model was on the assumption that the Cd(II) sorption occurred on heterogenous sites of BB. From Table 2, the maximum adsorption capacity (Q_m) of PE towards Cd(II) was 108.6 µg/g via monolayer sorption, which affirms that Cd(II) was able to sorbed onto PE and carried the co-contaminant properties, posing serious threats to aquatic environments.

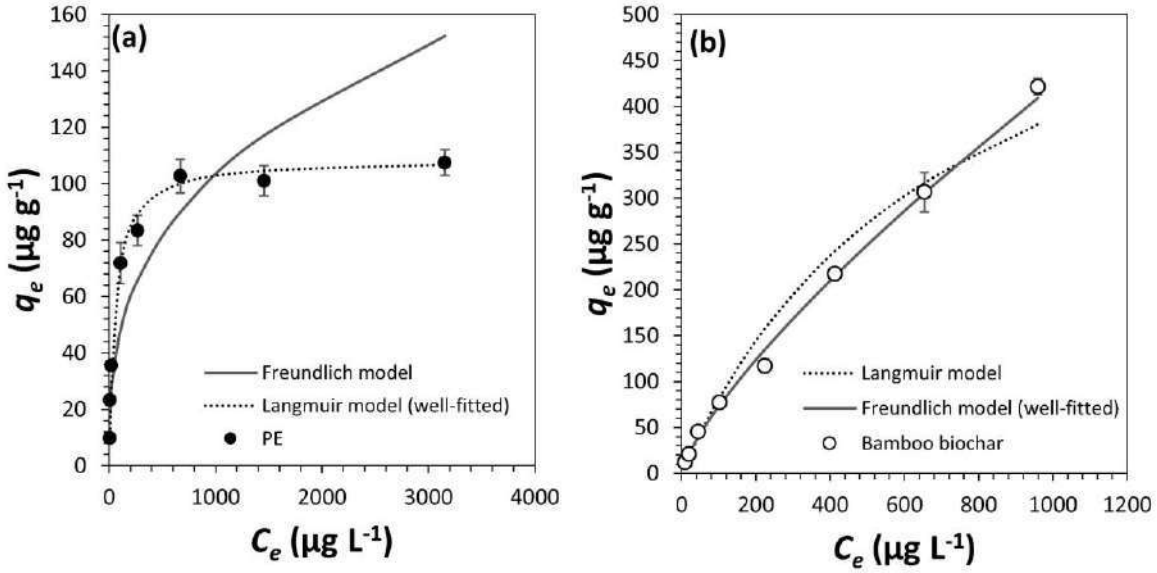

Figure 3. Adsorption isotherms of Cd(II) by polyethylene (PE) (a) and by bamboo biochar (BB) fitted with Langmuir and Freundlich isotherm models.

Regarding the well-fitting of Freundlich model (R^2≈0.9976) by bamboo biochar (BB), it served as a potential adsorbent for Cd(II) via multilayer sorption (Song et al., 2013). The sorption interactions of Cd on the BB can occur via surface complexation, due to available surface functional groups (e.g., O–H and C=C functional groups) detected by FTIR (Figure 1). Moreover, the XRF analysis shows that the BB contains mineral compositions, particularly K_2O (39%), that could be involved during the Cd sorption (Table 1). The physical adsorption could also be taken place for Cd sorption due to high specific surface area on the BB (BET surface area ≈ 136 m^2/g).

Table 2. Parameters calculated from adsorption isotherms for Cd(II) by polyethylene and bamboo biochar with the Langmuir and Freundlich models.

Pollutant	Langmuir			Freundlich		
	K_L[a] (L/µg)	Q_m[b] (µg/g)	R^2	K_f (µg/g)(L/µg)$^{1/n}$	n	R^2
Polyethylene	0.0172	108.6	0.9827	9.8257	2.9395	0.6723
Bamboo biochar	0.0013	669.5	0.9807	2.1824	1.3120	0.9976

Conclusion:

This study demonstrated the Cd adsorption on polyethylene (PE) microplastics and the capability of bamboo biochar (BB) to remove Cd from aqueous solutions through adsorption isotherm studies. Cadmium sorption on PE could be well-described by the Langmuir model, while the Freundlich model could explain the Cd sorption by BB. Results affirms that microplastics tend to accumulate with metals, which can enter the food chain and acts as carriers for metals in aquatic environments. Further investigation on the removal of microplastic-metal co-contaminants by biochars could be achieved to provide possible mitigation towards these pollutants entering into food chain and affecting the aquatic living organisms.

Acknowledgements:
This research project has received funding from the KMUTT Research Funding 2020.

References:
1. Agrafioti E, Kalderis D, Diamadopoulos E. J. Environ. Manage. 2014;146:444–450.
2. Cantrell KB, Hunt PG, Uchimiya M, Novak JM, Ro KS. Bioresour. Technol. 2012;107: 419–428.
3. Chaiyara R, Ngoendee M, Kruatrachue M. Sci. Asia. 2013;39:376–383.
4. Erni-Cassola G, Zadjelovic V, Gibson MI, Christie-Oleza JA. J. Hazard. Mater. 2019;369:691–698.
5. Li J, Li Y, Wu Y, Zheng M. J. Hazard. Mater. 2014;280:450–457.
6. Li Z, Xing B, Ding Y, Li Y, Wang S. Chin. J. Chem. Eng. 2020;28:2872–2880.
7. Liou TH, Wu SJ. J. Hazard. Mater. 2009;171:693–703.
8. Mclaren RG, Kanjanapa K, Navasumrit P, Gooneratne SR, Ruchirawat M. Water Air Soil Pollut. 2004;154:385–398.
9. Raul PK, Senapati S, Sahoo AK, Umlong IM, Devi RR, Thakur AJ, Veer V. RSC Adv. 2014;4:40580–40587.
10. Rybarczyk MK, Peng HJ, Tang C, Lieder M, Zhang Q, Titirici MM. Green Chem. 2016;18:5169–5179.
11. Sharma S, Chatterjee S. Environ. Sci. Pollut. Res. 2017;24:21530–21547.
12. Song X, Zhang Y, Yan C, Jiang W, Chang C. J. Colloid Interface Sci. 2013;389:213–219.
13. Thongra-ar W, Musika C, Wongsudawan W, Munhapol A. Environmentasia. 2008;1:37–45.
14. Tong M, He L, Rong H, Li M, Kim H. Water Res. 2020;169:115284.
15. Wongrod S, Simon S, Guibaud G, Lens PNL, Pechaud Y, Huguenot D, van Hullebusch, ED. J. Environ. Manage. 2018;219:277–284.
16. Worakhunpiset S. Int. J. Environ. Res. Public Health. 2018;15:1–15.
17. Yu F, Yang C, Zhu Z, Bai X, Ma J. Sci. Total Environ. 2019;694:133643.

Variation of the phytotoxicity of crumb rubbers waste on wheat (*Triticum aestivum* L.) seed germination with leaching conditions

Pimchanok Phatho,[1,2] Chanokphat Sengtrakun,[1] Khamphe Phongthong,[3*]
Thitipone Suwunwong [1,2*]
[1] School of Science, Mae Fah Luang University, Tasud, Muang, Chiang Rai, 57100, Thailand
[2] Center of Chemical Innovation for Sustainability (CIS), Mae Fah Luang University, Tasud, Muang, Chiang Rai, 57100, Thailand
[3] Environmental Assessment and Technology for Hazardous Waste Management Research Center, Faculty of Environmental Management, Prince of Songkla University, Songkhla 90112, Thailand
*e-mail: thitipone.suw@mfu.ac.th, khamphe.p@psu.ac.th

Abstract:
In recent years, recycling waste tires into crumb rubber, especially civil engineering applications and filler to reduce production costs in various industries has been gaining more and more interest. Crumb rubber is recycled rubber produced from automotive and truck scrap tires. However, the pollutants contained in crumb rubbers waste could potentially leach out and contaminate the local environment, which presents an obstacle to the reuse of the materials. To evaluate the environmental feasibility of using crumb rubbers waste as recycled material in construction, the leaching derived ecotoxicity was assessed. In the present work, an attempt has been made to study the environmental impact and physio-chemical properties of crumb rubber through Scanning Electron Microscopy (SEM), Fourier Transform Infrared Spectroscopy (FTIR), X-Ray Diffraction (XRD), X-ray fluorescence (XRF). Moreover, the leaching behaviour of crumb rubbers waste under various conditions, including the extractant type, leaching time, and leachate pH was investigated, and the phytotoxicity of these leachates on wheat (*Triticum aestivum* L.) seed germination was determined. It was found that heavy metal concentrations in the leachate were pH and leaching time. Heavy metals were the main pollutants present in wheat seeds. Heavy metals (especially Ba, Cr, Cu and Pb) had a substantial inhibitory effect on wheat seed germination and root elongation. To safely use crumb rubbers waste in construction, the potential risk and ecotoxicity of leached materials must be addressed.

SPECIES DIVERSITY OF LICHEN AT THE UTHOKKAWIPATPRASIT WATER GATE IN PAKPHANANG DISTRICT, NAKHON SI THAMMARAT PROVINCE

Kajonsak Vongshewarat1,[1] Supattara Phokaeo[1] and Vasun Poengsungnoen*,
Lichen Research Unit, Department of Biology, Faculty of Science, Ramkhamhaeng University, Bangkok, 10240
* email: kvongshewarat@hotmail.com

Abstract:
Lichen is a composite organism consisting of fungus and alga and/or cyanobacterium functioning in a symbiotic association. Survey and collection of lichens around Uthokkawipatprasit water gate in Pakphanang District, Nakhon Si Thammarat Province during October - November 2018 found 84 specimens. They were classified based on morphological and anatomical characteristics of thalli, ascomata, and colorless to grey-brown or brown color, ellipsoidal to fusiform shapes, muriform or trans-septate types of ascospores. In addition, chemical characteristics of KOH+ red purple on thalli or around ascomata were also observed. Nineteen species belonged to 10 families and 13 genera including *Bacidia, Coenogonium, Cresponea, Cryptothecia, Dyplolabia, Glyphis, Lecanora, Leucodecton, Malmidea, Nigrovothelium, Porina, Pyrenula* and *Trypethelium*. The highest diversity of lichens included 14 species which were found on *Calophyllum inophyllum* L., whereas the common lichens were *Bacidia submedialis* and *Cresponea proximata*

THE COMPARATIVE LEAF ANATOMY OF *Erycibe* ROXB. IN THAILAND

Ploypassorn Thirajitto[1,*], Benyawat Kongnarwa[1], Achiraya Manitkul[1], Paweena Traiperm[2] and Jiroat Sangrattanaprasert[1]

[1]Department of Biology and Health Science, Mahidol Wittayanusorn School, Nakhon Pathom 73170, Thailand

[2]Department of Plant Science, Faculty of Science, Mahidol University, Bangkok 10400, Thailand

*e-mail: s6208058@mwit.ac.th

Abstract:

The genus *Erycibe* belonging to the morning-glory family (Convolvulaceae) has small scented flowers and deeply lobed corolla; the genus is mostly distributed over tropical Asia. Eleven species of *Erycibe* have been reported in Thailand. Some species of *Erycibe* have been used as medicinal plants, such as arthritis-treated medicine from *E. schmidtii.* Owing to the morphological similarity within some species, the anatomical features could facilitate species identification. Thus, this study aims to investigate leaf anatomy using paraffin method in transverse section of nine species, including: *E. albida*, *E. citriniflora*, *E. cochinchinensis*, *E. coriacea*, *E. elliptilimba*, *E. expansa*, *E. griffithii*, *E. stapfiana*, and *E. subspicata*. The other two species were not studied due to the lack of specimens. All anatomical features were studied under the light microscopy. The observed anatomical patterns were considered. The outline and the vascular bundle arrangement of midvein are the main characters to discriminate species among *Erycibe*. A single layer of epidermal cells is found in almost all species except *E. griffithii* which has single to double layers. The patterns of adaxial and abaxial sclerenchyma arrangement are different among most species. Lastly, leaf margin characters, flat or revolute, are also valued in species identification. A key to the species based on leaf anatomy data is provided.

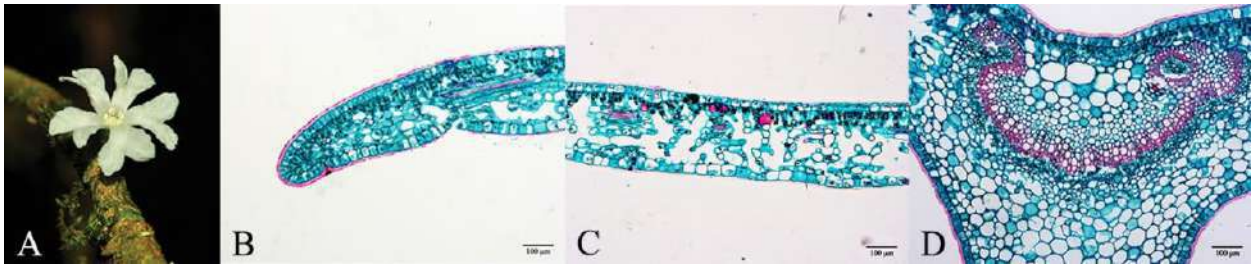

Figure 1. *Erycibe albida* (A) flower (B-D) leaf anatomy in transverse section: (B) margin, (C) blade, (D) midrib

Colorimetric method based on the Schiff's test for detection of methanol adulteration in hand sanitizer

Chirapha Prakobdi,[1,2] Duangjai Nacapricha,[1,2] Thanthapatra Bunchuay,[2] Phoonthawee Saetear[1,2,*]

[1]Flow Innovation-Research for Science and Technology Laboratories (Firstlabs), Department of Chemistry, Faculty of Science, Mahidol University, Bangkok 10400, Thailand.

[2]Department of Chemistry and Center of Excellence for Innovation in Chemistry, Faculty of Science, Mahidol University, Bangkok 10400, Thailand.

*e-mail: phoonthawee.sae@mahidol.edu

Abstract:

The outbreak of Corona virus disease 2019 (COVID-19) causes higher consumption of consumers in an alcohol gel/spray product for hand sanitizing. As a result, there is lacking of such product in markets. From this problem, some manufacturers smuggle to adulterate methanol into hand sanitizers, instead of use of ≥ 70 %(v/v) legal alcohols (i.e. ethanol, isopropanol and/or *n*-propanol). As widely known that methanol is harmful to human health. Thus, a screening method with accurate, rapid and cost-effective is appropriate for onsite detection. In this work, a colorimetric method based on an oxidation of methanol and the Schiff's test is presented for detection of methanol adulteration in hand sanitizer products. An analytical procedure includes 3 steps: (i) a ten-fold diluted sample is oxidized by permanganate reagent for 10 min to change methanol to formaldehyde; (ii) the excess of permanganate is then entirely reduced by oxalic acid reagent, and (iii) the Schiff reagent (fuchsin and bisulfite) is finally applied for 10 min as the colorimetric step to observe the color change due to the presence of formaldehyde converted from methanol. Pure or adulterated methanol in the product gives the distinguished color of magenta evaluated by naked eye. In contrast, pure legal alcohols give no color change after treatment with the Schiff's test. We found that linear detection ranges of methanol adulterated in legal alcohols were observed from 0.3 to 5.0 %(v/v) by UV-visible spectrophotometer (570 nm). Our proposed method would be useful as screening method for detection of adulterated methanol with fit to the maximum allowance concentration as 5 %(w/w) of the legal alcohol in the hand sanitizer products.

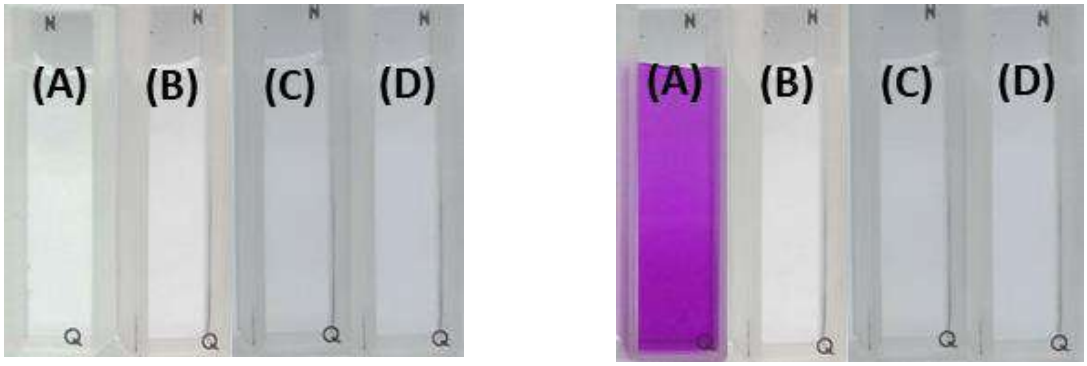

Figure 1.

Color observed from various types of 5 %(v/v) alcohol standards in water: (A) methanol, (B) ethanol, (C) isopropanol and (D) *n*-propanol as before (left) and after (right) treatment with the proposed method.

Development of lateral flow immunoassay for rapid and sensitive detection of anti-SARS-CoV-2 IgG

Umaporn Pimpitak[1,*] Abdulhadee Yakoh,[1] Sirirat Rengpipat,[2,3] Nattiya Hirankarn,[4,5] Orawon Chailapakul,[6] and Sudkate Chaiyo [1,6]

[1]Institute of Biotechnology and Genetic Engineering, Chulalongkorn University, Bangkok, 10330, Thailand
[2]Department of Microbiology, Faculty of Science, Chulalongkorn University, Bangkok, 10330, Thailand
[3]Qualified Diagnostic Development Center, Chulalongkorn University, Bangkok, 10330, Thailand
[4]Department of Microbiology, Faculty of Medicine, Chulalongkorn University, Bangkok, 10330, Thailand
[5]Center of Excellence in Immunology and Immune-mediated Diseases, Chulalongkorn University, Bangkok, 10330, Thailand
[6]Electrochemistry and Optical Spectroscopy Center of Excellence (EOSCE), Department of Chemistry, Faculty of Science, Chulalongkorn University, Bangkok, 10330, Thailand

*e-mail: Umaporn.P@chula.ac.th

Abstract: Coronavirus disease 2019 (COVID-19) caused by severe acute respiratory syndrome coronavirus 2 (SARS-CoV-2) is emerging as a global pandemic outbreak. The pandemic of COVID-19 is continuously spreading, becoming a worldwide emergency. Therefore, accurate testing devices are urgently needed among the international community to reduce the number of undetected cases. Serological assays to detect antibodies have been demonstrated to be a great accompaniment to the standard method of reverse transcription-polymerase chain reaction (RT-PCR), particularly after the second week of infection. Here, we have reported a colorimetric lateral flow immunoassay (LFIA) for the identification of the immunoglobulin G (IgG) produced against SARS-CoV-2. The presence of the targeted IgG can cause a visible color change from colorless to red, depending on the SARS-CoV-2 IgG concentration. Using a smartphone reader coupled with an ImageJ processing, the linear dynamic range was established in the range of 1 to 50 µg/mL with the lowest detectable level, which can be discriminated by naked eyes at 1 µg/mL. Benefiting from the fast (less than 15 min) and straightforward procedure, it can be concluded that the proposed LFIA holds excellent potential as point-of-care testing for serological detection of SARS-CoV-2 antibody.

PDMS AS A MATERIAL FOR DIGITAL MAGNETOFLUIDICS FOR APPLICATIONS IN BIOMEDICAL ANALYSIS

Pakakan Ngernpradab,[1] Numpon Insin,[2] Kanet Wongravee,[3] Monpichar Srisa-Art[1,*]

[1]Electrochemistry and Optical Spectroscopy Center of Excellence (EOSCE), Department of Chemistry, Faculty of Science, Chulalongkorn University, Bangkok 10330, Thailand

[2]Department of Chemistry, Faculty of Science, Chulalongkorn University, Pathumwan, Bangkok 10330, Thailand.

[3]Research Network NANOTEC-CU on Advanced Structural and Functional Nanomaterials, Faculty of Science, Chulalongkorn University, Pathumwan, Bangkok 10330 Thailand.

*e-mail: Monpichar.S@chula.ac.th

Abstract:

In this work, polydimethyl siloxane (PDMS), a well known material for microfluidic devices, was used to fabricate a digital magnetofluidic device. The superhydrophobic property of PDMS surface was easily achieved by coating with gold. The use of PDMS material allows for easy fabrication and flexibility of the digital magnetofluidic devices. The fabricated device was first demonstrated for titration experiments and colorimetric detection of phosphate based on the molybdenum blue method. A linear range for phosphate detection was between 10 and 100 ppm. From the preliminary results, the fabricated device will be further applied for complex analysis involving multi-step reactions. Therefore, this device could be an alternative platform for multi-step analysis, especially in the field of biomedical applications

Introduction:

Nowadays, microfluidic technology, which manipulates the fluids, such as liquids or gases in channels/chambers with dimensions of micrometers [1], has become important analytical tools because it provides the advantages including small volumes of sample and reagent consumption, possible automation, short analysis time, high analytical performance, and portability [2]. Therefore, microfluidics can be applied in a wide range of applications, such as chemistry, biology, medicine, and pharmaceuticals [3]. With microchannels, the clogging problem is a major concern. In addition, an external pump is required to deliver solutions. Accordingly, digital microfluidics, a part of microfluidic technology in which liquid droplets are manipulated on a surface using electric field, has been developed. Since the outstanding advantage of digital microfluidics is to manipulate individual droplets, it is highly suitable for multi-step reactions involving, washing, extraction and detection steps. Based on electrowetting, the transport path of the droplets depends on the number of the electrode arrays [4,5]. Thus, it is a challenge to fabricate an array of electrodes on a device [6]. Accordingly, digital magnetofluidics has been introduced as an alternative platform for manipulation of individual droplets. This microfluidic technology employs magnetic nanoparticles to control droplets on a superhydrophobic surface by the application of a magnetic field [7]. To fabricate digital magnetofluidic devices, a superhydrophobic material is key to allow for droplet movement when applying the external magnetic field. Previously, there have been different materials used for fabrication of digital magnetofluidic devices, such as silicon nanowire and low-density polyethylene [8], the Colocasia leaf [9] and Teflon-coated glass [10]. However, these materials are fragile and easily broken, and the fabrication process is complicated due to several steps in preparation. Recently, there has been research presenting polydimethylsiloxane (PDMS) coated with gold particles as a superhydrophobic substrate [11]. The gold film coating onto PDMS has microstructure and exhibits a superhydrophobic property. This method has the outstanding advantage of easy fabrication using a one-pot method. In addition, PDMS is also

a well-known material to fabricate microfluidic devices because it is easy to fabricate, cheap, environmentally friendly, gas permeable and flexible [12,13].

In this research, PDMS was used to fabricate a digital magnetofluidic device. The PDMS device was coated with gold to obtain a superhydrophobic property which allows for the movement of droplets on the PDMS surface. Iron oxide nanoparticles were used as a cargo to control the droplet movement on the PDMS device using an external magnetic force. Accordingly, each droplet can be controlled easily for reactions, especially for multi-step reactions involving washing, extraction, reaction and detection. The fabricated devices were first demonstrated for applications in titration experiments and phosphate colorimetric detection. In addition, the fabricated device will be further explored for complex reactions in the fields of biomedical analysis.

Methodology:

Materials

SYLGARD® 184 silicone elastomer kit, tetrachloroauric(III) acid trihydrate ($HAuCl_4.3H_2O$), sodium formate (HCOONa), sodium phosphate (Na_2HPO_4), L-ascorbic acid, phenol red and ammonium molybdate were purchased from Sigma-Aldrich. Hydrochloric acid (HCl) and sodium hydroxide (NaOH) were purchased form Merck. All reagents were analytical grade. Maghemite (γ-Fe_2O_3) nanoparticles were synthesized using the previous protocol [14].

Preparation of PDMS substrate

Sylgard 184 silicone elastomer base and a curing agent were mixed at a ratio of 10:1 by weight. The mixture was mixed well before being poured into a plastic box and then degassed in a refrigerator until no gas bubbles. The PDMS mixture was then cured in an oven at 60°C for 4 hours.

Fabrication of gold film on PDMS

Gold film coated on PDMS was fabricated by a simple wet chemical method using HCOONa as a reducing and stabilizing agent with $HAuCl_4$ as a gold ion source [11]. The gold growth solution (AuGS) was freshly prepared by mixing $HAuCl_4$ (0.24 mL, 0.5 M) with HCOONa (9.75 mL, 1 M). The mole ratio of gold and formate ions was kept at 1:80 and pH of AuGS was approximately 5.19. To fabricate gold film on PDMS, the AuGS solution was poured to cover the PDMS surface. Then, the gold coated PDMS was left at room temperature for 4 hours. The coating process involves the reduction of Au^{3+} by HCOONa to be Au^0 and the deposition of Au^0 on the PDMS surface. Subsequently, the excess AuGS solution was washed out form the gold film using milli Q water. Finally, the gold-coated PDMS was air dry at room temperature. The overall fabrication process is shown in Figure 1. To investigate the superhydrophobic property of the gold coated PDMS, a goniometer was used for contact angle (CA) measurements of a 2 µL DI water droplet on the gold film coated PDMS substrate.

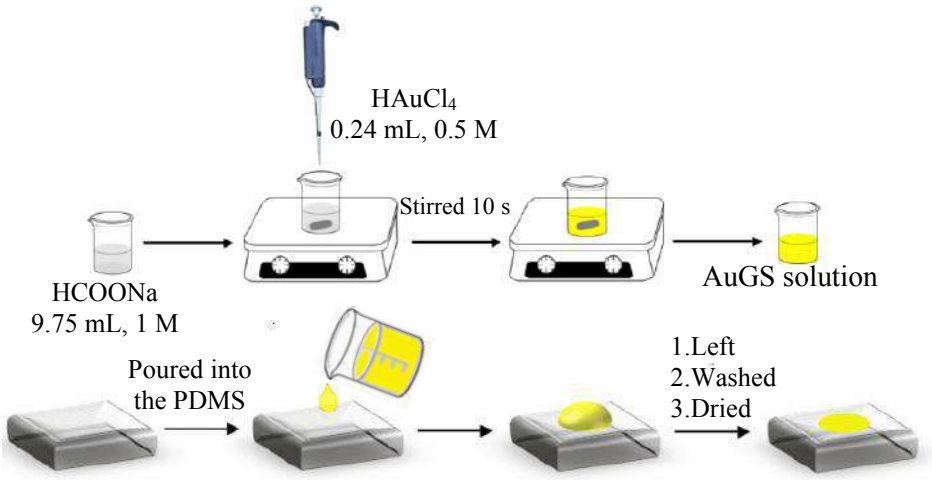

Figure 1. The overall fabrication process of gold film on PDMS.

Droplet movement and detection

To control the movement of reagent droplets on the gold-coated PDMS substrate, a 10 µL droplet containing iron oxide (γ-Fe_2O_3) nanoparticles was used as a cargo droplet that can be controlled by a permanent magnet. To perform reactions, the cargo drpolet was moved along to mix with each reagent droplets. Mixing of droplet content was achieved by magnetically moving the droplet in a circle. Colorimetric detection of droplet contents was performed by taking pictures of droplets, and the color intensity was analyzed using Image J software.

Titration experiment

First, the cargo droplet was magnetically moved to merge with a 10 µL droplet of phenol red (PR) as a pH indicator. The merged droplet was then moved to mix with a 10 µL HCl (0.1 M) droplet or a 10 µL NaOH (0.1 M) droplet, as shown in Figure 2 (left). The color of the final droplet was changed depending on the pH of the mixed solution.

Colorimetric detection of phosphate

The cargo droplet was first merged with a 10 µL Na_2HPO_4 droplet. The merged droplet was then moved along by the external magnet to mix with a 10 µL ammonium molybdate droplet and a 10 µL ascorbic acid droplet, respectively, as shown in Figure 2 (right)

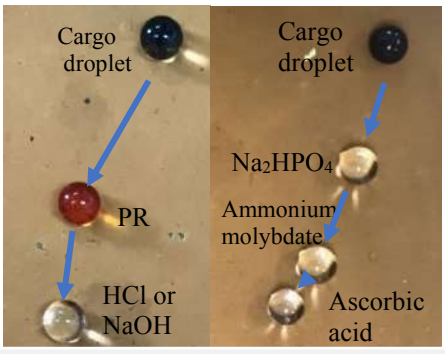

Figure 2. Titration experiments (left) and phosphate detection (right). The direction of droplet movement indicated by the arrow.

Results and Discussion:

Characterization of gold-coated PDMS substrate

From the previous work [11], wettability and morphological structure of gold-coated PDM was investigated, as shown in Figure 3. The SEM image shows the gold particles deposited on PDMS. To investigate the hydrophobicity of the gold-coated PDMS, the contact angle (CA) of a water droplet was measured by a goniometer. The static CA was measured to be 163.9° which was increased form the CA of bare PDMS (118.2°) [15], as shown in Figure 4.

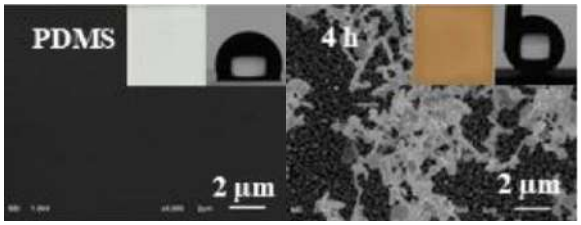

Figure 3. Water droplet and SEM pictures of bare PDMS (left) and gold-coated PDMS (right) [11].

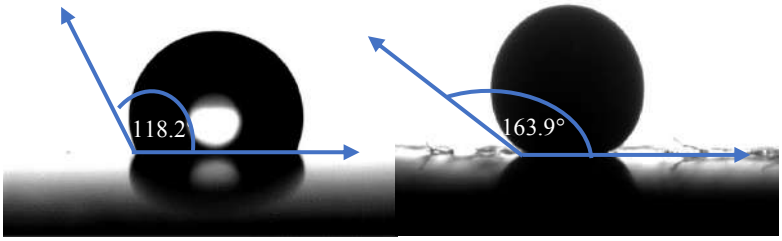

Figure 4. The static CAs of a water droplet on bare PDMS (left) and the gold-coated PDMS (right).

To confirm the superhydrophobic property of the gold film, the dynamic contact angles involving advancing (θ_a) and receding (θ_r) angles of a droplet on the superhydrophobic gold-coated PDMS were also measured. The hysteresis (H) is calculated from the difference between the angles ($H = \theta_a - \theta_r$). If it is lower than 10, the surface is categorized to be superhydrophobic. Results in Figure 5 show that the advancing and receding angles were not obviously different

and the hysteresis was calculated to be 0°. This indicates that the gold film rendered PDMS superhydrophobic.

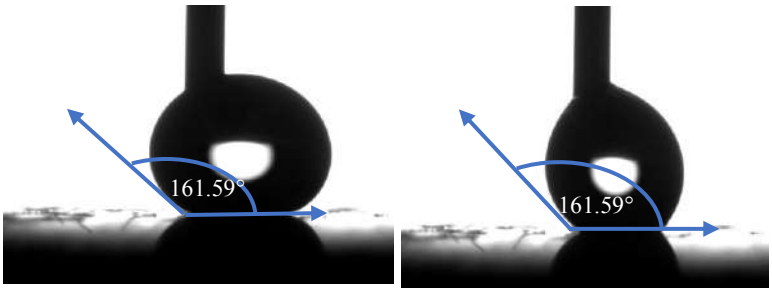

Figure 5. A water droplet on the gold-coated PDMS substrate for measuring dynamic CAs: advancing CA (left) and receding CA (right).

*Titration experiment*s

For the titration experiments, the cargo, PR and acid/base droplets were pipetted separately onto the gold-coated PDMS substrate. The acid (HCl) droplet appears colorless, while the PR droplet is dark yellow. After merging, the mixed droplet turned to light yellow, as shown in Figure 6 (middle). A similar experiment was carried out with the base (NaOH) droplet instead of the HCl droplet. The base droplet reacted with the indictor droplet to give a dark red color, as shown in Figure 6 (right). These results corresponded to the color change of PR from yellow to red over the pH range of 6.8 to 8.2.

Figure 6. Titration experiments showing the color change of PR indicator depending on the pH value. The color of PR droplet before mixing (left), the color of PR droplet mixed with an acid droplet (middle) and the color of PR droplet when mixing with a base droplet.

Colorimetric detection of phosphate

For the phosphate colorimetric detection, the reaction was based on the molybdenum blue method. Phosphate is reacted with ammonium molybdate in a strong acidic condition as shown in Equation (1) to form $[PO_4(MoO_3)_{12}]^{3-}$ which is then reduced by ascorbic acid to form $[H_4PMo(V)_4O_{40}]^{3-}$ (phosphomolybdenum blue), as shown in Equation (2) [16]. To perform these reactions on the device, each reagent droplets were subsequently merged. After 10 min, the mixed droplet generated the blue color, shown in Figure 7 (right). Images of each concentration of phosphate droplets as shown in Figure 8 (A) were taken for intensity analysis using Image J. A calibration curve was constructed by plotting color intensity as a function of concentration of phosphate (in ppm). The linear plot was obtained (R^2=0.99) in the range of 10 to 100 ppm, as shown in Figure 8B (inset).

$$PO_4^{3-} + 12MoO_4^{2-} + 27H^+ \rightarrow H_3PO_4(MoO_3)_{12} + 12H_2O \qquad (1)$$

$$H_3PMo(VI)_{12}O_{40} + \text{Ascorbic acid} \rightarrow [H_4PMo(V)_4O_{40}]^{3-} \qquad (2)$$

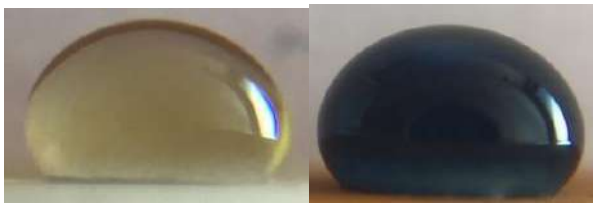

Figure 7. Colorimetric detection of phosphate. The reaction between sodium phosphate and ammonium molybdate before mixing with ascorbic acid (left). After mixing, the color of the mixed droplet was changed from colorless to blue within 10 min (right).

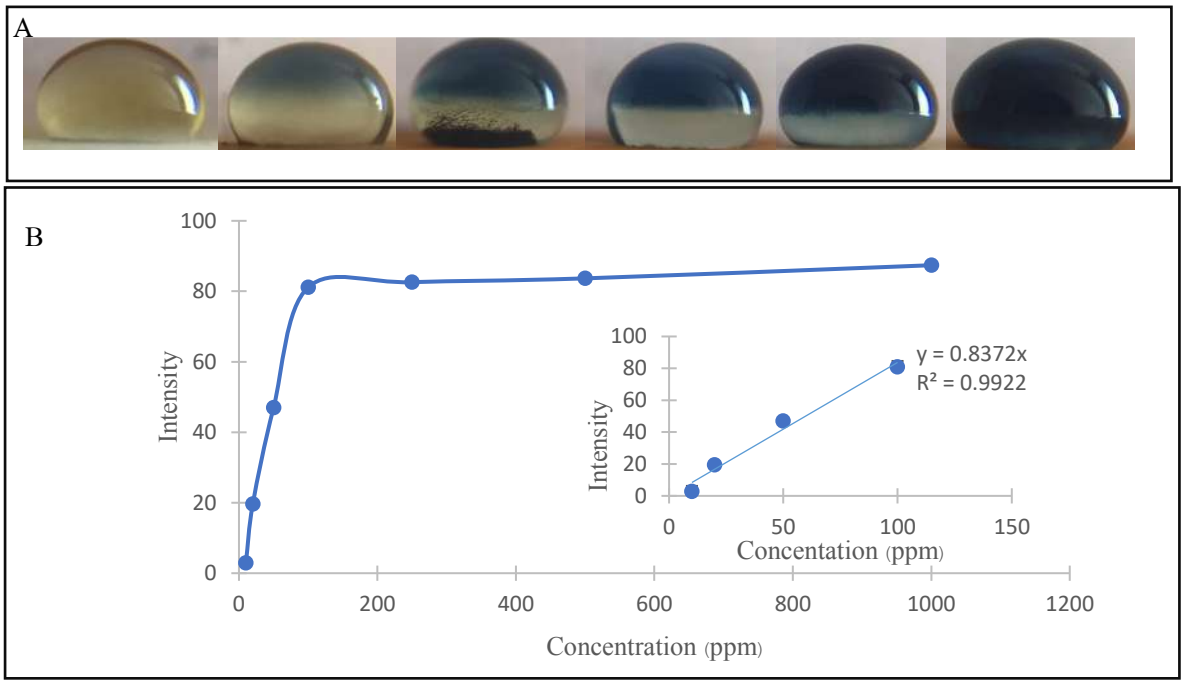

Figure 8. Colorimetric change for 10, 50, 100,250,500 and 1000 ppm of phosphate, respectively (A). The relation between intensity and difference concentration of phosphate. The inset shows a linear range used for quantitative analysis (B).

Conclusion:

Superhydrophobic gold-coated PDMS was successfully employed for fabrication of digital magnetofluidic devices. The wettability of the gold-coated PDMS surface was investigated and found that the CA was higher than 160º with low contact angle hysteresis (H=0º), indicating superhydrophobic. The device can be easily fabricated using a one-pot method and has shown its ability to control individual droplets. In addition, the fabricated device was successfully demonstrated for titration experiments and determination of phosphate using colorimetric detection. A calibration curve for determination of phosphate was found in the range of 10-100 ppm. Moreover, the developed devices showed high precision of phosphate detection with %RSD less than 5%; however, the limits of detection and quantitation of phosphate will be further studied. With ease of droplet controlling, this device will be further

applied for multi-step reactions, involving washing steps, extraction, chemical reaction, and detection, especially in biomedical analysis.

References:

1. Whiteside GM. Nature. 2006;442:368–373.
2. Reyes DR, Iossifidis D, Auroux PA, Manz A. Anal. Chem. 2002;74:2623–2636.
3. Situma C, Hashimoto M, Soper SA. Biomol. Eng. 2006;23:213–231.
4. Chou SA, Keimel C, Gu J. Nature. 2002;417:835–837.
5. Paik P, Pamula VK, Fair RB. Lap Chip. 2003;3:253–259.
6. Luk VK, Mo GCH, Wheeler AR. Langmuir. 2008;24:6382–6389.
7. Lehmann U, Hadjidi S, Parashar VK, Vandevyver C. Sens. Actuat. B: Chem. 2006;117:457–463.
8. Garcia AA, Egatz-Gomez A, Schneider J, Aella P, Dongging Y. Appl. Surf. Sci. 2007;254:330–334.
9. Oleschuk RD, Lili M, Rachel Y, Graham TTG. Sens. Actuat. B: Chem. 2015;220:5–12.
10. Nguyen NT, Lok KS, Koh WH. J. Fluids Eng. 2013;135:1–6.
11. Nootchanat S, Boonmeewiriya S, Parnsubsakul A, Insin N, Ekgasit S, Wongravee K. MTCHEM. 2021;21:1-9.
12. Sia SK, Whiteside GM. Electrophoresis. 2003;24:3563–3576.
13. McDonald JC, Duffy DC, Anderson JR, Chiu DT, Wu H, Schueller OJA, Whiteside GM. Electrophoresis. 2000;21:27–40.
14. Insin N, Lee H, Zimmer JP, Westervelt RM, Bawendi MG. ACS. 2008;2:197–202.
15. Tang J, Han Y, Chen H,Lin Q. Int. J. Polym. Sci. 2016:2016:1-5
16. Pradhan S, Pokhrel MR. Scientific World. 2013;11:58–62.

PROGRAM FOR COMPARING HIGH PERFORMANCE CHEMICAL FINGERPRINTING OF SAMPLES WITH COMPREHENSIVE TWO-DIMENSIONAL GAS CHROMATOGRAPHY TO EVALUATE THE SIMILARITY PERCENTAGE OF THE COMPONENTS IN 2 SUBSTANCES

Watcharapong Timklaypachara[1], Sira Duangnet[1], Pacharakrit Promsuwan[1], Amornsri Amornvatcharapong[2], Chadin Kulsing[3]
[1]Mahidol Wittayanusorn School, Nakhon Pathom, Thailand
[2]Department of Mathematics and Computing Science, Mahidol Wittayanusorn School, Nakhon Pathom, Thailand
[3]Department of Chemistry, Chulalongkorn University, Bangkok, Thailand
*e-mail: watcharapong,tim@gmail.com, s6208024@mwit.ac.th, s6208088@mwit.ac.th, amornsri.amo@mwit.ac.th, chadin.kul@chula.ac.th

Abstract:

Comprehensive two-dimensional gas chromatography is one of the valuable techniques in analytical chemistry. The technique is used during the COVID-19 pandemic. For example, to screen the infected person by their sweat. However, the analyzing step is challenging due to the processing time. The project's objective was to create the program in order (i) to identify the substances' compositions and (ii) to compare the similarity of any two substances. In this study, the novel comparison method was invented and divided into three steps, including data processing, data visualization and visual processing via Python programming. Moreover, the program output is reported in the percentage of similarity between 2 substances. For sample measurement, first, the raw data were processed by the conceived mathematical model, which stemmed from the machine procedure to evaluate another factor, second retention time. Then, the processed data were converted into a monochrome contour plot (also known as grayscale chromatogram), and Gaussian's filter smoothened the plot with a standard deviation of 5 to tolerate the experiment's errors. Finally, those two plots were analyzed by its Hue Saturation Value (HSV) pixel by pixel. The result was fascinating; the error of the program is only 0.967% approximately, obtained from four repeatedly experiment sets hence six comparisons. However, the program performance can be improved if more data are available.

STRAIGHTFORWARD SIGNAL AMPLIFICATION FOR A SENSITIVE DETECTION OF HORMONAL CORTISOL USING THE CONSTRICTED LATERAL FLOW TEST STRIP

Thanathip Kosawatphat[1], Abdulhadee Yakoh[1,2], Sirirat Rengpipat[3,4], Orawon Chailapakul[1], Sudkate Chaiyo[1,2]*, Narong Praphairaksit[1]*

[1] Electrochemistry and Optical Spectroscopy Center of Excellence (EOSCE), Department of Chemistry, Faculty of Science, Chulalongkorn University, Bangkok 10330, Thailand

[2] The Institute of Biotechnology and Genetic Engineering, Chulalongkorn University, Bangkok 10330, Thailand

[3] Qualified Diagnostic Development Center, Chulalongkorn University, Bangkok, 10330, Thailand

[4] Department of Microbiology, Faculty of Science, Chulalongkorn University, Bangkok, 10330, Thailand

*e-mail: narong.pr@chula.ac.th (N. P.), sudkate.c@chula.ac.th (S. C.)

Abstract:

Currently, monitoring cortisol levels can play a key role in understanding stress-related diseases. Several competitive immunoassay formats have been reported for the detection of this small hormone molecule. Lateral flow immunoassay (LFIA) is one of the most widely used platforms due to its simplicity and rapidity. Unlike previous sensors for cortisol sensing, in which most of them require complicated readers, specialized reagents, or even post-treatment methods to amplify the obtained signal, we demonstrated herein a concave test zone constructed on the LFIA device (cLFIA), which can directly enhance the signal response as the flowing sample was substantially concentrated before passing through the immobilized antibody. Nearly 2-fold sensitivity enhancement was obtained using this straightforward immunoassay format. Using a smartphone-based detection, the linear calibration plot of this cLFIA was established in the range of 5 to 5000 ng mL^{-1} with an LOD and LOQ of 1.6 and 4.84 ng mL^{-1}, respectively. This cLFIA device is believed to explore new possibilities for determination of other protein compounds and exploit them in point-of-care testing. This device design can be further applied for covid-19 diagnosis, which still requires massive diagnostic platforms.

Introduction:

Cortisol is a steroid hormone that is released from the adrenal cortex. This hormone can control blood pressure, metabolic activities, and cardiovascular function. Since the cortisol production is influenced by physical and psychological stress, monitoring of the cortisol levels can play a decisive role in understanding stress-related diseases [1]. Unusual high and low cortisol levels in the body lead to Cushing's syndrome and Addison's disease, respectively [2].

Currently, various standard methods to detect cortisol are usually ground on immunoassays coupled with a series of detection techniques such as chemiluminescent [3], surface plasmon resonance (SPR) [4], or electrochemical detection [5]. These detection methods generally rely on the utilization of sophisticated apparatuses, time-consuming and tedious procedures, impeding their practical implementation as a point-of-care (PoC) testing in actual clinical use. Although enzyme-linked immunosorbent assay (ELISA) with colorimetric, fluorescent or luminescent methods have been widely reported with sufficient sensitivity, their limitations arise from the use of the labor-intensive and expensive (microplate) readers, as well as the complexity from the measurement of enzyme activity [6]. Hence, a more straightforward, faster and cheaper method is of primary interest, especially for the on-site screening test. This has led to the uptake of the paper-based lateral flow immunoassay (LFIA) as the most prominent PoC diagnostic device due to its compromising sensitivity, simplicity, speed, and cost [7]. Therefore, the LFIA device is of interest in this study.

There are two commonly used immunoassay formats: competitive and non-competitive. Specifically, competitive immunoassays have been used effectively to measure small analytes such as drugs or hormones [8]. Indeed, cortisol is considered a low molecular weight hormone that fits the competitive assay [9]. In the competitive format, the unlabeled analyte competes with a fixed amount of labeled similar analyte (often gold nanoparticle (AuNP) labeled analyte). Only a small amount of analyte is efficient to produce a noticeable response. However, the sensitivity of this format is not considerably high compared to the sandwiched format and often yielded an inadequate limit of detection. Hence, the sensitivity enhancement of the competitive immunoassay is still challenging and yet to be explored.

Generally, there are two main strategies to improve the sensitivity: (i) chemical modification and (ii) geometrical modification of the device. However, the chemical modification usually requires additional steps and reagents and eventually prolongs the total analysis time. Therefore, a geometrical modification (ii) of the LFIA structure is far more promising for end-users. Different architectural modifications of the LFIA device have been proposed, mostly done by the constriction of the lateral flow channel to increase the binding event between immobilized antibody and analyte of interest.

In this work, we developed LFIA with a concave test line (cLFIA) fabricated using a straightforward office tool hole puncher. The cortisol presented in the sample and a fixed amount of AuNP-cortisol/BSA will be used in this competitive immunoassay. In the absence of cortisol, AuNP-cortisol/BSA will solely be captured by the immobilized antibody constricted at the concave test zone, thus revealing a red spot from AuNP within 10 min. Conversely, in the presence of cortisol, a small-size cortisol compound will compete with AuNP-cortisol/BSA to capture the antibody. This incoming cortisol will initially migrate to the test zone while less AuNP-cortisol/BSA can be bound with the antibody on the test zone, thus manifesting a less intense color (Figure 1). Benefitting from this concave flow path architecture, the increased binding events between antibody and antigen are demonstrated. Furthermore, a reduced amount of deposited antibody applied on the constricted test zone can also signify the advantages of the cLFIA proposed in this study.

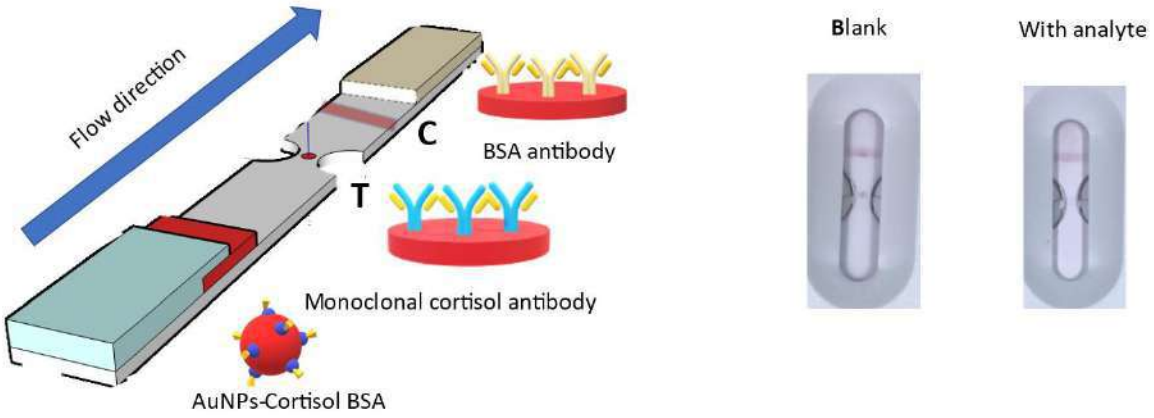

Figure 1. Schematic illustration of the cLFIA device in the absence and presence of cortisol. T and C are test spot and control line, respectively.

Methodology:

Materials

All commercial reagents were of analytical grade and handled according to the suppliers' material safety data sheets. Nitrocellulose (unicardsCN140), conjugated pads (GF33Glass), plastic backing card were purchased from SARTORU (USA). Sample pad (Fusion 5) and absorbance pad were obtained from GE healthcare Whatman (USA). Monoclonal cortisol antibody (CSB-MA0037110i0M) and Cortisol-BSA conjugated (CSB-MC00371b0105) were obtained from CUSABIO (USA). Gold nanoparticle solution 20 nm (AuNP), sucrose, phosphate saline buffer tablet (PBS), bovine serum albumin (BSA), cortisol, progesterone was acquired from Sigma-Aldrich (St. Louis, MO). Tween 20 was obtained from Glentham (UK).

Conjugation of cortisol-BSA with AuNP

A cortisol-BSA was conjugated with AuNP following the literature with a slight modification [12]. Initially, the pH of the AuNP solution was adjusted to pH 8 by 0.1 M NaOH to modify the charge at the surface of AuNP. After that, 1 mL of AuNP pH 8 was mixed with 100 µL of cortisol-BSA and incubated under the stirring condition for 30 min at RT. After incubation, 100 µL of 3% BSA was added to the solution to reduce nonspecific absorption. The mixed AuNP solution was then centrifuged at 12000 rpm (4°C) for 30 min. Lastly, the supernatant was removed while the residue was made up to the volume of 100 µL with 3% of BSA.

Fabrication of the cLFIA test strip for cortisol detection

To construct the concave test zone, the traditional LFIA strip was punched with the office hole puncher into two semicircles. The width between the two semicircles is 1 mm, while the distance between the conjugate pad and test zone was set at 2 cm. 0.2 µL of monoclonal

cortisol antibody was applied on the concave test zone of the nitrocellulose membrane. The control line, which is an anti-BSA antibody (600 µg mL^{-1}), was printed next to the test zone by ZX1010™ Dispense Platform (BIODOT, USA). Lastly, 4 µL of AuNP-cortisol/BSA was applied on the conjugate pad and dried at 37 °C for 30 min.

Cortisol detection procedure

To perform cortisol detection, 20 µL of the cortisol (working standard or serum sample) was loaded onto a sample pad, followed by 70 µL of running buffer containing 10 mM PBS, 0.1% tween, and 0.1%BSA. After 10 min, the LFIA test zone was captured by iPhone 7 (Apple Inc., USA) under an in-house light-controlled box with a movable strip tray using the Manual shot application. The color intensity (green channel intensity) of the test spot was then analyzed using Image J software.

Results and Discussion:

Microfluidic behavior of the cLFIA device

We investigated a signal amplification result by performing two sets of measurements using conventional LFIA and cLFIA. As presented in **figure 2A**, it can be seen that the concave LFIA markedly increases the sensitivity (slope) toward cortisol detection up to 2.4 times compared with that from conventional LFIA, simply by punching the paper device. Also, the intensity difference is almost 2.5-fold higher (tested at cortisol concentration of 5000 ng mL^{-1} and anti-cortisol concentration of 300 ng mL^{-1}) compared with the conventional test strip. All in all, it could be deduced that the cLFIA device can be used to enhance the sensitivity without requiring any tedious chemical modification method.

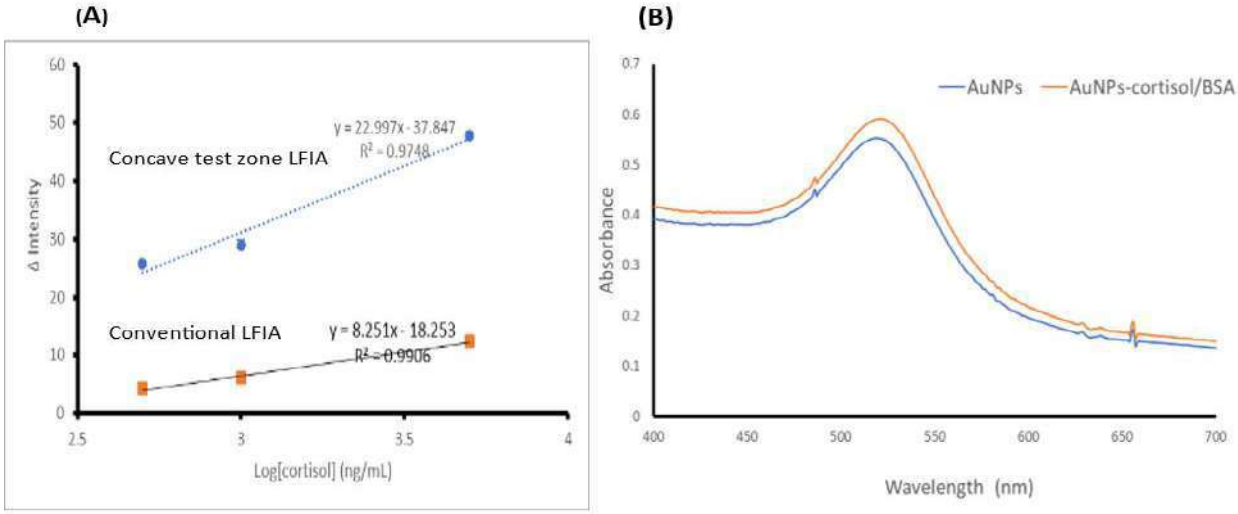

Figure 2. (A) a linear plot between Δintensity ($I_{tested\ cortisol}$ - I_{blank}) and logarithmic concentration of cortisol (500, 1000, and 5000 ng mL^{-1}) tested with a conventional LFIA and cLFIA. (B) UV-Vis absorption spectra of the AuNP before and after surface modification with cortisol/BSA.

Characterization of the AuNP-cortisol/BSA

In this section, the AuNP characterization (before and after modification with cortisol/BSA) was carried out using UV-Vis spectroscopy. The UV-Vis absorption spectroscopy was studied to monitor the size change and modification of biomolecules to the AuNP. Illustrated in **figure 2B** is the UV-Vis absorption spectra of the AuNP before and after modification with cortisol/BSA. It is well-known that the metallic nanoparticle (such as AgNP or AuNP) exhibited a strong absorption band in the visible region. Obviously, this characteristic peak of AuNP was distinctly seen at 518 nm (blue line), corresponding with the supplier's datasheet. Interestingly, when the cortisol/BSA was added and conjugated to the AuNP solution, the absorption peak of AuNP was shifted toward a longer wavelength (red-shift) from 518 to 521 nm due to an increase in the size of gold nanoparticle.

Analytical Performance of the cLFIA sensor

The sensing performance of the developed cLFIA was evaluated in this study. From inset of **figure 3**, it can be seen that the AuNP-cortisol/BSA is solely captured by the immobilized antibody on the test spot in the absence of cortisol (blank), thereby resulting in a red spot at the constricted zone. On the other hand, When the cortisol is presented in the solution, the red color spot from AuNP-cortisol/BSA is gradually disappeared (depending on the cortisol concentration) as the cortisol will compete with the fixed amount of AuNP-cortisol/BSA. Therefore, the color of the test spot will progressively change from red to colorless. For semi-quantitative interpretation, image processing software (ImageJ) was used to analyze the color intensity in the green channel of RGB mode. As shown in **figure 4A**, the Δintensity is increased proportionally with the cortisol concentration. A linear relationship between Δintensity and logarithmic concentration of cortisol was established in the range of 1 to 5000 ng mL^{-1} ($y = 13.176x-6.5861$, $R^2=0.9819$). The limit of detection (LOD) and limit of quantification (LOQ) were found to be 1.6 and 4.84 ng mL^{-1}, respectively. Interestingly, this LOD level is enough to detect cortisol in actual serum samples, thus showing a promising solution for on-site analysis.

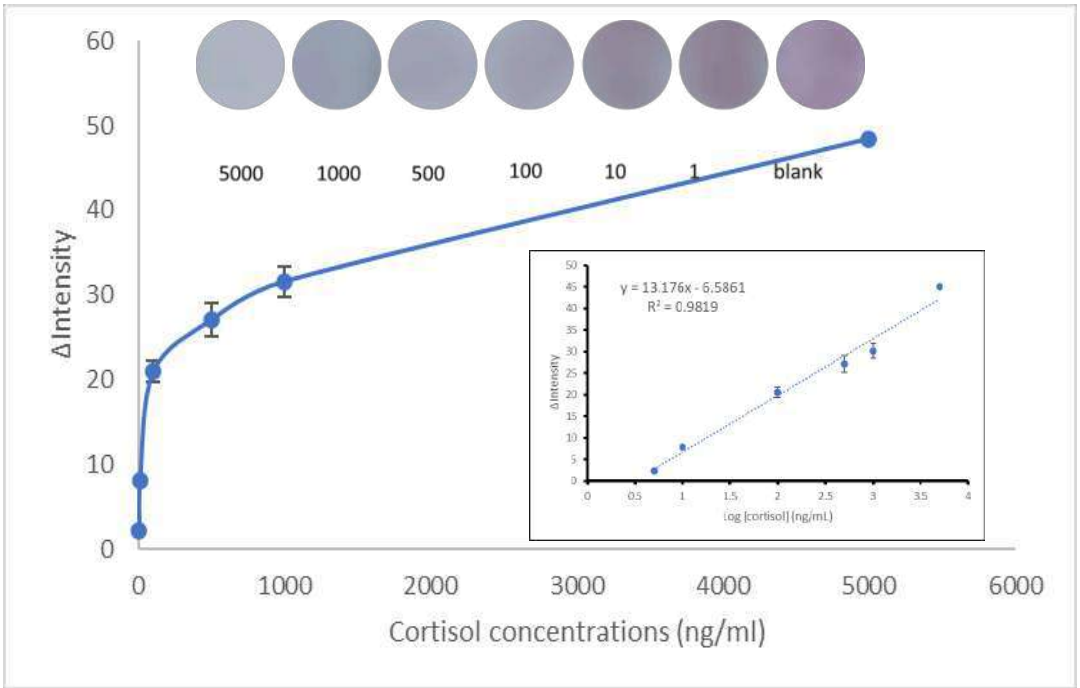

Figure 3. Signal response and linear relationship between ΔIntensity vs. logarithmic concentrations of cortisol; (inset) images showing the color of the test spot under the light controlled box.

Conclusion:

In closing, a paper-based LFIA device with a concave test zone was successfully developed to detect cortisol in human serum samples. This cLFIA test strip can be effortlessly manufactured using an available office hole puncher. Using such architecture, the sensitivity toward cortisol determination is greatly enhanced (almost 2.5 times) since the sample flowing was concentrated before entering the test spot, thus enabling more completed immunoreaction between antigen-antibody as compared with the traditional structure. Unlike previous reports, the proposed method shows a sensitive response without requiring any additional chemical modifications or a post-treatment amplification method. The LOD and LOQ of this device were found to be 1.6 ng mL^{-1} and 4.84 ng mL^{-1}, respectively, which are sufficient to extend the range for real serum samples analysis. Favorable advantages in terms of portability, user-friendliness and naked-eye detection without any modifications strongly signify the potential usefulness of this sensor. We believed that this cLFIA format could be used for other small protein molecules with good sensitivity.

Acknowledgment

This research was partially supported by the National Research Council of Thailand (NRCT, grant number: N41A640073).

References

1. Dedovic K, Duchesne A, Andrew J, Engert V, Pressner JC. NeuroImage. 2009;47:864-71.
2. Ahn CH, Lee C, Shim J,Kong SH, Kim S-j, Kim YH, et al. The Journal of Steroid Biochemistry and Molecular Biology. 2021;210:105856.
3. Abdulsattar JO, Greenway GM. J Anal Sci Technol. 2019;10:13.
4. Jo S, Lee w, Park J, Kim W, Lee G, et al. Sensors and Actuators B: Chemical. 2020;210:105856.
5. Kim KS, Lim SR, Kim W, Kim W, Lee G, et al. Sensors and Actuators B: Chemical. 2017;242:1121-8.
6. Barry TP, Lapp AF, Kayes TB, Malison JA. Aquaculture. 1993;117:351-63.
7. Nara S, Tripathi V, Singh H, Shrivastav TG. Anal Chim Acta. 2010;682:66-71.
8. Mahmoudi T, Guardia M, Shirdel B. TrAC Trends in Analytical Chemistry. 2019;116:13-30
9. Kosatsu T, Sato Y, Marki M, Ishida A, Tani H, Tokeshi M. Anal Chem Acta. 2021;1144:85-95.
10. Sena-Torralba A, Ngo DB, Parolo C, Hu L, Álvarez-Diduk R, Bergua JF, et al. 2020;168:112559.
11. Katis IN, He PJW, Eason RW, Sones CL. Biosensors and Bioelectronics. 2018;113:95-100.
12. Yakoh A, Siangproh W, Chailapakul O, Ngamrojanavanich N. ACS Applied Materials & Interfaces. 2020;12:22543.

A Perylene Diimide/Titanium Dioxide Hybrid as Electron Transporting Layer in Perovskite Solar Cells

Kanyaporn Thubthong,[1] Pisist Khumnorkeaw,[2] Vinich Promarak[3], Yingyot Infahsaeng[1,*]

[1] Division of Physics, Faculty of Science and Technology, Thammasat University, Klong Nueng, Klong Luang, Pathum-Thani, 12120 Thailand

[2] National Nanotechnology Center, National Science and Technology Development Agency Khlong Luang, 12120 Thailand

[3] Department of Materials Science and Engineering, School of Molecular Science and Engineering, Vidyasirimedhi Institute of Science and Technology, Wangchan, Rayong, 21210 Thailand

*e-mail: yingyot.infahsaeng.gmail.com

Abstract:

Perylene diimide derivatives as electron transport materials (ETMs) have been extensively attention for perovskite solar cells. In this work, we report an efficient electron transport material by the combination of novel perylene diimide, namely BPDIAQ, and titanium dioxide (TiO_2). The thin films of TiO_2:BPDIAQ at various annealing temperature were investigated for crystalline structure, functional groups, and surface morphologies. The results indicate that the BPDIAQ can be existed in the TiO_2 matrix at high annealing temperature of 400 ^oC. At this point, the PSCs based on TiO_2:BPDIAQ as electron transport layer achieves an excellent PCE of 11.38%. The concept using the perylene diimide derivative and TiO_2 hybrid for ETMs provides insights for future material engineering of the highly efficient perovskite solar cells.

Introduction:

Perovskite solar cells (PSCs) have been shown a promise of renewable energy sources due to their high-power conversion efficiency (PCE) up to 25.2%[1]. Up to the present time, the enhancement of cell performance has been still widely interested, especially, the material and device structure engineering and design. Typically, the wide bandgap formamidinium-methyl ammonium-cesium (FA-MA-Cs) lead iodide-bromide mixed perovskite with a bandgap of ≈ 1.7 eV exhibited the PCE of >11% [2–4]. Among of material layers of PSCs, the electron transport materials (ETMs) have received much attention[5]. In general, Titanium dioxide (TiO_2), has been used as ETMs in PSCs due to its outstanding charge transporting properties, which critically affect the photovoltaic performance. However, the structural and energy level modification of TiO_2 is rather limited. To improve the cell performance, proper electron mobility and compatible energy levels of both conduction band minimum (CBM) and valence band maximum (VBM) with perovskite are the criteria of ETMs. Recently, the TiO_2/ZnO electron transport bilayer shows a significantly efficiency enhancement up to 17%, which is the result of surface recombination suppression[6]. Moreover, doped TiO_2 was also shown to improve efficiency by modifying the energy level or surface morphology[7,8].

However, the compact TiO2 thin film require a high temperature annealing process (over 450 ^oC). Alternatively, organic, small molecular materials and theirs composites with TiO_2 have been proposed as ETMs for PSCs[9]. Therefore, low temperature solution-process can be

possibly applied for PSCs. One of the interested small molecules are perylene derivatives, which are, typically, the electron acceptor material and candidate as ETMs for PSCs.
Perylene diimide derivatives (PDI) have been used for the optoelectronic application because their high electron mobilities[10,11]. Several research of perylene derivatives have been reported for the enhancement of PSCs efficiency and stability[9,12–14]. The structural and energy band offset of PDI can be modified for the low temperature solution process, which is more advantage than TiO_2 electron transport layer. In particular, replacing TiO_2 layer by aminosubstituted perylene diimide can promote the power conversion efficiency up to 17.66%[12]. Moreover, the high PCE of 14.73% and stability were obtained from the PSCs with tetrachloroperylene diimide as ETMs[9]. In addition, the double electron transport layer (ETL) with a ladder-conjugated perylene diimide dimer showed a PCE that is better than typically fullerene based device[13]. Interestingly, the perylene diimide/fullerene hybrid was showed the effective ETMs with enhanced efficiency and stability[14]. At the current stage, the photovoltaic performance by using perylene diimide derivatives as ETMs are not high compared to the TiO_2 based device, but their proper stability can be obtained with low temperature process. On the other hand, the TiO_2 based device provide high PCEs of >25% but unsatisfactory device stability and high temperature process. In this context, the composites of PDI and TiO_2 is expected to provide the advantages of both materials. A high transparency of TiO_2 and high electron mobilities of PDI may improve the performance of PSCs. However, the temperature process of both materials is difference. Typically, the PDI thin film can be prepared at the temperature lower than 150 ^oC, but the TiO_2 layer require the temperature annealing higher than 400 ^oC. Because the PDI is small molecule that may be decomposed at high temperature, the proper annealing temperature is questioned for the composites of PDI and TiO_2 electron transport layer. Therefore, the investigation of fabrication process, especially annealing temperature, is required to optimize the high performance of PSCs.

In this work, PDI was mixed with TiO_2 with TiO_2:PDI ratio of 8:2 %V/V. Using the TiO_2:PDI as the ETL, the PSCs were successfully fabricated with various annealing temperature by the rapid convective deposition technique, which is one of the most effective solution-based coating methods[15]. The high PCE of 11.38% was achieved at the annealing temperature of 400 ^oC. Moreover, the crystalline structure, functional groups, and surface morphology of TiO_2:PDI thin films at various temperature were investigated.

Methodology:

TiO_2:PDI thin films preparation: N, N'-(9,10-dihydro-9,10-dioxo-2,6-anthracenediyl) bis(2ethylhexyl) perylene-3,4,9,10- tetracarboxylic diimide, namely BPDIAQ, was synthesized and received from Vidyasirimedhi Institute of Science and Technology (VISTEC). The BPDIAQ solutions were prepared in 2-butanol solution in a ratio of 10 milligrams: 250 microliters. The mixture was stirred at 70 ^oC for 1 hour and sonicated at room temperature for 30 minutes. Titanium Oxide (TiO_x) was diluted in isopropyl alcohol (IPA) in a ratio of 1 milliliter: 8 milliliters. BPDIAQ was dropwised in TiO_x solution. For ETL thin film fabrication, the TiO_x:BPDIAQ solution was coated onto the cleaned FTO substrate by the convective deposition technique at the speed of 4000 μm/s. The thin films were annealed at different temperatures of 100, 200, 300, 400 and 500 ^oC for 1 hour as shown in Table 1.

PSCs fabrication: Fluorine-doped tin oxide (FTO) glass substrates with dimension of 2.5×2.5 cm^2 were patterned by etching with zinc powder and 3 M hydrochloric acid, then were washed in ultrasonic baths of Alconox at 60 ºC for 30 min and cleaned in IPA for 30 min sequentially. For ETL, a compact TiO_x was coated onto the cleaned FTO substrate at 1250 □m/s by rapid convective deposition method for being reference device. The substrate was heated at 500 ºC for 1 hour, then a compact TiO_2 was formed. To study the perylene and annealing effects, the TiO_x:BPDIAQ solution was coated at 4000 µm/s and annealed at various temperatures (100, 200, 300, 400 and 500 ºC) for 1 hour. The FAI:MABr:CsI:PbI_2:$PbBr_2$ precursor solution was prepared from the mixture of FAI (1.00 M), PbI_2 (1.10 M), MABr (0.20 M), $PbBr_2$ (0.20 M), and CsI (0.02 M) in 1 mL of a mixed solvent of DMSO:DMF (4:1, v/v). For absorption layer, 100 µl of FAI:MABr:CsI:PbI_2:$PbBr_2$ precursor was spin-coated at 4000 rpm for 30 s. The substrate with perovskite precursor was heated at 120 ºC for 20 min and spiro-OMeTAD (in chlorobenzene, 72.5 mg/mL) of 70 µl was deposited at 3500 rpm by spin-coat technique. Finally, Au electrode was deposited via thermal evaporation under reduced pressure of 5×10^{-6} Torr. The active area of the devices was 0.04 cm^2. The device structure shows in Figure 1.

Table 1.
Annealing temperature and time of thin films and devices

NO.	Electrons Transporting Layer	Temperature	Time (min)
1.	TiO_2 (ref)	500	60
2.	BPDIAQ	100	30
3.	TiO_x: BPDIAQ	-	-
4.	TiO_x: BPDIAQ	100	60
5.	TiO_x: BPDIAQ	200	60
6.	TiO_x: BPDIAQ	300	60
7.	TiO_x: BPDIAQ	400	60
8.	TiO_x: BPDIAQ	500	60

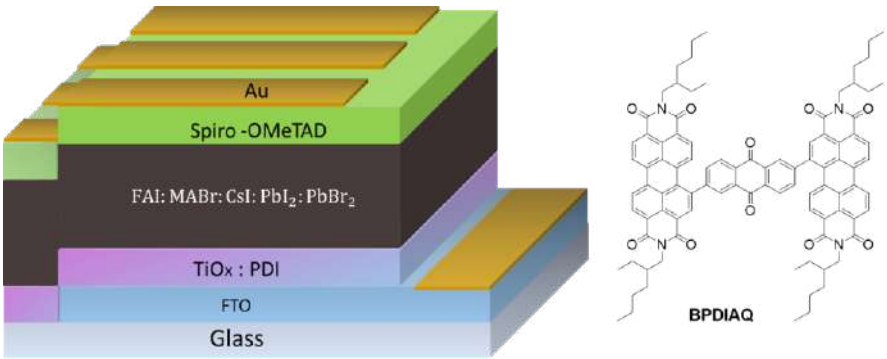

Figure 1.
Schematic drawing of a solar cells structure and chemical structure of BPDIAQ.

Characterization: The crystalline structure of TiO_2 and TiO_2:BPDIAQ thin films were examined using X-ray diffraction (XRD, model D8-discover, Bruker) technique using Cu-K□ radiation (□ = 1.542 Å). FTIR (PerkinElmer, spectrum 100) spectra were performed using attenuated total reflection (ATR) mode in the range 4000 – 400 cm^{-1}. The morphological properties were carried out using FE-SEM (Hitachi, S-4800) at an acceleration voltage of 10 kV. The current-voltage characteristics of PSCs were recorded from a solar simulator (ABET Technologies 10500 Solar Simulator) at the light intensity of 100 $mWcm^{-2}$ and an AM 1.5G solar light condition.

Results and Discussion:

Characterization of thin films: As shown in Figure 2(a), the XRD patterns of TiO_2 film exhibited the diffraction peaks at 25.5° and 48.3°, corresponding to (101) and (200) planes of anatase TiO_2, respectively. Thus, the results are in accordance with the previous report[16,17]. It should be noted that the broad spectrum about 20° represents the amorphous property of FTO glass substrate. The anatase TiO_2 peaks were less announced for TiO_2: BPDIAQ film at annealing temperature of 100 °C as shown in Figure 2(b). As the increasing of annealing temperature, the anatase TiO_2 peaks were more revealed. The clear evidence peaks of Figure 2(f) show that the anatase TiO_2 structure is formed. Note that a strong crystalline XRD peak of perylene derivatives is usually located at the 2θ of lower than 10°[18,19].

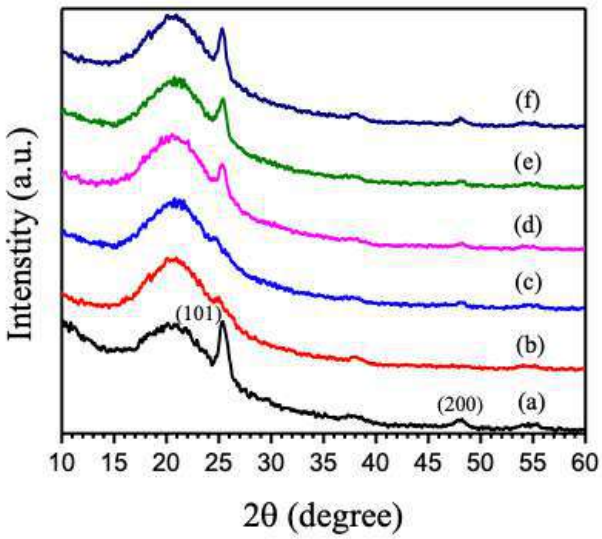

Figure 2.
X-ray diffraction spectra of (a) the pristine TiO_2 film and the annealed TiO_2:BPDIAQ films at (b) 100, (c) 200, (d) 300, (e) 400 and (f) 500 °C.

The ATR-FTIR measurements were investigated to confirm the formation of TiO_2 and TiO_2:BPDIAQ films at various annealing temperature. As shown in Figure 3, the broad band above 3500 cm^{-1} can be attributed to the stretching of the OH groups. The band between 700 – 480 cm^{-1} showed as the grey-box on the most right corresponds to Ti-O-Ti bonding[20,21]. Additionally, a signal between 1570 – 1440 cm^{-1} was detected for as-cast TiO_2:BPDIAQ film and the films at annealing temperature between 100 – 400 °C as indicated by the small greybox. This band is associated with -NO_x groups, which may indicate the bonding between TiO_2 and BPDIAQ. However, such band feature disappears at the annealing temperature of 500 °C, which may be a result of BPDIAQ evaporation or the change of chemical structure.

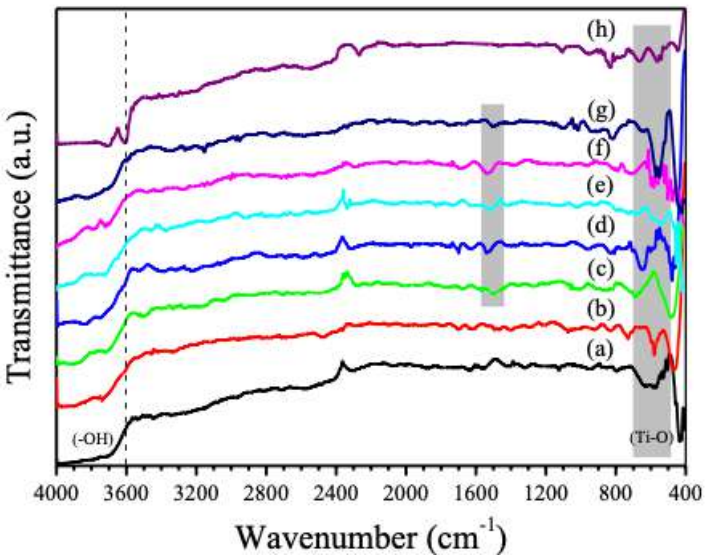

Figure 3.

Fourier-transform infrared (FTIR) spectra for (a) TiO_2, (b) BPDIAQ, TiO_2: BPDIAQ at (c) as-cast, and annealed at (d) 100, (e) 200, (f) 300, (g) 400 and (h) 500 ^oC.

The surface morphology of pure TiO_2 film was shown in Figure 4(a), which present slightly smooth surface of TiO_2 film. The crystalline phase of BPDIAQ film was observed as shown in Figure 4(b). For as-cast TiO_2:BPDIAQ film, the small fractures on the film surface can be observed as shown in Figure 4(c). From Figure 4(d) – (h), the size and depth of fractures were enlarged as the annealing temperature increase. However, these fractures were not distributed overall the film surface, but locate at some domain. From Figure 5, it is seen that the ETL layers of TiO_2 (a), TiO_2:BPDIAQ at 400 ^oC (g), and 500 ^oC (h) exhibited a compact layer. However, a mesoporous-like layer can be observed from the pristine TiO_2 layer. While, more dense and well packing can be obtained from the TiO_2:BPDIAQ layer at high annealing temperature.

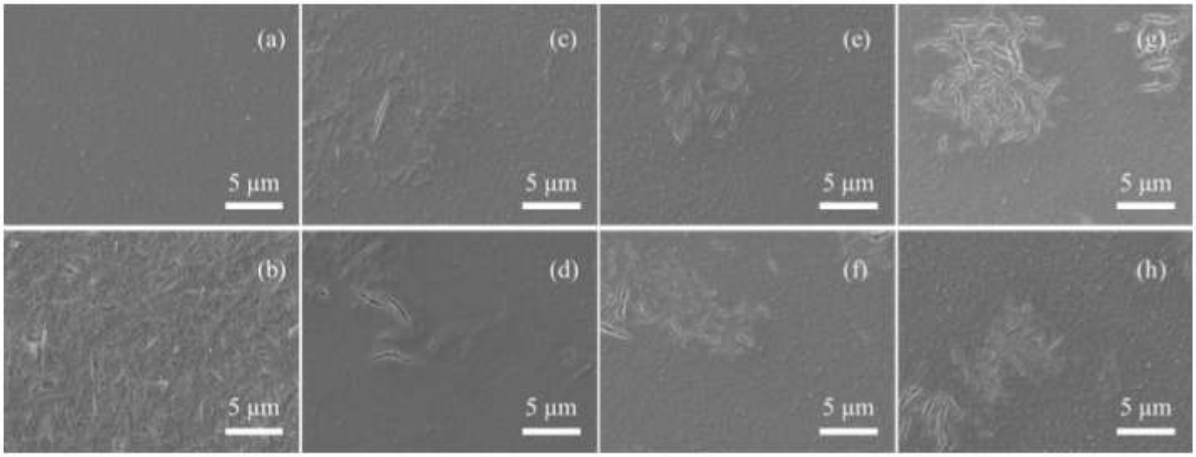

Figure 4.

SEM image of the top surface of (a) TiO_2, (b) BPDIAQ, (c) as-cast TiO_2: BPDIAQ and TiO_2: BPDIAQ thin films at various temperature of (d) 100, (e) 200, (f) 300, 400 and (h) 500 ^oC.

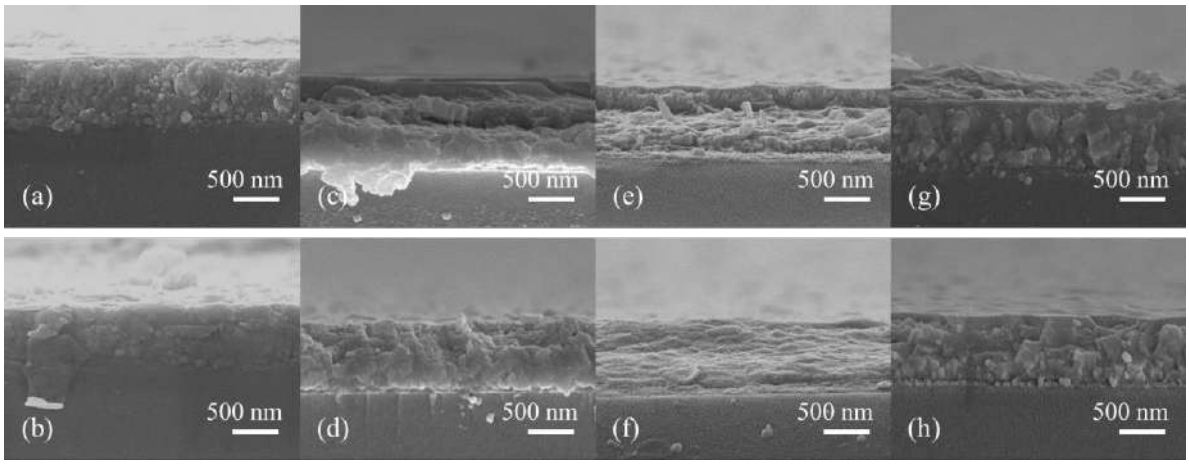

Figure 5.
Cross-section SEM image of (a) TiO_2, (b) BPDIAQ, (c) as-cast TiO_2: BPDIAQ and TiO_2: BPDIAQ thin films at various temperature of (d) 100, (e) 200, (f) 300, 400 and (h) 500 ^oC.

Characterization of PSCs: The perovskite solar cells were measured by reverse scan mode. A comparison of current density – voltage curves of PSCs with various ETLs and annealing temperature are shown in Figure 6. In general, the increasing of temperature is related with the increasing of crystallization for TiO_2. This plays a crucial role in improving the charge carrier transport, charge recombination, and consequently the fill factor of PSCs[22,23]. The PSCs with BPDIAQ as ETL exhibit the lowest PCE of 1.19%, which is the result of low open-circuit voltage of 0.26 V. Thus, there are the energy level mismatch between BPDIAQ and perovskite absorber. Interestingly, rather high short-circuit current of 14.92 $mAcm^{-2}$ was obtained, indicating that the BPDIAQ is a good electron acceptor. A reference TiO_2 based device show a promise PCE of 9.03% and rather high fill factor of 59.28%. When the annealing temperature increase, the PCE of TiO_2:BPDIAQ based device is also increased. A best PCE of 11.38% with an open-circuit voltage of 0.97 V, a short-circuit current of 17.11 $mAcm^{-2}$, and a fill factor of 68.55%, was achieved from the TiO_2:BPDIAQ based device with annealing temperature of 400 ^oC. The photovoltaic parameters of all PSCs conditions are shown in Table 2. From the crystalline structure, FTIR, and morphology results, it indicate that the TiO_2:BPDIAQ ETL at 400 ^oC annealing temperature exhibits the anatase TiO_2 incorporated with BPDIAQ. Interpenetrated pathways of BPDIAQ may provide the possibly channel for the electron transport from perovskite layer to TiO_2 or electrode. Due to the high electron mobility property of PDI derivatives, the existence of BPDIAQ may enhance the carrier transport and retard the possibility of surface recombination. As seen from Figure 6, higher short circuit current can be obtained as the annealing temperature increase above 400 ^oC. At this annealing temperature, the advantages of TiO_2 and BPDIAQ can dominate the performance of PSCs. Thus, the addition of BPDIAQ into TiO_2 can enhance the PSCs performance.

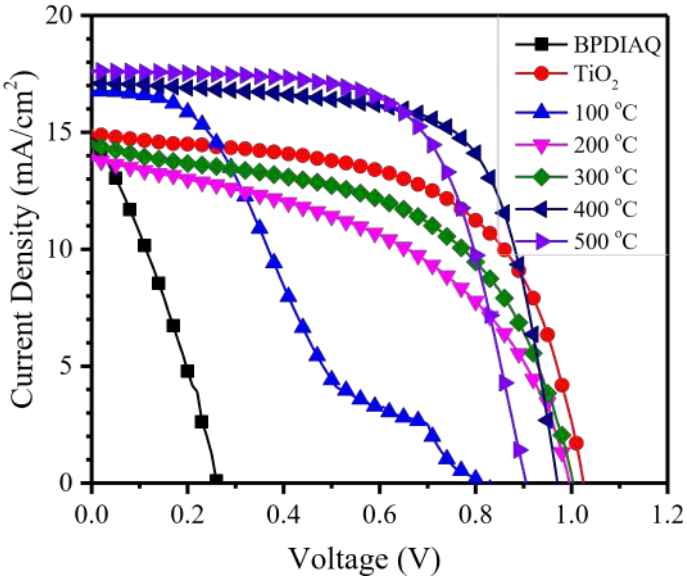

Figure 6.
The current density-voltage curves of PSCs of TiO_2, BPDIAQ and TiO_2: BPDIAQ devices at various temperature.

Table 2.
Photovoltaic Parameters of PSCs.

Device condition	V_{oc} (V)	J_{sc} (mA cm^{-2})	FF (%)	PCE (%)
BPDIAQ	0.26	14.92	30.79	1.19
TiO_2	1.02	14.93	59.28	9.03
TiO_2: BPDIAQ (100 °C)	0.81	16.78	29.85	4.06
TiO_2: BPDIAQ (200 °C)	0.99	13.83	48.41	6.63
TiO_2: BPDIAQ (300 °C)	1	14.48	54.08	7.83
TiO_2: BPDIAQ (400 °C)	0.97	17.11	68.55	11.38
TiO_2: BPDIAQ (500 °C)	0.9	17.63	65.35	10.37

Conclusion:

From this study, we develop a novel PDI/TiO_2 hybrid as an efficient ETMs. The thin films of TiO_2:BPDIAQ at various annealing temperature were investigated. The crystalline structure, functional groups, and morphology indicate that the BPDIAQ is existed in TiO_2 matrix at the annealing temperature of 400 °C. The PSCs based on TiO_2:BPDIAQ as ETL at 400 °C annealing achieves an excellent PCE of 11.38%. Thus, our results show the possibilities for the TiO_2 and perylene derivatives hybrid as electron transport materials in perovskite solar cells.

Acknowledgements:

The authors would like to thank for the financial support provided by the Thailand Research Fund (TRF) (MRG5980192).

References:

1. Kim, J. Y.,Lee, J.-W.,Jung, H. S.,Shin, H.,Park, N.-G. Chemical Reviews 2020;120 (15);7867–7918.
2. Lin, Y.,Chen, B.,Zhao, F.,Zheng, X.,Deng, Y.,Shao, Y.,Fang, Y.,Bai, Y.,Wang, C.,Huang, J. Advanced Materials 2017;29 (26);1700607.
3. Kaewprajak, A.,Kumnorkaew, P.,Sagawa, T. Journal of Materials Science: Materials in Electronics 2019;30 (4);4041–4055.
4. Kumnorkaew, P.,Rattanawichai, N.,Ratanatawanate, C.,Yoriya, S.,Lohawet, K.,Zhao, Y.,Vas-Umnuay, P. IEEE Journal of Photovoltaics 2020;10 (1);287–295.
5. Mahmood, K.,Sarwar, S.,Mehran, M. T. RSC Advances 2017;7 (28);17044–17062.
6. Xu, X.,Zhang, H.,Shi, J.,Dong, J.,Luo, Y.,Li, D.,Meng, Q. Journal of Materials Chemistry A 2015;3 (38);19288–19293.
7. Chandiran, A. K.,Abdi-Jalebi, M.,Yella, A.,Dar, M. I.,Yi, C.,Shivashankar, S. A.,Nazeeruddin, M. K.,Grätzel, M. Nano Letters 2014;14 (3);1190–1195.
8. Mahmood, K.,Swain, B. S.,Kirmani, A. R.,Amassian, A. Journal of Materials Chemistry A 2015;3 (17);9051–9057.
9. Zou, D.,Yang, F.,Zhuang, Q.,Zhu, M.,Chen, Y.,You, G.,Lin, Z.,Zhen, H.,Ling, Q. ChemSusChem 2019;12 (6);1155–1161.
10. Shi, Q.,Wu, J.,Wu, X.,Peng, A.,Huang, H. Chemistry – A European Journal 2020;26 (55);12510–12522.
11. Chatterjee, S.,Mandal, S. In *2017 International Conference on Trends in Electronics and Informatics (ICEI)*; IEEE, 2017; pp 400–406.
12. Zhang, H.,Xue, L.,Han, J.,Fu, Y. Q.,Shen, Y.,Zhang, Z.,Li, Y.,Wang, M. Journal of Materials Chemistry A 2016;4 (22);8724–8733.
13. Wang, H.,Yang, F.,Xiang, Y.,Ye, S.,Peng, X.,Song, J.,Qu, J.,Wong, W.-Y. Journal of Materials Chemistry A 2019;7 (42);24191–24198.
14. Luo, Z.,Wu, F.,Zhang, T.,Zeng, X.,Xiao, Y.,Liu, T.,Zhong, C.,Lu, X.,Zhu, L.,Yang, S.,Yang, C. Angewandte Chemie International Edition 2019;58 (25);8520–8525.
15. Kaewprajak, A.,Kumnorkaew, P.,Sagawa, T. Organic Electronics 2018;56;16–26.
16. Maryam, S.,Mufti, N.,Fuad, A.,Wisodo, H.,Sunaryono. IOP Conference Series: Materials Science and Engineering 2019;515;012007.
17. Srinivasu, P.,Singh, S. P.,Islam, A.,Han, L. Advances in OptoElectronics 2011;2011;1–5.
18. Mukherjee, B. Optik 2017;139;48–55.
19. Ishii, A.,Miyasaka, T. Chemical Communications 2012;48 (79);9900.
20. Castellanos-Leal, E. L.,Acevedo-Peña, P.,Güiza-Argüello, V. R.,Córdoba-Tuta, E. M. Materials Research 2017;20 (2);487–495.
21. Chougala, L. S.,Yatnatti, M. S.,Linganagoudar, R. K.,Kamble, R. R.,Kadadevarmath, J. S. Journal of Nano- and Electronic Physics 2017;9 (4);04005-1-04005–04006.
22. Le Corre, V. M.,Stolterfoht, M.,Perdigón Toro, L.,Feuerstein, M.,Wolff, C.,Gil-Escrig, L.,Bolink, H. J.,Neher, D.,Koster, L. J. A. ACS Applied Energy Materials 2019;2 (9);6280–6287.
23. Shalan, A. E.,Narra, S.,Oshikiri, T.,Ueno, K.,Shi, X.,Wu, H.-P.,Elshanawany, M. M.,Wei-Guang Diau, E.,Misawa, H. Sustainable Energy & Fuels 2017;1 (7);1533–1540.

EFFECTS OF TYPES OF ARYLAMINES BASED BENZOXAZINE BINDERS IN BRAKE PADS ON THERMAL DEGRADATION KINETICS

Juntasak Wangrangsimakul,[1] Lunjakorn Amornkitbamrung,[1] Chanchira Jubsilp,[2] and Sarawut Rimdusit[1, *]

[1]Polymer Engineering Laboratory, Department of Chemical Engineering, Faculty of Engineering, Chulalongkorn University, Bangkok 10330, Thailand
[2]Department of Chemical Engineering, Srinakharinwirot University, Nakhon Nayok 26120, Thailand
*E-mail: sarawut.r@chula.ac.th (Corresponding author)

Abstract: This research aimed to study the effects of the alkyl-substituted aromatic amines of polybenzoxazine resins used as binders in the non-asbestos friction composite materials. The effects of polybenzoxazine resins, BA-ot, BA-pt, BA-a, BA-mt and BA-35x, used as a binder of the brake pad on thermal stability, thermal degradation and kinetic behaviors were investigated using thermogravimetric analysis (TGA) at the different heating rates. For the friction composite system using BA-35x as binder, the derivative thermograms exhibited six stages of thermal decomposition reaction. The activation energies (E_a) were determined by Kissinger method, Flynn-Wall-Ozawa method and Coats-Redfern method of six stages to be 250, 240, 110, 220, 350 and 525 kJ/mol, respectively. Furthermore, from the calculation by Criado method, the thermal degradation mechanism was proposed to be the appropriated type of random nucleation with one nucleus on the individual particle (F1).

Introduction:

One of the most crucial parts in all automotive applications is the braking system requiring controlled friction, wear behavior, and thermal degradation. Friction materials play an important role in the brake system since brakes use friction to stop the motion of vehicle. A conventional automotive braking system consists of a disc and brake-lining pads, and must fulfill requirements such as good wear resistance, a stable coefficient of friction, reduced noise, decreased emission of particulate matter and proper mechanisms that affect thermal and frictional properties[1]. In the recent time, composite polymer-based friction materials have been finding greatly increased potentials for applications in several industries including automotive, self-lubricating materials, industrial equipment, and aerospace. Their typical benefits included ease in manufacturing, low cost, high damping of noise and vibrations, low friction, and self-lubrication[2]. Phenolic resins are a large family of polymers, consisting of a wide variety of structures based on the reaction products of phenols with formaldehyde. The traditional phenolic polymers have advantages including heat resistance, flame retardance, dielectric insulation properties; thus, they are employed in a wide range of applications[3]. Though phenolic-based materials are widely used to meet several desirable properties, such as good mechanical strength, moldability, economy, high thermal and dimensional stability, resistance against various chemicals and flame retardance, a number of short-comings are also associated with these materials. A typical binder in composite brake friction materials including phenolics is brittle, low impact resistance, highly toxic, and decomposes at relatively low temperature, while brake pads and brake shoes are exposed to high compressive and shear forces. Benzoxazines, a new type of phenolic resins, were developed to overcome the shortcomings of traditional phenolics while retaining their benefits.

Benzoxazine resins can be easily synthesized from phenol, formaldehyde, and amine by employing solution or solventless methods[4].The polymerization of benzoxazine resins proceeds via ring opening of oxazine rings by thermal cure. In addition, they did not require catalysts for polymerization and did not produce by-product upon curing. Polybenzoxazines, emerged as superior alternative to classical phenolic resins for the past few decades[5]. These resins had structural resemblance to classical phenolics and, thus, many properties were similar. However, the tertiary amine groups in polybenzoxazines had drastic effect on the structure resulting in inter-and intra-molecular hydrogen bonds between amino groups and phenolic hydroxyls which was unusual for classical phenolics[6,7]. Accordingly, polybenzoxazines had high mechanical strength, chemical resistance against acids and bases, high char yield, high glass transition (T_g) and relatively high service temperatures. Besides these important aspects, polybenzoxazines also bore in features that are uncommon for many resins such as low water adsorption that seemed to be in contrast to phenolic nature but stems from the intramolecular hydrogen bonds, and limited or no shrinkage upon curing due to the chain conformation of polybenzoxazines. Therefore, polybenzoxazines have found various industrial applications such as aerospace composites, electronic circuit boards, blends and alloys[8].

In this research, friction composites based on various polybenzoxazine binders were prepared. The thermal degradation kinetic parameters, such as activation energy (E_a), and kinetic behaviors were evaluated by using three well-known methods, i.e., Kissinger method, Flynn-Wall-Ozawa method, and Coats-Redfern method. Especially, Kissinger method and Flynn-Wall-Ozawa method were used in this study because they were mostly used in the literatures and could be used without prior knowledge of reaction mechanism. Additionally, Coats-Redfern method was used because it renders the degradation parameters and possible reaction mechanism. The thermal degradation mechanisms of the composites were also evaluated by using Criado method.

Methodology:

Preparation of Benzoxazine Resins

Polybenzoxazines were generally prepared by thermally activated polymerization of benzoxazines. According to the reported method[9,10], Aniline-based benzoxazine monomers were synthesized from bisphenol-A, para-formaldehyde, and aniline at a molar ratio of 1:4:2. The mixture was heated at about 110 °C in an aluminum pan and was mixed rigorously for about 30 min to yield a light-yellow solid monomer product. The same procedure was used to synthesize o-toluidine-based benzoxazine resin (BA-ot), p-toluidine-based benzoxazine resin (BA-pt), m-toluidine-based benzoxazine resin (BA-mt), and 3,5-xylidine-based benzoxazine resin (BA-35x).

Synthesis of Composite Friction Material

Each type of benzoxazine monomer was used to prepare friction material composites based five benzoxazine binders with the composite formulation following Akebono's patent no. US5360842A[11]. Each molding formulation was mixed at 120 °C for 40–45 min using an internal mixer to ensure uniform mixing. The compound was placed in iron mold with specified dimensions and then heated in a compression molder at 200 °C at a pressure of 15 MPa (using a hydraulic press) for 2 h. The fully cured composites were cooled to room temperature before being tested and characterized.

Characterizations

In this research, thermogravimetric analysis (TGA) was carried out and recorded on a thermogravimeter (model TGA1 STARe System, Mettler-Toledo). Degradation temperature

at 5% weight loss (T_{d5}) and char yield of all polybenzoxazines and arylamine based benzoxazine frictional composite were studied. A heating rate of 20 °C/min from room temperature (25 ºC) to the temperature about 1000 °C under nitrogen atmosphere was used to acquire TGA thermograms. The purge nitrogen gas flow rate was maintained at 50-100 ml/min. The sample mass used was measured to be approximately 10-15 mg. Weight loss of the sample was measured as a function of temperature. The degradation temperature (T_d) of polybenzoxazines and benzoxazine-composite were reported at their 5% weight loss. Char yield of the above specimens were also reported at 800 °C. With the evolved gases being released, the weight of the degradation residue is decreased gradually; thermogravimetry (TG) and the corresponding derivative thermogravimetry (DTG) curves of the composite is analyzed by peakfit to determine the thermal degradation step and calculated activated energy. To determine the kinetic parameters of thermal degradation, the conversion of the reaction was first evaluated. The kinetic parameters of thermal degradation can be determined by Kissinger method, Flynne-Walle-Ozawa method, and Coatse-Redfern method, an isoconversional method based on the principle that the reaction rate at constant extent of conversion is only a function of temperature, additionally, thermal degradation mechanism also determined by Criado method.

Results and Discussion:

Effects of Types of Arylamines Based Benzoxazine Binder in Brake Pad Composites on Thermal Stability

Thermal degradation and thermal stability are ones of crucial key thermal parameters for evaluating practical performances of composite friction materials. In this study, degradation temperatures of the polymer composites were defined as the temperature at 5% and 10% weight loss and the char yields were obtained at 800 ºC under nitrogen atmosphere for each composite. Five different arylamines based benzoxazine (BA-ot, BA-pt, BA-a, BA-mt and BA-35x) composites were selected to represent different types of brake pads in this study. Figure 1 showed the relationship between residual weight and temperature (ºC) from polybenzoxazines and arylamines based benzoxazine composites.

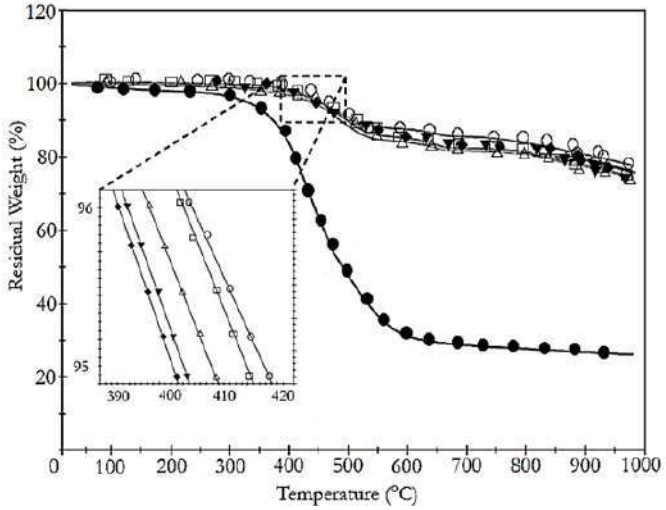

Figure 1

TGA thermogram from degradation of polybenzoxazine and friction composites prepared from different benzoxazine resin: (●) PBA-a polybenzoxazine, (▲) BA-ot based friction composite, (♦) BA-pt based friction composite, (Δ) BA-a based friction composite, (□) BA-mt based friction composite, (○) BA-35x based friction composite

The thermogram tends to decrease at higher temperature due to weight loss of the samples from thermal degradation. The higher residual weight at any temperature of arylamines based benzoxazine composites compare to polybenzoxazines shows higher thermal stability. The char yield determined at 800 ºC and weight loss data for each composite were also collected. From Figure 1, it could be explained the relationship between the thermal decomposition temperatures at 5% weight loss and the types of arylamine base in the composite. It clearly showed that the decomposition temperatures of the composites increase from about 131 ºC for pure PBA-a to about 402, 403, 406, 416 and 418 ºC for BA–ot, BA–pt, BA-a, BA-mt and BA-35x based binder friction composite, respectively. These temperatures increased with increasing crosslink densities[12,13], due to the increasing the amount of arylamine Mannich bridges and methylene bridges. Therefore, these results can be suggested that higher crosslink densities that found in different allylamine based binder could improve thermal stability of the polybenzoxazine composite friction materials. Moreover, the char yields of the composite systems exhibited the synergistic behavior as shown in Figure 1. As a result, the char yields of the composite were higher than those of neat polybenzoxazine. The highest char value at 800 ºC of about 80% was found for composite that apply PA-35x as based binder, while the value of pure PBA-a was only 30%.

From these results, the BA-35x based composite was selected for further kinetic studies of the friction composite systems since it provided the maximum decomposition temperature and char yield. After obtaining the TGA and DTG curves, using Seasolve Peakfit© v.4.12 program to separate the DTG curves of the composite at the various arylamine-based binders.

Analysis of The Thermal Degradation Kinetics of The Friction Composite

For the friction composite, BA-35x based composite was chosen to be represented, the composite began to lose weight at 260 ºC and go to the maximum at ca. 450 ºC. The result of the maximum thermal degradation temperature exhibited that composite sample of BA-35x has high degree of crosslinking thus it needs more energy to decompose and improve the thermal resistance. After resolving the TGA curves by using the computer software, Peakfit©, it can be noticed that the DTG curve of the composite, presented in Figure 2, composes of a three-stage weight-loss process.

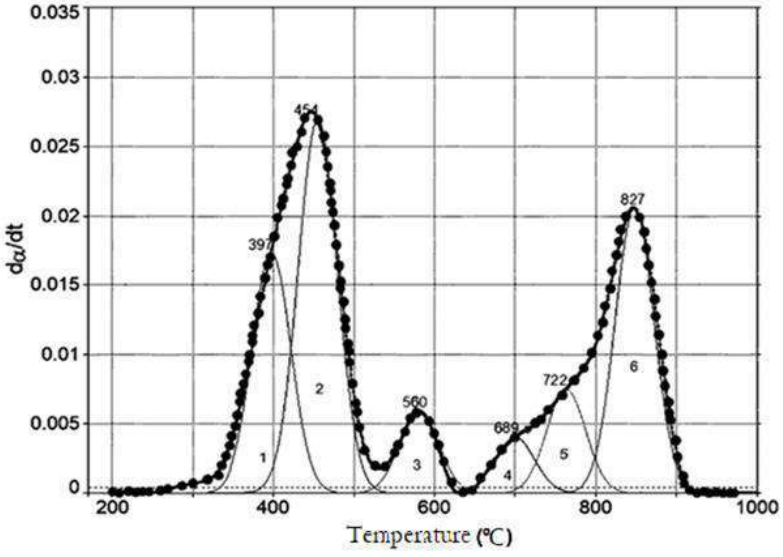

Figure 2

Derivative TGA thermogram of BA-35x brake pad composites and its separate peaks by using the Peakfit software: (●) experimental data, (—) simulated curve

From the Figure 2, the derivative thermograms for thermal degradation of friction composite at heating rate of 20 ºC/min, 6 peaks of weight-loss process were observed, centered approximately as per following

Peak 1 occurred at ca. 400 ºC represented the degradation of phenolic linkage in polybenzoxazine where the phenolic compound means the group of aromatics with hydroxyl group[9]

Peak 2 represented the decomposition of the Schiff base of the polybenzoxazine where the Schiff base is a basic compound with the general structure R1R2C=NR' from the condensation reaction between amine and aldehyde or ketone[12,13]

Peak 3 occurred at ca. 500-550 ºC displaying the degradation of rubber dust

Peak 4 and 5 observed approximately 700-750 °C presenting degradation of cashew dust and aramid pulp, respectively

Peak 6 displayed the degradation of barium sulphate occurred at 800-850 ºC.

Determine Thermal Degradation Kinetics Parameters: Kissinger Method (Differential Method)

The useful form of the Kissinger equation[14] for estimating the activation energy was

$$\ln\left(\frac{\beta}{T_p^2}\right) = \ln\left(\frac{AR}{\beta E_a}\right) + \ln[n(1-\alpha_p)^{n-1}] - \frac{E_a}{RT}$$

where T_p (K) is absolute peak temperature, α_p is weight loss at maximum weight-loss rate, n is the reaction order, β (K min^{-1}) is the heating rate and R (J/mol) is gas constant. The activation energy could be evaluated from the slope as the slope of the Kissinger plot of the straight-line $\ln(\beta/T^2)$ versus $1/T_p$. For peak 1, peak 2, peak 3, peak 4, peak 5, and peak 6, the activation energy can be evaluated as 248, 231, 115, 232, 365 and 523 kJ/mol, respectively.

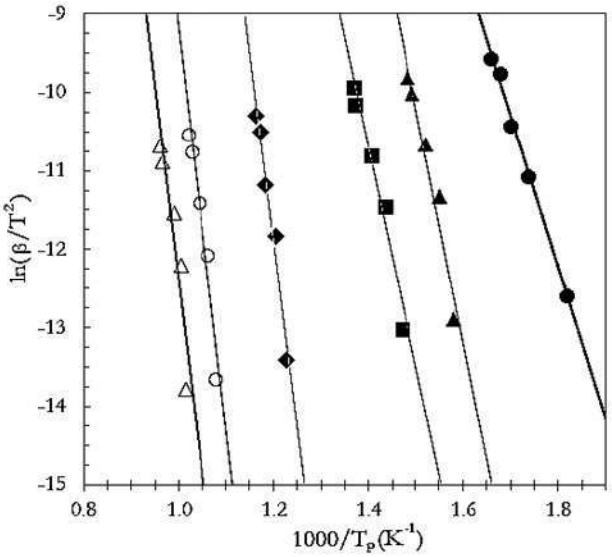

Figure 3

The relation between ln (β/T^2) and $1000/T_p$ as per Kissinger method (●) peak 1, (▲) peak 2, (■) peak 3, (♦) peak 4, (○) peak 5, (Δ) peak 6

Table 1

Activation energies determined by Kissinger method for the BA-35x based friction composite at different heating rates

Peak 1		Peak 2		Peak 3		Peak 4		Peak 5		Peak 6	
E_a (kJ/mol)	R^2	E_a (kJ/mol)	R^2	E_a (kJ/mol)	R^2	E_a (kJ/mol)	R^2	E_a (kJ/mol)	R^2	E_a (kJ/mol)	R^2
248.2	0.9507	231.3	0.9679	115.5	0.9723	232.4	0.9469	365.1	0.9723	522.5	0.9276

Determine Thermal Degradation Kinetics Parameters: Flynne-Walle-Ozawa Method (Integration Method)

Flynn-Wall-Ozawa method is relatively a simple method to calculate the value of activation energy from curve of weight loss versus temperature at different heating rates. This method can be applied to determine E_a without any knowledge of the reaction mechanisms[15],

$$\log \beta = \log\left(\frac{AE_a}{g(\alpha)R}\right) - 2.315 - \frac{0.457E_a}{RT}$$

where T (K) is the absolute temperature, α is conversion and β (K min^{-1}) is the heating rate. By this method, the Ea of the thermal degradation process of the brake pad composite was determined from the slope of the straight-line log β versus 1/T at constant value of fractional conversion. The activation energy for the thermal degradation reaction followed peak 1, peak 2, peak 3, peak 4, peak 5, and peak 6, were evaluated to be 241, 238, 107, 219, 362 and 531 kJ/mol, respectively.

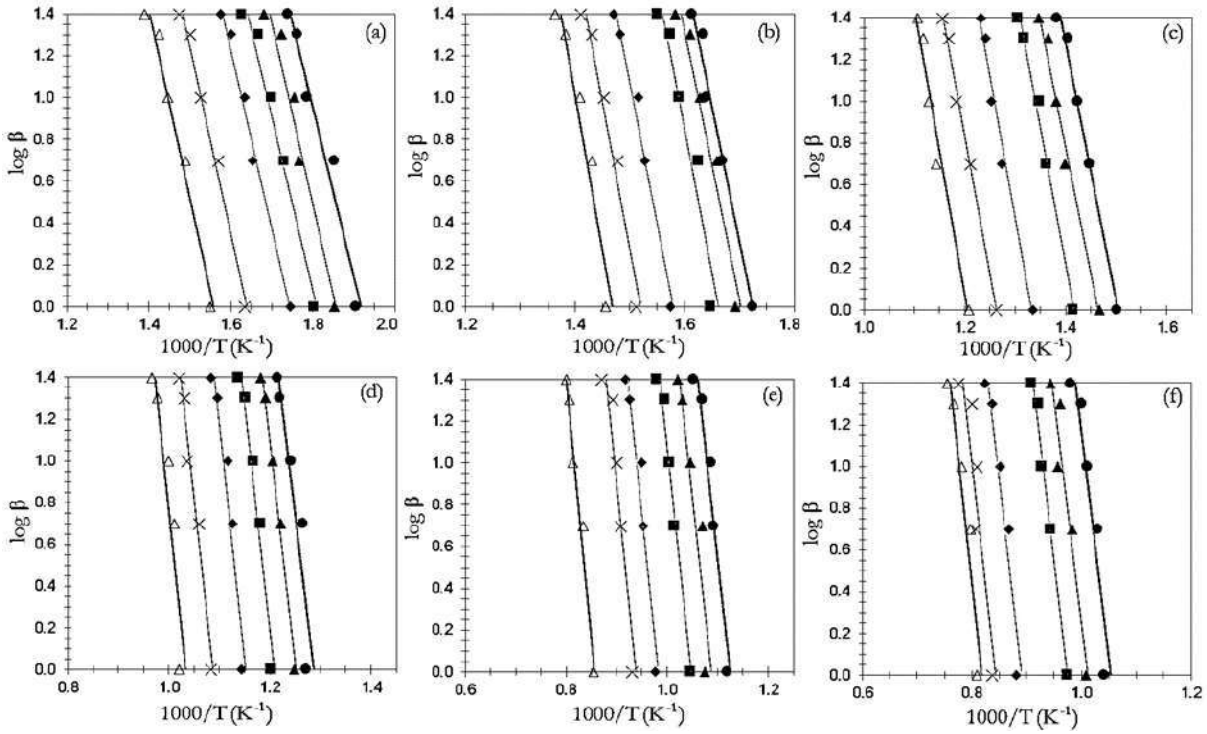

Figure 4

The relation between log β versus 1000/T according to Flynne-Walle-Ozawa method for the BA-35x brake pad composites with weight loss from 10% to 100% conversion for (a) peak 1, (b) peak 2, (c) peak 3, (d) peak 4, (e) peak 5, (f) peak 6, and (●) 10%, (▲) 20%, (■) 40%, (♦) 60%, (X) 80%, and (Δ) 100%.

Table 2

Activation energies obtained by using Flynne-Walle-Ozawa method for the BA-35x based frictional composite at various conversion

conversion (%)	E_a (kJ/mol)	R^2	E_a (kJ/mol)	R^2	E_a (kJ/mol)	R^2	E_a (kJ/mol)	R^2	E_a (kJ/mol)	R^2	E_a (kJ/mol)	R^2
	Peak1		Peak2		Peak3		Peak4		Peak5		Peak6	
10	225.3	0.9769	224.3	0.9569	95.2	0.9563	208.9	0.9236	319.8	0.9123	497.3	0.9587
20	234.8	0.9423	221.9	0.9556	99.2	0.9444	212.3	0.9563	336.5	0.9361	512.1	0.9658
40	237.1	0.9126	238.2	0.9235	104.1	0.9542	215.6	0.9514	345.9	0.9856	525.6	0.9123
60	244.2	0.9788	246.9	0.9485	108.3	0.9632	218.6	0.9854	371.2	0.9203	541.3	0.9021
80	250.1	0.9291	242.3	0.9632	113.9	0.9874	224.5	0.9658	382.6	0.9014	548.3	0.9632
100	257.4	0.9856	251.3	0.9514	119.8	0.9231	235.2	0.9745	423.1	0.9874	564.3	0.9741
average	**241.4**		**237.7**		**106.8**		**219.1**		**363.1**		**531.4**	

Determine Thermal Degradation Kinetics Parameters: Coats-Redfern Method

In order to determine kinetic parameters and thermal degradation mechanism, the Coats-Redfern method[16] was used

$$\ln \frac{g(\alpha)}{T^2} = \ln\left(\frac{AR}{\beta E_a}\right) - \frac{E_a}{RT}$$

According to this method, the E_a of the brake pad degradation process was determined from the slope of the straight-line $\ln [g(\alpha)/T^2]$ versus $1/T$ at different reaction mechanisms.

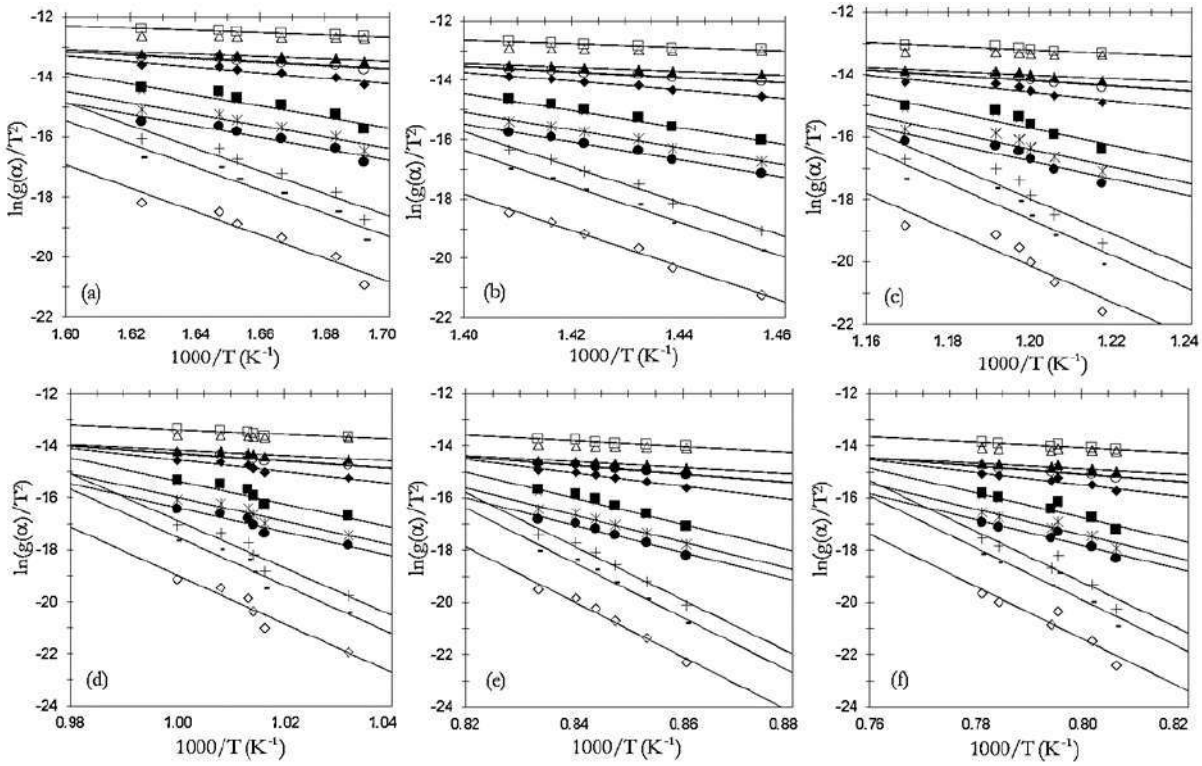

Figure 5

The relation between $\ln(g(\alpha)/T^2)$ versus 1000/T according to Coats-Redfern method for the BA-35x brake pad composites for various reaction mechanism at the heating rate of 10 ºC/min for (a) peak 1, (b) peak 2, (c) peak 3, (d) peak 4, (e) peak 5, (f) peak 6, and reaction mechanism for (♦) A2, (○) A3, (▲) A4, (X) R1, (*) R2, (●) R3, (+) D1, (-) D2, (□) D3, (◊) D4, (■) F1, (Δ) F2, and (□) F3.

Table 3

Activation energies obtained by using Coats-Redfern method for the BA-35x based frictional composite for various conversion at the 10 ºC/min heating rate (Mechanism: A2, A3, A4: Nucleation and growth, R1, R2, R3: Phase boundary-controlled reaction, D1, D2, D3, D4: 1, 2, 3-dimensional diffusion, F1, F2, F3: Random nucleation)

Model	Ea (kJ/mol)	R^2	Ea (kJ/mol)	R^2	Ea (kJ/mol)	R^2	Ea (kJ/mol)	R^2	Ea (kJ/mol)	R^2	Ea (kJ/mol)	R^2
	Peak1		Peak2		Peak3		Peak4		Peak5		Peak6	
A2	121.25	0.9547	113.72	0.9446	188.19	0.9864	213.1	0.9464	199.51	0.9964	124.17	0.9456
A3	77.21	0.9523	71.17	0.9115	120.01	0.9956	135.53	0.9846	126.03	0.9876	75.82	0.9245
A4	55.56	0.9611	49.89	0.9775	85.92	0.9806	96.74	0.9687	89.28	0.9732	51.65	0.9255
R1	239.03	0.9463	226.07	0.9235	369.7	0.9415	418.96	0.9964	393.97	0.9687	252.96	0.9818
R2	246.14	0.9841	233.63	0.9375	381.08	0.9632	432.24	0.9858	406.82	0.9864	261	0.9132
R3	249.59	0.9713	236.2	0.9642	384.93	0.9514	436.73	0.9832	403.17	0.9956	263.72	0.9687
D1	489.12	0.9035	466.07	0.9544	755.75	0.9464	857.53	0.9687	808.9	0.9235	926.79	0.9464
D2	499.22	0.9415	476.04	0.9476	770.75	0.9846	875.04	0.9464	825.83	0.9485	837.39	0.9236
D3	509.89	0.9232	486.33	0.9235	586.21	0.9702	493.08	0.9846	343.29	0.9532	448.31	0.9856
D4	502.03	0.9586	479.47	0.9485	775.9	0.9235	781.05	0.9712	631.65	0.9514	641.03	0.9464
F1	254.48	0.9215	241.38	0.9632	102.72	0.9484	221.83	0.9235	344.98	0.9564	525.22	0.9756
F2	19.32	0.9865	17.43	0.9504	30.75	0.9233	35.36	0.9732	32.28	0.9856	12.37	0.9532
F3	50.01	0.9122	48.79	0.9214	77.84	0.9895	90.34	0.9687	85.5	0.9752	45.61	0.9117

Table 2 listed the calculated kinetic parameters for different models and compared with Ea from the Flynn-Wall-Ozawa method. These results showed that at the specified heating rate, the thermal degradation mechanism of composite could be explained by the Random nucleation with one nucleus on the individual particle (F1) which the activation energy for the thermal degradation reaction were approximately evaluated as 254, 241, 103, 222, 345 and 525 kJ/mol for peak 1, peak 2, peak 3, peak 4, peak 5, and peak 6, respectively.

Table 4

Algebraic expressions for g(α) and f(α) for the most frequently used mechanisms of solid-state processes[17]

Mechanism	g(α)	f(α)
A2, Nucleation and growth (Avrami equation (1))	$[-\ln(1-\alpha)]^{1/2}$	$2(1-\alpha)[-\ln(1-\alpha)]^{1/2}$
A3, Nucleation and growth (Avrami equation (2))	$[-\ln(1-\alpha)]^{1/3}$	$3(1-\alpha)[-\ln(1-\alpha)]^{2/3}$
A4, Nucleation and growth (Avrami equation (3))	$[-\ln(1-\alpha)]^{1/4}$	$4(1-\alpha)[-\ln(1-\alpha)]^{3/4}$
R1, Phase boundary-controlled reaction (one-dimensional movement)	α	1
R2, Phase boundary-controlled reaction (contracting area)	$[1-(1-\alpha)^{1/2}]$	$2(1-\alpha)^{1/2}$
R3, Phase boundary-controlled reaction (contracting volume)	$[1-(1-\alpha)^{1/3}]$	$3(1-\alpha)^{2/3}$
D1, One-dimensional diffusion	α^2	$1/(2\alpha)$
D2, Two-dimensional diffusion (Valensi equation)	$(1-\alpha)\ln(1-\alpha)+\alpha$	$[-\ln(1-\alpha)]^{-1}$
D3, Three-dimensional diffusion (Jander equation)	$[1-(1-\alpha)^{1/3}]^2$	$(3/2)[1-(1-\alpha)^{1/3}]^{-1}(1-\alpha)^{2/3}$
D4, Three-dimensional diffusion (Ginstling Brounshtein equation)	$[1-(2/3)\alpha]-(1-\alpha)^{2/3}$	$(3/2)[1-(1-\alpha)^{1/3}]^{-1}$
F1, Random nucleation with one nucleus on the individual particle	$-\ln(1-\alpha)$	$1-\alpha$
F2, Random nucleation with two nuclei on the individual particle	$1/(1-\alpha)$	$(1-\alpha)^2$
F3, Random nucleation with three nuclei on the individual particle	$1/(1-\alpha)^2$	$(1/2)(1-\alpha)^3$

Thermal Degradation Mechanism of The Brake Pad Composites

According to the analysis by Coats-Redfern method, by evaluating and comparing the activation with the model, various possible mechanism (Table 4) can be determined, for example, reaction mechanism, R2, R3 and F1 were approximately evaluated from the thermal degradation stage-1 with compared the activation energy with the Flynn-Wall-Ozawa method and so on for the other stages. Criado model[17] give for more information and can be used as additional model to give the kinetics assessment of reactions to Coats-Redfern method.

The used models and the expressions of associated functions g(α) and f(α), could be used to construct the master curve. This curve for different mechanisms according to the Criado method for thermal degradation process of the brake pad composite was illustrated in Figure 6. The comparison of the experimental master plots with theoretical one, revealed that the kinetic process for the degradation of BA-35x based brake pad composite was most probably described by the reaction model F1 (Random nucleation with one nucleus on the individual particle).

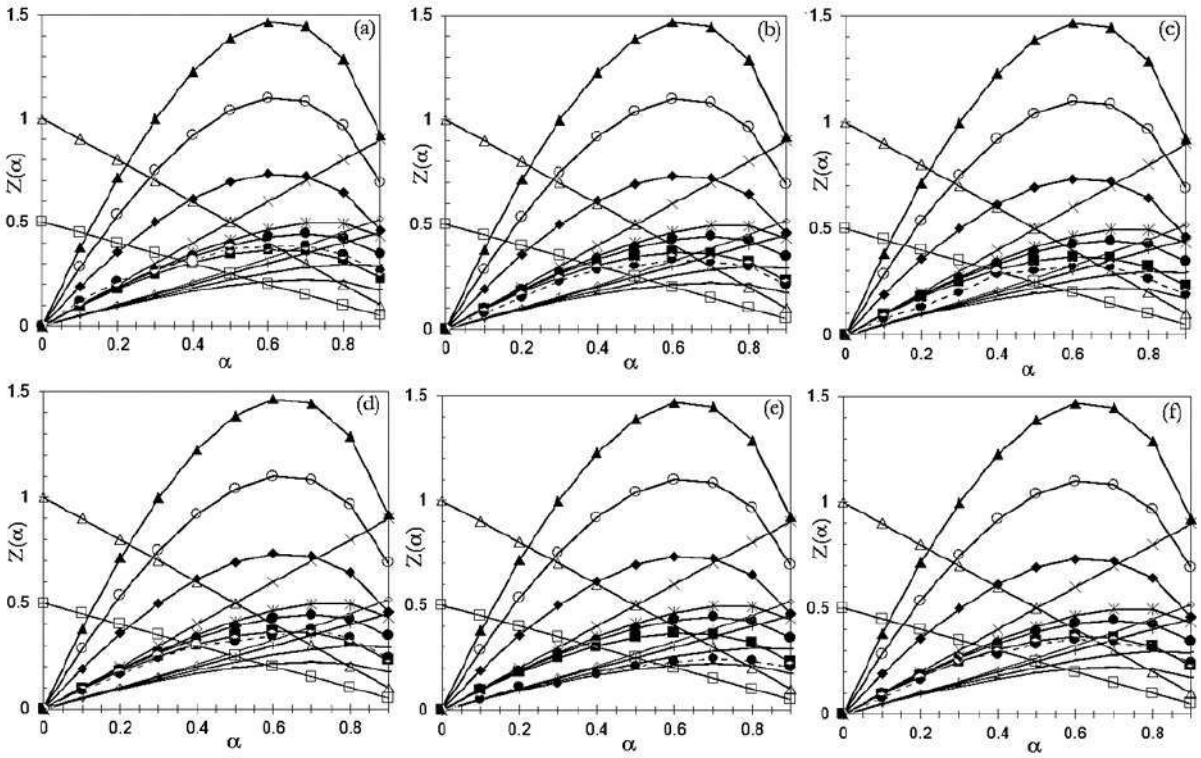

Figure 6

Master plots of different in kinetic models and experimental data plot according to Criado method for the BA-35x based brake pad composites for various reaction mechanism for (a) peak 1, (b) peak 2, (c) peak 3, (d) peak 4, (e) peak 5, (f) peak 6, and reaction mechanism for (♦) A2, (○) A3, (▲) A4, (X) R1, (*) R2, (●) R3, (+) D1, (-) D2, (□) D3, (◊) D4, (■) F1, (Δ) F2, (□) F3 and (-●-) experiment

Conclusion:

The investigation of thermal degradation processes of five different types of arylamines based polybenzoxazine binders applied in brake pad composite were carried on using thermogravimetric analysis technique under nitrogen atmosphere at different heating rates. The differentiation of thermogravimetric signal had detected six different peaks that showed various categories of degradation process occurred. The kinetic parameters, i.e., activation energy (E_a) was calculated by using Kissinger, Flynne-Walle-Ozawa and Coats-

Redfern methods. For applying Kissinger method, the activation energy for peak 1 to 6 were evaluated as 248, 231, 115, 232, 365 and 523 kJ/mol, respectively whereas the activation energy obtained by Flynne-Walle-Ozawa method for peak 1 to 6 were approximately estimated the averaged values as 241, 238, 107, 219, 362 and 531 kJ/mol, respectively and by Coats-Redfern method, the activation energy was evaluated as 254, 241, 103, 222, 343 and 525 kJ/mol for peak 1 to 6, respectively. This later, Coats-Redfern method, was acceptably consistent with the activation energy determined by Kissinger and Flynne-Walle-Ozawa approach. Finally, Coats-Redfern and Criado methods were utilized to predict the reaction mechanism of thermal degradation of the composite. The thermal degradation reaction mechanisms were described by the model of random nucleation with one nucleus on the individual particle (F1).

References:

1. Kchaou, M., Sellami, A., Elleuch, R., and Singh, H., Friction characteristics of a brake friction material under different braking conditions. Materials & Design (1980-2015), 2013.
2. Guarino, V., Gentile, G., Sorrentino, L., and Ambrosio, L., Encyclopedia of Polymer Science and Technology. 2017, John Wiley & Sons, Inc.
3. Takeichi, T., Kawauchi, T., and Agag, T., High performance polybenzoxazines as a novel type of phenolic resin. Polymer journal, 2008. 40(12).
4. Ghosh, N., Kiskan, B., and Yagci, Y., Polybenzoxazines-new high performance thermo setting resins: synthesis and properties. Progress in polymer Science, 2007. 32(11).
5. Nair, C.R., Advances in addition-cure phenolic resins. Progress in polymer science, 2004. 29(5).
6. Wirasate, S., Dhumrongvaraporn, S., Allen, D.J., and Ishida, H., Molecular origin of unusual physical and mechanical properties in novel phenolic materials based on benzoxazine chemistry. Journal of applied polymer science, 1998. 70(7).
7. Kim, H. and Ishida, H., Model compounds study on the network structure of polybenzoxazines. Macromolecules, 2003. 36(22).
8. Ishida, H. and Allen, D.J., Physical and mechanical characterization of near-zero shrinkage polybenzoxazines. Journal of polymer science Part B: Polymer physics, 1996. 34(6).
9. Ishida, H. and Agag, T., Handbook of benzoxazine resins. 2011: Elsevier.
10. Rimdusit, S., Kunopast, P., and Dueramae, I., Thermomechanical properties of arylamine-based benzoxazine resins alloyed with epoxy resin. Polymer Engineering & Science, 2011. 51(9).
11. Kurihara, S., Idei, H., Aoyagi, Y., Kuroe, M., Binder Resin for Friction Material. U.S. Patent 8,227,390 B2. 2012.
12. Tiptipakorn, S., Damrongsakkul, S., Ando, S., Hemvichian, K., and Rimdusit, S., Thermal degradation behaviors of polybenzoxazine and silicon-containing polyimide blends. Polymer degradation and stability, 2007. 92(7).
13. Dueramae, I., Jubsilp, C., Takeichi, T., and Rimdusit, S., Thermal degradation mechanism of highly filled nano-SiO2 and polybenzoxazine. Journal of Thermal Analysis and Calorimetry, 2014. 116(1).
14. Kissinger, H.E., Reaction kinetics in differential thermal analysis. Analytical chemistry, 1957. 29(11).
15. Ozawa, T., A new method of analyzing thermogravimetric data. Bulletin of the chemical society of Japan, 1965. 38(11).
16. Coats, A.W. and Redfern, J., Kinetic parameters from thermogravimetric data. Nature, 1964. 201(4914).
17. Criado, J.M., Malek, J., and Ortega, A., Applicability of the master plots in kinetic analysis of a non-isothermal rate. Thermochimica Acta, 1989.

RATIONALIZATION OF REACTIVITY OF NICKEL AND PALLADIUM PINCER COMPLEXES AS CATALYSTS FOR IODOBENZENE AND 1,2-DIMETHYLDISULFANE: THEORETICAL STUDY

Kann Jiwattayakul, Tavee Tangvijitsakul, Supawit Srisitthiporn, Sarote Boonseng*
Department of Chemistry, Mahidol Wittayanusorn School, Phutthamonthon, Nakorn Pathom, Thailand
*e-mail: sarote.bsg@mwit.ac.th

Abstract:

A pincer complex is a type of inorganic compound that has a tridentate ligand coordinating to a metal center. A pincer complex can be used in various applications such as a catalyst in organic reactions like the Heck reaction, the Suzuki reaction and the Kumada coupling reaction. The aim of this study is to understand the reactivity of Ni- and Pd-pincer complexes. An appropriate DFT method for determining Ni- and Pd-pincer complexes was evaluated. Ten popular density functionals (B3LYP, B3P86, B3PW91, B97D, HSEH1PBE, M06, M06-2X, PBE, PBE0, wB97XD) were investigated along with the two effective core potentials SDD and LanL2DZ for metal atoms. The optimized structures of Ni- and Pd-pincer complexes were compared to X-ray crystal structures. The best overall performance with relatively small statistical error was observed for M06. This level of DFT method was then used to determine the reaction mechanism between iodobenzene and 1,2-dimethyldisulfane using Ni- or Pd-pincer complexes as catalysts to investigate the role of the center atom. The reaction mechanism is comprised of four main steps; i) reductive elimination, ii) oxidative addition, iii) ligand exchange, and iv) C-S bond activation. The computational calculation showed that the C-S bond activation is a rate-determining step and the overall reaction is a spontaneous process for both Ni- and Pd-pincer complexes. Moreover, it was found that the Pd-pincer complex was more reactive than the Ni-pincer complex when the rate-determining step was used for studying reactivity.

STRUCTURAL CHARACTERIZATION OF ONE POT SYNTHESIZED NANO-SIZED β-TRICALCIUM PHOSPHATE

Supakorn Boonyuen,[1,*] Premjit Arpornmaeklong,[2] Napat Misrisuk,[3] Thanita Khunsap,[3] Nattamon Chaisitsanguan,[3] Unyakorn Chaiyakul,[4]

[1] Department of Chemistry, Faculty of Science and Technology, Thammasat University, Pathum Thani 12120, Thailand

[2] Faculty of dentistry, Thammasat University, Pathum Thani 12120, Thailand

[3] SCIUS TU, Faculty of Science and Technology, Thammasat University, Pathum Thani 12120, Thailand

[4] Faculty of Science and Mathematics, Saraburiwitthayakhom School, Saraburi 18000, Thailand

*e-mail: chemistrytu@gmail.com

Abstract:

The nano-β-tri-calcium phosphate (β-TCP) is a calcium phosphate compound also called whitlockite. This form is more widely used because of its chemical stability, high mechanical strength and better bio-sorption when compared with α-tri-calcium-phosphate. The nano-β-tri-calcium phosphate in this study was obtained from the reactions of calcium nitrate with ammonium hydrogen phosphate by co-precipitation and ultasonication methods. Precipitation were studied at various pH and sintering at 700 °C of 2 hours. Chicken and pig bone has rich in calcium carbonate (CaCO3) content 60-70 %, which were also used as a calcium source, while sintering at the same condition for comparison. The final nanoparticle products were characterized by BET, TEM, EDX and XRD to confirm the nano β-tri-calcium phosphate, further mechanical properties will be studied. The optimum reached of 72% at pH 8 and sintering temperature 700 °C for 2 hr. The nano crystal structure of β-tri-calcium phosphate formed is a rhombohedral crystal with a Ca / P ratio mole of 1.5 and the crystal size in ranged 50-90 nm. The nano-β- tri-calcium phosphate has antibacterial and antifungal properties which can be further studied for medical application. For example, it is used as a component to make artificial bones.

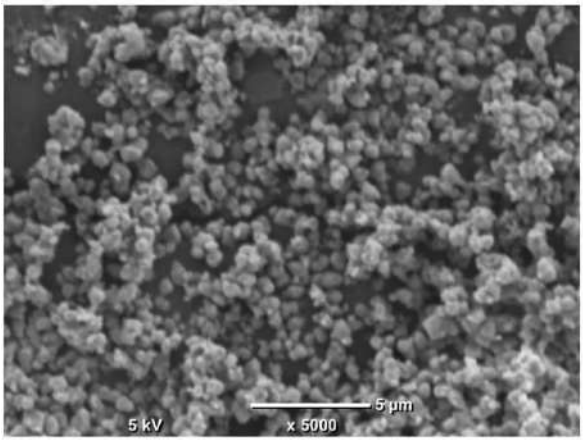

Figure 1.
SEM images of microstructure of nano-β-tri-calcium phosphate.

SYNTHESIS AND CHARACTERIZATION OF HETEROBIMETALLIC COMPLEXES SUPPORTED BY POLYETHYLENE GLYCOL CHAINS-APPENDED 2,6-PYRIDINEDIMETHANAMINE

Saran Sukchit, Teera Chantarojsiri*
Department of Chemistry and Center of Excellence for Innovation in Chemistry, Faculty of Science, Mahidol University, Thailand
*e-mail: teera.cha@mahidol.edu

Abstract:

Metal-organic composites containing heterobimetallic complexes have gained more interest in catalysis recently. Based on the enzymatic system, redox-inactive metals in multimetallic-cluster active sites significantly play important roles in the enzyme function. Proper designs of a heterobimetallic complex provide desirable properties of catalysts. Many studies reported biomimetic catalysts with more than one metal binding sites for binding both redox active and redox inactive metals. Using different redox-inactive metals also allows various activities of catalysts. However, the unselective metal-binding of the ligand is still challenging. Herein, we synthesized a 2,6-pyridinedimethanamine ligand platform appended with polyethylene glycol chains (PEG-chains) for selective heterobimetallic complex preparation. In our experiments, both UV-vis spectroscopy and nuclear magnetic resonance (NMR) revealed the coordination of transition metals (Ni^{2+} and Zn^{2+}) at NNN-cavity. In the presence of only redox-inactive cations (Na^{+}, K^{+}, Cs^{+}, Mg^{2+}, Ca^{2+}, Sr^{2+}, and Ba^{2+}), the ligand selectively bound to Ba^{2+}. Mass spectra also supported successful heterobimetallic complex preparation.

Introduction:

Redox-inactive metal ions play essential roles in many biological oxygen-containing complexes.[1] For example, Ca^{2+} in the oxygen evolving complex (OEC) of photosystem II. Even though the role of redox-inactive metal ion is still unwell-defined, many studies proposed that the redox-inactive metal, Ca^{2+} participates in hydrogen network that facilitate hydrogen transfer and adjusts the redox potential of the OEC.[2 – 5] Replacement of Ca^{2+} with other redox-inactive metal ions was also observed, only Sr^{2+} retains the activity of OEC.[6 – 8] This ion replacement study suggested that size and Lewis acidity of redox-inactive metal ions were found to affect the property of complex.[1,9]

Inspired by the biological system, numerous studies tried to use the combination between transition metals and redox-inactive metals for catalyst tuning. Redox-inactive metal ions, such as alkali and alkali earth, were present in many heterobimetallic complexes, together with transition metal ions to perform redox reactions. Many reports suggested that utilization of redox-inactive metals was found to increase the reactivity of catalyst,[10 – 12] tune the reactivity by means of changing redox potentials,[13,14] and change selectivity of the catalysts[15]. However, selective synthesis of heterobimetallic complex is not simple. The ligand that was used to bind both transition and redox-inactive metal ions must have at least two different binding sites. In general, transition-metal ions binding site usually contains soft or moderate base donor atoms such as nitrogen on pyridine or amine. For redox-inactive metal ions, these metal ions prefer hard base donor, especially oxygen atom, and the most common ligand for encapsulate redox-inactive cations is crown ether.[16]

In this work, we designed 2,6-bis[(phenylamino)methyl]pyridine ligand platform as transition metal binding sites. As the NNN-donor site is an intermediate Lewis-base, transition metals binding should bind at this site. Moreover, this ligand type has a potential to be used widely in chemical catalysis. The ligand was appended by polyethylene glycol chains (PEG-chains) for selective capturing redox-inactive cations. We used PEG-chains instead of crown ether because the opened-analog crown ether-like structure is rarely studies. Our proposed structure of heterobimetallic complex is shown in figure 1. Late transition metals, along with various redox-inactive cations, were used to study the selectivity in binding ligand with two types of binding sites. Some characterizations data are presented below.

Figure 1. Proposed structure of heterobimetallic complex.

Methodology:

General details

Compound 3 was synthesized following the literature procedure.[17] All other chemicals were purchased from commercial sources and used without further purification. Chemical reactions were performed under an ambient atmosphere. NMR spectra were obtained on a Bruker 400 MHz or Jeol 400 MHz spectrometer. UV-Vis spectrophotometry experiments were performed on a Shimadzu UV-2600 UV-Vis spectrophotometer.

*PEG-2,6-bis[(phenylamino)methyl]pyridine (**5**).*

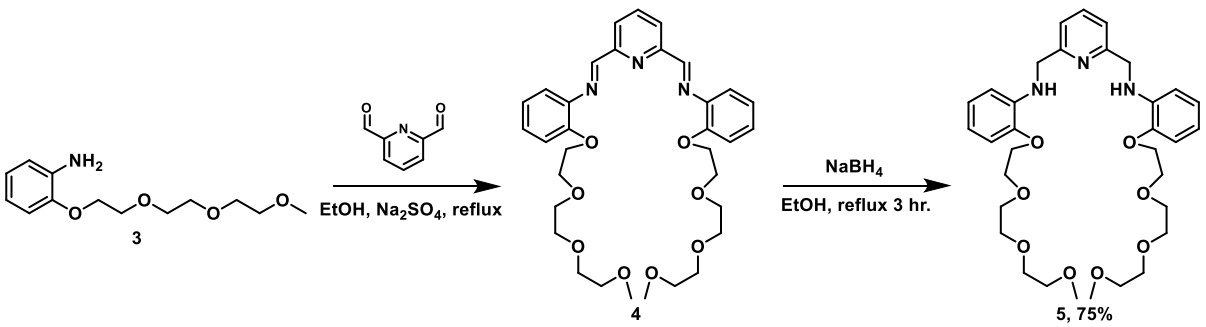

In a 50 mL round bottom flask, compound 3 (2.0424 g, 8 mmol, 5 equiv.) in 15 mL ethanol, was mixed with 2,6-pyridinedicarboxaldehyde (0.2162 g, 1.6 mmol, 1 equiv.). The reaction was refluxed overnight. ^{1}H NMR was used to confirm the complete formation of **4**, before the reaction was cooled down to ambient temperature. Afterward, $NaBH_4$ (0.6053 g, 16 mmol, 10 equiv.) was slowly added as a solid to the reaction mixture. The reaction was

refluxed for 3 hours. After that, solvent was removed under reduced pressure to obtain crude orange slurry. Saturated K_2CO_3 solution was used to dissolve all slurry and then extracted with dichloromethane (20 mL × 3). The combined organic layer was dried over Na_2SO_4 and all volatiles was removed under reduced pressure to get orange oil. After purifying by column chromatography (1% triethylamine in EtOAc as eluent), diamine ligand was obtained as yellow oil (75%).
^{1}H-NMR (400 MHz, $CDCl_3$, δ): 7.55 (t, 1H; Py H), 7.22 (d, 2H; Py H), 6.82 (m, 4H; Ar H), 6.65 (m, 2H; Ar H), 6.51 (m, 2H; Ar H), 5.30 (m, 2H; NH), 4.52 (s, 4H; CH_2), 4.20 (t, 4H; CH_2), 3.89(t, 4H; CH_2), 3.73 (m, 4H; CH_2), 3.62-3.66 (m, 8H; CH_2), 3.51 (m, 4H; CH_2), 3.34 (s, 6H; CH_3). MS-HR-ESI: $[M+Na]^+$, calc.=636.3255, found=636.3256

*[NiL](OTf)$_2$, **6** (L = compound 5)*

Compound 5 (0.0614 g, 0.1 mmol, 1 equiv.) was dissolved in 10 mL acetonitrile followed by addition of $Ni(OTf)_2$ (0.0357 g, 0.1 mmol, 1 equiv.). The reaction was stirred overnight at 85°C. Removal the organic solvent resulted in a dark yellow oil as product.

*[ZnL](OTf)$_2$, **7** (L = compound 5)*

Compound 5 (0.0614 g, 0.1 mmol, 1 equiv.) was dissolved in 10 mL acetonitrile followed by addition of $Zn(OTf)_2$ (0.0364 g, 0.1 mmol, 1 equiv.). The reaction was stirred overnight at ambient temperature. Removal the organic solvent resulted in a dark yellow oil as product.

*[NiBaL](OTf)$_x$, **6-Ba** (L = compound 5)*

Compound 5 (0.0614 g, 0.1 mmol, 1 equiv.) was dissolved in 10 mL acetonitrile following by addition of $Ni(OTf)_2$ (0.0357 g, 0.1 mmol, 1 equiv.). The reaction was stirred overnight at 85°C. $Ba(OTf)_2$ (0.0435 g, 0.1 mmol, 1 equiv.) was added to the solution and the reaction continue stirred at 85°C for 5 hours. Removal the organic solvent resulted in a dark brow oil as product.

*[ZnBaL](OTf)$_x$, **7-Ba** (L = compound 5)*

Compound 5 (0.0614 g, 0.1 mmol, 1 equiv.) was dissolved in 10 mL acetonitrile following by addition of $Zn(OTf)_2$ (0.0364 g, 0.1 mmol, 1 equiv.). The reaction was stirred overnight at ambient temperature. $Ba(OTf)_2$ (0.0435 g, 0.1 mmol, 1 equiv.) was added to the solution and the reaction continue stirred at room temperature 5 hours. Removal the organic solvent resulted in a dark brow oil as product.

General procedure for redox-inactive metal ion (A^{n+}) complexes $[A^{n+}L](OTf)_n$ preparation (n = 1 when A = Na^+, K^+, and Cs^+. n = 2 when A = Mg^{2+}, Ca^{2+}, Sr^{2+}, and Ba^{2+})

Compound 5 (0.1 mmol, 1 equiv.) was dissolved in 10 mL acetonitrile followed by addition of $A^{n+}(OTf)_n$ (0.1 mmol, 1 equiv.). The reaction was stirred overnight at ambient temperature. Removal the organic solvent resulted in a dark yellow oil as product.

Results and Discussion:

Transition-metal complex characterizations

The coordination between transition metals and ligand compound 5 (L) was first observed by using UV-Vis spectrophotometric titration method. Both Ni^{2+} and Zn^{2+} show similar titration profiles. As in figure 2, the absorption at 247 and 292 nm show a hypochromic shift, and the new absorption peak occurs around 225 nm (shoulder). Furthermore, for the nickel complex, the peak around 350 nm was also observed and denoted as d-d transition region. Zn complex, on the other hand, did not show any broad peak in the

visible region due to its d^{10} nature. Mass spectra of both complexes strongly confirm the binding between metals and ligand, as shown in figure 3, with the corrected isotopic pattern and charge for Ni^{2+} and Zn^{2+}. Both complexes were identified as Na^{+}-adduct from free Na^{+} in the liquid chromatography system that introduced the sample to the mass spectrometry system.

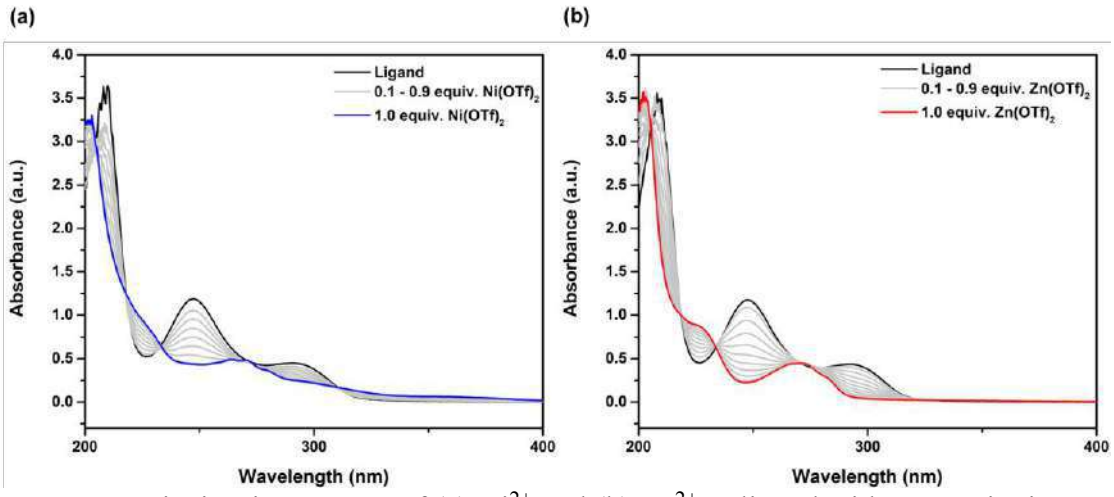

Figure 2. UV-Vis titration spectra of (a) Ni^{2+} and (b) Zn^{2+} to ligand with 0.1 equiv. increment in MeCN.

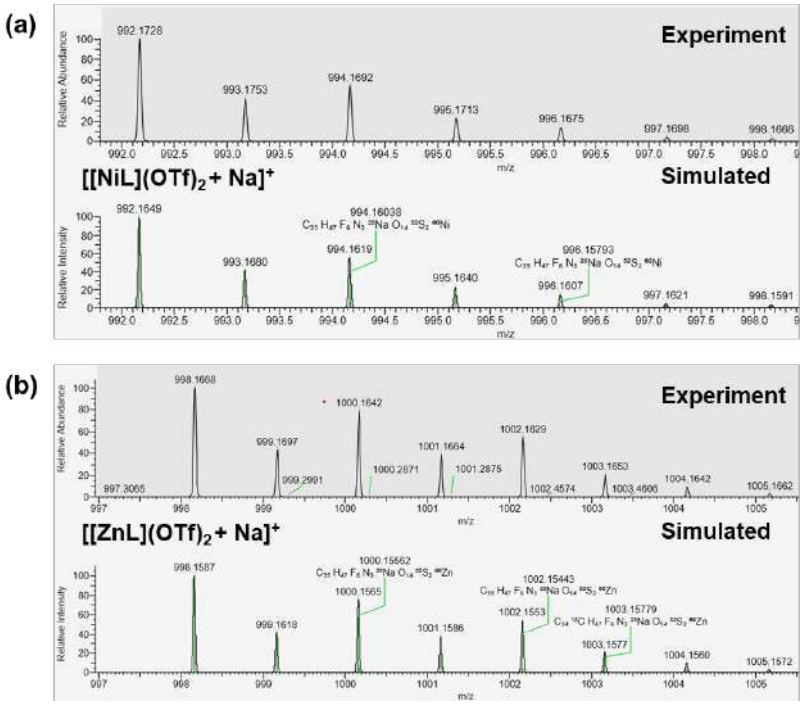

Figure 3. Mass spectra and isotope patterns of (a) $[NiLNa](OTf)_2$ and (b) $[ZnLNa](OTf)_2$ comparing between from experiment and simulation.

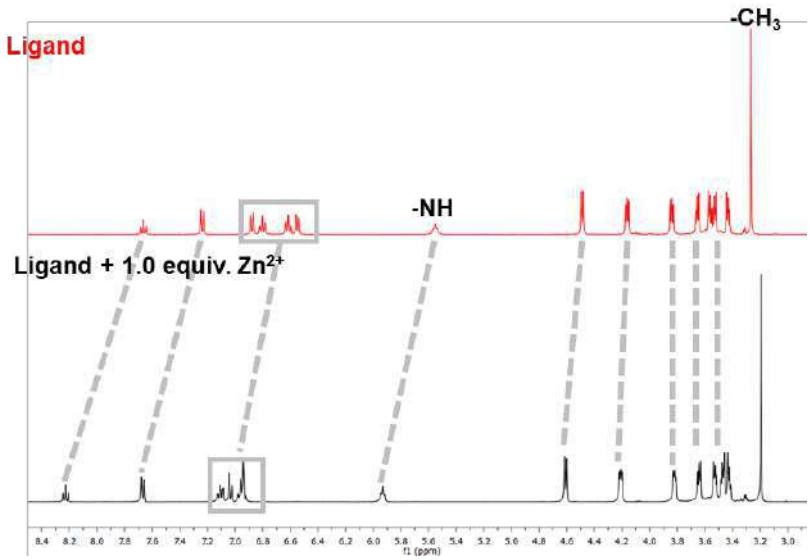

Figure 4. ^{1}H NMR spectrum of ligand (red) and ligand + 1.0 equiv. $Zn(OTf)_2$ (black) in CD_3CN.

To further prove the NNN-site as the preferred binding site for transition metal, NMR spectroscopy were used to study the diamagnetic Zn complex. According to the ^{1}H-NMR spectrum (figure 4), chemical shifts of protons on 2,6-bis[(phenylamino)methyl]pyridine moiety (4.60 – 8.30 ppm) shift to the downfield region while chemical shifts of proton on PEG-chains (3.00 – 4.25 ppm) have no significant change. This suggests that the metal-ion coordinates with NNN-donors of the pincer ligand which is in good agreement with the proposed structure. Hard and soft acids and bases theory (HSAB) was used to describe the result. Due to late transition metals (Zn^{2+} and Ni^{2+}) are intermediate acids, they prefer to bind at the NNN-site which is also intermediate bases. The PEG-chains with oxygen donors, on the other hand, are hard bases, which prefer to bind alkali and alkali-earth metal ions that are hard acids. The flexibility of the chains also accommodating the higher coordination numbers for bigger cations.

Binding studies of redox-inactive metals

UV-vis spectroscopy was used to study the electronic absorption of transition metal complexes in the presence of redox-inactive metals. In figure 5, only Ba^{2+} shows a different absorption wavelength comparing to other metals at the same equivalence. This suggests that the ligand favors binding Ba^{2+} more than other redox-inactive cations. We hypothesized that Ba^{2+} has more positive charge than group I metals (Na^{+}, K^{+}, Cs^{+}). So, it is more Lewis acidic than the group I metals. In the same group (group II metals; Mg^{2+}, Ca^{2+}, Sr^{2+}, Ba^{2+}), the ionic radii of Ba^{2+} are most likely to match to the size of crown ether binding cavity of the ligand.

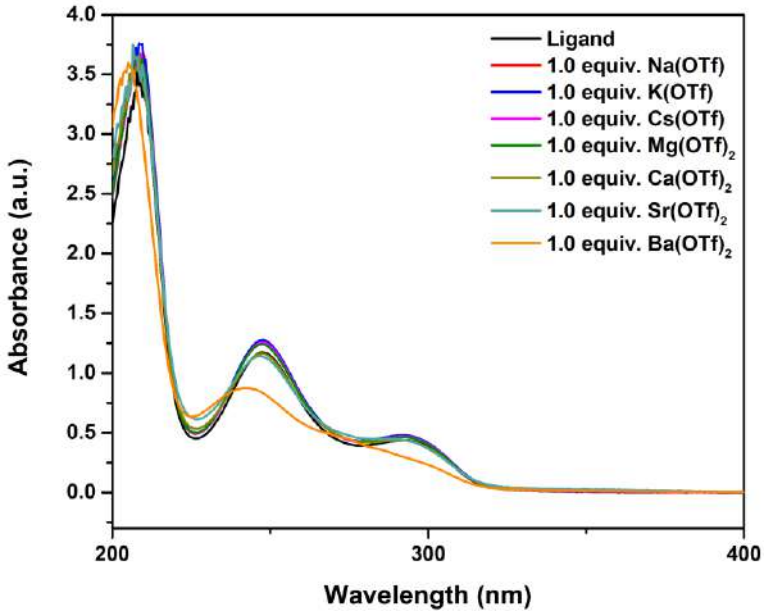

Figure 5. UV-Vis titration spectrum of 1.0 equiv. redox-inactive metals to ligand in MeCN.

To further confirm the results from UV-vis spectra, NMR spectroscopy was also used to study redox-inactive metal binding to the transition metal complexes. From figure 6, ^{1}H-NMR spectrum of ligand, 5, with Ba^{2+} (teal trace) shows completely different chemical shifts comparing with the free ligand (red trace), while the spectra of ligand with Na^{+} and K^{+} have no significant change in chemical shifts. Furthermore, the protons on the PEG chains regions shows downfield shifts which suggested coordination to Ba^{2+}, which was not observed in previous transition-metal complexes. This presumes that Ba^{2+} can bind at polyether-chains pocket. Due to low solubility in NMR solvent of other cations, NMR spectra of only Na^{+}, K^{+}, and Ba^{2+} ions were taken.

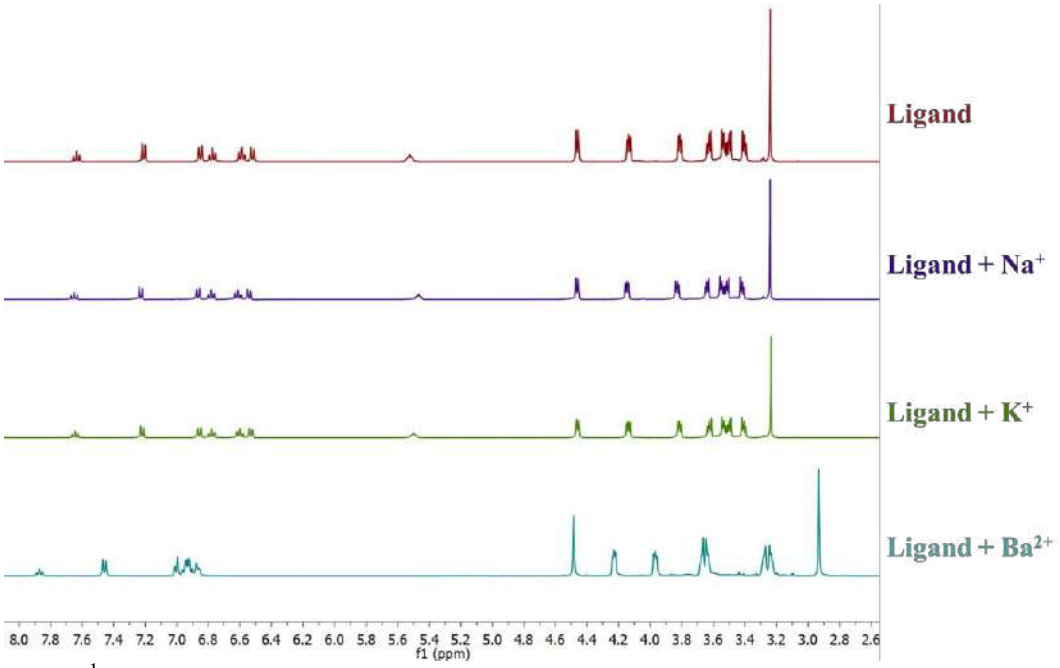

Figure 6. ^{1}H NMR spectra of ligand (red), 1.0 equiv. Na(OTf) (violet), 1.0 equiv. K(OTf) (green), and 1.0 equiv. $Ba(OTf)_2$ (teal) in CD_3CN.

However, adding Ba^{2+} into the solution of zinc complex does not show different chemical shifts of the PEG chain region (figure 7, green line) comparing to the spectrum of zinc complex without any cation (figure 7, yellow line). Even when Ba^{2+} was added to the ligand solution at first, followed by the addition of Zn^{2+}, the spectrum also shows no significant change from ligand with only Zn^{2+} (figure 7, blue line). Thus, this can be concluded that the ligand prefers Zn^{2+} to Ba^{2+}. Nevertheless, mass spectra of Zn complex, with the addition of Ba^{2+} showed the isotopic patterns of the heterobimetallic formation as shown in figure 8. The isotopic pattern from the experiment correlates to the simulated spectra supports the possibility of successful heterobimetallic complex preparation. Due to the open-chained nature of the ligand, it is possible that Ba^{2+} binds loosely and in equilibrium with free Ba^{2+}. Compound 6, Ni^{2+} complex of **5**, was also investigated by NMR spectroscopy. However, due to its paramagnetic nature, no further cation binding experiment can be conducted. More experiments will be conducted to further investigate the binding of redox-inactive metals into the transition metal complexes of 5.

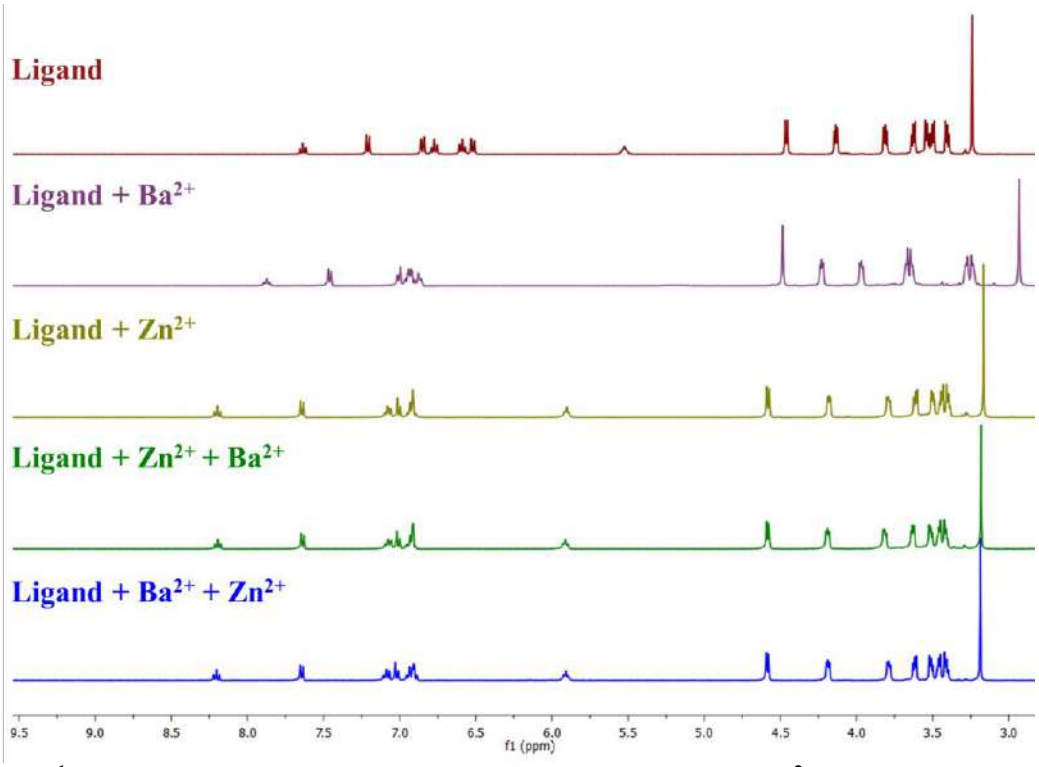

Figure 7. ^{1}H-NMR spectrum of ligand (red), ligand + 1.0 equiv. Ba^{2+} (purple), ligand + 1.0 equiv. Zn^{2+} (yellow), ligand + 1.0 equiv. Zn^{2+} and 0.1 equiv. Ba^{2+} (green), ligand + 1.0 equiv. Ba^{2+} and 1.0 equiv. Zn^{2+} (blue). The green line, Zn^{2+} was added first and followed by Ba^{2+}. The blue line, Ba^{2+} was added first and followed by Zn^{2+} in CD_3CN.

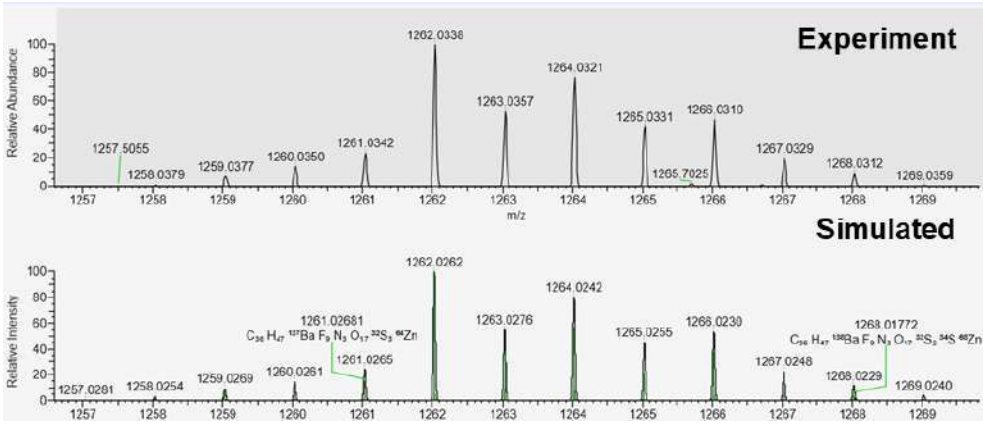

Figure 8. Experiment and simulation mass spectra of $[[ZnBaL](OTf)_3]^+$.

Conclusion:

In summary, we successfully synthesized PEG-2,6-bis[(phenylamino)methyl]pyridine ligand, compound 5, which can bind transition metals and possibly also redox-inactive metals. From results described above, transition metals are bound to the ligand at the NNN-cavity and we assumed that redox-inactive metals can be captured by PEG chains. However, further studies will be conducted to elucidate the binding affinity of redox-inactive metal to transition metal complex of 5.

Acknowledgements:

We would like to thank the Department of Chemistry, and the Center of Excellence for Innovation in Chemistry, Faculty of Science, Mahidol University for research funding. Saran Sukchit would like to acknowledge research assistantship from the Center of Excellence for Innovation in Chemistry. Teera Chantarojsiri would like to acknowledge the Thailand Research Fund, MRG6280152.

References:

1. Tsui EY, Tran R, Yano J, Agapie T. Nature Chem. 2013;5:293 – 299.
2. McEvoy JP, Brudvig GW. Chem Rev. 2006;106:4455 – 4483.
3. Zhang B, Sun L. Dalton Trans. 2018;48:14381 – 14387.
4. Baricuatro JH, Saadi FH, Carim AI, Velazquez JM, Kim YG, Soriaga MP. J. Phy Chem C. 2016;120:15618 – 15631.
5. Styring S, Feyziyev Y, Mamedov F, Hillier W, Babcock GT. Biochemistry. 2003;42:6185 – 6192.
6. Krewald V, Neese F, Pantazis DA. Phys Chem Chem Phys. 2016;16:10739 – 10750.
7. Boussac A, Rappaport F, Carrier P, Verbavatz JM, Gobin R, Kirilovsky D, Rutherford AW, Sugiura M. Journal of Biological Chemistry. 2004;279:22809 – 22819.
8. Cox N, Pantazis DA, Neese F, Lubitz W. Acc Chem Res 2013;46:1588 – 1596.
9. Kanady JS, Tsui EY, Day MW, Agapie T. Science. 2011;333:733 – 736.
10. Shao H, Muduli SK, Tran PD, Soo HS. Chem Commun. 2016;52:2948 – 2951.
11. Burns KT, Marks WR, Cheung PM, Seda T, Zakharov LN, Gilbertson JD. Inorg Chem. 2018;57:9601 – 9610.
12. Xiao D, Cai Z, Do LH. Dalton Trans. 2019;48:17887 – 17897.
13. Reath AH, Ziller JW, Tsay C, Ryan JA, Yang JY. Inorg Chem. 2017;56:3713 – 3718.
14. Kumar A, Lionetti D, Day VW, Blakemore JD. J Am Chem Soc. 2020;142:3032 – 3041.
15. Owens SB, Gray MG. Organometallics. 2008;27:4282 – 4287.
16. Haaf S, Kaifer E, Wadepohl H, Himmel HJ. Chem Eur J. 2021;27:959 – 970.
17. Wong W, Leung KC, Stoddart JF. Org Biomol Chem. 2010;8:2332 – 2343.

VALUE ADDED MANGO PEEL POWDER AS DIETARY FIBER IN CRISPY MIXED-VEGETABLE SHEET

Rachata Lueachan,[1] Wipaporn Ponklang,[1] Waraporn Sorndech,[1,*] Siwalee Rattanapunya,[2] Wiriyaporn Sumsakul, [1] Thongkorn ploypetchara, [1] Siriporn Butseekhot, [1] Sinee Siricoon, [1] Chiramet Auranwiwat, [3]

[1]Expert Center of Innovative Health Food, Thailand Institute of Scientific and Technological Research, Klong Ha, Klong Luang, Pathumtani, 12120, Thailand

[2] Public Health Department, Science and Technology Faculty, Chiang Mai Rajabhat University, Chang Phueak, Mueang Chiang Mai, Chiang Mai, 50300, Thailand

[3]Expert Center of Innovative Herbal Products, Thailand Institute of Scientific and Technological Research, Klong Ha, Klong Luang, Pathumtani, 12120, Thailand

*e-mail: waraporn_s@tistr.or.th

Abstract:

The crispy mixed-vegetable sheet is a novel snack recipe which is made from vegetables with fiber content from mango peel powder. Water convolvulus, sweet corn and potato were used as the main ingredients. Mango peel powder (1%, 3% or 5% w/w) was added to the mixed-vegetable and seasoning and dried. An increase in mango peel powder showed a significant increase in the lightness and firmness of the crispy mixed-vegetable sheet. The addition of 5% mango peel provided the highest calorie value (approx. 379.28 kcal/100g) and dietary fiber content (approx. 26.37 g/100g). Sensory evaluation data revealed that the overall-liking score of crispy mixed-vegetable with additional mango peel powder was not significantly different from that of control. However, the addition of mango peel powder provided a harder texture and greater astringency of the product. Consequently, it was found that the addition of 1% mango peel was the most appropriate amount of mango peel powder for a crispy mixed-vegetable sheet. These results should be adopted for vegetable snack production to achieve these specific attributes and to meet the needs of consumers for highly nutritious and cheap foods.

Introduction:

Nowadays, snacks are popular especially with young consumers. However, snacks are low in nutritional value due to their composition. Normally, the main ingredients of snacks consist of flour, sugar, salt and fat, and they are also low in fiber. Snacking has been considered as one of the main contributors to non-communicable diseases (NCDs), such as obesity because of an increase in consumption of high-energy, sugar, and fat foods.[1] Healthy snacks are now widely developed by adding fiber, protein or reduced salt and fat to satisfy health-conscious consumers. Dietary fiber is one of the most popular ingredients used in healthy snack recipes. Naturally, vegetables and whole grains are good sources of insoluble dietary fiber while fruits and nuts are sources of soluble fiber. Current recommendations for dietary fiber intake for adults in most European countries and in the US in a 2,000 calorie diet is approximately 25-30 grams per day. [2] Consumption of food with high dietary fiber content can slow digestion and absorption in the small intestine which reduces the postprandial blood glucose level and the glycemic response.[3] After dietary fiber reaches the ileum, it can stimulate the secretion of glucagon-like peptide 1 (GLP1) and the peptide YY (PYY) hormone which can lower the gastric emptying rate and decrease food intake.[4]

Mango (*Mangifera indica*) is an industrial crop which is widely grown in South East Asia. When mango is processed, a large amount (approx. 15-20% of total fruit weight) of peel is wasted. However, mango peel was previously tested for antioxidant activity and dietary fiber. The results showed that mango peel provides 2.32 g/mg of antioxidants and it is rich in dietary fiber content.[5] Utilization of mango waste is an important aspect of all mango processing industries for modification and recovery. Snacks made from vegetables are considered to be healthy snack and are widely produced these days. The addition of mango peel to a vegetable snack can increase its nutritional value and provide a high volume of soluble fiber which can reduce cholesterol and maintain blood sugar balance. Dietary fiber from mango peel can be used for bakery products in 10-15% of the total ingredients to reduce calories and increase fiber, or it can also be used in meat products with approx. 3-7% of the total ingredients. [5] In this study, we seek to produce a crispy mixed-vegetable sheet as a snack recipe with high dietary fiber content from mango peel powder. Our data demonstrate that mango peel powder provides has a high potential as a dietary fiber ingredient for the development of a new snack recipe.

Methodology:

1. Composition and preparation of a crispy mixed-vegetable sheet

Crispy mixed-vegetables were prepared as Control (See Table 1). The major ingredients consisted of water convolvulus, sweet corn, and potato and the minor ingredients were soy sauce, black pepper, sugar and agar. The water convolvulus and sweet corn were washed, cut and branched in boiling water. The potato was peeled, cut into small pieces and steamed until it became soft and mushy. The sweet corn was steamed for approx. 30 min or until done and chopped into fine pieces. All the ingredients were weighed and the sweet corn and water convolvulus were mixed and chopped together. Mashed potato, seasoning and agar were mixed with the previous mixture and spread onto a tray of 1-3 mm thickness. The mixed vegetables were baked in a hot air oven at 60ºC for 15 h until dry. For the crispy vegetables sheet which were mixed with 1%, 3% and 5% of mango peel, they were cooked in the same way as for Control. All the samples were kept in a plastic bag for further analysis.

Table 1
Composition of crispy vegetables.

Sample	Ingredients (%)							
	Water Convolvulus	Sweet corn	Potato	Light soy sauce	Pepper	Sugar	Agar	Mango peel powder
C	37.45	18.73	37.45	2.81	0.19	1.50	1.87	0.00
1%	37.45	18.73	37.45	2.81	0.19	1.50	1.87	1.00
3%	37.45	18.73	37.45	2.81	0.19	1.50	1.87	3.00
5%	37.45	18.73	37.45	2.81	0.19	1.50	1.87	5.00

Control (C), crispy vegetables mixed with 1% mango peel powder (1%), crispy vegetables mixed with 3% mango peel powder (3%) and crispy vegetables mixed with 5% mango peel powder (5%). Mango peel powder content was calculated based on the content of the major ingredients which were water convolvulus, sweet corn, and potato.

2. Crispiness and firmness

Crispiness and firmness were investigated by using a texture analyzer (TAPlus, LLOYD Instruments, United Kingdom). The three-point bend rig was chosen as a probe to determine the crispiness and firmness of the samples with 10 repeated measurements.

3. Color value

The color value was measured by using the HunterLab ColorQuest XE colorimeter (ColorQuest XE spectrophotometer, Hunter lab, USA) using CIE Lab color parameters. The results are displayed in the Hunter system and rectangular coordinates. The average recorded results were calculated. L* indicates lightness, a* is the red/green coordinate, and b* is the yellow/blue coordinate.

4. Chemical compositions

Water activity (a_w) was measured by using a_w meters (4TE, AQUALAB, USA). The calorie values and total carbohydrate content of all samples were analyzed according to the method of analysis for nutrition labeling of AOAC Official Methods of Analysis (1993). Total dietary fiber, protein content (%Nx6.25), total fat content, ash and moisture content of all samples were analyzed according to the AOAC Official Methods of Analysis (2019).

5. Sensory evaluation

Sensory evaluation of all samples was conducted by 10 panelists on a nine-point hedonic scale (9 = like very much; 1 = dislike very much) for different sensory parameters which were appearance, color, odor, crispness, astringency, sourness, texture, overall-taste and overall-liking. All panelists had had previous experience in evaluating the vegetables in snack products. The panel comprised assistant researchers and researchers who are employees at the Thailand Institute of Scientific and Technological Research. All the data were analyzed in a completely randomized design procedure using the general linear model procedure of the SPSS statistical package program (SPSS, Inc., Chicago, IL). Duncan's multiple range test was chosen to measure the significant differences between means ($P<0.05$).

Results and Discussion

The effects of additional mango peel powder on crispy mixed-vegetable sheet properties were investigated (Table 1). Generally, mango peel powder contains very low a_w (approx. 0.35), high lightness (L*) and yellowness (b*) values (approx. 71.43 and 19.30, respectively). A_w in the crispy mixed-vegetables sheets, was not significantly different while moisture content was lower than 3.48% indicating that the products were thoroughly dried. The colors of all the products were measured and the results showed that crispy mixed-vegetables sheets with 5% mango peel provided the highest lightness (L*) and yellowness (b*) values which were 56.35 and 15.84, respectively. These factors may explain the relatively good correlation between an increase in mango peel content and an increase in lightness and yellowness of the products due to the original color of the mango peel powder.

Table 1.

Physical properties of crispy mixed-vegetables sheets with mango peel powder.

Sample	a_w	Moisture content (%)	Color		
			L*	a*	b*
C	$0.37(0.00)^{ns}$	$3.33(0.04)^{a}$	$52.42(0.45)^{b}$	$-1.92(0.03)^{d}$	$13.71(0.23)^{b}$
1%	$0.38(0.01)^{ns}$	$3.48(0.08)^{a}$	$46.69(1.08)^{d}$	$0.06(0.09)^{a}$	$8.39(0.07)^{d}$
3%	$0.37(0.00)^{ns}$	$2.80(0.03)^{b}$	$50.76(0.37)^{c}$	$-0.70(0.03)^{c}$	$11.70(0.26)^{c}$
5%	$0.37(0.00)^{ns}$	$2.78(0.11)^{b}$	$56.35(0.38)^{a}$	$-0.55(0.02)^{b}$	$15.84(0.34)^{a}$

Values are expressed as mean ± standard deviation; Values with different letters in superscript in columns are significantly different ($p \leq 0.05$); ns = not significantly different ($p \leq 0.05$). Control (C), crispy mixed-vegetables sheets with 1% mango peel powder (1% MP), crispy mixed-vegetables sheets with 3% mango peel powder (3% MP) and crispy mixed-vegetables sheets with 5% mango peel powder (5% MP).

The appearance of crispy mixed-vegetables sheets with mango peel powder were displayed in Figure 1. The figure shows that there were no differences between these crispy vegetable sheets when compared to that of the control sample.

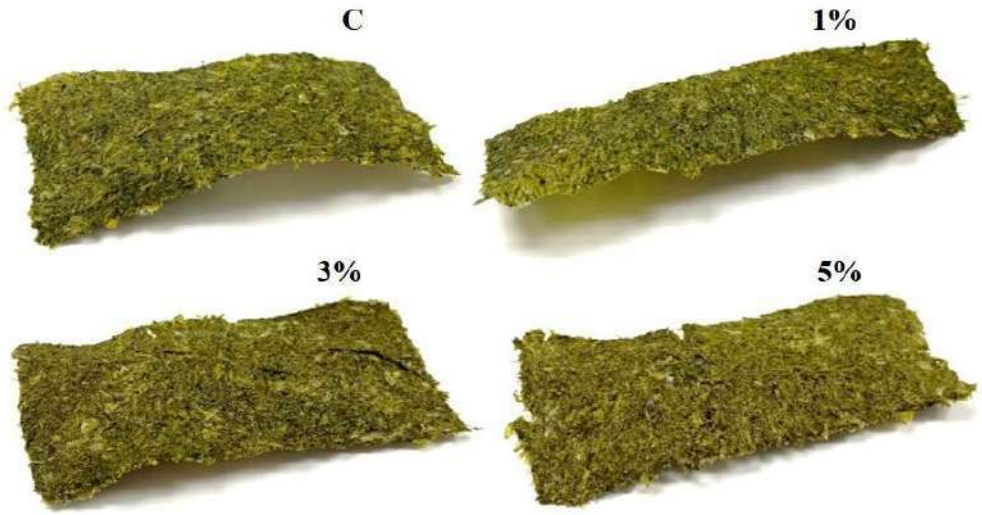

Figure 1.
Appearance of crispy vegetable sheets mixed with mango peel powder. Control (C), a crispy vegetable sheet mixed with 1% mango peel powder (1%), a crispy vegetable sheet mixed with 3% mango peel powder (3%) and a crispy vegetable sheet mixed with 5% mango peel powder (5%).

An analysis of the texture profile of crispy vegetable sheets mixed with mango peel powder is shown in Table 2. The results show that there was no correlation between crispiness and mango peel powder content in the crispy vegetable sheet. Nevertheless, a positive correlation was found between firmness and the mango peel powder content in the crispy vegetable sheets. A possible explanation for this might be that a high mango peel powder content was able to blend thoroughly with the other ingredients and maintain a stable crispy vegetable structure. This result further supports the idea of a previous study which reported that the production of vegetable sheets with several different types of vegetables produces a greater firmness in the vegetable sheets than those made from individual vegetables.[6]

Table 2.
Texture profile analysis of crispy vegetables mixed with mango peel powder

Sample	Crispiness	Firmness (N)
C	25.99(5.10)^{c}	3.03(0.88)^{b}
1%	51.59(2.81)^{a}	2.94(1.24)^{b}
3%	24.30(4.78)^{bc}	3.81(1.62)^{b}
5%	21.87(4.8)^{c}	6.04(2.06)^{a}

Values are expressed as mean ± standard deviation; Values with different letters in superscript in columns are significantly different ($p \leq 0.05$). Samples include Control (C), crispy mixed-vegetables sheets with 1% mango peel powder (1%), crispy mixed-vegetables sheets with 3% mango peel powder (3%) and crispy mixed-vegetables sheets with 5% mango peel powder (5%).

The chemical compositions of crispy vegetables mixed with different amounts of mango peel powder were investigated and the results are shown in Table 3. An addition of 5% mango peel provided the highest calorie value (approx. 379.28 kcal/100g), total carbohydrates (approx.75.31 g/100g), and total fat (approx. 3.60 g/100g). The total dietary fiber content of the 5% mango peel sample (approx. 26.37 g/100g) was higher than that of the control sample (approx. 22.72 g/100g) which reached 3.65g or 16.07%. This also accords with earlier observations, which showed that the total dietary fiber of *Mangifera indica* or Chonk Anan peel has a total of dietary fiber (TDF), soluble dietary fiber (SDF) and insoluble dietary fiber (IDF) equal to 84.53%, 33.84% and 50.69% (dry weight), respectively.[5] Hence, the addition of 5% mango peel in this product provided quantities of TSD, SDF and IDF in the sample. The results of a previous report[5] are comparable to our total dietary fiber results as shown in Table 3.

Table 3
Chemical compositions of crispy mixed-vegetables sheets with difference level of mango peel powder.

Sample	Proximate analysis (per 100 g)					
	Calories (kcal)	Total carbohydrate (g)	Protein (g)	Total fat (g)	Total dietary fiber (g)	Ash (g)
C	373.62(0.71)^{c}	72.96(0.69)^{c}	13.35(0.60)^{a}	3.16(0.12)^{c}	22.7(0.47)^{b}	7.21(0.01)^{a}
1%	373.47(0.40)^{c}	73.62(0.18)^{bc}	12.54(0.16)^{ab}	3.21(0.04)^{bc}	24.77(0.47)^{a}	7.16(0.03)^{b}
3%	377.93(0.13)^{b}	74.73(0.42)^{ab}	12.14(0.74)^{bc}	3.39(0.01)^{b}	25.19(0.59)^{a}	6.95(0.01)^{c}
5%	379.28(0.17)^{a}	75.31(0.09)^{a}	11.42(0.08)^{c}	3.60(0.06)^{a}	26.37(0.75)^{a}	6.90(0.00)^{d}

Control (C), crispy mixed-vegetables sheets with 1% mango peel powder (1 crispy mixed-vegetables sheets with 3% mango peel powder (3%) and crispy mixed-vegetables sheets with 5% mango peel powder (5%).

The sensory qualities of crispy vegetables mixed with different amounts of mango peel powder are shown in Figure 2. The supplementation of a high mango content of peel powder showed lower scores for textural properties, sourness and astringency of the crispy vegetables. This study supports evidence from previous observations on crispiness and firmness (Table 1) which showed a positive correlation between firmness and mango peel powder content in the crispy vegetable sheets. A high level of sourness and astringency in the crispy vegetable sheets were mentioned by one of the panelists due to the appropriate taste of mango peel powder. The overall crispy mixed-vegetable sheet supplemented with 1% mango peel powder was awarded the highest acceptance level (overall liking score) from the sensory panelists. Hence, these results should be used in the future for vegetable snack production to achieve these specific attributes and to meet the needs of consumers by provided highly nutritious and cheap foods.

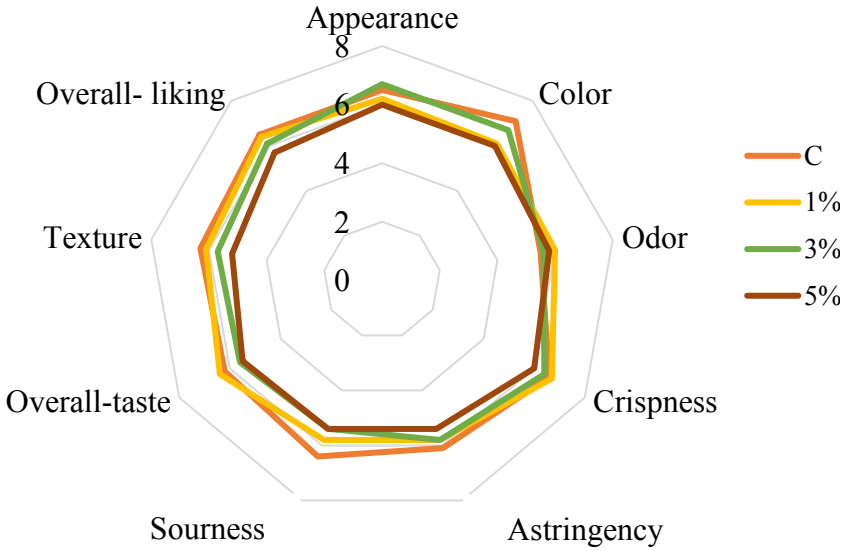

Figure 2.
This figure is based on a hedonic scale of sensory evaluation of crispy vegetables mixed with different levels of mango peel powder. Values are expressed as mean ± standard deviation; Values with different letters in superscript in columns are significantly different ($p \leq 0.05$); ns = not significantly different ($p \leq 0.05$). Categories: Control (C), crispy mixed-vegetables sheets with 1% mango peel powder (1%), crispy mixed-vegetables sheets with 3% mango peel powder (3%) and crispy mixed-vegetables sheets with 5% mango peel powder (5%)

Conclusion:
The results of the development of a crispy mixed-vegetable sheet with mango peel revealed that the addition of mango peel affects the physical, chemical and sensory qualities of a crispy vegetable sheet product. The addition of 5% mango peel provided an increase in crispiness and lightness. The results of a proximate analysis show that the moisture content decreases when the mango peel content increases which can affect the shelf-life of the product. The addition of 5% mango peel in the product showed an increase in total dietary fiber from the control recipe which reached 16.07%. The addition of mango peel provided better physical and chemical characteristics of the product. However, a high level of mango peel decreased the scores for sensory quality. Hence, the addition of 1% mango peel displayed the highest overall-liking score as compared to the additions of 3% and 5% mango peel and also provided an increase of 9.02% in total dietary fiber compared to control.

Acknowledgements:
This research was supported by the Thailand Institute of Scientific and Technological Research and Chiang Mai Rajabhat University (TISTR Project no. 6458202009).

References:

1. Bes-Rastrollo M, Sanchez-Villegas A, Basterra-Gortari FJ, Nunez-Cordoba JM, Toledo E, Serrano-Martinez M. Clin Nutr. 2010;29(3):323-330.
2. Lee B-H, Bello-Pérez LA, Lin AH-M, Kim CY, Hamaker B.R. Cereal Chem. 2013;90: 335-343.
3. Na-Nakorn K, Kulrattanarak T, Hamaker BR, Tongta S. Food Funct. 2019;10(8):4577-4583.
4. Barber TM, Kabisch S, Pfeiffer AFH, Weickert MO. Nutrients. 2020;12(10):3209.
5. Wachirasiri K, Wanlapa S, Sithisam-ang D, Suwannathap T. Agricultural Sci. J. 2010;41(3/1) (Suppl.):309-312.
6. Saengthongpinit W, Thakum S, Thepthubtim, P, Fuangfu, P. The 7th NPRU National Academic Conference. 2015:1-10.

EFFECTS OF SUPPORT AND STEAM ADDITION ON CALCIUM CARBONATE REGENARATION IN THE COMBINED SORPTION-ENHANCED STEAM METHANE REFORMING WITH BI-REFORMING PROCESS

Pasin Poung-Art[1,*], Jon Powell[2], Suwimol Wongsakulphasatch[1] and Suttichai Assabumrungrat[3]

[1]Department of Chemical Engineering, Faculty of Engineering, King Mongkut's University of Technology North Bangkok, Bangkok 10800, Thailand,

[2]International School of Engineering, Chulalongkorn University, Bangkok 10330, Thailand,

[3]Center of Excellence in Catalysis and Catalytic Reaction Engineering, Department of Chemical Engineering, Faculty of Engineering, Chulalongkorn University, Bangkok 10330, Thailand,

*e-mail: s6301031820031@email.kmutnb.ac.th

Abstract:

This research studied the effect of support and steam addition on the regeneration of calcium carbonate in the combined sorption-enhanced steam methane reforming with bi-reforming process. Multi-functional material, consisting of nickel oxide as a catalyst, calcium oxide as a CO_2 sorbent, and aluminum oxide and/or cerium oxide as a support, with fixed weight ratio of 15:70:30 wt% was applied in the reaction. The studies were conducted by feeding methane with/without steam (the ratio of methane to steam equal to 1:1) during regeneration process using fixed-bed reactor system at 850°C. The results showed that the multi-functional material having cerium oxide as a support could produce hydrogen and carbon monoxide with the ratio of 7.66, whereas the one using aluminum oxide as a support could produce hydrogen and carbon monoxide with the ratio of 5.42, for the co-feeding of methane and steam system.

HYDROGEN-RICH GAS PRODUCTION FROM STEAM REFORMING OF ETHANOL OVER Re-Ni/Al_2O_3 CATALYSTS

Peat Khemnarong,[1] Worapon Kiatkittipong,[1,*] Suwimol Wongsakulphasatch,[2] Pattaraporn Kim-Lohsoontorn,[3,4] Sakhon Ratchahat,[5] Navadol Laosiripojana,[6] Suttichai Assabumrungrat,[3,4]

[1] Department of Chemical Engineering, Faculty of Engineering and Industrial Technology, Silpakorn University, Nakhon Pathom 73000, Thailand

[2] Department of Chemical Engineering, Faculty of Engineering, King Mongkut's University of Technology North Bangkok, Bangkok 10800, Thailand

[3] Center of Excellence in Catalysis and Catalytic Reaction Engineering, Department of Chemical Engineering, Faculty of Engineering, Chulalongkorn University, Bangkok 10330, Thailand

[4] Bio-Circular-Green-economy Technology & Engineering Center, BCGeTEC, Department of Chemical Engineering, Faculty of Engineering, Chulalongkorn University, Bangkok 10330, Thailand

[5] Department of Chemical Engineering, Faculty of Engineering, Mahidol University, Nakhon Pathom 73170, Thailand

[6] The Joint Graduate School of Energy and Environment, King Mongkut's University of Technology Thonburi, Bangkok 10140, Thailand

*e-mail: kiatkittipong_w@su.ac.th

Abstract:

In this study, hydrogen production from steam reforming of ethanol was investigated in the presence of Re-Ni/Al_2O_3 catalysts. The catalysts were synthesized by the wetness impregnation method, using commercial γ-alumina support. The samplers were characterized by numerous techniques including N_2 physisorption (BET method), X-ray diffraction (XRD), scanning electron microscope with energy dispersive X-ray (SEM-EDX) and, hydrogen temperature-programmed reduction (H_2-TPR). The catalytic steam reforming activity of the catalysts was evaluated at ambient pressure in the temperature range of 450 to 650 ºC, with a stoichiometric ratio of ethanol and water (1:3 molar ratio). The results indicated a high catalytic activity as almost complete conversion (>99.7%) could be achieved at a temperature of 450 ºC, and 100% conversion at a higher temperature without any trace of intermediates. The addition of a small amount of rhenium (3 wt.%) on Ni/Al_2O_3 causes the beneficial effects to the reaction by greatly reduced the production of CO, thus increasing the selectivity toward hydrogen at 650 ºC. Moreover, a constant H_2 yield of 90% could be achieved for up to 60 h over the range of studied temperature without any deactivation, indicating high catalytic stability.

MAKE IT FLOW: ITS APPLICATION IN PHOTOCATALYTIC WATER SPLITTING FOR HYDROGEN PRODUCTION

Nopphon Weeranoppanant[1,2*], Chetsada Khositanon[1]
[1] Department of Chemical Engineering, Burapha University, Chonburi, 20131, Thailand.
[2] School of Biomolecular Science and Engineering (BSE), Vidyasirimedhi Institute of Science and Technology (VISTEC), Rayong 21210 Thailand
*e-mail: Nopphon.we@eng.buu.ac.th

Abstract:

Most of photocatalytic reactions are currently operated batchwise, typically in a vessel-like photoreactor. However, such type of the photoreactor is often found to have mass and photon transfer limitations. Flow chemistry emerges as a new platform for chemical synthesis. Reagents are mixed and flowed through a tubular reactor. The reactor can be designed to have small characteristic lengths so that the diffusion and light path lengths are small. Therefore, the mass and photon transfer efficiency can be enhanced. In this talk, two designs of tubular reactors will be presented for their applications in photocatalytic water splitting. A transport phenomena is modelled to assess the effect of different process parameters and to examine axial-dependent hydrogen content profile along the reactor. We also demonstrated the photocatalytic reaction in this tubular reactor. The flow reactor is proved to be a promising choice for the photocatalytic processes.

PRELIMINARY STUDY THE PALLADIUM CLUSTERS FOR HYDROGEN PRODUCTION FROM FORMALDEHYDE USING DFT CALCULATION

Patid Poolthongkam[1], Namfah Pattanarangsan[1], Phurich Deepentham[1], Rungroj Tuayjaroen[2], Sarote Boonseng[1,*]

[1]Department of Chemistry, Mahidol Wittayanusorn School, Phutthamonthon, Nakorn Pathom, Thailand

[2]Department of Physics, Mahidol Wittayanusorn School, Phutthamonthon, Nakorn Pathom, Thailand

*e-mail: sarote.bsg@mwit.ac.th

Abstract:

Hydrogen as one of the alternative energies is needed to overcome energy shortage and reduce amounts greenhouse gasses like carbon monoxides, carbon dioxides and nitrogen oxide, etc. There are several industrial hydrogen production processes such as steam reforming, decomposition of methane, electrocatalytic of fuel cell and especially production from organic decomposition using catalyst. In here, formaldehyde decomposition using palladium cluster is investigated. The efficiency and preliminary mechanism study of hydrogen production were examined. A Perdew-Burke-Ernzerhof (PBE) method with a Stuttgart-Dresden (SDD) for palladium (Pd) while 6-31G(d) for light atoms basis sets was carried out on whole reaction mechanism. The results from calculations reveal that the preliminary hydrogen production began with a hydroxycarbene produced from formaldehyde and then the hydroxycarbene changed to a methanediol. The formation of hydrogen product was produced during the methanediol was adsorbed on the palladium cluster with small activation energy barriers. For overall reaction, enthalpy energy (ΔH) of this reaction is -291.2 kJ/mol and Gibbs free energy (ΔG) is -201.6 kJ/mol. These indicate that the hydrogen production from formaldehyde using palladium cluster is exothermic and spontaneous processes. This study demonstrates the important role of the Pd catalyst which brings about a dramatic decrease in the energy barrier of the hydrogen production. The preliminary study of the Pd catalyst can be extended for the rational design of other metal catalysts for the hydrogen production in the future.

COMMUNITY STRUCTURE OF CORALS ON A NEW DIVE SITE, PRATHONG UNDERWATER PINNACLE IN THE ANDAMAN SEA

Makamas Sutthacheep,[1,*] Sittiporn Pengsakun,[1] Prarop Plangngan,[2] Wanlaya Klinthong,[1] Supawadee Hamanee[3] Thamasak Yeemin[1]
[1]Marine Biodiversity Research Group, Department of Biology, Faculty of Science, Ramkhamhaeng University, Huamark, Bangkok, Thailand
[2]Phuket Marine National Park Operation Center 2, Department of National Parks, Wildlife and Plant Conservation, Phuket Province, Thailand
[3]School of Business Administration, Sripatum University, Bangkok, Thailand
E-mail: smakamas@hotmail.com

Abstract:

Some underwater pinnacles in Thailand have been recognized as dive sites because of their unique environment and rich biodiversity. Most of the underwater pinnacles are coral communities that are as important as coral reefs that have the highest biodiversity in the sea. Marine ecotourism is one of the coral reef ecosystem services, greatly contributing to the economic growth and livelihoods of tropical coastal communities. Exploring new marine ecotourism sites is one of the solutions that could help reduce pressures on major dive sites. This study investigates the coral communities on a newly discovered dive site, Prathong Underwater Pinnacle, for assessing its potential for ecotourism development in the Andaman Sea. Our results showed that the dominant coral species found on the underwater pinnacle were *Porites lutea*, *Symphyllia radians*, *Pocillopora eydouxi*, *Tubastraea coccinea*, and *Tubastraea micranthus*. The major benthic invertebrates included *Heteractis magnifica*, *Acanthogorgia* spp., *Annella* spp., and *Dendronephthya* sp. The dominant reef fishes were *Chromis cinerascens*, *Chromis weberi*, *Pomacentrus moluccensis*, and *Thalassoma lunare*. Based on the assessment, Prathong Underwater Pinnacle has a high potential to be developed as a new dive site. This study serves as integrated baseline information of a newly discovered underwater pinnacle in the Andaman Sea, to support sustainable ecotourism management along with coral reef conservation in Thailand, which can be applied at other coral communities in the Indo-Pacific region.

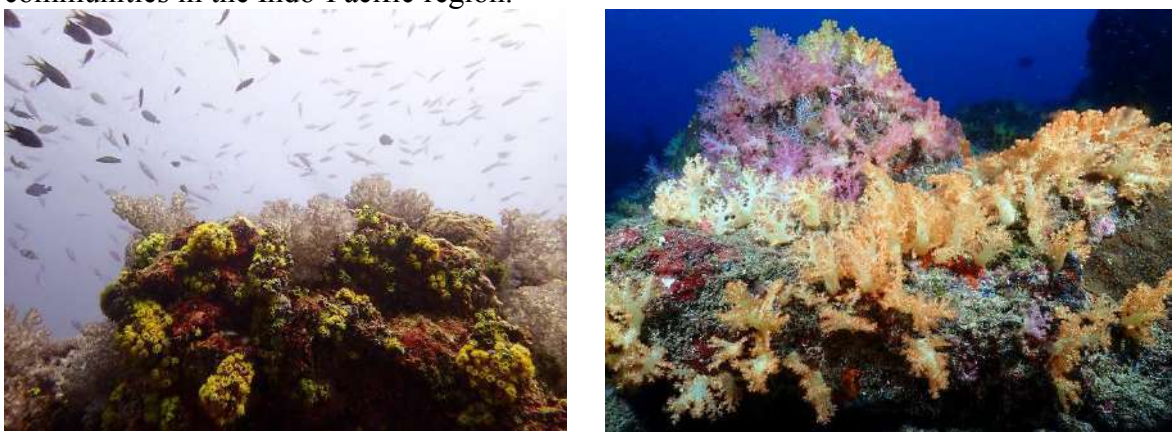

Underwater photos at Prathong Underwater Pinnacle in the Andaman Sea

DIVERSITY OF SMALL-SCALE FISHING GEARS IN RANONG, PHANG NGA AND PHUKET, THE NORTH ANDAMAN SEA

Wichin Suebpala,[1*] Thamasak Yeemin,[1] Makamas Sutthacheep,[1] Prarop Plangngan,[2] Arirush Wongnutpranont,[1] Ploypailin Rangseethampanya,[1] Suphakarn Phoaduang[1]
[1]Marine Biodiversity Research Group, Department of Biology, Faculty of Science, Ramkhamhaeng University, Huamark, Bangkok, Thailand
[2]Phuket Marine National Park Operation Center 2, Department of National Parks, Wildlife and Plant Conservation, Phuket Province, Thailand
*e-mail: wichin.s@gmail.com

Abstract:
Small-scale fisheries are essential sources of food, employment and income, making them vital for the local economy and livelihoods. Despite such important socio-economic contributions, fisheries can cause various impacts on marine biodiversity and habitats, leading to ecological imbalance and degraded ecosystem services. Knowing the diversity of fishing gears helps appropriately manage and mitigate the ecological impacts of fishing. In this study, we analyzed the diversity of small-scale fishing gears in Ranong, Phang Nga and Phuket, the north Andaman Sea, Thailand. Overall, as many as eight thousand fishing households were found in three provinces, most of which were in Phang Nga, followed by Ranong. The number of fishing households in Phuket was much low due to extensive tourism development. Phang Nga had the highest number of fishing vessels (4,147 vessels), followed by Ranong (3,772 vessels) and Phuket (2,351 vessels). About 76 - 78 percent of the vessels were small-scale (less than 10 GRT in size). The small-scale fishing gears in the study sites were diverse and locally varied. Overall, the common small-scale fishing gears were traps, trammel nets, drift nets, bottom nets, hook and lines. Most fishers owned multiple gears, which were used seasonally. The most diverse fishing gears were observed in Phang Nga, where handlines/poles and lines (15%) were mostly found, followed by shrimp trammel nets (12%), fish driftnets (9%). In Ranong, crab traps were mostly found (16%), followed by shrimp trammel nets (15%), crab nets (10%). Phuket exhibited the least diversity; the most common fishing gears were handlines/poles and lines (42%), crab traps (11%), fish driftnets (8%). The similarity of fishing gears between Phang Nga and Ranong were more similar, compared with that in Phuket. This study provides important information for ecosystem-based fisheries management to step towards the Sustainable Development Goals.

Figure 1.
Some small-scale fishing vessels (left) and common fishing gears:
handlines/pole and line (R1), trammel net (R2), fish driftnet (R3), crab trap (R4)

MACROBENTHIC FAUNA AND TOURISM ACTIVITIES WITHIN UNDERWATER PINNACLE DIVE SITES IN THE NORTH ANDAMAN SEA, THAILAND

Arirush Wongnutpranont,[1*] Siriluck Rongprakhon,[1] Nachaphon sangmanee,[1] Sittiporn Pengsakun,[1] Prarop Plangngan,[2] Makamas Sutthacheep[1], Thamasak Yeemin[1]
[1]Marine Biodiversity Research Group, Department of Biology, Faculty of Science, Ramkhamhaeng University, Bangkok 10240
[2]Phuket Marine National Park Operation Center 2, Department of National Parks, Wildlife and Plant Conservation, Phuket Province, Thailand
*e-mail: e.wongnut@gmail.com

Abstract:
Macrobenthic has importance for nutrient cycling and dispersion, pollutant metabolism, and secondary production in marine environments. They are the essential components of coral reef ecosystems, contributing to fishery resources and tourism. Some can be used as a bioindicator for environmental monitoring. However, understandings on macrobenthic communities at most underwater pinnacles are limited, especially those in the north Andaman Sea, Thailand. The line-intercept transect method combined with image analysis was used to investigate the macrobenthic communities in terms of their composition, distribution, and abundance at nine underwater pinnacles located between Mu Ko Surin and Mu Ko Similan in the north Andaman Sea, Thailand. The surveys were conducted about two years after the COVID-19 pandemic that has affected the diving tourism of Thailand. Before the pandemic, all of the observed underwater pinnacles were used as dive sites, having both snorkeling and SCUBA diving. Hin Pae was the most popular dive site among them. In this study, a total of 66 species were recorded at nine underwater pinnacles. The common species were soft coral *Dendronephthya* sp. (0 . 0 2-1 . 2 6 ind.m^{-2}), sea fan *Melithaea* sp. (0.06-0.55 ind.m^{-2}), feather star *Comantheria briareus* (0.03-0.47 ind.m^{-2}), and sea anemone *Heteractis magnifica* (0.02-0.39 ind.m^{-2}). The highest species diversity was recorded at Hin Pae in Mu Ko Similan (Shannon-Wiener index, H′ = 2.39), while the lowest was observed at Hin Kong Talueng in Mu Ko Surin (H′ = 1.20). Hin Pae in Mu ko Surin had the lowest abundance (0.01-0.08 ind.m^{-2}) but high diversity of macrobenthic fauna (H′ = 2.30). The lowest abundance at Hin Pae might be linked to the previous tourism activities. This area has been impacted by snorkeling that might affect the Thus, this area urgently requires an effective management plan to mitigate any anthropogenic impacts, particularly the impacts of tourism activities, on macrobenthic fauna and the marine environment. This study serves as valuable information for properly managing and conserving marine biodiversity along with the sustainable utilization of the underwater pinnacle in the north Andaman Sea.

Figure 1. Hin Pae in Mu Ko Similan, the north Andaman Sea, Thailand

SPECIES DIVERSITY AND ABUNDANCE OF MACROBENTHIC INVERTEBRATES IN SEAGRASS AT KO PHRA THONG, PHANG NGA PROVINCE

Laongdow Jungrak,[1,*] Makamas Sutthacheep,[1] Thamasak Yeemin,[1] Prarop Plangngan,[2] Sittiporn Pengsakun,[1] Wiphawan Aunkhongthong[1]
[1] Marine Biodiversity Research Group, Department of Biology, Faculty of Science, Ramkhamhaeng University, Huamark, Bangkok, Thailand
[2] Phuket Marine National Park Operation Center 2, Department of National Parks, Wildlife and Plant Conservation, Phuket Province, Thailand
*e-mail: Laongdow8853@gmail.com

Abstract:
Seagrass ecosystems are important as nurseries for marine animals, including economically important species. Ko Phra Thong, in Phang Nga Province, has a large seagrass community, covering an area of about 3.456 km^2 (2,160 rai). This study aimed to examine the diversity and abundance of macrobenthic invertebrates in the seagrass community. A total of nine seagrass species were found, namely, *Cymodocea rotundata, C. serrulata, Enhalus acoroides, Halodule pinifolia, H. uninervis, Halophila beccarii, H. decipiens, H. ovalis, and Syringodium isoetifolium*. The results showed that the soldier crabs (*Dotilla* spp.) and a sea star (*Astropecten* sp.) were dominant macrobenthic invertebrates, with population densities 165.0, 6.7 individuals/m^2, respectively. The economically important species included the sea cucumbers (*Holothuria arta, H. scabra*) and the dog conch (*Strombus canarium*). It was also found that the macrobenthic invertebrates were associated with the growth of certain marine organisms such as fish. The macrobenthic invertebrates are important in the food chains of marine and coastal ecosystems which act as primary or secondary consumers. The seagrass community is now threatened by human activities and natural factors such as overfishing and destructive fishing, unregulated coastal development, pollution from land and sea activities, and global climate change. Therefore, researches promoting the sustainability of small-scale fisheries in the Andaman Sea applying marine and coastal ecosystem-based management are essential through systematic scientific research.

Dotilla spp.

Holothuria scabra

THE COLONY SIZE STRUCTURE OF CORAL POPULATIONS ON SHALLOW REEF FLAT AT KO RANG KACHIU, MU KO CHUMPHON NATIONAL PARK

Charernmee Chamchoy,[1,] * Makamas Sutthacheep,[1] Sittiporn Pengsakun,[1] Wanlaya Klinthong,[1] Chaturathep Khowinthawong,[2], Chainarong Ruengthong[2], Wiphawan Aunkhongthong[1], Thamasak Yeemin[1]

[1]Marine Biodiversity Research Group, Department of Biology, Faculty of Science, Ramkhamhaeng University, Huamark, Bangkok, Thailand

[2]Department of National Parks, Wildlife and Plant Conservation, Bangkok, Thailand

E-mail: charernmee14@hotmail.com

Abstract:

Coral colony size distributions on shallow reef flats can be used to assess population responses to local environmental conditions. The size structure of coral colonies usually varies among- and within-species in different reef localities. In this study, we examined the community structure and colony size structure of coral populations on a shallow reef flat in Mu Ko Chumphon, the Western Gulf of Thailand, focusing on the abundance of large and small colonies. At the study site, coral communities were recorded using permanent belt-transects (30×1 m^2) for large coral colonies (>5 cm in diameter), while quadrats (16x16 cm^2 for each) were randomly placed on available substrates to observe small coral colonies (<5 cm in diameter). Coral colonies were identified to species level and the diameters of the coral colonies were measured. The results revealed that the percentage of live coral cover was 53.6. The numbers of a large coral colony of *Porites lutea*, *Pocillopora acuta*, and *Favites abdita* were 38.3%, 16.6% and 1.2% respectively, while those of small coral colonies of *P. lutea*, *P. acuta*, and *F. abdita* were 61.7%, 83.4% and 98.8% respectively. The sizes of coral colonies on the shallow reef flat ranged from 0.6 to over 100 cm. Most colonies of these coral species were in a range of 1 – 2 cm. Only colonies of *P. lutea* had the size over 50 cm in diameter. The small colony densities of *P. lutea*, *P. acuta*, and *F. abdita* were 2.3, 4.0 and 2.5 colonies.m-2. *P. acuta*, a brooder, exhibited the highest coral recruitment at the study site. The survival rate of juvenile colonies of *F. abdita* would be very low. A reduced abundance of small coral colonies may indicate highly threatened marine ecosystems due to stressors, probably driven by high post-settlement mortality. This study highlights the importance of the size structure data of coral populations for further ecological analyses. The small coral colonies are potential resources for active coral restoration projects to enhance coral recovery following severe disturbances, particularly coral bleaching events in the Gulf of Thailand.

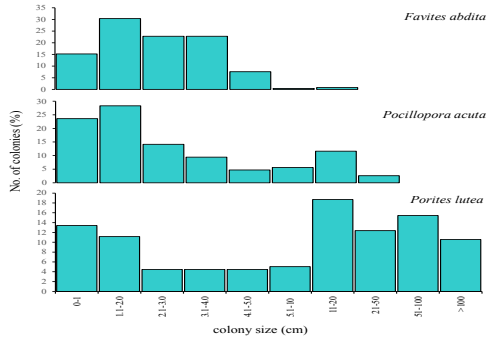

Colony size structure of corals at the study site

THE INITIAL STUDY OF FISH ASSEMBLAGE IN THE CORAL NURSERIES OF HIGH STRESS-TOLERANT CORAL FRAGMENTS IN THE WESTERN GULF OF THAILAND

Ploypailin Rangseethampanya,[1,] Makamas Suthacheep[1,*] Thamasak Yeemin,[1] Teerawat Sirisuwan,[2] Chaturathep Khowinthawong,[3]
[1] Marine Biodiversity Research Group, Department of Biology, Faculty of Science, Ramkhamhaeng University, Huamark, Bangkok, Thailand
[2] Chumphon Marine National Park Operation Center 2, Department of National Parks, Wildlife and Plant Conservation, Chumphon Province, Thailand
[3] Marine National Park Management Division, Department of National Parks, Wildlife and Plant Conservation, Bangkok, Thailand
*e-mail: ploypailinr@outlook.com

Abstract:
Corals on shallow reef flats in the Western Gulf of Thailand have a high potential for coral reef restoration projects because of their tolerance and adaptation for survival in high temperatures and environmental fluctuations. This initiative research project for coral reef restoration in Thailand is based on selecting stress-tolerant coral fragments and good traits for survival under the climate change crisis. The project established pilot nursery sites for innovative coral restoration projects in Thailand and study on biology, physiology, and ecology of coral fragments from pilot nursery sites and corals on shallow reef flats. The pilot nursery structure was proposed to be environmentally friendly structures dome-shaped with gaps to reduce weight and increase areas for the nursery. This study assessed the density and composition of fish in pilot nursery structures at Ko Rang Kachiu and Ko Ngam Yai, Mu Ko Chumphon National Park, Chumphon Province. Nine pilot nursery structures were placed at each study site on March 2021. After placed pilot nursery structures two months, fish communities were observed using Underwater Visual Census techniques (UVC). The results showed that the fish density in Ko Rang Kachiu was greater than Ko Ngam Yai (3,099.38 and 145.63 ind./100 m^2, respectively). Twenty-three species from 11 families were found in Ko Rang Kachiu, while Ko Ngam Yai had 36 species from 12 families. In comparison with Ko Rang Kachiu, Ko Ngam Yai is more diverse. This study suggests that the artificial structure provided valuable habitat for fish, which are ornamental and commercial fishes. Therefore, active restoration is helpful for the coral restoration and successful recovery of marine organisms in terms of density and diversity composition.


Pilot nursery structure


Rabbitfishes grazing on pilot nursery structure

THE RELATIONSHIP OF MEIOFAUNAL COMMUNITIES AND CORAL COVER AT MU KO SURIN NATIONAL PARK, THE ANDAMAN SEA

Nachaphon sangmanee[1,] * Makamas Sutthacheep,[1] Prarop Plangngan,[2] Laongdow Jungrak,[1] Siriluck Rongprakhon,[1] Sirirat Jaihan,[1] Thamasak Yeemin,[1]
[1] Marine Biodiversity Research Group, Department of Biology, Faculty of Science, Ramkhamhaeng University, Huamark, Bangkok, Thailand
[2] Phuket Marine National Park Operation Center 2, Department of National Parks, Wildlife and Plant Conservation, Phuket Province, Thailand
*e-mail: nachaphon.sangmanee@gmail.com

Abstract:
Coral reefs are complex ecosystems bearing the high biological diversity of the world's oceans. Assessing biodiversity and ecosystem functions is an essential step to predict the consequences of biodiversity loss. Meiofaunal are the main food source for the juveniles of various marine economic species in coral reef ecosystems. However, they have received much less attention. This study examined the composition and densities of meiofauna in coral communities and assessed the relationship of meiofauna density and ratio of live coral per dead coral at Mu Ko Surin National Park, the Andaman Sea, in February 2021. The results revealed that a total of seventeen taxa of meiofauna were found in six study sites. The major groups were Foramminifera, Nematoda, Polychaeta and Copepoda followed by Turbellaria, Nemertea, Ostracoda, Amphipoda, Ciliophora, Oligochaeta, Tardigrada, Isopoda, Gastropoda, Scaphopoda, Bivalvia, Echinoidea and Sipuncula. The highest average total density of meiofauna was observed at Ao Mai Ngam (77.45±5.47 inds. 10 cm^{-2}) and followed by Ao Chong Khad (71.85 ± 27.04 inds. 10 cm^{-2}). The density and composition of meiofauna were significantly varied among study sites. The correlations between meiofauna density and live coral per dead coral cover ratio were positive ($r = 0.455$, $p = 0.07$). A positive significant correlation was observed for Copepoda ($r = 0.64$, $p = 0.004$), Turbellaria ($r = 0.58$, $p = 0.01$) and Nematoda ($r = 0.27$, $p = 0.02$). These positive correlations indicate that live coral cover is a contributor to meiofauna community distribution. These results suggest that the meiofauna communities can play a major role in coral reef ecosystems, and they may be gradually changing in total population densities and their composition that may affect the coral reef food webs.

Nematoda Foramminifera Copepoda

A Review of New Tourism in the Post-COVID Era: Opportunities and Challenges for Sustainable Tourism Development

Chainarong Srirak,[1*] Patthaphon Sukjai[2,]
Faculty of Liberal Arts and Science, Kasetsart University
*e-mail: yaravee.add@gmail.com

Abstract:

Covid-19 epidemic situation has created a huge disruption phenomenon for the world, resulting in global economic activities including the tourism economy face an unprecedented halt. The situation immensely affected the service and tourism sectors causing an adjustment in both the demand and supply of the tourism system. The tourism is susceptible to all sorts of situations. As the tourism industry becomes more complicated as behaviors and lifestyles of consumers become more sophisticated, the tourism market is shaped in the way that customers expect unique products and services, especially travel experiences. Hence, the review of new tourism in the post-Covid era is both opportunity and challenge for sustainable tourism development in the post-Covid era.

Consumers have completely changed their behavior towards the expectations of products and services. It is expected that after this crisis, we will see the "new normal" that the behavior of people in daily life, work and leisure will apparently change as tourism has become part of the way of life of people around the world. It is also expected that technology will play a more crucial role in life than ever before, especially online communication It is an important turning point that all countries must review measures to maintain balance in tourism promotion. along with maintaining stability and sustainability in all dimensions both in terms of creating standards for screening tourists to reduce risks and create collateral for the tourism industry in their country and support new challenges that will occur in the future.

The changes in the new normal that will determine the tourism system in the post-Covid era are: 1) new tourism culture/needs of tourists; 2) lifestyle culture using intensive internet and social media; 3) The proportion of free independent travelers has increased; 4) technology, innovation and applications have changed the way of access to services; 5) tourism standards accommodate a changing group of tourists in both size, attribute and quality. Hence, improving and developing tourist attractions to accommodate the behavioral changes of tourists toward expectations is an opportunity and challenge for sustainable tourism development of all countries across the globe.

Keywords: Review of Tourism Post-Covid Era, Tourism Development, Sustainable Tourism

Developing agro-tourism standards to support new normal tourist groups: opportunities and challenges for sustainable tourism development in Thailand

Piyapong Katpiyarat,[1*] Chainarong Srirak,[2*] Patthaphon Sukjai[3]
Faculty of Liberal Arts and Science, Kasetsart University
*e-mail: piyapong.ka@ku.th

Abstract:

Thailand is an agricultural country, that deliver agricultural products around the world. but farmers in the country grow economic crops that are not diversified. When agricultural products come to the market at the same time in large numbers causing the price of agricultural products to fall. Most farmers suffer losses when they sell their produce. The agricultural sector of Thailand still relies on climatic conditions and sufficient water supply for the farming area. As a result, the agricultural sector of Thailand, they are often affected when the weather changes due to global warming. In some years, the whole country faces a drought crisis. This was so severe that farmers were asked by the government to refrain from cultivating crops or limit their planting areas. Due to insufficient water supply for farming. Poverty is a big problem that aggravates Thai farmers for a long time.

Covid-19 has rapidly attacked every country around the world. Thailand is also heavily attacked by the disease. How will we develop agro-tourism standards after COVID-19 comes and direction will it develop? Agricultural tourism development after COVID-19 by integrating with health tourism in conjunction with cultural tourism with agricultural activities / agricultural production as a link. The strategy is the 5R strategy as a mechanism for driving, consisting of 1) Reboot - Stimulate domestic tourism build consumer confidence for spending on tourism. 2) Rebuild - Rebuilding, adapting to the new normal increase long-term competitiveness. Develop products and services to increase added value. 3) Rebrand - Communicate marketing with a new image. Tourists are sure to be happy when they arrive and return safely. 4) Rebound - Stimulate the foreign tourist market to recover in a short period of time. especially tourists with high spending potential. Maintain a quality tourist base and target audience. and 5) Rebalance - Rebalancing for sustainability through responsible approach, preserving nature that has recovered from COVID-19. Support participation in promoting socially and environmentally responsible tourism.

Keywords: Developing Agro-Tourism Standards, Sustainable Tourism

GUIDELINES ON SELF-ADJUSTMENT OF TOURISM ENTREPRENEURS CAUSED BY EFFECTS OF COVID-19 IN PHRA NAKHON SI AYUTTHAYA

Jong saesong[1]
[1] Innovative Tourism and Hospitality Research Project Ratjamangala University Of Technology Suvarnabhumi.

Abstract:

The purpose of This research on the guidelines on self-adjustment of tourism entrepreneurs caused by effect of Covid-19 in Phra Nakhon Si Ayutthaya was conducted in the form of Qualitative Research by collecting data from various articles and documents incorporated with in-depth interviews conducted with the group of tourism entrepreneurs. This research aims to study on effects of Covid-19 affecting to tourism entrepreneurs in Phra Nakhon Si Ayutthaya in order to study on self-adjustment activities of tourisms and guidelines on self-adjustment of tourism entrepreneurs caused by effect of Covid-19 in Phra Nakhon Si Ayutthaya. The results revealed that effects of Covid-19 pandemic, for example, lockdown, vaccine provision, building confidence on tourism of Thai and foreign tourists, and severe reduction of income and purchasing power of tourists, hindered tourists from travelling in Phra Nakhon Si Ayutthaya. Moreover, behaviors of tourists were also changed rapidly causing tourism entrepreneurs in Phra Nakhon Si Ayutthaya to adjust themselves to meet with all situations and creative tourism styles in Phra Nakhon Si Ayutthaya were as follows:

1. New Normal Community-Based Tourism – This kind of tourism emphasized on sustainability and its goal was not only increased number of tourists but its goal was quality as well.
2. Artistic and Cultural Tourism – it was the way to create learning activities through community's artistic and cultural activities, for example, folk dances, earthenware, cultural tourist attractions, and outstanding uniqueness of Phra Nakhon Si Ayutthaya.
3. Digital Tourism – It is a kind of tourism in Phra Nakhon Si Ayutthaya via online digital platform in order to collect traveling score for actual travel at tourist attractions in Phra Nakhon Si Ayutthaya.
4. Tourism activities for tourists who are older persons and families

Guidelines on Self-Adjustment of Tourism Entrepreneurs in Phra Nakhon Si Ayutthaya

The examples of new normal tourism activities were promoting entrepreneurs and communities to participate in creating tourism activities with local tourism entrepreneurs, developing products under support of government agencies, community-based tourism activities for attracting Thai tourists, consideration on safety from Covid-19 pandemic, and consideration on maintenance of environment and community tourism for strengthening tourism entrepreneurs, communities, and creative tourism in Phra Nakhon Si Ayutthaya.

Phra Nakhon Si Ayutthaya and tourism entrepreneurs must apply the Guidelines for Creating MICE ECOSYSTEM and Basic Structure to drive tourism activities. The main issue was to connect value chain of health promotion, innovations, food, integrated connection, government/private/educational networks, provincial strategies driving, value adding for adding economic value driven by MICE ECOSYSTEM Guidelines for building confidence on travelling in Phra Nakhon Si Ayutthaya, and safety. Therefore, health tourism would become the distinctiveness on tourism of Phra Nakhon Si Ayutthaya after Covid-19 pandemic

plus with outstanding uniqueness on culture, food, recovered natural beauty, and kindness of Thai people.

Tourist attractions, tourism entrepreneurs, places of business, hotels and service sector, as well as digital platforms would help to give new experiences to tourists in New Normal era. Upskill and reskill of personnel in tourism industry of Phra Nakhon Si Ayutthaya was another important issue that must be firstly considered by Tourism Authority of Thailand.

The guidelines for developing tourism entrepreneurs in order to enable them to create activities to respond to tourists of Health & Wellness and Digital Transformation groups were developing manpower to have those skills for businesses whereas Phra Nakhon Si Ayutthaya Provincial Office cooperated with Tourism Authority of Thailand to establish a development center for developing tourism personnel and create activities via digital platform plus with health care and safety for supporting health tourism and services that is expected to be more interested after Covid-19 pandemic.

In conclusion, the guidelines on self-adjustment of tourism entrepreneurs caused by effect of Covid-19 in Phra Nakhon Si Ayutthaya are that tourism entrepreneurs must cooperate with all agencies and organizations of government and private sectors on tourism with integration and creativity. In addition, they must bring digital technology to participate in all tourism activities in order to develop creative tourism sustainably in the future. Moreover, they are also required to develop tourism innovations to respond to new normal traveling in the future.

Post New Normal Tourism

Thanakorn Thangruang[1,*]
[1] Lecture of Tourism Industry, Northern College, Tak, Thailand
[*] email: thanakorn.thangruang@gmail.com

Abstract:
Due to the COVID-19 pandemic, the travelling is limited all tourism has been stopped and the travel business has also decreased. To maintain the competitive advantage of tourism, the tourism attractions have to change and prepare for the risk to the meaning of The New Normal Tourism. The tourism sectors related including Government, Private, Local, and People's issued safety measures that consider with each attraction for tourist's confidence.
However, World Tourism Organization (UNWTO) looking further the tourism industry will be recovery as much as return to pre-pandemic levels in 2023. (UNWTO, 2021) The tourism attraction might be continue sustainable and keep strength from inside, the tourism development by using technology digital and innovation. Improve the quality of personnel and entrepreneurs in the tourism industry. Continuing the crisis into an opportunity to change and develop the tourism industry to be a next normal. (Office of the Board of Directors of the national tourism policy, 2021) How tourism and tourism attractions changing in post new normal?

SOCIOLOGY OF TOURISM IN THE DIMENSION OF TRAVEL EXPERIENCE DESIGN WITH DEMOCRATIC CONCEPT

Patthaphon Sukjai,[1*] Chainarong Srirak[2]
Faculty of Liberal Arts and Science, Kasetsart University
*e-mail: patthaphon.s@gmail.com

Abstract:

The COVID-19 pandemic outbreak has severely affected the global tourism system, leading to a change in all forms of tourism as well as the behavior of tourists that tend to change the need for more close-to-nature tourism and higher use of tourism services that emphasize intellectual skills.

The community ecotourism will play a greater role in tourism in the future. Therefore, the tourism experience design of tourist attractions must be carried out in connection with the cultural, lifestyle and environment basis to create an exchange of experiences between tourists and hosts. In addition, conducting tourism activities with regard to exchanging knowledge of local identities participatory through the five senses: sight, hearing, smell, taste test and touch, and through creative activities to create awareness of caring, cherishing, collecting impressions from participating in activities and bringing those good experiences to be conveyed and disseminated, leading to loyalty to tourist attractions.

The approach to building tourism products and services to accommodate the changing behavioral changes and new expectations of travelers should adopt a new concept of increasing access to information through personalization applications. The exclusive assistance platform where this assistant together with the host will jointly design the event and plan your itinerary that is more flexible and tailored to your individual needs. The core is on connecting tourists and tourism resource owners to exchange, dependency and equality in line with the concept "designing a tourism experience with a democratic concept".

Keywords: Sociology of Tourism, Tourism Experience Design, Democratic Concept

THE DEVELOPMENT OF A STAND UP PADDLE BOAT (SUP) ACTIVITY MODEL TO PROMOTE SUSTAINABLE SPORTS TOURISM.

Theeranan Tanphanich,[1] Amnauy Tanphanich,[2] Siriluk Pichainarong,[3] Satesh Bidaisee[4] Suppawan Vongsrangsap[5]
[1]Kasetsart University, Thailand
[2]Kasetsart University, Thailand
[3]Kasetsart University, Thailand
[4] St Georges University, Grenada
[5]Kasetsart University, Thailand
*e-mail: famtnt@ku.ac.th

Abstract

This research aimed to develop a model for the implementation and management of Stand-Up Paddle (SUP) sports activities to promote sustainable sports tourism in Thailand. A Participatory Action Research (PAOR) methodology was conducted including documents review, semi-structured informant interviews, group discussion and participant observation. Informants consisted of 1) Experts from the Standing Rowing Association of Thailand 2) Academics in sports tourism and 3) Members and related clubs for observations. Data were analyzed to create a model for SUP sport activities.

Analyzed results demonstrated that participation of the Rowing Association of Thailand, its members, clubs, and related agencies consisted of 4 management processes: 1) Planning, consisting of 9 elements, namely the determination of the main organization, responsible persons, goals, objectives, operational plans, activities, personnel, budgets, and suitable locations for organizing marketing activities. and community cooperation in the competition area 2) Organization framework consisting of 5 components including: jointly defined across related agencies, event design, classification of stand-up paddle sports, qualification and training for the implementation committee; 3) Implementation of 3 components: target group; event process and communities in the competition area to benefit from the activities 4) 3 aspects of control including: related agencies and community together, assessments by members, clubs, and communities in the tournament area. Additionally, for SUP marketing, there are 3 components including: set prices for tourism services, developing sports tourism products and promotion of SUP in markets.

Keywords : Participatory Action Research, Stand Up Paddle Boat, Sports Tourism Management

THE IMPORTANCE OF SERVICE QUALITY OF 5 STAR HOTELS IN RATCHAPRASONG AREA TO TRANSITION UNDER CORONAVIRUS-19 2019 SITUATION.

Niramol Khwakhong
Faculty of Liberal Arts and Science, Kasetsart University
* e-mail: niramolb5671@gmail.com

Abstract:

The Coronavirus pandemic has affected tourism and hotel businesses in the long run also leading to a huge change in the service system which causes tourism behaviors that need to be changed, such as tourism that focus more individual needs, Business model were changed and adoption to modern technology including attention more health. Changing of tourism behaviors also affects to the business model and hotel business operator. Therefore, hotel business operators need to accelerate the adjustment to maintain the level of income including looking for the strategy for new business opportunities that create value of tourism and service.

The factors that determine the hotel success it not only from hotel location, rooms, room rate or hotel facilities but also come from the ability to adapt and manage the quality of service as well. Therefore the hotel operators needs to adjust their business strategies in order for the hotel business to grow back. It also creates sustainability for the Thai tourism industry in the long run.

The quality of service as the essential and the key success of the hotel business. It is also one of the concepts that enable organized to produce the products and services that stand out when compared to their competitors and at the same time to bring back the confidence of tourists. Therefore, this article aims to present the importance of service quality, guidelines and service quality management models that hotel business can use to develop their business successfully under the midst of coronavirus pandemic 19 by applying a review of concepts, theories and research related to service quality (SERVQUAL) to lead to impressive service and tourists come back to use the service again and communicated to other interested tourists also the hotel business continues to maintain the standard able to develop sustainably in all situations.

Keywords: Service Quality, 5 Star Hotel, Coronavirus 2019

The Process of Coordinating Forces to Shake Society through the COVID-19 Crisis: Tour Leader's Youth Capacity Development for Sustainable Tourism Development

Apidet Changchai,[1] Chokechai Dongkaew,[2] Winai Poonsri,[3] Sumit Suwan[4]

[1]Kasetsart University, Thailand 1st author
[2]Kasetsart University, Thailand 2nd author
[3]Kasetsart University, Thailand 3rd author
[4]Kasetsart University, Thailand 4th author

*e-mail: faasadc@ku.ac.th

Abstract:

The coronavirus outbreak affects the society, economy and security of people's lives in the world and of course, this outbreak affects tourism, there were lacked of income, so it's to time for people to rise up shake society through the COVID-19 crisis because it's duty of everyone. This article was used triangulation technique (documentary analysis, observe and social phenomenon study) data collecting then synthesis data, found that the process of coordinating forces tour leader's youth capacity development (developing knowledge, skill, and attitudes of tour leader's youth) for sustainable tourism, was one approach which was through this crisis, however a coronavirus vaccination campaign was still necessary and creating an understanding of tourism management in the New - Normal era (get vaccinated, wear a mask, carry alcohol and test for corona virus) for people in the community was another important issue. This process was a solution to problems through democratic concepts. Therefore, it was proposed that the tourism communities in each area use this approach to develop and rehabilitate this tourist attraction because no one knows the problems and solutions to the problems that the community itself.

The Way of Survival of the Tha - Chin Riverside Market Communities: Approach of Stepping Through the COVID - 19 Crisis of Tourism Community

Apidet Changchai,[1] Sunti Srisuantang,[2] Prasong Tanpichai,[3]
[1]Kasetsart University, Thailand 1st author
[2]Kasetsart University, Thailand 2nd author
[3]Kasetsart University, Thailand 3rd author
*e-mail: faasadc@ku.ac.th

Abstract:

The coronavirus outbreak has shrunk the tourism of the Tha Chin riverside communities, resulting in a lack of income for people in the community. This problem requires urgent solutions through the participation of people in the community. This article aims to seeking the way of survival of the Tha - chin riverside market tourism communities. There were used triangulation technique [a) documentary analysis technique, i.e. articles, research report and other b) interview online technique, i.e. people in communities, people from government agencies and people from private sector and 3) observe the social phenomenon at Tha chin Riverside Market Communities area] then synthesis approach of stepping through the COVID - 19 crisis of tourism community, This study found that: The using learning space of all stakeholders is to find a common solution based on democratic thinking (seeking problem, planning, action, observe and reflections through participate) were the way of survival of the Tha - Chin riverside market communities, however a coronavirus vaccination campaign was still necessary and creating an understanding of tourism management in the after COVID-19 era (get vaccinated, wear a mask, carry alcohol and test for corona virus) to stakeholders was another important issue therefore, it was proposed to the community that organizes tourism on the Tha Chin River to be a guideline for drives the development of tourism for the community towards sustainability, after this crisis.

Way of Survival
Riverside Market
Crisis of Tourism

THE COMMUNICATION ACROSS CULTURE TO TOURISM IN THE NEW NORMAL WAY AFTER COVID-19

Varachoti Vitchalertphol

Abstract:

This study aims to use the online application to communicate between temple staff and tourists in various cultures or various social for support tourism in the period of new normal after COVID-19. Due to the problem of COVID-19 is spread over the world. The government of each country is taken policy about working from home (WFH) to separate each other workers to protect them from an infection of COVID-19, automatically a group of tourists does follow the policy of the government to avoid face-to-face communication.

Hence, the improvement of communication could handle this crisis when the researcher would bring the communication designed through the application of both Google form and Line to use with the tourists who travel at Veerachote Thammaram Temple, Klong Luang Phaeng Sub-district, Mueang District, Chachoengsao Province. The instrument of this study consisted of both online applications designed to communicate with tourists and questionnaires of tourists' satisfaction. Data collection was collected from the questionnaires of 60 tourists by simple random sampling and an interview with 10 tourists from 60 tourists. Data analysis of the study took as a pair sample T-test, the average, and standard deviation.

In conclusion, the results of this study by the use of the design of two online applications mentioned above summarized that it helps tourists communicate with various cultures more effectively to tourism in the new normal way. Moreover, they feel well-satisfied with communication via online application at a 0.05 statistical level.

IDENTIFICATION OF NOVEL SERINE/THREONINE PROTEIN KINASES B INHIBITORS AS ANTI-TUBERCULOSIS AGENTS FROM KINASE LIBRARY: MULTISTAGE VIRTUAL SCREENINGS AND PHAMACOKINETIC PREDICTIONS

Pharit Kamsri,[1,*] Auradee Punkvang,[1] Supa Hannongbua,[2] Patchreenart Saparpakorn,[2] Khomson Suttisintong,[3] Prasat Kittakoop,[4,5,6] James Spencer,[7] Adrian J. Mulholland[8], Galina V. Mukamolova,[9] Pornpan Pungpo[10]

[1]Division of Chemistry, Faculty of Science, Nakhon Phanom University, 48000 Nakhon Phanom, Thailand

[2]Department of Chemistry, Faculty of Science Kasetsart University, 10900 Bangkok, Thailand

[3]National Nanotechnology Center, National Science and Technology Development Agency, Thailand Science Park, 12120 Pathumthani, Thailand

[4]Chulabhorn Research Institute, 10210 Bangkok, Thailand

[5]Chulabhorn Graduate Institute, Chemical Biology Program, Chulabhorn Royal Academy, 10210 Bangkok, Thailand

[6]Center of Excellence on Environmental Health and Toxicology (EHT), CHE, Ministry of Education, 10300 Bangkok, Thailand

[7]School of Cellular and Molecular Medicine, University of Bristol, Biomedical Sciences Building, University Walk, BS8 1TD Bristol, United Kingdom

[8]Centre for Computational Chemistry, School of Chemistry, University of Bristol, BS8 1TS Bristol, United Kingdom

[9]Department Respiratory Sciences, University of Leicester, Leicester LE1 7RH, United Kingdom

[10]Department of Chemistry, Faculty of Science Ubon Ratchathani University, 34190 Ubon Ratchathani, Thailand

*e-mail: pharit.kamsri@npu.ac.th

Abstract:

The *M. tuberculosis* Serine/Threonine Protein Kinases B (PknB) has been validated as potential target for novel anti-tuberculosis drug development. The combinations of ligand and structure based virtual screening, biological activities predictions with three different programs (PASS, AntiBac-Pred and MycoCSM) and pharmacokinetic predictions were applied on kinase library to identify four novel hit compounds including **CHEMBL1257310**, **CHEMBL1356336**, **CHEMBL1403777** and **CHEMBL153843** as novel inhibitors of PknB. The Caseum FU(%) prediction of these hit compounds were 0.198 to 18.965 % which indicated that hit compounds will be more potent anti-tuberculosis agents with low MIC value. These compounds showed strong binding affinity in the ATP binding site of PknB and shared hydrogen bonding interaction with Val95 backbone as the key interaction for binding. In addition, sigma-pi and hydrophobic interactions of hit compounds with amino acid residues in ATP binding site of PknB enhanced the binding affinity of the compounds. Based on pharmacokinetic predictions, hit compounds showed high Caco2 permeability, intestinal absorption and poorly distribution to the brain. The low maximum tolerated dose and oral rat acute toxicity (LD_{50}) of hit compounds was obtained. These results demonstrated that his compounds were low toxicity. Therefore, the obtained result provides the novel scaffolds for rational design and development of highly potent PknB inhibitors as anti-tuberculosis agents.

INSIGHT INTO THE BINDING MODE AND BINDING INTERACTIONS OF BENZO[*d*]ISOTHIAZOLE DERIVATIVES AS POTENTIAL MTB DNA gyrase INHIBITORS USING MOLECULAR DYNAMICS SIMULATIONS

Bandit Khamsri,[1] Bongkochawan Pakamwong,[1] Paptawan Thongdee,[1] Naruedon Phusi,[1] Kampanart Chayajarus,[1] Somjintana Taveepanich,[1]
Kanchiyaphat Ariyachaokun,[2] Pharit Kamsri,[3] Auradee Punkvang,[3] Patchreenart Saparpakorn,[4] Supa Hannongbua,[4] Khomson Suttisintong,[5] Prasat Kittakoop,[6,7,8] James Spencer,[9] Adrian J. Mulholland,[10] and Pornpan Pungpo[1, *]

[1]Department of Chemistry, Faculty of Science, Ubon Ratchathani University, Ubon Ratchathani 34190, Thailand
[2]Department of Biological Science, Faculty of Science, Ubon Ratchathani University, Ubon Ratchathani 34190, Thailand
[3]Division of Chemistry, Faculty of Science, Nakhon Phanom University, Nakhon Phanom 48000, Thailand
[4]Department of Chemistry, Faculty of Science, Kasetsart University, Bangkok 10900, Thailand
[5]National Nanotechnology Center, NSTDA, 111 Thailand Science Park, Klong Luang, Pathum Thani 12120, Thailand
[6]Chulabhorn Research Institute, Kamphaeng Phet 6 Road, Laksi, Bangkok 10210, Thailand
[7]Chulabhorn Graduate Institute, Chemical Biology Program, Chulabhorn Royal Academy, Kamphaeng Phet 6 Road, Bangkok 10210, Thailand
[8]Center of Excellence on Environmental Health and Toxicology (EHT),
[9]School of Cellular and Molecular Medicine, University of Bristol, Bristol, BS8 1TD, United Kingdom
[10]Centre for Computational Chemistry, School of Chemistry, University of Bristol, Bristol, BS8 1TS, United Kingdom
*e-mail: pornpan_ubu@yahoo.com

Abstract:
DNA gyrase subunit B has been an attractive target for discovery of novel GyrB inhibitors that is a crucial enzyme used in DNA replication of *Mycobacterium tuberculosis*. In this study, we aim to explain the crucial interactions for binding of benzo[*d*]isothiazole derivatives in GyrB binding pocket using molecular dynamics (MD) simulations and binding free energy calculation. The results showed that the calculated binding free energy from MM/GBSA has a good correlation with the derived experimental binding energy. Recognizing the key residues in the binding site of the enzyme that are involved in the binding mode with the GyrB inhibitors was investigated by using decomposition energy. The key interactions showed pi-cation between benzo[*d*]isothiazole rings with ammonium site chain of Lys108 residue. The carbonyl substituent on the amide group formed a water-mediated interaction with Val76 residue. Hydrophobic interactions have been observed with Val49, Ala53, Ile84, Pro85, Val123, Val125 and Ile171 residues in GyrB binding pocket. The results from these simulations highlight the important residues in the ATP binding site that can be useful for rational design of potential new DNA gyrase inhibitors.

PROPOSING NOVEL *M. tuberculosis* InhA INHIBITORS USING STRUCTURE-BASED DRUG DESIGN APPROACHES: MD SIMULATIONS AND FMO CALCULATIONS

Naruedon Phusi,[1] Chayanin Hanwarinroj,[1] Chan Inntam,[1] Kampanart Chayajarus,[1] Somjintana Taveepanich,[1] Kanchiyaphat Ariyachaokun,[2] Pharit Kamsri,[3] Auradee Punkvang,[3] Patchreenart Saparpakorn,[4] Supa Hannongbua,[4] Khomson Suttisintong,[5] Prasat Kittakoop,[6,7,8] Noriyuki Kurita,[9] James Spencer,[10] Adrian J. Mulholland,[11] and Pornpan Pungpo[1]*

[1]Department of Chemistry, Faculty of Science, Ubon Ratchathani University, Ubon Ratchathani 34190, Thailand

[2]Department of Biological Science, Faculty of Science, Ubon Ratchathani University, Ubon Ratchathani 34190, Thailand

[3]Division of Chemistry, Faculty of Science, Nakhon Phanom University, Nakhon Phanom 48000, Thailand

[4]Department of Chemistry, Faculty of Science, Kasetsart University, Bangkok 10900, Thailand

[5]National Nanotechnology Center, NSTDA, 111 Thailand Science Park, Klong Luang, Pathum Thani 12120, Thailand

[6]Chulabhorn Research Institute, Kamphaeng Phet 6 Road, Laksi, Bangkok 10210, Thailand

[7]Chulabhorn Graduate Institute, Chulabhorn Royal Academy, Bangkok 10210, Thailand

[8]Center of Excellence on Environmental Health and Toxicology (EHT)

[9]Department of Computer Science and Engineering, Toyohashi University of Technology, Tempaku-cho, Toyohashi, Aichi, 441-8580, Japan

[10]School of Cellular and Molecular Medicine, University of Bristol, Bristol, BS8 1TD, United Kingdom

[11]Centre for Computational Chemistry, School of Chemistry, University of Bristol, Bristol, BS8 1TS, United Kingdom

*e-mail: pornpan_ubu@yahoo.com

Abstract:

In this research, structure-based drug design was applied to investigate and rational design of high potential of novel *M. tuberculosis* InhA inhibitors. The heteroaryl benzamide derivative as potential antituberculosis agents active against *M. tuberculosis* InhA was selected. Molecular dynamics (MD) simulations and fragment molecular orbital (FMO) calculations were applied to elucidate the important information of these inhibitors in the InhA binding site. The obtained result from MD simulations showed that the molecular dynamics simulations were reliable to predict the binding mode, binding interactions, and binding energy with MM-GBSA and waterswap calculations. The crucial interaction revealed that strong hydrogen bond interactions between the backbone of Met98 and NAD^+ cofactor in InhA binding pocket with heteroaryl benzamide derivative were obtained. In addition, FMO calculations highlight that some key interactions between InhA and heteroaryl benzamide inhibitors, indicating that the most potent inhibitor has strong hydrogen bonds with the backbone of Met98. These findings provide informative structural concepts for designing novel heteroaryl benzamide derivatives with higher binding affinity to InhA. Based on the integrated results, this study could provide important guidelines for the rational design of new and more potent InhA inhibitors.

SELECTIVE TARGETING OF MYCOBACTERIAL BIOFILMS AND INTRACELLULAR MYCOBACTERIA BY SYNTHETIC ANTIMICROBIAL POLYAMIDES

Prabhu Srinivas Yavvari,[1] Siddhi gupta,[2] Divya Arora,[3] Vinay Nandikoori,[3] Aasheesh Srivastava,[1,*] Avinash Bajaj[3,*]

[1]Department of Chemistry, Indian Institute of Science Education and Research, Bhopal By-pass Road, Bhopal-462066, Madhya Pradesh, India

[2]Laboratory of Nanotechnology and Chemical Biology, Regional Centre for Biotechnology, Third Milestone Faridabad-Gurgaon Expressway, NCR Biotech Cluster, Faridabad-121001, Haryana, India

[3] National Institute of Immunology, Aruna Asaf Ali Marg, New Delhi, Delhi-110067, India

*e-mail: asri@iiserb.ac.in, bajaj@rcb.res.in

Abstract:

Current membrane targeting antimicrobials fail to target mycobacteria, due to their hydrophobic membrane structure, ability to form drug-resistant biofilms, and their natural intracellular habitat within the confines of macrophages. We developed biocompatible synthetic antimicrobial polyamides that can target drug-sensitive and drug-resistant mycobacteria with high selectivity. Structure–activity relationship studies revealed that reduced hydrophobicity of cationic pendants induces enhanced and selective permeabilization of mycobacterial membranes. Besides achieving very high selectivity to target Mycobacteria over other Gram-positive and Gram-negative strains, these synthetic polyamides were able to disrupt the mycobacterial biofilms as well as mitigate the mycobacteria present within the infected mammalian cells.

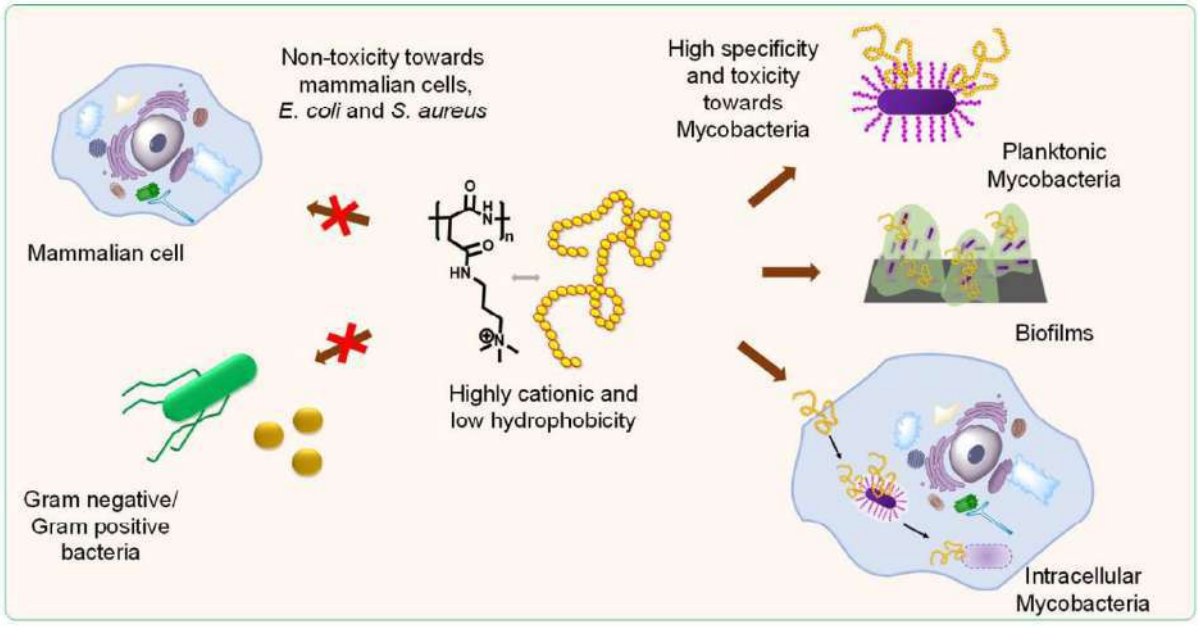

Figure 1. Schematic showing the activity of the synthetic cationic polyamides to selectively target the Mycobacteria (planktonic, biofilms and intracellular forms)

SYNTHESIS OF *Mycobacterium tuberculosis* ATP SYNTHASE INHIBITORS

Pattarakiat Seankongsuk,[1] Umayal Lakshmanan,[2] Priya Ragunathan,[3] Amaravadhi Venkata Krishna Harikishore,[1] Gerhard Grüber,[3] Roderick Wayland Bates[1,*]
[1]Division of Chemistry and Biological Chemistry, School of Physical and Mathematical Sciences, Nanyang Technological University, Singapore 637371
[2]Experimental Drug Development Centre, The Agency for Science, Technology and Research, Singapore
[3]School of Biological Science, Nanyang Technological University, Singapore
*e-mail: Roderick@ntu.edu.sg

Abstract:
Tuberculosis (TB) is a severe infectious disease, caused by *Mycobacterium tuberculosis* (Mtb). Currently, a number of drugs are used for treatment of this disease. However, the bacterium is able to mutate to become drug resistant Mtb, resisting against the recent therapy. Nowadays, 10 million active TB cases are reported worldwide leading to around 1.2 million deaths every year. By the World Health Organization's estimate, the TB situation will become more severe, and the number of deaths will increase significantly during Coronavirus disease 2019 (Covid-19) pandemic. Recently, GaMF1 was reported to exhibit a good inhibition in ATP synthesis of Mtb by binding at an unique and crucial peptide loop in the ɣ-subunit of *Mycobacterium* F_oF_1-ATP synthase. Nevertheless, water solubility and in *vivo* stability of GaMF1 are potentially problematic. In this work, 28 GaMF1 analogs are synthesized to overcome those aforementioned issues and to improve both enzymatic and growth inhibition. Inverted Membrane Vesicle (IMV) and growth inhibition assays were done to evaluate the synthetic analogs' properties. In summary, both the *p*-phenylenediamine moiety (ring B) and the pyrimidine (ring C) are crucial moieties for inhibition.

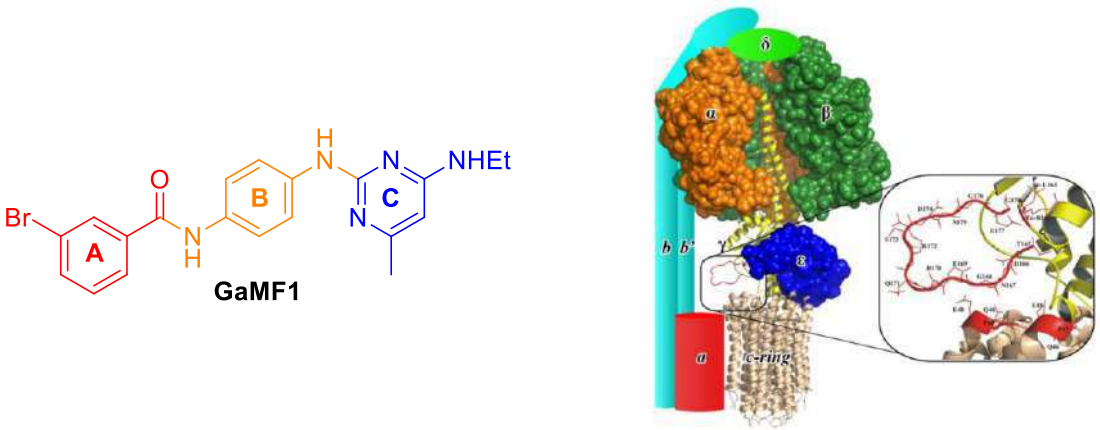

Figure 1.
Structure of GaMF1 (left) and Overall structure of *Mtb* F-ATP synthase (right)

EFFECT OF PHOSPHATE COMPOUND AS LIQUID PHASE SINTERING ADDITIVE ON PROPERTIES OF ALUMINA CERAMICS

Chayanit Sripradit[1,*], Charusporn Mongkolkachit[2], Mateekul Jiarawattananon[2], Thanakorn Wasanapiarnpong[1,3]
[1]Department of Materials Science, Faculty of Science, Chulalongkorn University, Bangkok
[2]National Metal and Materials Technology Center (MTEC), Klong Luang, Pathumthani
[3]Center of Excellence on Petrochemical and Materials Technology, Bangkok
*e-mail: pairchayanit02@gmail.com

Abstract:
High density alumina is used in a vast variety of applications such as refractory, insulator, biomedical, and mechanical components due to its outstanding physical and chemical properties in the term of electrical insulation, thermal stability, and high chemical stability. It can be used at maximum temperatures at 2000 ^{o}C. This research sets out to study the reduction of sintering temperature using the methodology of adding liquid phase sintering additives to produce high dense alumina ceramics with low rate of water absorption. The group of phosphate comprises monoammonium phosphate ($(NH_4)H_2PO_4$), calcium phosphate monobasic monohydrate ($Ca(H_2PO_4)_2.H_2O$) and sodium tripolyphosphate ($Na_5P_3O_{10}$). The characteristic of phosphate has a potential water-soluble property for homogenous mixture. The methodology in this study is, to mix phosphate following the proportion of 5-15 wt% with alumina powders — that has average size of particle size of 2.5 micrometers — then using mechanical stirrers with water about 50 wt% by weigh and continually mixing until it becomes slipped. Therefore, researchers evaporated evenly with a rotary evaporator then grinding with alumina mortar and a pestle. Ultimately, Alumina specimens were uniaxially pressed at 50 MPa in a form of 20 mm diameter and 5 mm of thickness. They were sintered at 1500-1600 ^{o}C for 2 hours in 5 ^{o}C/min heating rate. The study found that, the best optimum mixture condition and proportion—based on the defined constraints — is in the condition of alumina powder 90 wt% and calcium phosphate monobasic monohydrate 10 wt% with the sintering temperature of 1550 ^{o}C. As a result, alumina specimens have high bulk density of 3.68 g/cm^3 and water absorption as low as 0.12%.

Introduction:

High density alumina is widely well-known in ceramics materials, with some merit, it physically and chemically stands out in the term of refractoriness, high temperature oxidation resistance, electrical insulation, wear resistance and high chemical inertness, and corrosion resistance at high temperature. However, sintering alumina still has some drawbacks in the area of itself which require a high rate of sintering temperature at a melting point around 2000 ^{o}C [1] and production cost is way too high. A process technique that used to produce density materials from alumina powders by applying sintering can be divided into two types[1] consist of solid-state sintering and liquid phase sintering (LPS) which in this research, points out on a liquid phase sintering to reduce sintering temperature and production. Also, the addition of well-dispersed solid powder additives requires an enormous number of techniques — such as wet grinding with a ball mill[2] which can take a plenty of time to initiate the process. Moreover, this method either requires a removal of water or solution which can cause unevenness in dry evaporation, affecting the properties of the workpiece. Consequently, this research aims to use

a liquid additive or a liquid solution for more homogenous mixture. Particularly, solutions in the phosphate group —such as monoammonium phosphate, calcium phosphate monobasic monohydrate[3], and sodium tripolyphosphate — is melted to be a liquid phase for reduction sintering temperatures. Also, phosphate compound group can bond with refractories caused by their thermomechanical properties at 30-1000 ºC. Therefore, it would be meaningful to study the optimum ratio of liquid phase additive addition of phosphate groups to achieve the best formula of high-density alumina products and low water absorption since it is used in a wide range of formations such as furnace refractory panels, high-density bricks, medical materials, and engineering materials.

Alumina commonly exploits in the industry, in the type of high purity and high-density alumina. The density in these types is more than 3.75 g/cm^3 and must be sintered at high temperature (1500-1900ºC). Therefore, liquid phase sintering with the use of an additive that forms a liquid phase during sintering will allow the particles to rearrange[4], find a solution for re-precipitation and solid phase bonding as result alumina products that have high density at low sintering temperature.

Liquid phase sintering (LPS) is a well-known technique and widely published. B.A. Latella and O'Connor[5] study mentioned that the preparations of high purity alumina and liquid phase sintered (LPS alumina) consisting of 84 wt% alumina, 9 wt% kaolinite, 5 wt% talc and 2 wt% calcite powders. The addition of additive caused the glassy phase at the grain boundary so it can be prepared with high density alumina at low temperature but may affect some properties afterward. The result of this study said, LPS alumina with a density of 3.56 g/cm^3 from theoretical density of LPS alumina was 3.65 g/cm^3 and small grain size.

The purpose of this study aims to prepare sintered alumina by soluble additives to be easily mix well and homogeneously. It was found that, phosphate combined phosphoric acid, ammonia mixed of phosphates, alkali[6] of phosphate compounds and alumina of phosphate compounds. Some groups are soluble in water[3]. From the study of phase equilibrium diagrams, phosphoric oxide has a melting point at 580 °C[7]. A low melting point phase can be formed with alumina AlP_3O_9 and can transform to be $AlPO_4$ which has a high melting point. The study of phase equilibrium diagrams —Al_2O_3-CaO-P_2O_5 system from phase diagrams Al_2O_3-CaO-P_2O_5. L.Madecka[8] found that sintering at 1600 ºC could face 3 phases consist of Al_2O_3, $AlPO_4$, and $CaAl_{12}O_{19}$. Moreover, they found that $AlPO_4$ is a refractory material[8] which is highly robust. Eventually, in this study used phosphate compounds group to decrease the temperature for sintering. During the melting process, the alumina sintering was well-high density.

Methodology:

Researchers have carried out a series of academic research studies of each composition at different phosphate aiming to study the effect of phosphate compounds as liquid phase sintering additives consist of Almina powder size of 2.5 μm (P133SB, Alteo), phosphate compound group such as monoammonium phosphate (Wesco Chemicals Thailand Co., LTD.), monocalcium phosphate monobasic monohydrate (Sigma-aldrich) and sodium tripolyphosphate. The methodology consisted mixture of phosphate compound 0-15 wt% combined with R.O water by magnetic bar for 30 minutes. The methodology in this study is, to mix phosphate following the proportion of 0-15 wt% with alumina powders — that has average size of particle size of 2.5 micrometers — then using mechanical stirrers with water about 50 wt% of distilled water to be homogeneous slurry and evaporated evenly with a rotary evaporator and then dried power cakes were crushed and passed through a 100 μm. Alumina specimens are uniaxially dry pressed at 50 MPa to form 20 mm in diameter with 5 mm in thickness. After that, they are sintered at 1500-1600 ºC for 2 hours with a heating rate of 5 ºC /min.

The next step, we identified the water absorption and bulk density by using Archimedes' method and scanning electron microscope (SEM) to find microstructures. After all, we were verifying a phase composition by x-ray diffraction.

Results and Discussion:

As shown in figure 1, the addition of phosphate compound additive amount of each composition at a different phosphate compound additive content, we compared the three difference phosphate compounds in density of alumina 90 wt% and phosphate compound 10 wt%. The result shows that, in both temperature of sintering, 1500 ^{o}C and 1600 ^{o}C, calcium phosphate monobasic monohydrate has the highest density in both two temperature points of sintering for three phosphate compounds in this study. Thereby, we point up simply on calcium phosphate monobasic monohydrate.

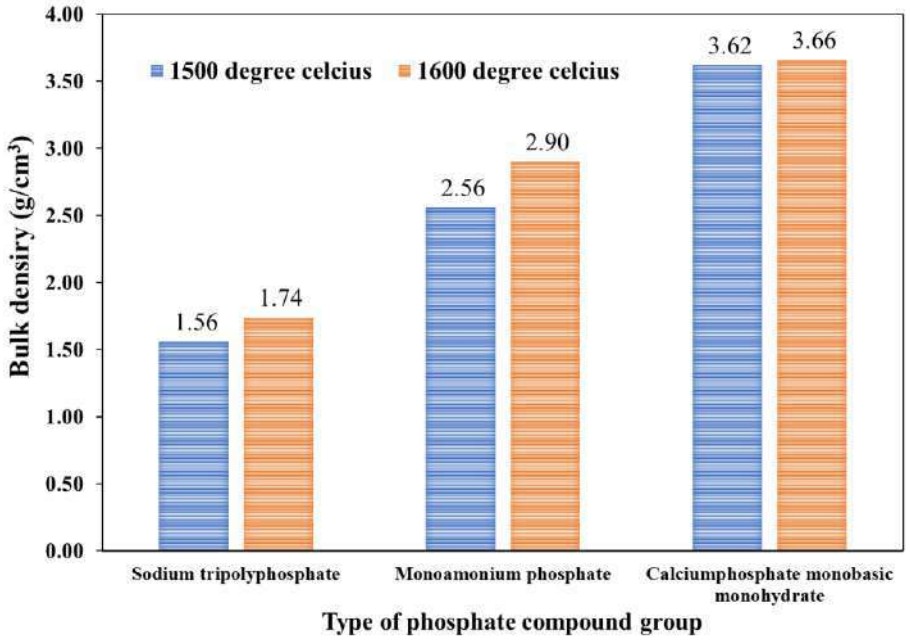

Figure 1. Bulk density of sintered alumina sample added with 10 wt% of phosphate compounds at 1500 ^{o}C and 1600 ^{o}C.

In this research, we used Almina powder size of 2.5 μm while we took alumina powder for sintering at 1500-1600 ^{o}C for 2 hours. The result found that, the range of bulk density was at 2.50 to 2.68 g/cm^3 and the range of percentage of water absorption was between 12.30 to 14.91. When adding additive at 1, 5, and 10 wt% of sodium tripolyphosphate in order to decrease temperature of sintering, found that, the density of products was in the range of 1.56 to 2.15 which was lower than estimation that we expected. Furthermore, we observed that, the products were bending and swelling on the disc in the 5wt% of additive, and the percentage of water absorption is at 25.25 to 37.62. In term of monoammonium phosphate additive, found that alumina has not melted yet relating to the microstructure images. Although, it showed that, for the most part, it had the similar particle when comparing with the initial alumina in the first place. In addition, we noticed the porosity and the bulk density of sintering at 1500-1600 ^{o}C in the range between 2.56 to 2.90 when adding additive 10 wt% and the percentage of water absorption in the range between 8.55 to 12.22. Eventually, in the last group, calcium phosphate monobasic monohydrate with adding additive 5 wt% and 10 wt% sintering at the same temperature, alumina got the highest density between 3.61 to 3.68 which was 93% of theory's

density and the percentage of water absorption was in the range between 0.12 to 0.38. Ultimately, the surface of this additive alumina product that had high density which related to the microstructure images has less perforation. In this study, phosphate compounds additive 10 wt% sintering at 1500-1600 ºC found that, calcium phosphate monobasic monohydrate produced the highest density of the group in this study which was represented in Figure 1 as below.

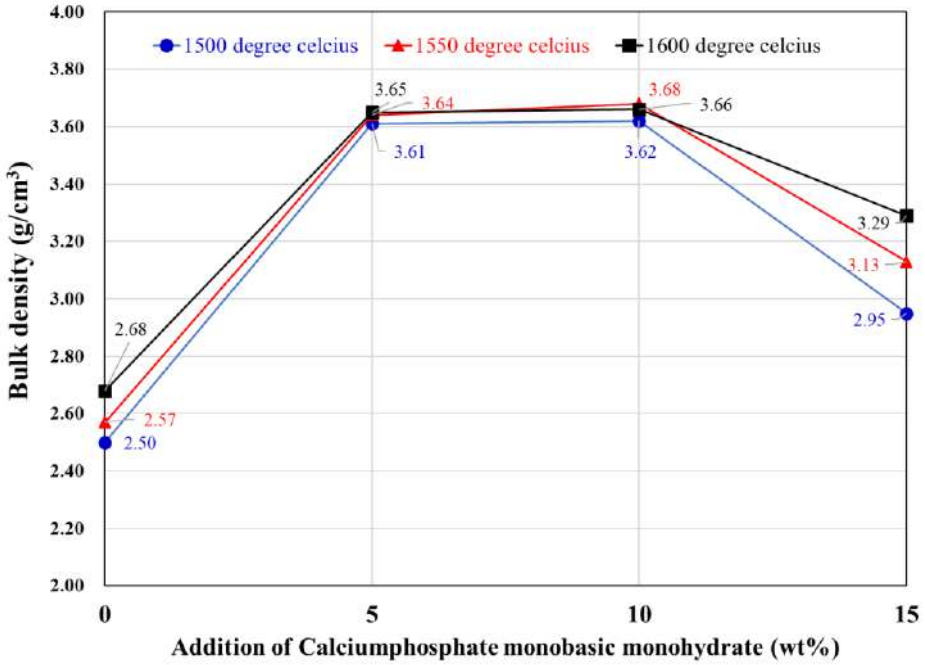

Figure 2. Bulk density of sintered alumina samples with added of 0-15 wt% calcium phosphate monobasic mono hydrate at 1500 ºC, 1550 ºC and 1600 ºC.

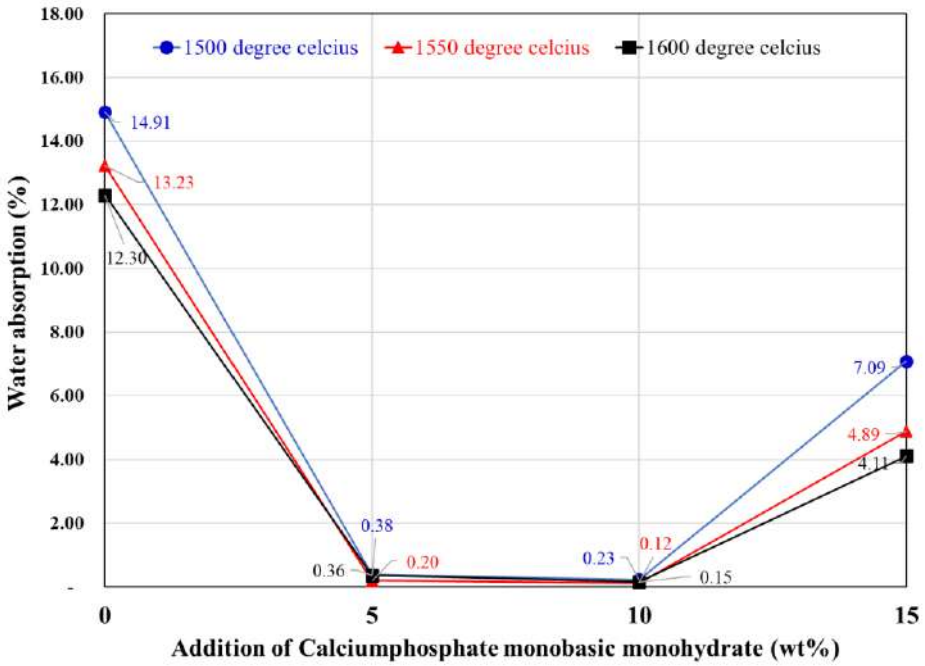

Figure 3. Water absorption of sintered alumina samples with added of 0-15 wt% calcium phosphate monobasic mono hydrate at 1500 ºC, 1550 ºC and 1600 ºC.

From the Figure 2 and 3 showed that, the bulk density and the percentage of water absorption of sintered alumina sample, were found at 1550 ^{o}C with the addition of additive calcium phosphate monobasic mono hydrate 10 wt%. As a result, alumina specimen had fully high bulk density of 3.68 g/cm^3 and water absorption was as low as 0.12%. On the other hand, when sintering at 1600 ^{o}C , it approximately had the density at the same level as 1500 ^{o}C, yet the percentage of water absorption was fewer and fewer than the previous one as you can see in Figure 7. The microstructure when sintering at 1600 ^{o}C had a high porosity which made the percentage of water absorption going high as well. Moreover, adding additive 15 wt% effects on high density, meanwhile, less the percentage of absorption. Consequently, we found the relationship between density and percentage of water absorption in this study.

The Figure 4a. showed that, in the circumstance of alumina which added additive monoammonium phosphate, the particle hasn't had any densification which related to density. The size of particle was generally similar the regular alumina. The particle which adding additive sodium tripolyphosphate has not melted as you can see in Figure 4b. Nevertheless, in the Figure 4c found that, the particle of alumina had been melting and bonding together which meant that the particle changed from the initial alumina. Due to the effect of adding calcium phosphate monobasic monohydrate, alumina had a high density at the sintering temperature at 1600 ^{o}C.

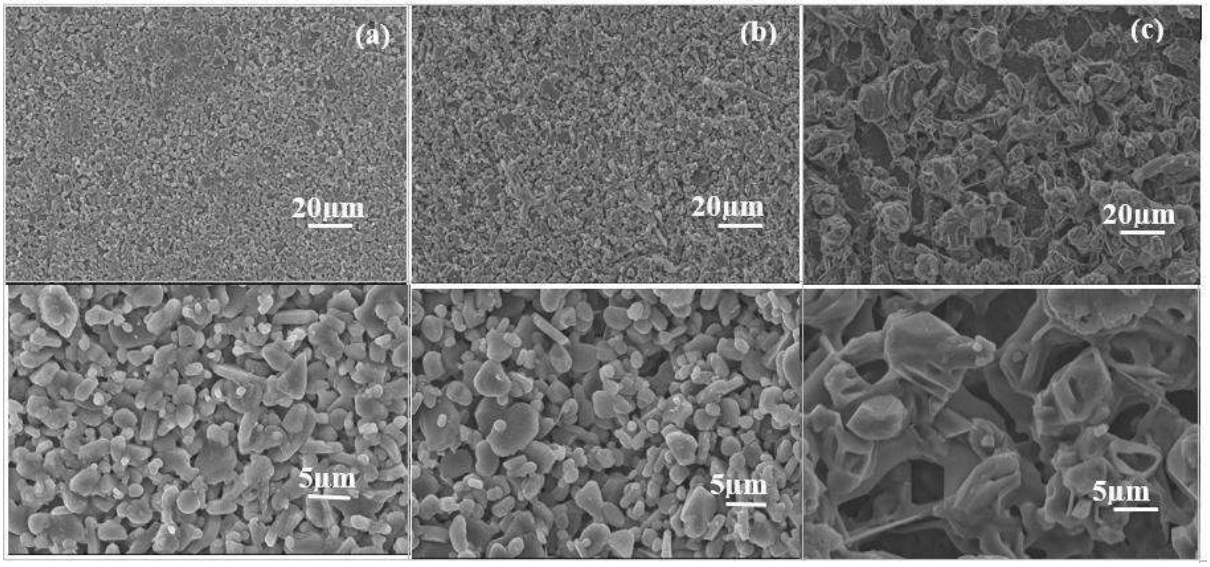

Figure 4. Scanning electron micrographs of surface of alumina at phosphate additive 10 wt% sintered 1600 ^{o}C (a) monoammonium phosphate (b) sodium tripolyphosphate (c) calcium phosphate monobasic monohydrate.

The calcium phosphate monobasic monohydrate at 10 wt% sintering at 1500-1600 ^{o}C which is represented in Figure 5 and Figure 6 showed that they sintered at 1550 ^{o}C, the particle of alumina had cohesion implicitly, and had the correlation between porosity and the percentage of water absorption.

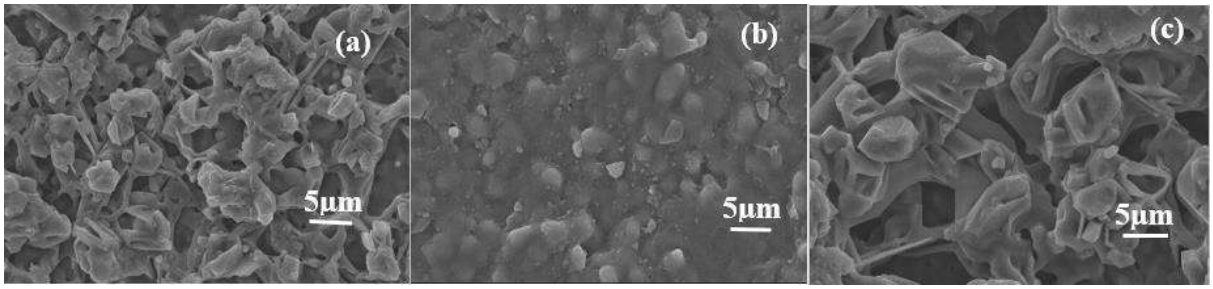

Figure 5. Scanning electron micrographs of surface of alumina at phosphate additive 10 wt% sintered (a) 1500 ^{o}C (b) 1550 ^{o}C (c) 1600 ^{o}C

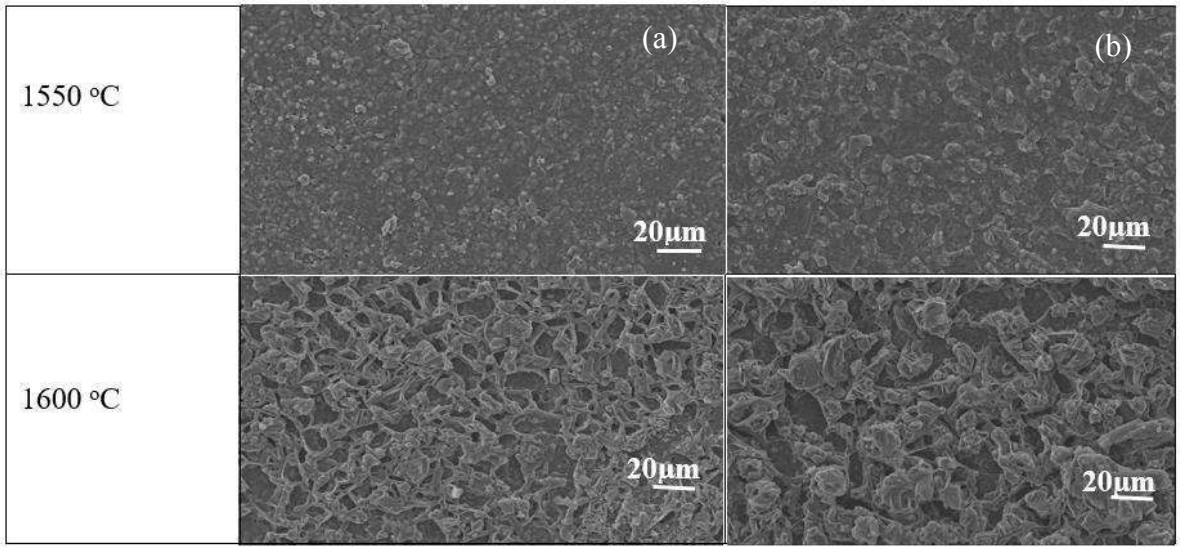

Figure 6. SEM pictures of surface of alumina at 1550 ^{o}C and 1600 ^{o}C with phosphate additive (a) 5 wt% (b) 10 wt%.

From X-ray diffraction analysis of disc-shape alumina samples containing 10 wt% of each phosphate group with sintering temperature at 1600 ^{o}C which was represented in Figure 7, corundum (Al_2O_3) occurred as main phases. Also, aluminum phosphate ($AlPO_4$) was found as minor phase which qualified as a heat-resistant property and highly compactness since its structure is isomorphous, for the most part as silica[9]. Accordingly, aluminum phosphate was qualified at its best in the part of the chemical and physical properties that was similar to silica[1]. However, aluminum phosphate tended to form at lower temperatures. As a result, less internal stress has an effect on high-density alumina at low temperature. Nevertheless, it could be considered as an economic advantage to produce suitable ceramics with low production cost. Compare with the addition of monoammonium phosphate and sodium tripolyphosphate additives, we found that, at the same temperature, there was no other the alumina phase formations from XRD analysis relevant to the result from the scanning of electron micrographs which presented the component of alumina particles with an average initial size of 2.5 microns, indicating that the alumina powder has not yet sintering.

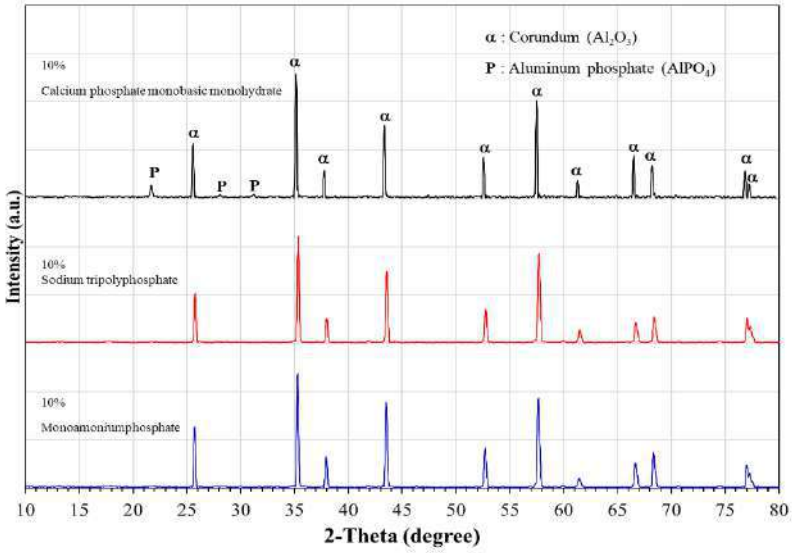

Figure 7. X-ray diffraction analysis of sintered alumina sample at 10 wt% of monoammonium phosphate, sodium tripolyphosphate, and calcium phosphate monobasic

Conclusion:

From this experiment of alumina adding additives in phosphate compounds group in order to reduce the temperature of sintering and the complexity of additives to form liquid phase while sintering. The result found that, the best optimized condition based on the defined constraints was obtained in the sample of alumina powder 90 wt% and calcium phosphate monobasic monohydrate 10 wt%. As a result, alumina specimens have high bulk density of 3.68 g/cm^3 and water absorption rate as low as 0.12% in the process of sintering at 1550 ^{o}C which can reduce the cost of production and complexity of additive. Additionally, $AlPO_4$ phase was found in this experiment which was highly robust and can transform at a low temperature point essentially. From this study, other pupils could use this study to perform products that have humidity such as an extrusion, since the phosphate compound additive can be dissolved in water and can make a homogeneous mixture that technically improves the quality of material, especially alumina additives.

Acknowledgements:

This study is funded by Thailand Graduate institute of Science, TGIST. The financial support has been provided by GAICCE Research Grant from ASEAN University Network/Southeast Asia Engineering Education Development Network (AUN/SEED-net) and I would like to thankful acknowledgment Department of Materials Science, Faculty of Science, Chulalongkorn University

References:

1. Liang X, I-Wei C. J Am Ceram Soc. 1991;74:2011-2013.
2. Peter S, Dusˇan G. Acta Mater. 2006;54:4853–4863.
3. Jaroslav S, Dusˇan G. Key Eng Mater. 2005;290:246-249.
4. Weimin D, Himanshu J. J Am Ceram. 2005;88:1702–1707.
5. Latella B, Brain O. J Mater Sci. 1998;33:877-886.877-886.
6. Jaroslav S, Reyes G. Ultrasonics Sonochem. 2013;20:948–954.
7. Philip E, Eward P. J Am Ceram. 1956;39:89-98.
8. Mandecka L, Rapacz A. Ceram Int. 2015;41:4093–4100.
9. Cassidy J. Am Cream Soc Bull. 1977;56:640-643.

PREPARATION OF PERVIOUS PAVING BRICK FROM CERAMIC PITCHER USING CERAMIC GLAZE AS BONDING MATERIAL

Pimrampa Kititarakul[1,2,*], Nithiwach Nawaukkaratharnant[2,3], Siriphan Nilpairach[2,3], Thanakorn Wasanapiarnpong[1,2,4]
[1]Department of Materials Science, Faculty of Science, Chulalongkorn University, Bangkok
[2]Water Resilient City Unit, Department of Geology, Chulalongkorn University, Bangkok
[3]Metallurgy and Materials Science Research Institute, Chulalongkorn University, Bangkok
[4]Center of Excellence on Petrochemical and Materials Technology, Bangkok
*e-mail: pimrampa1996@gmail.com

Abstract:
Urban flooding always occurs after heavy precipitation which is a serious issue in a big city that impacts on pedestrians. This study focuses on reusing waste products from the ceramic industries called pitcher in order to create pervious paving bricks. Ceramic pitcher from stoneware-grade tableware factory is crushed and sieved between 2-5 mm. Then, crushed pitcher is considered as the aggregate mixed with white-opaque glaze slurry and formed in a 5x5x5cm mold. After firing at 1200 °C with soaking time for 30 minutes and heating rate 5 °C/min, millimeters pore channels take place since ceramic pitcher pieces are connected by the fusing of glaze as binder. It is found that there are three major factors: grain size of aggregate, content of binder and aggregate, and content of glaze powder to water that affect to strength, density, porosity, and permeability rate of pervious paving brick. It is obvious that the brick using large grain aggregate provides lower strength with high porosity, leading to enhance the permeability rate. Moreover, the more glaze is added in the sample, the more porosity and permeability rate decreases. Therefore, this research tries to find out the most suitable condition to produce the brick that has both strength and permeability. The optimal condition for this research is 80 wt% of large aggregate (size 2-5 mm) and 20 wt% of glaze slurry. In the term of glaze slurry, the best combination is 71.43 wt% of glaze powder and 28.57 wt% of water, respectively. The result show that the brick samples have high compressive strength of 27.44 MPa, permeability rate at 937.6 $L/m^2 \cdot min$, bulk density of 1.65 g/cm^3 and apparent porosity of 30.53%.

Introduction:

Urban flooding after heavy rainfall is a serious issue in many cities which have a lot of impervious areas, impacting on the paths, roads, and people etc[1]. There are several perspectives to point out this problem such using permeable brick as Porous asphalt, Pervious concrete, Permeable Interlocking Concrete Pavement (PICP)[2] which has a high porosity and permeability rate of water drainage. The strength of the pervious brick depends on aggregate and binder; the small aggregate lead to high-strength on the brick, while the permeability rate is decreased[3].

The size and volume of pitcher affect to porosity and permeable rate. In other words, the size of pitcher at 2.36-4.00 mm (in 82 wt%) results in porosity and permeable rate at 26% and $3.2x10^2$ cm/sec, respectively. The strength of this brick could be loaded to 6.3 MPa which is quite stronger than that of the requirement in GB/T 25993-2010 standard[4]. In addition, the more binder content they put, the more porosity they gate. Since the binder such as glass powder receives the optimal temperature, it will melt to coat the ceramic grain's

surface which makes the brick be more porosity in products. Moreover, The performance of melting affects to strength[5].

This study aims to reuse the stone-ware pitcher from ceramic tableware industries to create pervious brick that has high porosity, high permeable rate, and high strength. It will solve the urban flooding issue by using pervious bricks instead of the regular pavement in order to release water as fast as possible. For this reason, this study will change the impact of pervious bricks made from the pitcher that not only produce the high-quality pervious bricks, but also reduce the waste from industries.

Methodology:

In the term of ceramic industries in Thailand, tableware is the most exported ceramic product contributed for 36.74%[6]. This research uses the pitchers from stone-ware tableware factories to aggregate which improves strength on pervious brick more than general porous asphalt[7]. The pitcher is crushed and selected; aggregate size between 2-5 mm for large aggregate and 0-2 mm for small aggregate. Usually, broken ceramic tableware is sharp, so it needs to be chamfered by grinding using a porcelain high-speed ball mill for 30 minutes and are then sieved out dust or small aggregate.

White-opaque glaze from Compound Clay Company Limited is used as a binder. The chemical compositions of glaze is analyzed by x-ray fluorescence (XRF) which is presented in **Table 1.** The main compositions of glaze are SiO_2, Al_2O_3, CaO, MgO, and ZrO_2, which not only exhibit good abrasion and good chemical resistance, but also increase mechanical properties of the produced pervious brick[8].

Table 1. Chemical composition of white-opaque glaze was detected by XRF

Oxide	SiO_2	Al_2O_3	CaO	MgO	ZrO_2	K_2O	Na_2O	Fe_2O_3	Total
Mass%	53.5	18.6	10.6	7.10	4.27	3.22	2.26	0.25	99.80

The preparation of the pervious paving brick starts from mixing pitcher with glaze slurry, then forming the mixture in a cubic mold (size 5×5×5 cm). After dried in an oven overnight at 110 ºC, the samples are fired at 1200 °C in a furnace with a soaking time of 30 minutes and a heating rate 5 °C/min. The samples are then cooling down in furnace to room temperature. The process of preparation is shown in **Figure 1.** This study has three main conditions, 1.T content of glaze powder: water, 2. content of aggregate : glaze slurry, 3. content of aggregate size large : small. All these conditions have impact on bulk density, water permeability rate, porosity, and compressive strength. The detail in each condition is shown in **Table 2.**

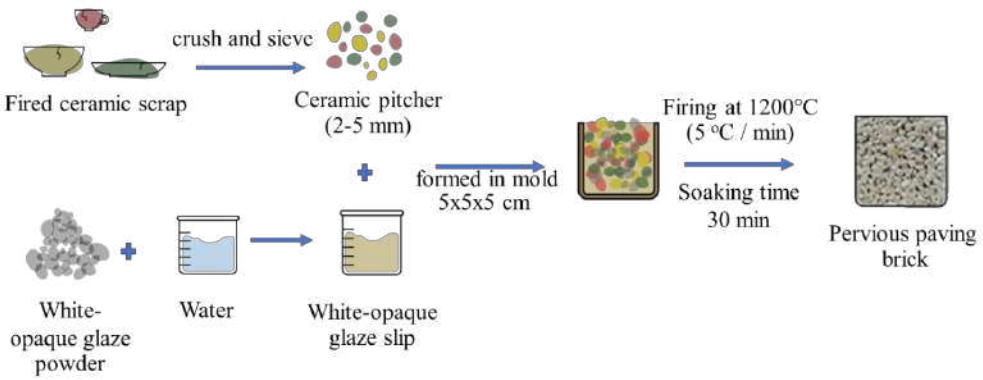

Figure.1 The preparation of pervious paving brick from pitcher

Table 2. Conditions in mixture of pervious brick

Condition	Formula (wt%)								
1. glaze powder: water	**A**			**B**			**C**		
	Small	-	80	Small	-	80	Small	-	80
	Large	100		Large	100		Large	100	
	Glaze	66.67	20	Glaze	68.96	20	Glaze	71.4	20
	Water	33.33		Water	31.04		Water	28.57	
2. aggregate: glaze slurry	**D**			**E**			**F**		
	Small	-	75	Small	-	80	Small	-	85
	Large	100		Large	100		Large	100	
	Glaze	71.43	25	Glaze	71.43	20	Glaze	71.43	15
	Water	28.57		Water	28.57		Water	28.57	
3. aggregate size large: small	**G**			**H**			**I**		
	Small	33.33	80	Small	25	80	Small	-	80
	Large	66.67		Large	75		Large	100	
	Glaze	71.43	20	Glaze	71.43	20	Glaze	71.43	20
	Water	28.57		Water	28.57		Water	28.57	

Bulk density of fired samples is calculated from dry weight and dimension. The compressive strength testing uses Instron Testing Machine 5843 followed ASTM C133 standard. The results show an average value from 5 samples. The permeability rate testing is calculated by **Equation 1**, using sample size 5×5×5 cm and wrapping specimen around by paraffin film after that pouring 1 liter of water on specimen then time. A constant level of water above the brick surface is 4 cm.

$$\text{Permeability rate}(\text{L}/\text{m}^2 \cdot \text{min}) = \frac{\text{V}}{\text{A} \times \text{t}} \quad (1)$$

Where V is volume of water (1 Liter)
A is area of specimen surface (m^2)
t is time of water permeated into a specimen (min)

The apparent density and apparent porosity are calculated by **Equation 2.** and **Equation 3.** respectively. The tests start from measuring the sample weight then immerse in water for 24 hours. The brick is saturated. next, dried for 24 hours.

$$\text{Apparent density}(\text{g}/\text{cm}^3) = \frac{\text{W}_{\text{dry}}}{\text{W}_{\text{sat}} - \text{W}_{\text{water}}} \quad (2)$$

Where W_{dry} is dry weight of specimen (g)
W_{sat} is saturate weight of specimen (g)
W_{water} is weight of specimen in water (g)

$$\text{Apparent porosity}(\%) = [1 - \left(\frac{\text{Apparent density}}{\text{Bulk density}}\right)] \times 100 \quad (3)$$

Results and Discussion:

The results of bulk density in each condition (aggregate size, content of glaze to water, and content of aggregate to glaze) are presented in **Figure 2.** In the content of aggregate to glaze condition, an increased binder generates a higher bulk density caused by the exceed coating. The reason for this incident because the exceed coating flows down and piles at the bottom, so it fills the pore in the brick while molding[7]. The result of the apparent porosity and permeability rate shown in **Figure 3**. and **Figure 4**. It is evident that the more an increased binder, the lower apparent porosity and permeability rate. On the other hand, the more content of glaze powder, the more viscosity of glaze slurry. In the molding process, the binder can adhere to the aggregate surface better, resulting in more porous in the structure and higher permeability rate.

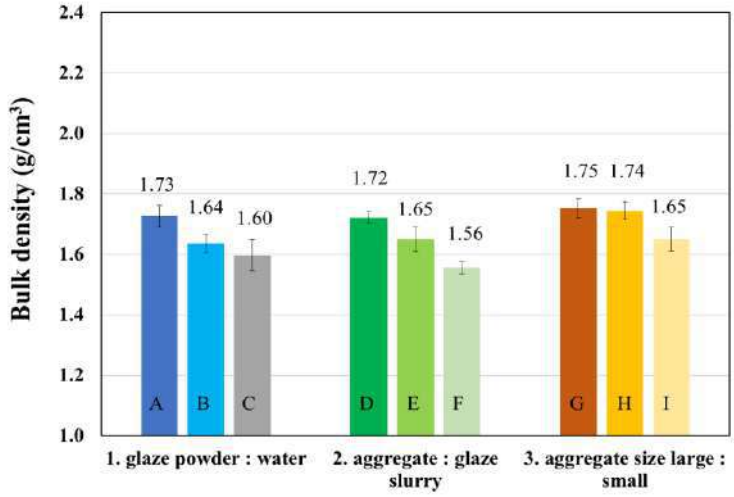

Figure 2. The results of bulk density in each condition

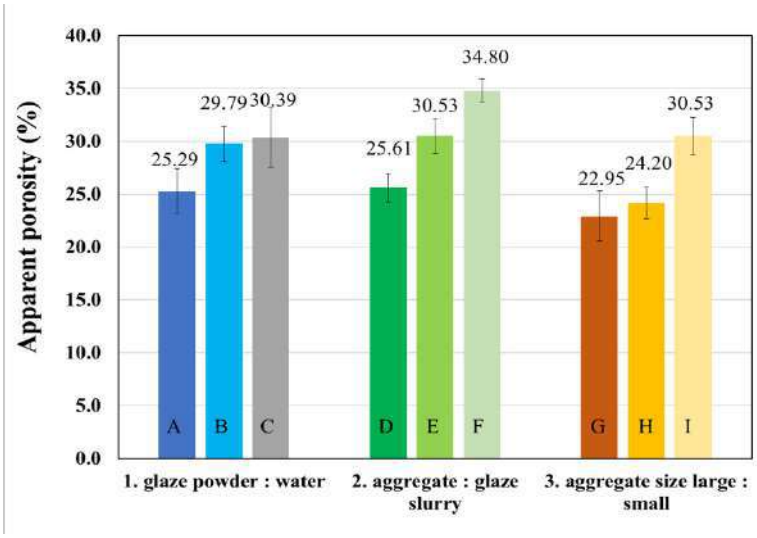

Figure 3. The results of apparent porosity in each condition

The trend of the graph in **Figure 5** shows that the small aggregate (size 0 - 2 mm) increases the compressive strength. The comparison between the brick using large aggregate 66.67 wt% and large aggregate 100 wt%, Illustrates the compressive strength increases 37% because the small aggregate forming in a mold will be arranged more tightly. According to **Figure 2** it is obvious that bulk density has direct variation with small grain content. In contrast, bulk density inverse variation with the porosity and permeability rate. In **Figure 4**, the permeability rate decreases from 930 L/m^2·min to 530 L/m^2·min or 43 %. From **Figure 6A**, the surface of the specimen with a small aggregate of 33.33 wt% shows that the volume and the pore size decrease compared to **Figure 6B** which uses only the large aggregate. Considering the GB/T 25993-2010 standard, the compressive strength of the sample (large aggreate 100 wt%) is 27.4 MPa, which is higher than the standard. Concerning with the suitable condition, this study considers only a large aggregate size of 2-5 mm. Since even the strength is lower, it generates higher permeability.

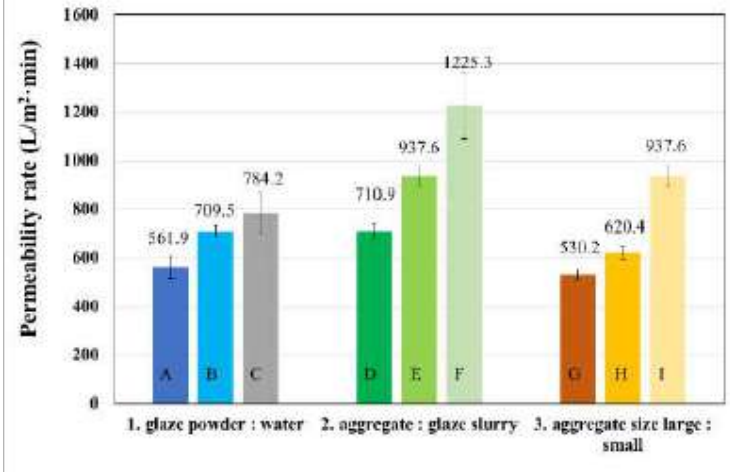

Figure 4. The results of permeability rate in each condition

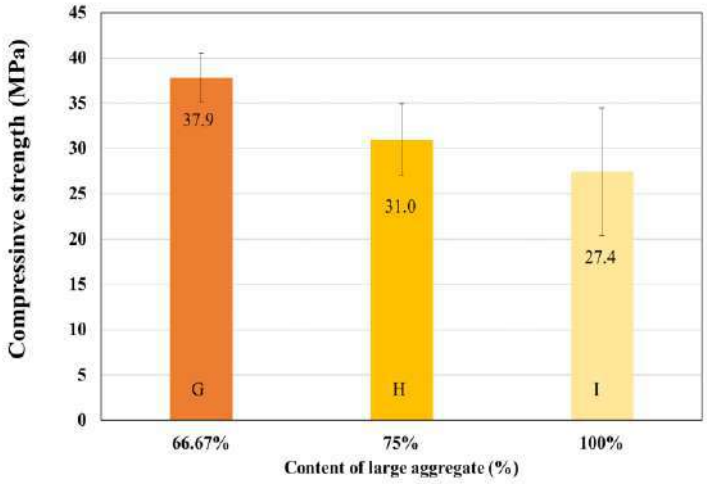

Figure 5. The results of compressive strength in content of large aggregate to small aggregate condition.

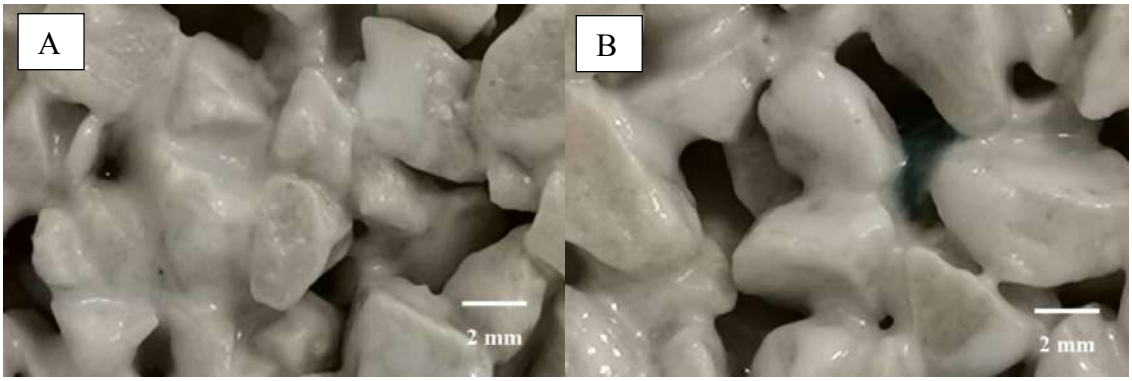

Figure 6. Surface of pervious brick that used (A) small aggregate size 33.33 wt% and (B) large aggregate size 100 wt%

Conclusion:

This study aims to find the suitable conditions for preparing pervious brick, in term of size aggregate, content of glaze powder to water, and content of aggregate to glaze, in order to create the brick that has high porosity, high permeability, and high strength. The suitable condition is large aggregate (size 2-5 mm) 80 wt%, 20 wt% of glaze slurry that has 71.43 wt% of glaze powder and 28.57 wt%. The brick samples exhibit high compressive strength of 27.44 MPa, permeability rate at 937.6 $L/m^2 \cdot min$, bulk density of 1.65 g/cm^3 and apparent porosity of 30.53%.

Acknowledgements:

The author would like to thank for financial supporting, which has been provided by GAICCE Research Grant from ASEAN University Network/Southeast Asia Engineering Education Development Network (AUN/SEED-net) and Department of Materials Science, Faculty of Science, Chulalongkorn University.

References:

1. Rahman M. J Environ Manage. 2021;295:113086.
2. Razzaghmanesh M, Borst M. Sci Total Environ. 2019;670:893-901.
3. AlShareedah O, Nassiri S. J Clean Prod. 2021;288:125095.
4. Yang Z. J Clean Prod. 2020;254.
5. Zhou, C. Construct Build Mater, 2018;188:850-859.
6. Riyakad P, Chiarakorn S. Energy Procedia. 2015;79:98-102.
7. Lu G. J Clean Prod. 2019;220:1052-1060.
8. Ercenk E, Guven B, Yilmaz S. J Non Cryst Solids. 2018;498:262-271.

USE OF BIOCHAR IMPREGNATED WITH IRON AND CHITOSAN FOR HEAVY METAL REMOVAL: SORPTION PERFORMANCES

Nattakarn Kruatong,[1*] Soydoa Vinitnantharat,[1,2] Anawat Pinisakul,[3] Arachaporn Wilamas,[4] Nareerat Sukkhe[2]
[1]Environmental and Energy Management for Community and Circular Economy (EEC&C) Research Group, King Mongkut's University of Technology Thonburi, Bangkok, Thailand
[2]Environmental Technology Program, School of Energy, Environment and Materials, King Mongkut's University of Technology Thonburi, Bangkok, Thailand
[3]Chemistry for Green Society and Healthy Living Research Unit (ChGSH), Department of Chemistry, Faculty of Science, King Mongkut's University of Technology Thonburi, Bangkok, Thailand
[4]Department of Biological Science, Faculty of Science, Ubon Ratchathani University, Ubon Ratchathani, Thailand
*e-mail: nattakarn973@gmail.com

Abstract:

The presence of pollutants in aqueous solution, particularly from heavy metals is an important environmental and social problem. Iron (Fe), manganese (Mn) and arsenic (As) can be found in groundwater, particularly if it is near gold mine. Thus, it is necessary to find the adsorbent that can remove these heavy metals and investigate its sorption performance. Synthetic water solutions with Fe(II), Mn(II) and As(V) at concentration of 5.0, 5.0 and 0.1 mg/L, respectively, were used in batch adsorption study using bamboo biochar (B) and impregnated with iron (BFe) and chitosan (BC) as adsorbents. The results indicated that iron and chitosan could enhance the sorption capacity of heavy metal solution, especially for the adsorption of arsenic (> 90%) in BFe.

Introduction:

The presence of heavy metal in groundwater is an important environmental and social problem, as groundwater is typically used in rural area. Few metals, such as Fe, Zn, Cu, Co, Cr, Mn and Ni, are required for biological metabolism in trace amounts; however, their high dosage may cause toxic effects. Others, such as Pb, Hg, Cd and As, are not suitable for biological functions and are positively toxic. Toxicity of these elements is considerable concern worldwide because of their environmental burden.[1] The removal of contaminants from polluted waters is a matter of great interesting in the field of water pollution. Amongst the numerous techniques of contaminant removal, adsorption using solid materials (adsorbents) is a simple, useful and effective process. The adsorbent can be mineral, organic or biological origin.[2] Adsorption is the accumulation of materials at an interface, the liquid/solid boundary layer. It is a mass transfer process where a substance is transferred from the liquid phase to the surface of a solid and becomes bound by chemical or physical forces. Adsorption can take place on suspended particles, as part of the process of coagulation/co-precipitation, or on fixed media. Since adsorption is a surface phenomenon, the greater the surface area of the medium, the greater it's capacity to accumulate materials. Recently, biochar is a popular filter media due to its physical characteristics, sustainable production, and global availability which high effective for removal pollutants in water and soil. In addition, biochar prepared from agricultural products and wastes leading to low cost production. Biochar was widely used for removal of organic substances and heavy metals due

to its adsorption properties. Fe, Mn and As can be found in groundwater, particularly if it is near gold mine. Thus, it is necessary to find the adsorbent that can simultaneously remove these heavy metals and investigate its sorption performance. Biochar normally has negative charge on surface, so it had less adsorption of anion such as arsenite ion in water. To enhance the adsorption capacity, it is needed to modify the biochar. Thus, this present study investigated the use of biochar derived from bamboo and impregnated with iron and chitosan for the removal of Fe, Mn and As in synthetic water solution.

Methodology:

Preparation of adsorbents and characterization:

Bamboo biochar (B) was derived from Ubon Ratchathani province. Biochar was prepared by carbonization of bamboo (*Bambusa beecheyana*) in a mound kiln. It was crushed to a uniform size in range of 2.0-3.0 mm.

Iron impregnated bamboo biochar (BFe) was adapted from method by Kalaruban et al.[3] Bamboo biochar at 20 g was mixed with iron solution (6.75 g/500 mL of $FeCl_3.6H_2O$) in 250 mL erlenmeyer flask. Then, agitated in a shaker at 100 rpm for 24 h at a room temperature. BFe was separated by filtering through plastic sieve, then it was rinsed with tap water until pH is 7.00±0.50 and rinsed with deionized water. Left it dried at room temperature and then kept in bottle.

As for chitosan impregnated bamboo biochar (BC) preparation, bamboo biochar was placed in an erlenmeyer flask containing chitosan gel solution (B: chitosan ratio of 5:1 w/w). The chitosan gel solution was prepared by dissolving 10 g chitosan powder in 1 L of 1% v/v acetic acid. The mixture was agitated at 100 rpm for 24 h. Then, they were rinsed with tap water until pH is 7.00±0.50 and rinsed with deionized water. Left it dried at room temperature and then kept in bottle.

Activated carbon (AC) at the size of 2.0-3.0 mm was derived from Charcoal Home Co., Ltd, Thailand. It was made from bamboo (*Dendrocalamus asper*) by carbonization in brick kiln at high temperature (1000 ^oC)

To characterize the physical properties of B, BFe, BC and AC, the Brunauer-Emmett-Teller (BET) surface area and porosity and scanning electron microscopy (SEM) were employed. The chemical composition was analyzed by X-ray fluorescence (XRF). In addition, the iodine number was analyzed followed ASTM D4607, the pH of the point of zero charge (pH_{pzc}) was followed by Newcombe, et al.[4] and pH of solution (pH_{sol}) was analyzed followed Al-Degs, et al.[5]

Preparation of synthetic water solution:

The synthetic water solution was prepared from tap water containing ions as showed in Table 1. Heavy metal at desirable concentration was spiked into tap water. The Fe(II), Mn(II) and As(V) ions were prepared from $FeSO_4.7H_2O$ (AR grade), $MnSO_4.H_2O$ (AR grade) and $Na_2HAsO_4.7H_2O$ (AR grade), respectively.

Table 1.
Characteristics of synthetic water

pH	Na^+ (mg/L)	NH_4^+ (mg/L)	K^+ (mg/L)	Ca^{2+} (mg/L)	Mg^{2+} (mg/L)	Cl^- (mg/L)	NO_3^- (mg/L)	SO_4^{2-} (mg/L)
7.55	11.95	0.03	4.66	57.05	9.52	12.75	4.03	34.90

Batch adsorption experiments:

The initial concentrations of 5.0, 5.0 and 0.1 mg/L were used for the Fe(II), Mn(II) and As(V), respectively. A series of plastic bottle containing 0.5 g adsorbents with 50 mL solutions of heavy metal were agitated in an incubator shaker at 100 rpm, 28 ± 0.5 °C and pH 7.00±0.50 for the interval of time. The suspensions at the period of time were then filtered and the filtrates were analyzed for Fe(II) and Mn(II) using an atomic absorption spectrometer (AAS) and As(V) concentration using an inductively coupled plasma (ICP-OES). All experiments and control experiment (without adsorbate) were done in duplicate.

The amount of Fe, Mn and As adsorbed onto adsorbent, q (mg/g), was calculated using the equation (1):

$$q_t = [(C_0-(C_t-C_c)) \cdot V]/m \quad (1)$$

where C_0 is the initial concentration of heavy metal ion (mg/L), C_t is the concentration of heavy metal ion at time t (mg/L), C_c is the concentration of heavy metal ion from control experiment at time t (mg/L), V is the volume of solution (L), and m is the mass of adsorbent (g). Percentage of adsorption was calculated using the equation (2):

$$\text{Percentage of adsorption (\%)} = [(C_0-(C_t-C_c))/C_0] \times 100 \quad (2)$$

The kinetics of adsorption were modelled using pseudo-first order and pseudo-second order in equations (3) and (4), respectively.

$$\log (q_e-q_t) = \log (q_e) - [(k_1 \cdot t)/2.303] \quad (3)$$

where q_e = amount of Fe, Mn and As adsorbed at equilibrium (mg/g), q_t = amount of Fe, Mn and As adsorbed at time (h), (mg/g), and k_1 = rate constant for pseudo-first order adsorption (min^{-1}).

$$t/q_t = (1/k_2 \cdot q_e^2) + (t/q_e) \quad (4)$$

where k_2 = rate constant for pseudo-second order adsorption (g $mg^{-1}h^{-1}$).

Results and Discussion:

Characteristics of adsorbents:

The BET surface area (S_{BET}), pore volume (V_p), pore width (D_p), iodine number, pH_{pzc} and pH_{sol} of each adsorbent are presented in Table 2.

Table 2.
Characteristics of adsorbents

Adsorbents	**S_{BET} (m^2/g)**	**V_p (cm^3/g)**	**D_p (A^0)**	**Iodine no. (mg/g)**	**pH_{pzc}**	**pH_{sol}**
B	191.949	0.104	21.641	75.300	7.630	8.660
BFe	127.715	0.070	22.055	45.540	3.610	2.590

BC	66.630	0.037	21.960	72.090	4.560	4.310
AC	136.016	0.110	19.523	267.380	8.340	9.350

B has the highest BET surface area followed by AC, BFe and BC, respectively. The decrease in surface area and pore volume of the BFe and BC are due to the blockage of some pores by the iron oxide and chitosan. Previous study also reported a reduction in surface area, pore volume and pore size after impregnation of activated carbon (AC) with Fe.[6] This is consistent with SEM as showed in Figure 1. The cross-section micrographs of adsorbent shows presence of the porous structure of B, whereas the rest adsorbents have fine particles on their surfaces. These particles could affect adsorption capability. The iodine adsorption analysis was tested to define the surface porosity of adsorbents. The higher iodine number implies the higher small porous of the adsorbent. The obtained iodine numbers ascertained that AC has the highest surface porosity in this study. The iodine adsorption of B after impregnation with iron (BFe) and chitosan (BC) were lower than B. The alkaline pH_{sol} of AC was due to high ash composition of biochar as the high temperature was used for carbonization. The iron and chitosan impregnation of the B surface has changed the pH of the B. The impregnation of Fe decreased the pH_{pzc} and pH_{sol}. The acidic solution pH of BFe was due to the consuming OH^- from water by Fe(III). The acidic pH of BC caused by the preparation BC used an acetic acid solution (1%) for preparing chitosan gel solution, H^+ can release into the BC solution. The results indicated that the surface of BFe and BC were more acidic (pH_{pzc} = 3.61 and 4.56, respectively) whereas the surface of B is close to neutrality (pH_{pzc} = 7.63). At the pH_{sol} below pH_{pzc}, the surface become positively charged renders BFe and BC to be more suitable in the removal of arsenic ($H_2AsO_4^-$, $HAsO_4^{2-}$). Whereas at pH_{sol} above the pH_{pzc}, the adsorbent surfaces of the B and AC are negatively charged[7]. As a result, B and AC can remove iron (Fe(II), $FeOH^+$) and manganese (Mn(II)).

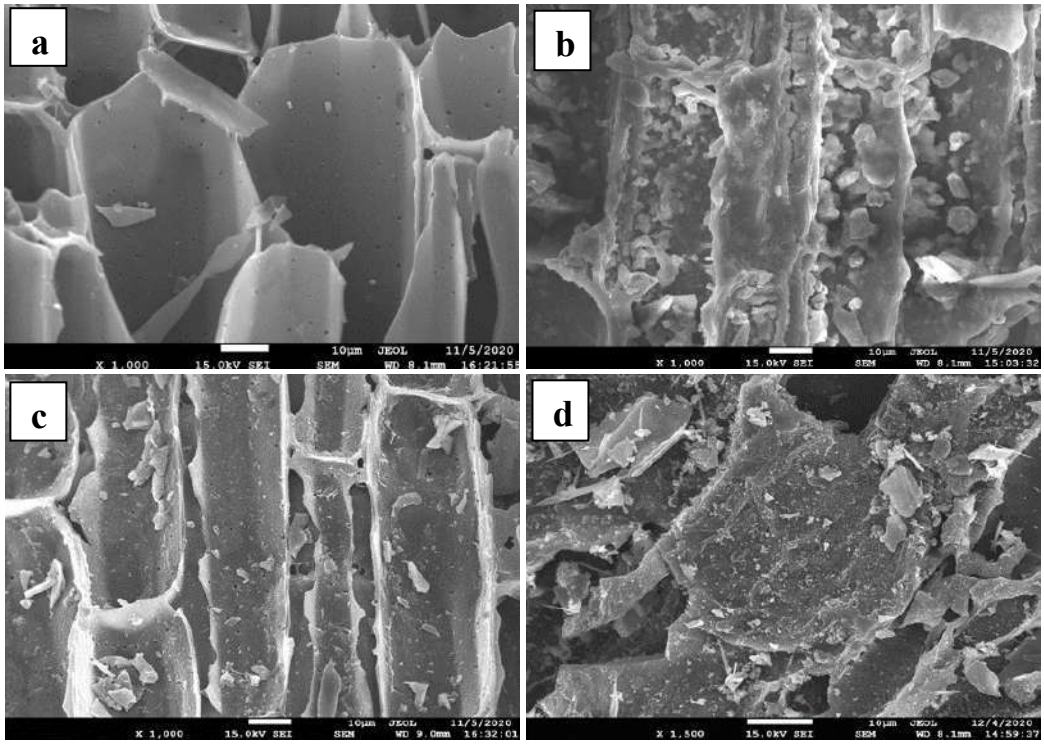

Figure 1.
Scanning electron micrographs of B (a), BFe (b), BC (c) and AC (d) (x1000)

Results from the X-ray fluorescence analysis (Table 3) show that all adsorbent contains Fe and Mn that can release to the solution. As for modified biochar, it was found that BFe has low Mn, whereas BC has low Fe.

Table 3.
X-ray fluorescence of the adsorbent

Adsorbents	%Wt.							
	Si	Ca	Fe	Ni	Cr	Mn	Br	As
B	9.54	29.23	3.48	ND[a]	ND	1.43	ND	ND
BFe	16.28	2.54	14.00	0.04	0.02	0.45	0.03	ND
BC	17.00	10.59	0.79	0.10	ND	1.24	ND	ND
AC	7.16	7.75	1.32	ND	ND	0.70	ND	ND

[a]ND = Non detectable

Kinetics of batch adsorption:

In general, Fe precipitated in high pH and the pH of a single solution in this research was 7.00 ± 0.5. In the presence of oxygen, ferrous iron (Fe(II)) oxidizes to ferric iron (Fe(III)), and ferric hydroxide forms a yellowish-orange solid, which precipitates at pH >4.5.[8] Therefore, the removal of iron is due to precipitation in combination with adsorption. This gives the Fe removal efficiencies more than 90 % from the first 30 minutes in all adsorbents. Figure 2 and Table 4 show kinetic parameters for adsorbent and the heavy metal removal efficiencies. For kinetic analysis of Fe(II), the pH values were adjusted to 4.30 with 1% HNO_3 solution for avoiding the Fe(II) precipitation. The adsorption of Fe(II) by all adsorbents were followed pseudo-second order, that means the adsorption mechanism was chemical process. The adsorption of Mn on the BFe and BC occurred slowly. The equilibration time for BFe and BC were 96 and 132 h, respectively. For BC cannot remove Mn (the Mn removal efficiencies < 1%) and BFe can remove Mn of approximately 12%. For B and AC were found for the Mn removal efficiencies of 70% occurred within 36 h, and this reached 80 and 90% in 84 and 60 h, respectively. Adsorption of Mn (II) onto B, BFe and AC were followed pseudo-second order, whereas adsorption of As(V) onto all adsorbents were followed pseudo-second order. However, it was found that correlation coefficient values of the pseudo-first order were not different from the pseudo-second order. It can be assumed that the sorption capacity could be achieved both of physical and chemical processes. The adsorption of As(V) on all adsorbents were rapid. Fifty percent adsorption occurred within 15 min and 2.3 h for BFe and BC, respectively, and this reached 90% in 2.3 h for BFe adsorbent.

(a) The Fe(II) adsorption (pseudo-first order)

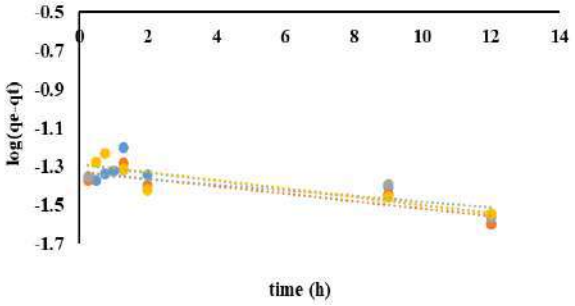

(b) The Fe(II) adsorption (pseudo-second order)

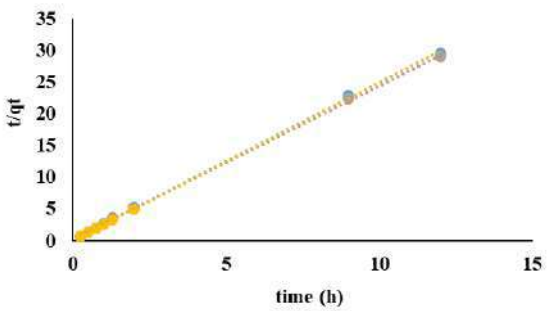

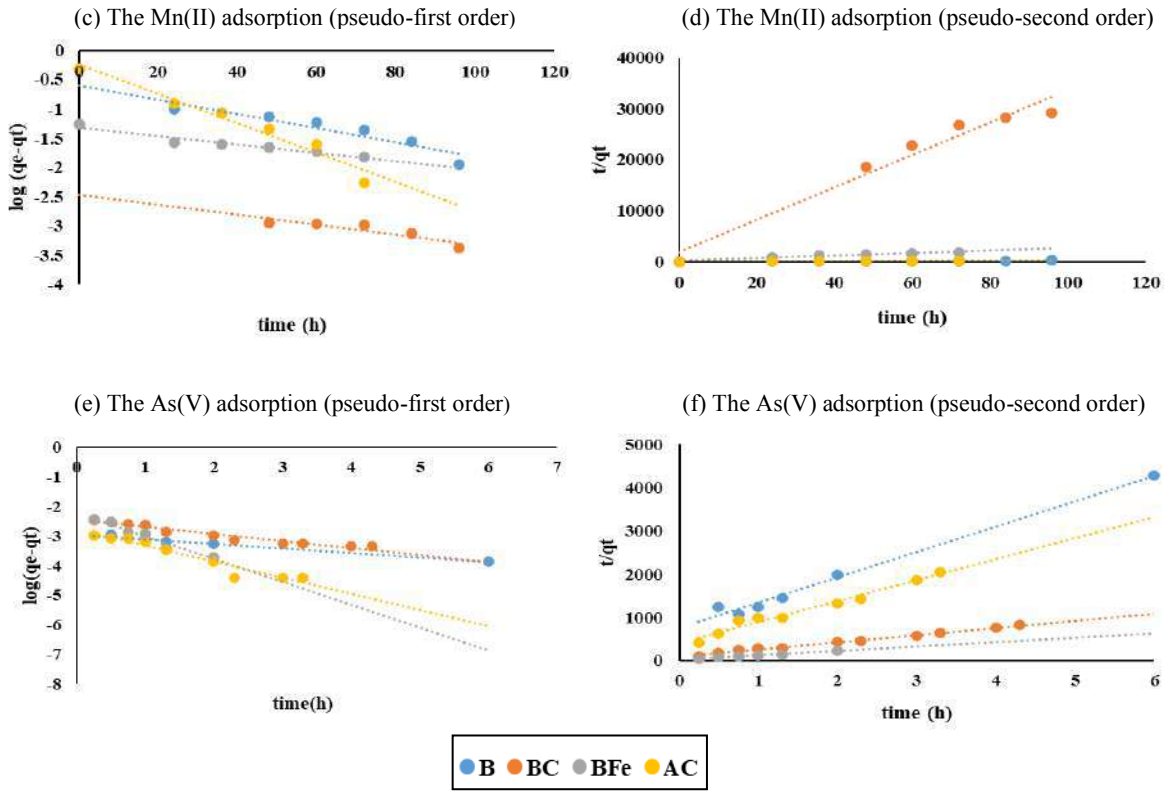

Figure 2.
Kinetics of batch adsorption

Table 4.
Kinetic parameters for adsorbent and the heavy metal removal efficiencies

Solution	Adsorbent	Removal efficiencies (%)[a]	q_e (exp)[b] (mg/g)	Pseudo-first-order			Pseudo-second-order		
				k_1 (min^{-1})	q_e (cal) (mg/g)	R^2	k_2 ($g\ mg^{-1}\ h^{-1}$)	q_e (cal) (mg/g)	R^2
Fe(II)[c]	B	95	0.434	0.048	0.051	0.670	29.429	0.404	1.000
	BFe	98	0.441	0.034	0.047	0.655	40.405	0.411	1.000
	BC	97	0.440	0.045	0.045	0.765	32.418	0.413	1.000
	AC	97	0.438	0.050	0.052	0.795	38.318	0.409	1.000
Mn(II)	B	86	0.443	0.032	0.334	0.929	0.452	0.435	1.000
	BFe	12	0.055	0.016	0.048	0.933	2.132	0.040	0.962
	BC	1	0.004	0.020	0.005	0.813	7.926	0.005	0.917
	AC	97	0.489	0.058	0.565	0.960	0.450	0.494	0.983
As(V)	B	14	0.002	0.352	0.001	0.978	591.898	0.002	0.990
	BFe	92	0.009	1.772	0.006	0.961	478.987	0.010	0.996
	BC	58	0.006	0.555	0.004	0.941	299.870	0.006	0.994
	AC	16	0.002	1.251	0.002	0.934	955.798	0.002	0.972

[a]The removal efficiencies of Fe(II), Mn(II) and As(V) at the equilibrium time were 3, 120 and 6 h, respectively.
[b]q_e(exp) = amount of heavy metal adsorbed from experiment.
[c]This experiment was done at initial concentration of 5.0 mg/l at pH 4.30 to avoid Fe precipitation.

Conclusion:

The overall results from this study indicate that iron and chitosan could enhance the sorption capacity of heavy metal solution, especially for the adsorption of arsenic (> 90%) by BFe. Batch adsorption studies showed that adsorptions were diffusion controlled and the process followed chemisorption (pseudo-second order models). It is recommended that bamboo biochar can be replaced activated carbon for adsorption of heavy metals in ground water and the mixed heavy metal should be further study.

Acknowledgements:

This project is funded by National Research Council of Thailand.

References:

1. Sanjay K. Sharma. Heavy Metals In Water: Presence. Removal and Safety. 2014;1-25.
2. Crini G, Lichtfouse E, Wilson L, Morin-Crini N. Adsorption-oriented processes using conventional and non-conventional adsorbents for wastewater treatment. Green Adsorbents for Pollutant Removal. Springer Nature. 2018;18:23-71.
3. Kalaruban M. Loganathan P. Nguyen T.V. Nur T. Johir Md. A.H. Nguyen T.H. Trinh M.V. Vigneswaran S. Iron-impregnated granular activated carbon for arsenic removal: Application to practical column filters. Journal of Environmental Management. 2019;239:235-243.
4. Newcombe G. Hayes R. Drikas M. Granular activated carbon: importance of surface properties in the adsorption of naturally occurring organics. Colloids Surf. A. 1993;78:65-71.
5. Al-Degs Y. Khraisheh M.A.M. Allen S.J. Ahmad M.N. Effect of Carbon Surface Chemistry on the Removal of Reactive Dyes from Textile Effluent. Water Research. 2000;34:927-935.
6. Luu T.L. Remarks on the current quality of groundwater in Vietnam. Environmental Science and Pollution Research volume. 2019;26:1163–1169.
7. Menéndez J. Illán-Gómez M. Leon, C. Radovic L. On the difference between the isoelectric point and the point of zero charge of carbons. Carbon. 1995;33:1655–1657.
8. Miklas S. Chapter 9 Coagulation and flocculation. Wetland Systems to Control Urban Runoff. Elsevier Science Ltd. 2006;43-50.

A REVIEW OF EDUCATIONAL PROGRAMMES AT THE RAMA 9 MUSEUM ASSOCIATED WITH THE UNITED NATIONS' SUSTAINABLE DEVELOPMENT GOALS (SDGS)

Napat Malathum, Siraprapah Srisupan, Jittikan Intamong
National Science Museum, Thailand
*e-mail: napat.m@nsm.or.th

Abstract:

The Rama 9 Museum, which first opened in December 2019, is one of the museums under the operation of the National Science Museum of Thailand. It is an ecological museum that aims to raise citizens' awareness of environmental issues and encourage them to take action. Aside from its spacious, immersive exhibitions, it also hosts numerous educational programmes that enhance visitors' learning experiences, ranging from self-guided booklets and pop-up demonstrations to lab experiments and special events. This abstract reviews the number of programmes that directly connect to the United Nations' Sustainable Development Goals (SDGs) at the museum because they align with our mission to raise environmental awareness.

We compiled a list of every educational programme at the Rama 9 Museum, then identified if they had associations with any of the SDGs. If they did, we further connected them to the specific Goals they met. Of the total 67 programmes, 34 of them could be associated with SDGs; some of them had connections with more than one SDG. Out of the 17 SDGs, the 34 programmes had links to eight of them, as shown in Figure 1 below. Most programmes (n = 18) were about biodiversity and conservation of terrestrial wildlife and habitats, which relates to Goal 15: Life on Land. The second-most most common was Goal 6: Clean Water and Sanitation (n = 6), followed by Goal 14: Life Below Water (n = 5).

One surprising result was that there was only one educational programme for Goal 13: Climate Action, considering that the climate crisis is one of the world's most significant environmental issues. However, this is not for lack of coverage within the contents of the education programmes or exhibitions; climate change is integrated and referred to within them. Nevertheless, this finding may lead to developing future programmes that are explicitly about climate change and action.

As educators at the Rama 9 Museum, we will use this study's findings to continue developing educational programmes that are in line with the SDGs to serve our visitors.

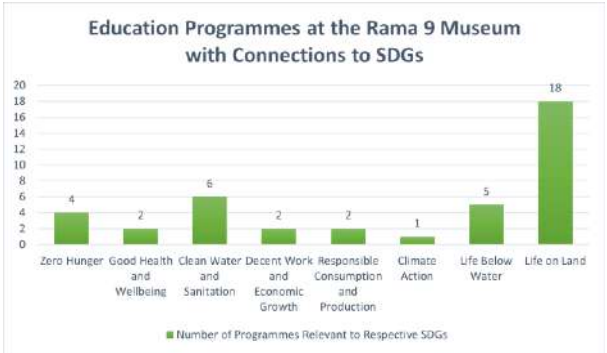

Figure 1. This bar chart shows the number of education programmes offered at the Rama 9 Museum that have direct connections to the SDGs.

A SIMPLE PIEZOELECTRIC CALIBRATION METHOD OF THE LOW-COST OPTICAL INTERFEROMETRY KIT FOR UNDERGRADUATE TEACHING LABORATORY

Tanyalak Nuntakulkaisak, Yingyot Infahsaeng,Ruchipas Bavontaweepanya and Ekkarat Pongophas*

Division of Physics, Faculty of Science and Technology, Thammasat University, Pathum Thani 12120 Thailand

***E-mail:** e_pongophas@staff.tu.ac.th

Abstract:

An optical interferometer is a classic apparatus for demonstrating the wave nature of light to science students. However, a very precise mechanical part in the interferometer is essentially required for the mirror moving at the nanometer scale. Typically, a piezoelectric actuator is used as the oscillating part which is needed to be precisely calibrated. The calibration method makes the interferometer kit unaffordable for a general university. Thus, development of low-cost calibrated actuator is considerably attractive. In this paper, the low-cost actuator is developed by adapting a piezoelectric loudspeaker which is inexpensive and easy to find.We present a simple method for the piezoelectric loudspeaker calibration by installing it in a Michelson interferometer set-up and measuring the intensity of the interference fringe after the voltage adjustment to the loudspeaker. We found that the piezoelectric loudspeaker has a nonlinear response, and this nonlinear correction must be considered to calibrate the actuator. In addition, the calibrated response equation can be linearized for the simplicity in the range of driving voltage from 0-20 V.

Introduction:

Optical interferometry is a well-known investigative tool that extensively used in many fields of science and engineering. Interferometers come in a variety of shapes and sizes due to their vast range of applications such as surface metrology, and gravitational waves detection[1]. An interference pattern can be constructed by superposing two or more sources of light. Such pattern consists of constructive and destructive fringes, which can be monitored and studied. In general, the interference fringes provide the information about the small displacement or phase shift, with wavefront shapes to one half of the light source wavelength. By this method, interferometers are then the high precision measuring technique. Among those interferometers, the famous techniques applied to different research areas are the Michelson interferometer, the Mach-Zehnder interferometer and the Sagnac interferometer. All of them are rather laborious in optics set-up for undergraduate and high school level. Moreover, the professional interferometers apparatus is rarely to access due to the cost of each apparatus, even for university laboratory. This is due to the requirement of very high precise mechanical actuator and control to oscillate one of mirrors in the interferometer. In addition, the precisely calibration method is crucially expected, which increase the cost of the interferometer kit due to their additional calibration apparatus.

Therefore, a low-cost and high-precise mechanical actuator with simple calibration method for the educational university is very important. Recently, the low-cost Michelson interferometer was introduced by using an inexpensive apparatus such as a thick transparent acrylic plate, an acrylic base, and the diaphragm of a loudspeaker for moving the mirror[2]. The correlation between the number of fringes shifted and the voltage applied to the speaker was used as the calibration

method. To obtain a very high sensitivity of interferometry, one must use a high precise piezoelectric stack transducer with high cost[3]. Thus, an inexpensive piezoelectric loudspeaker with cost of about 40 THB is introduced in this research, It can be used as a moderate precise actuator in an interferometer. Interestingly, a small stretch in the range of nanometer can be generated from the piezoelectric loudspeaker when the reverse bias is applied, and the metal diaphragm is fixed to a static base. Therefore, we choose the piezoelectric loudspeaker as a candidate for moving a mirror in an interferometer. In fact, the piezoelectric devices represent many applications that involve the production and detection of sound, generation of high voltages, electronic frequency generation,and microbalances. It is also the basis of several scientific instrumental techniques with atomic resolution, such as scanning probe microscope. However, the simple and precise calibration method of the piezoelectric loudspeaker is a challenging task for the interferometer. Many works have been proposed on these solutions[4-8].

However, those methods encounter numerous complicated procedures. The purpose of the present work is the simple and precise calibration method of the piezoelectric loudspeaker with the straightforward process, compact geometry, and nanometric accuracy. In particular, the piezoelectric loudspeaker is glued between a mirror and the mechanical mirror mount in one arm of a Michelson interferometer. The driving voltage is applied to the piezoelectric loudspeaker which cause the stretche and consequently, the shift of phase in the interferometer. The change in interference fringes is detected by a photodetector. Consequently, the data are analyzed to find the voltage dependent stretch curve, which is used as the calibration curve.

Material and Method:

The piezoelectric loudspeaker is a loudspeaker that uses the piezoelectric effect to generate sound. It is known by quite a few names, piezo, buzzer and crystal loudspeaker internal mechanical. This strain typically is converted into audible sound by a metal diaphragm or resonator that is attached to it. Piezoelectric loudspeakers are relatively easy to use compared to other types of loudspeakers The loudspeakers were controlled by directly applying a voltage signal from a signal generator. Furthermore, piezoelectric loudspeakers can operate well in a wide range frequency from 1 kHz up to 100 kHz.

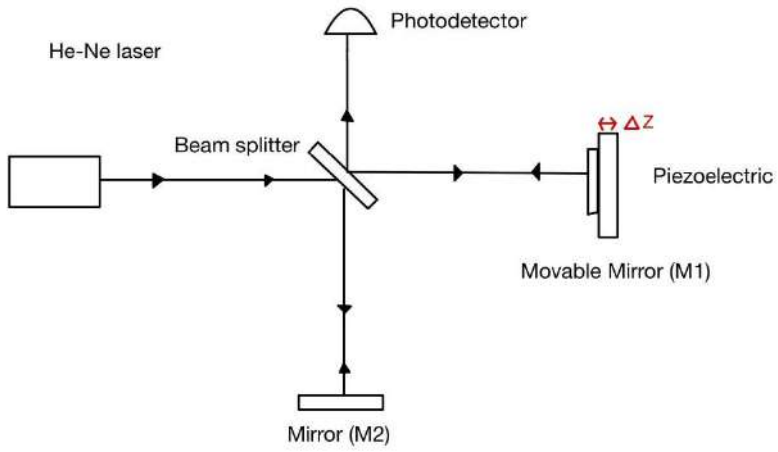

Figure 1. schematic diagram of Michelson interferometer

Figure 1. shows a diagram of a Michelson interferometer. The He-Ne laser with wavelength of 632.8 nm is used as a light source. The laser incident the beam splitter, which reflects and transmits 50:50 of the incident light. The incident beam is therefore split into two beams; first beam propagates toward the movable mirror M1, the other is reflected toward the fixed mirror M2. Both mirrors reflect light back toward the beam splitter. Half the light from M1 is reflected from the beam-splitter to the photodetector and the other half the light from M2 is transmitted through the beam-splitter to the photodetector. The piezoelectric loudspeaker is attached to the back the movable mirror M1 and the driving voltage from the high voltage source is varied. The varying voltages change the optical path difference of the laser which as a response the interference intensity is also changed. This intensity is then measured by the photodetector. The photodetector is an optical transducer that transform the intensity of light into the voltage measured at the output port of it. Thus, the output voltage of the photodetector, V_D at the output port of Michelson interferometer will be in the form of

$$V_D = V_0[1 + \cos(2k\Delta z)] \quad (1)$$

where $k=2\pi/\lambda$ is the wavenumber of light, V_0 is a constant relating to the initial light intensity and Δz is the stretch of piezoelectric. If the initial position of the moving mirror M1 is set to be the same distance of the fixed mirror M2 to the beam splitter. In this situation, the stretch of the piezoelectric loudspeaker is then the optical path difference of the Michelson interferometer. This situation can be used to measure the stretch of the piezoelectric loudspeaker. For example, if we focus only on the maximum voltage points, the stretch (Δz) in this case can be expressed as

$$\Delta z = m\left(\frac{\lambda}{2}\right) \quad (2)$$

where λ is the wavelength of the He-Ne laser and m=0,1,2,… This is the method to measure the stretch of the piezoelectric loudspeaker by exploiting the wavelength of laser. For more general, we can use every point of data to calibrate the stretch response of the piezoelectric loudspeaker by curve fitting using Eq.(1) with model that the stretch response of the piezoelectric loudspeaker (Δz) is a function of driving voltage (Vp) in the form of

$$\Delta z = aV_P + bV_p^2 \quad (3)$$

where a and b are the linear-proportional constant and nonlinear-proportional constant, respectively. These two constants are the important constants that we would like to find. The model that the stretch response of the piezoelectric loudspeaker be a nonlinear function of driving voltage is a proper model because the piezoelectric material must reach the maximum stretch at some value of the driving voltage. Moreover, the voltage-dependent stretch curves of piezoelectric actuators are subject to hysteresis due to the extrinsic domain contributions[9]

Results and Discussion:

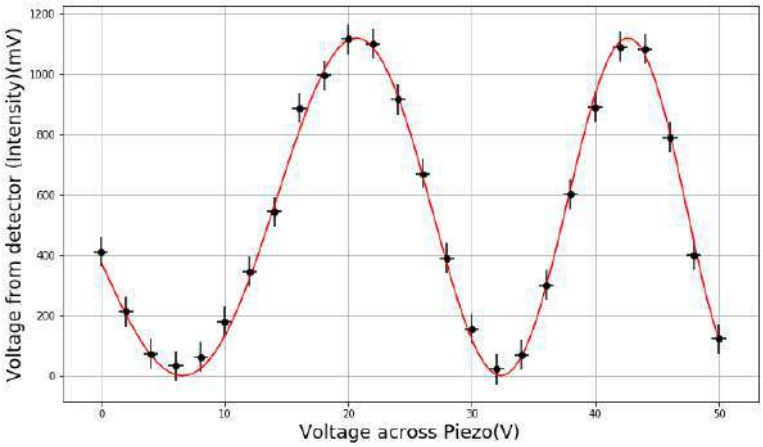

Figure 2. The graph of the driving voltage across piezoelectric loudspeaker and versus the voltage from photodetector

Figure 2 shows the measurement result of the driving voltage across piezoelectric loudspeaker and the voltage from photodetector. The uncertainty of the photodetector voltage is the uncertainty of the voltmeter used to measure the photodetector signal which is about ± 50 mV and the uncertainty of the voltage across the piezoelectric loudspeaker is the uncertainty of the high-voltage power supply use to drive it which is in the rang of ± 0.59 mV.The experimental result clearly shows nonlinear voltage-dependent of the stretch that can be seen from the chirping of the graph. By curve fitting with Python programming, we obtain the constants a = 8.908 nm/V and b = 0.086 nm/V^2 .Thus, the equation used to calibrate the piezoelectric speaker is

$$\Delta z = 8.908V_P + 0.086V_p^2 \quad (4)$$

With this equation, our DIY actuator can be controlled the stretch. For more simplicity, the Eq.(4) can be linearized by the equation $\Delta z = 11V_P - 10$. From Figure 3 it is obvious that this linear equation is fit in the calibrated voltage-dependent stretch curve the voltage range from 0 to 20 V which correspondent to a piezoelectric extension of 0 to 250 nm. After this calibration method, this simple actuator can be used in teaching the interferometry for undergraduate students.

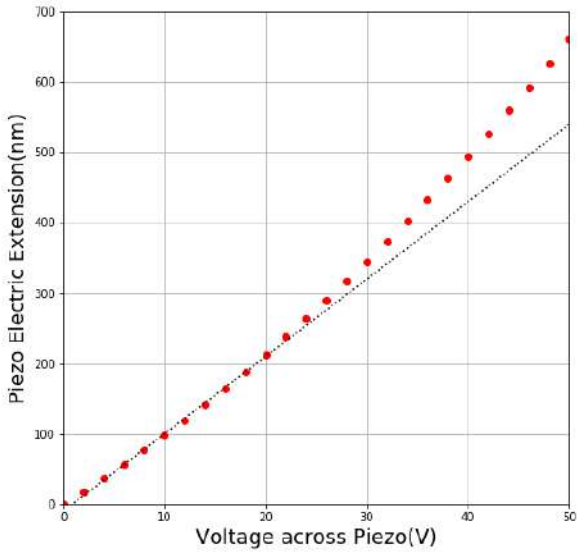

Figure 3. The plot of the calibrated voltage-dependent stretch curve from the equation $\Delta z = 8.908V_P + 0.086V_p^2$ (red dot) and the plot of linearized equation $\Delta z = 11V_P - 10$ (dash line)

Conclusion:

We developed the low-cost actuator by using a piezoelectric loudspeaker and calibrated it using Michelson interferometer. The calibration of a piezoelectric loudspeaker was successfully done by curve fitting the voltage dependent stretch data. Thus the calibrated curve is followed the equation $\Delta z=8.908V_P+0.086V_p^2$. However, the calibrated response equation can be linearized for the simplicity in the range of 0 - 20V by using equation $\Delta z=11V_P-10$.

Acknowledgements

This research was supported by the Program Management Unit for Human Resources & Institutional Development, Research and Innovation [grant number B05F630108]

Reference

1. Bizouard, M.-A., & Papa, M. A. Searching for gravitational waves with the LIGO and Virgo interferometers. Comptes Rendus Physique 2013;14(4);352–365.
2. Pathare, S., & Kurmude, V. Low cost Michelson–Morley interferometer. Physics Education 2016;51(6);063001.
3. Libbrecht, K. G., & Black, E. D. A basic Michelson laser interferometer for the undergraduate teaching laboratory demonstrating picometer sensitivity. American Journal of Physics 2015; 83(5);409–417.
4. Denker R, Shilling R, Haerlin V, Lau B. Phase-stepping for interferometry for less than 1 Euro. In: Jacquot P, Fournier JM, editors. Proc Interferometry in speckle light. Lausanne: Springer 2000; pp 52-445.
5. Ochoa NA, Huntley JM. Convenient method for calibrating nonlinear phase modulators for use in phase-shifting interferometry. Opt Eng 1998;37;5-2501.

6. Bruno L, Mainieri P, Poggialini A. Design and calibration of a low-cost open-loop PZT actuator for phase-shifting speckle interferome-try. Proc SPIE 2003;pp22-317.
7. Shen Y, Huntley JM. Simple method to calibrate phase modulators for use in dynamic phase-shifting interferometry. Opt Eng 2004; 43(12);2998–3002.
8. Kang CS, Nicolaus RA, Bonsch G. Automatic self-calibration of piezo systems in phase shifting fizeau interferometers. Proc of the pacific rim conference on lasers and electro-optics, CLEO'99 1999;pp1-330.
9. Li, H., Xu, Y., Shao, M., Guo, L., & An, D. Analysis for hysteresis of piezoelectric actuator based on microscopic mechanism. IOP Conference Series: Materials Science and Engineering 2018;399;012031.

BIOGENIC SYNTHESIS OF SILVER NANOPARTICLES USING THE EXTRACT OF ENVIRONMENTALLY BENIGN PLANT MATERIAL, BASIL (*OCIMUM BASILICUM*) AND DETERMINATION OF THEIR ANTIOXIDANT, ANTIBACTERIAL AND PHOTOCATALYTIC ACTIVITIES

Abinaya Sathiskumar[1] and Mathivathani Kandiah[1*]
[1]BMS, School of Science, 591 Galle Road, Colombo 06, Sri Lanka
[*]e-mail: mathi@bms.ac.lk

Abstract:

The synthesis of noble metal nanoparticles has gained the attention of researchers due to their enhanced physiochemical and biochemical characteristics compared to the macro scale. Even though there are numerous metals existing in nature, only a few of them such as silver, gold, platinum and palladium are widely synthesized in nanoscale. Among the mentioned metallic nanoparticles, silver nanoparticles (AgNPs) have given more importance due to their unique properties and non-toxic nature which makes it ideal for various applications in biology and medicine. This study focuses on discovering an ecofriendly and cost-effective method for the synthesis of AgNPs using five varieties of Basil and to evaluate antibacterial, antioxidant and photocatalytic activities. The colour change of the solution from yellow to reddish brown indicated the formation of AgNPs. The synthesized silver nanoparticles were characterized using UV-visible spectrophotometry which showed a resonance peak between 440-480 nm. SEM images of AgNPs showed that the diameter was around 40 nm and they were spherical in shape. Antioxidant activity of AgNPs was measured using TFC, TPC, TAC and DPPH assays where AgNPs showed higher activity compared to the water extracts due to their excellent radical scavenging properties. The lower IC50 values obtained in the study also proved the higher antioxidant capacity of AgNPs. Antibacterial activity tested against *Escherichia coli* and *Staphylococcus aureus* showed no significant difference between the water extracts and AgNPs. Silver nanoparticles at 500 ppm concentration with sodium borohydride catalyst showed greater potential in degrading Methyl orange dye molecules within 15 minutes. Therefore, the results obtained in this study indicated that AgNPs synthesized using *Ocimum basilicum* can be used as a therapeutic agent against antibiotic resistant pathogens, can treat cellular damages caused by free radicals and used for the degradation of toxic dye molecules to create pollution free environment.

CONTRIBUTIONS OF A WEED: MICROWAVE ASSISTED GREEN SYNTHESIS OF SILVER NANOPARTICLES USING MORNING GLORY (*IPOMOEA* SPP.) FOR THE ASSESSMENT OF ITS ANTIOXIDANT, ANTIBACTERIAL AND PHOTOCATALYTIC ACTIVITY.

Ramlah Mohamed Kamal[1] and Mathivathani Kandiah[1]*
[1]BMS School of Science, 591 Galle Road, Colombo 06, Sri Lanka
*email: mathi@bms.ac.lk

Abstract:
The *Ipomoea* spp. is a common weed that has untapped potential for the scientifically significant green synthesis of economical and environmentally friendly silver nanoparticles (AgNPs). AgNPs have multiple benefits in fields including medical treatment and environmental clean-up. In this study, eco-friendly water-based extraction was carried out on the leaves of 5 different *Ipomoea* spp. The synthesis of AgNPs was attempted using the extracts and *Ipomoea lacunosa* (S3) AgNPs were successfully generated through microwave-assisted synthesis. The formation of AgNPs caused the solution to deepen in colour and resulted in a peak of 420nm under UV-Vis spectroscopy. This peak corresponded to the surface plasmon resonance peak of AgNPs. The S3AgNPs, characterized by Scanning Electron Microscopy, were spherical and of 60nm in diameter. Furthermore, the antioxidant, antibacterial and photocatalytic activity of the S3AgNPs were compared against *I. aquatica, I. cairica, I. pes-caprae and I. purpurea* water extracts. The S3AgNPs showed elevated activity as opposed to the water extracts in the Total Flavonoid Content, Total Phenolic Content, Total Antioxidant Content and DPPH assays. It had an IC_{50} of 20.3% in the DPPH assay. The S3AgNPs demonstrated potent antibacterial activity against the Gram-negative *Escherichia coli* and the Gram-positive *Staphylococcus aureus* than the water extracts. A higher zone of inhibition was observed for the *S. aureus* compared to *E. coli*. In the presence of sodium borohydride, 100ppm of S3AgNPs degraded 94% of Methylene blue dye in 240 minutes. The implications of this research are widespread and can be used to develop novel antibiotics, antioxidants and water treatment compounds.

EXPERIMENTAL INVESTIGATION ON SOLAR CHIMNEY STACK FOR NATURAL VENTILATION

Waraporn Rattanongphisat*,[1] and Sakawrat Kumphon[2]
[1]Energy Technologies Building Laboratory, Department of Physics, Faculty of Science, Naresuan University, Phitsanulok, Thailand
[2] Graduated, Department of Physics, Naresuan University, Phitsanulok, Thailand
*e-mail: waraporn r@nu.ac.th

Abstract:
A solar chimney is used to provide natural ventilation for a building in certain climate. It operates based on solar energy and environmental parameters such as ambient temperature and humidity and wind flow. According to a buoyancy effect, the flow of air is created, due to the temperature difference caused variation of air density, and moves vertically along the height of chimney. Thus, it could induce outdoor air to indoor as well as withdraw indoor air to release outside. Prior study strongly suggested that square solar chimney could be used to create air flow under our hot and humid climate country. The current study aims to investigate solar chimney characteristics experimentally for practical use of natural ventilation in building application. Two identically simulated flat-roofed building were constructed by light weight wall and well insulated. One was performed as a base case while another has solar chimney stack and opening at the front. The demonstrated building dimension is 2 m width, 2.5 m length and 2 m height. The square steel solar chimney has the dimension of 0.4 m width, 0.4 m length and 1.5 m height. Three variations of opening, ambient air could enter to building space via this opening, were 0 m^2, 0.02 m^2, 0.04 m^2. It was found that the building with solar chimney stack has highest outlet air velocity of 0.43 m/s with 0.04 m^2 opening area and provide 3 ^oC indoor temperature reduction. Then followed by the condition of 0.02 m^2 opening area that reduces indoor temperature by 1.5 ^oC with air velocity of 0.34 m/s. The lowest performance found at 0 m^2 opening area. In addition, the solar radiation has influenced the performance of the chimney. It has shown that the higher solar radiation achieved the greater temperature difference and higher air velocity.

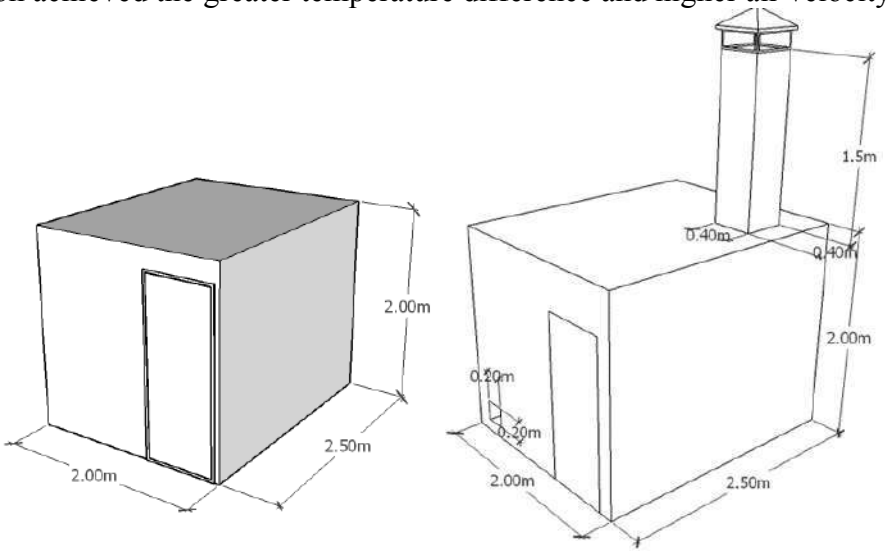

Figure 1. Dimension of base case building (left) and building with solar chimney stack (right)

N-DOPED REDUCED GRAPHENE OXIDE/GRAPHENE NANOPLATELET (RGO/GNP) AEROGEL -PREPARATION AND CHARACTERIZATION

Alvin Lim Teik Zheng,[1] Supakorn Boonyuen,[2,3*] Yoshito Andou[1,3]

[1] Department of Life Science and Systems Engineering, Graduate School of Life Science and Systems Engineering, Kyushu Institute of Technology, Fukuoka 808-0196, Japan.
[2] Department of Chemistry, Faculty of Science and Technology, Thammasat University, Pathumthani 12120, Thailand
[3] Collaborative Research Centre for Green Materials on Environmental Technology, Kyushu Institute of Technology, Fukuoka 808-0196, Japan
*e-mail: chemistrytu@gmail.com

Abstract:
In this study, hybrid N-doped reduced graphene oxide/graphene nanoplatelet hydrogel was prepared using the solvothermal method and freeze-drying technique by varying the ratio of GNP at various amounts (20 – 80 mg). Dimethylformamide (DMF) was selected for the nitrogen source and reducing agent during the thermal process to drive the self-assembly of the hybrid hydrogel. The effect of the GNP amount on the physicochemical properties of the hybrid hydrogel is reported and discussed in terms of their chemical, optical, electrical, morphology and textural properties. The physicochemical characterizations of the hybrid aerogel were carried out using FT-IR, XPS, XRD, Raman, BET and UV-Vis. The study indicated that the amount of GNP plays a significant role in altering the properties of the hybrid hydrogel.

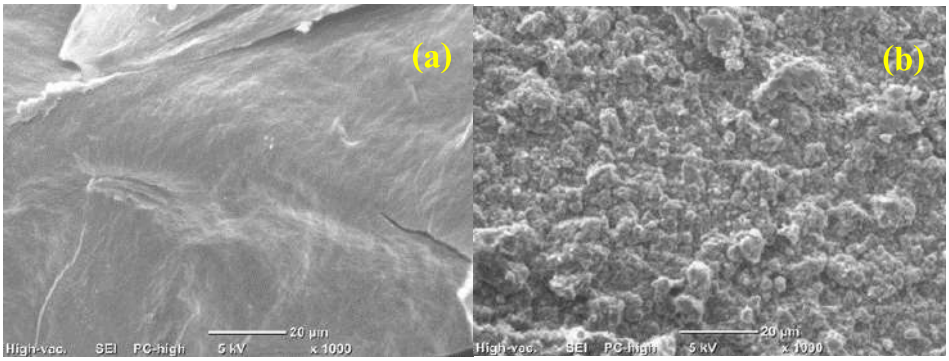

Figure 1. SEM images of (b) 0-GNP/rGH and (b) 40-GNP/rGH

PHYTOFABRICATION OF SILVER NANOPARTICLES (AgNPs) WITH PHARMACEUTICAL CAPABILITiES BY USING *Oroxylum indicum (L.) Kurz* BARK EXTRACT

Supakorn Boonyuen,[1*]Premjit Arpornmaeklong,[2] Supawan Tantayanon,[3] Rasitvich Panichvatana,[4] Karn Hassadang,[5] Suwattana Donkhunthod,[6]
[1]Department of Chemistry, Faculty of Science and Technology, Thammasat University, Pathum Thani 12120, Thailand
[2]Faculty of dentistry, Thammasat University, Pathum Thani 12120, Thailand
[3]Department of Chemistry, Green chemistry Research Laboratory, Chulalongkorn University, Bangkok 10330, Thailand
[4,5,6]SCIUS TU, Faculty of Science and Technology, Thammasat University, Pathum Thani 12120, Thailand
*e-mail:
chemistrytu@gmail.com

Abstract:
The current study was focused on the investigation of antibacterial of *Oroxylum indicum (L.) Kurz* bark extract embedded silver nanoparticles (*Oi*-AgNPs), which participate in nanoformulation synthesis. The synthesis process involved the addition of $AgNO_3$solution (1 mM) and color changes of the extract from light brown to dark, confirmed the formation of silver nanoparticles. Further, the characterization of synthesized *Oi*-AgNPs were done using different spectroscopical and microscopical techniques. FTIR spectra of So-AgNPs indicated vibrational peaks of polyphenolic hydroxyl groups, which are responsible for the stabilization of nanoformulation. Others microscopy methods such as TEM, XRD, and EDX. The results showed that the produced *Oi*-AgNPs were crystalline in nature and spherical in shape with an average size of 21.49 ± 0.32 nm, and indicated a localized surface plasmon resonance (LSPR) peak at around 420 nm. The zeta potential value of −39.1 mV pointed that the AgNPs were stable. The *Oi*- AgNPs showed a higher antioxidant activity as compared with the Oi-crude extract. They also exhibited significant antibacterial activity against both Gram-positive (*Staphylococcus aureus*) and Gram-negative (*Escherichia coli*) bacteria. The resulting phytofabricated *Oi*-AgNPs could be used as a promising antioxidant, antibacterial agent in the treatments of many medical complications.

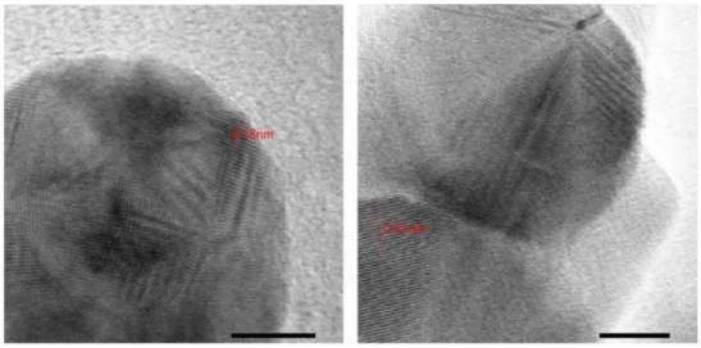

Figure 1.
HR-TEM image (x1,200,000) of *Oi*-Ag-NPs and it's structural lattice.

SILVER NANOPARTICLES: A SOLUTION FOR DEGRADING AZO DYES

Mathivathani Kandiah[1*], Dinithi Neelawala[1] and Supakorn Boonyuen[2]
[1]BMS, School of Science, 591 Galle Road, Colombo 06, Sri Lanka
[2]Department of Chemistry, Faculty of Science and Technology, Thammasat University Rangsit campus, Pathum Thani, 12120 Thailand
*e-mail: mathi@bms.ac.lk

Abstract:

Silver nanoparticles have gained high acceptability in recent decades as a result of their diverse applications in new electronic, medicinal, optical, magnetic fields and for their exclusionary, mechanical, physical and chemical properties. This study concentrates on using a cost-effective and ecofriendly bio-synthesis of silver nanoparticles from 5 varieties of Hibiscus flower water extracts and assessing their antioxidant, antibacterial and photocatalytic properties. The green synthesized Ag nanoparticles were characterized using an Ultraviolet- Visible Spectral Analysis followed by characterization *via* Scanning electron microscopy. The antioxidant properties of AgNPs were assessed by Total Phenolic Content (TPC), Total Flavonoid Content (TFC), Total Antioxidant Content (TAC), DPPH radical scavenging assay and Ferric Reducing Antioxidant Capacity (FRAP). AgNPs show higher antioxidant properties than water extracts. Additionally, phytochemical tests were carriedc out for all 5 *Hibiscus* samples. The photo-catalytic activity was assessed for 300ppm and 5000ppm concentrated AgNPs using the Methylene blue dye. The antibacterial properties were assessed against *Escherichia coli* and *Staphylococcus aureus.* AgNPs showed higher Total Phenolic Content (TPC), Total Flavonoid Content (TFC), Total Antioxidant Content (TAC), DPPH radical scavenging assay and Ferric reducing antioxidant power. 5000 ppm and 300 ppm could degrade MB in 60 and 2 hours respectively. Antibacterial studies indicated the nanoparticles of the samples were more effective against *Escherichia coli* and *Staphylococcus aureus.* Based on the overall results, it can be concluded, the green synthetic NPs can be widely utilized in Biotechnological and biomedical applications whereas to cure diseases caused due to free radicals and pathogenic microorganisms.

THE INTEGRATION OF GREEN CHEMISTRY AND SMALL SCALE FOR BASIC REDOX REACTIONS

Supakorn Boonyuen,[1*] Supawan Tantayanon,[2] Mathi Kandiah[3]
[1]Department of Chemistry, Faculty of Science and Technology, Thammasat University, Pathum Thani 12120, Thailand
[2]Department of Chemistry, Green chemistry Research Laboratory, Chulalongkorn University, Bangkok 10330, Thailand
[3]School of Science, BMS 591, Galle Road, Colombo 06, Sri Lanka
*e-mail: chemistrytu@gmail.com

Abstract:
Redox reactions are considered one of the most difficult chemistry subjects to teach and learn. However, this is an important content that permeates several topics and includes many everyday life-related phenomena. To understand the teaching and learning difficulties of the 'redox reactions' topic, a systematic literature review should conducted in the parallel with experiments. The article is focusing on the green chemistry and safety by using small scale chemistry idea for the students to practice at home during COVID-19 pandemic. The electrons transfer, galvanic and electrolytic experiments are combined with in 1 hr. Firstly the electrons transfer of each metals including, copper Cu, tin Sn, Zinc Zn and magnesium Mg with only a single drop of acid and their metal ion solution were practiced, the results are clearly shown the relationship of their metal reactivity in the metal displacement reactions. The galvanic cell was conducted by using ammonium nitrate soaked paper acting as a salt bridge, while each metal and their metal ion solution was put at each end of the soaked paper, finally the voltmeter was reading the voltage between two metals. The electrolysis of water was studied by using the modified simple equipment (from doing science company), which required only 6 ml solution and clearly yielded the 2:1 ratio of hydrogen gas: oxygen gas. The further electrolysis of 2 drops copper(II)sulfate can be studied by using the same tools. All these experiments required only small amount of reagents and the metal can be reused. Current study points to the real practice the small scale redox chemistry at home, with safe and less waste.

Figure 1.
Small scale experiments of electrons transfer, galvanic cell and electrolysis.

PRE-GELATINIZED COLORED SWEET POTATOES: AN APPROACH FOR ENHANCING EXTRACTABLE POLYPHENOLS AND ANTIOXIDANT POTENTIAL

Naraporn Phomkaivon,[1] Lina Yonekura,[2,*] Vipa Surojanametakul,[3] Prajongwate Satmalee,[3] Hirotoshi Tamura[2,*]

[1] The United Graduate School of Agricultural Sciences, Ehime University, Tarumi, Matsuyama 790-8556, Japan

[2] Graduate School of Agriculture, Kagawa University, Miki-cho, Kagawa 761-0795, Japan

[3] Institute of Food Research and Product Development, Kasetsart University, Bangkok 10900, Thailand

*e-mail: tamura.hirotoshi@kagawa-u.ac.jp/yonekura.lina@kagawa-u.ac.jp

Abstract:

The effect of pre-gelatinization of colored sweet potato powders on extractable polyphenols and antioxidant activity was investigated. Pre-gelatinized double drum-dried powders prepared with Torperk and Purple, purple-fleshed cultivars, were superior to the conventional hot air-dried powder in terms of total phenolic content and total anthocyanin content. Formation of TBA reactive substances (4.4 nM MDA/mg linoleic acid) and DPPH free radical (SC_{50} 72.1 µg/mL) were significantly lower in Torperk cultivars after pre-gelatinization. In consequence, pre-gelatinized powders of individual sweet potato cultivars showed higher extractable polyphenol content, including anthocyanins, and greater antioxidant activity than conventional powders, probably due to the destruction of cell matrix during the pre-gelatinization process. Moreover, the antioxidant activity (TBA value) of pre-gelatinized Torperk was statistically correlated to concentration of chlorogenic acid (peak **1**) ($r = 0.93$ with $p < 0.05$) and an acylated anthocyanin (peak **3**) ($r = 0.98$ with $p < 0.01$).

Introduction:

Colored sweet potatoes contain a different profile of phytochemicals and pigments depending on flesh color. Compared with white-fleshed potatoes, the colored sweet potatoes such as yellow, orange, and purple contain higher amounts of phenolic compounds and other phytochemicals[1,2]. The phytochemicals found in sweet potatoes, such as carotenoids (in orange-fleshed varieties), anthocyanins (in purple-fleshed varieties), as well as phenolic compounds exhibit strong antioxidant activity, anti-inflammatory, anticancer, antidiabetic, and anti-obesity effects [3,4,5]. Purple fleshed sweet potatoes feature a distinctive profile of anthocyanins, including 3,5-diglucoside derivatives of cyanidin or peonidin, acylated with *p*-hydroxybenzoic acid, ferulic acid, or caffeic acid[6,7]. Whereas the main phenolic compounds are caffeoylquinic acid (CQA) derivatives such as chlorogenic acid, 3,5-, 3,4-, and 4,5-diCQA[1]. The biological activity of sweet potatoes depends on the profile and concentration of phytochemicals, emphasizing the need to investigate these features in a range of sweet potato cultivars.

The high content of phytochemicals in colored sweet potato tubers makes it a nutritionally important foodstuff, with high potential as an ingredient of processed foods. As a strategy for value-added processing, pre-gelatinization combined with double drum-drying is expected to improve flour versatility by eliminating the need of pre-cooking and extending shelf-life. Therefore, pre-gelatinized powders can be applicable for improving the texture of dough, noodles, and instant products[8,9]. Drum-drying for making pre-gelatinized powder is

very suitable for drying high-viscosity materials, where drying is achieved by processing for short time at high temperatures. However, there is limited information on the effects induced by pre-gelatinization on phytochemicals and biological activity of processed sweet potatoes.

To evaluate the function of pre-gelatinized sweet potatoes, we report the advantages of pre-gelatinized powders against conventional hot air-dried ones in terms of total phenolics, total anthocyanins and antioxidant activity. In addition, the compounds related to the biological activities were statistically determined using Pearson's correlation coefficients.

Methodology:

Materials

Four cultivars of Thai sweet potatoes, Khai, Orange, Torperk, and Purple harvested in some Thai provinces, were purchased from a local market in Bangkok in 2018. Khai potatoes were from Ayutthaya province, and Orange, Torperk, and Purple were from Pathumthani province. The Japanese sweet potato, Naruto Kintoki, was obtained in 2018 from a supermarket in Miki-cho (Kagawa prefecture, Japan).

Preparation of conventional (hot air-dried) sweet potato powder

Five sweet potato fleshes (ca. 20 kg) were sliced into 2 mm thickness and dried in a hot air oven (Memmert GmbH + Co. KG, Schwabach, Germany) at 60°C for 18 h (moisture content < 10%). The dried slices (7 kg) were individually ground and kept under 4°C.

Preparation of pre-gelatinized sweet potato powder

Five sweet potato fleshes (ca. 20 kg) were cut into chunks, mixed with water (20 L), and then boiled at 100°C for 30 min. After that, the boiled sweet potatoes were homogenized into a paste, and dried at 110°C in a double-drum dryer (350 mm diameter drums, 1 mm gap between drums; Escher Wyss GmbH, Ravensburg, Germany) for 1 min at 4 rpm. The dried flakes (7.5 kg) were individually collected, ground, and kept under 4°C.

Light microscope observation of starch granules

The sweet potato powders (0.4 g) were suspended in 10 mL of 50% glycerol containing water. The suspension was spread on glass slides, and the size and shape of the granules was observed by light microscopy (200×, Nikon Diaphot TMD microscope; Nikon Co. Ltd., Tokyo, Japan).

Extraction of phytochemicals using the QuEChERS method

The quick, easy, cheap, effective, rugged, and safe (QuEChERS) method, which is a commonly used extraction method for agrochemicals, was applied to extract the phytochemicals in the sweet potatoes according to the method reported by Sato *et al*[10]. The five sweet potato powders (10 g) were individually placed in 250 mL centrifuge tubes (250PP; Hitachi Koki Co. Ltd., Tokyo, Japan). Water and acetonitrile (30 mL each) were added and then mixed well. Sodium chloride (3 g), trisodium citrate dihydrate (3 g), disodium hydrogen citrate sesquihydrate (1.5 g), and anhydrous magnesium sulfate (12 g) were added to each tube. After shaking by hand for 1 min, the tubes were centrifuged at 1,409 × g for 5 min (Hitachi Himac CR21N; Hitachi Koki Co. Ltd., Tokyo, Japan). The supernatants were collected and evaporated to dryness at 35°C under reduced pressure. The crude extracts were kept at −20°C until further analysis.

Total phenolic content

The total phenolic content (TPC) was measured using Folin-Ciocalteu's colorimetric assay[11] with minor modifications. Each crude extract was adjusted to a concentration of

2 mg/mL with 80% ethanol. Absorbance was measured at 760 nm. TPC was calculated using a calibration curve of gallic acid (0–50 μg/mL) and expressed as milligram gallic acid equivalent per g sample dry weight basis (mg GAE/g DW).

Total anthocyanin content

The total anthocyanin content (TAC) was determined using the pH differential method[12]. Each crude extract was adjusted to a concentration of 20 mg/mL. TAC which is expressed as milligram of cyanidin 3-glucoside per g sample dry weight basis (mg cy 3-glu/g DW) was calculated using equation (1):

$$TAC = (A \times MW \times DF \times 1000/\varepsilon)/L \quad (1)$$

where $A = (A_{520} - A_{700})_{pH1.0} - (A_{520} - A_{700})_{pH4.5}$, MW = molecular weight of cyanidin-3-glucoside (449.2), DF = dilution factor, and ε = molar absorptivity of cyanidin-3-glucoside (26,900) and L = pathlength in cm.

Free radical scavenging activity

The free radical scavenging activity**,** using 2,2-diphenyl-2-picrylhydrazyl (DPPH) was determined by following the method reported by Zhu *et al*.[13] Each crude extract was adjusted to 2 mg/mL concentration. The DPPH absorbance was recorded at 517 nm. The free radical scavenging activity (%) was expressed using equation (2):

$$\text{Free radical scavenging activity (\%)} = (A_{control} - A_{sample})/A_{control} \times 100 \quad (2)$$

The SC_{50} values (concentrations of dry extract that causes 50% scavenging of DPPH radical) determined by interpolation from five different concentrations (0.02–2 mg/mL) of samples were determined by GraphPad PRISM 5 (GraphPad Software Inc., La Jolla, CA, USA).

Lipid peroxidation inhibition determined by TBA assay

The lipid peroxidation inhibitory activity of the extracts (20 mg/mL) was evaluated by suppressing malondialdehyde formation (TBA method) from linoleic acid according to the method reported by Tamura and Shibamoto [14]. Linoleic acid (17.8 mM) was diluted with 4.85 mL of Tris-buffer (pH 7.4, containing 0.2% SDS and 0.75 mM potassium chloride) and mixed with sample solution (0.1 mL) and ferrous sulfate (0.05 mL, 20 mM aqueous solution). The mixture was incubated for 16 h at 37°C. TBA reactive substances of the 0.2 mL reacted solution were detected at 535 nm and then quantified it using a previous report[15]. TBA was expressed as nmol of MDA per 1 mg of linoleic acid (nM MDA/mg linoleic acid).

HPLC analysis of phenolic metabolites

The phenolic metabolites in five sweet potatoes were analyzed using a JASCO HPLC system (JASCO Corp., Tokyo, Japan) equipped with double PU-980 pumps, AS-950 autosampler, CO-965 column oven, and MD2010 plus with a photodiode array detector (200–600 nm). The HPLC analyses of the metabolites were conducted using a YMC-triart C18 column (250 × 4.6 mm, 5 μm; YMC Co. Ltd., Kyoto, Japan) with a gradient elution between solvent A (10% acetonitrile containing 0.1% TFA) and solvent B (acetonitrile containing 0.1% TFA) under a minor modification[7]. The gradient elution was programed from 2% B to 20% B (0–20 min), and then 20% B to 70% B (20–40 min). The column flow rate was set at 1.0 mL/min and the oven was kept at 35°C during the entire analysis. Finally, chemicals were detected at 290 and 530 nm.

Statistical analysis

All analyses were done in triplicate. The analytical data were expressed as mean ± SD. The Duncan's multiple range test was calculated for multiple comparisons using IBM SPSS statistics version 25 software. Pearson's correlation coefficients between the peak areas of individual phytochemicals and antioxidant activities were determined by using IBM SPSS statistics (version 25). Significant differences were considered at $p < 0.05$ and $p < 0.01$. A heatmap was plotted using Morpheus (https://software.broadinstitute.org/morpheus).

Results and Discussion:

Observation of starch granules

The size and shape of starch granules of pre-gelatinized sweet potatoes were compared with native ones. Native granules were less than 20 μm in diameter (Figure 1a). Pre-gelatinization resulted in granule aggregation and swelling up to about 40 μm or larger, with further change to irregular shapes (Figure 1b). The granules of yellow and purple sweet potatoes were irreversibly disrupted over 85 °C[16]. Thus, the permanent destruction and loss of granules indicated typical feature of complete gelatinization of colored sweet potatoes during heating at 100 °C for 30 min.

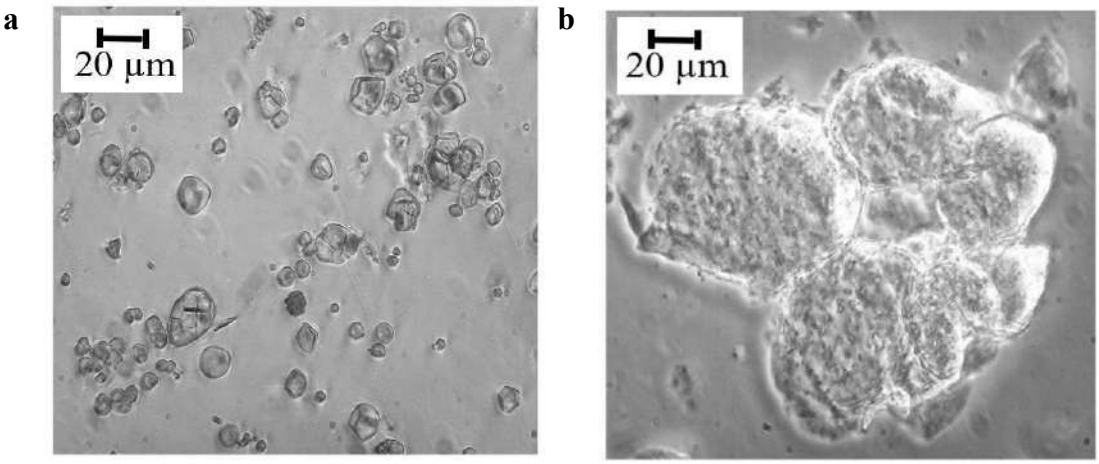

Figure 1. Native (a) and pre-gelatinized (b) sweet potato starch granules observed under a light microscope (magnification 200×).

Total phenolics, total anthocyanins and antioxidant activity

Total phenolic content (TPC) and antioxidant activities assessed by DPPH radical scavenging and TBA assays of QuEChERS extracts [13, 17] from colored sweet potato powders are presented in Table 1 and 2.

All pre-gelatinized colored sweet potato powders had higher TPC (mg GAE/g DW), compared to conventional hot air-dried ones, with approximately 7.5-fold increase in the case of Torperk and Purple powders, and 1.3-fold for Khai and Orange powders (Table1). However, pre-gelatinized and conventional dried powders prepared from Naruto Kintoki, had the lowest TPC values among all the cultivars with no significant effect on TPC (Table 1). The QuEChERS extracts of pre-gelatinized Purple and Torperk powders exhibited higher yields, phenolics and anthocyanins than those of yellow-orange fleshed sweet potatoes (Table 1). Total anthocyanin content (TAC) was detected only in pre-gelatinized Torperk (light

purple flesh, 0.484 mg cy 3-glu/g DW) and Purple (deep purple flesh, 1.609 mg cy 3-glu/g DW). The absence of anthocyanins in powders prepared with the conventional method may be linked to the enzymatic degradation of anthocyanins during hot-air drying at 60 °C[18]. Comprehensive consideration of this part may be summarized that pre-gelatinized powders give higher recoveries of polyphenols and anthocyanins by QuEChERS extraction than conventionally prepared powders.

Table 1. Total phenolics and total anthocyanins of colored sweet potatoes

Samples		**Yield**[1] (mg/g DW)	**TPC**[2] (mg GAE/g DW)	**TAC**[3] (mg cy 3-glu/g DW)
Khai	Conventional	4.9	0.429 ± 0.005bc	n.d.
	Pre-gelatinized	4.0	0.530 ± 0.004cd	n.d.
Orange	Conventional	4.4	0.348 ± 0.004b	n.d.
	Pre-gelatinized	3.8	0.455 ± 0.004bc	n.d.
Torperk	Conventional	3.4	0.631 ± 0.018cd	n.d.
	Pre-gelatinized	4.7	4.732 ± 0.004f	0.484 ± 0.061a
Purple	Conventional	5.7	0.682 ± 0.008d	n.d.
	Pre-gelatinized	7.3	4.453 ± 0.003e	1.609 ± 0.139b
Naruto Kintoki	Conventional	4.2	0.149 ± 0.001a	n.d.
	Pre-gelatinized	3.7	0.189 ± 0.001a	n.d.

[1] Yield: the value is presented in mg crude extract/g of sweet potato powder (dry weight basis)
[2]TPC: total phenolic content (mg GAE/g sweet potato powder (dry weight basis))
[3]TAC: total anthocyanin content (mg cyanidin 3-glucoside/g sweet potato powder (dry weight basis))
a-f: the mean values within the same column with different superscripts were significantly different ($p < 0.05$)
n.d.: non-detected

The DPPH SC_{50} values (concentration of dry extract that causes 50% scavenging of DPPH) were decreased in all pre-gelatinized powders, if compared to the conventional powders. Lower SC_{50} means a rise of free radical scavenging activity through pre-gelatinization (Table 2).

Torperk extract exhibited free radical scavenging activity (SC_{50} = 72.1 µg/mL) similar to that of Trolox (SC_{50} = 48.1 µg/mL). In contrast, free radical scavenging activity of pre-gelatinized Torperk (SC_{50} = 72.1 µg/mL) was 5-fold higher than that of the conventional counterpart (SC_{50} = 403.5 µg/mL) (Table 2). The lower SC_{50} value by gelatinization of Torperk may be caused by releasing of anthocyanins (and cell wall-bound phenolics). This is accordance to various reports of increased extractable polyphenols from vegetables by boiling [19,20]. In addition, pre-gelatinization could have inactivated the enzymatic degradation of phenolics and maintained the appearance of colored sweet potatoes [18].

The thiobarbituric acid (TBA) assay is based on suppression of malondialdehyde (MDA) formation by lipid peroxidation of linoleic acid. It can be used to assess the potential for oxidation states of biological membranes or cell tissue. Similarly, pre-gelatinized extracts efficiently suppressed lipid peroxidation more than conventional hot air-dried counterparts, except the Orange extract (Table 2). In addition, inhibition of lipid peroxidation of the extracts from purple-fleshed sweet potatoes (Torperk and Purple) was greater than those from the yellow-orange fleshed ones (Khai, Orange, and Naruto Kintoki). In all, Torperk showed 4.4 nM MDA/mg linoleic acid, which was close to that of the synthetic antioxidant BHT (3.9 nM MDA/mg linoleic acid). Enhancement of antioxidant activities in DPPH and TBA assays of Torperk were attributed to great amount of phenolics as well as anthocyanins.

Table 2. Total phenolics and antioxidant activities of QuEChERS extracts from colored sweet potatoes

Samples		TPC [1] (mg GAE/g extract)	SC_{50} of DPPH[2] (μg/mL)	TBA[3] (nM MDA/mg linoleic acid)
Khai	Conventional	69.5 ± 4.7c	558.9 ± 16.2g	14.5 ± 0.5f
	Pre-gelatinized	115.0 ± 15.4e	363.7 ± 27.1d	12.7 ± 0.2e
Orange	Conventional	59.2 ± 4.3b	651.9 ± 3.5i	8.2 ± 0.4c
	Pre-gelatinized	115.1 ± 11.8e	325.4 ± 13.3c	14.2 ± 0.8f
Torperk	Conventional	163.4 ± 6.1f	403.5 ± 16.1e	5.8 ± 0.5b
	Pre-gelatinized	936.2 ± 8.9h	72.1 ± 6.4a	4.4 ± 0.5a
Purple	Conventional	105.9 ± 8.6d	573.3 ± 26.6h	10.3 ± 0.2d
	Pre-gelatinized	554.8 ± 18.3g	103.2 ± 6.5b	9.7 ± 0.2d
Naruto Kintoki	Conventional	26.3 ± 6.9a	1,602.9 ± 50.8j	18.6 ± 0.9g
	Pre-gelatinized	23.8 ± 1.1a	450.4 ± 8.0f	13.9 ± 0.2f

[1]TPC: total phenolic content (mg GAE/g extract)
[2]SC_{50} of DPPH: sample concentration causes 50% scavenging of DPPH free radicals (μg/mL)
[3]TBA: the amount of MDA that occurred in linoleic acid peroxidation with sample extracts (20 mg/mL)
a-j: the mean values within the same column with different superscripts were significantly different ($p < 0.05$)

Overall, our results demonstrated a positive impact of pre-gelatinization on the releasing of phenolic compounds from plant matrix and activation of free radical scavenging activity. In plant cells, a considerable percentage of phenolic compounds is bound to the cell wall matrix, and pre-gelatinization might have facilitated the release of such compounds, as suggested by some studies[20,21]. In addition, anthocyanins are typically located within the vacuoles and the rupture of these organelles during the gelatinization process might have been responsible for the release of anthocyanins [18,22]. Paradoxically, the homogenization, drum-drying and pulverization after gelatinization implies contact with atmospheric oxygen and therefore the possibility of phytochemical degradation by oxidation, which clearly did not counteract the positive effect of polyphenol release. The gelatinization process hydrates and releases the starch from the granule, making gelatinized starch more available to form extractable complexes with polyphenols. Starch-polyphenol interactions have been reported in the literature[23], and may have played a role in stabilizing the released phenolics and keeping the high antioxidant activity during the post-gelatinization steps as well as during storage of the gelatinized powders.

Tentative assignment of metabolites in pre-gelatinized sweet potatoes

From the HPLC chromatograms, we can observe that peaks **1** to **10** were the main peaks of colored sweet potatoes (Figure 2a). Peaks **1**, **2**, **7**, **9**, and **10** detected at 290 nm were compatible to phenolic compounds, while peaks **3**, **4**, **5**, **6**, and **8** detected at 530 nm were compatible with anthocyanins. Increase of peaks **1**, **7**, **9**, and **10** were observed in all gelatinized powders, when compared with the conventional hot air-dried powders (data not shown), in agreement with the increasing of TPC in pre-gelatinized sweet potatoes. Peak **1** had same retention time and λ_{max} (327 and 295 nm) with those of authentic chlorogenic acid (Figure 2b). In addition, the UV spectra of peaks **7**, **9**, and **10** were also similar to chlorogenic acid, probably corresponding to 4,5-, 3,5-, and 3,4-dicaffeoylquinic acids (diCQAs), respectively[1,3].

In case of anthocyanins (λ = 530 nm), typical UV-VIS spectra feature, λ_{max} at 490–550, 310–340, and 260–280 nm were observed in peaks **3,4, 5, 6, 8**. The absorbance in the range 310–340 nm (λ_{acyl}) could indicate acylation of phenolic acids at the sugar moieties of anthocyanins. Major anthocyanins of Torperk and Purple were the peaks **3** and **8**, respectively. The λ_{max} at 527 nm is compatible with of anthocyanin structures such as

cyanidin and peonidin derivatives. Both peaks **3** and **8** can, therefore, be assigned as acylated cyanidin and/or peonidin due to the detection of λ_{acyl} at 331 and 327 nm (Figure 2b). The identification of peaks **3** and **8** is currently under investigation.

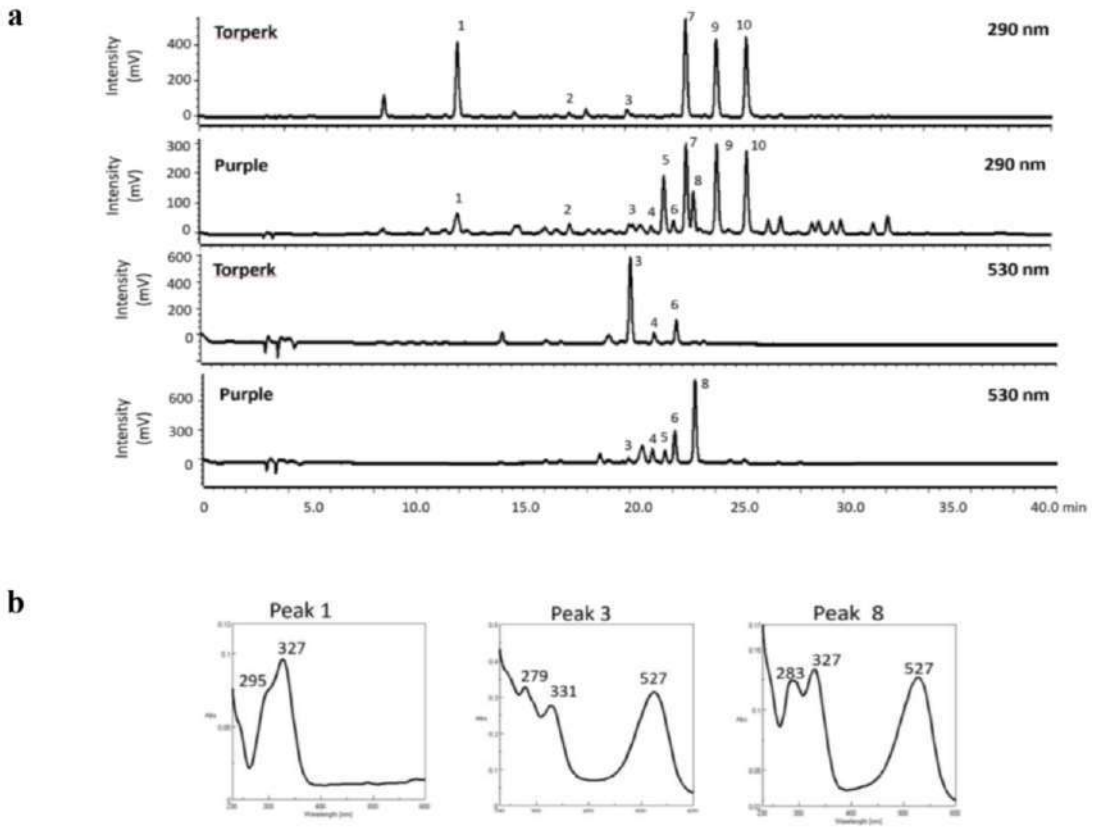

Figure 2. Metabolites of Torperk and Purple. HPLC chromatograms detected at 290 nm and 530 nm (a) and UV-VIS absorption spectra of peaks **1**, **3**, and **8** (b).

Putative antioxidant substances determined by Pearson's correlation coefficient

Pearson's correlation coefficients between the peak areas of 10 compounds and antioxidant activities (TPC, 1/DPPH, and 1/TBA) of QuEChERS extracts (data from Table 2) were applied for quick selection of the putative antioxidant substances in five sweet potatoes (Figure 3). Positive correlation with 1/TBA was observed for peak **1** (r=0.93, $p < 0.05$), whereas peak **3** showed the strongest positive correlation with 1/DPPH (r=0.92, $p < 0.05$) and 1/TBA (r=0.98, $p < 0.01$). Chlorogenic acid has been reported as a major phenolic in sweet potatoes, and contributed to great antioxidant activity, antimutagenicity, anti-HIV, and anticarcinogenic activities[3,5], while acylated anthocyanins played important roles in pH and thermal stabilities of colored intensity[18,24], as well as their biological activities including antioxidant activity, anti-inflammatory, and anticancer activity[4,14]. In this study, pre-gelatinized Torperk showed the highest antioxidant activity, which could be related to the high amount of an acylated anthocyanin (peak **3**).

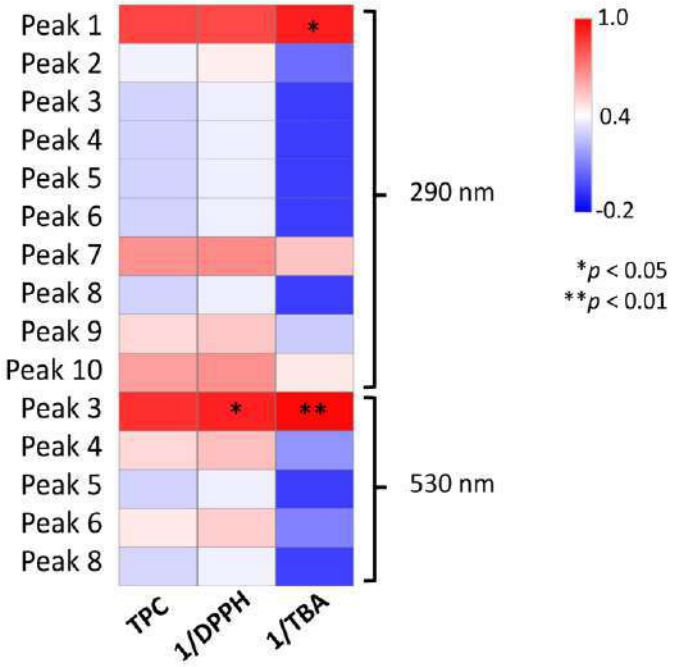

Figure 3. Heatmap showing the correlation of peak areas and antioxidant activities. The correlation is significantly different at $*p < 0.05$ and $**p < 0.01$, respectively

Conclusion:

Pre-gelatinization directly caused the breakdown of starch granules and the disruption of plant cell matrix. Phenolics of pre-gelatinized sweet potato powders were 1.3- to 7.5-fold higher in amount than conventional hot air-dried powders. The rise of antioxidant activity of pre-gelatinized samples was observed in all cultivars. The releasing of phenolics during pre-gelatinization contributed to antioxidant enhancement of colored sweet potatoes. The significantly positive correlation between chlorogenic acid (peak **1**) and an acylated anthocyanin (peak **3**) indicated as potent antioxidant substances released during the pre-gelatinization. Torperk, abundant of peak **3**, showed a high potential for antioxidant capacity. The advantages of pre-gelatinization indicate the potential for promoting health and commercial application in the food industry, health food market, natural food colorants, and nutraceuticals.

Acknowledgements: This research was financially supported by a Monbukagakusho Scholarship to N. Phomkaivon, provided by the Japanese Ministry of Education, Culture, Sports, Science and Technology.

References:

1. Park JS, Woo JW, Choi GH, Choi DS, Jung MY. J Food Chem Nanotechnol. 2015; 1(1): 3–12.
2. Wang A, Li R, Ren L, Gao X, Zhang Y, Ma D, Luo Y. Food Chem. 2018; 260: 124–134
3. Tamura H, Akioka T, Ueno K, Chujyo T, Okazaki K, King PJ, Robinson WE Jr. (2006) Mol Nutr Food Res. 2006; 50: 396–400.
4. Suda I, Oki T, Masuda M, Kobayashi M, Nishiba Y, Furuta S. JARQ. 2003; 37(3): 167–173.
5. Wang S, Nie S, Zhu F. Food Res Int. 2018; 89: 90–116.

6. Terahara N, Shimizu T, Kato Y, Nakamura M, Maitani T, Yamaguchi M, Goda Y. Biosci Biotechnol Biochem. 1999; 63(8): 1420–1424.
7. Oki T, Osame M, Masuda M, Kobayashi M, Furuta S, Nishiba Y, Kumagai T, Sato T, Suda I. Breed Sci. 2003; 53: 101–107.
8. Liu Y, Chen J, Luo S, Li C, Ye J, Liu C, Gilbert R. Carbohydr Polym 2017; 175: 265–272.
9. Laryea D, Wireko-Manu FD, Oduro I. Am J Food Technol. 2017; 5(5): 210–219.
10. Sato A, Zhang T, Yonekura L, Tamura H. J Funct Foods. 2015; 14: 581–589
11. Singleton VL, Rossi JA. Am J Enol Vitic. 1965; 16: 144–158.
12. Lee J, Durst RW, Wrolstad RE. J AOAC Int. 2005; 88: 1269–1278.
13. Zhu F, Asada T, Sato A, Koi Y, Nishiwaki H, Tamura H. J Agric Food Chem. 2014; 62: 885–892.
14. Tamura H, Shibamoto T. Lipids. 1991; 26: 170–173.
15. Tamura H, Yamagami A. J Agric Food Chem. 1994; 42: 1612–1615.
16. Guo K, Liu T, Zhang L, Bian X, Wei C. Food hydrocoll. 2019; 89: 829–836.
17. Sato A, Yamagami A, Tamura H. Chiang Mai Univ J Nat Sci. 2012; 11(1): 343–349.
18. Yang J, Gadi RL. Am J Food Technol. 2008; 3(4): 224–234.
19. Xu J, Su X, Lim S, Griffin J, Carey E, Katz B, Tomich J, Smith JS, Wang W. Food Chem. 2015; 186: 90–96.
20. Yamaguchi T, Mizobuchi T, Kajikawa R, Kawashima H, Miyabe F, Terao J, Takamura H, Matoba T. Food Sci Technol Res. 2001; 7(3): 250–257.
21. Zhu F. Trends Food Sci Technol; 2015: 129–143.
22. Soison B, Jangchud K, Jangchud A, Harnsilawat T, Piyachomkwan K, Charunuch C, Prinyawiwatkul W. IFST. 2014; 49: 2067–2075.
23. Gómez-Mascaraque LG, Dhital S, López-Rubio A, Gidley MJ. J Funct Foods. 2017; 283–292.
24. Kondo T, Kawai T, Tamura H, Goto T. Tetrahedron Lett. 1987; 28 (20): 2273–2276.

Replacement of Philangkasa extracts (*Ardisia elliptica* Thunb.) to nitrite in fermented meat product

Lalita Lakkham[1], Sasitorn Tongchitpakdee[1,2], Kanithaporn Vangnai[1,2], Chitsiri Rachtanapun[1,2,3,*]

[1]Department of Food Science and Technology, Faculty of Agro-Industry, Kasetsart University, Bangkok 10900, Thailand

[2]Center for Advanced Studied Agriculture and Food, Kasetsart University, Bangkok 10900, Thailand

[3]Advance Technology for Food Safety Specialty Unit, Kasetsart University, 10900. Thailand

*e-mail: chitsiri.t@ku.th

Abstract:

This research aims to apply Philangkasa extract (PLE) to replace nitrite in fermented meat products using Nham as a model. Philangkasa fruit was extracted with 95% ethanol assisted with an ultrasonic technique. The minimum inhibitory concentration (MIC) and the minimum bactericidal concentration (MBC) were determined by agar and broth dilution methods at pH 7.0 and 4.6. The anti-*Salmonella* effect of PLE was enhanced at acidic conditions by reducing their MIC values against *S.* Typhimurium from 0.70 to 0.30% (v/v) and MBC value from 0.80 to 0.40% (v/v), respectively. The 0.3% PLE showed bacteriostatic effect against *Salmonella* throughout 24 hr. Moreover, when the concentration of PLE increased to 0.5 and 1.0% (v/v), the bactericidal effect reduced to 9 and 6 hr, respectively. PLE was applied to Nham to replace nitrite (0, 50, and 100%). The production of Nham was divided into four batches, namely Nham without nitrite and PLE, Nham with 100% nitrite, Nham with 50% nitrite and 50% PLE, and Nham with 100% PLE that used as a benchmark for a commercial product. The chemical, physical and microbiological characteristics of Nham were determined after 3-day fermentation, at which the pH of Nham was below 4.6. Removal of all nitrite, a carcinogenic precursor, in Nham showed a beneficial effect on lactic acid bacteria and its activity on lactic acid fermentation. However, it drastically affected the red color and texture of the product. A replacement of PLE with 50% nitrite showed the best condition of not compromising the beneficial effect of nitrite in Nham regarding antibacterial activity, red color, and texture characteristics such as hardness, cohesiveness, gumminess, and chewiness. It also offered an anti-*Salmonella* impact on the product. To conclude, PLE can be used as a natural food preservative to replace 50% nitrite for fermented meat products. Therefore, this is a good alternative for reducing the nitrite content and providing safe food for the consumer.

Introduction:

Nham is a popular traditional fermented meat in Thailand due to its unique flavor and taste. It contains minced pork, chopped pork skin, cooked rice, and various spices. Nham is a preserved food by fermentation that is not heated. The fermentation relies on lactic acid bacteria to form lactic acid[1] and keeps the pH lower than 4.6 to prevent the growth of pathogenic bacteria in the food. However, suppose Nham is processed under non hygienic conditions. In that case, there is a chance that pathogenic bacteria such as *Clostridium botulinum*, *Salmonella* spp., *Staphylococcus aureus,* and *Listeria monocytogenes* are present and contaminated in Nham.[2] Therefore, it is crucial to control the pH of Nham below 4.6 to limit the growth of foodborne pathogenic bacteria. In addition, nitrates or nitrites are added to inhibit sporulation and the toxin formation of *C. botulinum*. Moreover, nitrites provide the meat a pink meat

appearance, a good taste, and flavor. However, nitrites can react with amino acids in meat to form carcinogenic nitrosamines (N-nitrosamines). It causes unsafe food for the consumers' health.[3] Nowadays, consumers are interested in a healthy diet and require meat products with fewer synthetic chemicals, including nitrates and nitrites.[4] Therefore, the meat industry tends to respond to consumers using natural additives or preservatives, mainly of plant origin.

Philangkasa extract (PLE) was an antimicrobial substance with red pigments. It contains anthocyanin, flavonols, and flavones such as myricetin, quercetin, and kaempferol, which carry strong antioxidant and antimicrobial activities.[5,6] In addition, PLE contains malvidin as anthocyanin and making it possible to act as a natural coloring agent. Therefore, this research aims to apply PLE as natural food additives, including antibacterial and coloring agents in Nham, to replace or reduce nitrite.

Methodology:

Preparation of Philangkasa extract

The fruit of Philangkasa (*Ardisia elliptica* Thunb.) were collected from Bang Kachao district, Samut Prakan, Thailand. Philangkasa fruits (removal seeds) were freeze- dried at - 18°C. Ground and sieved (80 mesh) for particle size uniformity. The powder was stored at -20°C until extract preparation.[7,8] Philangkasa powder was mixed with 95% (v/v) ethanol in a ratio of 1:10 (w/v) and was carried out using an ultrasonic technique (10 Amplitude microns, 23KHz; Soniprep 150 Ultrasonic Disinteragtor, London, UK) for 15 min, maintain its constant cool temperature during the extraction process. Then, centrifuged (5000 × g, 10 min) and kept the supernatant. The pellet was re-extracted. The supernatant was filtered through 0.45 µm nylon membrane under vacuum at 25°C and then the solvent was removed at 30°C by rotary evaporator under vacuum. The extract was stored in an amber bottle at -20ºC for subsequent use.[9]

Determination of minimum inhibitory concentration (MIC) and minimum bactericidal concentrations (MBC)

The MIC and MBC values of PLE against *S*. Typhimurium TISTR 292 were determined in normal (pH 7.0) and acidic (pH 4.6) conditions. At pH 4.6, the culture medium was adjusted using lactic acid.

The MIC was determined by the agar dilution method.[10] A test tube containing PLE was prepared to maintain a final concentration of 0.1 to 0.7% (v/v) using sterile deionized (DI) water as a diluent. After that, added the molten agar medium and quickly mixed it thoroughly. Then pour into the sterile petri dish and left to solidify. Dropped 0.1 µL of cell suspension of *S*.Typhimurium on the agar surface to obtain the number of cells at 3 Log CFU/spot. The control sample was agar media without PLE. The plates were incubated at 37ºC for 24 hr. After incubated, the plates were evaluated visually colony population density compare with the control sample. The MIC was defined as the lowest concentration that inhibited the visible growth of bacteria within 24 hr.

The MBC was evaluated according to the broth dilution method[11]. PLE was prepared at a concentration of 0.4 to 0.8% (v/v) by mixed with sterile DI to a volume of 5 mL in a test tube. Then added 5 mL of double-strength Mueller Hinton broth (MHB; Difco, Sparks, USA) and cell suspension of *S*.Typhimurium to give a final volume of 10 mL and an initial number of tested *Salmonella* was *ca*. 3 Log CFU/mL. The positive control was test tubes containing cell suspension and MHB medium without PLE, and the negative control was tubes containing PLE and MHB medium, without cell suspension. The test tubes were incubated at 37ºC for 24 hr. After that, the number of surviving *Salmonella* cells was examined by the spread plate method on TSA. The MBC was defined as the lowest concentration of antimicrobials that

reduced a cell concentration by 99.9% (3 Log reduction) at 24 hr. All experiments were run triplicated.

Determination of bactericidal activity by time-kill assay

A period of time to inactivate *Salmonella* at acidic conditions was determined by a time-kill assay.[12,11] A 15 mL of double-strength MHB broth at pH 4.6, containing *S*. Typhimurium was mixed with 15 mL of the PLE, to maintain a concentration of 0, 0.3, 0.5, and 1.0% (v/v) in the Erlenmeyer flask. The final volume of the mixtures was 30 mL. The final concentration of the initial cell was 3 Log CFU/mL. MBH broth at pH 4.6 was adjusted by lactic acid. The flasks were incubated at 37ºC in a shaker at 100 rpm for up to 24 hr. The numbers of survivors were enumerated at 0, 5, 10, and 30 min, 1, 3, 6, 9, 12, 15, 18, 21, and 24 hr using the spread plate technique on TSA.

Nham preparation

Nham was prepared as described by the Department of Livestock Development[13]. The formulation consisted with 52% ground pork, 35% chopped pork skin, 4.3% cooked sticky rice, 4.3% garlic, 1.7% fresh chili, 0.4% sugar, 0.2% sodium erythorbate, 0.2% sodium tripolyphosphate, 0.2% monosodium glutamate, and 1.9% sodium nitrite (NO_2). The production of Nham was divided into four batches, namely Nham without nitrite (NO_2) and Philangkasa extract (N 0%, P 0%), Nham with PLE and without nitrite (N 0%, P 100%), Nham with 50% nitrite reduction and 50% Philangkasa extract replacement (N 50%, P 50%), and Nham with nitrite and without Philangkasa extract (N 100%, P 0%). All ingredients were mixed until a homogeneous consistency. Then added starter culture (*Pediococcus pentosaceus* TBRC369) about 6 Log CFU/mL in each batch and mixed well. Packed in polypropylene vacuum bags by vacuum-sealed method and incubated at 30ºC for 3-day fermentation. After that, refrigerated at 4ºC for up to 7 days. The samples were withdrawn to evaluate the chemical, physical, and microorganism characteristics.

Chemical characteristics

pH and lactic acid content were measured using the AOAC method.[14]

Physical characteristics

Water activity (a_w) analysis was measured using a water activity meter 4TE (Aqualab, Pullman, USA). Color measurement was evaluated from[17]. Nham samples were measured in the L*, a*, b* mode of the CIE system by UltraScan PRO Spectrophotometer (Hunter Lab, Reston, USA). Texture measurements were modified from [17] and [18]. Texture profile analysis (TPA) program including hardness, cohesiveness, springiness, gumminess, and chewiness using a texture analyzer (TA-XT PLUS; Stable Micro Systems, Ltd., Surrey, UK).

Microorganism characteristics

An acid-tolerant bacteria was artificially inoculated to Nham to simulate the contamination by adding *S*. Typhimurium TISTR 292 to each batch. The final concentration of cell suspension was 4 Log CFU/mL. After the fermentation, the samples were tested for total viable count (TVC), total lactic acid bacteria (LAB), and *Salmonella*.[15,16]

25-g of Nham mixed with 225 mL sterile 0.1% peptone water (Peptone from meat; Merck, Darmstadt, Germany). The sample was homogenized in a stomacher (Seward Stomacher 400 Lab System, West Sussex, United Kingdom) for 2 min and spread plate technique for enumeration. The TVC and LAB were enumerated on trypticase soy agar (TSA; Merck, Darmstadt, Germany) and de Man Rogosa and Sharpe (MRS; Merck, Darmstadt, Germany) plates, respectively. *Salmonella* was determined using xylose lysine deoxycholate

agar (XLD agar, Difco, Sparks, USA). The presence of *Salmonella* with under detectable level was confirmed by enrichment method and qualitative analysis.

Statistical analysis

All experiments showed the mean of at least in duplicates determined and standard deviation (SD). The data were analyzed using analysis of variance (ANOVA). Duncan's multiple range tests carried out a means comparison at $p < 0.05$ by SPSS Software (version 16.0; SPSS Inc., Chicago, IL, USA) for Windows.

Results and Discussion:

Determination of minimum inhibitory concentration (MIC) and minimum bactericidal concentrations (MBC)

The results of the MIC and MBC values of PLE against *S*. Typhimurium are shown in Table 1. At neutral pH (pH 7.0), the MIC and MBC values are 0.70 and 0.80 % (v/v), respectively. When adjusted to an acid condition (pH 4.6), the inhibitory effect against *S*. Typhimurium enhances by reducing the MIC value to 0.30% (v/v) and MBC value to 0.40% (v/v).

According to the report[9], the ethanolic Philangkasa extract showed a broad-spectrum antimicrobial activity against foodborne microorganisms, including *Bacillus cereus*, *L. monocytogenes*, *S. aureus, Escherichia coli, Pseudomonas aeruginosa, S.* Enteritidis*, S.* Typhimurium*,* and *S.* Weltevreden. However, it did not affect lactic acid bacteria, namely *Lactobacillus plantarum* and *Pediococcus pentosaceus,* which are beneficial microorganisms mainly used in the food fermentation process. The PLE contains flavones and flavonols, which are the subclasses of flavonoid and phenolic compounds. The flavones in PLE are myricetin, quercetin and kaempferol. Flavones and flavonols in PLE had antimicrobial activity and affected the bacterial cell structure[19]. Flavones are polar molecules. When they enter the bacterial cell, they disrupt the plasma membrane containing the nonpolar phospholipid, destroy the cell membrane, and lead the bacterial death.[20]

Table 1.

The minimal inhibitory concentration (MIC) and minimal bactericidal concentration (MBC) values of PLE against *S*. Typhimurium at pH 4.6 and 7.0.

pH	MIC (% v/v)	MBC (% v/v)
4.6	0.30	0.40
7.0	0.70	0.80

Determination of bactericidal activity by time-kill assay

The bactericidal activity of PLE against *S.* Typhimurium was determined by a time-kill assay in an acidic condition (pH 4.6) to demonstrate a fermented food environment, as shown in Figure 1. *S*. Typhimurium is an acid-tolerant foodborne pathogen; therefore, it grew well in the control (no PLE added) sample and reached several 9 Log CFU/mL within 15 hr. When 0.3% PLE was added, PLE showed a bacteriostatic effect and slowed down the growth of *Salmonella* throughout 24 hr. The addition of 0.5% PLE reduced the bacterial cell to an undetectable level within 9 hr, indicating a bactericidal effect. Besides, the bactericidal effect showed within 6 hr when the concentration increased up to 1.0% (v/v).

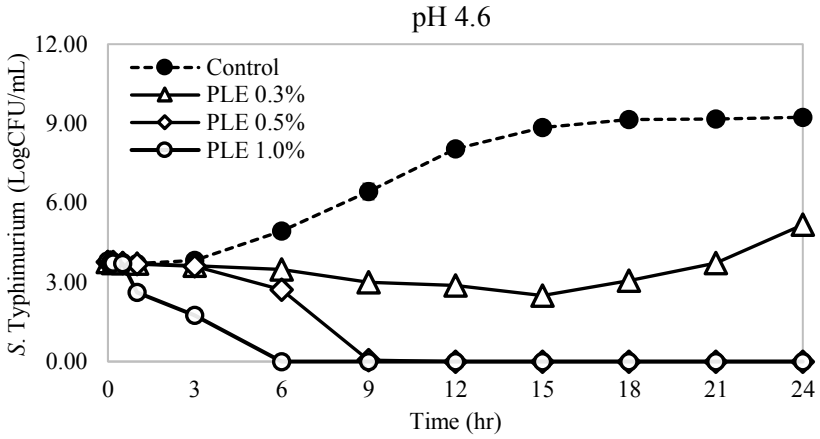

Figure 1.
Time-kill curve of PLE at different concentrations in MHB pH 4.6.

Chemical characteristic of Nham

The pH values of all samples gradually dropped from *ca* 6.4 to below 4.6 during 3-day fermentation (Figure 2, left) due to lactic acid production from the starter culture added, *P. pentosaceus*. The pH of Nham ranged from 4.24 to 4.53 and lactic acid contents ranged from 0.11% – 0.26% (Figure 2, right). Interestingly, lactic acid contents in samples without nitrite were significantly higher than samples added nitrite. The results implied that nitrite may retard the lactic acid fermentation of the starter culture, whereas PLE did not. After the fermentation, the samples were refrigerated at 4ºC, and their pH was relatively stable throughout the storage period because of less biological activity of the starter culture at low temperature and visibly shown in less lactic acid production rates (less slope of lactic acid).

All treatments of Nham showed pH below 4.6, which is safe for consumption as it can prevent the growth of pathogenic microorganisms[2], namely *C. botulinum*, a harmful foodborne pathogenic bacteria in vacuum packed food and fermented meat products.

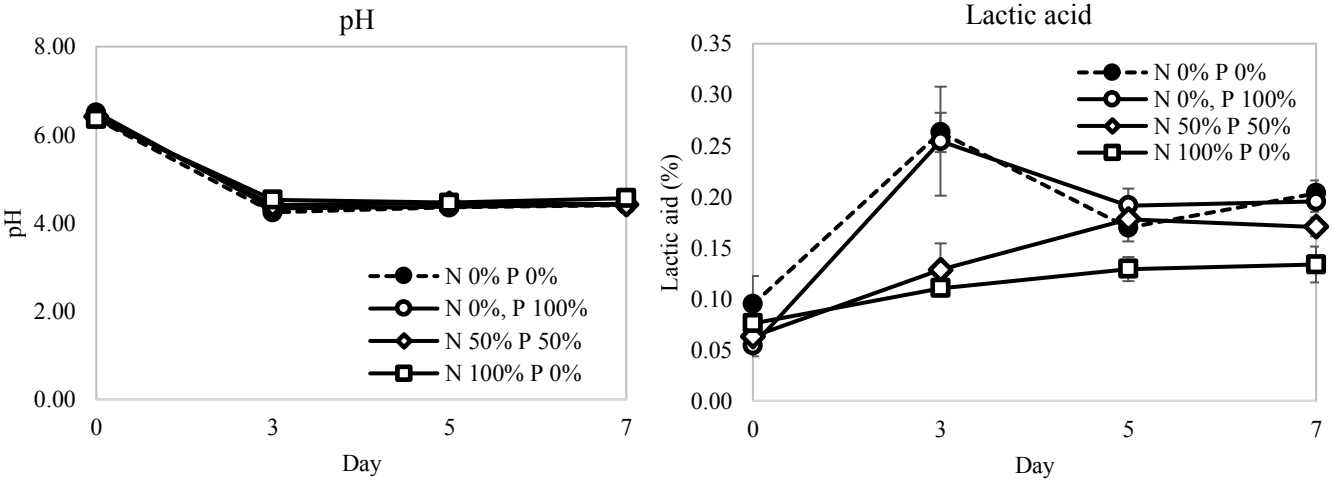

Figure 2.
Change in pH value (left) and lactic acid content (right) of Nham before fermentation (day 0), after fermentation (day 3) and store at 4ºC for 7 days.

Microorganism characteristic of Nham

Before fermentation, TVC of all samples ranged from 6.28-6.57 Log CFU/g (Figure 3, left), which corresponds to LAB ranging from 5.91-6.59 Log CFU/g (Figure 3, right) due to inoculation of starter culture at the initial of 6 LogCFU/g. The addition of starter culture can reduce the number of pathogenic bacteria and control the fermentation process. Some starter culture forming bacteriocin such as *Pediococcus pentosaceus* BCC 3772 produces bacteriocin against *L. monocytogenes*[21]. In addition,[22] reported that the use of starter culture (*Lactobacillus plantarum* strain BCC 9546) in the Nham fermentation process reduces biogenic amines toxins caused by bacteria to safe levels.

The numbers of TVC and LAB of all samples were not significantly different and constant throughout the storage. However, the numbers of LAB in Nham added nitrite (either 50% or 100%) were slightly lower than those numbers in Nham without nitrite. In contrast, the addition of 100% PLE did not affect the LAB numbers, which corresponds to the lactic acid contents in the product. This result proved that PLE did not show any adverse effect on the beneficial lactic acid bacteria, including a starter culture of fermented food related to beneficial microorganisms in the human gut.

Even though the fermented food at pH below 4.6 is safe from the *C. botulinum*, it is no guarantee to be safe from acid-tolerant bacteria such as *Salmonella*. Therefore, *Salmonella* (4 LogCFU/g) was artificially inoculated before fermentation to demonstrate unhygienic practices of Nham production. *Salmonella* tends to decrease during 3-day fermentation. However, Nham with 100% nitrite and Nham with 50% nitrite and 50% PLE showed by far the most anti-*Salmonella* effect, they reduced *Salmonella* by 4 LogCFU/g. *Salmonella* was inactivated in Nham with 100% nitrite within 3 days. Furthermore, Nham with 50% nitrite and 50% PLE and Nham with 100% PLE (without nitrite) inactivated *Salmonella* within 5 days after preparation.

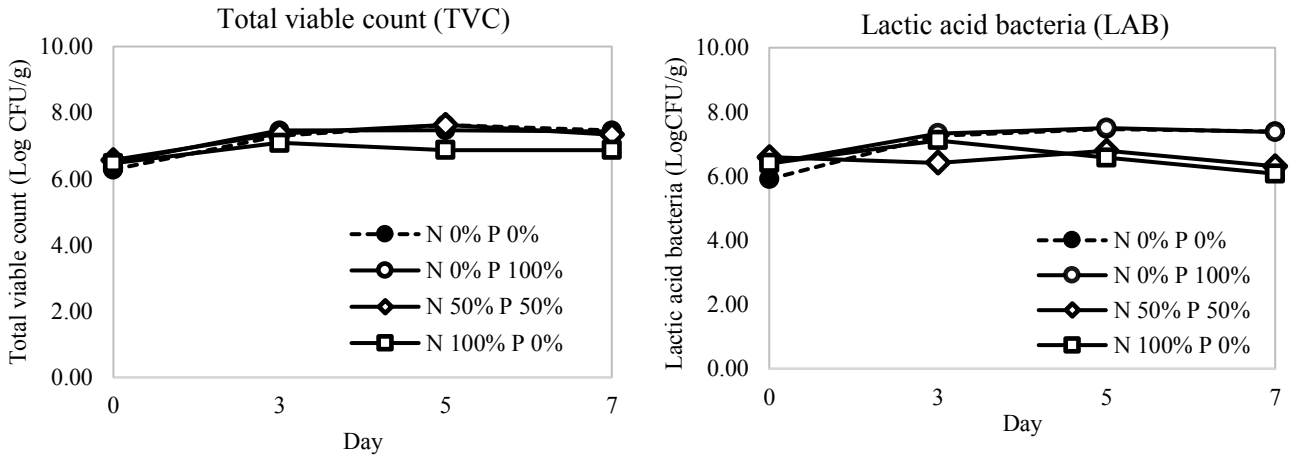

Figure 3.
Changes in TVC (left) and LAB (right) of Nham before fermentation (day 0), after fermentation (day 3), and storage at 4ºC for 7 days.

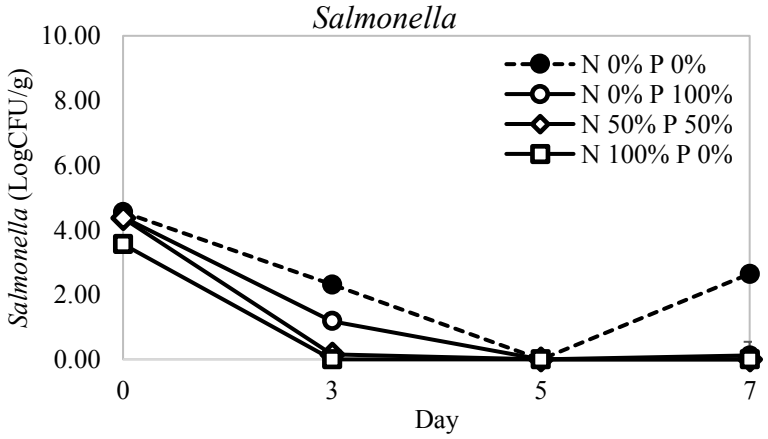

Figure 4.
Changes in *Salmonella* of Nham before fermentation (day 0), after fermentation (day 3), and storage at 4ºC for 7 days.

The physical characteristic of Nham

After 3-day fermentation, physical characteristics including a_w, color, and texture of Nham were analyzed. A sample added 100% nitrite was benchmark as a commercial product. The a_w values of Nham with nitrite were slightly lower than non nitrite added product (Table 2). A benchmark product, the addition of 100% nitrite, showed the lowest L* (lightness) and highest a* (redness). The fewer nitrite added showed the paler and less red color. Considering ΔE value, Nham added 50% nitrite and 50% PLE showed the most considerably similar to the benchmark.

Adding PLE into Nham showed more redness values as PLE contains malvidin which is anthocyanin and natural coloring agents[9]. However, Nham with 100% nitrite showed the highest redness value due to nitrite converts to nitric oxide (NO) which reacts with myoglobin in meat to form nitrosomyoglobin gives the meat a red color[3].

Table 2.
Change in water activity(a_w) and color of Nham after fermentation (day 3)

Sample	a_w	Color parameter			
		L*	a*	b*	ΔE
N 0% P 0%	0.98 ± 0.00a	60.22 ± 2.18a	1.12 ± 0.27d	11.93 ± 0.42a	9.73a
N 0% P 100%	0.98 ± 0.00a	57.04 ± 2.54b	2.21 ± 0.22c	8.96 ± 0.92c	6.93b
N 50% P 50%	0.97 ± 0.00b	56.03 ± 0.89b	4.31 ± 0.21b	10.80 ± 0.74b	4.64c
N 100% P 0%	0.97 ± 0.00b	51.67 ± 2.79c	5.53 ± 0.45a	10.62 ± 0.75b	-

Mean of three determinations ± standard deviation.
Small Letters means within the same vertical with different are significantly different ($p < 0.05$).

For the texture analysis, texture profile characteristics of Nham consisted of hardness, cohesiveness, springiness, gumminess and chewiness. Nham with 100% nitrite had the highest value of all characteristics. No significant differences in hardness, cohesiveness, gumminess,

and chewiness were observed between Nham with 50% nitrite and 50% PLE and the commercial formulation, Nham with 100% nitrite. The addition of PLE did not show any effect on texture characteristics.

Table 3.

Change in texture of Nham after fermentation (day 3)

Sample	Texture				
	Hardness	**Cohesiveness**	**Springiness**	**Gumminess**	**Chewiness**
N 0% P 0%	159.00 ± 12.72b	0.42 ± 0.01b	0.54 ± 0.05c	67.62 ± 6.30b	36.23 ± 4.27b
N 0% P 100%	163.84 ±13.84b	0.45 ± 0.03b	0.52 ± 0.05c	74.49 ± 8.39b	38.67 ± 6.16b
N 50% P 50%	289.24 ± 13.34a	0.53 ± 0.02a	0.70 ± 0.04b	153.57 ± 9.60a	106.50 ± 4.18a
N 100% P 0%	286.22 ±39.77a	0.54 ± 0.02a	0.77 ± 0.05a	156.33 ± 26.74a	121.38 ± 24.65a

Mean of three determinations ± standard deviation.
Small Letters means within the same vertical with different are significantly different ($p < 0.05$).

Conclusion:

Philangkasa extract can control *Salmonella* growth during fermentation. It can be applied as a natural food preservative to reduce nitrite in fermented meat products. A replacement of PLE to 50% nitrite in Nham did not compromise the chemical, physical, and texture characteristics of the products. Therefore, this is a good alternative for reducing the nitrite content and providing safer food for the consumer.

Acknowledgments:

This research was supported by Kasetsart University Research and Development Institute, FF(KU) 25.64.

References:

1. Thiravattanamontri P, Tanasupawat S, Noonpakdee W, Valyasev, R. Food Biotechnology. 2009;12: 221-238.
2. Paukatong K. V, Kunawasen S, Berl Munch Tierarztl Wochenschr. 2001;114: 327-30.
3. Martin M. Meat Science and Applications, 2001: 491-508.
4. Sindelar J. J, Cordray J. C, Sebranek J. G, Love J. A, Ahn D. U. J Food Sci. 2007;72: 324-332.
5. Rojsuntornkitti K, Jittrepotch N, Kongbangkerd T, Kraboun, K. International Food Research Journal. 20010;17: 153-161.
6. Riazi F, Zeynali F, Hoseini E. Behmadi, Homa. Nutrition and Food Sciences Research. 2016;3: 37-44.
7. Rodriguez-Saona L.E, Wrolstad R.E. 2001. Current Protocols in Food Analytical Chemistry 2001:1.1.1-1.1.11
8. Kim D.O, Lee C. Food Analytical Chemistry. 2003; 1.2.1-I1.2.12.
9. Jongrattanavit K, M.Sc. thesis, Faculty of Agro-Industry, Kasetsart University. Bangkok, Thailand. 2014.

10. Weckesser S, Engel K, Simon-Haarhaus B, Wittmer A, Pelz K, Schempp C.M. Phytomedicine. 2007;14: 508-516.
11. Naksang P, Tongchitpakdee S., Thumanu S., K., Oruna-Concha M.J., Niranjan K., Rachtanapun, C. Molecules. 2020;25: 1-14.
12. Thongson, C., Davidson P.M., Mahakarnchanakul W, Vibulsresth P. Journal of Food Protection. 2005;68: 2054-2058.
13. Department of Livestock Development. 2009:26.
14. AOAC. Official Method of Analysis of AOAC International. 17th ed. 2000.
15. Petchsing U, Woodburn M J. International Journal of Food Microbiology. 1989;10: 183-192
16. BAM. Food and Drug Administration Bacteriological Analytical Manual. 8th ed. 2002.
17. Sueprasarn J, Reabroy S, Pirak T, International Food Research Journal. 2017;24: 1667-1675
18. Bourne M. C. Food Technology. 1978;32: 62–72.
19. Ahmad A, Kaleem M, Ahmed Z, Shafiq H. Food Research International. 2015;77: 221-235.
20. Arora A., Byrem T.M., Nair, M.G.and Strasburg, G.M. Archives of Biochemistry and Biophysics.2000;373;102-109.
21. Kingcha, Y., Tosukhowong A., Zendo T, Roytrakul S, Luxananil P, Chareonpornsook K, Valyasevi R, Sonomoto K, Visessanguan W. Food Control. 2012;25: 190-196.
22. Tosukhowong A., Visessanguan W, Pumpuang L., Tepkasikul P, Panya A, Valyasevi R. Food Chemistry.2011;129: 846-853.

EFFECTS OF POTTERY STONE ON PHYSICAL – MECHANICAL PROPERTIES AND MICROSTRUCTURE OF PORCELAIN TABLEWARE FOR SINGLE-FAST FIRING

Soravich Mulinta[1, 2*], Sakdiphon Thiansem[1], Worapong Thiemsorn[1], Apinon Nantiya[1]

[1] Department of Industrial Chemistry, Faculty of Science, Chiang Mai University, Chiang Mai, 50200, Thailand
[2] Department of Production Innovation and Ceramic Design, Faculty of Industrial Technology, Lampang Rajabhat University, Lampang 52100 Thailand
*e-mail: Soravichcmu.pdh@gmail.com

Abstract:
The objective of this research was to study and investigate on effect of raw materials for artificial porcelain tableware body in Lampang province, Thailand. The raw materials used in the study were from local sources comprising Lampang pottery stone, Lampang clay, feldspar, and quartz. The characterization of the raw materials was analyzed by a particle analyzer, X-ray fluorescence (XRF) and X-ray diffraction (XRD). The mixing ratio of the artificial porcelain body was an addition to the Lampang pottery stone of 60 – 70%, Lampang clay of 0 – 15%, feldspar of 0 – 15%, and quartz of 0 – 40% on the physical-mechanical properties of the artificial porcelain body. The properties of the artificial porcelain body after firing at a temperature of 1,200°C and firing time of 2 h, 4h, and 8 h, in an oxidation atmosphere were studied, and the shrinkage, water absorption, bulk density, appearance porosity, crazing and bending strength of the artificial porcelain body were also tested. The results showed that the Formula 6 fired 8 h, components of 60% of Lampang pottery stone, 15% of Lampang clay, 15% of feldspar and 10% of quartz had optimum properties. Formula 6 fired 8 h, had a shrinkage of 13.5%, water absorption of 1.08%, bulk density of 1.88 g/cm^3, appearance porosity of 7.3 %, non-crazing and resistance to the bending strength at 1,198 kg/cm^2. The artificial porcelain body improved the requirements of the Thai industrial standard (TIS 564-2546).

Introduction:

Lampang province, Thailand is a noted ceramic source of the country, which has large, medium and small-sized entrepreneurs, including small and medium-sized enterprises (SMEs). However, most entrepreneurs lack basic knowledge and the techniques for applying innovation.

Lampang's ceramic products are mainly made of earthenware and stoneware porcelain clay that have particular characteristics. They are in general very siliceous, aluminous and contain significant proportions of potassium, which acts as flux. These clays have the property of gradually vitrifying without becoming deformed with a rise in temperature, and they yield an opaque material, often brown in color, though this varies according to the impurities contained in the initial mixture[1].

From the collection of the data from the Ban Nam Cho Factory, there was a production process of semi-porcelain, mainly chicken bowls, that was pottery painted by hand with a chicken, botan flowers and banana trees pattern. Their colors were white with transparent or turbid glaze, or creamy with transparent glaze with an estimated production of 100,000 units/month. Artificial porcelain products were normally fired at a temperature of around 1,200 –

1220 °C in a shuttle kiln 2.5 cubic capacity using LPG as the fuel and were fired for eight to ten hours. The quality of the semi-porcelain production is shown in Table 1. The mechanical strength of the semi-porcelain product was resistant from bending at 420 kg/cm^2. Thus, the mechanical property of the porcelainware was not exactly within the requirements of the Thai community's product standard.

The aim of this research was to study and investigate on effect of pottery stone, Lampang clay and quartz on physical and mechanical properties for single-fast firing porcelain tableware. The mixing ratios of clay body used in this study were 60 – 70% Lampang pottery stone, 0 – 15% Lampang clay, feldspar 0 – 15% and 0 – 40% quartz by the triaxial blend. All compositions were wet mixed and milled for 16 h and passed through a 325-mesh sieve. The specimen was formed and dried at 110°C for firing at 1200°C in an oxidation atmosphere, soaked for 30 minutes with a heating rate of 5 - 15°C/min, then fired in shuttle kiln.

Methodology:

1. Raw materials for experimental.

The raw materials used in the study came from local sources in Lampang province, Thailand. They were Lampang clay, Lampang pottery stone from Patra Ratana Clays and Minerals (1992) Company Limited, and feldspar and quartz from Sibelco Minerals (Thailand) Co., Ltd. The raw materials were controlled by grinding and passed through a 325-mesh sieve

2. Characterization analysis of the raw materials.

The particle size of the raw materials was analyzed by laser diffraction (Mastersizer S, Malvern, USA), and the chemical composition of the raw materials was analyzed by X-ray fluorescence (XRF, Megix Pro MUA/ USEP T84005, Philips, USA). The mineralogical composition of the raw materials was identified by X-ray diffraction: Cu anode, Kα1-1,544 A° (XRD, Smartlab, Rikaku, Japan).

3. Preparation of the specimens.

The component ratios of the artificial porcelain body used in this study were Lampang pottery stone of 60 – 70%, Lampang clay of 0 – 15%, feldspar of 0 – 15% and quartz of 0–40% (Table 1). All compositions were wet mixed and milled by a high-speed mill for 16 hours and passed through a 325-mesh sieve. The specimens were formed by a slip casting method and dried at 110°C then fired at a temperature of 1,200°C, soaked for 30 minutes with a heating rate of 5 ° C/min (firing time of 8h), heating rate of 10 °C (firing time of 4h), and heating rate of 15 °C/min (firing time of 2h) in a shutter kiln with LPG fuel.

Table 1.
Composition of the clay mixture in this study.

Raw Material	**Formula** (wt%)								
	1	2	3	4	5	6	7	8	9
Pottery stone	70	70	70	70	60	60	60	60	60
Lampang clay	15	10	5	0	20	15	10	5	0
Feldspar	15	10	5	0	20	15	10	5	0
Quartz	0	10	10	30	0	10	20	30	40

4. Properties measurement of the specimens.

The linear firing shrinkage was assessed as the difference between the diameter of the dried and fired specimens divided by the diameter of the dried specimen. The wet–to–fired shrinkage value was quoted on the basis of the wet size; wet–to–fired shrinkage is given by[2]:

$$\text{Shrinkage} = \frac{\text{wet length} - \text{fired length}}{\text{Wet length}} \times 100$$

The bulk density of a specimens has been defined as the relationship between the mass (weight) divided by the volume. The water absorption was calculated by premeasuring the weight of the test specimens after placing them in boiling water at 110°C for five hours. The samples were cooled in desiccators and weighed to an accuracy of 0.01g to give the dried weight (D). Then, the moisture was removed from the surface of the samples with a moist cloth, and the samples' weight was measured to give the soaked weight (S). The value of (D) and (S) are used in the formula[2]:

$$\text{Water absorption} = \frac{S - D}{D} \times 100$$

The bending strength for the clay was the determined by the universal testing machine (LLOYG Instrument model LRX5K) represented by the modulus of the rupture equation:

$$\text{MOR} = \frac{3LD}{2bd^2}$$

where L is the breaking load.
D is the distance between the supports.
b is the breadth of the rectangular rod.
and d is the depth of the rod [3].

The three-point loading system usually employed, the supper surface of the specimen is in compression whilst the lower surface is in tension, are shown in fig 1

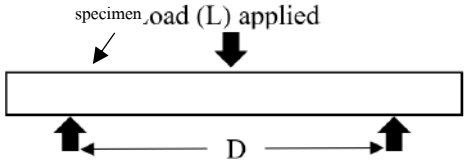

Figure 1.
three-point loading for MOR test.

Results and Discussion:

1. Characterization of the raw material.

The particle size of the raw materials were analyzed by laser diffraction X-ray fluorescence are shown in table 4. It was found that the Lampang clay had an average particle size of 10.59 μm whereas Lampang pottery stone had an average particle size of 22.41 μm. Potassium feldspar had an average particle size of 9.21 μm and Quartz had average particle size of 12.24 μm

Table 4.

Particle size of the raw materials.

Raw Material	**Particle Size** (μm)
Lampang pottery stone	22.41
Lampang clay	10.59
Feldspar	9.21
Quartz	12.24

The chemical composition of raw materials were analyzed by X-ray fluorescence, are shown in Table 5. The major components of Lampang clay included 67.47% of silicon oxide (SiO_2), 20.092% of aluminum oxide (Al_2O_3), and up to 1.81wt% of ferric oxide (Fe_2O_3). The amount of SiO_2 was much lower than Al_2O_3 and Fe_2O_3, respectively. CaO, K_2O, BaO MnO, ZrO_2, TiO_2, P_2O_5, MgO, Y_2O_3 and Rb_2O were found in small quantities. The major components of Lamapng pottery stone included 66.47wt% of silicon oxide, 11.52% of aluminum oxide, and 13.26% of ferric oxide, which would mostly affect the color of the fired product (Fe_2O_3, MnO, and TiO_2). Other elements (MgO, K_2O, and Na_2O) would act as fluxes and may have a strong effect during sintering[4]. Another important component of the studied Lampang pottery stone was the total amounts of the alkali and alkaline earth oxides (Na_2O, K_2O, MgO, and CaO) acting as flux materials were slightly high in the pottery stone[5]. The major components of Lampang clay included 66.9% of silicon oxide (SiO_2), 18.14% of aluminum oxide (Al_2O_3), and up to 11.17wt% of potassium oxide (K_2O). The major components of quartz included 97.2wt%.

Table 5.

Chemical composition of the raw materials.

Raw Material	**Composition** (wt%)										
	SiO_2	Al_2O_3	Fe_2O_3	K_2O	MgO	MnO	Na_2O	P_2O_5	TiO_2	CaO	LOI
Pottery stone	60.30	19.52	1.26	3.64	1.14	<0.01	0.20	0.18	0.04	0.05	5.96
Lampang clay	67.47	20.99	1.81	1.72	0.29	<0.01	0.12	0.04	1.23	0.27	6.77
Potassium feldspar	66.9	18.14	N/D	11.17	N/D	N/D	2.96	N/D	0.2	N/D	4.17
Quartz	99.16	0.45	N/D	0.03	0.004	N/D	0.06	0.01	N/D	0.01	0.276

N/D: non detector

The mineralogical composition of the standard clay was analyzed by X-ray diffraction**.** The results of the mineralogical analysis of raw materials in fig. 2(A), show the XRD pattern of the Lampang clay. The predominant peaks are associated with quartz (Q) while the secondary peaks identify the crystalline mineral phase of kaolinite (K) ($Al_2Si_2O_5(OH)_4$) and illite (I) $(K,H_3O)(Al,Mg,Fe)_2(Si,Al)_4O_{10}[(OH)_2\cdot(H_2O)]$. In Fig. 2(B), shows the XRD pattern of the Lampang pottery stone. The predominant peaks are associated with quartz (Q) while the secondary peaks identify the crystalline mineral phase of illite (I) $(K,H_3O)(Al,Mg,Fe)_2(Si,Al)_4O_{10}[(OH)_2\cdot(H_2O)]$.

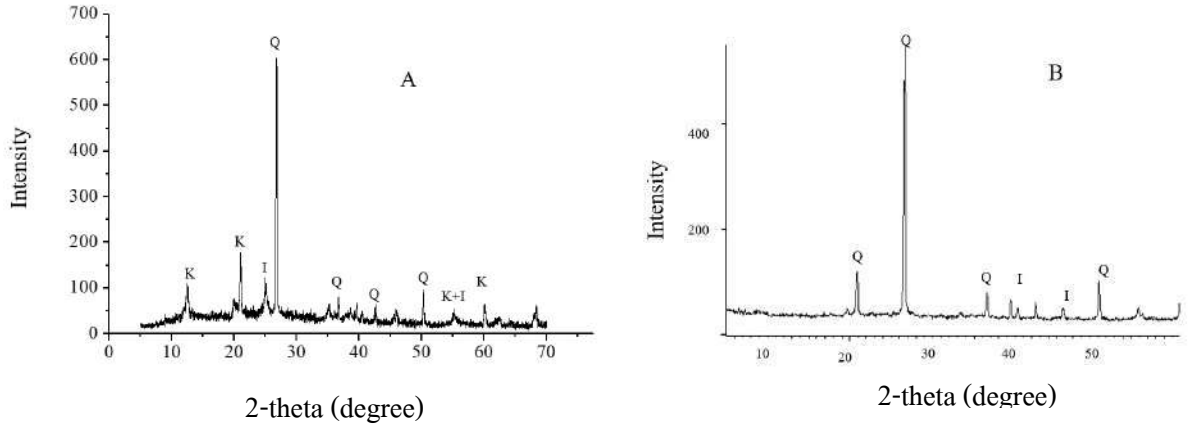

Figure 2.

X-ray diffraction patterns of the raw materials; Lampang clay (A) and Pottery stone (B).

2. Properties of the artificial porcelain body.

From the linear shrinkage of the fired porcelain body, the shrinkage of body at 100-180°C is due to hygroscopic water and is associated with weight loss. When was increased feldspar content and over firing temperatures at 900-1,100°C is due to the formation of mullite ($3Al_2O_3 \cdot 2SiO_2$) and another phase[6]. The primary mullite forms originated from the decomposition of the clay content whereas the secondary mullite forms resulted from the reaction of the alkaline (CaO, K_2O or Na_2O) in feldspar and Lampang pottery stone or Lampang clay[7]. The results showed that after firing, the clay body had low shrinkage of 6.6% (formula 9, fired 8h.) are shown in Fig 3.

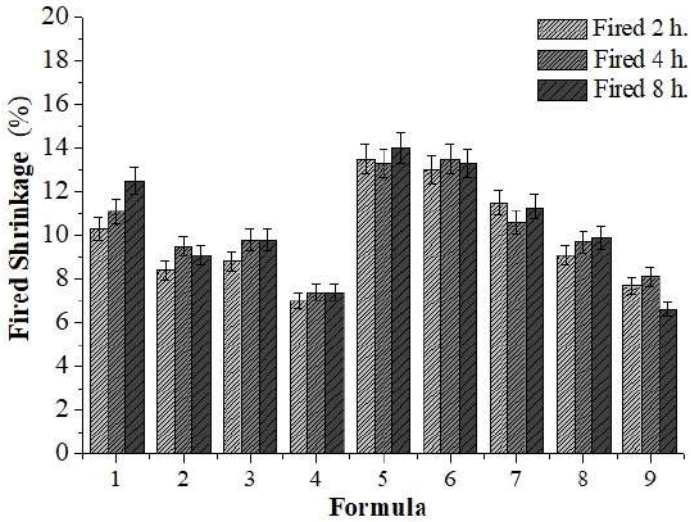

Figure 3.

Fired shrinkage of porcelain body.

For the water absorption of the porcelain body, the water absorption of specimens depends on the Lampang pottery stone had potassium oxide (K_2O) content in feldspar had an effect on a higher density and glassy phase than Lampang clay content. The feldspar content that the appropriate glassy phase and pore change size results could be obtained under the

firing temperatures at 1,200˚C. the results showed that after firing, the body had low water absorption of 1.08% (Formula 5, fired 8h.) are shown in Fig 4.

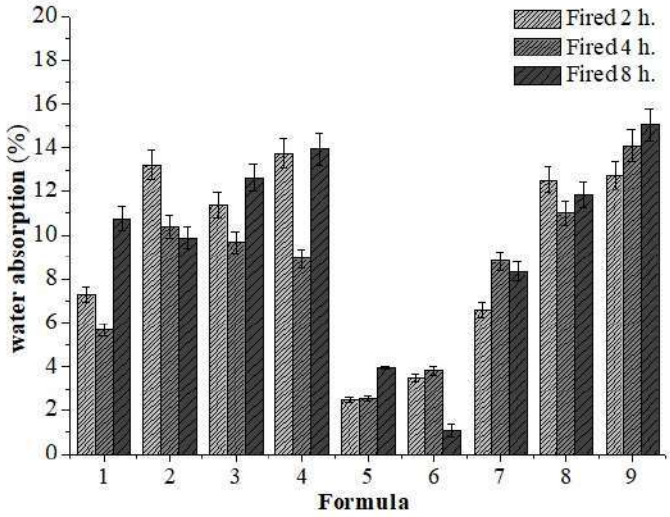

Figure 4.
Water absorption of the porcelain body.

The porcelain body was fired at 1200°C to obtain the appearance porosity. The appearance porosity of the porcelain body, the results showed that after firing, the body had low appearance porosity of 2.1% (Formula 5, fired 8h.) are shown in Fig 5. The bulk density was optimum with the addition of 70% of Lampang pottery stone. Formula 1 – 4 had a low bulk density than the addition of 60% of Lampang pottery stone, the result is shown as Fig 6.

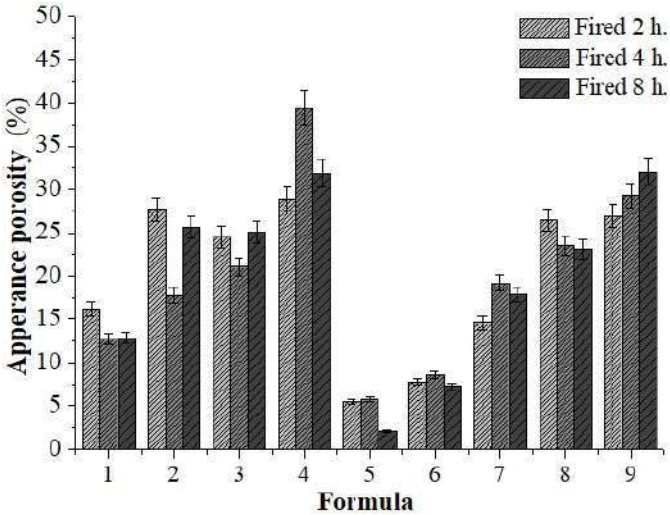

Figure 5.
Appearance porosity of porcelain body.

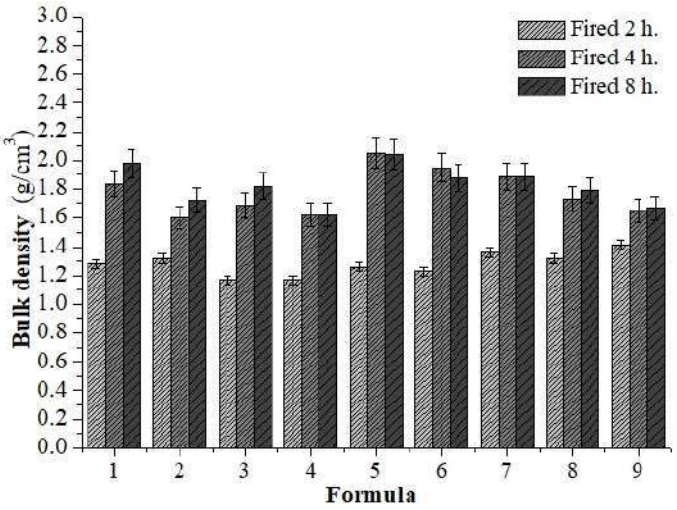

Figure 6.
Bulk density of porcelain body.

The bending strength of the fired porcelain body showed that before firing, the firing strength was associated with the development of strong crystals; such as, secondary mullite ($3Al_2O_3.2SiO_2$) and glassy matrix. Heating pottery stone and Lampang clay to a high temperature in the porcelain ware product of mullite contributed markedly to the strength of the fired body system. For the mechanical properties of firing in the porcelain body, the porcelain composition was prepared by mixing Lampang clay, alkaline earth and silica. The analysis revealed that the representative composition of the stoneware was produced by means of the firing process on the mechanical properties with several physical features and phase compositions including secondary mullite needles[8,9]. The porcelain body had a high bending strength of 1198 kg/cm^2 (Formula 6, fired 8h.), are shown in Fig 7.

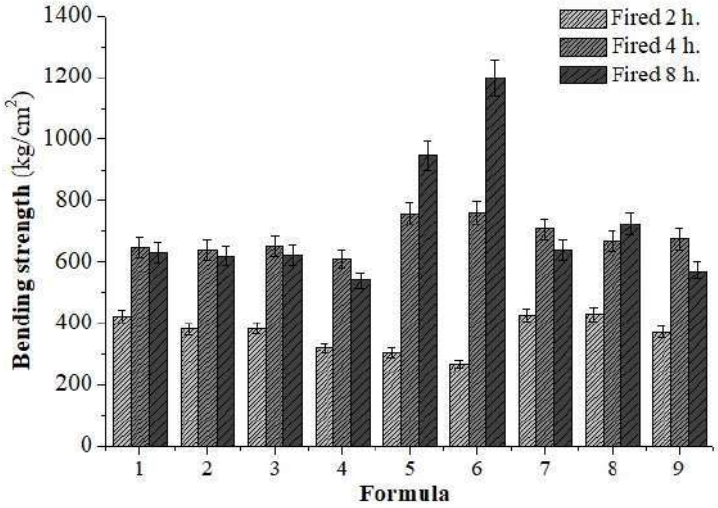

Figure 7.
Bending strength of porcelain body.

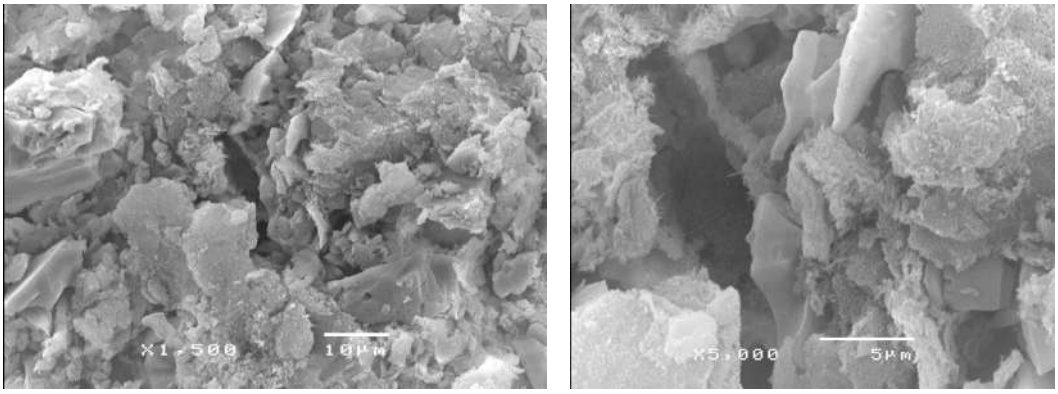

Figure 8.
Microstructure of the porcelain body of Formula 5.

The crystallographic analysis of the phases presents in the artificial porcelain body in formula 6, fired 8h is shown in Figure 8 indicating the presence of mullite and quartz. Such analysis confirmed the complete reaction of Lampang pottery stone, feldspar and silica in the microstructure of the artificial porcelain body fired at 1200°C (10% HF acid etching within 15 seconds). The phases formed in the clay body were much different than those formed in artificial porcelain, and this explained the difference of the physical and mechanical properties of porcelain body[10].

Conclusion:

The results concluded that Formula 6 (60%Lampang pottery stone, 15%Lampang, 15% feldspar and 10%quartz) had optimum properties. The properties of the porcelain body after firing at 1,200°C, heating rate of 15 °C/min (firing time of 2h) were studied. In the specimens, shrinkage of 13.5%, water absorption of 1.08%, bulk density of 1.88 g/cm^3, appearance porosity of 7.3 %, non-crazing and resistance to the bending strength at 1,198 kg/cm^2. This porcelain body achieved the requirements of the Thai industrial standard (TIS 564-2546).

Acknowledgements:

The authors would like to thank Chiang Mai University and Lampang Rajabhat University for providing the experiment and support for the research.

References:

[1] Philippe B. and N., 2007., *Ceramic Materials: Processes, Properties and Application.,* ISTE Ltd, UK.
[2] "Standard for Porcelain Tableware." Thai Industrial standard. (TIS-564-2546)
[3] Ray W. and Radford C., (1987), Pergamon press, London, 1987.
[4] Jone. J.T. and Berard. M.F., Ceramics Industrial Processing and Testing, second ed., Ames; Iowa; 1993.
[5] Thiansem, S., et al. Quality Improvement of Lampang Clay for Porcelain Bodies, *ScienceAsia*, 2002, (**28**), p.45-152.
[6] Chitwaree, S., et al. Energy saving in sintering of porcelain stoneware tile manufacturing by using recycled glass and pottery stone as substitute materials, *Thel Eng***,** 2018 (**11**), p. 81–88.
[7] Lee, W.E., I., Y., Mullite formation in clays and clay-derived vitreous ceramics. *J. Eur Cer Soc*, **21**(14) (2001) 2583-2586**.**
[8] Martín-Márquez, J., et al. Effect of microstructure on mechanical properties of porcelain stoneware, *J. Eur Cer Soc*, **30**(15) (2010), 3063–3069.

[9] Pakawadee S., et al. Influence of Lampang pottery stone: local materials in Thailand on C-Q-F ratio, key properties, mullite formation and glaze-body fit of vitreous ceramic sanitary ware. J Aust Cer Soc, 2019. (55), p.1153–1160.
[10] Sirilar, P., et al. Thermal and physical properties of white-opaque sanitary glazes using Lampang pottery stone as a raw materials. Mater. Sci. Forum. 2016, 872, p. 118–122

CLASSIFICATION OF DIFFERENT TEA TAXA FROM CHIANG RAI USING UHPLC-MS/MS COMBINED WITH CHEMOMETRICS

Patchayanan Suksamran,[1] Somrudee Nilthong,[1,2] Kanchana Watla-iad[1,2,3,*]
[1]School of Science, Mae Fah Luang University, Chiang Rai, 57100, Thailand
[2]Center of Chemical Innovation for Sustainability, School of Science, Mae Fah Luang University, Chiang Rai 57100, Thailand
[3]Tea and Coffee Institute of Mae Fah Luang University, Mae Fah Luang University, Chiang Rai 57100, Thailand
*e-mail: kanchana.wat@mfu.ac.th

Abstract:
Assam tea is the local tea of Chiang Rai province (Thailand). The Assam tea from different regions of Chiang Rai is produced from different variants of *Camellia sinensis* var. *assamica* grown under various climatic conditions, and thus, its important chemical compounds might be affected by these factors. Therefore, to select for the most suitable taxa for further applications, chemical composition in the methanolic extract of Assam tea samples collected from six areas in Chiang Rai province were analyzed using a sensitive liquid chromatography–triple quadrupole mass spectrometer (LC–MS/MS) combined with chemometrics in this work. The determined compounds were caffeic acid (CA), caffeine (CF), chlorogenic acid (CGA), gallic acid (GA), p-coumaric acid (PCA), catechin (C), catechin gallate (CG), epicatechin gallate (ECG), epicatechin (EC), epigallocatechin gallate (EGCG), epigallocatechin (EGC), gallocatechin gallate (GCG), gallocatechin (GC), o-Coumaric acid (OCA) and theobromine. The studied compound contents were reported as mg/g dried sample. The main compounds found in all extracted samples were caffeine and epigallocatechin gallate. Some taxa have potential for further study because of the high chemical content. The obtained chemical contents were performed principal component analysis (PCA) to study the natural clustering of data. The PCA screen plot showed that the studied tea taxa could be clustered into 3 groups. This work indicates that the combination of LC–MS/MS and chemometrics can be a useful technique for the classification of tea taxa from different regions of Chiang Rai.

DENSITY FUNCTIONAL THEORY STUDY OF THE GLYPHOSATE ADSORPTION ON LEWIS ACIDIC BEA ZEOLITES: EFFECT OF LEWIS ACID

Keeradara Hiruntrakool,[1] Athittaya Rasrichai,[1] Ornanong Opasmongkolchai,[1] Thana Maihom[1,*]
[1]Department of Chemistry, Faculty of Liberal Arts and Science, Kasetsart University, Kamphaeng Saen Campus, Nakhon Pathom 73140, Thailand
*e-mail: faastnm@ku.ac.th

Abstract:
The effect of Lewis acidity of BEA zeolite for glyphosate pesticide adsorption have been investigated with M06-L/6-31G(d,p) level of theory. The 38T BEA nanocluster model where T atoms are either Si or Al atoms are used to represent BEA zeolite. The four tetravalent metals including Sn, Zr, Hf and Ti substituted Si atom at T2 of BEA zeolite framework are used in this work. The glyphosate is adsorbed on BEA zeolite through the interaction between phosphoryl (P=O) group and the Lewis acid site of zeolites. The calculated adsorption energies are -55.1, -62.0, -64.2 and -46.6 kcal/mol for Sn-, Zr-, Hf- and Ti-BEA, respectively. Hf-BEA adsorbs glyphosate strongest due to its highest Lewis acidity and, in other words, is the best in attaching electrons from O of phosphoryl group. A linear correlation between the adsorption energies and lowest unoccupied molecular orbital (LUMO) levels is also observed, with an R^2 value 0.955. This result implies the significant role of interactions between surface LUMO level of Lewis acidic zeolites and highest occupied molecular orbital (HOMO) level of glyphosate molecule. The LUMO energies of Lewis acidic zeolites might be used as activity descriptors for an estimation of the adsorption energy of organophosphorus compounds.

DEVELOPMENT OF SEA BASS SCALES GELATIN/NANO-TiO_2 BLENDED FILMS FOR INHIBITION OF *Staphylococcus aureus* BY THE PHOTOCATALYTIC

Pheeraphong Bunroek,[1,*] Atiwat Wiriya-amornchai,[2,*] Chotimon Koomgate,[3] Rapatsorn Wongwatcharakerati,[4] Chutikarn Hmokmued
[1,3,4,5] College of Teacher Education, Phranakhon Rajabhat University, Bangkok, Thailand
[2]Materials and Processing Technology, Faculty of Engineering and Technology, King Mongkut's University of Technology North Bangkok Rayong campus, Rayong, Thailand
*e-mail: pheeraphong@pnru.ac.th,[1] atiwat.w@eat.kmutnb.ac.th[2]

Abstract:

The objectives of this research were 1) to study the extraction of gelatin from the sea bass scales and 2) to develop the inhibition properties of the gelatin/nano-TiO_2 blended film. Staphylococcus aureus bacteria were applied to the resistance of antibiotics via the Photocatalytic. The procedure of extraction was used 0.4% (w/v) sodium hydroxide solution and 0.4% (w/v) acetic acid solution. The gelatin/nano-TiO_2 blended films were prepared using the solution casting technique. Then, the spread plate technique was used to study the antibacterial of *Staphylococcus aureus* properties under the UV-light box. The results revealed that gelatin extraction from sea bass scales was produced about 8.04% w/w (gelatin/sea bass scales). The fingerprint by FTIR spectra of extracted gelatin from sea bass scales was similar to the functional groups as the commercial gelatin. Gelatin/nano-TiO_2 blended films had a smooth surface, were white color and opaque, and easily removed from the petri dish. Bacteria disruption of the gelatin/nano-TiO_2 blended films was observed from the prohibition of Staphylococcus aureus under testing of UV exposure. The increase of concentration of the nano-TiO_2 in the gelatin/nano-TiO_2 blended films was more effective than the antibacterial activity test.

Introduction:

Currently, plastic packaging and synthetic films from petrochemicals that could not be biodegradable were widely used, causing pollution and severe environmental problems. There could be a lack of understanding in the use of petrochemicals, which caused the contamination of food and beverages. Therefore, the misuses directly affected consumer health. The excessive use and consumption of single-use plastics also accumulated the plastic wastes, which was a burden on storage and destruction since some plastics could not be recycled and might eventually impact the ecosystem. (Sangrajrang et.al., 2013). The biodegradable plastics were used in many areas, such as agricultural materials, medical materials, and packaging for consumption. Biodegradable plastic was derived from proteins found throughout the mammal, fats, and carbohydrates in the plants that could be prevented steam permeability and strength beneficially. However, there were some restrictions for mammal gelatins. Fish scale gelatin was another option material that can be used in biofilms. The improvement of biofilms could be the effectiveness of antibiotic activity by adding the antibacterial activity reagent. Titanium dioxide (TiO_2) was an antimicrobial reagent with applications in food contact and packaging surfaces. The inhibition effect of TiO_2 was higher in the presence of light because of photocatalytic properties. When the reaction was stimulated by ultraviolet light on titanium dioxide, it reacted with water or moisture. Then, it formed super oxygen with hydroxyl radical, which decomposed organic matter used for anti-

microorganisms such as bacteria and fungi. Preparations of films were fabricated by nanoparticle powders coated on the materials. The nanoparticle of TiO_2 additives had the potential of gelatin-based films that disrupted the operation and growth of *Staphylococcus aureus,* which would be used in the future. By the way, it was the packaging for food or medicine (Nassiri and Mohammadi Nafchi, 2013). Therefore, this researcher aimed to 1) study the extraction of gelatin from sea bass scales 2) improve the sea bass scales gelatin/nano-TiO_2 blended film for disinfecting properties of *Staphylococcus aureus.* This research provided general guidelines and fundamental information to produce biofilms.

Methodology:

In this study, TiO_2 nanoparticles made in China with CAS No. 13463-67-7 were purchased from Krungthepchemi Co., Ltd. The microstructure of the crystalline structure was Anatase phase, with an average diameter of 21 nm and a specific surface area of 50 m^2/g. The sea bass scales were collected from the local fish market in Rayong province, Thailand. The fabrication of sea bass scales gelatin/nano-TiO_2 blended films to inhibit *Staphylococcus aureus* had three steps as follow:

1. Extraction of sea bass scales gelatin

Firstly, the 50 g of sea bass scales were washed with clean water to remove unnecessary material on the surface. Alkaline treatment with 0.4 % w/v NaOH solution was used to remove of non-Collagenous with the scales/solution ratio of 1:20 (w/v) for two hours at room temperature. Secondly, the scales were washed with clean water and immersed in 0.4 % w/v CH_3COOH solution for 150 mins to extract the collagenous material in the sea bass scales. Thirdly, the collagen mixture was subjected to water at 70^oC for two hours. Finally, the gelatin solution was filtrated and evaporated in the petri dish. The percentage of gelatin extracted from sea bass scales was determined by weighing the extracted gelatin and comparing with the initial sea bass scales. The functional groups of gelatin extracted from sea bass scales were analyzed by FTIR technique that was compared with commercial fish gelatin, the McGarrett brand.

2. Gelatin/nano-TiO_2 blended film preparation

The gelatin/nano-TiO_2 blended films were prepared using the solution casting technique. Firstly, nano titanium dioxide was mixed with distilled water varied at 0.1, 0.3, and 0.5% w/v. Then, the mixture of solid and dispersed particles was sonicated in the ultrasonic machine for one hour. Secondly, dried gelatin extracted was dissolved into the de-ionized water to prepare the 30%w/v of gelatin solution. Then, the different nano-TiO_2 solutions were mixed into the gelatin solution at 58 ^oC and stirred for one hour by using the glycerol as a plasticizer. Finally, 5 mL of gelatin/nano-TiO_2 blended solution was dried on the glass plate at room temperature for 24 hours to prepare the films of uniform thickness.

3. Study *Staphylococcus aureus* disinfecting properties

Staphylococcus aureus was diluted to 1 x 10^8 CFU/mL concentrations in the distilled water. Each proportion of the gelatin/nano-TiO_2 blended solution was mixed with *Staphylococcus aureus* by pipetted 5 mL from each concentration into the test tubes. The disinfecting properties test was carried out at 0, 30, 60, and 90 minutes under UV light (in UV box) at constant light intensity for the photocatalysis process. Agar disk-diffusion testing was the method used in the antimicrobial activity. Then, agar plates were incubated at 37°C for 24 hours. The incubation was done under proper conditions for varied time intervals (0, 30, 60, and 90 mins). Then, the number of living cells (CFU/mL) of each sample was counted using the agar plate.

Results and Discussion:

1. Extraction of sea bass scales gelatin

Physical characteristics of sea bass scales after immersion in 0.4% w/v NaOH and 0.4% w/v CH_3COOH solutions were swelled, white, and smooth texture like gel. Gelatin was obtained about 4.02 g / 50 g of sea bass scales (8.04 %w/w). The yield of gelatin varied depending on the species of fish due to the collagen contents in the fish scales (Karim and Rajeev, 2009). The fish scales were swelled with the acid solution by loosening the proteins and breaking the non-covalent bonds which were to prepared collagen for extraction. When fish scales were extracted, energy above the collagen temperature to gelatin conversion temperature (above 40 °C) broke the hydrogen bondings and lost the triple helix structure. Additionally, the heat could be caused the breakage of internal covalents and non-covalent bonds and external bonds between the peptide chains, forming smaller peptides (Karim and Rajeev, 2009). Using high temperature, collagen was altered into gelatin and dissolved more in the extract than low-temperature and short-time extraction. Gelatin from sea bass scales had less gel strength than bovine and pork gelatin. This was corresponded to the research objectives that required flexibility. This was due to the content of the amino acid; glycine and hydroxyproline and less proline which affected the stability of the gelatin structure. Gelatin from jellyfish had a lower gel strength than gelatin from bovine bone. The heat used for drying may result in a darkening of the gelatin color as well as causing some macromolecular proteins to coagulate during drying. As a result, the extracted gelatin has lower transparency than commercial gelatin. Identification of commercial gelatin and gelatin extracted from sea bass scales shown in Fig.1

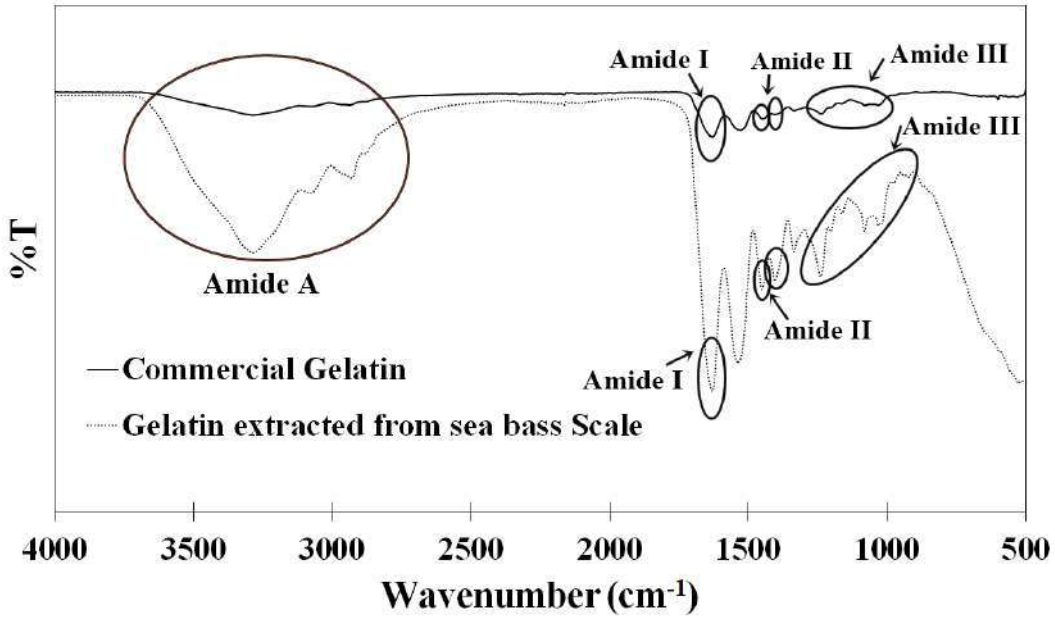

Figure 1. FTIR fingerprint of commercial gelatin and gelatin extracted from sea bass scales

According to the Figure 1, it was found that there were several amino acid components (Al-Hassan and Norziah, 2011). The stretching vibration of all amide groups was found at four positions: 3660 – 2300 cm^{-1}, 1661 cm^{-1}, 1450 – 1401 cm^{-1}, and 1236 – 698 cm^{-1} indicating the identity of the structure Amide A, Amide I, Amide II, and Amide III (Ran et.al, 2017). It was confirmed that there were various amino acid compositions obtained by extracting gelatin from sea bass scales. In this study, commercial fish gelatin, the McGarrett brand with 100% fish gelatin content (INS 428) was used to compare with the gelatin extracted from sea bass scales. The characteristic of the commercial showed at 3560 – 3412

cm^{-1} was an Amide Type A stretching group (N–H Group). It was indicated the degree of crosslinking among the gelatinous structures of the chain (Zhang, et al., 2013). Furthermore, the appearance peak about 1631 cm^{-1} introduced from Carbonyl stretching (C = O) group identity in the amide structure (Tongdeesoontorn et. al., 2012). Moreover, the peak at 1386 and 1313 cm^{-1} indicating $–CH_2–$ bending in-plane (Zaher, et. al., 2009) as well as at wave numbers about 1118 and 1021 cm^{-1} represented –C–O–C– antisymmetric bridge stretching (Rhim et. al., 1999). There was also a wave number 614 cm^{-1} that indicated the Skeletal Stretching structure (Muyonga, Cole, & Duodu, 2004). The researchers confirmed the FTIR spectra graph similarity pattern as the commercial gelatin at the market.

2. Gelatin/nano-TiO_2 blended film

The physical appearance of the pure gelatin film (0% nano-TiO_2) was demonstrated in the Fig.2-a. It had smooth surface, colorless, and translucent. Moreover, the film was hard and ductility, difficult to peel the film from the petri dish. While gelatin/nano-TiO_2 blended films showed in the Fig.2-b, they had smooth surface, white color, and opaque. Furthermore, the additional properties of films were tough, flexible, easily to remove from the glass plate. The white color of film was depending on the amount of nano titanium dioxide 0.1%, 0.3%, and 0.5% nano-TiO_2 respectively. The average film thickness was displayed as shown in Table 1. The average thickness of film samples was 0.11 mm. The volume of 5 mL of solution and glass plate sizes was equally controlled. Some films were thicker than others because, while evenly spreading took longer than others, Gelatin was gelatinized, resulting in high viscosity and difficult to flow. The gelatin/nano-TiO_2 blended films at varied concentrations had no different change of the thickness. The film thickness was the control variable in the disinfecting properties test at different nano-TiO_2 concentrations.

(a) (b)

Figure 2. physical appearance of films (a) pure gelatin film (b) gelatin/nano-TiO_2 blended films

Table 1 Gelatin/nano-TiO_2 blended films thickness

Nano-TiO_2 concentrations	Film thickness (mm)									
	1	**2**	**3**	**4**	**5**	**6**	**7**	**8**	**9**	**Average**
TiO_2 0% (Ref.)	0.19	0.20	0.10	0.10	0.10	0.10	0.10	0.10	0.10	0.12
TiO_2 0.1%	0.10	0.10	0.10	0.10	0.10	0.10	0.10	0.10	0.10	0.10
TiO_2 0.3%	0.10	0.20	0.19	0.10	0.10	0.10	0.10	0.10	0.10	0.12
TiO_2 0.5%	0.10	0.17	0.10	0.10	0.10	0.10	0.10	0.10	0.10	0.10

3. Antibacterial activity of films

Antibacterial activity test of films from *Staphylococcus aureus* was calculated the number of colonies on the agar surface. Before testing, the gelatin/nano-TiO_2 solutions were submitted to treatment under the UV light (in UV box) for different time intervals; 30 mins, 60 mins, 90 mins, and 0 min (no UV light) at constant light intensity for the photocatalysis

process. The counted number of colonies of *Staphylococcus aureus* bacteria had been produced as shown in Figure 3 and Table 2.

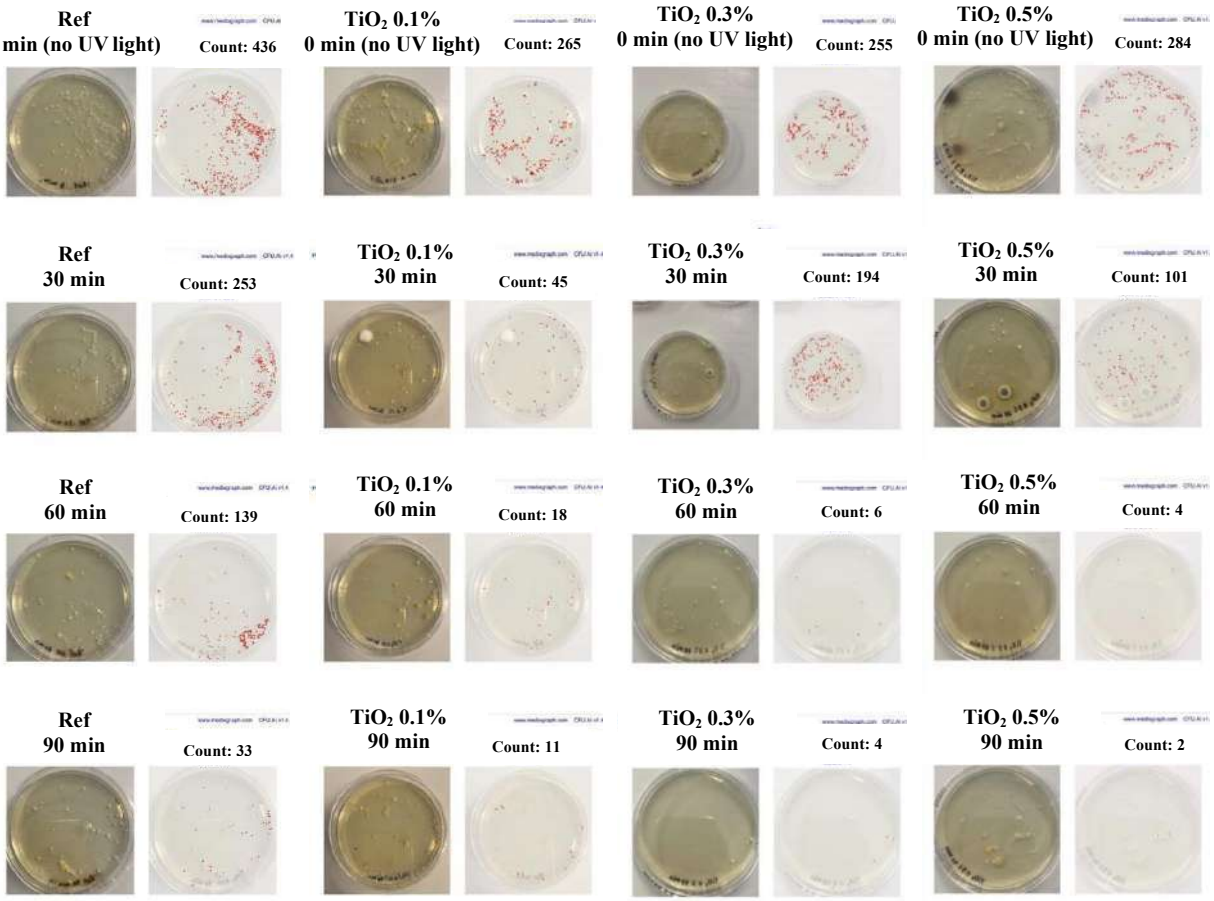

Figure 3. *Staphylococcus aureus* colonies on agar

Table 2 Number of colonies on agar surface

Time (min)	Colony (CFU/ml)							
	0% TiO_2 (Ref.)	% Reduction	0.1% TiO_2	% Reduction	0.3% TiO_2	% Reduction	0.5% TiO_2	% Reduction
0 (no UV light)	43.6×10^8	Ref.	26.5×10^8	Ref.	25.5×10^8	Ref.	28.4×10^8	Ref.
30	25.3×10^8	41.97%	4.5×10^8	83.02%	19.4×10^8	23.92%	10.1×10^8	64.44%
60	13.9×10^8	68.12%	1.8×10^8	93.21%	0.6×10^8	97.65%	0.4×10^8	98.59%
90	3.3×10^8	92.43%	1.1×10^8	95.85%	0.4×10^8	98.43%	0.2×10^8	99.30%

The gelatin/nano-TiO_2 solutions were found that the increased amount of nano-titanium dioxide and time interval in the UV box resulted in decreased colonies from the photocatalysis process of nano-titanium dioxide as shown in Figure 4. The production of evidence was confirmed synergistic mechanism between of UV-light and nano-TiO_2 to constrain *Staphylococcus aureus* in the samples.

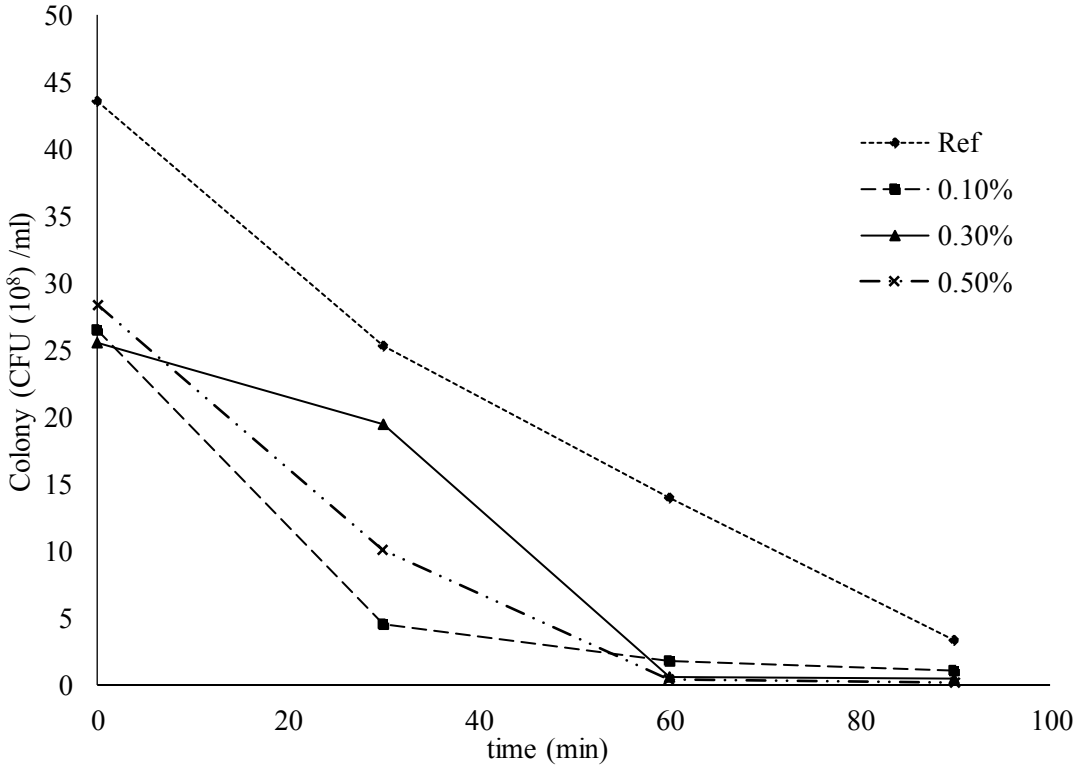

Figure 4. *Staphylococcus aureus* colonies on agar at different times

The disinfecting test of *Staphylococcus aureus* by the gelatin solution (0% nano-TiO_2) and gelatin/nano-TiO_2 solution were designed to accomplish the number of colonies on the agar surface. The %reduction can be calculated from the following equation;

$$\%\ \text{reduction at 90 mins} = \frac{\text{colony (CFU/ml) at 0 minutes} - \text{colony (CFU/ml) at 90 minutes}}{\text{colony (CFU/ml) in at 0 minutes}} \times 100$$

The condition of the reference sample (0% nano-TiO_2) presented as follows:

1) The number of colonies at 0 minute (no UV light) decreased from 43.6 x 10^8 CFU/ml to 3.3 x 10^8 CFU/ml within 90 minutes, that could be caused by the only UV light. As the result, the %reduction at 90 mins was 92.43%.

2) The result of this experiment would be used as a reference to compare with the efficiency of nano-TiO_2. The increase of nano TiO_2 in the gelatin solution showed the influence of surface area on the effectiveness of antimicrobial activity. When adding the amount of 0.1% nano-TiO_2 solution, the number of colonies at 0 minute (no UV light) decreased from 26.5 x 10^8 CFU/ml to 1.1 x 10^8 CFU/ml within 90 minutes, that could be caused by the UV light and nano-TiO_2 was effective when exposed to light. As the result, the %reduction at 90 mins was 95.85%.

3) When adding the amount of 0.3% nano-TiO_2 solution, the number of colonies at 0 minute (no UV light) decreased from 25.5 x 10^8 CFU/ml to 0.4 x 10^8 CFU/ml within 90 minutes, that could be caused by the UV light and nano-TiO_2 was effective when exposed to light. As the result, the %reduction at 90 mins was 98.43%.

4) When adding the amount of 0.5% nano-TiO_2 solution, the number of colonies at 0 minute (no UV light) decreased from 28.4 x 10^8 CFU/ml to 0.2 x 10^8 CFU/ml within 90

minutes, that could be caused by the UV light and nano-TiO_2 was effective when exposed to light. As the result, the %reduction at 90 mins was 99.30%.

In summary, the study found that when adding TiO_2 at 0.1%, 0.3%, and 0.5% nano-TiO_2 solution (w/v), the %reduction increased from 92.43% (0% nano-TiO_2) to 95.85%, 98.43%, and 99.30% respectively because the effects of the nano-TiO_2 were in solution which was effective when exposed to light.

In comparison, the % effective can be calculated from the following equation;

$$\% \text{ effective } = \frac{\text{colony (CFU/ml) at 0\% nano-TiO}_2 \text{ } - \text{colony (CFU/ml) at 0.5\% (w/v) nano-TiO}_2}{\text{colony (CFU/ml) 0\% nano-TiO}_2} \times 100$$

(at 90 minutes)

The antimicrobial activity of the 0.5% (w/v) nano-TiO_2 solution was 93.03% which was more effective than 0% nano-TiO_2 at 90 minutes based on the number of colonies.

The results showed that when increased the nano-TiO_2 in solution, the antimicrobial activity increased. The reduction of colonies was increased because the nano-TiO_2 was exposed to UV light as a catalyst. Hydroxyl radical, hydrogen peroxide, and superoxide anion, were strong oxidizing agents. It could destroy the structure and inhibit the biochemistry of bacteria and virus-infected cells or caused organic compounds to eventually oxidize to carbon dioxide and water (Theerakarun-wong, 2012).

Conclusion:

Gelatin extraction from sea bass scales was yielded 4.02 g or 8.04% gelatin (w/w). The characteristic of gelatin extracted from sea bass scales had the same functional group as commercial gelatin. The physical properties of gelatin film were hard and ductility, difficult to peel the film from the petri dish. Gelatin/nano-TiO_2 blended film had a smooth surface, white color, and opaque. The physical properties were tough and flexible, and the film can be easily removed from the mold. The average film thickness was 0.11 mm. The gelatin/nano-TiO_2 blended film at 0%, 0.1%, 0.3%, and 0.5% concentrations had no difference in thickness that was the control variable in the antimicrobial activity. Spread the sample evenly over the surface of the agar and incubated the plate at 37°C for 24 hours found that when the nano-TiO_2 increased in solution, the antimicrobial activity increased. It confirmed that, the amounts of nano-TiO_2 were directly affected by the Photocatalytic for application.

References:

1. Al-Hassan, A. A., Norziah, M. H. Food Hydrocolloids. 2011;26(1):108-117.
2. Karim, A.A. and Rajeev, B. Food Hydrocolloids. 2009;23:563-576.
3. Muyonga, J.H., Cole, C.G.B., Duodu, K.G. Food Chemistry. 2004;86(3):325-332.
4. Nassiri R., MohammadiNafchi A. Journal of Chemical Health Risks. 2013;3(3): 12 -28.
5. Ran, J., Hu, J., Chen, L., Shen, X., Tong, H. Polymer composites. 2017;38(8):1579-1590.
6. Rhim, J. W., Wu, Y., Weller, C. L., Schnepf, M. Journal of Food Science. 1999;64(1):149-152.
7. Sangrajrang, S., Ploysawang, P., Promhithatron, P. Thai J Toxicology. 2013;28(1), 39-50.
8. Theerakarunwong C., KKU Science Journal. 2012;40:1,049-1058.
9. Tongdeesoontorn, W., Mauer, L. J., Wongruong, S., Sriburi, P., Rachtanapun, P. International Journal of Polymeric Materials and Polymeric Biomaterials. 2012;61(10):778-792.
10. Zaher, K., Kolli, E. M., Riahi, F., Doufnoune, R. International Journal of Polymeric Materials and Polymeric Biomaterials. 2009;58(12):665-680.

DIRECT CARBOXYLATION OF METHANE WITH CARBON DIOXIDE OVER 3d-TRANSITION METALS SUPPORTED ON METAL–ORGANIC FRAMEWORK NU-1000: A DENSITY FUNCTIONAL THEORY STUDY

Ornanong Opasmongkolchai,[1] Keeradara Hiruntrakool,[1] Athittaya Rasrichai,[1] Thana Maihom[1,*]

[1]Department of Chemistry, Faculty of Liberal Arts and Science, Kasetsart University, Kamphaeng Saen Campus, Nakhon Pathom 73140, Thailand

*e-mail: faastnm@ku.ac.th

Abstract:

The catalytic conversion of methane (CH_4) and carbon dioxide (CO_2) to more valuable chemicals via direct C−C coupling is importance from both the environmental and industrial points of view. Herein, the direct carboxylation of CH_4 with CO_2 to acetic acid (CH_3COOH) over 3d-transition metals (Fe, Co, Ni and Cu) supported on metal−organic framework (MOF) NU-1000 has been investigated by means of density functional theory calculations with the M06-L functional. The 6-31G(d,p) basis set is employed for the O, C, and H atoms, while the transition metal atoms are described by the Stuttgart-Dresden effective core potential (SDD). NU-1000 is modelled by a cluster containing one Zr_6 node and the organic linkers 1,3,6,8-tetrakis(p-benzoate)pyrene ($TBAPy^{4-}$) reduced to capping formate groups. For the metals support on the Zr_6 nodes, two protons of the original terminal -OH_2 and -OH groups are substituted by metals in oxidation state +2. The reaction proceeds in three steps. First, the C−H bond of CH_4 is broken to form a methoxide intermediate. After that, the acetate intermediate is formed via C-C bond coupling process, and finally acetate abstracts the proton to form the acetic product. The studied reaction profiles reveals that the activation of the C–H bond is the rate-determining step for the reaction. Among the materials calculated, the Fe-NU-1000 are predicted to have lowest rate-determining step activation energy (29.7 kcal/mol) compared to other. The Fe-NU-1000 might be potential catalysts for the title reaction.

EFFECTS OF THE ZEOLITE FRAMEWORK ON THE ADSORPTION OF GLYPHOSATE ON HAFNIUM-CONTAINING ZEOLITES: A DFT STUDY

Athittaya Rasrichai,[1] Keeradara Hiruntrakool,[1] Ornanong Opasmongkolchai,[1] Thana Maihom[1,*]

[1]Department of Chemistry, Faculty of Liberal Arts and Science, Kasetsart University, Kamphaeng Saen Campus, Nakhon Pathom 73140, Thailand

*e-mail: faastnm@ku.ac.th

Abstract:

The adsorption of glyphosate pesticide on different types of Hf-containing zeolites (BEA, ZSM-5 and FAU) have been investigated with the M06-L method and the 6-31G(d,p) basis set. The zeolites have been modeled with a large quantum cluster to cover their nanocavity. The BEA, ZSM-5 and FAU zeolites are represented by 38T, 34T, and 38T nanocluster models, respectively where T atoms are either Si or Al atoms. A silicon at the position T2, T12, and T2; in BEA, ZSM-5, and FAU, respectively, is substituted by Hf atom. We first consider various possible adsorption configurations of glyphosate on Beta zeolite. The glyphosate prefers to interact on Hf active site of zeolite via its phosphoryl (P=O) group. The adsorption energies are predicted to be −64.2, −61.2, −43.3 kcal/mol for Hf-Beta, Hf-ZSM-5 and Hf-FAU, respectively. The results demonstrate that the medium-pore zeolites (Hf-Beta and Hf-ZSM-5) provide stronger interaction of glyphosate than the large-pore one (HF-FAU) which is mainly due to their higher confinement effect. From our findings, the better understanding of the zeolite framework effect on organophosphates adsorption provides hints to the rational adsorbent design.

ELEMENTAL CONTENT IN ARABICA GREEN COFFEE BEAN FROM NORTHERN THAILAND USING INDUCTIVELY COUPLED PLASMA MASS SPECTROMETRY COMBINED WITH CHEMOMETRICS

Chidchanok Tabtimhin[1], Plaipol Dedvisitsakul [1,2], Kanchana Watla-iad[1,2,3*]

[1]School of Science, Mae Fah Luang University, Chiang Rai, 57100, Thailand

[2]Microbial Products and Innovation Research Unit, School of Science, Mae Fah Luang University, Chiang Rai 57100, Thailand

[3]Center of Chemical Innovation for Sustainability, School of Science, Mae Fah Luang University, Chiang Rai 57100, Thailand

[4]Tea and Coffee Institute of Mae Fah Luang University, Mae Fah Luang University, Chiang Rai 57100, Thailand

*e-mail: Kanchana.wat@mfu.ac.th

Abstract:

Northern Thailand has a wide range of Arabica coffee plantations. But the weather in the north of Thailand is very different in each area. Different climates can affect the quality and chemical composition of coffee beans. The minerals in coffee beans can also reflect their quality. The coffee cherries were collected from four provinces (n=50 samples) for mineral analysis using an inductively coupled plasma mass spectrometry (ICP-MS). The coffee cherries were processed to be coffee green beans, and performed acid wet digestion before analysis. The concentration of studied elements in coffee green beans were various. The element content found in the samples were subsequently evaluated by chemometrics such as principal component analysis (PCA). The 3D score plot between the selected PCs found that coffee green beans tend to group by using the element content. The elements that were important for clustering were Na, Mg, Al, K, Ca, Cr, Mn, Fe, Co, Ni, Cu, Zn, As, Se, Cd, Ba, Tl and Pb. This work is beneficial for further development of quality of coffee green bean by fertilizer adjustment.

THE ANTIOXIDANT ACTIVITY AND THEIR CHEMICAL PROFILE FROM FRUITS OF *Lycium ruthenicum* BY LC-MS/MS

Chalinee Janta,[1,2] Surat Laphookhieo,[1,2] Tawanun Sripisut,[3] Rawiwan Charoensup,[2,4] Tharakorn Maneerat*[1,2]

[1] Center of Chemical Innovation for Sustainability (CIS) and School of Science, Mae Fah Luang University, Chiang Rai 57100, Thailand.

[2] Medicinal Plant Innovation Center (MPIC), Mae Fah Luang University, Chiang Rai 57100, Thailand.

[3] School of Cosmetic Science, Mae Fah Luang University, Chiang Rai 57100, Thailand.

[4] School of Integrative Medicine, Mae Fah Luang University, Chiang Rai 57100, Thailand.

*e-mail: wisanu.man@mfu.ac.th

Abstract:

The fruits of *Lycium ruthenium* are widely used to be functional foods and traditional medicinal herbs worldwide. This study demonstrated promising results for microwave-assisted extraction (MAE) of antioxidative from the fruits of *L. ruthenium*. The separation of *L. ruthenium* extract by C_{18} solid-phase extraction led to give water and ethanol fractions. The chemical composition of ethanol fraction from *L. ruthenium* has been investigated by high-performance liquid chromatography coupled to quadrupole time-of-flight mass spectrometry (HPLC-ESI-QTOF-MS/MS). A total of 32 compounds were identified in fruits and the most detected of 30 compounds of dicaffeoyl spermidines derivatives. Spermidine alkaloids were the most compounds that showed the most potent antioxidant activity in *L. ruthenium* fruits. For antioxidant activities, their ethanol fraction showed the powerful antioxidant in terms of DPPH and ABTS assays.

Introduction:

Microwave-assisted extraction (MAE) is an environmentally friendly technique known as "green extraction". MAE is the technique extraction of natural products by absorption of microwave energy through heating the water or alcohol as a solvent, hence accelerate the solvent dissipation into the material.[1,2] This extraction uses the MAE method because the advantages are more rapid, less solvent, more compact produces, and energy consumption compared to conventional extraction processes.[3,4] This method can extract bioactive compounds, including phenolic, flavonoid, and antioxidant compounds, that have the rich electron-donating ability of crude extract.[5] Therefore, the MAE process has been used to extract antioxidants or bioactive compounds from natural products.

Antioxidants are molecules or compounds that can be inhibitors in oxidation processes.[6] They can protect cells from the damage caused by unstable molecules or free radicals.[7,8] An effect from free radicals can occur in the human body or from outside factors such as exposure to X-rays, ultraviolet light, air pollutants, smoking, alcohol, industrial chemicals, and cooking (burned meat, fried food).[9,10] Free radicals can produce cardiovascular disease, inflammatory disease, diabetes mellitus, neurodegenerative diseases, cancer, cataract, asthma, autism, and rheumatoid arthritis.[10-12] However, many foods or plants contain chemical constituents for eliminating free radical scavenging molecules that have hydroxyl group and a double bond, e.g., phenolic compound (phenolic acid, etc.) nitrogen compounds (alkaloids, amines, etc.) which enhance antioxidants.[12,13]

Plants in the *Lycium* genus, especially *Lycium ruthenicum*, are wildly utilized for medicines and dietary supplements in Southeast Asia, such as in China.[14,15] This plant, known as "black goji berry," belong to the Solanaceae family, a wild perennial thorny shrub.[16] The fruit of this plant was used for traditional medicine in northwestern China to treat hypotension, diabetes, abnormal menstruation, heart disease, and menopause.[16-20] Previously reported the pharmacological activities of goji berries shown immunomodulation, anti-tumor activity, anti-aging, antioxidant, anti-fatigue, anti-cardiovascular disease, and hepatoprotective activity.[19-21] The fruits of *L. ruthenicum* have been found a rich source of polysaccharides, anthocyanins, alkaloids, amides, flavonoids, and organic acid.[20,22] Chemical constituents as the bioactive compound in the Solanaceae family are dicaffeoylspermidine and dicaffeoyl spermine derivative (spermidine alkaloids), a type of alkaloid group acylated hydroxycinnamic acid amides.[20,22,23] These secondary metabolites compounds in plants are connected with caffeoyl group or caffic acid derivative and spermidine or spermine via amide bonds.[24-26] This alkaloid has been outstanding for its antioxidant properties and low toxicity.[22,27] Also, it has been treated for cardiovascular disease such as obesity, dilates, and renal abnormalities.[22]

This study aims to establish chemical profiling of spermidine alkaloids from *L. ruthenicum* by HPLC-ESI-QTOF-MS coupled with MAE and SPE methods, along with their antioxidant properties.

Methodology:

Materials and Reagents

The dried fruits of *L. ruthenicum* were purchased from China. HPLC-grade acetonitrile, 2,2-diphenyl-1-picrylhydrazyl (DPPH), 2,2'-azino-bis(3-ethylbenzothiazoline-6-sulfonic acid) (ABTS), ascorbic acid, and formic acid were purchased from Sigma-Aldrich (St. Louis, MO, USA). SPE cartridge Sep-Pak Vac 35cc C18 10g obtained from Water™ (St. Milford, MA, USA). Water for LC-MS mobile phase was reverse osmosis Milli-Q water (Millipore, USA). Ethanol AR grade was purchased from Merck (Darmstadt, Germany).

Sample Preparation

The dried fruits of *L. ruthenicum* (5.0 g) were grounded and extracted under a microwave-assisted extractor with 50% methanol/water (1:10, w:v). In brief, The program was performed at 1000 W for 5 min, extraction temperature 85 ℃ to give *L. ruthenicum* extract (1.64 g). The solvent was removed under vacuum, and residue afforded a crude extract after freeze-drying. The crude extract was future separated by solid-phase extraction (SPE, 10g C_{18} cartridge, Water™, Milford, MA, USA) in a portion of 5 g dissolved in 2 mL of distilled water. Two fractions were collected in each separation eluent with 200 mL of distilled water and ethanol to obtain F1 (1.4 g) and F2 (190 mg), respectively. The solvents of each fraction were removed under vacuum distillation, and the residues were dissolved in distilled water and freeze-dried. HPLC-ESI-QTOF-MS analysis (1 mg of the sample) was dissolved with methanol and filtered with a 0.22 mm filter membrane.

Chromatographic Conditions

Agilent 1290 Infinity LC instrument (Agilent, USA) coupled to an Agilent 6540 series QTOF-MS (Agilent, USA) equipped with an ESI source, a diode-array detector (DAD), an automatic sample injector, a degasser, and a column Agilent ZORBAX Eclipse XDB column (100 x 2.1 mm i.d.; particle size 1.7 μm; Palo Alto, CA, USA) maintained at 35 ℃ was finally chosen for separation of these extracts. The mobile phase was water (0.1% formic acid, A) mixed with acetonitrile (B) at a 0.2 mL/min flow rate. The elution gradient mode was following: 0-5 min, 5% to 17% B; 5-6 min, 17% B; 6-30 min, 17% to 100% B; 30-35 min, 100% B; 35-40 min, 100% to 5% B; 40-45 min, 5% B. The injection volume was 1.0 μL and samples were set at 4 ℃.

For identification of the compounds, both positive and negative ion modes within the mass/charge (*m/z*) ratio range of 50–1000 at a resolution of 4,000 were used to confirm fragment ions in MS/MS data by energy collision dissociation (HCD, collision energy: 40, 20, 10 eV). The other parameters were as follows: gas temperature 350 ℃, drying gas flow rate 12 L min^{-1}, nebulizer gas pursuer 45 psi, sheath gas temperature 250 ℃, and sheath gas flow rate 12 Arb. Agilent mass Hunter workstation software B.08.00 was used analysis components for LC-MS/MS control and data handling.

Antioxidant Assay

DPPH radical scavenging assay

Free radical scavenging activity of the plant extract was performed according to the methodology modified.[28] The reaction of the DPPH radical scavenging activity was determined by the hydrogen atom donating ability of the extract to react with a solution of 2,2-diphenyl-1-picrylhydrazyl (DPPH). DPPH showed violet purple color in ethanol solution when the presence of antioxidants performed yellow color. A solution of 60 µM DPPH radical solution in ethanol (100 µL) was mixed with 100 µL of extract in ethanol at different concentrations. The reaction was incubated for 30 min at room temperature in the dark, and the absorbance was measured at 517 nm. Ascorbic acid was used as a positive control. The percentage of inhibitory concentration (IC_{50}) of crude extract was calculated by plotting inhibition percentages against the concentrations of extracts. Percentage DPPH radical scavenging activity was calculated as follow:

$$\% \text{ DPPH radical scavenging activity} = [(A_0 - A_1)/A_0] \times 100$$

where A_0 is the absorbance of DPPH radical solution, and A_1 is the absorbance of DPPH radical solution for the extractives/standard. The experiment was done in triplicate.

ABTS radical scavenging assay

The ABTS radical scavenging assay of samples was evaluated by modification.[26] The radical cations were prepared by mix seven mM aqueous ABTS with 2.45 mM potassium persulphate (1:1) in the dark at room temperature for 16-18 h before use. Dilute $ABTS^{\bullet+}$ solution was mixed with distilled water to an absorbance of 0.700 ± 0.020 at 734 nm. The reaction of $ABTS^{\bullet+}$ solution (160 µL) was added to 40 µL of sample in 50% ethanol at different concentrations, and the absorbance was recorded after 5 min at 734 nm. Ascorbic acid was used as a standard substance. The percentage inhibition and IC_{50} were calculated using the formula:

$$\% \text{ ABTS radical scavenging assay} = [(A_0 - A_1)/A_0] \times 100$$

where A_0 is the absorbance of $ABTS^{\bullet+}$ solution, and A_1 is the absorbance of $ABTS^{\bullet+}$ solution for tested samples/standard. All the measurements were performed in triplicates.

Total polysaccharide content

Total polysaccharide content was evaluated according to previous studies.[29] Dissolve solution of sample and glucose was prepared in distilled water. For reaction, 200 µL of 100 ug/mL sample was mixed 200 µL of 5% phenol solution and 1 mL of concentrated H_2SO_4. The absorbance was measured 10 min at 488 nm against a calibration curve with glucose standards (100-10 ug/mL).

Nitric oxide production inhibitory assay

The nitric oxide production inhibitory assay was previously described.[30] RAW 264.7 were seeded at 4 x 10^4 cell/wells in 96-well plates and incubated at 37°C under 5% CO_2 for 24 hr. Then cells were stimulated with 1 µg/mL of LPS for 1 hr and treated with different concentrations of samples for 24 h. After 24 hours, the samples were added 50 µl of Griess reagent for 10 min. The determination of nitric oxide was measured at 570 nm with a microplate reader.

Cell viability assay

The cell viability was used to determine by MTT (3-[4,5-dimethylthiazol-2-yl]-2,5-diphenyl tetrazolium bromide; Millipore Sigma) assay, as previously described.[30]

Statistical Analysis

Significant differences were analyzed using Graph-Pad Prism (GraphPad Software Inc.) by one-way ANOVA. The level of statistical significance was $p<0.05$. Agilent mass Hunter workstation software version B.08.00 (Agilent Technologies, Palo Alto, CA, USA) was used analysis components. Parameters for the program were using compound discovery workflow, molecular feature function, m/z range 50–1000, retention time (RT) range 0.1–2 min, with a minimum absolute abundance of 2000 counts. For identification of the compounds was performed by comparing specific fragments from databases including Mass Hunter PCDL Manager (Version B.08.00), Pubmed, Chemspider, MassBank, and literature data.[19,22,25]

Result and discussion:

The extraction of *L. ruthenicum* fruits was analyzed chemical constituents profile by comparison mass fragment in negative and positive ions. The MS conditions were optimized sensitivity for analysis components that key parameter is collision energies. CID represented an attractive approach for selectively yielding fragment ions. Different collision energies 10, 20 ,40 eV was tested for extraction. Abundant fragmentation ions were generated in the MS/MS spectra when the collision energy was raised to 40 eV. The result in the MS/MS spectra showed that dicaffeoylspermidine derivatives (spermidine alkaloids) were the most detected compounds in positive ion mode. According to the fragment ions and fragmentation analysis, some of the peaks in ethanol fraction (**Figure 1**) were identified as spermidine alkaloids that shown the greatest antioxidant activity. The detailed information of the 32 compounds found in fruits of *L. ruthenicum* is performed in **Table 1**.

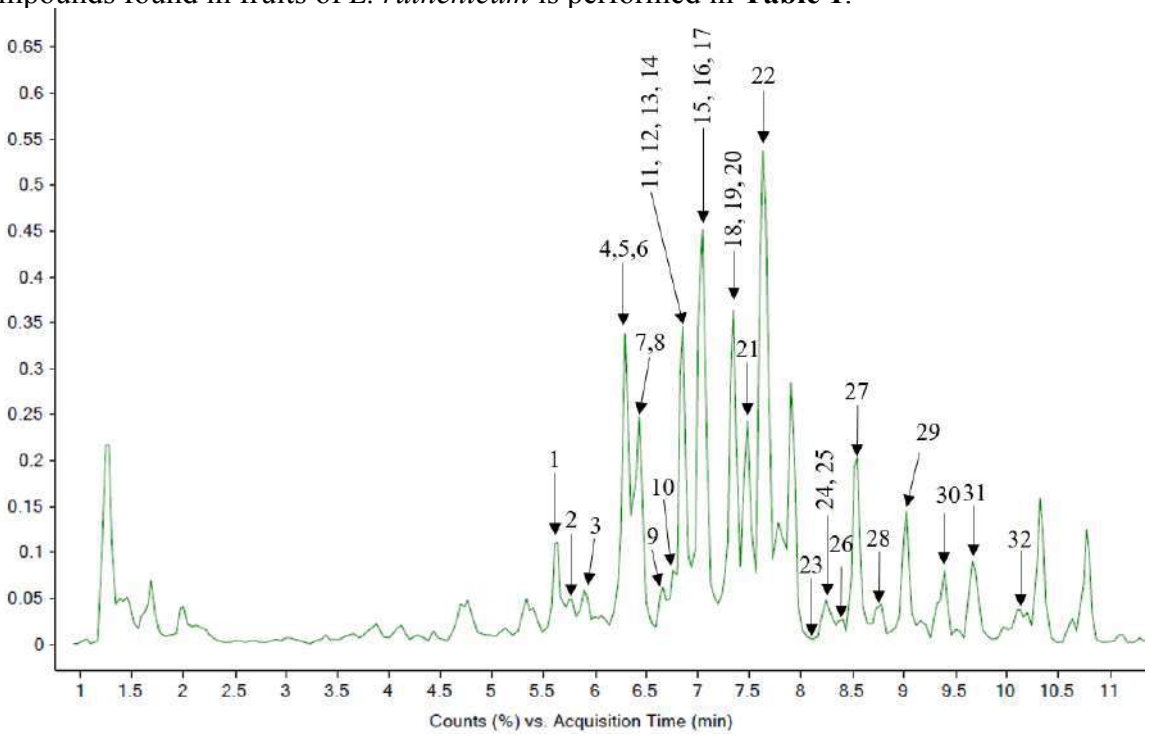

Figure 1. HPLC-ESI-QTOF-MS chromatogram of ethanol fraction from *L. ruthenicum* (positive ion)

Table 1. Compound identification from ethanol fraction of *L. ruthenicum* fruits by HPLC-QTOF-MS/MS (positive ion)

No	RT[1]	Formula	$[M + H]^+$	Mass error	MS/MS fragment ion[3]	Identification[4]
1	5.724	$C_{37}H_{53}O_{16}N_3$	796.3464	1.10	**634.2908**; 472.2582; 310.2221; 220.0947; 163.0371	N^1-caffeoyl-N^3-dhc-spermidine-di-hex
2	5.769	$C_{37}H_{55}O_{16}N_3$	798.3640	0.31	**636.3101**; 474.2568; 384.1652; 236.1263; 222.1131; 100.7360	N^1-N^3-bis-dhc-spermidine-di-hex
3	5.910	$C_{37}H_{53}O_{16}N_3$	796.3507	-0.37	**634.2981**; 472.2686; 384.1626; 310.2120; 293.1858; 234.1111; 222.1093; 163.0380	N^1-caffeoyl-N^3-dhc-spermidine-di-hex
4	6.223	$C_{25}H_{33}O_7N_3$	488.2395	0.35	308.1972; 234.1118; 220.0969; 185.5188; 172.1423; **163.0392**; 72.0811	Dihydrocaffeoyl spermidine derivative
5	6.244	$C_{31}H_{43}O_{11}N_3$	634.2962	-0.17	472.2426; 310.2102; 236.1267; **220.0966**; 163.0388	N^1-caffeoyl-N^3-dhc-spermidine-hex
6	6.325	$C_{31}H_{45}O_{11}N_3$	636.3120	0.77	474.2595; 310.2124; 293.1872; **222.1126**; 165.0550; 123.0430; 100.0752; 72.0808	N^1-N^3-dhc-spermidine-hex
7	6.405	$C_{16}H_{18}O_9$	355.1024	-0.03	**163.0392**; 145.0286; 135.0444; 117.0343	Chlorogenic acid
8	6.430	$C_{31}H_{43}O_{11}N_3$	634.2975	-1.49	474.2620; 310.2123; 293.1919; 236.1254; **222.1111**; 165.0543; 72.0807	N^1-caffeoyl-N^3-dhc-spermidine-hex
9	6.587	$C_{31}H_{39}O_9N_3$	598.2749	0.91	472.2412; 454.2351; 336.1897; 310.2142; 234.1110; **222.1126**; 163.0383	Dihydrocaffeoyl spermidine derivative
10	6.650	$C_{31}H_{43}O_{11}N_3$	634.2972	-0.03	472.2510; 310.2117; 293.1880; 236.1271; **220.0966**; 163.0392; 123.0469	N^1-caffeoyl-N^3-dhc-spermidine-hex
11	6.826	$C_{31}H_{41}O_{11}N_3$	632.2808	0.98	470.2297; 308.1952; 293.1784; 234.1130; **220.0936**; 163.0399	dhc-caffeoyl-cyclic-spermidine-hex
12	6.923	$C_{31}H_{39}O_9N_3$	598.2741	-0.14	472.2412; 455.2176; 310.2093; 23.1122; **222.1118**; 220.0962; 163.0398	Dihydrocaffeoyl spermidine derivative
13	6.930	$C_{31}H_{43}O_{11}N_3$	634.2967	0.07	472.2418; 384.1658; 310.2104; 293.1820; 234.11120; 222.1122; **163.0385**; 145.0281; 72.0807	N^1-caffeoyl-N^3-dhc-spermidine-hex
14	6.970	$C_{24}H_{25}O_7N_{11}$	580.2000	-1.54	455.1494; 293.0994; 275.0982; 231.1096; 147.0473; 129.0543; **126.0549**	Dihydrocaffeoyl spermidine derivative
15	7.033	$C_{25}H_{35}O_6N_3$	474.2564	-0.51	310.2116; 293.1895; 236.1272; **222.1124**; 165.0546; 123.0444; 100.0754; 72.0811	N^1,N^3-bis(dhc)spermidine
16	7.202	$C_{25}H_{35}O_6N_3$	474.2593	1.25	310.2176; 236.1250; **222.1121**; 165.0543;123.0445; 100.0748	N^1,N^3-bis(dhc)spermidine
17	7.249	$C_{15}H_{22}O_3N_4$	307.1768	-0.95	177.0546; 149.0591; **145.0282**; 117.0332	Feruloylagmatine
18	7.355	$C_{31}H_{43}O_{11}N_3$	634.2963	1.27	472.2441; 310.2118; 293.1853; 291.1679; 236.1271; 234.1094; **222.1105**; 220.1105; 163.0249; 123.0413	N^1-caffeoyl-N^3-dhc-spermidine-hex
19	7.434	$C_{26}H_{33}O_3N_{13}$	576.2906	-0.94	522.2633; 414.2371; 397.2071; 331.0507; 265.1436; 236.1205; **162.0912**; 147.0459	Dihydrocaffeoyl spermidine derivative
20	7.465	$C_{25}H_{33}O_6N_3$	472.2442	-0.02	310.2131; 293.1835; 253.1521; 236.1269; 220.0961; **163.0386**; 145.0287; 72.0812	N^1-dhc-N^3-caffeoyl-spermidine
21	7.525	$C_{26}H_{35}O_6N_3$	486.2598	0.30	237.1310; 222.1114; 193.0527;' 165.0540; 147.0452; 124.0460; **123.0432**	Dihydrocaffeoyl spermidine derivative
22	7.639	$C_{25}H_{33}O_6N_3$	472.2443	-0.02	293.1861; 234.1122; **222.1124**; 165.0542; 163.0390; 123.0440; 100.0750; 72.0821	N^1-caffeoyl-N^3-dhc-spermidine
23	8.193	$C_{24}H_{31}ON_3$	518.2848	-0.49	293.1792; **222.1116**; 173.1508; 163.0381; 84.0794; 72.0821	Dihydrocaffeoyl spermidine derivative

No	RT[1]	Formula	$[M + H]^+$	Mass error	MS/MS fragment ion[3]	Identification[4]
24	8.242	$C_{25}H_{31}O_6N_3$	470.2289	-0.70	308.1954; 291.1713; 234.1112; 220.0963; **163.0392**; 145.0280; 72.0813	N^1,N^3-bis(caffeoyl)spermidine
25	8.291	$C_{26}H_{37}O_6N_3$	488.2733	0.29	293.1872; **236.1277**; 222.1133; 179.0701; 165.0548; 137.0593; 123.0436; 100.0753	Dihydrocaffeoyl spermidine derivative
26	8.397	$C_{26}H_{33}O_6N_3$	484.2434	0.09	348.1928; 322.2118; 277.1550; 234.1127; **222.1116**; 163.0386; 84.0805	Dihydrocaffeoyl spermidine derivative
27	8.566	$C_{25}H_{33}O_5N_3$	456.2478	1.05	293.1828; 222.1093; 204.1012; **147.0441**; 119.0506	N^1-dhc-N^{10}-cou-spermidine
28	8.777	$C_{25}H_{33}O_5N_3$	456.2486	-0.35	253.0648; **222.1151**; 165.0671; 147.0449; 123.0495; 100.0741; 84.0804	N^1-dhc-N^{10}-cou-spermidine
29	8.992	$C_{26}H_{35}O_6N_3$	486.2593	0.60	306.0398; 293.1834; 278.0463; 236.1246; 222.1116; **177.0545**; 165.0541; 145.0291; 123.0443	Dihydrocaffeoyl spermidine derivative
30	9.170	$C_{26}H_{35}O_6N_3$	486.2592	1.62	293.1832; 278.0463; 236.1248; 222.1115; **177.0546**; 165.0540; 145.0288	Dihydrocaffeoyl spermidine derivative
31	9.580	$C_{26}H_{35}O_6N_3$	486.2590	1.85	469.2319; 336.1822; 293.1919; **222.1133**; 177.0528; 123.0433	Dihydrocaffeoyl spermidine derivative
32	10.164	$C_{34}H_{46}O_8N_4$	639.3387	0.42	512.2678; 439.2713; 383.1984; 293.1861; 291.1703; 236.1265; **222.1115**; 219.1484; 191.0543; 165.0534; 150.0906; 123.0436	Dihydrocaffeoyl spermidine derivative

[1] RT represent retention time (min)
[2] Mass error (ppm) show chemical formula was determined using a mass difference tolerance of ± 5 ppm
[3] MS/MS fragment show fragmentation ion which the number in **bold** represent the most abundant product ion.
[4]Abbreviations: dhc, dihydrocaffeyl; hex, hexose; cou, *p*-coumaroyl

Compound **2** had the $[M+H]^+$ at *m/z* 798.3640 ($C_{37}H_{55}O_{16}N_3$, cal. 798.3655, mass error 0.31 ppm) and obtained of fragment ion at *m/z* 636.3101, 474.2568, 222.1131 and 100.7360. The ion at *m/z* 636 was observed by the loss hexose unit. The one ion *m/z* 474 is performed after the loss of two glucosyl units. The fragment ion *m/z* 310 and 163 were formed by the cleavage of the caffeoyl unit. The fragment ion *m/z* 310 and 165 were formed by the cleavage of the dihydrocaffeoyl unit. The ion at *m/z* 293 resulted in a loss of the ammonia unit. The ion *m/z* 222 was formed by the cleavage of a rearrangement ion at *m/z* 72. The one ion *m/z* 123 was caused after losing of molecule ion at *m/z* 100 from fragment ion *m/z* 222. So, compound **2** was characterized as N^1-N^3-bis-dihydrocaffeyl-spermidine-di-hexose.

Compound **3** had molecular ion $[M+H]^+$ at *m/z* 796.3507 ($C_{37}H_{53}O_{16}N_3$, cal. 796.3499, mass error -0.37 ppm) and fragment ions at *m/z* 634.2981, 472.2686, 384.1626, 310.2120, 293.1858, 234.1111, 222.1093 and 163.0380. The ion at *m/z* 634 $[M+H-C_6H_{10}O_5]^+$ and *m/z* 472 $[M+H-C_6H_{10}O_5-C_6H_{10}O_5]^+$ were performed by the loss of one and two hexose units, respectively. The fragment ion *m/z* 310 was formed by the cleavage of the caffeoyl unit (163 Da). The ion at *m/z* 293 was detected with loss ammonia unit from the ion at *m/z* 310. The ion at m/z 222 was presented by leaving a rearrangement ion at m/z 72 from molecule ion m/z 293. The ions at m/z 220 and 253 were produced from another pathway after the ion 253 appeared a 234 by the loss of ammonia unit. In the same fragment ion with compound 1. Thus, compounds **1** and **3** were identified as N^1-caffeoyl-N^3-dihydrocaffeyl-spermidine-di-hexose.

Compound **5** had a $[M+H]^+$ at *m/z* 634.2962 ($C_{37}H_{43}O_{11}N_3$, cal. 634.2970, mass error -0.17 ppm) and produced fragment ions at *m/z* 472.2426, 310.2102, 236.1267, 220.0966 and 163.0388. The one ion *m/z* 472 $[M+H-C_6H_{10}O_5-C_6H_{10}O_5]^+$ is performed after the loss of two glucosyls. The fragment ion *m/z* 310 and 163 were resulted from the leave of the caffeoyl unit. The ion at *m/z* 293 was generated of ammonia unit from the ion at *m/z* 310. The ion at *m/z* 222 was produced by leaving a cyclization ion at *m/z* 72 from molecule ion *m/z* 293. The ions at m/z 220 and 253 were observed from another pathway after the ion 253 appeared a 236 by the cleaving of the ammonia unit. Compounds **8**, **10**, **13**, and **18** had the same $[M+H]^+$ at *m/z* 634, and In consequence, these compounds were confirmed to be N^1-caffeoyl-N^3-dihydrocaffeyl-spermidine-hexose.

Compound **6** had a $[M+H]^+$ at *m/z* 636.3120 ($C_{37}H_{45}O_{11}N_3$, cal. 636.3127, mass error 0.77 ppm) and yielded molecule ions at *m/z* 474.2595, 310.2124, 293.1872, 222.1126, 165.0550, 123.0430, 100.0752 and 72.0808. The ion at *m/z* 474 $[M+H-C_6H_{10}O_5]^+$ were detected by the hexose unit from the ion at *m/z* 636. The ion *m/z* 310 appeared after the loss of ion at *m/z* 165. The ion at *m/z* 293 was indicated when losing the ammonia unit from molecule ion at *m/z* 310. The ion at *m/z* 222 was presented by the leaving of a rearrangement ion at *m/z* 72. The fragment ion at *m/z* 123 was generated by losing the substitution rearrangement production ion at *m/z* 100 from the ion at *m/z* 222. Thereby, Compound **6** was assigned as N^1-N^3-dihydrocaffeyl-spermidine-hexose.

Compound **11** had molecular ion $[M+H]^+$ at *m/z* 632.2808 ($C_{37}H_{45}O_{16}N_3$, cal. 632.2893, mass error -0.37 ppm) and seven fragment ions at *m/z* 470.2297, 308.1952, 293.1784, 234.1130; 220.0936, and 163.0399. The ion at *m/z* 470 was formed by the loss of the sugar molecule (162 Da). The fragment ion *m/z* 308 was indicated when loss of caffeoyl unit (163 Da). The ion at *m/z* 293 was detected after the loss ammonia unit from the ion at *m/z* 308. The ion at *m/z* 220 was appeared by the loss of a rearrangement ion at *m/z* 72 from molecule ion *m/z* 291. The ions at m/z 220 and 253 were produced from another pathway after the ion 253 appeared a 234 by the loss of ammonia unit. As a result, compound **11** was determined to be dicaffeoyl-caffeoyl-cyclic-spermidine-hexose.

Compound **15** had molecular ion $[M+H]^+$ at *m/z* 474.2564 ($C_{25}H_{35}O_6N_3$, cal. 474.2599, mass error -0.51 ppm) and obtained of fragment ion at *m/z* 310.2116, 293.1895, 236.1272, 222.1124, 165.0546, 123.0444, 100.0754 and 72.0811. The fragment ion *m/z* 310 and 165 were formed by the cleavage of the dihydrocaffeoyl unit. The ion at *m/z* 293 was generated by the loss of the ammonia unit. The ion at *m/z* 222 was detected when cleavage of a rearrangement ion at *m/z* 72 from molecule ion *m/z* 293. The one ion at *m/z* 123 was produced after losing the substitution cyclization molecule ion at *m/z* 100 from the ion at *m/z* 222. The ions at m/z 220 and 253 occurred from another pathway after the ion 253 presented a 234 by the loss of ammonia unit. Compound **16** had similar $[M+H]^+$ and fragment ions with compound **15**. In this way, compounds **15** and **16** were recognized as N^1,N^3-bis(dicaffeoyl)spermidine.

Compound **20** had a $[M+H]^+$ at *m/z* 472.2442 ($C_{25}H_{33}O_6N_3$, cal. 472.2441, mass error -0.02 ppm) and fragment ions at *m/z* 310.2131, 293.1835, 253.1521, 236.1269, 220.0961, 163.0386, 145.0287 and 72.0812. The ion at *m/z* 310 and 163 was yielded after the loss of the caffeoyl unit from the protonated parent ion. The ion at *m/z* 293 was presented with a loss of ammonia unit from the ion at *m/z* 310. The cleavage of a rearrangement ion caused the ion at m/z 222 and 72 from molecule ion m/z 293. The ions at m/z 220 and 253 were produced from another pathway after the ion 253 appeared a 236 by the loss of ammonia unit. Compound **22** was exhibited a similar fragmentation ion with compound 22. Therefore, Compounds **20** and **22** were proposed to be N^1-dicaffeoyl-N^3-caffeoyl-spermidine.

Compound **24** had molecular ion $[M+H]^+$ at *m/z* 470.2289 ($C_{25}H_{31}O_6N_3$, cal. 470.2283, mass error -0.70 ppm) and produced fragment ions at *m/z* 308.1954, 291.1713, 234.1112, 220.0963, 163.0392, 145.0280 and 72.0813. The fragment ion *m/z* 308 was formed by the cleavage of the caffeoyl unit (163 Da). The ion at *m/z* 291 was observed by the loss ammonia unit from the ion at *m/z* 308. The ion at *m/z* 220 was produced by the loss of a rearrangement ion at *m/z* 72 from molecule ion *m/z* 291. Thus, Compound **24** was suggested as N^1,N^3-bis(caffeoyl)spermidine.

Compound **28** had a $[M+H]^+$ at *m/z* 456.2486 ($C_{25}H_{33}O_6N_3$, cal. 456.2493, mass error -0.35 ppm) and yielded molecule ions at *m/z* 253.0648, 222.1151, 165.0671, 147.0449, 123.0495, 100.0741, 84.0804. The ion at *m/z* 293 appeared after cleavage of the caffeoyl unit (163 Da) from the protonated parent ion. The fragment ion at *m/z* 222 and 123 was indicated by the leaving of rearrangement ion at *m/z* 72 and 100, respectively. From another pathway, the one ion at *m/z* 147 was formed by the loss of a coumaroyl group from the protonated parent ion. In the same manner, compound 27 was showed $[M+H]^+$ similar to compound 28. Hence, Compounds **27** and **28** were presented to be N^1-dicaffeoyl-N^{10}-coumaroyl-spermidine.

In this plant, *L. ruthenicum* can found phenolic amide compounds, which detected fragment ions at *m/z* 177 (feruloyl group), 163 (caffeoyl group), and 147 (coumaroyl group).[26,31] Compound 7 had a $[M+H]^+$ at *m/z* 355.1024 ($C_{16}H_{18}O_9$, cal. 355.1039, mass error -0.03 ppm) and four fragment ions at *m/z* 163.0392, 145.0286, 135.0444 and 117.0343. This compound was identified as Chlorogenic acid. The ion at *m/z* 163 was formed by loss of caffeoyl group from molecule ion. The one ion *m/z* 135 was presented with the leaving of CO (28 Da). The ion at *m/z* 145 and 117 were produced by the loss of a water molecule from the ion at *m/z* 163 and 135, respectively. Compound 17 was confirmed to be feruloylagmatine with $[M+H]^+$ at *m/z* 307.1768 ($C_{15}H_{22}O_3N_4$, cal. 307.1772, mass error -0.95 ppm) and generated fragment ions at *m/z* 177.0546, 149.0591, 145.0282, and 117.0332. The one ion at *m/z* 177 was observed after the loss of the agmatine (130 Da) from the ion at *m/z* 307. The ion at *m/z* 145 and 117 were detected by leaving molecule CH_4O and CO from molecule ion at *m/z* 177 and 145, respectively.[32]

In addition, compound **4**, **9**, **12**, **14**, **19**, **21**, **25**, **26**, **29**, **30**, **32** and **33** were presented to be dicaffeoylspermidine derivative. The dicaffoylspermidine can be performed by abundant fragment ion peak at *m/z* 310/308, 293/291, 222/220, or 165/163.26. The key characteristic for this group of compounds was obtained of fragment ion at *m/z* 222 and 220.[22] Summary, spermidine alkaloids were appeared by fragment ion at *m/z* 310/308 was formed by the cleavage of one caffeoyl unit, 293/291 was detected with loss ammonia unit, 222/220 represented the leaving of a rearrangement ion at *m/z* 72, and 165/163 was formed by further neutral loss of the spermidine unit. The possible fragmentation of dicaffeoylspermidine derivative was proposed in **Figure 2**.

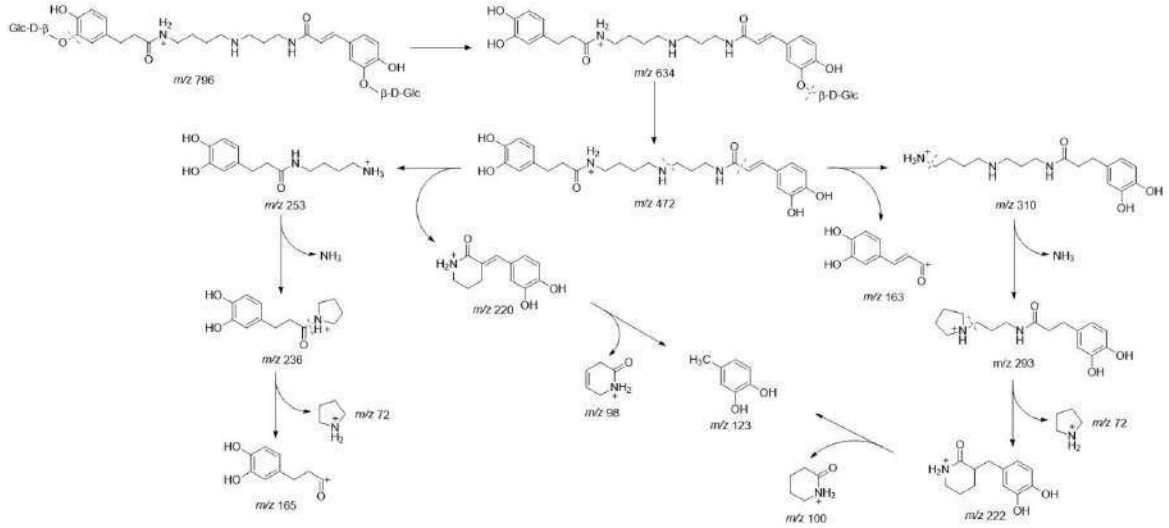

Figure 2. The proposed fragmentation pathway of dicaffeoylspermidine derivatives.

The antioxidant assay showed that ethanol fraction obtained the greatest value of IC_{50} at 2.04 ± 0.02 µg/mL and 4.70 ± 0.28 µg/mL in DPPH and ABTS assay, respectively. Water fraction preformed IC_{50} > 100 µg/mL and 78.37 ± 1.12 µg/mL while ascorbic acid showed 1.53 ± 0.02 µg/mL and 2.92 ± 0.02 µg/mL for DPPH and ABTS assay, respectively (**Table 2**). In addition, the result significant differences in water fraction, which showed low antioxidant properties. From this study was confirmed that the extract which contains a large amount of spermidine alkaloid showed the strongest antioxidant activity.[26]

Table 2. Antioxidant activities of extracts from *L. ruthenicum* fruits

Extracts	DPPH (IC_{50}, µg/mL)[1]	ABTS (IC_{50}, µg/mL)[2]
Crude extract	27.26 ± 1.62	76.01 ± 1.23
Part ethanol	2.04 ± 0.02	4.70 ± 0.28
Part water	> 100	78.37 ± 1.12
Ascorbic acid[3]	1.53 ± 0.02	2.92 ± 0.02

[1] DPPH (IC_{50}) represents the extract concentration scavenging 50% of DPPH radical
[2] ABTS (IC_{50}) represents the extract concentration scavenging 50% of ABTS radical
[3] represent the positive control; Results are expressed as means ± SD, n=3.

Nitric oxide (NO) are a highly reactive free radical however overproduction of NO cause many diseases in pathogenesis.[33,34] In this study, nitric oxide production, the crude extract of *L. ruthenicum* from microwave extraction showed %NO inhibition at 56.50 ± 0.84% (concentration at 200 µg/mL) while fraction part ethanol and water exhibited inactive (%NO inhibition < 50%). The IC_{50} value of crude extract showed 161.4 µg/mL more than the positive control, indomethacin at 34.67 µg/mL (**Table 3**). A previous study of significant

compounds from *L. ruthenicum* is polysaccharides for extract not found in this group.[20,22] Maybe because the column from the analyst cannot separate the mixtures of polysaccharides.[35,36] Therefore, it is necessary to test the quantity of polysaccharides content. Due to, polysaccharide content of crude extract, water, and ethanol fraction was evaluated as 80.63±3.82, 70.42±2.02, and 67.32±1.23 glucose equivalent µg/100µg of the sample, respectively. Moreover, the polysaccharide content of the crude extract was significantly higher than the other fractions. This study confirmed that the polysaccharide-contained extract presented the potential to inhibit the production of nitric oxide.[37,38]

Table 3. Nitric oxide production inhibitory of extracts from *L. ruthenicum* fruits

Samples	Concentration (µg/mL)	% NO inhibition	IC_{50} (µg/mL)	% cell viability
Crude extract	12.5	2.19 ± 0.69	161.4	98.62 ± 0.95
	25	5.74 ± 0.47		97.17 ± 1.21
	50	10.93 ± 1.22		97.10 ± 0.55
	100	28.87 ± 2.98		95.80 ± 1.60
	200	56.50 ± 0.84		95.32 ± 0.96
Indomethacin	6.25	3.95 ± 2.69	34.67	99.61 ± 2.24
	12.5	17.24 ± 3.48		92.66 ± 1.18
	25	38.36 ± 276		88.43 ± 1.30
	50	62.15 ± 3.28		85.36 ± 1.13
	100	96.07 ± 1.83		81.37 ± 0.72

Conclusions:

The fruits of *L. ruthenicum* were extracted by microwave-assisted extraction (MAE) and C_{18} solid-phase extraction for antioxidant compounds. In the study, ethanol fraction was performed as the most potent antioxidant activity in DPPH and ABTS assay. The chemical constituents in this part have been investigated by high-performance liquid chromatography coupled to quadrupole time-of-flight mass spectrometry (HPLC-ESI-QTOF-MS/MS). Dicaffeoyl spermidines derivatives were identified 30 compounds from 32 compounds in ethanol fraction, for the study was to evaluate the physiological activity of *L. ruthenicum* to investigate their potential as a raw material that can be used in the cosmetic industry.

Acknowledgments:

This study has supported the funding of this study by the Research and Researchers for Industries of Thailand Science Research and Innovation (Grant No. MSD60I0134) and Center of Chemical Innovation for Sustainability (CIS) and Office of the Postgraduate Studies, Mae Fah Luang University. We also thank Medicinal Plant Innovation Center (MPIC) for laboratory facilities. We would like to thank Miss. Wanpen Kanthathong for HPLC-ESI-QTOF-MS data.

References:

1. Veggi PC, Martinez J, Meireles MA. Springer, New York. 2013;4:15–28.
2. Duarte K, Justino CIL, Gomes AM, Rocha-Santos T, Duarte AC. Elsvier, The Netherland. 2014;65:59–78.
3. Li Y, Li S, Lin SJ, Zhang JJ, Zhao CN, Li HB. Molecules. 2017;22:1481.
4. Nitthiyah J, Nour AH, Kantasamy R, Akindoyo JO. Aust. J. Basic & Appl. Sci. 2017;11:22-29.
5. Azmir J, Zaidul ISM, Rahman MM, Sharif KM, Mohamed A, Sahena F, Jahurul MHA, Ghafoor K, Norulaini NAN. Omar AKM. J. Food Eng. 2013;117:426-436.
6. Mandal S, Yadav S, Yadav S, Nema RK. J. Chem. Pharm. 2009;1:102-104.

7. Hamid AA, Aiyalaagbe OO, Usman LA, Ameen OM, Lawal A. Afr. J. Pure Appl. Chem. 2010;4:142-151.
8. Salehi B, Martorell M, Arbiser JL, Sureda A, Martind N, Maurya PK, Sharifi-Rad M, Kumar P, Sharifi-Rad J. Biomolecules. 2018;8:124.
9. Lobo V, Patil A, Phatak A, Chandra N. Pharmacogn. Rev. 2010;4:118-127.
10. Phaniendra A, Jeatadi DB, Periyasamy L. 2015. Ind. J. Clin. Biochem. 2015;30:11-26.
11. Lu JM, Lin PH, Yao Q, Chen C. J. Cell. Mol. Med. 2010;14:840-860.
12. Atta EM, Mohamed NH, Abdelgawad AM. Eur. Chem. Bull. 2017;6:365-375.
13. Yadav A, Kumari R, Yadav A, Mishra JP, Srivatva S, Prabha S. Res. Environ. Life Sci. 2016;9:1328-1331.
14. Qian D, Zhao Y, Yang G, Huang L. Molecules. 2017;22:911.
15. Qian D, Chen J, Lai C, Kang L, Xiao S, Song J, Xie J, Huang L. Fitoterpia. 2020;143:104543.
16. Wu T, Lv H, Wang F, Wang Y. J. Agric. Food Chem. 2016;64:2280−2288.
17. Peng Q, Lv X, Xu Q, Li Y, Huang L, Du Y. Carbohydr. Polym. 2012;90:95-101.
18. Tian Z, Aierken A, Pang H, Du S, Feng M, Ma K, Gao S, Bai G, Ma C. J. Liq. Chrom. Relat. Tech. 2016;39:453-458.
19. Yossa Nzewe IB, Xia Y, Qiao Z, Feng F, Bian J, Liu W, Qu W. J. Sep. Sci. 2017;40:1234-1243.
20. Wang H, Li J, Tao W, Zhang X, Gao X, Yong J, Zhao J, Zhang L, Li Y, Duan J. Food Chem. 2018;1:759-766.
21. Hu N, Zheng J, Li W, Suo Y. Sep. Sci. Technol. 2014;49:2897-2906.
22. Ahad H, Jin H, Liu Y, Wang J, Sun G, Liang X, Akber Aisa H. J. Chromatogr. B, 2019;1137:121923.
23. Zhou ZQ, Fan H., He RR. World J. Tradit. Chin. Med. 2016;2:1–5.
24. Zhou ZQ, Fan H-, He R-R, Xiao J, Tsoi B, Lan KH, Kurihara H, So KF, Yao XS, Gao H. J. Agric. Food Chem. 2016;64:2223−2237.
25. Xiang J, Zhang M, Apea-Bah FB, Beta T. Food Chem. 2019;295:214-223.
26. Xiao X, Ren W, Zhang N, Bing T, Liu X, Zhao Z, Shangguan D. Molecules. 2019;24:1585.
27. Madao F, Eisenbery T, Pietrocola F, Kroemer G. Sci. 2018;359.
28. Rahman MM. Islam MB, Biswas M, Khurshid Alam AH. BMC Res. Notes. 2015;8:621.
29. Bhatti M, Kamboj A, Saluja AK. International Journal of Pharmacy and Pharmaceutical Sciences. 2013;5(2):40-41.
30. Raksat A, Maneerat W, Rujanapun N, Raymond J. Andersen Stephen G. Pyne, Laphookhieo S. J. Nat. Prod. 2019;82:2343-2348.
31. Onkokesung N, Gaquerel E, Kotkar H, Kaur H, Baldwin IT, Galis I. 2012. Plant Physiol. 2012;58:389-407.
32. Samulski GB, Gontijo DC, Moreira NC, Brandao GC, Oliveira AB. Biochem. Syst. Ecol., 2020;92:104114.
33. Antosova M, Plevkova J, Strapkova A, Buday T. Open J Mol Integr Physiol. 2012;2:98-106.
34. Peng Q, Liu H, Shi S, Li, M. Int.J. Biol. Macromol. 2014;64:330-335.
35. Guo N, Bai Z, Jia W, Sun J, Wang W, Chen S, Wang H. Molecules. 2019;24:2526.
36. Amicucci MJ, Galermo AG, Guerrero A, Treves G, Nandita E, Kailemia MJ, Higdon SM, Pozzo T, Labavitch JM, Bennett AB, Lebrilla CB. Analytical chemistry. 2019;91:7254-7265.
37. Vazirian M, Dianat S, Manayi A, Ziari R, Mousazadeh A, Habibi E, Saeidnia S, Amanzadeh Y. Research Journal of Pharmacognosy. 2014;1:13-19.
38. Minzanova ST, Mironov VF, Arkhipova DM, Khabibullina AV, Mironova LG, Zakirova YM, Milyukov VA. Polymers. 2018;14:1407.

MOLECULAR DOCKING INVESTIGATION TOWARDS GELDANAMYCIN ANALOGUES FOR HSP90 TARGETED ANTI-CANCER DRUG THERAPY

Satipat Suttayasorranakhom,[1] Chanjira Jaramornburapong,[2] Waya Phuthawong,[1] and Jitnapa Sirirak[1,*]
[1]Department of Chemistry, Faculty of Science, Silpakorn University, Nakhon Pathom, Thailand 73000
[2]Program of Chemistry, Faculty of Science and Technology Nakhon Pathom Rajabhat University, Nakhon Pathom, Thailand 73000
*e-mail: sirirak_j@su.ac.th

Abstract:
Cancer, a silent threat that most people do not expect, is a vital issue that has received increasing attention worldwide. To design anti-cancer drug, heat shock protein 90 (Hsp90) is one of the promising targets. Hsp90 is a chaperone protein responsible for the folding, stability, and activity of the oncoproteins that promote proliferation and survival of cancer. Herein, novel geldanamycin derivatives, **P1-P5** were designed as potential Hsp90 cancer drug by against oncogenic client protein. The binding of **P1-P5** in the cavity of Hsp90 were investigated by molecular docking using the iGEMDOCK v2.1 software. The results illustrated that **P1-P5** bound in the binding site of Hsp90 with similar manner to geldanamycin. The binding energies of **P1-P5** in Hsp90 (-155.08 to -120.67 kcal/mol) were comparable to that of geldanamycin (-133.06 kcal/mol). **P1-P5** interacted well by hydrogen bonding with key amino acids including Lys112 and Phe138 in the binding site of Hsp90. Additionally, **P1-P5** formed hydrogen bonding with other new amino acids including Asp54, Asn106, Gly132, and Gly137, which could inhibit the cancer cell. Additionally, experimental results reviewed that **P5** had potent cytotoxic effects on human breast cancer cells (HeLa) (IC_{50a}=52.76 µg/mL) with low cytotoxicity against Vero cells (IC_{50a}=220 µg/mL). Therefore, **P1-P5** could be a guide for future anti-cancer drug molecular design with Hsp90.

RIVER SNAIL SHELL AS HIGHLY EFFECTIVE RENEWABLE HETEROGENEOUS BASE CATALYST FOR BIODIESEL PRODUCTION

Achanai Buasri,[1,*] Supapisit Kooljaruswech,[1] Supapiwat Maneenil,[1] Surajit Duangjit,[1] Vorrada Loryuenyong[1]
[1]Department of Materials Science and Engineering, Faculty of Engineering and Industrial Technology, Silpakorn University, Nakhon Pathom, 73000, Thailand
*e-mail: achanai130@gmail.com

Abstract:
Biodiesel production process encourages use of heterogeneous catalyst over homogeneous catalysts. The major problems associated with the use of homogeneous catalysts are its non-renewable nature, separation and washing which can be overcome by the use of heterogeneous catalysts. This study is focused on the investigation of river snail (*Viviparidae*) shell improved with modified activated carbon (MAC) as heterogeneous solid base catalyst for transesterification of palm oil. The waste shell was repeatedly washed to remove any organic impurities attached to it and then dried in an oven. It was calcined at a high temperature of 900 °C for 2 h in an air atmosphere. The calcined sample (calcium oxide: CaO) was obtained as white powder and mixed with MAC. The calcium oxide (CaO)/MAC catalyst was characterized by X-ray diffraction (XRD), scanning electron microscopy (SEM) and Brunauer-Emmet-Teller (BET) method. The operating parameters such as methanol to oil mole ratio, amount of catalyst, reaction time and microwave electrical power were investigated in order to optimize the reaction condition for the biodiesel production. As a result, the optimum reaction parameters found were 12:1 methanol to oil mole ratio, 2.5 wt.% of the CaO/MAC, 4 min of reaction time and microwave electrical power at 600 watt. After further reused for 5 times, the yield of biodiesel could still reach 90%, which indicated that the novel catalyst had a good stability and recyclability. The fuel properties of biodiesel obtained in this work were compared with the biodiesel international standards ASTM D6751 and EN14214. River snail shell can be considered as a nature based benign and resourceful material for the biodiesel production providing a new route for sustainability of fuels.

AUTHOR INDEX

INTERNATIONAL ADVISORY BOARD

Prof. Dr. Michael Kramer

Germany

Prof. Howard Alper

Canada

Prof. Javier García Martínez

Spain

Prof. Dr. Daniel Solow

USA

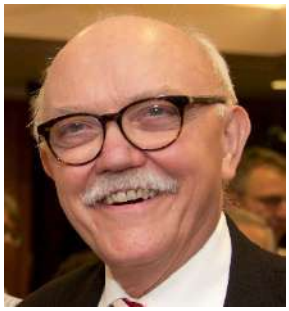

Dr. Peter Gölitz

Germany

Dr. Eva E. Wille

Germany

LOCAL ADVISORY BOARD

Prof. Dr. Supawan Tantayanon

Prof. Dr. Supa Hannongbua

Prof. Dr. Supachitra Chadchawan

Assoc. Prof. Dr. Utomporn Phalavonk

Assoc. Prof. Boonrucksar Soonthornthum

Asst. Prof. Dr. Anamai Damnet

Asst. Prof. Dr. Rajit Vadhanasindhu, Honorary Doctorate Degree

COMMITTEES

SCIENTIFIC COMMITTEE

1. Prof. Dr. Chanpen Chanchao (Thailand)
2. Prof. Dr. Gang Meng (China)
3. Prof. Dr. Nongnuj Muangsin (Thailand)
4. Prof. Dr. Orawon Chailapakul (Thailand)
5. Prof. Dr. Suchana Chavanich (Thailand)
6. Prof. Dr. Takeshi Yanagida (Japan)
7. Prof. Dr. Takiumi Konno (Japan)
8. Prof. Dr. Suttichai Assabumrungrat (Thailand)
9. Prof. Dr. Vudhichai Parasuk (Thailand)
10. Prof. Joseph S.M. Samec (Sweden)
11. Prof. Patrick Cognet (France)
12. Prof. Zuriati Zakaria (Malaysia)
13. Assoc. Prof. Dr. Anucha Watcharapasorn (Thailand)
14. Assoc. Prof. Dr. Chaleeda Borompichaichartkul (Thailand)
15. Assoc. Prof. Dr. Chartchai Leenawong (Thailand)
16. Assoc. Prof. Dr. Kazuki Nagashima (Japan)
17. Assoc. Prof. Dr. Nuttha Thongchul (Thailand)
18. Assoc. Prof. Dr. Taeng On Prommi (Thailand)
19. Assoc. Prof. Dr. Thamasak Yeemin (Thailand)
20. Assoc. Prof. Roderick Bates (Singapore)
21. Asst. Prof. Dr. Noppadon Kitana (Thailand)
22. Asst. Prof. Dr. Oraphan Sungkajanttranon (Thailand)
23. Dr. Chainarong Srirak (Thailand)
24. Dr. Ganigar Chen (Thailand)
25. Dr. Mati Horprathum (Thailand)
26. Dr. Rakhi Majumda (India)
27. Dr. Sumate Chareonchaidet (Thailand)
28. Dr. Suparerk Aukkaravittayapun (Thailand)
29. Dr. Verawat Champreeda (Thailand)
30. Dr. Worajit Setthapun (Thailand)
31. Miss Kanchana Un-Arom (Thailand)

ORGANIZING COMMITTEE

The Science Society of Thailand Under the Patronage of His Majesty the King

1.	Prof. Dr.	Somkiat Ngamprasertsith (Chairman)
2.	Assoc. Prof. Dr.	Benjapon Chalermsinsuwan (Secretary)
3.	Assoc. Prof. Dr.	Boonchoat Paosawatyanyong
4.	Assoc. Prof. Dr.	Onruthai Pinyakong
5.	Assoc. Prof. Dr.	Rajalida Lipikorn
6.	Assoc. Prof. Dr.	Saiwarun Chaiwanichsiri
7.	Assoc. Prof. Dr.	Tipaporn Limpaseni
8.	Dr.	Mati Horprathum
9.	Dr.	Ratchanon Piemjaiswang

Kasetsart University, Kamphaeng Saen Campus

9.	Assoc. Prof. Dr.	Saiwarun Chaiwanichsiri
10.	Assoc. Prof. Dr.	Taeng On Prommi
11.	Assoc. Prof. Dr.	Sakauwrat Jongpattanakorn
12.	Assoc. Prof. Dr.	Auttasit Tubtimtae
13.	Assoc. Prof. Dr.	Pongrawee Nimnoi
14.	Asst. Prof. Dr.	Weeranut Kaewwiset
15.	Asst. Prof. Dr.	Piyapong Laosrirattanachai
16.	Asst. Prof. Dr.	Potjaman Poolmee
17.	Asst. Prof. Dr.	Piched Anuragudom
18.	Asst. Prof. Dr.	Veeramol Vailikhit
19.	Asst. Prof. Dr.	Tissawas Thumrongsanta
20.	Asst. Prof. Dr.	Eakachai Suntonsinsoungvon
21.	Asst. Prof. Dr.	Pornpairin Rungcharoenthong
22.	Asst. Prof. Dr.	Sucheewan Krobthong
23.	Asst. Prof. Dr.	Jintanart Wongchawalit
24.	Asst. Prof. Dr.	Wisut Jarunthawatchai
25.	Asst. Prof. Dr.	Attapol Khamkhien
26.	Asst. Prof. Dr.	Suntree Sangjan
27.	Asst. Prof. Dr.	Aree Innun
28.	Asst. Prof. Dr.	Bundet Boekfa
29.	Asst. Prof. Dr.	Busara Pattanasiri
30.	Asst. Prof. Dr.	Siraprapha Premcharoen
31.	Asst. Prof. Dr.	Rudeerat Suntako
32.	Asst. Prof. Dr.	Pharima Phiriyangkul
33.	Asst. Prof.	Wuttipong sillapavisa
34.	Asst. Prof.	Patchara Jaturakomol
35.	Dr.	Danupon Sangnak
36.	Dr.	Aunchistha Poo-Udom
37.	Dr.	Arm Unartngam
38.	Dr.	Varangkana Jitchum
39.	Dr.	Tipawan Rungsawang
40.	Dr.	Thana Maihom
41.	Dr.	Adisorn Chaibang

42.	Dr.	Pemikar Srifa
43.	Dr.	Chananyoo Tintabura
44.	Mr.	Krit Leangphan
45.	Mr.	Sasin Tiendee
46.	Mr.	Jakkapan Boonwong
47.	Mr.	Chalermchai Aueviriyavit
48.	Mr.	Khwanchai Suksomboon
49.	Mr.	Ratchapad Chuangrangsee
50.	Mr.	Teerapong tippanthong
51.	Mr.	Prab Sathong-on
52.	Mr.	Pongpisit Amonpongpaisan
53.	Mr.	Suthawee Kryangan
54.	Mr.	Suchart Pornnapalai
55.	Mr.	Werapon Buntham
56.	Mr.	Jeerasak Thongdonkuang
57.	Mr.	Sataporn Chaisomparn
58.	Mr.	Punyarit Yasri
59.	Miss	Umaporn Boonphetkaew
60.	Miss	Pimtham Uafua
61.	Miss	Chudaporn Sonpakdee
62.	Miss	Wilai Jangboon
63.	Miss	Jongjit Nuchjareon
64.	Miss	Pornpun Laosomboon
65.	Miss	Kingdao Sudoke
66.	Miss	Weerada Thanapongthram
67.	Miss	Nattida Rungsri
68.	Miss	Supawan Laohasukpaisan
69.	Miss	Rungsiya Tongphud
70.	Miss	Tapanat Tanthanakit
71.	Miss	Siriwan Daothong
72.	Miss	Thanita Chaisuwan
73.	Miss	Kannika Pantean
74.	Miss	Wilawan Pliankham
75.	Miss	Sathita Chingthongkam
76.	Miss	Ruttanavadee Sawsawun
77.	Miss	Pojjanee Thongkhonghan
78.	Miss	Atikan Thirasinp
79.	Miss	Wassana Sam-ai
80.	Miss	Duangporn Chuwong
81.	Miss	Wilaiwan Nuchtongmuang
82.	Miss	Netnapa Pumhan
83.	Miss	Somying Thongyod
84.	Miss	Wipawan Roungsri
85.	Miss	Siraporn Meejumrus
86.	Miss	Nantawan Jaiyen
87.	Miss	Atitaya Sripranthong

88.	Miss	Kunniga Sukeewong
89.	Miss	Jitima Suangamiem
90.	Miss	Arisara Khunphithuk
91.	Miss	Wichuda Poonoi
92.	Miss	Orasa Satongkeaw
93.	Mrs	Wasana Hatthakij
94.	Mrs	Chanaporn Singtothong

REVIEWER COMMITTEE

1.	Prof. Dr.	Bunjerd Jongsomjit
2.	Prof. Dr.	David Ruffolo
3.	Prof. Dr.	Nongnuj Muangsin
4.	Prof. Dr.	Sirilux Poompradub
5.	Prof. Dr.	Sujittra Youngme
6.	Prof. Dr.	Supon Ananta
7.	Assoc. Prof. Dr.	Anchalee Samphao
8.	Assoc. Prof. Dr.	Aniruth Phon-On
9.	Assoc. Prof. Dr.	Anucha Watcharapasorn
10.	Assoc. Prof. Dr.	Apinpus Rujiwatra
11.	Assoc. Prof. Dr.	Arthit Intarasit
12.	Assoc. Prof. Dr.	Chartchai Leenawong
13.	Assoc. Prof. Dr.	Cheewarat Printrakoon
14.	Assoc. Prof. Dr.	Cheunjit Prakitchaiwattana
15.	Assoc. Prof. Dr.	Christopher Smith
16.	Assoc. Prof. Dr.	David J. Harding
17.	Assoc. Prof. Dr.	David James Harding
18.	Assoc. Prof. Dr.	Duangkamol Gleeson
19.	Assoc. Prof. Dr.	Gina B. Alcoriza
20.	Assoc. Prof. Dr.	Jonggol Tantirungrotechai
21.	Assoc. Prof. Dr.	Kuakarun Krusong
22.	Assoc. Prof. Dr.	Luckhana Lawtrakul
23.	Assoc. Prof. Dr.	Nooduan Muangsan
24.	Assoc. Prof. Dr.	Nuttha Thongchul
25.	Assoc. Prof. Dr.	Orawan Duangphakdee
26.	Assoc. Prof. Dr.	Pattaraporn Kim
27.	Assoc. Prof. Dr.	Pongtharin Lotrakul
28.	Assoc. Prof. Dr.	Poonpat Poonnoy
29.	Assoc. Prof. Dr.	Rojana Pornprasertsuk
30.	Assoc. Prof. Dr.	Sirichok Jungthawan
31.	Assoc. Prof. Dr.	Soorathep Kheawhom
32.	Assoc. Prof. Dr.	Supavadee Kiatisevi
33.	Assoc. Prof. Dr.	Suwattana Pruksasri
34.	Assoc. Prof. Dr.	Suwimol Wongsakulphasatch
35.	Assoc. Prof. Dr.	Taeng On Prommi
36.	Assoc. Prof. Dr.	Tawatchai Tanee
37.	Assoc. Prof. Dr.	Taweetham Limpanuparb
38.	Assoc. Prof. Dr.	Vudhichai Parasuk
39.	Asst. Prof. Dr.	Akekawat Vitheepradit
40.	Asst. Prof. Dr.	Amara Apilux
41.	Asst. Prof. Dr.	Amporn Wiwegweaw
42.	Asst. Prof. Dr.	Anukorn Boutson
43.	Asst. Prof. Dr.	Atipong Bootchanont

44.	Asst. Prof. Dr.	Atsalek Rattanawannee
45.	Asst. Prof. Dr.	Chan Inntam
46.	Asst. Prof. Dr.	Chitiphon Chuaicham
47.	Asst. Prof. Dr.	Chutima Jiarpinitnun
48.	Asst. Prof. Dr.	Dumrongkiet Arthan
49.	Asst. Prof. Dr.	Ekachai Chukeatirote
50.	Asst. Prof. Dr.	Inthawoot Suppavorasatit
51.	Asst. Prof. Dr.	Jarin Kanchanawarin
52.	Asst. Prof. Dr.	Jaursup Boonmak
53.	Asst. Prof. Dr.	Kamontip Kuttiyawong
54.	Asst. Prof. Dr.	Kanchana Uraisin
55.	Asst. Prof. Dr.	Kanogwan Seraypheap
56.	Asst. Prof. Dr.	Kheamrutai Thamaphat
57.	Asst. Prof. Dr.	Kittipong Chainok
58.	Asst. Prof. Dr.	Kom Campiranon
59.	Asst. Prof. Dr.	Muhammad Kashif
60.	Asst. Prof. Dr.	Nanthawat Wannarit
61.	Asst. Prof. Dr.	Narit Triamnak
62.	Asst. Prof. Dr.	Narupon Chattrapiban
63.	Asst. Prof. Dr.	Olarik Surinta
64.	Asst. Prof. Dr.	Orawan Chunhachart
65.	Asst. Prof. Dr.	Parsiri Khetpiyarat
66.	Asst. Prof. Dr.	Pawana Kangtia
67.	Asst. Prof. Dr.	Pongchai Dumrongrojwatthana
68.	Asst. Prof. Dr.	Pongsathorn Dechatiwongse Na Ayuthaya
69.	Asst. Prof. Dr.	Prasit Pattananuwat
70.	Asst. Prof. Dr.	Rakrudee Sarnthima
71.	Asst. Prof. Dr.	Sahanat Petchsri
72.	Asst. Prof. Dr.	Saisamorn Lumlong
73.	Asst. Prof. Dr.	Saowanit Saithong
74.	Asst. Prof. Dr.	Saranyu Khammuang
75.	Asst. Prof. Dr.	Sasipohn Prasertpalichat
76.	Asst. Prof. Dr.	Sirima Puangpraphant
77.	Asst. Prof. Dr.	Siriporn Sripinyowanich
78.	Asst. Prof. Dr.	Sittiporn Pattaradirokrat
79.	Asst. Prof. Dr.	Somjintana Taveepanich
80.	Asst. Prof. Dr.	Suchai Worachananant
81.	Asst. Prof. Dr.	Sujin Suwanna
82.	Asst. Prof. Dr.	Supakorn Boonyuen
83.	Asst. Prof. Dr.	Supareak Praserthdam
84.	Asst. Prof. Dr.	Supranee Phanthanawiboon
85.	Asst. Prof. Dr.	Suwicha Wannawichian
86.	Asst. Prof. Dr.	Thanachan Mahawanich
87.	Asst. Prof. Dr.	Theeranan Tanphanich
88.	Asst. Prof. Dr.	Tipwan Sappasat
89.	Asst. Prof. Dr.	Walailuck Chavanasporn

90.	Asst. Prof. Dr.	Warut Pannakkong
91.	Dr.	Abdulhadee yakoh
92.	Dr.	Adisorn Chaibang
93.	Dr.	Akawat Sirisuk
94.	Dr.	Anchalee Chankong
95.	Dr.	Assadawoot Srikhaow
96.	Dr.	Bongkot Witchachucherd
97.	Dr.	Ganigar Chen
98.	Dr.	Jurin Kanarat
99.	Dr.	Jutamas Kaewsuk
100.	Dr.	Khomson Suttisintong
101.	Dr.	Kitiyanee Asanok
102.	Dr.	Krieng Kanchanawatee
103.	Dr.	Laddawan Sangsawang
104.	Dr.	Mati Horprathum
105.	Dr.	Nipapan Ruecha
106.	Dr.	Nithiwadee Thaicharoen
107.	Dr.	Nontivich Tandavanitj
108.	Dr.	Nopporn Thasana
109.	Dr.	Nut Songvoravit
110.	Dr.	Nuttachai Jutong
111.	Dr.	Nuttapong Sanglerdsinlapachai
112.	Dr.	Panupong Thammachoti
113.	Dr.	Pimonpan Sompet
114.	Dr.	Piyachat Lilasilpzard
115.	Dr.	Punnarai Siricharoen
116.	Dr.	Rongrong Cheacharoen
117.	Dr.	Rungroj jintamethasawat
118.	Dr.	Sanit Piyapattanakorn
119.	Dr.	Sarawut Siriwong
120.	Dr.	Siwaruk Siwamogsatham
121.	Dr.	Suchana Chavanich
122.	Dr.	Sudkate Chaiyo
123.	Dr.	Suebpong Sa-nguansil
124.	Dr.	Supawadee Wichitchan
125.	Dr.	Thanakorn Prinyasart
126.	Dr.	Threeraphat Chutimasakul
127.	Dr.	Tossaporn Lertvanithphol
128.	Dr.	Uraiwan Waiwijit
129.	Dr.	Voranop Viyakarn
130.	Dr.	Watcharawuth Krittinatham
131.	Dr.	Witchaya Rattanametawee
132.	Dr.	Wittawin Susutti
133.	Mr.	Manasit Sarigaphuti

STT47 SPONSORS ACKNOWLEDGEMENT

PLATINUM

Bangkok Bank

SILVER

DOW

SCG

Siam Photon

NARIT

สกสว

สมาคมวิทยาศาสตร์แห่งประเทศไทยในพระบรมราชูปถัมภ์
https://www.scisoc.or.th/